



AFRL-RZ-ED-TR-2012-0031

Dynamics of Supercritical Flows

Bruce Chehroudi
Dustin Davis
Jeffrey Graham
Ann Karagozian

Ivett Leyva
Juan Rodriguez
Douglas Talley
Sophonias Teshome

Air Force Research Laboratory (AFMC)
AFRL/RQRC
10 E. Saturn Blvd
Edwards AFB CA 93524-7680

26 August 2012

In-House Final Report

Distribution A: To be approved for Public Release; distribution unlimited. PA No. 12789

**AIR FORCE RESEARCH LABORATORY
AEROSPACE SYSTEMS DIRECTORATE**

■ Air Force Materiel Command ■ United States Air Force ■ Edwards Air Force Base, CA 93524

- STINFO COPY -
NOTICE AND SIGNATURE PAGE

Using Government drawings, specifications, or other data included in this document for any purpose other than Government procurement does not in any way obligate the U.S. Government. The fact that the Government formulated or supplied the drawings, specifications, or other data does not license the holder or any other person or corporation; or convey any rights or permission to manufacture, use, or sell any patented invention that may relate to them.

Qualified requestors may obtain copies of this report from the Defense Technical Information Center (DTIC) (<http://www.dtic.mil>).

AFRL-RZ-ED-TR-2012-0031 HAS BEEN REVIEWED AND IS APPROVED FOR PUBLICATION IN ACCORDANCE WITH ASSIGNED DISTRIBUTION STATEMENT.

FOR THE DIRECTOR:

//SIGNED//

DOUGLAS G. TALLEY, Ph.D.
Project Manager

//SIGNED//

QUOC V. VO, Capt, USAF
Acting Chief, Combustion Devices Branch

//SIGNED//

LaDONNA J. DAVIS, LtCol, USAF
Deputy Chief – Senior Technical Advisor
Rocket Propulsion Division

This report is published in the interest of scientific and technical information exchange, and its publication does not constitute the Government's approval or disapproval of its ideas or findings.

REPORT DOCUMENTATION PAGE				Form Approved OMB No. 0704-0188	
<p>Public reporting burden for this collection of information is estimated to average 1 hour per response, including the time for reviewing instructions, searching existing data sources, gathering and maintaining the data needed, and completing and reviewing this collection of information. Send comments regarding this burden estimate or any other aspect of this collection of information, including suggestions for reducing this burden to Department of Defense, Washington Headquarters Services, Directorate for Information Operations and Reports (0704-0188), 1215 Jefferson Davis Highway, Suite 1204, Arlington, VA 22202-4302. Respondents should be aware that notwithstanding any other provision of law, no person shall be subject to any penalty for failing to comply with a collection of information if it does not display a currently valid OMB control number. PLEASE DO NOT RETURN YOUR FORM TO THE ABOVE ADDRESS.</p>					
1. REPORT DATE (DD-MM-YYYY) 26 August 2012		2. REPORT TYPE In-house Final Report		3. DATES COVERED (From - To) 27 Sep 2004 – 28 May 2012	
4. TITLE AND SUBTITLE Dynamics of Supercritical Flows				5a. CONTRACT NUMBER	
				5b. GRANT NUMBER	
				5c. PROGRAM ELEMENT NUMBER 61102F	
6. AUTHOR(S) Chehroudi, Bruce; Davis, Dustin; Graham, Jeffrey; Karagozian, Ann; Leyva, Ivett; Rodriguez, Juan; Talley, Douglas; Teshome, Sophonias				5d. PROJECT NUMBER	
				5e. TASK NUMBER	
				5f. WORK UNIT NUMBER 23080533 / Q0AY	
7. PERFORMING ORGANIZATION NAME(S) AND ADDRESS(ES) Air Force Research Laboratory (AFMC) AFRL/RQRC 10 E. Saturn Blvd Edwards AFB CA 93524-7680				8. PERFORMING ORGANIZATION REPORT NO.	
9. SPONSORING / MONITORING AGENCY NAME(S) AND ADDRESS(ES) Air Force Research Laboratory (AFMC) AFRL/RQR 5 Pollux Drive Edwards AFB CA 93524-7048				10. SPONSOR/MONITOR'S ACRONYM(S)	
				11. SPONSOR/MONITOR'S REPORT NUMBER(S) AFRL-RZ-ED-TR-2012-0031	
12. DISTRIBUTION / AVAILABILITY STATEMENT Approved for public release; distribution unlimited. PA No. 12789					
13. SUPPLEMENTARY NOTES					
14. ABSTRACT This research has concentrated on the characterization of mixing for typical liquid rocket injectors. The conditions of interest have encompassed subcritical to supercritical pressures with temperatures below and above the critical temperature, with and without an acoustic field. The project has been largely experimental in-house. A single shear coaxial injector element has been thoroughly studied. This type of injector element is commonly used in many rocket engines (e.g., Space Shuttle Main Engine (SSME), Vulcain, RS-68, etc). It was found that the mixing in these injectors is governed primarily by the presence or absence of an acoustic field, the outer to inner jet area ratio and the inner jet lip thickness to inner jet diameter, the outer to inner momentum flux ratio, the reduced density of the inner jet, and on whether the pressure is subcritical and supercritical.					
15. SUBJECT TERMS cold-flow effects, combustion instabilities, fundamental fluid, mechanics liquid rocket injectors, subcritical pressure, supercritical pressure, shear coaxial injector					
16. SECURITY CLASSIFICATION OF:			17. LIMITATION OF ABSTRACT	18. NUMBER OF PAGES	19a. NAME OF RESPONSIBLE PERSON Douglas Talley
a. REPORT Unclassified	b. ABSTRACT Unclassified	c. THIS PAGE Unclassified			19b. TELEPHONE NO (include area code) 661 275-6174

TABLE OF CONTENTS

Section	Page
LIST OF ABBREVIATIONS.....	iii
ABSTRACT.....	iv
1.0 EXECUTIVE SUMMARY	1
2.0 ACKNOWLEDGEMENTS.....	4
3.0 REFERENCES	4
APPENDIX A—COPIES OF REFERENCES	A-1
1. Measurements in an Acoustically Driven Coaxial Jet under Supercritical Conditions	A-2
2. Experiments on a Coaxial Injector under an Externally Forced Transverse Acoustic Field	A-31
3. Shear-Coaxial Jets from a Rocket-Like Injector in a Transverse Acoustic Field at High Pressures	A-51
4. A Rocket-Like Coaxial Injector In An Acoustic Field Under Sub-and Supercritical Conditions	A-69
5. Behavior of a Rocket-Like Coaxial Injector in an Acoustic Field.....	A-77
6. <i>On the Behavior of a Shear-Coaxial Jet, Spanning Sub- to Supercritical Pressures, With and Without an Externally Imposed Transverse Acoustic Field</i> , Ph.D. Thesis.....	A-89
7. Measurements in an Acoustically-Driven Coaxial Jet under Sub-, Near-, and Supercritical Conditions	A-351
8. Dark core analysis of coaxial injectors at sub-, near-, and supercritical conditions in a transverse acoustic field.....	A-362
9. Dark core analysis of coaxial injectors at sub-, near-, and supercritical pressures in a transverse acoustic field.....	A-373
10. Preliminary Results on Coaxial Jet Spread Angles and the Effects of Variable Phase Transverse Acoustic Fields	A-391
11. Effects of a Variable-Phase Transverse Acoustic Field on a Coaxial Injector at Subcritical and Near-Critical Conditions	A-406
12. Results on Subcritical One-Phase Coaxial Jet Spread Angles and Subcritical to Supercritical Acoustically Forced Coaxial Jet Dark Core Lengths.....	A-417
13. Effect of Phase Angle on Coaxial Jet Behavior Spanning Sub- to Supercritical Pressures	A-429
14. On the Inner Jet Spread Angles of Coaxial Jets from Subcritical to Supercritical Conditions with Preliminary Numerical Results	A-437

15. <i>Acoustic Excitation of Liquid Fuel Droplets and Coaxial Jets</i> , Ph.D. Dissertation	A-456
16. On the Effect of a Transverse Acoustic Field on a Flush Shear Coaxial Injector	A-732
17. Mixing Enhancement of Liquid Rocket Engine Injector Flow	A-745
18. Effect of Phase Angle of Transverse Acoustics on Shear Coaxial Jets for Two Geometries	A-767
19. Mixing under Transcritical Coaxial Injection Conditions: Experiments and Simulations	A-768
20. Physical Hypothesis for the Combustion Instability in Cryogenic Liquid Rocket Engines.....	A-785
21. Non-Reacting Shear Coaxial Jets in an Acoustic Field	A-793
22. Shear Coaxial Jets Subjected to an External Acoustic Field	A-817
23. Proper Orthogonal Decomposition Analysis of Shear-Coaxial Injector Flows With and Without Transverse Acoustic Forcing	A-823
24. Cryogenic High-Pressure Shear-Coaxial Jets Exposed to Transverse Acoustic Forcing	A-840
25. <i>Droplet Combustion and Non-Reactive Shear-Coaxial Jets with Transverse Acoustic Excitation</i> , Ph.D. Dissertation.....	A-862
26. Experiments and numerical simulation of mixing under supercritical conditions	A-1144
27. Split Stream Flow Past a Blunt Trailing Edge with Application to Combustion Instabilities	A-1173
28. Geometry Effects on Steady and Acoustically Forced Shear-Coaxial Jet Sprays	A-1189

LIST OF ABBREVIATIONS

AFRL	Air Force Research Laboratory
AR	Area Ratio
AVBP	The name of a large eddy simulation code originating in France
FFT	Fast Fourier Transform
SSME	Space Shuttle Main Engine
td/l	Inner jet lip thickness to inner jet diameter

ABSTRACT

This research has concentrated on the characterization of mixing for typical liquid rocket injectors. The conditions of interest have encompassed subcritical to supercritical pressures with temperatures below and above the critical temperature, with and without an acoustic field. The project has been largely experimental in-house. A single shear coaxial injector element has been thoroughly studied. This type of injector element is commonly used in many rocket engines (e.g., Space Shuttle Main Engine (SSME), Vulcain, RS-68, etc). It was found that the mixing in these injectors is governed primarily by the presence or absence of an acoustic field, the outer to inner jet area ratio and the inner jet lip thickness to inner jet diameter, the outer to inner momentum flux ratio, the reduced density of the inner jet, and on whether the pressure is subcritical and supercritical.

1.0 EXECUTIVE SUMMARY

This executive summary documents the extensive amount of work that was performed over the eight year duration of this project. The main themes are outlined below, and extensive references are given to guide readers to the details. Copies of all references are provided in Appendix A, both for convenience and in order to make this a self-contained document. Streamlined reference to most of the details may be found in the three Ph.D. theses that were completed under this project.

Mixing between propellants, as a necessary precursor to combustion, is a fundamental fluid mechanics problem to be understood in order to design liquid rocket injectors that meet all the performance and stability requirements implicit in modern rockets. The interaction or disruption of the mixing process when an injector is subject to an external acoustic field is believed to be a fundamental problem needed to be solved within the larger problem of combustion instabilities. Combustion instabilities arise from very complex interactions between fundamental processes happening in an injector such as atomization, vaporization, combustion, fluid mechanic instability modes, with acoustic modes derived from the combustion chamber geometry. Though combustion instability events have happened since the dawn of rocketry, their fundamental understanding and control has remained elusive. Because of the catastrophic effects that combustion instability can have on an engine (possible destruction in less than a second) and a development program (very large cost over runs if an unstable engine has to be fixed after it has been improperly designed), the Air Force Research Laboratory (AFRL) is interested in tackling this problem by gaining a understanding of the basic physics. The project to be summarized here has focused on understanding mixing in a particular liquid rocket injector and its interaction with an external acoustic field. This study isolates the effects of chemistry or combustion from the effects of fluid mechanics since it is conducted with non-reacting flows. The study that will follow this project will add chemistry to the experiments proving a very exciting opportunity to understand which cold-flow effects are present and absent in a hot-fire experiment. The effort has been mostly experimental.

The experimental facility is capable of operating up to 2000 psi (13.3 MPa) and at cryogenic temperatures (down to 162 R (90 K)). It is used only for non-reacting flows. All the experiments described here were conducted using only N₂, which has a critical pressure, P_{cr} , of 493 psi (3.4 MPa) and a critical temperature, T_{cr} , of 226 R (126.2 K). N₂ was used as the fluid for the injector streams and also to pressurize the chamber. This means that there is a unique critical point and clear determination of the thermodynamic state of the injector streams at different flow conditions. By being able to operate at pressures above P_r and temperatures above and below T_{cr} , this facility is capable of simulating realistic rocket operating conditions. The facility also has two piezo sirens that can produce acoustic pressure levels of up to ~2% of chamber pressure at around 3 kHz. This high frequency value is representative of actual frequencies recorded on high-frequency instability events.

The injector type chosen for this project is a shear coaxial injector. Shear coaxial injectors have received much attention in diverse engineering fields because of their simplicity (one inner jet separated from an annular flow by the thickness of the inner jet wall) and their ability to mix the two streams remarkably well via the shear developed due to differences in velocity between the two streams. This type of injector has been widely used in liquid rocket engines, from the J2 engine in Saturn I and V to the SSME to the Vulcan engine currently used in the Ariane launch vehicle.

The first set of experiments on shear coaxial jets is detailed in several papers from Davis et al. [1-5, 7] which form the core of Davis' Ph.D. thesis [6]. The shear coaxial injector geometry chosen has a Large outer to inner jet Area Ratio and a Thick inner jet lip thickness to inner jet diameter ratio, therefore it is denoted as LAR_thick. Of special interest was to conduct experiments in realistic operating conditions, given that many modern rockets operate at pressures that are higher than the individual propellant critical pressures. Most data available had been obtained at subcritical pressures with two-phase mixtures (liquid-gas) or one-phase mixtures (liquid-liquid or gas-gas). In fact, a wealth of literature has been published since the 1960's on observations, theoretical treatments and numerical simulations for shear coaxial jets.

Davis et al. showed that the mixing of the inner and outer jets is heavily determined by the outer to inner jet momentum flux ratio ($J = \rho_o u_o^2 / \rho_i u_i^2$). Mixing is completed closer to the injector exit plane as J increases. However, the rate at which the mixing is enhanced by J is different for subcritical (2-phase mixtures) and supercritical mixtures (one-phase mixtures). They found an experimental correlation of the form $L/D1 \sim AJ^n$ to describe mixing. Here L is a measurement made from back-lit pictures where the inner jet shows as a dark region connected to the injector exit plane. The inner jet appears darker because in all the experiments it is at a lower temperature, thus denser, than the outer jet. The distance from the injector exit plane, along the axial direction, to where the first break in the inner jet appears, is called the inner jet dark core length and is denoted by L . To make the results non-dimensional, the dark core is divided by the inner jet diameter. The exponent n , was found to be 0.2 for subcritical pressures and 0.5 for supercritical pressures. Davis was also able to excite the jets with a single acoustic driver, which due to the geometrical arrangement of the driver and the injector subjected the flow mostly to a pressure node (velocity antinode). His results showed that for the cases when the injector responded to acoustics, it did so by taking on a sinuous shape. His movies were very similar qualitatively to movies taken in the 1960's by Heideman during a combustion instability event, which gave even more confidence to the relevance of studying cold flows for the successful design of rocket injectors.

Leyva et al [8-10] completed a thorough study of the time-response of the same geometry used by Davis to acoustics. Davis had started this course of research by taking data of three representative flow conditions. Leyva et al [8-10] found that the shear coaxial jets are most sensitive to acoustics in a set range of J values. For subcritical and supercritical pressures, this range is about $1 < J < 10$. They also found that even though the inner jet attains a sinuous shape when subject to a velocity antinode, the total length of the inner jet (taking into account its curvature) is still shorter for cases when the acoustics is turned on. That is, acoustics has the effect of enhancing mixing for a given range of J . The movies of the injector flow subject to acoustics showed the sinuous shape shrinking and expanding in the axial direction as the acoustic cycle progresses. An Fast Fourier Transform (FFT) analysis of the dark core length demonstrated that the dark core variations were at the same frequency as the acoustic disturbance being applied to the jet. No other frequencies (e.g., those due to the natural instabilities of the jets, or acoustic modes of the injector geometry) were found. Finally, Leyva et al measured the spread angle of the outer jet for different flow conditions to compare with other available data from the literature. It was found [10] that for the conditions studied the spread angles were less than those for planar shear layers or other shear coaxial jets at subcritical pressures for the same chamber-to-outer-jet density ratios. A new parameter, $(\rho_{\text{chamber}}/\rho_{\text{outer}})\sqrt{J}$ was proposed that seemed to collapse the available data better.

The next logical step was to subject the injector flow to both pressure nodes and antinodes to see how differently the injector responds. Both cases could be present in a real rocket environment. To accomplish this, a second piezo siren was installed, so that two independent waves can be formed at each end of the chamber. By controlling the phase angle between the two waves, the injector, which is placed in the middle between the two sirens, can be subjected to a pressure node (phase angle between sources = 180 degrees) or a pressure antinode (phase angle = 0 degrees). Both of these cases correspond to stationary waves. For any other phase angle a travelling wave is set up in the chamber. A very detailed study ensued in which two geometries were carefully characterized at two operating pressures (subcritical and near critical) and a wide range of J . The results at higher supercritical pressures were found to be similar to those at near critical pressures, so higher pressures were not further investigated for safety and operability reasons. The new geometry resembled the one used in the SSME. This new geometry has a *small* outer to inner jet *area ratio* (AR) and a *thin* inner jet lip thickness to inner jet diameter ratio, denoted as SAR_thin, in contrast to the previous geometry LAR_thick. The results of this study are detailed in Rodriguez et al [11-12], Leyva et al [13], Rodriguez et al [14], Rodriguez's Ph.D. thesis [15], Graham et al [16] and Rodriguez et al [17-18].

The results obtained with SAR_thin provided evidence that different geometries for shear coaxial injectors of similar size could have an impact on the dynamics of a coaxial jet. The range at which acoustics had a noticeable effect on the coaxial flow was broader for SAR_thin ($0.1 < J < 10$). The largest reduction of the inner jet core was observed around the pressure antinode at both subcritical and supercritical pressures. That is, the injector responded more to pressure fluctuations than velocity fluctuations. In contrast, the inner jet dark core showed a weak effect with phase angle for LAR_thick, but when an effect was captured it was greater at pressure nodes.

An interesting observation was made for SAR_thin: at large J values, the relative reduction of the dark core length compared to its baseline value, as a function of phase angle, collapses into a single curve for subcritical and near critical pressures. This observation points to the possibility of having a limit cycle where only a small perturbation is needed to achieve the same relative reduction of the dark core. If this proposition is true, even small pressure perturbations could have a large impact on the stability behavior of liquid rocket injectors and other applications of coaxial flows.

A very interesting study was carried out by Schmitt et al [19, 26] where three of the experimental conditions obtained at near critical pressures for SAR_thick were simulated using a Large Eddy Simulation code (AVBP). AVBP is widely used in Europe and has been validated for real gas models which are needed for simulating mixing at transcritical conditions. The numerical simulations captured our experimental observations quite well in a qualitative sense. A new study is underway where two more geometries will be studied and more quantitative experimental data will be available to compare with the numerical simulations. Chehroudi [20] put forth a hypothesis for combustion instability based on experimental observations from previous cold-flow experiments.

Based on the intriguing results that had been obtained at this point with two different geometries, the next logical step was to complete a design of experiments where four different but related geometries were studied: SAR_thin, SAR_thick, LAR_thin, and LAR_thick. By varying the outer to inner AR and the inner jet lip thickness to inner jet diameter (t/d_1) independently, it was possible to explore how those two important parameters govern mixing. This work has been reported in Teshome et al [21-25, 28].

Teshome et al have reported, we believe for the first time in the literature, a comprehensive study of the effect of flow parameters (pressure, J , inner jet temperature) and geometry (AR and t/d_1) on mixing for shear coaxial jets. Teshome also completed a proper orthogonal decomposition study which has enabled a better understanding of the stability characteristics of the different geometries at different flow conditions. This analysis has already improved our understanding by figuring out which geometries seem to be more sensitive to acoustic disturbances, knowledge which certainly can be very useful for a rocket designer.

In summary, the main conclusions of this study were: mixing in shear coaxial jets at subcritical and supercritical pressures with temperatures below and above the critical temperature is governed primarily by the following sets of parameters. First there is the presence or absence of an acoustic field. There are three main kinds of response when an acoustic field is present. The jet can respond either in a sinuous fashion, it can respond in a vortex shedding fashion, or it can fail to respond at all to any appreciable extent. There are two main geometrical parameters, namely the outer to inner jet area ratio, and the inner jet lip thickness to inner jet diameter ratio. The geometry of the injectors determines to a great extent its sensitivity to an external acoustic field. Then there two main flow parameters, namely the outer to inner jet momentum flux ratio (J) and the inner jet reduced density. For most cases, the injectors are sensitive to acoustics only in a range of about $1 < J < 10$. Finally, the dependence on these parameters is in general different depending on whether the pressure is subcritical or supercritical.

2.0 ACKNOWLEDGEMENTS

The people involved in this project wish to thank very sincerely Randy Harvey, head mechanic, who works assiduously to ensure the lab functions properly and goes the extra mile to ensure students meet test deadlines; Foster Beasley, who has helped with the modeling and drawings of many designs; Todd Newkirk who has lent a helping hand with electronics and instrumentation projects, and the rest of the mechanics crew, Earl Thomas, Dave Hill, and Paul Rue who always step in when their help is needed. Support from AFOSR, Mitat Birkan, Program Manager, is gratefully acknowledged.

3.0 REFERENCES

1. Davis, D.W., Chehroudi, B., and Sorensen, I., "Measurements in an Acoustically Driven Coaxial Jet under Supercritical Conditions" 43rd AIAA Aerospace Sciences Meeting and Exhibit," paper AIAA 2005-0736, Reno, NV, January 10-13, 2005.
2. Davis, D.W., Chehroudi, B., and Talley, D.G., "Experiments on a Coaxial Injector under an Externally Forced Transverse Acoustic Field," Defense Technical Information Center paper ADA442936, June 2005.
3. Davis, D.W., and Chehroudi, B., "Shear-Coaxial Jets from a Rocket-Like Injector in a Transverse Acoustic Field at High Pressures," paper AIAA-2006-758, 44th AIAA Aerospace Sciences Meeting and Exhibit, Reno, NV, January 9-12, 2006.
4. Davis, D.W., Chehroudi, B., and Talley, D.G., "A Rocket-Like Coaxial Injector In An Acoustic Field Under Sub-And Supercritical Conditions," 10th International Conference on Liquid Atomization and Spray Systems, paper ICLASS06-270, Kyoto, Japan, August 27 – September 1, 2006.

5. Davis, D. W., Chehroudi, B., and Talley, D.G., "Behavior of a Rocket-Like Coaxial Injector in an Acoustic Field," 19th Conference on Liquid Atomization and Spray Systems, Toronto, Ontario, May 23-26, (2006) (Winner of Marshall best paper award, 2007).
6. Davis, Dustin W., *On the Behavior of a Shear-Coaxial Jet, Spanning Sub- to Supercritical Pressures, With and Without an Externally Imposed Transverse Acoustic Field*, Ph.D. Thesis, The Pennsylvania State University, May 2006.
7. Davis, D.W., and Chehroudi, B., "Measurements in an Acoustically-Driven Coaxial Jet under Sub-, Near-, and Supercritical Conditions," *Journal of Propulsion and Power* 23(2), 366-376, March-April 2007.
8. Leyva, I.A., Chehroudi, B., and Talley, D.G., "Dark core analysis of coaxial injectors at sub-, near-, and supercritical conditions in a transverse acoustic field," Defense Technical Information Center paper ADA467843, May 2007.
9. Leyva, I., Chehroudi, B., and Talley, D.G., "Dark core analysis of coaxial injectors at sub-, near-, and supercritical pressures in a transverse acoustic field," paper AIAA 2007-5456, 43rd AIAA/ASME/SAE/ASEE Joint Propulsion Conference & Exhibit, Cincinnati, OH, July 8-11, 2007.
10. Leyva, I., Rodriguez, J., Chehroudi, B., and Talley, D., "Preliminary Results on Coaxial Jet Spread Angles and the Effects of Variable Phase Transverse Acoustic Fields," 46th AIAA Aerospace Sciences Meeting and Exhibit, paper AIAA-2008-950, Reno, Nevada, January 7-10, 2008.
11. Rodriguez, J., Leyva, I., Chehroudi, B., and Talley, D., "Effects of a Variable-Phase Transverse Acoustic Field on a Coaxial Injector at Subcritical and Near-Critical Conditions," 21st Annual Conference on Liquid Atomization and Spray Systems - Americas, Orlando, Florida, May 18-21 2008.
12. Rodriguez, J.I., Leyva, I.A., Chehroudi, B., and Talley, D., "Results on Subcritical One-Phase Coaxial Jet Spread Angles and Subcritical to Supercritical Acoustically Forced Coaxial Jet Dark Core Lengths," 44th AIAA/ASME/SAE/ASEE Joint Propulsion Conference and Exhibit, paper AIAA-2008-4561, Hartford, CT, July 21-23, 2008.
13. Leyva, I., Rodriguez, J., Chehroudi, B., and Talley, D., "Effect of Phase Angle on Coaxial Jet Behavior Spanning Sub- to Supercritical Pressures," 22nd Annual conference of the Institute of Liquid Atomization and Spray Systems (ILASS) – Europe, paper ILASS08-A142, Como Lake, Italy, September 8-10, 2008.
14. Rodriguez, J.I., Graham, J.J., Leyva, I.A., Lyu, H.-Y., and Talley, D., "On the Inner Jet Spread Angles of Coaxial Jets from Subcritical to Supercritical Conditions with Preliminary Numerical Results," Defense Technical Information Center paper ADA502385, October 2008.
15. Rodriguez, J.I., *Acoustic Excitation of Liquid Fuel Droplets and Coaxial Jets*, Ph. D. Dissertation, Department of Mechanical and Aerospace Engineering, University of California, Los Angeles, 2009.
16. Graham, J., Leyva, I., Rodriguez, J., and Talley, D., "On the Effect of a Transverse Acoustic Field on a Flush Shear Coaxial Injector," 45th AIAA/ASME/SAE/ASEE Joint Propulsion Conference and Exhibit, paper AIAA-2009-5142, Denver, Colorado, August 2-5, 2009.

17. Rodriguez, J., Leyva, I., Graham, J., and Talley, D., "Mixing Enhancement of Liquid Rocket Engine Injector Flow," 45th AIAA/ASME/SAE/ASEE Joint Propulsion Conference and Exhibit, paper AIAA-2009-5143, Denver, Colorado, August 2-5, 2009.
18. Rodriguez, J.I., Leyva, I.A., and Talley, D., "Effect of Phase Angle of Transverse Acoustics on Shear Coaxial Jets for Two Geometries," poster presented at the 11th International Conference on Liquid Atomization and Spray Systems, Vail, Colorado, July 26-30, 2009.
19. Schmitt, T., Rodriguez, J., Candel, S., and Leyva, I., "Mixing under Transcritical Coaxial Injection Conditions: Experiments and Simulations," 8th EuroMech Conference, Bad Reichenhall, Germany, September 2010.
20. Chehroudi, B., "Physical Hypothesis for the Combustion Instability in Cryogenic Liquid Rocket Engines," *Journal of Propulsion and Power*, vol. 26 no. 6, pp 1153-1160 (2010) doi: 10.2514/1.38451
21. Teshome, S., Rodriguez, J., Graham, J., Leyva, I.A., Talley, D., and Karagozian, A., "Non-Reacting Shear Coaxial Jets in an Acoustic Field," presented at Joint French/German/United States Symposium on Liquid Rocket Combustion Instabilities, London, UK, June 15-16, 2011.
22. Leyva, I.A., Talley, D., Teshome, S., Rodriguez, J., and Graham, J., "Shear Coaxial Jets Subjected to an External Acoustic Field," 23rd International Conference on Detonations and Explosions in Reactive Systems (ICDERS), Irvine, Ca, July 24-29, 2011.
23. Teshome, S., Leyva, I., and Talley, D., "Proper Orthogonal Decomposition Analysis of Shear-Coaxial Injector Flows With and Without Transverse Acoustic Forcing," Defense Technical Information Center paper ADA554901, October 2011.
24. Teshome, S., Leyva, I., Talley, D., and Karagozian, A., "Cryogenic High-Pressure Shear-Coaxial Jets Exposed to Transverse Acoustic Forcing," 50th AIAA Aerospace Sciences Meeting including the New Horizons Forum and Aerospace Exposition, paper AIAA-2012-1265, Nashville, Tennessee, January 9-12, 2012.
25. Teshome, S., *Droplet Combustion and Non-Reactive Shear-Coaxial Jets with Transverse Acoustic Excitation*, Ph.D. dissertation, The University of California at Los Angeles, 2012.
26. Schmitt, T., Rodriguez, J., Leyva, I., and Candel, S., "Experiments and numerical simulation of mixing under supercritical conditions," *Physics of Fluids* 24, 055104 (2012).
27. Tian, V, McKeon, B., and Leyva, I.A., "Split Stream Flow Past a Blunt Trailing Edge with Application to Combustion Instabilities," to be presented at the 48th AIAA/ASME/SAE/ASEE Joint Propulsion Conference & Exhibit and 10th International Energy Conversion Engineering Conference, Atlanta, GA, July 30 – August 1, 2012.
28. Teshome, S., Leyva, I., Talley, D., and Karagozian, A., "Geometry Effects on Steady and Acoustically Forced Shear-Coaxial Jet Sprays," to be presented at the 12th Triennial International Conference on Liquid Atomization and Spray Systems, Heidelberg, Germany, September 2-6, 2012.

This Page Intentionally Left Blank

APPENDIX A—COPIES OF REFERENCES

Measurements in an Acoustically Driven Coaxial Jet under Supercritical Conditions

Dustin W. Davis^{*} and Bruce Chehroudi[†]

Engineering Research Consultants, Inc. , Edwards AFB, CA, 93524

Ira Sorensen[‡]

California State University, Fresno, Fresno, CA 93740-8030

An experimental investigation was conducted on a coaxial jet similar to those used in cryogenic liquid rockets, under sub-, near-, and supercritical conditions, with the ultimate intent of gaining a better understanding of an aspect of combustion instability that pertains to interactions of an externally-imposed acoustic field with the jet. Past research works on this subject have shown both the relevance and importance of geometrical changes in an injector's exit-area and its nearby physical and fluid mechanical processes. On this basis, special attention is paid in collecting spatially-resolved mean temperatures and documenting the aforementioned interactions at the exit of this injector. Short duration and high-speed framing digital cameras provided information on the behavior of this jet under variety of conditions. Mean and rms values of the "dark core" length fluctuations were measured from the acquired images via a computer-automated method and the ensuing results are discussed. There appears to be a good correlation between this length and the outer-to-inner jet momentum ratio, but the form of this dependence was found to be different at subcritical than the rest of the conditions. The rms values of the length fluctuations suggested a possible explanation for the observed improvement in instability limit at increasingly higher outer-to-inner jet velocity ratios.

Nomenclature

A, B, C	=	constants
$D_{1,2,3,4}$	=	diameter with subscripts 1 through 4 indicating the four different diameters of a coaxial injector
L	=	length of dark core, length of injector tube
M	=	momentum flux ratio of outer jet to inner jet
\dot{m}	=	mass flow rate
P	=	pressure
$R_{1,2,3,4}$	=	radius with subscripts 1 through 4 indicating the four different radii of a coaxial injector
R_h	=	hydraulic radius of outer jet, equal to the gap width
T	=	temperature
U_i	=	velocity
VR	=	velocity ratio of outer jet to inner jet
μ	=	viscosity
ρ	=	density
σ	=	surface tension
i	=	subscript denoting inner jet
o	=	subscript denoting outer jet

^{*} Ph.D. Candidate Penn State University , and Scientist, AFRL/PRSA/ERC, 10 E. Saturn Blvd., AIAA Member.

[†] Corresponding Author, Sr. Scientist, AFRL/PRSA/ERC, 10 E. Saturn Blvd. ChehroudiB@aol.com, AIAA Member.

[‡] Adjunct Faculty, Department of Mechanical Engineering, 2320 E. San Ramon MS/EE-94, AIAA Member.

Approved for public release; distribution unlimited. PAS #2005-182.

I. Introduction

COMBUSTION instability is a problem that has been observed with liquid rocket engines since the late 1930's.¹ Three types of combustion instabilities have been identified based on the frequencies involved. Low frequency instability (chugging) is when the wavelength is much longer than the characteristic dimension of the chamber and the feed system. Generally, chugging frequencies are less than a few hundred Hz. High frequency instability (screaming) is the second type which is also referred to as acoustic instability due to the closeness of the measured pressure oscillation frequencies to the computed acoustic resonance modes of the thrust chamber. High frequency combustion instability is the most destructive type, and it is generally agreed that it is not influenced by the propellant feed system of the rocket engine. An intermediate frequency (buzz) consists of the lumping of the instabilities that do not fall into either chugging or screaming categories.²

Typically, for cryogenic propellant systems consisting of liquid oxygen (LOX) – hydrogen (H₂), a shear coaxial type injector is used. Examples are the designs presently employed in the Space Shuttle Main Engine (SSME) or the Ariane 5 Vulcain engine³, and the RL-10 and J-2 engines from the late 1950's.⁴ One method for eliminating acoustic instability in liquid rocket engines is to modify the spray combustion field,² which is usually achieved through modifications to the injector design. One such modification to the Ariane 5 Vulcain, which increased the mean droplet diameter size, improved the stability of the engine.³ These changes to the injector design ultimately affect the mixing characteristics of the propellant streams in the thrust chamber. The fundamental physics of the breakup of a liquid jet and its subsequent mixing with another fluids have been studied since Rayleigh's study in 1878.⁵ Much progress has been made since then,⁶ and as a result we are approaching a fundamental understanding of fluid jet break up and atomization processes. However, full understanding is not yet available⁷. A review of liquid jet atomization processes from a coaxial-type injector has recently been presented by Lasheras and Hopfinger⁸ discussing some of the more recent developments in this area.

Since the 1970s, the importance of interactions between the acoustic field and a fluid jet in the context of combustion instability has been realized. This notion arises from designers' ability to bring about improvements in engine stability through modifications in injector designs. Combustion in a rocket engine is controlled by, or at least intimately related to, the jet breakup and mixing processes of the oxidizer and fuel streams. Some early works on the interaction of high-amplitude acoustic waves with fluid jets were done by Miesse.⁹ Miesse excited atmospheric-pressure round water jets with a high-intensity acoustic field and observed a decrease in the breakup length of the jet. Buffum and Williams¹⁰ also investigated the effects of a transverse acoustic wave at frequencies in the range of 100 to 500 Hz and at amplitudes up to 161 dB on round liquid jets, measuring jet lateral deflection from its stable position. They observed that at acoustic amplitudes below 130 dB the deflection of the jet was unobservable.

Hulka and Hutt⁴ have compiled an extensive review of coaxial injectors used in reported LOX/H₂ rocket engine stability works by others with the objective of identifying key injector design or operating conditions contributing to combustion instability in these engines. What they found, and also reported by others, was that the outer-to-inner jet exit velocity ratio played a key role in many of the studies defining stability. Although a lot of scatter is seen in the accumulated results, generally speaking, high velocity ratio values tended to improve engine stability limits. For a wide variety of injector designs and operating conditions, a velocity ratio of about 10 was the maximum where combustion instability occurred, with the exception of the M-1 engine. Additionally, they point out that a velocity ratio as low as 1 has been stable and a ratio as high as 15 was required to stabilize the M-1 engine. One method for LOX/H₂ rocket engine stability rating is to perform "temperature ramping" of the H₂ (flowing into the outer annular region of the coaxial injector) by reducing its temperature from a high value to low enough temperature until an onset of instability in the engine is measured. An engine, injector or combined injector/engine design as a system, which produces a lower H₂ temperature at the onset of the instability, implies a more stable system. One issue with the data accumulated by Hulka and Hutt is that the original researchers reporting the results usually measured propellant temperatures well upstream of the injector exit area which could provide calculated velocity ratios quite different from its true values at the exit. Additionally, under near- or supercritical conditions, as also pointed by them, small changes in temperature, even if measured at the injector exit plane, can produce large changes in density, strongly affecting the accuracy of estimates for velocity ratios. It is this lack of accurate information that partly motivated the current authors to initiate research providing details and accurate measurements of temperature radial profiles at the exit of a coaxial injector design, something we are unaware has ever been undertaken before to the detail presented here.

As indicated by Wanhainen et al.¹¹, although velocity ratio seems to serve quite well as a correlating parameter, it is difficult to relate it to a physical combustion model and it may indeed be a symbolic of other fundamental parameters. It is our ultimate intention to shed some light and contribute towards such a key physical understanding. It is also interesting to mention a related work reported by Hiedmann¹² in a circular combustor with LOX jets

injecting radially from the side walls of the combustor. The H_2 streams were introduced into the chamber in a diffuse manner, somewhat similar to a coaxial design. The combustion instability was induced by injection of nitrogen streams circumferentially to be perpendicular to the LOX injection direction. In images, Hiedmann¹² observed that the length of the LOX dark core decreased during every screaming combustion instability event. This motivated us to pay special attention to the observed “dark core” impression of the jets seen in our studies.

Therefore, to gain physical insight on the effects of an externally-imposed acoustic field on the flow and thermodynamic conditions of a coaxial jet near its exit area, experiments were designed and conducted to have as many of the key features of a LOX/ H_2 rocket engine as possible in a cold flow environment. Chehroudi and co-workers^{13,14} have assembled a single-element coaxial-jet non-combusting test rig operating at cryogenic temperatures, transcritical temperature ranges, sub- to supercritical pressures, realistic outer-to-inner jet velocity ratios, and activation of an acoustical field inside the test chamber simulating one important aspect of the environment when combustion instability intensifies. Of course, combustion processes cannot be simulated in this facility, a subject to be considered in a design of a new facility. It is hoped that such a cold flow analysis will provide an initial insight into some, but not all, of the key interactions during an episode of combustion instability in a rocket engine. This work is an extension of previous papers by Davis and Chehroudi^{13,14} in which a coaxial jet injector was designed, based on a well-characterized single-jet injector investigated by Chehroudi and coworkers.¹⁵⁻¹⁹

II. Experimental Facility

The experimental facility previously described by Chehroudi and co-workers¹³⁻¹⁹ has undergone considerable upgrades and modifications in order to improve the quality of the data and expand the operating range of the facility. A schematic of the key components of the improved facility is shown in Fig. 1, along with its photograph in Fig. 2. Gaseous nitrogen (GN2) from the laboratory feed line was used to pressurize the test chamber and also to produce the jets issuing from a coaxial injector’s center post and its outer annular coaxial region. The feed GN2 flow rates, used to produce the inner and outer jets, are measured separately with Porter Mass flow meters. Subsequently, the GN2 streams flow through a series of heat exchangers (HX) to be cooled, see Fig. 1. These HXs are cooled by the “facility liquid nitrogen (LN2)” stored in a cryogenic tank outside the test cell. The GN2 feeding the inner jet is passed through a counter-flow HX cooled to a liquid state (if subcritical). The exiting nitrogen (now LN2) from the center-post HX is then directly sent to the injector. The GN2 for the outer flow passes through two HXs (primary and secondary) before it is directed to the injector. The facility LN2 flow rate to the secondary HX is adjusted to produce a desired temperature of the outer jet at the exit plane of the injector. Independent control over the outer jet exit temperature was not previously available in our facility. For reference, the critical temperature and pressure of nitrogen are 126.2 K and 3.4 MPa, respectively.

The injector used in this study (Figs. 3 and 4), previously explained by Davis and Chehroudi,¹³ produces a cryogenic jet that is injected through a sharp-edged stainless steel inner tube having a length (L) of 50 mm and an inner and outer diameters of $D_1 = 0.508$ mm and $D_2 = 1.59$ mm, respectively. The resulting L/D_1 is 100, considered sufficient to ensure a fully-developed pipe flow at the injector exit plane. The gap width (R_h) between the inner and outer tubes, defining the annular region, was 0.415 mm. The injector had an 8% bias of the mean gap width and the inner post was recessed by about $\sim 0.5 D_1$.

The chamber is designed to withstand pressures up to 14 MPa. There is a smaller rectangular-shaped chamber within a main chamber. The purpose of the main chamber is to contain the pressure whereas that of the inner one is to act as a cavity resonator at the same pressure as the main chamber, with the intention of achieving the highest amplitude of the acoustically-induced velocity in the vicinity of the jet. The inner-chamber cavity was driven by a piezo-siren, specially-designed by Hersh Acoustical Engineering, Inc. This device is capable of producing sound pressure levels (SPL) of up to 180 dB (measured in an impedance tube) at resonant frequencies lying between 1000 to 8000 Hz and at pressures up to 14 MPa. The siren is physically coupled to the inner chamber via a circular-to-rectangular transition piece to guide the acoustic waves into the measurement zone of the inner chamber. Actual SPL levels in the inner chamber were between 161 dB and 171 dB at its first two resonance frequencies of 3.0 kHz and 5.2 kHz. The resonance frequencies change slightly with changes in chamber pressure and temperature.

Radial temperature profiles of the jet at the exit of the injector were measured with a Type-E thermocouple (TC) installed on a traversing stage that protrudes into the inner chamber region (see Fig. 5). The best estimate of the measurement accuracy of a standard calibration of the Type-E TC within our range of interest is on the order of ± 5 K. This is considered too large, especially near the critical point of nitrogen, producing large uncertainties in density and injection velocity calculations. The uncertainty is due to composition variations of the particular bead and wire materials used within the manufacturing specification. Typically, a curve fit to the calibration data over a large

range is quite adequate and has only a few degrees of uncertainty at room temperatures or warmer. However, at cryogenic temperatures, the uncertainties grow because the output voltage from a TC decreases at low temperatures and in addition the “multiple TC effect” within the circuit becomes a larger portion of the output signal. When the local composition of a TC wire varies along the length of the wire leading to the bead and a temperature gradient exists along the wire, the voltage signal from this TC is changed. This is because these compositional changes along the wire act as a network of connected individual TC beads throughout the wire including any circuitry used. This will produce “the multiple TC effect”. Therefore, it was necessary to re-calibrate the TCs in-house to mitigate these effects. The calibration was performed against a precision platinum resistance temperature detector (Pt-RTD) over a range of 77 to 300 K. The Pt-RTD was manufactured and calibrated by Hart and had an accuracy of ± 0.01 K. No Pt-RTD was available in the small size required to make measurements in the jet, but the size was unimportant for the calibration procedure itself. The maximum estimated uncertainty over the range of interest for the re-calibrated thermocouples was ± 0.8 K.

The addition of the exit plane temperature measurement system was a significant improvement to the facility. Previous temperature measurements¹³ were performed with the standard calibration of a Type E TC which had a large bead diameter of approximately 0.4mm, and had no mechanism for removing the bead from the jet flow without opening the main chamber. This means that no images could be acquired during temperature measurements and another repeat run was required to accumulate such information. Additionally, the improved temperature measurement system uses a TC with a much smaller bead diameter than before (~ 0.1 mm), which induces less disturbance to the jet flow, particularly for the inner-jet temperature measurements. Also, the TC is attached to a traversing mechanism, which permits measurements of radial profiles at a fixed axial distance of $0.28 D_i$ downstream of the injector exit plane. Once temperature measurements are made, the TC can be traversed out of the flow far from the coaxial jet area, enabling imaging of the undisturbed jet in the same run.

Backlit images (12 bit) of the coaxial jet were taken at 10 Hz frame rate with resolution of 1280x1024 pixels using a PixelFly CCD camera manufactured by the Cooke Corporation. A General Radio Strobotac strobe light was used for illumination purposes. The image was defined by the strobe flash duration of approximately 0.5 μ s. Additionally, for some of the conditions, images were taken with a Phantom CMOS camera model version 5.1, manufactured by the Vision Research Company. The Phantom camera has the capability of producing 10-bit images at 93 kHz. However, in this study, and to increase the clarity of the features, the framing rate was set to 18 kHz at a resolution of 256x128 pixels. For this case, the images were backlit with a continuous light source, and were defined by the exposure time of the camera at 2 μ s duration. Unfortunately, the Phantom camera was acquired during the latter part of the project and was not used for all the conditions presented here. It is our intention to use the Phantom camera for those data sets already acquired with the PixelFly camera in the future.

The operation of a typical test consisted of a cool-down process for a certain period, allowing establishment of a steady-state condition for the entire facility including the plumbing system and the chamber. Once this condition is reached, radial traverses towards the coaxial jet centerline were made for temperature measurements, starting from a distance sufficiently far away from the jet to establish a background chamber temperature value. Measurements continued past the centerline until a large enough increase in temperature was observed, and sufficient data collected, to allow determination of a true jet centerline position. The TC traversing mechanism was then pulled entirely away from the jet area until it stopped near the wall of the inner chamber. With the TC clearing the path of the jet, images were taken while the acoustic driver was off, immediately followed by a set of images when the driver was operating and tuned to the first and second resonance frequencies of the inner chamber. Only 30 images were recorded when the PixelFly camera was in use. In contrast, the Phantom camera collected a large set of images of up to a 1000 for each condition.

III. Experimental Results and Discussion

The experimental matrix was organized to enable comparisons between results at different outer-to-inner jet velocity ratios. Thermodynamic conditions of the jet at the exit of the injector, calculated from temperature measurements, are shown in Fig. 6. Because of a large variation in density with small changes in temperature near the critical point (see Fig 6), two nominal outer-jet temperatures (around 140K (low) and around 190K (high)) were selected, and then the jet’s mass flow rates were varied to obtain a desired outer-to-inner jet velocity ratio. We will refer to these cases as “low or lower” and “high or higher” temperatures and should be clear in the context of the discussion.

A. Temperature Measurements

Radial profiles of the coaxial jet averaged temperature were measured at a normalized axial location (x/D_i) of about 0.28 from the injector exit plane using a Type-E thermocouple as described above. Figure 7 shows the measured temperature and the associated density radial profiles computed using the NIST REFPROP²⁰ equation-of-state (EOS) program accepting the radial temperature and chamber pressure as input data. The horizontal axis is radial distance measured from the jet centerline and is normalized by the inner-jet tube inside radius. The top, middle, and bottom rows plots in Fig. 7, are at the chamber pressures of 1.5 (subcritical), 3.5 (near-critical), 4.9 (supercritical) MPa, respectively. Scales for temperature profiles are read from the left axis and those for densities from the right axis. The left and right columns in Fig. 7 are at the low (~ 140 K) and high (~ 190 K) outer-jet temperatures respectively. The solid lines and symbols represent measured temperature profiles, and the dashed lines and hollow symbols show computed densities.

An attribute that the temperature profiles in Fig. 7 possess is that there are three distinct zones where the temperature gradient is fairly small: the core or region near the centerline of the jet, the region that defines the flow of the outer jet, and the far-field inner-chamber environment. The temperatures in these three regions were used to compute physical properties such as densities and viscosities, which in turn were used to compute quantities such as velocity, momentum, and their appropriate ratios.

At a given subcritical chamber pressure (i.e. 1.5 MPa, the top row in Figs. 7a & b), both the temperature and density profiles representing the core region of the inner jet at the injector exit area are flat in shape, producing “top-hat” density profiles. The profiles then sharply change to quite different values, typical of a transition from a liquid to a gas phase, as expected. Note that for the low outer-jet temperature case, and at the measured axial location, this constant core temperature value penetrates well beyond the inner-tube radius, up to about r/R_i of 2.5, independent of the velocity ratios used. Under this condition, variations of the velocity ratio have no impact on the radial extent of the inner jet as defined by either the temperature or density profiles. Also, small variations in the outer jet temperature have no effect on the calculated values for densities. However, at the higher outer-jet temperature in Fig. 7b, the radial extent or penetration of the inner jet is strongly affected by the value of the outer-to-inner velocity ratio, primarily due to the increased heat transfer to the inner jet from the outer jet, both inside and immediately outside the injector. Note that the outer jet temperature is controlled manually by changes in the LN2 flow rate to the secondary HX, and the manual nature of this control system accounts for the variations seen in the outer jet temperatures. The variability of the inner-chamber temperature at the far field is related to changes in several factors, including mass flow rates of all nitrogen streams into the inner-chamber, their respective temperatures, and the length of time spent running the experiment (see Fig. 7b). Under the higher outer-jet temperature shown in Fig. 7b, the HX control system was able to maintain this temperature at a reasonably constant value and, again, small changes in temperature has no impact on the calculated densities.

As the chamber pressure is elevated to a near-critical value (i.e. 3.5 MPa, the middle row of Figs. 7c and d), the “top-hat” nature of the radial profiles is lost and more rounded shapes are observed, perhaps due to drastic changes of the heat transfer characteristics inside the tube under elevated, especially near-critical, conditions. Additionally, the temperature of the core (of the jet) at the centerline is greater than the corresponding temperatures at the subcritical pressure discussed above. The density increase within the outer jet zone from that of the far-field chamber value, especially at lower outer-jet temperature, is quite larger and more noticeable than that observed under subcritical pressures (see Figs. 7a & b). It is also noted that for the “case 55” plot (Fig. 7c), the temperature at the centerline is slightly higher (by approximately 5 K) than all other cases, causing the density profile to exhibit its maximum value at a slightly off-axis radial location. It is believed that the thermocouple may have moved off the plane defining a diameter to a plane defining a chord of the circular cross-section of the jet as the centerline was approached during a traverse operation. However, this remains to be verified in future.

Further increase in chamber pressure to a supercritical condition (i.e. 4.9 MPa, the bottom row of Figs. 7e & f) leads to an insignificant change in the qualitative behavior of the profiles as compared to the 3.5 MPa case. Again, a strong contrast is seen between the far-field chamber and outer-jet densities, indicating sensitivity of the density to small changes in temperature under this condition. It is also noticed that at all velocity ratios, the value of the centerline temperature at the higher outer-jet temperature (Fig. 7f) is supercritical (i.e. > 126.2 K), whereas it is subcritical for all other cases in Fig. 7. For the lower outer-jet temperature cases, the difference in density between the outer-jet region and the far-field value is in excess of 200 kg/m^3 , which makes this feature easily observable in images of the jet, but does not permit easy and clear distinction of the inner jet dark core areas.

Because of the modifications to the system made since the results of Davis and Chehroudi¹³ were presented, a direct one-to-one comparison of temperature measurements cannot be performed. However, some of the same trends were observed in the current study, such as the finding that the centerline temperature increases as the chamber pressure is elevated. Others will be investigated in the future.

B. Flow Visualization

Flow visualization of the jet with backlit photography provides many details about the flow structure and was used here to catalogue the coaxial jet behavior and its responses to the acoustic field. Figures 8, 9, and 10 are sample images of the coaxial jet under different conditions discussed in the ensuing paragraphs. One prominent feature of these images is the so-called “dark core”, which represents the high-density region of the inner jet. In these images, the inner jet has a much higher density than anywhere else in the field, thus minimizing the light penetration and causing it to appear dark and black. In many of the conditions, identification of the outer jet is made difficult because of the low density and low density gradient between the outer jet and the inner-chamber environment. However, under some conditions (see Fig. 7 at the low temperature for near- and super-critical conditions) the density and the density gradient are large enough to easily distinguish the periphery of the outer jet.

Figure 8(i) shows realizations of the coaxial jet under a subcritical chamber pressure. From left to right, they correspond to cases 17 to 20 in Table 1. For the top row (Fig. 8(i) a to d), the acoustic driver is *off* and the bottom row (Fig. 8(i) e to h) shows the corresponding images when the acoustic driver is turned *on*. Images in the same column correspond to the same operating conditions and were taken at the same test run. The velocity ratio increases from left to right in Fig. 8(i), while the inner-jet velocity is approximately constant. At the lowest velocity ratio (Fig. 8(i)a), the breakup of the jets appears to fall into the non-axisymmetric Rayleigh category, and the next higher velocity ratio (Fig. 8(i)b) is of the membrane-breakup type, even though the aerodynamic Weber number is much greater than what was observed for water-into-air injection by Faragó and Chigier²¹. At the next two higher velocity ratios (Fig. 8(i)c and d) a fiber-type breakup is observed with a pulsating mode. The exit width of the dark core is noticeably thinner for the case 18 (Fig. 8(i)b). If one compares the width of the high-density region defined in Fig. 7b with those of the dark core at the exit plane of the injector, the same trend will be observed. Upon increase in velocity ratio, the atomization process is enhanced, which is qualitatively visible from the decrease in droplet sizes, particularly in high magnification images.

Comparing the top and bottom row images, a clear effect of the acoustic field is noticed for all four conditions in Fig. 8(i). The breakup of the dark core of the inner jet is accelerated and large-amplitude wave structures are formed. From these visualizations and the limited high speed movies, it appears that, near to the injector exit area, the dark core of the inner jet is “pushed out” into the path of the outer jet flow and is then convected downstream away from the injector. The dark core develops a cusp-like structure at a distance from the injector which subsequently separates from the attached region of the jet and ultimately disappears, becoming fully mixed with the outer jet fluid.

Figure 8(ii) shows the impact of the velocity ratio and acoustic field on the coaxial jet under the low outer-jet temperature condition. As seen in the temperature measurements, the core jet also appears thicker here and the breakup seems to be of the fiber type. The jet responds to the acoustic field at all conditions with increasingly dramatic effects at higher velocity ratios. The length of the dark core region (with the acoustic driver on) appears to be considerably larger than those seen in Fig. 8(i).

Images from a near-critical chamber pressure (~ 3.5 MPa) are shown in Fig. 9, and are arranged in the same fashion as those in Fig. 8. The droplets which were clearly present under the subcritical chamber pressure disappear as expected (see Chehroudi et al¹⁶). Judging purely from the dark region of the jet, the effect of the acoustic field is less pronounced. However, from the high speed movies taken with the Phantom camera and shown in the fourth row from the top of Fig. 10, the oscillation of the jet is quite visible due to the increased framing rate and the illumination arrangement, which allowed the outer jet boundaries to be visualized. Figure 10 is composed of ten consecutive frames taken from an acquired high-speed movie of the jet. The first and second, the third and fourth, and the fifth and sixth pair of rows are at sub-, near-, and supercritical chamber pressures, respectively. In the first, third, and fifth rows the acoustic driver is *off*, and in the second, fourth, and sixth rows it is *on* at 3kHz. The framing rate was 18 kHz, producing a time interval of $55.6\mu\text{s}$ between frames. Previously reported¹³ observations that the effect of the acoustic field was lesser under near- and supercritical pressures are still valid. However, the oscillations of the jet in the acoustic field under near- and supercritical conditions seen here were not previously detected. The dark core (i.e. regions of high density) is the most visible structure, and as the density field becomes more uniform the discrimination of this effect diminishes.

Not immediately obvious in Fig. 10, but seen when played as a movie, the structures in the far-field background of the frame begin to oscillate laterally at the same frequency of the acoustic driver. One can measure the magnitude of these velocity fluctuations from the movies. Assuming that the acoustic wave in the chamber is a plane wave, the estimated pressure fluctuations from these measurements agreed with previous-measured pressure fluctuations. The velocity of the coaxial gas can also be estimated from these images. If one draws a line connecting the same structure seen in adjacent frames, the slope of this line is related to the axial convection velocity of these structures (see Fig. 10). Similarly, if each of the individual images are rotated by 90 degrees, one can measure the radial

velocity using the same method. Although further analysis is required, initial crude estimates are consistent with the computed values based on mass flow rate measurements.

By tracking the structures shown in Fig. 10 for the cases when the acoustic field is on, a possible explanation for the behavior of the jet is proposed. Once the dark high-density core of the inner jet leaves the injector, it experiences a force in the direction of the local acoustic field velocity at that moment, directing the fluid elements into the high-velocity of the outer jet areas. While these elements are accelerated in the axial direction to speeds close to the outer jet values, they nearly maintain the component of velocity in the wave propagation direction. However, once the dense region of these fluid elements (i.e. dark core) approaches the shear layer between the outer jet and chamber fluid, it experiences further mixing and heat transfer until it is no longer discernable. A fraction of these fluid elements from the dark core is convected downstream with the outer jet and experiences heat up and mixing until the elements eventually disappear into the rest of the background.

C. Dark Core Measurements

When a region of an image is referred to as a “dark core”, we simply are referring to an intact area of the jet, always defined by the inner jet, which clearly stands out in darkness level with respect to the remaining areas. This will be explained further in a quantitative term in this section. Some of the work most relevant to the present study was performed by Glogowski et al.²², in which a shear coaxial injector was utilized with a design derived from a prototype SSME fuel preburner element using liquid nitrogen (LN2) and gaseous nitrogen (GN2). They stated that the length of the dark core in the acquired images increased significantly upon increasing the chamber pressure from sub- to supersonic, with mass flow rates kept constant. They attributed this to the drop in the relative velocity between the inner and outer (annular) streams. Although temperature measurements were made somewhere downstream of the critical flow venturi location in the feed system, it was not clear how far upstream of the injector exit area this occurred. It is known that small changes in temperature in this thermodynamic region can bring about large changes in density, affecting the parameters, especially outer-to-inner velocity ratio, used to characterize the injector exit conditions. Close examination of the figures presented by Glogowski et al.²² suggests that the dark core (that is, the flow issuing from the center-post) of the jet actually appears to contract in length, while the visual impression of the outer annular flow is that it grows in length.

Measurements of both the liquid core and dark core lengths of a variety of different jets from photographs have been performed by others and reported in the past (see Eroglu et al.⁷). However, the measurement methods are often not discussed in sufficient details. There are many difficulties in performing quantitative measurements of this quantity from images of a jet. For example, if using a strobe light for illumination purposes, the intensity of the background will most likely vary from shot to shot. Another difficulty is the selection of a criterion to assess the location where the core is broken up into separated pieces. It is then possible for two people to make different measurement judgments. Also, with the use of digital cameras capable of collecting thousands of images, a manual measurement becomes an extremely tedious and time consuming task. Therefore, in order to produce repeatable measurements, to account for the variability in the light source intensity, and to be able to process thousands of images, an algorithm is necessary for automated computer processing.

A judicious choice of a threshold level on the brightness scale of an image is necessary, and a single fixed value is not sufficient for all images to consistently determine the end or the break points of the dark core. Figure 11 is a sample image illustrating an automated thresholding procedure for determination of the length of the dark core. Figures 11 a, b, c, and d are, respectively, the untouched original photograph, the image threshold applied between 0-128 to indicate the injector, the image threshold applied between 128-929 to represent the dark core, and the image threshold applied between 929-4095 to depict the background. Figure 12 is the image histogram corresponding to Fig. 11 indicating the number of pixels versus a 12-bit gray scale level. The ability of an algorithm to successfully predict the proper threshold level is based on the physical implications of different gray level zones in an image as shown in Fig. 12. The peak to the left of the dashed line in this figure indicates the injector metal surface areas. With the object (i.e., injector) being backlit and the injector being absolutely opaque, one would expect that the zero level intensity should all represent the injector itself. However, the slight shift of the peak to a higher value is due to stray light being reflected by the chamber windows and other surfaces towards the injector which is then reflected back into the camera. The low number of pixels at gray level values between the dashed and dotted lines in Fig. 12 physically represents the dark core of interest, and the broad noisy peak at gray levels to the right of the dotted line in this figure defines the background.

As mentioned previously, variations of the light intensity from shot to shot are usually significant and a matter of concern. For example, in the case of Fig. 12, the threshold level distinguishing the end of the dark core and the beginning of the background is at a gray level of about 929. However, this value varies from shot to shot in a sequence of images taken at the same operating conditions. Also, it varies more widely when the chamber conditions

are changed due to differences in the refractive index field. Therefore, it is necessary to devise a methodology for an accurate and repeatable determination of the rise of the portion of the curve representing the contribution of the background in these images. More importantly, the outcome should conform to what human eyes determine to be the end of the dark core. To select the threshold level identifying the rise of the background, data from the histogram in this region was curve-fitted, using a non-linear Levenberg - Marquardt least squares algorithm, to a piece of a Gaussian function. This function is then differentiated and the point where the derivative of this curve is equal to e^{-1} was determined to be the threshold level corresponding to the dotted line shown in Fig. 12. Evidence to support the soundness and consistency of this algorithm is shown in Figs. 11 and 13.

Figure 13 is a plot of the dark core length (L) in number of pixels and presents a comparison between a manual measurement by visual inspection and the previously described algorithm using an averaged image of those taken at a fixed operating condition. The error bars in Fig. 13 represent the sensitivity of the measurements to the variations of the automatically-selected threshold level when changed by $\pm 10\%$. The large error bars on several points indicate that a proper selection of this threshold is essential in achieving a reliable result and a good agreement with manual measurements. A large positive error bar indicates a truly-disconnected fluid ligament misinterpreted as being connected and a large negative error bar indicates a truly-connected fluid ligament which is misjudged as disconnected. As seen in Fig. 13, the automated algorithm clearly selects the proper value that agrees well with the manual measurements. This allows for a repeatable measurement procedure of a large set of images. Once a proper threshold is established, direct measurement of the geometrical dimensions of the dark core is made possible by identifying the injector exit plane.

For each condition, an averaged dark core length was calculated based on analysis of each individual image within a set of 30 images and then averaging the results. The dark core lengths are shown in Figs. 14(a) and 15(a) as a function of velocity ratio (VR). The RMS of the variations of this quantity is also shown in Figs. 14(b) and 15(b). Figures 14 and 15 present results for both higher and lower outer-jet temperatures of ~ 190 K ~ 140 K, respectively. The error bars on Figs 14 and 15 represent \pm one standard deviation from the mean values. According to Eroglu et al.⁷, the average of the length measured from individual images of a set can be regarded as the time average. It should be noted that, for each operating condition in this work, length measurements were also made from an averaged image of a set. In general, the length measured from the averaged image is shorter than the average of the individual dark core values calculated in a given set.

Evident in Figs. 14(a) and 15(a) is the fact that the length of the dark core decreases as the chamber pressure is increased. The dark core provides an indication of high-density regions of the flow. A possible explanation of this effect is that, as the chamber pressure increases in the present system, the temperature of the inner jet also increases, causing the density of the inner jet to decrease and leading to a shortened length of the dark core, as seen in Fig. 7. Since the jet begins with a lowered density, less time is then required to fully mix the dark inner jet with the background. At a constant chamber pressure, as VR is increased, the length of the dark core decreases and approaches a plateau region. In a mean sense, when the dark core feels the imposed external acoustic field, its length is shorter than or equal to the length when the acoustic driver is turned off. Under the near- and supercritical chamber pressures, as the VR parameter increases, the difference between the lengths of the dark core, measured with and without the acoustic field, diminishes. The RMS values of the dark-core length fluctuations, shown in Figs. 14(b) and 15(b), exhibit somewhat similar trends to those seen with their mean values. It is known that for a liquid-fueled rocket, atomization and breakup processes, interactions between the propellant jets, droplet formation, and vaporization are all affected by the pressure and, particularly, velocity fluctuations. Also, for any chemically-reacting system, the rate at which energy is released is sensitive to the rate of change of temperature, density, pressure, and, of course, mixture ratio. It is then quite intuitive to relate, in some form, the RMS values of the dark core length fluctuations to mixture ratio variations. On the other hand, a low RMS value can be interpreted as the jet's inherent steadiness and vice versa. Examination of Figs. 14b and 15b clearly shows that this property is drastically reduced as the velocity ratio is increased. Although these results are for a single injector, it is then quite possible that the observed improvement in combustion stability at higher values of velocity ratio is a result of the jet's inability to generate large mass flow rate fluctuations under these conditions, weakening a key feedback line for the self-excitation process. In temperature ramping exercises for instability rating of LOX/H₂ engines, the mass flow rate is usually maintained at a constant value⁴. Therefore, as the temperature of the H₂ is decreased during a ramping episode, the H₂ becomes denser, which decreases the injector velocity ratio. The RMS plots shown here suggest that such a decline in this ratio amplifies the jet's inherent unsteadiness, providing a possible explanation for the engine's eventual arrival into an unstable zone as a temperature ramping test proceeds. Also, the observation reported by Wanhainen¹¹, who found that a decline in LOX density was de-stabilizing, can be explained in a similar manner. Unfortunately, due to small sample sizes, a distinct impact of the acoustic field on the RMS fluctuations is

not evident. A sufficiently large sample size can be acquired through applications of high-resolution and high-speed cameras, such as the one acquired towards the latter part of this project. This is planned for future studies.

A plot of the difference between the dark core lengths when the acoustic field is turned off and on at ~ 3 kHz as a function of the outer-to-inner mass flow rate ratio is shown in Fig. 16. This plot shows that the greatest difference in length occurs near a mass flow rate ratio of approximately 5. If the difference in the dark core lengths is an indication of an impact of the acoustics on the jet, then this plot is similar to previous results presented by Davis and Chehrودي¹³. However, the range of the present data is extended from a mass flow rate ratio of approximately 10 to 25.

Many expressions for the prediction of the liquid core length have been proposed, which often involve parameters such as the Webber number (We), the Reynolds number (Re), the momentum flux ratio (M) = $((\rho U^2)_o / (\rho U^2)_i)$ (sometimes called the dynamic pressure ratio), and VR .⁸ Most expressions having a term to represent surface tension predict a core length of zero when the surface tension becomes negligible (i.e. supercritical). One interesting formula for the core length, proposed by Lasheras et al.²³, is Eq. (1), which was derived from a simple entrainment model, suggested by Rehab et al.²⁴, based on a dynamic pressure continuity at the interface between the outer and inner jets. It is argued by Lasheras et al.²³ that when the We is large, surface tension has no effect on interfacial stability, and therefore does not appear in Eq. (1). Raynal²⁵ modified the dynamic pressure continuity condition to incorporate the effects of surface tension, resulting in Equation (2). This equation contains surface tension and gives a non-zero limit as the surface tension approaches zero. Lasheras and Hopfinger⁸ reported that the constant A should be equal to 6, and the constant B , which was evaluated from Raynal's²⁵ experiments, to be about 10^{-3} for water and air coaxial jets. In these equations, U_i and U_o are inner and outer jet mean velocities, and M is the outer-to-inner momentum flux ratio.

$$\frac{L}{D_i} \cong \frac{A}{\sqrt{M}} \left(1 - \frac{U_i}{U_o} \right)^{-1} \quad (1)$$

$$\frac{L}{D_i} \cong \frac{A}{\sqrt{M}} \left(1 - \frac{B\sigma}{\mu_o U_o} \right)^{-1/2} \quad (2)$$

Comparison of the present measurements for the average length of the dark core with values predicted by Equations (1) and (2) are given in Fig. 17 (a) and (b). It is plotted as measured normalized length (L/D_i) with no externally-forced acoustic field versus the predicted L/D_i values from these equations. In our case, the constant A was selected to be equal to 13 for supercritical and near-critical pressures and 26 for subcritical pressures, with the constant $B = 10^{-5}$ in order to obtain the agreement level seen in Fig. 17. In Fig. 17, the diamond, circle, and up-triangle symbols represent sub-, near-, and supercritical pressures, respectively. The hollow and solid symbols represent the higher and lower outer-jet temperatures, respectively. Equation (1) is intended for use with high We numbers. The range of the We numbers for our data set ranges from 32 to 4000, based on the relative velocity of the inner and outer jets. For $M > 0.1$, the average deviation for the values calculated using Eqs. (1) and (2) are to within 37% and 22% of the measured values, respectively. Apparent in Fig. 17 is that the subcritical data set (the diamond symbols) has a slightly different slope than that calculated using the near- and supercritical information. This may indicate a different dependence on M for these two sets of data.

Figure 18 is a plot of L/D_i versus M with the same symbol definition as those shown in Fig. 17. The dashed and dotted curves in Fig. 18 represent the following functional form: $L/D_i = C/M^n$, where C and n are 26 and 0.2 for subcritical pressures (dashed line) and 13 and 0.5 for near- and supercritical pressures. Engelbert et al.²⁶ proposed equations of this type with $n = 0.3$ for coaxial air-blast atomizers. From Fig. 18, there is an apparent difference in the exponent of M between the subcritical and supercritical pressure data. However, the exponent of 0.5 for the near- and supercritical pressure cases is consistent with Eqs. (1) and (2). The lowest momentum point for the near-critical chamber pressure at the lower outer-jet temperature (solid circle and for $M < 1$) shows a length that instead agrees with the subcritical dashed line having an exponent of 0.2. This point exhibited a bimodal distribution in dark core length values as opposed to a Gaussian distribution seen for most of the data shown here.

IV. Summary and Conclusions

Radial mean temperature measurements were made from a coaxial jet under sub-, near-, and supercritical pressures at a fixed axial location very near the injector exit plane at a variety of outer-to-inner jet velocity ratios. Two nominal temperature levels (~140K and 190K) were selected for the outer jet to investigate the impact of the velocity ratios and acoustic field on the coaxial jet considering a nominal cryogenic temperature for the inner jet. To the best of the authors' knowledge, this level of detailed measurements has not been previously performed. True exit velocity ratios, as opposed to ratios based on upstream values, can now be calculated with sufficient accuracy, especially under near- and supercritical conditions, to aid in interpretation of the results. Under subcritical pressures, temperature profiles exhibit a top-hat behavior at two distinct levels with an abrupt transition from a high (liquid-like for the inner jet) to a low value representative of compressed gases. The transition point is somewhere in the region between the outer and the inner jet flows. Large changes in velocity ratio had no impact on these profiles at the low outer jet temperature, whereas the location of the transition point was affected under the higher outer jet temperature. At near- and supercritical chamber pressures, the inner jet loses its top-hat shape and the temperature profiles exhibit a more gradual transition from the inner to outer jet.

Backlit images were taken at both low (10 Hz) and high speeds (18 kHz) with and without the acoustic driver turned on at 3 kHz. Using images taken at high framing rates, velocity fluctuations in the chamber background fluid and within the jets were observed when the acoustic driver was on. Velocities can be measured by tracking isolated structures in these images. Initial crude measurements of the velocities agreed with the predicted values.

A prominent feature seen in most of the images in the study is the existence of a high-density region, referred to as the "dark core", which is defined by the fluids in the inner jet. An automated method for measurement of the dark core was produced to enable rapid analysis of a large number of images in a repeatable and consistent manner. It is seen that the dark core length decreases at higher chamber pressures, due to the combined effects of inner-tube heat transfer and better inter-jet mixing. As the velocity ratio increases at a constant chamber pressure, the length of the dark core shortens and asymptotically approaches a constant value. This constant value appears to be different for subcritical pressures. The general form of the equations, which were theoretically-derived and experimentally verified for water-to-air injections, agrees reasonably well with data acquired under conditions tested here. Results show the dependence of the outer-to-inner jet momentum ratio to an exponent, with the exponent having a different value for subcritical pressures as opposed to near- and supercritical pressures.

It is hypothesized that a connection to combustion instability can be obtained from the data analyzed thus far by way of the magnitude of the RMS values of the dark core length fluctuations. It is possible that decreases in the fluctuation levels, which were shown here to occur at higher velocity ratios, could weaken a key feedback mechanism for the self-excitation process that is believed to drive the combustion instability in rocket engines. This offers a possible means for improvements in our understanding of combustion instability experienced in engines under higher outer-to-inner jet velocity ratios. Additional analysis and data acquisition are planned to further investigate this initial finding.

Figures and Table

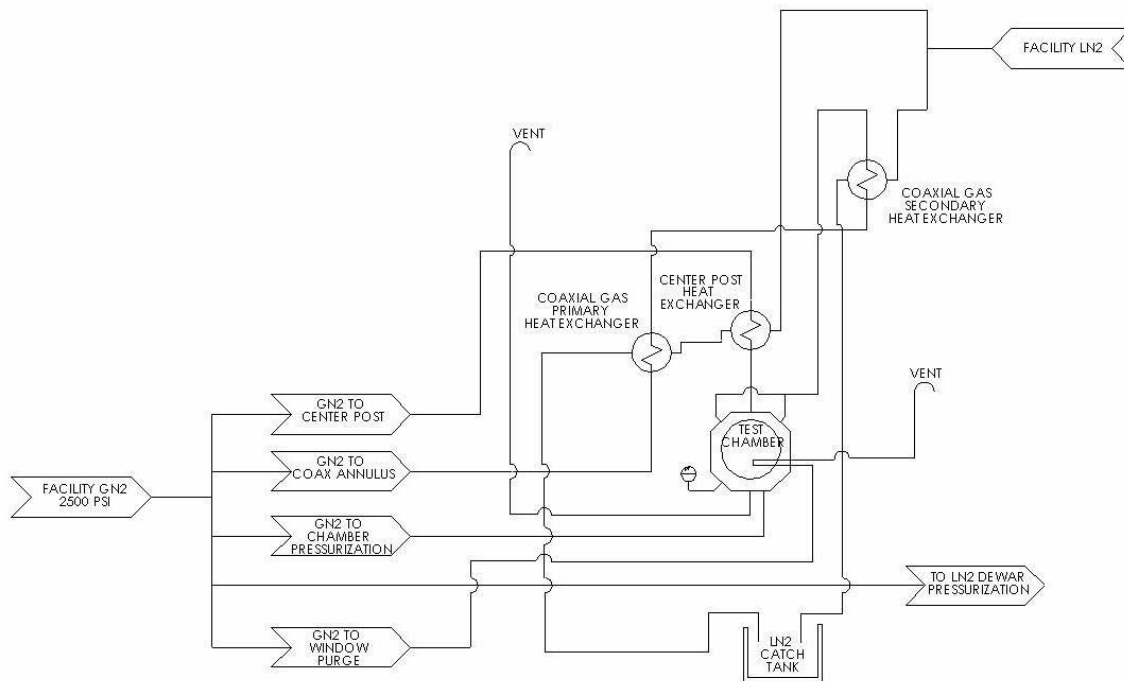


Figure 1. Schematic diagram of the Supercritical Facility at AFRL

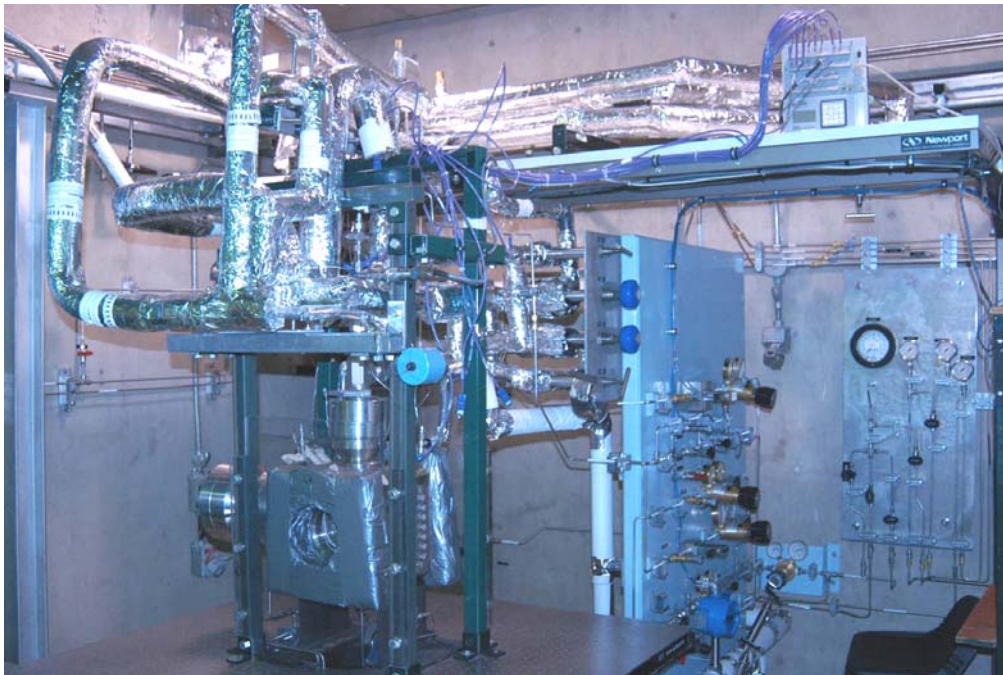


Figure 2. Picture of Supercritical Facility at AFRL

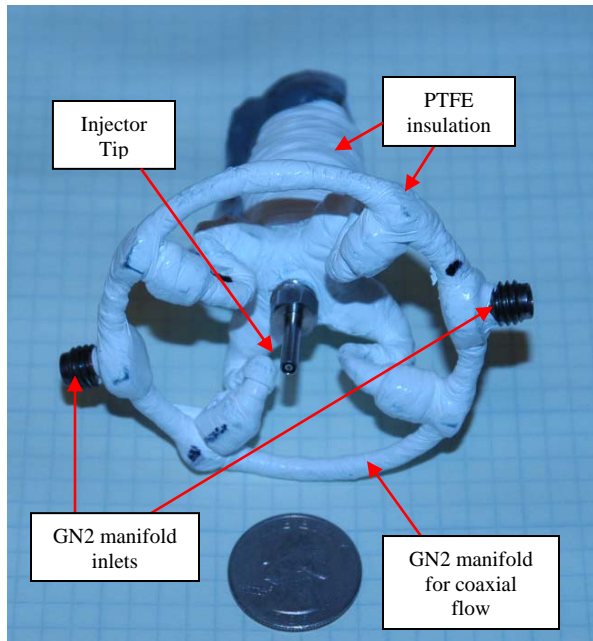


Figure 3. Coaxial injector

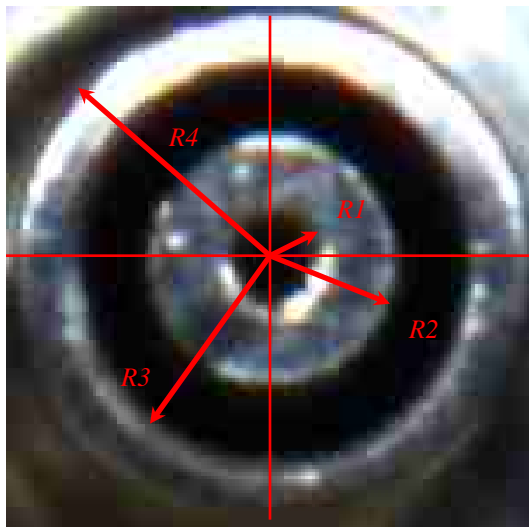


Figure 4. Close-up image of the coaxial injector tip area.
The dimensions of the injector are: $R_1 = 0.25$ mm,
 $R_2 = 0.79$ mm, $R_3 = 1.21$ mm, and $R_4 = 1.59$ mm.

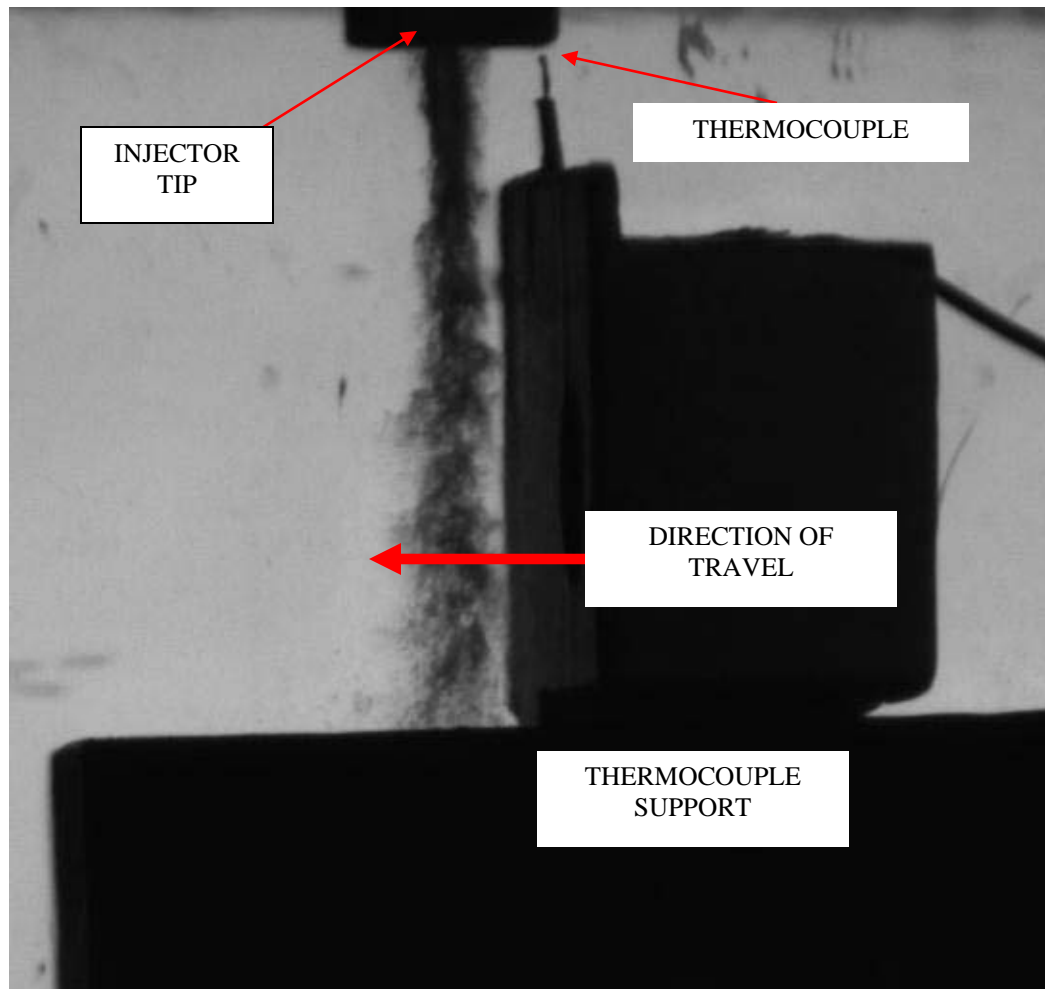


Figure 5. Thermocouple and the support mechanism used to perform radial temperature measurements in the coaxial jet. The thermocouple bead diameter is 0.10 mm. The resolution of the radial distance is 0.01 mm. The distance from the injector exit plane to the thermocouple bead is 0.14 mm or $0.28 D_I$.

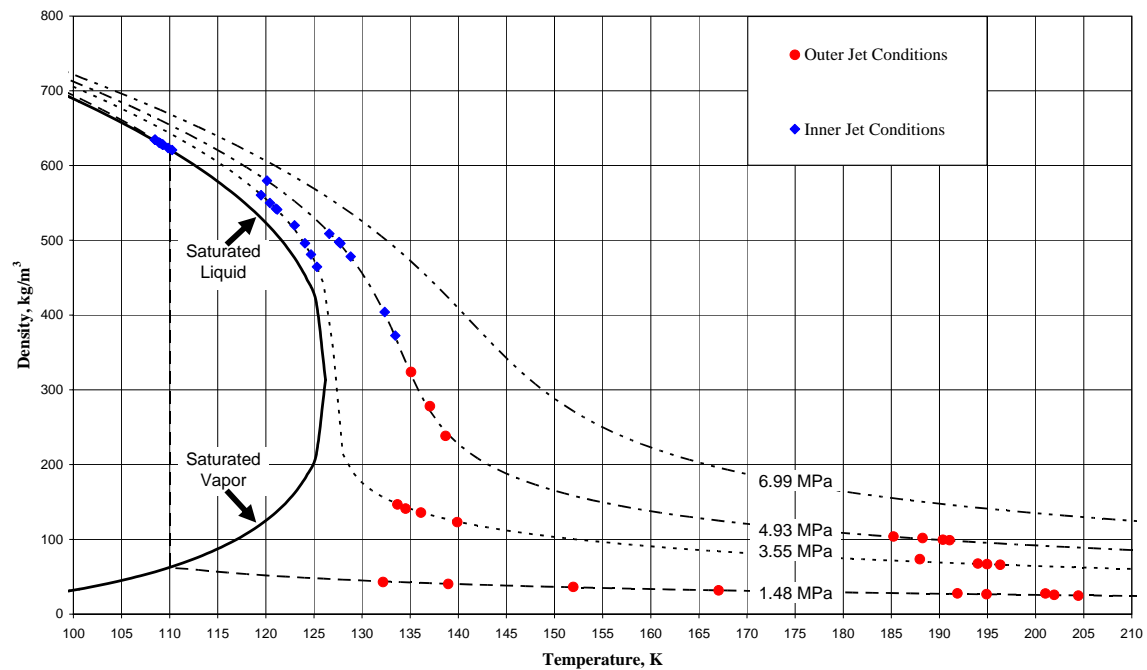


Figure 6. Thermodynamic conditions of the data.

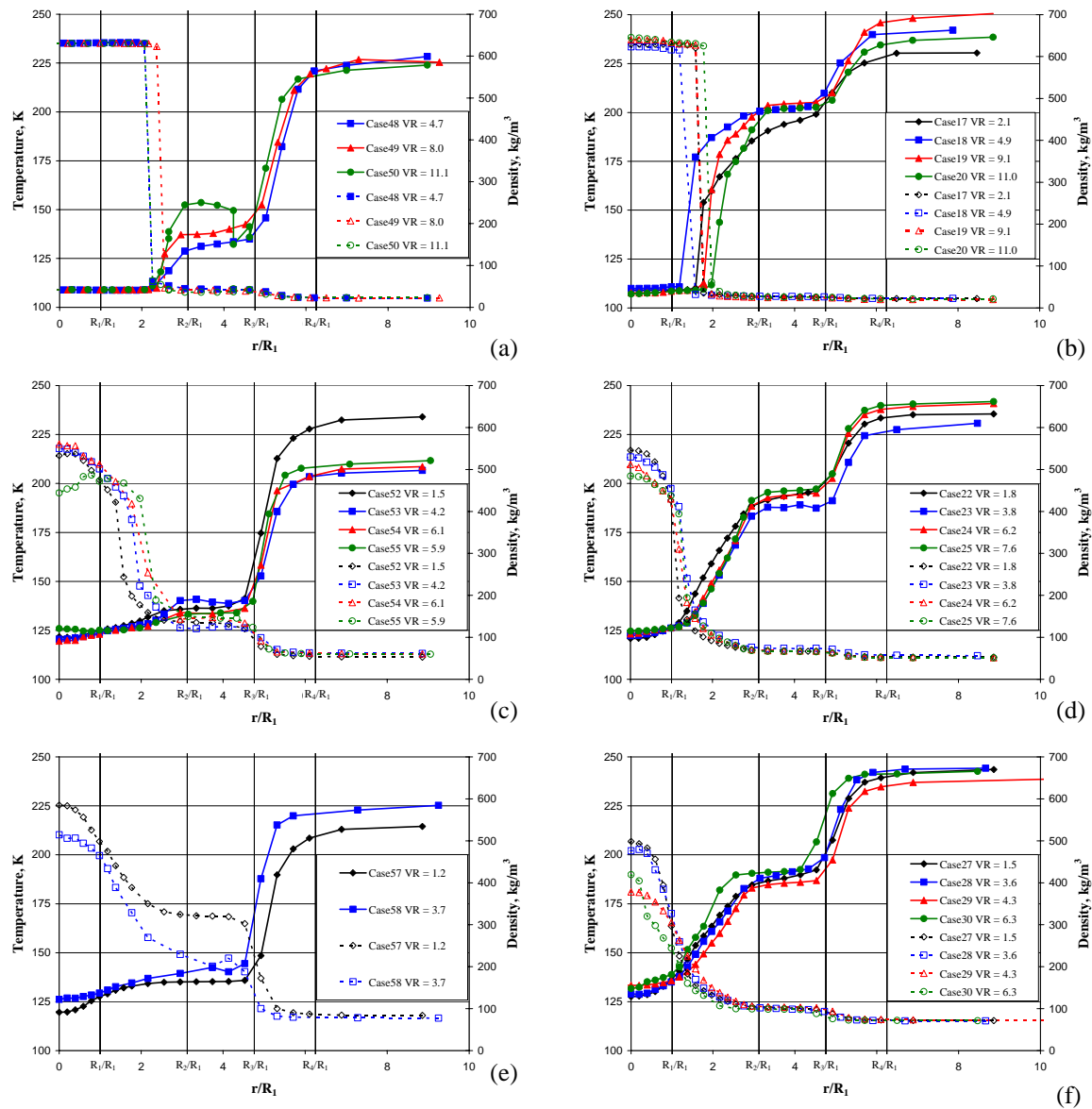


Figure 7. Radial profiles of the measured average temperature and calculated density. Conditions of cases are listed in Table 1. The chamber pressure in the top row is ~ 1.5 MPa, in the middle row is ~ 3.5 MPa, and in the bottom row is ~ 4.9 MPa. The nominal outer jet temperatures in the left and right columns are about 140 K and 190 K, respectively. See Fig. 6 for exact values.

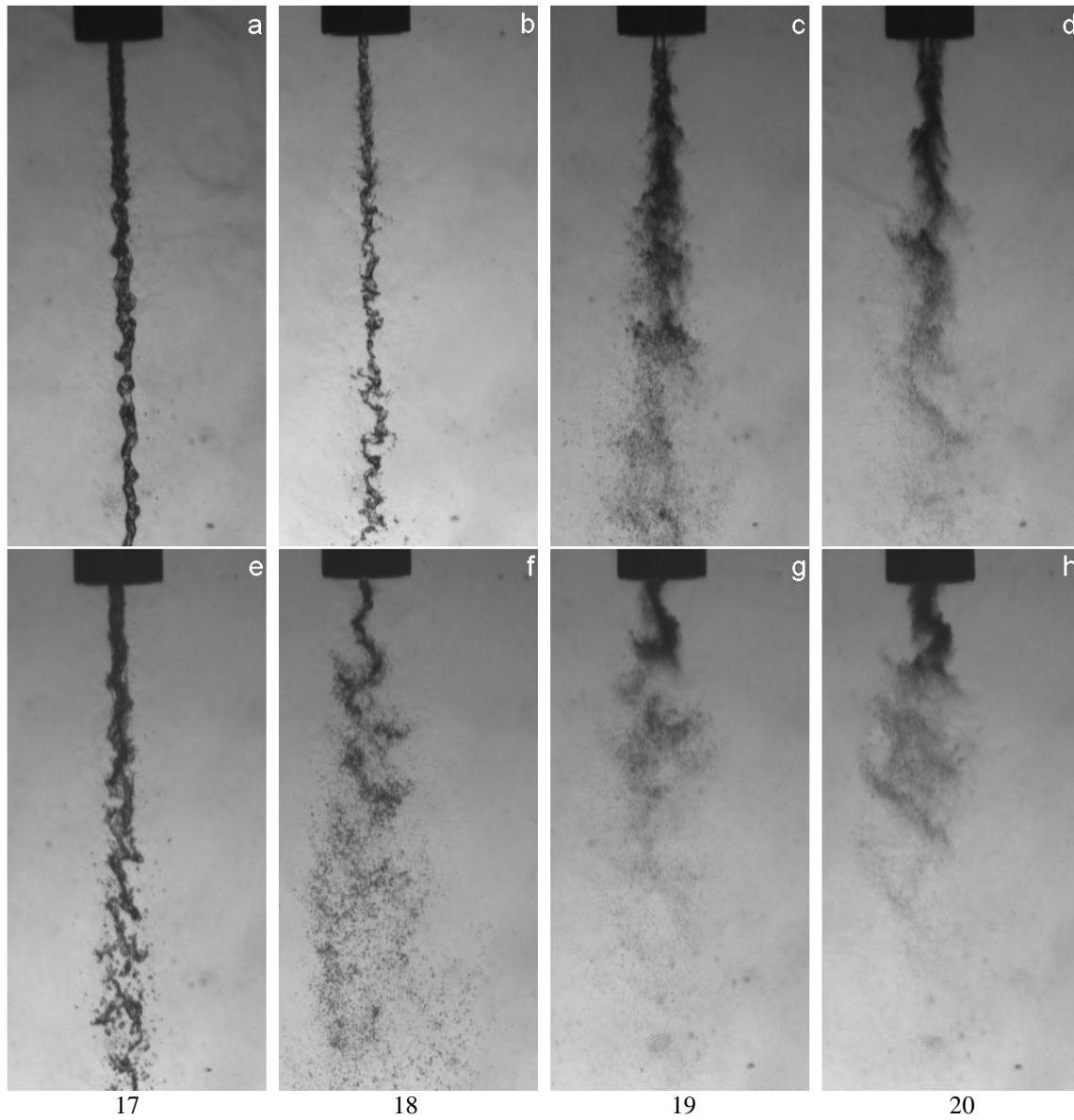


Figure 8(i). Backlit images of coaxial jet at subcritical chamber pressure ($\sim 1.5\text{MPa}$) and at the higher outer jet temperature ($\sim 190\text{ K}$) corresponding to cases 17-20 from left to right. The acoustic driver is *off* for images in the top row and *on* for the bottom row at $\sim 3\text{ KHz}$. The velocity ratio increases from left to right.

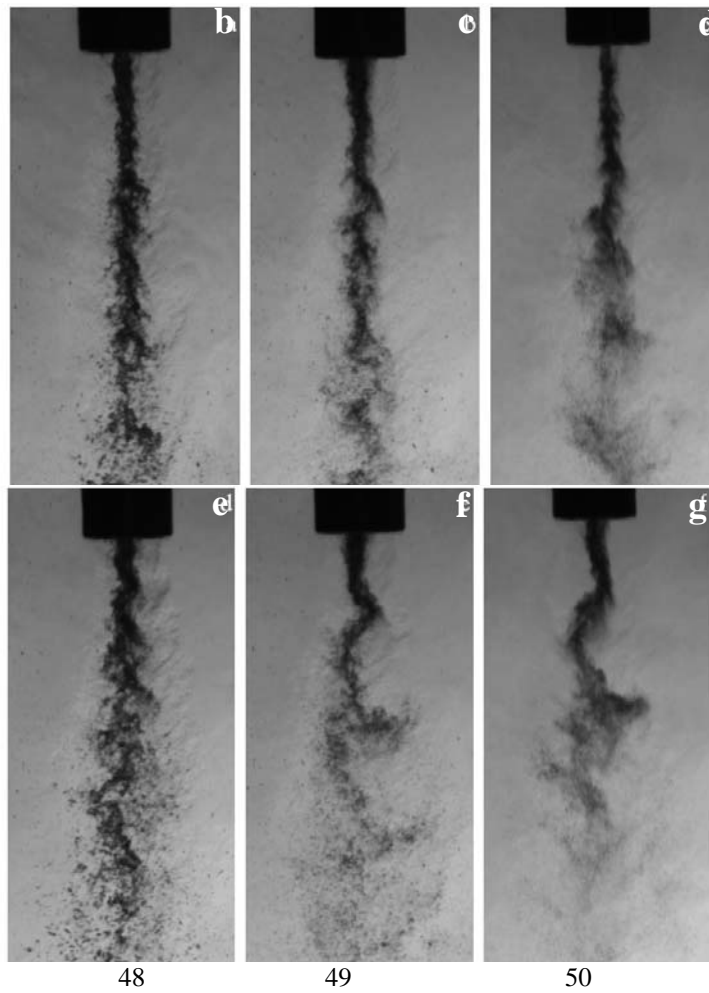


Figure 8(ii). Backlit images of coaxial jet at subcritical chamber pressure ($\sim 1.5\text{MPa}$) and at the lower outer jet temperature ($\sim 140\text{ K}$) corresponding to cases 48-50 from left to right. The acoustic driver is off for images in the *top row* and *on for the bottom row* at $\sim 3\text{ KHz}$. The velocity ratio increases from left to right. The lowest flow rate condition was unattainable experimentally.

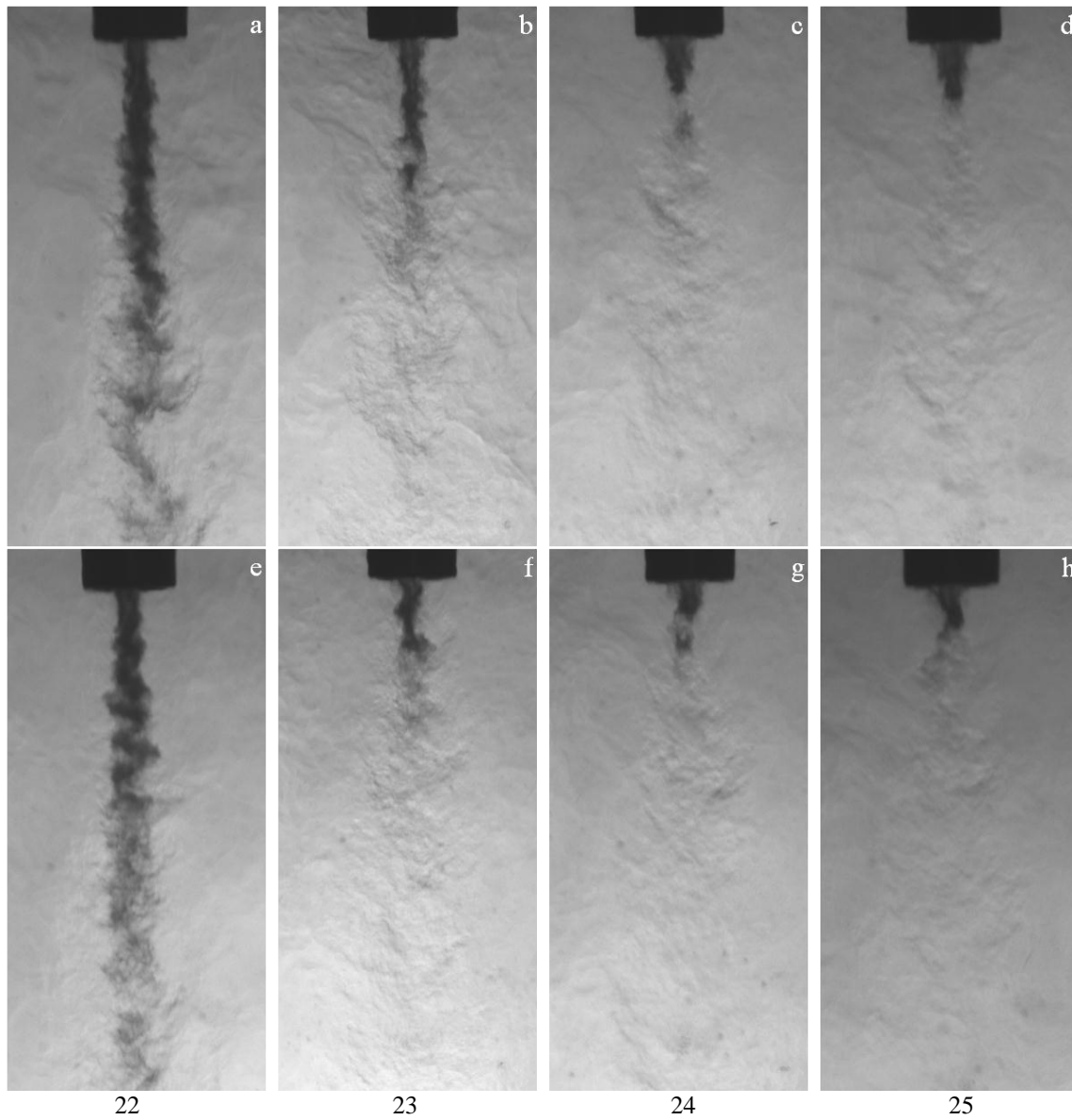


Figure 9. Backlit images of a coaxial jet at nearcritical chamber pressure (~ 3.5 MPa) and at a high outer jet temperature (~ 190 K) corresponding to cases 22-25 from left to right. Images in the *top row* the acoustic driver is *off*, and the *bottom row* the acoustic driver is *on* at ~ 3 KHz. The velocity ratio increases from left to right.

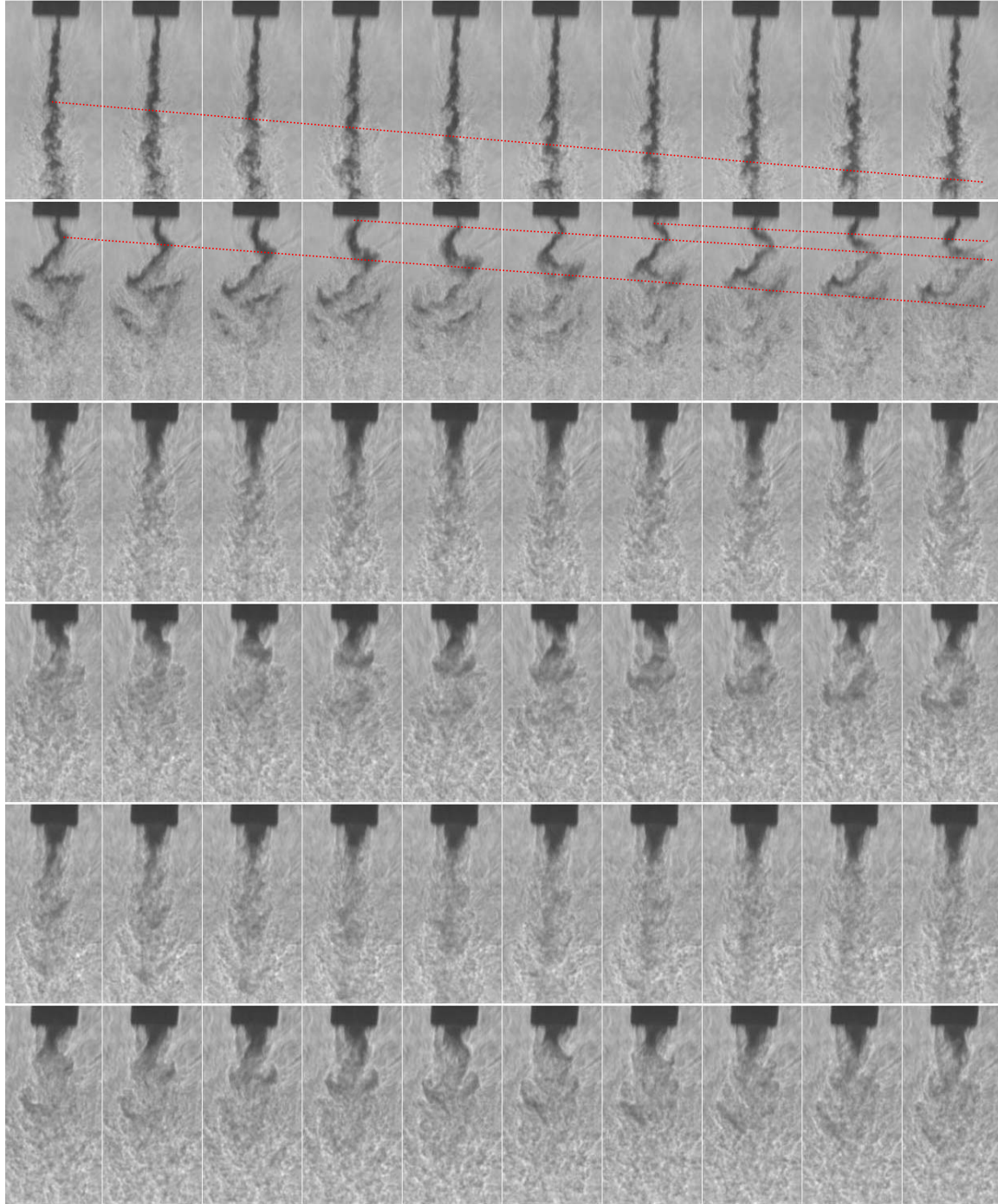


Figure 10. Consecutive frames from high-speed shadowgraph images of case 19, 24, and 29 with the acoustic driver turned on and off. Time increases from left to right with an interval of $55.6\mu s$ between frames. The first two rows are at a subcritical chamber pressure (~ 1.5 MPa, case 19), the third and fourth rows are at a near-critical chamber pressure (~ 3.5 MPa), and the fifth and sixth rows are at a supercritical chamber pressure (~ 4.9 MPa). The acoustic driver is *off* for the first, third, and fifth rows and on for the second, fourth, and sixth at ~ 3 kHz.

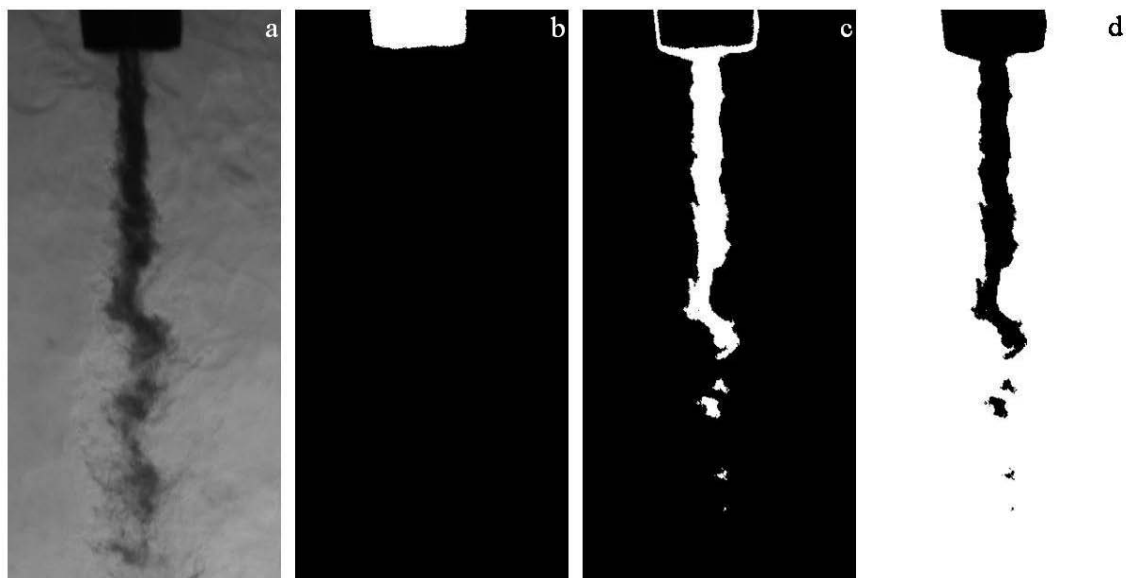


Figure 11. Sample images indicating the effect of threshold levels. Images a, b, c, and d are the original photograph, thresholded between 0-128 indicating the injector, thresholded between 0-128 indicating the injector, thresholded between 128-929 indicating the dark core, and threshold applied between 929-4095 indicating the background, respectively.

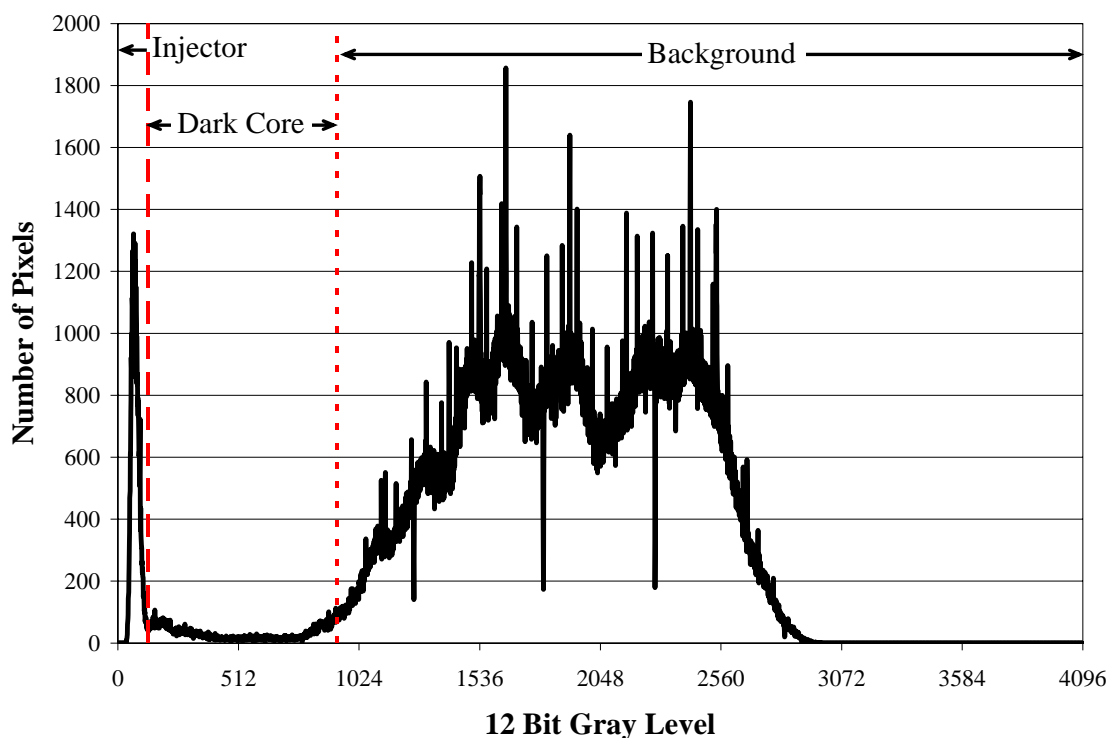


Figure 12. Shows histogram for the image in Fig. 11. The peak between 0-128 (the dashed line) gray levels represent the injector, the low region between 128-929 (between the dashed line and the dotted line) indicates dark core, and the noisy broad peak greater than 929 (beyond the dotted line) indicates the background.

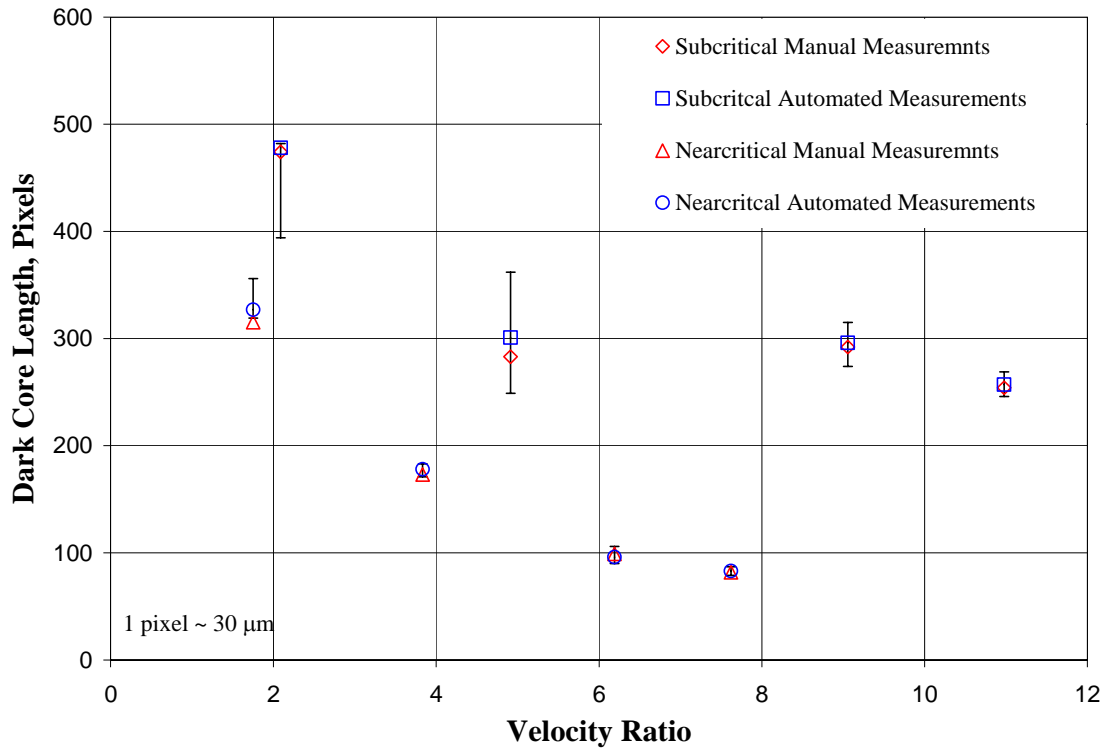


Figure 13. Dark core length (in pixels) versus velocity ratio (outer-to-inner jet) comparing the manual measurement with that of an algorithm programmed for automated calculations of this length using an average image representative for each of the conditions. The error bars represent a sensitivity analysis, varying the automatically-selected threshold level by $\pm 10\%$. The diamonds and the up-triangles are for manual measurements under sub- and nearcritical chamber pressures and the squares and circles are for corresponding pressures using automated computer measurements.

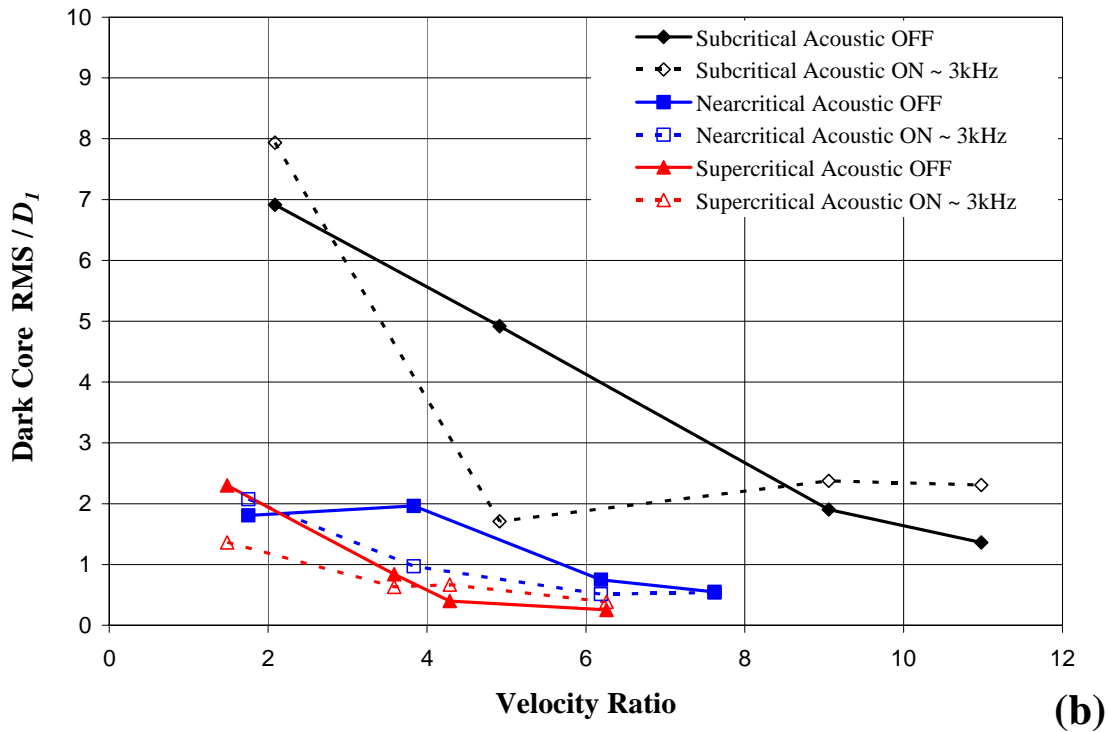
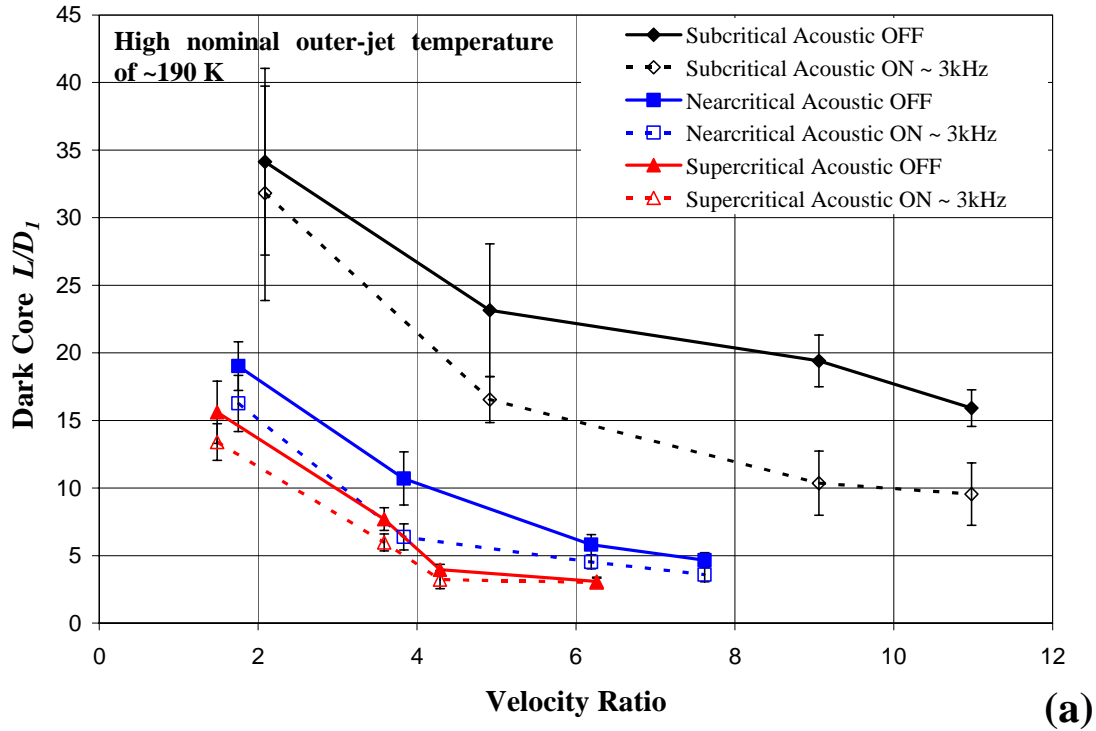


Figure 14. Plots of the dark core length (a) and the RMS of the variations (b) normalized by the inner diameter. The solid symbols and lines represent the data for when the acoustic driver is *off*, and the hollow symbols and dotted lines show the data when the acoustic driver operates at ~3kHz. The diamond, square, and up-triangle symbols are for cases 17-20, 22-25, and 27-30, respectively. The error bars are \pm one standard deviation from the mean. All cases are for the higher nominal outer-jet temperature of ~190 K. Data for each of the cases is listed in Table 1.

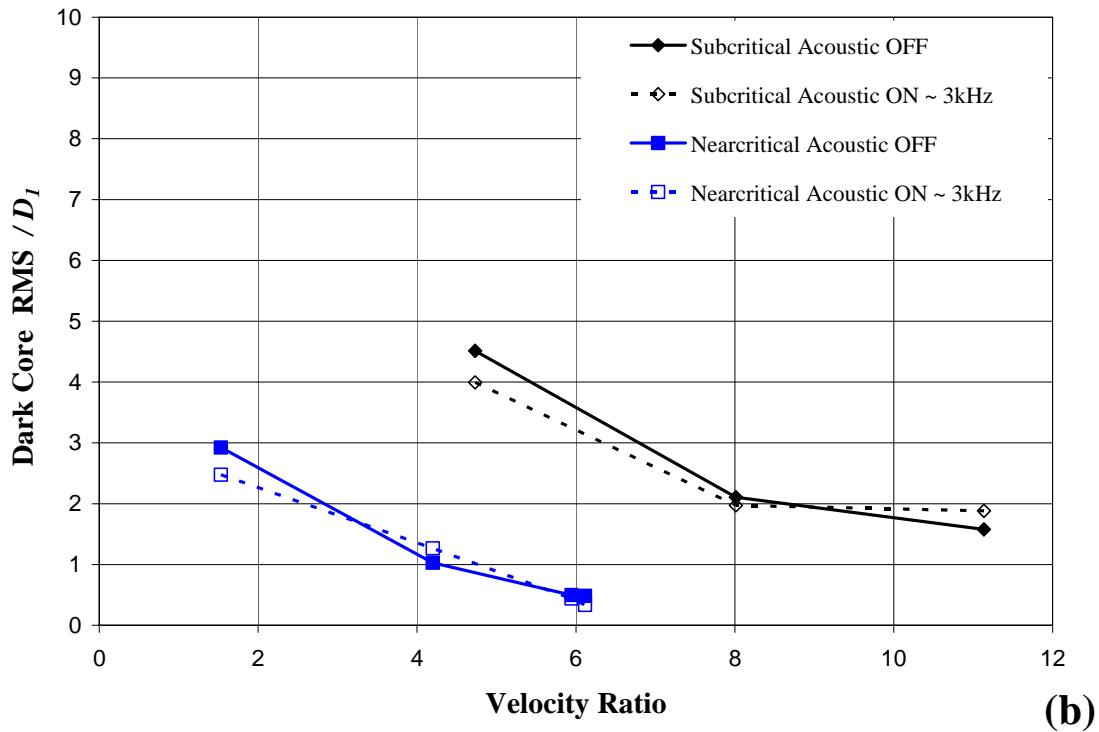
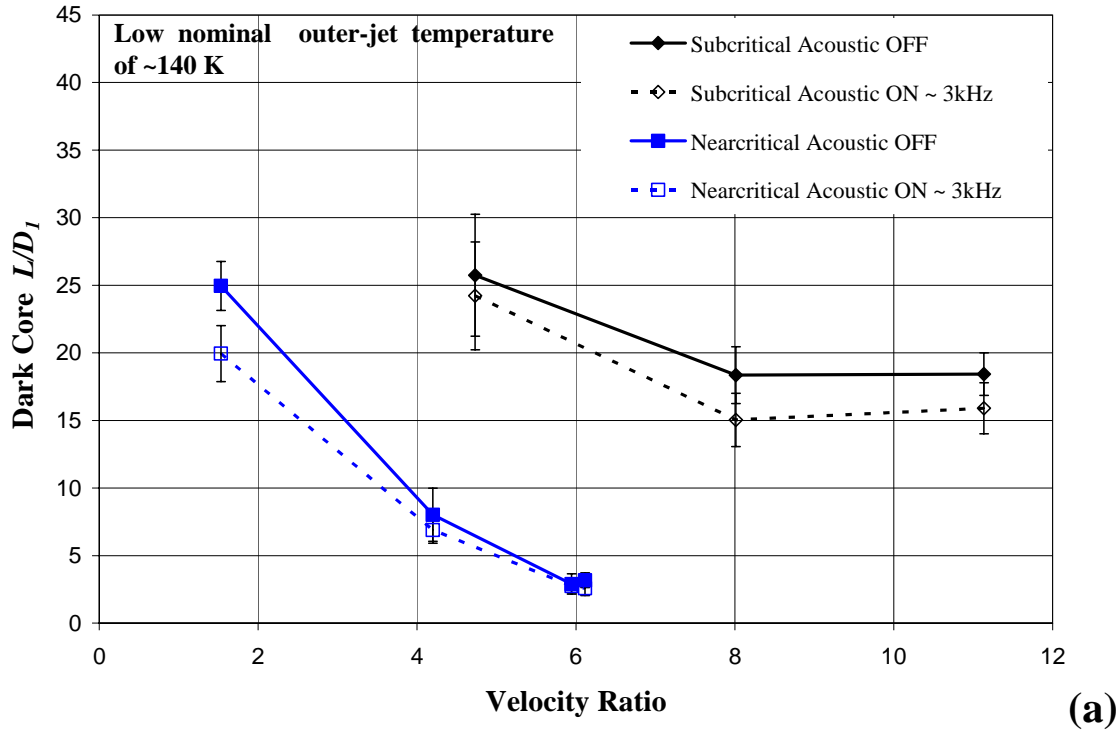


Figure 15. Plot of the dark core length (a) and the RMS of the variations (b) normalized by the inner diameter. The solid symbols and lines represent data for when the acoustic driver *off*, and the hollow symbols and dotted lines show results when the acoustic driver is operated at ~3kHz. The diamond and square symbols are for cases 48-50 and 52-55, respectively. The error bars are \pm one standard deviation from the mean. All cases are for the lower nominal outer-jet temperature of ~140 K. Data for each of the cases is listed in Table 1.

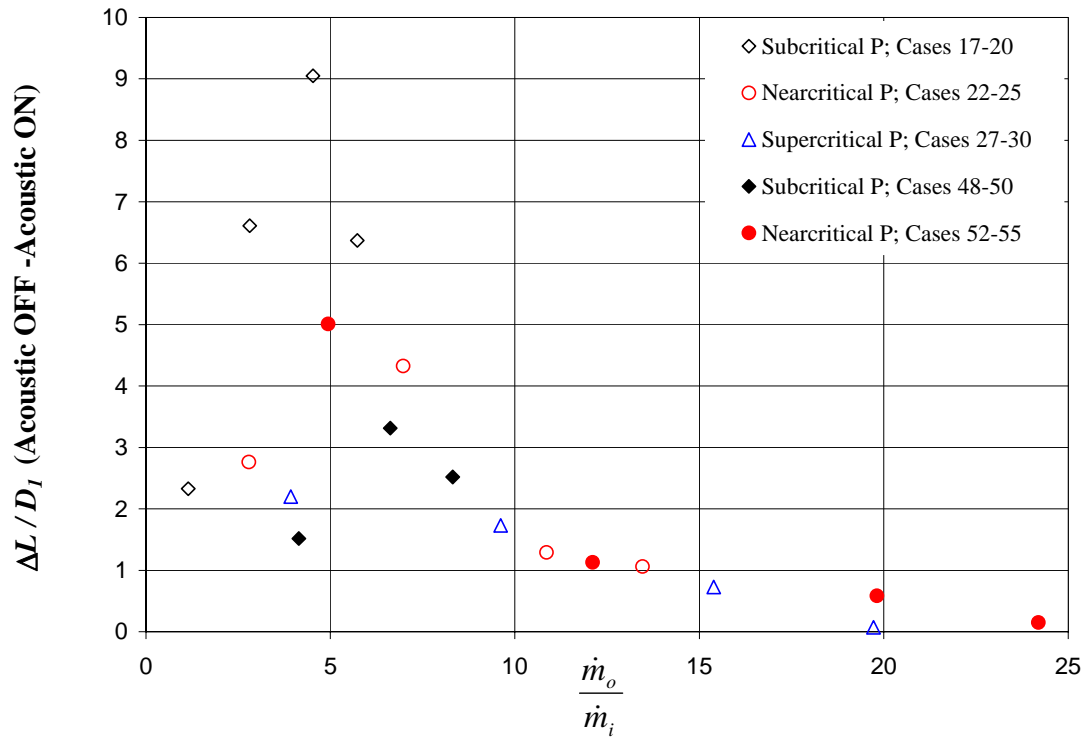


Figure 16. Plots of differences in the dark core length between cases when the acoustic field is off and on at 3 kHz for the same flow conditions as a function of the outer-jet to inner-jet mass flow rate ratio.

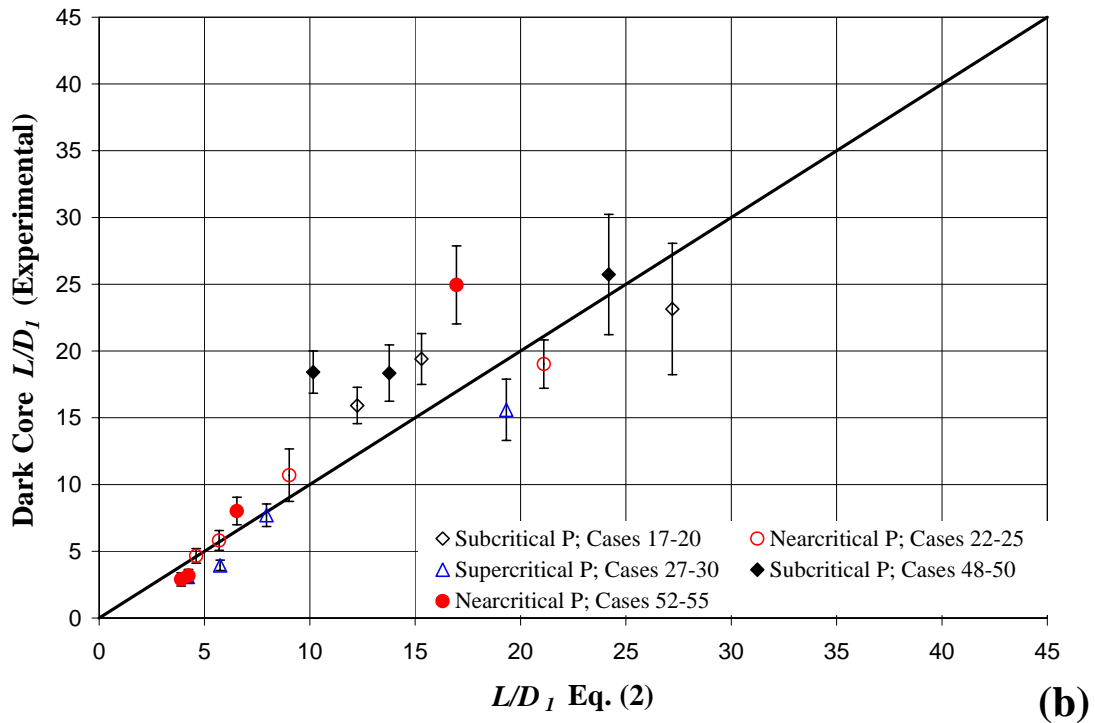
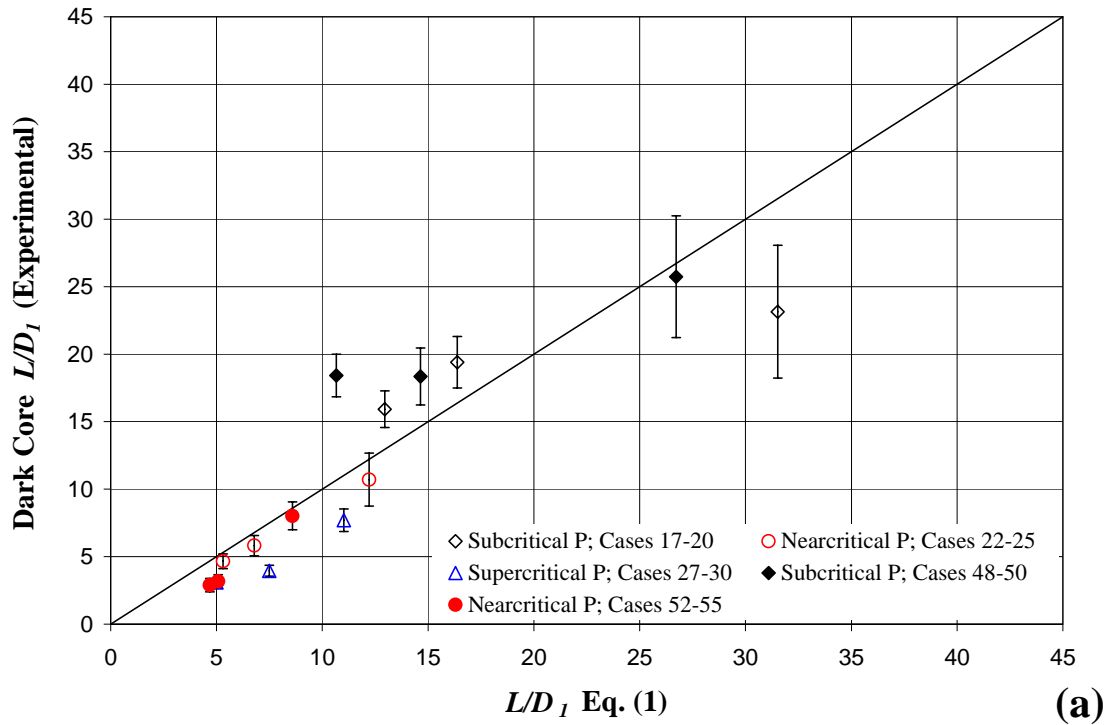


Figure 17. Comparison of the measured L / D_1 from present work with those predicted from equations (1), shown in (a) and (2), shown in (b) which give a non-zero limit as surface tension goes to zero. The diamond, circle, and up-triangle symbols represent sub-, near-, and supercritical chamber pressure respectively. The hollow symbols are at a higher outer-jet temperature (~ 190 K) and solid symbols are at a lower outer-jet temperature (~ 140 K).

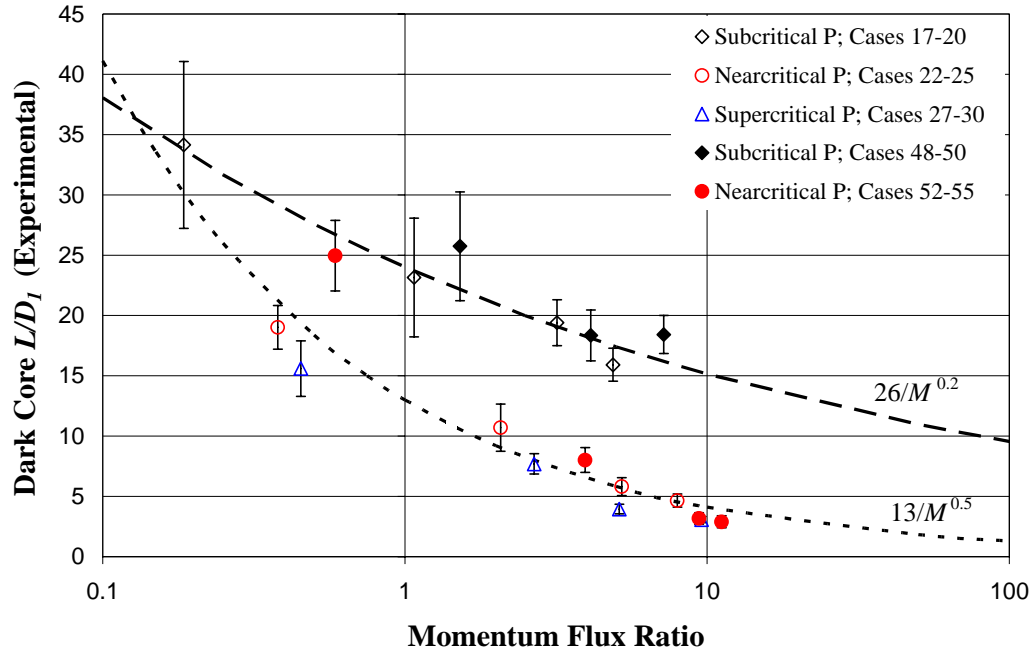


Figure 18. Dark core length versus momentum flux ratio. The diamond, circle, and up-triangle symbols represent sub-, near-, and supercritical chamber pressure, respectively. The hollow symbols are at a higher outer-jet temperature (~ 190 K) and solid symbols are at a lower outer-jet temperature. The dashed line is $26/M^{0.2}$ and the dotted line is $13/M^{0.5}$.

Table1. Data conditions for the various cases.

CASE	Chamber P (MPa)	Outer Jet \dot{m}_o (mg/s)	Inner Jet \dot{m}_i (mg/s)	Chamber T (K)	Outer Jet T (K)	Inner Jet T (K)	Chamber ρ (kg/m ³)	Outer Jet ρ (kg/m ³)	Inner Jet ρ (kg/m ³)
17	1.49	316	276	238	195	109	21.4	26.7	627.9
18	1.59	787	280	248	201	110	21.9	27.6	620.8
19	1.45	1271	281	249	204	108	19.9	24.6	634.5
20	1.49	1602	280	237	202	108	21.6	25.7	634.6
22	3.56	801	287	238	195	121	51.9	66.9	541.1
23	3.70	2001	287	233	188	123	55.4	73.4	520.0
24	3.57	3132	288	235	194	124	53.1	67.5	495.9
25	3.55	3899	290	235	196	125	52.6	66.0	481.1
27	4.97	1156	294	240	188	128	72.6	101.8	495.9
28	4.95	2821	293	237	190	129	73.4	99.5	478.3
29	4.94	4558	296	228	185	133	77.1	103.8	372.5
30	4.94	5812	295	233	191	132	75.0	98.8	404.0
48	1.45	1159	280	231	132	109	21.5	42.9	630.8
49	1.47	1858	281	224	139	109	22.6	40.4	630.0
50	1.50	2328	280	219	152	109	23.6	36.4	627.9
52	3.54	1436	291	228	136	121	54.6	135.8	542.4
53	3.53	3521	291	202	140	120	63.2	123.1	549.9
54	3.52	5731	289	197	135	119	65.2	141.0	560.4
55	3.54	7076	293	197	134	125	65.7	146.8	464.5
57	4.97	2603	293	218	137	128	82.2	278.1	497.7
58	4.88	6547	296	203	139	127	88.8	238.4	508.8
CASE	Outer Jet U_o (m/s)	Inner Jet U_i (m/s)	Outer Jet Re	Inner Jet Re	VR o/i	M o/i	Acoustic Frequency (kHz)		
17	4.5	2.2	7.7E+03	1.2E+04	2.1	0.2	2.96		
18	10.9	2.2	1.9E+04	1.3E+04	4.9	1.1	2.99		
19	19.8	2.2	3.0E+04	1.2E+04	9.1	3.2	2.98		
20	23.9	2.2	3.8E+04	1.2E+04	11.0	4.9	2.98		
22	4.6	2.6	1.9E+04	1.8E+04	1.8	0.4	2.99		
23	10.4	2.7	4.7E+04	1.9E+04	3.8	2.1	2.99		
24	17.8	2.9	7.3E+04	2.1E+04	6.2	5.2	2.95		
25	22.6	3.0	9.0E+04	2.2E+04	7.6	8.0	2.96		
27	4.4	2.9	2.6E+04	2.1E+04	1.5	0.5	3.06		
28	10.9	3.0	6.3E+04	2.2E+04	3.6	2.7	2.99		
29	16.8	3.9	1.0E+05	3.2E+04	4.3	5.1	2.98		
30	22.5	3.6	1.3E+05	2.9E+04	6.3	9.6	2.95		
48	10.3	2.2	3.8E+04	1.2E+04	4.7	1.5	2.94		
49	17.6	2.2	5.9E+04	1.2E+04	8.0	4.1	2.94		
50	24.5	2.2	6.9E+04	1.2E+04	11.1	7.2	2.91		
52	4.1	2.6	3.8E+04	1.8E+04	1.5	0.6	3.06		
53	11.0	2.6	9.5E+04	1.7E+04	4.2	3.9	3.05		
54	15.6	2.5	1.5E+05	1.7E+04	6.1	9.4	3.06		
55	18.5	3.1	1.9E+05	2.4E+04	5.9	11.2	3.01		
57	3.6	2.9	4.7E+04	2.1E+04	1.2	0.8	2.95		
58	10.5	2.9	1.3E+05	2.0E+04	3.7	6.3	2.99		

Acknowledgments

The authors would like to acknowledge Dr. Douglas Talley for his interest, support, and contributions with this ongoing project, and many valuable discussions. Also, the authors would like to acknowledge Mr. Mike Griggs for his valuable contributions in the improvements to the experimental facility. Lt. Matthew Raskie, Mr. Earl Thomas, Mr. Randy Harvey, Mr. David Hill, and Mr. Mark Wilson are thanked for their efforts. Additionally, Ms. Jennie Paton is thanked for making literature available in a timely manner. A great appreciation is extended to Mr. Steven Martin for loaning the authors the Phantom Camera. This work is sponsored by the Air Force Office of Scientific Research under Dr. Mitant Birkan, program manager.

References

- ¹Culick F. E. and Yang, V., "Overview of Combustion instabilities in Liquid-Propellant Rocket Engines," Liquid Rocket Engine Combustion Instability, edited by V. Yang and W. Anderson, Progress in Astronautics and Aeronautics, AIAA, Washington, DC, 1995, pp. 3-38.
- ²Harrje, D. T., and Reardon, F. H. (eds.) "Liquid Propellant Rocket Combustion Instability," NASA SP-194, 1972, pp. 17-19.
- ³Vingert, L., Gicquel, P., Lourme, D., and Ménoret, L., "Coaxial Injector Atomization," Liquid Rocket Engine Combustion Instability, edited by V. Yang and W. Anderson, Progress in Astronautics and Aeronautics, AIAA, Washington, DC, 1995, pp.145-190.
- ⁴J. Hulka, and J. Hutt, "Liquid Oxygen / Hydrogen Instability Phenomena," Liquid Rocket Engine Combustion Instability, edited by V. Yang and W. Anderson, Progress in Astronautics and Aeronautics, AIAA, Washington, DC, 1995, pp. 39-72
- ⁵Rayleigh, Lord, "On the instability of Jets," Proceedings of London Mathematical Society, Vol. 10, 1878.
- ⁶Lefebvre, A. H. Atomization and Sprays, Hemisphere, New York, 1989.
- ⁷Eroglu, H., Chigier, N., and Farago, Z., "Coaxial Atomizer Intact Lengths," Physics of Fluids A, Vol. 3, No. 2, Jan. 1991, pp. 303-308.
- ⁸Lasheras, J. C., and Hopfinger, E. J., "Liquid Jet Instability and Atomization in a Coaxial Gas Stream," Annual Review of Fluid Mechanics, Vol. 32, 2000, pp. 275-308.
- ⁹Miesse, C. C., "The effect of Ambient Pressure Oscillations on the Disintegration and Dispersion of a Liquid Jet," Jet Propulsion, Vol. 25, Oct. 1955, pp. 525-530,534
- ¹⁰Buffum, F. G., and Williams, F. A., "Response of Turbulent Jets to Transverse Acoustic Fields," Proceedings of the 1967 Heat Transfer and Fluid Mechanics Institute, edited by P. A. Libby, D. B. Olfe, and C. W. Van Atta, 1967, pp. 247-276.
- ¹¹Wanhainen, J. P., Feiler, C. E., and Morgan, C. J., "Effect of Chamber Pressure, Flow per Element, and Contraction Ratio on Acoustic-Mode Instability in Hydrogen - Oxygen Rockets," NASA TN D-4733, August 1968.
- ¹²Heidmann, M. F., "Oxygen-Jet Behavior during Combustion Instability in a Two-Dimensional Combustor," NASA TN D-2725, March 1965.
- ¹³Davis, D. W. and Chehroudi, B., "The effects of Pressure and Acoustic Field on a Cryogenic Coaxial Jet," 42nd AIAA Aerospace Sciences Meeting & Exhibit, AIAA, Washington, DC, 5-8 Jan. 2004.
- ¹⁴Chehroudi, B., Davis, D. W., and Talley, D. G., "Initial Results from A Cryogenic Coaxial Injector In An Acoustic Field," 41st AIAA Aerospace Sciences Meeting & Exhibit, AIAA, Washington, DC, 6-9 Jan. 2003.
- ¹⁵Chehroudi, B., Cohn, R., and Talley, D. G., "Cryogenic Shear Layers: Experiments and Initial Growth Rates of Round Cryogenic Jets at Subcritical and Supercritical Pressures," International Journal of Heat and Fluid Flow, Vol. 23, 2002, pp. 554-563.
- ¹⁶Chehroudi, B., Talley, D. G., and Coy, E. B. "Visual Characteristics and Initial Growth Rates of Round Cryogenic Jets at Subcritical and Supercritical Pressures," Physics of Fluids, Vol.4, No. 2, Feb. 2002. pp. 850-861.
- ¹⁷Chehroudi, B., Cohn, R., Talley, D. G. and Badakhshan, A., "Raman Scattering Measurements in the Initial Region of Sub- and Supercritical Jets," 36th AIAA/ASME/SAE/ASEE Joint Propulsion Conference and Exhibit, AIAA, Washington, DC, 17-19 Jul. 2000.
- ¹⁸Chehroudi, B., Talley, D., and Coy, E. B., "Initial Growth Rate and Visual Characteristics of a Round Jet into a Sub- to Supercritical Environment of Relevance to Rocket, Gas turbine, and Diesel Engines," 37th AIAA Aerospace Science Meeting and Exhibit, AIAA, Washington, DC, 11-14 Jan. 1999.
- ¹⁹Chehroudi, B., Talley, D. G., and Coy, E. B., "Fractal Geometry and Growth Rate Changes of Cryogenic Jets Near the Critical Point," 35th AIAA/ASME/SAE/ASEE Joint Propulsion Conference and Exhibit, AIAA, Washington, DC, 20-24 Jun. 1999.
- ²⁰REFPROP, Reference Fluid Thermodynamic and Transport Properties, Software Package, Ver. 7.0, NIST, U.S. Department of Commerce, Gaithersburg, MD, 2002.
- ²¹Faragó, Z., and Chigier, N., "Morphological Classification of Disintegration of Round Liquid Jets in a Coaxial Air Stream," Atomization and Sprays, Vol. 2, 1992, pp. 137-153.
- ²²Glogowski, M., Bar-Gil, M., Puissant, C., Kaltz, T., Milicic, M., and Micci, M., "Shear Coaxial Injector Instability Mechanisms" 30th AIAA/ASME/SAE/ASEE Joint Propulsion Conference, AIAA, Washington, DC, 27-29 Jun. 1994.

²³Lasheras, J. C, Villiermaux, E., and Hopfinger, E. J., "Breakup and Atomization of a Round Water Jet by a High Speed annular Air Jet," J. Fluid Mech. Vol. 357, 1998, pp. 351-379.

²⁴Rehab, H., Villiermaux, E., Hopfinger, E. J., "Flow Regimes of Large Velocity Ratio Coaxial Jets," J. Fluid Mech., 1997, pp.357-381.

²⁵Raynal, L. Instabilite et entrainement a l'interface d'une couche de mélange liquid-gaz, Thèse de Doctorat, Université Joseph Fourier, Grenoble, France, 1997. In Ref. 8.

²⁶Englebert, C., Hardalupas, Y., and Whitlaw, J. H., "Breakup Phenomena in Coaxial Air-Blast Atomizers," *Proc. R. Soc.*, Vol. 451, London, 1995, pp. 189-229.

PREPRINT

EXPERIMENTS ON A COAXIAL INJECTOR UNDER AN EXTERNALLY-FORCED TRANSVERSE ACOUSTIC FIELD

D. W. Davis and B. Chehroudi

ERC, Inc.

Edwards AFB, CA

and

D. G. Talley

AFRL/PRSA

Edwards AFB, CA

ABSTRACT

In order to gain a better understanding of some of the underlying physics associated with the interaction of high-amplitude acoustic waves and a coaxial-jet type injector similar to those used in cryogenic liquid rockets, a non-reacting-flow experimental investigation was conducted under sub-, near-, and supercritical chamber pressures, with and without acoustical excitation. Past research works on this subject have shown both the relevance and importance of geometrical changes in an injector's exit-area and its nearby physical and fluid mechanical processes. On this basis, special attention is paid in collecting spatially-resolved mean temperatures and documenting the aforementioned interactions at the exit of this injector. Short-duration and high-speed digital cameras provided information on the dynamic behavior of this jet under a variety of conditions. Mean and root mean square (RMS) values of the coaxial-jet dark-core length fluctuations were measured from the acquired images via a computer-automated method. It is seen that as the outer-to-inner jet velocity ratio increases, the RMS of the dark-core length fluctuations decreases. It is hypothesized that a connection to rocket instability can be obtained from the data analyzed thus far by way of the magnitude of the RMS values of the dark-core length fluctuations. It is possible that decreases in the fluctuation levels, which were shown here to occur at higher velocity ratios, could weaken a key feedback mechanism for the self-excitation process that is believed to drive the combustion instability in rocket engines. This could offer a possible explanation of the combustion stability improvements experienced in engines under higher outer-to-inner jet velocity ratios. Additional analysis and data acquisition are planned to further investigate this initial finding. Finally, there also appears to be a good correlation between the dark-core length and the outer-to-inner jet momentum flux ratio, but the form of this dependence was found to be different at subcritical pressures than the rest of the chamber conditions (i.e., near- and supercritical cases).

INTRODUCTION

Most, if not all, liquid rocket engines (LRE) experienced a problem with combustion instability during the development phase. The combustion instabilities span from low-frequency, which is a feed-system coupled instability, to high-frequency acoustic instabilities, which depends on the acoustic modes of the chamber. As a consequence, the resulting high-amplitude pressure oscillations can damage the injection and combustion chamber hardware, causing catastrophic failure of the engine. A great deal of work remains to be done to understand the root causes of combustion instability, although two fairly comprehensive treatises on this subject, such as those compiled by Harje and Reardon¹ and Yang and Anderson², have been published.

Many fundamental questions remain to be answered regarding the physical behavior of the propellant jets and other phenomena governing the combustion instability. One such

question is how the fuel and oxidizer jets change behavior during an unstable combustion event. One early study by Heidmann³ investigated the behavior of liquid oxygen (LOX) jets during a

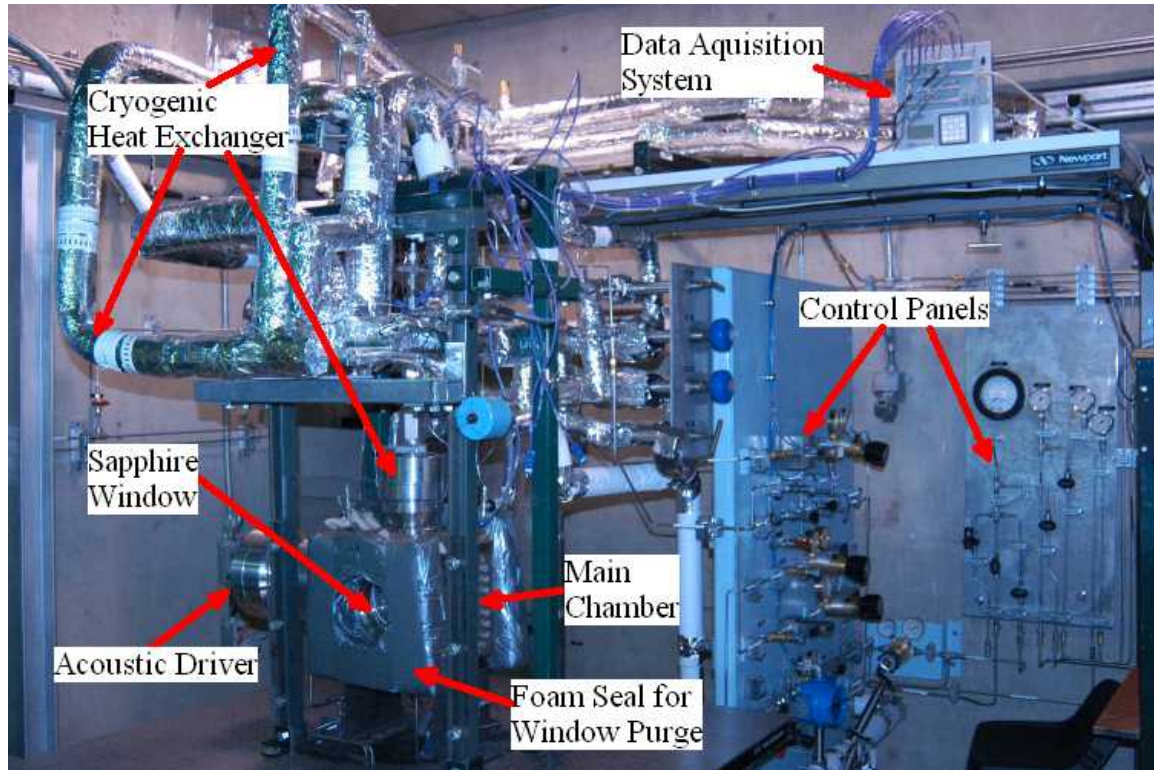


Figure 1. AFRL Supercritical Cold Flow Facility.

period when combustion instability was induced. Hydrogen was introduced into the combustor in a diffuse manner near the LOX jets, making it quite similar to a shear-coaxial injector used in many liquid rocket engines. The LOX jet contracted, once the combustor became unstable. Similar observations were made by Miesse⁴ and Buffum and Williams⁵ under cold flow conditions when a single round jet was excited with an externally-forced acoustic field.

Mixing of the propellant streams, if not controlling, is at least intimately related to the combustion process. To accomplish combustion in a chamber a given chamber size is required to mix and burn the propellants. With a desire to make smaller combustors possessing high efficiencies, while achieving proper thermal management to prevent burnout of the injection hardware, the need for detailed knowledge of the mixing process becomes critical. To a first order approximation, one measure of the mixing process is the so-called liquid-core length, which has been extensively studied by many researchers in the past.⁶⁻²⁴ A compilation of the experimental core-length correlations, semi-empirical theories, and other data for shear coaxial injector studies involving core length are summarized in Table 1 in the appendix. Although the intent of Table 1 is to compile a comprehensive list of papers reporting the core length of different shear-coaxial jets, it is possible that omissions may have occurred. Many of the correlations and semi-empirical theories reviewed indicate scaling of the core length with outer-jet to inner-jet velocity ratio (V_o), outer-jet to inner-jet momentum flux ratio (M), density ratio (ρ_o / ρ_i), Reynolds number (Re), and Weber number (We). Supercritical pressures and transcritical temperatures are found in liquid rocket engines. One difficulty with applying these relationships to the conditions that may be found in liquid rocket engines is the predicted core length is very small or zero in magnitude, because one of the parameters in the equation is We and surface tension diminishes greatly or vanishes all together. Transcritical temperatures means that when the fluid is introduced into the combustion chamber it is initially at subcritical temperature, then is heated to a supercritical temperature. To overcome the difficulty of core length prediction associated

large We , one group of researchers¹⁵⁻²⁰, proposed that M can be used to describe the scaling of core length for shear-coaxial injectors, and need not include We if the We is sufficiently high.

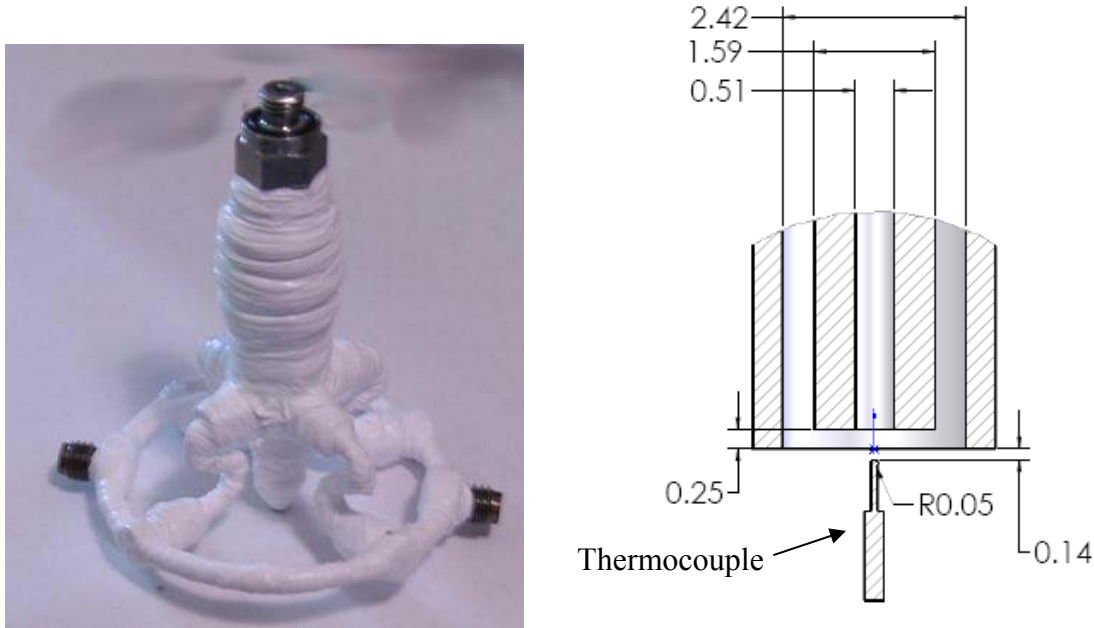


Figure 2. Picture of shear-coaxial injector (left) and cross-section drawing of the injector tip. The thermocouple used to measure exit-plane temperature profiles is shown in the drawing, indicating the relative size and axial position of the measurement.

Chehroudi and co-workers²²⁻³³ have investigated supercritical jet flows at higher Reynolds numbers and turbulent jets of interest to practical applications in propulsion systems. The single round-jet work by Chehroudi et al.²⁵⁻³¹ was produced from two different injectors made from 50 mm long sharp-edged tubes with the inner jet diameters of 0.254 mm and 0.508 mm, (L/D of 200 and 100, respectively). They injected pure N_2 and O_2 into N_2 , He, Ar, and mixtures of CO and N_2 and the arrangement was studied with shadowgraphs and Raman imaging. It was determined that the initial growth rate of a supercritical jet was different from that of a subcritical jet. Furthermore, they quantitatively proved, for the first time, that the initial growth rate of supercritical jet behaved similar to variable-density gas jets.²⁸ From this observation, a phenomenological model of the initial growth rate based upon time scale arguments was proposed which agreed well with the results acquired under sub- and supercritical pressures.²⁸ It is also important to note that Chehroudi et al.²⁹ showed that the growth rate measured from shadowgraphs was about twice as large as the growth rate of the jet measured by Raman imaging of the jet, based on the full width at half maximum (FWHM) jet thickness values. The fractal dimension of the initial region of the jet under sub- and supercritical pressures was also measured for the first time by Chehroudi et al.^{26, 29, 31} and compared to liquid and gas jets in a similar fashion to that of the growth rate. A transition from a liquid jet to a gas jet, from sub- to supercritical, in fractal dimension was observed.

EXPERIMENTAL SET-UP

The experimental facility, shown in Fig. 1, has been described in details previously^{22-24, 31}, and only a brief description will be given here. High-pressure gaseous nitrogen (GN_2) flows into the system, its flow rate measured with Porter Mass Flow meters, and controlled with micrometer needle valves. Temperature conditioning is accomplished by passing the GN_2 through a shell and tube type heat exchanger using liquid nitrogen (LN_2) to cool the GN_2 . The nitrogen flows into both the inner and outer tubes. Temperature of the flow to the inner round jet

of the shear-coaxial injector is considerably lower than that of the outer annular jet, reaching the liquid state. However, the outer jet is cooled well below the room temperature, but is still in gaseous state. The chamber is pressurized with GN_2 at ambient temperature. For reference, the critical pressure and temperature of N_2 is 3.4 MPa and 126.2 K, respectively. The pressure inside the main chamber is maintained by adjusting the outlet flow rate using a triplet of valves to provide an optimum level of control.

The test article consists of a chamber within a chamber. The main, external, chamber is used to create a pressurized environment and is fitted with two sapphire windows for observation of the jet behavior. The smaller, internal chamber, acting as an acoustic resonator cavity, is used to keep the amplitude of the acoustic driver (attached at one end) high in the vicinity of the jet. The Piezo Siren acoustic driver, developed by Hersch Acoustical, is capable of producing amplitudes in an impedance tube of up to 180dB at pressures up to 14 MPa. To obtain sufficiently high amplitudes, the driver must resonate the normal modes of the inner chamber. Therefore, the frequency at which the effects are studied is limited to the first two modes of the inner chamber, being about 3 kHz and 5.25 kHz, respectively. The frequency shifts slightly depending on the chamber fluid, temperature, and pressure. The resulting wave length is much larger than the diameter of the jet. The injector is positioned at a pressure node (a velocity anti-node) to produce maximum velocity fluctuations near the jet.

The shear coaxial injector used in this work (see Fig. 2) is based on the well-characterized design of the single-jet injector used in all previous studies²⁴⁻³⁰ in this apparatus. The center-post made from a stainless steel tube with an I.D. (D_1) of 0.51 mm (0.020") and an O.D. (D_2) of 1.59 mm (0.063") with a length of 50.8 mm (2.00") used to produce the inner jet. The resulting length to I.D. ratio is 100, which is sufficient to ensure a fully-developed turbulent pipe flow conditions at the exit. The outer stainless steel tube creating the annular passage had an I.D. (D_3) of 2.42 mm (0.095") and an O.D. (D_4) of 3.18 mm (0.125") used to produce the outer annular jet. The resulting mean gap width of the annular passage, the hydraulic radius, is 0.415 mm (0.016"), measured from an image taken at the exit of the injector. The injector has a small bias of 8% of the mean gap width. The recess of the inner tube was $0.5 D_1$, 0.25 mm (0.010") from the end of the outer tube.

Because of the proximity of the experimental conditions to the critical point of nitrogen, accurate measurements of temperature were necessary to obtain reliable estimates of density and other quantities computed from the density. Radial temperature profiles were measured using a type E exposed bead thermocouple that was traversed through the jet measuring mean temperature. At cryogenic temperatures, the accuracy of thermocouples is not reliable. However, due to the small size of the system of interest, a Pt-RTD was not feasible. Therefore, it was necessary to calibrate the individual thermocouples against a precision Pt-RTD. The temperature profiles and the details of the calibration were reported elsewhere.^{22,23}

Shadowgraph images of the jet were taken using either a PixelFly CCD camera or a Phantom v5.1 or v7.1 CMOS camera. The advantage that the CMOS cameras presented was the ability to produce high-speed movies of the jet for a period lasting up to several seconds. The framing rate for the movies in this work was 18.00 kHz.

RESULTS AND DISCUSSION

ACOUSTIC WAVE INTERACTION WITH SHEAR-COAXIAL JET

High speed movies of the jet present a large amount of information about the flow being studied. A sample of ten consecutive images at sub- (rows one and two from top), near- (rows three and four), and supercritical (rows five and six) chamber pressures are shown in Fig. 3. Rows one, three, and five are for when the acoustic driver is off and the remaining ones are when it is activated at $\sim 3\text{kHz}$. The evolution of the jet in time is from left to right in Fig. 3, with the time

between frames being $55.6 \mu\text{s}$. Prominent in all the visualizations of the jet is existence of a dark central region which we refer to as a dark core. The dark core under the unexcited subcritical

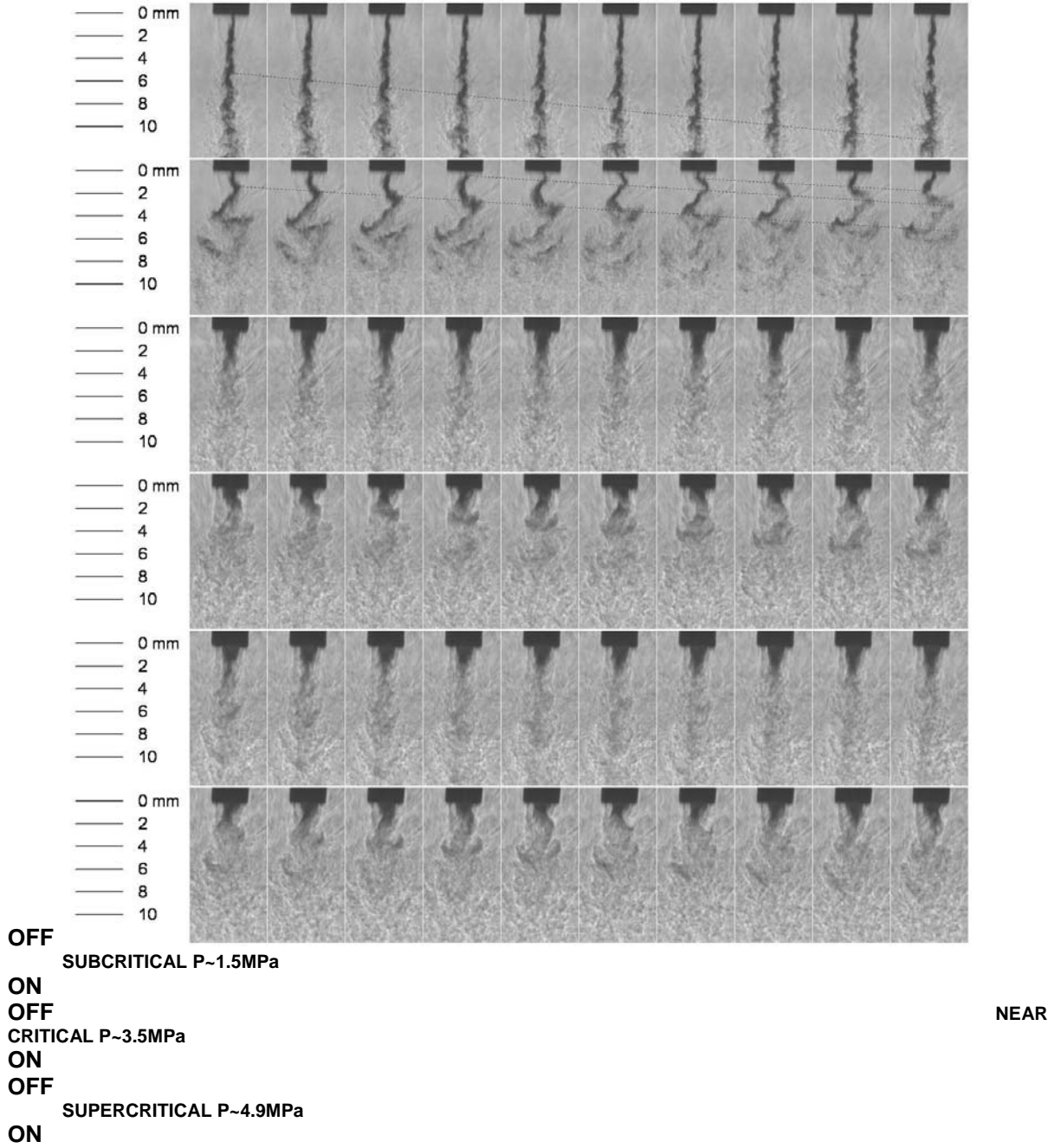


Figure 3. Consecutive frames from high-speed shadowgraph images with the acoustic driver turned off and on at $\sim 3\text{kHz}$. Time increases from left to right with an interval of $55.6 \mu\text{s}$ between frames. The first two rows are at a subcritical chamber pressure ($\sim 1.5 \text{ MPa}$), the third and fourth rows are at a near-critical chamber pressure ($\sim 3.5 \text{ MPa}$), and the fifth and sixth rows are at a supercritical chamber pressure ($\sim 4.9 \text{ MPa}$). The acoustic driver is turned off for the first, third, and fifth rows and on for the second, fourth, and sixth at $\sim 3 \text{ kHz}$. The light gray lines in the first and second rows connect fluid structure as they evolve in time.

pressures (Fig. 3, row one) can be approximated as a cylindrical-like structure with unstable surface waves of low amplitude. However, upon increasing the pressure to near- and supercritical pressures (rows three and five) this structure changes to a more conical shape. The conical structure of the dark core has been reported before for single-phase coaxial jets by Lasheras and Hopfinger.²⁰ As clearly demonstrated in images of Fig. 3 and the other visualizations obtained in this work (not shown here), the conical-shape structure was not observed under two-phase conditions (i.e. subcritical chamber pressure).

Excitation of the jet with acoustic driver yields significantly different behavior of the dark core compared to that of the unexcited one. The strongest effect is observed under subcritical pressures. The cause of this effect is not completely clear at this time. However, it is believed to be as a result of the operation of the acoustic driver at a constant power level at the three

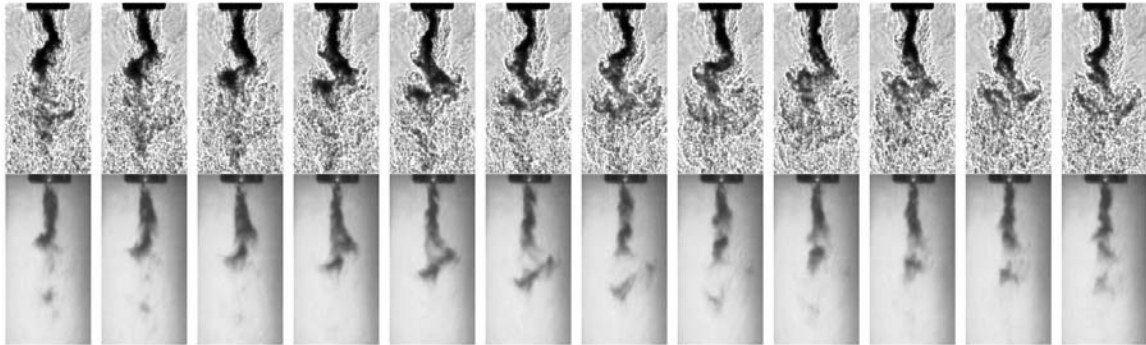


Figure 4. Simultaneous images of the acoustically-excited jet under subcritical conditions viewed from the direction perpendicular (top row) and parallel (bottom row) to the acoustic velocity. The top row was back-lit, but due to geometrical limitations of the apparatus it was necessary to illuminate the jet from the front in the bottom row. Time increases from left to right. The framing rate of the two cameras was 18 kHz and the driving frequency was 3 kHz, approximately two cycles of the acoustic driver are represented in these images.

pressure levels tested. This is a limitation of the current equipment. As the chamber pressure is increased the density of the chamber fluid increases also. Therefore, there is more mass for the driver to move and oscillate, thus the amplitude of the velocity fluctuations is reduced at higher pressures. This remains to be verified, as more data is acquired and analyzed.

The direction of the acoustically-induced velocity fluctuations is horizontal (towards left and right) in images of Fig. 3. The core of the jet forms large-scale sinusoidal structures as a result of this imposed velocity field oscillations. To investigate the modal behavior of the jet, two Phantom CMOS cameras were synchronized and the jet imaged both perpendicular and parallel to the acoustic velocity fluctuations. Twelve consecutive images of the jet (approximately two cycles of the acoustic oscillation period), viewed perpendicular (top row) and parallel (bottom row) to the acoustic velocity field, are shown in Fig. 4. The large-scale oscillations of the dark core are principally in the direction of the acoustic velocity. Some three-dimensional movement of the core does occur, but these motions do not occur in a periodic manner, as do the jet oscillations in the direction of the acoustic velocity. The large-scale oscillations of the dark core seen in the top row of Fig. 4 are periodic and correspond to the driving frequency, as tested at the two resonance modes of the chamber (~ 3 and 5.2 kHz). It appears from these movies, as fluid leaves the injector tip the momentum from the acoustically-induced motion causes a transverse displacement pushing the core of the jet into the higher speed annular jet. The dense fluid from the core experiences acceleration in the axial direction, which is caused by the high speed annular jet. Upon reversal of the acoustic field, the dense fluid, initially from the core now in higher speed annular flow, appears to maintain the transverse component of momentum imparted to it upon leaving the injector and the dense fluid particle does not reverse direction. The dense fluid parcel then slows (both in the axial and transverse directions) as it arrives at the shear layer

between the outer jet and the chamber fluid farther downstream, where a “cusp-shaped” structure is formed from the dense fluid originating in the core of the jet . Subsequent mixing and heat transfer from the outer jet to the inner jet core fluid ultimately causes the fluid parcel to be indistinguishable from the outer jet fluid.

DARK CORE LENGTH MEASUREMENT

As indicated in Table 1 (in the appendix), many techniques have been employed to measure the core length of a coaxial jet, ranging from Pitot tube measurements to analysis of images. The measurements in this work are taken from a great number of images in a systematic fashion to provide repeatable results. In the past, final results have been reported on as few as four number of images.¹⁰

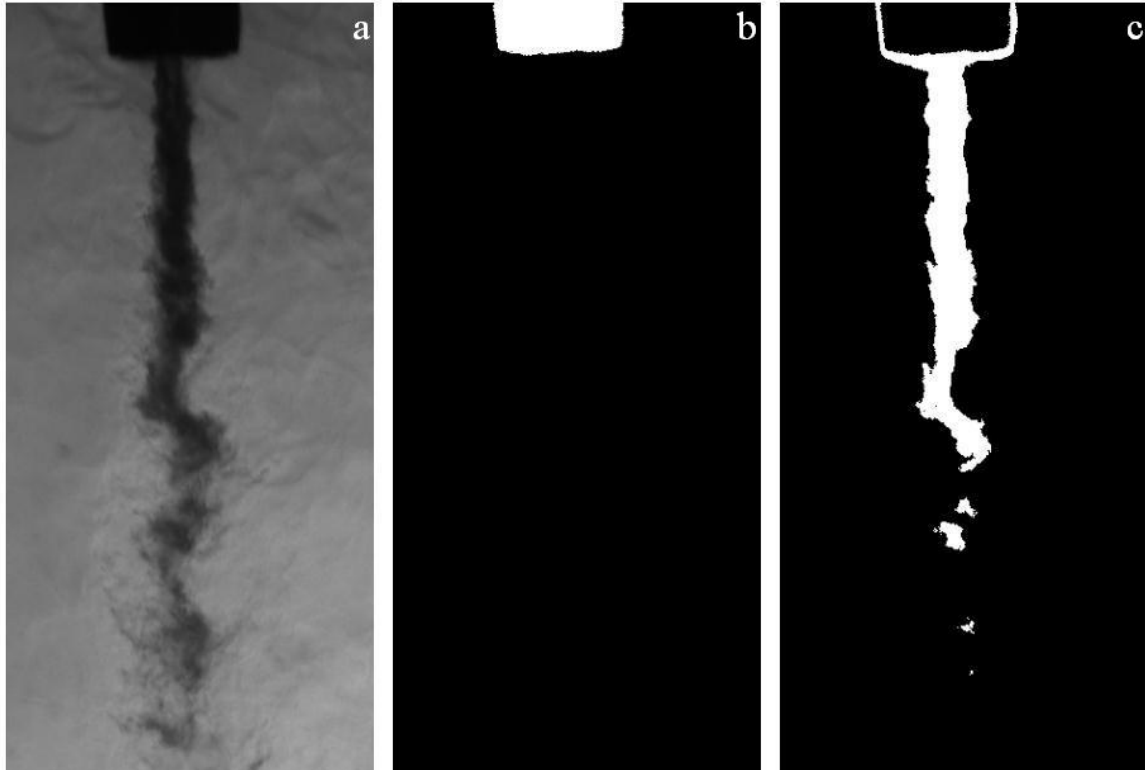


Figure 5. The image of (a) coaxial jet as captured, (b) threshold applied for injector, (c) threshold applied for dark core.

The algorithm for measuring the dark-core length starts with an individual image, such as Fig. 5(a). From this image, the image histogram, that is, number of pixels vs. gray level, is computed, as shown in Fig.6 for the image shown in Fig. 5(a). The first peak, located within the gray-scale values below that of the dashed (vertical) line level denotes those corresponding to the injector tip. Ideally, the

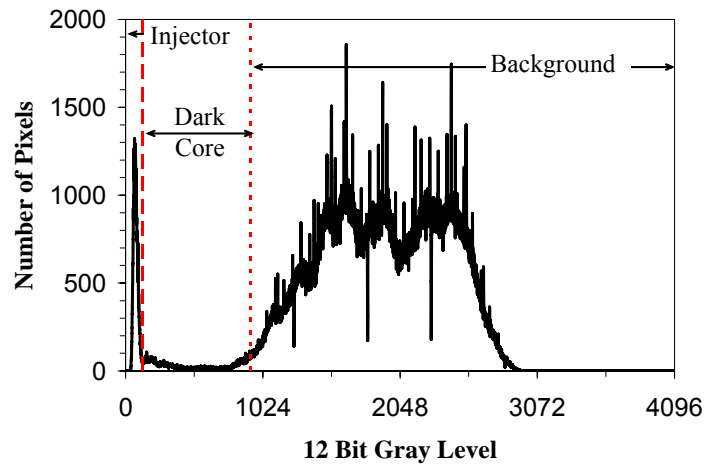


Figure 6. Histogram of image in Fig. 3a.

injector tip should be completely opaque (corresponding to a zero gray-scale value), but due to internal reflections within the chamber this peak shifts slightly off the zero value. The gray levels defining the dark core, ends with the rise of large broad peak on the right, denoting the background, see the dotted vertical line in Fig. 6. This dotted-line gray level is determined by a non-linear curve fitting technique using a Gaussian function to fit to the region of the histogram in the vicinity of the rise of the background information. The slope of this fitted curve is then calculated by differentiation and the gray level at which the slope of the histogram exceeds e^{-1} is determined to be the end of the gray levels defining the dark core, which corresponding to the dotted line in Fig. 6.. A binary threshold is then applied to the image between the gray levels indicated by the injector tip (Fig. 5(b)) and the rise of the background information. The resulting image is shown in Fig. 5(c). Such images are then used to measure the axial length of what we refer to as the “dark core” from the injector exit to the end of the interconnected white region seen in this figure. Results from this technique compared well with those when visual judgments were used, see Davis et al.²³

It should be mentioned that confusion exists in the literature especially when vague definitions are used when defining a core length. The terms potential-core, potential-cone, intact-length, intact-liquid-length, and breakup-length are all used along with various measurement techniques (see Table 1). To be clear, and remove any possible ambiguity from the data, dark-core length is defined here as the connected dark fluid region between the injector exit area and the first break in the core as defined by the adaptive thresholding procedure outlined above.

INFLUENCE OF VELOCITY RATIO ON THE DARK CORE

Velocity ratio (outer-to-inner jet) has been a design parameter for shear-coaxial injectors, particularly, as a criterion to ensure the stable operation of LREs. For LOX/H₂ engines. the design rule-of-thumb has been to keep the velocity ratio greater than about 10 to keep the engine stable.³⁴ Although experimental data suggests this criterion, no physical explanation has been provided. One method to rate a LRE for combustion instability is temperature ramping, which is accomplished by lowering the temperature of the H₂ while maintaining mass flow rate at a constant value. The lower the H₂ temperature is at the onset of the measured combustion instability, the greater the stability margin of that particular LRE. Note that as the H₂ temperature is lowered at a constant mass flow rate, the velocity ratio is also lowered.

To determine the effects of the outer-jet temperature (which is GN₂ in this work) on the coaxial jet, two nominal temperatures were studied (called high and low). The averaged dark-core lengths are shown in Figs. 7(a) and 8(a) as a function of velocity ratio (V_r). The RMS of the variations of the dark core length is also shown in Figs. 7(b) and 8(b). Figures 7 and 8 present results for conditions when the external acoustic field is turned on and off for both nominal high and low outer-jet temperatures of ~190 K and ~140 K, respectively. According to Eroglu et al.¹⁰, the average of the length measured from individual images of a set can be regarded as the time averaged value. It should be noted that, for each operating condition in this work, length measurements were also made from an averaged image of a set. In general, the length measured from the averaged image is slightly shorter than the average of the individual dark-core values calculated in a given set.

Evident in Figs. 7(a) and 8(a) is the fact that the length of the dark core decreases as the chamber pressure is increased. The dark core provides an indication of high-density regions of the flow. At a constant chamber pressure, as V_r is increased, the length of the dark core decreases and appears to approach a constant value. In a mean sense, when the dark core feels the imposed external acoustic field, its length is shorter than or equal to the that when the acoustic driver is turned off. Under the near- and supercritical chamber pressures, as the V_r increases, the difference between the lengths of the dark core, measured with and without the acoustic field, diminishes. The RMS values of the dark-core length fluctuations, shown in Figs. 7 (b) and 8(b), exhibit somewhat similar trends to those seen with the mean values. It is known that

for a liquid-fueled rocket, atomization and breakup processes, interactions between the propellant jets, droplet formation, and vaporization are all affected by the pressure and, particularly, velocity fluctuations. Also, for any chemically-reacting system, the rate at which energy is released is sensitive to the rate of change of temperature, density, pressure, and, of course, mixture ratio. It is then quite intuitive to relate, in some form, the RMS values of the dark-core length fluctuations to mixture ratio variations. On the other hand, a low RMS value can be interpreted as the jet's inherent steadiness and vice versa. Examination of Figs. 7b and 8b clearly shows that this property is drastically reduced as the velocity ratio is increased. Although these results are for a single injector, it is then quite possible that the observed improvement in combustion stability at higher values of velocity ratio is a result of the inability of the jet to generate large mass flow rate

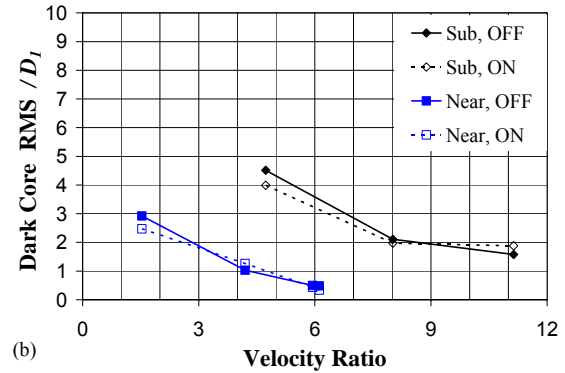
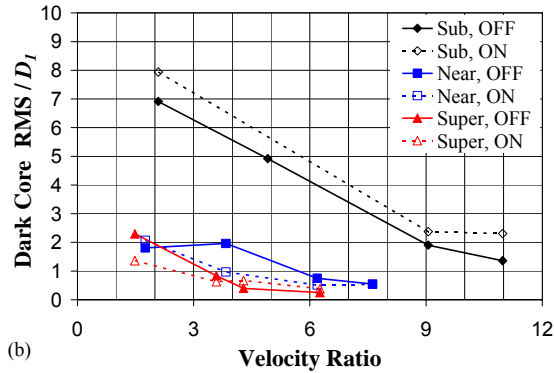
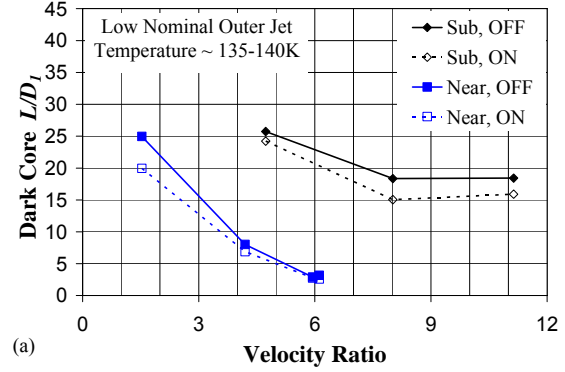
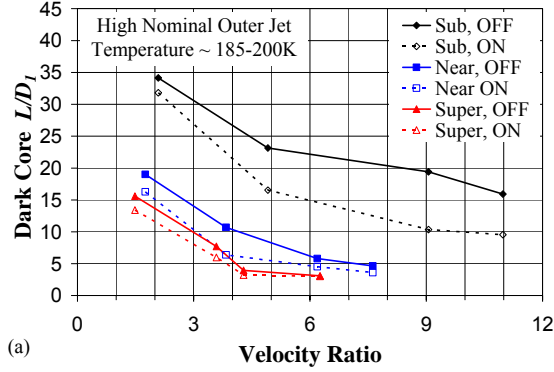


Figure 7. Plot of the averaged dark-core length (a) and the RMS of the length variations (b) normalized by the inner diameter. The solid symbols and lines represent the data for when the acoustic driver is off, and the hollow symbols and dotted lines show the data when the acoustic driver was operated at ~ 3 kHz. The diamond, square, and up-triangle symbols are sub-, near and supercritical chamber pressures, respectively. All cases are for the higher nominal outer-jet temperature of ~ 190 K. In the inset the words sub, near, and super refer to subcritical, nearcritical, and supercritical pressure respectively, and the words OFF and ON refer to the acoustic driver being off and on at ~ 3 kHz, respectively.

Figure 8. Plot of the averaged dark-core length (a) and the RMS of the length variations (b) normalized by the inner diameter. The solid symbols and lines represent data for when the acoustic driver is off, and the hollow symbols and dotted lines show results when the acoustic driver is operated at ~ 3 kHz. The diamond and square symbols are for sub- and nearcritical chamber pressures, respectively. All cases are for the lower nominal outer-jet temperature of ~ 140 K. In the inset the words sub and near refer to subcritical and nearcritical pressure respectively, and the words OFF and ON refer to the acoustic driver being off and on at ~ 3 kHz, respectively.

fluctuations under these conditions, weakening a key feedback line for the self-excitation process. In temperature ramping exercises for stability rating of LOX/H₂ engines, the mass flow rate is usually maintained at a constant value.³⁴ Therefore, as the temperature of the H₂ is decreased during a ramping episode, the H₂ becomes more dense, which decreases the injector velocity ratio. The RMS plots shown here suggest that such a decline in this ratio amplifies the jet's inherent unsteadiness, providing a possible explanation for the engine's eventual arrival into an unstable zone as a temperature ramping test proceeds.

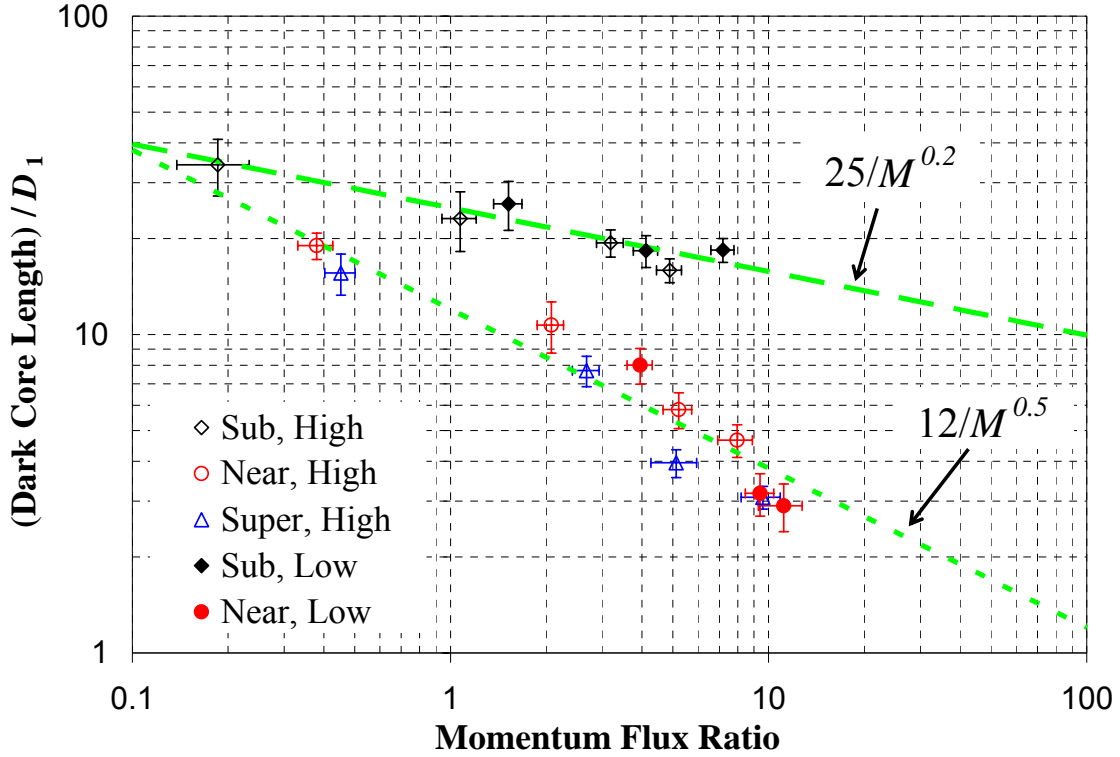


Figure 9. Dark-core length versus momentum flux ratio. The diamond, circle, and up-triangle symbols represent sub-, near-, and supercritical chamber pressure, respectively. The hollow symbols are at a high outer-jet temperature (~ 190 K) and solid symbols are at a low outer-jet temperature. The dashed line is $25/M^{0.2}$ and the dotted line is $12/M^{0.5}$.

SCALING OF THE DARK CORE

As mentioned above, the core length has been scaled with many parameters. In some work, We and Re numbers were used to represent velocity values in nondimensionalized forms, as physical parameters, such as surface tension and viscosity, were not varied. In other work, based on single-phase results, velocity ratio (V_r) or momentum flux ratio (M) were considered as the scaling parameters. The semi-empirical theory of Rehab et al.¹⁷ which is based on an entrainment velocity of the inner jet into the outer jet and a resulting mass balance on the core of the jet, produces an equation suggesting that the length of the core scales with $M^{-0.5}$. This equation was then quantitatively compared to single-phase shear-coaxial jet data, often with equal densities.¹⁶⁻¹⁸ Note that for (inner and outer) jets of equal densities, $M^{-0.5}$ reduces to V_r . The same dependence on M was also reported qualitatively for single-phase shear-coaxial jets of

different densities by Favre-Marinet and Samano-Shettini.²¹ Additionally, Lasheras et al.¹⁹ stated applicability of the same $M^{-0.5}$ dependence form for two-phase shear-coaxial jets. However, they were unable to make core length measurements from their images.

A plot of the measured dark-core length values, of this work, versus momentum flux ratio is shown in Fig. 9. A clear distinction between the subcritical dark-core length (diamond symbols) and that for the near- and supercritical chamber pressures are seen. Subcritical data indicates a much longer length than the supercritical pressure for a given momentum flux ratio.. It should be noted that the near-critical pressure data is slightly supercritical, and both the near- and supercritical pressure conditions produce a single-phase coaxial jet. The dashed line in Fig. 9 is a least-square curve fit to the subcritical data, and the dotted line is a least squares curve fit to the near- and supercritical data. As indicated by the equations on Fig. 9, the single-phase

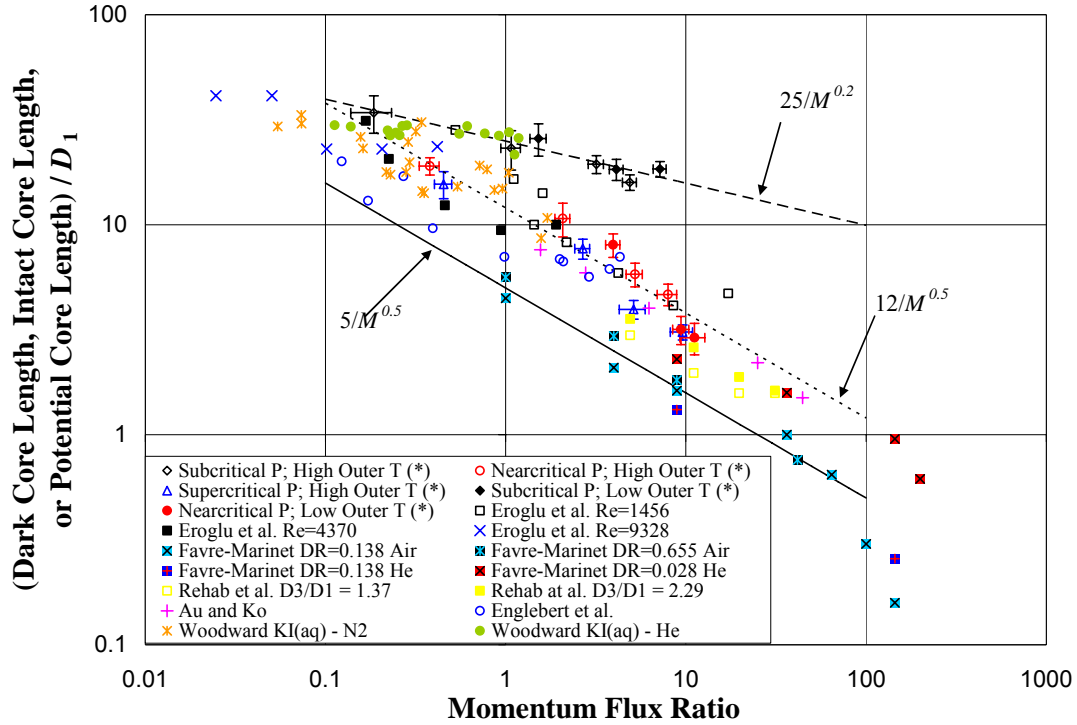


Figure 10. Comparison of present dark-core length with all the core-length data available in the literature vs. momentum flux ratio. Of the data from the literature, Eroglu et al, Englebert et al., and Woodward are two-phase flows and the rest are single phase. The references for the data are found in Table 1.

(i.e., near- and supercritical pressures), data have the same $M^{-0.5}$ dependence form as reported by others.^{16-18, 21} However, the two-phase subcritical data has a weaker dependence, $M^{-0.2}$, than the single-phase dark-core length. Other quantitative differences between subcritical and supercritical have been reported before. For single round jets, Chehroudi^{28,29, 31} and co-workers found that under supercritical pressures the spreading rate and fractal dimension values were the same as those for a gaseous jet injected into a gaseous ambient with different densities (i.e., variable-density, single-phase, gaseous jet). This is a similar observation but for the dark-core length. Under supercritical pressures, our coaxial jet scales with $M^{0.5}$. Therefore, it appears that this form of the dependency to M is not only valid for gas-gas shear-coaxial jets, but as any single-phase shear-coaxial jet, such as the system where the original dependence $f M^{-0.5}$ was found from the water-water work of Rehab et al.^{16,17}

Figure 10 was constructed with the objective of comparing the dark-core length with all of the available data that exists in the literature for the potential-core length, intact-core length, and breakup-length. Figure 10 represents all of the available data in the literature concerning core length spanning 5 orders of magnitude in momentum flux ratio. Also, note that as M approaches zero, one reaches a limit defining a single round jet configuration because the outer velocity becomes zero. From data in Fig 10, it seems that for $M < 1$, data points converge and approach the core length range expected for single round jets reported by Oschwald et al.³³. The single-phase data presented in Fig. 10 follows the dependence of $L/D_1 = A M^{0.5}$, where the constant A is between 5 and 12. At $M > 100$, the data points of Favre-Marinet and Samano-Shettini²¹ exhibit a recirculation bubble at the end of the core, and thus the core length decreases. The injectors used to produce the two-phase coaxial jets of Eroglu et al.¹⁰ and Englebert et al.¹² have much larger outer jet gap widths (see Table 1) than what is typical of rocket type injectors. Additionally, the apparatus of Eroglu et al.¹⁰, reported in Farago and Chigier³⁵, does not produce fully-turbulent inner jet until when $Re > 10^4$. The lack of a fully-turbulent inner jet and the significant differences between their injector and shear-coaxial ones used in rockets could be the reasons the core length measured by Eroglu et al.¹⁰ is shorter than those observed in our work. Englebert et al.¹² reported that the core length scaled with $M^{0.3}$. The core length by Woodward¹¹ for the water potassium iodide solution with helium, however, obeys very nearly the trends for the subcritical data points (i.e., $25M^{0.2}$). Considering that momentum flux ratios near 10 are of importance for LRE, to the best of the authors' knowledge, the data for the subcritical (two-phase) case is the only reported information in the neighborhood of the $M = 10$.

SUMMARY AND CONCLUSIONS

A non-reacting flow study of a cryogenic shear-coaxial injector was conducted at pressures spanning subcritical to supercritical values. The flow from the inner jet of the coaxial injector was liquid nitrogen (or liquid-like, if at supercritical pressures) and cold gaseous nitrogen flowed from the outer annular jet, both injected into a chamber pressurized with nitrogen at room temperature. The resulting coaxial jet was imaged with a camera framing at a rate of up to 18 kHz. The jet was excited with a high-amplitude acoustic driver, with the jet located at a velocity anti-node (pressure node). The following conclusions are offered:

1. The high-amplitude acoustic wave alters the behavior of the shear-coaxial jet. The resulting structure of the jet exhibits a periodic shape corresponding to the transverse-velocity field created by the acoustic waves. The periodic oscillation of the core of the jet is predominately in the direction of the transverse acoustic velocity. No helical mode of for the jet was observed.
2. The quantitative behavior of the dark-core length for the coaxial jet at near- and supercritical pressure follows similar momentum flux ratio (M) dependency reported for the single-phase shear-coaxial jets (i.e., $12M^{-0.5}$). The dark-core length for the subcritical pressures, however, scales with $M^{-0.2}$.
3. Within a range of momentum flux ratios in between 1 and 10, the dark-core lengths for the coaxial jet under the subcritical (two-phase) ambient pressure used here appear longer than those measured at the supercritical (single-phase) condition. Considering the upper bound of this range represents relevant values for liquid rocket engines, subcritical data define a new regime which was not reported previously.

NOMENCLATURE

A	= area
B	= a constant on the order of 10^{-3}
C	= 0.5 constant
c	= a constant
D	= diameter

PREPRINT

E_R	= energy ratio $(\rho_o U_o^3 A_o) / (\rho_i U_i^3 A_i)$
L	= dark-core length, potential core, intact core, or breakup length
L_{post}	= length of undisturbed entrance length of inner tube of the coaxial injector
R	= radius
r	= correlation parameter dependent on gas properties
Re	= Reynolds Number $(\rho U D) / \mu$
M	= momentum flux ratio of the outer jet to inner jet $(\rho_o U_o^2) / (\rho_i U_i^2)$
M_R	= momentum ratio $(\rho_o U_o^2 A_o) / (\rho_i U_i^2 A_i)$
U	= velocity
V_r	= velocity ratio of the outer jet to inner jet
We	= Weber number $(\rho_o (U_o - U_i)^2 D_1) / \sigma$
Z	= Ohnesorge Number

GREEK SYMBOLS

α	= 0.17 constant
μ	= viscosity
ρ	= density
σ	= surface tension

SUBSCRIPTS

1, 2, 3, 4	the four diameters defining the edges of a coaxial injector from innermost to outermost
i	inner
o	outer

ACKNOWLEDGMENTS

The authors would like to acknowledge Mr. Mike Griggs for his valuable contributions in the improvements to the experimental facility. Lt. Matthew Raskie, Lt. Jason Szuminski, Mr. Earl Thomas, Mr. Randy Harvey, Mr. David Hill, and Mr. Mark Wilson are thanked for their efforts. Additionally, Ms. Jennie Paton is thanked for making literature available in a timely manner. A great appreciation is extended to Mr. Steven Martin for loaning the authors one of the Phantom Cameras. A special gratitude is expressed to M. Favre-Marinet, E. B. Camano Schettini, and R. D. Woodward for providing us with their core length data in tabular form. The first author would like to thank his thesis advisor, Dr. R. J. Santoro, for many helpful discussions permitting his thesis work to be performed off-campus at AFRL. This work is sponsored by the Air Force Office of Scientific Research under Dr. Mitat Birkan, program manager.

REFERENCES

1. Harje, D. T. and Reardon, F. H. (eds.), ***Liquid Propellant Rocket Combustion Instability***, NASA SP-194, 1972.
2. Yang, V. and Anderson, W. (eds.), ***Liquid Rocket Engine Combustion Instability***, Progress in Astronautics and Aeronautics, AIAA, Washington, DC, 1995.
3. Heidmann, M. F. ***Oxygen Jet Behavior During Combustion Instability in a Two-Dimensional Combustor***, NASA TN D-2725, 1965.
4. Miesse, C. C., "The effect of ambient pressure oscillations on the disintegration and dispersion of a liquid jet", ***Jet Propulsion***, Vol. 25, 1955, pp. 525-530, 534.

5. Buffum, F. G., and Williams, F. A., "Response of turbulent liquid jets to transverse acoustic fields", **Proceedings of the 1967 Heat Transfer and Fluid Mechanics Institute**, Edited by P. A. Libby, D. B. Olfe, and C. W. Van Atta, 1967, pp. 247-276.
6. Forstall, W., and Shapiro, A. H., "Momentum and Mass Transfer in Coaxial Gas Jets," **J. Applied Mechanics**, Trans. ASME, Vol. 72, 1950, pp. 399-408.
7. Chigier, N. A., and Beer, J. M., "The Flow Region Near the Nozzle in Double Concentric Jets," **J. of Basic Engineering**, Trans. ASME, Vol. 4, 1964, pp. 797-804.
8. Champagne, F. H., and Wygnanski, I. J., "An experimental Investigation of Coaxial Turbulent Jets," **International Journal of Heat and Mass Transfer**, Vol. 14, 1971, pp. 1445-1464.
9. Au, H., and Ko, N. W. M., "Coaxial Jets of Different Mean Velocity Ratios, Part 2," **Journal of Sound and Vibration**, Vol. 116, No. 3, 1987, pp. 427-443.
10. Eroglu, H., Chigier, N., and Farago, Z., "Coaxial Atomizer Intact Lengths," **Physics of Fluids A**, Vol. 3, No. 2, Jan. 1991, pp. 303-308.
11. Woodward, R. D., **Primary Atomization of Liquid Jets Issuing from Rocket Engine Coaxial Injectors**, Ph.D. Thesis, Mechanical Engineering Dept., The Pennsylvania State University, University Park, PA, 1993.
12. Englebert, C., Hardalupas, Y., and Whitlaw, J. H., "Breakup Phenomena in Coaxial Air-Blast Atomizers," **Proc. R. Soc.**, Vol. 451, London, 1995, pp. 189-229.
13. Carreau, J. L., Porcheron, E., LeVisage, D., Prevost, L., and Roger, F., "Liquid Core Characterization of Coaxial Liquid Oxygen/Inert Gas Jets," **Int. J. of Fluid Mech. Research**, Vol. 24, Nos. 4-6, 1997, pp. 498-507.
14. Porcheron, E., Carreau, J. L., Prevost, L., LeVisage, D., and Roger, F., "Effect of Density on Coaxial Liquid Jet Atomization," **Atomization and Sprays**, Vol. 12, 2002, pp. 209-227.
15. Villermaux, E., Rehab, H., and Hopfinger, E. J., "Breakup Regimes and Self-Sustained Pulsations in Coaxial Jets," **Meccanica**, Vol. 29, 1994, pp. 393-401.
16. Rehab, H., Villermaux, E., and Hopfinger, E. J., "Geometrical Effects of Near-Field Flow Structure of Coaxial Jets," **AIAA Journal**, Vol. 36, No. 5, 1998, pp. 867-869.
17. Rehab, H., Villermaux, E., and Hopfinger, E. J., "Flow Regimes of Large Velocity Ratio Coaxial Jets," **J. Fluid Mech.**, 1997, pp. 357-381.
18. Villermaux, E., "Mixing and Spray Formation in Coaxial Jets," **J. Propulsion and Power**, Vol. 14, No. 5, 1998, pp. 807-817.
19. Lasheras, J. C., Villermaux, E., and Hopfinger, E. J., "Breakup and Atomization of a Round Water Jet by a High Speed annular Air Jet," **J. Fluid Mech.**, Vol. 357, 1998, pp. 351-379.
20. Lasheras, J. C., and Hopfinger, E. J., "Liquid Jet Instability and Atomization in a Coaxial Gas Stream," **Annual Rev. Fluid Mech.**, Vol. 32, 2000, pp. 275-308.
21. Favre-Marinet, M., and Camano Schettini, E. B., "The Density Field of Coaxial Jets with Large Velocity Ratio and Large Density Differences," **International Journal of Heat and Mass Transfer**, Vol. 44, 2001, pp. 1913-1924.
22. Davis, D. W. and Chehroudi, B., "The Effects of Pressure and Acoustic Field on a Cryogenic Coaxial Jet," **42nd AIAA Aerospace Sciences Meeting & Exhibit**, AIAA, Washington, DC, 5-8 Jan. 2004.
23. Davis, D. W., Chehroudi, B., and Sorensen, I. "Measurements in an Acoustically Driven Coaxial Jet under Supercritical Condition," **43rd AIAA Aerospace Sciences Meeting & Exhibit**, AIAA, Washington, DC, 10-13 Jan. 2005.
24. Davis, D. W., and Chehroudi, B., "Measurements of an Acoustically Driven Coaxial Jet under Sub-, Near-, and Supercritical Conditions," **J. of Propulsion and Power**, 2005 (submitted).
25. Chehroudi, B., Talley, D., and Coy, E. B., "Initial Growth Rate and Visual Characteristics of a Round Jet into a Sub- to Supercritical Environment of Relevance to Rocket, Gas turbine, and Diesel Engines," **37th AIAA Aerospace Science Meeting and Exhibit**, AIAA, Washington, DC, 11-14 Jan. 1999.
26. Chehroudi, B., Talley, D. G., and Coy, E. B., "Fractal Geometry and Growth Rate Changes of Cryogenic Jets near the Critical Point," **35th AIAA/ASME/SAE/ASEE Joint Propulsion Conference and Exhibit**, AIAA, Washington, DC, 20-24 Jun. 1999.
27. Chehroudi, B., Cohn, R., Talley, D. G. and Badakhshan, A., "Raman Scattering Measurements in the Initial Region of Sub- and Supercritical Jets," **36th**

- AIAA/ASME/SAE/ASEE Joint Propulsion Conference and Exhibit**, AIAA, Washington, DC, 17-19 Jul. 2000.
28. Chehroudi, B., Talley, D. G., and Coy, E. B. "Visual Characteristics and Initial Growth Rates of Round Cryogenic Jets at Subcritical and Supercritical Pressures," **Physics of Fluids**, Vol.4, No. 2, Feb. 2002. pp. 850-861.
 29. Chehroudi, B., Cohn, R., and Talley, D. G., "Cryogenic Shear Layers: Experiments and Initial Growth Rates of Round Cryogenic Jets at Subcritical and Supercritical Pressures," **International Journal of Heat and Fluid Flow**, Vol. 23, 2002, pp. 554-563.
 30. Chehroudi, B., and Talley, D. G., "Interaction of Acoustic Waves with a Cryogenic Nitrogen Jet at Sub- and Supercritical Pressures," **40th AIAA Aerospace Meeting and Exhibit**, AIAA, Washington, DC, 14-17 Jan. 2002.
 31. Chehroudi, B. and Talley, D., "Fractal Geometry of a Cryogenic Nitrogen Round Jet Injected into Sub- and Super-critical Conditions", **Atomization and Sprays**, Vol. 14, 2004, pp. 81-91.
 32. Chehroudi, B., Davis, D. W., and Talley, D. G., "Initial Results from A Cryogenic Coaxial Injector In An Acoustic Field," **41st AIAA Aerospace Sciences Meeting & Exhibit**, AIAA, Washington, DC, 6-9 Jan. 2003.
 33. Oschwald, M., Smith, J. J., Branam, R., Hussong, J., Schik, A., Chehroudi, B., and Talley, D. G., "Injection of Fluids into Supercritical Environments," **Comb. Sci. Tech.**, Accepted, 2005.
 34. Hulka, J., and Hutt, J., "Liquid Oxygen / Hydrogen Instability Phenomena," Liquid Rocket Engine Combustion Instability, edited by V. Yang and W. Anderson, **Progress in Astronautics and Aeronautics**, AIAA, Washington, DC, 1995, pp. 39-72.
 35. Faragó, Z., and Chigier, N., "Morphological Classification of Disintegration of Round Liquid Jets in a Coaxial Air Stream," **Atomization and Sprays**, Vol. 2, 1992, pp. 137-153.

APPENDIX

Table 1. Summary of Core Length Literature for Shear-Coaxial Jets

REF#	Author	Date	Fluid	Fluid	Fluid	Pressure	T _i	T _o	T _∞
			Inner Jet	Outer Jet	Ambient	(MPa)	(K)	(K)	(K)
6	Forstall & Shapiro	1950	Air+ 10 %He	Air	Air	0.1*	Ambient ^a	Ambient	Ambient
7	Chigier & Beer	1964	Air	Air	Air	0.1*	Ambient	Ambient	Ambient
8	Champagne & Wygnanski	1971	Air	Air	Air	0.1	Ambient	Ambient	Ambient
9	Au and Ko	1987	Air	Air	Air*	0.1*	Ambient	Ambient	Ambient
10	Eroglu et al.	1991	Water	Air	Air	0.1*	Ambient	Ambient	Ambient
11	Woodward	1993	KI (aq.)	N ₂ , He	N ₂ , He	0.1 - 2.17	Ambient	Ambient	Ambient
15	Villermaux et al. ^g	1994	Water	Water	Water	0.1*	Ambient	Ambient	Ambient
12	Englebert et al.	1995	Water	Air	Air	0.1	293	293 - 636	293
13	Carreau et al.	1997	LOX	He, N ₂ , Ar	NC ^c	0.1	82 ^d	245 - 272 ^d	NC
16	Rehab et al. ^g	1997	Water	Water	Water	0.1*	Ambient	Ambient	Ambient
17	Rehab et al. ^g	1997	Water	Water	Water	0.1*	Ambient	Ambient	Ambient
18	Villermaux ^{g,h}	1998	Water	Water	Water	NR	NR	NR	NR
19	Lasheras et al. ^g	1998	Water	Air	Air	0.1	Ambient	Ambient	Ambient
20	Lasheras & Hopfinger ^{g,i}	2000	NR	NR	NR	NR	NR	NR	NR

PREPRINT

21	Favre-Marinet & Schettini	2001	Air, SF6	Air,He	Air, He	0.1	Ambient	Ambient	Ambient
14	Porcheron et al.	2002	LOX, Water	He, N2, Ar, Air	Air	0.1	82, 293	245 - 293	293
This work	Davis et al.	2005	N2	N2	N2	1.4 – 4.9	108 - 133	132 - 204	197 - 249

Table 1. Summary of Core Length Literature for Shear-Coaxial Jets (continued).

REF#	Author	Density Ratio	Velocity Ratio	M	Re Inner	Re Outer	We
		Outer/Inner	Outer/Inner	Outer/Inner	(10^4)	(10^4)	
6	Forstall & Shapiro	1.09	0.2 - 0.75	0.04 - 0.61	NR	NR	NA
7	Chigier & Beer	1*	0.024 - 2.35	5.8e-4 - 5.52	$\sim 10^b$	$\sim 10^b$	NA
8	Champagne & Wygnanski	1*	0 - 10	0 - 100	1.01 - 10.15	0 - 9.6	NA
9	Au and Ko	1*	1.25 - 6.67	1.5 - 44	NR	NR	NA
10	Eroglu et al.	0.001	4.5 - 131.2	0.02 - 17.2	0.15 - 0.93	2.0 - 11.6	15 - 530
11	Woodward	0.0006 - 0.018	0 - 30	0 - 1.7	7.86 - 18.9	NR	12 - 3600
15	Villermaux et al. ^g	1	1 - 6	1 - 36	>5000	>5000	NA
12	Englebert et al.	0.0008 - 0.0012	10.25 - 66.75	0.12 - 4.3	0.54 - 3.4	4.8 - 16.5	76 - 2610
13	Carreau et al.	NR	NR	3 - 21.5	5.32 - 8.11	NR	9.19×10^3 - 3.48×10^4
16	Rehab et al. ^g	1	2.2 - 5.6	4.9 - 31	1 - 10	1 - 10	NA
17	Rehab et al. ^g	1	2 - 5	4 - 25	NR ^f	NR ^f	NA
18	Villermaux ^{g,h}	1*	NR	NR	NR	NR	NR
19	Lasheras et al. ^g	0.001	NR	NR	NR	NR	NR
20	Lasheras & Hopfinger ^{g,i}	NR	NR	NR	NR	NR	NR
21	Favre-Marinet & Schettini	0.028 - 1	3.0 - 70	1 - 200	NR	3200, 11000	NA
14	Porcheron et al.	1.6×10^{-4} - 2.3×10^{-3}	NR	2 - 21.6	NR	NR	0 - 14000
This work	Davis et al.	0.04 - 0.56	1.2 - 11.1	0.19 - 11.2	1.2 - 3.2	0.8 - 19	32 - ∞

Table 1. Summary of Core Length Literature for Shear-Coaxial Jets (continued).

REF#	Author	D_1	D_2	D_3	$(D_3 - D_2)/2$	Area Ratio	Post Recess	Injector
		(mm)	(mm)	(mm)	(mm)	Outer/Inner	(mm)	L_{post}/D_1
6	Forstall & Shapiro	6.4, 25	NR	102	NR	NR	NR	NR
7	Chigier & Beer	25	64	97	16.5	8.50	0*	NR
8	Champagne & Wygnanski	25	NR	NR	NR	1.28, 2.94	0*	NR
9	Au and Ko	2	2.2	4	0.9	2.79	0*	NR
10	Eroglu et al.	0.971	1.262	10.36	4.549	112.15	-0.6	57
11	Woodward	4.76	6.35	9.86	1.76	2.51	0.0	85
15	Villermaux et al. ^g	40	51	55	0.2	0.27	0*	"long"
12	Englebert et al.	2.3	2.95	14.95	6.00	40.60	0.0	22
13	Carreau et al.	5 ^d	5.57 ^d	16 ^d	5.2 ^d	9	0.0	NR
16	Rehab et al. ^g	NR	NR	NR	NR	1.82, 1.87, 5.24 ^e	0*	NR
17	Rehab et al. ^g	20	21	27	3	1.82	0	NR
18	Villermaux ^{g,h}	NR	NR	NR	NR	NR	NR	NR
19	Lasheras et al. ^g	3.8	4.2	5.6	0.7	0.95	0	29
20	Lasheras & Hopfinger ^{g,i}	NR	NR	NR	NR	NR	NR	NR
21	Favre-Marinet & Schettini	20	20.4	27	3.3	0.78	0.0	6.75
14	Porcheron et al.	5, 2.1	5.57, 2.5	16, 7	2.25	9, 9.69	0*	NR
This work	Davis et al.	0.51	1.59	2.42	0.415	12.80	0.25	100

Table 1. Summary of Core Length Literature for Shear-Coaxial Jets (continued).

REF	Author	Diagnostic	Quantity	Equation
			Measured	
6	Forstall & Shapiro	Pitot tube, Sampling Tube	Potential Core	$L / D_1 = 4 + 12V_r$
7	Chigier & Beer	Pitot tube	Potential Core	
8	Champagne & Wygnanski	Hot wire anemometer	Inner Core	
9	Au and Ko	Hot wire anemometer	Potential Core	
10	Eroglu et al.	Back-lit still	Liquid Intact Length	$L / D_1 = 0.66 We^{-0.4} Re^{0.6}$
11	Woodward	x-ray Radiography	Intact Liquid Core Length	$L / D_1 = 0.0095 \left(\frac{\rho_o}{\rho_i} \right)^{-0.36/r} We^{-0.22/r} Re^{0.68}$
15	Villermaux et al. ⁹	Hot film anemometer	Potential Core / Cone	$L / D_1 = 7 / V_r$
12	Englebert et al.	Back-lit high-speed 16mm film	Breakup Length	$L / D_1 = 40 We^{-0.27}$ $\frac{2L}{D_3 - D_2} = 10.6 M_R^{-0.3} = 13.7 E_R^{-0.2}$
13	Carreau et al.	Fiber optic Probe	Breakup Length, Potential Cone Length	$L / D_1 = 0.0012 \left(\frac{\rho_o}{\rho_i} \right)^{-0.32} We^{-0.33} Re^{0.55}$
16	Rehab et al. ⁹	Hot film anemometer	Potential Core	$L / D_1 = 6 / V_r; \quad L / D_1 = 7.5 / V$
17	Rehab et al. ⁹	Hot-film anemometer, Pitot tube, LIF image	Potential Cone	$L / D_1 = 6 / V_r; \quad L / D_1 = 8 / V$ $L / D_1 = 0.5 \left(\frac{1}{(C\alpha V_r)^2} - 1 \right)^{1/2} \approx \frac{1}{2C\alpha V_r}$
18	Villermaux ^{9,h}	^h	Potential Cone, Liquid intact length	$L / D_1 = c / V_r; \quad 6 < c < 8$

Table 1. Summary of Core Length Literature for Shear-Coaxial Jets (continued).

REF	Author	Diagnostic	Quantity	Equation
19	Lasheras et al. ^g	Photo-graph	Liquid intact length	$L / D_1 = \left(\frac{1}{4 (C \alpha)^2 M} - \frac{1}{4} \right)^{1/2} \approx \frac{6}{M^{1/2}}$
20	Lasheras & Hopfinger ^{g,i}			$L / D_1 = \frac{1}{2 c M^{2/3}} \left(\frac{\sigma}{\mu_i U_i} \right)^{1/3}$ $L / D_1 \approx \frac{6}{M^{1/2}} \left(1 - \frac{U_i}{U_o} \right)^{-1}$ $L / D_1 \approx \frac{6}{M^{1/2}} \frac{1}{\left(1 - \frac{B \sigma}{\mu_o U_o} \right)^{0.5}}$
21	Favre-Marinet & Schettini	Aspirating Probe w/ hot-wire	Potential Core	$L / D_1 \propto M^{-0.5}$
14	Porcheron et al.	Fiber optic Probe		$L / D_1 = 2.85 \left(\frac{\rho_o}{\rho_i} \right)^{-0.32} Z^{0.34} M^{-0.13}$
This work	Davis et al.	Shadow-graph	Dark Core	$L / D_1 \approx \frac{12}{M^{1/2}}$ $L / D_1 \approx \frac{25}{M^{0.2}}$

Table 1 Notes

NR = not reported

NA = not applicable

NC = not clear from report

* assumed from the context, but not directly reported

^a Ambient temperature assumed from the context of discussion, but generally not specifically stated in report.^b reported as approximately 10^5 ^d The dimensions of the injector and the temperatures were not given in the paper, but were given in the paper by Porcheron et al.¹⁴^e This number is the diameter ratio squared, which is approximately the area ratio for a very thin lip injector. The only dimensional information given was the diameter ratios (1.35, 1.37, and 2.29 mm) and the lip thickness (D2-D1) of 0.3 mm.^f A Re based on momentum conservation reported and defined asRe = $\rho_o U_o D_3 / \mu^* (1 - (D_1/D_3))^{0.5}$ ranged from 10^4 - 10^5 .^g These papers are from the same collaboration / research group over several years.^h This paper was an analysis paper that presented a different equation based on the data from the same group of researchers¹⁵⁻¹⁷ⁱ This paper was a review paper encompassing the work from this same collaboration of researchers¹⁵⁻¹⁹, as well as others.^j Unable to make measurements from images, and therefore not compared quantitatively to theory for core length.

Shear-Coaxial Jets from a Rocket-Like Injector in a Transverse Acoustic Field at High Pressures

Dustin W. Davis* and Bruce Chehroudi.†
ERC, Inc., Edwards AFB, CA, 93524

In order to gain a better understanding of some of the underlying physics associated with the interaction of high-amplitude acoustic waves and a coaxial-jet injector similar to those used in cryogenic liquid rockets, a non-reacting-flow experimental investigation was conducted under sub-, near-, and supercritical chamber pressures, with and without acoustical excitation. Past research works on this subject have shown both the relevance and importance of geometrical changes in an injector's exit-area and its nearby physical and fluid mechanical processes. On this basis, special attention is paid in collecting spatially-resolved mean temperatures and documenting the aforementioned interactions at the exit of this injector. Short-duration and high-speed digital cameras provided information on the dynamic behavior of this jet under a variety of conditions. Mean and root mean square (RMS) values of the coaxial-jet dark-core length fluctuations were measured from the acquired images via a computer-automated method. It is seen that as the outer-to-inner jet velocity ratio increases, the RMS of the dark-core length fluctuations decreases. It is hypothesized that a connection to rocket instability can be obtained from these data through examination of the RMS values of the dark-core length fluctuations. It is possible that decreases in the fluctuation levels, which were shown here to occur at higher velocity ratios, could weaken a key feedback mechanism for the self-excitation process that is believed to drive the combustion instability in rocket engines. This could offer a possible explanation of the combustion stability improvements experienced in engines under higher outer-to-inner jet velocity ratios. Additional analysis and data acquisition are planned to further investigate this finding. Finally, after a careful review of relevant data taken here and by others, there appears to be a good correlation between the dark-core length and the outer-to-inner jet momentum flux ratio, but the form of this dependency was found to be different at subcritical pressures than the rest of the chamber conditions (i.e., near- and supercritical cases).

Nomenclature

A	= area
B	= a constant on the order of 10^{-3}
C	= 0.5 constant
c	= a constant
D	= diameter
E_R	= energy ratio $(\rho_o U_o^3 A_o) / (\rho_i U_i^3 A_i)$
L	= dark-core length, potential core, intact core, or breakup length
L_{post}	= length of undisturbed entrance length of inner tube of the coaxial injector
R	= radius
r	= correlation parameter dependent on gas properties
Re	= Reynolds Number $(\rho U D) / \mu$
M	= momentum flux ratio of the outer jet to inner jet $(\rho_o U_o^2) / (\rho_i U_i^2)$
M_R	= momentum ratio $(\rho_o U_o^2 A_o) / (\rho_i U_i^2 A_i)$
U	= velocity

* Scientist AFRL/PRSA and PhD Candidate Penn State University, 10 E. Saturn Blvd., and AIAA Member.

† Sr. Scientist, AFRL/PRSA, ChehroudiB@aol.com, 10 E. Saturn Blvd., and AIAA Member.

V_r = velocity ratio of the outer jet to inner jet
 We = Weber number $(\rho_o (U_o - U_i)^2 D_i / \sigma$
 Z = Ohnesorge Number

Greek Symbols

α = 0.17 constant
 μ = viscosity
 ρ = density
 σ = surface tension

Subscripts

1, 2, 3, 4 the four diameters defining the edges of a coaxial injector from innermost to outermost
 i inner
 o outer

I. Introduction

Most, if not all, liquid rocket engines (LRE) experienced a problem with combustion instability during the development phase. The combustion instabilities span from low-frequency, which is a feed-system coupled instability, to high-frequency acoustic instabilities, which depends on the acoustic modes of the chamber. As a consequence, the resulting high-amplitude pressure oscillations can damage the injection and combustion chamber hardware, causing catastrophic failure of the engine and loss of life. A great deal of work remains to be done to understand the root causes of combustion instability, although two fairly comprehensive treatises on this subject, such as those compiled by Harrje and Reardon¹ and Yang and Anderson², have been published.

Many fundamental questions remain to be answered regarding the physical behavior of the propellant jets and other phenomena governing the combustion instability. One such question is how the fuel and oxidizer jets change behavior during an unstable combustion event. One early study by Heidmann³ investigated the behavior of liquid oxygen (LOX) jets during a period when combustion instability was induced. Hydrogen was introduced into the combustor in a diffuse manner near the LOX jets, making it quite similar to a shear-coaxial injector used in many liquid rocket engines. The LOX jet contracted, once the combustor became unstable. Similar observations were made by Miesse⁴ and Buffum and Williams⁵ under cold flow conditions when a single round jet was excited with an externally-forced acoustic field.

Mixing of the propellant streams, if not controlling, is at least intimately related to the combustion process. To accomplish combustion in a chamber, a given chamber size is required to mix and burn the propellants. With a desire to make smaller combustors possessing high efficiencies, while achieving proper thermal management to prevent burnout of the injection hardware, the need for detailed knowledge of the mixing process becomes critical. To a first order approximation, one measure of the mixing process is the so-called liquid-core length, which has been extensively studied by many researchers in the past.⁶⁻²⁴ A compilation of the experimental core-length correlations, semi-empirical theories, and other data for shear coaxial injector studies involving core length are summarized in Table 1 in the Appendix. Although the intent of Table 1 is to compile a comprehensive list of papers reporting the core length of different shear-coaxial jets, it is possible that omissions may have occurred. Many of the correlations and semi-empirical theories reviewed indicate scaling of the core length with outer-jet to inner-jet velocity ratio (V_r), outer-jet to inner-jet momentum flux ratio (M), density ratio (ρ_o / ρ_i), Reynolds number (Re), and Weber number (We). Supercritical pressures and transcritical temperatures are found in liquid rocket engines. One difficulty with applying these relationships to the conditions that may be found in liquid rocket engines is the predicted core length is very small or zero in magnitude, because one of the parameters in the equation is We and surface tension diminishes greatly or vanishes all together. Transcritical temperatures means that when the fluid is introduced into the combustion chamber it is initially at subcritical temperature, then is heated to a supercritical temperature. To overcome the difficulty of core length prediction associated large We , one group of researchers¹⁵⁻²⁰, proposed that M can be used to describe the scaling of the core length for shear-coaxial injectors, and need not include We if the We is sufficiently high.

Chehroudi and co-workers²²⁻³³ have investigated supercritical jet flows at higher Reynolds numbers and turbulent jets of interest to practical applications in propulsion systems. The single round-jet work by Chehroudi et al²⁵⁻³¹ was produced from two different injectors made from 50 mm long sharp-edged tubes with the inner jet diameters of 0.254 mm and 0.508 mm, (L/D of 200 and 100, respectively). They injected pure N₂ and O₂ into N₂,

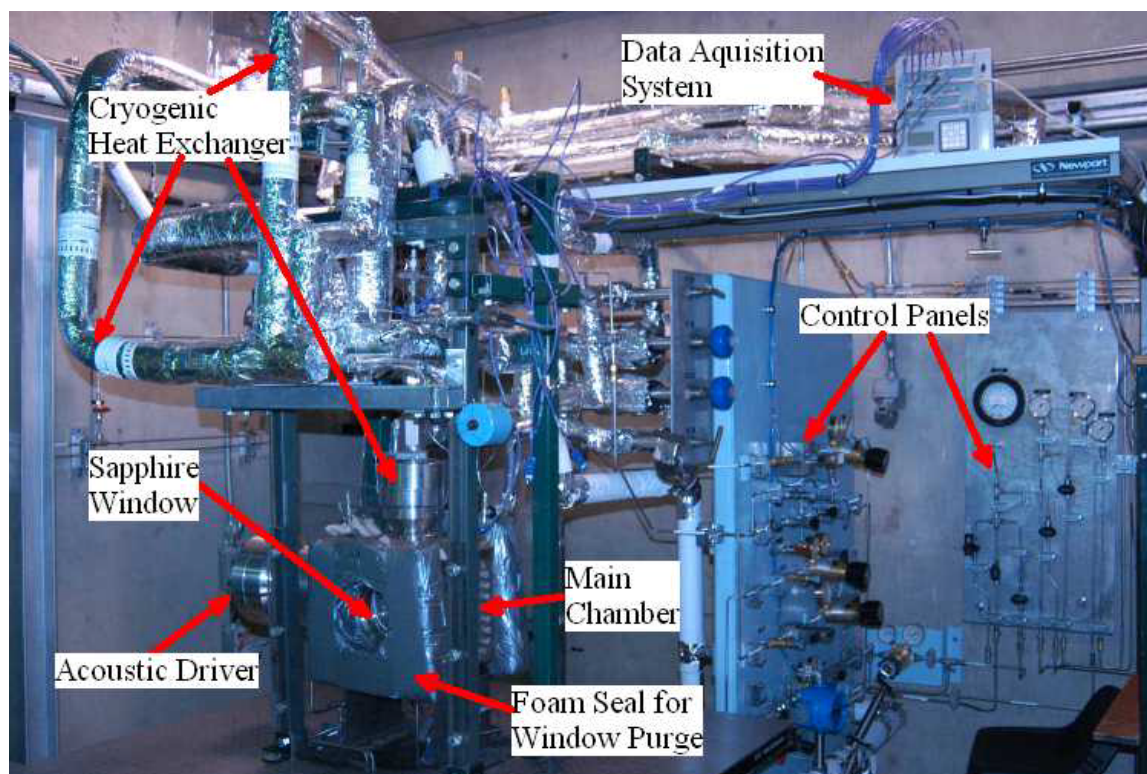


Figure 1. AFRL supercritical non-reacting flow facility.

He, Ar, and mixtures of CO and N₂ and the arrangement was studied with shadowgraphs and Raman imaging. It was determined that the initial growth rate of a supercritical jet was different from that of a subcritical jet. Furthermore, they quantitatively proved, for the first time, that the initial growth rate of supercritical jet behaved similar to variable-density gas jets.²⁸ From this observation, a phenomenological model of the initial growth rate based upon time scale arguments was proposed which agreed well with the results acquired under sub- and supercritical pressures.²⁸ It is also important to note that Chehroudi et al.²⁹ showed that the growth rate measured from shadowgraphs was about twice as large as the growth rate of the jet measured by Raman imaging of the jet, based on the full width at half maximum (FWHM) jet thickness values. The fractal dimension of the initial region of the jet under sub- and supercritical pressures was also measured for the first time by Chehroudi et al.^{26, 29, 31} and compared to liquid and gas jets in a similar fashion to that of the growth rate. A transition from a liquid jet to a gas jet, from sub- to supercritical, in fractal dimension was observed.

II. Experimental Set-Up

The experimental facility, shown in Fig. 1, has been described in details previously^{22-24, 31}, and only a brief description will be given here. High-pressure gaseous nitrogen (GN₂) flows into the system, its flow rate measured with Porter Mass Flow meters, and controlled with micrometer needle valves. Temperature conditioning is accomplished by passing the GN₂ through a shell and tube type heat exchanger using liquid nitrogen (LN₂) to cool the GN₂. The nitrogen flows into both the inner and outer tubes. Temperature of the flow to the inner round jet of the shear-coaxial injector is considerably lower than that of the outer annular jet, reaching the liquid state. However, the outer jet is cooled well below the room temperature, but is still in gaseous state. The chamber is pressurized with GN₂ at ambient temperature. For reference, the critical pressure and temperature of N₂ is 3.4 MPa and 126.2 K, respectively. The pressure inside the main chamber is maintained by adjusting the outlet flow rate using a triplet of valves to provide an optimum level of control.

The test article consists of a chamber within a chamber. The main, external, chamber is used to create a pressurized environment and is fitted with two sapphire windows for observation of the jet behavior. The smaller, internal chamber, acting as an acoustic resonator cavity, is used to keep the amplitude of the acoustic driver (attached at one end) high in the vicinity of the jet. The Piezo-Siren acoustic driver, developed by Hersch Acoustical, is capable of producing amplitudes in an impedance tube of up to 180dB at pressures up to 14 MPa. To

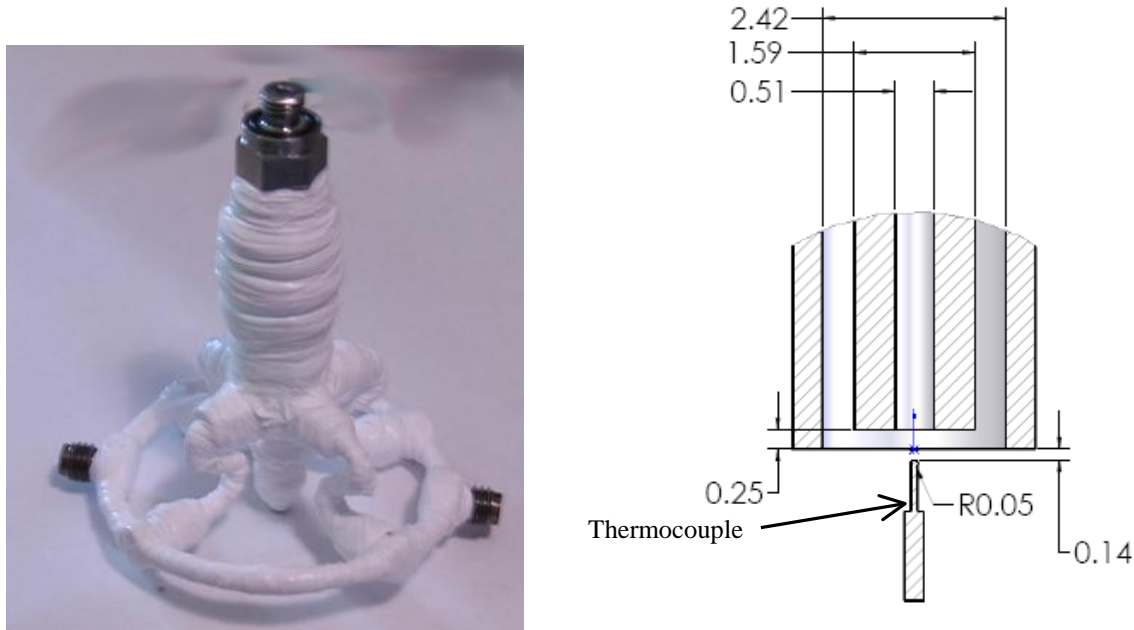


Figure 2. Picture of the shear-coaxial injector (left) and a cross-section drawing of the injector tip. The thermocouple used to measure exit-plane temperature profiles is shown in the drawing, indicating its relative size and the axial position at which measurements are made.

obtain sufficiently high amplitudes, the driver must resonate the normal modes of the inner chamber. Therefore, the frequency at which the effects are studied is limited to the first two modes of the inner chamber, being about 3 kHz and 5.25 kHz, respectively. The frequency shifts slightly depending on the chamber fluid, temperature, and pressure. The resulting wavelength is much larger than the diameter of the jet. The injector is positioned at a pressure node (a velocity anti-node) to produce maximum velocity fluctuations near the jet.

The shear coaxial injector used in this work (see Fig. 2) is based on the well-characterized design of the single-jet injector used in all previous studies²⁴⁻³⁰ in this apparatus. The center-post made from a stainless steel tube with an I.D. (D_1) of 0.51 mm (0.020") and an O.D. (D_2) of 1.59 mm (0.063") with a length of 50.8 mm (2.00") used to produce the inner jet. The resulting length to I.D. ratio is 100, which is sufficient to ensure a fully-developed turbulent pipe flow conditions at the exit. The outer stainless steel tube creating the annular passage had an I.D. (D_3) of 2.42 mm (0.095") and an O.D. (D_4) of 3.18 mm (0.125") used to produce the outer coaxial annular jet. The resulting mean gap width of the annular passage, the hydraulic radius, is 0.415 mm (0.016"), measured from an image taken at the exit of the injector. The injector has a small bias of 8% of the mean gap width. The recess of the inner tube was 0.5 D_1 , 0.25 mm (0.010") from the end of the outer tube.

Because of the proximity of the experimental conditions to the critical point of nitrogen, accurate measurements of temperature were necessary to obtain reliable estimates of density and other quantities computed from the density. Radial temperature profiles were measured using a type E exposed bead thermocouple that was traversed through the jet measuring mean temperature. At cryogenic temperatures, the accuracy of thermocouples is not reliable. However, due to the small size of the system of interest, a Pt-RTD was not feasible. Therefore, it was necessary to calibrate the individual thermocouples against a precision Pt-RTD. The temperature profiles and the details of the calibration were reported elsewhere, see Davis and Chehroudi²² and Davis et al.²³

Shadowgraph images of the jet were taken using either a PixelFly CCD camera or a Phantom v5.1 or v7.1 CMOS camera. The advantage that the CMOS cameras presented was the ability to produce high-speed movies of the jet for a period lasting up to several seconds. The framing rate for the movies in this work was 18 kHz.

III. Results and Discussion

A. Acoustic Wave Interaction with Shear-Coaxial Jet

High-speed movies of the jet present a large amount of information about the flow being studied. A sample of ten consecutive images at sub- (rows one and two from top), near- (rows three and four), and supercritical (rows five

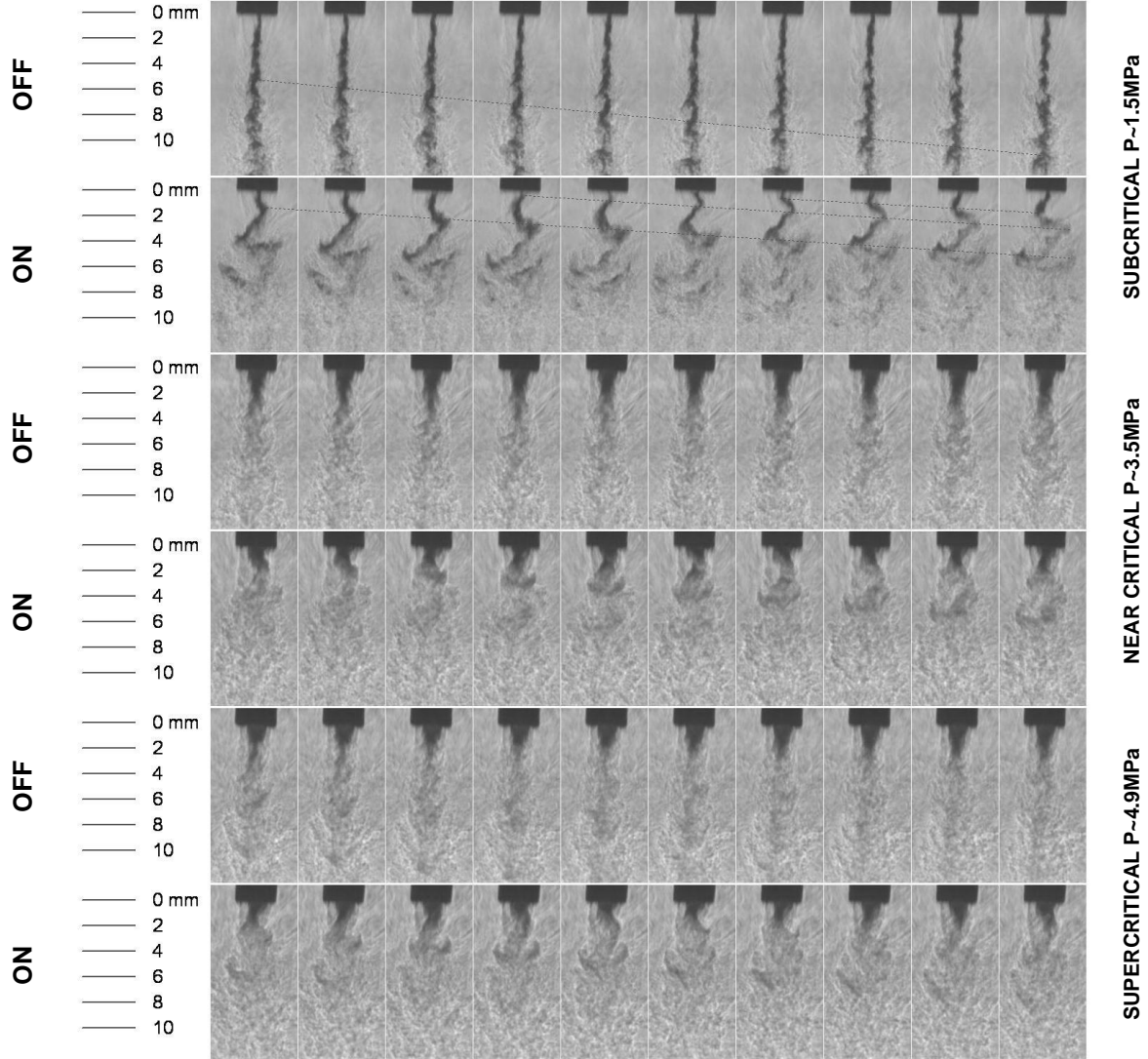


Figure 3. Consecutive frames from high-speed shadowgraph movies with the acoustic driver turned off (in rows 1, 3, and 5) and on (in rows 2, 4, and 6) at $\sim 3\text{kHz}$. Time increases from left to right with an interval of $55.6\ \mu\text{s}$ between frames. The first two rows are at a subcritical chamber pressure ($\sim 1.5\ \text{MPa}$), the third and fourth rows are at a near-critical chamber pressure ($\sim 3.5\ \text{MPa}$), and the fifth and sixth rows are at a supercritical chamber pressure ($\sim 4.9\ \text{MPa}$). The acoustic driver is turned off for the first, third, and fifth rows and on for the second, fourth, and sixth at $\sim 3\ \text{kHz}$. The light gray lines in the first and second rows connect fluid structure as they evolve in time.

and six) chamber pressures are shown in Fig. 3. Rows one, three, and five are for when the acoustic driver is off and the remaining ones are when it is activated at $\sim 3\text{kHz}$. The evolution of the jet in time is from left to right in Fig. 3, with the time interval between frames of $55.6\ \mu\text{s}$. Prominent in all the visualizations of the jet is the existence of a dark central region which we refer to as a “dark core”. The dark core under the unexcited subcritical pressures (Fig. 3, row one) can be approximated as a cylindrical-like structure with unstable surface waves of low amplitude. However, upon increasing the pressure to near- and supercritical pressures (rows three and five) this structure changes to a more conical shape. The conical structure of the dark core has been reported before for single-phase coaxial jets by Lasheras and Hopfinger.²⁰ As clearly demonstrated in images of Fig. 3 and the other visualizations obtained in this work (not shown here), the conical-shape structure was not observed under two-phase conditions (i.e., subcritical chamber pressure).

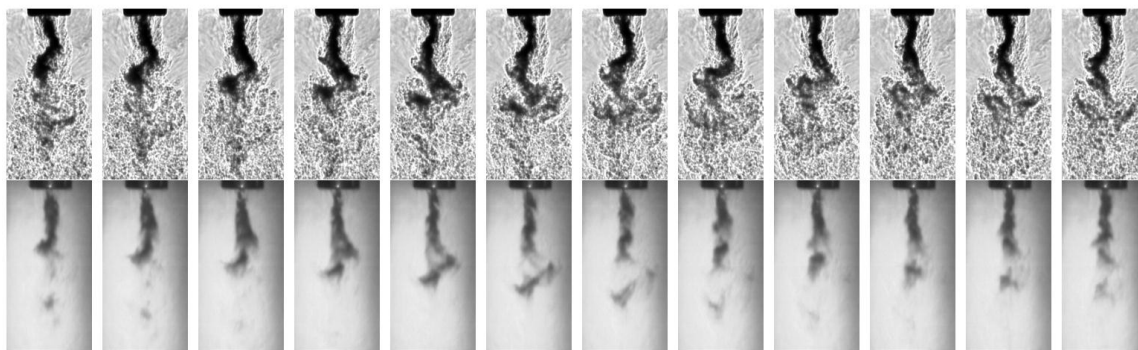


Figure 4. Simultaneous images of the acoustically-excited jet under subcritical conditions viewed from the direction perpendicular (top row) and parallel (bottom row) to the acoustic field velocity. The top row was back-lit and the jet in the lower row is illuminated from the front side. Time increases from left to right. The framing rate for both cameras was 18 kHz and the driving frequency was set at 3 kHz. Approximately two cycles of the acoustic driver oscillations are represented in these images.

Excitation of the jet with acoustic driver yields significantly different behavior of the dark core compared to that of the unexcited one. The strongest effect is observed under subcritical pressures. The cause of this effect is not completely clear at this time. However, it is believed to be as a result of the operation of the acoustic driver at a constant power level at the three pressure levels tested. This is a limitation of the current equipment. As the chamber pressure is increased, the density of the chamber fluid increases also. Therefore, there is more mass for the driver to move and oscillate, thus the amplitude of the velocity fluctuations is reduced at higher pressures. This remains to be verified, as more data is acquired and analyzed.

The direction of the acoustically-induced velocity fluctuations is horizontal (towards left and right) in images of Fig. 3. The core of the jet forms large-scale sinusoidal structures as a result of this imposed velocity field oscillations. To investigate the modal behavior of the jet, two Phantom CMOS cameras were synchronized and the jet imaged both perpendicular and parallel to the acoustic velocity fluctuations. Twelve consecutive images of the jet (approximately two cycles of the acoustic oscillation period), viewed perpendicular (top row) and parallel (bottom row) to the acoustic velocity field, are shown in Fig. 4. The large-scale oscillations of the dark core are principally in the direction of the acoustic velocity. Some three-dimensional movement of the core does occur, but these motions do not occur in a periodic manner, as do the jet oscillations in the direction of the acoustic velocity. The large-scale oscillations of the dark core seen in the top row of Fig. 4 are periodic and correspond to the driving frequency, as tested at the two resonance modes of the chamber (~ 3 and 5.2 kHz). It appears from these movies that as a piece of fluid leaves the injector tip, the momentum from the acoustically-induced motion causes a transverse displacement pushing the core of the jet into the higher speed annular jet. The dense fluid from the core experiences acceleration in the axial direction, which is caused by the high speed annular jet. Upon reversal of the acoustic field, the dense fluid, initially from the core but now in the high-speed annular flow, appears to maintain its transverse component of the momentum imparted upon leaving the injector and hence the dense fluid particle does not reverse its direction. The dense fluid parcel then slows (both in the axial and transverse directions) as it arrives at the shear layer between the outer jet and the chamber fluid farther downstream, where a “cusp-shaped” structure is formed from the dense fluid originating in the core of the jet. Subsequent mixing and heat transfer from the outer jet to the inner jet core fluid ultimately causes the fluid parcel to be indistinguishable from the outer jet fluid.

B. Dark Core Length Measurement Technique

As indicated in Table 1 (in the appendix), many techniques have been employed to measure the core length of a coaxial jet, ranging from Pitot tube measurements to analysis of images. The measurements in this work are taken from a great number of images in a systematic fashion to provide repeatable results. In the past, final results have been reported on as few as four number of images.¹⁰

The algorithm for measuring the dark-core length starts with an individual image, such as Fig. 5(a). From this image, the image histogram, that is, number of pixels vs. gray level, is computed, as shown in Fig. 6 for the image shown in Fig. 5(a). The first peak, located within the gray-scale values below that of the dashed (vertical) line level denotes those corresponding to the injector tip. Ideally, the injector tip should be completely opaque (corresponding

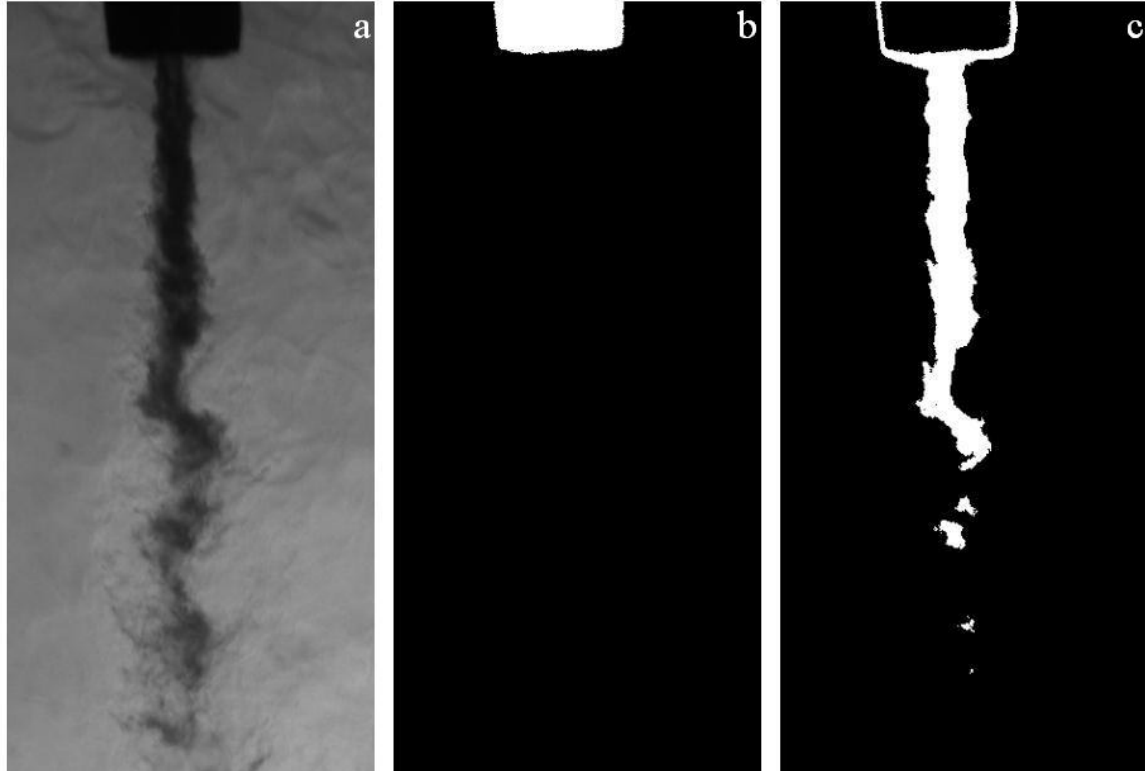


Figure 5. The image of, (a) coaxial jet as captured, (b) threshold applied for injector, (c) threshold applied for identification of the dark core.

to a zero gray-scale value), but due to internal reflections within the chamber this peak shifts slightly off the zero value. The gray levels defining the dark core, ends with the rise of large broad peak on the right, denoting the background, see the dotted vertical line in Fig. 6. This dotted-line gray level is determined by a non-linear curve fitting technique using a Gaussian function to fit to the region of the histogram in the vicinity of the rise of the background information. The slope of this fitted curve is then calculated by differentiation and the gray level at which the slope of the histogram exceeds e^{-1} is determined to be the end of the gray levels defining the dark core, which corresponding to the dotted line in Fig. 6. A binary threshold is then applied to the image between the gray levels indicated by the injector tip (Fig. 5(b)) and the rise of the background information. The resulting image is shown in Fig. 5(c). Such images are then used to measure the axial length of what we refer to as the “dark core” from the injector exit to the end of the interconnected white region seen in this figure. Results from this technique compared well with those when visual judgments were used, see Davis et al.²³

It should be mentioned that confusion exists in the literature especially when vague definitions are used defining a core length. The terms potential-core, potential-cone, intact-length, intact-liquid-length, and breakup-length are all used along with various measurement techniques (see Table 1). To be clear, and remove any possible ambiguity from the data, dark-core length is defined here as the connected dark fluid region between the injector exit area and the first break in the core as defined by the adaptive thresholding procedure outlined above.

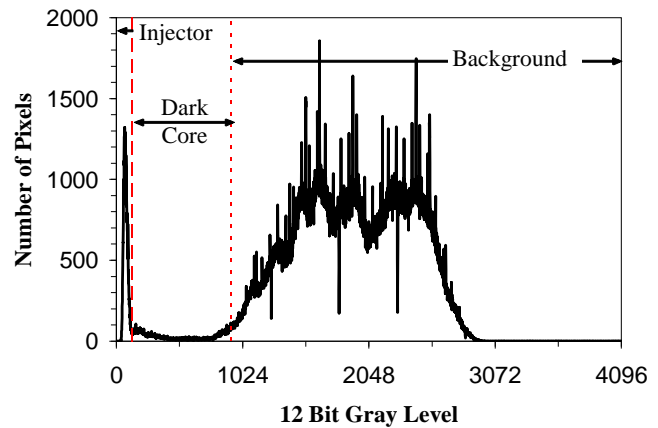


Figure 6. Histogram of the image in Fig. 3a.

C. Influence of Velocity Ratio on Dark Core Length

Velocity ratio (outer-to-inner jet) has been a design parameter for shear-coaxial injectors, particularly, as a criterion to ensure the stable operation of LREs. For LOX/H₂ engines, the design rule-of-thumb has been to keep the velocity ratio greater than about 10 to keep the engine stable, see Hulka and Hutt³⁴. Although experimental data suggests this criterion, no physical explanation has been provided. One method to rate a LRE for combustion instability is temperature ramping, which is accomplished by lowering the temperature of the H₂ while maintaining mass flow rate at a constant value. The lower the H₂ temperature is at the onset of the measured combustion instability, the greater the stability margin of that particular LRE. Note that as the H₂ temperature is lowered at a constant mass flow rate, the velocity ratio is also lowered.

To determine the effects of the outer-jet temperature (which is GN₂ in this work) on the coaxial jet, two nominal temperatures were studied (called high and low). The averaged dark-core lengths are shown in Figs. 7(a) and 8(a) as a function of velocity ratio (V_r). The RMS of the variations of the dark-core length is also shown in Figs. 7(b) and 8(b). Figures 7 and 8 present results for conditions when the external acoustic field is turned on and off for both nominal high and low outer-jet temperatures of ~190 K and ~140 K, respectively. According to Eroglu et al.¹⁰, the average of the length measured from individual images of a set can be regarded as the time averaged value. It should be noted that, for each operating condition in this work, length measurements were also made from an averaged image of a set. In general, the length measured from the averaged image is slightly shorter than the average of the individual dark-core values calculated in a given set.

Evident in Figs. 7(a) and 8(a) is the fact that the length of the dark core decreases as the chamber pressure is increased. The dark core provides an indication of high-density regions of the flow. At a constant chamber pressure, as V_r is increased, the length of the dark core decreases and appears to approach a constant value. In a mean sense, when the dark core feels the imposed external acoustic field, its length is shorter than or equal to that when the acoustic driver is turned off. Under the near- and supercritical chamber pressures, as the V_r increases, the difference between the lengths of the dark core, measured with and without the acoustic field, diminishes. The RMS values of the dark-core length fluctuations, shown in Figs. 7 (b) and 8(b), exhibit somewhat similar trends to those seen with the mean values. It is known that for a liquid-fueled rocket, atomization and breakup processes, interactions between the propellant jets, droplet formation, and vaporization are all affected by the pressure and, particularly, velocity fluctuations. Also, for any chemically-reacting system, the rate at which energy is released is sensitive to the rate of change of temperature, density, pressure, and, of course, mixture ratio. It is then quite intuitive to relate, in some form, the RMS values of the dark-core length fluctuations to mixture ratio variations. On the other hand, a low RMS value can be interpreted as the jet's inherent steadiness (or insensitivity to external stimuli) and vice versa. Examination of Figs. 7b and 8b clearly shows that this property is drastically reduced as the velocity ratio is increased. Although these results are for a single injector (i.e., no inter-injector interaction), it is then quite possible that the observed improvement in combustion stability at higher values of velocity ratio is a result of the inability of the jet to generate large mass flow rate fluctuations under these conditions, weakening a key feedback line for the self-excitation process. In temperature ramping exercises for stability rating of LOX/H₂ engines, the mass flow rate is usually maintained at a constant value.³⁴ Therefore, as the temperature of the H₂ is decreased during a ramping episode, the H₂ becomes more dense, which decreases the injector velocity ratio. The RMS plots shown here suggest that such a decline in this ratio amplifies the jet's inherent unsteadiness, providing a possible explanation for the engine's eventual arrival into an unstable zone as a temperature ramping test proceeds.

D. Scaling of the Dark Core Length

As mentioned above, the core length has been scaled with many parameters. In some work, We and Re numbers were used to represent velocity values in nondimensionalized forms, as physical parameters, such as surface tension and viscosity, were not varied. In other work, based on single-phase results, velocity ratio (V_r) or momentum flux ratio (M) were considered as the scaling parameters. The semi-empirical theory of Rehab et al.¹⁷ which is based on an entrainment velocity of the inner jet into the outer jet and a resulting mass balance on the core of the jet, produces an equation suggesting that the length of the core scales with $M^{-0.5}$. This equation was then quantitatively compared to single-phase shear-coaxial jet data, often with equal densities.¹⁶⁻¹⁸ Note that for (inner and outer) jets of equal densities, $M^{-0.5}$ reduces to V_r . The same dependence on M was also reported qualitatively for single-phase shear-coaxial jets of different densities by Favre-Marinet and Samano-Shettini.²¹ Additionally, Lasheras et al.¹⁹ stated applicability of the same $M^{-0.5}$ dependence form for two-phase shear-coaxial jets. However, they were unable to make core length measurements from their images.

A plot of the measured dark-core length values, of this work, versus momentum flux ratio is shown in Fig. 9. A clear distinction between the subcritical dark-core length (diamond symbols) and that for the near- and supercritical chamber pressures are seen. Subcritical data indicates a much longer length than the supercritical pressure for a

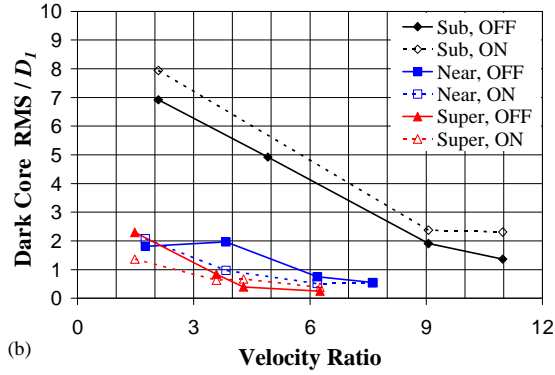
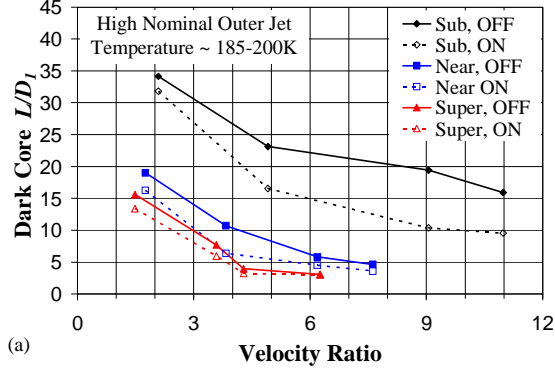


Figure 7. Plot of the averaged dark-core length (a) and the RMS of the length variations (b) normalized by the inner diameter. The solid symbols and lines represent the data for when the acoustic driver is off, and the hollow symbols and dotted lines show the data when the acoustic driver was operated at $\sim 3\text{kHz}$. The diamond, square, and up-triangle symbols are sub-, near-, and supercritical chamber pressures, respectively. All cases are for the high nominal outer-jet temperature of $\sim 190\text{ K}$. In the inset, the words sub, near, and super refer to subcritical, nearcritical, and supercritical pressure respectively, and the words OFF and ON refer to the acoustic driver being off and on at $\sim 3\text{kHz}$, respectively.

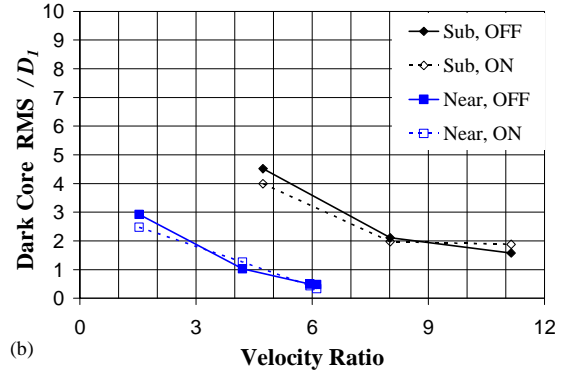
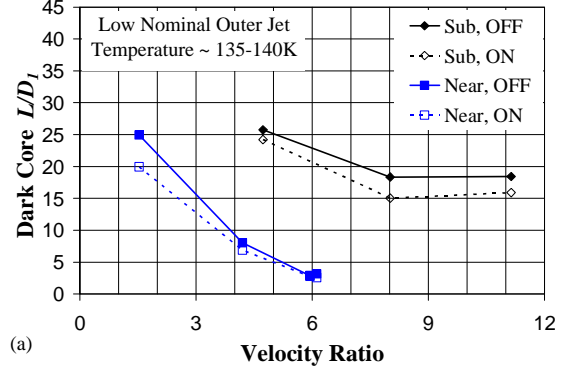


Figure 8. Plot of the averaged dark-core length (a) and the RMS of the length variations (b) normalized by the inner diameter. The solid symbols and lines represent data for when the acoustic driver off, and the hollow symbols and dotted lines show results when the acoustic driver is operated at $\sim 3\text{kHz}$. The diamond and square symbols are for sub- and nearcritical chamber pressures, respectively. All cases are for the low nominal outer-jet temperature of $\sim 140\text{ K}$. In the inset, the words sub and near refer to subcritical and nearcritical pressure respectively, and the words OFF and ON refer to the acoustic driver being off and on at $\sim 3\text{kHz}$, respectively.

given momentum flux ratio. It should be noted that the near-critical pressure data is slightly supercritical, and both the near- and supercritical pressure conditions produce a single-phase coaxial jet. The dashed line in Fig. 9 is a least-square curve fit to the subcritical data, and the dotted line is a least squares curve fit to the near- and supercritical data. As indicated by the equations on Fig. 9, the single-phase (i.e., near- and supercritical pressures), data have the same $M^{-0.5}$ dependence form as reported by others.^{16-18, 21} However, the two-phase subcritical data has a weaker dependence, $M^{0.2}$, than the single-phase dark-core length. Other quantitative differences between the subcritical and supercritical cases have been reported before. For single round jets, Chehroudi^{28,29, 31} and co-workers found that under supercritical pressures the spreading rate and fractal dimension values were the same as those for a gaseous jet injected into a gaseous ambient with different densities (i.e., variable-density, single-phase, gaseous jet). This is a similar observation but for the dark-core length. Under supercritical pressures, our coaxial jet scales with $M^{0.5}$. Therefore, it appears that this form of the dependency to M is not only valid for gas-gas shear-coaxial jets, but as any single-phase shear-coaxial jet, such as the system where the original dependence $f M^{-0.5}$ was found from the water-water work of Rehab et al.^{16,17}

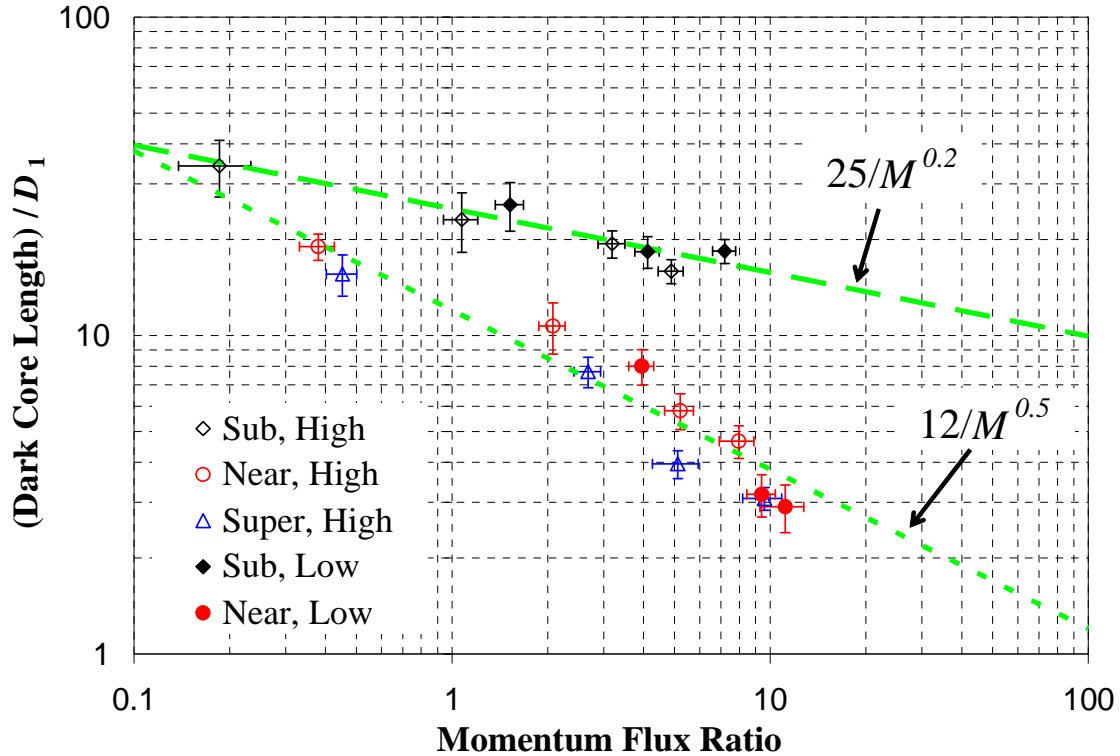


Figure 9. Dark-core length versus momentum flux ratio. The diamond, circle, and up-triangle symbols represent sub-, near-, and supercritical chamber pressure, respectively. The hollow symbols are at a high outer-jet temperature (~ 190 K) and solid symbols are at a low outer-jet temperature. The dashed line is $25/M^{0.2}$ and the dotted line is $12/M^{0.5}$.

Figure 10 was constructed with the objective of comparing the dark-core length with all of the available data that exists in the literature for the potential-core length, intact-core length, and breakup-length. Figure 10 represents all of the available data in the literature concerning core length spanning 5 orders of magnitude in momentum flux ratio. Also, note that as M approaches zero, one reaches a limit defining a single round jet configuration because the outer velocity becomes zero. From data in Fig 10, it seems that for $M < 1$, data points converge and approach the core length range expected for single round jets reported by Chehroudi et al.³⁵ and Oschwald et al.³³ The single-phase data presented in Fig. 10 follows the dependence of $L/D_i = A M^{0.5}$, where the constant A is between 5 and 12. At $M > 100$, the data points of Favre-Marinet and Samano-Shettini²¹ exhibit a recirculation bubble at the end of the core, and thus the core length decreases. The injectors used to produce the two-phase coaxial jets of Eroglu et al.¹⁰ and Englebert et al.¹² have much larger outer jet gap widths (see Table 1) than what is typical of rocket injectors. Additionally, the apparatus of Eroglu et al.¹⁰, reported in Farago and Chigier³⁶, does not produce fully-turbulent inner jet until when $Re > 10^4$. The lack of a fully-turbulent inner jet and the significant differences between their injector and shear-coaxial ones used in rockets could be the reasons the core length measured by Eroglu et al.¹⁰ is shorter than those observed in our work. Englebert et al.¹² reported that the core length scaled with $M^{-0.3}$. The core length by Woodward¹¹ for the water potassium iodide solution with helium, however, obeys very nearly the trends for the subcritical data points (i.e., $25M^{0.2}$). Considering that momentum flux ratios near 10 are of importance for LRE, to the best of the authors' knowledge, the data for the subcritical (two-phase) case is the only reported information in the neighborhood of the $M = 10$.

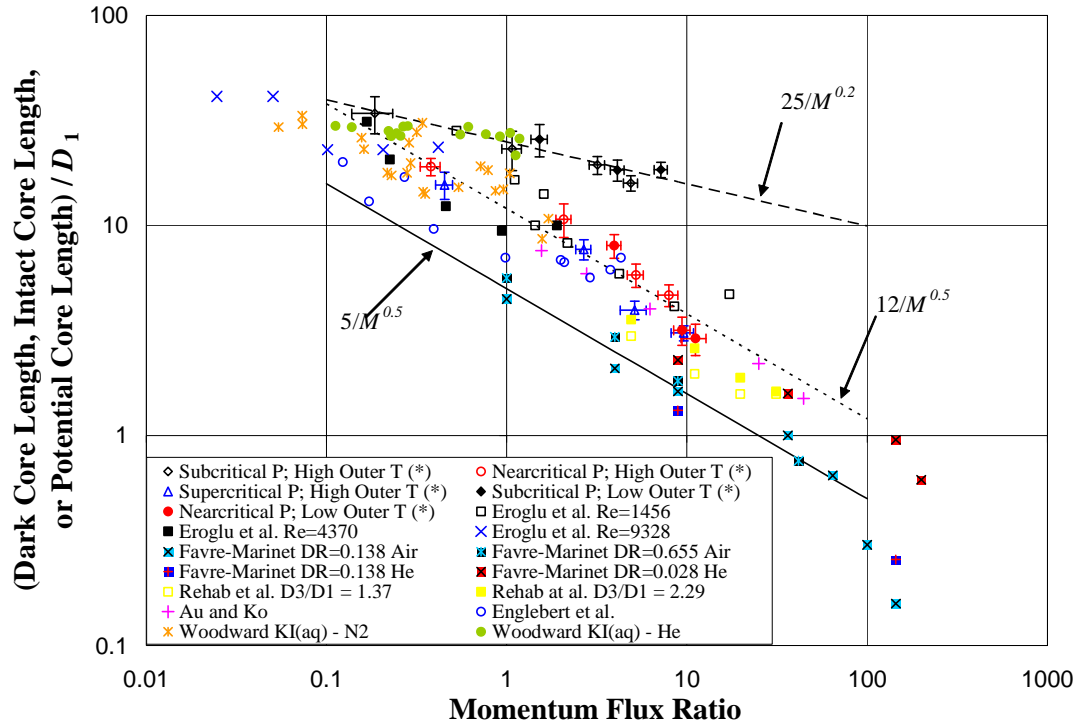


Figure 10. Comparison of present dark-core length measurements with all other core-length data available in the literature vs. momentum flux ratio. Amongst the data reported by others, Eroglu et al., Englebert et al., and Woodward are two-phase flows and the rest are single phase. The references for the data are found in Table 1.

IV. Summary and Conclusions

A non-reacting flow study of a cryogenic shear-coaxial injector was conducted at pressures spanning subcritical to supercritical values. The flow from the inner jet of the coaxial injector was liquid nitrogen (or liquid-like, if at supercritical pressures) and cold gaseous nitrogen flowed from the outer annular jet, both injected into a chamber pressurized with nitrogen at room temperature. The resulting coaxial jet was imaged with a camera framing at a rate of up to 18 kHz. The jet was excited with a high-amplitude acoustic driver, with the jet located at a velocity anti-node (pressure node). The following conclusions are offered:

1. Existence of high-amplitude acoustic waves alter the behavior of the shear-coaxial jet. The resulting structure of the jet exhibits a periodic shape corresponding to the transverse-velocity field created by the acoustic waves. The periodic oscillations imposed on the dark core of the jet is predominately in the direction of the transverse acoustic velocity. No helical mode for the jet was observed.
2. The root mean square (RMS) variation of the dark-core length decreases with increasing velocity ratio at a given chamber pressure and asymptotically approaches a constant level. The RMS of the dark-core length is greatest at subcritical pressures. To the best of the authors' knowledge, this quantity was not previously reported in the literature.
3. Previous research showed that an episode of so-called "temperature ramping", used for stability rating, could lead the engine to an unstable behavior. Also, from other works, it is shown that coaxial injectors with high outer-to-inner jet velocity ratios (greater than ~10 for LOX/H₂) are more stable. In the current work, the observation that the RMS of the dark-core length fluctuations decreased at high velocity ratio under both high and low outer-jet temperatures, is considered as a potential explanation of the injector-induced combustion instabilities. It is possible that decreases in the RMS fluctuation levels could weaken a key feedback mechanism for the self-excitation process that is believed to drive the combustion instability in rocket engines. This offers a possible improvement in understanding of the combustion instability in LRE. Ultimately, this hypothesis requires further testing in a multi-element, fired rocket experimental facility, for validation purposes.

4. The quantitative behavior of the dark-core length of the coaxial jet at near- and supercritical pressure follows a similar momentum flux ratio (M) dependency reported for the single-phase shear-coaxial jets (i.e., $12M^{-0.5}$). The dark-core length for the subcritical chamber pressures, however, scales with $M^{-0.2}$.
5. Within a range of momentum flux ratios in between 1 and 10, the dark-core lengths for the coaxial jet under the subcritical (two-phase) ambient pressure used here appear longer than those measured at the supercritical (single-phase) condition. This range represents relevant values for liquid rocket engines, subcritical data define a new regime which was not reported previously.

Appendix

Table 1. Summary of published operating conditions, geometries, measurement techniques, and proposed equations from the literature, measuring or correlating core length for shear-coaxial jets.

REF	Author	Date	Fluid Inner Jet	Fluid Outer Jet	Fluid Ambient	Pressure (MPa)	T_i (K)	T_o (K)	T_∞ (K)
6	Forstall & Shapiro	1950	Air+ 10 %He	Air	Air	0.1*	Amb. ^a	Amb.	Amb.
7	Chigier & Beer	1964	Air	Air	Air	0.1*	Amb.	Amb.	Amb.
8	Champagne & Wygnanski	1971	Air	Air	Air	0.1	Amb.	Amb.	Amb.
9	Au and Ko	1987	Air	Air	Air*	0.1*	Amb.	Amb.	Amb.
10	Eroglu et al.	1991	Water	Air	Air	0.1*	Amb.	Amb.	Amb.
11	Woodward	1993	KI (aq.)	N2, He	N2, He	0.1 – 2.17	Amb.	Amb.	Amb.
15	Villermaux et al. ^g	1994	Water	Water	Water	0.1*	Amb.	Amb.	Amb.
12	Englebert et al.	1995	Water	Air	Air	0.1	293	293 – 636	293
13	Carreau et al.	1997	LOX	He, N2, Ar	NC ^c	0.1	82 ^d	245 – 272 ^d	NC
16	Rehab et al. ^g	1997	Water	Water	Water	0.1*	Amb.	Amb.	Amb.
17	Rehab et al. ^g	1998	Water	Water	Water	0.1*	Amb.	Amb.	Amb.
18	Villermaux ^{g,h}	1998	Water	Water	Water	NR	NR	NR	NR
19	Lasheras et al. ^g	1998	Water	Air	Air	0.1	Amb.	Amb.	Amb.
20	Lasheras & Hopfinger ^{g,i}	2000	NR	NR	NR	NR	NR	NR	NR
21	Favre-Marinet & Schettini	2001	Air, SF6	Air,He	Air, He	0.1	Amb.	Amb.	Amb.
14	Porcheron et al.	2002	LOX, Water	He, N2, Ar, Air	Air	0.1	82, 293	245 – 293	293
This work	Davis	2005	N2	N2	N2	1.4 – 4.9	108 – 133	132 – 204	197 – 249

Table 1. Summary of published operating conditions, geometries, measurement techniques, and proposed equations from the literature, measuring or correlating core length for shear-coaxial jets. (continued)

REF	Author	Density Ratio Outer / Inner	Velocity Ratio Outer / Inner	M Outer / Inner	Re Inner ($\times 10^4$)	Re Outer ($\times 10^4$)	We
6	Forstall & Shapiro	1.09	0.2 - 0.75	0.04 - 0.61	NR	NR	NA
7	Chigier & Beer	1*	0.024 - 9.22	5.8×10^{-4} - 85.0	$\sim 10^b$	$\sim 10^b$	NA
8	Champagne & Wygnanski	1*	0 - 10	0 - 100	1.01 - 10.15	0 - 9.6	NA
9	Au and Ko	1*	1.25 - 6.67	1.5 - 44	NR	NR	NA
10	Eroglu et al.	0.001	4.5 - 131.2	0.02 - 17.2	0.15 - 0.93	2.0 - 11.6	15 - 530
11	Woodward	0.0006 - 0.018	0 - 30	0 - 1.7	7.86 - 18.9	NR	$12 - 3.6 \times 10^4$
15	Villiermaux et al. ^g	1	1 - 6	1 - 36	>5000	>5000	NA
12	Englebert et al.	0.0008 - 0.0012	10.25 - 66.75	0.12 - 4.3	0.54 - 3.4	4.8 - 16.5	76 - 2610
13	Carreau et al.	NR	NR	3 - 21.5	5.32 - 8.11	NR	9.19×10^3 - 3.48×10^4
16	Rehab et al. ^g	1	2 - 5	4 - 25	NR ^f	NR ^f	NA
17	Rehab et al. ^g	1	2.2 - 5.6	4.9 - 31	1 - 10	1 - 10	NA
18	Villiermaux ^{g,h}	1*	NR	NR	NR	NR	NR
19	Lasheras et al. ^g	0.001	NR	NR	NR	NR	NR
20	Lasheras & Hopfinger ^{g,i}	NR	NR	NR	NR	NR	NR
21	Favre-Marinet & Schettini	0.028 - 1	3.0 - 70	1 - 200	NR	3.2, 11.0	NA
14	Porcheron et al.	1.6×10^{-4} - 2.3×10^{-3}	NR	2 - 21.6	NR	NR	0 - 14000
This work	Davis	0.04 - 0.56	1.2 - 11.1	0.19 - 11.2	1.2 - 3.2	0.8 - 19	32 - ∞

Table 1. Summary of published operating conditions, geometries, measurement techniques, and proposed equations from the literature, measuring or correlating core length for shear-coaxial jets. (continued)

REF	Author	D_1 (mm)	D_2 (mm)	D_3 (mm)	$(D_3-D_2)/2$ (mm)	Area Ratio Outer / Inner	Post Recess (mm)	Injector L_{post}/D_1
6	Forstall & Shapiro	6.4, 25	NR	102	NR	NR	NR	NR
7	Chigier & Beer	25	64	97	16.5	8.50	0*	NR
8	Champagne & Wagnanski	25	NR	NR	NR	1.28, 2.94	0*	NR
9	Au and Ko	2	2.2	4	0.9	2.79	0*	NR
10	Eroglu et al.	0.971	1.262	10.36	4.549	112.15	-0.6	57
11	Woodward	4.76	6.35	9.86	1.76	2.51	0.0	85
15	Villiermaux et al. ^g	40	51	55	0.2	0.27	0*	"long"
12	Englebert et al.	2.3	2.95	14.95	6.00	40.60	0	22
13	Carreau et al.	5 ^d	5.57 ^d	16 ^d	5.2 ^d	9	0	NR
16	Rehab et al. ^g	20	21	27	3	1.82	0	NR
17	Rehab et al. ^g	NR	NR	NR	NR	1.82, 1.87, 5.24 ^e	0 – 2 D_1	NR
18	Villiermaux ^{g,h}	NR	NR	NR	NR	NR	NR	NR
19	Lasheras et al. ^g	3.8	4.2	5.6	0.7	0.95	0	29
20	Lasheras & Hopfinger ^{g,i}	NR	NR	NR	NR	NR	NR	NR
21	Favre-Marinet & Schettini	20	20.4	27	3.3	0.78	0	6.75
14	Porcheron et al.	5, 2.1	5.57, 2.5	16, 7	2.25	9, 9.69	0*	NR
This work	Davis	0.51	1.59	2.42	0.415	12.80	0.25	100

Table 1. Summary of published operating conditions, geometries, measurement techniques, and proposed equations from the literature, measuring or correlating core length for shear-coaxial jets. (continued)

REF	Author	Diagnostic	Quantity Measured	Equation
6	Forstall & Shapiro	Pitot tube, Sampling Tube	Potential Core	$L/D_1 = 4 + 12V_r$
7	Chigier & Beer	Pitot tube	Potential Core	NR
8	Champagne & Wagnanski	Hot wire anemo-meter	Inner Core	NR
9	Au and Ko	Hot wire anemo-meter	Potential Core	$L/D_1 = 9.9/V_r$
10	Eroglu et al.	Back-lit still	Liquid Intact Length	$L/D_1 = 0.66 We^{-0.4} Re^{0.6}$
11	Woodward	x-ray Radiography	Intact Liquid Core Length	$L/D_1 = 0.0095 \left(\frac{\rho_o}{\rho_i} \right)^{\frac{-0.36}{H}} We^{-0.22/H} Re^{0.68}$
15	Villiermaux et al. ^g	Hot film anemo-meter	Potential Core / Cone	$L/D_1 = 7/V_r$
12	Englebert et al.	Back-lit high-speed 16mm film	Breakup Length	$L/D_1 = 40 We^{-0.27}$ $\frac{2L}{D_3 - D_2} = 10.6 M_R^{-0.3} = 13.7 E_R^{-0.2}$
13	Carreau et al.	Fiber optic Probe	Breakup Length, Potential Cone Length	$L/D_1 = 0.0012 \left(\frac{\rho_o}{\rho_i} \right)^{-0.32} We^{-0.33} Re^{0.55}$
16	Rehab et al. ^g	Hot film anemo-meter, Pitot tube, LIF image	Potential Core	$L/D_1 = 6/V_r; L/D_1 = 8/V$ $L/D_1 = 0.5 \left(\frac{1}{(C\alpha V_r)^2} - 1 \right)^{1/2} \approx \frac{1}{2C\alpha V_r}$
17	Rehab et al. ^g	Hot-film anemo-meter	Potential Cone	$L/D_1 = c/V_r; 6 < c < 8$
18	Villiermaux ^{g,h}	^h	Potential Cone, Liquid intact length	$L/D_1 = 6/M^{1/2}$

Table 1. Summary of published operating conditions, geometries, measurement techniques, and proposed equations from the literature, measuring or correlating core length for shear-coaxial jets. (continued)

REF	Author	Diagnostic	Quantity Measured	Equation
19	Lasheras et al. ^g	Photo-graph	Liquid intact length	$L / D_1 = \left(\frac{1}{4 (C \alpha)^2 M} - \frac{1}{4} \right)^{1/2} \approx \frac{6}{M^{1/2}}$
20	Lasheras & Hopfinger ^{g,i}	i	i	$L / D_1 = \frac{1}{2 c M^{2/3}} \left(\frac{\sigma}{\mu_i U_i} \right)^{1/3}$ $L / D_1 \approx \frac{6}{M^{1/2}} \left(1 - \frac{U_i}{U_o} \right)^{-1}$ $L / D_1 \approx \frac{6}{M^{1/2}} \frac{1}{\left(1 - \frac{B \sigma}{\mu_o U_o} \right)^{0.5}}$
21	Favre-Marinet & Schettini	Aspirating Probe w/ hot-wire	Potential Core	$L / D_1 \propto M^{-0.5}$
14	Porcheron et al.	Fiber optic Probe	Liquid Core	$L / D_1 = 2.85 \left(\frac{\rho_o}{\rho_i} \right)^{-0.38} Z^{0.34} M^{-0.13}$
This work	Davis	Shadow-graph	Dark Core	$L / D_1 \approx \frac{12}{M^{1/2}}$ $L / D_1 \approx \frac{25}{M^{0.2}}$

Table 1. Notes

NR = not reported

NA = not applicable

NC = not clear from report

Amb. = ambient

* assumed from the context, but not directly reported

^a Ambient temperature assumed from the context of discussion, but not specifically stated in report.

^b reported as approximately 10^5

^d The dimensions of the injector and the temperatures were not given in the paper, but were given in the paper by Porcheron et al.¹⁴

^e This number is the diameter ratio squared, which is approximately the area ratio for a very thin lip injector. The only dimensional information given was the diameter ratios (1.35, 1.37, and 2.29 mm) and the lip thickness $(D_2 - D_1)/2$ of 0.3 mm.

^f A Re based on momentum conservation reported and defined as

$$Re = \rho_o U_o D_3 / \mu^* (1 - (D_1/D_3))^{0.5} \text{ ranged from } 10^4 - 10^5.$$

^g These papers are from the same collaboration / research group over several years.

^h This paper was an analysis paper that presented a different equation based on the data from the same group of researchers^{16,17}

ⁱ This paper was a review paper encompassing the work from this same collaboration of researchers, as well as others.

^j Unable to make measurements from images, and therefore not compared quantitatively to theory for core length.

Acknowledgments

The authors would like to acknowledge Dr. Douglas Talley for his interest, support, and contributions with this ongoing project, and many valuable discussions. The authors would like to recognize Mr. Mike Griggs for his valuable contributions in the improvements to the experimental facility. Lt. Matthew Raskie, Lt. Jason Szuminski, Mr. Earl Thomas, Mr. Randy Harvey, Mr. David Hill, and Mr. Mark Wilson are thanked for their efforts. Additionally, Ms. Jennie Paton is thanked for making literature available in a timely manner. A great appreciation is extended to Mr. Steven Martin for loaning the authors one of the Phantom Cameras. A special gratitude is expressed to M. Favre-Marinet, E. B. Camano Schettini, and R. D. Woodward for providing us with their core length data in tabular form. D. W. Davis would like to thank his thesis advisor, Dr. R. J. Santoro, for many helpful discussions and permitting his thesis work to be performed off-campus at AFRL. This work is sponsored by the Air Force Office of Scientific Research under Dr. Mitat Birkan, program manager..

References

- ¹Harje, D. T. and Reardon, F. H. (eds.), *Liquid Propellant Rocket Combustion Instability*, NASA SP-194, 1972.
- ²Yang, V. and Anderson, W. (eds.), *Liquid Rocket Engine Combustion Instability*, Progress in Astronautics and Aeronautics, AIAA, Washington, DC, 1995.
- ³Heidmann, M. F. *Oxygen Jet Behavior During Combustion Instability in a Two-Dimensional Combustor*, NASA TN D-2725, 1965.
- ⁴Miesse, C. C., "The effect of ambient pressure oscillations on the disintegration and dispersion of a liquid jet", *Jet Propulsion*, Vol. 25, 1955, pp. 525-530, 534.
- ⁵Buffum, F. G., and Williams, F. A., "Response of turbulent liquid jets to transverse acoustic fields", *Proceedings of the 1967 Heat Transfer and Fluid Mechanics Institute*, Edited by P. A. Libby, D. B. Olfe, and C. W. Van Atta, 1967, pp. 247-276.
- ⁶Forstall, W., and Shapiro, A. H., "Momentum and Mass Transfer in Coaxial Gas Jets," *J. Applied Mechanics*, Trans. ASME, Vol. 72, 1950, pp. 399-408.
- ⁷Chigier, N. A., and Beer, J. M., "The Flow Region Near the Nozzle in Double Concentric Jets," *J. of Basic Engineering*, Trans. ASME, Vol. 4, 1964, pp. 797-804.
- ⁸Champagne, F. H., and Wagnanski, I. J., "An experimental Investigation of Coaxial Turbulent Jets," *International Journal of Heat and Mass Transfer*, Vol. 14, 1971, pp. 1445-1464.
- ⁹Au, H., and Ko, N. W. M., "Coaxial Jets of Different Mean Velocity Ratios, Part 2," *Journal of Sound and Vibration*, Vol. 116, No. 3, 1987, pp. 427-443.
- ¹⁰Eroglu, H., Chigier, N., and Farago, Z., "Coaxial Atomizer Intact Lengths," *Physics of Fluids A*, Vol. 3, No. 2, Jan. 1991, pp. 303-308.
- ¹¹Woodward, R. D., "Primary Atomization of Liquid Jets Issuing from Rocket Engine Coaxial Injectors," Ph.D. Dissertation, Department of Mechanical Engineering, The Pennsylvania State University, University Park, PA, 1993.
- ¹²Englebert, C., Hardalupas, Y., and Whitlaw, J. H., "Breakup Phenomena in Coaxial Air-Blast Atomizers," *Proc. R. Soc.*, Vol. 451, London, 1995, pp. 189-229.
- ¹³Carreau, J. L., Porcheron, E., LeVisage, D., Prevost, L., and Roger, F., "Liquid Core Characterization of Coaxial Liquid Oxygen/Inert Gas Jets," *Int. J. of Fluid Mech. Research*, Vol. 24, Nos. 4-6, 1997, pp.498-507.
- ¹⁴Porcheron, E., Carreau, J. L., Prevost, L., LeVisage, D., and Roger, F., "Effect of Density on Coaxial Liquid Jet Atomization," *Atomization and Sprays*, Vol. 12, 2002, pp. 209-227.
- ¹⁵Villermaux, E., Rehab, H., and Hopfinger, E. J., "Breakup Regimes and Self-Sustained Pulsations in Coaxial Jets," *Meccanica*, Vol. 29, 1994, pp. 393-401.
- ¹⁶Rehab, H., Villermaux, E., and Hopfinger, E. J., "Geometrical Effects of Near-Field Flow Structure of Coaxial Jets," *AIAA Journal*, Vol. 36, No. 5, 1998, pp. 867-869.
- ¹⁷Rehab, H., Villermaux, E., and Hopfinger, E. J., "Flow Regimes of Large Velocity Ratio Coaxial Jets," *J. Fluid Mech.*, 1997, pp.357-381.
- ¹⁸Villermaux, E., "Mixing and Spray Formation in Coaxial Jets," *J. Propulsion and Power*, Vol. 14, No. 5, 1998, pp. 807-817.
- ¹⁹Lasheras, J. C., Villermaux, E., and Hopfinger, E. J., "Breakup and Atomization of a Round Water Jet by a High Speed annular Air Jet," *J. Fluid Mech.*, Vol. 357, 1998, pp. 351-379.
- ²⁰Lasheras, J. C., and Hopfinger, E. J., "Liquid Jet Instability and Atomization in a Coaxial Gas Stream," *Annual Rev. Fluid Mech.*, Vol. 32, 2000, pp. 275-308.
- ²¹Favre-Marinet, M., and Camano Schettini, E. B., "The Density Field of Coaxial Jets with Large Velocity Ratio and Large Density Differences," *International Journal of Heat and Mass Transfer*, Vol. 44, 2001, pp. 1913-1924.
- ²²Davis, D. W. and Chehrودي, B., "The Effects of Pressure and Acoustic Field on a Cryogenic Coaxial Jet," *42nd AIAA Aerospace Sciences Meeting & Exhibit*, AIAA, Washington, DC, 5-8 Jan. 2004.
- ²³Davis, D. W., Chehrودي, B., and Sorensen, I. "Measurements in an Acoustically Driven Coaxial Jet under Supercritical Condition," *43rd AIAA Aerospace Sciences Meeting & Exhibit*, AIAA, Washington, DC, 10-13 Jan. 2005.
- ²⁴Davis, D. W., and Chehrودي, B., "Measurements of an Acoustically Driven Coaxial Jet under Sub-, Near-, and Supercritical Conditions," *J. of Propulsion and Power*, 2005 (submitted).

- ²⁵Chehroudi, B., Talley, D., and Coy, E. B., "Initial Growth Rate and Visual Characteristics of a Round Jet into a Sub- to Supercritical Environment of Relevance to Rocket, Gas turbine, and Diesel Engines," *37th AIAA Aerospace Science Meeting and Exhibit*, AIAA, Washington, DC, 11-14 Jan. 1999.
- ²⁶Chehroudi, B., Talley, D. G., and Coy, E. B., "Fractal Geometry and Growth Rate Changes of Cryogenic Jets near the Critical Point," *35th AIAA/ASME/SAE/ASEE Joint Propulsion Conference and Exhibit*, AIAA, Washington, DC, 20-24 Jun. 1999.
- ²⁷Chehroudi, B., Cohn, R., Talley, D. G., and Badakhshan, A., "Raman Scattering Measurements in the Initial Region of Sub- and Supercritical Jets," *36th AIAA/ASME/SAE/ASEE Joint Propulsion Conference and Exhibit*, AIAA, Washington, DC, 17-19 Jul. 2000.
- ²⁸Chehroudi, B., Talley, D. G., and Coy, E. B. "Visual Characteristics and Initial Growth Rates of Round Cryogenic Jets at Subcritical and Supercritical Pressures," *Physics of Fluids*, Vol.4, No. 2, Feb. 2002. pp. 850-861.
- ²⁹Chehroudi, B., Cohn, R., and Talley, D. G., "Cryogenic Shear Layers: Experiments and Initial Growth Rates of Round Cryogenic Jets at Subcritical and Supercritical Pressures," *International Journal of Heat and Fluid Flow*, Vol. 23, 2002, pp. 554-563.
- ³⁰Chehroudi, B., and Talley, D. G., "Interaction of Acoustic Waves with a Cryogenic Nitrogen Jet at Sub- and Supercritical Pressures," *40th AIAA Aerospace Meeting and Exhibit*, AIAA, Washington, DC, 14-17 Jan. 2002.
- ³¹Chehroudi, B. and Talley, D., "Fractal Geometry of a Cryogenic Nitrogen Round Jet Injected into Sub- and Super-critical Conditions", *Atomization and Sprays*, Vol. 14, 2004, pp. 81-91.
- ³²Chehroudi, B., Davis, D. W., and Talley, D. G., "Initial Results from A Cryogenic Coaxial Injector In An Acoustic Field," *41st AIAA Aerospace Sciences Meeting & Exhibit*, AIAA, Washington, DC, 6-9 Jan. 2003.
- ³³Oschwald, M., Smith, J. J., Branam, R., Hussong, J., Schik, A., Chehroudi, B., and Talley, D. G., "Injection of Fluids into Supercritical Environments," *Comb. Sci. Tech.*, Accepted, 2005.
- ³⁴Hulka, J., and Hutt, J., "Liquid Oxygen / Hydrogen Instability Phenomena," *Liquid Rocket Engine Combustion Instability*, edited by V. Yang and W. Anderson, *Progress in Astronautics and Aeronautics*, AIAA, Washington, DC, 1995, pp. 39-72.
- ³⁵Chehroudi, B., Chen, S. H., Bracco, F. V., and Onuma, Y., 1985. On the Intact Core of Full-Cone Sprays, Society of Automotive Engineers, 1985 Congress and Exposition, *SAE Transaction Paper 850126*, February 25-March 1.
- ³⁶Faragó, Z., and Chigier, N., "Morphological Classification of Disintegration of Round Liquid Jets in a Coaxial Air Stream," *Atomization and Sprays*, Vol. 2, 1992, pp. 137-153.

Paper ID ICLASS06-270

A ROCKET-LIKE COAXIAL INJECTOR IN AN ACOUSTIC FIELD UNDER SUB- AND SUPERCRITICAL CONDITIONS

Davis, D. W. ¹, Chehroudi, B. ², and Talley, D. G. ³

¹ERC, Inc., Dustin.Davis@ge.com (Presently at GE Global Research Center, Niskayuna, NY)

²ERC, Inc., Bruce.Chehroudi@Edwards.af.mil (or, ChehroudiB@aol.com, corresponding author)

³Air Force Research Laboratory, Douglas.Talley@Edwards.af.mil

ABSTRACT An experimental investigation was undertaken under non-reacting condition to gain a physical understanding of the interaction of acoustic waves and a coaxial-jet injector similar to those used in cryogenic liquid rockets. Liquid nitrogen (the round inner jet) and gaseous nitrogen (the annular outer jet) were used under subcritical, near critical, and supercritical chamber pressures, with and without presence of an external acoustic field. High-speed images of the jet provided information on the dynamic behavior of the jet at a variety of conditions. It is found that when the jet is at the pressure minimum, an externally-imposed acoustic field excites the dark-core of the jet to a wavy-shaped structure consistent with the field's characteristics. Mean and root mean square (RMS) values of the dark-core length fluctuations were measured from images. It is found that when the outer-to-inner-jet velocity ratio increases, the RMS of the dark-core length fluctuations decreases both with and without the existence of the acoustic field. A connection to the rocket instability may be established from these data through examination of the RMS values. It is possible that decreases in the fluctuation levels, observed at higher velocity ratios, could weaken a key feedback mechanism for the self-excitation process that could be driving combustion instability in rocket engines. This can offer a possible explanation of the combustion stability improvements experienced in engines when a transition to higher values of the outer-to-inner-jet velocity ratio is made. Finally, after a careful review of relevant data taken here and elsewhere, there appears to be a good correlation between the dark-core length and the momentum flux ratio.

Keywords: Supercritical fluids, Acoustic, Combustion Instability, Liquid Rocket Engine, Coaxial Injector, Atomization, Liquid Core, Spray

1. BACKGROUND

Combustion instabilities, manifested as pressure variations, in liquid rocket engines (LREs) can reach amplitudes of 100% of chamber pressure and damage an engine in a fraction of a second [1, 2]. The combustion instability mechanisms span from low-frequency mechanisms, which is a feed-system coupled instability, to high-frequency mechanisms, which depend on the acoustic modes of the chamber. Often LREs operate at chamber pressures which exceed the critical pressure of the propellants. In such cases, while the pressure is supercritical, the initial temperature of the propellants is often subcritical, but heats to supercritical temperatures during mixing and combustion processes.

Many fundamental questions remain to be answered regarding the physical behavior of the propellant jets and other phenomena governing the combustion instability. One such question is how the fuel and oxidizer jets change behavior during an unstable combustion event. One early study by Heidmann [3] investigated the behavior of liquid oxygen (LOX) jets in a coaxial-jet-like injector during a period when combustion instability was induced. The LOX jet became shorter once the combustor became unstable. Similar observations were made by Miesse [4] and Buffum and Williams [5] under cold flow conditions when a single round jet was excited with an externally-forced acoustic field.

Mixing of the propellant streams, if not controlling, is at least intimately related to the combustion process. To a first order approximation, one measure of the mixing process is the so-called liquid-core length, which has been extensively studied by many researchers in the past [6-24]. A compilation of experimental core-length correlations, semi-empirical theories, and other data for shear coaxial injectors involving core length is summarized in Table 1. Many of the correlations and semi-empirical theories suggest scaling of the core length with outer-jet to inner-jet velocity ratio (V_o), outer-jet to inner-jet momentum flux ratio (M), density ratio (ρ_o/ρ_i), Reynolds number (Re), and Weber number (We). One difficulty with applying these relationships at supercritical pressures is that the predicted core length is very small or zero in magnitude, because of the use of the We number and the fact that surface tension diminishes greatly or vanishes. To overcome the difficulty of core length prediction associated with large We , one group of researchers [15-20], proposed that M can be used, and need not include We if the We is sufficiently high.

Chehroudi and co-workers [22-34] have investigated supercritical jet flows at higher Reynolds numbers and turbulent jets of interest to practical applications in propulsion systems. The single round-jet work by Chehroudi et al. [26-32] was produced from two different injectors made from 50 mm long sharp-edged tubes with the inner jet diameters of 0.254 mm and 0.508 mm, (L/D of 200 and 100, respec-

tively). They injected pure N_2 and O_2 into N_2 , He, Ar, and mixtures of CO and N_2 and the arrangement was studied with shadowgraphs and Raman imaging. It was determined that the initial growth rate of a supercritical jet was different from that of a subcritical jet. Furthermore, they quantitatively showed that this growth rate for a supercritical jet behaved similar to variable-density gas jets [29]. From this observation, a phenomenological model of the initial growth rate based upon time scale arguments was proposed which agreed well with the results acquired under subcritical and supercritical pressures [29]. It is also important to note that Chehroudi et al. [30] showed that the growth rate measured from shadowgraphs was about twice as large as the growth rate of the jet measured by Raman imaging of the jet, based on the full width at half maximum (FWHM) jet thickness values. The fractal dimension of the initial region of the jet under subcritical and supercritical pressures was also measured by Chehroudi et al. [27, 30, 32] and compared to the fractal dimension of other liquid and gas jets. It was found that the fractal dimension of supercritical jets was similar to that of gas jets, while the fractal dimension of the subcritical jets was similar to that of other liquid jets.

2. EXPERIMENTAL SETUP

Detailed description of the experimental facility can be found in [22–24, 31, 39], and only a brief description will be given here. High-pressure gaseous nitrogen (GN_2) flows into the system and its flow rate is controlled with micrometer needle valves. Temperature conditioning is accomplished by passing the GN_2 through a shell-and-tube type heat exchanger using liquid nitrogen (LN_2) to cool the GN_2 . The nitrogen flows into both the inner and outer tubes of a coaxial injector. The temperature of the flow to the inner round jet of the shear-coaxial injector is considerably lower than that of the outer annular jet, reaching the liquid (subcritical) or densified (supercritical) state. However, the outer jet is cooled well below the room temperature, but is still in gaseous state. The chamber is pressurized with GN_2 at ambient temperature. For reference, the critical pressure and temperature of N_2 is 3.4 MPa and 126.2 K, respectively. The pressure inside the main chamber is maintained by adjusting the outlet flow rate to provide an optimum level of control.

The test article consists of a chamber within a chamber. The main, outer, chamber is used to create a pressurized environment and is fitted with two sapphire windows for observation of the jet behavior. The smaller, inner chamber, channels and focuses acoustic waves onto the jet at high intensity. The waves are generated by a high pressure acoustic driver developed by Hersch Acoustical Engineering. To obtain sufficiently high amplitudes, the driver must resonate the normal modes of the inner chamber. Therefore, the frequency at which the effects are studied is limited to the first two modes of the inner chamber, being about 3 kHz and 5.25 kHz, respectively. The acoustic wavelength is much longer than the characteristic transverse jet dimensions at both of these frequencies and the conclusions drawn were similar. Consequently, only the 3 kHz results are reported here. The

injector is positioned at a pressure minimum to produce maximum velocity fluctuations near the jet. Because of the nonlinear nature of the high amplitude waves the pressure amplitude experiences a minimum but is still finite, and therefore not a pressure node.

The acoustic driver was always operated at its maximum power, which was the same for all pressures. As a consequence, the acoustic amplitude decreased as pressure increased, due to the increase in density. The amplitude was

Table 1. Summary of published operating conditions, geometries, measurement techniques, and proposed equations from the literature, measuring or correlating core length for shear-coaxial jets.

REF	Author	Date	Fluid Inner Jet	Fluid Outer Jet	Fluid Ambient	Pressure (MPa)	T_i (K)	T_o (K)	T_a (K)
6	Forstall & Shapiro	1950	Air + 10 %He	Air	Air	0.1*	Amb. *	Amb.	Amb.
7	Chigier & Beer	1964	Air	Air	Air	0.1*	Amb.	Amb.	Amb.
8	Champagne & Wygnanski	1971	Air	Air	Air	0.1	Amb.	Amb.	Amb.
9	Au and Ko	1987	Air	Air	Air*	0.1*	Amb.	Amb.	Amb.
10	Eroglu et al.	1991	Water	Air	Air	0.1*	Amb.	Amb.	Amb.
11	Woodward	1993	KI (aq.)	N_2 , He	N_2 , He	0.1 – 2.17	Amb.	Amb.	Amb.
15	Villermaux et al. ⁹	1994	Water	Water	Water	0.1*	Amb.	Amb.	Amb.
12	Englebert et al.	1995	Water	Air	Air	0.1	293	293 – 636	293
13	Carreau et al.	1997	LOX	He, N_2 , Ar	NC ^c	0.1	82 ^d	245 – 272 ^d	NC
16	Rehab et al. ⁹	1997	Water	Water	Water	0.1*	Amb.	Amb.	Amb.
17	Rehab et al. ⁹	1998	Water	Water	Water	0.1*	Amb.	Amb.	Amb.
18	Villermaux ^{9,h}	1998	Water	Water	Water	NR	NR	NR	NR
19	Lasheras et al. ⁹	1998	Water	Air	Air	0.1	Amb.	Amb.	Amb.
20	Lasheras & Hopfinger ^{9,i,j}	2000	NR	NR	NR	NR	NR	NR	NR
21	Favre-Marinet & Schettini ^{9,i}	2001	Air, SF6	Air, He	Air, He	0.1	Amb.	Amb.	Amb.
14	Porcheron et al.	2002	LOX, Water	He, N_2 , Ar, Air	Air	0.1	82, 293	245 – 293	293
This work	Davis	2005	N_2	N_2	N_2	1.4 – 4.9	108 – 133	132 – 204	197 – 249

about 183 dB at 1.49 MPa, about 180 dB at 3.5 MPa, and about 178 dB at 4.9 MPa.

The shear coaxial injector used in this work (see Fig. 1) is based on the well-characterized design of the single-jet injector used in all previous studies by Chehroudi [24–30] in this apparatus. The center-post is made from a stainless steel tube with an I.D. (D_1) of 0.51 mm (0.020”) and an O.D. (D_2) of 1.59 mm (0.063”) with a length of 50.8 mm (2.00”). This is used to produce the inner jet. The resulting length-to-inner-diameter ratio is 100, which is sufficient to ensure a fully-developed turbulent pipe flow condition at the exit. The outer stainless steel tube creating the annular passage had an I.D. (D_3) of 2.42 mm (0.095”) and an O.D. (D_4) of 3.18 mm (0.125”). This is used to produce the outer coaxial annular jet. The resulting mean gap width of the annular passage is 0.415 mm (0.016”), measured from an image taken at the exit of the injector. The recess of the inner tube was 0.5 D_1 , 0.25 mm (0.010”) from the end of the outer tube.

Because of the proximity of the experimental conditions to the critical point of nitrogen, accurate measurements of temperature were necessary to obtain reliable estimates of density and other quantities computed from the density. The

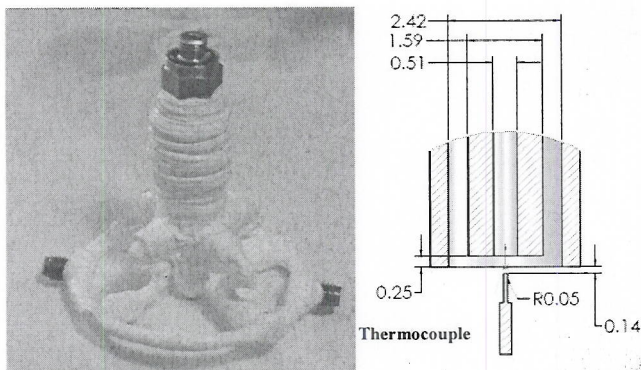


Figure 1. Picture of the shear-coaxial injector (left) and a cross-section drawing of the injector tip. The thermocouple used to measure exit-plane temperature profiles is shown in the drawing.

temperature profiles and the details of the calibration were reported elsewhere (Davis and Chehroudi [22] and Davis et al. [23]).

Shadowgraph images of the jet were taken using either a PixelFly CCD camera or a Phantom v5.1 or v7.1 CMOS camera. The advantage that the CMOS cameras presented was the ability to produce high-speed movies of the jet for a period lasting up to several seconds. The framing rate for the movies in this work was 18 kHz.

3. RESULTS AND DISCUSSIONS

3.1. Acoustic Wave Interaction with Shear-Coaxial Jet

The jets were studied by high-speed movies at three different pressures: a subcritical pressure of nominally 1.5 MPa, a near-critical pressure of nominally 3.5 MPa, and a supercritical pressure of nominally 4.9 MPa. A sample of ten consecutive images at the subcritical, near-critical, and supercritical chamber pressures are shown in Fig. 2. Prominent in all the visualizations of the jet is the existence of a dark central region which we refer to as a “dark core”. The dark core under the unexcited (i.e., acoustic driver off) subcritical pressures (Fig. 2, row one) can be approximated as a cylindrical-like structure with unstable surface waves of low amplitude. However, upon increasing the pressure to near-critical and supercritical pressures (rows three and five) this structure changes to a more conical shape. The conical structure of the dark core has been reported before for single-phase coaxial jets by Lasheras and Hopfinger [20]. As demonstrated in images of Fig. 2 and the other visualizations obtained in this work (not shown here), the conical-shape structure was not observed under two-phase conditions (i.e., subcritical chamber pressure.)

Excitation of the jet with acoustic driver yields significantly different behavior of the dark core compared to that of the unexcited one. The strongest effect was observed at subcritical pressures. It is not clear at this point whether this was due to the subcritical nature of the flow or to the fact that the acoustic amplitude was the highest at subcritical pressures.

3.2. Dark Core Length Measurement Method

The algorithm for measuring the dark-core length in this work starts with an individual image from which an image histogram is computed. A threshold value is then carefully defined to identify the shape of the dark core of the jet.

It should be mentioned that confusion exists in the literature especially when vague definitions are used to define a core length. The terms potential-core, potential-cone, intact-length, intact-liquid-length, and breakup-length have all been used along with various measurement techniques. To be clear, and to remove any possible ambiguity from the data, the dark-core length is defined here as the visually-connected dark fluid region between the injector exit area and the first break in the core as defined by an adaptive thresholding procedure, see Davis [39] or Davis and Chehroudi [25] for more details.

3.3. Influence of Velocity Ratio on Dark Core Length

Velocity ratio V_r has been a design parameter for shear-coaxial injectors, particularly, as a criterion to ensure the stable operation of LREs. For LOX/H₂ engines, the design rule-of-thumb has been to keep the velocity ratio greater than about 10 to keep the engine stable, as is discussed by Hulka and Hutt [35]. Although this criterion has been suggested by the experimental data, no physical explanation has been provided. Related to this is a method to rate a LRE for combustion instability, known as temperature ramping. Temperature ramping is accomplished by lowering the temperature of the H₂ (outer jet) while maintaining mass flow rate at a constant value. The lower the H₂ temperature is at the onset of the measured combustion instability, the greater the stability margin that particular LRE. Temperature ramping is related to the velocity ratio because one of the effects of lowering H₂ temperature at constant mass flow rate is increased density and consequently lower velocity of H₂.

To determine the effects of the outer-jet temperature (which is gaseous N₂ in this work) on the coaxial jet, two nominal temperatures of ~190 K and ~140 K were studied, called “high” and “low,” respectively. The averaged dark-core lengths are shown in Figs. 3(a) and 4(a) as a function of velocity ratio (V_r). The RMS of the variations of the dark-core length is also shown in Figs. 3(b) and 4(b). Figures 3 and 4 present results for conditions when the external acoustic field is turned on and off for both nominal high and low outer-jet temperatures.

Evident in Figs. 3(a) and 4(a) is the fact that the length of the dark core decreases as the chamber pressure is increased. The dark core provides an indication of high-density regions of the flow. At a constant chamber pressure, as V_r is increased, the length of the dark core decreases and appears to approach a constant value. In a mean sense, when the dark core feels the imposed external acoustic field, its length is shorter than or equal to that when the acoustic driver is turned off. At the near-critical and supercritical chamber pressures, as the V_r increases, the difference between the lengths of the dark core, measured with and without the acoustic field, diminishes. The RMS values of the dark-core length fluctuations, shown in Figs. 3 (b) and 4(b), exhibit

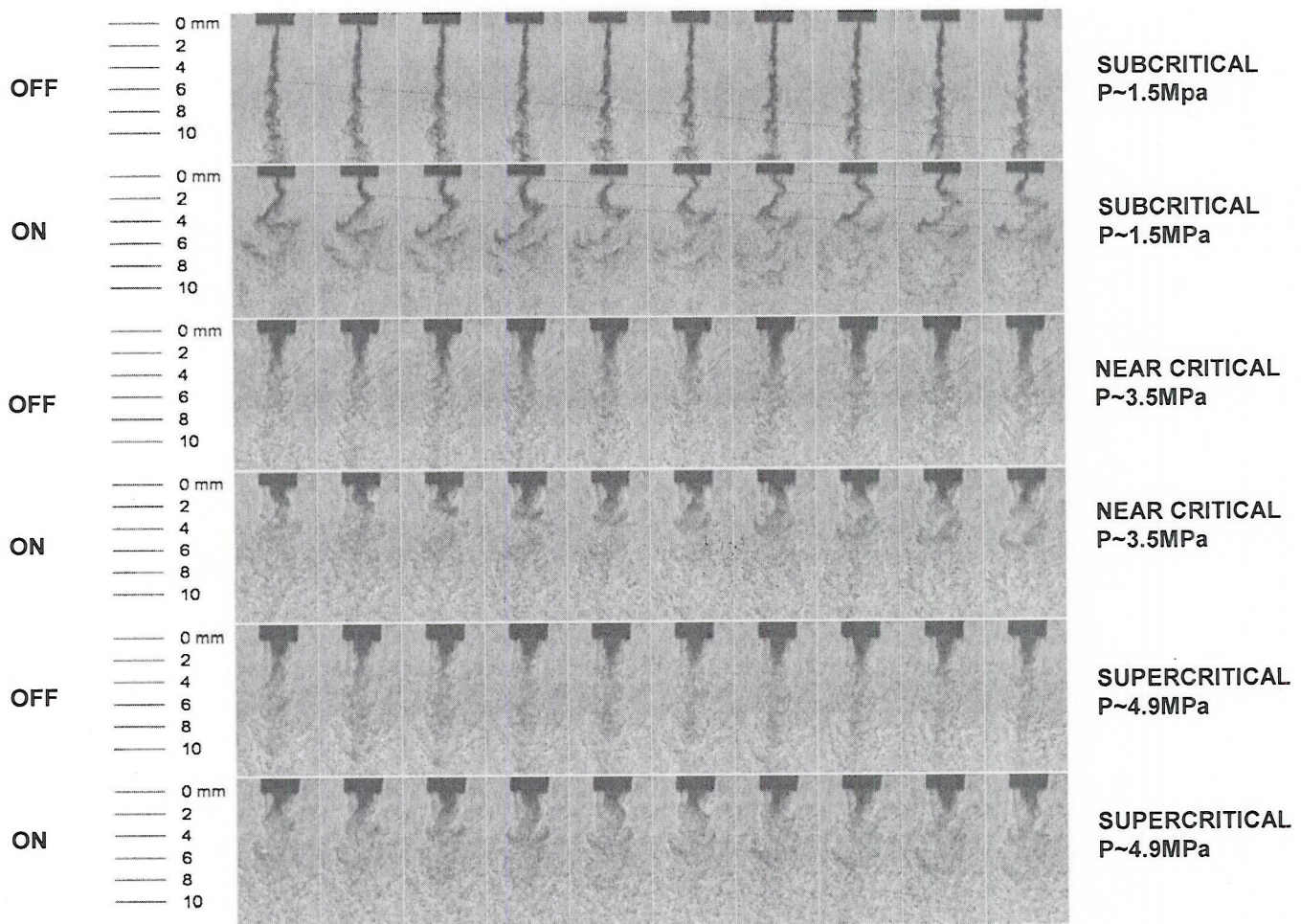


Figure 2. Consecutive frames from high-speed shadowgraph movies with the acoustic driver turned off (in rows 1, 3, and 5) and on (in rows 2, 4, and 6) at $\sim 3\text{kHz}$. Time increases from left to right with an interval of 55.6 ms between frames. The first two rows are at a subcritical chamber pressure ($\sim 1.5\text{ MPa}$), the third and fourth rows are at a near-critical chamber pressure ($\sim 3.5\text{ MPa}$), and the fifth and sixth rows are at a supercritical chamber pressure ($\sim 4.9\text{ MPa}$). The acoustic driver is turned off for the first, third, and fifth rows and on for the second, fourth, and sixth at $\sim 3\text{ kHz}$. The light gray lines in the first and second rows connect fluid structure as they evolve in time.

somewhat similar trends to those seen with the mean values. It is known that for a liquid-fueled rocket, atomization and breakup processes, interactions between the propellant jets, droplet formation, and vaporization are all affected by the pressure and, particularly, velocity fluctuations. Also, for any chemically-reacting system, the rate at which energy is released is sensitive to the rate of change of temperature, density, pressure, and, of course, mixture ratio. It is then quite intuitive to relate, in some form, the RMS values of the dark-core length fluctuations to mixture ratio variations. On the other hand, a low RMS value can be interpreted as the jet's inherent steadiness (or insensitivity to external stimuli) and vice versa. Examination of Figs. 3(b) and 4(b) clearly shows that this property is drastically reduced as the velocity ratio is increased. It is then quite possible that the observed improvement in combustion stability at higher values of velocity ratio is a result of the inability of the jet to generate large mass flow rate fluctuations under these conditions,

weakening a key feedback mechanism for the self-excitation process. In temperature ramping exercises for stability rating of LOX/ H_2 engines, the mass flow rate is usually maintained at a constant value [24]. Therefore, as the temperature of the H_2 is decreased during a ramping episode, the H_2 becomes more dense, which decreases the injector velocity ratio. The RMS plots shown here suggest that such a decline in this ratio amplifies the jet's inherent unsteadiness, providing a possible explanation for the engine's eventual arrival into an unstable zone as a temperature ramping test proceeds.

3.4. Scaling of the Dark Core Length

As mentioned above, the core length has in the past been scaled with many parameters. In some works, We and Re numbers were used to represent velocity values in non-dimensionalized forms, since physical parameters, such as surface tension and viscosity, were not varied. In other works, based on single-phase results, velocity ratio (V_r) or

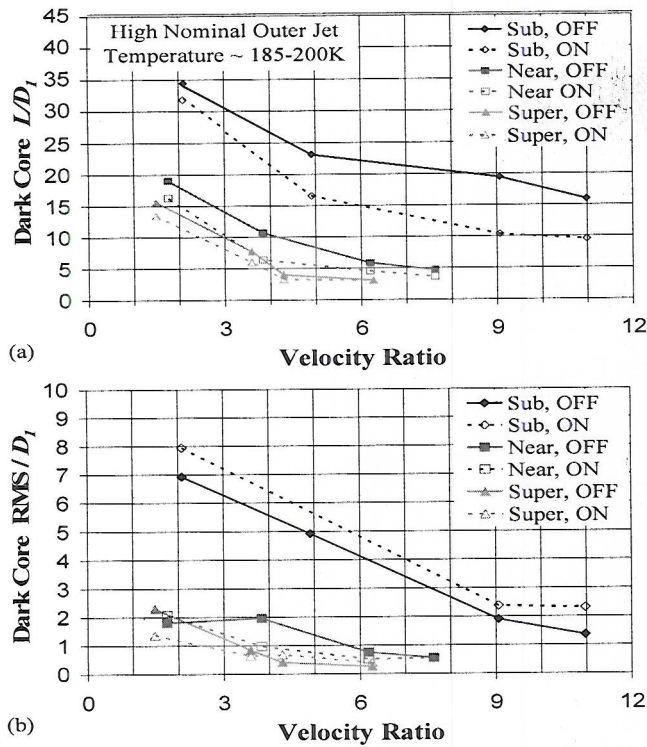


Figure 3. Plot of the averaged dark-core length (a) and the RMS of the length variations (b) normalized by the inner diameter. The solid symbols and lines represent the data for when the acoustic driver is off, and the hollow symbols and dotted lines show the data when the acoustic driver was operated at ~ 3 kHz. The diamond, square, and up-triangle symbols are sub-, near, and supercritical chamber pressures, respectively. All cases are for the high nominal outer-jet temperature of ~ 190 K. In the inset, the words sub, near, and super refer to subcritical, nearcritical, and supercritical pressure respectively, and the words OFF and ON refer to the acoustic driver being off and on at ~ 3 kHz, respectively.

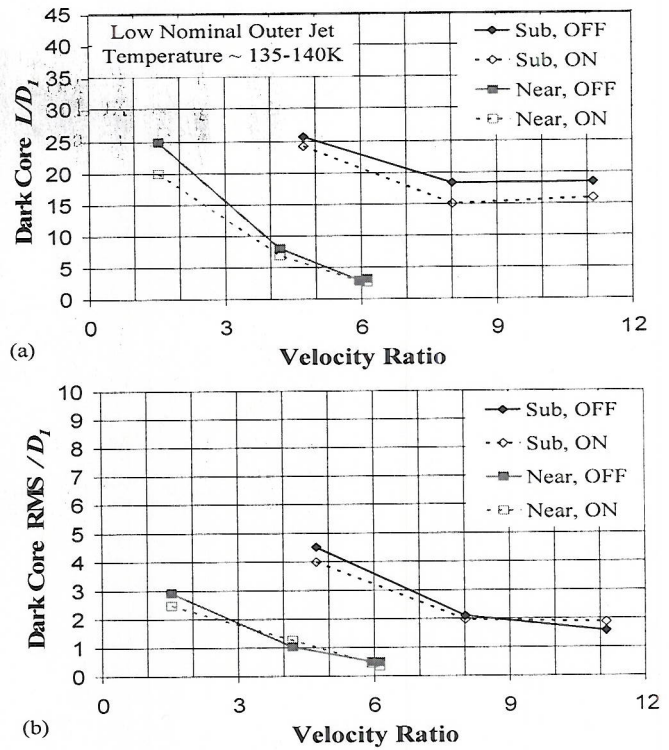


Figure 4. Plot of the averaged dark-core length (a) and the RMS of the length variations (b) normalized by the inner diameter. The solid symbols and lines represent data for when the acoustic driver is off, and the hollow symbols and dotted lines show results when the acoustic driver is operated at ~ 3 kHz. The diamond and square symbols are for sub- and nearcritical chamber pressures, respectively. All cases are for the low nominal outer-jet temperature of ~ 140 K. In the inset, the words sub and near refer to subcritical and nearcritical pressure respectively, and the words OFF and ON refer to the acoustic driver being off and on at ~ 3 kHz, respectively.

momentum flux ratio (M) were considered to be the scaling parameters. The semi-empirical theory of Rehab et al. [17] produces an equation suggesting that the length of the core scales with $M^{-0.5}$. This equation was then quantitatively compared to single-phase shear-coaxial jet data, often with equal densities [16-18]. Note that for (inner and outer) jets of equal densities, $M^{-0.5}$ reduces to V_r . The same dependence on M was also reported qualitatively for single-phase shear-coaxial jets of different densities by Favre-Marinet and Samano-Shettini [21]. Additionally, Lasheras et al. [19] stated the applicability of the same $M^{-0.5}$ dependence for two-phase shear-coaxial jets. However, they were unable to make core length measurements from their images.

A plot of the measured dark-core length values, of this work, versus momentum flux ratio is shown in Fig. 5. A clear distinction between the subcritical dark-core length (diamond symbols) and that for the near-critical and super-

critical chamber pressures are seen. Subcritical data indicates a much longer length than at supercritical pressures for a given momentum flux ratio. It should be noted that the near-critical pressure data is slightly supercritical, and both the near-critical and supercritical pressure conditions produce a single-phase coaxial jet. The dashed line in Fig. 5 is a least-square curve fit to the subcritical data, and the dotted line is a least squares curve fit to the near-critical and supercritical data. As indicated by the equations on Fig. 5, the single-phase (i.e., near-critical and supercritical pressures) data have the same $M^{-0.5}$ dependence form as reported by others [16-18, 21]. However, the two-phase subcritical data has a weaker dependence, $M^{-0.2}$, than the single-phase dark-core length. Other quantitative differences between the subcritical and supercritical cases have been reported before. For single round jets, Chehroudi and co-workers [29, 30, 32] found that at supercritical pressures the spreading rate and fractal

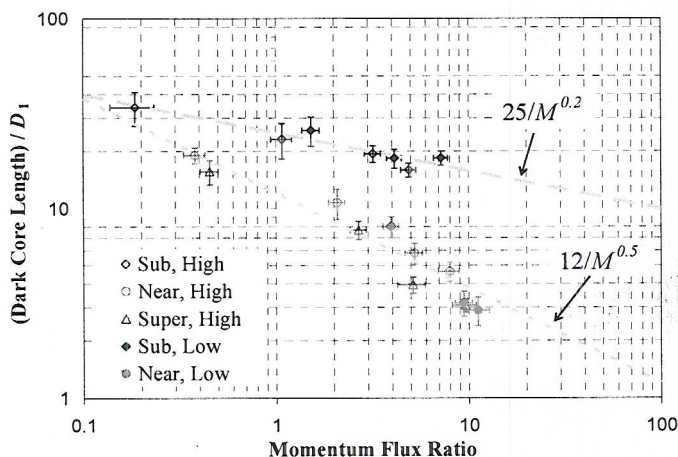


Figure 5. Dark-core length versus momentum flux ratio. The diamond, circle, and up-triangle symbols represent sub-, near-, and supercritical chamber pressure, respectively. The hollow symbols are at a high outer-jet temperature (~ 190 K) and solid symbols are at a low outer-jet temperature. The dashed line is $25/M^{0.2}$ and the dotted line is $12/M^{0.5}$.

dimension values were the same as those for a gaseous jet injected into a gaseous ambient with different densities (i.e., variable-density, single-phase, gaseous jet). This is similar to the present dark-core length observations. Under supercritical pressures, our coaxial jet scales with $M^{0.5}$. Therefore, it appears that this form of the dependency on M is not only valid for gas-gas shear-coaxial jets, but for any single-phase shear-coaxial jet.

Figure 6 was constructed with the objective of comparing the dark-core length with all of the available data that exists in the literature for the potential-core length, intact-core length, and breakup-length. This figure represents all of the available data in the literature concerning core length spanning 5 orders of magnitude in momentum flux ratio. Also, note that as M approaches zero, one reaches a limit defining a single round jet configuration because the outer velocity becomes zero. From data in Fig. 6, it seems that for $M < 1$, data points converge and approach the core length range expected for single round jets reported by Chehrودي et al. [37] and Oschwald et al. [35]. The single-phase data presented in Fig. 6 follows the dependence of $L/D_1 = A M^{0.5}$, where the constant A is between 5 and 12. At $M > 100$, the experiments of Favre-Marinet and Samano-Shettini [21] exhibit a recirculation bubble at the end of the core, and thus the core length decreases. The injectors used to produce the two-phase coaxial jets of Eroglu et al. [10] and Englebert et al. [12] have much larger outer jet gap widths (see Table 1) than what is typical of rocket injectors. Additionally, the apparatus of Eroglu et al. [10], reported in Farago and Chigier [38], does not produce fully-developed turbulent inner jet until when $Re > 10^4$. The lack of a fully-developed turbulent inner jet and the significant differences between their injector and shear-coaxial ones used in rockets could be

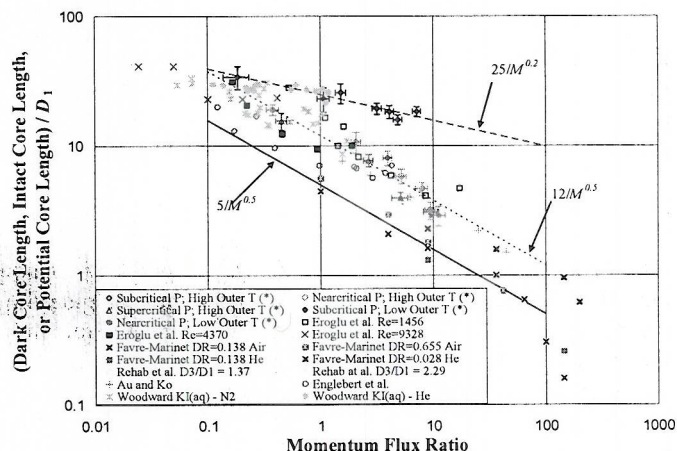


Figure 6. Comparison of the present dark-core length measurements with all other core length data available in the literature vs. momentum flux ratio. Amongst the data reported by others, Eroglu et al., Englebert et al. and Woodward are two-phase flows and the rest are single phase.

the reason why the core length measured by Eroglu et al. [10] is shorter than those observed in our work. Englebert et al. [12] reported that the core length scaled with $M^{0.3}$. The core length by Woodward [11] for the water potassium iodide solution with helium, however, obeys very nearly the trends for the subcritical data points (i.e., $25M^{0.2}$). Considering that momentum flux ratios near 10 are of importance for LRE, to the best of the authors' knowledge, the data for the subcritical (two-phase) case is the only reported information in the neighborhood of the $M = 10$.

4. SUMMARY AND CONCLUSIONS

A non-reacting flow study of a cryogenic shear-coaxial injector was conducted at pressures spanning subcritical to supercritical values. The flow from the inner jet of the coaxial injector was liquid nitrogen (or liquid-like, if at supercritical pressures) and cold gaseous nitrogen flowed from the outer annular jet, both injected into a chamber pressurized with nitrogen at room temperature. The resulting coaxial jet was digitally imaged with a camera framing at a rate of up to 18 kHz. The jet was excited transversely with a high-amplitude acoustic driver, with the jet positioned at a minimum of the pressure amplitude. The following conclusions are offered:

1. The existence of high-amplitude acoustic waves alters the behavior of the shear-coaxial jet. The resulting structure of the jet exhibits a periodic shape corresponding to the transverse-velocity field created by the acoustic waves. The periodic oscillations imposed on the dark core of the jet is predominately in the direction of the transverse acoustic velocity.

2. The root mean square (RMS) variation of the dark-core length decreases with increasing velocity ratio at a given chamber pressure and asymptotically approaches a constant level. The RMS of the dark-core length is greatest at subcritical pressures.

3. Previous research showed that an episode of so-called "temperature ramping", used for stability rating of LREs, could lead the engine to an unstable behavior. Also, from other research, it is shown that coaxial injectors with high outer-to-inner jet velocity ratios (greater than ~ 10 for LOX/H₂) tend to be more stable. In the current work, the observation that the RMS of the dark-core length fluctuations decreased at high velocity ratio under both high and low outer-jet temperatures is considered to be a potential explanation for the observed combustion instability behavior. It is possible that decreases in the RMS fluctuation levels could weaken a key feedback mechanism for the self-excitation process that could be driving combustion instability in rocket engines. This offers a possible improvement in understanding of the combustion instability in LREs. Ultimately, this hypothesis requires further testing in a multi-element, fired rocket experimental facility.

4. The quantitative behavior of the dark-core length of the coaxial jet at near- and supercritical pressures follows a similar momentum flux ratio (M) dependency reported for the single-phase shear-coaxial jets (i.e., $12M^{0.5}$). The dark-core length for the subcritical chamber pressures, however, scales with $M^{0.2}$.

5. Within a range of momentum flux ratios in between 1 and 10, the dark-core lengths for the coaxial jet under the subcritical (two-phase) ambient pressure used here appear longer than those measured at the supercritical (single-phase) condition. This range represents relevant values for liquid rocket engines, subcritical data define a new regime which was not reported previously.

5. ACKNOWLEDGEMENT

The authors would like to recognize Mr. Mike Griggs for his valuable contributions in the improvements to the experimental facility. Lt. Matthew Raskie, Lt. Jason Szuminski, Mr. Earl Thomas, Mr. Randy Harvey, Mr. David Hill, and Mr. Mark Wilson are thanked for their efforts. Additionally, Ms. Jennie Paton is thanked for making literature available in a timely manner. A great appreciation is extended to Mr. Steven Martin for loaning the authors one of the Phantom Cameras. A special gratitude is expressed to M. Favre-Marinet, E. B. Camano Schettini, and R. D. Woodward for providing us with their core length data in tabular form. D. W. Davis would like to thank his thesis advisor, Dr. R. J. Santoro, for many helpful discussions and permitting his thesis work to be performed off-campus at AFRL. This work is sponsored by the Air Force Office of Scientific Research under Dr. Mitat Birkan, program manager.

6. REFERENCES

1. Harje, D. T. and Reardon, F. H. (eds.), Liquid Propellant Rocket Combustion Instability, NASA SP-194, 1972.
2. Yang, V. and Anderson, W. (eds.), Liquid Rocket Engine Combustion Instability, Progress in Astronautics and Aeronautics, AIAA, Washington, DC, 1995.
3. Heidmann, M. F. Oxygen Jet Behavior During Combustion Instability in a Two-Dimensional Combustor, NASA TN D-2725, 1965.
4. Miesse, C. C., Jet Propulsion, Vol. 25, pp. 525-530, 534, 1955.
5. Buffum, F. G., and Williams, F. A., Proceedings of the 1967 Heat Transfer and Fluid Mechanics Institute, Edited by P. A. Libby, D. B. Olfe, and C. W. Van Atta, pp. 247-276, 1967.
6. Forstall, W., and Shapiro, A. H., J. Applied Mechanics, Trans. ASME, Vol. 72, pp. 399-408, 1950.
7. Chigier, N. A., and Beer, J. M., "The Flow Region Near the Nozzle in Double Concentric Jets," J. of Basic Engineering, Trans. ASME, Vol. 4, pp. 797-804, 1964.
8. Champagne, F. H., and Wignanski, I. J., International Journal of Heat and Mass Transfer, Vol. 14, pp. 1445-1464, 1971.
9. Au, H., and Ko, N. W. M., Journal of Sound and Vibration, Vol. 116, No. 3, pp. 427-443, 1987.
10. Eroglu, H., Chigier, N., and Farago, Z., Physics of Fluids A, Vol. 3, No. 2, pp. 303-308, 1991.
11. Woodward, R. D., Primary Atomization of Liquid Jets Issuing from Rocket Engine Coaxial Injectors, Ph.D. Dissertation, Department of Mechanical Engineering, The Pennsylvania State University, University Park, PA, 1993.
12. Englebert, C., Hardalupas, Y., and Whitlaw, J. H., Proc. R. Soc., Vol. 451, London, pp. 189-229, 1995.
13. Carreau, J. L., Porcheron, E., LeVisage, D., Prevost, L., and Roger, F., Int. J. of Fluid Mech. Research, Vol. 24, Nos. 4-6, pp. 498-507, 1997.
14. Porcheron, E., Carreau, J. L., Prevost, L., LeVisage, D., and Roger, F., Atomization and Sprays, Vol. 12, pp. 209-227, 2002.
15. Villermaux, E., Rehab, H., and Hopfinger, E. J., Meccanica, Vol. 29, pp. 393-401, 1994.
16. Rehab, H., Villermaux, E., and Hopfinger, E. J., AIAA Journal, Vol. 36, No. 5, pp. 867-869, 1998.
17. Rehab, H., Villermaux, E., and Hopfinger, E. J., J. Fluid Mech., pp. 357-381, 1997.
18. Villermaux, E., J. Propulsion and Power, Vol. 14, No. 5, pp. 807-817, 1998.
19. Lasheras, J. C., Villermaux, E., and Hopfinger, E. J., J. Fluid Mech., Vol. 357, pp. 351-379, 1998.
20. Lasheras, J. C., and Hopfinger, E. J., Annual Rev. Fluid Mech., Vol. 32, pp. 275-308, 2000.
21. Favre-Marinet, M., and Camano Schettini, E. B., International Journal of Heat and Mass Transfer, Vol. 44, pp. 1913-1924, 2001.

22. Davis, D. W. and Chehrودي, B., 42nd AIAA Aerospace Sciences Meeting & Exhibit, AIAA, Washington, DC, 5-8 Jan. 2004.
23. Davis, D. W., Chehrودي, B., and Sorensen, I. Measurements of an Acoustically Driven Coaxial Jet under Supercritical Conditions 43rd AIAA Aerospace Sciences Meeting & Exhibit, AIAA, Washington, DC, 10-13 Jan. 2005.
24. Davis, D. W., and Chehrودي, B., Measurements of an Acoustically Driven Coaxial Jet under Sub-, Near-, and Supercritical Conditions *J. of Propulsion and Power*, 2005 (accepted).
25. Davis, D. W., and Chehrودي, B., 2006. Shear-Coaxial Jets from a Rocket-Like Injector in a Transverse Acoustic Field at High Pressures. 44^{ed} AIAA Aerospace Sciences Meeting and Exhibit, Paper No. AIAA-2006-0758, Reno, Nevada, January 9-12, 2006.
26. Chehrودي, B., Talley, D., and Coy, E. B., 37th AIAA Aerospace Science Meeting and Exhibit, AIAA, Washington, DC, 11-14 Jan. 1999.
27. Chehrودي, B., Talley, D. G., and Coy, E. B., "Fractal Geometry and Growth Rate Changes of Cryogenic Jets near the Critical Point," 35th AIAA/ASME/SAE/ASEE Joint Propulsion Conference and Exhibit, AIAA, Washington, DC, 20-24 Jun. 1999.
28. Chehrودي, B., Cohn, R., Talley, D. G., and Badakhshan, A., Raman Scattering Measurements in the Initial Region of Sub- and Supercritical Jets, 36th AIAA/ASME/SAE/ASEE Joint Propulsion Conference and Exhibit, AIAA, Washington, DC, 17-19 Jul. 2000.
29. Chehrودي, B., Talley, D. G., and Coy, E. B. Visual Characteristics and Initial Growth Rates of Round Cryogenic Jets at Subcritical and Supercritical Pressures, *Physics of Fluids*, Vol.4, No. 2, pp. 850-861, 2002.
30. Chehrودي, B., Cohn, R., and Talley, D. G., Cryogenic Shear Layers: Experiments and Initial Growth Rates of Round Cryogenic Jets at Subcritical and Supercritical Pressures, *International Journal of Heat and Fluid Flow*, Vol. 23, pp. 554-563, 2002.
31. Chehrودي, B., and Talley, D. G., Interaction of Acoustic Waves with a Cryogenic Nitrogen Jet at Sub- and Supercritical Pressures, 40th AIAA Aerospace Meeting and Exhibit, AIAA, Washington, DC, 14-17 Jan. 2002.
32. Chehrودي, B. and Talley, D., Fractal Geometry of a Cryogenic Nitrogen Round Jet Injected into Sub- and Super-critical Conditions, *Atomization and Sprays*, Vol. 14, pp. 81-91, 2004.
33. Chehrودي, B., Davis, D. W., and Talley, D. G., Initial Results from A Cryogenic Coaxial Injector In An Acoustic Field, 41st AIAA Aerospace Sciences Meeting & Exhibit, AIAA, Washington, DC, 6-9 Jan. 2003.
34. Chehrودي, B., Supercritical Fluids: Nanotechnology And Select Emerging Applications, Invited Review Article, *Combust. Sci. and Tech.*, 178, pp. 555-621, 2006.
35. Oschwald, M., Smith, J. J., Branam, R., Hussong, J., Schik, A., Chehrودي, B., and Talley, D. G., Injection of Fluids into Supercritical Environments, Invited Review Article, *Combust. Sci. and Tech.*, 178, pp. 49-100, 2006.
36. Hulka, J., and Hutt, J., Liquid Oxygen / Hydrogen Instability Phenomena, *Liquid Rocket Engine Combustion Instability*, edited by V. Yang and W. Anderson, Progress in Astronautics and Aeronautics, AIAA, Washington, DC, pp. 39-72, 1995.
37. Chehrودي, B., Chen, S. H., Bracco, F. V., and Onuma, Y., 1985. On the Intact Core of Full-Cone Sprays, Society of Automotive Engineers, 1985 Congress and Exposition, SAE Transaction Paper 850126, February 25-March 1, 1985.
38. Faragó, Z., and Chigier, N., Morphological Classification of Disintegration of Round Liquid Jets in a Coaxial Air Stream, *Atomization and Sprays*, Vol. 2, pp. 137-153, 1992.
39. Davis, D. W., On the Behavior of a Shear-Coaxial Jet Spanning Sub- to Supercritical Pressures, with and without an Externally Imposed Transverse Acoustic Field, Ph.D. Dissertation, Department of Mechanical Engineering, The Pennsylvania State University, University Park, PA, 2006.

Behavior of a Rocket-Like Coaxial Injector in an Acoustic Field

D. W. Davis* and B. Chehroudi
ERC, Inc., Edwards AFB, CA

D.G. Talley
Air Force Research Laboratory, Edwards AFB, CA

Abstract

A non-reacting-flow experimental investigation was undertaken to gain a better understanding of some of the underlying physics associated with the interaction of acoustic waves and a coaxial-jet injector similar to those used in cryogenic liquid rockets. Liquid nitrogen (the round inner jet) and gaseous nitrogen (the annular outer jet) were used under subcritical, near critical, and supercritical chamber pressures, with and without acoustic excitation. High-speed digital imaging provided information on the dynamic behavior of the jet under a variety of conditions. It is found that when the jet is at the pressure node, an externally-imposed acoustic field excites the dark-core of the jet to a wavy-shaped structure consistent with the field's characteristics. Mean and root mean square (RMS) values of the dark-core length fluctuations were measured from images. It is seen that as the outer-to-inner-jet velocity ratio increases, the RMS of the dark-core length fluctuations decreases both with and without the existence of the acoustic field. It is thought that a connection to the rocket instability may be established from these data through examination of the RMS values. It is possible that decreases in the fluctuation levels, shown to occur at higher velocity ratios, could weaken a key feedback mechanism for the self-excitation process that could be driving combustion instability in rocket engines. This could offer a possible explanation of the combustion stability improvements experienced in engines when a transition to higher values of the outer-to-inner-jet velocity ratio is made. Finally, after a careful review of relevant data taken here and those by others, there appears to be a good correlation between the dark-core length and the momentum flux ratio

Introduction

Combustion instabilities in liquid rocket engines (LREs) can reach amplitudes of 100% of chamber pressure and damage an engine in a fraction of a second [1,2]. The combustion instability mechanisms span from low-frequency mechanisms, which is a feed-system coupled instability, to high-frequency mechanisms, which depend on the acoustic modes of the chamber. Often LRE's operate at chamber pressures which exceed the critical pressure of the propellants. In such cases, while the pressure is supercritical, the initial temperature of the propellants is often subcritical, but heats to supercritical temperatures during mixing and combustion. The term "transcritical" has often been used to describe this process.

Many fundamental questions remain to be answered regarding the physical behavior of the propellant jets and other phenomena governing the combustion instability. One such question is how the fuel and oxidizer jets change behavior during an unstable combustion event. One early study by Heidmann [3] investigated the behavior of liquid oxygen (LOX) jets in a coaxial-jet-like injector during a period when combustion instability was induced. The LOX jet became shorter once the combustor became unstable. Similar observations were made by Miesse [4] and Buf-

fum and Williams [5] under cold flow conditions when a single round jet was excited with an externally-forced acoustic field.

Mixing of the propellant streams, if not controlling, is at least intimately related to the combustion process. To a first order approximation, one measure of the mixing process is the so-called liquid-core length, which has been extensively studied by many researchers in the past [6-24]. A compilation of experimental core-length correlations, semi-empirical theories, and other data for shear coaxial injector studies involving core length is summarized in Table 1. Many of the correlations and semi-empirical theories reviewed indicate scaling of the core length with outer-jet to inner-jet velocity ratio (V_r), outer-jet to inner-jet momentum flux ratio (M), density ratio (ρ_o/ρ_i), Reynolds number (Re), and Weber number (We). One difficulty with applying these relationships at supercritical pressures is that the predicted core length is very small or zero in magnitude, because one of the parameters in the equation is We and surface tension diminishes greatly or vanishes all together. To overcome the difficulty of core length prediction associated large We , one group of researchers [15-20], proposed that M can be used to describe the scaling of the core length for shear-coaxial injectors, and

need not include We if the We is sufficiently high.

Chehroudi and co-workers [22-33] have investigated supercritical jet flows at higher Reynolds numbers and turbulent jets of interest to practical applications in propulsion systems. The single round-jet work by Chehroudi et al. [26-32] was produced from two different injectors made from 50 mm long sharp-edged tubes with the inner jet diameters of 0.254 mm and 0.508 mm, (L/D of 200 and 100, respectively). They injected pure N_2 and O_2 into N_2 , He, Ar, and mixtures of CO and N_2 and the arrangement was studied with shadowgraphs and Raman imaging. It was determined that the initial growth rate of a supercritical jet was different from that of a subcritical jet. Furthermore, they quantitatively showed that the initial growth rate of a supercritical jet behaved similar to variable-density gas jets [29]. From this observation, a phenomenological model of the initial growth rate based upon time scale arguments was proposed which agreed well with the results acquired under subcritical and supercritical pressures [29]. It is also important to note that Chehroudi et al. [30] showed that the growth rate measured from shadowgraphs was about twice as large as the growth rate of the jet measured by Raman imaging of the jet, based on the full width at half maximum (FWHM) jet thickness values. The fractal dimension of the initial region of the jet under subcritical and supercritical pressures was also measured by Chehroudi et al. [27, 30, 32] and compared to the fractal dimension of other liquid and gas jets. It was found that the fractal dimension of supercritical jets was similar to that of gas jets, while the fractal dimension of the subcritical jets was similar to that of other liquid jets.

Experimental Setup

The experimental facility, shown in Fig. 1, has been described in detail previously [22-24, 31, 38], so only a brief description will be given here. High-pressure gaseous nitrogen (GN_2) flows into the system and its flow rate is controlled with micrometer needle valves. Temperature conditioning is accomplished by passing the GN_2 through a shell-and-tube type heat exchanger using liquid nitrogen (LN_2) to cool the GN_2 . The nitrogen flows into both the inner and outer tubes. The temperature of the flow to the inner round jet of the shear-coaxial injector is considerably lower than that of the outer annular jet, reaching the liquid (subcritical) or densified (supercritical) state. However, the outer jet is cooled

well below the room temperature, but is still in gaseous state. The chamber is pressurized with GN_2 at ambient temperature. For reference, the critical pressure and temperature of N_2 is 3.4 MPa and 126.2 K, respectively. The pressure inside the main chamber is maintained by adjusting the outlet flow rate using a triplet of valves to provide an optimum level of control.

The test article consists of a chamber within a chamber. The main, external, chamber is used to create a pressurized environment and is fitted with two sapphire windows for observation of the jet behavior. The smaller, internal chamber, channels and focuses acoustic waves onto the jet at high intensity. The waves are generated by a high pressure acoustic driver developed by Hersch Acoustical Engineering. To obtain sufficiently high amplitudes, the driver must resonate the normal modes of the inner chamber. Therefore, the frequency at which the effects are studied is limited to the first two modes of the inner chamber, being about 3 kHz and 5.25 kHz, respectively. The acoustic wavelength is much longer than the characteristic transverse jet dimensions at both of these frequencies and the conclusions drawn were similar. Consequently, only the 3 kHz results are reported here. The injector is positioned at a pressure node (a velocity anti-node) to produce maximum velocity fluctuations near the jet.

The acoustic driver was always operated at its maximum power, which was the same for all pressures. As a consequence, the acoustic amplitude decreased as pressure increased, due to the increase in density. The amplitude was about 183 dB at 1.49 MPa, about 180 dB at 3.5 MPa, and about 178 dB at 4.9 MPa.

The shear coaxial injector used in this work (see Fig. 2) is based on the well-characterized design of the single-jet injector used in all previous studies [24-30] in this apparatus. The center-post is made from a stainless steel tube with an I.D. (D_1) of 0.51 mm (0.020") and an O.D. (D_2) of 1.59 mm (0.063") with a length of 50.8 mm (2.00"). This is used to produce the inner jet. The resulting length to inner diameter ratio is 100, which is sufficient to ensure a fully-developed turbulent pipe flow conditions at the exit. The outer stainless steel tube creating the annular passage had an I.D. (D_3) of 2.42 mm (0.095") and an O.D. (D_4) of 3.18 mm (0.125"). This is used to produce the outer coaxial annular jet. The resulting mean gap width of the annular passage is 0.415 mm (0.016"), measured from an image taken at the exit of the injector. The injector has a small bias of 8% of the mean gap width.

The recess of the inner tube was $0.5 D_I$, 0.25 mm (0.010") from the end of the outer tube.

Because of the proximity of the experimental conditions to the critical point of nitrogen, accurate measurements of temperature were necessary to obtain reliable estimates of density and other quantities computed from the density. The temperature profiles and the details of the calibration were reported elsewhere (Davis and Chehrودي [22] and Davis et al. [23]).

Shadowgraph images of the jet were taken using either a PixelFly CCD camera or a Phantom v5.1 or v7.1 CMOS camera. The advantage that the CMOS cameras presented was the ability to produce high-speed movies of the jet for a period lasting up to several seconds. The framing rate for the movies in this work was 18 kHz.

Results and Discussion

A. Acoustic Wave Interaction with Shear-Coaxial Jet. High-speed movies of the jet present a large amount of information about the flow being studied. The jets were studied at three different pressures: a subcritical pressure of nominally 1.5 MPa, a near-critical pressure of nominally 3.5 MPa, and a supercritical pressure of nominally 4.9 MPa. A sample of ten consecutive images at the subcritical (rows one and two from top), near-critical (rows three and four), and supercritical (rows five and six) chamber pressures are shown in Fig. 3. Rows one, three, and five are for when the acoustic driver is off and the remaining ones are when it is activated at ~ 3 kHz. The evolution of the jet in time is from left to right in Fig. 3, with the time interval between frames of 55.6 μ s. Prominent in all the visualizations of the jet is the existence of a dark central region which we refer to as a "dark core". The dark core under the unexcited (i.e. acoustic driver off) subcritical pressures (Fig. 3, row one) can be approximated as a cylindrical-like structure with unstable surface waves of low amplitude. However, upon increasing the pressure to near-critical and supercritical pressures (rows three and five) this structure changes to a more conical shape. The conical structure of the dark core has been reported before for single-phase coaxial jets by Lasheras and Hopfinger [20]. As demonstrated in images of Fig. 3 and the other visualizations obtained in this work (not shown here), the conical-shape structure was not observed under two-phase conditions (i.e., subcritical chamber pressure).

Excitation of the jet with acoustic driver yields significantly different behavior of the dark core compared to that of the unexcited one. The

strongest effect was observed at subcritical pressures. It is not clear at this point whether this was due to the subcritical nature of the flow or to the fact that the acoustic amplitude was the highest at subcritical pressures.

It appears from the movies, similar to those used to generate Fig. 3, that as a portion of fluid originating from the inner jet leaves the injector tip, the momentum from the acoustically-induced motion causes a transverse displacement, pushing the core of the jet into the higher speed annular jet. The dense fluid from the core is then accelerated by the outer jet. Upon reversal of the acoustic field, the dense fluid, initially from the core but now in the high-speed annular jet, appears to maintain its transverse component of the momentum imparted upon leaving the injector tip and hence the dense fluid particle does not reverse its direction. The dense fluid parcel then slows (both in the axial and transverse directions) as it arrives at the shear layer between the outer jet and the chamber fluid farther downstream, where a "cusp-shaped" structure is formed from the dense fluid originating in the core of the jet. Subsequent mixing and heat transfer from the outer jet to the inner jet core fluid ultimately causes the fluid parcel to be indistinguishable from the outer jet fluid.

An investigation was also conducted to determine whether the side-to-side oscillation of the jet was occurring in a 3D helical mode or in a 2D planar mode. Visualization of the jet from a direction orthogonal to the perspective of Fig. 3 revealed that the jet oscillation was largely 2D in the direction of the planar acoustic waves.

B. Dark Core Length Measurement Technique. The algorithm for measuring the dark-core length in this work starts with an individual image from which an image histogram is computed. A threshold value is then carefully defined to identify the shape of the dark core of the jet.

It should be mentioned that confusion exists in the literature especially when vague definitions are used to define a core length. The terms potential-core, potential-cone, intact-length, intact-liquid-length, and breakup-length have all been used along with various measurement techniques. To be clear, and to remove any possible ambiguity from the data, the dark-core length is defined here as the connected dark fluid region between the injector exit area and the first break in the core as defined by an adaptive thresholding procedure. See Davis [38] or Davis and Chehrودي [25] for more details.

C. Influence of Velocity Ratio on Dark Core Length. Velocity ratio V_r has been a design pa-

parameter for shear-coaxial injectors, particularly, as a criterion to ensure the stable operation of LREs. For LOX/H₂ engines, the design rule-of-thumb has been to keep the velocity ratio greater than about 10 to keep the engine stable, as is discussed by Hulka and Hutt [35]. Although this criterion has been suggested by the experimental data, no physical explanation has been provided. Related to this is a method to rate a LRE for combustion instability, known as temperature ramping. Temperature ramping is accomplished by lowering the temperature of the H₂ while maintaining mass flow rate at a constant value. The lower the H₂ temperature is at the onset of the measured combustion instability, the greater the stability margin that particular LRE is considered to have. Temperature ramping is related to the velocity ratio because one of the effects of lowering H₂ temperature at constant mass flow rate is increased density and consequently lower velocity.

To determine the effects of the outer-jet temperature (which is GN₂ in this work) on the coaxial jet, two nominal temperatures of ~190 K and ~140 K were studied, called “high” and “low,” respectively. The averaged dark-core lengths are shown in Figs. 4(a) and 5(a) as a function of velocity ratio (V_r). The RMS of the variations of the dark-core length is also shown in Figs. 4(b) and 5(b). Figures 4 and 5 present results for conditions when the external acoustic field is turned on and off for both nominal high and low outer-jet temperatures. According to Eroglu et al. [10], the average of the length measured from individual images of a set can be regarded as the time averaged value. It should be noted that, for each operating condition in this work, length measurements were also made from an averaged image of a set. In general, the length measured from the averaged image is slightly shorter than the average of the individual dark-core values calculated in a given set.

Evident in Figs. 4(a) and 5(a) is the fact that the length of the dark core decreases as the chamber pressure is increased. The dark core provides an indication of high-density regions of the flow. At a constant chamber pressure, as V_r is increased, the length of the dark core decreases and appears to approach a constant value. In a mean sense, when the dark core feels the imposed external acoustic field, its length is shorter than or equal to that when the acoustic driver is turned off. At the near-critical and supercritical chamber pressures, as the V_r increases, the difference between the lengths of the dark core, measured with and without the acoustic field,

diminishes. The RMS values of the dark-core length fluctuations, shown in Figs. 4 (b) and 5(b), exhibit somewhat similar trends to those seen with the mean values. It is known that for a liquid-fueled rocket, atomization and breakup processes, interactions between the propellant jets, droplet formation, and vaporization are all affected by the pressure and, particularly, velocity fluctuations. Also, for any chemically-reacting system, the rate at which energy is released is sensitive to the rate of change of temperature, density, pressure, and, of course, mixture ratio. It is then quite intuitive to relate, in some form, the RMS values of the dark-core length fluctuations to mixture ratio variations. On the other hand, a low RMS value can be interpreted as the jet’s inherent steadiness (or insensitivity to external stimuli) and vice versa. Examination of Figs. 4b and 5b clearly shows that this property is drastically reduced as the velocity ratio is increased. It is then quite possible that the observed improvement in combustion stability at higher values of velocity ratio is a result of the inability of the jet to generate large mass flow rate fluctuations under these conditions, weakening a key feedback mechanism for the self-excitation process. In temperature ramping exercises for stability rating of LOX/H₂ engines, the mass flow rate is usually maintained at a constant value [24]. Therefore, as the temperature of the H₂ is decreased during a ramping episode, the H₂ becomes more dense, which decreases the injector velocity ratio. The RMS plots shown here suggest that such a decline in this ratio amplifies the jet’s inherent unsteadiness, providing a possible explanation for the engine’s eventual arrival into an unstable zone as a temperature ramping test proceeds.

D. Scaling of the Dark Core Length. As mentioned above, the core length has in the past been scaled with many parameters. In some works, We and Re numbers were used to represent velocity values in nondimensionalized forms, since physical parameters, such as surface tension and viscosity, were not varied. In other works, based on single-phase results, velocity ratio (V_r) or momentum flux ratio (M) were considered to be the scaling parameters. The semi-empirical theory of Rehab et al. [17] produces an equation suggesting that the length of the core scales with $M^{-0.5}$. This equation was then quantitatively compared to single-phase shear-coaxial jet data, often with equal densities [16-18]. Note that for (inner and outer) jets of equal densities, $M^{-0.5}$ reduces to V_r . The same dependence on M was also reported qualitatively for single-phase

shear-coaxial jets of different densities by Favre-Marinet and Samano-Shettini [21]. Additionally, Lasheras et al. [19] stated the applicability of the same $M^{-0.5}$ dependence for two-phase shear-coaxial jets. However, they were unable to make core length measurements from their images.

A plot of the measured dark-core length values, of this work, versus momentum flux ratio is shown in Fig. 6. A clear distinction between the subcritical dark-core length (diamond symbols) and that for the near-critical and supercritical chamber pressures are seen. Subcritical data indicates a much longer length than at supercritical pressures for a given momentum flux ratio. It should be noted that the near-critical pressure data is slightly supercritical, and both the near-critical and supercritical pressure conditions produce a single-phase coaxial jet. The dashed line in Fig. 6 is a least-square curve fit to the subcritical data, and the dotted line is a least squares curve fit to the near-critical and supercritical data. As indicated by the equations on Fig. 6, the single-phase (i.e., near-critical and supercritical pressures) data have the same $M^{-0.5}$ dependence form as reported by others [16-18, 21]. However, the two-phase subcritical data has a weaker dependence, $M^{0.2}$, than the single-phase dark-core length. Other quantitative differences between the subcritical and supercritical cases have been reported before. For single round jets, Chehroudi and co-workers [29, 30, 32] found that at supercritical pressures the spreading rate and fractal dimension values were the same as those for a gaseous jet injected into a gaseous ambient with different densities (i.e., variable-density, single-phase, gaseous jet). This is similar to the present dark-core length observations. Under supercritical pressures, our coaxial jet scales with $M^{-0.5}$. Therefore, it appears that this form of the dependency on M is not only valid for gas-gas shear-coaxial jets, but for any single-phase shear-coaxial jet.

Figure 7 was constructed with the objective of comparing the dark-core length with all of the available data that exists in the literature for the potential-core length, intact-core length, and breakup-length. This figure represents all of the available data in the literature concerning core length spanning 5 orders of magnitude in momentum flux ratio. Also, note that as M approaches zero, one reaches a limit defining a single round jet configuration because the outer velocity becomes zero. From data in Fig 7, it seems that for $M < 1$, data points converge and approach the core length range expected for single round jets reported by Chehroudi et al. [36]

and Oschwald et al. [34]. The single-phase data presented in Fig. 7 follows the dependence of $L/D_I = A M^{0.5}$, where the constant A is between 5 and 12. At $M > 100$, the experiments of Favre-Marinet and Samano-Shettini [21] exhibit a recirculation bubble at the end of the core, and thus the core length decreases. The injectors used to produce the two-phase coaxial jets of Eroglu et al. [10] and Englebert et al. [12] have much larger outer jet gap widths (see Table 1) than what is typical of rocket injectors. Additionally, the apparatus of Eroglu et al [10], reported in Farago and Chigier [37], does not produce fully-turbulent inner jet until when $Re > 10^4$. The lack of a fully-turbulent inner jet and the significant differences between their injector and shear-coaxial ones used in rockets could be the reason why the core length measured by Eroglu et al. [10] is shorter than those observed in our work. Englebert et al. [12] reported that the core length scaled with $M^{0.3}$. The core length by Woodward [11] for the water potassium iodide solution with helium, however, obeys very nearly the trends for the subcritical data points (i.e., $25M^{-0.2}$). Considering that momentum flux ratios near 10 are of importance for LRE, to the best of the authors' knowledge, the data for the subcritical (two-phase) case is the only reported information in the neighborhood of the $M = 10$.

Summary and Conclusions

A non-reacting flow study of a cryogenic shear-coaxial injector was conducted at pressures spanning subcritical to supercritical values. The flow from the inner jet of the coaxial injector was liquid nitrogen (or liquid-like, if at supercritical pressures) and cold gaseous nitrogen flowed from the outer annular jet, both injected into a chamber pressurized with nitrogen at room temperature. The resulting coaxial jet was imaged with a camera framing at a rate of up to 18 kHz. The jet was excited transversely with a high-amplitude acoustic driver, with the jet located at a pressure amplitude minimum. The following conclusions are offered:

1. The existence of high-amplitude acoustic waves alters the behavior of the shear-coaxial jet. The resulting structure of the jet exhibits a periodic shape corresponding to the transverse-velocity field created by the acoustic waves. The periodic oscillations imposed on the dark core of the jet is predominately in the direction of the transverse acoustic velocity. No helical mode for the jet was observed.

2. The root mean square (RMS) variation of the dark-core length decreases with increasing

velocity ratio at a given chamber pressure and asymptotically approaches a constant level. The RMS of the dark-core length is greatest at subcritical pressures.

3. Previous research showed that an episode of so-called "temperature ramping", used for stability rating, could lead the engine to an unstable behavior. Also, from other research, it is shown that coaxial injectors with high outer-to-inner jet velocity ratios (greater than ~ 10 for LOX/H₂) tend to be more stable. In the current work, the observation that the RMS of the dark-core length fluctuations decreased at high velocity ratio under both high and low outer-jet temperatures is considered to be a potential explanation observed combustion instability behavior. It is possible that decreases in the RMS fluctuation levels could weaken a key feedback mechanism for the self-excitation process that could be driving combustion instability in rocket engines. This offers a possible improvement in understanding of the combustion instability in LRE. Ultimately, this hypothesis requires further testing in a multi-element, fired rocket experimental facility.

4. The quantitative behavior of the dark-core length of the coaxial jet at near- and supercritical pressures follows a similar momentum flux ratio (M) dependency reported for the single-phase shear-coaxial jets (i.e., $12M^{-0.5}$). The dark-core length for the subcritical chamber pressures, however, scales with $M^{-0.2}$.

5. Within a range of momentum flux ratios in between 1 and 10, the dark-core lengths for the coaxial jet under the subcritical (two-phase) ambient pressure used here appear longer than those measured at the supercritical (single-phase) condition. This range represents relevant values for liquid rocket engines, subcritical data define a new regime which was not reported previously.

Acknowledgments

The authors would like to recognize Mr. Mike Griggs for his valuable contributions in the improvements to the experimental facility. Lt. Matthew Raskie, Lt. Jason Szuminski, Mr. Earl Thomas, Mr. Randy Harvey, Mr. David Hill, and Mr. Mark Wilson are thanked for their efforts. Additionally, Ms. Jennie Paton is thanked for making literature available in a timely manner. A great appreciation is extended to Mr. Steven Martin for loaning the authors one of the Phantom Cameras. A special gratitude is expressed to M. Favre-Marinet, E. B. Camano Schettini, and R. D. Woodward for providing us with their core length data in tabular form. D. W. Davis would

like to thank his thesis advisor, Dr. R. J. Santoro, for many helpful discussions and permitting his thesis work to be performed off-campus at AFRL. This work is sponsored by the Air Force Office of Scientific Research under Dr. Mitat Birkan, program manager.

References

1. Harje, D. T. and Reardon, F. H. (eds.), *Liquid Propellant Rocket Combustion Instability*, NASA SP-194, 1972.
2. Yang, V. and Anderson, W. (eds.), *Liquid Rocket Engine Combustion Instability*, Progress in Astronautics and Aeronautics, AIAA, Washington, DC, 1995.
3. Heidmann, M. F. *Oxygen Jet Behavior During Combustion Instability in a Two-Dimensional Combustor*, NASA TN D-2725, 1965.
4. Miesse, C. C., *Jet Propulsion*, Vol. 25, 1955, pp. 525-530, 534.
5. Buffum, F. G., and Williams, F. A., *Proceedings of the 1967 Heat Transfer and Fluid Mechanics Institute*, Edited by P. A. Libby, D. B. Olfe, and C. W. Van Atta, 1967, pp. 247-276.
6. Forstall, W., and Shapiro, A. H., *J. Applied Mechanics*, Trans. ASME, Vol. 72, 1950, pp. 399-408.
7. Chigier, N. A., and Beer, J. M., "The Flow Region Near the Nozzle in Double Concentric Jets," *J. of Basic Engineering*, Trans. ASME, Vol. 4, 1964, pp. 797-804.
8. Champagne, F. H., and Wygnanski, I. J., *International Journal of Heat and Mass Transfer*, Vol. 14, 1971, pp. 1445-1464.
9. Au, H., and Ko, N. W. M., *Journal of Sound and Vibration*, Vol. 116, No. 3, 1987, pp. 427-443.
10. Eroglu, H., Chigier, N., and Farago, Z., *Physics of Fluids A*, Vol. 3, No. 2, Jan. 1991, pp. 303-308.
11. Woodward, R. D., "Primary Atomization of Liquid Jets Issuing from Rocket Engine Coaxial Injectors," Ph.D. Dissertation, Department of Mechanical Engineering, The Pennsylvania State University, University Park, PA, 1993.
12. Englebert, C., Hardalupas, Y., and Whitlaw, J. H., *Proc. R. Soc.*, Vol. 451, London, 1995, pp. 189-229.
13. Carreau, J. L., Porcheron, E., LeVisage, D., Prevost, L., and Roger, F., *Int. J. of Fluid Mech. Research*, Vol. 24, Nos. 4-6, 1997, pp. 498-507.
14. Porcheron, E., Carreau, J. L., Prevost, L., LeVisage, D., and Roger, F., *Atomization and Sprays*, Vol. 12, 2002, pp. 209-227.
15. Villermaux, E., Rehab, H., and Hopfinger, E. J., *Meccanica*, Vol. 29, 1994, pp. 393-401.
16. Rehab, H., Villermaux, E., and Hopfinger, E. J., *AIAA Journal*, Vol. 36, No. 5, 1998, pp. 867-869.
17. Rehab, H., Villermaux, E., and Hopfinger, E. J., *J. Fluid Mech.*, 1997, pp. 357-381.
18. Villermaux, E., *J. Propulsion and Power*, Vol. 14, No. 5, 1998, pp. 807-817.

19. Lasheras, J. C., Villiermaux, E., and Hopfinger, E. J., *J. Fluid Mech.*, Vol. 357, 1998, pp. 351-379.
20. Lasheras, J. C., and Hopfinger, E. J., *Annual Rev. Fluid Mech.*, Vol. 32, 2000, pp. 275-308.
21. Favre-Marinet, M., and Camano Schettini, E. B., *International Journal of Heat and Mass Transfer*, Vol. 44, 2001, pp. 1913-1924.
22. Davis, D. W. and Chehrودي, B., *42nd AIAA Aerospace Sciences Meeting & Exhibit*, AIAA, Washington, DC, 5-8 Jan. 2004.
23. Davis, D. W., Chehrودي, B., and Sorensen, I. Measurements of an Acoustically Driven Coaxial Jet under Supercritical Conditions *43rd AIAA Aerospace Sciences Meeting & Exhibit*, AIAA, Washington, DC, 10-13 Jan. 2005.
24. Davis, D. W., and Chehrودي, B., Measurements of an Acoustically Driven Coaxial Jet under Sub-, Near-, and Supercritical Conditions *J. of Propulsion and Power*, 2005 (submitted).
25. Davis, D. W., and Chehrودي, B., 2006. Shear-Coaxial Jets from a Rocket-Like Injector in a Transverse Acoustic Field at High Pressures. *44th AIAA Aerospace Sciences Meeting and Exhibit*, Paper No. AIAA-2006-0758, Reno, Nevada, January 9-12.
26. Chehrودي, B., Talley, D., and Coy, E. B., *37th AIAA Aerospace Science Meeting and Exhibit*, AIAA, Washington, DC, 11-14 Jan. 1999.
27. Chehrودي, B., Talley, D. G., and Coy, E. B., "Fractal Geometry and Growth Rate Changes of Cryogenic Jets near the Critical Point," *35th AIAA/ASME/SAE/ASEE Joint Propulsion Conference and Exhibit*, AIAA, Washington, DC, 20-24 Jun. 1999.
28. Chehrودي, B., Cohn, R., Talley, D. G., and Badakhsan, A., "Raman Scattering Measurements in the Initial Region of Sub- and Supercritical Jets," *36th AIAA/ASME/SAE/ASEE Joint Propulsion Conference and Exhibit*, AIAA, Washington, DC, 17-19 Jul. 2000.
29. Chehrودي, B., Talley, D. G., and Coy, E. B. "Visual Characteristics and Initial Growth Rates of Round Cryogenic Jets at Subcritical and Supercritical Pressures," *Physics of Fluids*, Vol. 4, No. 2, Feb. 2002. pp. 850-861.
30. Chehrودي, B., Cohn, R., and Talley, D. G., "Cryogenic Shear Layers: Experiments and Initial Growth Rates of Round Cryogenic Jets at Subcritical and Supercritical Pressures," *International Journal of Heat and Fluid Flow*, Vol. 23, 2002, pp. 554-563.
31. Chehrودي, B., and Talley, D. G., "Interaction of Acoustic Waves with a Cryogenic Nitrogen Jet at Sub- and Supercritical Pressures," *40th AIAA Aerospace Meeting and Exhibit*, AIAA, Washington, DC, 14-17 Jan. 2002.
32. Chehrودي, B. and Talley, D., "Fractal Geometry of a Cryogenic Nitrogen Round Jet Injected into Sub- and Super-critical Conditions", *Atomization and Sprays*, Vol. 14, 2004, pp. 81-91.
33. Chehrودي, B., Davis, D. W., and Talley, D. G., "Initial Results from A Cryogenic Coaxial Injector In An Acoustic Field," *41st AIAA Aerospace Sciences Meeting & Exhibit*, AIAA, Washington, DC, 6-9 Jan. 2003.
34. Oschwald, M., Smith, J. J., Branam, R., Hussong, J., Schik, A., Chehrودي, B., and Talley, D. G., "Injection of Fluids into Supercritical Environments," *Comb. Sci. Tech.*, Accepted, 2005.
35. Hulka, J., and Hutt, J., "Liquid Oxygen / Hydrogen Instability Phenomena," Liquid Rocket Engine Combustion Instability, edited by V. Yang and W. Anderson, *Progress in Astronautics and Aeronautics*, AIAA, Washington, DC, 1995, pp. 39-72.
36. Chehrودي, B., Chen, S. H., Bracco, F. V., and Onuma, Y., 1985. On the Intact Core of Full-Cone Sprays, Society of Automotive Engineers, 1985 Congress and Exposition, *SAE Transaction Paper 850126*, February 25-March 1.
37. Faragó, Z., and Chigier, N., "Morphological Classification of Disintegration of Round Liquid Jets in a Coaxial Air Stream," *Atomization and Sprays*, Vol. 2, 1992, pp. 137-153.
38. Davis, D. W., "On the Behavior of a Shear-Coaxial Jet Spanning Sub- to Supercritical Pressures, with and without an Externally Imposed Transverse Acoustic Field", Ph.D. Dissertation, Department of Mechanical Engineering, The Pennsylvania State University, University Park, PA, 2006.

Table 1. Summary of published operating conditions, geometries, measurement techniques, and proposed equations from the literature, measuring or correlating core length for shear-coaxial jets.

REF	Author	Date	Fluid Inner Jet	Fluid Outer Jet	Fluid Ambient	Pressure (MPa)	T_i (K)	T_o (K)	T_∞ (K)
6	Forstall & Shapiro	1950	Air+ 10 %He	Air	Air	0.1*	Amb. ^a	Amb.	Amb.
7	Chigier & Beer	1964	Air	Air	Air	0.1*	Amb.	Amb.	Amb.
8	Champagne & Wagnanski	1971	Air	Air	Air	0.1	Amb.	Amb.	Amb.
9	Au and Ko	1987	Air	Air	Air*	0.1*	Amb.	Amb.	Amb.
10	Eroglu et al.	1991	Water	Air	Air	0.1*	Amb.	Amb.	Amb.
11	Woodward	1993	KI (aq.)	N2, He	N2, He	0.1 – 2.17	Amb.	Amb.	Amb.
15	Villermaux et al. ^g	1994	Water	Water	Water	0.1*	Amb.	Amb.	Amb.
12	Englebert et al.	1995	Water	Air	Air	0.1	293	293 – 636	293
13	Carreau et al.	1997	LOX	He, N2, Ar	NC ^c	0.1	82 ^d	245 – 272 ^d	NC
16	Rehab et al. ^g	1997	Water	Water	Water	0.1*	Amb.	Amb.	Amb.
17	Rehab et al. ^g	1998	Water	Water	Water	0.1*	Amb.	Amb.	Amb.
18	Villermaux ^{g,h}	1998	Water	Water	Water	NR	NR	NR	NR
19	Lasheras et al. ^g	1998	Water	Air	Air	0.1	Amb.	Amb.	Amb.
20	Lasheras & Hopfinger ^{g,i}	2000	NR	NR	NR	NR	NR	NR	NR
21	Favre-Marinet & Schettini	2001	Air, SF6	Air,He	Air, He	0.1	Amb.	Amb.	Amb.
14	Porcheron et al.	2002	LOX, Water	He, N2, Ar, Air	Air	0.1	82, 293	245 – 293	293
This work	Davis	2005	N2	N2	N2	1.4 – 4.9	108 – 133	132 – 204	197 – 249

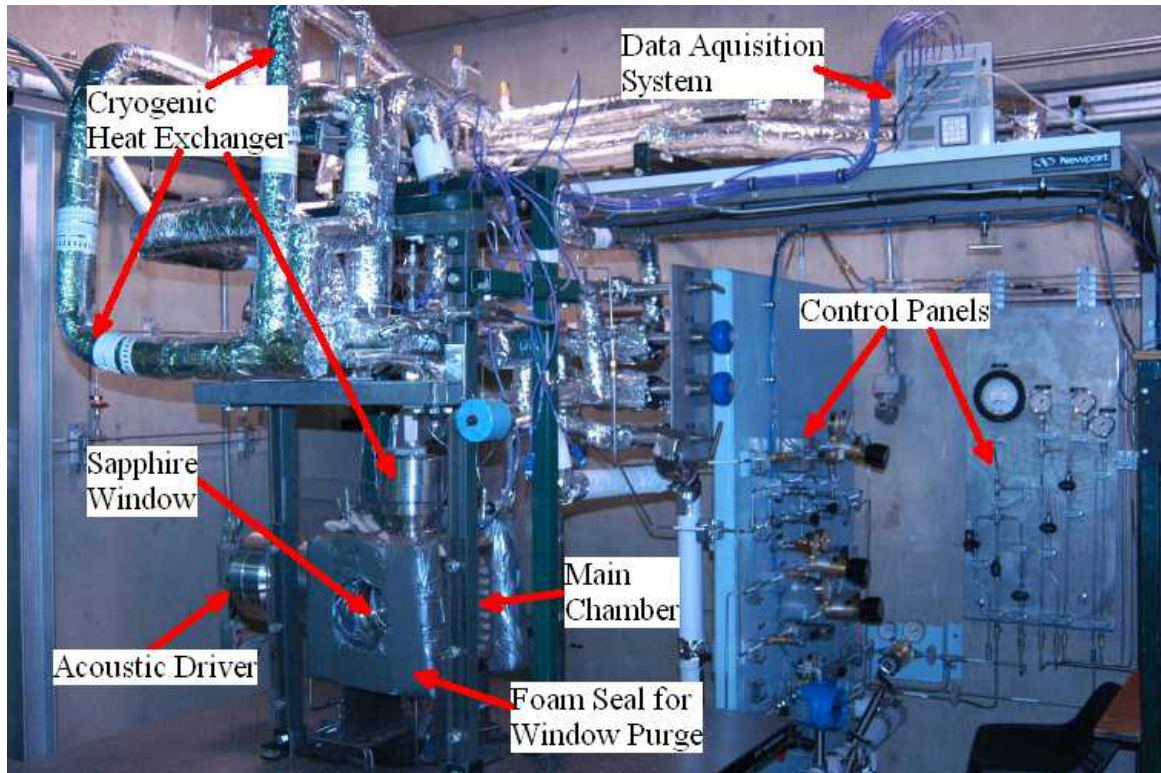


Figure 1. Picture of the experimental facility

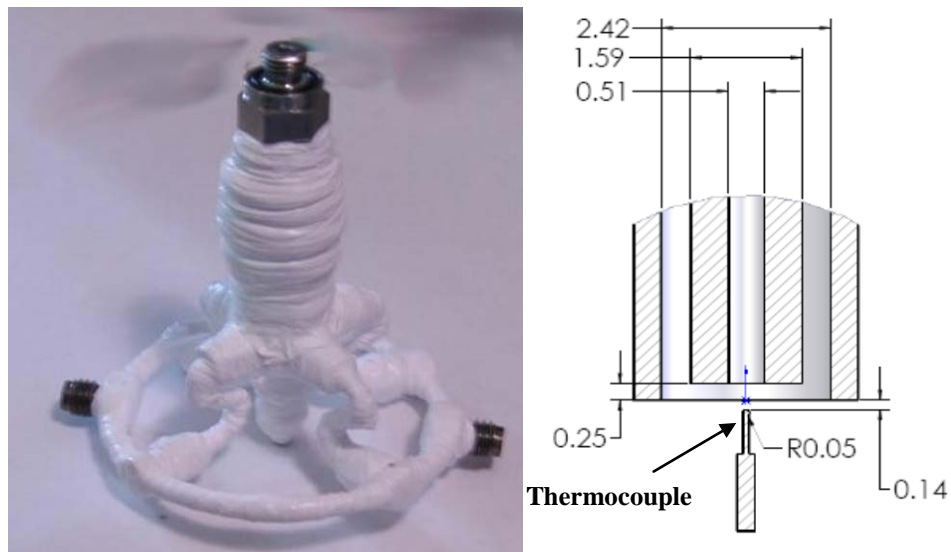


Figure 2. Picture of the shear-coaxial injector (left) and a cross-section drawing of the injector tip. The thermocouple used to measure exit-plane temperature profiles is shown in the drawing.

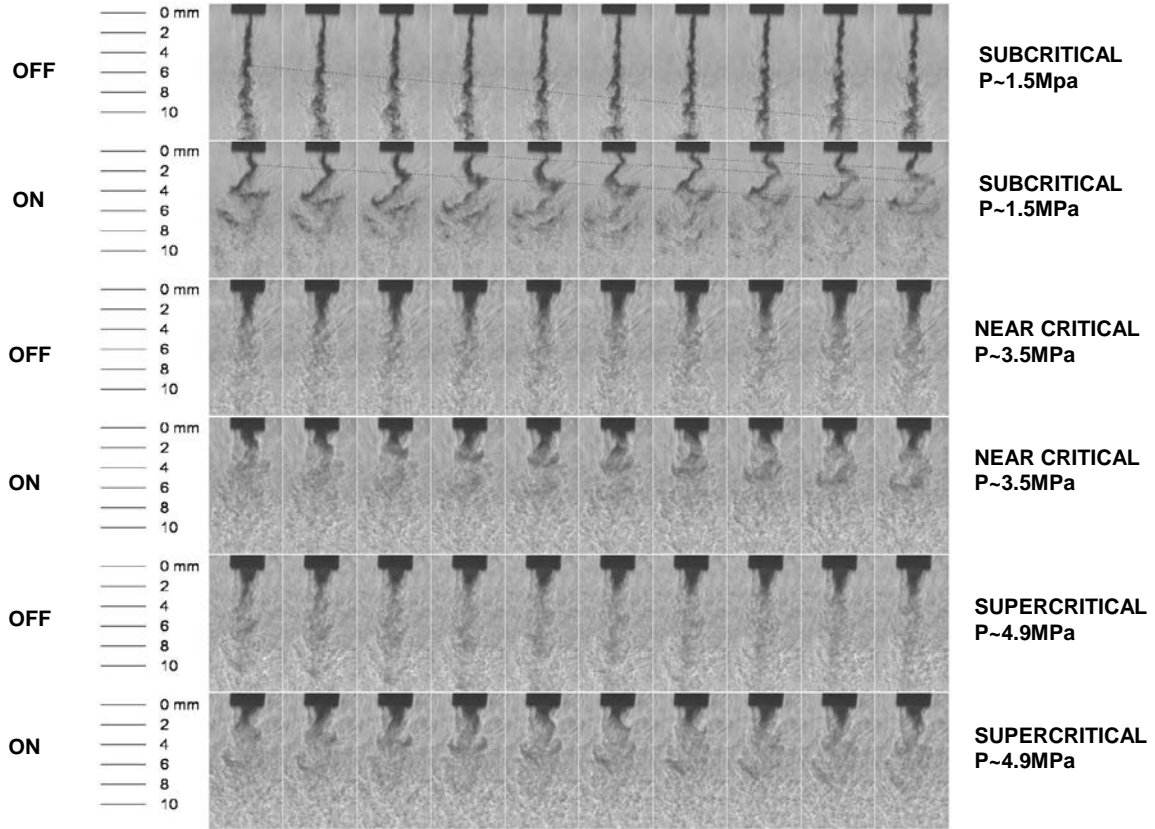


Figure 3. Consecutive frames from high-speed shadowgraph movies with the acoustic driver turned off (in rows 1, 3, and 5) and on (in rows 2, 4, and 6) at $\sim 3\text{kHz}$. Time increases from left to right with an interval of 55.6 ms between frames. The first two rows are at a subcritical chamber pressure ($\sim 1.5\text{ MPa}$), the third and fourth rows are at a near-critical chamber pressure ($\sim 3.5\text{ MPa}$), and the fifth and sixth rows are at a supercritical chamber pressure ($\sim 4.9\text{ MPa}$). The acoustic driver is turned off for the first, third, and fifth rows and on for the second, fourth, and sixth at $\sim 3\text{ kHz}$. The light gray lines in the first and second rows connect fluid structure as they evolve in time.

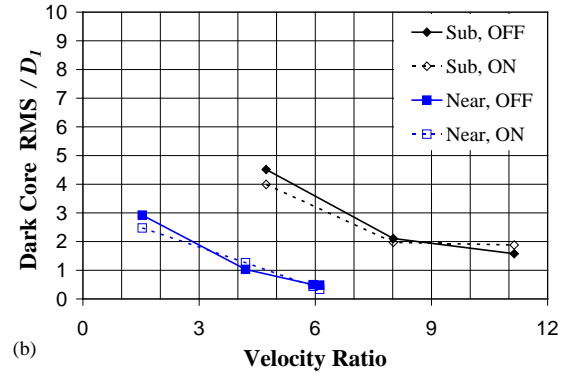
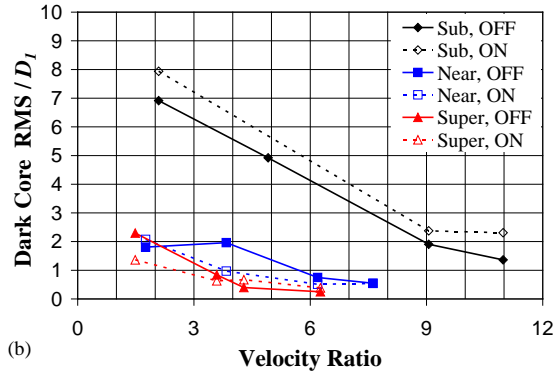
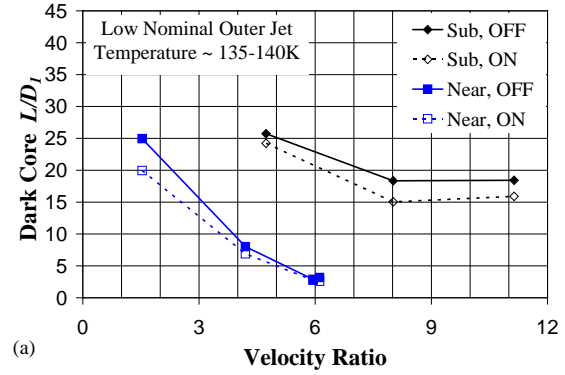
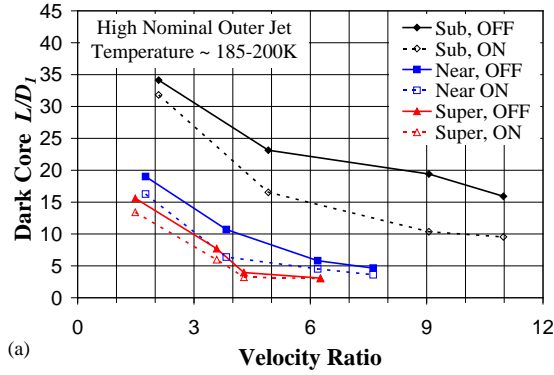


Figure 4. Plot of the averaged dark-core length (a) and the RMS of the length variations (b) normalized by the inner diameter. The solid symbols and lines represent the data for when the acoustic driver is off, and the hollow symbols and dotted lines show the data when the acoustic driver was operated at ~3kHz. The diamond, square, and up-triangle symbols are sub-, near, and supercritical chamber pressures, respectively. All cases are for the high nominal outer-jet temperature of ~190 K. In the inset, the words sub, near, and super refer to subcritical, nearcritical, and supercritical pressure respectively, and the words OFF and ON refer to the acoustic driver being off and on at ~3kHz, respectively.

Figure 5. Plot of the averaged dark-core length (a) and the RMS of the length variations (b) normalized by the inner diameter. The solid symbols and lines represent data for when the acoustic driver is off, and the hollow symbols and dotted lines show results when the acoustic driver is operated at ~3kHz. The diamond and square symbols are for sub- and near-critical chamber pressures, respectively. All cases are for the low nominal outer-jet temperature of ~140 K. In the inset, the words sub and near refer to subcritical and nearcritical pressure respectively, and the words OFF and ON refer to the acoustic driver being off and on at ~3kHz, respectively.

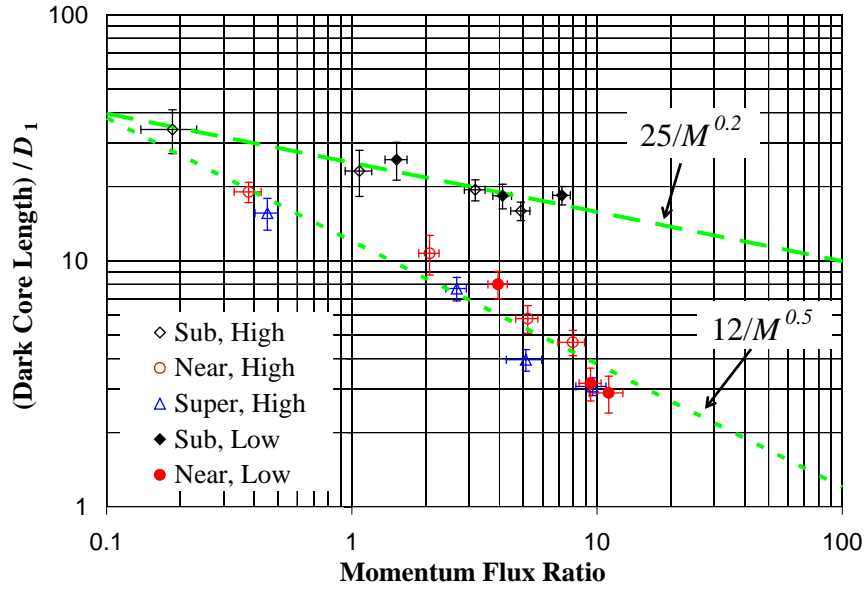


Figure 6. Dark-core length versus momentum flux ratio. The diamond, circle, and up-triangle symbols represent sub-, near-, and supercritical chamber pressure, respectively. The hollow symbols are at a high outer-jet temperature (~ 190 K) and solid symbols are at a low outer-jet temperature. The dashed line is $25/M^{0.2}$ and the dotted line is $12/M^{0.5}$.

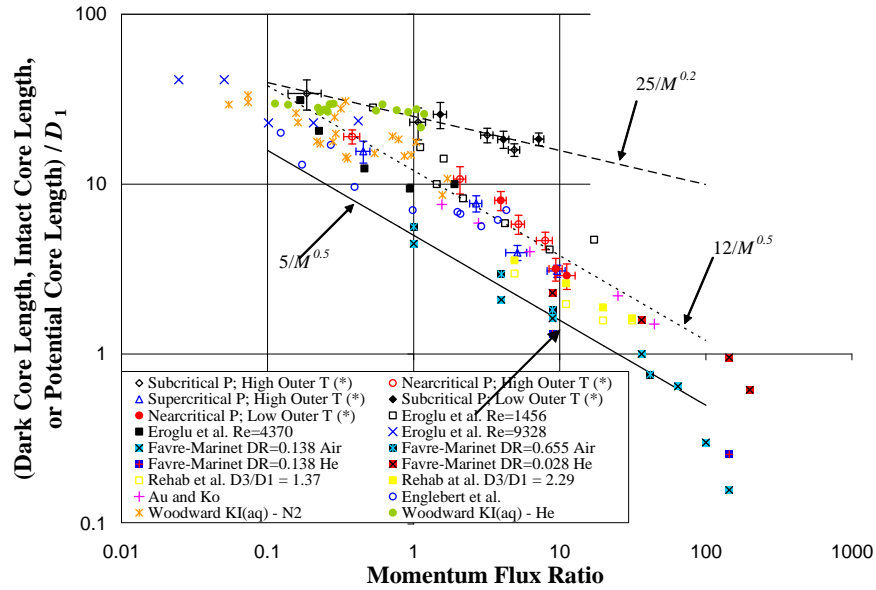


Figure 7. Comparison of the present dark-core length measurements with all other core length data available in the literature vs. momentum flux ratio. Amongst the data reported by others, Eroglu et al., Englebert et al. and Woodward are two-phase flows and the rest are single phase.

The Pennsylvania State University

The Graduate School

Department of Mechanical and Nuclear Engineering

**ON THE BEHAVIOR OF A SHEAR-COAXIAL JET,
SPANNING SUB- TO SUPERCRITICAL PRESSURES, WITH AND WITHOUT
AN EXTERNALLY IMPOSED TRANSVERSE ACOUSTIC FIELD**

A Thesis in

Mechanical Engineering

by

Dustin Wayne Davis

© 2006 Dustin Wayne Davis

Submitted in Partial Fulfillment
of the Requirements
for the Degree of

Doctor of Philosophy

May 2006

Approved for public release; distribution unlimited. PAS #2006-081.

The thesis of Dustin Wayne Davis was reviewed and approved* by the following:

Robert J. Santoro
George L. Guillet, Professor of Mechanical Engineering
Thesis Advisor
Chair of Committee

André L. Boehman
Associate Professor of Fuel Science

Bruce Chehroudi
Chief Scientist, ERC, Inc.
Special Member

Domenic A. Santavicca
Professor of Mechanical Engineering

Vigor Yang
Distinguished Professor of Mechanical Engineering

H. Joseph Sommer III
Professor of Mechanical Engineering
Head of the Department of Mechanical and Nuclear Engineering

*Signatures are on file in the Graduate School

ABSTRACT

In the past, liquid rocket engines (LRE) have experienced high-frequency combustion instability, which impose an acoustic field in the combustion chamber. The acoustic field interacts with the fluid jets issuing from the injectors, thus altering the behavior of the jet compared to that of stable operation of the LRE. It is possible that this interaction could be a substantial feed back mechanism driving the combustion instability. In order to understand the problem of combustion instability, it is necessary to understand the interaction of the jet with the acoustic waves. From past combustion instability studies of the liquid oxygen and hydrogen propellant combination in a shear-coaxial injector configuration, a design guideline of outer-to-inner jet velocity ratio greater than about ten was proposed in order to avoid high-frequency acoustic combustion instability problems. However, no satisfactory physical explanation was provided. To promote this understanding, a cold-flow experimental investigation of a shear-coaxial jet interacting with a high-amplitude non-linear acoustic field was undertaken under chamber pressures extending into the supercritical regime. Liquid nitrogen (LN₂) flowed from the inner tube of a coaxial injector while gaseous nitrogen (GN₂) issued from its annular region. The injector fluids were directed into a chamber pressurized with gaseous nitrogen. The acoustic excitation was provided by an external driver capable of delivering acoustic field amplitudes up to 165 dB. The resonant modes of the chamber governed the two frequencies studied here, with the first two modes being about 3 and 5.2 kHz. High-speed images of the jet were taken with a Phantom CMOS camera. The so-called “dark core” of the jet is among the most salient features in the

acquired images, and therefore, was defined and measured. The core length was found to decrease with increasing velocity and momentum flux ratio. Because of the ability of the camera to capture thousands of images and an automated routine to measure the dark core of the jet, meaningful statistics and time histories of the core length were determined. The root mean square (RMS) fluctuation of the dark-core length decreases and approaches a low constant value as the velocity ratio of the jet increases. The RMS of the dark core length, in some fashion is related to variations in mixture ratio within the combustion chamber. By decreasing this variation, at high velocity ratios under cold-flow conditions, this may lead to a physical explanation of the observed stable behavior of the LRE at high velocity ratios. The decreased RMS fluctuations at high velocity ratios reduce mixture ratio variations, which in turn leads to a more uniform heat release zone in the chamber, thus possibly weakening a key feed back mechanism to drive the combustion instability. Comparisons of the dark core length measured here to those reported by others for both single-phase coaxial jets (i.e. gas-gas or liquid-liquid) and two-phase coaxial jets (i.e. water-air or $\text{LN}_2\text{-GN}_2$) establish two regimes on the dependence of this length to the outer-to-inner jet momentum flux ratio (M). The core length of single-phase jets quantitatively agrees with the dark-core length and its M -dependence measured in our studies under supercritical conditions. However, under subcritical conditions the dark core tends to be much longer and depends more weakly on M than when under supercritical conditions. At $M < 1$ the two regimes meet and approach the values reported for single round turbulent jets (at the limit of $M = 0$). However, at higher values of M , divergence between the two regimes is observed.

TABLE OF CONTENTS

LIST OF FIGURES	vii
LIST OF TABLES	xv
NOMENCLATURE	xvi
ACKNOWLEDGEMENTS	xix
Chapter 1 Introduction	1
1.1 Motivation.....	1
1.2 Objectives	6
1.3 Method of Approach.....	7
Chapter 2 Literature Review	9
2.1 Thermodynamics of High-Pressure Systems	9
2.2 Experiments in Supercritical Cold-Flow Jets and Sprays.....	15
2.3 Shear-Coaxial Jets	20
2.3.1 Core-Length of Single-Phase Shear-Coaxial Jets.....	21
2.3.2 Core-Length of Two-Phase Shear-Coaxial Jets	28
2.4 Interaction of a Transverse Acoustic Waves with Jet Flows	32
2.5 Velocity Measurements from High-Speed Shadowgraph Images	35
Chapter 3 Experimental Facility, Apparatus, and Technique	37
3.1 High Pressure Chamber	39
3.2 Fluid Systems.....	42
3.3 Shear-Coaxial Injector	47
3.4 Acoustic Driver.....	49
3.5 Instrumentation	52
3.6 Imaging Set-up.....	58
Chapter 4 Results and Discussion.....	61
4.1 Uncertainty Analysis	65
4.2 Exit-Plane Temperature Measurements	69
4.3 Flow Visualizations	82
4.3.1 Qualitative Behavior of Single Round Jets	82
4.3.2 Qualitative behavior of Shear-Coaxial Jets	91
4.4 Characterization of Acoustic Wave – Jet Interaction Mechanism.....	100
4.4.1 Acoustic Pressure Measurement.....	100
4.4.2 Acoustically-Driven Mode of the Shear-Coaxial Jet.....	105

4.4.3 Acoustic Velocity Measurements.....	113
4.4.4 Acoustic Wave Jet Interaction Mechanism	135
4.5 Dark-Core Length.....	146
4.5.1 Adaptive Thresholding Measurement of Dark-Core Length.....	153
4.5.2 Influence of Velocity Ratio on the Dark-Core Length.....	163
4.5.3 Scaling of the Dark Core with Momentum Flux Ratio	171
Chapter 5 Summary, Conclusion, and Recommendations for Future Work	185
5.1 Summary and Conclusions	185
5.2 Recommendations for Future Work	191
Bibliography	194
Appendix A Experimental Procedure and Flow Diagram	202
Appendix B Tabular Data	229

LIST OF FIGURES

Figure 1.1: Critical pressures and critical temperatures for species of interest to combustion systems. Superimposed, are the operating conditions of liquid oxygen/hydrogen engines (x symbols), and the range of operating conditions for liquid oxygen/RP-1 rocket, and existing and future jet engines. The critical properties of jet fuels and RP-1 are shown as a range and do not exist as a single point because these fuels are mixtures of many hydrocarbons.	5
Figure 2.1: T, P diagram for a pure fluid. Adapted from Smith et al.[10].....	10
Figure 2.2: Mixture critical pressure (a) and temperature (b) variation with composition for the $N_2 - H_2$ system, and phase diagram (c). The supercritical regime is indicated by the dotted arrows. Mixture critical data (hollow points) from Street and Calado [12] and saturation curve from NIST RERPROP [14]. The dashed-double-dotted lines denote the possible three-phase equilibria regime, and are hypothetical but typical of Type III critical point systems.	13
Figure 3.1: Photograph of the EC-4 Supercritical Facility.	39
Figure 3.2: Drawing of Main Chamber. All dimensions are in mm and approximate.	41
Figure 3.3: Process Flow Diagram of the AFRL Supercritical Facility. Larger format of this figure presented in the Appendix.	45
Figure 3.4: Photograph of Shear-coaxial injector (a) without gas manifold and insulation, (b) with gas manifold and PTFE insulation. Scale cross-section drawing (c) of injector exit-plane area also indicating relative size and position of thermocouple used for temperature measurement. Dimensions in mm.	48
Figure 3.5: Piezo-Siren, high-amplitude high pressure acoustic driver.....	49
Figure 3.6: Plan view cross-section drawing of acoustic driver housing, wave guide, and assembly for attachment to main chamber.....	50
Figure 3.7: Photograph of Inner-chamber.....	51
Figure 3.8: Acoustic Wave Guide.....	52
Figure 3.9: Calibration of the chamber pressure transducer. Difference between the measured pressure (using the linear fit) and the set pressure of the precision calibration device. The circle symbols indicate the increasing	

pressure, followed by decreasing the pressure (square symbols), finally increasing the pressure a second time (triangle symbols).	54
Figure 3.10: Traversing stage for Kistler transducer	55
Figure 3.11: Thermocouple Calibration Curve	57
Figure 3.12: Optical layout for the two Phantom camera arrangement.....	60
Figure 4.1: Density – Temperature ($\rho - T$) diagram displaying the pair of conditions of the inner and outer-jets of the shear-coaxial jet. The red circles are the outer-jet conditions, and the blue diamonds are the inner-jet conditions. The numbers listed near the points correspond to the case number listed in Table 4.1.	63
Figure 4.2: Thermocouple (TC) and the support mechanism used to perform radial temperature measurements in the coaxial jet. The thermocouple bead diameter is 0.10 mm. The resolution of the radial distance is 0.01 mm. The distance from the injector exit-plane to the thermocouple bead is 0.14 mm or $0.28 D_I$	71
Figure 4.3: Radial profiles of the measured average temperature and calculated density. Conditions of cases are listed in Table 4.1. The chamber nominal pressure in the top row is 1.5 MPa, in the middle row is 3.5 MPa, and in the bottom row is 4.9 MPa. The nominal outer-jet temperatures in the left and right columns are about 140 K and 190K, respectively, see Table 4.1 for exact values. The letters “T” or “D” in the inset of the figures refers to temperature or density, respectively, the next number indicates the particular case number for the data corresponding to the case listed in Table 1, and the number in parenthesis is the corresponding outer-to-inner jet velocity ratio.	72
Figure 4.3(a). Radial temperature and density profiles of subcritical pressure and low outer-jet temperature.....	73
Figure 4.3(b) Radial temperature and density profiles of subcritical pressure and high outer-jet temperature.....	74
Figure 4.3 (c). Radial temperature and density profiles of nearcritical pressure and low outer-jet temperature.....	75
Figure 4.3 (d) Radial temperature and density profiles of nearcritical pressure and high outer-jet temperature.....	76
Figure 4.3 (e) Radial temperature and density profiles of supercritical pressure and low outer-jet temperature.....	77

- Figure 4.3 (f) Radial temperature and density profiles of supercritical pressure and low outer-jet temperature..... 78
- Figure 4.4: Subcritical liquid nitrogen single round jet injected into gaseous nitrogen. Nine sequential frames, starting at the top left, with a time interval between frames of $222\ \mu\text{s}$ are shown. Time increases down the column. The chamber pressure was 1.50 MPa, and the velocity of the jet was 2.2 m/s. The acoustic driver is off. The scale can be determined from the injector tip outer diameter of 3.18 mm..... 84
- Figure 4.5: Droplet formation and ejection from liquid jet surface. Fifteen sequential frames are shown starting at the top left, with a time interval between frames of $56\ \mu\text{s}$. Time increases across a row. The pressure was 1.50 MPa, and the velocity of the jet was 2.2 m/s. The acoustic driver is off..... 86
- Figure 4.6: Acoustic wave interaction with subcritical liquid nitrogen single round jet injected into gaseous nitrogen. The pressure was 1.50 MPa, and the velocity of the jet was 2.2 m/s. The acoustic driver is on at 3.03 kHz, amplitude is about 170 dB. The top of the frame is about $10 D_1$ down stream of the injector exit-plane..... 88
- Figure 4.7: Near-critical cryogenic nitrogen single round jet injected into gaseous nitrogen. Fifteen sequential frames, starting at the top left, with a frame-to-frame time interval of $222\ \mu\text{s}$. Time increases across a row. The pressure was 3.47 MPa, and the velocity of the jet was 2.2 m/s. The acoustic driver is off. The scale can be determined from the injector width of 3.18 mm..... 90
- Figure 4.8: Shadowgraph images of coaxial jet at subcritical chamber pressure ($\sim 1.5\text{MPa}$) and at the *high outer-jet temperature* ($\sim 190\text{ K}$) corresponding to cases 1 – 4 listed in Table 4.1 from left to right. The acoustic driver is off for images in the top row and on for the bottom row at $\sim 3\text{ KHz}$. The velocity ratio is the same for each column and increases from left to right. 94
- Figure 4.9: Shadowgraph images of coaxial jet at subcritical chamber pressure ($\sim 1.5\text{MPa}$) and *low outer-jet temperature* ($\sim 140\text{ K}$) corresponding to cases 13 – 15 listed in Table 4.1 from left to right. The acoustic driver is off for images in the top row and on for the bottom row at $\sim 3\text{ KHz}$. The velocity ratio is the same for each column and increases from left to right. The lowest flow rate condition was unattainable experimentally. 95
- Figure 4.10: Shadowgraph images of a coaxial jet at nearcritical chamber pressure ($\sim 3.5\text{ MPa}$) and at a *high outer-jet temperature* ($\sim 190\text{ K}$) corresponding to cases 5-8 listed in Table 4.1 from left to right. Images in

the top row the acoustic driver is off, and the bottom row the acoustic driver is on at ~ 3 KHz. The velocity ratio increases from left to right.	96
Figure 4.11: Consecutive frames from high-speed shadowgraph images of case 3, 7, and 11 (from Table 4.1) with the acoustic driver turned on and off. Time increases from left to right with an interval of $55.6 \mu\text{s}$ between frames. The first two rows are at a subcritical chamber pressure (~ 1.5 MPa, case 19 of Table 4.1), the third and fourth rows are at a near-critical chamber pressure (~ 3.5 MPa), and the fifth and sixth rows are at a supercritical chamber pressure (~ 4.9 MPa). The acoustic driver is off for the first, third, and fifth rows and on for the second, fourth, and sixth at ~ 3 kHz.	99
Figure 4.12: Variations of the RMS of acoustic pressure oscillations (in kPa on the left axis, and in dB on the right axis) along the length of the inner-chamber. The static chamber pressure was 1.49 MPa, and the temperature was ambient $\sim 300\text{K}$. The acoustic driver is located at the far left position.....	102
Figure 4.13: Variation of the RMS of the acoustic pressure with the chamber pressure, measured 1.75 mm to the right of the injector centerline in the direction away from the acoustic driver.	104
Figure 4.14: Synchronized images viewed both perpendicular and parallel to acoustic velocity direction. Columns 1 and 2 acoustic driver is off, 3 and 4 on at 3.03 kHz.....	108
Figure 4.15: Consecutive images framed at 18kHz of case 3 of Table 4.1. Column 1 acoustics off, column 2 acoustics on at 2.98 kHz, column 3 acoustics on at 5.16 kHz.....	110
Figure 4.16: Ratio of the wavelength measured from the dark core of the jet multiplied by the frequency of the acoustic driver for the second resonance frequency (subscript 2) to the first resonance frequency (subscript 1) as a function of momentum flux ratio.....	112
Figure 4.17: An image frame from a movie with boxes indicating the locations of the source windows for the spatial cross-correlation calculations (a), and (b) shows the spatial cross-correlation space for the fifth source window from the left in (a).	116
Figure 4.18: Power spectrum of the transverse velocity signal normalized by the dc component. The acoustic driver frequency was (a) 3.06 kHz and (b) 5.16 kHz, respectively.	118
Figure 4.19: Spatial cross-correlation space for image resolution of 512×256	120

- Figure 4.20: Transient transverse velocity after start of the acoustic driver, at chamber pressures of (a) 1.49 MPa and (b) 3.56 MPa, respectively. The acoustic driver frequency was (a) 3.01 kHz and (b) 3.04 kHz, respectively. 122
- Figure 4.21: The instantaneous transverse velocity measured at $1.4 D_1$ downstream of injector exit-plane, at progressively closer radial distances to the injector centerline: (a) $4.86 D_1$ from the centerline of the jet in the chamber fluid, (b) $2.24 D_1$ from the centerline at the edge of the outer-jet, and (c) $0.73 D_1$ from the centerline at the edge of the inner-jet. The chamber pressure was 1.49 MPa. 124
- Figure 4.22: RMS of the velocity signal variations with transverse direction (x). The error bars on the figure correspond to the n^{th} order uncertainty as described in the beginning of chapter 4. The vertical gridlines are the four important radii of the shear-coaxial injector. The chamber pressure was 1.49 MPa. 125
- Figure 4.23: Power spectra of the acoustic velocity signals shown in Fig. 4.21 at distances from the centerline of the jet of: (a), $4.86 D_1$ in the chamber fluid; (b), $2.24 D_1$ at the edge of the outer-jet; and (c), $0.73 D_1$ at the edge of the inner-jet. The chamber pressure was 1.49 MPa. 127
- Figure 4.24: Amplitude of the transverse acoustic velocity fluctuations from the chamber pressure measurements (circle symbols) and directly measured from the images (square symbols). The solid and dashed lines represent curve fits using the equation indicated in the figure. 130
- Figure 4.25: Variation of acoustic momentum flux ($\rho \mathcal{U}^2$) with the outer-to-inner jet momentum flux ratio. The words sub, near, and super in the figure inset correspond to subcritical, near-critical, and supercritical chamber pressure, respectively. The words “high” and “low” in the figure inset are for the nominal high and low outer-jet temperature cases. The hollow diamond symbols (“Sub, High”) are cases 1-4; the hollow circles (“Near, High”) are case 5-8; the hollow triangle symbols (“Super, High”) are cases 9-12; the solid diamond symbols (“Sub, Low”) are case 13-15; the solid cycle symbols (“Near, Low”) are cases 16-19. The case numbers correspond to Table 4.1. 132
- Figure 4.26: Variation of the ratio of acoustic momentum flux ($\rho \mathcal{U}^2$) to the momentum flux of the inner-jet with the outer-to-inner-jet momentum flux ratio. The words sub, near, and super in the figure inset correspond to subcritical, near-critical, and supercritical, respectively. The words “high” and “low” in the figure inset are for the nominal high and low outer-jet temperature cases. The hollow diamond symbols (“Sub, High”) are cases 1-4; the hollow circles (“Near, High”) are case 5-8; the hollow triangle symbols

- (“Super, High”) are cases 9-12; the solid diamond symbols (“Sub, Low”) are case 13-15; the solid cycle symbols (“Near, Low”) are cases 16-19. The case numbers correspond to Table 4.1..... 133
- Figure 4.27: Variation of the ratio of acoustic momentum flux (ρU^2) to the momentum flux of the outer-jet with the outer-to-inner jet momentum flux ratio. The words sub, near, and super in the figure inset correspond to subcritical, near-critical, and supercritical, respectively. The words “high” and “low” in the figure inset are for the nominal high and low outer-jet temperature cases. The hollow diamond symbols (“Sub, High”) are cases 1-4; the hollow circles (“Near, High”) are case 5-8; the hollow triangle symbols (“Super, High”) are cases 9-12; the solid diamond symbols (“Sub, Low”) are case 13-15; the solid cycle symbols (“Near, Low”) are cases 16-19. The case numbers correspond to Table 4.1..... 134
- Figure 4.28: Annotated consecutive images of a subcritical pressure shear-coaxial jet. 140
- Figure 4.29: Annotated consecutive images of the shear-coaxial jet at subcritical chamber pressure. Images show magnified views of the near-injector region. Horizontal arrow length is quantitative and proportional (amplified by 10 for clarity) to velocity measured in Fig. 4.21 (a). Two parallel vertical lines in the center show the inside diameter of the inner tube. The chamber pressure was 1.49 MPa (subcritical), and the acoustic driver frequency was at 3.01 kHz..... 144
- Figure 4.30 Magnified view of frame number 10 from Fig. 4.29. The dashed curves denote the approximate boundary of the recirculation zone, and the arrows within the recirculation region indicate the direction of the rotation. The vortex structures that form on the outer rim of the injector are identified by the arrows pointing to the outer edge of the injector tip. The two vertical lines with the dimension D_2 denote the extent of the outer diameter of the inner tube, $D_2 = 1.59\text{mm}$ 145
- Figure 4.31: The image of (a) coaxial jet as captured, (b) threshold applied for injector, (c) threshold applied for dark core. 156
- Figure 4.32: Histogram of image in Fig. 4.31 (a). 157
- Figure 4.33: Dark core length (in pixels) versus velocity ratio (outer-to-inner jet) comparing the visual measurement with that of the algorithm programmed for automated measurement of this length using an average image representative for each of the conditions. The error bars represent a sensitivity analysis, varying the automatically-selected threshold level by $\pm 10\%$. The diamonds and the up-triangles are for manual visual

- measurements under sub- and nearcritical chamber pressures and the squares and circles are for corresponding pressures using automated computer measurements. 160
- Figure 4.34: Comparison of the average dark-core length measured from of set of individual images versus the dark-core length measured from the average image of the same set..... 162
- Figure 4.35: Plot of the averaged dark-core length (a) and the RMS of the length variations (b) normalized by the inner diameter. The solid symbols and lines represent the data for when the acoustic driver is OFF, and the hollow symbols and dotted lines show the data when the acoustic driver was operated at $\sim 3\text{kHz}$ (ON). The diamond, square, and up-triangle symbols are sub-, near and supercritical chamber pressures, respectively. All cases are for the high nominal outer-jet temperature of $\sim 190\text{ K}$ 164
- Figure 4.36: Plot of the averaged dark-core length (a) and the RMS of the length variations (b) normalized by the inner diameter. The solid symbols and lines represent data for when the acoustic driver off, and the hollow symbols and dotted lines show results when the acoustic driver is operated at $\sim 3\text{kHz}$ (ON). The diamond and square symbols are for sub- and near-critical chamber pressures, respectively. All cases are for the lower nominal outer-jet temperature of $\sim 140\text{ K}$ 165
- Figure 4.37: Comparison of measured core length data vs. velocity ratio (outer /inner). Data series indicated by (*) denotes this work. References for the data taken from other work listed in Table 4.2. DR denotes density ratio of the outer-jet to the inner-jet. 170
- Figure 4.38: Dark core length versus momentum flux ratio. The diamond, circle, and up-triangle symbols represent sub-, near-, and supercritical chamber pressure, respectively. The hollow symbols are at a high outer-jet temperature ($\sim 190\text{ K}$) and solid symbols are at a low outer-jet temperature. The error bars on the data points in Fig. 12 for the dark core length represent on standard deviation from the mean, and the error bars for the momentum flux ratio are the n^{th} order uncertainty as described at the beginning of this chapter. The dashed line is $25/M^{0.2}$ and the dotted line is $12/M^{0.5}$ 173
- Figure 4.39: Comparison of dark core length, intact core length, or potential-core length for single-phase coaxial jets. This work (denoted by *), Favre-Marinet and Camano Schettini [60], Rehab et al. [52], Au and Ko [48]. DR denotes density ratio of the outer-jet to inner-jet. 176
- Figure 4.40: Comparison of the dark-core length, intact core length, or potential-core length for two – phase coaxial jets. This work (denoted by *), Eroglu et

al. [8], Engelbert et al. [63], Woodward [62]. Porcheron et al. [65] did not report core length measurements because of the measurement technique of liquid probability presence, but only an equation, see Table 4.2 for a summary of the work, and Chapter 2 for more details. Dashed-dotted line is the equation of Porcheron et al. evaluated at the average conditions of the subcritical data of this work with the LPP = 50%, and the dotted line is their equation evaluated at the same conditions except LPP = 2.5%..... 180

Figure 4.41: Comparison of the dark-core length, intact core length, or potential-core length vs. momentum flux ratio for shear-coaxial injectors, both single-phase and two-phase shear-coaxial jets. The same symbol definitions and references used here as Fig. 4.39 and Fig. 4.40 182

Figure 4.42: Comparison of dark core length, for $M < 1$, with Eq. 4.9 developed for single round jets. 184

Figure A.1: Process Flow Diagram of the AFRL Supercritical Facility. Regions denoted with “A” corresponds to Fig. A.1(A) and so on..... 203

LIST OF TABLES

Table 3.1: Fluid Subsystem Number Designation.....	46
Table 4.1: Summary of conditions for coaxial jet.....	64
Table 4.2: Summary of published operating conditions, geometries, measurement techniques, and proposed equations from the literature, measuring or correlating core length for shear-coaxial jets.....	148
Table B.1: Radial temperature and density profiles.....	230
Table B.2: Dark Core Length Data.....	241

NOMENCLATURE

A	cross-sectional area
c	speed of sound
C, c	a constant
D_1	inner-diameter of the inner-jet
D_2	outer-diameter of the inner-jet
D_3	inner-diameter of the outer-jet
D_4	outer-diameter of the outer-jet
\mathcal{E}	energy density of acoustic wave integrated over one time period
E_R	kinetic energy ratio $\equiv \frac{\rho_o U_o^3 (D_3^2 - D_2^2)}{\rho_i U_i^3 D_1^2}$
f	frequency, region of interest in an image
g	region of interest in an image
H	ratio of fluid of interest to that of nitrogen $\equiv \frac{\sqrt{\gamma R}}{\sqrt{\gamma_{N2} R_{N2}}}$
L	core-length, dark-core length, length
M	momentum flux ratio of the outer-jet to inner-jet $\equiv (\rho_o U_o^2) / (\rho_i U_i^2)$
M_R	momentum ratio of the outer-jet to inner-jet $\equiv (\rho_o U_o^2 A_o) / (\rho_i U_i^2 A_i)$
p	relative coordinate in the transverse direction
P	pressure
\mathcal{P}	amplitude of the acoustic pressure
q	relative coordinate in the axial direction

R radius, gas specific gas constant, cross-correlation

Re Reynolds number $\equiv \frac{\rho U D}{\mu}$

St Strouhal number $\equiv \Lambda f / u$

t time

T temperature

u velocity, characteristic velocity

U average axial velocity

\mathcal{U} is the amplitude of the acoustic velocity

V_r velocity ratio

We Weber Number $\equiv \frac{\rho_o (U_o^2 - U_i^2) D_1}{\sigma}$

x transverse dimension

y axial dimension

Z Ohnesorge Number $\equiv \frac{\mu_i}{\sqrt{\rho_i \sigma D_1}}$

Greek Symbols

α a constant

γ ratio of specific heats

κ a constant

Λ wavelength measured from the core of the jet

μ	viscosity
ρ	density
σ	surface tension
τ_A	characteristic time associated with core wavelength

Subscripts

e	denoting entrainment quantity
i	denoting a quantity relating to the inner-jet
o	denoting a quantity relating to the outer-jet
$post$	denoting a dimension of the inner tube

Superscript

$'$	denoting root-mean-square fluctuating velocity
sat	denoting saturation condition

ACKNOWLEDGEMENTS

I wish to thank my thesis advisor, Dr. Robert Santoro, particularly for many helpful discussions, and permitting me to go to AFRL to perform the experiments with Dr. Bruce Chehroudi and Dr. Douglas Talley. I would like to extend my appreciation to Dr. Chehroudi for his close mentorship and guidance during this work. The patient and gentle nature of Dr. Chehroudi was instrumental in the transition from a mentor to a friend, and I sincerely value his friendship. I would also like to thank the rest of my committee, Dr. Boehman, Dr. Santavicca, and Dr. Yang, for their interest in this research.

Without the support of the people at AFRL, this work would not have been possible. I would like to extend my appreciation to Dr. Talley for his interest, leadership, and support. Also, I would like to express my gratitude our mechanical crew, particularly Mr. Mike Griggs, for his valuable insight and experience. Mr. Griggs was a cornerstone in the modification and building of the experimental facility, and his opinion was always held in high esteem. Additionally, the AFRL Librarian, Jennie Paton, is thanked for her efforts to make literature available in a timely manner. The funding for this work from AFOSR, Dr. Mitat Birkin program manager, and NASA, Walter Duvall contract monitor, was greatly appreciated.

My deepest gratitude is to my wife Holly and sons Drew and Parker for enduring the long journey required to complete the degree. Also I would like to thank my parents, and grandparents for their support, especially my maternal grandfather, Homer Miller, for his inspiration to wonder how things work.

In all your ways acknowledge Him, and He shall direct your paths. Prov. 3:6

Chapter 1

Introduction

1.1 Motivation

Combustion instability in liquid rocket engines was the problem in mind at the onset of this study, and the motivation starts there. Culick and Yang [1] indicated that combustion instability has plagued almost all liquid rocket engine programs since the late 1930's. Three types of combustion instabilities have been identified based on the frequencies involved. Low frequency instability (chugging) corresponds to when the wavelength is much longer than the characteristic dimension of the chamber and the feed system. Generally, chugging frequencies are less than a few hundred Hz. High frequency instability (screaming) is the second type, which is also referred to as acoustic instability, due to the closeness of the measured pressure oscillation frequencies to the computed acoustic resonance modes of the thrust chamber. High-frequency combustion instability is the most destructive type, and generally agreed that it is not influenced by the propellant feed system of the rocket engine. An intermediate frequency (buzz) consists of the lumping of the instabilities that do not fall into either chugging or screaming categories, see Harrje and Reardon [2].

With acoustic instabilities being the most destructive [2], they pose the greatest risk to preventing the development of a new engine, or may lead to a loss of vehicle and payload, or worse, to a loss of human life. A great deal of research primarily in the

1950's and 1960's during the space race [2] was undertaken attempting to gain fundamental understanding of combustion instability. This was later somewhat revitalized briefly in the 1990's [1]. Now, in part, enhancing our fundamental understanding is under consideration again. A large portion of the initial combustion instability research often involved a trial and error approach to the design of a new injector or a new combustion chamber. Many times, design and development of a new large-scale LRE starts with subscale models that proves to be stable, but an acoustic instability appears when a full-scale testing of this new LRE begins for flight verification. Historically, in these situations, the solution to the problem often has been to eliminate instability with baffles and Helmholtz resonators or modify the injectors (or both). Consequently, the modifications make the combustion chamber more complex, and add cost, time delays, and most importantly, additional mass to the vehicle. Despite these previous efforts, the fact of the matter is that a fundamental understanding of high-frequency combustion instability does not exist even today. The impediments to a full understanding of combustion instability in a rocket engine are due, in part, to the complex nature of the system itself, and mainly to a lack of fundamental understanding of the sub-processes such as liquid atomization, combustion, and their couplings with the acoustic waves.

Considering that the experiments in this study are done in a non-reacting environment, it would be an unjustifiable statement to claim, as an objective of this study, a quest for a full understanding of combustion instability. However, fundamental understanding about the sub-process associated with combustion instability may be gained. Hulka and Hutt [3] compiled an extensive review of combustion instability data

for liquid rocket engines using liquid oxygen (LOX) / hydrogen (H_2) propellants. Because of the complex nature of combustion instability, the development of liquid rocket engines has focused and emphasized mapping of the stability margins of the engine, instead of understanding of the fundamental cause of the combustion instability. General observations about the stability regions of LOX / H_2 rocket engines indicates that higher hydrogen temperature, velocity ratios (outer-to-inner or H_2 -to-LOX), and momentum ratios (outer-to-inner) had a stabilizing effect. Because of the complex nature of a rocket engine, exceptions were found, but for the majority of the data, velocity ratios greater than about 10 proved to produce stable engines. One method for determining the stability margin of an engine is the so-called “temperature ramping” method. The temperature ramping method consists of lowering the hydrogen temperature feeding the engine at a constant hydrogen flow rate until a combustion instability event is initiated. Hulka and Hutt [3] point out that during the J-2 engine development, when the temperature was ramped down to somewhere between 28 and 42 K, combustion instabilities were observed even for high velocity ratios. The critical temperature of hydrogen is 33.2 K (DCAPII [4]), which is near the middle of this range. Note that in this range, small (~ 5 K) changes in temperature produce large changes in density (factor of 2 to 3). It was not always clear where, with respect to the injector, the hydrogen temperature was measured. However, it is certain that it was not at the exit-plane of the injector. Physical mechanisms have been proposed on how temperature ramping causes combustion instability, but all have limited ranges of applicability (see Hulka and Hutt [3]).

Liquid rocket engines, burning cryogenic propellants of liquid oxygen (LOX) / hydrogen (H_2), often use shear-coaxial injectors. Examples are the designs presently employed in the Space Shuttle Main Engine (SSME) or the Ariane 5 Vulcain engine (Vingert et al. [5]), and the RL-10 and J-2 engines from the late 1950's (Hulka and Hutt [3]). One method for eliminating acoustic instability in liquid rocket engines is to modify the spray combustion field, which is usually achieved through modifications to the injector design (see Harrje and Reardon [2]). One such modification to the Ariane 5 Vulcain reported by Vingert et al. [5], increased the mean droplet diameter size and improved the stability of the engine. Changes to the injector design ultimately influence the mixing characteristics of the propellant streams in the thrust chamber.

The fundamental physics of the breakup of a liquid jet and its subsequent mixing with other fluids have been studied since Rayleigh's study in 1878 [6]. Significant progress has been made since then, and as a result the scientific community is approaching a fundamental understanding of fluid jet break up and atomization processes, see for example Lefebvre [7]. However, Eroglu et al. [8] make it clear that a full understanding is not yet reached.

Interestingly enough, the majority of non-reacting flow studies related to propulsion applications were performed at low pressure, even though many liquid rocket engines are operated at pressures well above the critical pressures of the propellants or the major products of combustion, with the exception of water. Figure 1.1 shows the critical pressures and temperatures for possible chemical species of interest to combustion systems. Superimposed on the plot is the chamber pressure and fuel inlet temperature of several liquid oxygen/hydrogen rocket engines, the regime of liquid

oxygen/kerosene engines, and the current and proposed operating regime of jet engines. What is important to note in Fig. 1.1 is that many rockets and future jet engines are at supercritical pressures with respect to the propellants. Despite this observation, much less work has been done regarding mixing and atomization processes at elevated pressures as compared to atmospheric pressure.

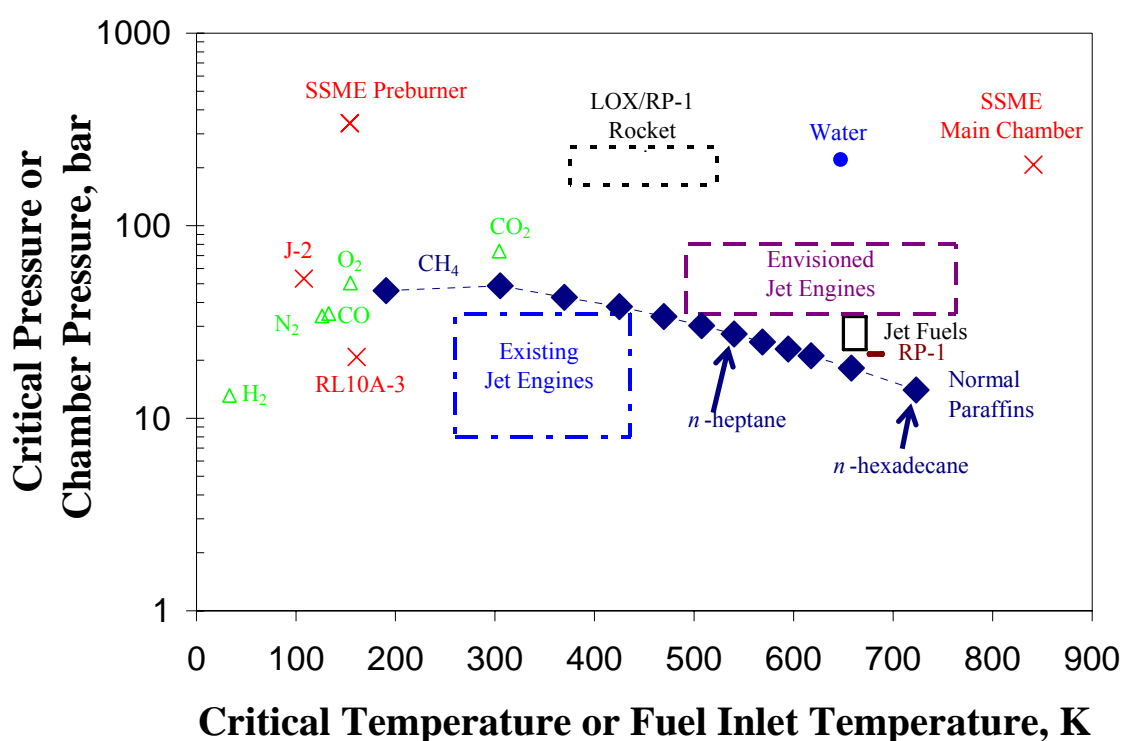


Figure 1.1: Critical pressures and critical temperatures for species of interest to combustion systems. Superimposed, are the operating conditions of liquid oxygen/hydrogen engines (x symbols), and the range of operating conditions for liquid oxygen/RP-1 rocket, and existing and future jet engines. The critical properties of jet fuels and RP-1 are shown as a range and do not exist as a single point because these fuels are mixtures of many hydrocarbons.

1.2 Objectives

Because of the observations of Hulk and Hutt [3] regarding the relationship of the hydrogen temperature (during the ramping exercise) and velocity ratio to combustion stability, several questions were pondered. Why does temperature ramping cause an onset of combustion instability? Why are engines more stable at high velocity ratios? How does the shear-coaxial jet behave during combustion instability? Does the nearcritical conditions of the hydrogen account for temperature ramping observations? Clearly the complex nature of combustion instability is far too large of a problem to answer in one dissertation. But perhaps, something can be learned from a cold-flow study of a shear-coaxial jet, in which similar conditions to those in liquid rocket engines during a combustion instability event are created. This could provide an opportunity to understand how the character of the jet may change during such an event. Therefore, the objectives of this study are:

1. To eliminate ambiguity in the real exit-plane temperature conditions making accurate temperature measurements at the injector exit-plane to determine initial conditions of the jet with high precision.
2. Determine if any one of the dynamic behaviors of the shear-coaxial jet could be a potential trigger for combustion instability, which would also be consistent with the observed stability impact of the velocity ratio.
3. Determine how the jet may behave during a combustion instability event, by driving the jet with externally-imposed high-amplitude transverse acoustic waves.

4. Assess the impact of the velocity and momentum flux ratios on the core of the shear-coaxial jet (physically related to mixing) both with and without the presence of acoustic waves.

One may expect to find a hypothesis statement to come at this point. However, at the onset of the study because of the complex nature of the problem, the outcome was quite unpredictable. Nevertheless, past efforts have shown that the core of the jet is an important component defining the character of the jet and could potentially be related to combustion instability. Therefore, special emphasis is put on the behavior of the core of a shear-coaxial jet.

1.3 Method of Approach

The approach is then to create a shear-coaxial jet in a chamber with pressures spanning subcritical to supercritical. Using only a single chemical species, nitrogen, to remove any ambiguity about the conditions being subcritical or supercritical associated with the composition dependence on mixture critical properties. Make accurate temperature measurements so the initial conditions of the jet are well known. Adjust the temperature of the outer-jet to two nominal temperatures to simulate temperature ramping effects while maintaining independent control over velocity ratio. One temperature is selected to be in a region where small changes in temperature produce only small changes in density, and the other temperature where small changes could produce large changes in density. At these conditions, study the behavior of the jet both with and without acoustic forcing to simulate the effect of what might happen during transverse combustion

instability. Assess the behavior and mixing characteristics of the jet by taking images at framing rates fast enough to capture the dynamic behavior of the jet. From the images establish a repeatable method for determination of the effects of mixing in a consistent and repeatable fashion. One assessment for mixing of coaxial jets in the past has been core length. This parameter may also be of use to injector designers. Therefore, the assessment of mixing will be core length of the jet.

Chapter 2 presents a review of relevant literature. In particular, the review focuses on the core length measurements obtained by other researchers. However, relevant concepts concerning supercritical jets are also reviewed. Additionally, information concerning past studies involving the interaction of high-amplitude acoustic waves and jet flows are also presented.

The equipment used to perform the experiments in this work is presented in Chapter 3. A concise description of the experiment is presented first, then followed by details about the specific equipment used. A complete experimental procedure is contained in Appendix A.

Chapter 4 presents the experimental results and discussion. Chapter 4 is broken into several sections, but three sections contain the bulk of the information. Section 4.3 discusses general observations from the visualizations of the jet. Section 4.4 presents the characterization of the interaction mechanism of the acoustic wave and the jet. Finally, the discussion on the dark-core of the jet is placed in section 4.4.

Finally, the conclusions and recommendations for extensions to the study are presented in Chapter 5.

Chapter 2

Literature Review

2.1 Thermodynamics of High-Pressure Systems

Considering a broader pool of readers, beyond that of the propulsion community, a brief review and discussion of high-pressure thermodynamics is presented first. The intent of this section is not to produce a comprehensive review of the literature on supercritical flows and applications, but rather present the relevant concepts which may be unfamiliar to those working outside the propulsion community.

Typically, fluids are divided into two classes, gases (or vapors) and liquids. However, in the supercritical regime a clear distinction between liquid and gas cannot be drawn. Moran and Shapiro [9] define the critical temperature (T_c) of a pure chemical substance as a temperature above which vapor and liquid phases cannot simultaneously co-exist in equilibrium. The pressure at the critical point is called the critical pressure (P_c). Figure 2.1 shows a phase diagram for a pure fluid, including a saturation curve in T - P space. The critical point is the terminal point of the saturation curve. According to Smith et al. [10], pure fluids at conditions of $T < T_c$ and P greater than the saturation pressure (P^{sat}) are referred to as liquids, if $P < P^{\text{sat}}$ then the fluid is referred to as a gas (or a vapor if $T < T_c$, also). The dashed and dotted lines on Fig. 2.1 do not represent physical phase boundaries, but rather identify different regions, as a result of semantics associated with the words liquid and gas [10]. For pure fluids, several anomalies occur

with the physical properties of the fluid as the critical point is approached. For example, the heat capacity diverges and becomes theoretically infinite. Additionally, the latent heat of vaporization and surface tension become zero. However, this subject becomes more complicated when multiple chemical species are added to the system as is the case in a reacting system.

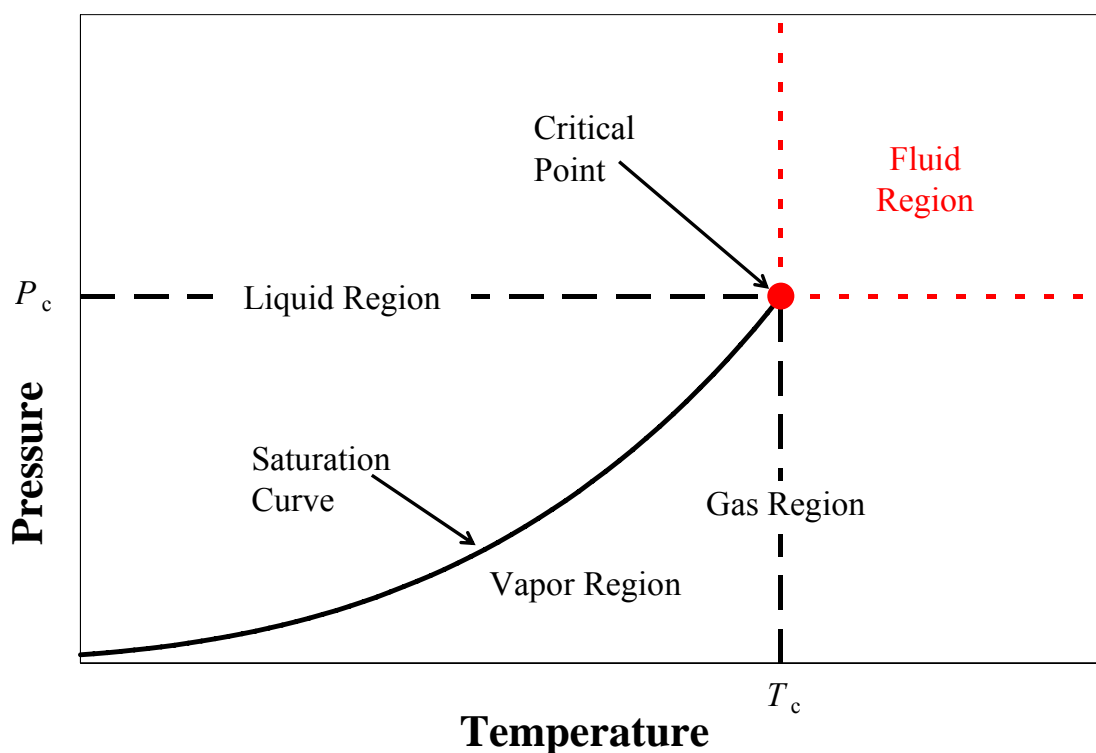


Figure 2.1: T, P diagram for a pure fluid. Adapted from Smith et al.[10].

The critical point of a mixture of two or more pure species is expanded to critical lines or surfaces depending on the number of species in the mixture, and is called the critical locus. Multi-component fluid systems have phase diagrams that fall into one of the six fundamental types, first classified by van Konynenburg and Scott [11] with critical loci of phases other than vapor-liquid equilibrium critical phases (such as liquid-liquid). The vapor-liquid critical locus is the most relevant to liquid rocket engines, but the propellant combination may exhibit other types of phase behavior other than the simple vapor-liquid co-existence curve.

The critical locus of the mixture depends on the composition of the mixture. The critical pressure of a mixture can exceed many times the critical pressure of any component in the mixture. In the case of $\text{H}_2 - \text{O}_2$ system, because of the reactive nature of the system, mixture critical point measurements are not easily attainable. However, N_2 is similar in thermodynamic behavior to that of O_2 and it is often used as a simulant. Mixture critical properties were measured for the $\text{N}_2 - \text{H}_2$ system by Street and Calado [12] and are shown in Fig. 2.2. Figure 2.2 (a) and (b) show the variation in mixture critical pressure and temperature with composition, respectively. Figure 2.2 (c) is a phase diagram for the $\text{N}_2 - \text{H}_2$ system, with the supercritical regime indicated by the red arrows. Although the liquid – liquid equilibrium (LLE) or vapor – liquid – liquid (VLLE) data are not available at the lower temperatures for this system, the phase diagram most likely exhibits Type III critical locus behavior (as classified by van Konynenburg and Scott [11]), due to the sharp divergence in the critical pressure with increasing composition (see Fig. 2.2(a)). For reference, the critical pressures and temperatures for pure N_2 and H_2 are 3.4 MPa, 126.2 K and 1.313 MPa, 33.19 K,

respectively (DCAPII [4]). The maximum measured critical pressure in the $\text{H}_2 - \text{N}_2$ system is 58 MPa (~ 8400 psi), which is 17 times greater than the critical pressure of pure N_2 .

In general, the composition in a combustion device varies both spatially and temporally. Therefore, the critical pressure and temperature of the mixture are functions of space and time, and are not fixed quantities as is the case for a pure fluid. It can then be expected that in a high-pressure combustion environment, especially near the injector exit-plane region where the temperature may be relatively low, the fluids could have regions which are subcritical. Additionally, if one of the products of combustion is water, with a critical pressure of 22.06 MPa [4] then the equilibrium two-phase region is likely to be expanded. As the water is transported away from the flame (especially in the direction of the lower temperatures) it is possible that more two-phase regions are created in the flow of the mixture.

The importance of the discussion in the last paragraph is that surface (or interfacial) tension may not be zero, and this can play a role in the mixing and atomization processes. For example, Zuo and Stenby [13] used a modified form of the Soave Redlich Kwong equation of state along with the assumption of a linear density gradient through the interface to compute non-zero interfacial tensions up to 60 MPa for the $\text{N}_2 - n$ -octane system, well above the critical pressure for either pure species in the mixture (P_c of $\text{N}_2 = 3.4$ MPa, P_c of n -octane = 2.49 MPa [4]). The computed results agreed fairly well with the experimental measurements of Gielessen and Schmatz [15] over the same range. A much more detailed computation of surface tension using

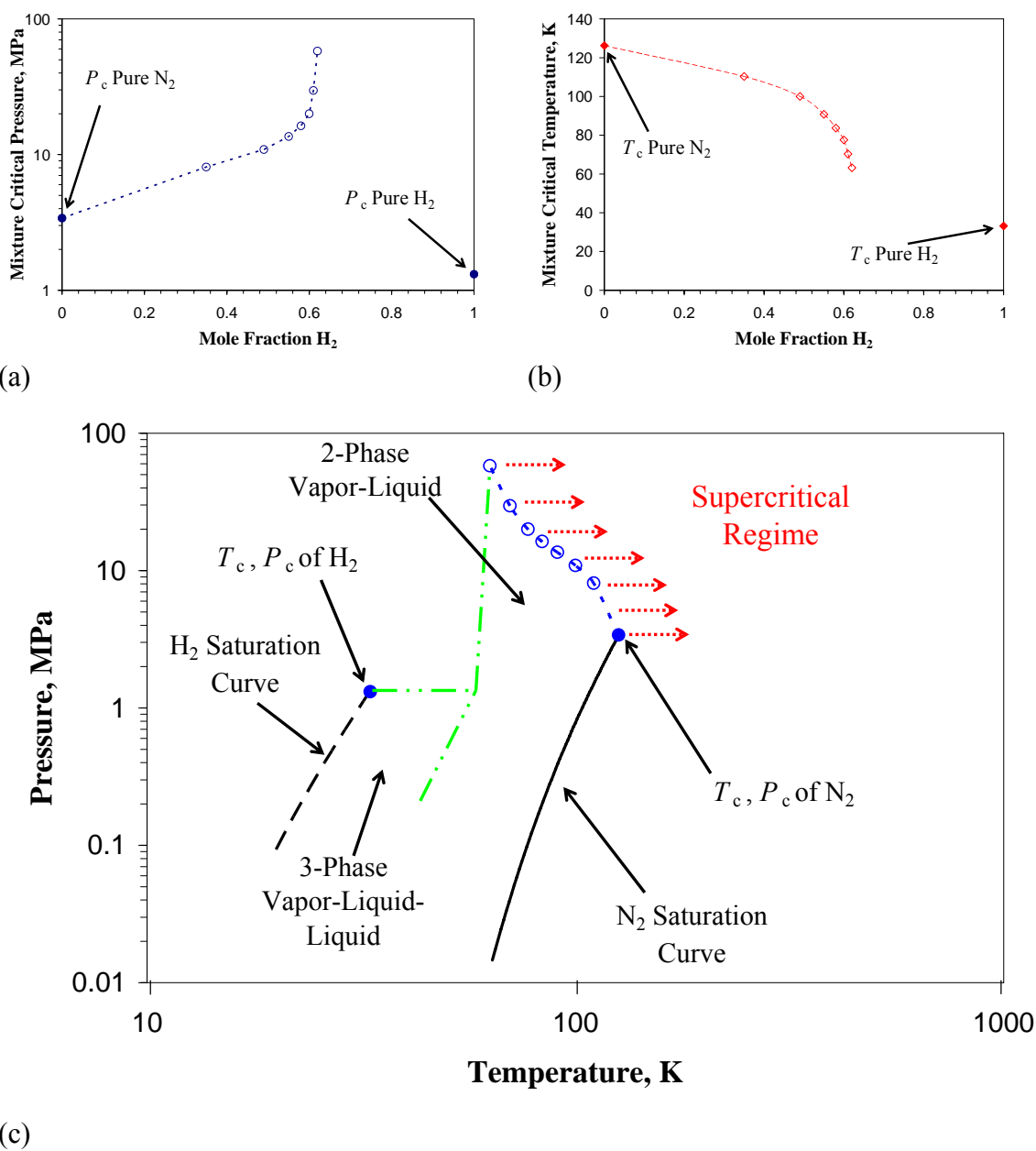


Figure 2.2: Mixture critical pressure (a) and temperature (b) variation with composition for the N_2-H_2 system, and phase diagram (c). The supercritical regime is indicated by the dotted arrows. Mixture critical data (hollow points) from Street and Calado [12] and saturation curve from NIST RERPROP [14]. The dashed-double-dotted lines denote the possible three-phase equilibria regime, and are hypothetical but typical of Type III critical point systems.

molecular dynamics was done by Lee [16] for the $O_2 - He$ system up to 8 MPa (P_c of $O_2 = 5.043$ MPa, P_c of $He = 0.2275$ MPa [4]). Lee [16] demonstrated good agreement between the simulation and experimental results of Vieille [17] over the pressure range tested.

Caution should be exercised when referring to supercritical region to avoid ambiguity, and to ensure that some of the relevant physics are not neglected in the problem of interest. The supercritical system can be defined as the impossibility of two phases being simultaneously present as defined by Harstad and Bellan [18]. However, the impossibility of two phases existing when the system is at conditions greater than T_c or P_c is only true for systems consisting of a single pure substance. For a mixture it is not necessarily true as indicated by Fig. 2.2. Specifically, for $N_2 - H_2$ system the temperature and pressure of the system must be greater than T_c and P_c of N_2 to ensure that the system is at a supercritical condition by relying on only the critical properties of one of the components in the mixture, see Fig. 2.2. If the temperature of the system is less than that of the T_c of N_2 and the pressure is greater than P_c of N_2 the possibility of the coexistence of two equilibrium phases exists, depending on the specific values of the temperature of the system and the composition.

In some liquid rocket engines, gas-turbines, and diesel engines the fuel and/or oxidizer in the injector may be at a pressure greater than the critical pressure and a temperature below the critical temperature, and is introduced into a combustion chamber that is also at a supercritical pressure, but at a temperature supercritical with respect to the propellants. For instance, Woodward and Talley [19] call this “transcritical” injection. For a single chemical species undergoing a transcritical injection process the

impossibility of crossing a phase boundary is true. However, for a multiple chemical species system the potential for portions of the flow in different locations to be both subcritical and supercritical at the same time exists.

2.2 Experiments in Supercritical Cold-Flow Jets and Sprays

While much can be learned from the study of droplets under supercritical conditions, a thorough review is beyond the scope of this work and will not be discussed in great detail here. Extensive reviews on the subject of supercritical droplets have been done in the past by Givler and Abraham [20], Yang [21], and Bellan [22], to name a few. The review articles of Yang [21] and Bellan [22] do not restrict themselves to droplets only, but include other relevant flows for propulsion applications such as jets and sprays. In particular, both address difficulties associated with modeling supercritical flows.

One of the earlier jet studies under nearcritical conditions was done by Newman and Brzustowski [23]. A single round jet of liquid carbon dioxide (CO_2) at 295 K was injected into a gaseous N_2 environment under (chamber) pressures around the critical pressure of CO_2 ($P_c = 7.383$ MPa, $T_c = 304.2$ K). Shadowgraph images of the jet were taken with a 0.5 μs strobe flash at three chamber pressures of 6.21, 7.58, and 8.96 MPa and a variety of chamber far-field temperatures spanning sub- to supercritical values, with respect to the pure CO_2 . The results of the photographic study under isothermal conditions indicated that the atomization of the jet near the critical pressure of the pure CO_2 was similar to previous observations at high, but well below the critical pressure. Therefore, they concluded that in an isothermal system, the fact that the chamber pressure

was near or greater than the critical pressure of pure CO₂ is of no consequence for the atomization, and is only related to the fluid dynamic processes. The composition of the chamber fluid was found to have an effect on droplet size distribution (qualitatively determined). Their results indicated that increased concentration of CO₂ in the gas resulted in the formation of larger droplet sizes at a given axial distance from the injector. This was attributed to processes associated with evaporation. Under conditions of higher chamber temperatures, the atomization of the jet is controlled by the decreased surface tension associated with heat transfer to the jet [23]. Finally, they concluded that at low evaporation rates and at velocities that produce small (qualitative) droplet sizes, the jet can be characterized as a single-phase variable-density turbulent jet, spanning sub- to supercritical chamber pressures (with respect to the CO₂). A discussion about the effect of the mixture critical properties of the N₂ – CO₂ system was not presented. It is possible (and is most likely) that the system, although reported supercritical, was in fact subcritical in nature. Additionally, axial velocity measurements of the jet were made from high-speed film movies. It is unclear from the report as to how these measurements were made, but perhaps by tracking structures in the movie.

Woodward and Talley [19] produced cryogenic nitrogen jets under subcritical and supercritical conditions injected into gaseous nitrogen (N₂) and N₂ and helium (He) mixture. The injector was a long ($L_{\text{post}} / D \sim 300$) tube with a diameter of 0.25 mm. Chamber temperatures ranged from 280 to 310 K and injection temperatures were between 88 and 115 K. Back-lit and Raman scattering images of the jet were made. From the shadowgraph results at subcritical injection temperatures and supercritical pressures (transcritical) for N₂-into-N₂ injection (i.e., a single component system),

droplets were not present. However, once even a small amount of He gas was introduced into the chamber, the jet underwent the classical break-up mechanism as a result of presence of surface tension. These observations are consistent with the discussion of the thermodynamics of critical phenomena of single component and multi-component mixtures given above. If a single component system is at a pressure greater than the critical pressure, but at a subcritical temperature, then as the temperature is increased at relatively constant pressure (as is the case in this type of flow) then the fluid does not pass through the two phase region (see Fig. 2.1). Consequently, without passing through the two phase region, a surface tension cannot exist. However, as shown in Fig. 2.2(c) phase boundaries can be crossed for a transcritical injection process of a multi-component system. Recall, that a transcritical injection process is when the pressure is greater than the critical pressure of both of the chemical species, and the initial temperature is less than the critical temperature of one of the species at injection. After injection, the fluids are subsequently heated to a supercritical temperature.

Chehroudi and co-workers [24-37] extended the preliminary laminar-jet work of Woodward and Talley [19] at the Air Force Research Laboratory (AFRL) to higher Reynolds numbers and turbulent jets of interest to practical applications in propulsion systems. The single round-jet studies by Chehroudi et al. [24-30] were produced from two different injectors made from 50 mm long sharp-edged tubes with the inner diameters (D_I) of 0.254 mm and 0.508 mm, (L_{post}/D_I of 200 and 100, respectively). Pure N_2 and O_2 were injected separately into N_2 , He, Ar, and mixtures of CO and N_2 . The single round jets were studied with shadowgraphs and Raman imaging. It was determined that the initial growth rate (initial spreading angle) of a supercritical jet was

different from that of a subcritical jet. Furthermore, they quantitatively proved for the first time that the initial growth rate of a supercritical jet behaved similar to a variable-density gas jet [27]. From this observation, a phenomenological model of the initial growth rate based upon time scale arguments was proposed that agreed well with the results acquired under sub- and supercritical conditions [28]. It is also important to note that Chehroudi et al. [28] showed that the growth rate measured from shadowgraphs was about twice as large as the growth rate of the jet measured from Raman imaging of the jet, based on the full-width at half-maximum (FWHM) jet thickness (diameter) values. The fractal dimension of the initial region of the jet under sub- and supercritical conditions was also measured by Chehroudi et al. [25, 28, and 30] and compared to liquid and gas jets in a similar fashion to that of the growth rate. A transition of the fractal dimension from values associated with a liquid jet under subcritical conditions to values associated with those of a gas jet under supercritical critical conditions was observed.

Similar research work to that of Chehroudi et al. has been undertaken at Deutsches Zentrum für Luft und Raumfahrt (DLR). Recently, a joint article by Chehroudi and co-workers at AFRL and Oswald and co-workers at DLR summarized the work performed at both laboratories, see Oswald et al. [37]. Independent confirmation of the results published by Chehroudi and his colleagues was shown in this article. Both laboratories had difficulties making Raman scattering measurements at subcritical conditions, and reported that under supercritical conditions, Raman scattering information was more useful. Correspondence between the spreading rates from shadowgraph and Raman scattering images using twice the FWHM rule might not be universally true at all axial locations from the injector exit-plane [37, 38]. This was

found to be especially true for single round jets under supercritical conditions approaching self-similar profiles at about 10 diameters downstream from the injector exit. Oswald and Micci [38] have shown that the spreading rate from the shadowgraph images is approximately twice the spreading rate from the Raman images using FWHM for $15 < x/D < 32$ in the DLR experimental setup. Oswald and Schik [39], using Raman scattering demonstrated the effects of the initial temperature of the jet, considering whether it was initially below or above the “pseudo-boiling” temperature (this temperature is also called the transposed critical temperature in other supercritical literature). The pseudo-boiling temperature is an extrapolation of the saturation curve in T - P space based upon the temperature at which a maximum in the heat capacity exists for a given pressure greater than the critical pressure. They reported that the temperature of the jet, measured along its centerline, remained roughly constant many diameters downstream if the initial temperature was below the pseudo-boiling temperature. However, if the initial temperature was greater than the pseudo boiling temperature, the jet temperature decreased from the injector exit-plane.

Zong et al. [40] and Zong [41] performed a large-eddy simulation of the supercritical cryogenic nitrogen jet studied experimentally by Chehroudi et al. [27-28]. Real fluid transport properties and thermodynamic properties were used in the model, and the subgrid scales were addressed using modified Smagorinsky models extended for compressible flow. The simulations produced good quantitative agreement with the experimentally-measured visual spreading angle of the jet to within 5%. The dynamics of the jet were largely governed by the local thermodynamic state of the fluid [40]. Classification of the supercritical jet could be broken into three regimes: potential-core,

transition regime, and a variable-density gas jet downstream. Therefore, Zong [41] notes simulating the entire jet as an incompressible variable-density jet could produce errors in the near-field region of the jet computation.

2.3 Shear-Coaxial Jets

Shear-coaxial jets are characterized by a flow issuing from an inner central tube, surrounded by a second outer tube, defining an annular opening from which an additional flow exits the injector. Typically, in shear-coaxial injectors for rocket applications, the oxidizer forms the inner-jet and the fuel defines the outer-jet region. Improved combustion stability characteristics of liquid oxygen (LOX) / hydrogen (H_2) engines were observed when the outer-jet to inner-jet velocity ratio (V_r) was greater than about 10, as indicated by Hulka and Hutt [3]. Therefore, many LOX / H_2 liquid rocket engines have velocity ratios in this range and thus ratio of the momentum flux ratio (M) typically falls into range $1 < M < 10$. For example the Space Shuttle main engine (SSME) preburner and main chamber velocity ratios are about 10 and 11.5, respectively, and momentum flux ratios are about 3.4 and 1.2, respectively [42,43].

Core length of the shear-coaxial jets is an important physical structure for the present study, particularly when the velocity ratio and momentum flux ratio are in the range relevant to that of liquid rocket engines. A summary of the studies that reported core length measurements or an equation correlating core length is presented in Table 4.2 in Chapter 4. This summary includes the fluids used, operating conditions, relevant injector dimensions, the diagnostic tools used in the study, the physical quantity

measured, and the correlation equation for the core length. This table is comprehensive, and to the best of the author's knowledge includes all of the relevant core length measurements and data in the open literature for non-reacting shear-coaxial jets.

2.3.1 Core-Length of Single-Phase Shear-Coaxial Jets

The term “single-phase” coaxial jet is defined as a shear-coaxial jet where all three fluid components (i.e., the inner-jet, the outer-jet, and the chamber or ambient fluid) are the same phase, either all gas, all liquid or all supercritical fluid.

One of the first experimental studies in the U.S. on coaxial gas jets was published by Forstall and Shapiro [44], shortly after WWII. Two different inner-jet tubes were used in this work with diameters of 6.4 mm and 25.4 mm, through which air with 10 ppm of helium (He) as a tracer gas flowed. The jet was studied with a Pitot tube, which was also used as a gas sampling tube. The gas samples were analyzed with a thermal conductivity cell measuring the He concentrations. The potential-core length was determined from the axial He concentration profiles. The length of the potential-core was found to increase with velocity ratio ($V_r = U_o / U_i$) for velocity ratios of less than one. Additionally, it is interesting to note that in the limit of $U_2 = 0$ (i.e., single round jet), the length of the potential-core predicted by their equation is $4 D_I$.

Chigier and Beer [45] also studied air – air coaxial jets at atmospheric pressure. Both the inner-jet diameter and the outer-jet annular gap were tapered to smaller dimensions near the injector exit-plane. Static pressure measurements were made with an impact tube and disk-type static probe, and velocities were calculated from these static

measurements. Carbon dioxide was used as a tracer gas to measure the axial concentration profile, similar to Forstall and Shapiro [44]. By extending the range of velocity ratios up to 9.22 (well beyond that of Forstall and Shapiro [44]), Chigier and Beer [45] determined that both the axial velocity and the concentration on the centerline decay as velocity ratio was increased. Therefore, they concluded that the potential-core length decreased as a velocity ratio increased, which is opposite to what Forstall and Shapiro [44] found for their lower velocity ratios studies ($U_o / U_i < 1$).

Effects of the velocity ratio range spanning 0 to 10, for coaxial all-air jets, was investigated by Champagne and Wygnanski [46]. Velocity and turbulence intensities were measured using two hot wire anemometers. The potential-core for the outer-jet region was determined not to vary with velocity ratio. However, the potential-core of the inner-jet was strongly dependent on velocity ratio and the area ratio. They pointed out that for $0 < U_o / U_i < 1$, the length of the potential-core was extended as velocity ratio increased, and for $U_o / U_i > 1$, the potential-core decreased with increases in velocity ratio. Thus confirming the explanation offered by Chigier and Beer [45] for the disagreements between their data on the behavior of the core length variation with velocity ratio compared to that reported by Forstall and Shapiro [44].

Au and Ko [47-48], also studied shear-coaxial jets using air as the only fluid. The velocity field was measured with a hot-wire anemometer and static pressure fluctuations were measured with a microphone. Vortices were found to shed from the lip of the inner tube, with alternating direction when the velocity ratio was less than 1.25. Once the velocity ratio was increased to a number greater than 2, the vortices originated from the outer edge of the inner tube lip with a rotation direction inwards toward the inner-jet.

These inward-rotating vortices were considered the reason for the decrease in the core length as velocity ratio increased. The velocity ratio was adjusted by varying the inner-jet velocity while maintaining a constant initial velocity for the outer-jet (50 m/s). Changing the inner-jet velocity had little impact on the potential-core of the annular outer-jet, which remained roughly constant at a value 1.7 times larger than the outer-jet diameter. Upon comparing their work to others, they concluded that the outer-jet potential-core was relatively unaffected by the velocity ratio and was a function of the area ratio between the inner and outer streams. Finally, the inner potential-core length was found to be inversely proportional to the velocity ratio, and for the first time was reported in the form of an equation (see Table 4.2) indicating this inverse proportionality. It is also important to note that for a shear-coaxial jet with equal inner-jet and outer-jet densities, the velocity ratio is equal to the square root of momentum flux ratio.

Coaxial water jets with equal densities injected into a tank filled with water were studied by Dahm et al. [49]. The injector was contoured inward to the inner-tube exit diameter of 53.3 mm and the annular gap inner and outer diameters were 54.6 and 76.5 mm, respectively. The velocity ratio covered a range of $0.59 < U_o / U_i < 4.16$. The flow was visualized using planar laser induced fluorescence (PLIF) with a different color fluorescent dye in each fluid issuing from the inner and outer-jets. The fluorescent dyes were excited with a “thin” continuous wave argon ion laser sheet. The jets were imaged with 35 mm film, and 16 mm movie camera framing at 60 Hz. The shear layer between the inner- and outer-jet, and the outer-jet and the stagnant chamber fluid can be seen very clearly with this visualization technique. The vortex structure changed significantly over the small range of velocity ratios studied. The vortices evolving from each layer can be

wake-like (alternating rotation), shear-layer-like (single direction of rotation turning into the slower velocity region) with either axisymmetric or helical modes. They determined that the changes in potential-core length are governed by the near-injector vortex dynamics. Also, they found that this length did not depend on velocity ratio alone, and that it did not behave in a monotonic fashion with velocity ratio. Finally, a coupling between the instability, roll-up and vortex structure interactions in the outer shear layer (between the outer-jet and the chamber fluid) and vortex structures located in the inner shear layer (between the inner-jet and outer-jet) was observed.

The momentum flux ratio, in particular $M^{-0.5}$, has been taken to be an important parameter for coaxial jets by one group of researchers [50-58]. Recall that the velocity ratio is equal to the square root of momentum flux ratio ($M = \rho_o U_o^2 / (\rho_i U_i^2)$) when the density ratio is unity. A review of coaxial jet literature considering the works of this group and others is given by Lasheras and Hopfinger [54] covering both single-phase experiments and two-phase experiments of coaxial jet flows.

Villermaux et al. [50] performed experiments on coaxial jets with water issuing from both the inner-jet and outer-jet, into a chamber filled with water studying the self pulsation phenomenon of the jet. The injector inner tube diameter was 40 mm, with an outward taper of 6° to a knife edge tip. The outer diameter of the annular gap was 55 mm. Oscillations were measured with a pressure transducer and a hot film anemometer. For velocity ratios between 1 and 6, they reported the potential-core length to be inversely proportional to velocity ratio (see Table 4.2). At velocity ratios greater than 6, a recirculation bubble was observed at the end of the potential core. Using a mixing layer argument and the pressure drop caused by the mixing layer, a criterion for the onset of

the recirculation was derived as $\sqrt{M} > 6$. The recirculation bubble caused oscillations that are convected downstream in the jet. The oscillation Strouhal number based on the inner diameter and the outer-jet velocity was fixed at a value approximately equal to 0.3.

Rehab et al. [51] expanded upon the work of Villiermaux et al. [50] making measurements with a hot-film anemometer, a Pitot tube, and flow visualizations from a single-dye PLIF images excited by an argon ion laser. A definition of potential core was offered, clarifying that the flow in the potential core is not necessarily irrotational flow, but indicates a region of weak turbulence intensity where small-scale dissipation is nearly zero. The length of the potential core was defined as the distance from the injector exit to the axial location where the velocity on the centerline of the jet reached a minimum value, and was stated to follow the inverse proportionality to the velocity ratio. A theoretical analysis of the length of the potential core was given starting with the same estimate of pressure drop for the mixing layer as Villiermaux et al. [50]. The pressure drop in the mixing layer is given by:

$$\Delta P = \rho u'^2 / 2 \quad (2.1)$$

Where,

$\rho u'^2 / 2$ is the dynamic turbulent pressure.

The assumed that the potential core is an inverted cone in shape with the inner diameter (of inner tube) defining the base, and the length of the potential core for its height. Also, they hypothesized that the entrainment velocity (u_e) is proportion to the root-mean-square

(RMS) fluctuating velocity (u'). The entrainment velocity (u_e) is an averaged velocity that satisfies the equation for the conservation of mass for the core of the jet. From their measurements, they showed that $u' \approx 0.17 (U_o - U_i) = 0.12 U_o$, and in general assumed that $u' \approx \alpha U_o$. Then, applying conservation of mass on this conical control volume, the resulting length of the potential core was determined and given by Eq. 2.2.

$$\frac{L}{D_1} \approx \frac{1}{2} \left(\frac{1}{C^2 \alpha^2 \frac{U_o}{U_i}} - 1 \right)^{1/2} \approx \frac{1}{2C\alpha \frac{U_o}{U_i}} \quad (2.2)$$

Where,

C is a constant approximately 0.5

With $\alpha = 0.17$, the term $1/(2 C \alpha)$ is 5.88, and when $\alpha = 0.12$, the term $1/(2 C \alpha)$ is 8.33, which is consistent with their data. If the RMS of the velocity fluctuations is given by $u' \approx \alpha (U_o - U_i)$, the resulting expression for the potential core length is given by the Eq. 2.3. A comment was made that for fluids of unequal densities the velocity ratio term should be replaced with $M^{0.5}$. Rehab et al. [51] stated that Eq. 2.3 is limited to the range $1 < U_o / U_i < 8$, without any statement about momentum flux ratio. However, if the same limitation were to apply, then the momentum flux ratio range of applicability would be $1 < M < 64$.

$$\frac{L}{D_1} \approx \frac{1}{2} \left(\frac{1}{C^2 \alpha^2 \left(\frac{U_o}{U_i} - 1 \right)^2} - 1 \right)^{1/2} \quad (2.3)$$

Favre-Marinet and co-workers [59, 60] investigated the effects of the density ratio on coaxial gaseous jets spanning a wide range of velocity, density, and momentum flux ratios (see Table 4.2 for the values). The variations in density ratio were achieved using different gas combinations of air, He, and sulfur hexafluoride (SF_6). Favre-Marinet et al. [59] performed flow visualization by illuminating the jets with a 1mm thick laser sheet from a pulsed copper vapor laser operating at 10 kHz, and images were recorded with a video camera at 50 Hz. The shutter speed was set at 1/4000 s, therefore each frame captured two pulses from the laser. The flow was seeded with incense smoke, except when He and SF_6 were used as the fluids, for this case, the inner-jet was seeded with “very-small” droplets of a mixture of water, glycerin, and fluorescein dye. A Laser Doppler Velocimetry (LDV) system used for the air-air and He-air jets, were combined with results using a hot-wire probe. Favre-Marinet and Schettini [60] used the same apparatus, but with a different diagnostic method and were able to measure the density field of the jet. The measurement was made with an aspirating probe, which is a “very thin” tube with a hot-wire at its end. This tube is connected to a vacuum pump and when the pressure reaches a critical value, the hot-wire is no longer sensitive to velocity, but only to density variation. The results of these two works indicated that the onset of the recirculation bubble at the end of the potential core begins at $M \approx 50$, which is larger than that reported by Villermaux et al. [50]. For $M < 50$, they claimed that the potential core length varied with $M^{-0.5}$. However, at the same M value but at different density ratios the potential-core lengths of the jet are different values.

2.3.2 Core-Length of Two-Phase Shear-Coaxial Jets

The term “two-phase” coaxial jet here means a shear-coaxial jet where the inner-jet is liquid phase, and the outer-jet and the chamber (i.e. ambient fluid) are gas phases.

Eroglu, Chigier, and Farago [8] measured liquid intact lengths for a coaxial water-air jet at atmospheric pressure, and later Farago and Chigier [61] classified the break-up of the liquid jet according to the value of Weber number (We). Note that Eroglu et al. [8] used a definition of We which has a factor of 2 in the denominator. This expression is different than the definition given by Farago and Chigier [61] and the definition listed in the Nomenclature section of this dissertation. To be clear, all values and equations reported in this work are consistent with the definition of We presented in the Nomenclature section. Images of the coaxial jet were acquired with a 35 mm camera back-lit with a 0.5 μ s pulse duration strobe light. The injector had an inner-tube inside diameter of 0.971 mm. The inner and outer diameters at the exit of the annular gap were 1.262 mm and 10.36 mm, respectively, which was obtained by contracting a 16 mm duct in order to produce a flat velocity profile at the exit. The area ratio (outer-to-inner) of this injector was about 112, which is much greater than a rocket-type coaxial injector (for example, SSME injector area ratio is about 2.8). The inner tube of the injector used in many rocket engines is recessed back into the outer tube. However, the inner tube, in this case protruded (a negative post recess) beyond the outer tube by 0.6 mm, but they reported no noticeable effects of moving the inner-jet by ± 1 mm. The inner tube flow was in the laminar regime when $Re < 6000$, with transition occurring somewhere within the range $6 \times 10^3 < Re < 10^4$, and fully turbulent regime occurring for $Re > 10^4$ [61]. The

Re in this study was in the range $1097 < Re < 9328$, and therefore, being less than 10^4 , it is likely that the exit-plane velocity profile from the inner tube was not a fully-developed turbulent profile. Eroglu et al. [8] measured the intact liquid length by analysis of four to seven images taken at each condition for six different Re numbers. Mean values were then computed, and it was noted that the individual measurements values can be as much as $\pm 15\%$ from the mean value. A correlation equation (see Table 4.2) of the intact liquid lengths was deduced from these measurements, and found to depend on the Re and We .

Three liquid breakup modes were found by Farago and Chigier [61]: (1) Rayleigh breakup for $We < 25$, (2) jet disintegration via membrane-type ligaments for $25 < We < 70$, and (3) jet disintegration via fiber-type ligaments for $100 < We < 500$. The Rayleigh breakup regime was further divided into two sub-categories, axisymmetric Rayleigh breakup for $We < 15$, and non-axisymmetric for $15 < We < 25$. Each of the breakup modes had sub-modes of pulsating and super-pulsating. The authors determined that the atomization process was always a pulsating process. The super-pulsation mode existed when the liquid mass flow rate was “low” and the gas flow rate was “very high”.

Woodward [62] made liquid core measurements from a coaxial jet with real time x-ray radiography. The inner tube of the injector had an undisturbed entrance length of 85 inner diameters, sufficiently long to produce a fully-developed turbulent velocity profile at the inner tube exit. The outer-jet fluids were nitrogen (N_2) and helium (He), and the inner-jet fluid was an aqueous solution of potassium iodide ($KI_{(aq)}$) to attenuate the x-rays. The chamber was initially pressurized with the same fluid as that used for the outer-jet from 0.1 to 2.17 MPa, which is still well below the critical pressure of water (H_2O $P_c = 22.06$ MPa). It is important to note that the study of Woodward [62] is the

only study in the open literature, other than this work, to experimentally investigate the core length of shear-coaxial jets at pressures greater than atmospheric (see Table 4.2). The intact core measurements from the x-ray radiography were correlated (Eq. 2.4) using Re and We , similar to that of Eroglu et al. [8], but the additional parameters of density ratio, and a ratio (H) involving the square root of the ratio of heat capacities and the specific gas constant of the fluid of interest to the same quantities evaluated for the nitrogen. At a constant temperature, this parameter (H) is essentially the ratio of sound speeds for the outer flow compared to that of N_2 . Woodward notes that this could imply a Mach number effect for coaxial jet liquid breakup, but states that the real physical significance is not known.

$$\frac{L}{D_1} = 0.0095 \left(\frac{\rho_o}{\rho_i} \right)^{-0.36/H} Re^{0.68} We^{-0.22/H} \quad (2.4)$$

Where,

$$H = \frac{\sqrt{\gamma R}}{\sqrt{\gamma_{N_2} R_{N_2}}},$$

γ is the ratio of heat capacities = C_P/C_V , and

R is the specific gas constant.

Englebert et al. [63] examined shear-coaxial jets with water as the inner-jet liquid and air as the outer-jet gas. The area ratio (outer-to-inner) was about 40, which again is much larger than a typical injector used in rocket engines (SSME injector area ratio is about 2.8). Images of the jet were taken with a high-speed 16 mm camera framing at 12 kHz, and back-lit with a continuous halogen lamp. Breakup length was correlated as a

function of We , kinetic energy ratio (E_R , see Eq. 2.5), and momentum ratio (M_R , see Eq. 2.6). With the velocity of the inner-jet at a constant value of 4 m/s, the breakup lengths were fitted to a function of We , with a similar exponent to that of Woodward [62], but were much shorter in length. The correlations of their data involving E_R and M_R were normalized by the annular gap-width (i.e. $(D_3 - D_2)/2$). The dependence on the M_R to the -0.3 power was observed. Notice that M_R is the momentum ratio and incorporates the area ratio of the injector, and is not to be confused with M , the momentum flux ratio, which does not include the area ratio of the injector.

$$E_R = \frac{\rho_o U_o^3 (D_3^2 - D_2^2)}{\rho_i U_i^3 D_1^2} \quad (2.5)$$

$$M_R = \frac{\rho_o U_o^2 (D_3^2 - D_2^2)}{\rho_i U_i^2 D_1^2} \quad (2.6)$$

Carreau et al. [64] and Porcheron et al. [65] studied coaxial jets with a fiber optic probe to measure what they refer to as the “liquid-presence probability (LPP).” The probe had a sapphire tip, and an infrared light at 850 nm, modulated at 2.5 MHz, passed through it. In principle, because the shape of the probe end, if liquid was present, then the light would pass through of the tip, however, if gas was present at the tip, the light would be internally reflected back through the fiber optics and the signal would be recorded. A double-thresholding technique was used to determine the amount of time the probe was in contact with liquid and gas. The fraction of time the voltage signal was high indicated the gas time, and the fraction of time the signal was low indicated the

amount of time the probe was in contact with liquid. The LPP was computed from these measurements. The experiments were done with LOX and either He, N₂, or Ar, and water – air. The LPP was correlated as a function of axial distance, as well as other parameters. Upon defining the LPP to be 0.5 at the end of the breakup length, a breakup length correlation could be determined. Note that changes in the selection of the LPP value from 0.5 at the breakup length would only result in variations in the constant used in their proposed correlation. The initial correlation (see Table 4.2) presented by Carreau et al. [64] was for LOX with either He, N₂, or Ar, and was of the same form as that by Woodward [62]. Later Porcheron et al. [65] included water-air and LOX-inert-gas experiments and modified their earlier correlation by replacing explicit dependencies on We and Re to those of Ohnesorge number (Z) and M parameters.

2.4 Interaction of a Transverse Acoustic Waves with Jet Flows

The number of reports involving the interaction of transverse-acoustic waves and fluid jets are limited. One of the earliest studies was done by Miesse [66] with single round jets. Two “sound sources” (acoustic drivers) were positioned along a common axis, perpendicular to the flow of the jet, opposing one another. The phase angle between the two drivers was adjusted to be 180° to maximize the “push-pull” effect on the jet, using frequencies of less than 200 Hz. Images showed that the amplitude of the jet deflection in the transverse direction decreased with increase in both the frequency of the driver and pressure drop across the injector (i.e. flow rate). It was also noted that the sound field considerably reduced the length of the solid stream. Maximum dispersion of

the jet was observed at the natural frequency of the jet. The intact length of the jet decreased when excited by the acoustic drivers.

Newman [67] studied laminar single round jets in an externally-imposed acoustic field inside a resonant chamber at a frequency of 880 Hz. The mean chamber pressure varied up to about 0.6 MPa (70 psig). The breakup length of the jet was measured from images both with and without the presence of the acoustic field. The jet was placed at both a pressure node and a velocity node. At low mean chamber pressures (atmospheric pressure) the differences between the two nodal placements of the jet exhibited a small effect on the breakup length. However, at higher chamber pressures the pressure oscillations were more effective at decreasing the breakup length. Overall, the effect of the acoustic field diminished with increasing chamber pressure.

Buffum and Williams [68] investigated the interaction of externally imposed transverse acoustic waves at frequencies ranging from 100 to 500 Hz on a turbulent liquid jet at atmospheric pressure. The primary physical quantity measured was the oscillatory displacement of the liquid jet as it passed through an acoustic standing wave field in a resonant tube. Resonance effect at different frequencies was achieved through variations of the tube length in this study. It was found that the peak-to-peak jet deflection distance decreased when jet diameter or velocity was increased due to increased fluid mass in the acoustic field. The jet deflection was unobservable below 130 dB and immeasurable below 140 dB. At about 161 dB the acoustic waves induced shearing atomization of the jet, which produced large scale periodic structures. These periodic structures were proposed to act as reactant sources in a combustion case to sustain or amplify combustion instabilities. The drag coefficients for turbulent liquid jets in transverse acoustic field

were about an order of magnitude larger than that of a solid cylinder having a diameter the same as that of the injector orifice. This caused enhanced jet deflections in the acoustic field and may be one source for sustaining the instability in liquid rocket engines.

Heidmann and Groeneweg [69] produced images of unstable liquid oxygen (LOX) / hydrogen (H_2) combustion. The LOX was injected in the form of a round jet from a multi-element ring surrounding the perimeter of disk-shaped combustion chamber. In a diffuse manner, H_2 flowed from slots both above and below the LOX jets. The propellants were injected inward in the radial direction from the perimeter of the combustor, and the burned gases turned 90 degrees to flow through the nozzle located on the bottom plate. Time varying jet length was observed to be coupled with the acoustic field which raised suspicion that unstable combustion was directly related to the dynamic behavior of the liquid jet.

More recently, Rhys [70] considered the interaction of acoustic waves with flat liquid (water) sheets and swirl-coaxial jets (water and air). The amplitude of the surface waves on the flat liquid sheet decreased in magnitude as the frequency was increased over the range of 600 to 1700 Hz. The author indicated that the preferred frequency of the surface waves on the liquid sheet of the swirl-coaxial spray increased as We increased up to a values of about 10^4 , where the atomization character of the driven sheet changed. When We is greater than about 10^4 the liquid sheet disintegration of the swirl-coaxial spray made a transition from surface-wave breakup to aerodynamic stripping mode. Additionally, Rhys stated that for swirl-coaxial injectors high velocity ratios eliminate

fundamental atomization frequencies. Therefore, he postulated that the surface wave combustion instability pathway could be eliminated by operating at high velocity ratio.

2.5 Velocity Measurements from High-Speed Shadowgraph Images

An early report of velocity measurements from shadowgraph images was done by Newman and Brzustowski [23] in the experimental work reviewed in section 2.2 above. Measurements of the axial velocity of a single round jet were reported. However, no details were presented on how the measurements were made. One may only surmise that they visually tracked fluid structures on the core of the jet to estimate velocities.

Ota et al. [71] and Okamoto et al. [72] investigated supercritical carbon dioxide flow over a heated wall. The flow was driven by a pump vertically upward, but the fluid near the heated wall experienced a buoyant acceleration. Shadowgraph images were taken with a high-speed charge coupled device (CCD) camera framing at 250 Hz. The light source was a pulsed infrared laser with a wavelength 808 nm. The laser pulses were frame straddled, that is, the first pulse occurred near the end of one frame exposure time and the next pulse near the start of the next frame, and so on. Therefore, the effective time difference between frames was reduced to 0.48 ms, rather than 4 ms. A spatial cross-correlation was then computed for two consecutive images, using a 32 by 32 pixel interrogation source window. In the images, there were pixels that their intensities did not vary between images, and they were considered as noise points and not included in the spatial cross-correlation calculations. The intensity variations, caused by the density gradients in the shadowgraph served as fluid elements (or particles) for the spatial cross-

correlation. The authors refer to this process of velocity measurement using unseeded shadowgraphs as a “new technique”. Instantaneous two-dimensional velocity fields were constructed indicating a higher velocity near the heated wall. Also, the transient velocity signal at one point in space revealed the unsteady nature of the flow, which corresponded to the frequency of the diaphragm pump used to drive the flow. The uncertainties of the measurement are not specifically addressed in these reports and it is stated that error elimination should be part of future work.

Chapter 3

Experimental Facility, Apparatus, and Technique

The experiments presented in this work were performed in test cell EC-4 at the Air Force Research Laboratory (AFRL) at Edwards Air Force Base, CA. Portions of the experimental apparatus preexisted prior to the work described in this thesis, but the facility required significant upgrades and modifications, which will be outlined in the following sections of this chapter.

A concise operational description of the facility shown in Fig. 3.1 is given here. Detailed descriptions of key components appear in the subsequent sections. Also, the detailed standard operating procedure developed for this work is presented in Appendix A.

The experimental apparatus and system components were designed to achieve a cold flow injection of cryogenic liquid (when subcritical) or liquid-like (when supercritical) nitrogen through the inner tube of a shear-coaxial type injector with cold nitrogen gas passing through the annular region of this injector. The fluids from the injector flow into a main chamber pressurized with gaseous (or gas-like, if supercritical) nitrogen. All flows entering the chamber including those from the injector are supplied by the high pressure nitrogen line to the facility. The flow rates are monitored and controlled while still in gaseous phase because of the difficulties associated with controlling and measuring high-pressure cryogenic flows. The high-pressure gaseous nitrogen is liquefied by passing the gas through heat exchangers, chilled with low-

pressure liquid nitrogen. During the “chill down” procedure, the temperature of the outer-jet is monitored by a thermocouple positioned near the exit-plane of the injector in the outer-jet fluid. Adjustments to the outer-jet temperature are made by changing the liquid nitrogen flow rate to a secondary heat exchanger. Once a steady-state operating condition within the chamber has been achieved, radial temperature profiles near the injector exit-plane area were measured using a very fine (bead diameter 0.10 mm) exposed-bead thermocouple. Upon completion of these temperature measurements, the thermocouple was traversed out of the jet to a far-field position, and images of the jet were captured using either a low-speed camera with a framing rate of 10 Hz, or a high-speed camera with a framing rate of 18 kHz. Most of the images and movies were taken with a back-lit illumination arrangement producing shadowgraphs, but in some instances it was necessary to illuminate the jet from the front. An acoustic driver was driven with a sinusoidal signal to excite the first resonance mode of the inner-chamber, which is approximately 3 kHz, depending on the chamber temperature and pressure. The inner-chamber is embedded inside the main chamber, and is used to reduce the cross-sectional area of the main chamber to keep the amplitude of the acoustic waves high in the vicinity of the jet. Images of the excited jet were then acquired. Subsequently, the acoustic driver frequency was then set to the second resonance mode of the inner-chamber, at approximately 5 kHz, and then the imaging process was repeated. In other test runs, several variations of this imaging process were executed in order to gain additional information about startup transients or modal behavior of the jet.

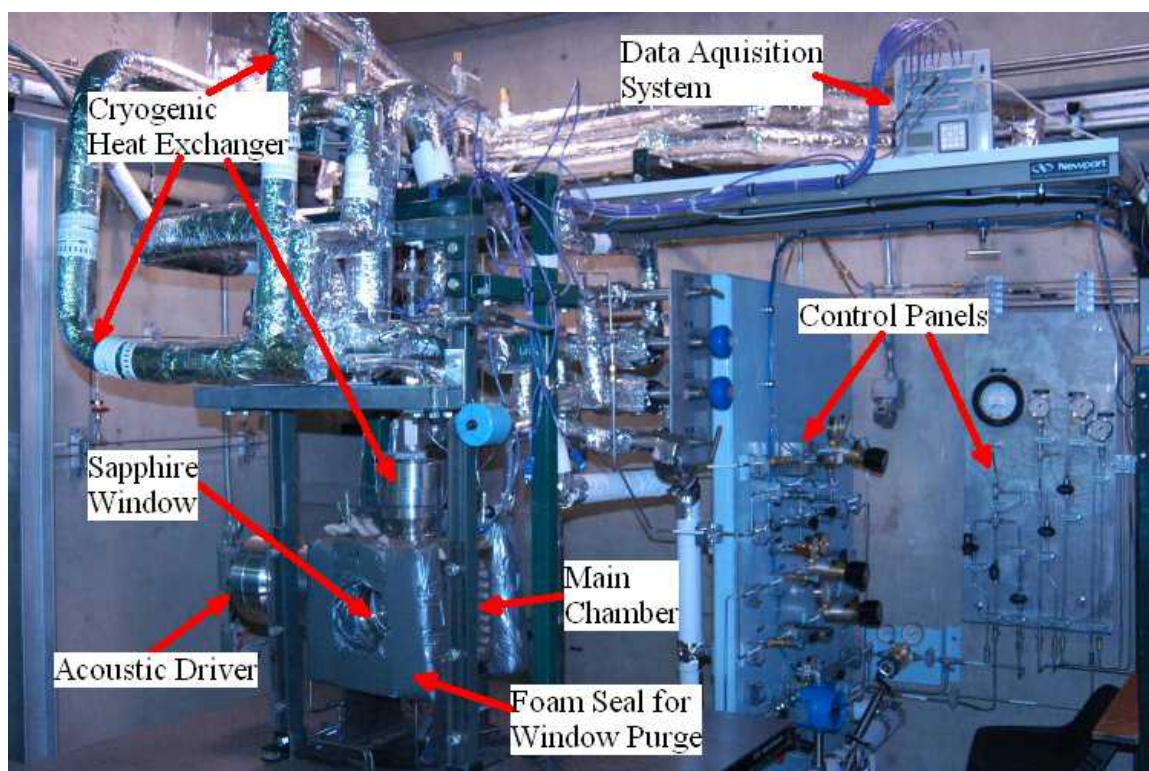


Figure 3.1: Photograph of the EC-4 Supercritical Facility.

3.1 High Pressure Chamber

The main chamber (Figs. 3.1 and 3.2) was originally designed by General Physics Corp. for the purpose of studying supercritical droplets at AFRL and was completed in 1995. The main chamber was designed in accordance with the American Society of Mechanical Engineers (ASME) Boiler and Pressure Vessel Code capable of withstanding 13.8 MPa (2000 psig) over a temperature range of 76 K to 473 K (-323°F to 392°F). The main chamber is made of 304 stainless steel. The chamber has four ports for providing optical access to the injector region (see Fig. 3.2). The two larger circular openings have round sapphire (Al_2O_3) windows, and the smaller oblong shaped window openings can be

used to house fused silica (quartz) windows, the acoustic driver (discussed below), the thermocouple traversing stage (discussed below), or the piezoelectric pressure transducer traversing stage (discussed below). The opening at the top of the chamber is used to mount the cooling tower used to cool and/or liquefy (when the pressure is subcritical) the gaseous nitrogen (GN_2) into liquid nitrogen (LN_2) that is then injected into the chamber through the shear-coaxial injector. The chamber is equipped with multiple ports for flow connections and instrumentation such as thermocouples and pressure transducers.

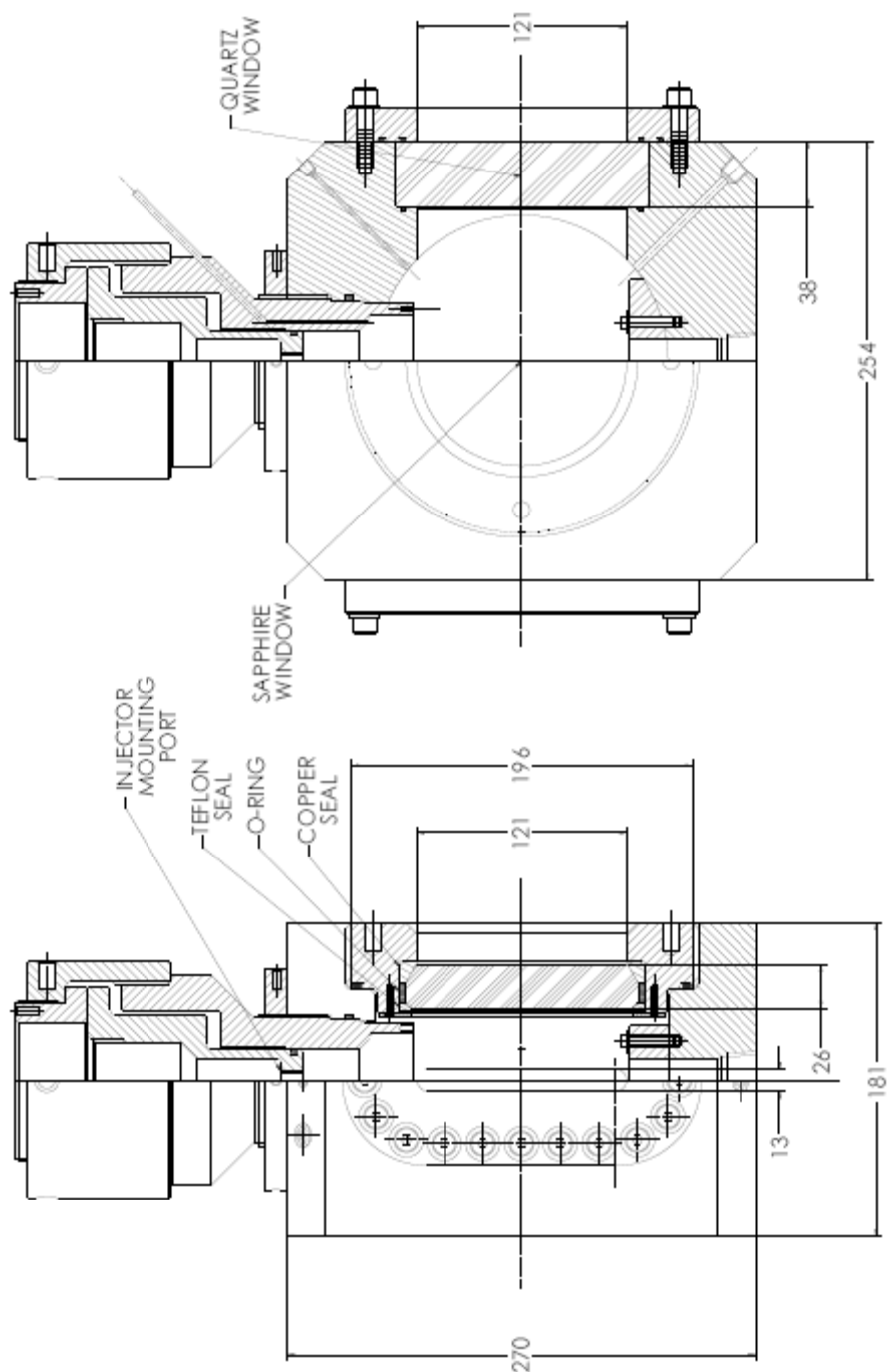


Figure 3.2: Drawing of Main Chamber. All dimensions are in mm and approximate.

The sapphire windows are contained within a specially-designed stainless steel window retainer. With approximately 121 mm diameter optical access, the retainer is fitted with acme threads on the outer diameter, and screws into the chamber resulting in a face-sealed design against the main chamber with an o-ring. The sapphire windows are beveled at the edge that are used in conjunction with the seals. The sealing of the window is assured using a combination of three types of seals, see Fig. 3.2. The edge facing inside the main chamber is sealed within the retainer using a Teflon seal ring that acts as a primary seal. To provide an additional seal, the outer edge is sealed using a copper gasket inside the window retainer. Between the two beveled edges there is an o-ring with a backup ring on both side of it to enhance the sealing action. The window retainer entirely encapsulates the large and expensive sapphire windows to provide protection from physical damage during removal and assembly. The window retainer is also sized in a manner to prevent stress on the window from thermal gradients causing changes in the critical dimensions.

3.2 Fluid Systems

It was necessary to make several upgrades to the plumbing system of the facility prior to the start of this work in order to produce the desired flow rates and temperature conditions. A process flow diagram (PFD) of the modified plumbing system is shown in Fig. 3.3. Magnified versions are presented in Appendix A. The fluid handling components in Fig. 3.3 are systematically labeled with a two or three letter designation followed by a dash and a four-digit number. The letters indicate the type of fluid

component, such as, HV for hand valve and PSV for pressure safety valve. A detailed list of the letter designation for the flow controls is in Appendix A. The first digit of the number indicates the fluid in the line, for example, 0 designates nitrogen and 1 designates helium. Helium was not used in this work, but was included in the system for ease of upgrades in the future. The second digit, ranging from 0 – 9 listed in Table 3.1, indicates the fluid subsystem based upon its function. The last two digits indicate the component number.

Gaseous nitrogen (GN_2) is introduced into the facility from a supply line available at AFRL and regulated to a nominal high pressure of 17 MPa (2500 psi) and a nominal low pressure of 0.85 MPa (125 psi). The high-pressure GN_2 is split to feed the subsystems 1 – 4. The flows sent to the injector are first thermally conditioned using heat exchangers cooled with low-pressure liquid nitrogen (LN_2). It is more convenient to control flow rates while the nitrogen is in the gaseous phase than to liquefy and then meter the high-pressure LN_2 . Four heat exchangers (designated by the letters HE) are used in the system (see Fig. 3.3) to fully control the temperatures of the flows to the injector. The heat exchangers are of counter-flow design, with the exception of HE-0107, which has the ability to operate either in counter-flow or co-flow modes. The purpose for retaining the co-flow operating mode is to provide the ability to repeat tests that were conducted prior to all the upgrades made in this system. The temperature of the annular flow is controlled by adjusting the flow rate of the low-pressure LN_2 into the heat exchangers. However, due to heat transfer within the injector passages, the exit temperature of the flow issuing from the inner tube depends upon the mass flow rates of the inner and outer flows, the temperature of the outer flow at the inlet to the injector, and

the chamber pressure. It was discovered that flow from the external LN₂ tank produced fewer and lower oscillations in temperature than the flow from the Dewar. Therefore, for all of the data presented in this work, the chilling operation used only the external LN₂ tank as the flow source for the heat exchangers.

The chamber pressure can be adjusted to within ± 0.14 bar (2 psi), using a combination of three valves controlling the vent system. The three “hand valves”, see Fig. 3.3, HV-0604, HV-0605, and HV-0606 are a Hoke 1/4” ball valve with a $C_V = 0.8$, a Parker 1/4” needle valve with a C_V ranging from 0.0 – 0.43, and a Swagelok 1/4” needle valve with a C_V ranging from 0.0 – 0.04, respectively. This large range in C_V values for the three valves allows accurate control of the venting of the chamber fluid, thus controlling the chamber pressure within a tight tolerance (± 0.14 bar).

Even with the dry climate in the desert where experimental facility is located, significant frost build up on the apparatus occurs due to freezing of moisture in the laboratory air. Therefore, in order to eliminate obscuring of visual access inside the chamber it was necessary to purge the windows with dry nitrogen to eliminate frost formation. A low pressure, 1.12 bar (1.5 psig), dry nitrogen purge was introduced through the void created by a 10 cm (4”) foam seal between the main chamber and an acrylic shield as shown in Fig. 3.1.

Table 3.1: Fluid Subsystem Number Designation.

Subsystem Number	Function
0	High Pressure Facility GN ₂
1	N ₂ to Feed Center Post of Injector
2	N ₂ to Feed Annular Flow of Injector
3	N ₂ to Pressurize the Chamber
4	N ₂ for Pressurization of LN ₂ Systems
5	Low Pressure GN ₂ for Window Purge
6	GN ₂ Vent
7	LN ₂ from Dewar
8	LN ₂ from External Tank
9	Future He System

3.3 Shear-Coaxial Injector

The shear-coaxial injector used in this study (Fig. 3.4) was based on the well-characterized design of the single-jet injector used in this facility previously described by Chehroudi and co-workers [24-30]. The cryogenic nitrogen feeding the inner tube, producing the inner-jet, flows into the cooling tower in the injector mounting port as indicated in Fig. 3.2. The cold, but still gas or gas-like, nitrogen flow generating the annular outer-jet is introduced into two ports in a manifold ring (see Fig. 3.4). The fluid in the manifold ring is then split into four tubes flowing into the annular passage through four holes located 28 mm (1.1") upstream of the injector exit area. Teflon[®] (PTFE) was used as an insulating material for the injector to minimize heat transfer from the warm chamber to the cold injector assembly.

The inner-tube (center-post) was made from a stainless steel tube with an inside diameter (D_I) of 0.51 mm (0.020") and an outside diameter (D_2) of 1.59 mm (0.063") with a length of 50.8 mm (2.00"). The resulting length-to-inside-diameter ratio (L_{post}/D_I) is 100, which is sufficiently long enough to ensure fully-developed turbulent pipe flow conditions at the exit. The outer stainless steel tube creating the annular passage had an inside diameter (D_3) of 2.42 mm (0.095") and an outside diameter (D_4) of 3.18 mm (0.125"). The resulting mean gap width of the annular passage, the hydraulic diameter, is 0.415 mm (0.016"), measured from an image of the injector. The entrance length to hydraulic diameter ratio is 67 for the annular passage. The injector has a small bias of 8% of the mean gap width. The post (inner tube) is recessed by 0.5 D_I , 0.25 mm (0.010").

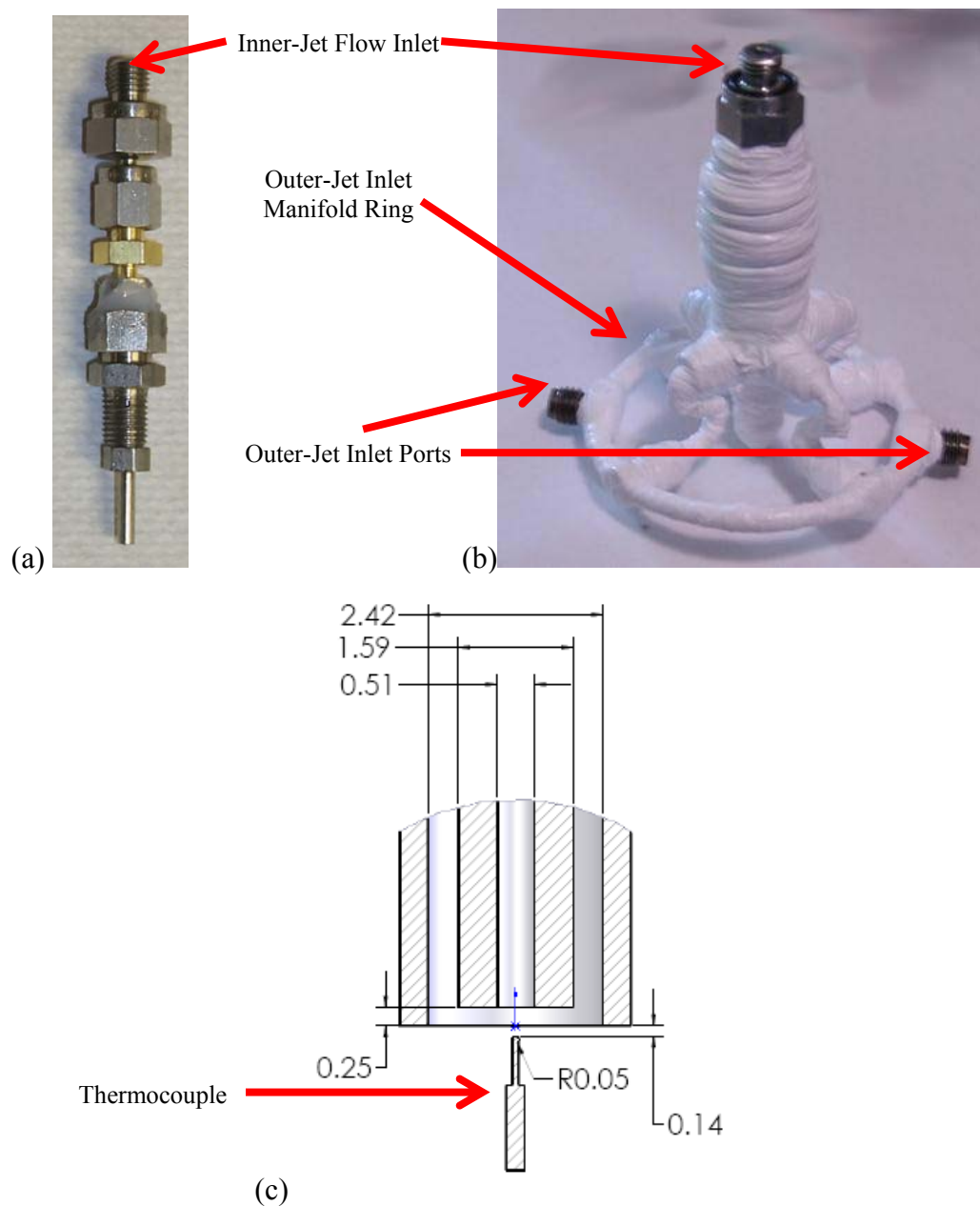


Figure 3.4: Photograph of shear-coaxial injector (a) without gas manifold and insulation, (b) with gas manifold and PTFE insulation. Scale cross-section drawing (c) of injector exit-plane area also indicates relative size and position of thermocouple used for temperature measurement. Dimensions in mm.

3.4 Acoustic Driver

The acoustic driver, Piezo-Siren (Fig. 3.5), used in this experiment was developed especially for this apparatus as part of a Small Business Innovative Research (SBIR) contract with the U.S. Air Force and Hersh Acoustical Engineering, Inc. A unique quality of this Piezo-Siren is the ability to produce high-amplitude acoustic waves in a high-pressure static environment. The actuator for the acoustic driver is a piezo-ceramic crystal, contained within an aluminum housing with an aluminum cone on one side to produce the acoustic waves.

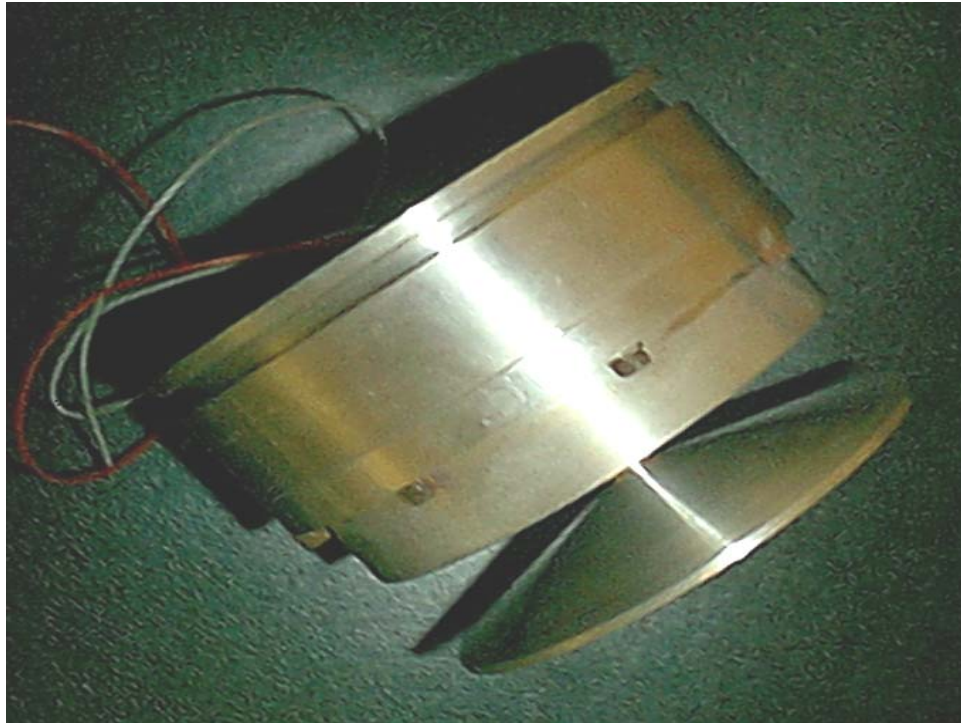


Figure 3.5: Piezo-Siren, high-amplitude high pressure acoustic driver.

The Piezo-Siren along with the wave guide (discussed below) that directs the acoustic waves to the inner-chamber are housed inside a high-pressure adaptor, externally connected to the main chamber (Fig. 3.6). The Piezo-Siren housing and the adaptor as a unit is bolted to the main chamber (see Fig. 3.1) at the location of the oblong window opening (see Fig. 3.2) and is sealed to the main chamber with o-ring face seals.

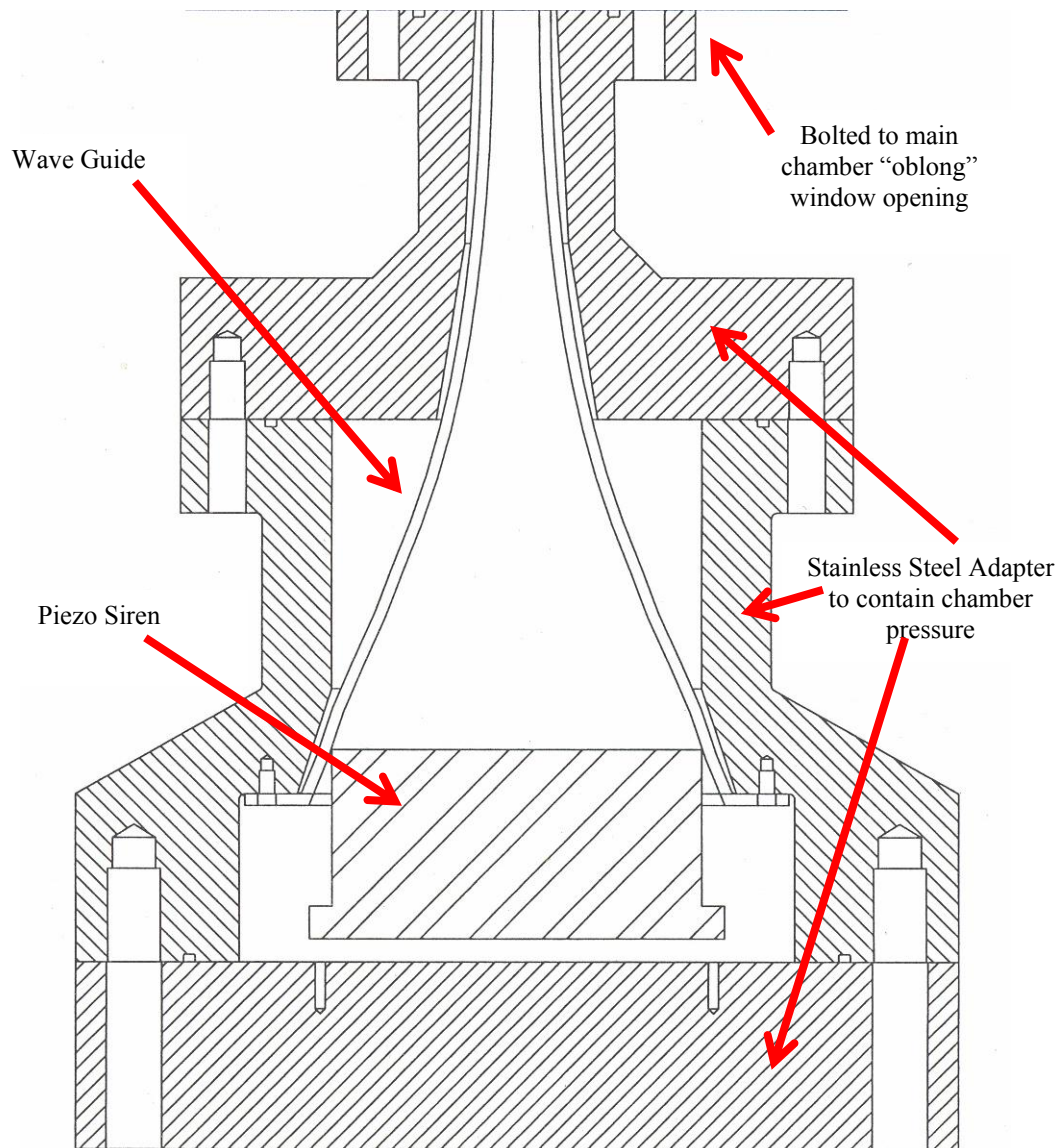


Figure 3.6: Plan view cross-section drawing of acoustic driver housing, wave guide, and assembly for attachment to main chamber.

In order to maintain the amplitude of the acoustic waves at a high level near the jet, a smaller inner-chamber, see Fig. 3.7, is housed within the main high-pressure chamber. The inner-chamber support structure is made of stainless steel, and has acrylic windows for jet visualizations. The width of the rectangular cross-section of the inner-chamber is 13 mm (0.5"). Because of the rectangular cross-section of the inner-chamber and the circular cross-section of the acoustic driver, a transition wave guide shown in Fig. 3.8 was necessary to minimize losses from the acoustic driver. The wave guide is made of copper and has a catenary contour which was designed also by Hersh Acoustical Engineering, Inc. The diaphragm of the acoustic driver has a diameter larger than the height of the inner-chamber. The rectangular cross-section of the wave guide is oriented with the longest side being parallel to the axis of the jet.

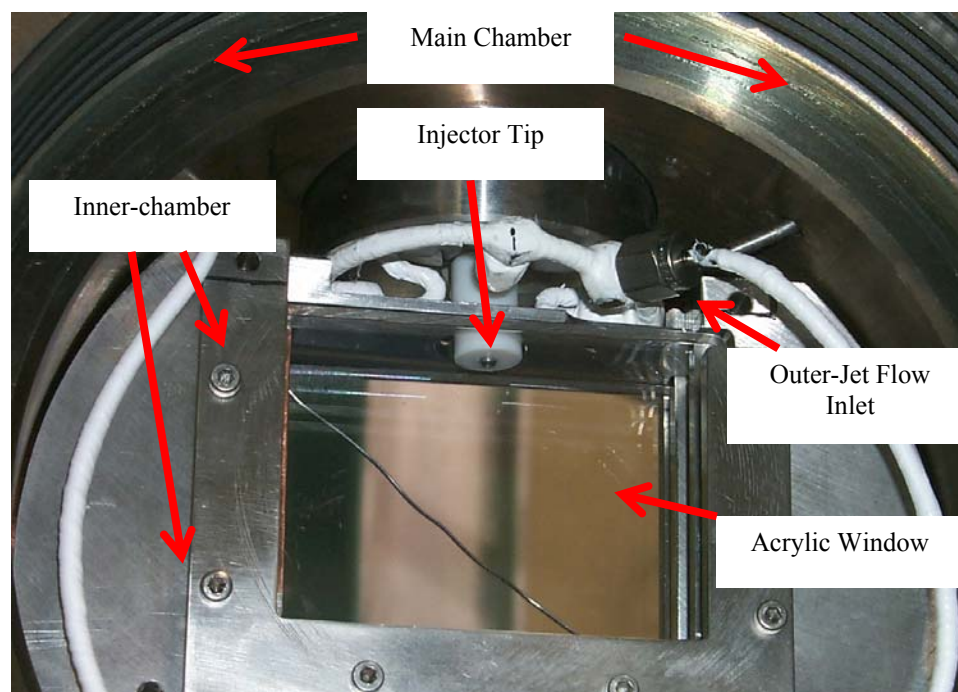


Figure 3.7: Photograph of Inner-chamber.



Figure 3.8: Acoustic Wave Guide

3.5 Instrumentation

The data acquisition system used for the collection of temperature, chamber pressure, and mass flow rate measurements was a Campbell Scientific CR5000 data logger. The data logger has 20 differential analog input channels, capable of acquiring data at an aggregate rate of 1000 Hz (50 Hz per channel) at 16 bits. The input channels recorded the temperature, chamber pressure, and various mass flow rate measurements.

The chamber pressure was measured by a Stellar ST 1500 pressure transducer, with a full scale range of 70 bar (1000 psi). The transducer used in the system was ordered with special manufacturer's limits of error of $\pm 0.05\%$ of full scale (FS), which

is approximately ± 3.5 kPa (0.5 psi). However, the transducer was calibrated with a precision pressure measurement and calibration system, Ruska Model 7310, which has an accuracy of $\pm 0.01\%$ of full scale (1.4 kPa, 0.2 psi). The calibration outcome is a plot of transducer voltage versus the reference set pressure. A linear fit to the data was then used to relate voltage to the reference pressure. Figure 3.9 shows the difference between the measured pressure (using the linear fit) and the set pressure on the Ruska precision calibrator. The calibration procedure was to first increase the pressure from the atmospheric value to 90% of the full scale. Next, the pressure was decreased from 90% FS to atmospheric, finally increasing the pressure again to 90% of the FS range a second time. The accuracy over the range of the transducer is actually about double of that reported by the manufacture (i.e., $\pm 0.1\%$ FS), which is approximately ± 7 kPa (1 psi). This was determined to be sufficient accuracy for this work, despite being twice the value reported by the manufacturer.

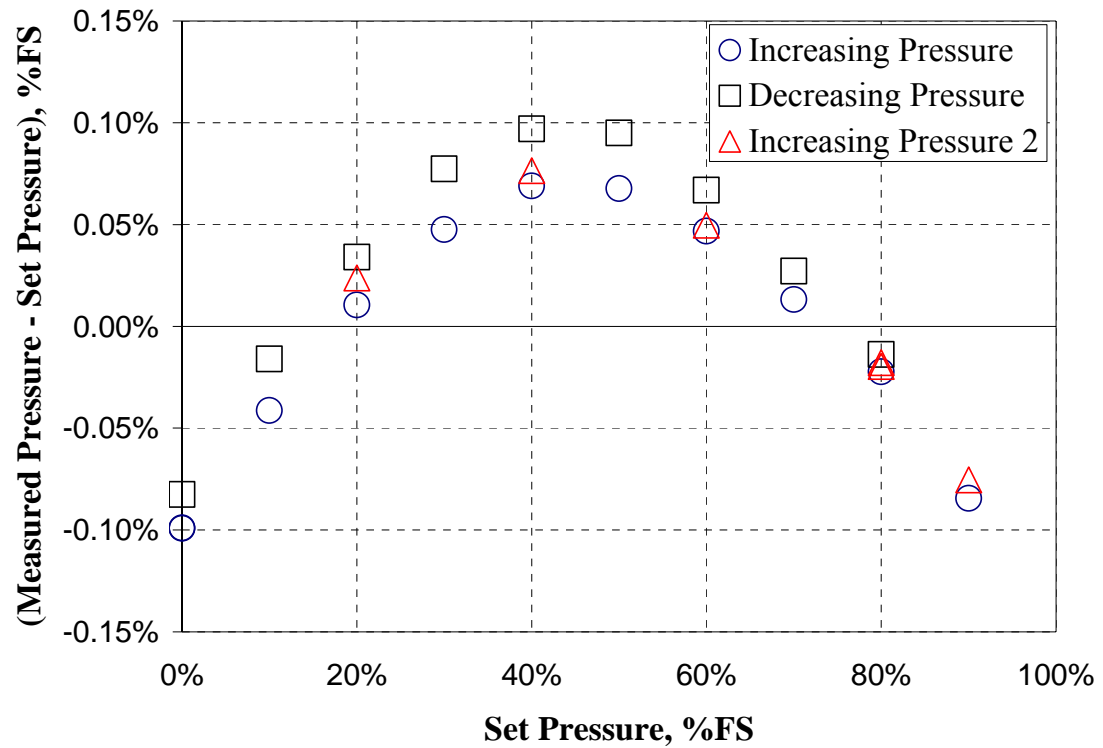


Figure 3.9: Calibration of the chamber pressure transducer. Difference between the measured pressure (using the linear fit) and the set pressure of the precision calibration device. The circle symbols indicate the increasing pressure, followed by decreasing the pressure (square symbols), finally increasing the pressure a second time (triangle symbols).

The acoustic pressure in the inner-chamber was only measured under warm chamber conditions without any fluids flowing through the injector. The pressure transducer used to measure the acoustic pressure was a Kistler model 601B1, connected to a dual mode charge amplifier Kistler Type 5010. The data acquisition system used to collect data from the Kistler transducer was a Lab Master DMA from Scientific Solutions with a maximum aggregate data rate of 100 kHz (with a 12bit A/D converter). The Kistler transducer was mounted on a traversing stage, a drawing of which is shown in Fig. 3.10. The traversing stage mounts into one of the openings for the oblong windows

of the main chamber (Fig. 3.2) using a stainless steel window blank (instead of the window) with a 13 mm diameter hole bored through to permit the traversing rod to pass into the pressure chamber. The position of the transducer is determined using a micrometer handle, Model BM32.80 from Newport Corp. The precision of the micrometer is 0.01 mm.

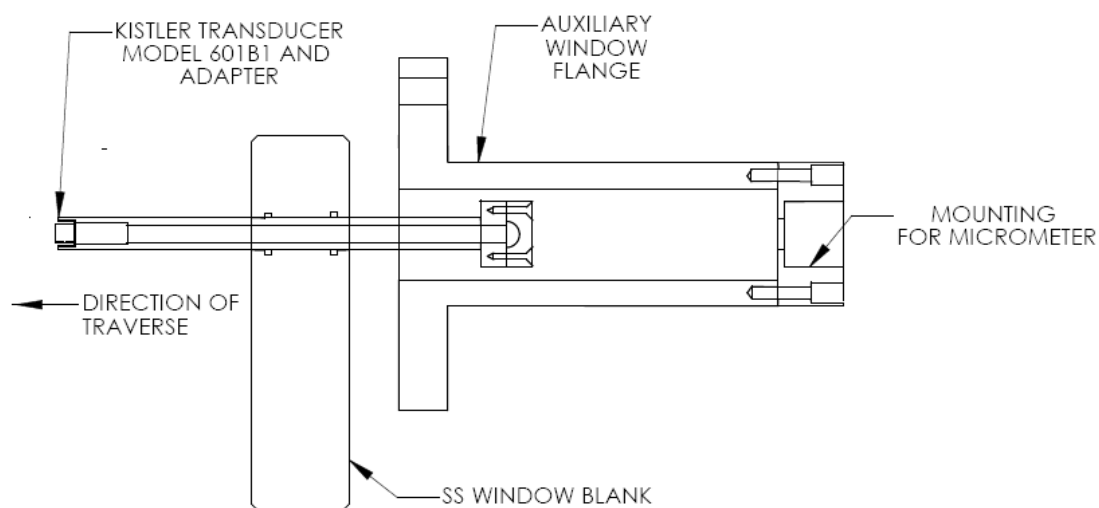


Figure 3.10: Traversing stage for Kistler transducer

Temperature measurements in the entire facility are made with Type E (chromel – constantan) thermocouples (TC). Type E thermocouples have the largest Seebeck coefficient (dV/dT), which permits the greatest sensitivity amongst thermocouples. Accurate cryogenic temperature measurement with thermocouples is difficult. The only thermocouple type with ANSI limits of error at cryogenic temperatures is Type T (copper – constantan), but the Seebeck coefficient is about 30% smaller than a Type E [73]. Very accurate measurements were not necessary for most of the temperature measurements in this work. However, at the injector exit-plane high accuracy is required due to the need to

compute density (ρ) from the temperature and chamber pressure measurements. These measurements are then used for the calculations of the injector exit velocities. At high chamber pressures, especially near the critical pressure of the fluid, small uncertainties in temperature can produce large uncertainties in density.

Resistance temperature detectors (RTD) are usually the thermometer of choice at cryogenic temperatures. However, due to the small probe sizes required to make high-resolution spatially-resolved measurements near the injector exit-plane area, an exposed-junction thermocouple with a bead size of 0.1 mm (0.004") in diameter was selected. Upon comparison between values obtained from the thermocouple and a precision RTD probe in saturated liquid nitrogen, it was noted that a difference of about 5 K exists between the thermocouple and the RTD data. Over the conditions of interest, errors of 5 K could produce errors in density as great as 600 kg/m³. Clearly, the high errors in density calculations from the associated uncertainties in temperature at the 5 K level are large and need to be reduced if meaningful results are to be obtained. Therefore, it was necessary to individually calibrate each thermocouple, along with its the extension wire and the data acquisition system as a system against a precision Pt-RTD.

The precision RTD probe was from the Hart Scientific company, model number 5622-05, precision calibrated with an accuracy of ± 0.04 K. Several constant-temperature baths were selected to perform the calibration. The constant temperature baths used were, saturated LN₂, LN₂/isopentane, LN₂/methylcyclopentane, ice/water, and room temperature air. At each temperature, 500 points were collected over two minutes and averaged. The resulting calibration curve in Fig. 3.11 shows a high degree of linearity in the curve fit as indicated by the correlation coefficient of nearly one. The maximum

deviation from the data to the curve fit was 0.7 K. A reasonably conservative estimate of the uncertainty using the maximum deviation and Student's t-distribution, resulted in the associated uncertainty of the thermocouple measurement of ± 0.8 K.

The calibrated thermocouple was then traversed through the jet near the exit-plane using a modified form of traversing stage described earlier for the acoustic pressure measurements (Fig. 3.10). The relative size and axial position of the thermocouple used for exit-plane measurements is shown in Fig. 3.4(c).

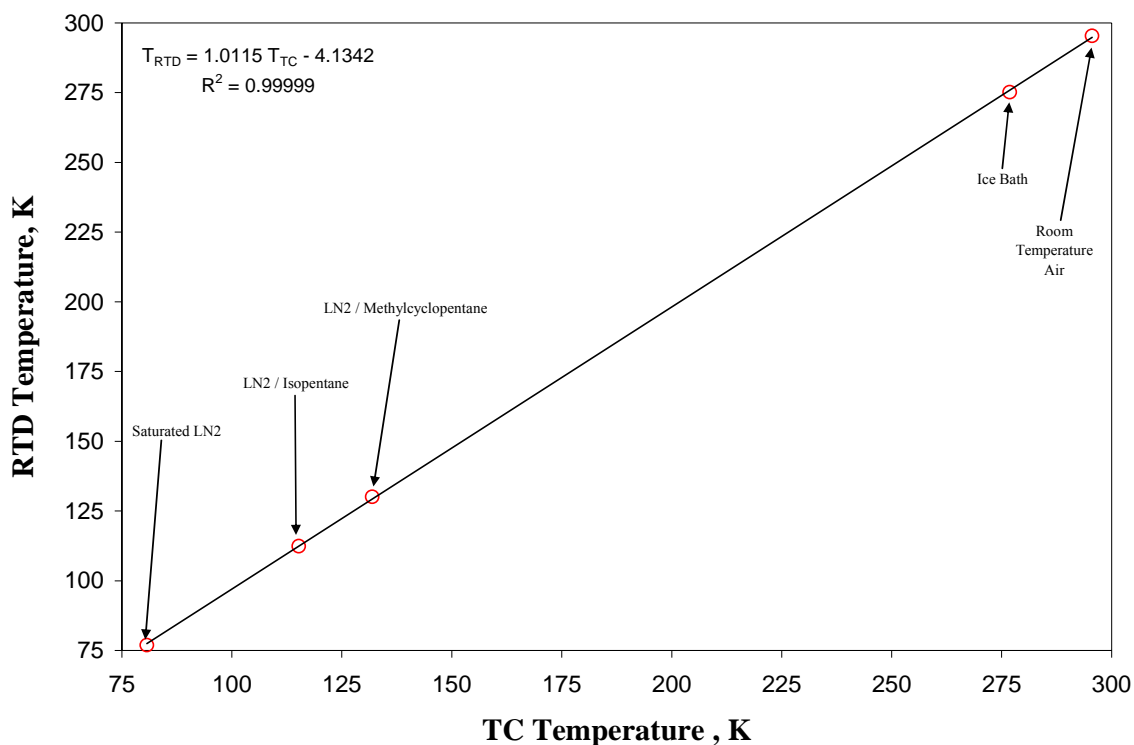


Figure 3.11: Thermocouple Calibration Curve

Mass flow rates of the gaseous streams were measured with Porter Instrument Company, Inc mass flow meters. The flow to the inner-jet was measured with a Type 122 mass flow meter calibrated for nitrogen, with a range of 0 to 50 standard liters per

minute (SLPM) (967 mg/s). The mass flow meter used to measure the flow rate of the outer-jet was a Type 123 with 0 to 200 SLPM (3868 mg/s) range, which was used for all flows less than 200 SLPM or a Type 123 with a range of 0 to 500 SLPM (9670 mg/s) for high values. The factory calibrated accuracy for all mass flow meters was $\pm 1\%$ of FS, this accuracy was doubled for the uncertainty calculations.

3.6 Imaging Set-up

Most of the information about the behavior of the jet in this work comes from the flow visualizations. The jets were imaged using a back-lit arrangement with various lenses on digital cameras. One of the cameras used to capture images was a PixelFly HiRes CCD camera made by the Cooke Corporation. The resolution of the camera is 1360 by 1024 pixels with a 12 bit (A/D) dynamic range. The PixelFly was fitted with a Sigma macro zoom 28 – 200 mm lens and a c-mount-to-f-mount adapter. The framing rate of the camera was 10 Hz. The shutter speed was set at 30 μ s. A digital delay pulse generator was used to synchronize the camera with the strobe for backlighting the jets. The digital delay pulse generator was a Stanford Research Systems, Inc. model DG535. The strobe was a General Radio Stroboslave Type 1539-A, with approximately a 0.6 μ s flash time. A light diffuser was placed in between the strobe and the chamber which provided better quality images. Since the amount of the stray light from the room picked up by the camera was small, the images were primarily defined by the strobe flash.

High-speed framing cameras used in this work was a Phantom version 5.1 CMOS high-speed framing digital camera from Vision Research, Inc. with a maximum framing

rate of 95 kHz. However, the highest framing rate used here was 18.0 kHz, which provided the best trade-off between resolution (128 by 256) and framing rate. The Phantom ver. 5.1 has a dynamic range of 10 bits. Another high-speed camera used was a Phantom version 7.1 CMOS camera. The Phantom ver. 7.1 has a 12 bit dynamic range, and is capable of framing at even faster rates than the Phantom 5.1. The lens for the high-speed cameras were a 105-mm Micro Nikkor f/2.8, and a 200-mm macro Micro Nikkor f/4. Various extension tubes were also used to optimize the field of view. The high-speed images were illuminated with one of two continuous light sources available for these studies. One was a Cuda Product Corp. continuous fiber optic light source model I-150 using a 150 W Quartz halogen lamp. The other source was a 200 to 500 W mercury –xenon (Hg-Xe) arc-lamp from Oriel Instrument Corp. model number 66905. The arc-lamp was fitted with the Asperab[®] condenser lens to collimate the light. The shutter speed of Phantom V5.1 was set at 2 μ s, and thus the images were defined by this speed because of the continuous light source used for back illumination. The Phantom V7.1 had a 1 μ s shutter speed option.

For one particular set of tests, the two Phantom cameras were used synchronously and arranged as shown in Fig. 3.12. Synchronization of multiple Phantom cameras is accomplished by connecting the two via a communication cable and choosing one to be the master clock. Because of the available windows, it was necessary to have one of the cameras (V.5) front-lit rather than in a shadowgraph-type configuration.

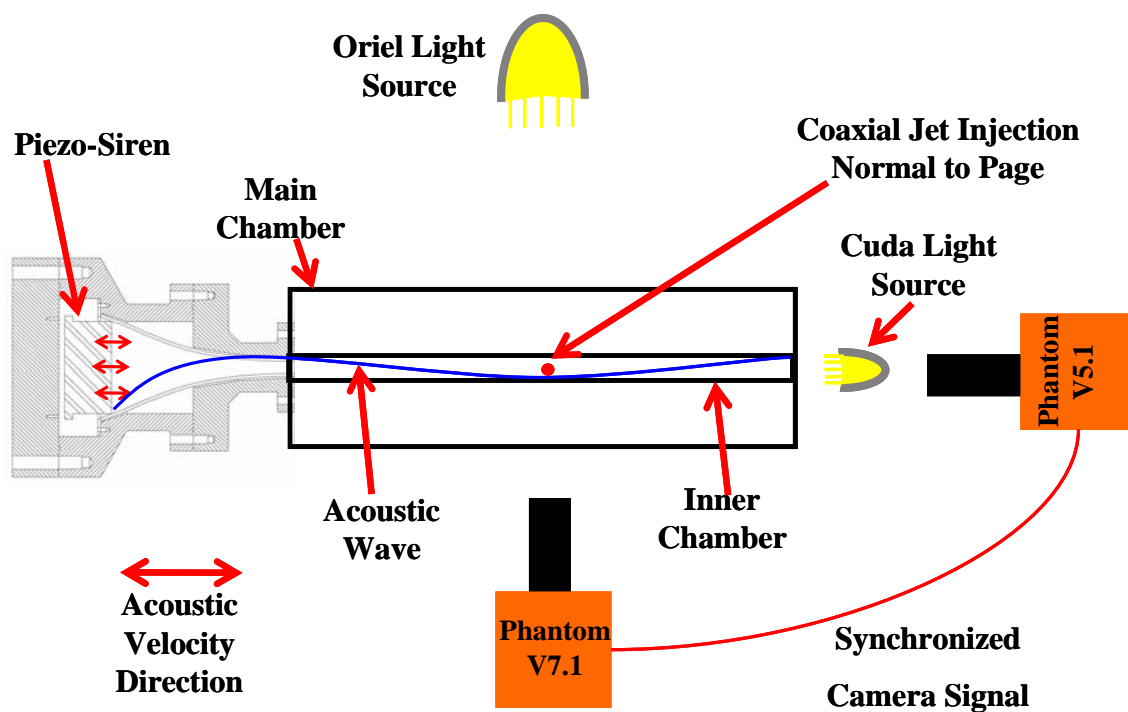


Figure 3.12: Optical layout for the two Phantom camera arrangements.

Chapter 4

Results and Discussion

For a given injector design, there are several major operating parameters one can vary such as the outer-jet exit temperature, outer-to-inner jet velocity ratio, and chamber pressure. Ideally, one would like to change only one of these parameters, keeping the others constant. However, in practice, this is an exceedingly difficult task. On this basis, the experimental setup was designed in such a way as to facilitate near-independent variation of these parameters. For example, changes in the outer-jet exit temperature alone affect the fluid density and therefore velocity ratio at a given fixed flow rate. Hence, to maintain a near-constant velocity ratio, the outer-jet flow rate is adjusted accordingly when its temperature is changed. The experimental matrix was organized to enable comparisons between the results at different outer-to-inner jet velocity (and momentum) ratios. Thermodynamic conditions of the jets at the exit of the injector, calculated from temperature and pressure measurements, are shown in Fig. 4.1. The vertical bars represent the uncertainty of the density values, the details of which are discussed below. The number near each data point in Fig. 4.1 corresponds to the case number listed in Table 4.1. In order to simulate and understand the effect of temperature ramping as performed in a stability rating of a liquid rocket engine, two nominal outer-jet temperatures (around 135–140 K (low) and around 185–200 K (high)) were selected, and then the mass flow rate of the outer-jet was varied to obtain a desired outer-to-inner jet velocity ratio. Some minor adjustments on the inner-jet were also required. References

to these cases in the text are made as “low” and “high” outer-jet temperatures and should be clear in the context of the discussion. The flow issuing from the center-post of the injector is referred to as the inner-jet, and that issuing from the annular coaxial region of the injector is the outer-jet. The shear-coaxial jet was excited at the first two resonance modes of the inner-chamber, which are listed in Table 4.1. The resonant modes vary slightly in frequency because of changes in the chamber temperature and pressure, ultimately affecting the speed of sound in the chamber fluid. The outer-jet temperature reported in Table 4.1 computed from by integrating the temperature profile over the region of space defining the outer-jet. The inner-jet temperature reported in Table 4.1 was taken as the centerline temperature.

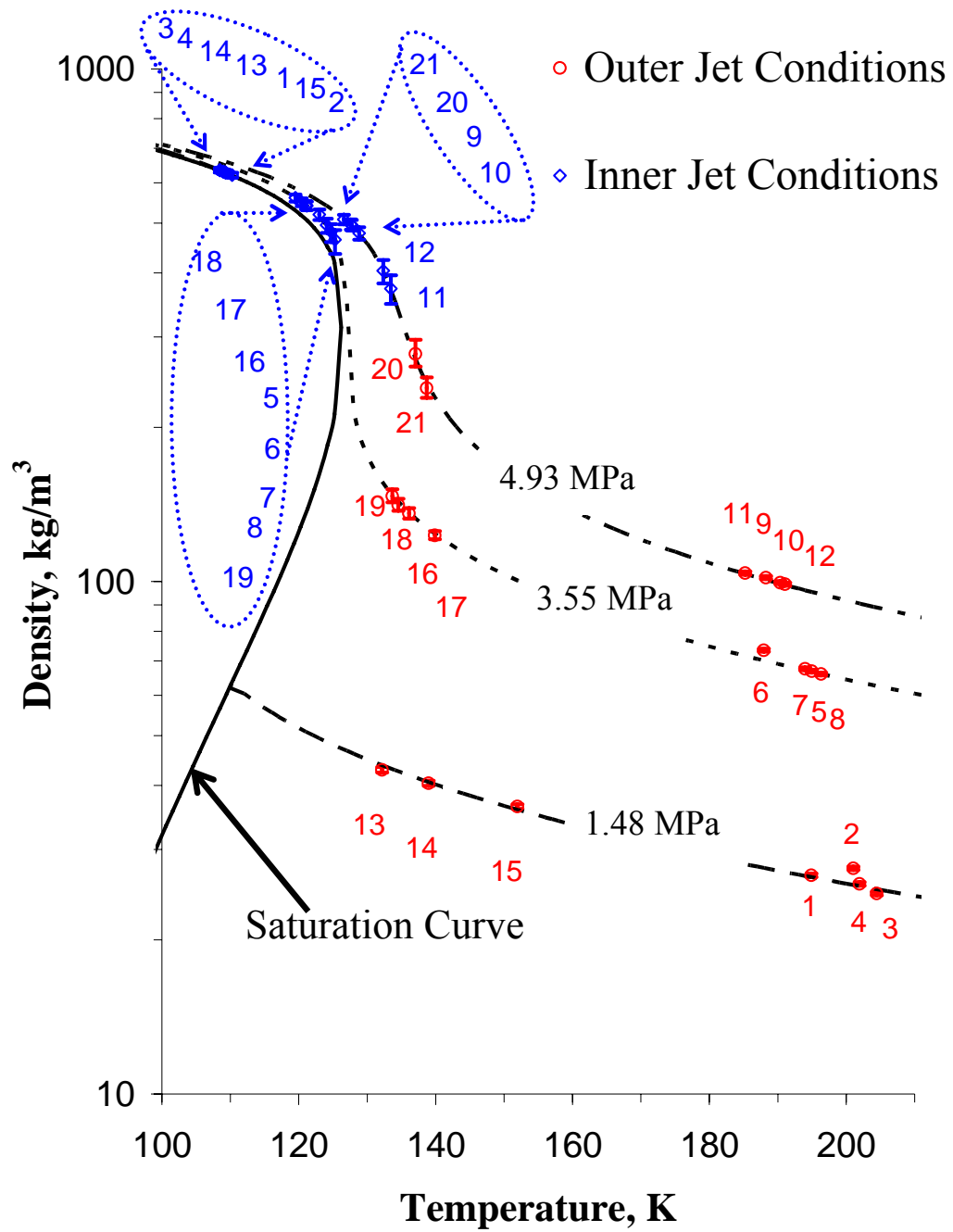


Figure 4.1: Density – Temperature (ρ - T) diagram displaying the conditions of the inner- and outer-jets of the shear-coaxial jet. The red circles are the outer-jet conditions, and the blue diamonds are the inner-jet conditions. The numbers listed near the points correspond to the case number listed in Table 4.1.

4.1 Uncertainty Analysis

In order to determine the measurement uncertainty, it is necessary to have both the measured value and the true value of a particular physical quantity. However, the true value is almost never known, with possible exceptions of calibration experiments when a reference point is defined by a physical state of matter, such as triple point of water. Conducting an uncertainty analysis early in the planning stages usually aides the analysis of the data after completion of the experiments. The purpose of estimating the uncertainties in an experiment is not only to determine “how good the data are”, but, more importantly, to decide whether differences between various experimental points in a given plot have a significance and lead to a proper conclusion of the trend. For example, it is known that density is very sensitive to temperature in regions near the critical point of a fluid. Therefore, great care was taken with those measurements, particularly in the calibration of the thermocouples as described in Chapter 3.

Measured quantities have uncertainties associated with them based on the accuracy of the instrument, the calibration, and the usage of the instrument. When calculating parameters from these measured independent variables, the uncertainty of a derived quantity increases based on the uncertainties of the individual terms and it varies according to the root-sum square rule. Moffat [74] describes the estimation of the derived-quantity uncertainty as:

$$\delta Q_{derived} = \sqrt{\sum_{i=1}^n \left(\frac{\partial Q_{derived}}{\partial x_i} \delta x_i \right)^2} \quad (4.1)$$

Where,

$Q_{derived}$ is the derived quantity,

x_i are the independent variables used to calculate $Q_{derived}$,

δx_i is the individual uncertainty of the independent variables, and

n is the number of parameters in the equation used to compute $Q_{derived}$.

To use Eq. 4.1 correctly, the individual uncertainties of the independent variables (δx_i) must be known. Often the manufacture of an instrument will report the accuracy of an instrument as a fraction of the full scale reading. To use this information it must be converted to a standard deviation, in some manner. According to Moffat [74], this is a choice that is somewhat subjective, and the experience of the user should be relied upon. For example, in this work, the pressure transducers described in Chapter 3 have a manufacturer's reported accuracy of $\pm 0.05\%$ of full scale reading. To gain an appreciation of what that accuracy represented, the pressure transducers were calibrated using the data acquisition system, which accounts for possible fixed errors in the measuring system and enables an interpretation of the accuracy reported by the manufacture. Fortunately, a precision pressure calibration device (Ruska, as described in Chapter 3), which has a precision of 0.01% of full scale, was available to test the reported accuracy of the pressure transducers, and offer an interpretation of the results. The value used in the uncertainty analysis was not the $\pm 0.05\%$ of full scale output from the transducer reported by the manufacturer, but rather $\pm 0.1\%$ (see Fig. 3.9). Part of the increase was most likely a contribution of the data acquisition system. However, an additional part was due to the manufacturer, only reporting the accuracy for the increasing pressure calibration and not accounting for the hysteresis of the transducer

upon decreasing pressure. Individual calibration of each instrument in conjunction with the data acquisition system was not possible with all the available equipment, as was the case with the mass flow meters in this work. The reported calibration sheet from the manufacture of the mass flow meters was $\pm 1\%$ of full scale output, and a precision calibration device for the mass flow measurement was not available for this work. The manufacturer's calibration was judged to represent one half of the standard deviation. Thus the uncertainty in the mass flow measurements was doubled and then combined with the uncertainties of the data acquisition system according to the root-sum-square procedure. The temperature measurements at the exit-plane of the injector required great care. The thermocouples were individually calibrated against a precision Pt-RTD as described in Chapter 3. However, to compute the uncertainty of the temperature measurements, it was necessary to include random errors in the measurements, and then combine these using the root-sum-square process, resulting in the n^{th} order uncertainty of the measurement. Once one has the uncertainties of the individual measurements (i.e., δx_i) and an equation that relates the independent variables to the dependent variables, then Eq. 4.1 may be applied.

However, there are instances where a simple equation relating the independent variables to the dependent variables does not exist, as in the present case with the density calculations using the NIST REFPROP [14] equations of state. Moffat [74] suggests that for difficult-to-differentiate quantities, one should compute the uncertainties based upon the evaluation of $Q_{derived\pm}$ at $x_i \pm \delta x_i$, and then compute the root-sum-square deviation of the finite differences in $Q_{derived\pm}$ for the positive and negative variation in x_i as shown in Eq. 4.2. Caution should be exercised as to the direction of the deviation, for example

with density, a positive deviation in temperature causes a negative deviation in density. Therefore it is necessary to consider the negative deviation of temperature and the positive deviation in pressure to compute the positive deviation in density, and the opposite temperature and pressure deviations for the negative deviation in density. Moffat [74] recommends averaging the positive and negative deviations, but suggests this with caution, because a definitive analysis has not been performed as to the consequences of this averaging process. Because of the non-linear behavior of density in the regions of interest in this work, a more conservative approach to capturing the uncertainty in the variation of density was used by retaining both positive and negative deviations rather than averaging the two. Thus, occasionally producing asymmetric error bars.

$$\delta Q_{derived\pm} = \sqrt{\sum_{i=1}^n (Q_{derived}(x_i \pm \delta x_i) - Q_{derived}(x_i))^2} \quad (4.2)$$

Unless otherwise noted, all error bars on the figures in this work were computed in the fashion outlined above.

4.2 Exit-Plane Temperature Measurements

Owing to sensitivities of density to temperature changes, careful measurements of the temperature at the exit-plane of the jet were necessary. As previously mentioned, the thermocouple used to measure the exit-plane temperature was calibrated using a precision Pt-RTD. Because of the small size of the injector ($D_I = 0.508$ mm), a probe of small size was necessary and a Pt-RTD was not available in the required dimensions. Therefore, the smallest thermocouple commercially available was selected, with a bead diameter of 0.10 mm. The thermocouple, attached to a support structure shown in Fig. 4.2, traversed through the jet at an axial location of about $0.28 D_I$ downstream of the injector exit-plane (i.e., the exit edge of the outer tube, and note that the inner tube is recessed). At each radial location, 1500 measurements were taken over 30 seconds and averaged. It is also important to note that during the initial chill-down phase, this thermocouple was positioned in the outer-jet so the temperature could be monitored to achieve the desired operating conditions. However, only a coarse control over this temperature was achievable by adjusting the liquid nitrogen flow rate to the heat exchanger (see Fig. 3.3, HE-0209).

Figure 4.3 shows the measured temperature and the associated radial profiles of density computed using the NIST REFPROP [14] program with the measured temperature and chamber pressure as input data. The data in Fig. 4.3 are presented in tabular format in Table B.1 in Appendix B. The horizontal axis is the radial distance from the jet centerline and is normalized by the inner-tube inside radius (R_I). The top, middle,

and bottom rows in Fig. 4.3, are at the nominal chamber pressures of 1.5 (subcritical), 3.5 (near-critical), and 4.9 (supercritical) MPa, respectively. The scale for the temperature profiles is read from the left axis and density on the right axis. The left and right columns in Fig. 4.3 are at the low (135 – 140 K) and high (185 – 200 K) outer-jet temperatures, respectively. The solid lines and symbols represent measured temperature profiles, and the dashed lines and hollow symbols show computed densities. Although low in resolution, temperature profiles for different conditions are shown on one page in order to facilitate comparisons of the global effects of different operating conditions as shown in Figs. 4.3 (a) – (f). However, the small-size format may not permit viewing the details, thus the individual figures are presented in full-page format as well.

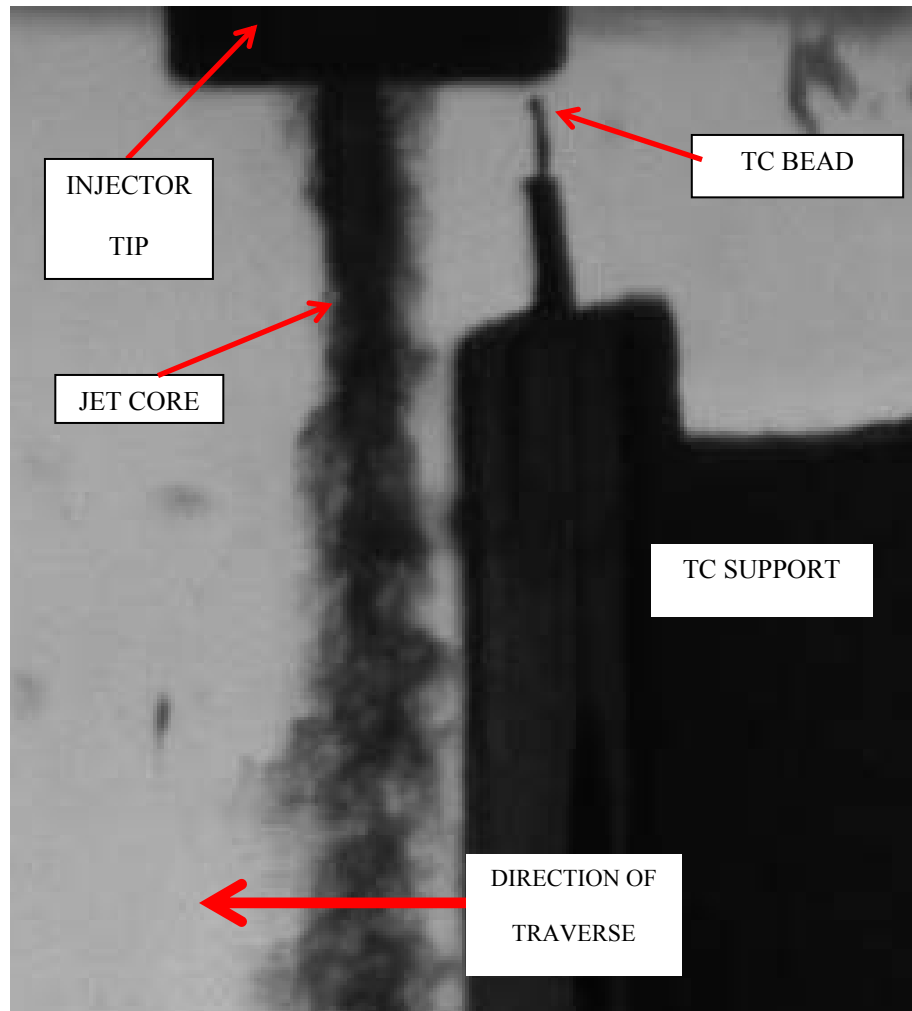


Figure 4.2: Thermocouple (TC) and the support mechanism used to perform radial temperature measurements in the coaxial jet. The thermocouple bead diameter is 0.10 mm. The resolution of the radial distance is 0.01 mm. The distance from the injector exit-plane to the thermocouple bead is 0.14 mm or $0.28 D_I$.

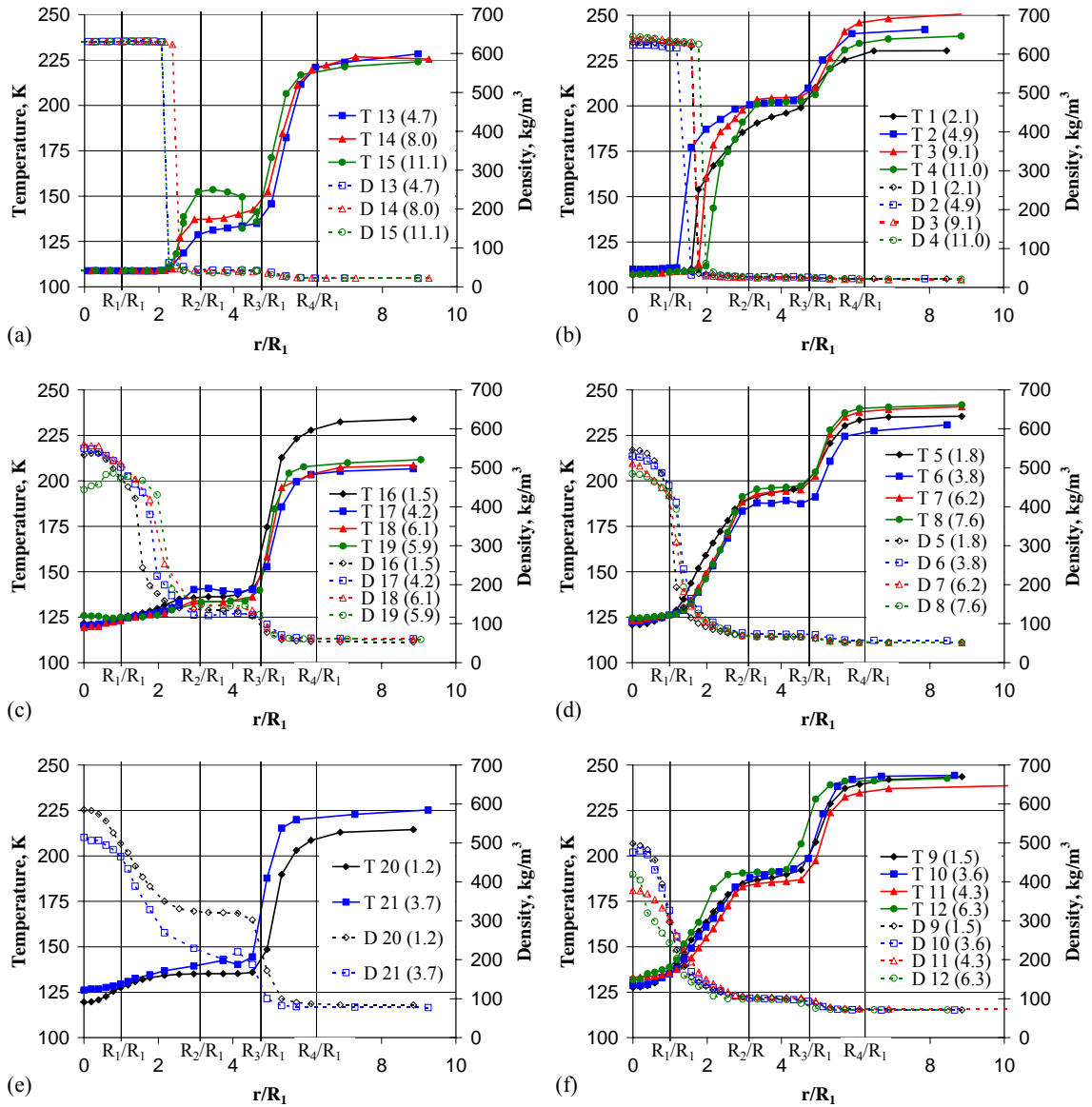


Figure 4.3: Radial profiles of the measured average temperature and calculated density. Conditions of cases are listed in Table 4.1. The chamber nominal pressure in the top row is 1.5 MPa, in the middle row is 3.5 MPa, and in the bottom row is 4.9 MPa. The nominal outer-jet temperatures in the left and right columns are about 140 K and 190 K, respectively, see Table 4.1 for exact values. The letters “T” or “D” in the inset of the figures refers to temperature or density, respectively, the next number indicates the particular case number for the data corresponding to the case listed in Table 1, and the number in parenthesis is the corresponding outer-to-inner jet velocity ratio. R_1 , R_2 , R_3 , R_4 are the radii of the surfaces of the coaxial injector. For example, R_1 is the inner-diameter of the inner-tube, and R_2 is the outer-diameter of the inner-tube.

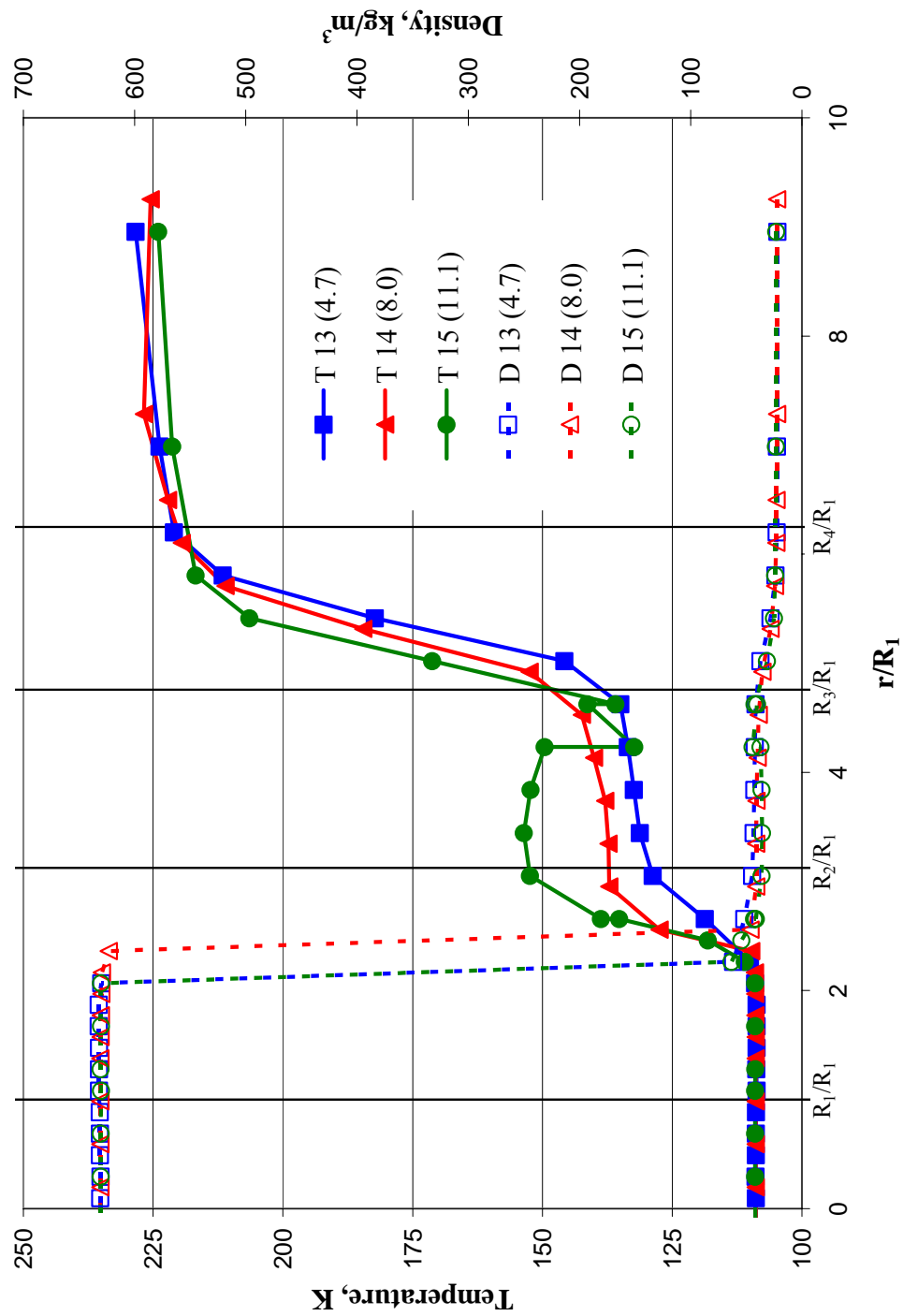


Figure 4.3(a). Radial temperature and density profiles of subcritical pressure and low outer-jet temperature.

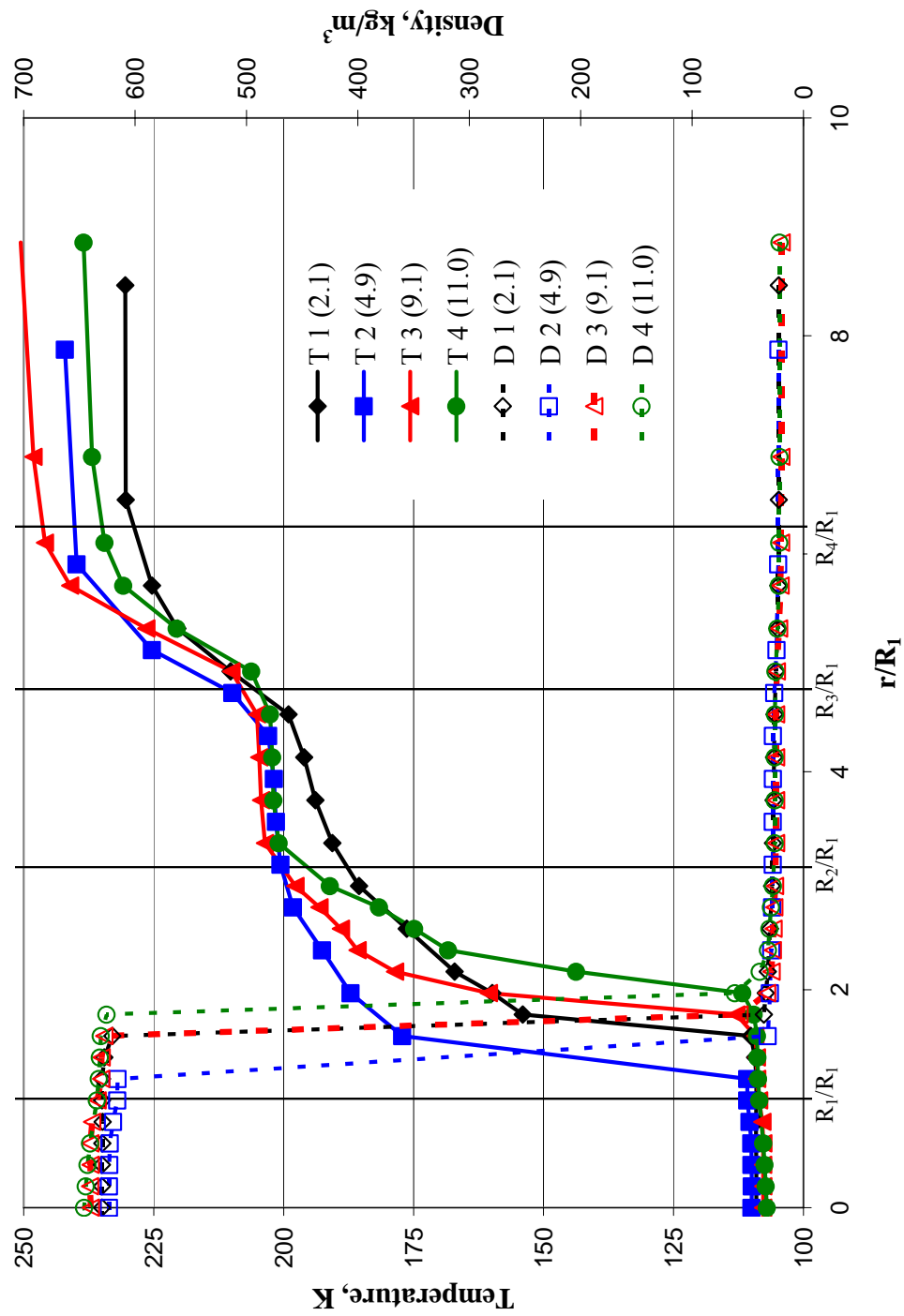


Figure 4.3(b) Radial temperature and density profiles of subcritical pressure and high outer-jet temperature.

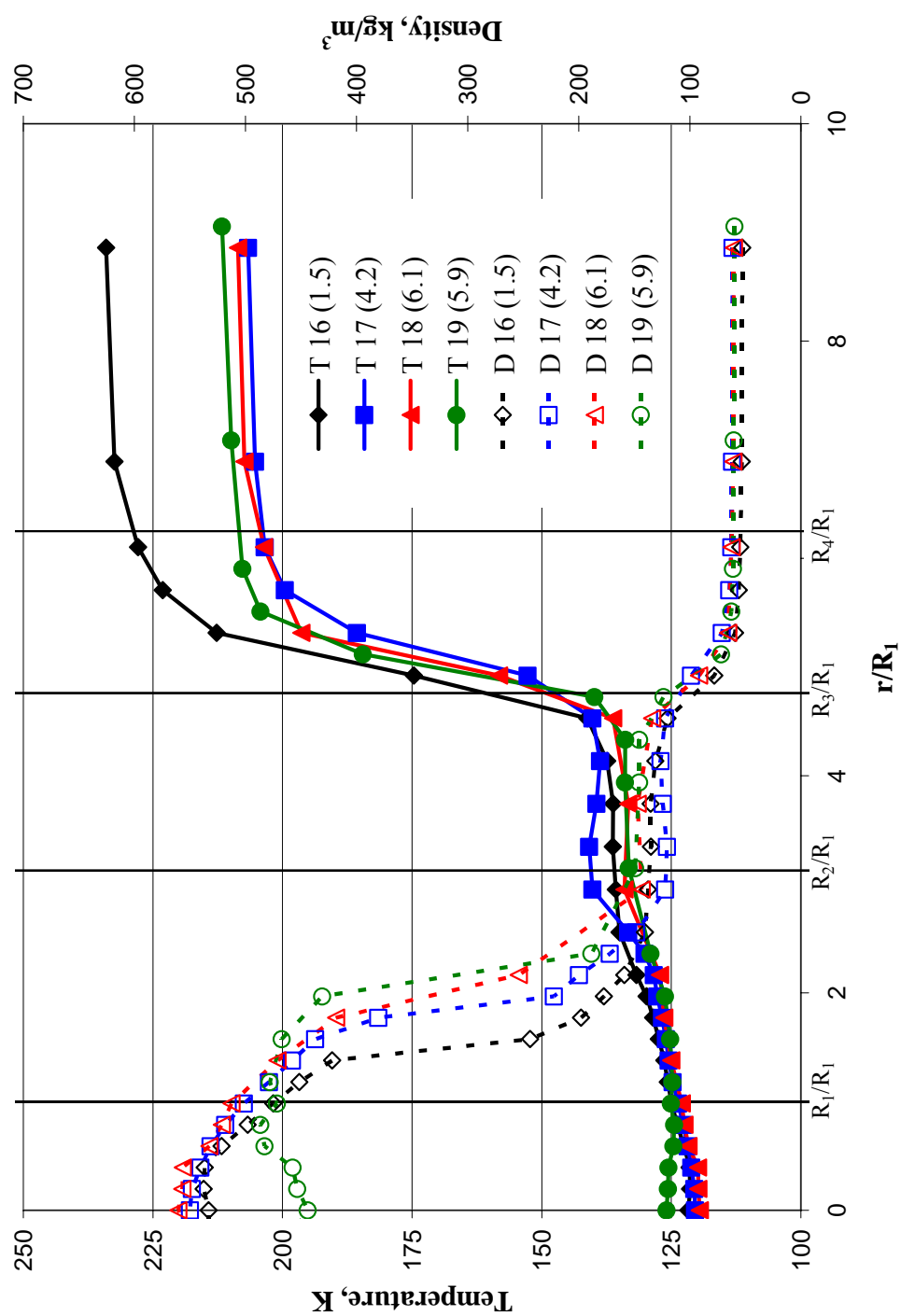


Figure 4.3 (c). Radial temperature and density profiles of nearcritical pressure and low outer-jet temperature.

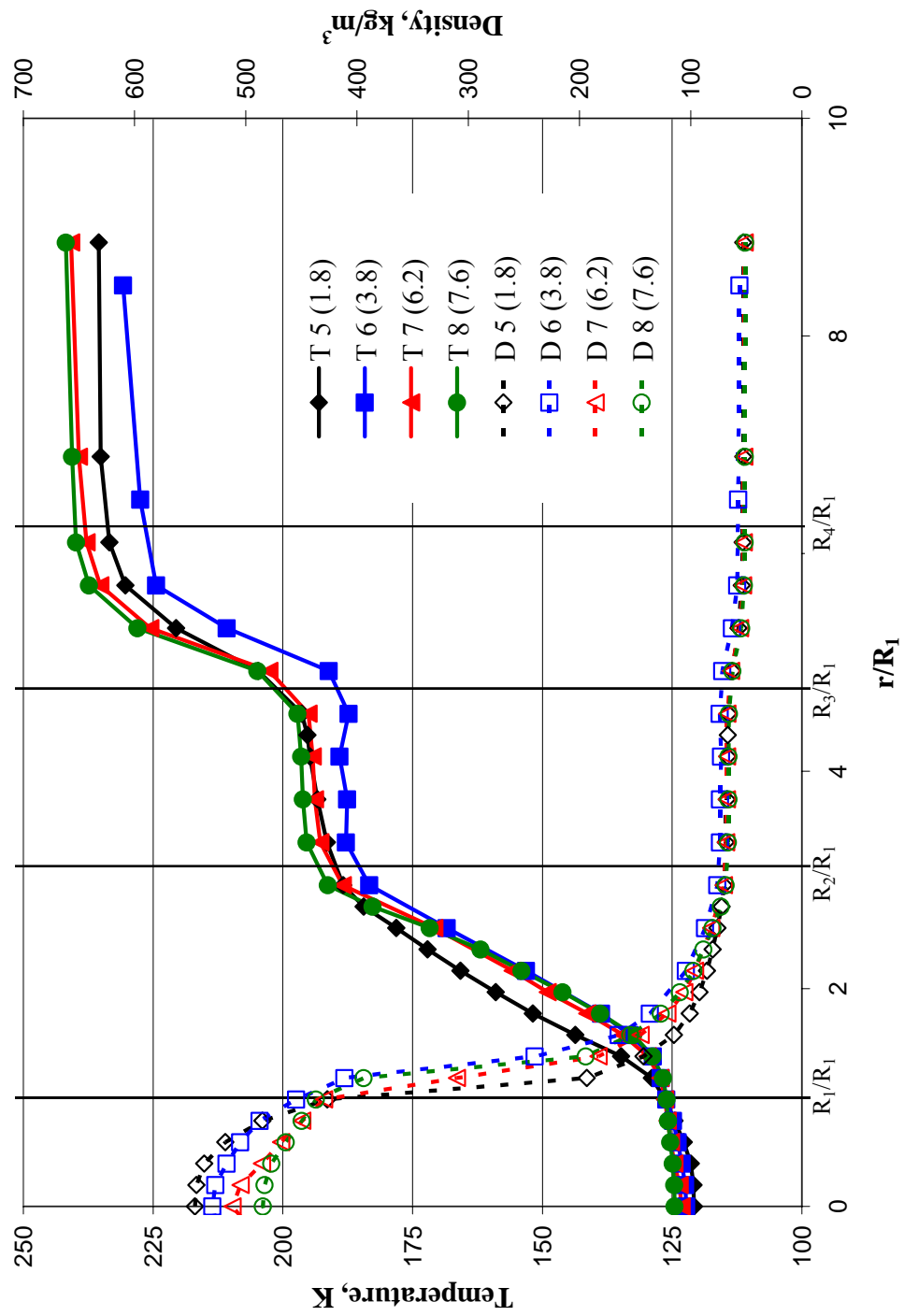


Figure 4.3 (d) Radial temperature and density profiles of nearcritical pressure and high outer-jet temperature.

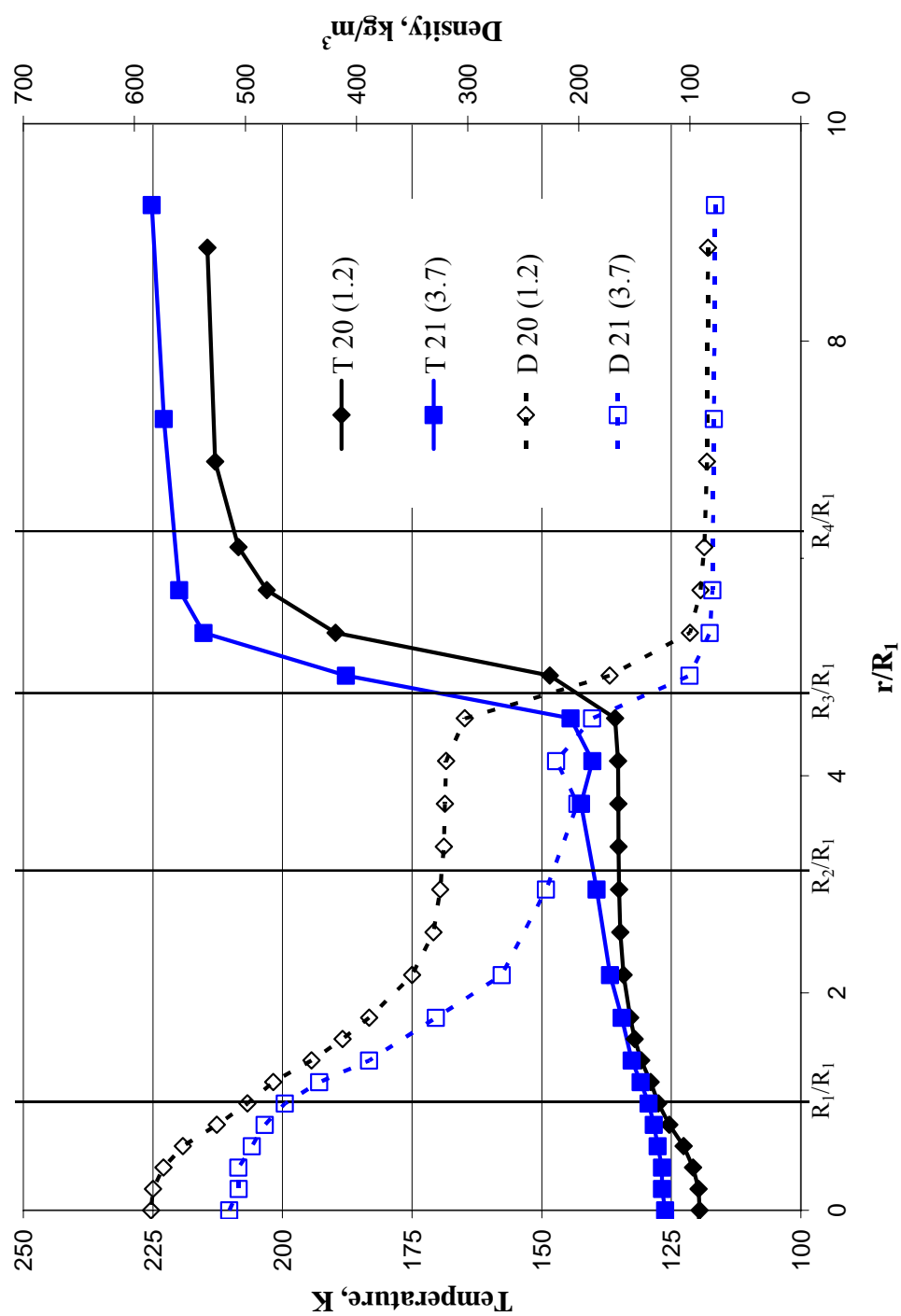


Figure 4.3 (e) Radial temperature and density profiles of supercritical pressure and low outer-jet temperature.

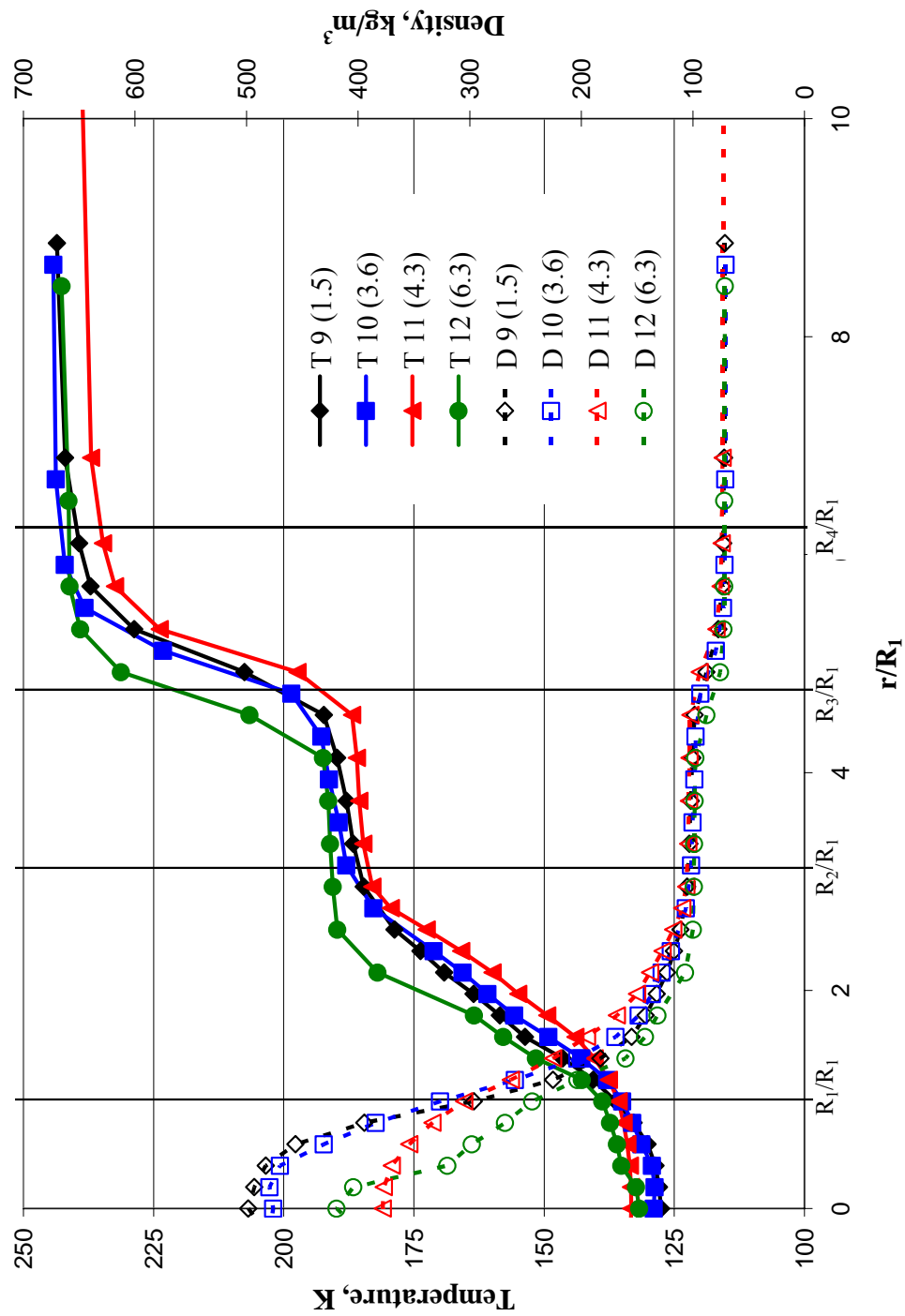


Figure 4.3 (f) Radial temperature and density profiles of supercritical pressure and low outer-jet temperature.

An attribute that the temperature profiles in Fig. 4.3 possess is that there are three distinct zones where the temperature gradient is fairly small: the core or region near the centerline of the jet, the region that defines the flow of the outer-jet, and the far-field inner-chamber environment. The temperatures in these three regions were used to compute physical properties such as densities and viscosities, which in turn were used to compute quantities such as velocity, momentum, and their appropriate ratios.

At a given subcritical chamber pressure (i.e., nominally 1.5 MPa, the top row in Figs. 4.3 (a) and (b)), both the temperature and density profiles representing the core region of the inner-jet at the injector exit area are flat in shape, producing “top-hat” density profiles. The profiles then sharply change to quite different values, typical of a transition from a liquid to a gas phase, as chamber pressure is raised. Note that for the low outer-jet temperature case (i.e., Fig. 4.3 (a)), and at the measured axial location, this constant core temperature value penetrates well beyond the inner-tube radius, up to about r/R_I of 2.5, independent of the velocity ratios used. Under this condition, variations of the velocity ratio have little impact on the radial extent of the inner-jet as defined by either the temperature or density profiles. Also, small variations in the outer-jet temperature have little effect on the calculated values for densities. However, at the higher outer-jet temperature in Fig. 4.3 (b), the radial extent or penetration of the inner-jet is strongly affected by the value of the outer-to-inner velocity ratio, primarily due to the increased heat transfer to the inner-jet from the outer-jet, both inside and immediately outside the injector. Note that the outer-jet temperature is controlled manually by changes in the liquid nitrogen flow rate to the secondary heat exchanger used to cool the outer-jet flow, see Fig. 3.3. The control over this temperature is somewhat coarse and it

is a manual adjustment, which accounts for the variations seen in the outer-jet temperatures shown in Fig. 4.3 (a). The variability of the inner-chamber temperature at the far field is related to changes in several factors, including mass flow rates of all nitrogen streams into the inner-chamber, their respective temperatures, and the length of time spent running the experiment, see Fig. 4.3 (b). Under the higher outer-jet temperature shown in Fig. 4.3 (b), the heat exchanger control system was able to maintain this temperature at a reasonably constant value and, again, small changes in temperature has only a small impact on the calculated densities at this pressure.

As the chamber pressure is elevated to a near-critical value (i.e., nominally 3.5 MPa, the middle row of Fig. 4.3, Figs. 4.3 (c) and (d)), the “top-hat” nature of the radial density profiles is lost and more rounded shapes are observed, perhaps due to the changes in the heat transfer characteristics inside the tube under elevated pressures, especially at near-critical pressures. Additionally, the temperature of the core (of the jet) at the centerline is greater than the corresponding temperatures at the subcritical pressure discussed above. The density increase within the outer-jet zone from that of the far-field chamber value, especially at lower outer-jet temperature, is larger ($\sim 15 - 20 \text{ kg/m}^3$) and more noticeable than that observed under subcritical pressures (see Figs. 4.3 (a) and (b)). It is also noted that for the case “T 19” on the plot Fig. 4.3 (c), the temperature at the centerline is slightly higher (by approximately 5 K) than all the other cases, causing the density profile to exhibit its maximum value at a slightly off-axis radial location. It is believed that the thermocouple traverse plane may have moved off the axis of symmetry of the jet.

A further increase in chamber pressure to a supercritical condition (i.e., ~ 4.9 MPa, the bottom row of Figs. 4.3 (e) and (f)) leads to an insignificant change in the qualitative behavior of the profiles as compared to the 3.5 MPa near-critical pressure data. Again, a strong contrast is seen between the far-field chamber and outer-jet densities, indicating the sensitivity of the density to small changes in temperature under this condition. It is also noticed that at all velocity ratios, the value of the centerline temperature at the higher outer-jet temperature (Fig. 4.3 (f)) is supercritical (i.e. > 126.2 K), whereas it is subcritical for all other cases in Fig. 4.3. For the lower outer-jet temperature cases, the difference in density between the outer-jet region and the far-field value is in excess of 200 kg/m^3 , which makes this feature easily observable in images of the jet, but does not permit easy and clear distinction of the inner-jet dark-core area.

4.3 Flow Visualizations

Flow visualization of fluid flows allows for both qualitative and sometimes quantitative measurements from images. The discussion in this section will be limited to qualitative descriptions of the phenomena observed in the images of the jets.

4.3.1 Qualitative Behavior of Single Round Jets

Full characterization of the behavior of single round jets is beyond the scope of this work and was done by Chehroudi et al. [24-30]. However, during validation experiments of the apparatus, interesting results were obtained from the high-speed movies. As the same injector assembly as the one described in Chapter 3 was used to produce all jet flows in this work, a single round jet was produced by turning off the outer-jet flow through the coaxial injector.

Nine sequential frames from the movie of the subcritical single round jet with a fixed inter-frame duration of 222 μs and at a subcritical pressure (1.50 MPa) are shown in Fig. 4.4. Visible droplets on the order of 100 to 500 μm are being ejected from the jet. Recall that the inner diameter of the inner tube (D_1) for this injector is 0.508 mm, and the center post (or inner tube) is recessed by $0.5 D_1$. The apparent width of the jet at the exit-plane of the injector is about 0.85 mm, which is larger than the D_1 . The increase in exit diameter of the jet is attributed to the post recess, which allows the jet to spread before being visible downstream of the recessed injector post.

The average exit velocity of the jet is 2.2 m/s ($Re \approx 1.2 \times 10^4$), determined by the mass flow rate and the density calculations. From the movies, the estimated velocity of the droplets in the direction of their motion, leaving the liquid core, ranges from about 0.75 to 2.2 m/s. Once a droplet leaves the jet, the drag acting on it slows the droplet to an extent that sometimes the droplet appears to stop entirely in the chamber fluid. Because of the large temperature differences of about 175 K between the chamber fluid and the injected liquid, strong droplet vaporization is expected. The droplets that appear to come to a stop eventually evaporate completely and disappear into the chamber fluid. The combination of the motion of the droplet and the evaporation results in a visible wake behind the droplets because of the higher density of the wake relative to the chamber fluid. The combination of the droplet and the wake appear to look like a comet (see Fig. 4.4). The estimated droplet ejection angles formed between the jet's axis of symmetry and droplet trajectories vary between 20° and 60° , with an averaged angle of about 30° . Also, occasionally some droplets are ejected from the dark core, which are later entrained back into the jet farther downstream.

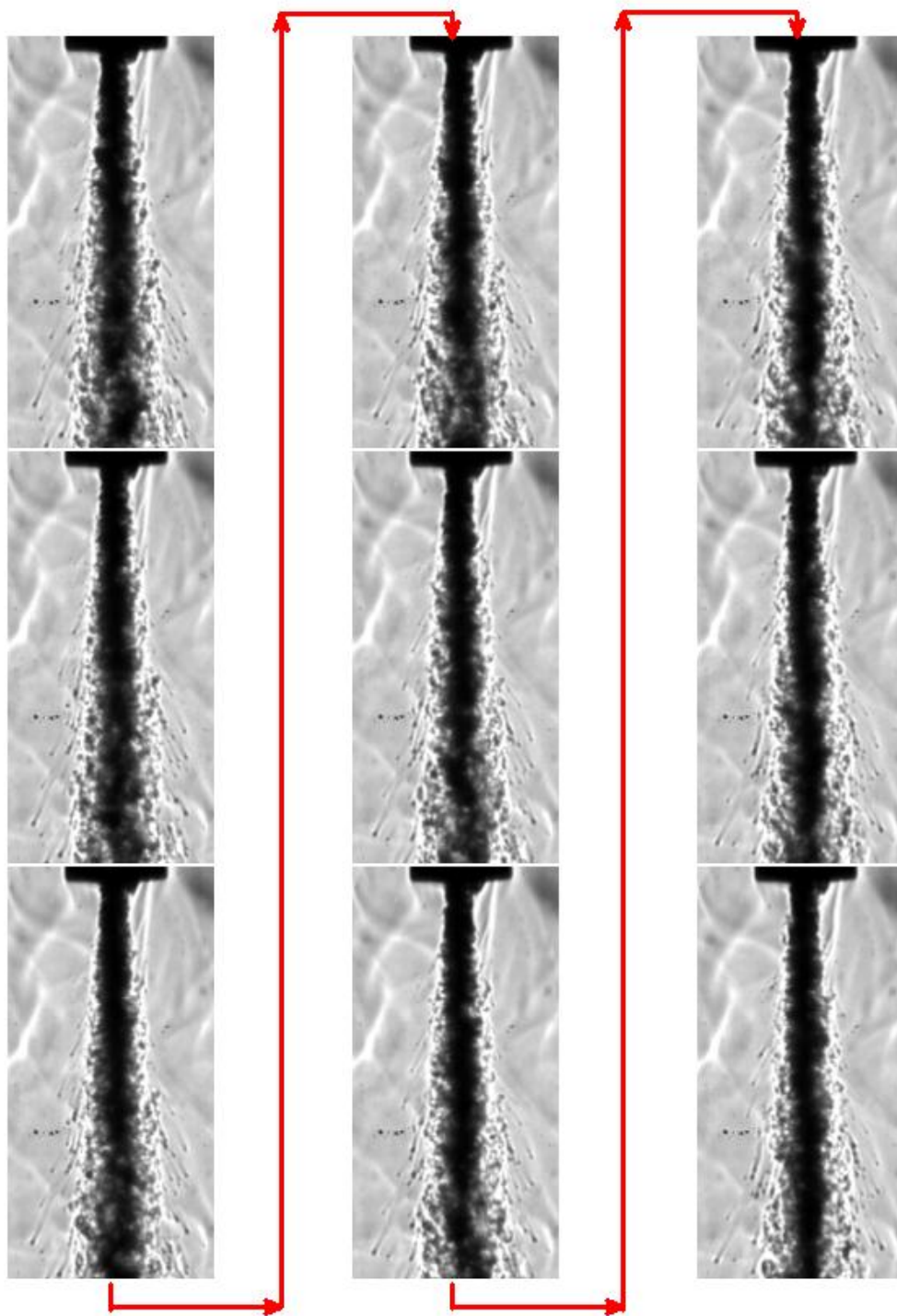


Figure 4.4: Subcritical liquid nitrogen single round jet injected into gaseous nitrogen. Nine sequential frames, starting at the top left, with a time interval between frames of $222 \mu\text{s}$ are shown. Time increases down the column of images. The chamber pressure was 1.50 MPa, and the velocity of the jet was 2.2 m/s. The acoustic driver is off. The scale can be determined from the injector tip outer diameter of 3.18 mm.

The vaporizing character of the dark-core of the jet along with the variable-density shear layer in the same region of space obscures high-contrast visualization of the droplet formation details in the periphery of the liquid jet. However, in the vicinity of the injector exit, where the shear layer and the vaporizing region are thin, some information on the droplet ejection mechanism is revealed. Figure 4.5 shows the formation and ejection of a droplet from the dark-core liquid surface. A bulge on the liquid surface in the first image (top left) turns into a ligament, protruding from the liquid surface, which subsequently shears off forming a droplet. As the droplet passes through the shear layer (or, vaporizing peripheral region of the jet), it becomes more difficult to discern the drop until it emerges from the layer. The wake of the vaporizing droplet is evident, particularly in the last row of images in Fig. 4.5.

The visual appearance of the drop formation is consistent with the phenomenological mechanism proposed by Wu et al. [75]. The initial ligament on the surface of the liquid jet is formed by a turbulent eddy of the size on the order of the integral length scale within the liquid jet that breaks through the surface and is subsequently sheared off from the core of the jet.

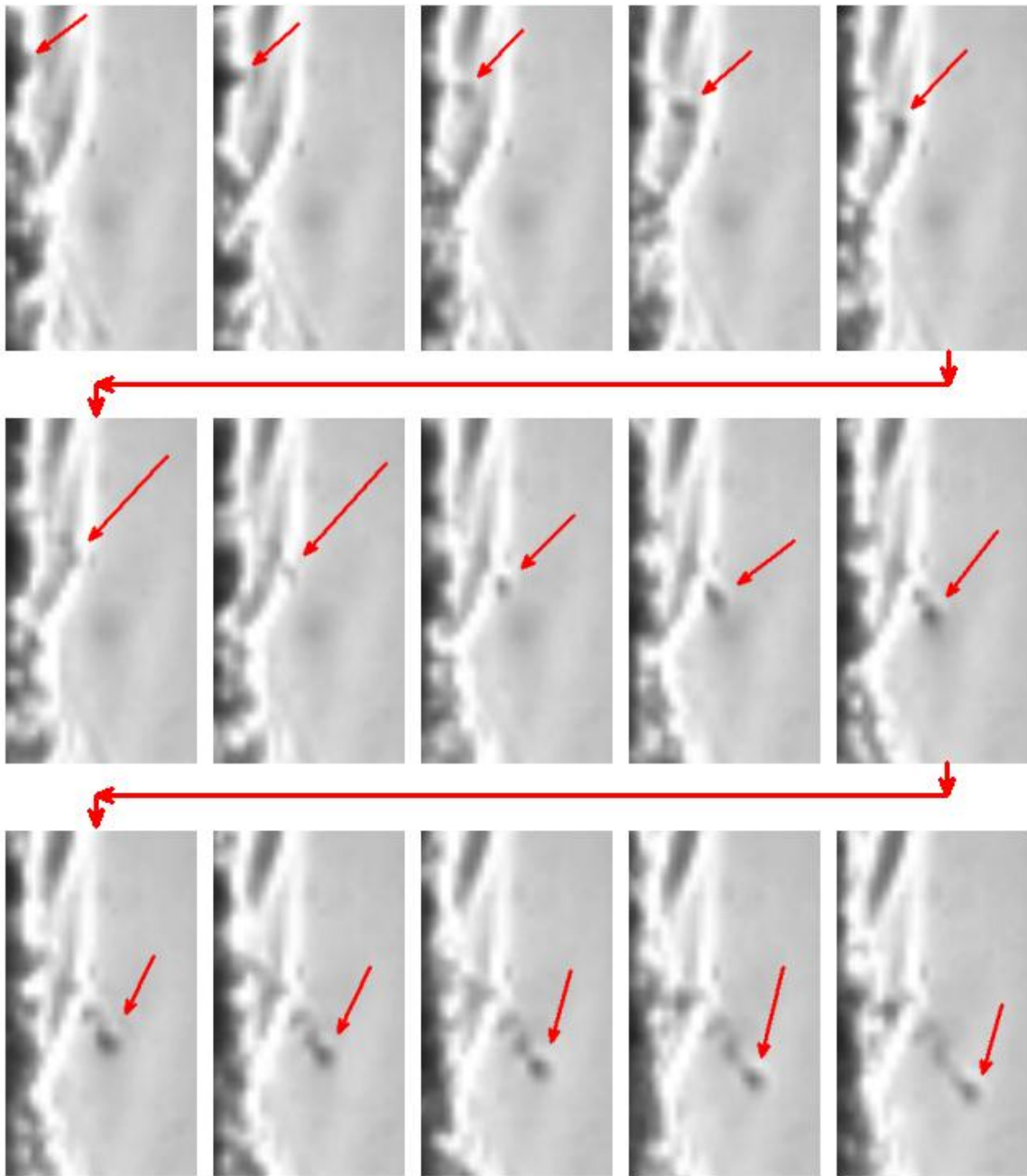


Figure 4.5: Droplet formation and ejection from liquid jet surface. Fifteen sequential frames are shown starting at the top left, with a time interval between frames of $56 \mu\text{s}$. Time increases across a row. The pressure was 1.50 MPa, and the velocity of the jet was 2.2 m/s. The acoustic driver is off.

Acoustic excitation of the single jet under subcritical pressures produced interesting behavior of the droplets. Figure 4.6 (a) shows an image of the jet impacted by a transverse acoustic field. The upper edge of the frame is located at about $10 D_1$ downstream, and two expanded views of droplets are also shown in Fig. 4.6 (b) and (c). As droplets travel away from the jet, a transverse acoustic (fluctuating) velocity is imposed on the droplet motion. Evident in Figs. 4.6 (b) and (c) is a sinusoidal structure in the wake of the droplets. As time passes, droplets are completely vaporized and subsequently this wake structure disappears. In short, consider a droplet moving with some mean velocity, as it evaporates it leaves behind a wake that has a greater density than that of the chamber fluid, thus making it visible in the images. When the acoustic velocity field exists in the chamber, the observed wake indicates an approximate trajectory a given droplet has taken. Once, the droplet slows down and its mean penetration velocity approaches zero, it begins to oscillate with the chamber fluid. However, because the mean velocity of the drop is very small (or, approaching zero) at that time, the high-density wake is not visible, rather the droplet continues to vaporize until the fluid becomes indistinguishable from the chamber fluid.

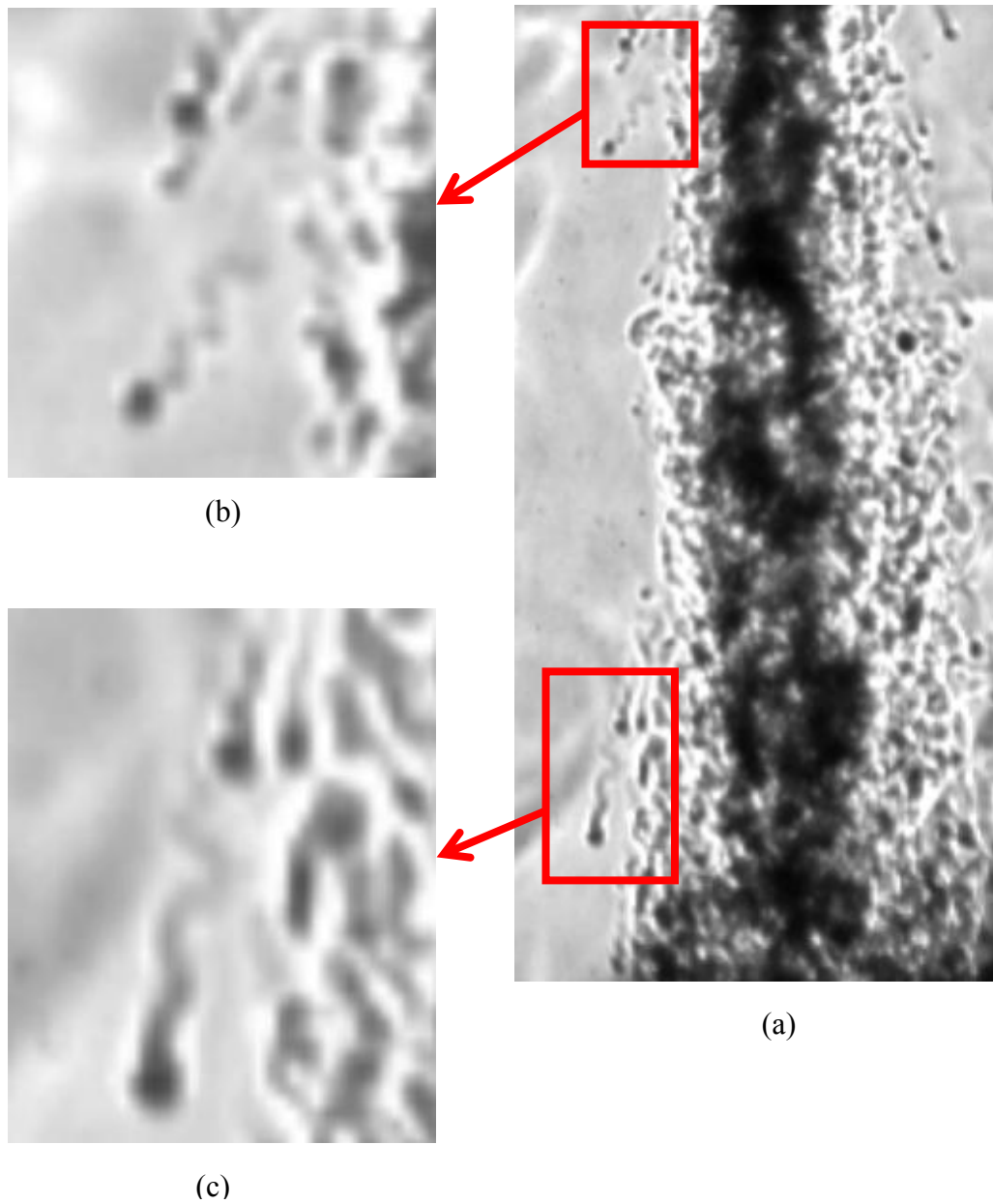


Figure 4.6: Acoustic wave interaction with subcritical liquid nitrogen single round jet injected into gaseous nitrogen. The pressure was 1.50 MPa, and the velocity of the jet was 2.2 m/s. The acoustic driver is on at 3.03 kHz, amplitude is about 170 dB. The top of the frame is about $10 D_1$ down stream of the injector exit-plane..

Upon an increase in chamber pressure to a near, but slightly supercritical condition, substantial differences in the behavior of the single round jet are observed. Figure 4.7 shows fifteen sequential frames of the single round jet at a pressure of 3.47 MPa, which is slightly supercritical (P_c of N_2 is 3.40 MPa). Droplets are not observed at this pressure, as expected. Occasionally, a fluid parcel forming from a ligament on the surface of the jet would become separated from the core similar to the droplet formation scenario observed at subcritical pressures. However, in contrast to the subcritical-pressure droplet formation, the fluid parcel remained at approximately the same location until it warms and subsequently disappeared into the chamber fluid, or was entrained back into the jet.

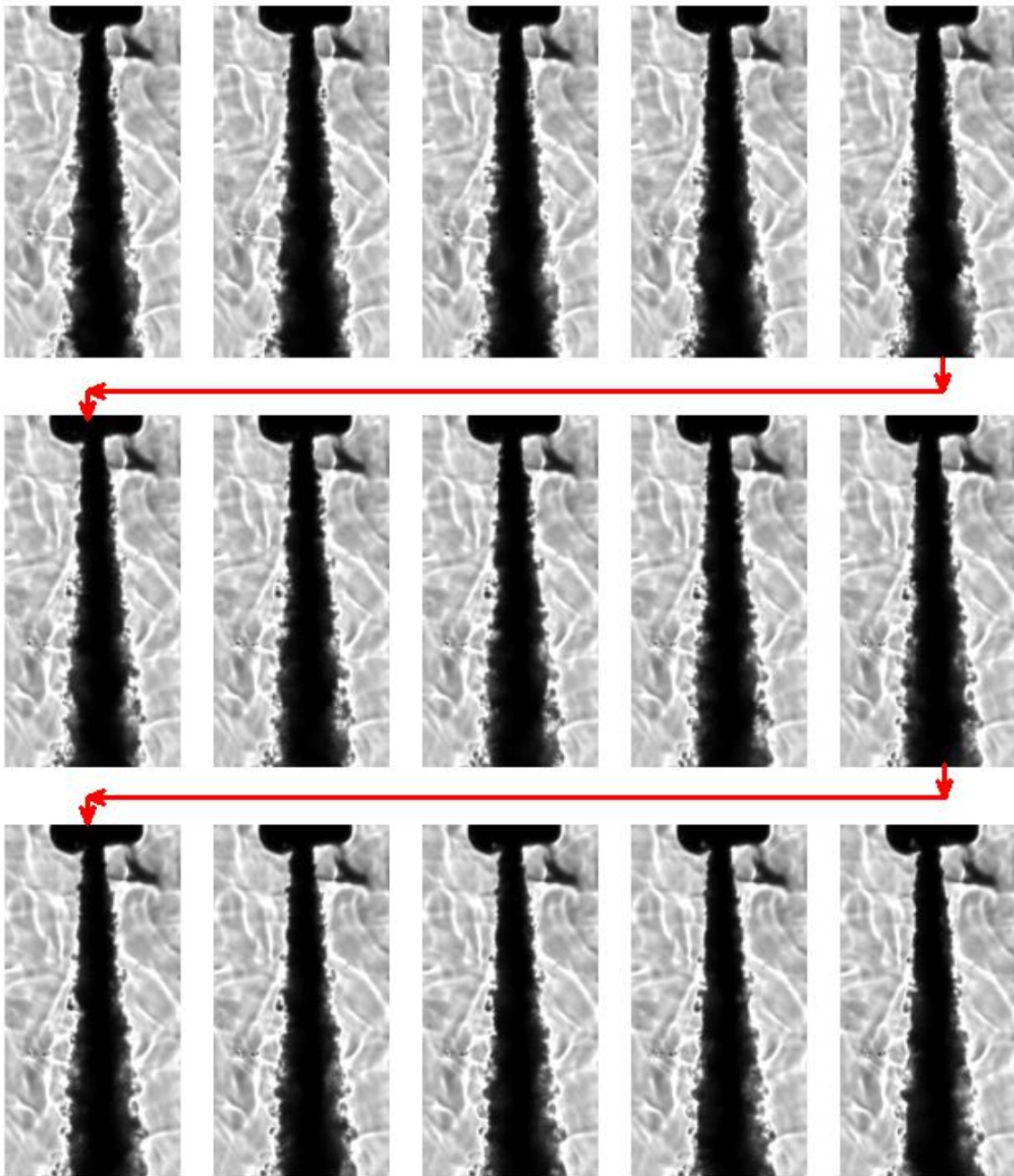


Figure 4.7: Near-critical cryogenic nitrogen single round jet injected into gaseous nitrogen. Fifteen sequential frames, starting at the top left, with a frame-to-frame time interval of $222\ \mu\text{s}$. Time increases across a row. The pressure was 3.47 MPa, and the velocity of the jet was 2.2 m/s. The acoustic driver is off. The scale can be determined from the injector width of 3.18 mm.

4.3.2 Qualitative behavior of Shear-Coaxial Jets

Flow visualization of the shear-coaxial jet provides detailed information on the flow structure, in particular, it could provide information about the atomization or breakup processes under different operating conditions (spanning sub- to supercritical chamber pressures) and on the interaction of the acoustic field with the jet. For this reason, this section is dedicated to cataloguing some of the shear-coaxial jet behavior both with and without acoustical excitation.

Figures 4.8 – 4.10 are sample images of the coaxial jet under different conditions discussed in the ensuing paragraphs. The scale presented in Fig. 4.9 is the same as those for Figs. 4.8 and 4.10. One prominent feature of these images is the so-called “dark core”, which represents the high-density region of the inner-jet. In these images, the inner-jet has a much higher density than anywhere else in the field, thus the light rays passing through this region experience large deflections causing the light rays to not be collected by the camera lens, and hence the reason for the dark, black appearance of the high-density regions. Details of this process are presented in Davis [76]. In many of the conditions, identification of the outer-jet is made difficult because of the low density and low density gradient between the outer-jet and the inner-chamber environment. However, under some conditions (see Figs. 4.3 (c) and (e) at the low temperature for near- and super-critical conditions), the density and the density gradient are large enough to easily distinguish the periphery of the outer-jet. This periphery is made visible in the high-speed images presented later in this chapter due to the choice of a new high-performance camera and improved illumination system.

Figure 4.8 shows the visualization of the coaxial jet under a subcritical chamber pressure and low outer-jet temperature. From left to right, in both rows, they correspond to cases 1 to 4 in Table 1. For the top row, Figs. 4.8 (a) to (d), the acoustic driver is off and the bottom row, Fig. 4.8 (e) to (h), shows the images corresponding to the same flow conditions as the top row but the acoustic driver is turned on. Images in the same column correspond to the same operating conditions and were taken in the same test run. The outer-to-inner jet velocity ratio increases from left to right in Fig. 4.8, while the inner-jet velocity is approximately constant. At the lowest velocity ratio (Fig. 4.8 (a)), the breakup of the jets appears to fall into the non-axisymmetric Rayleigh category, and the next higher velocity ratio (Fig. 4.8 (b)) is of the membrane-breakup type, even though the aerodynamic Weber number is much greater than that observed for water-into-air injection by Faragó and Chigier [61]. At the next two higher velocity ratios (Fig. 4.8 (c) and (d)), a fiber-type breakup is observed with a pulsating or superpulsating mode. Faragó and Chigier [61] describe the pulsating and superpulsating sub-modes of atomization as the periodic change in the axial flow direction of the liquid volume fraction, which is evident in images by the periodic appearance of dark regions downstream of the end of the core. The exit diameter of the dark core at the injector exit-plane for case 2 (Fig. 4.8 (b)) is noticeably smaller than the others. Comparison between the diameters of the high-density region defined through temperature measurements in Fig. 4.3 (b) and those of the dark core seen in the images at the exit-plane of the injector, reveals very similar trends. Upon an increase in the velocity ratio, the atomization process is enhanced, which is qualitatively visible, particularly when viewed in high-magnification images, from the decrease in the droplet sizes.

Comparing the top and bottom rows of images, a clear effect of the acoustic field is noticed for all four conditions in Fig. 4.8. The breakup of the dark core of the inner-jet is accelerated and large-amplitude wave structures are formed. From these visualizations and the high-speed movies, it appears that, near the injector exit area, the dark core of the inner-jet is “pushed out” into the path of the outer-jet flow and is then convected downstream away from the injector. The dark core develops a cusp-like structure at a distance from the injector which subsequently separates from the attached region of the jet and ultimately disappears, becoming fully mixed with the outer-jet fluid. A more detailed description of the mechanism of interaction of the acoustic wave and the jet is given later in this chapter.

Figure 4.9 shows the impact of the velocity ratio and acoustic field on the coaxial jet under the low outer-jet temperature condition. The relatively low velocity ratio condition, which would correspond to Figs. 4.8(a) and (e), is absent from the images shown in Fig. 4.9, because that particular condition was unattainable with the experimental apparatus used in this study. As seen in the temperature measurements (see Fig. 4.3), the core of the jet also appears thicker under the low outer-jet temperature case. The breakup seems to be of the fiber type with a pulsating or superpulsating sub-mode, evident from the periodic high-density structures visible in Figs. 4.9 (b) to (d). The jet responds to the acoustic field at all conditions with increasingly dramatic effects at higher velocity ratios. Comparing the linear extent of the dark core for the acoustically-excited jets of Figs. 4.9 (f) to (h) with those of Figs. 4.8 (f) to (h) show that it is somewhat longer for the former (i.e., the low outer-jet temperature case).

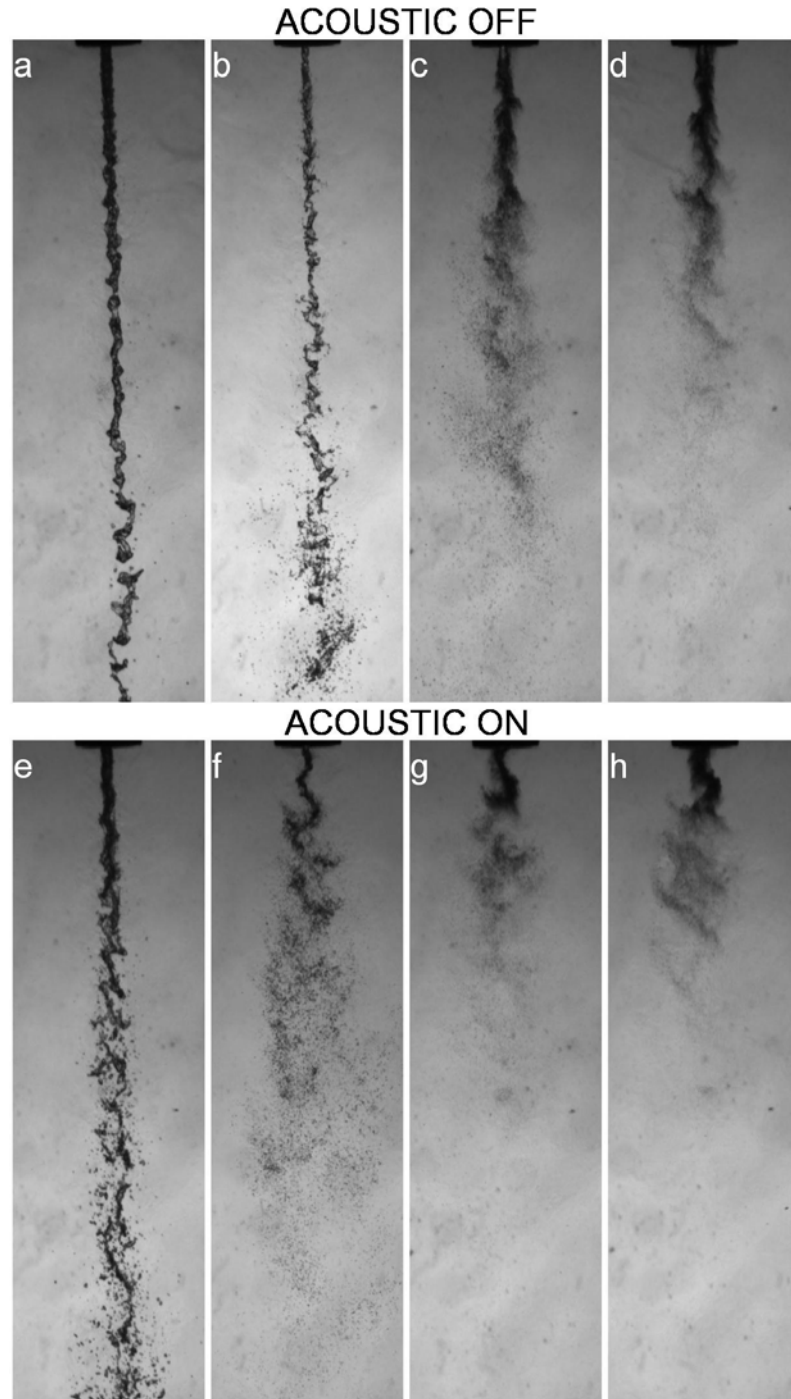


Figure 4.8: Shadowgraph images of coaxial jet at subcritical chamber pressure ($\sim 1.5\text{MPa}$) and at the *high outer-jet temperature* ($\sim 190\text{ K}$) corresponding to cases 1 – 4 listed in Table 4.1 from left to right. The acoustic driver is off for images in the top row and on for the bottom row at $\sim 3\text{ KHz}$. The velocity ratio is the same for each column and increases from left to right.

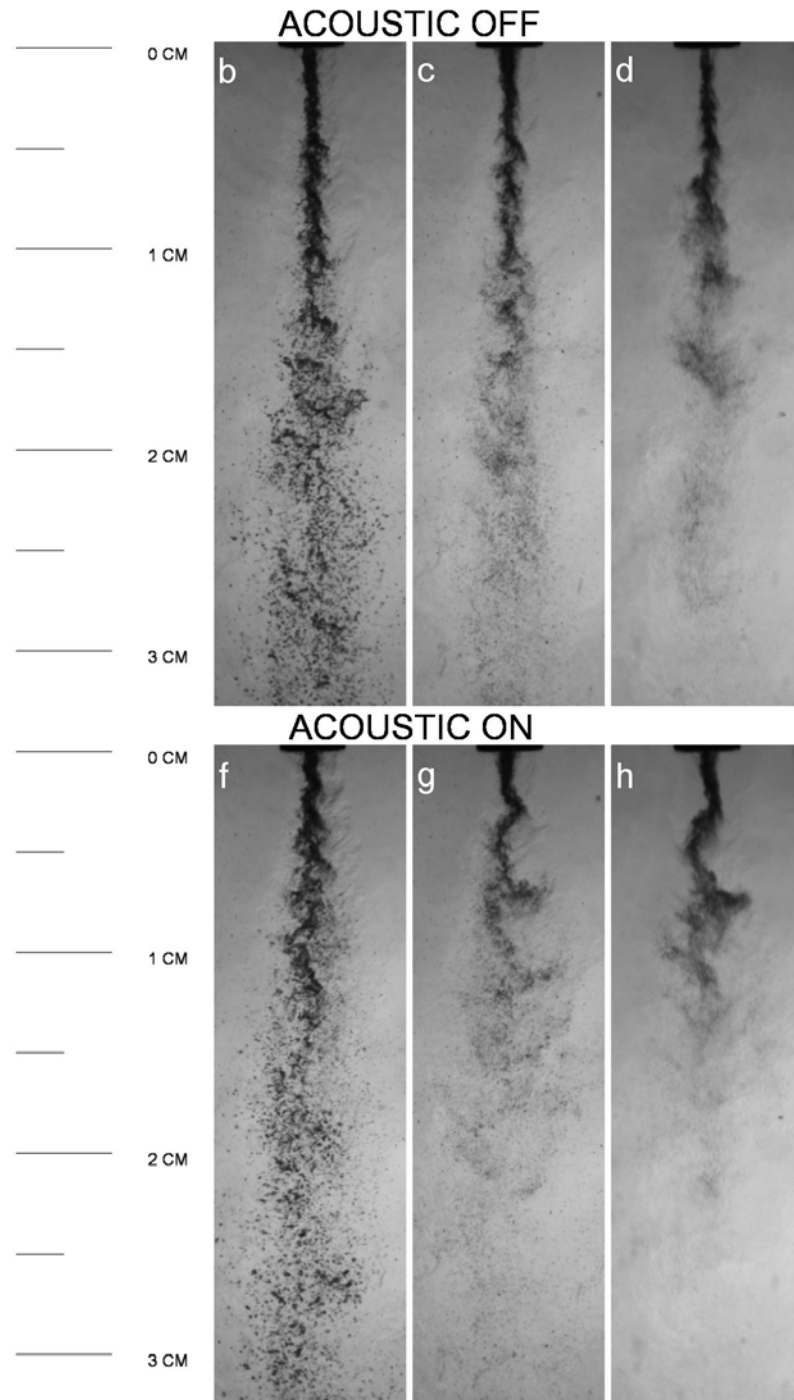


Figure 4.9: Shadowgraph images of coaxial jet at subcritical chamber pressure ($\sim 1.5\text{MPa}$) and *low outer-jet temperature* ($\sim 140\text{ K}$) corresponding to cases 13 – 15 listed in Table 4.1 from left to right. The acoustic driver is off for images in the top row and on for the bottom row at $\sim 3\text{ KHz}$. The velocity ratio is the same for each column and increases from left to right. The lowest flow rate condition was unattainable experimentally.

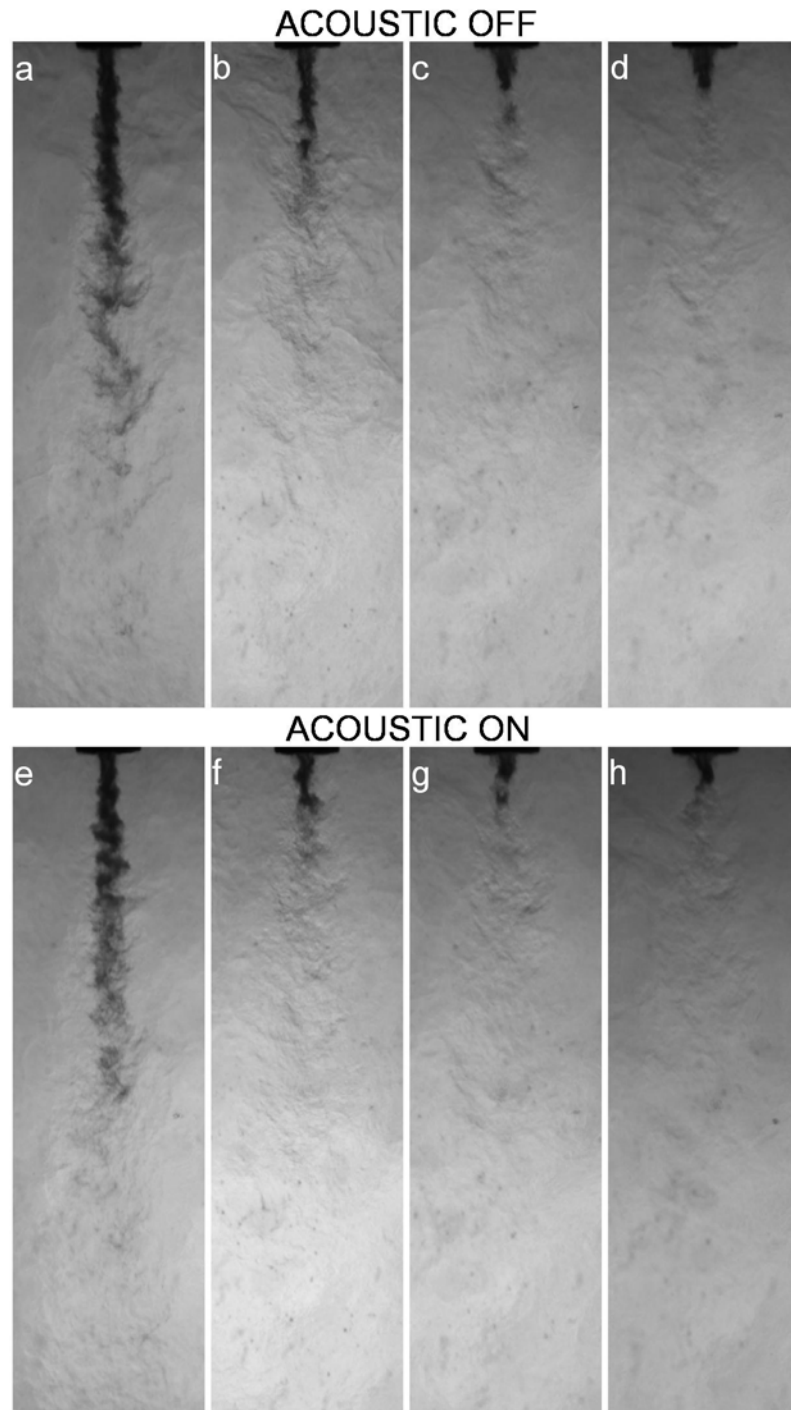


Figure 4.10: Shadowgraph images of a coaxial jet at nearcritical chamber pressure (~ 3.5 MPa) and at a *high outer-jet temperature* (~ 190 K) corresponding to cases 5-8 listed in Table 4.1 from left to right. Images in the top row the acoustic driver is off, and the bottom row the acoustic driver is on at ~ 3 KHz. The velocity ratio increases from left to right.

Shadowgraph images of the coaxial jet at a near-critical (but slightly supercritical) chamber pressure (~ 3.5 MPa) are shown in Fig. 4.10, and are arranged with the same format and scale as those in Figs. 4.8 and 4.9. Droplets that were clearly detected under the subcritical chamber pressure are not present as expected (see Chehroudi et al. [27]). The length of the dark-core decreases significantly as the momentum flux ratio is increased from less than unity (Fig. 4.10 (a)) to greater than one (Figs. 4.10 (b) to (d)). For the higher momentum flux ratio (and velocity ratio) the shape of the dark core changes from cylindrical to conical. The conical shape of the core was observed only for shear-coaxial jets that were at supercritical chamber pressures.

Judging solely from the dark region of the jet, the effects of the acoustic field are less pronounced. However, from the high-speed movies taken with the Phantom camera and shown in the fourth row from the top of Fig. 4.11, the oscillation of the jet is quite visible due to the increased framing rate and the improved illumination arrangement, which allowed the outer-jet boundaries to be visualized. Figure 4.11 is composed of ten consecutive frames acquired from high-speed movie of the jet. The first and second, the third and fourth, and the fifth and sixth pair of rows are at sub-, near-, and supercritical chamber pressures, respectively. In the first, third, and fifth rows the acoustic driver is off, and in the second, fourth, and sixth rows it is on at approximately 3 kHz. The framing rate was 18 kHz, producing a time interval of $55.6 \mu\text{s}$ between the frames. Previously reported observations by Davis and Chehroudi [32] that the effect of the acoustic field was less under near- and supercritical pressures are still valid. However, the jet oscillations in the acoustic field under near- and supercritical conditions seen in

Fig. 4.11 (using high-framing-rate camera) were not previously detected because of the low-framing-rate camera used in the early report [32].

Not immediately obvious in Fig. 4.11, but seen when played as a movie, the structures in the far-field background of the frame begin to oscillate laterally at the same frequency of the acoustic driver. One can measure the magnitude of these velocity fluctuations from the movies. Assuming that the acoustic wave in the chamber is a plane wave, the estimated pressure fluctuations from these measurements agreed with previously-measured pressure fluctuations. Details of the quantitative velocity measurements are discussed later in this chapter.

Surprisingly, at the subcritical pressures, the top two rows of Fig. 4.11, droplets are not visible, something one might expect to see under subcritical pressures. The inability to visualize droplets can be attributed to several factors. First, the resolution of the images is low, and only the largest droplets would be visible. However, because of the high velocity ratio, about 9.1, atomization is expected to be quite good and only small droplets would be produced. Also, the temperature of the outer-jet is about 96 K warmer than the inner-jet, which produces rapid vaporization of these small droplets.

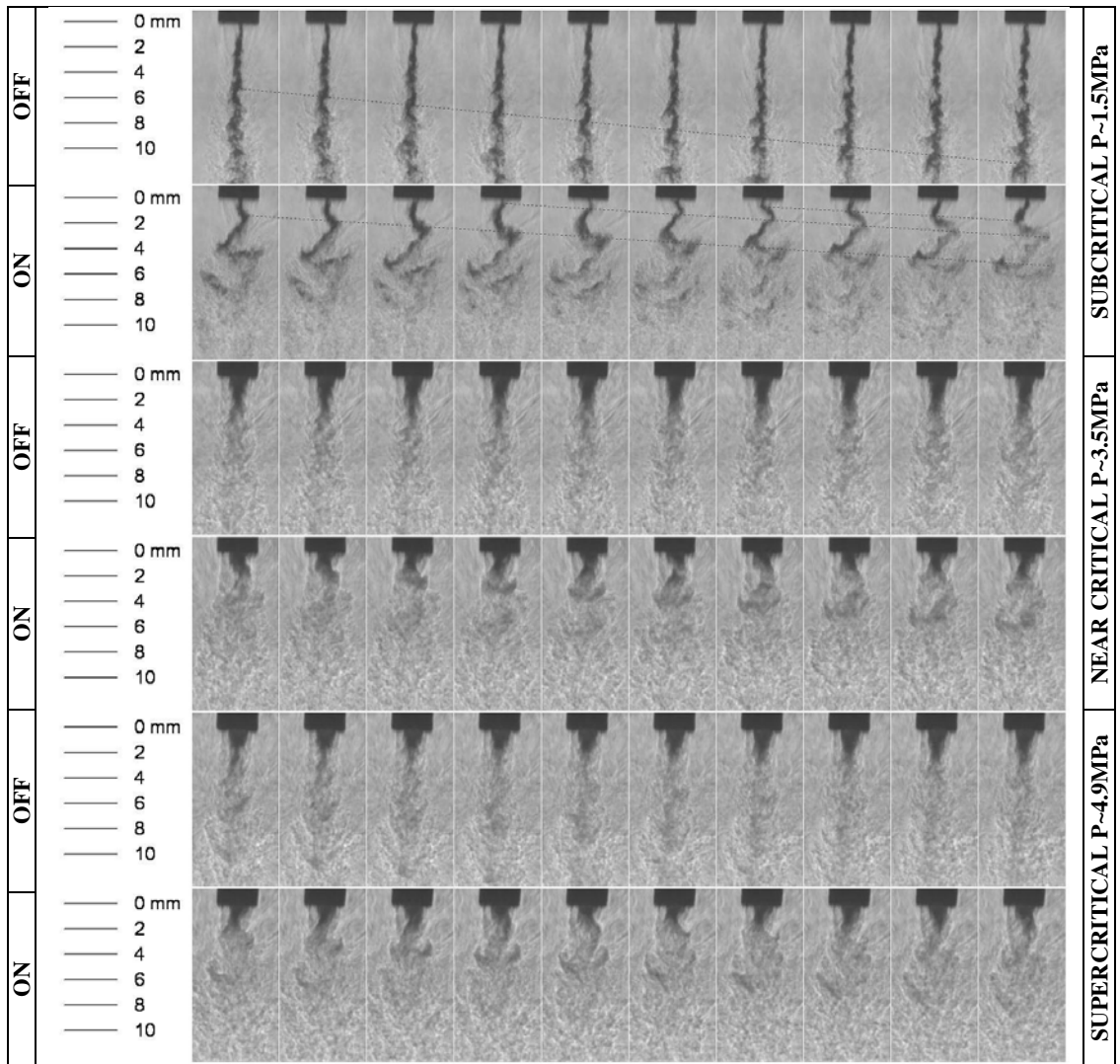


Figure 4.11: Consecutive frames from high-speed shadowgraph images of case 3, 7, and 11 (from Table 4.1) with the acoustic driver turned on and off. Time increases from left to right with an interval of $55.6 \mu\text{s}$ between frames. The first two rows are at a subcritical chamber pressure ($\sim 1.5 \text{ MPa}$, case 19 of Table 4.1), the third and fourth rows are at a near-critical chamber pressure ($\sim 3.5 \text{ MPa}$), and the fifth and sixth rows are at a supercritical chamber pressure ($\sim 4.9 \text{ MPa}$). The acoustic driver is off for the first, third, and fifth rows and on for the second, fourth, and sixth at $\sim 3 \text{ kHz}$.

4.4 Characterization of Acoustic Wave – Jet Interaction Mechanism

As seen from the images in the previous section, the acoustic waves can have a profound effect on the behavior of the jet. The intent of this section is to document and characterize this interaction.

4.4.1 Acoustic Pressure Measurement

Pressure measurements were made under warm, ambient temperature conditions in the inner-chamber with a piezoelectric pressure transducer described in Chapter 3. The pressure transducer was traversed through the inner-chamber in order to map the variations of the acoustic pressure in the chamber at the first resonance frequency of 2.80 kHz under these conditions. Figure 4.12 is a plot of the root-mean-square (RMS) amplitude of the acoustic pressure variations in kPa on the left axis, and in dB using the standard reference pressure of 20 μ Pa on the right axis, versus the transverse distance measured from the centerline of the jet at the static chamber pressure of 1.49 MPa. The acoustic driver is located on the left side of the jet in this figure. Because of the limited range of the micrometer used for traversing the pressure transducer, and in order to be able to map the entire range of the inner-chamber, it was necessary to use a spacer bar. The right and left edges of the inner-chamber window are indicated by the dashed vertical lines, and for visual aid, the outer diameter of the injector's outer tube is indicated by the dotted vertical lines.

The mode shape suggested by the RMS of the acoustic pressure is not a pure standing wave arising from a sinusoidal source. The acoustic field shows some

asymmetry which can be seen through differences in the peak values. The amplitude of the acoustic pressure is large and finite everywhere that it was measured ranging from 2% to 7% of the chamber pressure, suggesting a potential for nonlinear wave effects. The injector is located at the minimum amplitude of the acoustic pressure field of about 183 dB. There is a step in the internal chamber where the inner-chamber window is attached to the mounting hardware. Kinsler et al. [77] state that the normal modes of an enclosure, which were based on the linear acoustic theory, can be altered significantly by changing the shape of the enclosure. The wavelength (λ) measured as the distance between the local maxima on either side of the injector is 69 mm, which is much larger than the characteristic length of the injector ($\lambda / D_1 \approx 135$), placing this in the long-wavelength limit.

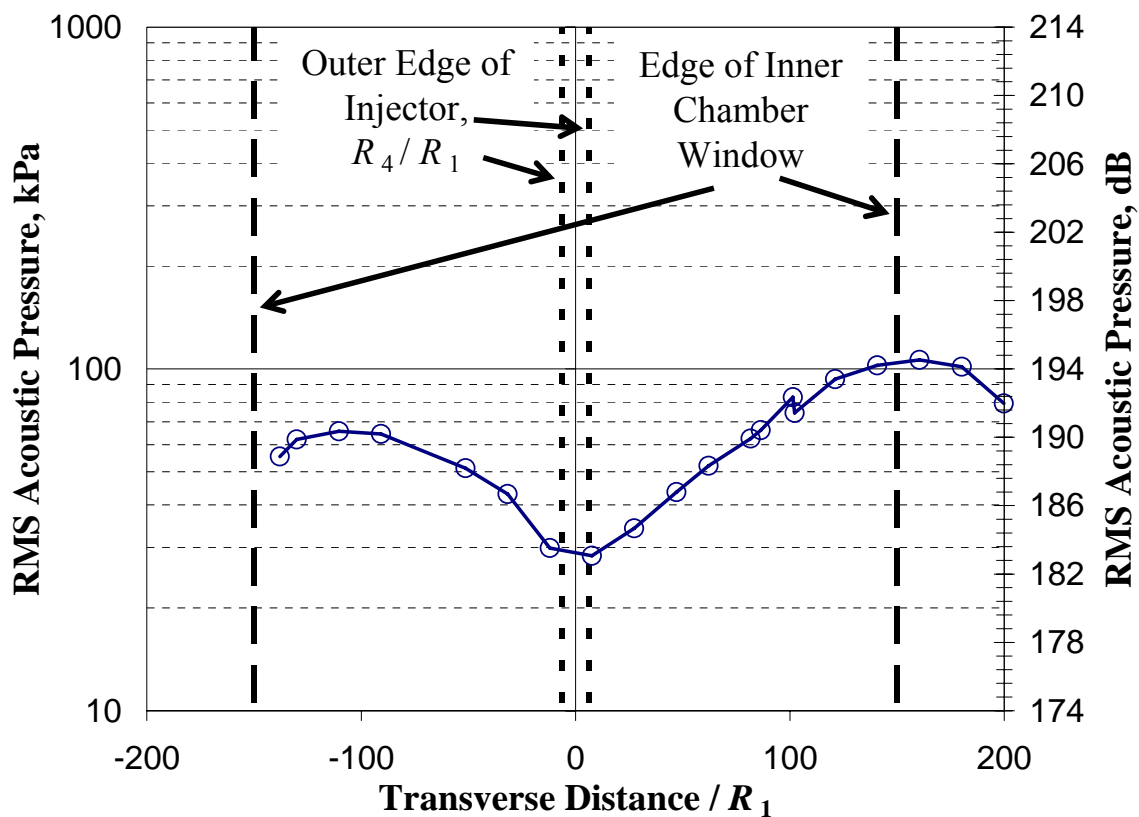


Figure 4.12: Variations of the RMS of acoustic pressure oscillations (in kPa on the left axis, and in dB on the right axis) along the length of the inner-chamber. The static chamber pressure was 1.49 MPa, and the temperature was ambient $\sim 300\text{K}$. The acoustic driver is located at the far left position.

It was found that if the acoustic driver operated at power levels below the maximum available with the equipment used in this work, the effects of the acoustic field on the jet were greatly reduced or not discernable. A plot of the RMS amplitude of the acoustic pressure oscillations at the first resonance frequency of the inner-chamber with chamber pressure is shown in Fig. 4.13. The acoustic driver was operated at its maximum power setting for the data in this figure as well as all data acquired in this work. In Fig. 4.13, the transverse position of the piezoelectric pressure transducer was 1.75 mm away from the jet centerline on the right side of the injector (using Fig. 4.12 as the reference for right and left sides). The reduction in the RMS of the acoustic pressure oscillations with an increase in chamber pressure was due to increased density of the chamber fluid considering that a constant input power was supplied to the driver. Details of this statement are discussed in section 4.4.3 below.

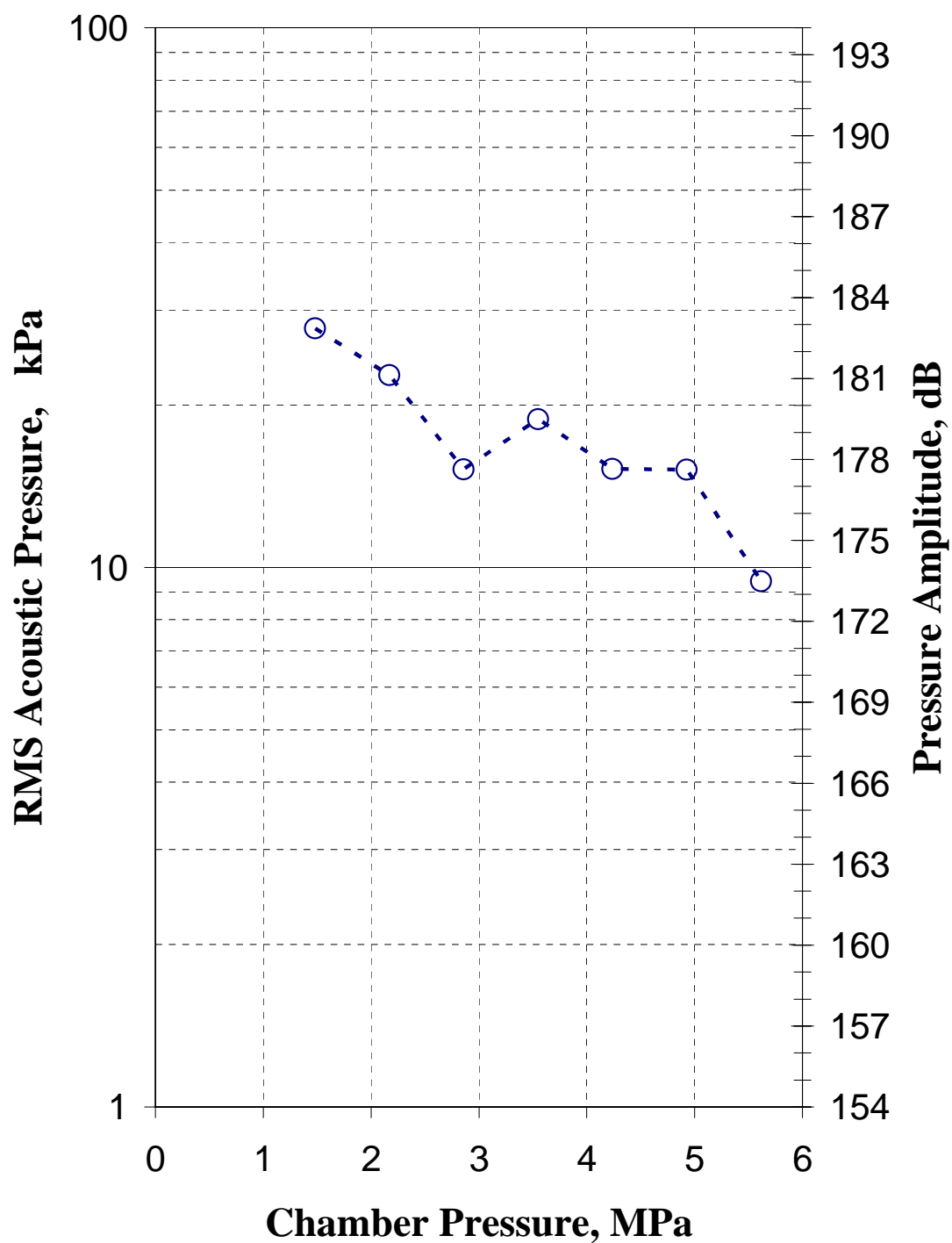


Figure 4.13: Variation of the RMS of the acoustic pressure with the chamber pressure, measured 1.75 mm to the right of the injector centerline in the direction away from the acoustic driver.

4.4.2 Acoustically-Driven Mode of the Shear-Coaxial Jet

The oscillatory mode of the jet was expected to be three dimensional and possibly helical by inspection of the movies of the type used to construct Fig. 4.11. Many phenomena in nature are three dimensional, and a natural instability mode of a jet can be helical. Particularly in this case, the “cusp-shaped” structures, formed from the dense dark-core fluid when approaching the shear layer between the outer-jet and the chamber fluid, suggested that the mode may be helical. Movies of the acoustically-excited jet, viewed perpendicular to the acoustic velocity direction, can only capture a portion of the information. An analogy, albeit crude, can be made to that of a spinning string. If one holds a given length of a string at one end and spins it (helically), while looking only perpendicular to the length of the string with one eye closed (to eliminate depth perception), then the string would appear to have a “cusp-like” structure. However, upon oscillating the end of the string with a “back and forth” motion (as opposed to spinning) and viewing the string in the same manner, the “cusp-like” structure is not observed. Only by looking at the string with both eyes open is that the true behavior of the string is revealed. Therefore, it was necessary to view the jet with two synchronized high-speed cameras to reveal the true modal behavior of the jet.

The two phantom cameras were synchronized, oriented orthogonal to one another as described in Chapter 3, and then images of the jet were taken. One camera viewed the jet perpendicular to the acoustic velocity fluctuations and the other parallel, or pointed into the acoustic velocity direction. Figure 4.14 consists of twelve sequential images in

each column, with direction of increasing time indicated by the arrows. The images in columns one and two show results for when the acoustic driver is off, and columns three and four indicate results when the acoustic driver is turned on at 3.03 kHz. In each row, the images in columns one and two are taken at the same time. Similarly, the images within the same row in columns three and four are taken simultaneously. The images in columns one and three view the jet perpendicular to the acoustic velocity fluctuations, and columns two and four see the jet parallel to it. The images taken perpendicular to the acoustic velocity fluctuations (columns one and three) are shadowgraphs, but images viewed in the parallel direction are forward-illuminated. A different light configuration for the parallel case was required because of the location of the acoustic driver which was blocking the optical access for back-illumination. This accounts for the differences in the background and the outer-jet region of the flow seen between the two cases in Fig. 4.14. The chamber pressure of the jet in Fig. 4.14 was 1.57 MPa (subcritical). In these tests, it was necessary to reconfigure the chamber by replacing the traversing thermocouple assembly with a window in its opening to view the jet in the direction parallel to the acoustic velocity. Therefore, no exit-plane temperature measurements were made and consequently the values for density, velocity ratio, and momentum flux ratio are not as accurate as the other measurements reported in this work. The outer-to-inner-jet velocity ratio and momentum-flux ratio are estimated to be 10.4 and 4.6, respectively.

Comparing the jets in the first two columns of Fig. 4.14, with the acoustic driver off, periodic structures in the jet are visible, which are associated with the pulsating or superpulsating sub-mode of atomization in both viewing directions. However, upon exciting the jet, a large-scale sinusoidal structure of the dark core was observed only

when viewed perpendicular to the acoustic velocity direction. Viewing the jet in the parallel direction does not reveal the same large-scale oscillations of the core. This suggests that oscillatory motion of the jet is predominantly in the direction of the acoustic velocity direction and no helical mode exists. Some three-dimensional movement of the core does occur, but these motions do not take place in the same periodic manner as do the jet oscillations in the direction of the acoustic velocity. The large-scale oscillations of the dark core seen in the third column of Fig. 4.14 are periodic and correspond to the acoustic driving frequency.

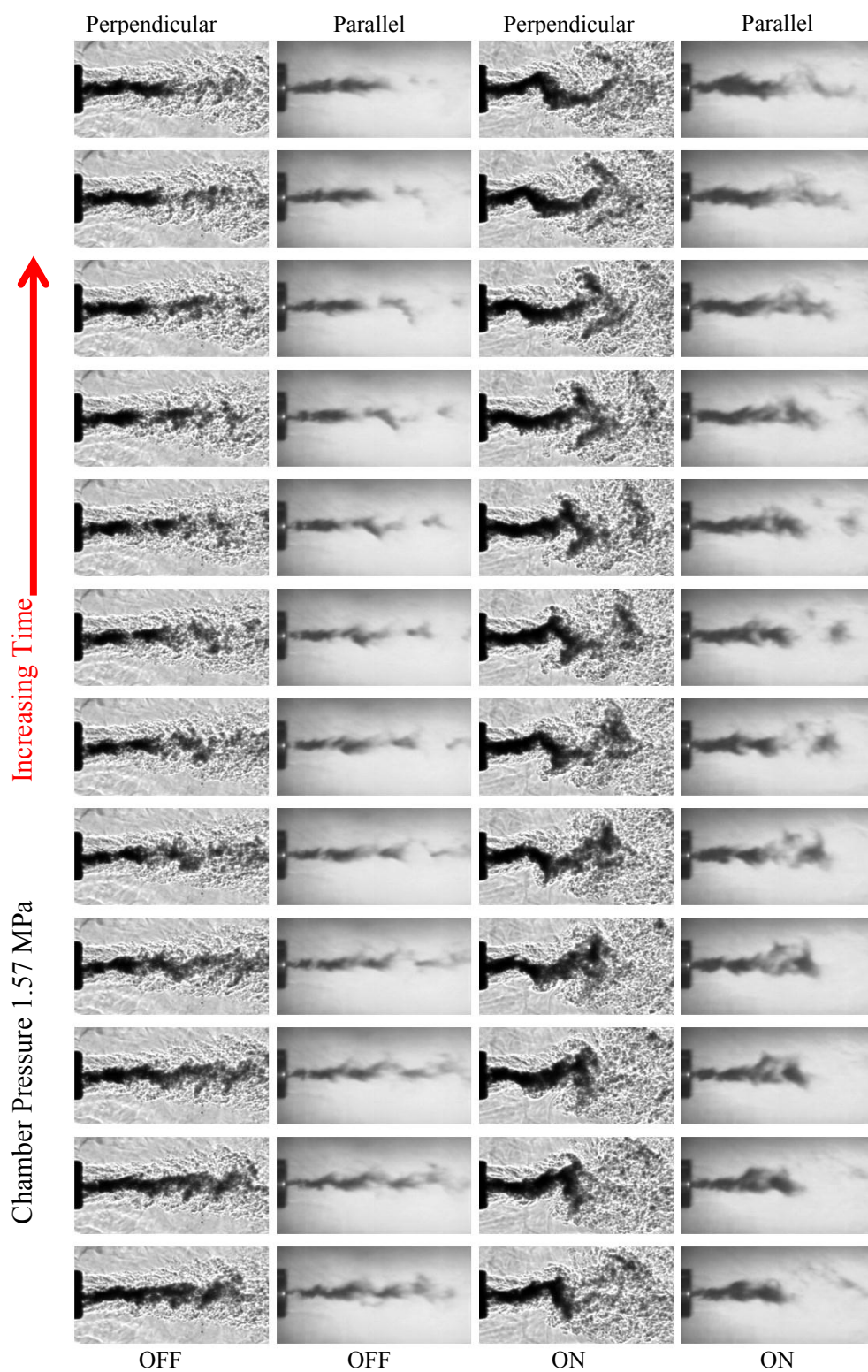


Figure 4.14: Synchronized images viewed both perpendicular and parallel to acoustic velocity direction. Columns 1 and 2 acoustic driver is off, 3 and 4 on at 3.03 kHz.

By changing the driving frequency to the second resonance frequency of the inner-chamber a decrease in the wavelength defined by the core of the jet is observed. Figure 4.15 is composed of six sequential frames taken at 18 kHz of the shear-coaxial jet at the same conditions with the acoustic driver turned off in the first column, on at 2.98 kHz in the second column, and on at 5.16 kHz in the third column. A wavelength, Λ , can be defined as the distance between the peaks of the sinusoidal structure formed by the dark core of the jet. When the frequency of the acoustic driver was increased to the second resonance mode, the wavelength, Λ , of the dark core decreased. For the images a wavelength could be identified from the core of the jet, the mean wavelength was always shorter for the higher frequency mode than the lower one.

The characteristic time for a fluid particle to move from one peak to the next peak, τ_Λ , should be given by the distance traveled, which is approximately, Λ , divided by some characteristic velocity, u . The acoustic time scale is given by the time period for one cycle, f^{-1} , or inverse frequency. If indeed the acoustic driving force is the cause for the oscillation of the core, the ratio of these two time scales, a Strouhal number, $St = \Lambda f / u$, should be unity. A difficulty with this relationship is the determination of an appropriate velocity scale, u . In the absence of such a velocity scale, a ratio of St evaluated at two frequencies at the same velocity conditions of the jet, should be constant. Measuring Λ from the images is not always easy to perform, particularly at near- and supercritical chamber pressures. Therefore, measurements were made from the subcritical pressure jets from 30 images where the wavelength could be measured on most images to within ± 10 pixels accuracy.

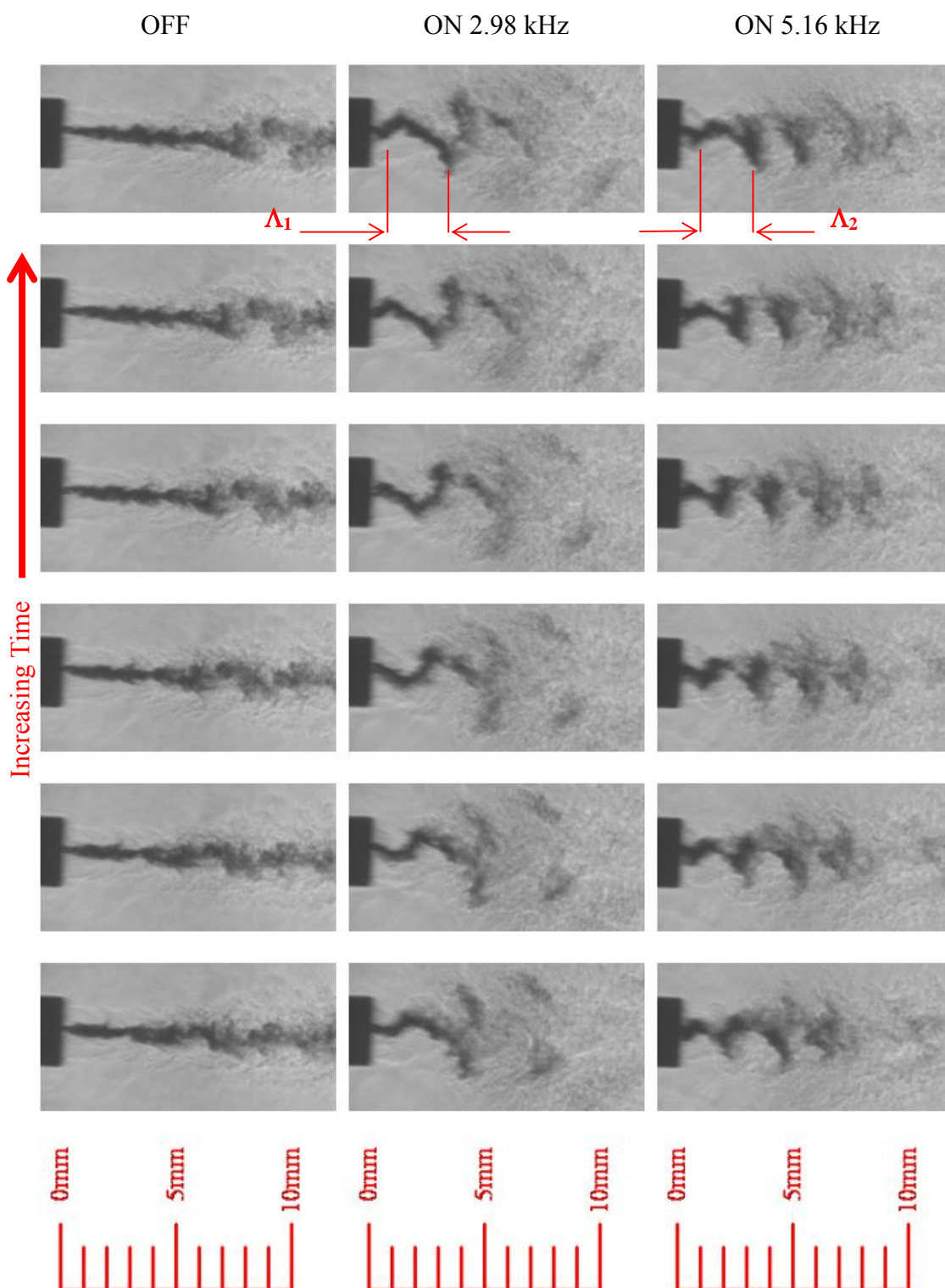


Figure 4.15: Consecutive images framed at 18kHz of case 3 of Table 4.1. Column 1 acoustics off, column 2 acoustics on at 2.98 kHz, column 3 acoustics on at 5.16 kHz.

Figure 4.16 is a ratio of the St for the jet at the same flow conditions, evaluated at the second resonance frequency to that of the first resonance frequency. As described above, this ratio should be a constant if the acoustic driver is controlling the oscillation of the core. The error bars on the figure represent the n^{th} order uncertainty analysis (as described in the beginning of this chapter) for 30 images taken at a 10 Hz sampling rate while the jet was excited at the two resonance frequencies of the inner-chamber. Although this only represents two frequencies and results carry large error bars, with the exception of one point, the ratio of the averaged St evaluated at the two frequencies is constant (mean value of ~ 1.4) at various velocities of the jet to within $\pm 25\%$.

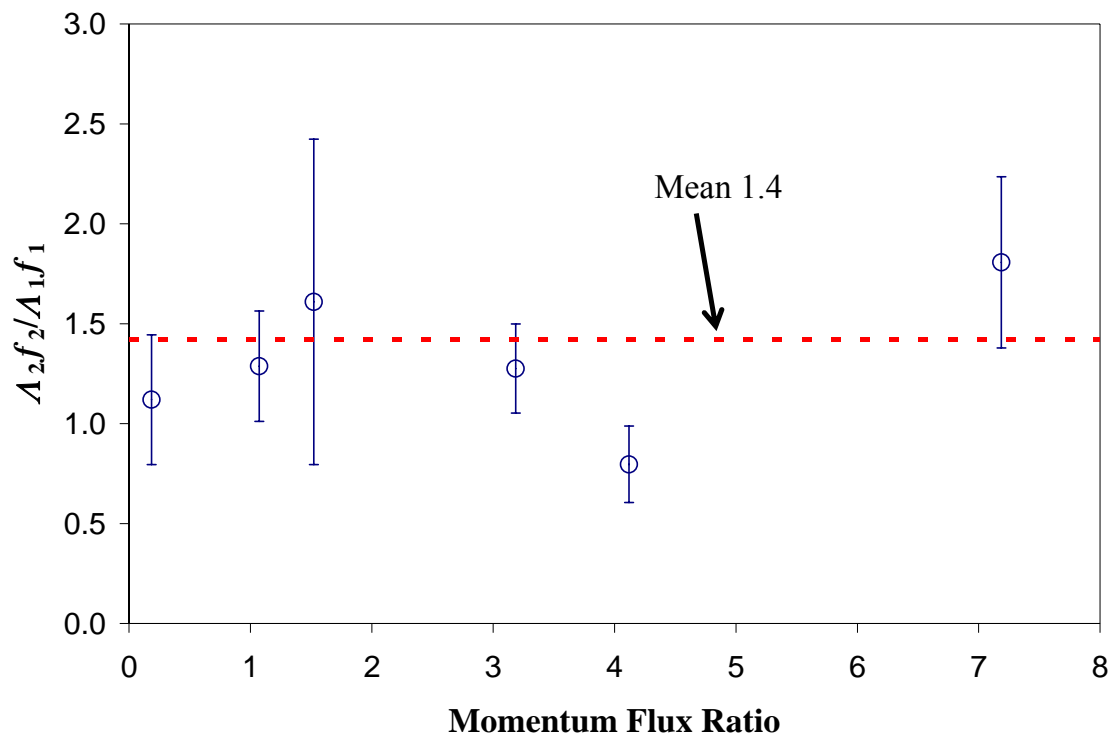


Figure 4.16: Ratio of the wavelength measured from the dark core of the jet multiplied by the frequency of the acoustic driver for the second resonance frequency (subscript 2) to the first resonance frequency (subscript 1) as a function of momentum flux ratio.

4.4.3 Acoustic Velocity Measurements

When viewing the movies of the jet, one can visually track fluid structures, possibly suggesting that velocity can be measured from these consecutive images. These structures in the fluid could be treated as though they were seed particles such as usually done with particle imaging velocimetry (PIV) or molecular tagging velocimetry (MTV). Velocity from unseeded flows has been attempted previously by Okamoto et al. [72] using a spatial cross-correlation between shadowgraph frames to determine motion, and ultimately velocity.

To compute velocity, the displacement of a fluid structure (i.e., Δx or Δy) and a time interval (Δt) between frames are required. Velocity is then simply approximated by $\Delta x / \Delta t$. A difficulty arises in obtaining the displacement of the fluid for an unseeded flow. From the movies taken in this work, structures are visible in the background and in the jet. Using a spatial cross-correlation (Eq. 4.3) between consecutive frames, these structures, which may or may not be identifiable to the human eye, can serve as particles from which displacements can be measured. However, the difficulty is that, unlike solid particles, fluid particles have the ability to dilate in addition to translation and rotation. Additionally, the shadowgraph is a line integral technique. Thus it not only obtains information from a very narrow slice of the flow field similar to PIV, but also collects data from the entire depth of field.

$$R_{p,q} = \frac{\sum_{i=0}^n \sum_{j=0}^m f_{i,j} g_{(i+p,j+q)}}{\sqrt{\left(\sum_{i=0}^n \sum_{j=0}^m f_{i,j}^2 \right) \left(\sum_{i=0}^n \sum_{j=0}^m g_{(i+p,j+q)}^2 \right)}} \quad (4.3)$$

Where,

f is the region of interest in the first image of size $n \times m$ pixels,
 g is the region of interest in the second image of size $n \times m$ pixels,
 p and q are the displacement of the $n \times m$ window in the second image in the x
and y directions, and
 R is the value of the spatial cross-correlation.

The method for determining the displacement at a given location starts with selecting an n by m region of interest (ROI) in an image (named, source window) centered at that location. Next, a region of interest of the same size in an image taken at a later time, but displaced from the first image ROI (or, source window) by (p,q) (named, search window) is selected, and a correlation coefficient, $R_{p,q}$ is computed. This process is repeated for various p,q combinations, moving the search window, creating a spatial cross-correlation for each p,q pair. The location of the maximum of the spatial cross-correlation (p_l, q_l) for the interrogation domain, is assumed to correspond to the displacement of the fluid particle (i.e., $\Delta x = p_l$ and $\Delta y = q_l$). The attainable maximum resolution is ± 1 pixel, although some authors [78] performing similar MTV measurements have reported subpixel accuracy by fitting high-order polynomials to the spatial cross-correlation space. However, in this work no physical reason presents itself to justify that the spatial cross-correlation space should vary as a high-order polynomial for improvement of the measurement accuracy.

Initially, the movies used to measure velocities were of low resolution (128 x 256 pixels) images because of the high-framing rate (18 kHz) and the limitations of the Phantom v.5 camera. Also, the available camera lenses used with this camera produced a scale for the image that was equal to 19.2 pixels per mm. The cross-correlation technique, described above, was applied to the acquired movies, a frame of which is represented by the image in Fig. 4.17 (a). Small boxes drawn on this image, each indicates a source box at which frame-to-frame fluid displacement was measured by calculation of the cross-correlations. The spatial cross-correlation space for the fifth source window from the left in Fig. 4.17 (a) is shown in Fig. 4.17 (b). To obtain reliable estimates of the displacements, it is necessary to have a strong gradient in cross-correlation space in two orthogonal directions. The spatial cross-correlation space shown in Fig. 4.17 (b) possesses the strongest gradients of all the source windows shown in Fig. 4.17. The shape of the spatial cross-correlation space indicates that only the transverse direction, the direction of the acoustic velocity, possesses a strong gradient, and thus the displacement measurements in that direction is reliable. It should also be mentioned that in PIV and MTV work, the spatial cross-correlation values are lower than what is obtained here. Nearly all values of the spatial cross-correlations for reasonable search distances is greater than 0.9. Generally, in a PIV approach, the field is illuminated with a laser sheet, producing images by elastic scattering from the particles. The resulting images are mostly black (low gray scale values), with some white particles (high gray scale values) producing typically lower values of the spatial cross-correlations. The images here, however, have intensities spanning the entire dynamic range, and correlating gray with gray yields higher spatial cross-correlation values.

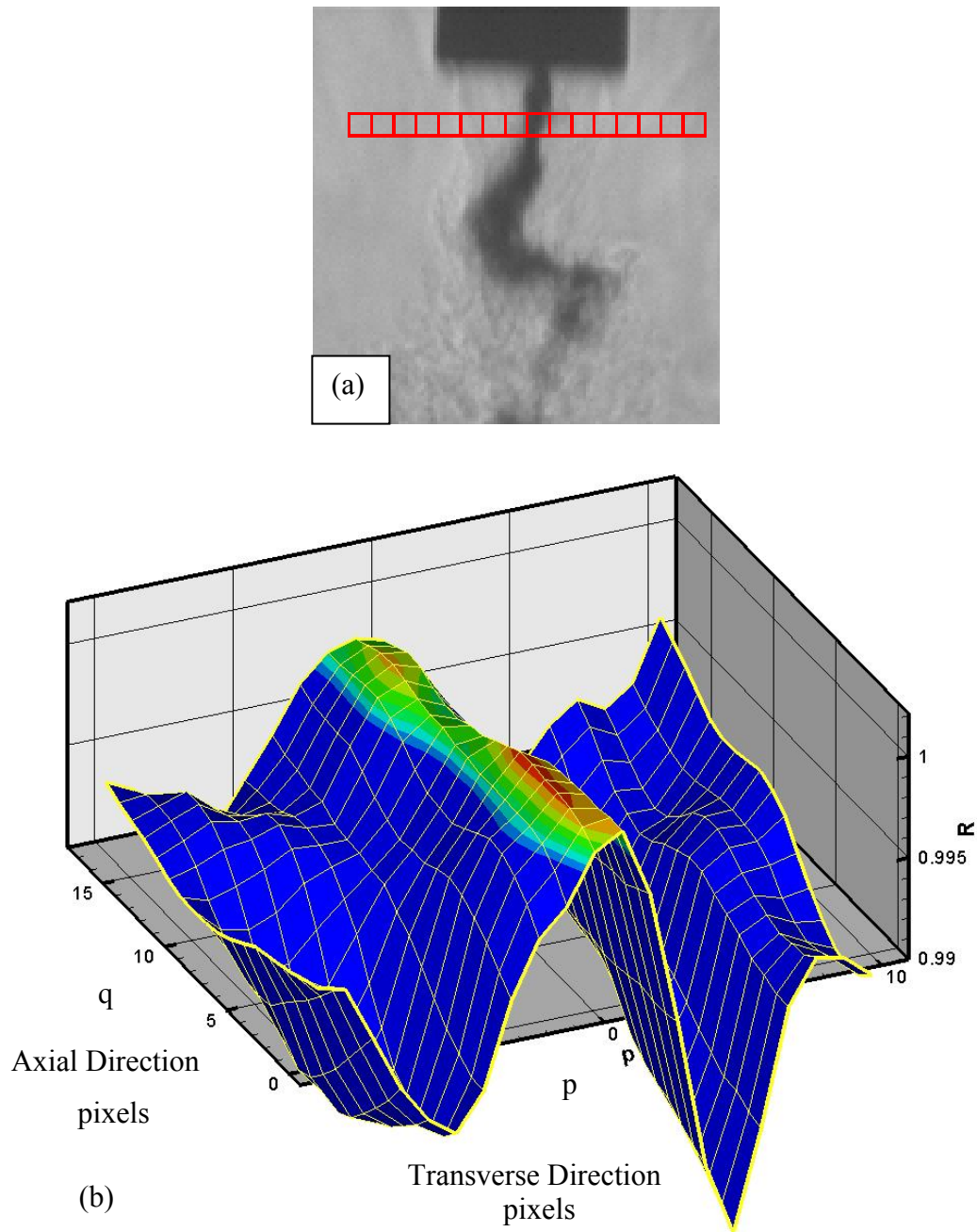


Figure 4.17: An image frame from a movie with boxes indicating the locations of the source windows for the spatial cross-correlation calculations (a), and (b) shows the spatial cross-correlation space for the fifth source window from the left in (a).

The transverse velocity measurements obtained from a sequence of images in a high-speed movie like that shown in Fig. 4.17 resulted in displacements with a very limited range, that is, -1 to 1 pixel. This is due to the resolution, field of view, and sampling time of the image frames. A balance between this range of motion and the sampling frequency needs to be made. On one hand, large displacements from longer times between frames enhances the dynamic range of the velocity measurement, but, on the other, it increases detection noise due to more distortion of fluid structures. Alternately, decreasing the sample time decreases the noise in velocity measurements, but can severely limit its dynamic range.

Despite the low dynamic range of the transverse velocity, a Fourier transform (128-point fast-Fourier transform (FFT) of the transverse velocity signal) was performed on the velocity. A power spectrum normalized by the dc component is shown in Fig. 4.18 for the first two resonance modes of the chamber at (a) 3.06 kHz and (b) 5.16 kHz, respectively. Evident from the large peak of the power spectrum is that the transverse velocity in the chamber responds to the acoustic driver at the same frequency, see Fig. 4.18 (a). At the higher resonance mode (Fig. 4.18 (b)), a measurable peak is observed at the driving frequency of 5.16 kHz. The sampling frequency (i.e., the image framing rate) was 18 kHz, resulting in only about 3.5 samples per cycle at 5.16 kHz. Consequently, a small peak due to aliasing appears at half the driver frequency.

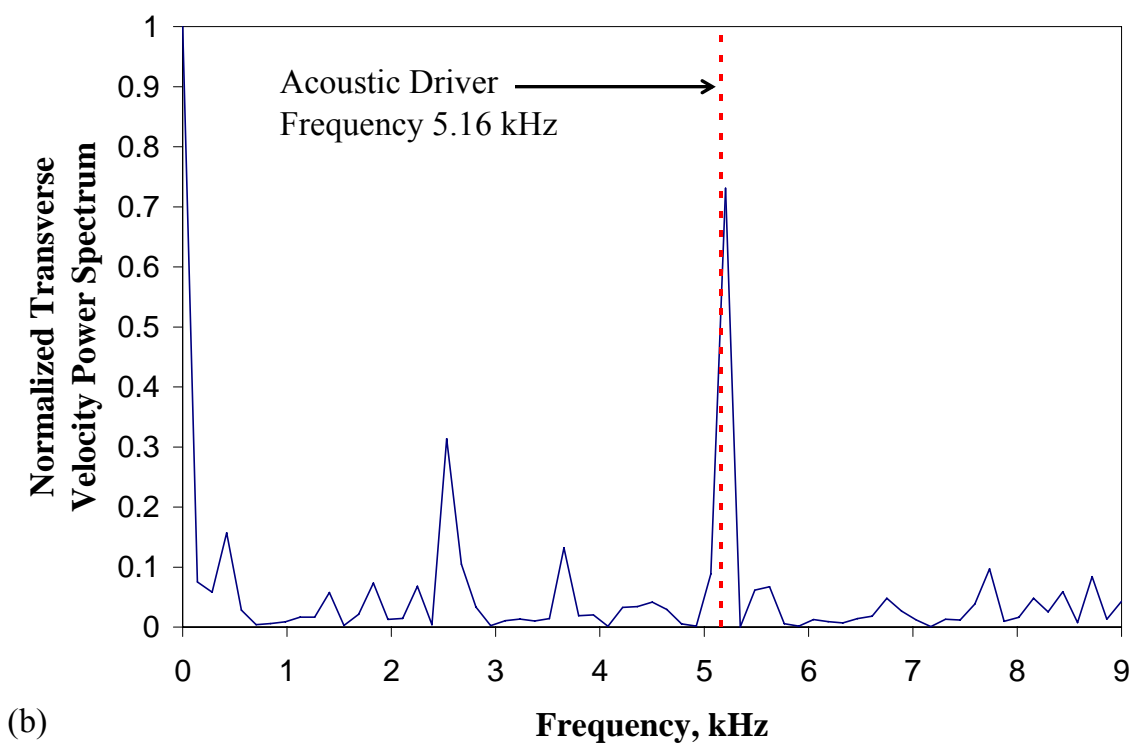
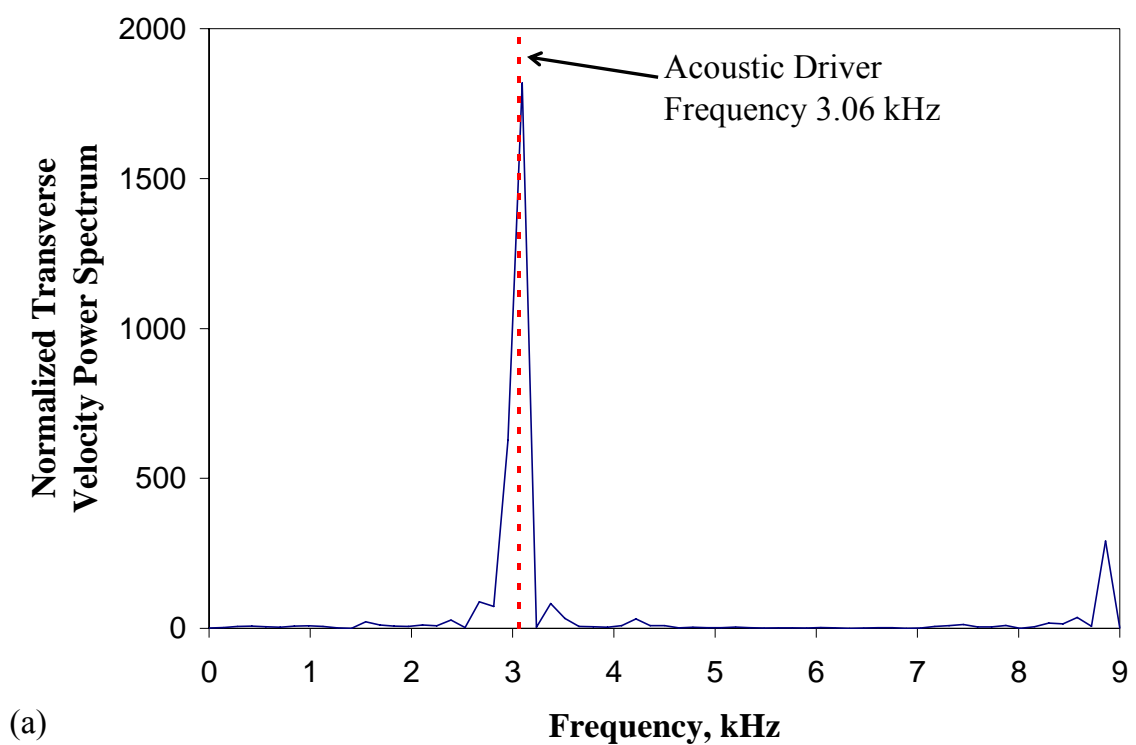


Figure 4.18: Power spectrum of the transverse velocity signal normalized by the dc component. The acoustic driver frequency was (a) 3.06 kHz and (b) 5.16 kHz, respectively.

Upon obtaining a Phantom v.7 camera, which has enhanced resolution at higher framing rates and a lens capable of increasing the magnification, the dynamic range of the velocity measurements was increased without suffering increased detection noise in the velocity signal. Additionally, the spatial cross-correlation space improved by showing a stronger gradient in two orthogonal directions. Figure 4.19 is the spatial cross-correlation space of the increased magnification and resolution image. This configuration gives an image scale of 62.4 pixels per mm, an increase of more than three times over the image shown in Fig. 4.17 (a). Improvements in the dynamic range of the transverse velocity measurements resulted in increased range of displacement to ± 4 pixels, at the same 18 kHz sample rate for subcritical jet, at the expense of a decreased field of view. From these improved velocity measurements, it was estimated that the fluid element displacements can be measured to within ± 1 pixel. The source window was selected to be square in shape and its size for the rest of the velocity measurements was 21 by 21 pixels. A study of the size of the square source window was done by varying its dimension from 3 by 3 pixels to 33 by 33 pixels. Once the size of the square was greater than 15 by 15 pixels, the velocity signal, in the form of displacements, did not change by more than the ± 1 pixel. The source window size for the rest of the velocity measurements was then set at 21 by 21 pixels. Rectangular pixel windows were not investigated.

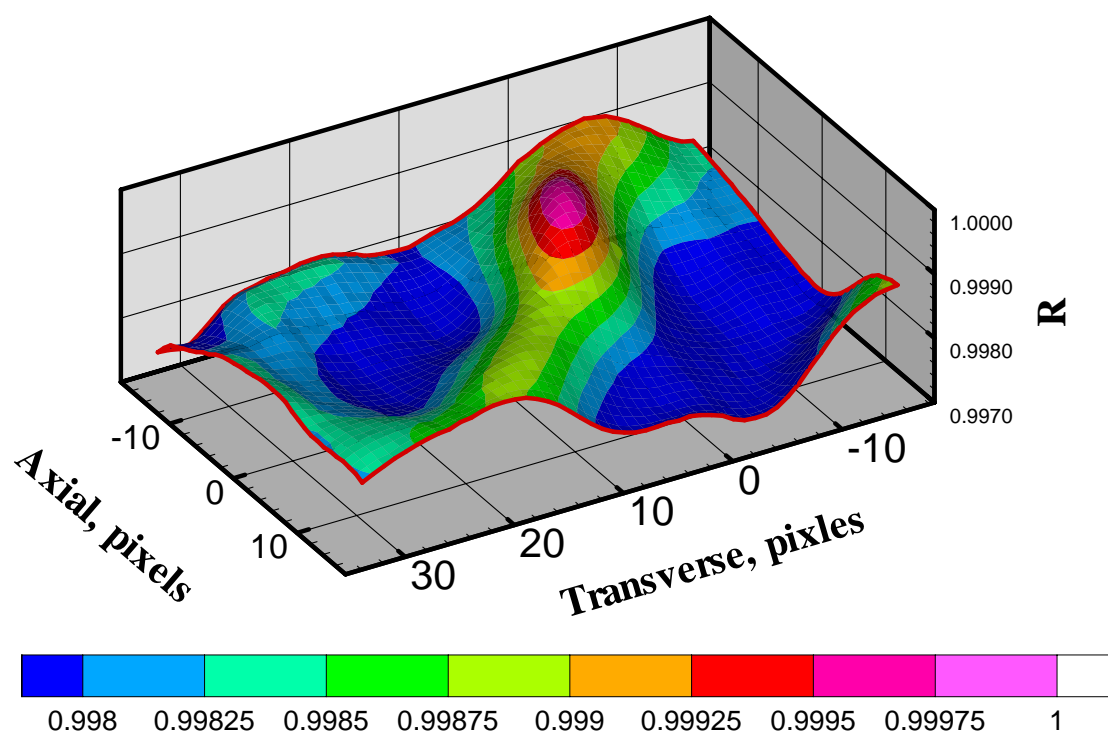


Figure 4.19: Spatial cross-correlation space for image resolution of 512 x 256.

From displacement measurements of chamber fluid elements, the transient start-up phase of the acoustic driver was captured. Figure 4.20 shows the start-up transient of the transverse velocity fluctuations of the chamber fluid for, (a) a subcritical chamber pressure of 1.49 MPa and, (b) for a near-critical chamber pressure of 5.36 MPa. The positive velocity points in the direction of the push stroke of the acoustic driver (i.e., left to right in Fig. 4.12), and the negative velocity direction is in the pull stroke. At the subcritical pressure (Fig. 4.20 (a)), the behavior of the acoustic velocity resembles that of a transient pressure trace for the onset of a combustion instability, resulting in a limit-cycle. A bias in the maximum amplitude exists in the positive direction by equivalent of one more pixel of motion in the images. Because the uncertainty of the measurement is ± 1 pixel, the conclusion from this observation is not certain. However, at times greater than about 23 ms after the start of the acoustic driver, the measured amplitude does not change. At the near-critical chamber pressure (Fig. 4.20 (b)), the transverse velocity range is reduced to the equivalent of ± 1 pixel. Although the same optical arrangement was used at both pressures, most likely the amplitude of the acoustic wave was reduced at higher pressures, a subject further discussed in the next section. The first observable motion at both pressures, however, occurs within one frame of each other, at approximately 2.17 ms after the start of the acoustic driver.

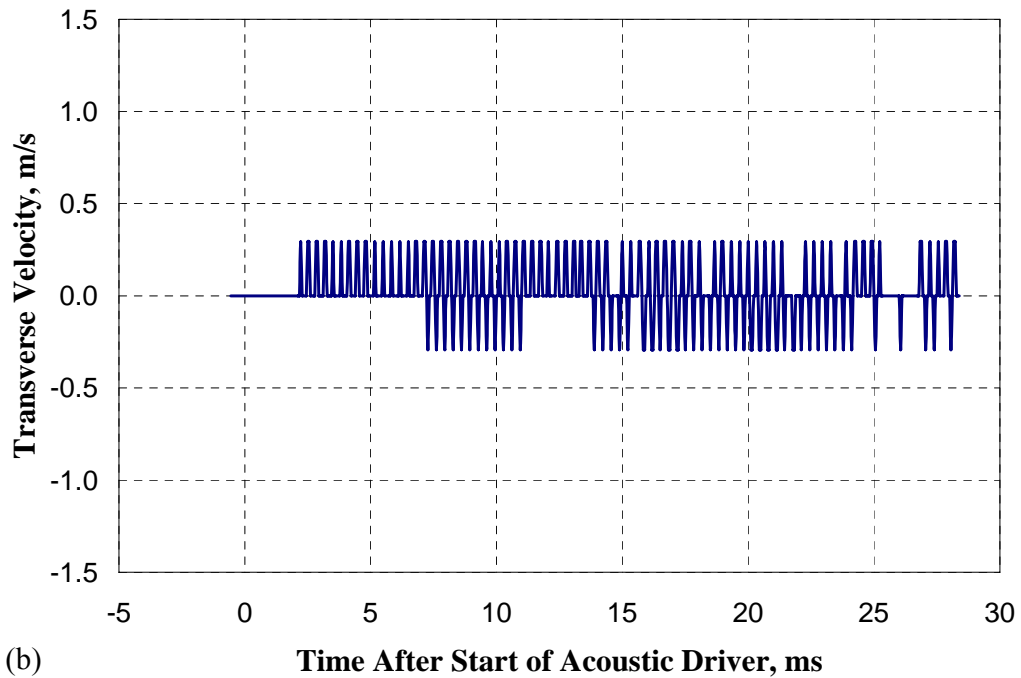
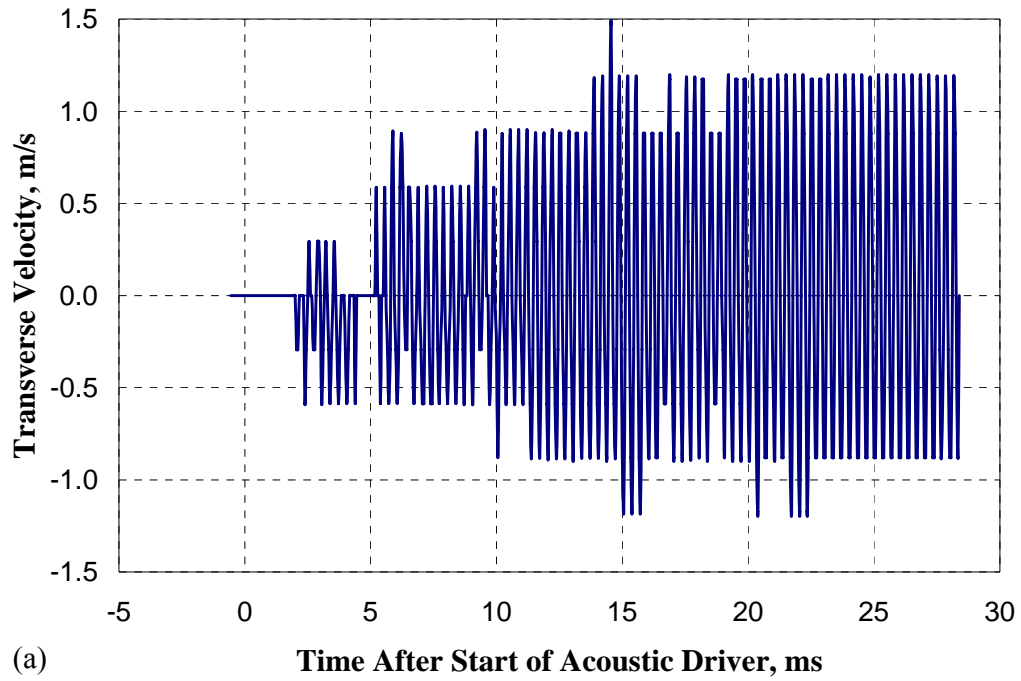


Figure 4.20: Transient transverse velocity after start of the acoustic driver, at chamber pressures of (a) 1.49 MPa and (b) 3.56 MPa, respectively. The acoustic driver frequency was (a) 3.01 kHz and (b) 3.04 kHz, respectively.

Because of the limited dynamic range of the system at the higher pressure conditions, the analysis of the velocity was restricted to a subcritical pressure. Figure 4.21 is the transverse velocity signal measured at an axial distance of $1.4 D_1$ downstream of the injector exit-plane and at transverse distances measured from the jet centerline of $4.86 D_1$ (in the chamber fluid), $2.24 D_1$ (at the edge of the outer-jet), and $0.73 D_1$ (at the edge of the inner-jet), moving toward the acoustic driver. These measurements were made from the same movie used to make the measurements in Fig. 4.20 (a), except about 100 ms after the limit cycle behavior was established. The transverse velocity measured in the chamber fluid (Fig. 4.21(a)), far from the influence of the jet, appears to be sinusoidal in nature. However, the velocities measured at the edge of the outer- and inner-jets, Figs. 4.21 (b) and (c), respectively, have a certain level noise superimposed on the sinusoidal variations, which is possibly due to the jet turbulence.

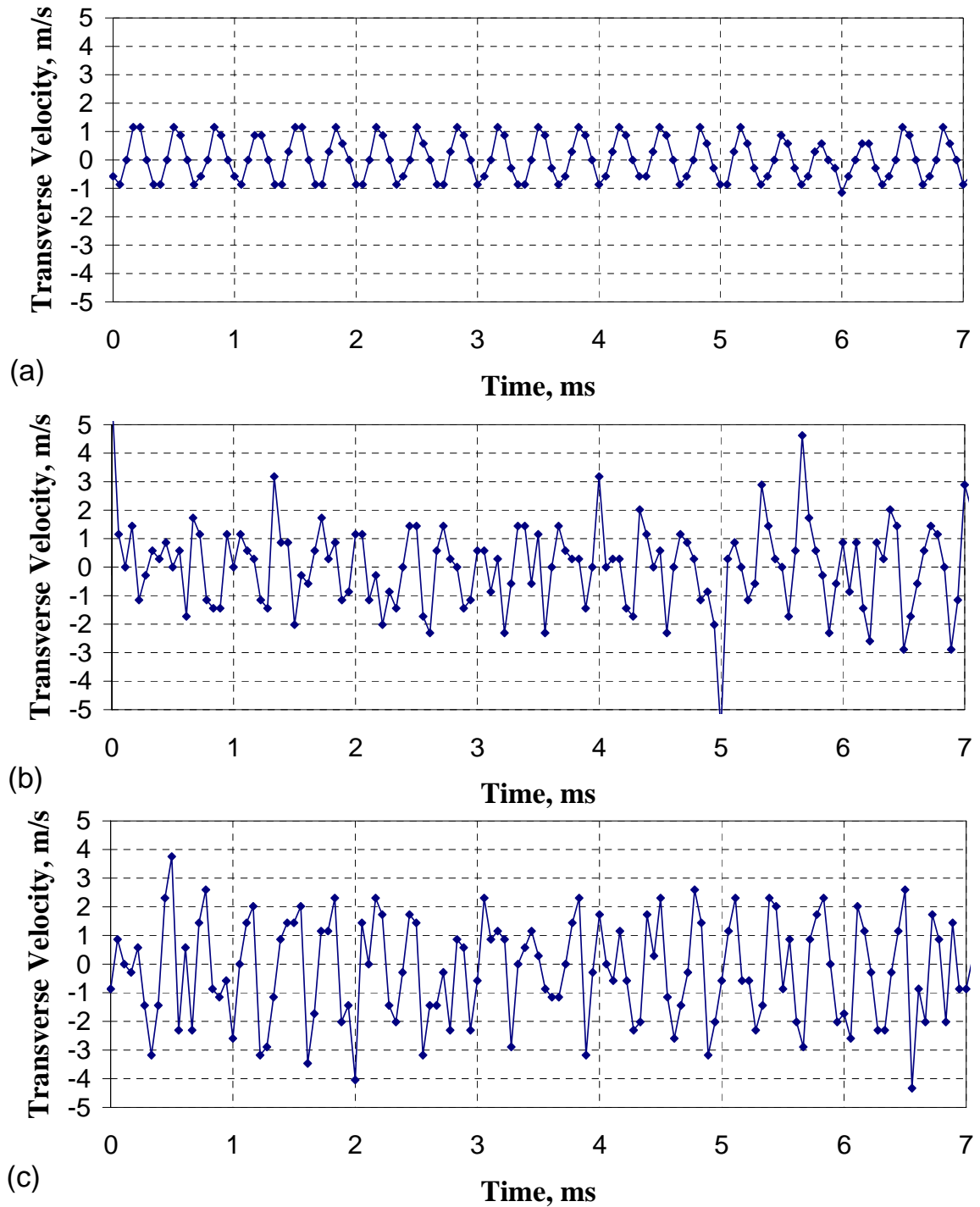


Figure 4.21: The instantaneous transverse velocity measured at $1.4 D_1$ downstream of injector exit-plane, at progressively closer radial distances to the injector centerline: (a) $4.86 D_1$ from the centerline of the jet in the chamber fluid, (b) $2.24 D_1$ from the centerline at the edge of the outer-jet, and (c) $0.73 D_1$ from the centerline at the edge of the inner-jet. The chamber pressure was 1.49 MPa.

Within the uncertainty of the measurements, the mean of the three transverse velocity signals shown in Fig. 4.21 is zero. The root mean square (RMS) of the transverse velocity (V_{RMS}) variations plotted versus the transverse position (x) is shown in Fig. 4.22. The RMS transverse velocity in the chamber fluid is lower than what is measured at the edge of either the outer-jet or inner-jet. It appears that V_{RMS} at the edge of the inner-jet is the largest, but, to within the uncertainty of the measurement, it can not be reliably determined to be different from the V_{RMS} at the edge of the outer-jet.

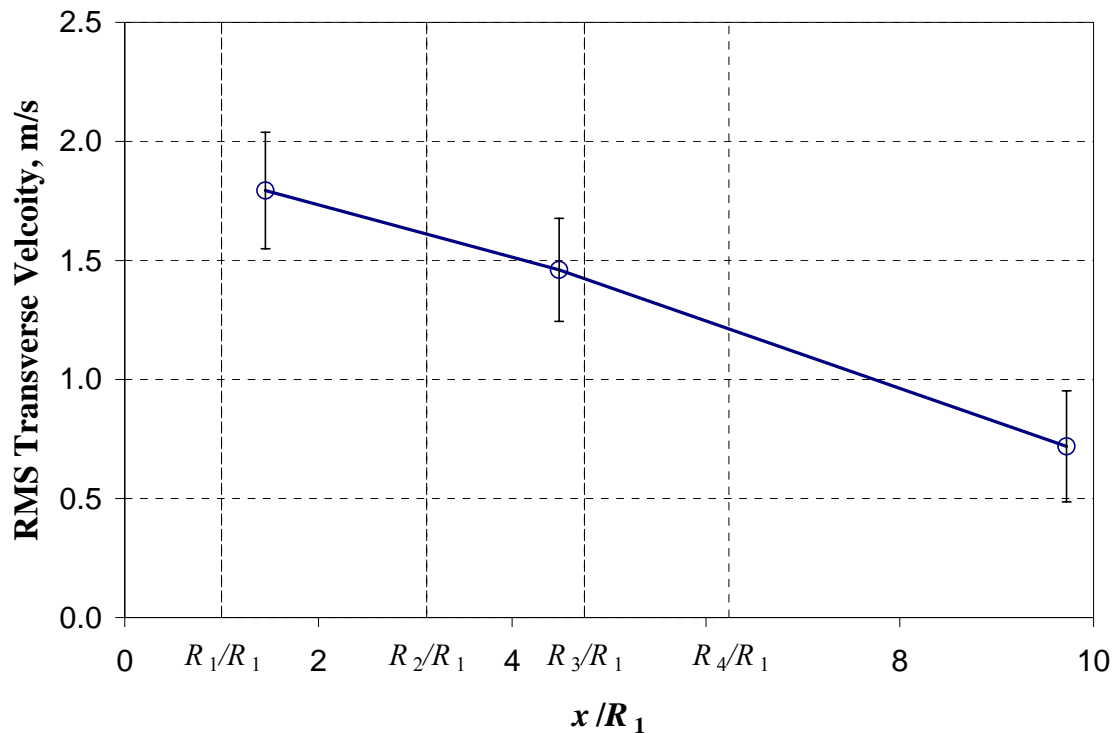


Figure 4.22: RMS of the velocity signal variations with transverse direction (x). The error bars on the figure correspond to the n^{th} order uncertainty as described in the beginning of chapter 4. The vertical gridlines are the four important radii of the shear-coaxial injector. The chamber pressure was 1.49 MPa.

The power spectra of the three velocity signals in Fig. 4.21, computed from a 128 point FFT, are shown in Fig. 4.23. All of the power spectra in Fig. 4.23 are normalized by the value at the peak value of the power spectrum of the velocity signal measured in the chamber fluid (Fig. 4.23(a)), located at the acoustic driver frequency. Evident in the power spectra is the fact that the maximum energy is contained at the frequency of the acoustic driver. The magnitude of the peak at the acoustic driver frequency increases at both the edge of the outer-jet and the edge of the inner-jet by about 1.75 and 2.8 times greater than that of the chamber fluid, respectively. A second harmonic peak is observed also in the power spectrum of the velocity signal measured at the edge of the outer-jet (Fig. 4.23 (b)), which is believed to be due to the noise and is not seen in the other spectra.

Analysis of the complex portion of the FFT allowed for phase angle determination between the velocity signals. At the axial distance of $1.4 D_1$ downstream of the injector exit-plane, the phase angle difference calculated between velocity signals at the frequency of maximum peak in the power spectra (i.e., the acoustic driver frequency) in the chamber fluid ($x/D_1 = 4.86$) and at the edge of outer-jet ($x/D_1 = 2.24$) was 155° , and the phase angle difference between the velocity measured in the chamber fluid and at the edge of the inner-jet was 70° . At this axial location, this indicates that the transverse velocities measured within the chamber fluid and at the edge of the outer-jet are almost completely out of phase.

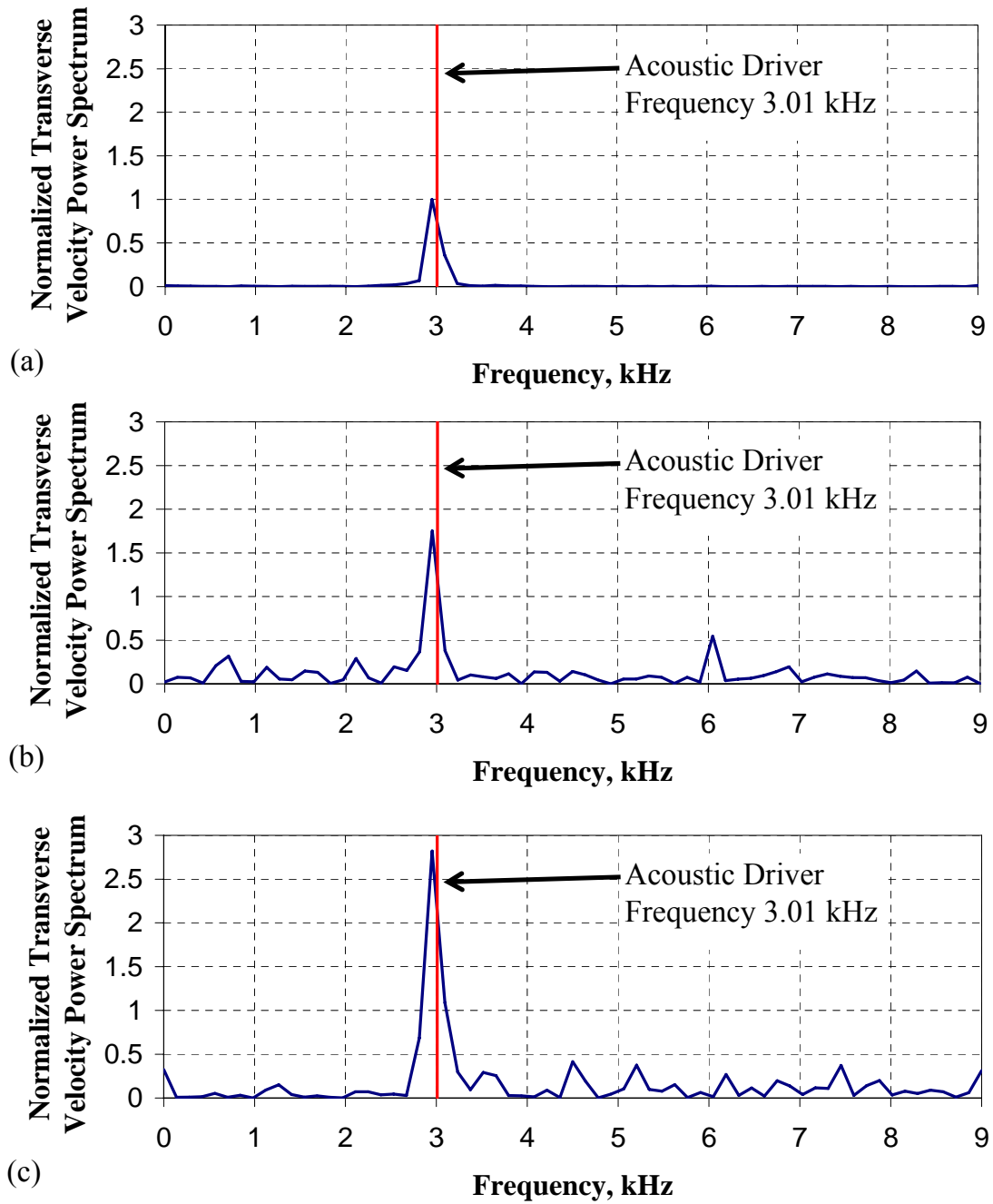


Figure 4.23: Power spectra of the acoustic velocity signals shown in Fig. 4.21 at distances from the centerline of the jet of: (a), $4.86 D_1$ in the chamber fluid; (b), $2.24 D_1$ at the edge of the outer-jet; and (c), $0.73 D_1$ at the edge of the inner-jet. The chamber pressure was 1.49 MPa.

Using the information from the measured variations of the acoustic pressure with chamber pressure shown in Fig. 4.13, the acoustically-induced velocity amplitude was computed by taking advantage of the simple relationship from linear acoustic theory for plane waves as shown in Eq. 4.4, using the characteristic acoustic impedance (ρc). In complicated geometries, where the wave may not be planar and with nonlinear acoustics, there is no guarantee that the relationship in Eq. 4.4 will be valid [77]. However, continuing along with this assumption, and using a relationship, derived in Kinsler et al. [77], between the averaged (integrated over one time period) energy density (\mathcal{E} , energy per unit volume) and the acoustic velocity amplitude shown in Eq. 4.5, one arrives at a possible explanation for the decay in amplitude of the acoustic pressure with increases in chamber pressure. Note the volume of the chamber and the supplied power to the acoustic driver were constant in this work. Therefore, from Eq. 4.5, one expects that the amplitude of the acoustic velocity to decrease with $\rho^{-0.5}$.

$$\mathcal{P} = \rho c \mathcal{U} \quad (4.4)$$

$$\mathcal{E} = \rho \mathcal{U}^2 / 2 \quad (4.5)$$

Where,

\mathcal{P} is the amplitude of the acoustic pressure,

\mathcal{U} is the amplitude of the acoustic velocity,

ρ is density,

c is the speed of sound, and

\mathcal{E} is the integrated energy density over one time period.

Figure 4.24 presents the acoustic velocity computed from two different methods: first, the pressure measurements (the circle symbols) and using Eq. 4.4, and second, the velocity measurement approach described earlier using images (the square symbols) with examples shown in Fig. 4.20. The solid line is a curve fit to velocity amplitude, which is Eq. 4.5 with the addition of a constant (κ) to account for the nonlinear and non-plane-wave effects and using the energy and the constant κ as the parameters. The dashed line is the curve fit to the same equation, but with a different energy and constant term for the velocity amplitudes measured from images.

It appears that the proposed functional form describes the decay of the velocity amplitude with increased chamber density as estimated through pressure measurements, see Fig. 4.24. However, the velocities measured from the images are somewhat lower. This is considered not a surprising effect because estimated velocities from the pressure measurements were performed under room temperature and computed using a linear theory. Because of the low dynamic range and the displacement uncertainty of ± 1 pixel, the higher-density point in Fig. 4.24, calculated using the velocity information in Fig. 4.20 (b), has a rather large uncertainty. Considering the velocity measurements from the images as a closer representation of the true values, estimates of the momentum of the acoustic wave can now be made, with \mathcal{E} and κ being 33 J/m^3 and -0.85 m/s , respectively. The estimation of the acoustic velocity should not be extrapolated to chamber densities outside the range measured here.

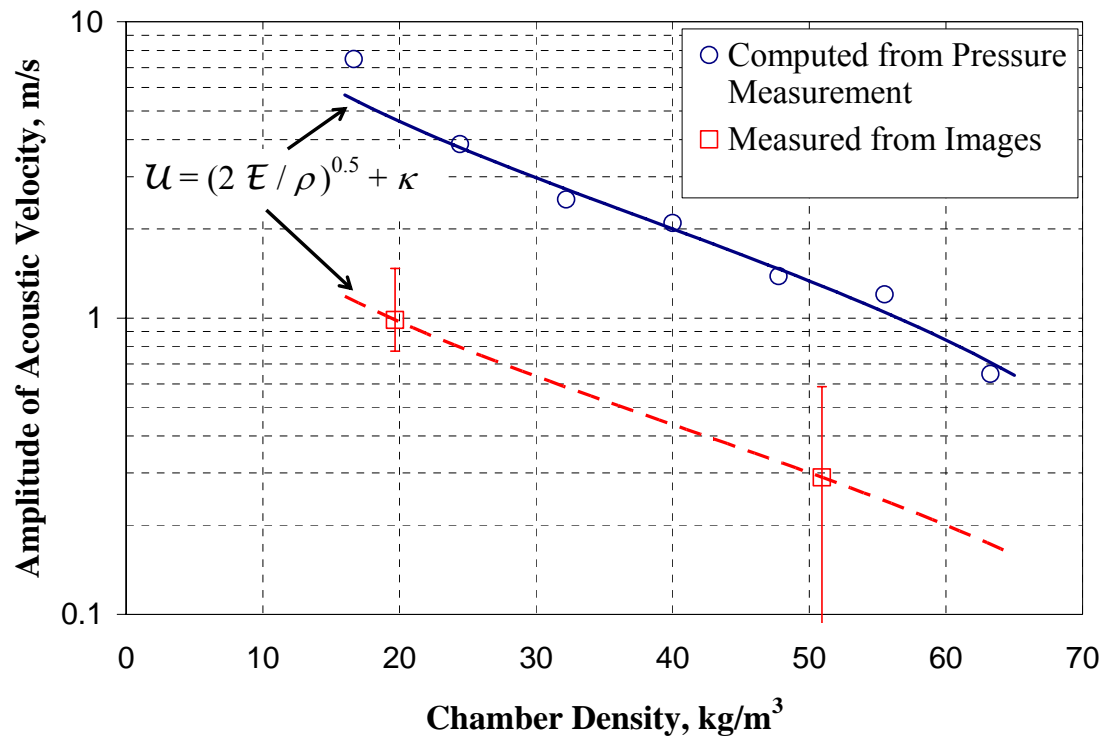


Figure 4.24: Amplitude of the transverse acoustic velocity fluctuations from the chamber pressure measurements (circle symbols) and directly measured from the images (square symbols). The solid and dashed lines represent curve fits using the equation indicated in the figure.

The estimates of the acoustic wave momentum flux ($\rho \mathcal{U}^2$), based on the chamber density and the computed amplitude of the acoustic velocity from images are shown in Fig. 4.25, plotted against the outer-to-inner jet momentum flux ratio. Also, the ratio of the acoustic momentum flux to that of the inner-jet and the outer-jet are shown in Fig. 4.26 and Fig. 4.27, respectively. The momentum flux of the inner-jet is essentially constant at a given pressure for the conditions tested in this work, hence explaining the similar appearance of Figs. 4.25 and 4.26. A decreasing trend seen in the acoustic-to-outer-jet momentum flux ratio with increases in the outer-to-inner momentum flux ratio is primarily due to increase in the outer-jet momentum flux. This plot is shown for ease of comparison between the momentum flux of the acoustic wave and that of the outer-jet. It is evident from these figures that the amplitude of the acoustic velocity fluctuations is highest at the lowest pressure conditions (i.e., low chamber density). This is consistent with the observed qualitative effect of the acoustic waves on the jet. The acoustic momentum flux is about an order of magnitude larger at the subcritical pressures than that under the supercritical pressure (see Fig. 4.25)

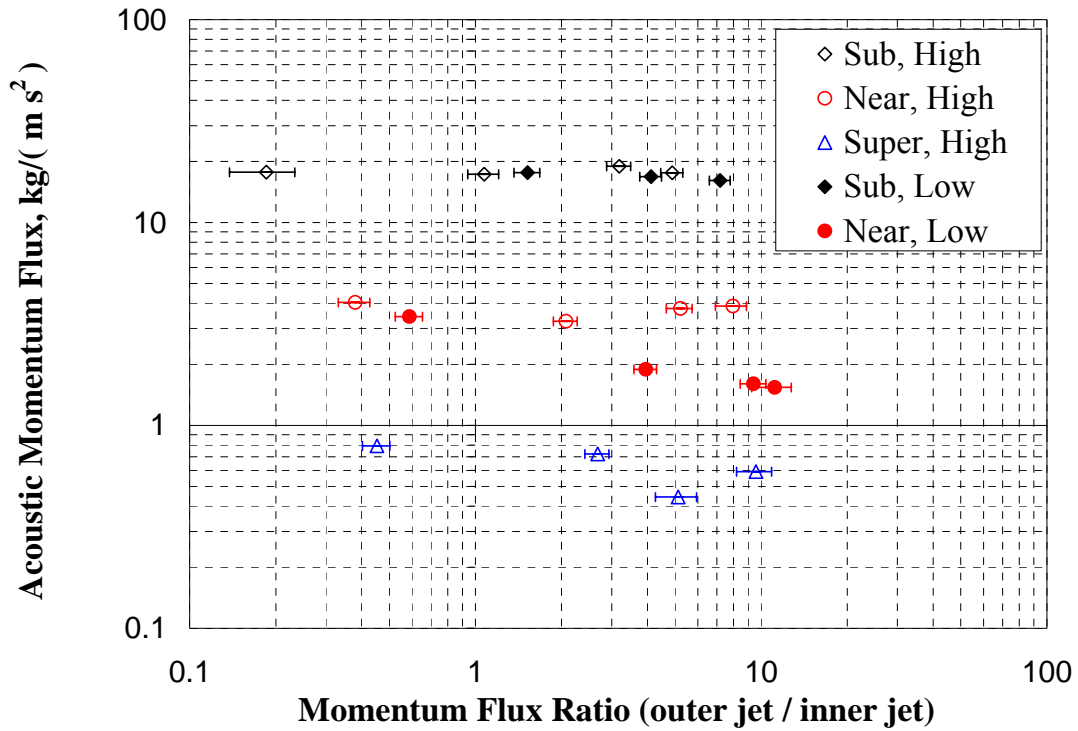


Figure 4.25: Variation of acoustic momentum flux ($\rho \mathcal{U}^2$) with the outer-to-inner jet momentum flux ratio. The words sub, near, and super in the figure inset correspond to subcritical, near-critical, and supercritical chamber pressure, respectively. The words “high” and “low” in the figure inset are for the nominal high and low outer-jet temperature cases. The hollow diamond symbols (“Sub, High”) are cases 1-4; the hollow circles (“Near, High”) are case 5-8; the hollow triangle symbols (“Super, High”) are cases 9-12; the solid diamond symbols (“Sub, Low”) are case 13-15; the solid circle symbols (“Near, Low”) are cases 16-19. The case numbers correspond to Table 4.1.

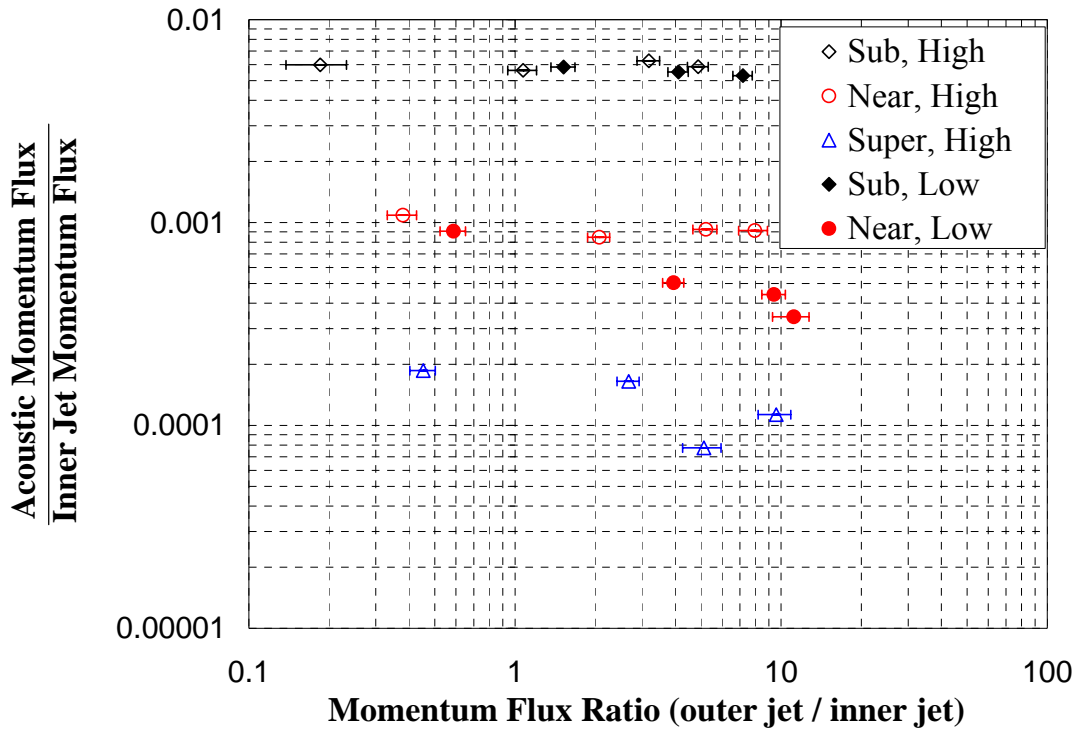


Figure 4.26: Variation of the ratio of acoustic momentum flux ($\rho \mathcal{U}^2$) to the momentum flux of the inner-jet with the outer-to-inner jet momentum flux ratio. The words sub, near, and super in the figure inset correspond to subcritical, near-critical, and supercritical, respectively. The words “high” and “low” in the figure inset are for the nominal high and low outer-jet temperature cases. The hollow diamond symbols (“Sub, High”) are cases 1-4; the hollow circles (“Near, High”) are case 5-8; the hollow triangle symbols (“Super, High”) are cases 9-12; the solid diamond symbols (“Sub, Low”) are case 13-15; the solid circle symbols (“Near, Low”) are cases 16-19. The case numbers correspond to Table 4.1.

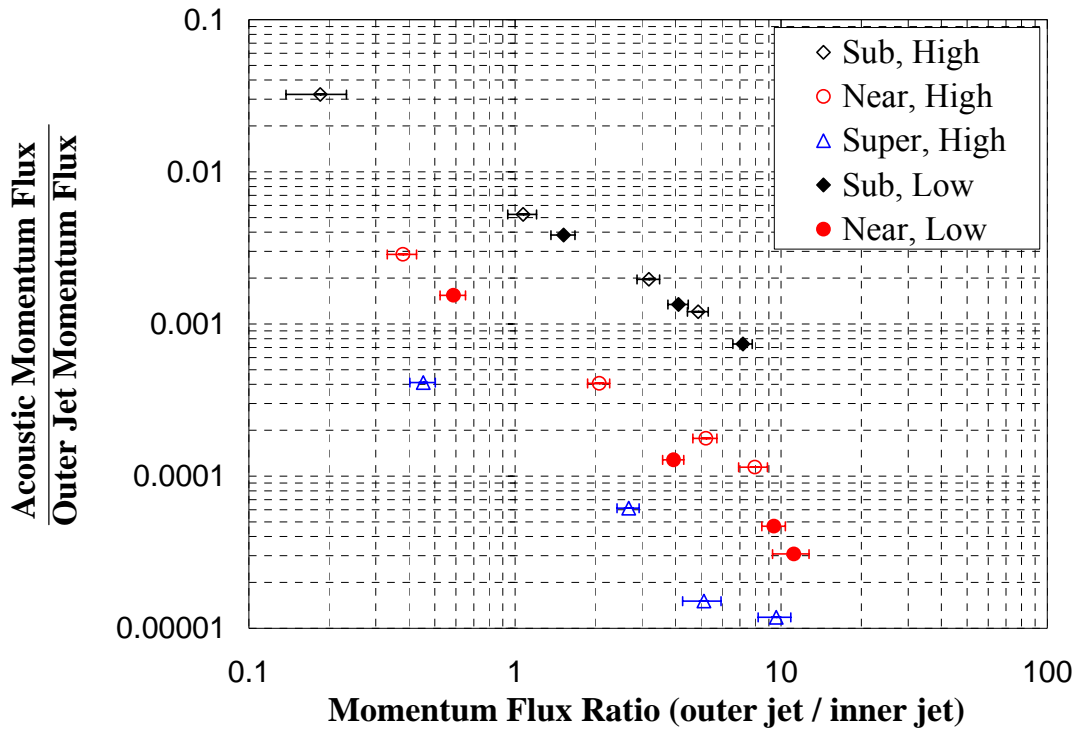


Figure 4.27: Variation of the ratio of acoustic momentum flux ($\rho \mathcal{U}^2$) to the momentum flux of the outer-jet with the outer-to-inner jet momentum flux ratio. The words sub, near, and super in the figure inset correspond to subcritical, near-critical, and supercritical, respectively. The words “high” and “low” in the figure inset are for the nominal high and low outer-jet temperature cases. The hollow diamond symbols (“Sub, High”) are cases 1-4; the hollow circles (“Near, High”) are case 5-8; the hollow triangle symbols (“Super, High”) are cases 9-12; the solid diamond symbols (“Sub, Low”) are case 13-15; the solid circle symbols (“Near, Low”) are cases 16-19. The case numbers correspond to Table 4.1.

4.4.4 Acoustic Wave Jet Interaction Mechanism

Using the data and observations presented in the previous sections, a picture of the interaction mechanism between the jet and the acoustic wave can now be presented. Figure 4.28 presents 13 consecutive images of the shear-coaxial jet framed at 18 kHz. These images were taken from the same movie and test run used to construct the third column of Fig. 4.14. The chamber pressure was 1.57 MPa, and the acoustic driver frequency was set at 3.03 kHz. The velocity ratio and momentum flux ratio were 10.4 and 4.6, respectively. The eight horizontal arrows in each image represent the direction and magnitude of the acoustic velocity estimated by visual inspection from the movie. The arrows were not computed by the spatial cross-correlation technique, because of the lower resolution of these images, which was necessary in order to have a larger field of view. As a visual aid, the two vertical lines near the center of each frame indicate the extent of the inner diameter of the inner tube, D_1 . The curves starting at the edge of the outer-jet represent the averaged boundary, delineating the extent of the outer-jet with no acoustical excitation. These lines were determined by applying a variance filter, which uses a 7x7 region of interest (ROI) which computes the variance of the ROI then replaces the center pixel with the variance for that particular ROI. The texture of the outer-jet fluid is different from the chamber fluid and the inner-jet. The variance filter converts what the human eye perceives as texture (vaguely defined) and converts it to intensity variations. The reader is referred to Russ [79] for more details on image textures. Two hundred variance images of the jet without acoustic excitation were averaged from which a line denoting the boundary can be easily distinguished. These averaged outer-jet

boundaries were then superimposed in the form of the curves drawn at the edge of the outer-jet starting from the injector tip.

Qualitatively speaking, fluid structures may be tracked sequentially in time. Starting in the first frame of Fig. 4.28, a bold circle is drawn around a fluid structure at the interface between the inner and outer-jets near the injector tip. In the second frame, the bold circle from the first frame is redrawn at the same position, but not in bold, and a bold circle is then drawn around the updated location of the same fluid structure, initially identified in frame number one, with a bold arrow connecting the centers of the two circles. This process is then repeated for consecutive frames with the bold circle and arrow denoting the movement from the last frame for the same fluid structure, until the structure is no longer distinguishable, which in this case occurs after about the tenth frame. In the fifth frame, a second fluid structure on the left side of the core is identified and tracked in the same manner.

By tracking a given fluid structure, identified by the circles in Fig. 4.28, a trajectory can be constructed. Despite reversal of the acoustic velocity in the chamber fluid several times, indicated by the direction of the horizontal arrows, the trajectory of a fluid feature on the dark core of the jet shown in Fig. 4.28 does not exhibit a periodic pattern. Recall from section 4.4.3 that there is a phase difference between the transverse velocity measured in the chamber fluid (sufficiently away from the jet) and that at the edge of the core of about 70° at an axial location of $1.4D_1$ downstream from the injector tip. This phase difference is due to the inertia that the dense core possesses. From the first two frames in Fig. 4.28, the horizontal arrows suggest that the acoustic velocity in the chamber fluid, and consequently its momentum, is at a maximum value in the

direction towards the left side of the jet. However, the direction of the transverse momentum at the edge of the core is in the direction of the left-right-oscillatory motion of the core. Because of the phase differences between the transverse velocity in the chamber fluid and that at the core of the jet, this is opposite to the direction of the transverse momentum of the chamber fluid. The momentum of the transverse wave at the edge of the core causes the portion of the core near the injector tip to be displaced in the same direction at this location, which is most likely due the force created by the drag on the core of the jet. Buffum and Williams [68] observed an order of magnitude increase in drag coefficient for the single jet in an acoustic field compared to that of a solid cylinder of an equal diameter. One may hypothesize that the transverse motion of the core is a result of the vibration of the inner tube of the injector excited by the acoustic vibrations. However, the wavelength of the acoustic wave is much longer than the annular gap width of the injector, $(D_3 - D_2)/2$, as indicated by Fig. 4.12. Even if one accounts for the radial variation in sound speed using temperature profiles shown in Fig. 4.3, the computed wavelength is still two orders of magnitude larger than the annular gap width of the injector. This suggests that the acoustic driver is not resonating the annular cavity in the injector formed between the inner- and outer-injector tubes in a transverse mode. Additionally, although the inner tube is recessed and is not visible in the images or movies, the outer tube of the injector is. Meticulous examination of the movies showed that the outer tube remains vibration free, suggesting that mechanical vibrations of the injector are not a probable cause of the jet behavior.

The ensuing sinusoidal shape of the dense core results directly from the fluid in the core being displaced near the injector tip and subsequently convected downstream.

The transverse momentum reverses its direction at the frequency of the acoustic driver (see Figs. 4.16, 4.18, 4.20, 4.21, and 4.23), and as fluid elements continually leave the injector, they are eventually displaced in accordance with the local momentum direction at that time near the injector tip. Then, within a short axial distance from the injector tip, the fluid elements of the dark core largely become insensitive to the existence of the transverse momentum, and follow nearly linear trajectories. A consistency check of this scenario was performed by fitting a line to the transverse position (x) versus time data from the identified fluid parcels of Fig. 4.28 producing lines with an R^2 correlation coefficient of 0.97. The trajectory of the fluid particle was judged visually, and therefore is somewhat subjective and errors are unknown. Therefore, the curve fit to the trajectory does not provide definitive proof that the transverse velocity (i.e., the time derivative of the curve fit) is constant, but it is consistent with the observations. The consequence of this linear variation of the fluid parcel transverse displacement is that if it were to continually be affected by the forces resulting from the transverse acoustic momentum while being convected downstream, then it would not exhibit this linear behavior. However, if one looks at images 7 to 13 in Fig. 4.28, approximately one cycle later from the image 1, and follows the portion of the core in time that grows into a large displacement peak, nearly the same trajectory of a similar nature to the previous cycle is traced.

The motion of the core appears to dominate the behavior of the jet. The displacement of the outer-jet seems to be governed by the displacement of the dense core. Looking at Fig. 4.28, the displacement of the outer edge of the jet is relatively small compared to the averaged outer edge boundary of the unexcited coaxial jet at the same

conditions, until farther downstream where the core begins to break up and becomes well mixed with the chamber fluid. However, in the near-field region of the jet, when a transverse displacement of the edge of the outer-jet occurs, it correlates well with a large lateral displacement of the core. The relatively large displacement of the dark and dense core compared to that of the chamber fluid suggests a possible amplification of the transverse velocity (see Figs. 4.22 and 4.23) caused in some way by the existence of the outer-jet. An examination of a single jet, produced by merely turning off the outer-jet flow and maintaining the other conditions constant, does not show an imposed large-scale sinusoidal structure on the core of the jet, see Chehrودي [29]. A possible reason for this amplification, at least in part, is due to the existence of the high-speed outer-jet. Once fluid from the core is displaced into the higher-speed outer-jet, the momentum of the outer-jet is much greater than that of the acoustic waves which controls the forces acting on the core, accelerating the fluid elements from the core very quickly in the axial direction within a short distance from the injector tip.

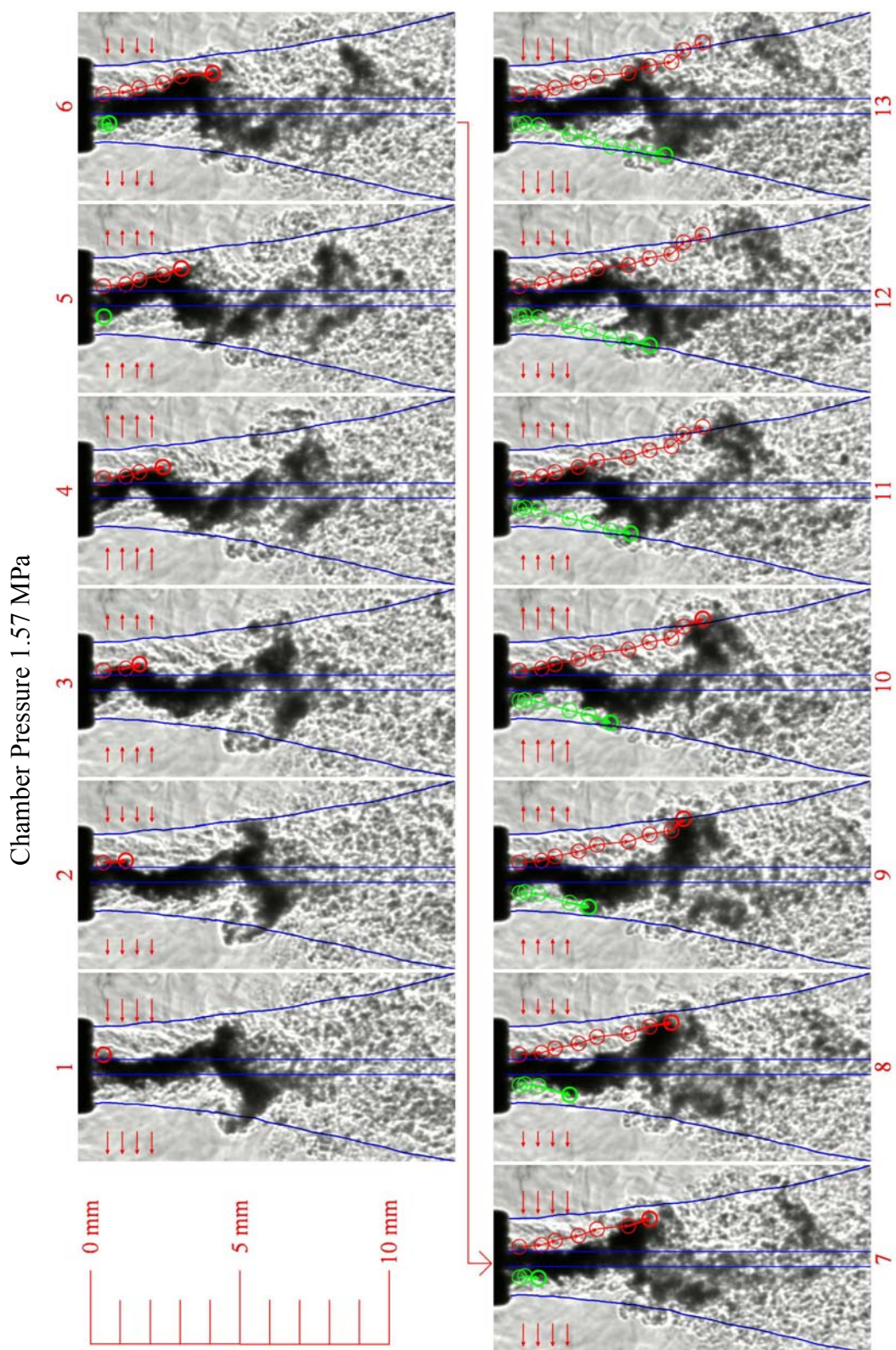


Figure 4.28: Annotated consecutive images of a subcritical pressure shear-coaxial jet.

Figure 4.29 presents 18 sequential images taken at an 18 kHz framing rate from the near-injector region at a subcritical chamber pressure. The images were from the same movie (test run) used to compute the velocities in Fig. 4.21. The chamber pressure was 1.49 MPa (subcritical) and the acoustic driver frequency was tuned at 3.01 kHz. Because of the arrangement of the images, the sampling frequency, and the acoustic driver frequency, the images in each row are approximately 180° out of phase (for example, frames 1 and 10). The velocity ratio and momentum flux ratio were 11.3 and 5.5, respectively. The length of the horizontal arrows drawn in each frame of Fig. 4.29 is the displacement, in pixels, extracted from the velocity measurements reported in Fig. 4.21 (a), scaled up by a factor of ten for clarity of presentation. Although four arrows are drawn indicating the direction of the acoustic velocity in the chamber fluid, only one axial measurement was made, being at a position $1.4 D_1$ downstream of the injector exit-plane (between the second and third arrow from the top of each frame). Because the time interval between the frames is constant, the length of the arrows is directly proportional to the velocity. The two vertical lines drawn near the center of the injector represent the extent of the inner diameter of the inner tube (D_1). The two curves originating from the tip of the injector represent the averaged edge of the outer-jet without acoustical excitation, which were determined from the averaged unexcited jet images in the same manner as in Fig. 4.28.

One structure that can be observed in the magnified images of Fig. 4.29 is the recirculation region attached to the lip of the inner tube. A magnified image of the frame number 10 in Fig. 4.29 is shown in Fig. 4.30. A similar recirculation zone was also predicted by Zong and Yang [80] in a coaxial injector attached to the lip of the inner tube

in an unexcited jet. The darker appearance of this region (compared with that of the outer-jet fluid) is due to an increase in density above that of the outer-jet, which results from the mixing of fluid elements from the high-density inner core region which was also predicted by Zong and Yang [80]. In some instances, the recirculation zone entrains enough of the inner-jet fluid leading to a decrease in the inner diameter of the core (identified by a very dark core). It is speculated that this recirculation region and the interaction with the acoustic wave is what causes the large-scale motions of the dark-core. Recall that the fluid from the dense dark-core appears to be strongly effected by the acoustic wave in the vicinity of the injector tip. The conjecture is that the acoustic wave momentum causes a collapse of the recirculation zone. For example, if the acoustic velocity direction is pointing to the right, then the left recirculation zone collapses, and vice-versa. At the same time, on the opposite side of the core, the low pressure recirculation zone pulls the core in the direction of low pressure which is the same direction as the momentum of the acoustic wave is pointing. This speculation would also account for the increased displacements of the core observed for shear-coaxial jets over that of a single round jet (no coaxial flow), because the recirculation is not present there. This cannot be definitively proven given the available data in this work.

An interesting vortex structure forms on the lip of the outer tube of the injector. This region and the vortex are denoted by the arrows pointing to the outer edge of the injector tip in Fig. 4.30, and are also visible to a lesser extent in Fig. 4.29 because of the reduced magnification. The vortex appears toroidal in shape from the examination of the movies, and continues to form during the push stroke of the acoustic driver. Once the acoustic velocity field reverses its direction, the vortex is formed and then broken up by

another change in velocity field direction, which is then entrained into the outer-jet or is mixed into the chamber fluid. This vortex appears to have little or no effect on the behavior of the jet with acoustic excitation

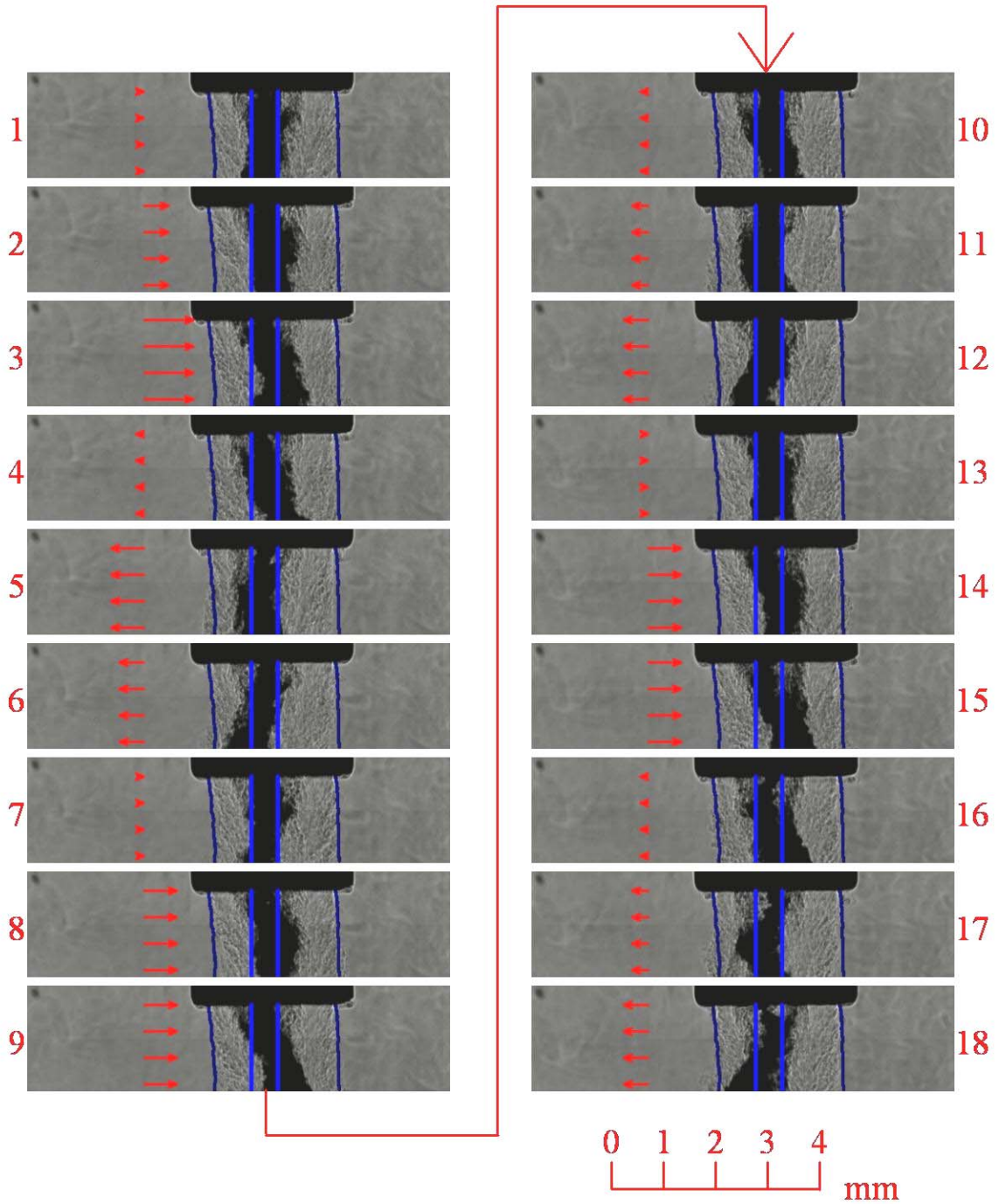


Figure 4.29: Annotated consecutive images of the shear-coaxial jet at subcritical chamber pressure. Images show magnified views of the near-injector region. Horizontal arrow length is quantitative and proportional (amplified by 10 for clarity) to velocity measured in Fig. 4.21 (a). Two parallel vertical lines in the center show the inside diameter of the inner tube. The chamber pressure was 1.49 MPa (subcritical), and the acoustic driver frequency was at 3.01 kHz.

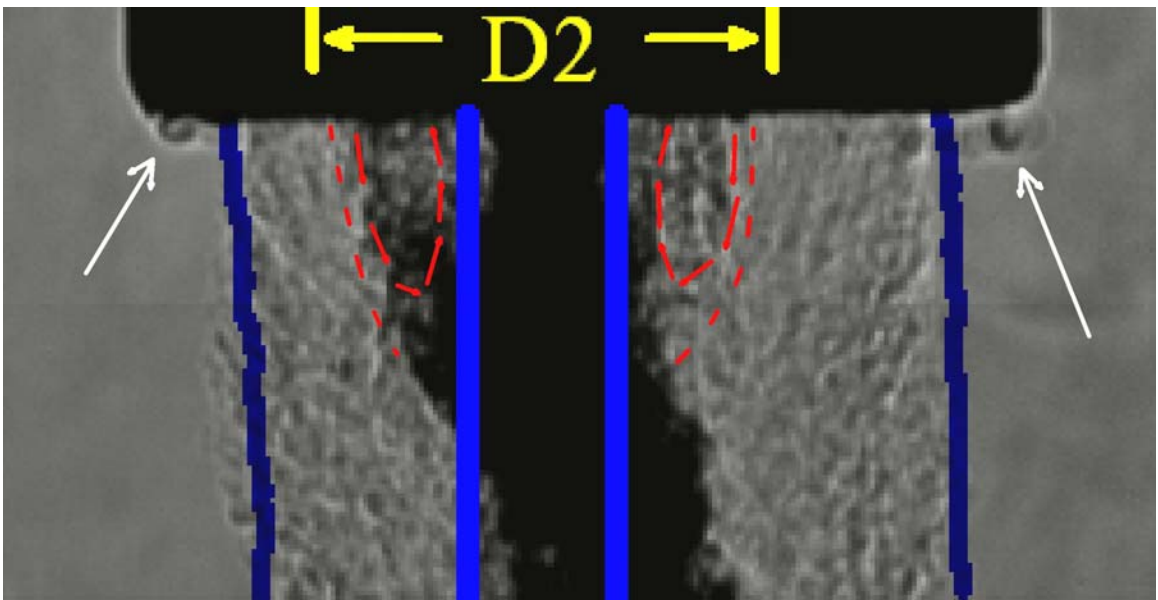


Figure 4.30 Magnified view of frame number 10 from Fig. 4.29. The dashed curves denote the approximate boundary of the recirculation zone, and the arrows within the recirculation region indicate the direction of the rotation. The vortex structures that form on the outer rim of the injector are identified by the arrows pointing to the outer edge of the injector tip. The two vertical lines with the dimension D_2 denote the extent of the outer diameter of the inner tube, $D_2 = 1.59\text{mm}$.

4.5 Dark-Core Length

Many researchers measured core length of different shear-coaxial jets in the past, and Table 4.2 presents a summary of all the works reported in the open literature. The core length was either measured or an equation correlating core length was reported. The intent of Table 4.2 is to provide detailed information on all relevant works, including the operating conditions, geometries, measurement techniques, and proposed equations correlating core lengths in one convenient location. Often, the terms potential-core, potential cone, intact liquid length, and breakup length are used interchangeably, and vaguely defined (see references in Table 4.2). The potential-core does exist for all coaxial jets, but is usually only reported for single-phase coaxial jets, and liquid intact length or breakup length is generally reported for “two-phase” coaxial jets. By “single-phase” coaxial jet, it is meant a shear-coaxial jet where all three fluid components (i.e., the inner-jet, the outer-jet, and the chamber or ambient fluid) are the same phase, either all gas, all liquid, or all supercritical fluid. The term “two-phase” coaxial jet here means a shear-coaxial jet where the inner-jet is liquid phase, and the outer-jet and the chamber (or ambient fluid) are gas phases.

Different techniques are used to measure core length (see Table 4.2) ranging from Pitot tube pressure measurements to analysis of photographs. It seems that images were used in most measurements of the core for two-phase jets. With a few exceptions, notably Woodward [62], often the measurement methods from images are not discussed with sufficient details. Therefore, in order to produce repeatable measurements, to

account for the variability in the light source intensity, and to be able to process a large number of images in a repeatable fashion, an accurate computer algorithm is necessary. When a region of an image is referred to as a “dark core”, this is simply referring to a contiguous area of the jet, always defined by the inner-jet, which clearly stands out in darkness level with respect to the remaining areas. This will be explained further in a quantitative manner below.

All of the dark core length data of the present study in figures in Section 4.5 is also presented in Table B.2 in Appendix B.

Table 4.2: Summary of published operating conditions, geometries, measurement techniques, and proposed equations from the literature, measuring or correlating core length for shear-coaxial jets.

REF	Author	Date	Fluid Inner Jet	Fluid Outer Jet	Fluid Ambient	Pressure (MPa)	T_i (K)	T_o (K)	T_∞ (K)
[44]	Forstall & Shapiro	1950	Air+ 10 %He	Air	Air	0.1*	Amb. ^a	Amb.	Amb.
[45]	Chigier & Beer	1964	Air	Air	Air	0.1*	Amb.	Amb.	Amb.
[46]	Champagne & Wygnanski	1971	Air	Air	Air	0.1	Amb.	Amb.	Amb.
[48]	Au and Ko	1987	Air	Air	Air*	0.1*	Amb.	Amb.	Amb.
[8]	Eroglu et al.	1991	Water	Air	Air	0.1*	Amb.	Amb.	Amb.
[62]	Woodward	1993	KI (aq.)	N2, He	N2, He	0.1 – 2.17	Amb.	Amb.	Amb.
[50]	Villermaux et al. ^g	1994	Water	Water	Water	0.1*	Amb.	Amb.	Amb.
[63]	Englebert et al.	1995	Water	Air	Air	0.1	293	293 – 636	293
[64]	Carreau et al.	1997	LOX	He, N2, Ar	NC ^c	0.1	82 ^d	245 – 272 ^d	NC
[51]	Rehab et al. ^g	1997	Water	Water	Water	0.1*	Amb.	Amb.	Amb.
[52]	Rehab et al. ^g	1998	Water	Water	Water	0.1*	Amb.	Amb.	Amb.
[53]	Villermaux ^{g,h}	1998	Water	Water	Water	NR	NR	NR	NR
[58]	Lasheras et al. ^g	1998	Water	Air	Air	0.1	Amb.	Amb.	Amb.
[54]	Lasheras & Hopfinger ^{g,i}	2000	NR	NR	NR	NR	NR	NR	NR
[60]	Favre-Marinet & Schettini	2001	Air, SF6	Air, He	Air, He	0.1	Amb.	Amb.	Amb.
[65]	Porcheron et al.	2002	LOX, Water	He, N2, Ar, Air	Air	0.1	82, 293	245 – 293	293
This work	Davis	2005	N2	N2	N2	1.4 – 4.9	108 – 133	132 – 204	197 – 249

Table 4.2: Summary of published operating conditions, geometries, measurement techniques, and proposed equations from the literature, measuring or correlating core length for shear-coaxial jets. (continued)

REF	Author	Density Ratio Outer / Inner	Velocity Ratio Outer / Inner	M Outer / Inner	Re Inner ($\times 10^4$)	Re Outer ($\times 10^4$)	We
[44]	Forstall & Shapiro	1.09	0.2 - 0.75	0.04 - 0.61	NR	NR	NA
[45]	Chigier & Beer	1*	0.024 - 9.22	5.8×10^{-4} - 85.0	$\sim 10^b$	$\sim 10^b$	NA
[46]	Champagne & Wygnanski	1*	0 - 10	0 - 100	1.01 - 10.15	0 - 9.6	NA
[48]	Au and Ko	1*	1.25 - 6.67	1.5 - 44	NR	NR	NA
[8]	Eroglu et al.	0.001	4.5 - 131.2	0.02 - 17.2	0.15 - 0.93	2.0 - 11.6	15 - 530
[62]	Woodward	0.0006 - 0.018	0 - 30	0 - 1.7	7.86 - 18.9	NR	$12 - 3.6 \times 10^4$
[50]	Villermaux et al. ^g	1	1 - 6	1 - 36	>5000	>5000	NA
[63]	Englebert et al.	0.0008 - 0.0012	10.25 - 66.75	0.12 - 4.3	0.54 - 3.4	4.8 - 16.5	76 - 2610
[64]	Carreau et al.	NR	NR	3 - 21.5	5.32 - 8.11	NR	9.19×10^3 - 3.48×10^4
[51]	Rehab et al. ^g	1	2 - 5	4 - 25	NR ^f	NR ^f	NA
[52]	Rehab et al. ^g	1	2.2 - 5.6	4.9 - 31	1 - 10	1 - 10	NA
[53]	Villermaux ^{g,h}	1*	NR	NR	NR	NR	NR
[58]	Lasheras et al. ^g	0.001	NR	NR	NR	NR	NR
[54]	Lasheras & Hopfinger ^{g,i}	NR	NR	NR	NR	NR	NR
[60]	Favre-Marinet & Schettini	0.028 - 1	3.0 - 70	1 - 200	NR	3.2, 11.0	NA
[65]	Porcheron et al.	1.6×10^{-4} - 2.3×10^{-3}	NR	2 - 21.6	NR	NR	0 - 14000
This work	Davis	0.04 - 0.56	1.2 - 11.1	0.19 - 11.2	1.2 - 3.2	0.8 - 19	32 - ∞

Table 4.2: Summary of published operating conditions, geometries, measurement techniques, and proposed equations from the literature, measuring or correlating core length for shear-coaxial jets. (continued)

REF	Author	D_1 (mm)	D_2 (mm)	D_3 (mm)	$(D_3-D_2)/2$ (mm)	Area Ratio Outer / Inner	Post Recess (mm)	Injector L_{post}/D_1
[44]	Forstall & Shapiro	6.4, 25	NR	102	NR	NR	NR	NR
[45]	Chigier & Beer	25	64	97	16.5	8.50	0*	NR
[46]	Champagne & Wygnanski	25	NR	NR	NR	1.28, 2.94	0*	NR
[48]	Au and Ko	2	2.2	4	0.9	2.79	0*	NR
[8]	Eroglu et al.	0.971	1.262	10.36	4.549	112.15	-0.6	57
[62]	Woodward	4.76	6.35	9.86	1.76	2.51	0.0	85
[50]	Villiermaux et al. ^g	40	51	55	0.2	0.27	0*	"long"
[63]	Englebert et al.	2.3	2.95	14.95	6.00	40.60	0	22
[64]	Carreau et al.	5 ^d	5.57 ^d	16 ^d	5.2 ^d	9	0	NR
[51]	Rehab et al. ^g	20	21	27	3	1.82	0	NR
[52]	Rehab et al. ^g	NR	NR	NR	NR	1.82, 1.87, 5.24 ^e	0 – 2 D_1	NR
[53]	Villiermaux ^{g,h}	NR	NR	NR	NR	NR	NR	NR
[58]	Lasheras et al. ^g	3.8	4.2	5.6	0.7	0.95	0	29
[54]	Lasheras & Hopfinger ^{g,i}	NR	NR	NR	NR	NR	NR	NR
[60]	Favre-Marinet & Schettini	20	20.4	27	3.3	0.78	0	6.75
[65]	Porcheron et al.	5, 2.1	5.57, 2.5	16, 7	2.25	9, 9.69	0*	NR
This work	Davis	0.51	1.59	2.42	0.415	12.80	0.25	100

Table 4.2: Summary of published operating conditions, geometries, measurement techniques, and proposed equations from the literature, measuring or correlating core length for shear-coaxial jets. (continued)

REF	Author	Diagnostic	Quantity Measured	Equation
[44]	Forstall & Shapiro	Pitot tube, Sampling Tube	Potential Core	$L / D_1 = 4 + 12V_r$
[45]	Chigier & Beer	Pitot tube	Potential Core	NR
[46]	Champagne & Wagnanski	Hot wire anemometer	Inner Core	NR
[48]	Au and Ko	Hot wire anemometer	Potential Core	$L / D_1 = 9.9 / V_r$
[8]	Eroglu et al.	Back-lit still	Liquid Intact Length	$L / D_1 = 0.66 We^{-0.4} Re^{0.6}$
[62]	Woodward	x-ray Radiography	Intact Liquid Core Length	$L / D_1 = 0.0095 \left(\frac{\rho_o}{\rho_i} \right)^{\frac{-0.36}{H}} We^{-0.22/H} Re^{0.68}$
[50]	Villermaux et al. ^g	Hot film anemometer	Potential Core / Cone	$L / D_1 = 7 / V_r$
[63]	Englebert et al.	Back-lit high-speed 16mm film	Breakup Length	$\frac{L}{D_1} = 40 We^{-0.27}$ $\frac{2L}{D_3 - D_2} = 10.6 M_R^{-0.3} = 13.7 E_R^{-0.2}$
[64]	Carreau et al.	Fiber optic Probe	Breakup Length, Potential Cone Length	$L / D_1 = 0.0012 \left(\frac{\rho_o}{\rho_i} \right)^{-0.32} We^{-0.33} Re^{0.55}$
[51]	Rehab et al. ^g	Hot film anemometer, Pitot tube, LIF image	Potential Core	$L / D_1 = 6 / V_r; L / D_1 = 8 / V$ $L / D_1 = 0.5 \left(\frac{1}{(C\alpha V_r)^2} - 1 \right)^{1/2} \approx \frac{1}{2C\alpha V_r}$
[52]	Rehab et al. ^g	Hot-film anemometer	Potential Cone	$L / D_1 = c / V_r; 6 < c < 8$
[53]	Villermaux ^{g,h}	^h	Potential Cone, Liquid intact length	$L / D_1 = 6 / M^{1/2}$

Table 4.2: Summary of published operating conditions, geometries, measurement techniques, and proposed equations from the literature, measuring or correlating core length for shear-coaxial jets. (continued)

REF	Author	Diagnostic	Quantity Measured	Equation
[58]	Lasheras et al. ^g	Photo-graph	Liquid intact length	$L / D_1 = \left(\frac{1}{4 (C \alpha)^2 M} - \frac{1}{4} \right)^{1/2} \approx \frac{6}{M^{1/2}}$
[54]	Lasheras & Hopfinger ^{g,i}	i	i	$L / D_1 = \frac{1}{2 c M^{2/3}} \left(\frac{\sigma}{\mu_i U_i} \right)^{1/3}$ $L / D_1 \approx \frac{6}{M^{1/2}} \left(1 - \frac{U_i}{U_o} \right)^{-1}$ $L / D_1 \approx \frac{6}{M^{1/2}} \frac{1}{\left(1 - \frac{B \sigma}{\mu_o U_o} \right)^{0.5}}$
[60]	Favre-Marinet & Schettini	Aspirating Probe w/ hot-wire	Potential Core	$L / D_1 \propto M^{-0.5}$
[65]	Porcheron et al.	Fiber optic Probe	Liquid Core	$L / D_1 = 2.85 \left(\frac{\rho_o}{\rho_i} \right)^{-0.38} Z^{0.34} M^{-0.13}$
This work	Davis	Shadow-graph	Dark Core	$L / D_1 \approx \frac{12}{M^{1/2}}$ $L / D_1 \approx \frac{25}{M^{0.2}}$

Table 4.2 Notes

NR = not reported

NA = not applicable

NC = not clear from report

Amb. = ambient

* assumed from the context, but not directly reported

^a Ambient temperature assumed from the context of discussion, but not specifically stated in report.

^b reported as approximately 10^5

^d The dimensions of the injector and the temperatures were not given in the paper, but were given in the paper by Porcheron et al.[65]

^e This number is the diameter ratio squared, which is approximately the area ratio for a very thin lip injector. The only dimensional information given was the diameter ratios (1.35, 1.37, and 2.29 mm) and the lip thickness $(D_2 - D_1)/2$ of 0.3 mm.

^f A Re based on momentum conservation reported and defined as

$$Re = \rho_o U_o D_3 / \mu^* (1 - (D_1/D_3))^{0.5} \text{ ranged from } 10^4 - 10^5.$$

^g These papers are from the same collaboration / research group over several years.

^h This paper was an analysis paper that presented a different equation based on the data from the same group of researchers [50]-[52]

ⁱ This paper was a review paper encompassing the work from this same collaboration of researchers, as well as others.

^j Unable to make measurements from images, and therefore not compared quantitatively to theory for core length.

4.5.1 Adaptive Thresholding Measurement of Dark-Core Length

There are many difficulties in performing quantitative measurements from a large number of images of a jet. Typically, a thresholding technique is used for making measurements from digital images. A threshold technique is applied to convert a gray-scale image to a binary image (only black and white). This is done by determining a gray-scale level (or a threshold level) and assigning all pixels that have gray-scale intensities greater than that number to a white color, and the pixels with gray-scale intensities below that particular gray-scale number to a black color. Other variations of this method exist, such as dual thresholding, which selects a range of gray level intensities to be white, and the intensities outside of this range to be black. The purpose of applying a threshold is to make a region of the image easily identifiable to either a human or computer, or both. The difficulty with applying this technique is determining the gray-scale level that should be defined as a threshold. For example, if using a strobe light for illumination purposes, the intensity of the background of the image will most likely vary from shot to shot. Additionally, if the chamber pressure or temperature field varies significantly, then the refractive index field can change the appearance of the background. Another difficulty is the selection of a criterion to assess the location where the core is broken up into separated pieces. It is then possible for two people to make different measurement judgments as to the core length. Also, with the use of digital cameras, capable of collecting a large number of images, a manual measurement becomes an extremely tedious and time consuming task.

A judicious choice of a threshold level on the gray-scale intensity level of each image is necessary, primarily because a single fixed value is not sufficient for all images to consistently determine the end or break point of the dark core. Figure 4.31 is a sample image illustrating an automated thresholding procedure for the determination of the length of the dark core. Figures 4.31 a, b, and c are, respectively, the untouched original photograph, the image threshold applied between 0-128 to indicate the injector, and the image threshold applied between 128-929 to represent the dark core. Figure 4.32 is the image histogram corresponding to Fig. 4.31 indicating the number of pixels versus a 12-bit gray-scale level. The ability of an algorithm to successfully predict the proper threshold level is based on the physical meaning of different gray level zones in an image as shown in Fig. 4.32. For example, the peak to the left of the dashed line in this figure indicates the metal surface of the injector. With the object (i.e., injector) being backlit and the injector being absolutely opaque, one would expect that the zero-level intensity should all represent the injector itself. However, the slight shift of the peak to a higher value is due to stray light being reflected by the chamber windows and other surfaces towards the injector which is then reflected back into the camera. The low number of pixels at gray level values between the dashed and dotted lines in Fig. 4.32 physically represents the dark core of interest, and the broad noisy peak at gray levels to the right of the dotted line in this figure defines the background. A difficulty with the adaptive thresholding is selecting the proper gray level denoting the difference between the dark core and the background.

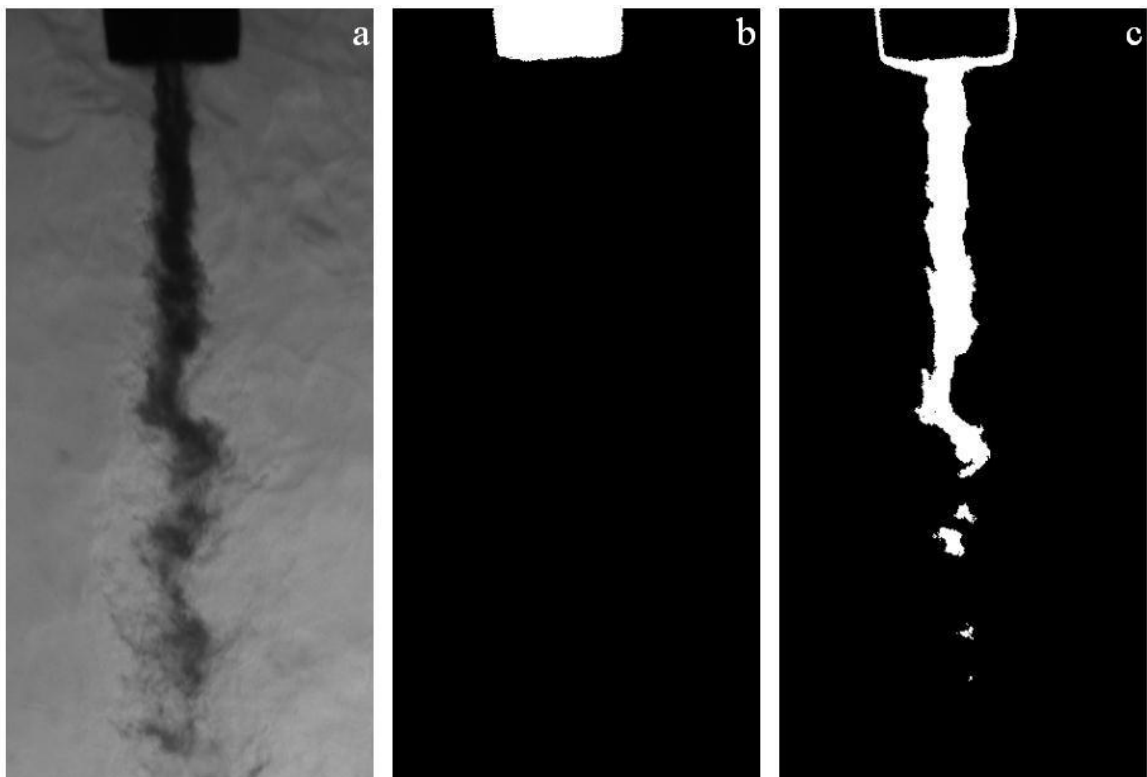


Figure 4.31: The image of (a) coaxial jet as captured, (b) threshold applied for injector, (c) threshold applied for dark core.

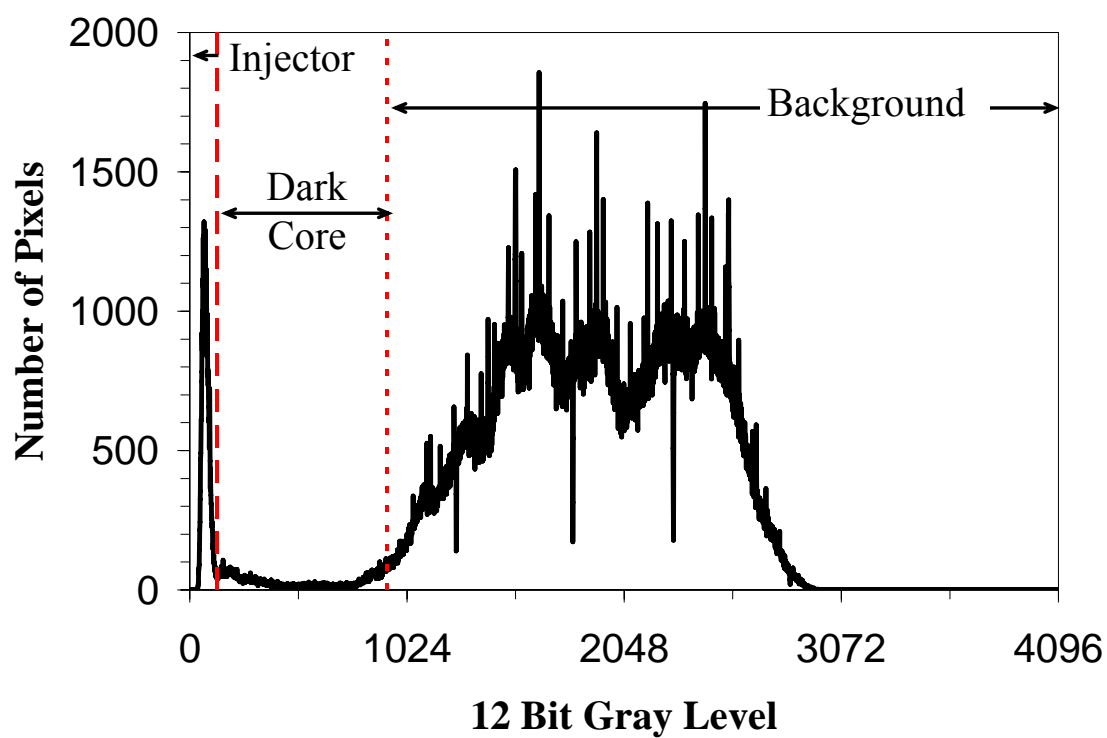


Figure 4.32: Histogram of image in Fig. 4.31 (a).

As mentioned previously, variations of the light intensity from shot to shot are usually significant and a matter of concern. For example, in the case of Fig. 4.32, the threshold level distinguishing the end of the dark core and the beginning of the background is at a gray level of 929. However, this value varies from shot to shot in a sequence of images taken at the same operating conditions. Also, it varies more widely when the chamber conditions are changed due to differences in the refractive index field. Therefore, it was necessary to devise a methodology for an accurate and repeatable determination of the rise of the portion of the curve representing the contribution of the background in these images. More importantly, the outcome should conform to what the human eye visually determines to be the end of the dark core. To select the threshold level identifying the rise of the background, data from the histogram in this region was curve-fitted, using a non-linear Levenberg – Marquardt least squares algorithm [81], to a piece of a Gaussian function (Eq. 4.6). This function is then differentiated and the point where the derivative of this curve is equal to e^{-1} was assigned to be the threshold level corresponding to the dotted line shown in Fig. 4.32 and the image of Fig. 4.31 (c). Once the proper threshold levels are determined, the program then searches for the first break in the core, and the difference between the location of the end of the injector tip and the first break in the core is taken as the dark core length (L).

$$f(I) = A \exp\left(-\frac{(B-I)^2}{C}\right) + D \quad (4.6)$$

Where,

I is the gray level intensity, and
 A , B , C , and D are constants.

Completion of an algorithm is only the first step in the analysis. A more important step is the verification that the adaptive thresholding algorithm gives results corresponding to the visual perception of the image. Evidence of the soundness and consistency of this algorithm is presented in Fig. 4.33. This figure is a plot of the dark-core length (L) in number of pixels and presents a comparison between a careful manual measurement by visual inspection and the previously-described algorithm using an averaged image of those taken at a fixed operating condition. The averaged image was used for the comparison and evaluation between the results of the algorithm and the visual measurements. An averaged image is formed by first computing the mean intensity at a given pixel location from a set of images, then repeating this process for all the pixels. In the next step, the maximum and the minimum intensity values are found for the averaged-image. Lastly, this image is rescaled by mapping the minimum and maximum intensity values (and all others in between) to a 12-bit gray-scale ranging from 0 to 4095. The error bars in Fig. 4.33 represent the sensitivity of the measurements to the variations of the automatically-selected threshold level when changed by $\pm 10\%$. The large error bars on several points indicate that a proper selection of this threshold is essential in achieving a reliable result and a good agreement with manual measurements. A large positive error bar indicates a truly-disconnected fluid ligament (judged visually) misinterpreted as being connected and a large negative error bar indicates a truly-connected fluid ligament which is misjudged as disconnected.

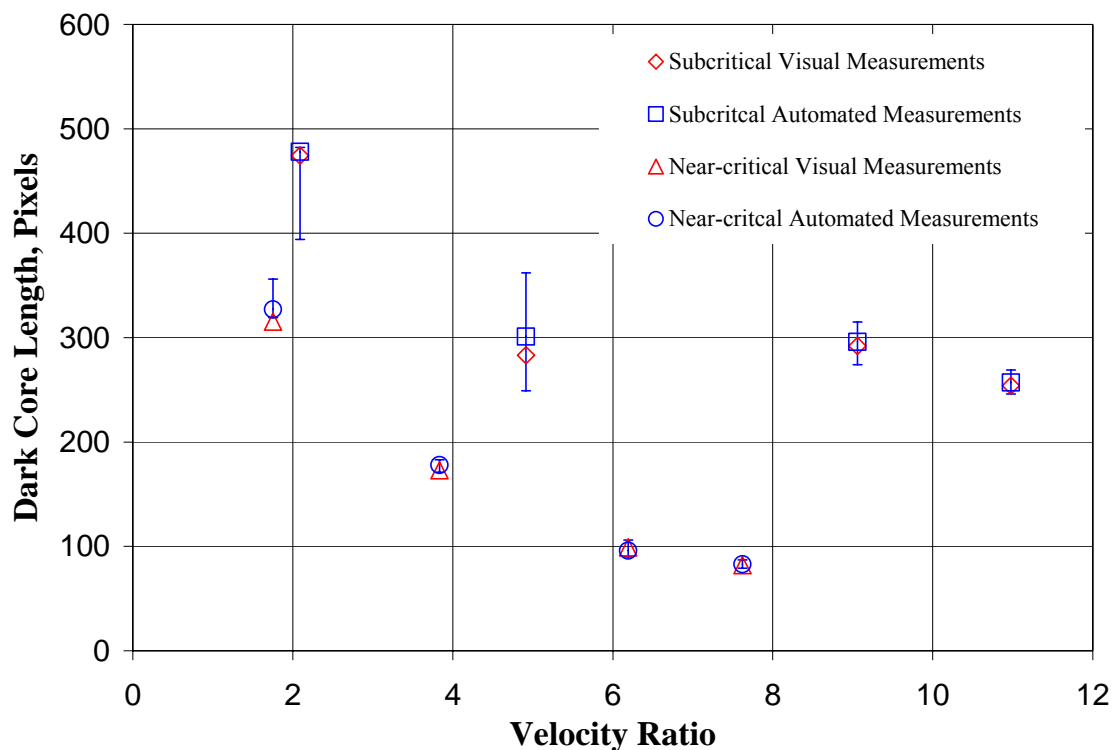


Figure 4.33: Dark core length (in pixels) versus velocity ratio (outer-to-inner jet) comparing the visual measurement with that of the algorithm programmed for automated measurement of this length using an average image representative for each of the conditions. The error bars represent a sensitivity analysis, varying the automatically-selected threshold level by $\pm 10\%$. The diamonds and the up-triangles are for manual visual measurements under sub- and nearcritical chamber pressures and the squares and circles are for corresponding pressures using automated computer measurements.

According to Eroglu et al.[8], the average of the length measured from individual images of a set can be regarded as the time-averaged length. It should be noted that, for each operating condition in this work, length measurements were also made from an averaged image from the set. A comparison between the averaged dark-core length measured from a set of 30 individual images and the dark-core length from the averaged-image from the same set of images is presented in Fig. 4.34, with the 45° line ($y = x$) drawn for ease of comparison. The length measured from the averaged image is somewhat shorter than the average of the individual dark core values calculated in a given set. This decreased length in the averaged image is due to the fluctuations of the dark core, causing occasional appearance of the core at a give position around the end of the core, while leading to its disappearance in other images of a set. Recall that the averaged image is calculated by computing the mean intensity at any pixel location from a set of images, then rescaling this mean value to integers between a gray-scale range (in this case, 0 and 4095, for a 12-bit resolution). The net result of the averaging process is that, for example, a black pixel (or, low gray-scale intensities) with a corresponding white pixel (or, higher gray-scale intensities) in a different image of a set of two images result in gray-scale level in the averaged image that is shifted to a higher intensity value (i.e., 0.5). This effect, particularly in the region of space near the end of the dark core, causes a length measured by the averaged image to be shorter than the average of the individual images of a set. It was found that the difference between the averaged dark-core length from a set of individual images and the dark-core length measured from the averaged image increases as the root-mean-square length fluctuations increases. For the remainder

of this work the averaged dark core length measured from 30 individual images is reported.

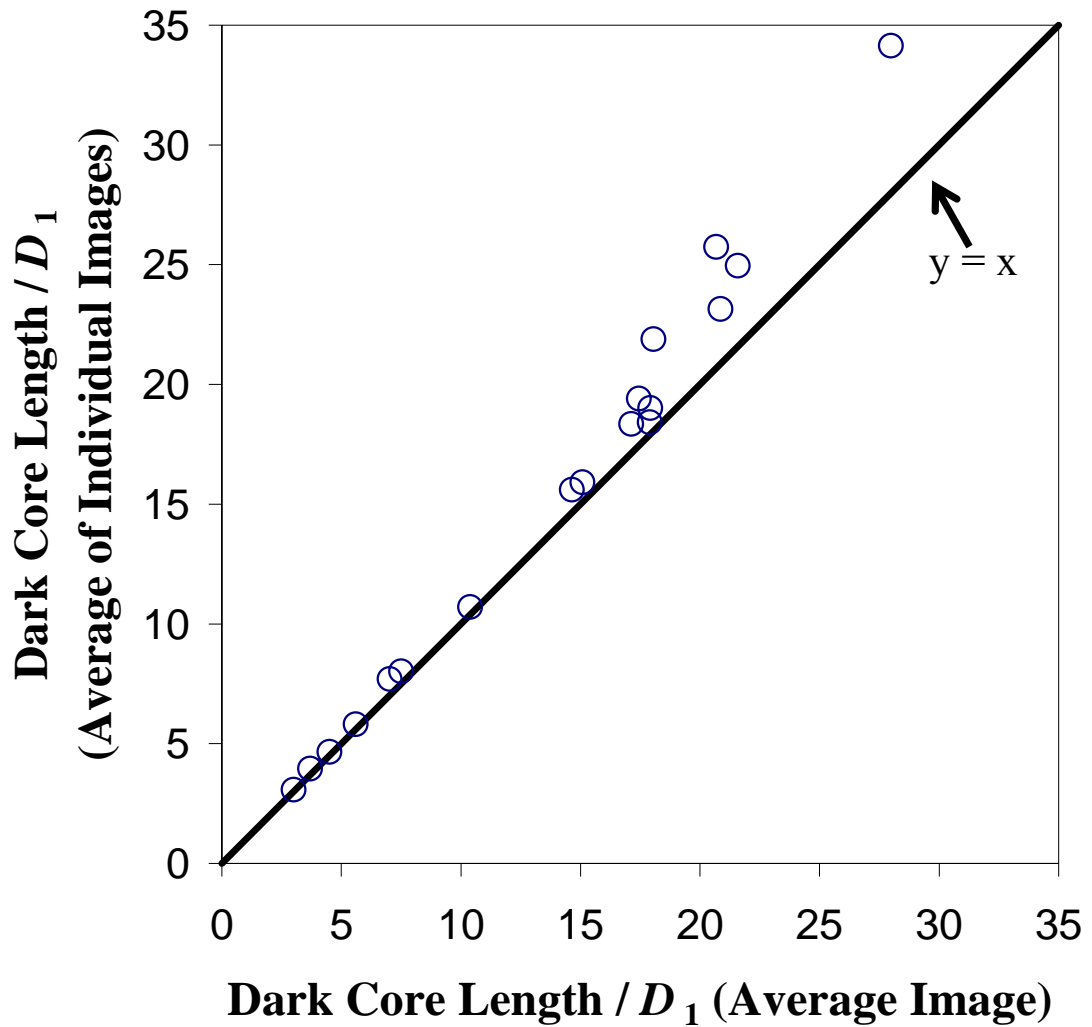


Figure 4.34: Comparison of the average dark-core length measured from of set of individual images versus the dark-core length measured from the average image of the same set.

4.5.2 Influence of Velocity Ratio on the Dark-Core Length

Velocity ratio (outer-to-inner jet) has been a design parameter for shear-coaxial injectors, particularly, as a criterion to ensure the stable operation of liquid rocket engines (LRE). For liquid oxygen (LOX) / hydrogen (H_2) engines, the design rule-of-thumb has been to keep the velocity ratio greater than about ten to prevent or minimize the occurrence of combustion instabilities (see Hulka and Hutt [3]). Although experimental data suggested this criterion, no physical explanation has been provided. One method to rate a liquid rocket engine (LRE) for combustion instability is the so-called “temperature ramping”, which is accomplished by lowering the temperature of the H_2 while maintaining H_2 mass flow rate at a constant value. The lower the H_2 temperature is at the onset of the measured combustion instability, the greater the stability margin of that particular LRE. Note that as the H_2 temperature is lowered at a constant mass flow rate, the actual velocity ratio is also lowered.

The dark-core lengths normalized by the inner-jet diameter are shown in Fig. 4.35 (a) and Fig. 4.36 (a) as a function of velocity ratio (V_r). The root-mean-square (RMS) of the variations of this physical quantity is also shown in Fig. 4.35 (b) and Fig. 4.36 (b). Figures 4.35 and 4.36 present results for both high and low outer-jet temperatures of ~ 190 K and ~ 140 K, respectively. The error bars on the plots represent the n^{th} order uncertainty as described at the beginning of this chapter.

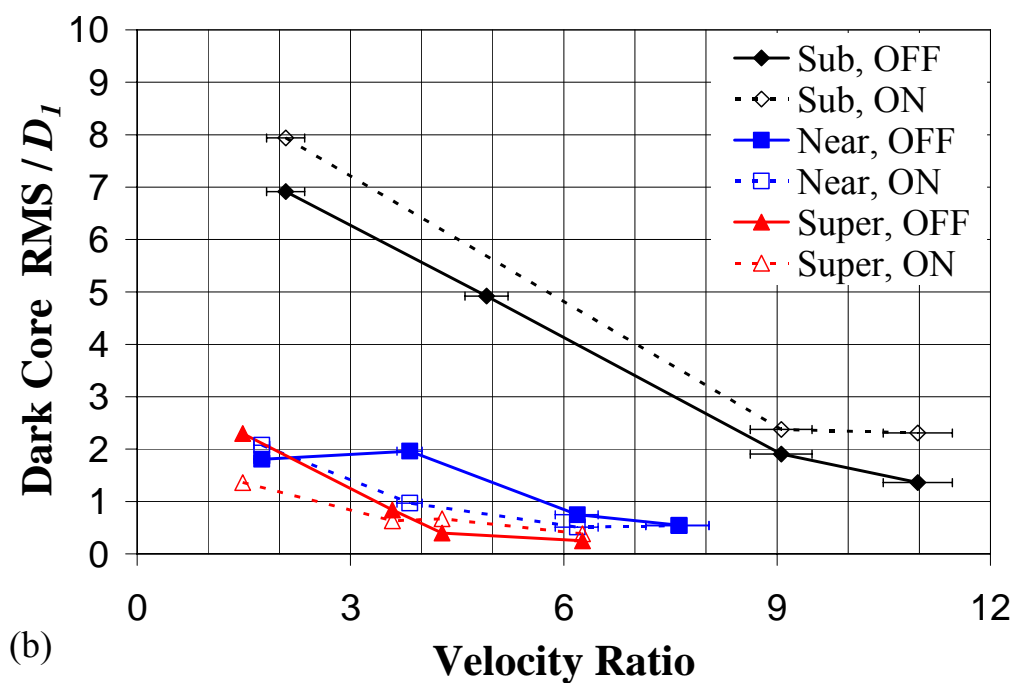
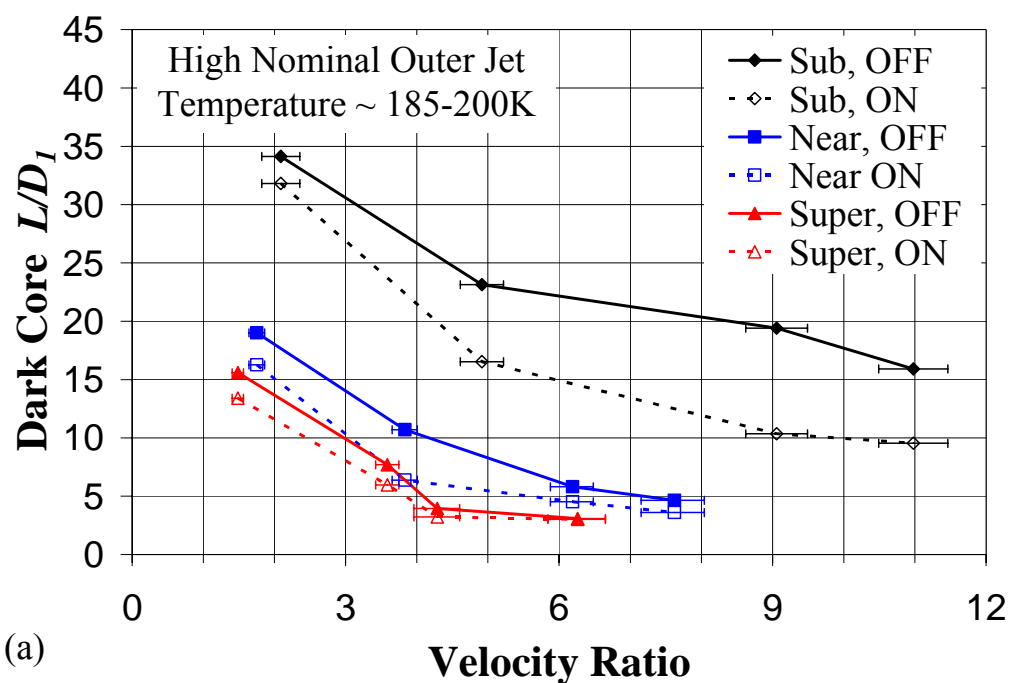
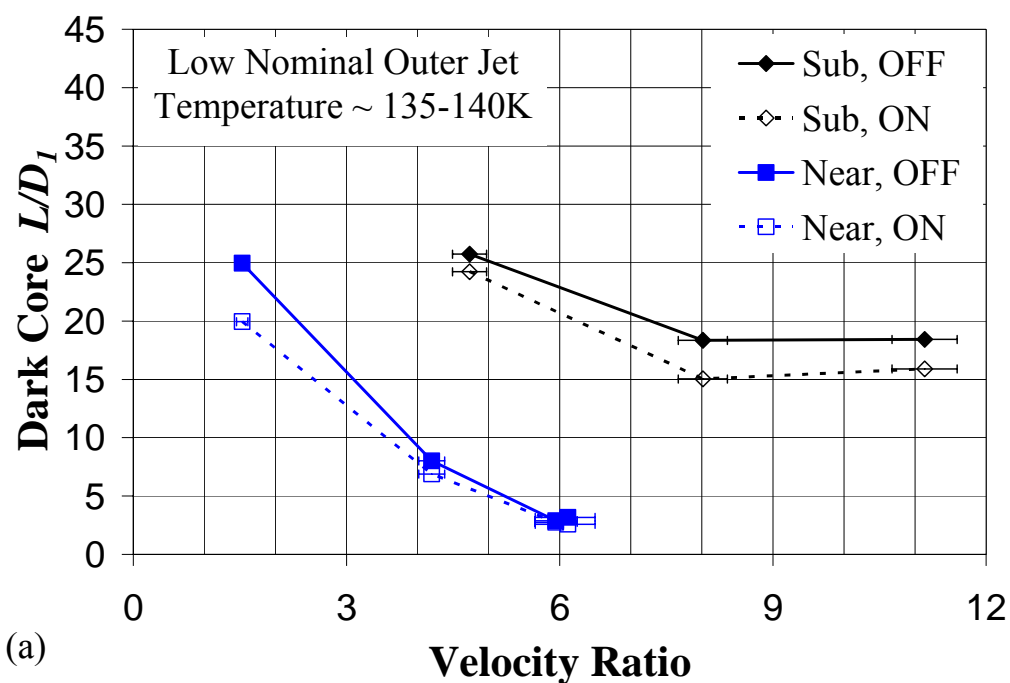
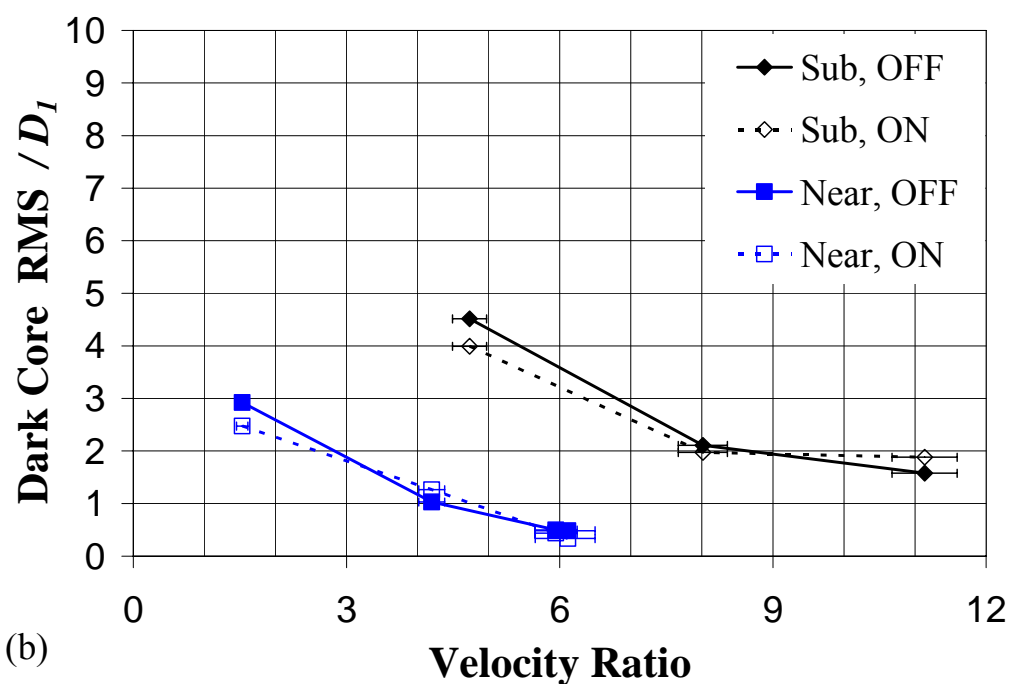


Figure 4.35: Plot of the averaged dark-core length (a) and the RMS of the length variations (b) normalized by the inner diameter. The solid symbols and lines represent the data for when the acoustic driver is OFF, and the hollow symbols and dotted lines show the data when the acoustic driver was operated at $\sim 3\text{kHz}$ (ON). The diamond, square, and up-triangle symbols are sub-, near and supercritical chamber pressures, respectively. All cases are for the high nominal outer-jet temperature of $\sim 190\text{ K}$.



(a)



(b)

Figure 4.36: Plot of the averaged dark-core length (a) and the RMS of the length variations (b) normalized by the inner diameter. The solid symbols and lines represent data for when the acoustic driver off, and the hollow symbols and dotted lines show results when the acoustic driver is operated at ~ 3 kHz (ON). The diamond and square symbols are for sub- and near-critical chamber pressures, respectively. All cases are for the lower nominal outer-jet temperature of ~ 140 K.

Evident in Figs. 4.35 (a) and 4.36 (a) is that the mean length of the dark core, which provides an indication of high-density regions of the flow, decreases as the chamber pressure is increased. A possible explanation of this effect is that as the chamber pressure increases in the present system, the temperature of the inner-jet also increases. The net effect causes the density of the inner-jet to decrease (as seen in Figs. 4.3 (a)-(f)), which leads to a shortened length of the dark core. Since the jet begins with a lower density, less time is then required to fully mix the dark inner-jet with the background. Work that is relevant to the present study was performed by Glogowski et al. [82] and Vingert et al. [83], in which a shear-coaxial injector was utilized with a design derived from a prototype SSME fuel preburner element using liquid nitrogen (LN2) and gaseous nitrogen (GN2). They stated that the length of the dark core in the acquired images increased significantly upon elevation of the chamber pressure from sub- to supercritical, at constant mass flow rates. They attributed this to the drop in the relative velocity between the inner and outer (annular) streams. Although temperature measurements were made somewhere downstream of the critical flow venturi location in the feed system, it was not clear how far upstream of the injector exit area this temperature measurement was made. It is known that small changes in temperature in this thermodynamic region can bring about large changes in density, affecting the parameters, especially outer-to-inner velocity ratio, used to characterize the injector exit conditions. Close examination of the figures presented by Vingert et al. [83] suggests that the dark core (that is, the flow issuing from the inner tube) of the jet actually appears to contract in length, while the visual impression of the outer annular flow is that it grows in length.

At a constant chamber pressure, as the velocity ratio (V_r) is increased, the mean length of the dark core decreases and approaches a somewhat constant region. In a mean sense, when the dark core feels the imposed external acoustic field, the length of the core is shorter than or equal to the length when the acoustic driver is turned off. Miesse [66] also observed a contraction, but for single round jets excited by an external acoustic field. Under the near- and supercritical chamber pressures, as the V_r parameter increases, the difference between the lengths of the dark core, measured with and without the acoustic field, diminishes.

The RMS values of the dark-core length fluctuations, shown in Figs. 4.35(b) and 4.36(b), exhibit somewhat similar trends to those seen with their mean values. It is known that for a liquid-fueled rocket, atomization and breakup processes, interactions between the propellant jets, droplet formation, and vaporization are all affected by the pressure and, particularly, velocity fluctuations. Also, for any chemically-reacting system, the rate at which energy is released is sensitive to the rate of change of temperature, density, pressure, and, of course, mixture ratio. It is then quite intuitive to relate, in some form, the RMS values of the dark-core length fluctuations to mixture ratio variations. On the other hand, a low RMS value can be interpreted as the jet's inherent steadiness and vice versa. Examination of Figs. 4.35(b) and Fig. 4.36(b) clearly shows that this property is reduced significantly as the velocity ratio is increased when the chamber pressure is subcritical. Although these results are for a single injector design, it is then quite possible that the observed improvement in combustion stability for liquid rocket engines at higher values of velocity ratio is a result of the jet's inability to generate large mass flow rate fluctuations under these conditions, weakening a key feedback line

for the self-excitation process. In temperature ramping exercises for stability rating of LOX/H₂ engines, the mass flow rate is usually maintained at a constant value [3]. Therefore, as the temperature of the H₂ is decreased during a ramping episode, the H₂ becomes more dense, which decreases the injector velocity ratio (V_r). Hence, the decrease in V_r causes a shift in the operating condition to those providing higher RMS fluctuations of the core. Additionally, considering that a liquid rocket engine may have regions, particularly near the LOX core, where they exist under subcritical condition even if both propellants are individually injected at supercritical conditions (described in Chapter 2), these RMS plots suggest that such a decline in the velocity ratio amplifies the jet's inherent unsteadiness. This provides a possible explanation for the engine's eventual arrival into an unstable zone as a temperature ramping test proceeds. Also, the observation reported by Wanhainen et al. [84], who found that a decline in LOX density was de-stabilizing, can be explained in a similar manner. Ultimately, this initial finding requires testing under multi-element injector combustion conditions for verification, which is considered beyond the scope of this work.

As indicated in Table 4.2 V_r has been used as a correlating parameter for core length by many investigators. Figure 4.37 is a comparison between the data taken from all of the available and relevant core length measurements reported in the literature. The hatched region in Fig. 4.37 represents the region of separation between single-phase and two-phase shear-coaxial jet results. All points below the hatched region are for single-phase coaxial jet cases, and the remaining points located above the hatched region are for two-phase coaxial jets. The important observation here is that the mean dark-core lengths for the near-critical and supercritical pressure conditions from this work, which were

measured from images and are in fact single-phase, fall on the single-phase side of the hatched region. Although the spatial discrimination between the single- and two-phase cases is interesting in Fig. 4.37, and will be discussed later, the large level of scatter might be explained by one or any combination of three reasons. Initially, one might suppose a reason for this observation to be related to the measurement technique. For example, all of the two-phase core lengths presented in Fig. 4.37 were measured from images of one type or another and the core-length measurements for the single-phase cases were acquired from some type of velocity measurement, estimating the potential-core (see Table 4.2). Another reason emerges from different definitions of these terms. For example, there is truly a difference between potential-core length and other names used referring to liquid-intact lengths. Thus, caution should be exercised when using these terms interchangeably, because physically they represent different quantities. Additionally, the velocity ratio may not be the proper parameter to represent the physical phenomenon. This matter will be discussed further in the next section.

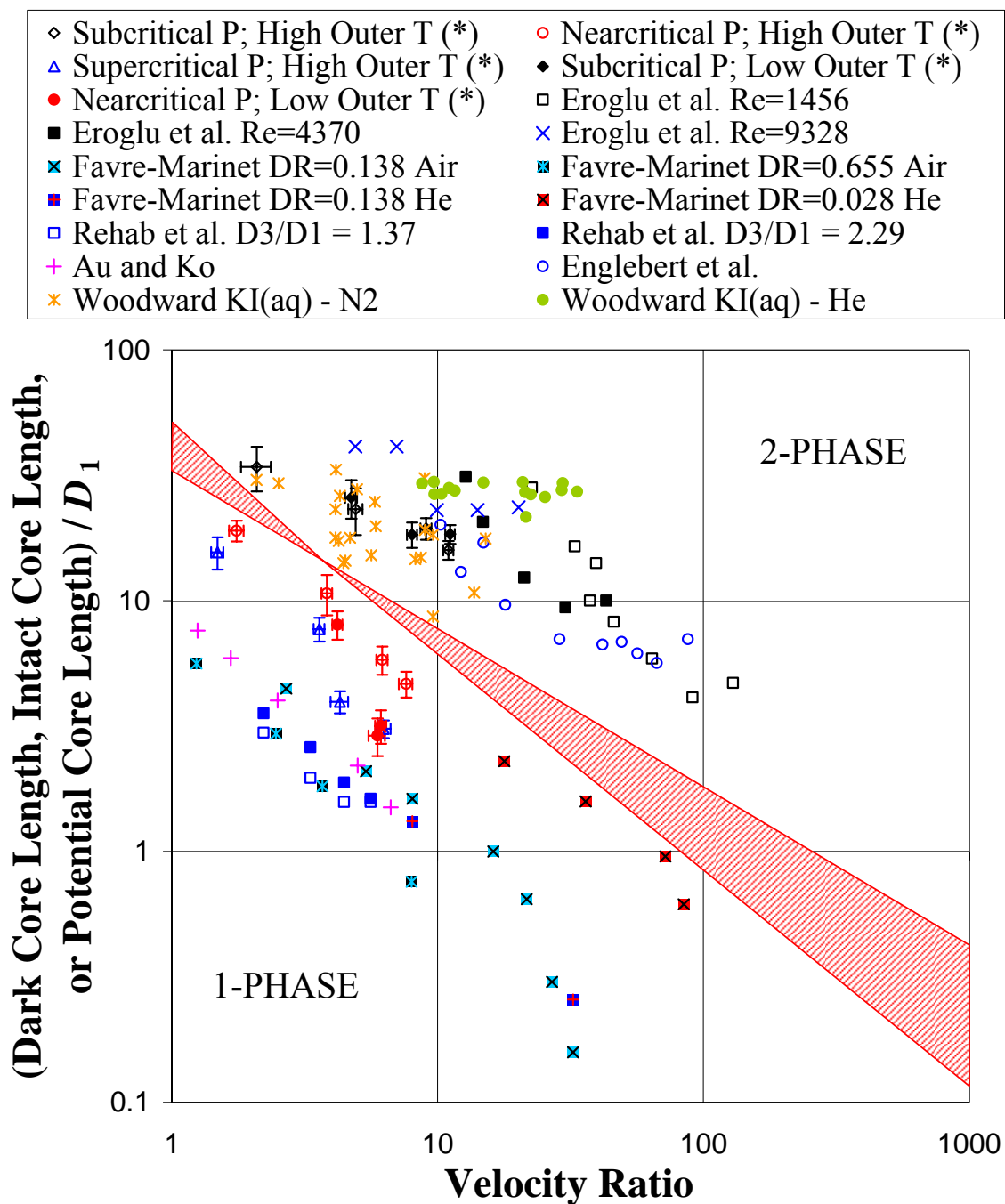


Figure 4.37: Comparison of measured core length data vs. velocity ratio (outer /inner). Data series indicated by (*) denotes this work. References for the data taken from other work listed in Table 4.2. DR denotes density ratio of the outer-jet to the inner-jet.

4.5.3 Scaling of the Dark Core with Momentum Flux Ratio

Scaling of the core length with momentum flux ratio ($M = (\rho_o U_o^2) / (\rho_i U_i^2)$) has been suggested by several authors with the dependence ranging from $M^{-0.5}$ to $M^{-0.13}$ (see Table 4.2). Note that for a uniform-density coaxial jet, the velocity ratio is equal to the square root of the momentum flux ratio. A plot of the measured dark-core length values in this work versus the momentum flux ratio is shown in Fig. 4.38. The dashed line in Fig. 4.38, corresponding to Eq. 4.7, is a least-square curve fit to the subcritical data, and the dotted line, corresponding to Eq. 4.8, is a least squares curve fit to the near- and supercritical data. A clear distinction exists between the dark-core length for the subcritical case (diamond symbols) and that for the near- and supercritical chamber pressures, with the subcritical dark-core length being longer for a given M . This is similar to the observation made with the velocity ratio in Fig. 4.37. It should be noted that the near-critical pressure data is slightly supercritical, and both the near- and supercritical pressure conditions produce a single-phase coaxial jet.

As indicated by Eq. 4.8 and the data in Fig. 4.38, the single-phase data (i.e., near- and supercritical pressures), have the same $M^{-0.5}$ dependence form, which were also reported by others (see Table 4.2). However, the two-phase subcritical data has a weaker dependence, $M^{-0.2}$, than the single-phase dark-core length. Other quantitative differences between jet flows at subcritical and supercritical pressures have been reported before. For single round jets, Chehroudi and co-workers [27, 28, and 30] found that at supercritical pressures the spreading rate and fractal dimension values were the same as those for a gaseous jet injected into a gaseous ambient with different densities (i.e.,

variable-density, single-phase, gaseous jet). This is considered a similar observation, but for the dark-core length. Under supercritical pressures, our coaxial jet results scales with $M^{-0.5}$. From Table 4.2 and the data presented in Fig. 4.38, it appears that the inverse square root of the momentum flux ratio, originally found from the equal-density water-water work of Rehab et al. [51], [52], and later extended to gas-gas coaxial jet with different densities by Favre-Marinet and Camano-Schettini [60], also applies as well to the dark-core length for supercritical shear-coaxial jets. The similarity between the dark-core length at supercritical pressures and single-phase shear-coaxial jets is possibly due to a lack of surface tension under near- and supercritical conditions. However, caution should be exercised when extrapolating these results to systems containing multiple chemical species. A system containing a mixture of different chemical species at a pressure greater than the critical pressure of any of the individual components, may in fact still be below the critical pressure of the mixture at various locations of the jet, as previously discussed in Chapter 2.

$$\frac{L}{D_1} = \frac{25}{M^{0.2}} \quad (4.7)$$

$$\frac{L}{D_1} = \frac{12}{M^{0.5}} \quad (4.8)$$

Where,

L is the dark core length,
 D_1 is the inner diameter of the inner-jet, and
 M is the momentum flux ratio outer-jet to inner-jet.

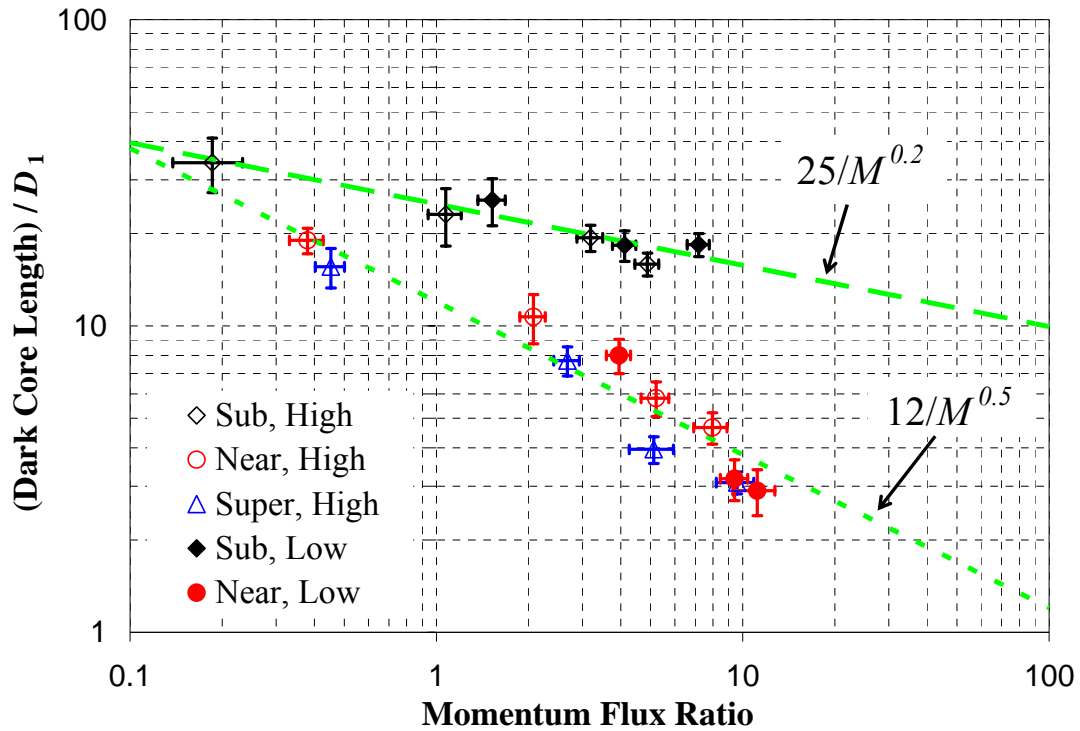


Figure 4.38: Dark core length versus momentum flux ratio. The diamond, circle, and up-triangle symbols represent sub-, near-, and supercritical chamber pressure, respectively. The hollow symbols are at a high outer-jet temperature (~ 190 K) and solid symbols are at a low outer-jet temperature. The error bars on the data points in Fig. 12 for the dark core length represent one standard deviation from the mean, and the error bars for the momentum flux ratio are the n^{th} order uncertainty as described at the beginning of this chapter. The dashed line is $25/M^{0.2}$ and the dotted line is $12/M^{0.5}$.

The near- and supercritical pressure dark-core length data for all of the single-phase cases taken from the references listed in Table 4.2 are plotted against momentum flux ratio in Fig. 4.39. Rehab et al. [51, 52] indicate that injector geometrical effects are attributed to the variation of a constant in the equation of the form given by Eq. 4.8. In addition, this constant was reported to be between 5 and 9 in [51] while to be suggested between 6 and 8 in [52]. Certainly, geometrical differences in injector design can influence the core length, but other differences in the experiment can also change this value.

Figure 4.39 also shows four data points from Favre-Marinet and Camano Schettini [60] (data series denoted by x, +, and * inscribed within a square) at a momentum flux ratio of about 8.9 for different density ratios and fluids with the same injector and measurement technique. Note that the injector produces shear-coaxial jets with different core lengths. This suggests that even though momentum flux ratio incorporates the effect of density differences between cases in some manner, it may not capture the entire effect.

Regarding the data by Rehab et al. [52], the authors reported reasonably good agreement with the $M^{-0.5}$ dependency when a semi-empirical theory was used, although a curve fit to their extracted experimental data indicates a somewhat slower fall of L/D_1 with momentum flux ratio, see dashed-dotted line in Fig. 4.39. It appears that the majority of the core-length data can be captured using the inverse square root dependence on momentum flux ratio with the constant varying from the low value of 5, reported by Rehab et al. [51], to a value of 12 for the dark core length data at near and supercritical pressures up to a momentum flux ratio of about 100. Favre-Marinet and Camano

Schettini [60] reported that for their data at the high momentum flux ratios a recirculation bubble forms at the end of the core causing a decrease in length as shown in Fig. 4.39.

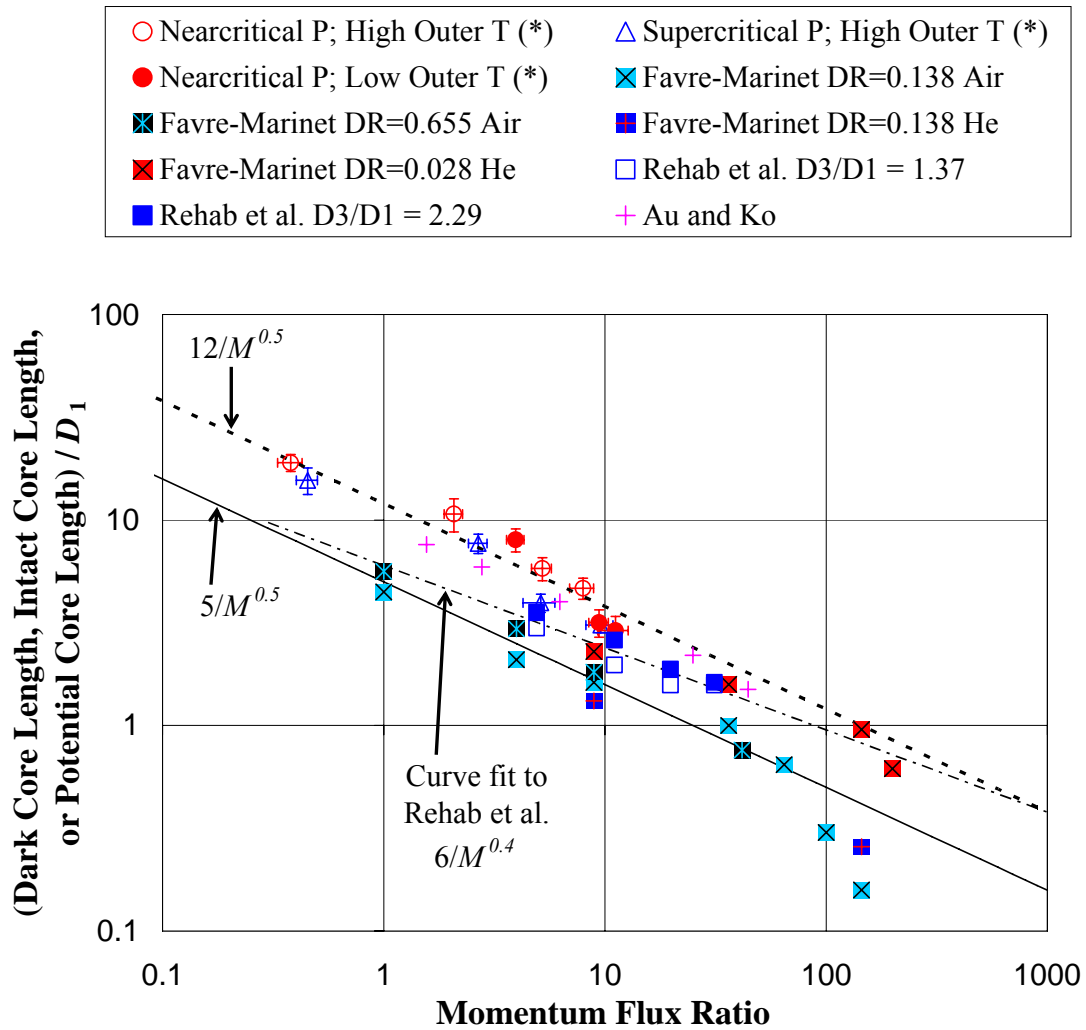


Figure 4.39: Comparison of dark core length, intact core length, or potential-core length for single-phase coaxial jets. This work (denoted by *), Favre-Marinet and Camano Schettini [60], Rehab et al. [52], Au and Ko [48]. DR denotes density ratio of the outer-jet to inner-jet.

The measured results for the core length in two-phase shear-coaxial jets reported by others listed in Table 4.2 are compared with the subcritical pressure dark-core length measured in this work in Fig. 4.40 plotted as a function of momentum flux ratio. Some information is important to keep in mind when comparing these results as follows. There are only three references in the literature that report measurements of core length for two-phase shear-coaxial jets. Also, only one, Porcheron et al. [65], reports an equation that was developed, in part, for a cryogenic liquid core (see Table 4.2). However, because the measuring technique involved acquisition of a quantity named “liquid-presence probability (LPP)” (see Chapter 2 for details), quite different from all the other techniques, only the computed values from the equation indicated by the dashed-dotted line in Fig. 4.40 can be compared. Englebert et al [63], Eroglu et al. [8], and Woodward [62] all used water or a water solution as the fluid flowing from the inner-jet. In the experiments of Eroglu et al. [8], using the same apparatus as in Farago and Chigier [61], they observed laminar flow for $Re < 6000$, and a transition regime to turbulent flow in the range of $6000 < Re < 10^4$. Therefore, it is unlikely that any of the measurements made by Eroglu et al. [8] had a fully-developed turbulent velocity profile at the injector exit-plane. The entrance length of the injector used by Englebert et al. [63] was $22 D_1$. At the range of Re reported by Englebert et al. [63] (see Table 4.2) the required entrance length, estimated from the equation reported in White [85], ranges from about 18 to $25 D_1$. It is possible that some of the data points were not taken under fully-developed condition. This was acknowledged by Englebert et al. [63] and another injector with an entrance length of $50 D_1$ was reported to not influence the breakup mechanism or the diameter of droplets after breakup. However, the effect on the core length was not reported. In

addition, both injectors used by Eroglu et al. [8] and Engelbert et al. [63] had much larger injector gap widths (i.e., annular outer-jet thickness), compared to the inner-jet diameter (see Table 4.2), than that typically associated with rocket engine shear-coaxial injectors. On the other hand, the injector used by Woodward [62] had a gap-width-to-inner-jet diameter more inline with those of typical rocket injectors. The required entrance length of the injector for the Re range reported by Woodward [62] was between 29 and 33 D_1 , whereas the actual length of the injector was 85 D_1 . Therefore, it is likely that the data of Woodward [62] did indeed have a fully-developed turbulent exit velocity profile. However, due to the high density of the aqueous solution of potassium iodide (KI(aq.)) used by Woodward [62], most of the data were for $M < 1$, even at velocity ratios as high as 30.

Evident in Fig. 4.40 is the fact that for the $1 < M < 10$, the dark-core length at the subcritical condition are longer than the laminar or transition regime jets of Eroglu et al. [8] and Englebert et al. [63] and appears to follow the trend of the aqueous solution of potassium iodide with helium (KI(aq) – He) data of Woodward [62]. The equation from Porcheron et al. [65] (see Table 4.2), indicated by the dashed-dotted line, was evaluated at the average Ohnesorge number (Z) and density ratio (outer-to-inner jet) equivalent to the subcritical data of this work, cases 1-4 and 13-15 from Table 4.1. Note that the equation of Porcheron et al. [65], despite having a similar dependence on momentum flux ratio ($M^{-0.13}$) as the subcritical data of this work ($M^{-0.2}$), and the seemingly relevant non-dimensional parameters of Ohnesorge number and density ratio, under-predicts the subcritical dark-core lengths by about 1.5 orders of magnitude. This is most likely due to their definition of core length and the measurement technique mentioned earlier. The

liquid–presence probability (LPP) was measured by a fiber optic method, and correlated with density ratio, Ohnesorge number, momentum flux ratio, and axial distance from the injector. When the LPP dropped to 50%, that axial distance was defined as the core length. By adjusting this LPP to about 2.5%, which results in a change to the constant in their equation, the agreement with the subcritical data of this work is quite good. However, their equation is very sensitive to the choices of the LPP value. For example, changing LPP by 1% causes the equation to over-predict by about one-half order of magnitude, and changing it by 5% causes an under-prediction of the same order. Another observed problem with changing the LPP to 2.5% to fit the data of this work is that the water data of Englebert et al [63], Eroglu et al. [8], and Woodward [62] is then over-predicted by about an order of magnitude. This kind of behavior suggests a lack of generality of this equation despite its appearance, incorporating seemingly-relevant parameters such as Ohnesorge number and density ratio.

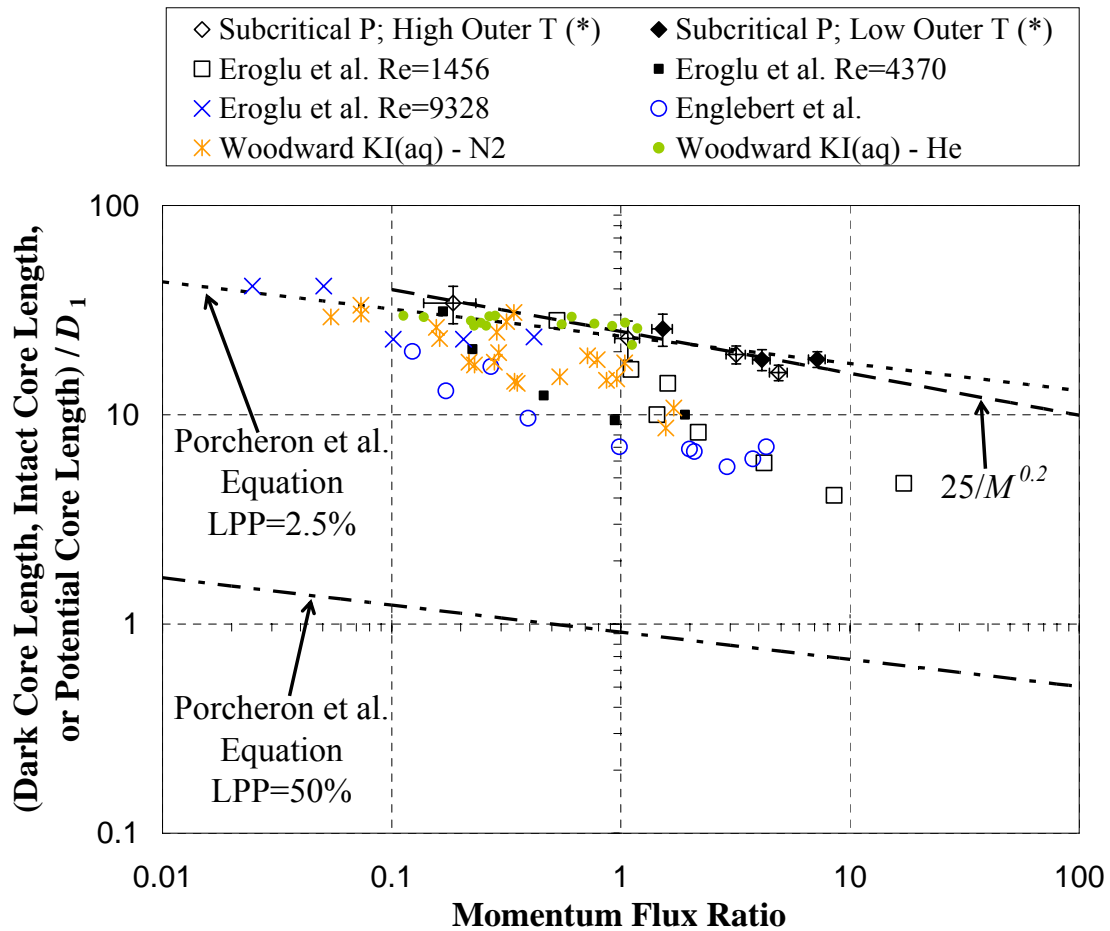


Figure 4.40: Comparison of the dark-core length, intact core length, or potential-core length for two – phase coaxial jets. This work (denoted by *), Eroglu et al. [8], Engelbert et al. [63], Woodward [62]. Porcheron et al. [65] did not report core length measurements because of the measurement technique of liquid probability presence, but only an equation, see Table 4.2 for a summary of the work, and Chapter 2 for more details. Dashed-dotted line is the equation of Porcheron et al. evaluated at the average conditions of the subcritical data of this work with the LPP = 50%, and the dotted line is their equation evaluated at the same conditions except LPP = 2.5%

Figure 4.41 combines the single-phase core length data in Fig. 4.39 with the two-phase data shown in Fig. 4.40. This plot is unique in the sense that, to the best of the author's knowledge, presents all of the relevant core length data available in the open literature, spanning five orders of magnitude in momentum flux ratio. In the range of $1 < M < 10$, which is relevant for cryogenic liquid rocket engines (SSME preburner and main chamber momentum flux ratios are about 3.4 and 1.2, respectively [42], [43]), two distinct regimes in core length exist. The single-phase coaxial jets are shorter and scale differently than the two-phase dark-core lengths of this work. An interesting aspect of these data is that for the momentum flux ratios less than about one, all data points seem to converge to single narrow range. Additionally, in the limit of momentum flux ratio approaching zero (i.e. $U_o \rightarrow 0$), results fall near the upper bound of single round jets (no coaxial jet). More specifically, the data in this limit tends to fall near the upper bound of the intact-core length range expected for single round jets as predicted by the Eq. 4.9 suggested in Chehroudi et al. [86]. This range for the single jet indicated in Fig. 4.41 was calculated using the recommended constant by Chehroudi et al. [86] of 7.15 using the density ratios (outer to inner jet) that spanned this work (see Table 4.1).

$$\frac{L}{D_1} = \frac{C}{\sqrt{\frac{\rho_o}{\rho_i}}} \quad (4.9)$$

Where,

L is the intact core length,

D_1 is the inner diameter of the inner-jet, and

ρ is the density, and

C is a constant ranging from 3.3 to 11, with the optimum being 7.15.

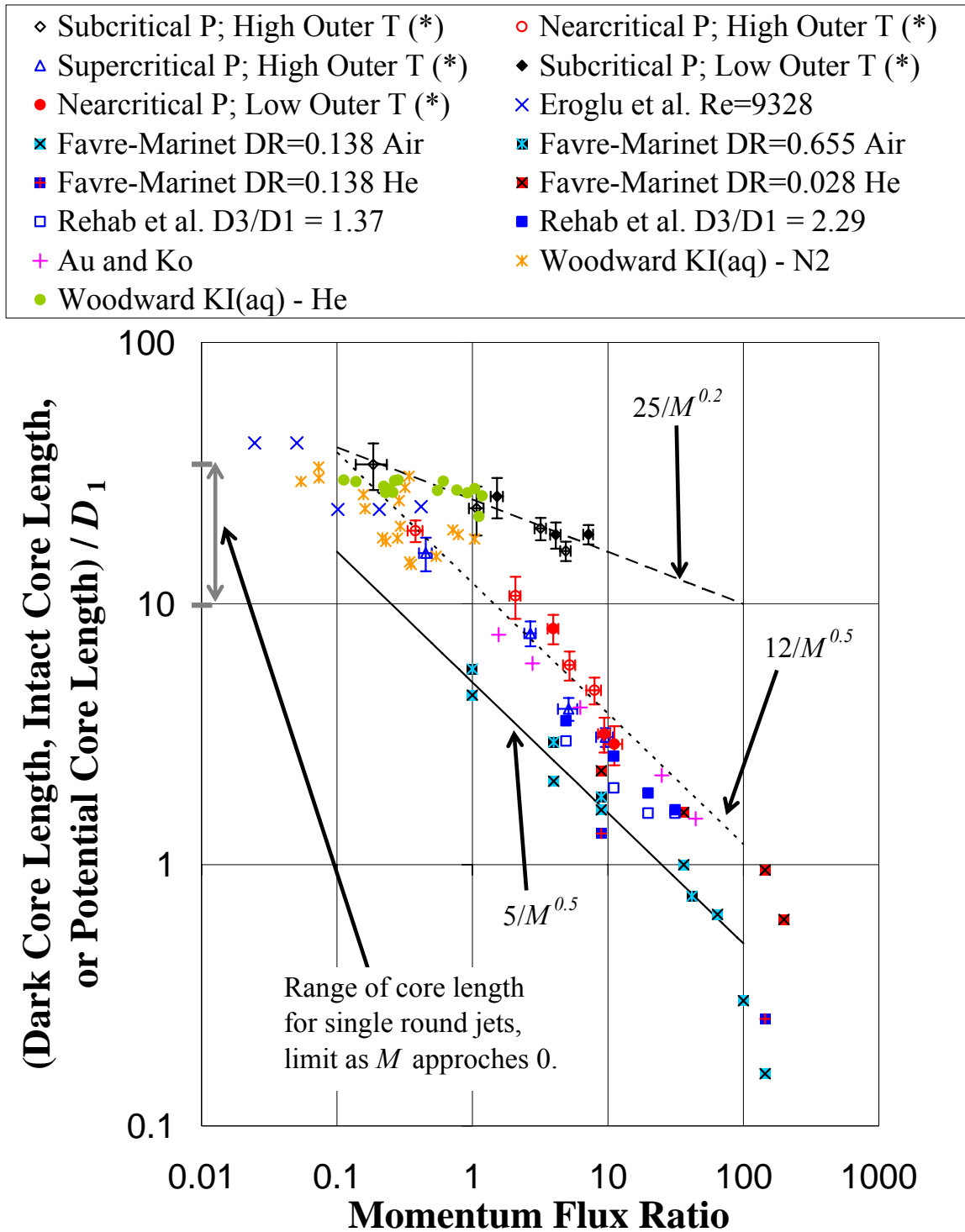


Figure 4.41: Comparison of the dark-core length, intact core length, or potential-core length vs. momentum flux ratio for shear-coaxial injectors, both single-phase and two-phase shear-coaxial jets. The same symbol definitions and references used here as Fig. 4.39 and Fig. 4.40 .

The dark-core length data from this work for momentum flux ratios less than one are plotted in Fig. 4.42 against outer-to-inner jet density ratio, and compared with Eq. 4.9 using the optimum value of $C = 7.15$ suggested by Chehrودي et al. [86]. It is clear from Fig. 4.42 that in the low-momentum-flux-ratio limit, the controlling nature of the high-speed outer-jet is diminished and the core length values are similar to those of single round jets.

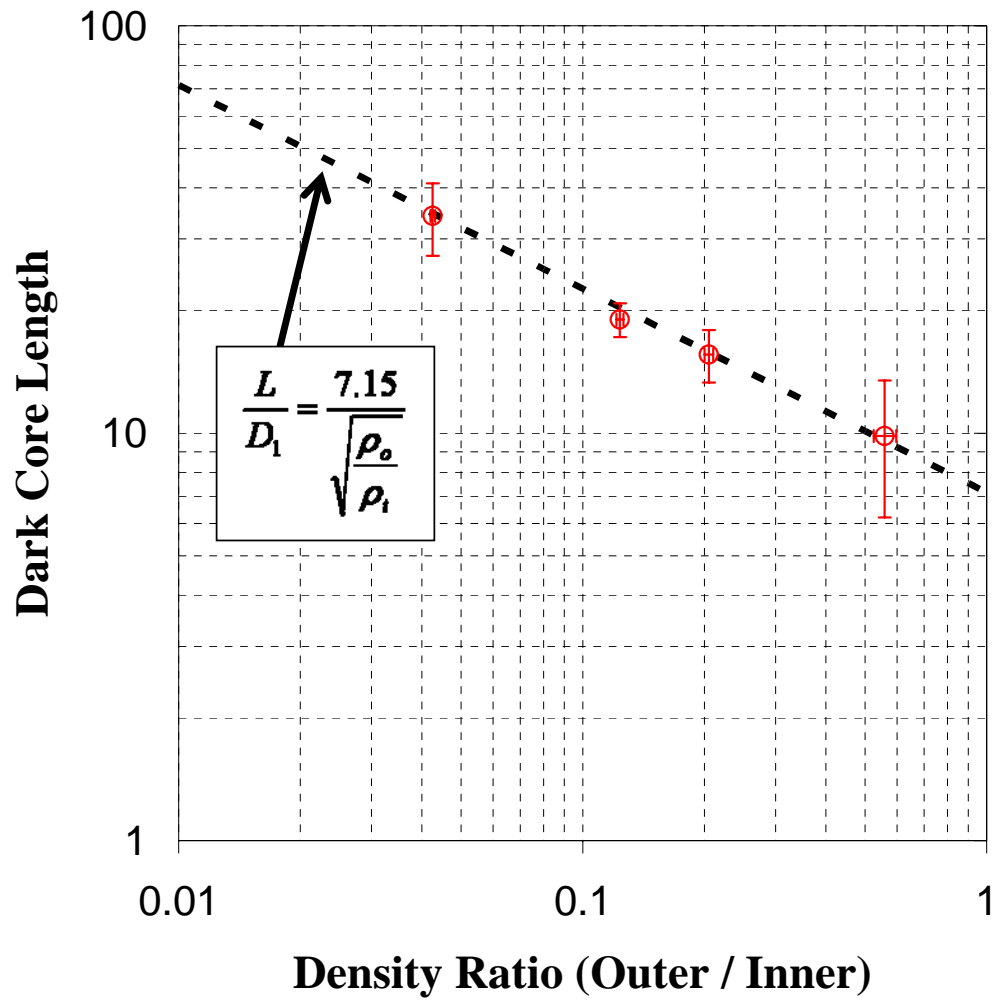


Figure 4.42: Comparison of dark core length, for $M < 1$, with Eq. 4.9 developed for single round jets.

Chapter 5

Summary, Conclusion, and Recommendations for Future Work

5.1 Summary and Conclusions

A flow study was conducted on a cryogenic shear-coaxial injector at pressures spanning from subcritical to supercritical values, both with and without high-amplitude external acoustic excitation. This injector design was based on the experience gained from a single round jet exposed to similar conditions, see Chehroudi and coworkers [16-22]. The injector was placed in a chamber, near the minimum of the pressure oscillation amplitude of its acoustic mode. The flow from the inner-jet of the coaxial injector was liquid nitrogen (or liquid-like, if at supercritical pressures) and cold gaseous nitrogen flowed from the outer annular jet, both injected into a chamber pressurized with nitrogen at ambient temperature. Radial temperature profiles were measured at the exit-plane of cryogenic shear-coaxial jets using a traversing mechanism holding a very small thermocouple to ensure proper characterization of the boundary conditions. To the best of the author's knowledge, this is the first reported exit-plane temperature profiles of a cryogenic coaxial jet at supercritical chamber pressures. The coaxial jet was imaged with cameras with framing rates up to 18 kHz. Visualizations of the jet were taken both with and without the external transverse acoustic field. The field was initiated by an activation of an acoustic driver at a wavelength two orders of magnitude longer than the

characteristic dimensions of the injector. Both qualitative and quantitative information were obtained from the images.

An algorithm for measuring the dark-core length from an image has been developed. This method, named an adaptive thresholding technique, accounts for the variability of the light source and changes in the refractive index field reflected in images. For this work, the rise of the background light in an image histogram was suitably identified by the slope of the intensity histogram increasing above the e^{-1} value. There is no guarantee that images of other flows have the same criteria. However, the information from image histograms provided a consistent and repeatable method for identification of the dark-core length of the jet.

Velocity measurements can be made from high-speed shadowgraph movies. Much work must still be done to determine the optimum interrogation source window size and image magnifications to improve overall accuracy of velocity measurements. The velocity measurement relies on the assumption (or approximation) that the motion of shadows of fluid elements in an image from one frame to another represents the motion of the fluid elements. Improvements on this approximation are achieved when the velocity gradient along the direction of light source to the camera is zero, or when the fluid structure is easily identified as a particle. A direct comparison to a proven velocimetry measurement technique, such as laser Doppler velocimetry (LDV), would allow for a better quantification of the technique and prove the validity.

Based on the results of the experiments summarized above the following conclusions are offered:

1. Transient start of the acoustic driver results in a limit cycle behavior, which is evident from the transient velocity measurements, and from the behavior of the jet observed in the high-speed movies. This presents one of the first transient measurements of velocity from shadowgraph images reported in the literature.
2. The amplitude of the acoustic pressure waves and the resulting transverse velocity fluctuations, driven at a resonance frequency of the chamber, decreases as the density of the chamber fluid increases. This is a consequence of operating acoustic driver at a constant maximum power.
3. The wavelength measured from the amplitude of the acoustic pressure measurements (in time or spatially) is two orders of magnitude longer than the characteristic dimensions of the jet. Therefore, the wavelength is too long to excite coherent structures in the shear layer.
4. The acoustic driver governs the behavior of the transverse velocity in the chamber fluid and the jet, which is evident from the peaks in the power spectra of the velocity signals and the movies. The velocity fluctuations measured in the jet are amplified compared to that of the chamber fluid far from the influence of the jet. Also, the most energetic peak in the power spectra of the transverse velocity is at the acoustic driver frequency.
5. The motion of the core dominates the behavior of the jet. The oscillations of the core are predominately in the direction of the acoustic velocity. Some motions of the core do occur in other directions, but are not in the same periodic fashion and are lower in amplitude. The transverse velocity fluctuations impart a force to the core of the jet near the injector tip causing the core to be displaced in the

transverse direction corresponding to the direction of the local momentum at a given time. As a portion of the core is displaced near the injector tip, and convected downstream, it continues to travel in the same transverse direction, despite a reversal of the acoustic velocity field.

6. The mean dark-core length, which is the axial distance from the injector tip to the first break in the core, shortens upon exposure to the acoustic field. However, a clear difference between the acoustically-excited and unexcited jets can be discerned at the highest velocity ratios, high outer-jet temperature, and under subcritical chamber pressure.
7. The dark-core length (for unexcited jet) measured from the averaged image of a set is shorter than the mean of the dark-core length measured from the individual images of the same set. When the fluctuations in the dark-core length are very small, the two quantities are nearly equal.. However, when the fluctuations of the dark-core length are large, differences as high as 20% is seen. This is a consequence of the averaging process of the image.
8. As the chamber pressure is increased at a constant velocity ratio, the dark-core length decreases. Because of the variability of the dark-core length, differences in the dark-core length, comparing the near- and supercritical chamber pressures, cannot always be distinguished. However, the dark-core length under subcritical chamber pressure at the same velocity ratio (or momentum flux ratio) is longer than those measured under near- or supercritical pressures.
9. The scaling of the dark-core length with the inverse-square-root of the momentum flux ratio, which was developed from all water shear-coaxial jets [37]-[42], and

later applied to gaseous jets of different densities [43], also applies to supercritical shear-coaxial jets. For this work, the dark-core length at near- and supercritical pressures is approximately given by the equation: $L/D_1 \approx 12 M^{-0.5}$. Within the momentum flux ratio range of $0.1 < M < 100$, nearly all of the single-phase shear-coaxial jet core length data in the open literature can be contained in a region defined by $L/D_1 \approx C M^{-0.5}$ when the constant C is between 5 and 12.

10. At subcritical pressures, the scaling of the dark-core length with momentum flux ratio, for this work, is given by $L/D_1 \approx 25 M^{-0.2}$. Limited core length data for two-phase shear-coaxial jets with fully-developed turbulent inner-jet flow exists in the open literature in the range of momentum flux ratios between 1 and 10, considered relevant for liquid rocket engines.
11. When comparing all of the available core length data in the open literature, for a given velocity ratio, the core length of two-phase (i.e., a liquid inner-jet with a gaseous outer-jet and chamber fluid) shear-coaxial jets are longer than those for single-phase shear-coaxial jets, and a clear region of demarcation between the two types can be drawn.
12. In the limit of momentum flux ratio approaching zero (for example, when the velocity of the outer-jet goes to zero), the dark-core length should approach that of a single round jet. For momentum flux ratios less than unity, where the controlling nature of the outer-jet momentum is diminished, the dark-core length scales with the inverse square root of the outer-to-inner density ratio, as predicted by an equation in Chehroudi et al. [52].

13. The root mean square (RMS) variation of the dark-core length decreases with increasing velocity ratio at a given chamber pressure and asymptotically approaches a constant level. The RMS of the dark-core length is greatest at subcritical pressures. To the best of the author's knowledge, this quantity was not previously reported in the literature.
14. From the past works, it was shown that an episode of so-called "temperature ramping", used for stability rating, could lead the engine to an unstable behavior. Also, from other works, it is shown that coaxial injectors with high outer-to-inner jet velocity ratios (greater than ~ 10 for LOX/H₂) are more stable. In the current work, the observation that the RMS of the dark-core length fluctuations decreased at high velocity ratio under both high and low outer-jet temperatures, is considered as a potential explanation the injector-induced combustion instabilities. It is possible that decreases in the RMS fluctuation levels could weaken a key feedback mechanism for the self-excitation process that is believed to drive the combustion instability in rocket engines. This offers a possible improvement in understanding of the combustion instability in LRE. Ultimately, this hypothesis requires further testing in a multi-element, fired rocket experimental facility, for validation purposes

5.2 Recommendations for Future Work

The data in the literature come from a variety of different injectors. A systematic variation of all the important dimensions of the injector geometry should allow for an accurate assessment of the impact the injector has on the length of the dark core. This ought to be combined with measurements from sufficiently large number of images to permit more accurate determination of the variability of the dark-core length. Some relevant dimensions that may produce first-order effects on the behavior of the core are the inner-tube (post) recess and the thickness of the inner-tube lip.

In addition to varying the injector dimensions, systematic changes of the fluids used, particularly with two-phase shear-coaxial jet operation is recommended. By using a single chemical species for both the inner and outer-jets, a clear distinction between subcritical and supercritical can be drawn. However, what may be more relevant to a liquid rocket engine is using a pair of fluids, such as liquid nitrogen and either hydrogen or helium at elevated pressures. The resulting system would have closely related properties to that of a cryogenic liquid rocket engine. Recall that a combusting system, or any system of multiple chemical species, may not be supercritical everywhere because of the highly non-linear behavior of the critical locus dependence on composition. Therefore, it is possible that even though the propellants are injected at pressures greater than the critical pressure, dark-core length may behave similar to a two-phase jet. This is because the region near the core is in fact a two-phase flow. Momentum flux ratio is an important parameter governing core length of a shear-coaxial jet and does a better job at collapsing the data from the open literature than the velocity ratio. However, the

bifurcation that exists between the fully-turbulent two-phase shear-coaxial jets and the single-phase shear-coaxial jets cannot be described with the inverse square root of the momentum flux ratio. There is an inherent difference between the single-phase and two-phase shear-coaxial jets. Perhaps, surface tension is the important quantity explaining the difference. Collapse of the core length data for both single-phase and two-phase jets to a single curve is desirable and has been considered by many researchers, even was claimed by a few. However, preponderance of evidence from this work suggests that a satisfactory collapse to a single curve is not yet achieved, and perhaps may not even exist. However, systematic variations of the viscosity, surface tension, and density of the inner and outer-jets in a given injector is a step in the right direction.

The application of high-speed shadowgraphs for measuring velocity proved to be a promising technique. However, more work is required to determine the accuracy of the approach. This could be accomplished by using some proven velocimetry measurement technique, such as laser Doppler velocimetry (LDV), which would allow examination of this method's limitations.

The acoustic field within the inner-chamber is not completely characterized. The injector in this work was placed at a pressure minimum. A liquid rocket engine experiencing a transverse mode combustion instability will undoubtedly have injectors at many phase angles with respect to the pressure amplitude. By fully characterizing the inner-chamber pressure field and moving the location of the injector, various effects on the jets behavior can be investigated. Additionally, by acoustically driving multiple injectors and analyzing the interaction between the jets, would provide useful information towards better understanding of the rocket combustion instability.

Finally, a computational model that can use the data reported in this dissertation, would provide a wealth of information. The model capable of satisfactory predication could provide the baseline validation on the fluid mechanics portion of a combustion instability code.

Bibliography

1. Culick F. E. and Yang, V., "Overview of Combustion Instabilities in Liquid-Propellant Rocket Engines," Liquid Rocket Engine Combustion Instability, edited by V. Yang and W. Anderson, Progress in Astronautics and Aeronautics, AIAA, Washington, DC, 1995, pp. 3-38.
2. Harje, D. T., and Reardon, F. H. (eds.) "Liquid Propellant Rocket Combustion Instability," NASA SP-194, 1972, pp. 17-19.
3. Hulka, J., and Hutt, J., "Liquid Oxygen / Hydrogen Instability Phenomena," in Liquid Rocket Engine Combustion Instability, edited by V. Yang and W. Anderson, Progress in Astronautics and Aeronautics, AIAA, Washington, DC, 1995, pp. 39-72.
4. DCAPII, ver. 2.1, The Design Institute for Physical Property Data (DIPPR) of The American Institute of Chemical Engineers, 1985.
5. Vingert, L., Gicquel, P., Lourme, D., and Ménoret, L., "Coaxial Injector Atomization," Liquid Rocket Engine Combustion Instability, edited by V. Yang and W. Anderson, Progress in Astronautics and Aeronautics, AIAA, Washington, DC, 1995, pp.145-190.
6. Rayleigh, J. W. S., "On the instability of Jets," Proceedings of London Mathematical Society, Vol. 10, 1878. pp. 4-21.
7. Lefebvre, A. H., *Atomization and Sprays*, Hemisphere, New York, 1989.
8. Eroglu, H., Chigier, N., and Farago, Z., "Coaxial Atomizer Intact Lengths," Physics of Fluids A, Vol. 3, No. 2, Jan. 1991, pp. 303-308.
9. Moran, M. J. and Shapiro, H. N., *Fundamentals of Engineering Thermodynamics*, 3rd ed., J. Wiley and Sons, New York, 1995.
10. Smith, J. M., Van Ness, H. C., and Abbott, M. M., *Introduction to Chemical Engineering Thermodynamics*, 5th ed., McGraw-Hill, New York, 1996.
11. van Konynenburg, P. H., and Scott, R. L., "Critical Lines and Phase Equilibria in a Binary van der Waals Mixtures," Phil. Trans. R. Soc. London, Vol. 298, 1980, pp 495.

12. Street, W. B., and Calado, J. C. G., "Liquid Vapor Equilibrium for Hydrogen + Nitrogen at Temperatures from 63 to 110K and Pressures to 57 MPa," J. Chem. Thermodynamics, Vol. 10, 1978, pp 1089-1100.
13. Zuo, Y. X., and Stenby, E. H., "A Linear Gradient Theory Model for Calculating Interfacial Tensions of Mixtures," J. of Colloid and Interface Science, Vol. 182, 1996, pp. 126-132.
14. REFPROP, Reference Fluid Thermodynamic and Transport Properties, Software Package, Ver. 7.0, NIST, U.S. Department of Commerce, Gaithersburg, MD, 2002.
15. Gielessen, J. and Schmatz, W, Z. Phys. Chem., Neue Folge, Vol. 27, 1961.
16. Lee, S. J., The Surface Tension of LOX Droplets at Near-Critical Conditions Using Molecular Dynamics, M.S. Thesis, Aerospace Engineering, The Pennsylvania State University, 2001.
17. Vieille, B., Étude expérimentale de l'atomisation secondaire de gouttes d'oxygène liquide, Thèse par Docteur de L'Université D'Orléans, 1998.
18. Harstad, K. and Bellan, J., "Evaluation of commonly used assumptions for isolated and cluster drops, in nitrogen at all pressures," Combustion and Flame, Vol. 127, 2001, pp. 1861.
19. Woodward, R. D., and Talley, D. G., "Raman Imaging of Transcritical Cryogenic Propellants," 34th Aerospace Sciences Meeting and Exhibit, AIAA, Washington, DC, 15-18 Jan. 1996.
20. Givler, S. D., and Abraham, J., "Supercritical Droplet Vaporization and Combustion Studies," Progress in Energy and Combustion Science, Vol. 22, 1996, pp. 1-28.
21. Yang, V. "Modeling of supercritical vaporization, mixing, and combustion processes in liquid-fueled propulsion systems," Proc. Combust. Inst., Vo. 28, 2000, pp. 925.
22. Bellan, J., "Supercritical (and subcritical) fluid behavior and modeling: drops, streams, shear and mixing layers, jets and sprays," Progress in Energy and Combustion Science, Vol. 26, 2000, pp. 329-366.
23. Newman, J. A., and Brzustowski, T. A., "Behavior of a Liquid Jet near the Thermodynamic Critical Region," AIAA J., Vol. 9, No. 8, 1971, pp. 1595-1602.
24. Chehroudi, B., Talley, D., and Coy, E. B., "Initial Growth Rate and Visual Characteristics of a Round Jet into a Sub- to Supercritical Environment of

- Relevance to Rocket, Gas turbine, and Diesel Engines,” 37th AIAA Aerospace Science Meeting and Exhibit, AIAA, Washington, DC, 11-14 Jan. 1999.
25. Chehroudi, B., Talley, D. G., and Coy, E. B., “Fractal Geometry and Growth Rate Changes of Cryogenic Jets near the Critical Point,” 35th AIAA/ASME/SAE/ASEE Joint Propulsion Conference and Exhibit, AIAA, Washington, DC, 20-24 Jun. 1999.
 26. Chehroudi, B., Cohn, R., Talley, D. G., and Badakhshan, A., “Raman Scattering Measurements in the Initial Region of Sub- and Supercritical Jets,” 36th AIAA/ASME/SAE/ASEE Joint Propulsion Conference and Exhibit, AIAA, Washington, DC, 17-19 Jul. 2000.
 27. Chehroudi, B., Talley, D. G., and Coy, E. B. “Visual Characteristics and Initial Growth Rates of Round Cryogenic Jets at Subcritical and Supercritical Pressures,” *Physics of Fluids*, Vol.4, No. 2, Feb. 2002. pp. 850-861.
 28. Chehroudi, B., Cohn, R., and Talley, D. G., “Cryogenic Shear Layers: Experiments and Initial Growth Rates of Round Cryogenic Jets at Subcritical and Supercritical Pressures,” *International Journal of Heat and Fluid Flow*, Vol. 23, 2002, pp. 554-563.
 29. Chehroudi, B., and Talley, D. G., “Interaction of Acoustic Waves with a Cryogenic Nitrogen Jet at Sub- and Supercritical Pressures,” 40th AIAA Aerospace Meeting and Exhibit, AIAA, Washington, DC, 14-17 Jan. 2002.
 30. Chehroudi, B. and Talley, D., “Fractal Geometry of a Cryogenic Nitrogen Round Jet Injected into Sub- and Super-critical Conditions”, *Atomization and Sprays*, Vol. 14, 2004, pp. 81-91.
 31. Chehroudi, B., Davis, D. W., and Talley, D. G., “Initial Results from a Cryogenic Coaxial Injector In An Acoustic Field,” 41st AIAA Aerospace Sciences Meeting and Exhibit, AIAA, Washington, DC, 6-9 Jan. 2003.
 32. Davis, D. W. and Chehroudi, B., “The Effects of Pressure and Acoustic Field on a Cryogenic Coaxial Jet,” 42nd AIAA Aerospace Sciences Meeting and Exhibit, AIAA, Washington, DC, 5-8 Jan. 2004.
 33. Davis, D. W., Chehroudi, B., and Sorensen, I. “Measurements in an Acoustically Driven Coaxial Jet Under Supercritical Condition,” 43rd AIAA Aerospace Sciences Meeting and Exhibit, AIAA, Washington, DC, 10-13 Jan. 2005.
 34. Davis, D. W., and Chehroudi, B., “Measurements of an Acoustically Driven Coaxial Jet under Sub-, Near-, and Supercritical Conditions,” *J. of Propulsion and Power*, 2005 (submitted).

35. Davis, D. W., Chehroudi, B., and Talley, D. G., "Experiments on a Coaxial Injector under an Externally-Forced Transverse Acoustic Field," 53rd JANNAF Propulsion / 2nd Liquid Propulsion Subcommittee / 1st Spacecraft Propulsion Subcommittee Meeting, CPIA, Monterey, CA, 5-8 Dec. 2005.
36. Davis, D. W., and Chehroudi, B., "Shear- Coaxial Jets from a Rocket- Like Injector in a Transverse Acoustic Field at High Pressures," 44th AIAA Aerospace Sciences Meeting and Exhibit, AIAA, Washington, DC, 9-12 Jan. 2006.
37. Oswald, M., Smith, J. J., Branam, R., Hussong, J., Schik, A., Chehroudi, B., and Talley, D. G., "Injection of Fluids into Supercritical Environments," Comb. Sci. Tech., to appear 2005.
38. Oswald, M., and Micci, M., "Spreading Angle and Centerline Variation of Density of Supercritical Nitrogen Jets," Atomization and Sprays, Vol. 11, 2002, pp. 91-106.
39. Oswald, M., and Schik, A., "Supercritical nitrogen free jet investigated by spontaneous Raman scattering," Experiments in Fluids, Vol. 27, 1999, pp. 497-506.
40. Zong, N., Meng, H., Hsieh, S.-Y., Yang, V., "A Numerical Study of Cryogenic Fluid Injection and Mixing under Supercritical Conditions," Physics of Fluids, Vol. 16, No. 12, 2004, pp. 4248-4261.
41. Zong, N., Modeling and Simulation of Cryogenic Fluid Injection and Mixing Dynamics under Supercritical Conditions, Ph.D. Thesis, Department of Mechanical and Nuclear Engineering, The Pennsylvania State University, University Park, PA, <http://etda.libraries.psu.edu/>, 2005.
42. Strakey, P. A., Talley, D. G., and Hutt, J. J., "Mixing Characteristics of Coaxial Injectors at High Gas/Liquid Momentum Ratios," Journal of Propulsion and Power, Vol. 17, No. 2, 2001, pp. 402-410.
43. Strakey, P. A., Talley, D. G., Tseng, L. K., Miner, K. I., "Effects of Liquid-Oxygen Post Biasing on SSME Injector Wall Compatibility," Journal of Propulsion and Power, Vol. 18, No. 2, 2002, pp. 240-246.
44. Forstall, W., and Shapiro, A. H., "Momentum and Mass Transfer in Coaxial Gas Jets," J. Applied Mechanics, Trans. ASME, Vol. 72, 1950, pp. 399-408.
45. Chigier, N. A., and Beer, J. M., "The Flow Region Near the Nozzle in Double Concentric Jets," J. of Basic Engineering, Trans. ASME, Vol. 4, 1964, pp. 797-804.

46. Champagne, F. H., and Wygnanski, I. J., "An Experimental Investigation of Coaxial Turbulent Jets," *International Journal of Heat and Mass Transfer*, Vol. 14, 1971, pp. 1445-1464.
47. Ko, N. W. M., and Au, H., "Coaxial Jets of Different Mean Velocity Ratios," *Journal of Sound and Vibration*, Vol. 100, No. 2, 1985, pp. 211-232.
48. Au, H., and Ko, N. W. M., "Coaxial Jets of Different Mean Velocity Ratios, Part 2," *Journal of Sound and Vibration*, Vol. 116, No. 3, 1987, pp. 427-443.
49. Dahm, W., Frieler, C., and Tryggvason, G., "Vortex Structure and Dynamics in the Near Field of a Coaxial Jet," *J. Fluid Mechanics*, Vol. 241, 1992, pp. 371-402.
50. Villiermaux, E., Rehab, H., and Hopfinger, E. J., "Breakup Regimes and Self-Sustained Pulsations in Coaxial Jets," *Meccanica*, Vol. 29, 1994, pp. 393-401.
51. Rehab, H., Villiermaux, E., and Hopfinger, E. J., "Flow Regimes of Large Velocity Ratio Coaxial Jets," *J. Fluid Mech.*, 1997, pp. 357-381.
52. Rehab, H., Villiermaux, E., and Hopfinger, E. J., "Geometrical Effects of Near-Field Flow Structure of Coaxial Jets," *AIAA Journal*, Vol. 36, No. 5, 1998, pp. 867-869.
53. Villiermaux, E., "Mixing and Spray Formation in Coaxial Jets," *J. Propulsion and Power*, Vol. 14, No. 5, 1998, pp. 807-817.
54. Lasheras, J. C., and Hopfinger, E. J., "Liquid Jet Instability and Atomization in a Coaxial Gas Stream," *Annual Rev. Fluid Mech.*, Vol. 32, 2000, pp. 275-308.
55. Hopfinger, E. J., and Lasheras, J. C., "Breakup of A Water Jet in High Velocity Co-Flowing Air," *ICLASS-94*, Rouen, France, Paper I-15, July 1994, pp. 110 – 117.
56. Raynal, L., Instabilite et entrainement a l'interface d'une couche de mélange liquid-gaz, Thèse de Doctorat, Université Joseph Fourier, Grenoble, France, 1997.
57. Raynal, L., Villiermaux, E., Lasheras, J. C., and Hopfinger, E. J., "Primary Instability in Liquid-Gas Shear Layers," 11th Symposium on Turbulent Shear Flows, Grenoble-France, Sept. 8-11, 1997.
58. Lasheras, J. C., Villiermaux, E., and Hopfinger, E. J., "Breakup and Atomization of a Round Water Jet by a High Speed annular Air Jet," *J. Fluid Mech.*, Vol. 357, 1998, pp. 351-379.
59. Favre-Marinet, M., Camano, E. B., and Sarboch, J., "Near-Field Coaxial Jets with Large Density Differences," *Experiments in Fluids*, Vol. 26, 1999, pp. 97-106.

60. Favre-Marinet, M., and Camano Schettini, E. B., "The Density Field of Coaxial Jets with Large Velocity Ratio and Large Density Differences," *International Journal of Heat and Mass Transfer*, Vol. 44, 2001, pp. 1913-1924.
61. Farago, Z., and Chigier, N., "Morphological Classification of Disintegration of Round Liquid Jets in a Coaxial Air Stream," *Atomization and Sprays*, Vol. 2, 1992, pp. 137-153.
62. Woodward, R. D., Primary Atomization of Liquid Jets Issuing from Rocket Engine Coaxial Injectors, Ph.D. Thesis, Department of Mechanical Engineering, The Pennsylvania State University, University Park, PA, 1993.
63. Englebert, C., Hardalupas, Y., and Whitlaw, J. H., "Breakup Phenomena in Coaxial Air-Blast Atomizers," *Proc. R. Soc.*, Vol. 451, London, 1995, pp. 189-229.
64. Carreau, J. L., Porcheron, E., LeVisage, D., Prevost, L., and Roger, F., "Liquid Core Characterization of Coaxial Liquid Oxygen/Inert Gas Jets," *Int. J. of Fluid Mech. Research*, Vol. 24, Nos. 4-6, 1997, pp.498-507.
65. Porcheron, E., Carreau, J. L., Prevost, L., LeVisage, D., and Roger, F., "Effect of Density on Coaxial Liquid Jet Atomization," *Atomization and Sprays*, Vol. 12, 2002, pp. 209-227.
66. Miesse, C. C., "The effect of ambient pressure oscillations on the disintegration and dispersion of a liquid jet", *Jet Propulsion*, Vol. 25, 1955, pp. 525-530, and 534.
67. Newman, "A Preliminary Study of the Effects of Vaporization and Transverse Oscillations on Liquid Jet Breakup," NASA CR-72258, 1967.
68. Buffum, F. G., and Williams, F. A. Response of turbulent liquid jets to transverse acoustic fields, *Proceedings of the 1967 Heat Transfer and Fluid Mechanics Institute*, Edited by P. A. Libby, D. B. Olfe, and C. W. Van Atta, 1967, pp. 247-276.
69. Heidmann, M. F. and Groenweg, J. F. "Analysis of the dynamic response of liquid jet atomization to acoustic oscillations," NASA Technical Note, NASA TN D-5339, July, 1969.
70. Rhys, N. O., Acoustic Excitation and Destruction of Liquid Sheets, PhD Thesis, Department of Mechanical and Aerospace Engineering, The University of Alabama in Huntsville, 1999.
71. Ota, J., Sakurai, K., Okamoto, K., and Madarame, H., "Application of Image Analysis with Noise Removal for Supercritical CO₂," *Proceedings of ICONE*,

- 10th International Conference on Nuclear Engineering, Arlington Virginia, 14-18 Apr. 2002.
72. Okamoto, K., Ota, J., Sakurai, K., Madarame, H., "Transient Velocity Distributions for the Supercritical Carbon Dioxide Forced Convection Heat Transfer," *Journal of Nuclear Science and Technology*, Vol. 40, No. 10, 2003, pp. 763-767.
 73. *Omega Temperature Hand Book*, 5th ed., Curtis Publishing, Indianapolis, IN, 2004, Chap. Z
 74. Moffat, R. J., "Describing Uncertainties in Experimental Results," *Experimental Thermal and Fluid Science*, Vol. 1, 1988, pp. 3-17.
 75. Wu, P.-K., Tseng, L.-K., and Faeth, G. M., "Primary Breakup in Gas/Liquid Mixing Layers for Turbulent Liquids," *Atomization and Sprays*, Vol. 2, 1992, pp. 295-317.
 76. Davis, D. W. Supercritical Fuel Injection Studies for Advanced Gas Turbine Engines, M.S. Thesis, The Pennsylvania State University, 2001.
 77. Kinsler, L. E., Frey, A. R., Coppens, A. B., Sanders, J. V., *Fundamentals of Acoustics*, 4th Ed., J. Wiley and Sons, New York, 2000.
 78. Gendrich, C. P., Koochesfahani, M. M., and Nocera, D.G., "Molecular Tagging Velocimetry and Other Novel Applications of a New Phosphorescent Supramolecule," *Experiments in Fluids*, Vol. 23, 1997, pp. 361-372.
 79. Russ, J. C., *The Image Processing Handbook*, CRC Press, Boca Raton FL, 1992.
 80. Zong, N. and Yang, V., "A Numerical Study of High-Pressure Oxygen/Methane Mixing and Combustion of A Shear Coaxial Jet," 43rd AIAA Aerospace Sciences Meeting and Exhibit, AIAA, Washington, DC, 10-13 Jan. 2005.
 81. Eagle, David, BNALib, A BASIC Numerical Analysis Library for Personal Computers, Littleton, CO, www.vbonline.com, 2002.
 82. Glogowski, M., Bar-Gil, M., Puissant, C., Kaltz, T., Milicic, M., and Micci, M., "Shear Coaxial Injector Instability Mechanisms" 30th AIAA/ASME/SAE/ASEE Joint Propulsion Conference, AIAA, Washington, DC, 27-29 Jun. 1994.
 83. Vingert, L., Gicquel, P., Ledoux, M., Care, I., Micci, M., and Glogowski, M., "Atomization in Coaxial-Jet Injectors", in *Liquid Rocket Thrust Chambers: Aspects of Modeling, Analysis, and Design*, edited by Yang, V., Habiballah, M., Hulka, J., and Popp, M., Progress in Astronautics and Aeronautics, AIAA, Washington, DC, 2004, pp. 105-140.

84. Wanhainen, J. P., Feiler, C. E., and Morgan, C. J., "Effect of Chamber Pressure, Flow per Element, and Contraction Ratio on Acoustic-Mode Instability in Hydrogen – Oxygen Rockets," NASA TN D-4733, August 1968.
85. White, F. M., *Fluid Mechanics*, 2nd Ed., McGraw-Hill, Inc. New York, 1986.
86. Chehroudi, B., Chen, S. H, Bracco, F., and Onuma, Y., "On the intact core of full-cone sprays," Society of Automotive Engineers, Paper 850126, 1985.

Appendix A

Experimental Procedure and Flow Diagram

The standard operating procedure and an expanded view of the process flow diagram presented in Fig. 3.3 spanning 4 pages here in Figs. A.1 (A) – (D).

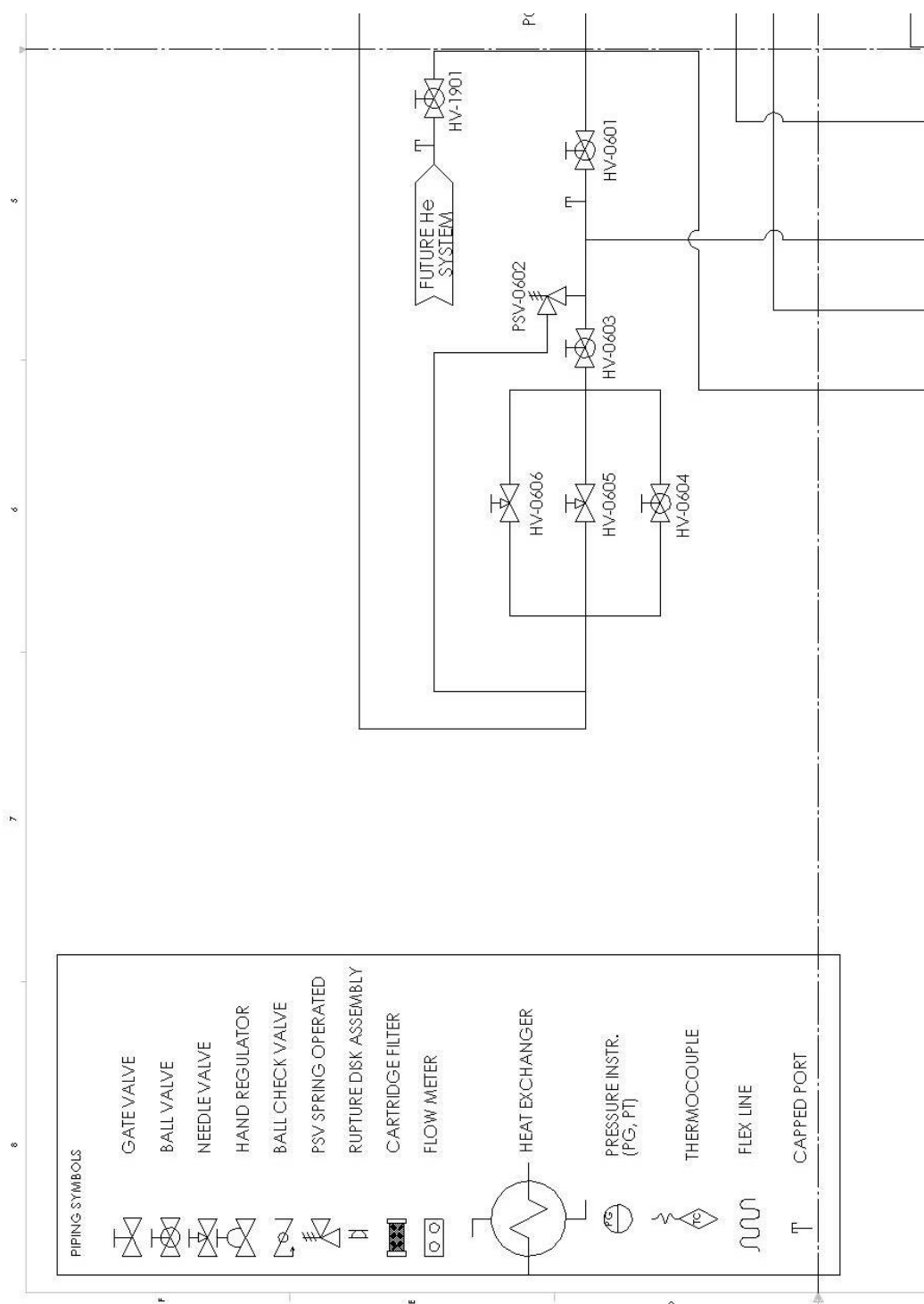


Figure A.2(A): Process Flow Diagram corresponding to region “A” Fig. A.1

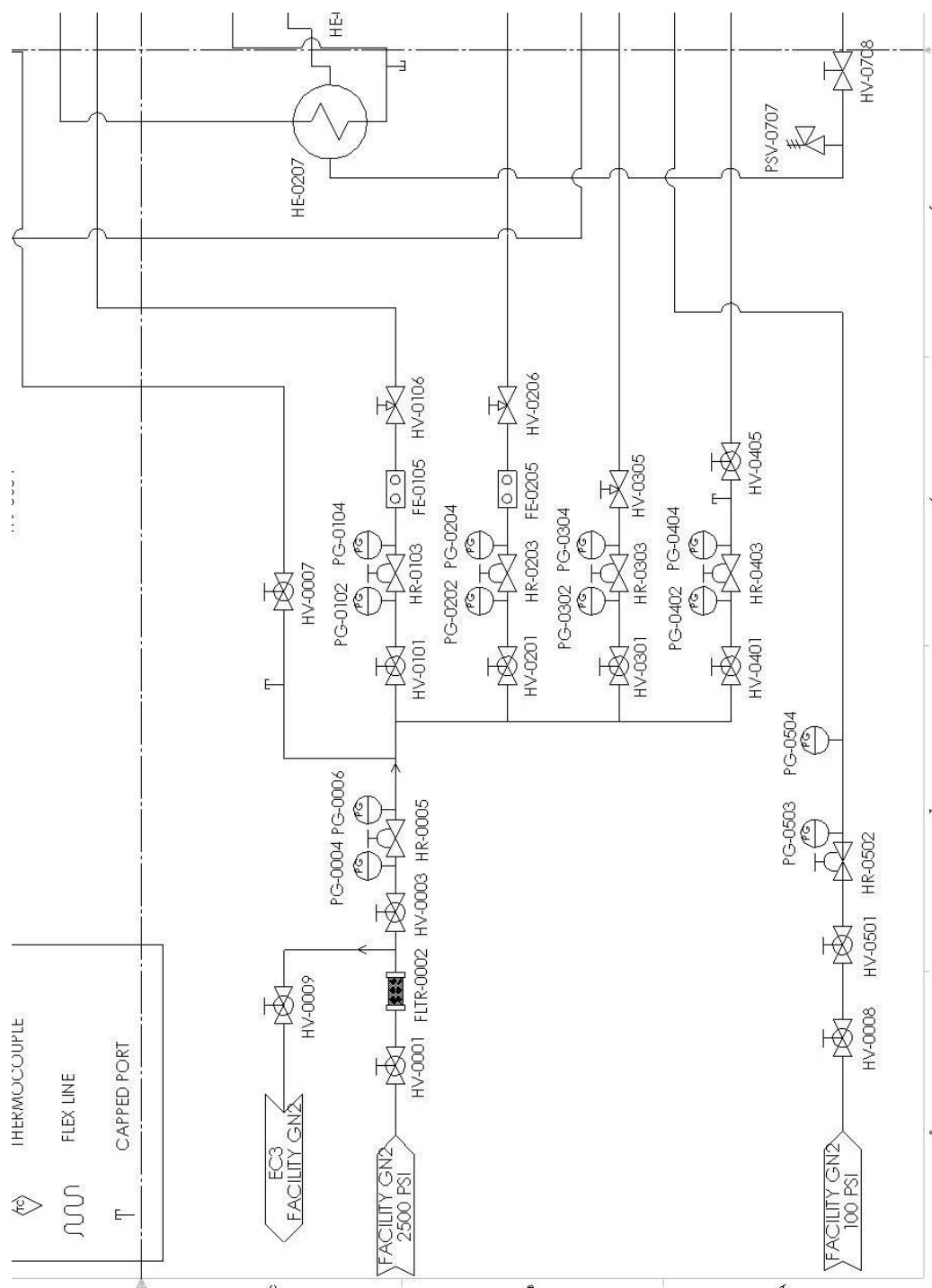


Figure A.4(C): Process Flow Diagram corresponding to region “C” Fig. A.1

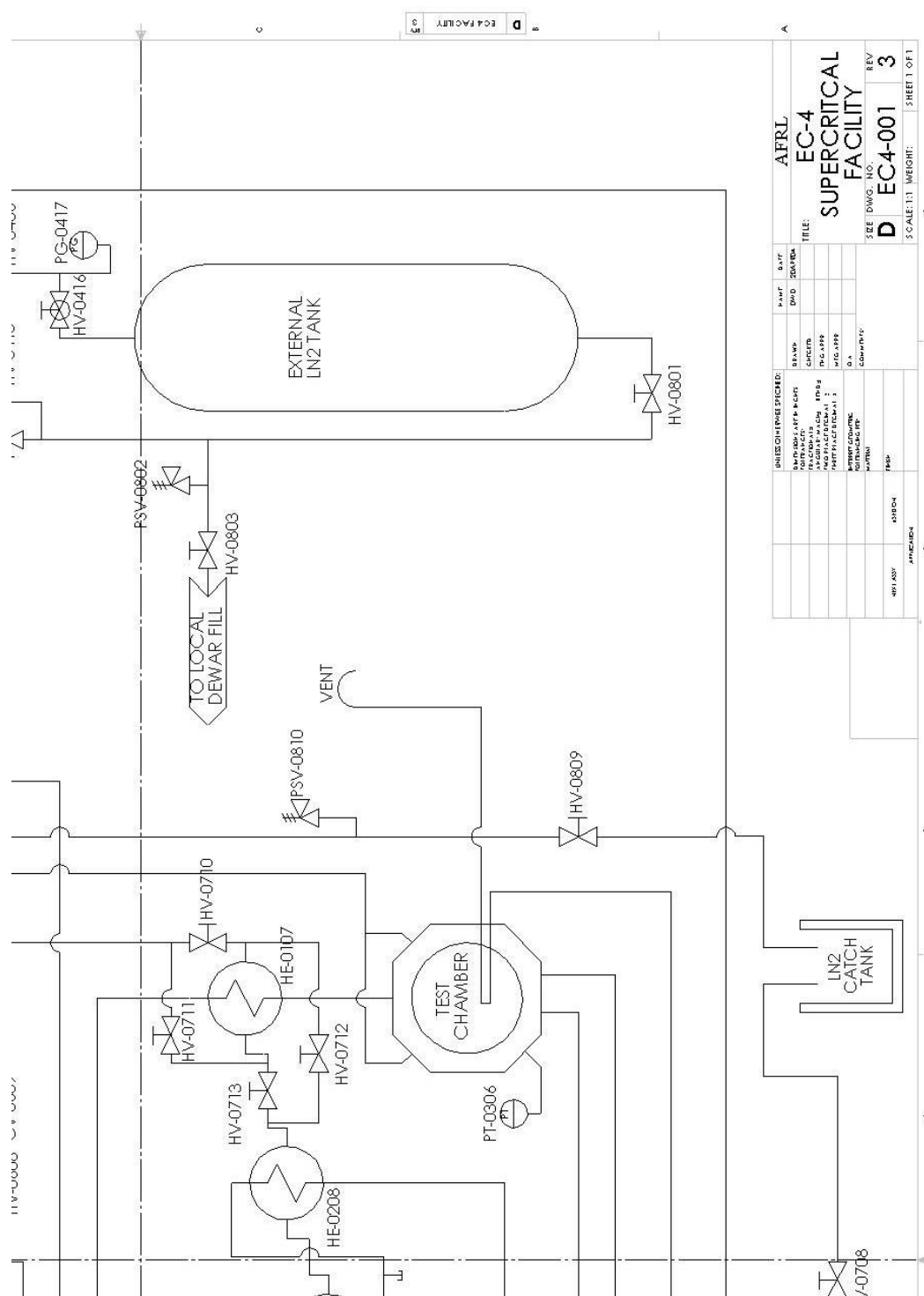


Figure A.5(D): Process Flow Diagram corresponding to region "D" Fig. A.1

BUILDING 8451 EXPERIMENTAL CELL, EC-4 AIR FORCE RESEARCH LABORATORY EDWARDS AFB, CA	PROCEDURE: REVISION: DATE REVISED: NUMBER OF PAGES:	SOP-PRSA-EC4-0001 0 24 Jun 2004 25
--	--	---

**BUILDING 8451
EXPERIMENTAL CELL, EC-4
OPERATIONS**

PROCEDURE TITLE

**SUPERCritical COLD FLOW
FACILITY
OPERATIONS**

PREPARED BY:
 Test Engineer _____ DATE _____
 EC-4

REVIEW:
 ERC, Principle Investigator Review _____ DATE _____
 Air Force Research Laboratory
 AFRL, Technical Representative Review _____ DATE _____
 Air Force Research Laboratory
 AFRL, Safety Representative Review _____ DATE _____
 Air Force Research Laboratory
 AFRL, Quality Assurance Review _____ DATE _____
 Air Force Research Laboratory

APPROVAL:
 AF Program Manager _____ DATE _____
 Air Force Research Laboratory
 ERC Program Manager _____ DATE _____
 Air Force Research Laboratory
 ERC Safety Manager _____ DATE _____
 Air Force Research Laboratory
 Building 8451 Facility Manger _____ DATE _____
 Air Force Research Laboratory
 AFRL Chief, Aerophysics Branch _____ DATE _____
 Air Force Research Laboratory
 AFRL Chief, Safety Branch _____ DATE _____
 Air Force Research Laboratory

Revision	Notes	Prepared By
0	-Initial procedure written	D. Davis June 24, 2004
1	-Added -Deleted	

PERSONNEL

EXPERIMENTAL CELL EC-4

DATE_____

AEROPHYICS BRANCH, BLDG 8451
AUTHORIZATION#_____

WORK

The following personnel are designated as test team members, and are charted to perform their assignment as follows:

Test Conductor (TC) – Responsible for the timely performance of the test as written and for overall facility and test safety. This includes coordinating and directing the activities of the Red Crew and other test support teams. TC is responsible for coordinating all pretest activities and outside support required, including (but not limited to) security, fire, medical, and safety. TC is responsible for initialing completion on each step of the master test procedure and ensuring all test goals are met and all critical data is acquired. Has authority to perform real-time redlines on test procedures as required to ensure test requirements and goals are met. All safety-related redlines will be coordinated and approved by AFRL and/or ERC Safety.

Name_____ Signature_____

Red Crew Leader (RCL) – Responsible for directing the activities of Red Crew members. Reports directly to the TC and ensures all Red Crew tasks are completed. Responsible for ensuring all RCM's have all required certifications and training. Responsible for ensuring all required equipment is available, accessible, and serviceable.

Name_____ Signature_____

Other Test Team Members – Responsible for performing ancillary duties in support of test, support of anomaly resolution, and other necessary activities.

Name_____ Signature_____

Name_____ Signature_____

Name_____ Signature_____

Name_____ Signature_____

ALL TEST TEAM MEMBERS – Responsible for the safe performance of the test. Have read and understood all portions of the test procedure. Any Test Team Member can declare an emergency or unsafe condition.

____ 1.

ABBREVIATIONS AND ACRONYMS

CPR	- Cardiopulmonary Resuscitation
CV	- Check Valve
EC	- Experimental Cell
ER	- Engineering Request
FE	- Flow Element
FLTR	- Filter
FLX	- Flexible Line
GN2	- Gaseous Nitrogen
HE	- Heat Exchanger
He	- Helium
HR	- Hand Regulator
HV	- Hand Valve
LN2	- Liquid Nitrogen
N2	- Nitrogen
PC	- Chamber Pressure
PG	- Pressure Gauge
PI	- Principle Investigator
PM	- Program Manager
PPE	- Personal Protective Equipment
PSV	- Pressure Safety Valve
PT	- Pressure Transducer
QA	- Quality Assurance
RCL	- Red Crew Leader
RD	- Rupture Disk
SCF	- Supercritical Facility
SOCC	- Site Operations Control Center
SOP	- Standard Operating Procedure
TC	- Test Conductor
TOP	- Test Operation Procedure

_____ 2.	TEST DESCRIPTION AND OBJECTIVES
_____ 2.1.	<p>PURPOSE</p> <p>This procedure performs a stand-alone operation of the EXPERIMENTAL CELL, EC-4. This procedure may be used in conjunction with other Test Operation Procedures (TOP) or Work Authorizations (WA) as required to support operations or checkouts.</p>
_____ 2.2.	<p>SCOPE</p> <p>This procedure will verify proper configuration before operation including purges and valve configuration and sequential steps to perform the Supercritical Cold Flow (SCF) Operation. Securing the SCF post operation and emergency shutdown are also included in the procedure.</p>
_____ 3.	DOCUMENTATION
	<p>The completion of each applicable event shall be verified by marking to the left of the item number by the TC. Deviations from these procedures will be coordinated with the Test Engineer, TC, RCL</p>
_____ 3.1.	<p>APPLICABLE DOCUMENTS</p> <p>AFRL/PR OI 91-202, Environmental, Safety, and Occupational Health (ESOH) Programs, 7 Aug 2000.</p> <p>Space & Missile Propulsion Division, Chemical Hygiene Plan (CHP), Bldg 8451.</p>
_____ 3.2.	REFERENCE DOCUMENTS: NONE
_____ 3.3.	<p>SPECIFICATIONS</p> <p>Nitrogen Purge Gas: Pressurizing agent, nitrogen, Grade B, Type I, Spec. Mil-P-27401.</p> <p>Water: Facility domestic water supply</p>
_____ 3.4.	<p>DRAWINGS</p> <p>EC4-001, EC-4 Supercritical Facility</p>

4.

4.1.

4.2.

4.3.

4.4.

TEST REQUIREMENTS AND RESTRICTIONS

TRAINING

The following training is required for personnel using these procedures:

CPR & First Aid

High Pressure

Noise

Initial HAZCOM

Cryogenics

Job Site HAZCOM

Lock-Out/Tag-Out

(Laser training will be required in the future)

MAXIMUM PERSONNEL ALLOWED IN EC-4:

Five (5): Workers – (3) (RCL and TC),
Supervision – (1) (PI, PM, etc.),
Casual (Bio, Safety, QA, etc) – (1)

LIST OF EQUIPMENT

Vapor Detection Equipment: One permanent (fixed) O2 sensor mounted in EC-4 and two (2) portable oxygen sensors (one for each worker in the cell).

Mechanics tool kit, torque wrench and Caliper.

Ensure all tools associated with this experiment/test/operation are accounted for prior to initiating system/item test. Assure all trash, debris, and FOD is picked up from around the test stand.

METEOROLOGICAL LIMITATIONS/ RESTRICTIONS

A. No hazardous operations will be started when thunderstorms are within 25 nautical miles (28.75 miles) of AFRL unless the operation can meet the requirements for stopping the operation for lightning within 10 nautical miles. Operations in progress may be completed if it is safe to do so; however supervisors must assess individual operations to determine the appropriate action.

B. All hazardous operations will be stopped when thunderstorms are within 10 nautical miles (11.5 miles) of the AFRL. The operation should be secured and personnel evacuated to Bldg 8451 and remain indoors.

C. All outside work must stop when thunderstorms are within 5 nautical miles (5.75 miles) of the AFRL and all personnel must seek safety in Bldg 8451 until the lightning warning is cancelled.

_____ 5.	SAFETY REQUIREMENTS
_____ 5.1.	TEST HAZARDS:
	<p>Nitrogen gas (GN2) is used for pressurization of the chamber and production of the supercritical jet in the chamber. Nitrogen gas can cause asphyxiation hazards to personnel working in EC-4. Oxygen deficiency monitors will be used to warn personnel working in EC-4 of the hazard.</p> <p>Liquid nitrogen (LN2) is used for temperature conditioning of the supercritical jet in the chamber. This presents a cryogenic hazard to test crew working inside and outside EC-4. LN2 will also convert to GN2.</p> <p>The Acoustic test can produce hazardous noise levels (>120 dB). Personnel are required to wear ear muffs to reduce exposure.</p>
_____ 5.2.	PERSONNEL PROTECTIVE CLOTHING REQUIREMENTS
	<p>Test PPE: Fire retardant lab coat or coveralls, safety goggles, safety shoes, leather gloves, and ear muffs (noise protection as required).</p> <p>Cryogenic PPE: Cryogenic gloves, Cryogenic Body Apron, Full-Face shield.</p>
_____ 5.3.	TEST AREA ACCESS DURING OPERATIONS
	<p>EC-4 GREEN: Normal test preparation activities. There are no pressure or chemical hazards in the test cell. The RCL will limit access to the affected operational area of interest.</p> <p>EC-4 AMBER: Hazardous chemicals in the test cell. No pressure or flows (static condition). RCL will monitor the Test Cell entrance, and prevent access to the cell. Personnel will not be allowed access to the test area unless cleared by the RCL and TC.</p> <p>EC-4 RED Hazardous test operations including propellant chill downs, purging operations. The TC will maintain access control to the area. Personnel will not be allowed access to EC-4 unless cleared by the TC.</p>

____ 6.

EXPLOSIVE LIMITS: NONE

____ 7.

EMERGENCY PROCEDURES

In the event of a major nitrogen leak or other emergency that jeopardizes the safety of the operators or other personnel perform Section 20 emergency procedures at the end of this document.

____ 8.

SPECIAL INSTRUCTIONS

Red Crew Member shall notify Test Engineer of any leaks from the system.

Any lines, which require maintenance or re-torquing, should be coordinated with Test Engineering to maintain SCF system cleanliness. Work must be authorized in order to break into clean and sealed systems.

9.		PRETEST PREPARATIONS
9.1.	ALL	DON Test PPE listed in step 5.2
9.2.	RCL	Verify Oxygen Sensor in EC-4 is not at an ALARM condition and is reading greater than 20.0% +2.0% / -0.5% oxygen concentration by volume.
9.3.	RCL	Verify portable oxygen sensors are operational and calibrated.
9.4.	RCL	Turn ON or Verify ON EC-4 Air Handler ventilation system
9.5.	ALL	UNLOCK EC-4 outside door
9.6.	ALL	NOTE any potential hazards in and outside EC-4
9.7.	ALL	Verify GREEN, AMBER, and RED lights are functional and return to GREEN
9.8.	TC	If Acoustic Testing Verify Gain or Turn Gain on Amplifier to the ZERO position
9.9.	TC	If Acoustic Testing, Turn ON Amplifier to allow warm up as per ER_____
9.10.	RCL	If Acoustic Testing, POST Hearing Protection Required signs on the out side of the doors to EC-4, Room 19, foam door and adjacent hallway.
9.11.	TC	Turn on Data Acquisition System and System Electronics.

_____ 10.		INITIAL SETUP
_____ 10.1.	RCL	CLOSE / Verify CLOSED HV-0001 (EC-3, EC-4 Primary Facility Isolation Valve)
_____ 10.2.	RCL	CLOSE / Verify CLOSED HV-0003 (EC-4 Secondary Facility Isolation Valve)
_____ 10.3.	RCL	CLOSE / Verify CLOSED HV-0008 (EC-4 Low Pressure Facility Isolation Valve)
_____ 10.4.	RCL	CLOSE / Verify CLOSED HV-0009 (EC-3 Secondary Facility Isolation Valve)
_____ 10.5.	RCL	CLOSE / Verify CLOSED HV-0701 (LN2 Isolation Valve)
_____ 10.6.	RCL	CLOSE / Verify CLOSED HV-0408 (Dewar GN2 Isolation Valve)
_____ 10.7.	RCL	OPEN / Verify OPEN HV-0610 (Supply Dewar GN2 Vent Valve)
_____ 10.8.	RCL	CLOSE / Verify CLOSED HV-0406 (Tank GN2 Pressurization Isolation Valve)
_____ 10.9.	RCL	CLOSE / Verify CLOSED HV-0409 (Dewar Pressurization Vent Isolation Valve)
_____ 10.10.	RCL	CLOSE / Verify CLOSED HV-0709 (Dewar LN2 Supply Isolation Valve)
_____ 10.11.	RCL	CLOSE / Verify CLOSED HV-0704 (Heat Exchanger LN2 Flow Meter Isolation Valve)
_____ 10.12.	RCL	CLOSE / Verify CLOSED HV-0706 (Heat Exchanger LN2 Flow Meter Bypass Valve)
_____ 10.13.	RCL	CLOSE / Verify CLOSED HV-0801 (Tank LN2 Isolation Valve) NOTE: Valve located outside
_____ 10.14.	RCL	CLOSE / Verify CLOSED HV-0803 (Local Dewar Fill Isolation Valve) NOTE: Valve located outside
_____ 10.15.	RCL	CLOSE / Verify CLOSED HV-0804 (Tank-Dewar Separation Valve) NOTE: Valve located outside
_____ 10.16.	RCL	CLOSE / Verify CLOSED HV-0415 (Vacuum Jacketed Line Purge Valve) NOTE: Valve located outside
_____ 10.17.	RCL	CLOSE / Verify CLOSED HV-0416 (Tank GN2 Pressurization Valve) NOTE: Valve located outside
_____ 10.18.	RCL	CLOSE / Verify CLOSED HV-0614 (Dewar Gauge Vent Valve)

_____10.19.	RCL	CLOSE / Verify CLOSED HV-1901 (He System Isolation Valve)
_____10.20.	RCL	CLOSE / Verify CLOSED HV-0601 (PC Vent PG Isolation Valve)
_____10.21.	RCL	OPEN / Verify OPEN HV-0608 (Gauge Vent Valve)
_____10.22.	RCL	CLOSE / Verify CLOSED HV-0007 (Upstream Regulator Pressure Valve)
_____10.23.	RCL	OPEN / Verify OPEN HV-0603 (Chamber Pressure Build Valve)
_____10.24.	RCL	OPEN / Verify OPEN HV-0604 (Primary Chamber Pressure Vent Valve)
_____10.25.	RCL	CLOSE / Verify CLOSED HV-0605 (Secondary Chamber Pressure Vent Valve)
_____10.26.	RCL	CLOSE / Verify CLOSED HV-0606 (Tertiary Chamber Pressure Vent Valve)
_____10.27.	RCL	CLOSE / Verify CLOSED HV-0708 (Heat Exchanger LN2 Throttle Vent Valve)
_____10.28.	RCL	CLOSE / Verify CLOSED HV-0809 (Coax Heat Exchanger LN2 Throttle Vent Valve)
_____10.29.	RCL	OPEN / Verify OPEN HV-0710 (Primary Co-Flow Valve)
_____10.30.	RCL	OPEN / Verify OPEN HV-0711 (Primary Counter Flow Valve)
_____10.31.	RCL	OPEN / Verify OPEN HV-0712 (Secondary Counter Flow Valve)
_____10.32.	RCL	OPEN / Verify OPEN HV-0713 (Secondary Co-Flow Valve)
_____10.33.	RCL	CLOSE / Verify CLOSED HV-0806 (Coax LN2 Flow Meter Isolation Valve)
_____10.34.	RCL	CLOSE / Verify CLOSED HV-0808 (Coax LN2 Flow Meter Bypass Valve)
_____10.35.	RCL	CLOSE / Verify CLOSED HV-0101 (Center Jet GN2 Isolation Valve)
_____10.36.	RCL	CLOSE / Verify CLOSED HV-0106 (Center Jet GN2 Throttle Valve)
_____10.37.	RCL	CLOSE / Verify CLOSED HV-0201 (Coax Jet GN2 Isolation Valve)
_____10.38.	RCL	CLOSE / Verify CLOSED HV-0206 (Coax Jet GN2 Throttle Valve)
_____10.39.	RCL	CLOSE / Verify CLOSED HV-0301 (Chamber Pressurization Isolation Valve)
_____10.40.	RCL	CLOSE / Verify CLOSED HV-0305 (Chamber Pressurization Throttle Valve)

_____ 10.41.	RCL	CLOSE / Verify CLOSED HV-0401 (Dewar and Tank Pressurization Isolation Valve)
_____ 10.42.	RCL	CLOSE / Verify CLOSED HV-0405 (Dewar LN2 Supply Dewar Tank Isolation Valve)
_____ 10.43.	RCL	CLOSE / Verify CLOSED HV-0501 (Window Purge Isolation Valve)
_____ 10.44.	RCL	Verify and Record Dewar Pressure from PG-0613 (Dewar Pressure Gauge) _____psig
_____ 10.45.	RCL	Verify PG-0504 (Window Purge Pressure Gauge) reads 0 psig
_____ 10.46.	RCL	Verify PG-0417 (LN2 Tank Pressure Gauge) reads 0 psig
_____ 10.47.	RCL	Verify PG-0607 (Chamber Pressure Gauge) reads 0 psig
_____ 10.48.	RCL	DECREASE FULLY / Verify FULLY DECREASED HR-0005 (EC-4 Facility Pressure Regulator)
_____ 10.49.	RCL	Verify PG-0004 (EC-4 System Inlet Pressure Gauge) reads 0 psig
_____ 10.50.	RCL	DECREASE FULLY / Verify FULLY DECREASED HR-0103 (Center Jet GN2 Pressure Regulator)
_____ 10.51.	RCL	Verify PG-0102 (Center Jet GN2 System Inlet Pressure Gauge) reads 0 psig
_____ 10.52.	RCL	DECREASE FULLY / Verify FULLY DECREASED HR-0203 (Coax Jet GN2 Pressure Regulator)
_____ 10.53.	RCL	Verify PG-0202 (Coax Jet GN2 System Inlet Pressure Gauge) reads 0 psig
_____ 10.54.	RCL	DECREASE FULLY / Verify FULLY DECREASED HR-0303 (Chamber Pressurization Regulator)
_____ 10.55.	RCL	Verify PG-0302 (Chamber Pressurization System Inlet Pressure Gauge) reads 0 psig
_____ 10.56.	RCL	DECREASE FULLY / Verify FULLY DECREASED HR-0403 (Dewar and Tank GN2 Pressure Regulator)
_____ 10.57.	RCL	Verify PG-0402 (Dewar and Tank GN2 System Inlet Pressure Gauge) reads 0 psig
_____ 10.58.	RCL	DECREASE FULLY / Verify FULLY DECREASED HR-0502 (Window Purge Pressure Regulator)
_____ 10.59.	RCL	Verify PG-0504 (Window Purge Pressure Gauge) reads 0 psi

_____ 11.		WINDOW PURGE
_____ 11.1.	TC	Notify SOCC via hotline in EC-1, EC-2 control room that EC-4 is going into a RED condition for SCF testing.
_____ 11.2.	ALL	Verify all personnel are wearing Test PPE
_____ 11.3.	RCL	Change EC-4 light to RED.
_____ 11.4.	TC	Record Time _____
_____ 11.5.	RCL	Verify window purge apparatus is in satisfactory condition
_____ 11.6.	RCL	OPEN HV-0008 (EC-4 Low Pressure Facility Isolation Valve)
_____ 11.7.	RCL	OPEN HV-0501 (Window Purge Isolation Valve)
		CAUTION: Do NOT Increase HR-0502 so that PG-0504 reads greater than 2.0 psig as it will damage PG-0504
_____ 11.8.	RCL	INCREASE HR-0502 (Window Purge Pressure Regulator) until PG-0504(Window Purge Pressure Gauge) reads 1.5 psig +/- 0.5 psig
_____ 11.9.	RCL	Permit window purge to continue according to ER _____

_____ 12.		FACILITY GN2 SETUP
_____ 12.1.	RCL	OPEN HV-0001 (EC-3, EC-4 Facility Isolation Valve)
_____ 12.2.	RCL	OPEN HV-0003 (EC-4 Facility Isolation Valve)
_____ 12.3.	RCL	Verify PG-0004 (EC-4 System Inlet Pressure Gauge) reads a pressure greater than 2000 psig
_____ 12.4.	RCL	OPEN HV-0007 (Upstream Regulator Pressure Valve)
_____ 12.5.	RCL	CLOSE HV-0608 (Gauge Vent Valve)
_____ 12.6.	RCL	INCREASE HR-0005 (EC-4 Facility Pressure Regulator) until PG-0607 (Chamber Pressure Gauge) reads 2000 psig +/- 50 psig.
_____ 12.7.	RCL	CLOSE HV-0007 (Upstream Regulator Pressure Valve)
_____ 12.8.	RCL	OPEN HV-0608 (Gauge Vent Valve)
_____ 12.9.	RCL	Verify PG-0607 (Chamber Pressure Gauge) reads 0 psig
_____ 12.10.	RCL	CLOSE HV-0608 (Gauge Vent Valve)
_____ 12.11.	RCL	OPEN HV-0601 (PC Vent PG Isolation Valve)
_____ 12.12.	RCL	Verify PG-0607 (Chamber Pressure Gauge) reads 0 psig

_____ 13.		CHAMBER PURGE
_____ 13.1.	TC	Record Time _____
_____ 13.2.	RCL	OPEN HV-0301 (Chamber Pressurization Isolation Valve)
_____ 13.3.	RCL	Verify PG-0302 (Chamber Pressurization System Inlet Pressure Gauge) reads 2000 psig +/- 150 psig
_____ 13.4.	RCL	INCREASE HR-0303 (Chamber Pressure GN2 Pressure Regulator) until PG-0304 (Chamber Pressure Purge Pressure Gauge) reads 400 psig +0/-100 psig
_____ 13.5.	RCL	OPEN HV-0305 (Chamber Pressurization Throttle Valve) as per ER_____
_____ 13.6.	RCL	CLOSE HV-0603 (Chamber Pressure Build Valve)
_____ 13.7.	RCL	Verify PG-0607 (Chamber Pressure Gauge) indicates that PC is increasing to indicate purge is flowing.
_____ 13.8.	RCL	OPEN HV-0603 (Chamber Pressure Build Valve)

_____ 14.		CENTER JET PURGE
_____ 14.1.	RCL	OPEN HV-0101 (Center Jet GN2 Isolation Valve)
_____ 14.2.	RCL	Verify PG-0102 (Center Jet GN2 System Inlet Pressure Gauge) reads 2000 psig +/- 150 psig
_____ 14.3.	RCL	INCREASE HR-0103 (Center Jet GN2 Pressure Regulator) until PG-0104 (Center Jet Pressure Gauge) reads 400 psig +0/-100 psig
_____ 14.4.	RCL	OPEN HV-0106 (Center Jet GN2 Throttle Valve) as per ER_____
_____ 14.5.	TC	Verify FE-0105 (Center Jet GN2 Flow Meter) indicates purge is flowing

_____ 15.		COAXIAL JET PURGE
_____ 15.1.	RCL	OPEN HV-0201 (Coax Jet GN2 Isolation Valve)
_____ 15.2.	RCL	Verify PG-0202 (Coax Jet GN2 System Inlet Pressure Gauge) reads 2000 psig +/- 150 psig
_____ 15.3.	RCL	INCREASE HR-0203 (Coax Jet GN2 Pressure Regulator) until PG-0204 (Coax Jet GN2 Pressure Gauge) reads 400 psig +/-100 psig
_____ 15.4.	RCL	OPEN HV-0206 (Coax Jet GN2 Throttle Valve) as per ER_____
_____ 15.5.	TC	Verify FE-0205 (Coax Jet GN2 Flow Meter) indicates purge is flowing
_____ 15.6.	RCL	OPEN HV-0605 (Secondary Chamber Pressure Vent Valve)
_____ 15.7.	RCL	CLOSE HV-0604 (Primary Chamber Pressure Vent Valve)
_____ 15.8.	RCL	ADJUST HV-0605 (Secondary Chamber Pressure Vent Valve) and HV-0606 (Tertiary Chamber Pressure Vent Valve) until PG-0607 (Chamber Pressure Gauge) reads INITIAL CHAMBER PRESSURE as per ER_____
_____ 15.9.	RCL	Wait for required time to elapse from step 13.1 as per ER_____

_____ 16.		SYSTEM CHILL DOWN
_____ 16.1.	TC	Verify Red Crew has donned Cryogenic PPE as outlined in Step 5.2
_____ 16.2.	RCL	OPEN HV-0801 (Tank LN2 Isolation Valve)
_____ 16.3.	RCL	OPEN HV-0804 (Tank-Dewar Separation Valve)
_____ 16.4.	RCL	OPEN HV-0409 (Dewar Pressurization Vent Isolation Valve)
_____ 16.5.	RCL	CLOSE HV-0610 (Supply Dewar GN2 Vent Valve)
_____ 16.6.	RCL	OPEN HV-0701 (LN2 Isolation Valve)
_____ 16.7.	RCL	OPEN HV-0408 (Dewar GN2 Isolation Valve)
_____ 16.8.	RCL	OPEN HV-0706 (Heat Exchanger LN2 Flow Meter Bypass Valve)
_____ 16.9.	RCL	If operating HE-0107 (Cooling Tower) in CO-FLOW as per ER_____
_____ 16.9.1.	RCL	CLOSE HV-0711 (Primary Counter Flow Valve)
_____ 16.9.2.	RCL	CLOSE HV-0712 (Secondary Counter Flow Valve)
_____ 16.10.	RCL	If operating HE-0107 (Cooling Tower) in COUNTER-FLOW as per ER_____
_____ 16.10.1.	RCL	CLOSE HV-0710 (Primary Co-Flow Valve)
_____ 16.10.2.	RCL	CLOSE HV-0713 (Secondary Co-Flow Valve)
_____ 16.11.	RCL	OPEN HV-0808 (Coax LN2 Flow Meter Bypass Valve)
_____ 16.12.	RCL	OPEN HV-0401 (Dewar and Tank Pressurization Isolation Valve)
_____ 16.13.	RCL	Verify PG-0402 (Dewar and Tank GN2 System Inlet Pressure Gauge) reads 2000 psig +/-150 psig
_____ 16.14.	RCL	Increase HR-0403 (Dewar and Tank GN2 Pressure Regulator) until PG-0404 (Dewar, Tank Pressurization Pressure Gauge) reads as per ER_____
_____ 16.15.	RCL	OPEN HV-0405 (Dewar LN2 Supply Dewar Tank Isolation Valve)
_____ 16.16.	TC	Record Time _____
_____ 16.17.	RCL	OPEN HV-0809 (Coax Heat Exchanger LN2 Throttle Vent Valve) as per ER_____
_____ 16.18.	RCL	OPEN HV-0708 (Heat Exchanger LN2 Throttle Vent Valve) as per ER_____

_____ 16.19.	ALL	ADJUST HR-0403 (Dewar and Tank GN2 Pressure Regulator) to maintain 22 psig +/- 1 psig on PG-0613 (Dewar Pressure Gauge)
_____ 16.20.	ALL	Wait Required time for chill down as per ER_____
_____ 16.21.	RCL	OPEN HV-0704 (Heat Exchanger LN2 Flow Meter Isolation Valve)
_____ 16.22.	RCL	CLOSE HV-0706 (Heat Exchanger LN2 Flow Meter Bypass Valve)
_____ 16.23.	RCL	OPEN HV-0806 (Coax LN2 Flow Meter Isolation Valve)
_____ 16.24.	RCL	CLOSE HV-0808 (Coax LN2 Flow Meter Bypass Valve)
_____ 16.25.	RCL	Remove Cryogenic PPE and don Test PPE as listed in Step 5.2

_____ 17.		TESTING
_____ 17.1.	RCL	If acoustic testing, Place foam door into position
_____ 17.2.	TC	Verify all personnel are wearing ear muffs if acoustic testing.
_____ 17.3.	RCL	INCREASE HR-0103 (Center Jet GN2 Pressure Regulator) until PG-0104 (Center Jet Pressure Gauge) reads 1500 psig +/- 50 psig
_____ 17.4.	RCL	INCREASE HR-0203 (Coax Jet GN2 Pressure Regulator) until PG-0204 (Coax Jet GN2 Pressure Gauge) reads 1500 psig +/- 50 psig
_____ 17.5.	RCL	INCREASE HR-0303 (Chamber Pressurization Regulator) until PG-0304 (Chamber Pressurization Pressure Gauge) reads 1500 psig +/- 50 psig
_____ 17.6.	TC	Direct RCL to operate system as per test needs
_____ 17.7.	RCL	OPERATE System as directed by test conductor

_____ 18.	RCL	SHUT DOWN
_____ 18.1.	RCL	OPEN HV-0808 (Coax LN2 Flow Meter Bypass Valve)
_____ 18.2.	RCL	CLOSE HV-0806 (Coax LN2 Flow Meter Isolation Valve)
_____ 18.3.	RCL	OPEN HV-0706 (Heat Exchanger LN2 Flow Meter Bypass Valve)
_____ 18.4.	RCL	CLOSE HV-0704 (Heat Exchanger LN2 Flow Meter Isolation Valve)
_____ 18.5.	RCL	CLOSE HV-0001 (EC-3, EC-4 Primary Facility Isolation Valve)
_____ 18.6.	RCL	CLOSE HV-0701 (LN2 Isolation Valve)
_____ 18.7.	RCL	CLOSE HV-0408 (Dewar GN2 Isolation Valve)
_____ 18.8.	RCL	OPEN HV-0610 (Supply Dewar GN2 Vent Valve)
_____ 18.9.	RCL	CLOSE HV-0008 (EC-4 Low Pressure Facility Isolation Valve)
_____ 18.10.	RCL	CLOSE HV-0801 (Tank LN2 Isolation Valve)
_____ 18.11.	RCL	Wait for PG-0004 (EC-4 System Inlet Pressure Gauge) to read 0 psig
_____ 18.12.	RCL	CLOSE HV-0003 (EC-4 Secondary Facility Isolation Valve)
_____ 18.13.	RCL	Verify PG-0102 (Center Jet GN2 System Inlet Pressure Gauge) reads 0 psig
_____ 18.14.	RCL	CLOSE HV-0101 (Center Jet GN2 Isolation Valve)
_____ 18.15.	RCL	CLOSE HV-0106 (Center Jet GN2 Throttle Valve)
_____ 18.16.	RCL	Verify PG-0202 (Coax Jet GN2 System Inlet Pressure Gauge) reads 0 psig
_____ 18.17.	RCL	CLOSE HV-0201 (Coax Jet GN2 Isolation Valve)
_____ 18.18.	RCL	CLOSE HV-0206 (Coax Jet GN2 Throttle Valve)
_____ 18.19.	RCL	Verify PG-0302 (Chamber Pressurization System Inlet Pressure Gauge) reads 0 psig
_____ 18.20.	RCL	CLOSE HV-0301 (Chamber Pressurization Isolation Valve)
_____ 18.21.	RCL	CLOSE HV-0305 (Chamber Pressurization Throttle Valve)
_____ 18.22.	RCL	Verify PG-0402 (Dewar and Tank GN2 System Inlet Pressure Gauge) read 0 psig
_____ 18.23.	RCL	CLOSE HV-0401 (Dewar and Tank Pressurization Isolation Valve)
_____ 18.24.	RCL	CLOSE HV-0405 (Dewar LN2 Supply Dewar Tank Isolation Valve)

_____ 18.25.	RCL	Verify PG-0504 (Window Purge Pressure Gauge) reads 0 psig
_____ 18.26.	RCL	CLOSE HV-0501 (Window Purge Isolation Valve)
_____ 18.27.	RCL	Fully DECREASE HR-0005 (EC-4 Facility Pressure Regulator)
_____ 18.28.	RCL	Fully DECREASE HR-0103 (Center Jet GN2 Pressure Regulator)
_____ 18.29.	RCL	Fully DECREASE HR-0203 (Coax Jet GN2 Pressure Regulator)
_____ 18.30.	RCL	Fully DECREASE HR-0303 (Chamber Pressurization Regulator)
_____ 18.31.	RCL	Fully DECREASE HR-0403 (Dewar and Tank GN2 Pressure Regulator)
_____ 18.32.	RCL	Fully DECREASE HR-0502 (Window Purge Pressure Regulator)
_____ 18.33.	RCL	OPEN HV-0608 (Gauge Vent Valve)
_____ 18.34.	RCL	Verify PG-0607 (Chamber Pressure Gauge) reads 0 psig
_____ 18.35.	RCL	CLOSE HV-0601 (PC Vent PG Isolation Valve)
_____ 18.36.	RCL	OPEN / Verify OPEN HV-0603 (Chamber Pressure Build Valve)
_____ 18.37.	RCL	OPEN HV-0604 (Primary Chamber Pressure Vent Valve)
_____ 18.38.	RCL	CLOSE HV-0605 (Secondary Chamber Pressure Vent Valve)
_____ 18.39.	RCL	CLOSE HV-0606 (Tertiary Chamber Pressure Vent Valve)
_____ 18.40.	RCL	CLOSE HV-0808 (Coax LN2 Flow Meter Bypass Valve)
_____ 18.41.	RCL	OPEN / Verify OPEN HV-0710 (Primary Co-Flow Valve)
_____ 18.42.	RCL	OPEN / Verify OPEN HV-0711 (Primary Counter Flow Valve)
_____ 18.43.	RCL	OPEN / Verify OPEN HV-0712 (Secondary Counter Flow Valve)
_____ 18.44.	RCL	OPEN / Verify OPEN HV-0713 (Secondary Co-Flow Valve)
_____ 18.45.	RCL	CLOSE HV-0708 (Heat Exchanger LN2 Throttle Vent Valve)
_____ 18.46.	RCL	CLOSE HV-0809 (Coax Heat Exchanger LN2 Throttle Vent Valve)
_____ 18.47.	RCL	CLOSE HV-0409 (Dewar Pressurization Vent Isolation Valve)
_____ 18.48.	RCL	CLOSE HV-0706 (Heat Exchanger LN2 Flow Meter Bypass Valve)
_____ 18.49.	RCL	CLOSE HV-0804 (Tank-Dewar Separation Valve)

____ 19.		LN2 DEWAR FILL
		NOTE: If filling Dewar without testing go through Initial Setup
____ 19.1.	TC	Verify Red Crew has donned Cryogenic PPE as outlined in Step 5.2
____ 19.2.	RCL	OPEN HV-0408 (Dewar GN2 Isolation Valve)
____ 19.3.	RCL	OPEN HV-0801 (Tank LN2 Isolation Valve)
____ 19.4.	RCL	OPEN HV-0804 (Tank-Dewar Separation Valve)
____ 19.5.	RCL	OPEN HV-0709 (Dewar LN2 Supply Isolation Valve)
____ 19.6.	RCL	OPEN HV-0701 (LN2 Isolation Valve) as per ER_____
____ 19.7.	RCL	Monitor Dewar Level until full
____ 19.8.	RCL	CLOSE HV-0701 (LN2 Isolation Valve)
____ 19.9.	RCL	CLOSE HV-0801 (Tank LN2 Isolation Valve)
____ 19.10.	RCL	CLOSE HV-0804 (Tank-Dewar Separation Valve)
____ 19.11.	RCL	CLOSE HV-0709 (Dewar LN2 Supply Isolation Valve)
____ 19.12.	RCL	CLOSE HV-0408 (Dewar GN2 Isolation Valve)
____ 19.13.	TC	Notify SOCC via hotline in EC-1, EC-2 control room that EC-4 is going from a RED condition to GREEN. Testing is complete.
____ 19.14.	RCL	Change EC-4 light from RED to GREEN.

_____ 20.	RCL	EMERGENCY PROCEDURE (GN2 or LN2 line leak or burst)
		IF OXYGEN DEFICIENCY MONITORS ALARMS:
_____ 20.1.	ALL	Exit the facility to a safe zone given in safety brief.
_____ 20.2.	TC	Contact SOCC and report the emergency. Have the SOCC contact the Fire Dept.
_____ 20.3.	TC	Contact the Facility Manager and isolate the cell or area.
		IF POSSIBLE AND WHEN SAFE, DO THE FOLLOWING:
_____ 20.4.	RCL	CLOSE HV-0001 (EC-3, EC-4 Primary Facility Isolation Valve)
_____ 20.5.	RCL	CLOSE HV-0701 (LN2 Isolation Valve)
_____ 20.6.	RCL	HV-0801 (Tank LN2 Isolation Valve)

Appendix B

Tabular Data

Table B.1 presents the data for the radial temperature and density profiles plotted in Fig. 4.3. The details about the conditions for the individual case numbers correspond to the case numbers in Table 4.1.

Table B.2 contains the dark core length measured from the averaged image, the average dark core length of the individual images, and the root mean square deviation of the dark core length. These three quantities are normalized by the inner-tube diameter of the injector. The details about the conditions for the individual case numbers correspond to the case numbers in Table 4.1.

Table B.1: Radial temperature and density profiles.

CASE 1				CASE 2			
Micrometer	r/R_1	Average	Calculated	Micrometer	r/R_1	Average	Calculated
Position		Temperature	Density	Position		Temperature	Density
(mm)	-	(K)	(kg/m^3)	(mm)	-	(K)	(kg/m^3)
18.00	8.46	230.4	22.2	18.00	7.87	242.1	22.5
17.50	6.50	230.4	22.2	17.50	5.91	239.8	22.7
17.30	5.71	225.3	22.7	17.30	5.12	225.3	24.3
17.20	5.31	220.4	23.3	17.20	4.72	209.9	26.3
17.10	4.92	210.2	24.5	17.10	4.33	202.9	27.3
17.00	4.53	199.1	26.1	17.00	3.94	201.9	27.4
16.90	4.13	196.0	26.5	16.90	3.54	201.5	27.5
16.80	3.74	193.9	26.9	16.80	3.15	200.6	27.6
16.70	3.35	190.6	27.4	16.70	2.76	198.2	28.0
16.60	2.95	185.5	28.3	16.60	2.36	192.6	29.0
16.50	2.56	176.3	30.0	16.50	1.97	187.1	30.0
16.40	2.17	167.1	32.0	16.40	1.57	177.2	31.9
16.35	1.97	159.9	33.9	16.30	1.18	110.8	615.7
16.30	1.77	154.0	35.5	16.25	0.98	110.8	616.0
16.25	1.57	110.1	620.5	16.20	0.79	110.4	619.8
16.20	1.38	109.3	627.6	16.15	0.59	110.0	622.8
16.15	1.18	109.1	629.7	16.10	0.39	110.0	623.1
16.10	0.98	109.1	629.7	16.05	0.20	110.0	623.4
16.05	0.79	109.1	629.3	16.00	0.00	110.0	623.3
16.00	0.59	109.1	629.5	15.95	-0.20	110.0	622.8
15.95	0.39	109.1	629.9	15.90	-0.39	110.0	622.8
15.90	0.20	109.0	629.9	15.85	-0.59	110.0	622.6
15.85	0.00	109.1	629.7	15.80	-0.79	110.1	621.9
15.80	-0.20	109.1	629.3	15.75	-0.98	110.2	621.3
15.75	-0.39	109.2	628.5	15.70	-1.18	111.0	614.5
15.70	-0.59	109.2	628.4	15.65	-1.38	127.8	50.5
15.65	-0.79	109.3	627.7				
15.60	-0.98	109.4	627.3				
15.55	-1.18	109.4	627.3				
15.50	-1.38	109.3	627.4				
15.45	-1.57	109.9	622.3				
15.40	-1.77	125.4	48.2				

Table B.1: Radial temperature and density profiles. (continued)

CASE 3			
Micrometer Position (mm)	r/R_1 -	Average Temperature (K)	Calculated Density (kg/m^3)
18.00	8.86	250.6	19.7
17.50	6.89	248.1	20.0
17.30	6.10	245.9	20.1
17.20	5.71	241.1	20.6
17.10	5.31	226.5	22.0
17.00	4.92	210.1	23.9
16.90	4.53	205.1	24.5
16.80	4.13	204.7	24.6
16.70	3.74	204.3	24.6
16.60	3.35	203.6	24.7
16.50	2.95	197.7	25.6
16.45	2.76	193.1	26.3
16.40	2.56	189.0	26.9
16.35	2.36	185.8	27.5
16.30	2.17	178.6	28.8
16.25	1.97	160.5	32.8
16.20	1.77	112.9	57.6
16.15	1.57	109.3	627.6
16.10	1.38	109.0	630.1
16.05	1.18	108.9	630.6
16.00	0.98	108.5	633.8
15.95	0.79	107.9	638.5
15.90	0.59	107.7	640.3
15.85	0.39	107.8	639.9
15.80	0.20	107.7	640.4
15.75	0.00	107.8	639.7
15.70	-0.20	107.8	639.8
15.65	-0.39	107.8	639.7
15.60	-0.59	108.0	638.2
15.55	-0.79	108.8	631.2
15.50	-0.98	109.0	629.7
15.45	-1.18	109.1	629.4
15.40	-1.38	109.2	628.6
15.35	-1.57	109.3	627.2
15.30	-1.77	111.5	59.5
15.25	-1.97	147.7	36.5

CASE 4			
Micrometer Position (mm)	r/R_1 -	Average Temperature (K)	Calculated Density (kg/m^3)
18.00	8.86	238.5	21.4
17.50	6.89	236.9	21.6
17.30	6.10	234.5	21.8
17.20	5.71	230.9	22.2
17.10	5.31	220.6	23.3
17.00	4.92	206.2	25.1
16.90	4.53	202.6	25.6
16.80	4.13	202.2	25.7
16.70	3.74	202.0	25.7
16.60	3.35	200.9	25.9
16.50	2.95	191.1	27.4
16.45	2.76	181.7	29.0
16.40	2.56	174.9	30.4
16.35	2.36	168.4	31.8
16.30	2.17	143.7	39.1
16.25	1.97	111.8	61.7
16.20	1.77	109.6	625.5
16.15	1.57	108.9	630.9
16.10	1.38	108.8	631.8
16.05	1.18	108.7	632.7
16.00	0.98	108.5	634.3
15.90	0.59	107.8	640.5
15.85	0.39	107.5	642.6
15.80	0.20	107.3	644.2
15.75	0.00	107.1	645.8
15.70	-0.20	107.6	641.5
15.65	-0.39	108.0	638.6
15.60	-0.59	108.1	637.5
15.55	-0.79	108.4	635.4
15.50	-0.98	108.8	632.1
15.45	-1.18	109.0	630.7
15.40	-1.38	109.0	630.2
15.35	-1.57	109.0	630.0
15.30	-1.77	109.1	629.6
15.25	-1.97	109.2	628.9
15.20	-2.17	109.4	627.4
15.15	-2.36	110.2	619.9
15.10	-2.56	150.2	36.8

Table B.1: Radial temperature and density profiles. (continued)

CASE 5				CASE 6			
Micrometer	r/R_1	Average	Calculated	Micrometer	r/R_1	Average	Calculated
Position		Temperature	Density	Position		Temperature	Density
(mm)	-	(K)	(kg/m^3)	(mm)	-	(K)	(kg/m^3)
18.00	8.86	235.5	52.7	18.00	8.46	230.8	56.2
17.50	6.89	235.1	52.8	17.50	6.50	227.5	57.2
17.30	6.10	233.4	53.2	17.30	5.71	224.4	58.1
17.20	5.71	230.4	54.1	17.20	5.31	210.8	62.9
17.10	5.31	220.6	57.0	17.10	4.92	191.2	71.7
17.00	4.92	204.8	62.6	17.00	4.53	187.3	73.8
16.90	4.53	196.4	66.2	16.90	4.13	189.1	72.8
16.85	4.33	195.3	66.7	16.80	3.74	187.6	73.6
16.80	4.13	194.8	66.9	16.70	3.35	187.8	73.5
16.70	3.74	193.3	67.6	16.60	2.95	183.3	76.1
16.60	3.35	191.5	68.5	16.50	2.56	168.4	87.0
16.50	2.95	188.4	70.1	16.40	2.17	153.2	104.2
16.45	2.76	184.4	72.3	16.30	1.77	138.7	136.6
16.40	2.56	178.1	76.1	16.25	1.57	133.1	164.6
16.35	2.36	172.1	80.3	16.20	1.38	128.7	240.2
16.30	2.17	165.8	85.4	16.15	1.18	127.2	411.3
16.25	1.97	159.0	92.0	16.10	0.98	126.1	454.7
16.20	1.77	151.8	100.9	16.05	0.79	124.8	487.5
16.15	1.57	143.7	115.2	16.00	0.59	123.9	505.1
16.10	1.38	134.8	142.5	15.95	0.39	123.2	517.4
16.05	1.18	128.9	193.5	15.90	0.20	122.5	527.4
16.00	0.98	126.4	426.7	15.85	0.00	122.3	530.0
15.95	0.79	124.6	485.0	15.80	-0.20	122.6	525.6
15.90	0.59	122.8	518.4	15.75	-0.39	123.5	512.6
15.85	0.39	121.4	537.5	15.70	-0.59	124.4	495.7
15.80	0.20	120.9	544.4	15.65	-0.79	126.2	452.4
15.75	0.00	120.8	545.7	15.60	-0.98	126.9	427.3
15.70	-0.20	121.1	542.0	15.55	-1.18	127.5	383.6
15.65	-0.39	121.6	535.8	15.50	-1.38	129.4	214.6
15.60	-0.59	122.1	528.8				
15.55	-0.79	123.2	510.7				
15.50	-0.98	124.8	479.0				
15.45	-1.18	126.5	419.7				
15.40	-1.38	131.3	164.1				
15.35	-1.57	141.9	119.3				

Table B.1: Radial temperature and density profiles. (continued)

CASE 7			
Micrometer Position (mm)	r/R_1 -	Average Temperature (K)	Calculated Density (kg/m^3)
18.00	8.86	240.8	51.5
17.50	6.89	239.3	51.9
17.30	6.10	237.8	52.2
17.20	5.71	235.2	52.9
17.10	5.31	225.6	55.7
17.00	4.92	202.6	63.7
16.90	4.53	195.1	67.0
16.80	4.13	194.3	67.4
16.70	3.74	193.8	67.6
16.60	3.35	192.8	68.1
16.50	2.95	188.5	70.3
16.40	2.56	170.8	81.6
16.30	2.17	155.7	96.2
16.25	1.97	149.0	105.7
16.20	1.77	141.4	121.1
16.15	1.57	134.4	145.2
16.10	1.38	129.7	183.0
16.05	1.18	127.3	310.1
16.00	0.98	126.3	429.6
15.95	0.79	125.9	449.3
15.90	0.59	125.3	468.2
15.85	0.39	124.6	485.5
15.80	0.20	123.6	504.8
15.75	0.00	123.2	511.8
15.70	-0.20	124.0	496.6
15.65	-0.39	124.9	476.7
15.60	-0.59	125.3	467.9
15.55	-0.79	125.7	456.6
15.50	-0.98	126.1	441.4
15.45	-1.18	126.3	432.4
15.40	-1.38	126.8	397.2
15.35	-1.57	127.8	231.5
15.30	-1.77	129.8	181.4
15.25	-1.97	133.4	150.9

CASE 8			
Micrometer Position (mm)	r/R_1 -	Average Temperature (K)	Calculated Density (kg/m^3)
18.0	8.9	241.8	50.9
17.5	6.9	240.6	51.2
17.3	6.1	239.8	51.4
17.2	5.7	237.4	52.0
17.1	5.3	228.0	54.6
17.0	4.9	204.9	62.4
16.9	4.5	197.2	65.6
16.8	4.1	196.5	65.9
16.7	3.7	196.2	66.1
16.6	3.3	195.4	66.4
16.5	3.0	191.3	68.4
16.5	2.8	182.7	73.0
16.4	2.6	171.7	80.3
16.4	2.4	161.9	88.6
16.3	2.2	154.0	97.5
16.3	2.0	146.1	109.7
16.2	1.8	138.9	126.8
16.1	1.6	132.5	154.2
16.1	1.4	128.7	194.3
16.0	1.2	126.7	394.1
16.0	1.0	126.1	437.1
15.9	0.8	125.8	449.7
15.9	0.6	125.3	464.1
15.9	0.4	124.9	477.1
15.8	0.2	124.6	483.1
15.8	0.0	124.5	484.6
15.7	-0.2	124.8	479.5
15.6	-0.4	125.0	473.0
15.6	-0.6	125.3	464.1
15.6	-0.8	125.7	452.4
15.5	-1.0	126.0	441.2
15.4	-1.2	126.4	421.9
15.4	-1.4	127.0	349.2
15.4	-1.6	128.3	205.0
15.3	-1.8	130.8	166.9
15.3	-2.0	134.6	142.7

Table B.1: Radial temperature and density profiles. (continued)

CASE 9				CASE 10			
Micrometer	r/R_1	Average	Calculated	Micrometer	r/R_1	Average	Calculated
Position		Temperature	Density	Position		Temperature	Density
(mm)	-	(K)	(kg/m^3)	(mm)	-	(K)	(kg/m^3)
18.00	8.86	243.6	71.3	18.00	8.66	244.3	70.8
17.50	6.89	242.0	71.9	17.50	6.69	243.8	70.9
17.30	6.10	239.3	72.9	17.30	5.91	242.0	71.6
17.20	5.71	237.1	73.8	17.20	5.51	238.3	73.0
17.10	5.31	228.7	77.2	17.10	5.12	223.2	79.3
17.00	4.92	207.5	88.0	17.00	4.72	198.5	93.3
16.90	4.53	192.3	98.4	16.90	4.33	192.8	97.5
16.80	4.13	189.8	100.5	16.80	3.94	191.3	98.7
16.70	3.74	187.9	102.1	16.70	3.54	189.4	100.3
16.60	3.35	186.7	103.2	16.60	3.15	188.0	101.5
16.50	2.95	184.6	105.1	16.50	2.76	182.8	106.3
16.40	2.56	178.8	111.1	16.40	2.36	171.2	119.6
16.35	2.36	173.7	117.0	16.35	2.17	165.7	128.0
16.30	2.17	169.2	123.2	16.30	1.97	160.8	136.8
16.25	1.97	163.5	132.4	16.25	1.77	155.7	148.5
16.20	1.77	158.5	142.5	16.20	1.57	149.2	169.4
16.15	1.57	153.7	155.1	16.15	1.38	142.8	203.5
16.10	1.38	146.5	182.9	16.10	1.18	137.9	259.3
16.05	1.18	140.6	225.3	16.05	0.98	135.0	326.6
16.00	0.98	136.2	296.4	16.00	0.79	133.1	384.3
15.95	0.79	132.8	394.5	15.95	0.59	131.3	430.7
15.90	0.59	130.1	456.2	15.90	0.39	129.3	470.0
15.85	0.39	128.6	482.9	15.85	0.20	128.7	479.4
15.80	0.20	127.9	493.2	15.80	0.00	128.9	476.2
15.75	0.00	127.6	498.5	15.75	-0.20	128.8	479.3
15.70	-0.20	128.5	484.7	15.70	-0.39	129.3	470.7
15.65	-0.39	128.9	477.2	15.65	-0.59	130.5	446.6
15.60	-0.59	129.2	472.7	15.60	-0.79	132.0	414.0
15.55	-0.79	130.2	455.3	15.55	-0.98	132.9	389.3
15.50	-0.98	132.3	407.8	15.50	-1.18	133.8	362.7
15.45	-1.18	135.5	316.8	15.45	-1.38	135.1	322.1
15.40	-1.38	140.5	226.0	15.40	-1.57	137.1	272.9
15.35	-1.57	147.8	176.3	15.35	-1.77	140.6	223.2

Table B.1: Radial temperature and density profiles. (continued)

CASE 11				CASE 12			
Micrometer	r/R_1	Average	Calculated	Micrometer	r/R_1	Average	Calculated
Position		Temperature	Density	Position		Temperature	Density
(mm)	-	(K)	(kg/m^3)	(mm)	-	(K)	(kg/m^3)
19.00	12.80	240.1	72.2	18.0	8.5	242.7	71.3
18.50	10.83	239.0	72.6	17.5	6.5	241.3	71.7
17.50	6.89	237.0	73.3	17.3	5.7	241.1	71.8
17.30	6.10	234.7	74.2	17.2	5.3	239.1	72.6
17.20	5.71	232.4	75.2	17.1	4.9	231.2	75.7
17.10	5.31	223.8	78.9	17.0	4.5	206.6	88.0
17.00	4.92	197.4	94.0	16.9	4.1	192.5	97.7
16.90	4.53	186.9	102.3	16.8	3.7	191.4	98.5
16.80	4.13	186.0	103.1	16.7	3.3	191.1	98.8
16.70	3.74	185.5	103.5	16.6	3.0	190.6	99.2
16.60	3.35	184.7	104.2	16.5	2.6	189.7	99.9
16.50	2.95	183.0	105.9	16.4	2.2	182.0	106.9
16.45	2.76	179.5	109.5	16.3	1.8	163.4	131.6
16.40	2.56	172.6	117.6	16.3	1.6	157.8	143.0
16.35	2.36	166.0	127.2	16.2	1.4	151.6	160.3
16.30	2.17	159.9	138.4	16.1	1.2	142.8	203.6
16.25	1.97	155.0	150.1	16.1	1.0	138.8	244.0
16.20	1.77	149.4	168.1	16.0	0.8	137.3	268.4
16.15	1.57	144.0	195.0	16.0	0.6	136.0	298.1
16.10	1.38	140.3	225.4	15.9	0.4	135.2	320.1
16.05	1.18	137.6	263.3	15.9	0.2	132.3	404.4
16.00	0.98	135.7	305.0	15.9	0.0	131.7	419.4
15.95	0.79	134.7	333.5	15.8	-0.2	132.5	400.4
15.90	0.59	134.0	354.3	15.8	-0.4	132.8	390.7
15.85	0.39	133.5	369.8	15.7	-0.6	133.7	366.5
15.80	0.20	133.3	377.2	15.6	-0.8	135.1	321.5
15.75	0.00	133.3	378.0	15.6	-1.0	136.8	279.1
15.70	-0.20	133.4	374.2				
15.65	-0.39	133.7	363.3				
15.60	-0.59	134.5	340.4				
15.55	-0.79	135.8	303.4				

Table B.1: Radial temperature and density profiles. (continued)

CASE 13				CASE 14			
Micrometer	r/R_1	Average	Calculated	Micrometer	r/R_1	Average	Calculated
Position		Temperature	Density	Position		Temperature	Density
(mm)	-	(K)	(kg/m^3)	(mm)	-	(K)	(kg/m^3)
18.00	8.96	228.4	21.8	18.00	9.25	225.5	22.4
17.50	6.99	223.8	22.3	17.50	7.28	226.8	22.3
17.30	6.20	221.0	22.6	17.30	6.50	222.1	22.8
17.20	5.81	211.6	23.7	17.20	6.10	219.5	23.1
17.10	5.41	182.2	28.1	17.10	5.71	211.1	24.1
17.00	5.02	145.8	37.2	17.00	5.31	184.5	28.1
16.90	4.63	135.0	41.6	16.90	4.92	152.5	35.5
16.80	4.23	133.5	42.2	16.80	4.53	142.4	39.0
16.70	3.84	132.4	42.8	16.70	4.13	140.0	40.0
16.60	3.44	131.2	43.4	16.60	3.74	137.9	40.9
16.50	3.05	128.7	44.8	16.50	3.35	137.3	41.1
16.40	2.66	118.7	51.7	16.40	2.95	137.1	41.2
16.30	2.26	110.0	61.9	16.30	2.56	127.4	46.2
16.25	2.07	109.0	629.9	16.25	2.36	109.8	623.3
16.20	1.87	108.7	632.2	16.20	2.17	109.1	629.5
16.15	1.67	108.7	632.3	16.15	1.97	109.0	629.9
16.10	1.48	108.7	632.0	16.10	1.77	109.0	630.4
16.05	1.28	108.8	631.9	16.05	1.57	108.9	630.6
16.00	1.08	108.8	632.0	16.00	1.38	108.9	630.9
15.95	0.89	108.8	631.4	15.90	0.98	108.9	630.9
15.90	0.69	108.9	631.1	15.80	0.59	108.9	630.8
15.85	0.49	108.9	631.0	15.70	0.20	108.9	630.8
15.80	0.30	108.9	630.5	15.60	-0.20	108.9	631.1
15.75	0.10	108.9	630.8	15.50	-0.59	108.9	630.9
15.70	-0.10	108.9	631.1	15.40	-0.98	109.0	630.5
15.65	-0.30	108.8	631.2	15.30	-1.38	108.9	630.8
15.60	-0.49	108.9	631.1	15.20	-1.77	108.9	630.7
15.55	-0.69	108.9	631.0	15.10	-2.17	108.9	630.7
15.50	-0.89	108.9	631.1	15.05	-2.36	109.0	630.3
15.45	-1.08	108.8	631.3	15.00	-2.56	109.4	627.0
15.40	-1.28	108.8	631.3				
15.35	-1.48	108.8	631.5				
15.30	-1.67	108.8	631.4				
15.25	-1.87	108.8	631.5				
15.20	-2.07	108.8	631.2				
15.15	-2.26	109.1	629.1				
15.05	-2.66	224.3	22.3				

Table B.1: Radial temperature and density profiles. (continued)

CASE 15			
Micrometer Position (mm)	r/R_1 -	Average Temperature (K)	Calculated Density (kg/m^3)
18.00	8.96	224.0	23.0
17.50	6.99	221.3	23.3
17.20	5.81	216.8	23.8
17.10	5.41	206.5	25.2
17.00	5.02	171.2	31.3
16.90	4.63	135.9	42.6
16.90	4.63	141.3	40.2
16.80	4.23	132.3	44.4
16.80	4.23	149.6	37.2
16.70	3.84	152.3	36.3
16.60	3.44	153.6	35.9
16.50	3.05	152.4	36.3
16.40	2.66	138.7	41.3
16.40	2.66	135.2	42.9
16.35	2.46	118.2	54.4
16.30	2.26	111.0	63.2
16.25	2.07	109.0	630.2
16.15	1.67	109.0	630.2
16.05	1.28	109.0	630.6
16.00	1.08	109.0	630.2
15.90	0.69	109.0	630.4
15.80	0.30	109.0	630.3
15.70	-0.10	109.0	630.5
15.60	-0.49	109.2	628.8
15.50	-0.89	109.3	628.1
15.40	-1.28	109.2	628.4
15.30	-1.67	109.3	628.3
15.20	-2.07	109.3	628.0
15.15	-2.26	109.8	623.2
15.05	-2.66	122.0	51.1

Table B.1: Radial temperature and density profiles. (continued)

CASE 16			
Micrometer Position (mm)	r/R_1 -	Average Temperature (K)	Calculated Density (kg/m^3)
18.00	8.86	234.0	52.8
17.50	6.89	232.4	53.2
17.30	6.10	227.9	54.5
17.20	5.71	223.1	55.9
17.10	5.31	212.7	59.3
17.00	4.92	174.6	78.0
16.90	4.53	141.2	120.0
16.80	4.13	137.4	131.1
16.70	3.74	136.2	135.3
16.60	3.35	136.3	135.2
16.50	2.95	135.7	137.5
16.40	2.56	135.0	140.4
16.30	2.17	131.7	159.0
16.25	1.97	129.8	177.2
16.20	1.77	128.5	198.0
16.15	1.57	127.4	243.8
16.10	1.38	126.4	422.0
16.05	1.18	125.7	451.6
16.00	0.98	124.9	474.9
15.95	0.79	123.9	498.0
15.90	0.59	122.5	521.6
15.85	0.39	121.5	536.7
15.80	0.20	121.4	537.6
15.75	0.00	121.7	533.1
15.70	-0.20	121.7	533.1
15.65	-0.39	121.5	536.6
15.60	-0.59	121.1	542.1
15.55	-0.79	121.1	540.9
15.50	-0.98	122.2	526.2
15.45	-1.18	123.8	500.2
15.40	-1.38	125.1	470.7
15.35	-1.57	126.7	400.0
15.30	-1.77	129.1	186.4
15.25	-1.97	132.1	156.2

CASE 17			
Micrometer Position (mm)	r/R_1 -	Average Temperature (K)	Calculated Density (kg/m^3)
18.00	8.86	206.6	61.4
17.50	6.89	205.3	62.0
17.30	6.10	203.4	62.7
17.20	5.71	199.5	64.3
17.10	5.31	185.7	71.0
17.00	4.92	152.7	98.8
16.90	4.53	140.2	122.2
16.80	4.13	138.7	126.4
16.70	3.74	139.4	124.4
16.60	3.35	140.8	120.6
16.50	2.95	140.2	122.2
16.40	2.56	133.3	148.2
16.35	2.36	130.2	171.9
16.30	2.17	128.4	199.7
16.25	1.97	127.7	222.2
16.20	1.77	126.8	380.4
16.15	1.57	126.0	437.1
16.10	1.38	125.5	458.0
16.05	1.18	124.7	478.8
16.00	0.98	123.7	501.4
15.95	0.79	122.7	518.2
15.90	0.59	121.8	531.4
15.85	0.39	121.2	540.6
15.80	0.20	120.6	548.2
15.75	0.00	120.4	549.9
15.70	-0.20	120.7	546.9
15.65	-0.39	121.1	541.5
15.60	-0.59	121.7	533.2
15.55	-0.79	122.4	523.7
15.50	-0.98	123.2	511.0
15.45	-1.18	123.9	497.9
15.40	-1.38	124.7	480.9
15.35	-1.57	125.3	464.2
15.30	-1.77	125.9	443.4
15.25	-1.97	126.4	418.7
15.15	-2.36	127.8	215.0

Table B.1: Radial temperature and density profiles. (continued)

CASE 18			
Micrometer Position (mm)	r/R_1 -	Average Temperature (K)	Calculated Density (kg/m^3)
18.00	8.86	208.6	60.5
17.50	6.89	207.4	60.9
17.30	6.10	203.6	62.4
17.10	5.31	196.4	65.5
17.00	4.92	158.2	91.6
16.90	4.53	136.2	134.0
16.70	3.74	133.3	147.0
16.50	2.95	134.0	143.3
16.30	2.17	127.2	254.1
16.20	1.77	126.3	418.4
16.10	1.38	125.0	471.1
16.00	0.98	123.0	512.6
15.95	0.79	122.5	521.3
15.90	0.59	121.7	532.5
15.85	0.39	119.8	556.5
15.80	0.20	119.8	556.9
15.75	0.00	119.5	560.4
15.70	-0.20	120.0	554.3
15.65	-0.39	120.2	552.5
15.60	-0.59	121.0	542.0
15.50	-0.98	122.3	523.9
15.40	-1.38	124.1	493.2

CASE 19			
Micrometer Position (mm)	r/R_1 -	Average Temperature (K)	Calculated Density (kg/m^3)
18.0	9.1	211.7	59.7
17.5	7.1	209.9	60.4
17.2	5.9	207.7	61.2
17.1	5.5	204.2	62.5
17.0	5.1	184.5	71.9
16.9	4.7	139.8	123.7
16.8	4.3	133.9	145.6
16.7	3.9	133.9	145.5
16.5	3.1	133.2	149.3
16.3	2.4	129.0	188.6
16.2	2.0	126.2	430.9
16.1	1.6	125.2	467.5
16.0	1.2	124.8	478.2
15.9	1.0	125.0	471.7
15.9	0.8	124.4	486.6
15.9	0.6	124.6	482.8
15.8	0.4	125.5	457.6
15.8	0.2	125.7	453.4
15.7	0.0	125.9	444.0
15.6	-0.2	125.5	457.4
15.6	-0.4	125.5	459.9
15.5	-0.8	125.7	452.0
15.4	-1.2	125.8	448.0
15.3	-1.6	126.2	429.5

Table B.1: Radial temperature and density profiles. (continued)

CASE 20				CASE 21			
Micrometer	r/R_1	Average	Calculated	Micrometer	r/R_1	Average	Calculated
Position		Temperature	Density	Position		Temperature	Density
(mm)	-	(K)	(kg/m^3)	(mm)	-	(K)	(kg/m^3)
18.00	8.86	214.5	83.6	18.00	9.25	225.2	77.2
17.50	6.89	213.0	84.5	17.50	7.28	222.9	78.3
17.30	6.10	208.5	87.0	17.10	5.71	219.9	79.7
17.20	5.71	203.1	90.3	17.00	5.31	215.2	82.0
17.10	5.31	189.8	100.0	16.90	4.92	187.8	100.1
17.00	4.92	148.5	172.3	16.80	4.53	144.4	187.8
16.90	4.53	135.9	302.5	16.70	4.13	140.2	220.2
16.80	4.13	135.2	319.3	16.60	3.74	142.4	201.0
16.70	3.74	135.2	320.5	16.40	2.95	139.4	229.4
16.60	3.35	135.2	321.3	16.20	2.17	136.8	269.3
16.50	2.95	135.1	324.7	16.10	1.77	134.5	328.6
16.40	2.56	134.9	330.7	16.00	1.38	132.6	388.8
16.30	2.17	134.2	350.1	15.95	1.18	130.9	433.7
16.20	1.77	132.9	388.6	15.90	0.98	129.4	464.6
16.15	1.57	132.0	412.5	15.85	0.79	128.3	482.7
16.10	1.38	130.8	440.5	15.80	0.59	127.6	494.3
16.05	1.18	129.0	475.1	15.75	0.39	126.8	506.3
16.00	0.98	127.5	498.2	15.70	0.20	126.8	506.2
15.95	0.79	125.4	525.9	15.65	0.00	126.2	514.5
15.90	0.59	122.6	556.5	15.60	-0.20	126.5	510.3
15.85	0.39	120.8	573.9	15.55	-0.39	126.8	506.4
15.80	0.20	119.7	583.3	15.50	-0.59	127.4	497.4
15.75	0.00	119.5	585.0	15.45	-0.79	128.5	479.5
15.70	-0.20	119.9	581.9	15.40	-0.98	129.2	467.6
15.65	-0.39	120.1	580.1	15.35	-1.18	130.3	447.5
15.60	-0.59	120.7	574.7	15.30	-1.38	131.6	417.5
15.55	-0.79	121.1	570.7				
15.50	-0.98	123.1	551.5				
15.45	-1.18	127.9	492.5				
15.40	-1.38	130.0	457.6				

Table B.2: Dark Core Length Data.

CASE #	Acoustic OFF			Acoustics ON First Mode			Acoustics ON Second Mode		
	Averaged Image L/D1	Average of Instantaneous L/D1	RMS/D1	Averaged Image L/D1	Average of Instantaneous L/D1	RMS/D1	Averaged Image L/D1	Average of Instantaneous L/D1	RMS/D1
1	28.0	34.1	6.9	18.8	31.8	7.9	20.5	30.7	6.9
2	20.9	23.1	4.9	15.1	16.5	-	15.2	19.3	3.2
3	17.4	19.4	1.9	6.7	10.4	2.4	10.9	12.7	1.8
4	15.1	15.9	1.4	7.2	9.5	2.3	11.2	12.6	1.9
5	17.9	19.0	1.8	14.6	16.3	2.1	18.4	19.2	1.5
6	10.4	10.7	2.0	5.5	6.4	1.0	6.3	6.5	1.3
7	5.6	5.8	0.7	4.2	4.5	0.5	3.4	4.0	0.9
8	4.5	4.7	0.5	3.4	3.6	0.5	3.8	4.1	0.5
9	14.6	15.6	2.3	12.2	13.4	1.4	15.0	16.0	2.1
10	7.0	7.7	0.8	5.4	6.0	0.6	5.5	5.9	0.9
11	3.7	4.0	0.4	2.8	3.2	0.7	3.2	3.4	0.5
12	3.0	3.1	0.3	3.0	3.0	0.4	3.0	2.9	0.4
13	20.7	25.7	4.5	18.8	24.2	4.0	16.5	20.7	2.6
14	17.1	18.4	2.1	11.9	15.0	2.0	8.9	9.1	1.5
15	17.9	18.4	1.6	14.9	15.9	1.9	9.7	11.2	1.5
16	21.6	25.0	2.9	17.9	19.9	2.5	17.1	17.4	1.9
17	7.5	8.0	1.0	5.8	6.9	1.3	4.9	5.7	0.9
18	3.6	3.2	0.5	2.8	2.6	0.3	3.4	3.2	0.5
19	3.7	2.9	0.5	4.2	2.7	0.4	3.2	2.5	0.5
20	6.9	9.8	3.6	7.7	12.3	4.0	27.3	29.0	2.8

VITA

Dustin Wayne Davis

Dustin W. Davis was born on December 3, 1975, and raised in Rockwood, Pennsylvania with humble beginnings. He graduated from Rockwood Area High School in June of 1994. After high school, the author went to The Pennsylvania State University, where he wanted to attend since five years of age. He completed his Bachelor of Science degree in Chemical Engineering, with a focus on Fuel Science in December of 1998. The faculty and courses in Fuel Science inspired him to attend graduate school with the intention of focusing on propulsion and power research in Mechanical Engineering. Upon completion of his Master of Science degree in Mechanical Engineering in August of 2001 and an additional year of course work, he went to the Air Force Research Laboratory at Edwards AFB, CA to perform the experimental work pursuing his doctoral degree in Mechanical Engineering. After three continuous years experimental work at AFRL, the author completed his experiments and doctoral degree.

While in graduate school, Dustin married Holly Beth Lee, and now have two sons Drew Anthony and Parker William. Presently, the author is working at GE Global Research Center in Niskayuna, New York.

Measurements in an Acoustically Driven Coaxial Jet under Sub-, Near-, and Supercritical Conditions

Dustin W. Davis* and Bruce Chehroudi†
ERC, Inc., Edwards Air Force Base, California 93524

DOI: 10.2514/1.19340

An experimental investigation was conducted on a coaxial jet, similar to those used in cryogenic liquid rockets, under sub-, near-, and supercritical pressures, with the intent of gaining a better understanding of an aspect of combustion instability pertaining to interactions of an externally imposed acoustic field with the jet. Past research on this subject has shown both the relevance and importance of geometrical changes in an injector's exit-area and its nearby physical and fluid mechanical processes. Special attention is paid in collecting spatially resolved time averaged temperatures and documenting the aforementioned interactions at the exit of this injector. Short-duration and high-speed framing digital images provided information on the behavior of this jet under various conditions. Mean and root mean square values of the "dark-core" length fluctuations were measured from the acquired images via a computer-automated method, and results are discussed. There appears to be a good correlation between this length and the outer-to-inner-jet momentum ratio, but the form of this dependence was found to be different at subcritical pressures than the rest of the conditions. The root mean square values of the dark-core length fluctuations suggested a possible explanation for the observed improvement in instability limit at increasingly higher outer-to-inner-jet velocity ratios.

Nomenclature

C	=	constant
D	=	diameter with subscripts
L	=	length of dark core, length of injector tube
M	=	momentum flux ratio of outer-jet to inner-jet
m	=	mass flow rate
n	=	exponent of M
P	=	pressure
R	=	radius with subscripts
R_h	=	hydraulic radius of outer-jet, equal to the gap width
T	=	temperature
U	=	velocity
VR	=	velocity ratio of outer-jet to inner-jet
μ	=	viscosity
ρ	=	density
σ	=	surface tension

Subscripts

1, 2, 3, 4	=	four diameters or radii of the coaxial injector from the smallest to largest values
i	=	subscript denoting inner-jet
o	=	subscript denoting outer-jet

I. Introduction

COMBUSTION instability is a problem that has been observed with liquid rocket engines since the late 1930s (see Culick and Yang [1]). Three types of combustion instabilities have been

identified based on the frequencies involved. Low frequency instability (chugging) is when the wavelength is much longer than the characteristic dimension of the chamber and the feed system. Generally, chugging frequencies are less than a few hundred Hz. High frequency instability (screaming) is the second type which is also referred to as acoustic instability due to the closeness of the measured pressure oscillation frequencies to the computed acoustic resonance modes of the thrust chamber. An intermediate frequency (buzz) consists of the lumping of the instabilities that do not fall into either chugging or screaming categories (see Harje and Reardon [2]).

Typically, for cryogenic propellant systems consisting of liquid oxygen (LOX)—hydrogen (H_2), a shear coaxial-type injector is used. Examples are the designs presently employed in the space shuttle main engine (SSME) or the Ariane 5 Vulcain engine (Vingert et al. [3]), and the RL-10 and J-2 engines from the late 1950s (Hulka and Hutt [4]). One method of eliminating the acoustic instability in liquid rocket engines is to modify the spray combustion field, which is usually achieved through modifications to the injector design, see Harje and Reardon [2]. One such modification to the Ariane 5 Vulcain reported by Vingert et al. [3] increased the mean droplet diameter size and improved the stability of the engine. These changes to the injector design ultimately affect the mixing characteristics of the propellant streams in the thrust chamber. The fundamental physics of the breakup of a liquid jet and its subsequent mixing with other fluids have been studied since Rayleigh's study in 1878 [5]. Much progress has been made since then and, as a result, we are approaching a fundamental understanding of fluid jet break up and atomization processes (see, for example, Lefebvre [6]). However, full understanding is not yet available (Eroglu et al. [7]). A review of liquid jet atomization processes from a coaxial-type injector has recently been presented by Lasheras and Hopfinger [8], discussing some of the more recent developments in this area.

The importance of interactions between the acoustic field and a fluid jet in the context of combustion instability has been realized for some time. This notion arises from designers' ability to bring about improvements in engine stability through modifications in injector designs. Combustion in a rocket engine is controlled by, or at least intimately related to, the jet breakup and mixing processes of the oxidizer and fuel streams. Some early works on the interaction of high-amplitude acoustic waves with fluid jets were done by Miesse [9]. Miesse excited atmospheric-pressure round water jets with a high-intensity acoustic field and observed a decrease in the breakup

Received 12 October 2005; accepted for publication 5 July 2006. Copyright © 2006 by the American Institute of Aeronautics and Astronautics, Inc. The U.S. Government has a royalty-free license to exercise all rights under the copyright claimed herein for Governmental purposes. All other rights are reserved by the copyright owner. Copies of this paper may be made for personal or internal use, on condition that the copier pay the \$10.00 per-copy fee to the Copyright Clearance Center, Inc., 222 Rosewood Drive, Danvers, MA 01923; include the code 0748-4658/07 \$10.00 in correspondence with the CCC.

*Scientist, ERC, Inc., and Ph.D. Candidate Pennsylvania State University. Currently Combustion Research Engineer, General Electric Global Research Center, One Research Circle, Niskayuna, NY 12309. AIAA Member.

†Principal Scientist, ERC, Inc., Air Force Research Laboratory, 10 East Saturn Boulevard; ChehroudiB@aol.com. AIAA Member.

Approved for public release; distribution unlimited. PAS #2005-181.

length of the jet. Buffum and Williams [10] also investigated the effects of a transverse acoustic wave at frequencies in the range of 100–500 Hz and at amplitudes up to 161 dB on round liquid jets, measuring jet lateral deflection from its stable position. They observed an induced deflection of the jet at acoustic amplitudes above 130 dB.

Hulka and Hutt [4] have compiled an extensive review of coaxial injectors used in reported LOX/H₂ rocket engine stability tests by others with the objective of identifying key injector design or operating conditions contributing to combustion instability in these engines. What they found, and also reported by others, was that the outer-to-inner-jet exit velocity ratio played a key role in many of the studies defining stability. Although much scatter is seen in the accumulated results, generally speaking, high-velocity ratio values tended to improve engine stability limits. For a wide variety of injector designs and operating conditions, a velocity ratio of about 10 was the maximum where combustion instability occurred, with the exception of the M-1 engine. Additionally, they point out that a velocity ratio as low as one has been stable and a ratio as high as 15 was required to stabilize the M-1 engine.

One method for LOX/H₂ rocket engine stability rating is to perform so-called temperature-ramping of the H₂ (flowing into the outer annular region of the coaxial injector) by reducing its temperature from a high value to low enough temperature until an onset of instability in the engine is measured. An engine, injector or combined injector/engine design as a system, which produces a lower H₂ temperature at the onset of the instability, implies a more stable system. One issue with the data accumulated by Hulka and Hutt [4] is that the original researchers reporting the results usually measured propellant temperatures well upstream of the injector exit area which could provide calculated velocity ratios quite different from its true values at the exit. Additionally, under near- or supercritical conditions, as also pointed out by them [4], small changes in temperature, even if measured at the injector exit plane, can produce large changes in density, strongly affecting the accuracy of estimates for velocity ratios. It is this lack of accurate information that partly motivated the current authors to initiate research providing details and accurate measurements of temperature radial profiles at the exit of a coaxial injector design, something we are unaware has ever been undertaken before to the detail presented here.

As indicated by Wanhainen et al. [11], although velocity ratio seems to serve quite well as a correlating parameter, it is difficult to relate it to a physical combustion model and it may indeed be symbolic of other fundamental parameters. It is our ultimate intention to shed some light and contribute towards such a key physical understanding. It is also interesting to mention a related work reported by Hiedmann [12] in a circular combustor with LOX jets injecting radially from the side walls of the combustor. The H₂ streams were introduced into the chamber in a diffuse manner, somewhat similar to a coaxial design. The combustion instability was induced by injection of nitrogen streams circumferentially to be perpendicular to the LOX injection direction. In images, Hiedmann observed that the length of the LOX dark core decreased during every screaming combustion instability event. This motivated us to pay special attention to the observed dark-core impression of the jets as seen in our studies.

Therefore, to gain physical insight on the effects of an externally-imposed acoustic field on the flow and thermodynamic conditions of a coaxial jet near its exit area, experiments were designed and conducted to have as many of the key features of a LOX/H₂ rocket engine as possible in a cold flow environment. Davis et al. [13,14] have assembled a single-element coaxial-jet noncombusting test rig operating at cryogenic temperatures, transcritical temperature ranges, sub- to supercritical pressures, realistic outer-to-inner-jet velocity ratios, and activation of an acoustical field inside the test chamber simulating one important aspect of the environment when combustion instability intensifies. Additional details on the development of this work can be found in previous papers by Davis et al. [13–15] in which a coaxial jet injector was designed, based on a well-characterized single-jet injector investigated by Chehroudi et al. [16–20].

II. Experimental Facility

The experimental facility, previously described by Chehroudi et al. [13–20], has undergone considerable upgrades and modifications to improve the quality of the data and expand the operating range of the facility. Gaseous nitrogen (GN2) from the laboratory feed line was used to pressurize the test chamber and also to produce the jets issuing from a round coaxial injector's center post (or inner tube) and its outer annular coaxial region. The feed GN2 flow rates, used to produce the inner and outer jets, are measured separately with Porter mass flow meters. Subsequently, the GN2 streams flow through a series of heat exchangers to be cooled. These heat exchangers are cooled by the "facility liquid nitrogen (LN2)" stored in a cryogenic tank outside the test cell. The GN2 feeding the inner jet is passed through a counter-flow heat exchanger (HX) cooled to below the critical temperature. The nitrogen (now in liquid phase) exiting from the center-post HX is then directly sent to the injector. The GN2 for the outer flow passes through two HXs (primary and secondary) before it is directed to the injector. The facility LN2 flow rate to the secondary HX is adjusted to produce a desired temperature of the outer jet at the exit plane of the injector. Independent control over the outer-jet exit temperature is an important feature which was not previously available in our facility. For reference, the critical temperature and pressure of nitrogen are 126.2 K and 3.4 MPa, respectively.

The coaxial injector used in this study, the details of which were previously given by Davis et al. [13–15], produces a cryogenic round jet that is injected through a sharp-edged stainless-steel inner tube having a length L of 50 mm, an inner diameter D_1 of 0.508 mm, and an outer diameter D_2 of 1.59 mm. The inner D_3 and outer D_4 diameters of the outer tube are 2.42 and 3.18 mm, respectively. The resulting L/D_1 is 100, which is considered sufficient to ensure a fully developed turbulent pipe flow at the injector exit plane. The exit plane of the inner tube was recessed by about $0.5D_1$ from that of the outer tube. The gap width R_h between the inner and outer tubes, defining the annular region, was 0.415 mm. The outer-jet exit area was measured from a highly magnified image of the injector exit plane, and R_h was computed from the exit area measured on this image. The concentricity of the inner tube of the injector was measured to be 0.03 mm, approximately 8% of the mean gap width. The inner tube was 0.03 mm closer to the outer tube on one side (this is the left side of the jet images presented in this work). Because the area was measured, this will have no effect on the computed mean velocities. However, the local velocity on the narrower side is most likely slightly higher than the other side. The effect of this level of eccentricity on the jet was not discernible from the data collected here.

The main chamber is designed to withstand pressures up to 14 MPa. There is a smaller rectangular-shaped cross section chamber inside the main chamber. Figure 1 shows a transparent portion of the side walls for the inner chamber, with a close-up image of the coaxial injector tip area. The injector outer tube is covered with thick Teflon material for heat insulation. The purpose of the main chamber is to

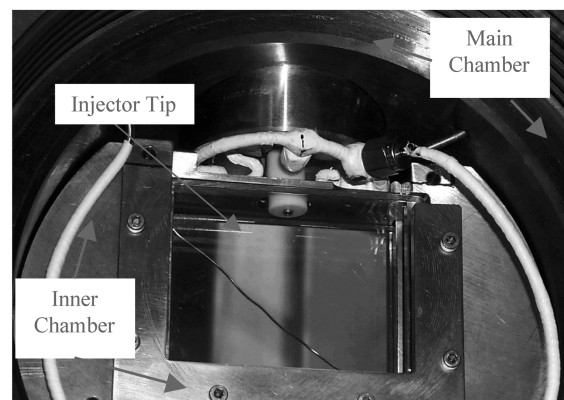


Fig. 1 View of inner chamber measurement zone.

contain the pressure, whereas that of the inner one is to act as a cavity resonator operating at the same (mean) pressure as the main chamber, with the intention of achieving the highest amplitude of the acoustically induced velocity in the vicinity of the jet. The inner-chamber cavity was driven by a piezo siren, specially designed by Hersh Acoustical Engineering, Inc. This device is capable of producing sound pressure levels (SPL) of up to 180 dB (measured in an impedance tube) at resonant frequencies lying between 1000 to 8000 Hz and at pressures up to 14 MPa. The siren is physically coupled to the inner chamber via a circular-to-rectangular transition piece (not shown in Fig. 1) to guide the acoustic waves into the measurement zone of the inner chamber. The measurement zone is evident in Fig. 1. Actual SPL in the inner chamber were between 161 and 171 dB at its first two resonance frequencies of 3.0 and 5.2 kHz. The pressure fluctuations represent about 4–7% of the mean chamber pressure at the highest and lowest chamber pressures. The resonance frequencies of the inner chamber change slightly with changes in chamber pressure and temperature. The jet from the injector is located at a pressure node of the inner chamber.

Radial temperature profiles of the jet at the exit of the injector were measured with a Type-E thermocouple (TC) installed on a traversing stage that protrudes into the inner-chamber region (see Fig. 2). The thermocouple bead diameter is 0.10 mm and the resolution of the radial distance is 0.01 mm. The distance from the injector exit plane to the thermocouple bead is 0.14 mm or $0.28D_1$. The best estimate of the measurement accuracy of a standard calibration of the Type-E TC within our range of interest is on the order of ± 5 K. This is considered too large, especially near the critical point of nitrogen, producing large uncertainties in density and injection velocity calculations. The uncertainty is due to composition variations of the particular bead and wire materials used within the manufacturing specification. Typically, a curve fit to the calibration data over a large range is quite adequate and has only a few degrees of uncertainty at room temperatures or warmer. However, at cryogenic temperatures, the uncertainties grow because the output voltage from a TC decreases at low temperatures and electrical noise becomes a larger portion of the output signal. Therefore, it was necessary to recalibrate the TCs in-house to mitigate these effects. The calibration was performed against a precision platinum resistance temperature detector (Pt-RTD) over a range of 77–300 K. The Pt-RTD was manufactured and calibrated by Hart and had an accuracy of

± 0.04 K. No Pt-RTD was available in the small size required to make measurements in the jet, but the size was unimportant for the calibration procedure itself. The maximum estimated uncertainty over the range of interest for the recalibrated thermocouples was ± 0.8 K. To assess the effect of the TC on the temperature field in the vicinity of the TC, CFD calculations were performed and determined to be insignificant.

The addition of the exit-plane temperature measurement system was a significant improvement to the facility. Previous temperature measurements by Davis et al. [14] were performed with the standard calibration of a Type-E TC which had a large bead diameter of approximately 0.4 mm, and had no mechanism for removing the bead from the jet flow without opening the main chamber. This means that no images could be acquired during temperature measurements and another repeat run was required to accumulate such information. Additionally, the improved temperature measurement system uses a TC with a much smaller bead diameter than before (~ 0.1 mm), which introduces less disturbance to the jet flow, particularly for the inner-jet temperature measurements. Also, the TC is attached to a traversing mechanism, which permits measurements of radial profiles at a fixed axial distance of $0.28D_1$ downstream of the injector exit plane. Once temperature measurements are made, the TC can be traversed out of the flow, far from the coaxial jet area, enabling imaging of the undisturbed jet in the same run.

Backlit images (12-bit) of the coaxial jet were taken at 10 Hz frame rate with resolution of 1280×1024 pixels using a PixelFly CCD camera manufactured by the Cooke Corp. A General Radio Stroboscopes® strobe light was used for illumination purposes. The image was defined by the strobe flash duration of approximately $0.5 \mu\text{s}$. Additionally, for some of the conditions, images were taken with a Phantom CMOS camera model version 5.1, manufactured by the Vision Research Co. The Phantom camera has the capability of producing 10-bit images at 93 kHz. However, in this study, and to increase the clarity of the features, the framing rate was set to 18 kHz at a resolution of 256×128 pixels. For this case, the images were backlit with a continuous light source, and were defined by the exposure time of the camera at $2 \mu\text{s}$ duration. Unfortunately, the Phantom camera was acquired for a short time during the latter part of the project and was not used for all the conditions presented here.

The operation of a typical test consisted of a cool-down process for a certain period, allowing establishment of a steady-state condition for the entire facility including the plumbing system and the chamber. Once this condition was reached, radial traverses towards the coaxial jet centerline were made for temperature measurements, starting from a distance sufficiently far away from the jet to establish a background chamber temperature value. Measurements continued past the centerline until a large enough increase in temperature was observed, and sufficient data collected, to allow determination of a true jet centerline position. The TC traversing mechanism was then pulled entirely away from the jet area until it stopped near the wall of the inner chamber. With the TC clearing the path of the jet, images were taken while the acoustic driver was off, immediately followed by a set of images when the driver was operating, and tuned to the first and second resonance frequencies of the inner chamber. Only 30 images were recorded when the PixelFly camera was in use. In contrast, the Phantom camera collected a large set of images of up to 1000 for each condition.

III. Experimental Results and Discussion

The experimental matrix was organized to enable comparisons between results at different outer-to-inner-jet velocity ratios. Thermodynamic conditions of the jet at the exit of the injector, calculated from temperature measurements, are shown in Fig. 3. The number near each of the data points in Fig. 3 represents the case number in Table 1. Because of a large variation in density with small changes in temperature near the critical point (see Fig. 3), two nominal outer-jet temperatures [around 135–140 K (low) and around 185–200 K (high)] were selected, and then the jet's mass flow rates were varied to obtain a desired outer-to-inner-jet velocity ratio. References to these cases are made as "low" and "high" temperatures and should be clear in the context of the discussion.

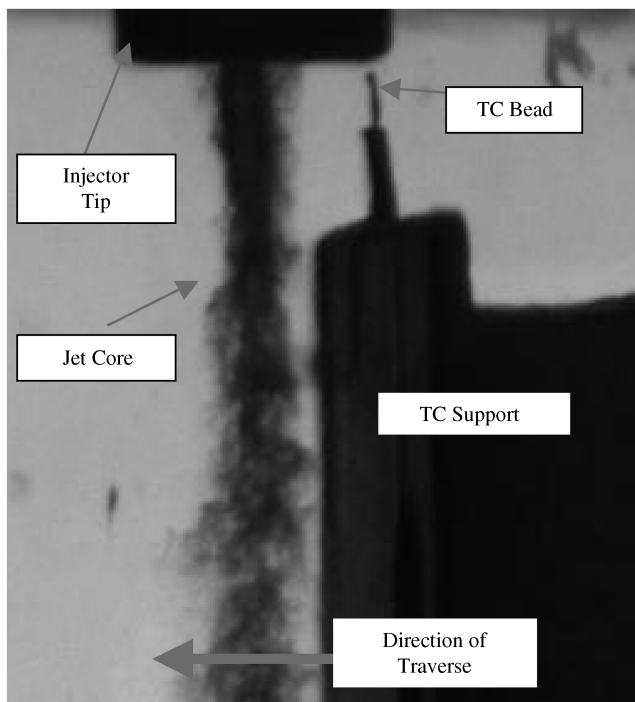


Fig. 2 Thermocouple and support mechanism used to perform radial temperature measurements in the coaxial jet.

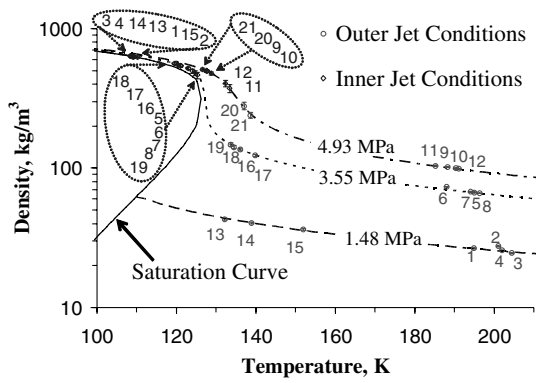


Fig. 3 Thermodynamic conditions of the data.

A. Temperature Measurements

Radial profiles of the coaxial jet averaged temperature were measured at a normalized axial location (x/D_1) of about 0.28 from the injector exit plane (i.e., the exit edge of the outer tube) using a Type-E thermocouple as described in the preceding section. Figure 4 shows the measured temperature and the associated density radial profiles computed using the NIST REFPROP [21] program accepting the radial temperature profile and chamber pressure as input data. The horizontal axis is radial distance measured from the jet centerline and is normalized by the inner tube inside radius (R_1). The vertical grid lines correspond to the four radii of the coaxial injector. The top, middle, and bottom rows in Fig. 4 are at the chamber pressures of 1.5 (subcritical), 3.5 (near-critical), and 4.9 (supercritical) MPa, respectively. Scales for temperature profiles are read from the left axis and those for densities from the right axis. The letters T or D in the inset of the figures refers to temperature or density, respectively, the next number indicates the particular case number for the data corresponding to the case listed in Table 1, and the number in parenthesis is the corresponding velocity ratio. The left and right columns in Fig. 4 are at the low (~ 135 – 140 K) and high (~ 185 – 200 K) outer-jet temperatures, respectively. (See Table 1 for exact values and conditions of cases.) The solid lines and symbols represent measured temperature profiles, and the dashed lines and hollow symbols show computed densities.

An attribute that the temperature profiles in Fig. 4 possess is that there are three distinct zones where the temperature gradient is fairly small: the core or region near the centerline of the jet, the region that defines the flow of the outer jet, and the far-field inner-chamber environment. The temperatures in these three regions were used to compute physical properties such as densities and viscosities, which in turn were used to compute quantities such as velocity, momentum, and their appropriate ratios.

At a given subcritical chamber pressure (i.e., 1.5 MPa, the top row in Fig. 4, i.e., Figs. 4a and 4b), both the temperature and density profiles representing the core region of the inner jet at the injector exit area are flat in shape, producing “top-hat” density profiles. The profiles then sharply change to quite different values, typical of a transition from a liquid to a gas phase, as expected. Note that for the low outer-jet temperature case, and at the measured axial location, this constant core temperature value penetrates well beyond the inner tube radius, up to about r/R_1 of 2.5, independent of the velocity ratios used. Under this condition, variations of the velocity ratio have no impact on the radial extent of the inner jet as defined by either the temperature or density profiles. Also, small variations in the outer-jet temperature have no effect on the calculated values for densities. However, at the higher outer-jet temperature in Fig. 4b, the radial extent or penetration of the inner jet is affected by the value of the outer-to-inner velocity ratio, primarily due to the increased heat transfer to the inner jet from the outer jet, both inside and immediately outside the injector. Note that the outer-jet temperature is controlled manually by changes in the LN2 flow rate to the secondary HX, and the manual nature of this control system accounts for the variations seen in the outer-jet temperatures. The variability of the inner-chamber temperature at the far field is related to changes in

Table 1 Data conditions for the various cases

Case	Chamber P MPa	Inner jet m mg/s	Chamber T K	Outer jet T K	Inner jet T K	Chamber ρ kg/m ³	Outer jet ρ kg/m ³	Inner jet ρ kg/m ³	Outer jet U m/s	Inner jet U m/s	Outer jet $Re \times 10^4$	Inner jet $Re \times 10^4$	VR o/i	M o/i	Acoustic freq. kHz	L/D_1
1	1.49	276	238	195	109	21.4	26.7	627.9	4.5	2.2	0.77	1.21	2.1	0.2	2.96	34.1
2	1.59	280	248	201	110	21.9	27.6	620.8	10.9	2.2	1.87	1.27	4.9	1.1	2.99	23.1
3	1.45	281	249	204	108	19.9	24.6	634.5	19.8	2.2	2.99	1.20	9.1	3.2	2.98	19.4
4	1.49	280	237	202	108	21.6	25.7	634.6	23.9	2.2	3.81	1.19	11.0	4.9	2.98	15.9
5	3.56	287	238	195	121	51.9	66.9	541.1	4.6	2.6	1.86	1.76	1.8	0.4	2.99	19.0
6	3.70	287	233	188	123	55.4	73.4	520.0	10.4	2.7	4.73	1.90	3.8	2.1	2.99	10.7
7	3.57	288	235	194	124	53.1	67.5	495.9	17.8	2.9	7.28	2.08	6.2	5.2	2.95	5.8
8	3.55	290	235	196	125	52.6	66.0	481.1	22.6	3.0	9.00	2.20	7.6	8.0	2.96	4.7
9	4.97	294	240	188	128	72.6	101.8	495.9	4.4	2.9	2.61	2.11	1.5	0.5	3.06	15.6
10	4.95	293	237	199	129	73.4	99.5	478.3	10.9	3.0	6.34	2.24	3.6	2.7	2.99	7.7
11	4.94	296	228	185	133	77.1	103.8	372.5	16.8	3.9	10.39	3.20	4.3	5.1	2.98	4.0
12	4.94	295	233	191	132	75.0	98.8	404.0	22.5	3.6	13.05	2.88	6.3	9.6	2.95	3.1
13	1.45	280	231	132	109	21.5	42.9	630.8	10.3	2.2	3.82	1.21	4.7	1.5	2.94	25.7
14	1.47	281	224	139	109	22.6	40.4	630.0	17.6	2.2	5.90	1.22	8.0	4.1	2.94	18.4
15	1.50	280	219	152	109	23.6	36.4	627.9	24.5	2.2	6.90	1.23	11.1	7.2	2.91	18.4
16	3.54	291	228	136	121	54.6	135.8	542.4	4.1	2.6	3.84	1.78	1.5	0.6	3.06	8.0
17	3.53	291	202	140	120	63.2	123.1	549.9	11.0	2.6	9.49	1.73	4.2	3.9	3.05	3.2
18	3.52	289	197	135	119	65.2	141.0	560.4	18.5	2.5	15.26	1.65	6.1	9.4	3.06	2.9
19	3.54	293	197	134	125	65.7	146.8	464.5	18.5	3.1	18.66	2.35	5.9	11.2	3.01	2.9
20	4.97	293	218	137	128	82.2	278.1	497.7	3.6	2.9	4.75	2.09	1.2	0.8	2.95	9.8
21	4.88	296	203	139	127	88.8	238.4	508.8	10.5	2.9	13.31	2.03	3.7	6.3	2.99	—

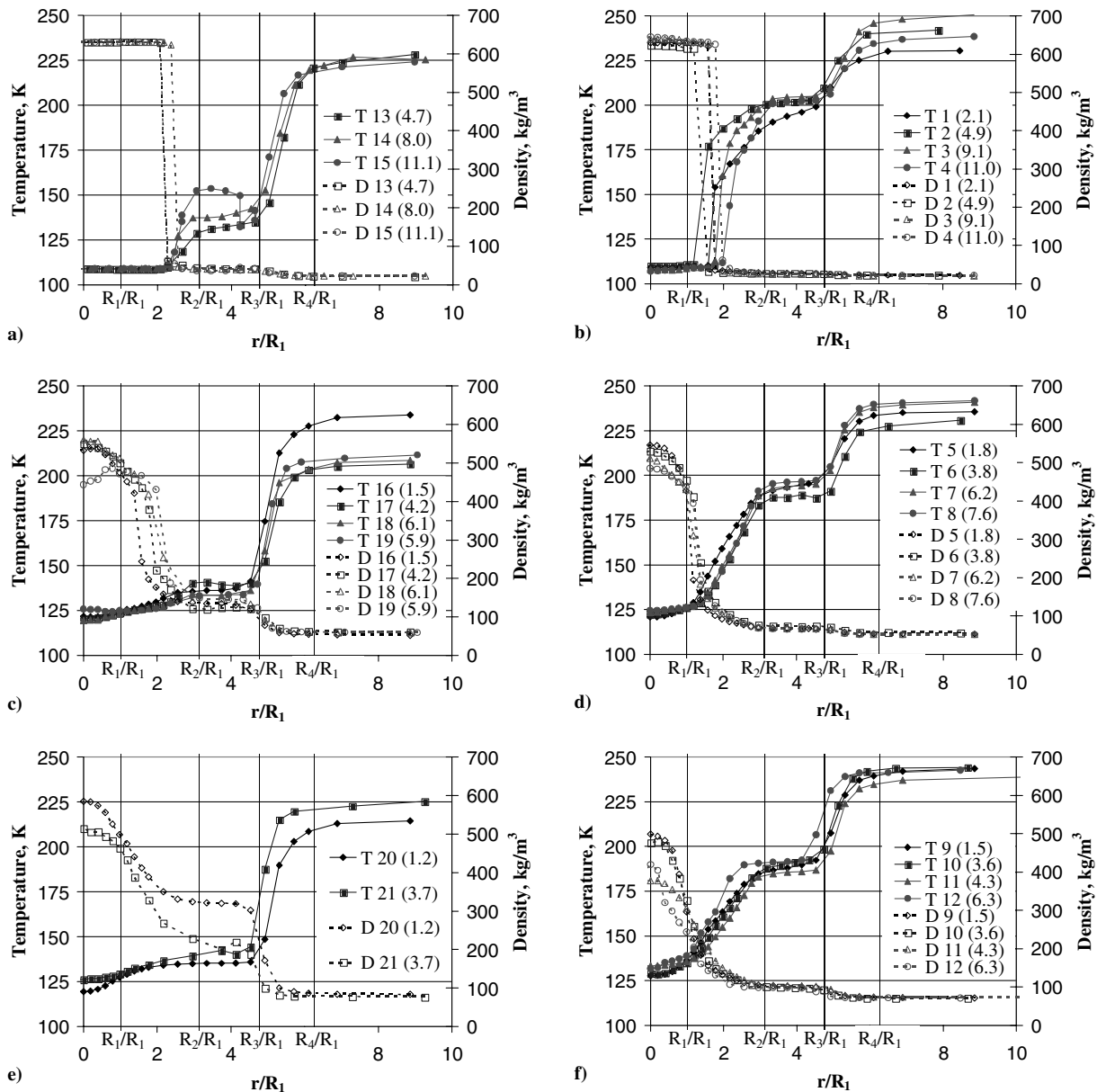


Fig. 4 Radial profiles normalized by the inner-radius of the inner tube.

several factors, including mass flow rates of all nitrogen streams into the inner-chamber, their respective temperatures, and the length of time spent running the experiment (see Fig. 4b). Under the higher outer-jet temperature shown in Fig. 4b, the HX control system was able to maintain this temperature at a reasonably constant value and, again, small changes in temperature has no impact on the calculated densities.

As the chamber pressure is elevated to a near-critical value (i.e., 3.5 MPa, the middle row of Fig. 4, i.e., Figs. 4c and 4d), the top-hat nature of the radial profiles is lost and more rounded shapes are observed, perhaps due to drastic changes of the heat transfer characteristics inside the tube under elevated, especially near-critical, conditions. Additionally, the temperature of the core (of the jet) at the centerline is greater than the corresponding temperatures at the subcritical pressure discussed in the previous paragraph. The density increase within the outer-jet zone from that of the far-field chamber value, especially at lower outer-jet temperature, is quite large and more noticeable than that observed under subcritical pressures (see Figs. 4a and 4b). It is also noted that for the case 19 plot (Fig. 4c), the temperature at the centerline is slightly higher (by approximately 5 K) than all other cases, causing the density profile to exhibit its maximum value at a slightly off-axis radial location. It is believed that the thermocouple may have moved off the plane defining a A-355

diameter to a plane defining a chord of the circular cross section of the jet as the centerline was approached during a traverse operation. However, this remains to be verified in the future.

Further increase in chamber pressure to a supercritical condition (i.e., 4.9 MPa, the bottom row of Figs. 4e and 4f) leads to an insignificant change in the qualitative behavior of the profiles as compared with the 3.5 MPa case. Again, a strong contrast is seen between the far-field chamber and outer-jet densities, indicating sensitivity of the density to small changes in temperature under this condition. It is also noticed that at all velocity ratios, the value of the centerline temperature at the higher outer-jet temperature (Fig. 4f) is supercritical (i.e., >126.2 K), whereas it is subcritical for all other cases in Fig. 4. For the lower outer-jet temperature cases, the difference in density between the outer-jet region and the far-field value is in excess of 200 kg/m^3 , which makes this feature easily observable in images of the jet, but does not permit easy and clear distinction of the inner-jet dark-core areas.

B. Flow Visualization

Flow visualization of the jet with backlit photography provides many details about the flow structure and was used here to catalog the coaxial jet behavior and its responses to the acoustic field. Figures 5–8 are sample images of the coaxial jet under different conditions

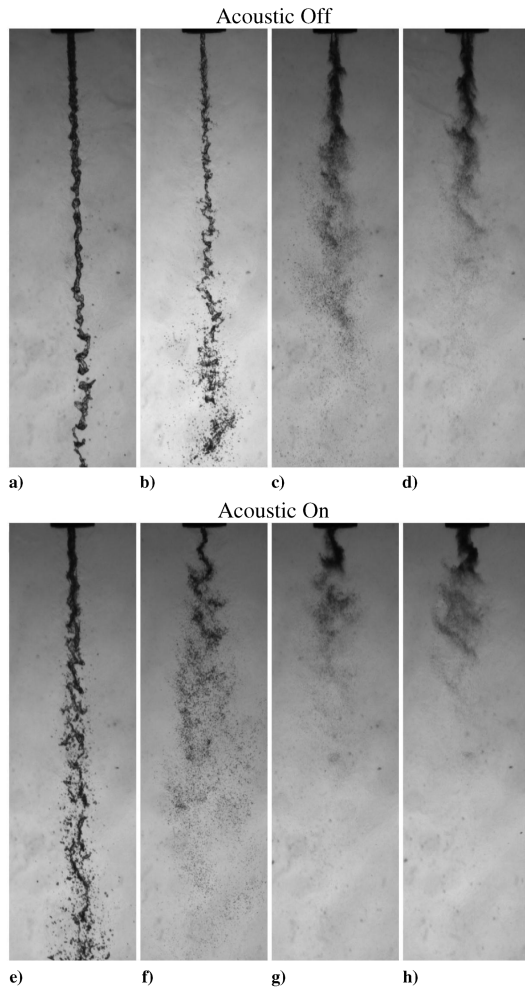


Fig. 5 Backlit images of coaxial jet at subcritical chamber pressure and higher outer-jet temperature.

discussed in the ensuing paragraphs. The scale presented in Figure 6 is the same for Figs. 5 and 7. One prominent feature of these images is the so-called dark core, which represents the high-density region of the inner jet. In these images, the inner jet has a much higher density than anywhere else in the field, and consequently a higher density gradient between the core and the surrounding fluid, thus minimizing the light passing through the core that reaches the camera causing it to appear dark and black. In many of the conditions, identification of the outer jet is made difficult because of the low density and low density gradient between the outer jet and the inner-chamber environment. However, under some conditions (see Fig. 4 at the low temperature for near- and supercritical conditions), the density and the density gradient are large enough to easily distinguish the periphery of the outer jet.

Figure 5 shows realizations of the coaxial jet under a subcritical chamber pressure (~ 1.5 MPa) and high outer-jet temperature (~ 190 K) corresponding to cases 1–4 from left to right. For the top row, Figs. 5a–5d, the acoustic driver is off and the bottom row, Figs. 5e–5h, shows the corresponding images when the acoustic driver is turned on (~ 3 KHz). Images in the same column correspond to the same operating conditions and were taken at the same test run. The velocity ratio increases from left to right in Fig. 5, whereas the inner-jet velocity is approximately constant. At the lowest velocity ratio (Fig. 5a), the breakup of the jets appears to fall into the nonaxisymmetric Rayleigh category, and the next higher velocity ratio (Fig. 5b) is of the membrane-breakup type, even though the aerodynamic Weber number is much greater than what was observed for water-into-air injection by Faragó and Chigier [22]. At the next two higher velocity ratios (Figs. 5c and 5d) a fiber-type breakup is observed with a pulsating mode. The exit width of the dark core is noticeably thinner for the case 2 (Fig. 5b). If one compares the

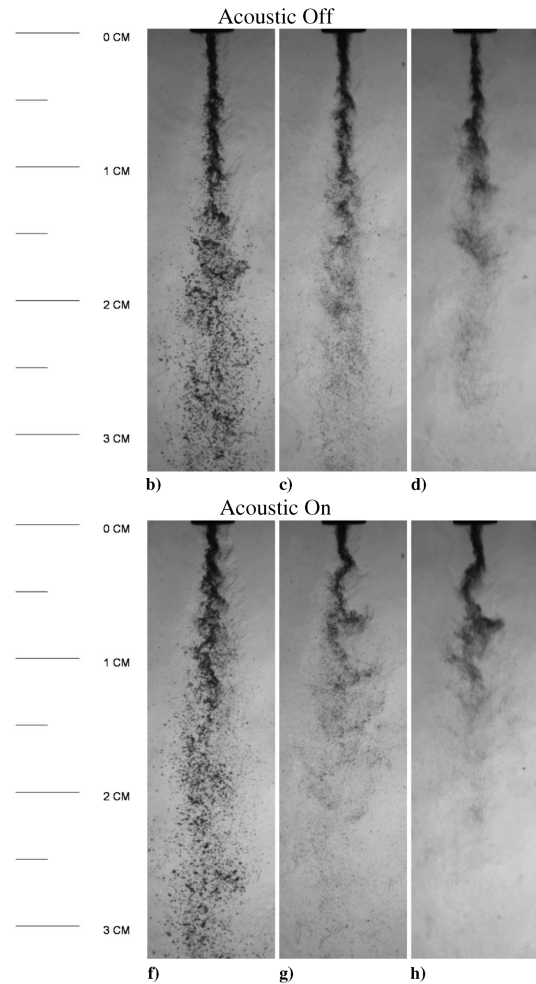


Fig. 6 Backlit images of coaxial jet at subcritical chamber pressure and lower outer-jet temperature.

width of the high-density region defined in Fig. 4b with those of the dark core at the exit plane of the injector, the same trend will be observed. Upon an increase in velocity ratio, the atomization process is enhanced, which is qualitatively visible from the decrease in droplet sizes, particularly in high magnification images.

Comparing the top and bottom row images, a clear effect of the acoustic field is noticed for all four conditions in Fig. 5. The breakup of the dark core of the inner jet is accelerated and large-amplitude wave structures are formed. From these visualizations and the limited high-speed movies, it appears that, near to the injector exit area, the dark core of the inner jet is pushed out into the path of the outer-jet flow and is then convected downstream away from the injector. The dark core develops a cusplike structure at a distance from the injector which subsequently separates from the attached region of the jet and ultimately disappears, becoming fully mixed with the outer-jet fluid.

Figure 6 shows the impact of the velocity ratio and acoustic field on the coaxial jet under the low outer-jet temperature (~ 140 K) condition. The velocity ratio increases from left to right, and in both rows, they correspond to cases 13–15 in Table 1. The acoustic driver is off for images in the top row and on for the bottom row at ~ 3 KHz. As seen in the temperature measurements, the core jet also appears thicker here and the breakup seems to be of the fiber-type. The jet responds to the acoustic field at all conditions with increasingly dramatic effects at higher velocity ratios. The lowest flow rate condition was unattainable experimentally. The length of the dark-core region (with the acoustic driver on) appears to be considerably larger than those seen in Fig. 5.

Images from a near-critical chamber pressure (~ 3.5 MPa) and a high outer-jet temperature (~ 190 K) corresponding to cases 5–8 from left to right are shown in Fig. 7, and are arranged in the same fashion as those in Figs. 5 and 6. The droplets which were clearly

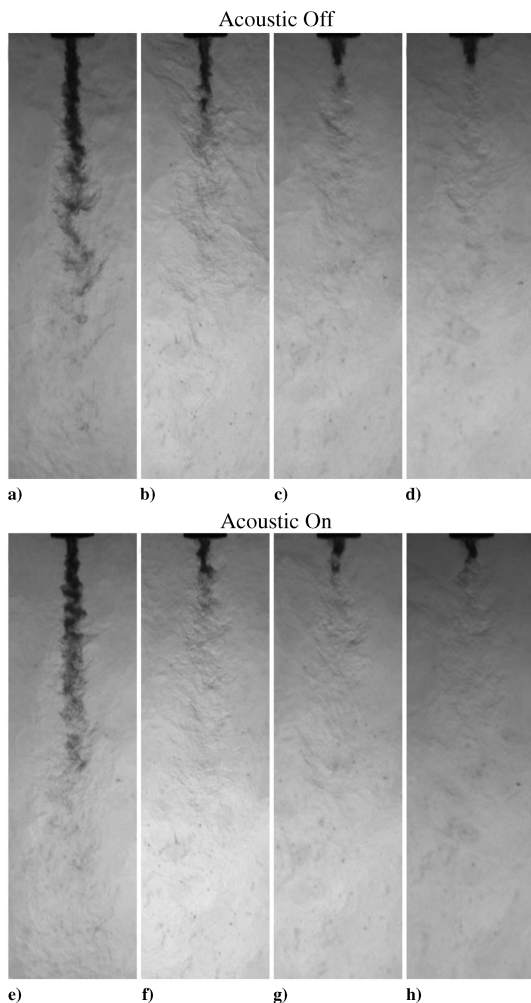


Fig. 7 Backlit images of a coaxial jet at near-critical chamber pressure.

present under the subcritical chamber pressure disappear as expected (see Chehroudi et al. [17]). Judging purely from the dark region of the jet, the effect of the acoustic field is less pronounced. However, from the high-speed movies taken with the Phantom camera and shown in the fourth row from the top of Fig. 8, the oscillation of the jet is quite visible due to the increased framing rate and the illumination arrangement, which allowed the outer-jet boundaries to be visualized. Figure 8 is composed of ten consecutive frames taken from an acquired high-speed movie of the jet. The first and second, the third and fourth, and the fifth and sixth pair of rows are at sub-, near-, and supercritical chamber pressures, respectively. In the first, third, and fifth rows the acoustic driver is off, and in the second, fourth, and sixth rows it is on at 3 kHz. The framing rate was 18 kHz, with time increasing from left to right, producing a time interval of $55.6 \mu\text{s}$ between frames. Previously reported [14] observations that the effect of the acoustic field was lesser under near- and supercritical pressures are still valid. However, the oscillations of the jet in the acoustic field under near- and supercritical conditions seen here were not previously detected because of the low framing rate available. The dark core (i.e., regions of high density) is the most visible structure, and as the density field becomes more uniform the discrimination of this effect diminishes.

Not immediately obvious in Fig. 8, but seen when played as a movie, the structures in the far-field background of the frame begin to oscillate laterally at the same frequency of the acoustic driver. One can measure the magnitude of these velocity fluctuations from the movies. Assuming that the acoustic wave in the chamber is a plane wave, the estimated pressure fluctuations from these measurements agreed with previously measured pressure fluctuations. The velocity of the annular gas from the injector can also be estimated from these images. If one draws a line connecting the same structure seen in

adjacent frames, the slope of this line is related to the axial convection velocity of these structures (see Fig. 8). Similarly, if each of the individual images are rotated by 90 deg, one can measure the radial velocity using the same method. Although further analysis is required, initial crude estimates are consistent with the computed values based on mass flow rate measurements.

By tracking the structures shown in Fig. 8 for the cases when the acoustic field is on, a possible explanation for the behavior of the jet is proposed. Once the dark high-density core of the inner jet leaves the injector, it experiences a force in the direction of the local acoustic field velocity at that moment, directing the fluid elements into the high-velocity of the outer-jet areas. Although these elements are accelerated in the axial direction to speeds close to the outer-jet values, they nearly maintain the component of velocity in the wave propagation direction. However, once the dense region of these fluid elements (i.e., dark core) approaches the shear layer between the outer jet and chamber fluid, it experiences further mixing and heat transfer until it is no longer discernible. A fraction of these fluid elements from the dark core is convected downstream with the outer jet and experiences heat up and mixing until the elements eventually disappear into the rest of the background.

C. Dark Core Measurements

When a region of an image is referred to as a dark-core, we simply are referring to an intact area of the jet, always defined by the inner jet, which clearly stands out in darkness level with respect to the remaining areas. This will be explained further in a quantitative term in this section. Some work that is relevant to the present study was performed by Glogowski et al. [23], in which a shear-coaxial injector was used with a design derived from a prototype SSME fuel preburner element using liquid nitrogen (LN2) and gaseous nitrogen (GN2). They stated that the length of the dark core in the acquired images increased significantly upon elevation of the chamber pressure from sub- to supercritical, at constant mass flow rates. They attributed this to the drop in the relative velocity between the inner and outer (annular) streams. Although temperature measurements were made somewhere downstream of the critical flow venturi location in the feed system, it was not clear how far upstream of the injector exit area this occurred. It is known that small changes in temperature in this thermodynamic region can bring about large changes in density, affecting the parameters, especially outer-to-inner velocity ratio, used to characterize the injector exit conditions. Close examination of the figures presented by Glogowski et al. [23] suggests that the dark core (that is, the flow issuing from the inner tube) of the jet actually appears to contract in length, while the visual impression of the outer annular flow is that it grows in length.

Measurements of both the liquid-core and dark-core lengths of a variety of different jets from photographs have been performed by others and reported in the past (see Eroglu et al. [7]). However, the measurement methods are often not discussed in sufficient detail. There are many difficulties in performing quantitative measurements from this quantity of images of a jet. For example, if using a strobe light for illumination purposes, the intensity of the background will most likely vary from shot to shot. Another difficulty is the selection of a criterion to assess the location where the core is broken up into separated pieces. It is then possible for two people to make different measurement judgments. Also, with the use of digital cameras capable of collecting thousands of images, a manual measurement becomes an extremely tedious and time consuming task. Therefore, to produce repeatable measurements, to account for the variability in the light source intensity, and to be able to process thousands of images, an algorithm is necessary for automated computer processing.

A judicious choice of a threshold level on the brightness scale of an image is necessary, and a single fixed value is not sufficient for all images to consistently determine the end or the break points of the dark core. Figure 9 is a sample image illustrating an automated thresholding procedure for determination of the length of the dark core. Figures 9a–9d are, respectively, the untouched original photograph, the image threshold applied between 0–128 to indicate

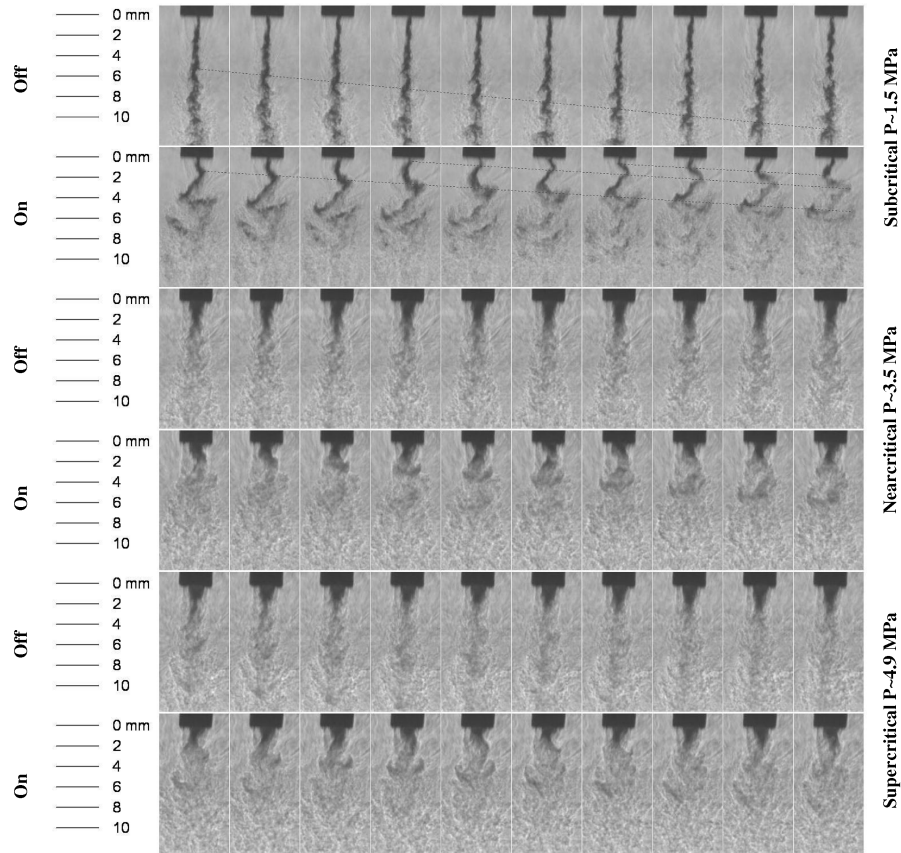


Fig. 8 Consecutive frames from high-speed shadowgraph images of cases 3, 7, and 11 (from Table 1).

the injector, the image threshold applied between 128–929 to represent the dark core, and the image threshold applied between 929–4095 to depict the background. Figure 10 is the image histogram corresponding to Fig. 9 indicating the number of pixels vs a 12-bit gray scale level. The ability of an algorithm to successfully predict the proper threshold level is based on the physical implications of different gray level zones in an image as shown in Fig. 10. The peak to the left of the dashed line in this figure (between 0–128) indicates the injector metal surface areas. With the object (i.e., injector) being backlit and the injector being absolutely opaque, one would expect that the zero level intensity should all represent the injector itself. However, the slight shift of the peak to a higher value is due to stray light being reflected by the chamber windows and other surfaces towards the injector which is then reflected back into the camera. The low number of pixels at gray level values between the dashed and dotted lines (128–929) in Fig. 10 physically represents the dark core of interest, and the broad noisy peak at gray levels to the right of the dotted line (greater than 929) in this figure defines the background.

As mentioned earlier in this paper, variations of the light intensity from shot to shot are usually significant and a matter of concern. For

example, in the case of Fig. 10, the threshold level distinguishing the end of the dark core and the beginning of the background is at a gray level of about 929. However, this value varies from shot to shot in a sequence of images taken at the same operating conditions. Also, it varies more widely when the chamber conditions are changed due to differences in the refractive index field. Therefore, it is necessary to devise a methodology for an accurate and repeatable determination of the rise of the portion of the curve representing the contribution of the background in these images. More important, the outcome should conform to what human eyes determine to be the end of the dark core. To select the threshold level identifying the rise of the background, data from the histogram in this region was curve-fitted, using a nonlinear Levenberg–Marquardt least squares algorithm, to a piece of a Gaussian function. This function is then differentiated and the point where the derivative of this curve is equal to e^{-1} was determined to be the threshold level corresponding to the dotted line shown in Fig. 10. Evidence to support the soundness and consistency of this algorithm is shown in detail by Davis et al. [13] and is visually shown in Fig. 9. For each condition, an averaged dark-core length was calculated based on analysis of each individual image within a

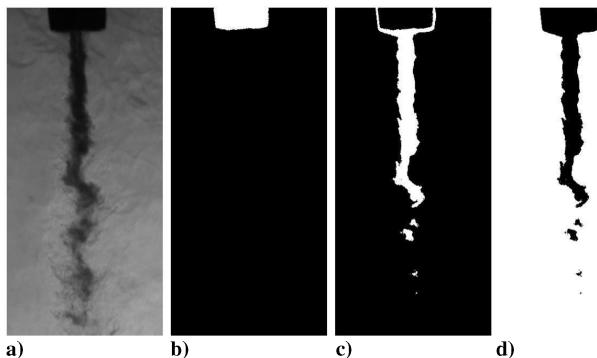


Fig. 9 Sample images indicating the effect of threshold levels.

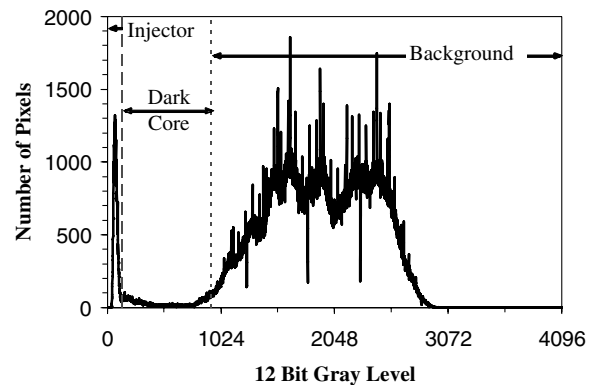


Fig. 10 Histogram for the image in Fig. 9.

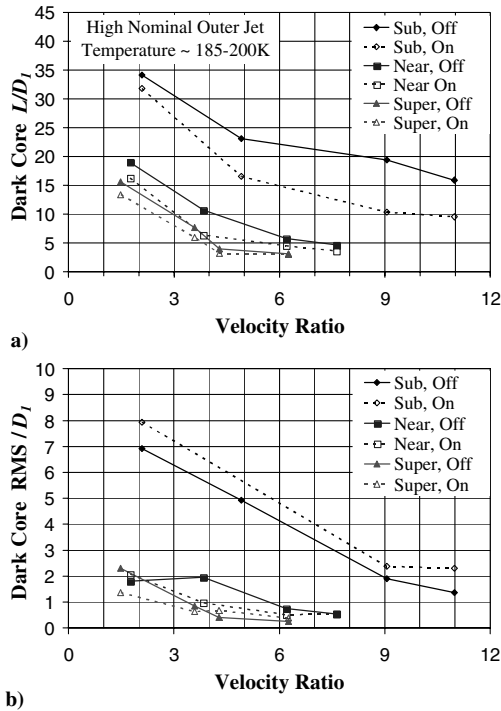


Fig. 11 Plot a) dark-core length, and b) rms of variations, normalized by the inner diameter (cases 1–12).

set of 30 images and then averaging the results. The dark-core lengths are shown in Figs. 11a and 12a as a function of velocity ratio. The rms of the variations of this quantity is also shown in Figs. 11b and 12b. Figures 11 and 12 present results for both higher and lower outer-jet temperatures of ~ 190 K and ~ 140 K, respectively. The diamond, square, and up-triangle symbols in Fig. 11 are for cases 1–4, 5–8, and 9–12, respectively. The diamond and square symbols in Fig. 12 are for cases 13–15 and 16–19, respectively. Data for each of the cases are listed in Table 1. The words “sub,” “near,” and “super” in the inset refer to subcritical, near-critical, and supercritical chamber pressure, respectively. According to Eroglu et al. [7], the average of the length measured from individual images of a set can be regarded as the time average. It should be noted that, for each operating condition in this work, length measurements were also made from an averaged image of a set. In general, the length measured from the averaged image is slightly shorter than the average of the individual dark-core values calculated in a given set.

Evident in Figs. 11a and 12a is the fact that the length of the dark core decreases as the chamber pressure is increased. The dark core provides an indication of high-pressure regions of the flow. A possible explanation of this effect is that, as the chamber pressure increases in the present system, the temperature of the inner jet also increases, causing the density of the inner jet to decrease and leading to a shortened length of the dark core, as seen in Fig. 4. Because the jet begins with a lowered density, less time is then required to fully mix the dark inner jet with the background. At a constant chamber pressure, as VR is increased, the length of the dark core decreases and approaches a plateau region. In a mean sense, when the dark core feels the imposed external acoustic field (operating at ~ 3 kHz), the length of the core is shorter than or equal to the length when the acoustic driver is turned off. Under the near- and supercritical chamber pressures, as the VR parameter increases, the difference between the lengths of the dark core, measured with and without the acoustic field, diminishes. The rms values of the dark-core length fluctuations, shown in Figs. 11b and 12b, exhibit somewhat similar trends to those seen with their mean values. It is known that for a liquid-fueled rocket, atomization and breakup processes, interactions between the propellant jets, droplet formation, and vaporization are all affected by the pressure and, particularly, velocity fluctuations. Also, for any chemically reacting system, the rate at which energy is released is sensitive to the rate of change of A-359

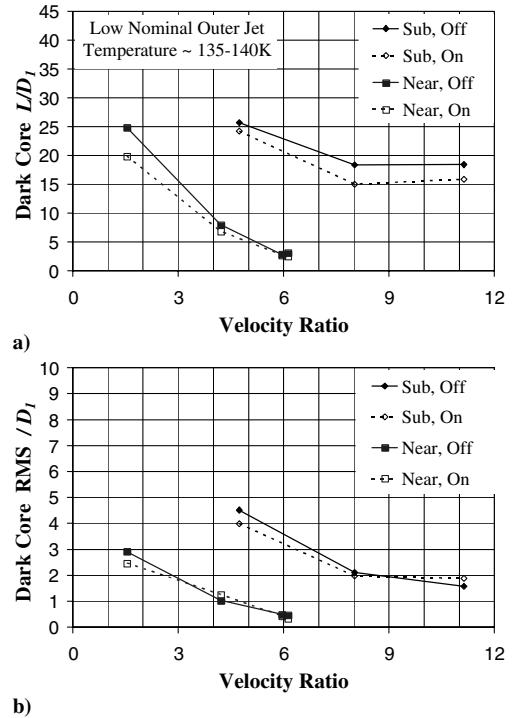


Fig. 12 Plot a) dark-core length, and b) rms of variations, normalized by the inner diameter (cases 13–19).

temperature, density, pressure, and, of course, mixture ratio. It is then quite intuitive to relate, in some form, the rms values of the dark-core length fluctuations to mixture ratio variations. On the other hand, a low rms value can be interpreted as the jet's inherent steadiness and vice versa. Examination of Figs. 11b and 12b clearly shows that this property is drastically reduced as the velocity ratio is increased. Although these results are for a single injector, it is then quite possible that the observed improvement in combustion stability at higher values of velocity ratio is a result of the jet's inability to generate large mass flow rate fluctuations under these conditions, weakening a key feedback line for the self-excitation process. In temperature-ramping exercises for stability rating of LOX/ H_2 engines, the mass flow rate is usually maintained at a constant value [4]. Therefore, as the temperature of the H_2 is decreased during a ramping episode, the H_2 becomes more dense, which decreases the injector velocity ratio. The rms plots shown here suggest that such a decline in this ratio amplifies the jet's inherent unsteadiness, providing a possible explanation for the engine's eventual arrival into an unstable zone as a temperature-ramping test proceeds. Also, the observation reported by Wanhainen et al. [11], who found that a decline in LOX density was destabilizing, can be explained in a similar manner. Unfortunately, due to small sample sizes, a distinct impact of the acoustic field on the rms fluctuations is not evident in some cases. A sufficiently large sample size can be acquired through applications of high-resolution and high-speed cameras, such as the one acquired towards the latter part of this project.

Figure 13 shows a plot of L/D_1 vs M , with the diamond, circle, and up-triangle symbols representing sub-, near-, and supercritical pressures, respectively. The hollow and solid symbols represent the higher and lower outer-jet temperatures, respectively. The dashed and dotted curves in Fig. 13 represent the least squares fits following a functional form of $L/D_1 = C/M^n$, where C and n constant pair are 25 and 0.2 for subcritical pressures (dashed line) and 12 and 0.5 for near- and supercritical pressures (dotted line). The error bars on the data points in Fig. 13 for the dark-core length represent on standard deviation from the mean, and the error bars for the momentum flux ratio represent the combined uncertainty from all the measurements used to compute the quantity. From Fig. 13, there is an apparent difference in the exponent of M between the subcritical and supercritical pressure data. Other researchers [24–29] observed a dependence of core length on M ranging from $M^{-0.5}$ to $M^{-0.13}$. For a

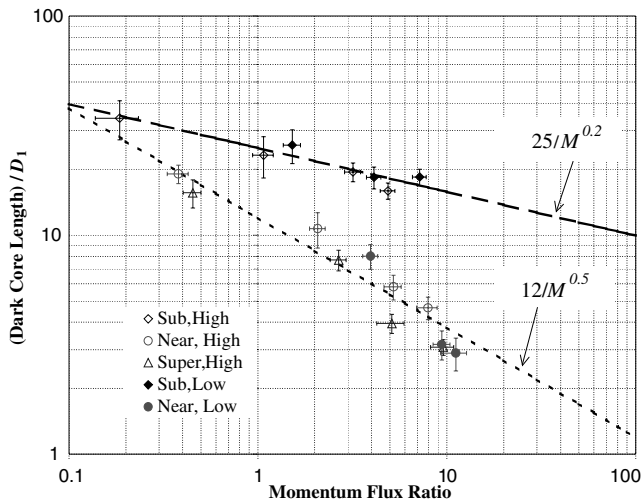


Fig. 13 Dark-core length versus momentum flux ratio.

coaxial jet where there is a single phase and therefore no surface tension, such as the water–water experiments of Rehab et al. [25] and the gas–gas experiments of Favre-Marinet and Camano Schettini [27], the dependence of the core length was $M^{-0.5}$, which is consistent with the present near-critical and supercritical results. Chehroudi et al. [17] noted a difference in behavior of subcritical and supercritical jets. They showed that the initial growth rate of a supercritical single round jet behaved like a variable-density gas jet. Figure 13 gives evidence to the fact that supercritical single-component coaxial jets behave like their subcritical single-phase counterparts. Caution should be exercised when extrapolating these results to systems containing multiple chemical species. A system which contains a mixture of chemical species, at a pressure greater than the critical pressure of any of the individual components, may in fact still be below the critical pressure of the mixture. For example, the critical pressures of carbon dioxide (CO_2), toluene, and H_2 are 7.49, 4.1, and 1.3 MPa, respectively. A mixture of approximately 95% by mole of CO_2 and 5% toluene has a critical pressure of 10.5 MPa, and a 90.75, 1.55, 7.70% mixture of CO_2 , toluene, and H_2 , respectively, has a critical pressure of 11.4 MPa [30].

IV. Summary and Conclusions

Radial mean temperature measurements were made from a coaxial jet under sub-, near-, and supercritical pressures at a fixed axial location very near the injector exit plane at a variety of outer-to-inner-jet velocity ratios. Two nominal temperature levels [low (~ 135 – 140 K) and high (~ 185 – 200 K)] were selected for the outer jet to investigate the impact of the velocity ratios and acoustic field on the coaxial jet considering a nominal cryogenic temperature for the inner jet. To the best of the authors' knowledge, measurements at this level of detail have not been previously performed. True exit velocity ratios, as opposed to ratios based on upstream values, can now be calculated with sufficient accuracy, especially under near- and supercritical conditions, to aid in interpretation of the results. Under subcritical pressures, temperature profiles exhibit a top-hat behavior at two distinct levels with an abrupt transition from a high (liquidlike for the inner jet) to a low value representative of compressed gases. The transition point is somewhere in the region between the outer and the inner jet flows. Large changes in velocity ratio had no impact on these profiles at the low outer-jet temperature, whereas the location of the transition point was affected under the higher outer-jet temperature. At near- and supercritical chamber pressures, the inner jet loses its top-hat shape and the temperature profiles exhibit a more gradual transition from the inner to outer jet.

Backlit images were taken at both low (10 Hz) and high speeds (18 kHz) with and without the acoustic driver turned on at 3 kHz. Using images taken at high framing rates, velocity fluctuations in the chamber background fluid and within the jets were observed when the acoustic driver was on. Velocities can be measured by tracking

isolated structures in these images. Initial crude measurements of the velocities agreed with the predicted values based on mass flow rate measurements.

A prominent feature seen in most of the images in the study is the existence of a high-density region, referred to as the dark core, which is defined by the fluids in the inner jet. An automated method for measurement of the dark core was produced to enable rapid analysis of a large number of images in a repeatable and consistent manner. It is seen that the dark-core length decreases at higher chamber pressures, due to the combined effects of inner tube heat transfer and better interjet mixing. As the velocity ratio increases at a constant chamber pressure, the length of the dark core shortens and asymptotically approaches a constant value. This constant value appears to be different for subcritical pressures. Results show the dependence of the outer-to-inner-jet momentum ratio to an exponent, with the exponent having a different value for subcritical pressures as opposed to near- and supercritical pressures. The exponent for near- and supercritical pressures is consistent with previous measurements of the potential core for single-phase systems.

It is hypothesized that a connection to combustion instability can be obtained from the data analyzed thus far by way of the magnitude of the rms values of the dark-core length fluctuations. It is possible that decreases in the fluctuation levels, which were shown here to occur at higher velocity ratios, could weaken a key feedback mechanism for the self-excitation process that is believed to drive the combustion instability in rocket engines. This offers a possible means for improvements in our understanding of combustion instability experienced in engines under higher outer-to-inner-jet velocity ratios. Additional analysis and data acquisition are planned to further investigate this initial finding.

Acknowledgments

The authors would like to acknowledge Douglas Talley for his support of this ongoing project. Also, the authors would like to recognize Mike Griggs for his valuable contributions in the improvements to the experimental facility. The first author would like to thank his thesis advisor, R. J. Santoro, for permitting his thesis work to be performed off-campus at U.S. Air Force Research Laboratory. This work is sponsored by the U.S. Air Force Office of Scientific Research under Mitat Birkan, program manager.

References

- [1] Culick, F. E., and Yang, V., "Overview of Combustion Instabilities in Liquid-Propellant Rocket Engines," *Liquid Rocket Engine Combustion Instability*, edited by V. Yang, and W. Anderson, Progress in Astronautics and Aeronautics, AIAA, Washington, DC, 1995, pp. 3–38.
- [2] "Liquid Propellant Rocket Combustion Instability," edited by D. T. Harje, and F. H. Reardon, NASA SP-194, 1972, pp. 17–19.
- [3] Vingert, L., Gicquel, P., Lourme, D., and Ménéret, L., "Coaxial Injector Atomization," *Liquid Rocket Engine Combustion Instability*, edited by V. Yang and W. Anderson, Progress in Astronautics and Aeronautics, AIAA, Washington, DC, 1995, pp. 145–190.
- [4] Hulka, J., and Hutt, J., "Liquid Oxygen/Hydrogen Instability Phenomena," *Liquid Rocket Engine Combustion Instability*, edited by V. Yang and W. Anderson, Progress in Astronautics and Aeronautics, AIAA, Washington, DC, 1995, pp. 39–72.
- [5] Rayleigh, J. S. W., "On the Instability of Jets," *Proceedings of London Mathematical Society*, Vol. 10, 1878, pp. 4–13.
- [6] Lefebvre, A. H., *Atomization and Sprays*, Hemisphere, New York, 1989.
- [7] Eroglu, H., Chigier, N., and Farago, Z., "Coaxial Atomizer Intact Lengths," *Physics of Fluids A*, Vol. 3, No. 2, Jan. 1991, pp. 303–308.
- [8] Lasheras, J. C., and Hopfinger, E. J., "Liquid Jet Instability and Atomization in a Coaxial Gas Stream," *Annual Review of Fluid Mechanics*, Vol. 32, 2000, pp. 275–308.
- [9] Miesse, C. C., "The Effect of Ambient Pressure Oscillations on the Disintegration and Dispersion of a Liquid Jet," *Jet Propulsion*, Vol. 25, Oct. 1955, pp. 525–530, 534.
- [10] Buffum, F. G., and Williams, F. A., "Response of Turbulent Jets to Transverse Acoustic Fields," *Proceedings of the 1967 Heat Transfer and Fluid Mechanics Institute*, edited by P. A. Libby, D. B. Olfe, and C. W. Van Atta, Stanford Univ. Press, Palo Alto, CA, 1967, pp. 247–276.

- [11] Wanhainen, J. P., Feiler, C. E., and Morgan, C. J., "Effect of Chamber Pressure, Flow per Element, and Contraction Ratio on Acoustic-Mode Instability in Hydrogen-Oxygen Rockets," NASA TN D-4733, Aug. 1968.
- [12] Heidmann, M. F., "Oxygen-Jet Behavior During Combustion Instability in a Two-Dimensional Combustor," NASA TN D-2725, March 1965.
- [13] Davis, D. W., Chehroudi, B., and Sorensen, I., "Measurements in an Acoustically Driven Coaxial Jet Under Supercritical Condition," *43rd AIAA Aerospace Sciences Meeting & Exhibit*, AIAA, Washington, DC, 2004.
- [14] Davis, D. W., and Chehroudi, B., "The Effects of Pressure and Acoustic Field on a Cryogenic Coaxial Jet," *42nd AIAA Aerospace Sciences Meeting & Exhibit*, AIAA, Washington, DC, 2004.
- [15] Chehroudi, B., Davis, D. W., and Talley, D. G., "Initial Results from a Cryogenic Coaxial Injector in an Acoustic Field," *41st AIAA Aerospace Sciences Meeting & Exhibit*, AIAA, Washington, DC, 2003.
- [16] Chehroudi, B., Cohn, R., and Talley, D. G., "Cryogenic Shear Layers: Experiments and Initial Growth Rates of Round Cryogenic Jets at Subcritical and Supercritical Pressures," *International Journal of Heat and Fluid Flow*, Vol. 23, No. 5, 2002, pp. 554–563.
- [17] Chehroudi, B., Talley, D. G., and Coy, E. B., "Visual Characteristics and Initial Growth Rates of Round Cryogenic Jets at Subcritical and Supercritical Pressures," *Physics of Fluids A*, Vol. 4, No. 2, Feb. 2002, pp. 850–861.
- [18] Chehroudi, B., Cohn, R., Talley, D. G., and Badakhsan, A., "Raman Scattering Measurements in the Initial Region of Sub- and Supercritical Jets," *36th AIAA/ASME/SAE/ASEE Joint Propulsion Conference and Exhibit*, AIAA, Washington, DC, 2000.
- [19] Chehroudi, B., Talley, D., and Coy, E. B., "Initial Growth Rate and Visual Characteristics of a Round Jet into a Sub- to Supercritical Environment of Relevance to Rocket, Gas Turbine, and Diesel Engines," *37th AIAA Aerospace Science Meeting and Exhibit*, AIAA, Washington, DC, 1999.
- [20] Chehroudi, B., Talley, D. G., and Coy, E. B., "Fractal Geometry and Growth Rate Changes of Cryogenic Jets near the Critical Point," *35th AIAA/ASME/SAE/ASEE Joint Propulsion Conference and Exhibit*, AIAA, Washington, DC, 1999.
- [21] REFPROP, Reference Fluid Thermodynamic and Transport Properties, Software Package, Ver. 7.0, National Inst. of Standards and Technology, U.S. Dept. of Commerce, Gaithersburg, MD, 2002.
- [22] Faragó, Z., and Chigier, N., "Morphological Classification of Disintegration of Round Liquid Jets in a Coaxial Air Stream," *Atomization and Sprays*, Vol. 2, No. 2, 1992, pp. 137–153.
- [23] Glogowski, M., Bar-Gil, M., Puissant, C., Kaltz, T., Milicic, M., and Micci, M., "Shear Coaxial Injector Instability Mechanisms," *30th AIAA/ASME/SAE/ASEE Joint Propulsion Conference*, AIAA, Washington, DC, 1994.
- [24] Lasheras, J. C., Villermaux, E., and Hopfinger, E. J., "Breakup and Atomization of a Round Water Jet by a High Speed Annular Air Jet," *Journal of Fluid Mechanics*, Vol. 357, No. 1, 1998, pp. 351–379.
- [25] Rehab, H., Villermaux, E., Hopfinger, E. J., "Flow Regimes of Large Velocity Ratio Coaxial Jets," *Journal of Fluid Mechanics*, No. 1, 1997, pp. 357–381.
- [26] Raynal, L., *Instabilité et Entrainement à l'Interface d'une Couche de Mélange Liquid-Gaz*, Thèse Ph.D, Université Joseph Fourier, Grenoble, France, 1997.
- [27] Favre-Marinet, M., and Camano Schettini, E. B., "The Density Field of Coaxial Jets with Large Velocity Ratio and Large Density Differences," *International Journal of Heat and Mass Transfer*, Vol. 44, No. 10, 2001, pp. 1913–1924.
- [28] Englebert, C., Hardalupas, Y., and Whitlaw, J. H., "Breakup Phenomena in Coaxial Air-Blast Atomizers," *Proceedings of the Royal Society of London*, Vol. 451, No. 19411995, pp. 189–229.
- [29] Porcheron, E., Carreau, J. L., Prevost, L., LeVisage, D., and Roger, F., "Effect of Density on Coaxial Liquid Jet Atomization," *Atomization and Sprays*, Vol. 12, Nos. 1–3, 2002, pp. 209–227.
- [30] Zhang, H., Liu, Z., and Han, B., "Critical Points and Phase Behavior of Toluene-CO₂ and Toluene-H₂-CO₂ mixture in CO₂-Rich Region," *Journal of Supercritical Fluids*, Vol. 18, No. 3, 2000, pp. 185–192.

J. Oefelein
Associate Editor

Dark core analysis of coaxial injectors at sub-, near-, and supercritical conditions in a transverse acoustic field

Ivett A. Leyva[#], Bruce Chehroudi*, Douglas Talley[#]

[#] Air Force Research Laboratory/PRSA Edwards AFB, CA 93524

*ERC Inc., Edwards AFB, CA 93524

ABSTRACT

An experimental study on the effects of an externally-imposed transverse acoustic field in sub-, near-, and supercritical N₂ coaxial jets is presented. Such fields and their interaction with the jets (i.e., breakup, mixing, etc.) is believed to play a critical role during combustion instabilities in liquid rocket engines. The shear coaxial injector used here is similar to those used in cryogenic liquid rockets. By using N₂ as the working fluid, the chemistry effects on combustion instability are separated from the effects of a transverse acoustic field on coaxial jets. Furthermore, through this choice, ambiguities associated with composition dependence on mixtures critical properties are eliminated. The acoustic oscillations are generated by a piezo-siren and have a frequency of ~3kHz. The pressures in the chamber range from 215-716 psia to span sub-, near-, and supercritical conditions. The outer to inner jet velocity ratio varies from ~1.2 to 23 and the momentum flux ratio varies from ~0.2 to 23. These ratios are mainly varied by changing the temperature and flow rates of the outer jet. At least 2000 backlit images were taken at 41kHz for each run. The main metric investigated is the length of the dark, or inner jet, core length. Both the axial length of the jet and the total, or curved, length are studied. A functional relation of the form A/MR^n describes the behavior of the axial length with the exponent being 0.2 (A:20-25) for subcritical conditions and 0.5 (A:5-12) for near and supercritical conditions. These results agree with historical data. The standard deviation of the axial length, which due to the large number of data points is within 0.03% of the RMS of the jet lengths fluctuations, also decreases with velocity ratio, for sub-, near-, and supercritical conditions. For momentum flux ratios $\sim O(1)$ the axial and total length differences between acoustics off and on are bigger than the error bars. For $MR < \sim 1$ and $MR > \sim 5$, the differences fall within the error bars. This preliminary result could imply that the dark core is in fact shortened by acoustics for $MR \sim O(1)$.

NOMENCLATURE

A = constant
D = diameter with subscripts
H = gap between the injector exit plane and the thermocouple
HX = heat exchanger
L = axial dark core length
L_t = total or curved dark core length
MR = outer to inner jet momentum flux ratio
n = exponent for MR
R = radius with subscripts
T = temperature
VR = outer to inner jet velocity ratio

Subscripts

1, 2, 3, 4 = four diameters or radii of the coaxial injector from smallest to largest values
i = inner-jet
o = outer-jet
cr = critical point

INTRODUCTION

There are two main motivations for this study. On the one hand, in the pursuit of higher specific impulse, the designs of liquid rocket engines (LRE's) are driven to higher chamber pressures. As the pressure increases the propellants go from subcritical to supercritical conditions. The Space Shuttle Main Engine (SSME) and the Vulcan engine for the Ariane 5 launch vehicles are examples of LRE's designed to operate above the critical pressures of each propellant individually. Our interest then is to understand the effects of transitioning from subcritical to supercritical pressure on an injector's jet characteristics such as mixing, atomization and breakup. We choose to study a coaxial injector since this design has proven effective for LRE's. In a typical coaxial injector for an LOX/LH2 engine, the oxygen is injected at subcritical temperatures in the center jet while the hydrogen is injected at supercritical temperatures, after being used as a coolant for the engine nozzle, in the coaxial jet. A typical velocity ratio between the outer and inner jets is about 10^1 . In this situation, as pointed out by previous researchers¹ the mixture no longer has a singular critical point but rather critical mixing lines that define its thermodynamic state. Therefore a phase-diagram becomes necessary when studying mixtures at supercritical pressures with respect to their individual propellants. Because of the added complexity introduced when working with mixtures, we choose to first use N2 as the sole working fluid.

The second motivation for the study is the problem that has been encountered since the late 1930's in LRE's, namely combustion instability². Of the different types of instabilities, high frequency or acoustic instabilities are the most destructive to an engine. The damage can range from minor to catastrophic failure of an engine³. While a comprehensive understanding of what triggers these instabilities and how they evolve is still underway, a few things seem to be agreed upon. These instabilities are the result of coupling between the chamber acoustic modes and the injector fluid processes such as propellant injection, atomization, droplet vaporization, mixing and combustion heat release⁴. Of the different high-frequency acoustic modes, tangential modes (in the case of cylindrical chambers) seem to be the most damaging in rocket engines^{5,6}. The equivalent of this mode is a transverse mode in a rectangular chamber. In the present study we have a coaxial jet with cryogenic N2 in a rectangular chamber. We excite this jet with a piezo-siren that produces high amplitude (max ~ 184 db) pressure oscillations and sets up a transverse acoustic field. We then study the effects of the acoustics on the jet by measuring the jet's dark core length and its standard deviation. By doing the experiments with cryogenic N2 we aim to study the sub-process of acoustics interaction with jet metrics such as dark core length (indicative of mixing efficiency) in isolation from the heat release created by the combustion process. In this sense, these cryogenic cold flow experiments at high pressure can be viewed as an intermediate step between atmospheric water cold flow experiments and fully reacting experiments.

Several series of experiments have previously been carried out at the present facility to study the effects of a transverse acoustic field on coaxial jets at sub-, near-, and supercritical conditions using N2^{7,8}. In these studies, it was found that the jet's dark core length for an undisturbed jet decreases as the outer to inner momentum flux ratio (MR) and outer to inner velocity ratio (VR) increase. A good correlation was found between the dark core length and the MR. Two branches were found; one for two-phase conditions (at subcritical pressures) and another one for single-phase (at near- and supercritical pressures) conditions. The two-phase branch follows a correlation of the form $A/MR^{0.2}$ where A is a constant, and the single-phase branch follows a correlation of the form $A/MR^{0.5}$. These observations are in agreement with a wealth of historical data⁷. Furthermore, it was found that the dark core length standard deviation decreases at higher VR. This decrease, was suggested, could weaken a key feedback mechanism for the self-excitation process believed to play a fundamental role in LRE's combustion instability⁷. Most of the runs in that study consisted of 30 backlit images per run taken at 10 Hz. In the present study, we revisit most of the conditions run previously and expand the VR and MR in the subcritical regime. The new runs consist of at least 2000 backlit images taken at 41000 Hz. With the higher number of data points for each run, we aim to get statistically significant mean and standard deviations of the dark core length and compare the results with the previous trends. For example, with 2000 images, the standard deviation of the jet length is within 0.02% of the RMS of the jet length fluctuations, and they can be considered the same for all practical purposes. Also as part of this study we computed the total dark core length. That is, when the jet is excited by the acoustics, its shape changes

from mostly straight to curved. We compute the curved length to find out if the jet's length does decrease with acoustics, implying better mixing, or if it is only being curved.

EXPERIMENTAL SETUP

The facility used for this study is the Cryogenic Supercritical Laboratory (EC-4) at the Air Force Research Laboratory (AFRL) at Edwards Air Force Base, CA. An overview of the facility is shown in Figure 1. This facility has been extensively described in previous references^{7,8}. The gaseous N₂ used to supply the inner and outer jets, and to pressurize the chambers, is obtained from the main supply line to the lab. The outer and inner jets are cooled by three separate counter-flow heat exchangers (HX's). The coolant is liquid nitrogen obtained from a cryogenic tank. One heat exchanger cools the inner jet and the other two cool the outer jet. The temperature (T) is controlled by adjusting the flow rate of liquid nitrogen through the HX's. The mass flow rate through the inner and outer jets is measured, before they are cooled, with Porter mass flow meters. This is because it was found that it is much easier to measure the flow rates for ambient temperature gases than for cryogenic fluids. The chamber pressure is measured with a Stellar 1500 transducer. To keep the amplitude of the acoustic oscillations to a maximum near the jet, an inner chamber was created (Figure 1). The inner chamber has nominal height of 2.6", width 3" and depth 0.5". Details for the injector used are shown in Figure 2. The diameter of the inner jet is 0.020". The outer jet has an inner diameter, D₂ of 0.063" and outer diameter, D₃ of 0.095". The length to inside diameter is 100 for the inner jet and 67 for the outer jet (taking as reference the mean width of the annular passage, or hydraulic diameter). There is a small bias of about 8% of the mean gap width. As can be seen from the same figure, the inner jet is recessed by 0.010" from the outer jet.

The temperature of the jets is measured with a type E thermocouple which has a bead diameter of 0.004". The accuracy of this thermocouple was checked with an RTD and found to be $\pm 1.8^\circ\text{F}$ (1K). This thermocouple is traversed across the outer and inner jets to obtain a reading as close as possible to the injector exit plane. The radial profiles of the temperature were taken at intervals of 0.004" or 0.002" if the temperature varied significantly. The average distance from the exit plane, denoted H in Figure 2A is ~ 0.012 ". The density is computed from the measured flow rates, chamber pressure and jet temperature, using NIST's REFPROP⁹. From this, the VR and MR can be computed. Table 1 shows the range of test conditions used.

Chamber pressure, P (psia)	Outer to inner jet Velocity ratio, VR	Outer to inner jet momentum flux ratio, MR	Range of inner jet temperature (F)	Nominal inner jet mass flow rate (lb/s) x10-6	Range of outer jet temperature (F)
215	1.9-22.5	0.2-23.2	-262	617	-200 – -109
515	1.3-5.3	0.3-6.6	-235 to -227	637	-211 – -109
716	1.2-4.8	0.4-10.3	-222 to -211	648	-190 – -109

Table 1. Ranges of running conditions studies

The jet is visualized by taking backlit images using a Phantom 7.1 CMOS camera. The images have 128x256 pixels, and each pixel represents an area of about 0.003"x0.003". The framing rate was 41kHz. The exposure time varies from 7-9 μ s. The jet is backlit using a Newport variable power arc lamp set at 300W. The acoustic waves are generated using a piezo-siren custom-designed for AFRL by Hersh Acoustical Engineering, Inc. (Figure1). A piezo-ceramic element is externally excited with a sinusoidal wave at the desired driving frequency for the system. This frequency is chosen by manually varying the frequency on a signal generator until the highest amplitudes for the pressure waves are obtained. This signal is amplified and then fed to the piezo-siren. The movement of the piezo element is transmitted to the aluminum cone attached to it, and the cone then produces acoustics waves. To accommodate for the rectangular chamber a waveguide with a catenary contour is used to guide the waves from a circular cross-section to a rectangular cross-section (also shown in Figure 2). The sound pressure levels (SPL) in

the inner chamber range from 161 dB to 171 dB at for the first two resonance frequencies (~ 3.0 kHz and ~ 5.2 kHz). In this study only the first resonant frequency is studied.

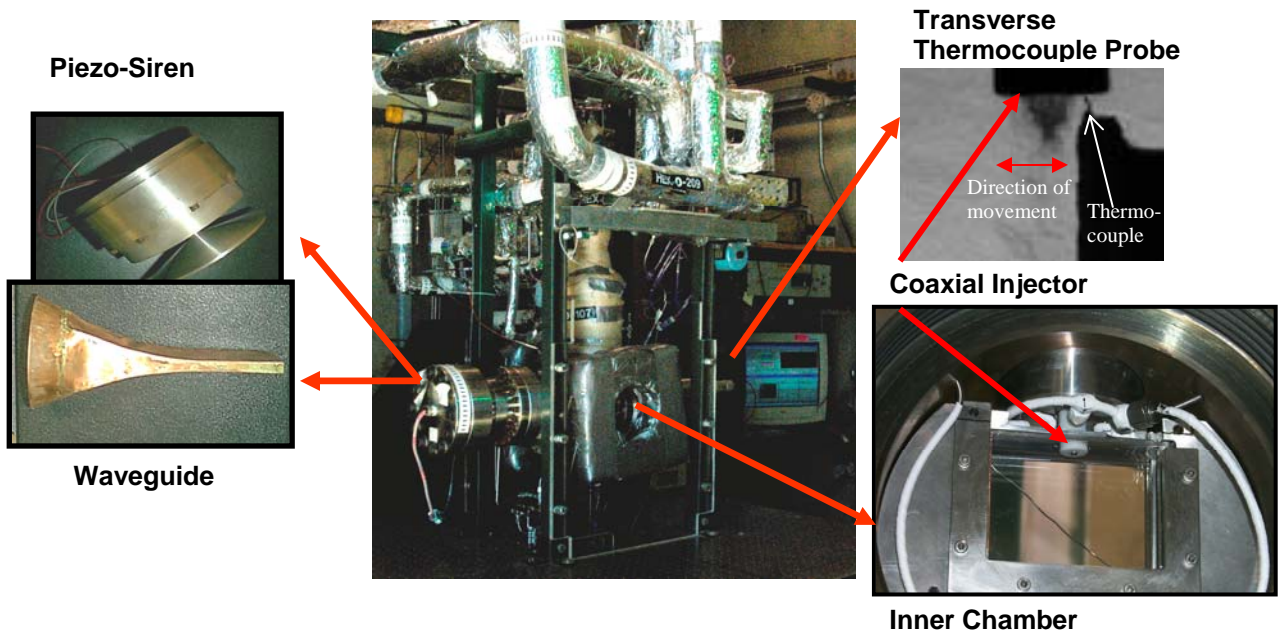


Figure 1. Overview of test facility used for this study, EC-4 at AFRL, Edwards.

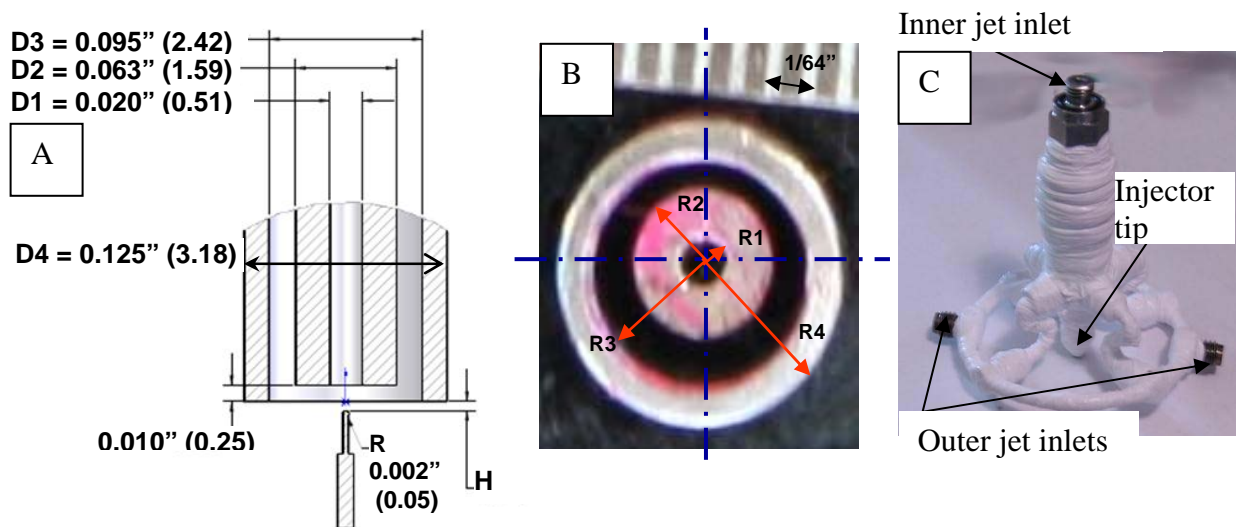


Figure 2. Injector Details. A: Schematic (dimension in parenthesis are in mm). B: Picture of coaxial injector tip. C: Injector overview.

RESULTS AND DISCUSSION

The main metric for this study is the dark core length. A typical image obtained is shown in Figure 3. In this case, $P_{\text{chamber}} = 217$ psia, $VR = 7.50$, $MR = 2.64$ and the acoustic field is on. As you can see from the left picture, the inner jet, being colder and denser than the outer jet shows darker in the backlit image. It is the length of this denser core that is measured. There are many valid ways to define the dark core length. One only has to be cautious that the method chosen agrees with the intuitive length measured by the naked eye. In the present case, the images are first converted to a multi-page tiff format and then analyzed using Matlab. The raw image is converted, or thresholded, to a black and white image using

Matlab's subroutine "im2bw" (Figure 3B). The threshold level or pixel intensity value above which all pixels will be white and below which all pixels will be black, is determined using the matlab subroutine "graythresh". This subroutine uses Otsu's method¹⁰ and it is based on the zeroth and first cumulative moments of the gray-level histogram. Once a black and white (b&w) image is obtained, the length of the jet is finally determined by drawing a contour around the b&w image (using matlab subroutine "imcontour") and measuring the axial length of the longest contour attached to the injector as shown in Figure 3C. This length is an axial length, in the sense that it does not take into account any curviness of the jet, which is typically seen when the acoustic field is on. In an attempt to investigate whether the axial acoustic field does shorten the length of the jet or only curves it, the curved or total length was also measured. In this case, the same contour already used to measure the axial length is divided into a left and a right side (see Figure3D). The total length is defined as the average of the left and right side. The lengths given by the matlab subroutines were manually checked by selecting 50-60 images from each set of 2000 images and comparing the results with what the authors would select to be the length using the naked eye. Using these images the threshold level could be modified from the one automatically computed and then used to process the complete set of images.

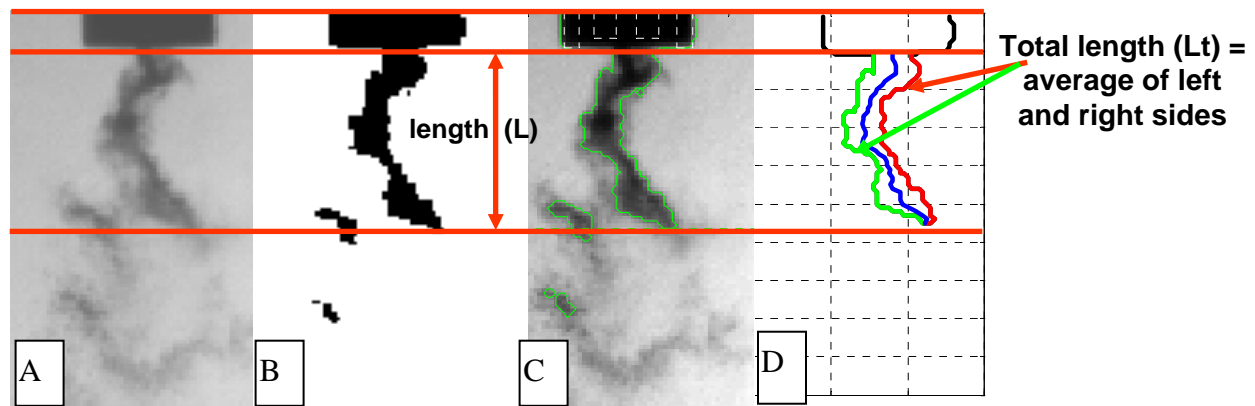


Figure 3 Measuring the dark core length. A: original image. B: Black and white image after thresholding. C: Contour used to define axial length (L). D: Schematic of how the total length is computed.

Three values for the chamber pressure are selected for the study to span subcritical to supercritical values: 215 (1.5), 515 (3.6), and 716 (4.9), psia (MPa). For reference, for N₂, P_{cr} =493 psia (3.4 MPa), T_{cr} = -232.4 F (126.26 K). The temperature of the inner jet is nominally the saturation T, -261F, while for near and supercritical pressures T is kept as close as possible to the critical value. There are two ranges of operating T for the outer jet for each pressure value: a "high" range from about -153 to -100 F (170 to 200 K) and a "low" range of about -208 to -172 (140-160) F (K). In a previous study by Davis et al.⁷, two sets of outer jet T's were also chosen for each pressure. However, the dark core length seemed to be a function of the VR and MR and not of the outer jet T specifically. In this study, therefore, the emphasis was to sweep as large as possible a range of VR and MR even if the outer jet temperature was not constant. For subcritical pressure, the inner jet is liquid and the outer jet is a gas, so this is a two-phase system. For near and supercritical pressures, the inner jet is mostly above the T_{cr} and the outer jet is warmer still. Therefore, for those cases there is a one-phase system. As a verification of the low impact of the outer jet T, a sweep was made on VR at subcritical conditions with the outer jet T being -136 to -134 F (180-181K). These data points blended with the rest of the data points taken at outer jet T from -208 to -100 F as will be shown later. For the case of nearcritical pressure (515 psia) at the high outer T range, there are two cases of the inner jet T, one within 2 F (1 K) from T_{cr} (which is within the accuracy of the thermocouple, so the temperatures could span the critical point) and the other case with temperatures about 5 F (3 K) above the critical temperature. For the nearcritical pressure low T case, the inner jet is below T_{cr} . For supercritical pressures, the inner jet T is above T_{cr} .

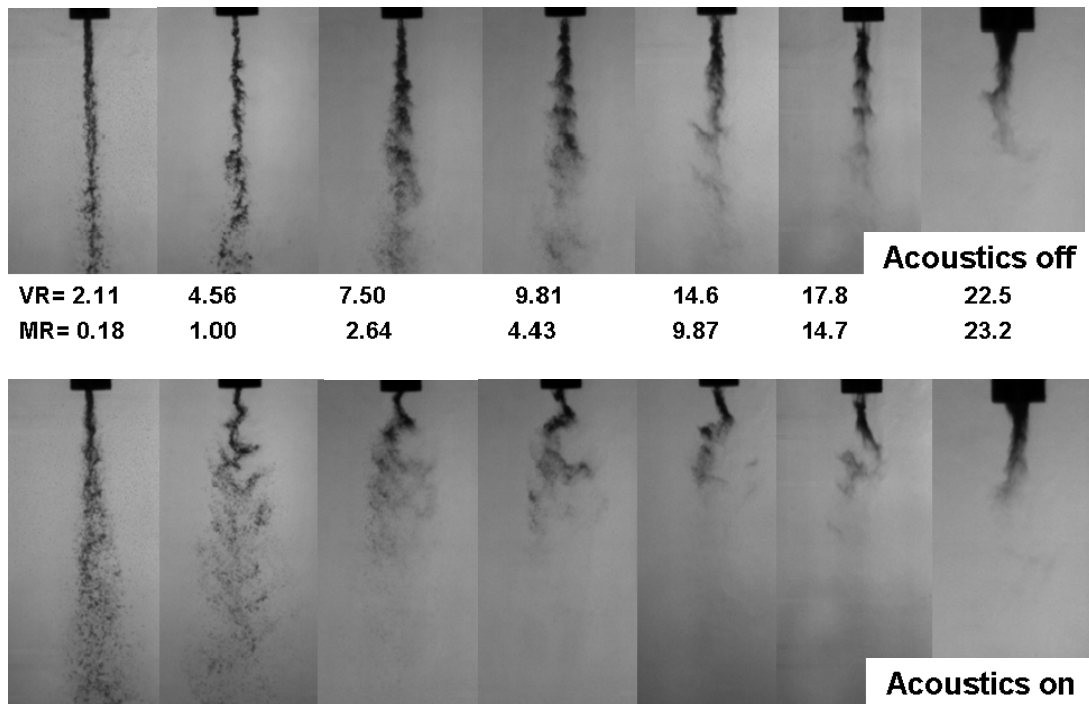


Figure 4. Collection of coaxial jet at subcritical pressure (~215 psia) with acoustics on and off for MR:0.18-23.2 and VR:2.11-22.5. The driving frequency is ~3kHz.

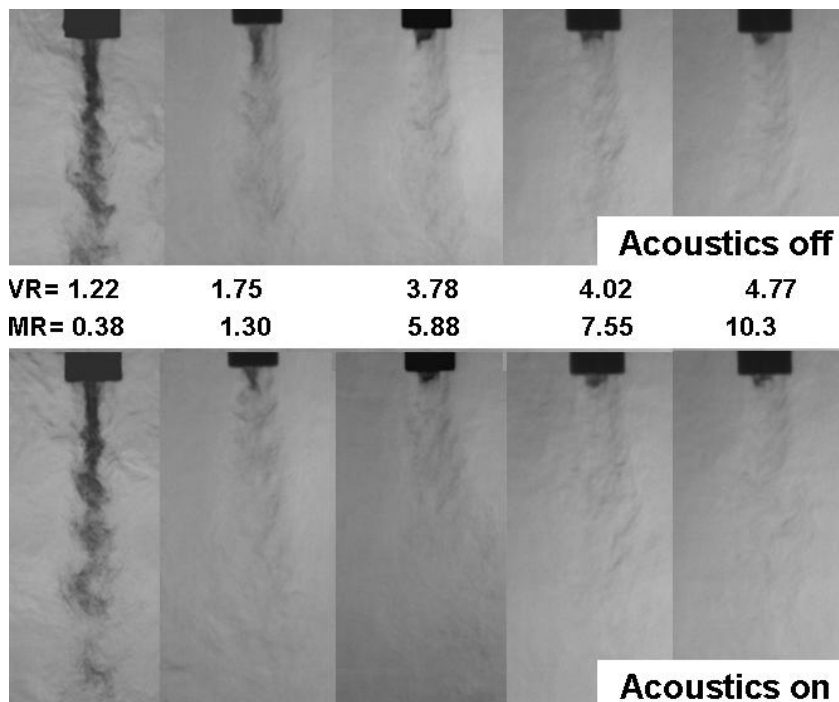


Figure 5. Collection of coaxial jet at supercritical pressure (~716psia) with acoustics on and off for MR:0.38-10.3 and VR:1.22-4.77. The driving frequency is ~3kHz.

A qualitative assessment of the coaxial jet at subcritical and supercritical conditions is shown in Figure 4Figure 5. The results for nearcritical pressures are not shown since they are very similar to those for the supercritical case. In these figures the top row represents the jet with no acoustics and the bottom row the jet with acoustics on ($\sim 3\text{kHz}$). VR and MR increase from the left to the right images. A few features can be observed from these figures. The axial length decreases with VR and MR for both acoustics on and off confirming previous results⁷. However, observe that for low MR and VR values (left-most images for both figures) the impact of the acoustics on the jet, in terms of the number of bends of the jet, seems to be small. As MR and VR increase the jet curves more (more bends seen in the jet). However, for high values of MR and VR ($\text{MR} > \sim 10$ for subcritical and $\text{MR} > \sim 6$ for supercritical) the jet does not curve as much again. The reasons for this behavior are being further investigated. Note that at supercritical conditions the jet is shorter for a given value of MR or VR and by values of $\text{VR} \sim 4$ and $\text{MR} \sim 6$, the jet is very short and hardly any bends can be accommodated by the short jet.

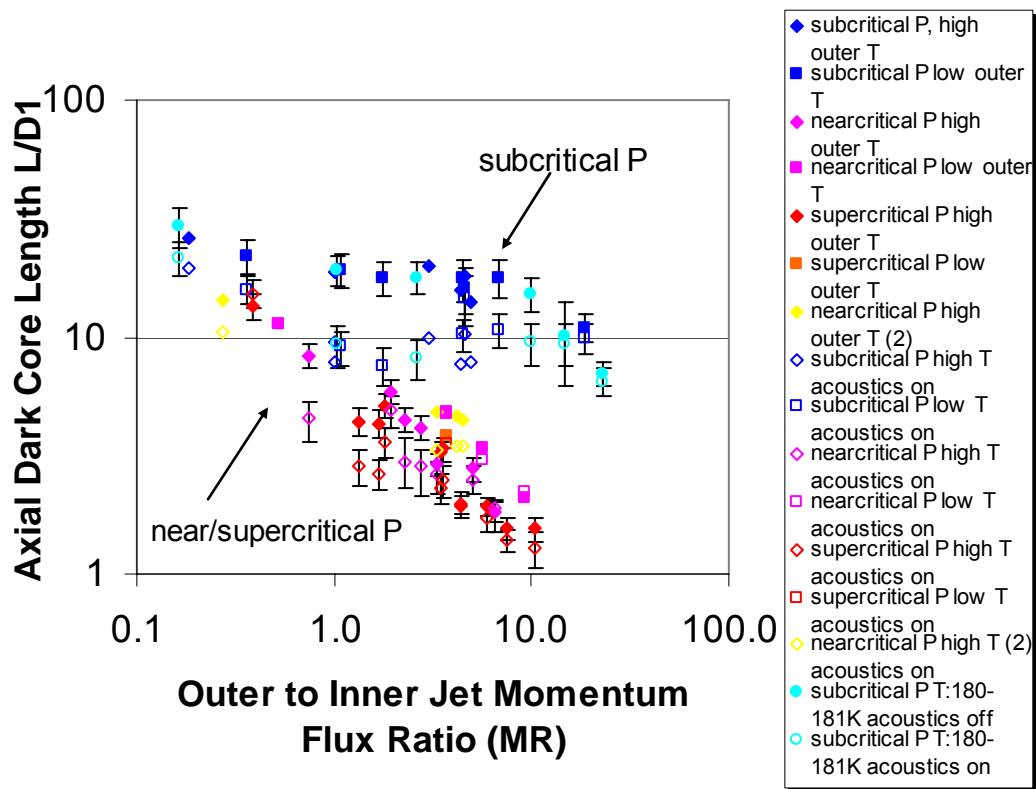


Figure 6. Axial Dark Core Length, L vs Outer to Inner Jet Momentum Flux Ratio (MR) for sub-, near-, and supercritical conditions with acoustics on and off.

Figure 6 shows the sub-, near-, and supercritical data with acoustics off (full symbols) and acoustics on (corresponding shallow symbol for a given full symbol). All the core length data presented here is normalized by the diameter of the inner jet, $D1$. The data called "Nearcritical P high T(2)" denotes the cases where the inner jet temperature was within 2F of the critical temperature. The dark core length for subcritical conditions (blue) is consistently higher than for the near- and supercritical conditions (red, pink, and yellow). The data for near- and supercritical conditions blends into one set of data consistent with previous results⁷. Note that for subcritical conditions, the entire set taken with outer jet temperatures ranging from -208 to -100 F (dark blue) blends with the data points taken at -136 to -134 F for the outer jet temperature (cyan), for both acoustics on and off. Therefore, for simplicity, in the next plots the data taken at 136 to -134 F will be included within the "subcritical P high T" data. Note that for all conditions the axial length of the jet gets shorter when the acoustics are on. For the few cases, where this is not the

case, the differences between the two lengths are within one pixel resolution. Finally, note that the percentage change between the length with acoustics off and on is largest for $MR \sim O(1)$ for the subcritical case. The reason for this feature is being investigated.

Now let's focus on the axial length with acoustics off only and compare it with all the historical data compiled by Davis et al¹¹, including his own data (

Figure 7). The current data has error bars. It can be seen that the current data agrees well with past correlations. For the two-phase case (subcritical regime) the axial length has a functional relation with MR of the form $L \sim A/MR^n$ where n is 0.2 and A is a constant, in this case 20-25. Also the near and supercritical regimes are in a lower branch roughly bounded by $A/M^{0.5}$ where A :5-12.

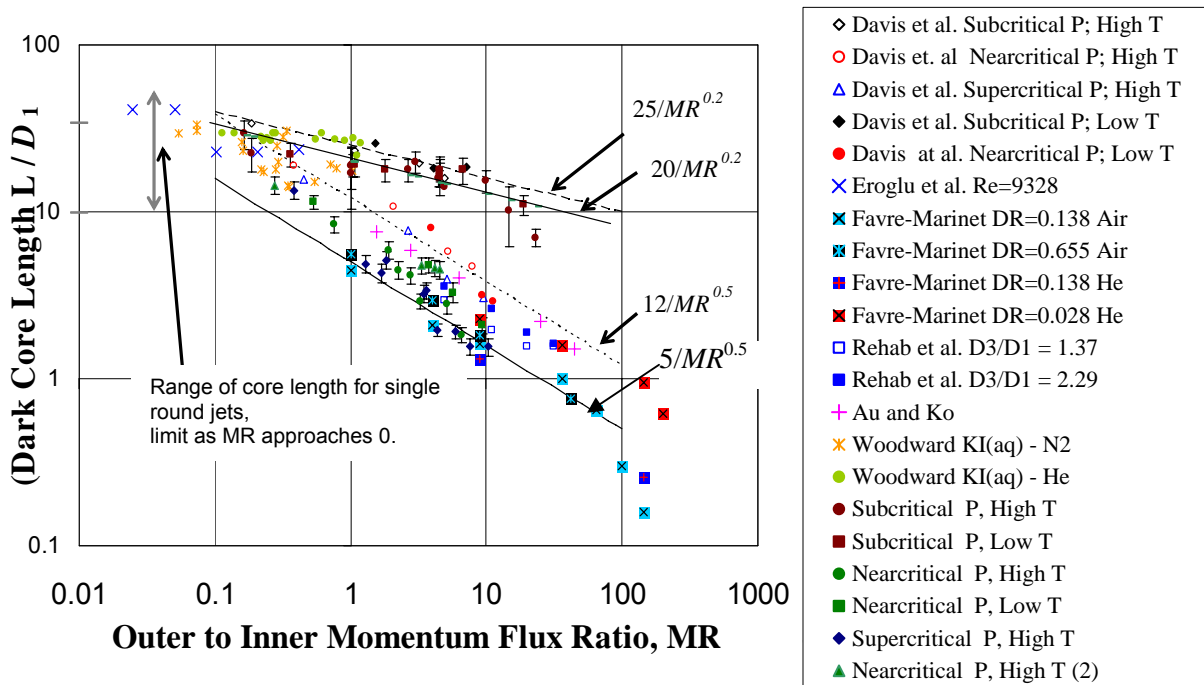
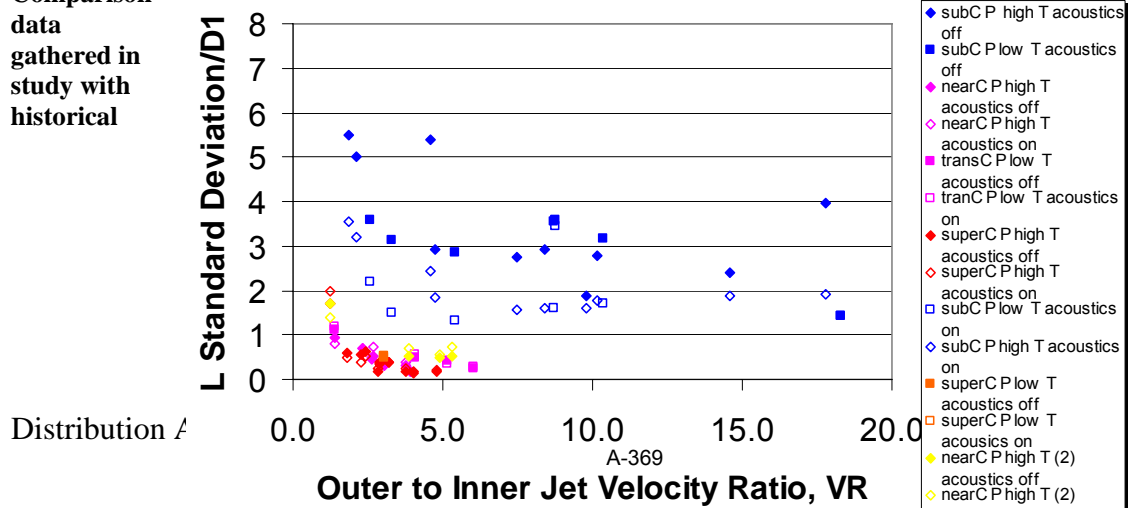


Figure 7.
Comparison
data
gathered in
study with
historical



of
this
data.

Figure 8. Standard deviation or RMS of dark core length fluctuations vs. outer to inner Velocity Ratio, VR

Having compared the axial dark core length of the jet with historical data and having found agreement, let's turn to the standard deviation. The results are shown in Figure 8. Again, there are two branches, one for subcritical and one for near and supercritical conditions. The standard deviation of the jet length for all conditions decreases as VR increases in agreement with previous results⁷. The faster decrease seems to happen for $VR \leq \sim 5$ which corresponds to $MR \leq \sim 1$. Then the standard deviation seems to plateau. Also for this case, the standard deviation decreases for both acoustics on and off. For the case of near and supercritical conditions, when the standard deviations/ D_1 gets smaller than 1, it is hard to make accurate statements about the differences between the cases with acoustics on and off because the pixel resolution is $0.2 D_1$.

The final metric to study is the total or curved length. The results, for acoustics on and off, are shown Figure 9. The same symbols and colors denote the same conditions as in Figure 6 for consistency. The results are consistent with those obtained for the axial length. Here too, the maximum percentage change of the length with and without acoustics is for $MR \sim O(1)$. For this range the difference between the lengths with acoustics on and off are larger than the error bars. For lower ($MR < \sim 1$) and higher ($MR > \sim 5$) the differences between the jet length for acoustics on and off fall within the error bars. As expected, for a given condition the curved length is longer than the axial length. That the acoustics do shorten the dark core length for a certain range of MR, even when taking into account the waviness of the jet, has implications for the effects of acoustics on mixing. The shorter the dark core length is for a given condition, the faster the mixing occurred with the outer jet. Thus, acoustics seems to have an effect on mixing for $MR \sim O(1)$.

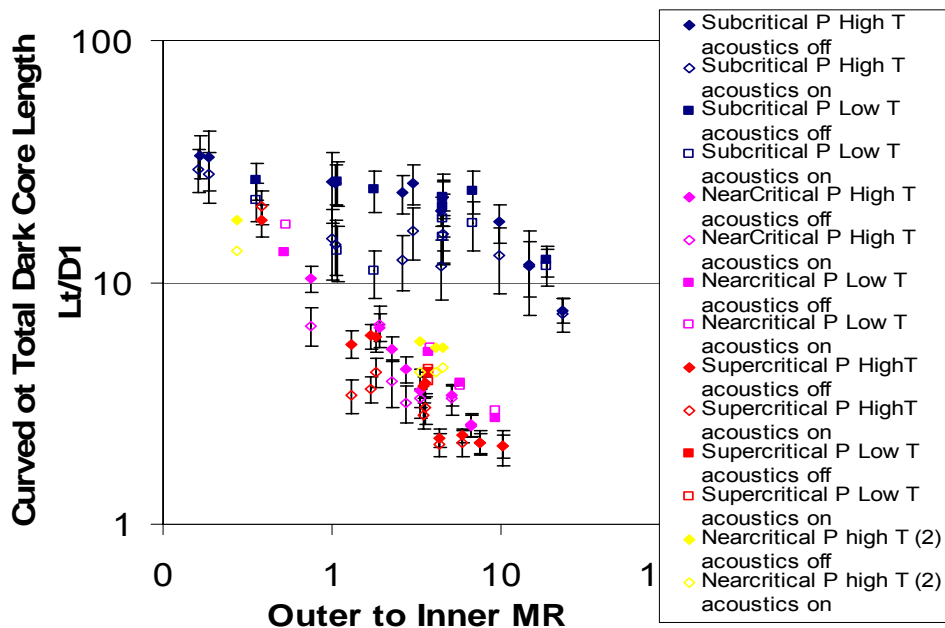


Figure 9. Curved or Total Dark Core Length L_t vs. Momentum Flux Ratio

CONCLUSIONS

An experimental study was completed to study the effects of chamber pressure, from subcritical to supercritical, outer to inner jet velocity ratio (VR) and outer to inner momentum flux ratio (MR) on a coaxial jet, which is either unexcited or under the influence of a transverse acoustic field at ~3kHz. The working fluid is cryogenic N₂. For a given chamber pressure, the inner jet mass flow rate was kept nearly constant while the outer jet temperature and flow rate were varied to change VR and MR. The main metric to judge the effect of these variables on the jet was the dark core jet length, which is the length of the inner jet before its first break as it mixes with the outer jet. In this study, two lengths were defined, an axial length, L , and a curved or total length L_t . The choice of the latter definition arose from the fact that under most conditions, when the jet is excited by an acoustic field, the jet becomes curved and one wants to know if the acoustics shorten the dark core's length or only change its shape from more or less straight to curved. Each run consisted of at least 2000 backlit images taken at 41kHz. It was found that, consistent with previous results, the axial length decreases as VR and MR increase. A functional relation of the form A/MR^n describes the behavior of the axial length with the exponent being 0.2 (A :20-25) for subcritical conditions and 0.5 (A :5-12) for near and supercritical conditions. These trends agree with a wealth of historical data including previous data obtained in the same facility but with 30 frames per run at 10Hz. The standard deviation of the axial length, which due to the large number of data points is within 0.03% of RMS of the jet length fluctuations, also decreases with VR, for sub-, near-, and supercritical conditions. It is empirically well known that LRE's designed to operate at $VR \sim 10$ are more stable than those designed for lower VR's. The fact that the standard deviation of the axial length decrease with increasing VR can result on the jet being less affected by acoustic disturbances as VR increases. The curved or total length was found to decrease when acoustics were on for the cases studied. For $MR \sim O(1)$ the curved length differences between acoustics off and on are bigger than the error bars. For $MR < 1$ and $MR \sim 5$, the differences fall within the error bars. This could imply that the dark core is in fact shortened by acoustics for $MR \sim O(1)$. The reason for this behavior is being further investigated.

ACKNOWLEDGEMENTS

The authors would like to recognize Randy Harvey for his invaluable contributions on running and maintaining the facility. This work is sponsored by the U.S. Air Force Office of Scientific Research under Mitat Birkan, program manager.

REFERENCES

1. Oschwald, M., Smith, J. J., Branam, R., Hussong, J., Schik, A., Chehroudi, B., Talley, D., "Injection of Fluids into Supercritical Environments", Combustion Science and Technology, Vol. 178, No. 1-3, 2006, pp. 49-100.
2. Culick F. E. and Yang, V., "Overview of Combustion Instabilities in Liquid-Propellant Rocket Engines," Liquid Rocket Engine Combustion Instability, edited by V. Yang and W. Anderson, Progress in Astronautics and Aeronautics, AIAA, Washington, DC, 1995, pp. 3-38.
3. Muss, J., Chakroborty, S., Leyva, I. A., "Development of the Scorpius LOX/Kerosene engine family", JANNAF 2005-0356, 2nd Liquid Propulsion and 1st Spacecraft Propulsion Subcommittee Meeting, Monterey, California, December 5-8, 2005.
4. Marshall, W., Pal, S., Woodward, R., Santoro, R. J., Smith, R., Xia, G., Sankaran, V., Merkle, C. L., "Experimental and Computational Investigation of Combustor Acoustics and Instabilities, Part II: Transverse Modes"; AIAA 2006-538
5. Yang, V., Anderson W., editors, "Liquid Rocket Engine Combustion Instability", Progress in Astronautics and Aeronautics, Vol. 169, 1995
6. Sutton, G. P., "Rocket Propulsion Elements", Sixth Edition, John Wiley & Sons, Inc., NY, 1992
7. Davis, D. W., Chehroudi, B., "Measurements in an acoustically driven coaxial jet under sub-, near-, and supercritical conditions", JPP, Vol. 23, No. 2, March- April 2007
8. Davis, D. W., Chehroudi, B., Sorensen, I., "Measurements in an acoustically driven coaxial jet under supercritical conditions", AIAA 2005-736
9. REFPROP, Reference Fluid Thermodynamic and Transport Properties, Software Package, Ver. 7.0, NIST, U.S. Department of Commerce, Gaithersburg, MD, 2002.
10. Otsu, N., "A threshold selection method from gray-level histograms", IEEE transactions on Systems, Man, and Cybernetics, Vol. 9, No. 1, 1979, pp. 62-66.
11. Davis, D., "On the behavior of a shear-coaxial jet, spanning sub- to supercritical pressures, with and without an externally imposed transverse acoustic field", Ph.D. Thesis, 2005

Dark core analysis of coaxial injectors at sub-, near-, and supercritical pressures in a transverse acoustic field

Ivett A. Leyva¹, Bruce Chehroudi² and Douglas Talley³
Air Force Research Laboratory, Edwards AFB, CA 93524

An experimental study on the effects of an externally-imposed transverse acoustic field in a N₂ shear coaxial jet at sub-, near-, and supercritical pressures is presented. Such fields and their interaction with the jet (i.e., breakup, mixing, etc.) are believed to play a critical role during combustion instabilities in liquid rocket engines. The shear coaxial injector used here is similar to those used in cryogenic liquid rockets. By using N₂ as the working fluid, the chemistry effects on combustion instability are separated from the effects of a transverse acoustic field on coaxial jets. Furthermore, through this choice, ambiguities associated with composition dependence on mixture critical properties are eliminated. The acoustic field is generated by a piezo-siren and the resonant frequency studied is ~3kHz. The pressures in the chamber range from 1.5-4.9 MPa to span subcritical to supercritical pressures. The outer to inner jet velocity ratio varies from ~1.2 to 23 and the momentum flux ratio (MR) varies from ~0.2 to 23. These ratios are mainly varied by changing the temperature and flow rates of the outer jet. At least 2000 backlit images were taken at 41kHz for each run. The main metric investigated is the length of the dark, or inner jet, core. This length is related to the mixing processes in a coaxial jet. The shorter the core length the faster the mixing occurs. Both the axial and the total, or curved, dark core lengths are studied. For momentum flux ratios ~1<MR<~4 the differences in the axial and curved dark core lengths between acoustics on and off are statistically significant, which means acoustics do shorten the core for this range. For subcritical pressures the MR range where the jet is shortened is larger. Preliminary results on the frequency analysis of the dark core lengths and width is also presented.

Nomenclature

A	=	constant
D	=	diameter with subscripts
LRE	=	liquid rocket engine
HE	=	heat exchanger
L	=	axial dark core length
L_t	=	total or curved dark core length
MR	=	outer to inner jet momentum flux ratio
n	=	exponent for MR
P	=	pressure
R	=	radius with subscripts
T	=	temperature
VR	=	outer to inner jet velocity ratio

¹ Sr. Aerospace Engineer, AFRL/PRSA, Edwards AFB, CA 93524, AIAA Member.

² Principal Scientist, ERC Inc., AFRL, Edwards AFB, CA 93524, AIAA Member.

³ Sr. Aerospace Engineer, AFRL/PRSA, Edwards AFB, CA 93524, AIAA Member.

Approved for public release; distribution unlimited. PA #07238A.

I. Introduction

THIS study is conducted with two overarching objectives in mind. The first objective is to understand the effects of transitioning from subcritical to supercritical pressure on a coaxial injector's jet characteristics such as mixing, atomization and breakup. This is because as liquid rockets engines (LRE's) have evolved into higher specific impulse designs, the chamber pressures have simultaneously increased reaching supercritical values for some propellants. The Space Shuttle Main Engine (SSME) and the Vulcan engine for the Ariane 5 launch vehicles are examples of LRE's designed to operate above the critical pressures of each propellant individually. We choose to study a coaxial injector since this design has proven effective for LRE's. In a typical coaxial injector for an LOX/LH2 engine, the oxygen is injected at subcritical temperatures in the center jet while the hydrogen is injected at supercritical temperatures, after being used as a coolant for the engine nozzle, in the coaxial jet. A typical velocity ratio between the outer and inner jets is about 10^1 . For these flows, as pointed out by previous researchers¹, the mixture no longer has a singular critical point but rather critical mixing lines that define its thermodynamic state. Therefore, a phase-diagram becomes necessary when studying mixtures that are at supercritical pressures with respect to their individual propellants. Because of the added complexity introduced when working with mixtures, N_2 is used as the sole working fluid.

The second objective is related to a problem that has been encountered since the late 1930's in LRE's, namely combustion instability². Of the different types of instabilities, high frequency or acoustic instabilities are the most destructive to an engine. The damage can range from minor to catastrophic failure of an engine³. While a comprehensive understanding of what triggers these instabilities and how they evolve is still underway, a few things seem to be agreed upon. These instabilities are the result of coupling between the chamber acoustic modes and the injector fluid processes such as propellant injection, atomization, droplet vaporization, mixing and heat release from combustion⁴. Of the different high-frequency acoustic modes, tangential modes (in the case of cylindrical chambers) seem to be the most damaging in rocket engines⁵⁻⁶. The equivalent of this mode in a rectangular chamber is a transverse mode. In the present study the coaxial jet with cryogenic N_2 is installed in a rectangular chamber. We excite this jet with a piezo-siren that produces high amplitude (max ~ 184 db) pressure oscillations and sets up a transverse standing acoustic field. The second objective is then to study the effects of the acoustics on the jet. This is done mostly by measuring the jet's dark core length (indicative of mixing efficiency) and its standard deviation as the outer-to-inner jet momentum flux ratio, MR, the outer-to-inner jet velocity ratio, VR, and the chamber pressure are varied. By doing the experiments with cryogenic N_2 , the aim is to study the sub-process of acoustic interaction with the jet in isolation from the heat release created by the combustion process. In this sense, these cryogenic cold flow experiments at high pressure can be viewed as an intermediate step between atmospheric water cold flow experiments and fully reacting experiments. The data gathered in this study (with and without the imposed acoustic field) also serves as a first step in validating CFD codes aimed to tackle combustion at supercritical pressure.

Previous studies done at the same facility at AFRL reported preliminary findings on the effects of a transverse acoustic field on a coaxial jet going from subcritical to supercritical pressures⁷⁻⁸. The current study is in part an extension of that work. The main differences are, 1) the ranges of MR and VR are larger in this study, 2) each data set now consists of at least 2000 images taken at a minimum sampling frequency of 41kHz (vs. 30 images taken at 10Hz), 3) introduction of the curved or total dark core length to look in more detail to the effects on mixing from acoustics, 4) different definitions and smoothing techniques applied for computing the dark core length are compared, and 5) a preliminary frequency analysis of the dark core length is given. With these enhancements, we have more confidence in the statistics of the dark core length and the conclusions drawn from these measurements.

II. Experimental Setup

The facility used for this study is the Cryogenic Supercritical Laboratory (EC-4) at the Air Force Research Laboratory (AFRL) at Edwards Air Force Base, CA. An overview of the facility is shown in Fig. 1. This facility has been extensively described in previous references⁷⁻⁸. Gaseous N_2 is used to supply the inner and outer jet flows and to pressurize the chamber. It is obtained from the main supply line to the lab. The outer and inner jets are cooled by three heat exchangers (HE's). The coolant is liquid nitrogen obtained from a cryogenic tank. One heat exchanger cools the inner jet and the other two cool the outer jet. The temperature (T) of the two jets is controlled by adjusting the flow rate of liquid nitrogen through the HE's. The mass flow rate through the inner and outer jets is measured, before they are cooled, with Porter mass flow meters (122 and 123-DKASVDAA). It was found that it is much easier to measure the flow rates at ambient rather than at cryogenic temperatures. The chamber pressure is measured

with a Stellar 1500 transducer. To keep the amplitude of the acoustic oscillations to a maximum near the jet, an inner chamber was created (Fig. 1). The inner chamber has nominal height of 6.6cm, width 7.6cm and depth 1.3cm. Details for the coaxial injector used are shown in Fig. 2. The inner diameter of the inner jet, D_1 , is 0.51 mm. The outer jet has an inner diameter, D_2 , of 1.59 mm and outer diameter, D_3 , of 2.42 mm. The length to inside diameter ratio is 100 for the inner jet and 67 for the outer jet (taking as reference the mean width of the annular passage, or hydraulic diameter). There is a small bias of about 8% of the mean gap width. As can be seen from the same figure, the inner jet is recessed by 0.3 mm from the outer jet.

The temperature of the jets is measured with a type E thermocouple which has a bead diameter of 0.1mm. The accuracy of this thermocouple was checked with an RTD and found to be $\pm 1K$. This thermocouple is traversed across the outer and inner jets to obtain a reading as close as possible to the injector exit plane (also seen in Fig. 1). The radial profiles of the temperature were taken at intervals of 0.1mm, or 0.05mm if the temperature varied significantly. The average distance from the exit plane, denoted H in Fig. 2 is $\sim 0.3mm$. Properties such as density, viscosity, and surface tension are computed from the measured flow rates, chamber pressure and jet temperature, using NIST's REFPROP⁹. From this, the Re , We , VR and MR for a given condition can be computed.

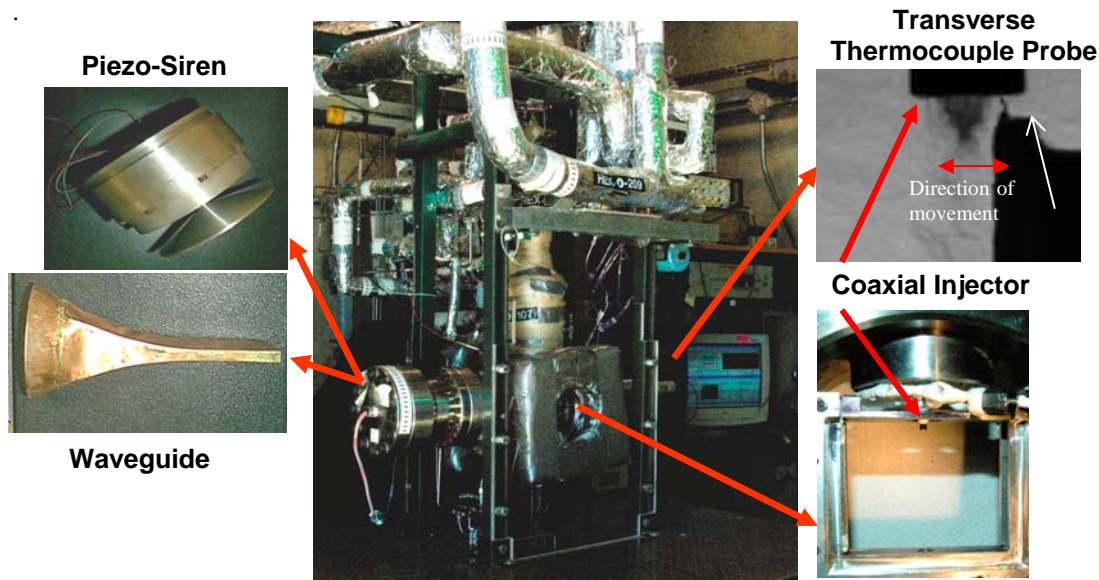


Figure 1. Overview of the Supercritical Flow Facility, EC-4 at AFRL/Edwards used for this study

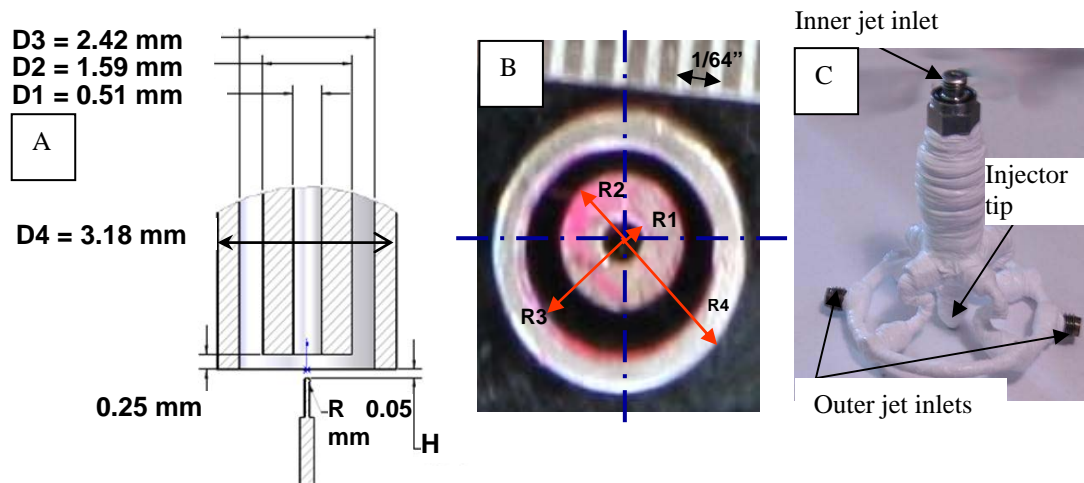


Figure 2. Details on the coaxial injector used for the present study

The jet is visualized by taking backlit images using a Phantom 7.1 CMOS camera. The images have 128x256 pixels, and each pixel represents an area of about 0.08mmx0.08mm. The framing rate is 41kHz. The exposure time varies from 7-9 μ s. The jet is backlit using a Newport variable power arc lamp set at 300W. The acoustic waves are generated using a piezo-siren custom-designed for AFRL by Hersh Acoustical Engineering, Inc. (Fig.1). A piezo-ceramic element is externally excited with a sinusoidal wave at the desired driving frequency for the system. This frequency is chosen by manually varying the frequency on a signal generator until the highest amplitudes for the pressure waves are obtained. This signal is amplified and then fed to the piezo-siren. The movement of the piezo element is transmitted to the aluminum cone attached to it, and the cone then produces acoustics waves. To accommodate for the rectangular chamber a waveguide with a catenary contour is used to guide the waves from a circular cross-section to a rectangular cross-section (also shown in Fig.1). The sound pressure levels (SPL) in the inner chamber range from 161 dB to 171 dB at for the first two resonance frequencies (~3.0 kHz and ~5.2 kHz). In this study only the first resonant frequency is studied.

IV. Results and Discussion

A total of 44 runs were completed spanning chamber pressures from 1.5 to 4.9 MPa. The runs are divided into subcritical, nearcritical and supercritical pressures. For reference, for N₂, the critical P is 3.40 MPa, and the critical T is 126.26 K. Within each pressure range, there is a subset of high T outer jet and a subset of low T outer jet. Details of the test conditions are presented in the Appendix. Table 1 summarizes the range of conditions for each chamber pressure. Since the major parameter of interest for this study is the core length, a graphical representation of the definitions for the axial and curved or total length is shown in Fig. 3 (P_{chamber} =1.49 MPa, VR=7.49, MR=2.64 and the acoustic field is on).

Table 1. Summary of range of conditions for each pressure range

Mean Chamber pressure, P (MPa)	Outer to inner jet Velocity ratio, VR	Outer to inner jet momentum flux ratio, MR	Range of inner jet temperature (K)	Nominal inner jet mass flow rate (mg/s)	Range of outer jet temperature (K)
1.48	1.9 – 22.6	0.2 – 23.3	109 – 110	280	144 – 195
3.55	1.3 – 5.9	0.3 – 9.1	123 – 132	289	138 – 195
4.93	1.2 – 4.8	0.3 – 10.3	132 – 147	294	150 – 195

The first observation in the unprocessed image (leftmost image) is that the inner jet, which is colder and denser than the outer jet, appears darker in the backlit image. It is the length of this denser core, before its first break, that is called the dark core length. Historically, people have defined the dark core length or intact length as the projection of the core in the axial direction (y) as shown in Fig. 3. In this study, this is called the axial dark core length. There are many valid ways to define this length. One only has to be cautious that the method chosen agrees with the intuitive length judged by the naked eye. Several methods to compute the axial dark core length were analyzed by this group. In general, to arrive at a length from raw images, a series of steps need to be taken. The first step is to convert the grayscale images to black and white (b&w) images. This is typically done by choosing a threshold value of pixel intensity below which all pixels are set to black and above which all pixels is set to white. Choosing an adequate threshold is the first logic rule that is implemented when automating the length measurements. After converting the image to b&w one has to define the first break in the jet. This would be the second logic rule that is implemented. Finally, if a total or curved length is desired (Fig 3), then one needs to decide if the curve needs to be smoothed before the final curve measurement is made.

In the present case, the raw images taken with the Phantom camera are first converted to a multi-page tiff format and then analyzed using Matlab. Matlab is chosen over other image processing programs such as ImagePro because it is faster. The raw images are converted, or thresholded, to a b&w image using Matlab's subroutine "im2bw" (Fig. 3B). The threshold level is determined using Matlab subroutine "graythresh". This subroutine uses Otsu's method¹⁰ and it is based on the zeroth and first cumulative moments of the gray-level histogram. In previous studies from this lab⁷⁻⁸ the threshold was found by constructing a histogram of the image and defining the threshold value as the pixel

intensity where the slope of histogram is equal to $1/e$. The current method to define a threshold is preferred due to its robustness. Once a b&w image is obtained, the axial length of the jet is determined by drawing a contour around the image (using Matlab subroutine “imcontour”) and measuring the y coordinate of the longest contour that is attached to the injector as shown in Fig. 3. Other ways to define the length include measuring the location when the standard deviation of the pixel intensity of a row is zero. This method tends to overpredict the length when the jet break is not clean and there are dark lumps clustered around the jet breakup region. For clean breaks both methods agree very well. It is noteworthy to say that even though the magnitudes might be different with the different definitions for the lengths, the trends of the axial dark core length and its standard deviation with respect to MR and VR are preserved.

In an attempt to investigate whether the transverse acoustic field shortens the length of the jet or only bends it, a curved or total length was also measured. In this case, the same contour already used to measure the axial length is divided into a left and a right side (see Figure3C). The total length is defined as the average of the left and right sides. Because the curves had a lot of small scale spatial features believed not to be significant to the computation of the total length, the right and left sides were smoothed by three methods: 1) simple averages in the x and y direction (5 points), 2) median filtering, and 3) median filtering followed by simple averages. The simple average was chosen because it smoothed out the small scale features mentioned above while preserving the shapes of the larger scale structures which is what we are interested in. Similarly in the case of filtering, even though the magnitude of the curved length changes, the trends with respect to MR and VR are preserved.

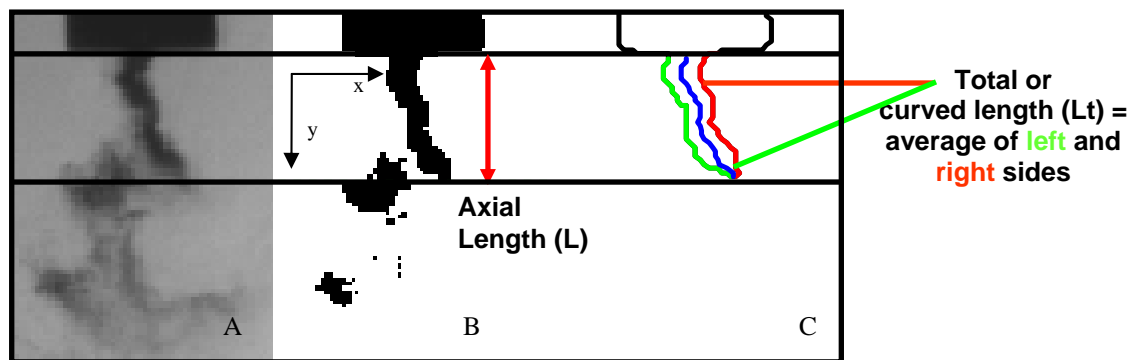


Figure 3. A. Raw image. B. Black and white image after thresholding showing definition of axial dark core length. C. Definition of total or curved length.

The lengths given by the Matlab subroutines were manually checked by selecting 50-60 images from each set of 2000 images and comparing the results with what the authors would select to be the length using the naked eye. Using these images the threshold level could be modified, if needed, from the one automatically computed and then used to process the complete set of images. In all cases, the axial and curved dark core lengths are normalized by the inner diameter of the inner jet ($D_1=0.51\text{mm}$)

A. Qualitative Characterization of Images

A collection of images taken at the three different chamber pressures is shown in Figs. 4-6. The first set of images (Fig. 4) corresponds to a subcritical pressure. For this case, the inner jet is a liquid with temperature of 109-110K and the outer jet is a gas with temperature from 175-195K. This is a two-phase mixture. The upper row of images has the acoustic field turned off. In the leftmost image the presence of droplets is evident, but as the VR and MR increase the dark core and the droplets become smaller and finally, for the conditions of the rightmost image, the droplets have become irresolvable by the pixel size of the image. This behavior is consistent with previous data^{7-8,11} where as MR and VR increase the mixing becomes more efficient between the two jets and the inner jet mixes faster with its surroundings. When the transverse acoustic field is turned on (lower row in Fig. 4) the jet also moves in the transverse direction. As will be shown later, the movement of the jet has the same frequency as the driving frequency of the piezo-siren. We can also intuitively see that the acoustics have the most effect on the jet, in terms of the decrease in axial dark core length and the amount of discernable bends, in a range of MR from about 1-4, which we will also confirm quantitatively later.

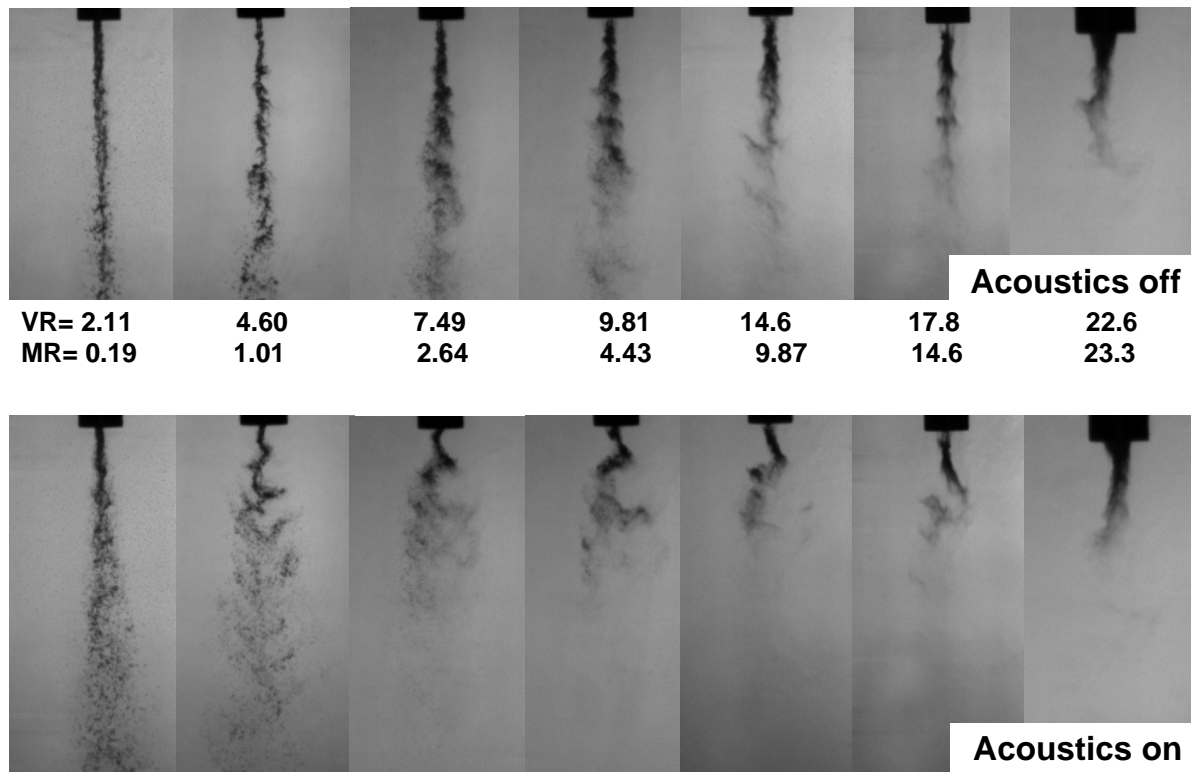


Figure 4. Collection of images at subcritical pressure (~ 1.5 MPa) with acoustics on and off for MR:0.19-23.3 and VR:2.11-22.6. The driving frequency is ~ 3 kHz

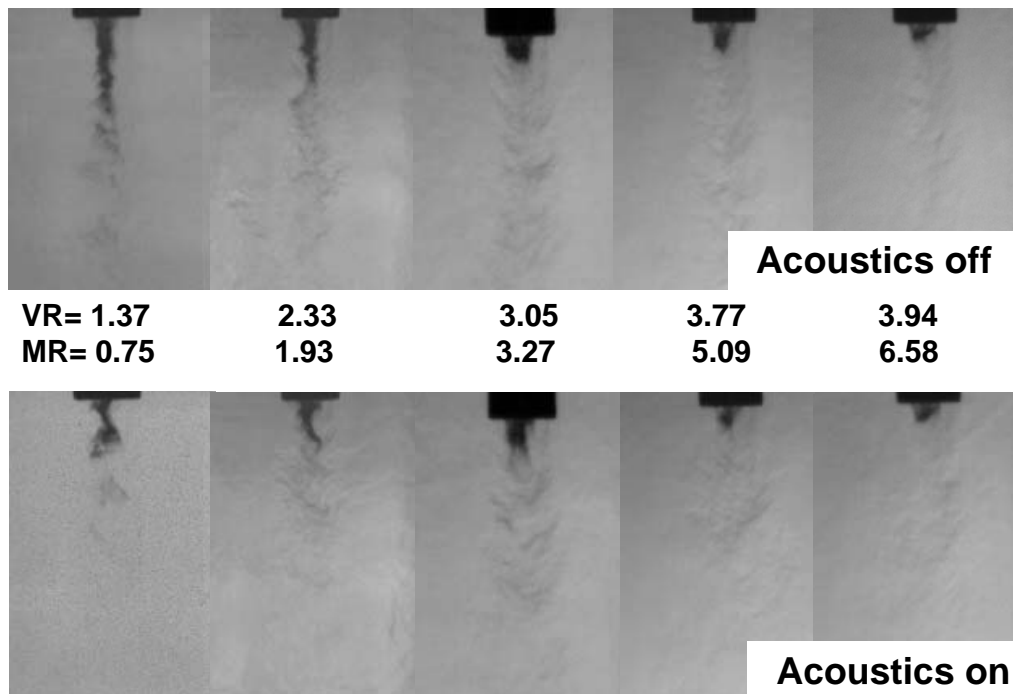


Figure 5. Collection of images at nearcritical pressures (~ 3.6 MPa) for acoustics on and off for MR:0.75-6.58 and VR:1.37-3.94. The driving frequency is ~ 3 kHz.

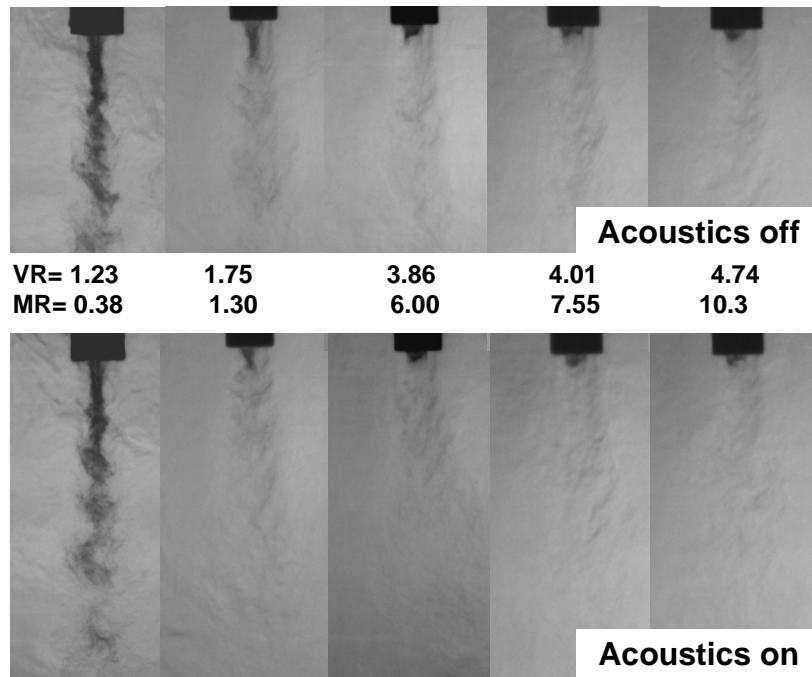


Figure 6. Collection of coaxial jet at supercritical pressure (~4.9 MPa) with acoustics on and off for MR: 0.38-10.3 and VR: 1.23-4.74. The driving frequency is ~3 kHz.

As the pressure increases to nearcritical values (Fig. 5) we notice some differences. In this case the inner jet is a few degrees above the critical temperature and the outer jet temperature varies from 171-195K. Both jets are in a supercritical state. This is a one-phase mixture. Notice that there are no more visible droplets in this situation, even for the low VR's, as we would expect since the inner jet is not a liquid anymore. At this pressure, the dark core length has become smaller for a given MR and VR due in part to the fact that the difference in temperatures between the two jets is smaller than for subcritical P's. By VR values of ~4, the length of the jet has become $< \sim 5 D_1$. In this case, when the acoustics are turned on, a dramatic shrinkage in the axial length is visible for the two leftmost images, but as the MR increases the changes become less

discernable and the bending of the jet becomes more of a straight motion of the short jets in the transverse direction. Similar observations apply for Fig. 6 which depicts jets at supercritical pressures and supercritical temperatures as well.

B. Axial Dark Core Length

Next, a quantitative characterization of the jet's response to the acoustic field is offered by plotting the axial dark core length as a function of MR. The results are shown in Fig. 7. This figure includes all the data gathered in this study. Solid symbols correspond to data with no acoustics and the corresponding hollow symbols denote data when the acoustics are on. The color codes and symbols are also applicable to the rest of the figures in this paper. The error bars denote $\pm 1\sigma$ (standard deviation). The two sets of blue data correspond to subcritical pressures. Within subcritical pressure data, the light blue or cyan corresponds to a set of data taken with a nearly constant outer jet temperature of 180-181K. This is done to compare with the other subcritical data to see if there is a direct effect of the outer jet temperature (besides its implicit effect through density and MR) on the dark core length. As the figure shows, these data blend well with the rest of the subcritical data which includes a broad range of outer jet temperatures from 112-195K. Therefore, there is no direct effect of the outer jet temperature on the axial dark core length within the range of MRs tested here. The other point to indicate has to do with the system repeatability in the subcritical regime. For a few conditions (namely around MR=1 and MR=5), run conditions were repeated within a few weeks to a couple of months. In all cases the variability is within the error bars of the test data.

The magenta diamonds correspond to nearcritical pressures with the inner jet at supercritical T while the magenta squares have inner jet temperatures below or within 1K of the critical T. The yellow data points are also at nearcritical pressures but the temperature of the inner jet is within 1K of the critical T while the outer jet temperatures are $> 180K$. Finally the red data corresponds to supercritical pressures. One of the most striking things from this figure is that there are two branches for the dark core length plotted versus MR. This new data confirms previous data gathered in this facility and other historical data^{7,11}.

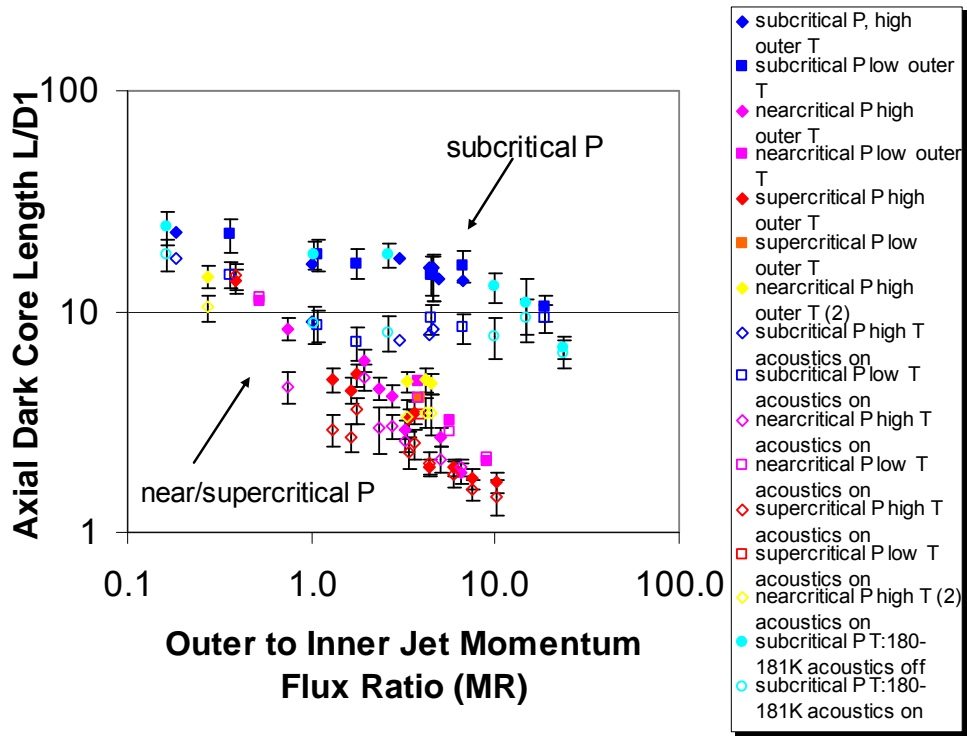


Figure 7. Variation of the axial dark core length as a function of MR for both acoustics on and off

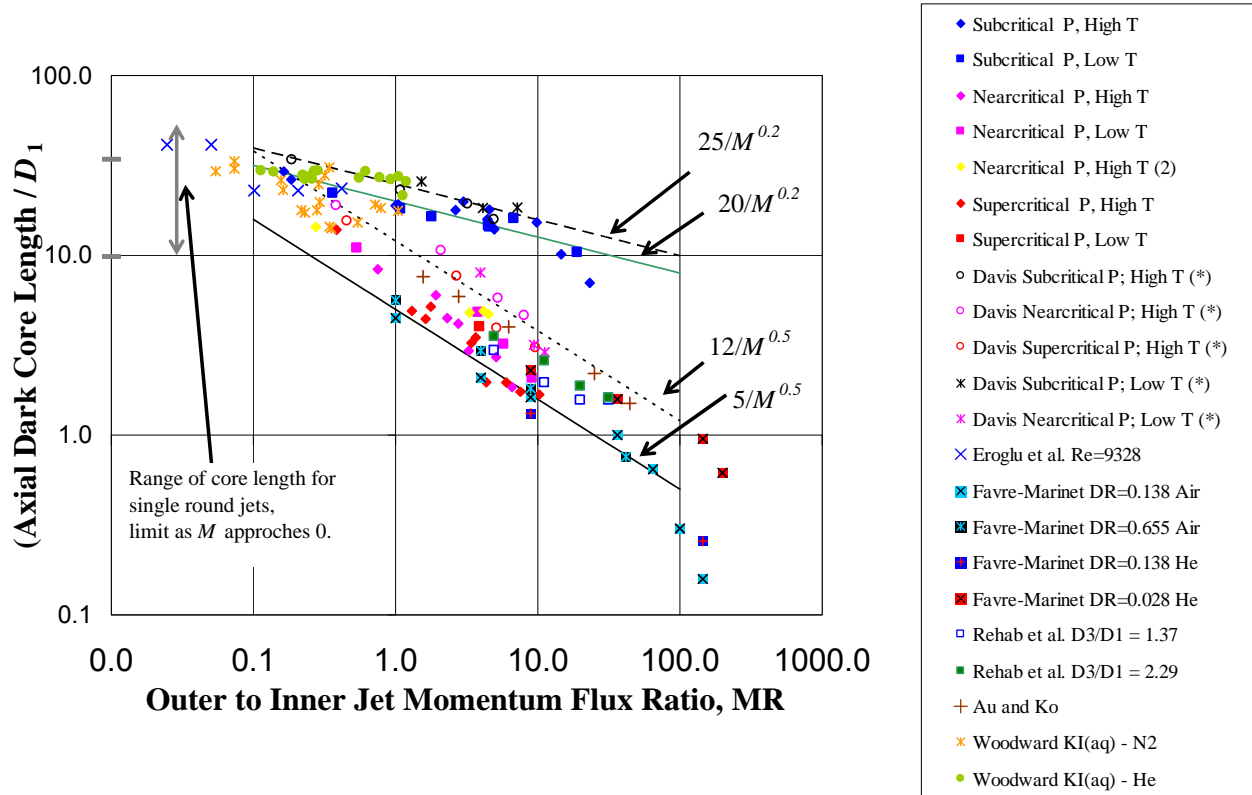


Figure 8. Summary of historical and current data on the trends of the axial dark core length vs. MR

In fact this was one of the objectives of the present study, to verify the trends of the axial dark core length vs. MR with more robust statistics due to the fact that the new runs have more data points per run than before and there are more points per pressure range. Also, note that differences in the axial dark core length for acoustics on and off are statistically significant for $1 < MR < 4$ under all chamber pressures. This is especially clear for the subcritical pressures. Next, this data is plotted along with the previously gathered data from this facility and historical data by others^{7-8,11} (Fig. 8). In previous studies^{7,11} the trend for the single-phase mixtures (near and supercritical P) was shown to follow a functional relation of the form A/MR^n where n is 0.5 and A : [5-12] whereas for the two-phase mixtures (subcritical P) the exponent was 0.2 and A was 25. For the current data, although a least squares fit for near and supercritical P gives $7.3/MR^{0.58}$, all but one point (including error bars) are included in the previous bracket. Similarly for the subcritical data, a least square fit gives $18.4/MR^{0.19}$ but all the data except for one point (including error bars) are contained in $A/MR^{0.5}$ if A is 20-25.

A trend we wanted to examine with this study is the effect of VR on the standard deviation (std. dev.) of the axial dark core length. This is because preliminary data^{7-8,11} indicated that the std. dev. decreased with VR offering perhaps insight into why injectors for cryogenic liquid rocket engines designed for high VR provide more stable combustion than those working at lower VR's. That is, a lower std. dev. is indicative of the jet's insensitivity to externally imposed acoustics which would make it more "stable". Of course, this and the previous studies are performed with N_2 instead of combusting gases, and this hypothesis needs to be further verified using reacting mixtures. The results for the axial length std. dev. are presented in Fig. 9 for all the data gathered in this study. The general trend, with the exception of a few outliers, is the same as observed before. The std. dev. decreases with VR, and the magnitudes are lower for near and supercritical pressures. Two new observations can be made from this data set; the first is that the fastest drop in std. dev. values happens at low VR's. At around VR=5, the std. dev. decrease becomes more gentle. The second observation is that for subcritical pressures, the std. dev.'s of the cases with acoustics on are lower than their no-acoustics counterparts and follow the same trend. For the near and supercritical pressure cases no conclusions can be drawn as the differences in the std. dev. mostly fall within the pixel resolution for these images, which is $\sim 0.2D1$.

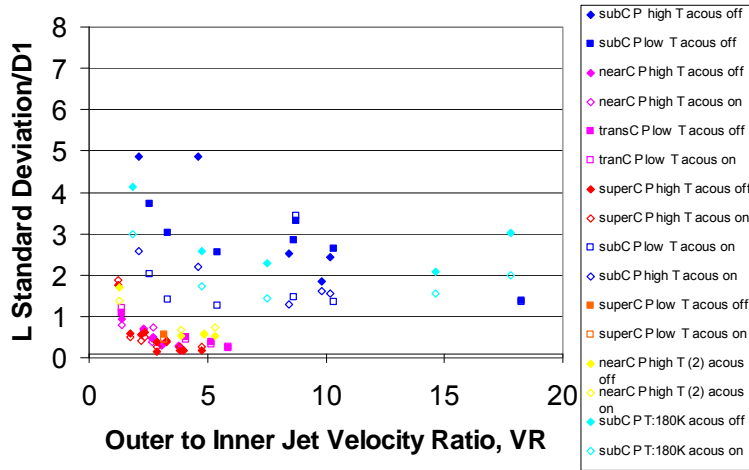


Figure 9. Standard deviation of the axial dark core length vs. VR

C. Curved or Total Dark Core Length

One of the questions that arose while conducting this study was whether the acoustics were indeed shortening the dark core or merely bending it. If the core is only being bent then we would expect the acoustics not to have much effect on mixing but if the core is being bent and shortened then acoustics are expected to have an impact on mixing. To answer this question, the definition of curved length described in Fig. 3 was employed. As mentioned previously, the curved lengths were smoothed by using a five point average around every point both in the x and y directions. Fig. 10 shows the results for the curved dark core length vs. MR. The data for these lengths with no smoothing was previously reported but the trends do not change¹². This figure is the counterpart to Fig. 7. One interesting observation is the great resemblance between both figures. Except for the fact that the lengths are larger

(as intuitively expected) all the observations made for Fig. 7 still apply. However, by virtue of Fig. 10 having curved as supposed to axial lengths, the fact that we see statistically significant differences between the cases with and without acoustics means that the jet is indeed shortened by the acoustic field when $\sim 1 < MR < \sim 4$. These differences are clearer in the curved dark core lengths. Finally, to conclude the comparison between the curved and axial dark core lengths, the std. dev. has been plotted against VR in Fig. 11. The data shows more scatter than those for the axial dark core length but the general trends are the same.

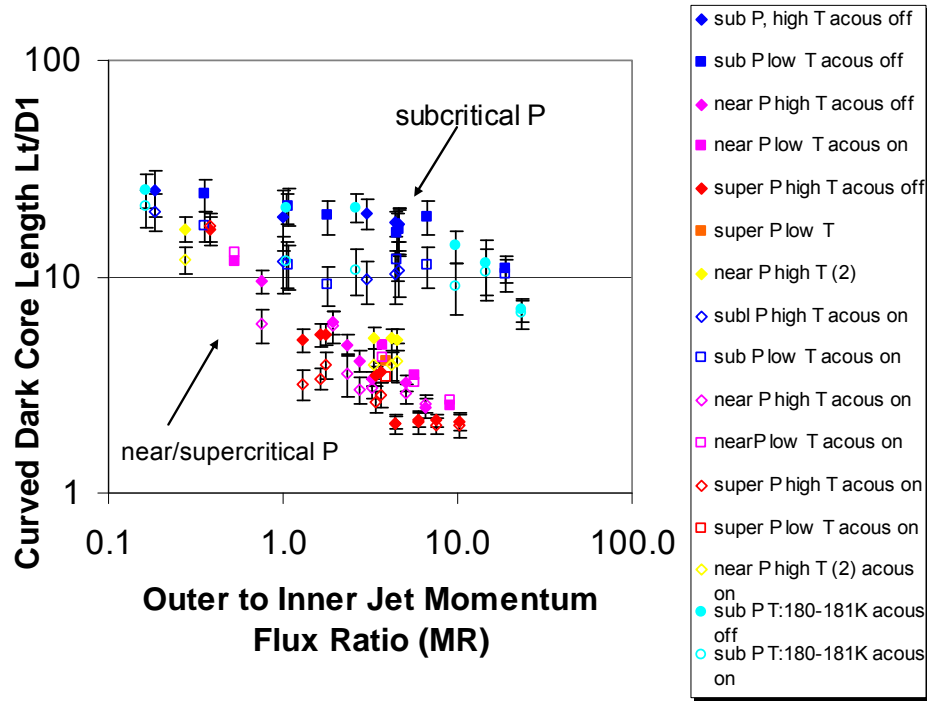


Figure 10. Trend of the Curved Dark Core Length vs. MR

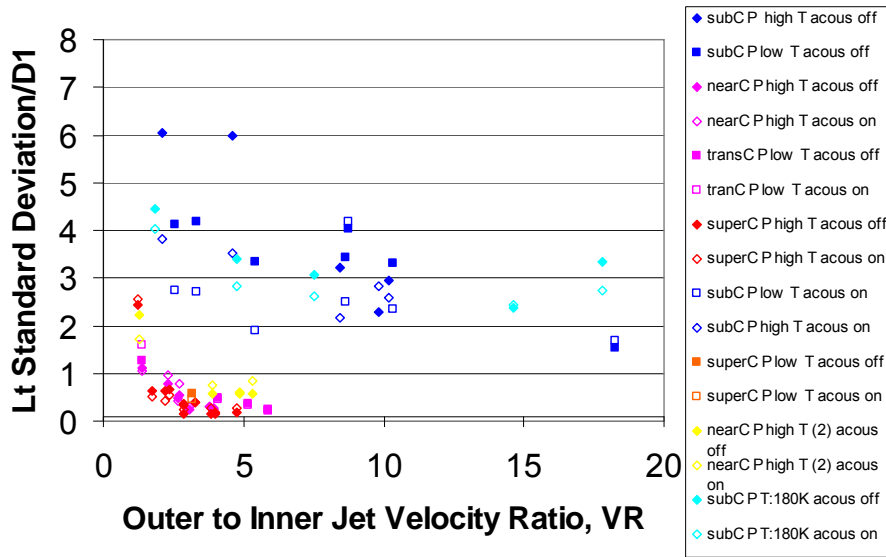


Figure 11. Standard Deviation of the Curved Dark Core Length vs. Velocity Ratio, VR

D. Frequency analysis

The last part of this paper is a preliminary presentation of the frequency analysis done on the transverse and axial movements of the dark core of the jet. Fig. 12 A&B shows a sample of the axial and curved lengths as a function of time for Run sb14 (Appendix) with acoustics on. In both cases, the dominant frequency is so prevalent that one can estimate it by merely counting the peaks. Also, note that the lengths have a saw tooth shape vs. the sinusoidal shape of the signal that is fed into the piezo-siren. Fig. 13 A&B show the FFT's of the axial and smooth curved lengths. The fundamental frequency in both cases is also about 3.043 kHz vs 3.06 kHz fed into the piezo-siren, which is a very good agreement (0.6% difference). Fig. 14 A shows a sample of the movement of the midpoint of the inner jet with time for the 10th row from the injector's exit plane. This row was chosen arbitrarily. The movement of the midpoint is evident in Fig. 14 B which shows two snapshots of the jet at about half a cycle apart highlighting the row examined. The FFT's of the width of the jet and the midpoint again at the 10th row from the injector's exit plane is shown in Fig. 14 C&D. We see that the main frequency is again 3.043kHz. Together, the movement of the inner jet's midpoint and width tell the story of the dynamics of the jet. Because the midpoint of the inner jet is moving, the peak in the width can be attributed to both the movement of the entire jet's width left and right and to its contraction and expansion. These preliminary results hint to the complex motion of the dark core of the jet in the transverse and axial directions when affected by a transverse acoustic field. A more detailed study of the frequency analysis of the behavior of the jet will be the subject of a future paper.

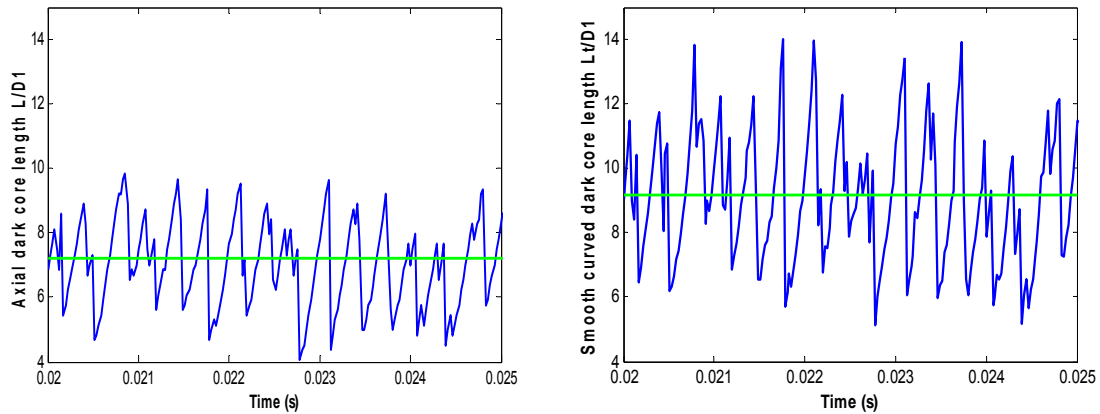


Figure 12. A. Time trace of axial dark core length. B. Time trace of curved dark core length.

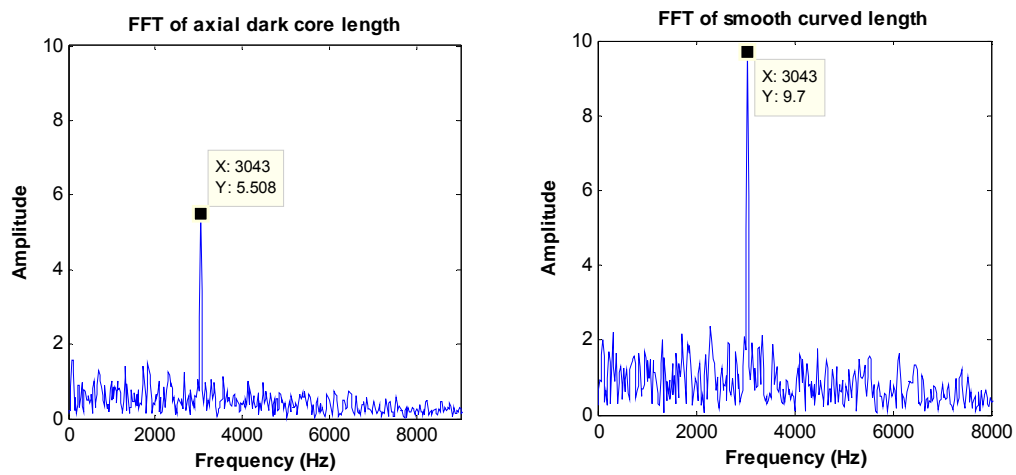


Figure 13. A. FFT of axial dark core length. B. FFT of curved dark core length

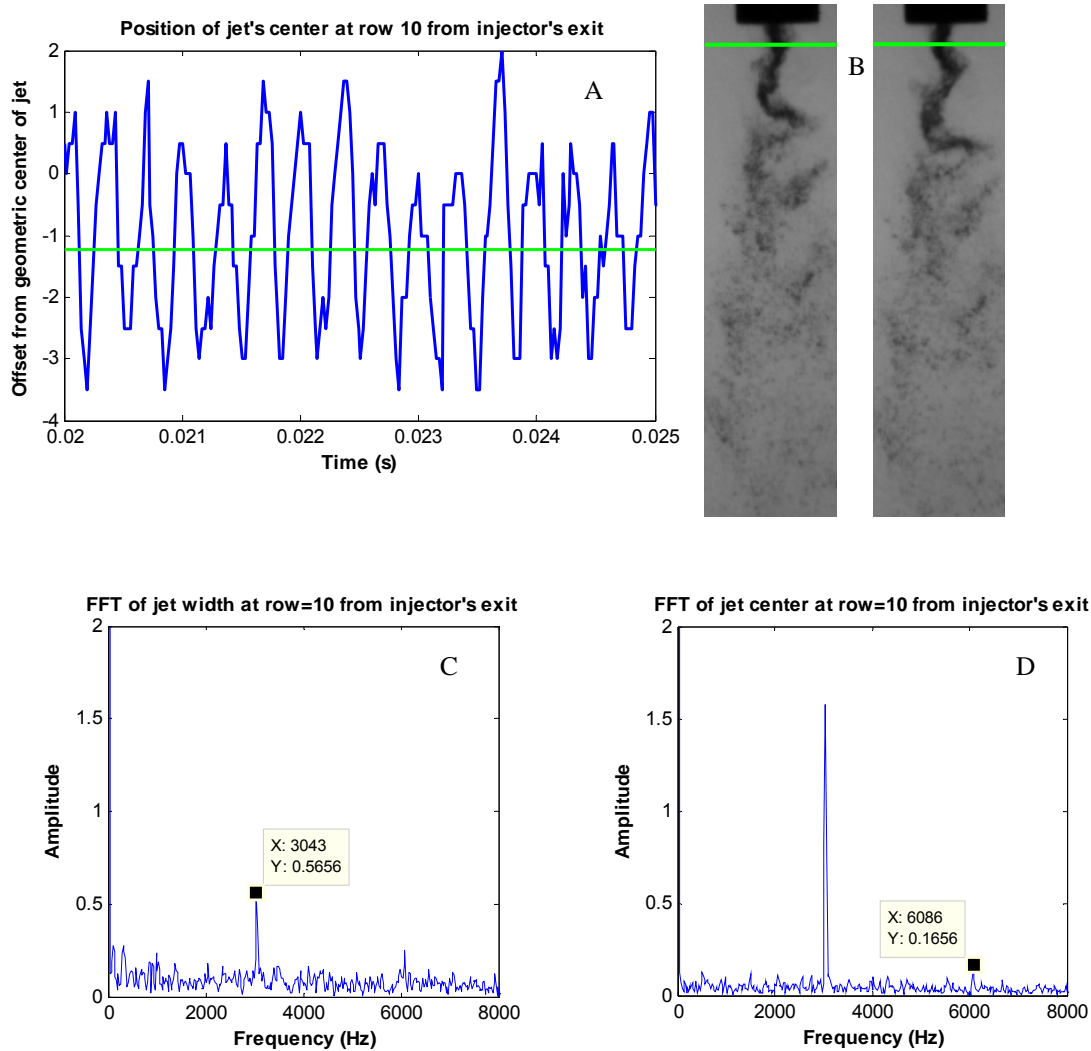


Figure 14. A. Sample of position of the inner jet's center with time at row 10 from injector's exit. B. Jet at two different times highlighting row 10 from injector's exit. C. FFT of jet width at row 10 from injector's exit. D. FFT of jet's center at row 10 from injector's exit.

V. Conclusion

An extensive study was carried out to characterize the effects of a transverse acoustic field on a coaxial jet spanning subcritical to supercritical chamber pressures. The main parameter used to assess the effects of the acoustics and operating conditions on the jet is the dark core length. Both the axial and the total, or curved, dark core lengths were investigated. In this study, at least 2000 images were taken at 41 kHz for each test condition giving more robust statistics such as the mean and the standard deviation of the dark core length than previously obtained (30 frames per condition at 10 Hz). The new data confirmed that the standard deviation of the axial dark core length decreases as VR increases. This trend was also observed in the curved or total dark core length

introduced in this paper. As the standard deviation decreases the jet becomes more insensitive to external fluctuations which can offer insight into why liquid rocket engine injectors designed to operate at $VR > \sim 10$ are more stable than those designed to operate at lower VR values. At subcritical pressures, the std. dev. of both lengths decreases when the acoustics are turned for a given MR and VR. For the near and supercritical pressure cases no conclusions can be drawn as the differences in the std. dev. mostly fall within the pixel resolution for these images. The current axial dark core length data falls within a band defined by $L = A/MR^n$, with the exponent being 0.2 (A:20-25) for subcritical pressures, and 0.5 (A:5-12) for near and supercritical pressures. With the exception of opening the band from A=20 to A:20-25 for subcritical pressures, the results agree with previous data.

A new key finding, resulting from the study of the total dark core length, is that for $\sim 1 < MR < \sim 4$, acoustics do shorten the dark core which implies that acoustics enhance mixing in this range. This answers the question of whether the acoustic field imposed on the jet only bends the jet or bends it and shortens it. For this range of MR's the differences in the curved lengths are larger than the error bars ($\pm \sigma$) in the data. This range is even larger for subcritical pressures. Outside this range the differences between the curved dark core length with and without acoustics fall within the statistical uncertainty of the measurements. Especially for $MR > \sim 4$ in the near and supercritical pressures, the core becomes small enough that the differences between acoustics on and off mostly fall within the resolution of the camera. Preliminary data is also presented to characterize the frequencies of the jet's movement in the transverse and axial directions. As one would expect, the frequency describing the transverse and axial movements of the jet is the same as the driving frequency of the acoustic field. Future work will include further characterization of the acoustic pressure field which will give a precise measurement of the acoustic pressure field for every test condition. Also, further frequency analysis of the jet, and variation of the position of the pressure and velocity nodes with respect to the jet center will be performed. This last part will allow us to see the effects not only of magnitude but also of gradient of the acoustic pressure and velocity on the jet's behavior.

Appendix

	SUBCRITICAL PRESSURE										
	HIGH OUTER JET TEMPERATURE										
	sb1	sb2	sb3	sb4	sb5	sb6	sb7	sb8	sb9	sb10	sb11
T chamber (K)	231	237	252	240	243	241	250	243	245	250	214
ρ chamber (kg/m ³)	22.4	21.1	19.9	21.1	21.0	20.8	20.3	20.9	20.6	20.1	24.0
P chamber (MPa)	1.51	1.46	1.47	1.49	1.49	1.47	1.49	1.49	1.48	1.48	1.49
P chamber (psia)	220	212	213	216	217	213	216	216	214	214	216
T outer (K)	181	195	175	180	181	195	184	189	181	181	184
\dot{m} outer (mg/s)	316	315	785	787	1270	1260	1620	1600	2410	2950	3680
ρ outer (kg/m ³)	29.6	26.2	29.8	29.2	29.2	26.4	28.6	27.5	28.8	28.8	28.5
u outer (m/s)	4.09	4.61	10.1	10.3	16.6	18.3	21.6	22.2	32.1	39.1	49.4
Re outer (x10 ³)	4.14	3.89	10.5	10.3	16.6	15.6	20.9	20.2	31.6	38.6	47.7
T inner (K)	110	109	110	109	110	110	110	110	110	110	110
\dot{m} inner (mg/s)	281	281	280	280	282	278	280	278	279	280	279
ρ inner (kg/m ³)	625	629	626	629	621	625	621	624	623	623	626
u inner (m/s)	2.21	2.21	2.21	2.20	2.24	2.19	2.22	2.20	2.21	2.22	2.20
Re inner (x10 ³)	12.4	12.3	12.4	12.2	12.7	12.3	12.6	12.4	12.5	12.6	12.4
VR	1.86	2.11	4.60	4.73	7.49	8.43	9.81	10.2	14.6	17.8	22.6
MR	0.164	0.185	1.01	1.04	2.64	3.00	4.43	4.59	9.87	14.6	23.3
Acoustics Off											
L/d1	24.0	22.7	16.5	18.1	18.2	17.5	15.9	15.7	12.9	10.9	6.89
L _T /d1	25.1	24.8	19.0	20.9	20.9	19.6	17.7	17.4	13.8	11.5	7.06
Acoustics On											
Frequency (kHz)	2.97	2.95	2.99	2.97	2.97	2.97	2.99	2.97	2.97	3.00	3.03
L/d1	18.2	17.4	8.90	8.79	8.05	7.47	7.86	8.28	7.71	9.31	6.43
L _T /d1	21.0	20.1	11.8	11.7	10.8	9.65	10.3	10.6	9.03	10.5	6.77

	SUBCRITICAL PRESSURE							NEARCRITICAL PRESSURE			
	LOW OUTER JET TEMPERATURE										
	sb12	sb13	sb14	sb15	sb16	sb17	sb18	nr12	nr13	nr14	nr15
T chamber (K)	233	221	228	234	213	213	213	216	210	215	209
ρ chamber (kg/m³)	21.5	23.3	22.1	21.5	23.9	24.2	24.1	58.7	60.3	58.7	60.5
P chamber (MPa)	1.46	1.49	1.48	1.47	1.47	1.50	1.48	3.57	3.54	3.54	3.54
P chamber (psia)	212	217	214	213	214	217	215	517	513	514	513
T outer (K)	157	112	146	148	148	144	154	138	143	157	141
\dot{m} outer (mg/s)	504	1170	1170	1860	1860	2320	3690	1410	3450	4040	5650
ρ outer (kg/m³)	33.9	61.0	37.8	37.1	37.1	39.1	35.2	130	115	94.3	121
u outer (m/s)	5.69	7.36	11.9	19.1	19.2	22.7	40.1	4.14	11.5	16.4	17.8
Re outer (x10^3)	7.36	21.7	18.1	28.5	28.5	36.3	54.6	19.1	47.0	53.6	77.0
T inner (K)	109	110	110	110	110	110	110	125	123	126	125
\dot{m} inner (mg/s)	284	281	279	281	279	278	280	291	292	286	287
ρ inner (kg/m³)	628	619	625	623	621	619	624	482	508	442	465
u inner (m/s)	2.23	2.24	2.20	2.23	2.21	2.22	2.21	2.98	2.84	3.19	3.05
Re inner (x10^3)	12.4	12.8	12.4	12.6	12.6	12.7	12.5	22.0	20.2	24.9	23.1
VR	2.58	3.31	5.43	8.66	8.74	10.3	18.3	1.40	4.09	5.17	5.89
MR	0.358	1.08	1.78	4.47	4.55	6.73	18.8	0.530	3.77	5.72	9.06
Acoustics Off											
L/d1	22.3	18.2	16.5	14.7	14.5	16.1	10.4	11.1	4.85	3.23	2.09
L _T /d1	24.1	21.2	19.1	16.0	16.6	19.0	10.9	11.7	4.80	3.50	2.52
Acoustics On											
Frequency (kHz)	2.96	3.04	3.06	3.07	3.05	3.04	3.02	3.12	3.11	3.13	3.13
L/d1	14.7	8.72	7.21	9.32	14.5	8.43	9.37	11.6	4.09	2.85	2.18
L _T /d1	17.1	11.3	9.17	12.1	16.6	11.2	10.2	13.0	4.19	3.22	2.68

	NEARCRITICAL PRESSURE – HIGH OUTER JET TEMPERATURE										
	ABOVE CRITICAL TEMPERATURE INNER JET							NEAR CRITICAL TEMP. INNNER JET			
	nr1	nr2	nr3	nr4	nr5	nr6	nr7	nr8	nr9	nr10	nr11
T chamber (K)	254	228	251	251	234	247	238	237	232	236	230
ρ chamber (kg/m ³)	47.6	54.8	49.2	48.8	53.1	49.8	51.9	51.7	52.5	54.3	53.6
P chamber (MPa)	3.52	3.56	3.58	3.54	3.56	3.55	3.54	3.53	3.56	3.55	3.56
P chamber (psia)	510	517	518	514	516	515	514	511	517	515	516
T outer (K)	194	179	179	186	171	192	195	182	189	184	194
\dot{m} outer (mg/s)	2030	3070	3130	3850	3950	4950	6120	802	3140	3140	3130
ρ outer (kg/m ³)	66.4	75.5	75.9	70.9	80.8	68.0	66.7	72.9	69.7	72.6	67.2
u outer (m/s)	11.7	15.5	15.8	20.8	18.7	27.9	35.1	4.21	16.51	17.8	17.22
Re outer (x10 ³)	23.8	37.9	38.7	46.4	50.1	58.5	71.8	9.81	38.2	36.8	37.4
T inner (K)	130	128	128	129	128	129	132	126	127	127	126
\dot{m} inner (mg/s)	289	290	289	290	288	287	286	287	288	288	288
ρ inner (kg/m ³)	167	213	244	182	230	190	157	422	319	416	420
u inner (m/s)	8.56	6.72	5.84	7.88	6.18	7.44	8.97	3.35	3.43	3.38	4.52
Re inner (x10 ³)	58.2	52.1	47.5	56.4	49.4	54.6	58.5	26.7	27.5	26.9	38.2
VR	1.37	2.33	2.72	2.66	3.05	3.77	3.94	1.26	3.89	4.88	5.32
MR	0.751	1.93	2.31	2.76	3.27	5.09	6.59	0.28	3.31	4.15	4.52
Acoustics Off											
L/d1	8.39	6.00	4.47	4.17	2.94	2.71	1.85	14.7	4.80	4.89	4.69
L _T /d1	9.48	6.14	4.86	4.07	3.35	3.23	2.47	16.6	5.23	5.17	5.10
Acoustics On											
Frequency (kHz)	3.00	2.99	3.05	3.05	3.01	3.06	3.05	3.06	3.01	3.02	3.00
L/d1	4.57	5.06	2.99	3.00	2.60	2.15	1.97	10.4	3.33	3.49	3.50
L _T /d1	6.00	5.91	3.57	3.01	3.05	2.87	2.58	12.0	3.88	3.88	4.06

SUPERCritical PRESSURE											
HIGH OUTER JET TEMPERATURE											LOW T
	sp1	sp2	sp3	sp4	sp5	sp6	sp7	sp8	sp9	sp10	sp11
T chamber (K)	240	251	241	245	234	232	236	225	236	227	209
ρ chamber (kg/m ³)	73.1	68.3	71.6	70.2	74.4	75.2	73.8	78.7	72.9	77.1	86.7
P chamber (MPa)	5.00	4.93	4.93	4.93	4.94	4.92	4.94	4.95	4.89	4.93	4.96
P chamber (psia)	725	715	715	714	716	714	716	718	709	715	719
T outer (K)	184	176	173	172	175	185	195	183	188	191	150
\dot{m} outer (mg/s)	1170	2800	2780	2810	4550	4240	5750	5810	7050	8140	4620
ρ outer (kg/m ³)	106	113	117	118	115	104	95.7	107	100	99.0	165
u outer (m/s)	4.23	9.46	9.09	9.10	15.2	15.7	23.0	20.9	26.9	31.5	10.7
Re outer (x10 ³)	13.5	32.9	32.9	33.3	53.6	48.8	64.6	67.3	80.9	92.5	54.6
T inner (K)	132	137	134	133	137	136	147	138	141	141	132
\dot{m} inner (mg/s)	293	294	291	293	296	295	295	292	293	293	294
ρ inner (kg/m ³)	416	266	342	373	271	302	179	264	214	216	423
u inner (m/s)	3.47	5.45	4.20	3.88	5.38	4.83	8.12	5.45	6.76	6.69	3.42
Re inner (x10 ³)	27.5	43.7	34.7	31.7	43.4	39.7	53.4	43.6	49.8	49.4	26.9
VR	1.23	1.75	2.18	2.36	2.85	3.27	2.86	3.86	4.01	4.74	3.15
MR	0.384	1.30	1.63	1.77	3.42	3.66	4.35	6.00	7.55	10.3	3.87
Acoustics Off											
L/d1	13.9	4.91	4.42	5.18	3.25	3.49	1.97	1.96	1.74	1.68	4.03
L _T /d1	16.4	5.12	5.35	5.45	3.46	3.64	2.11	2.17	2.17	2.12	4.08
Acoustics On											
Frequency (kHz)	3.10	3.11	3.29	3.26	3.26	3.22	3.08	3.19	3.08	3.05	3.10
L/d1	10.2	2.92	2.70	3.58	2.32	2.54	2.05	1.84	1.55	1.45	3.40
L _T /d1	12.2	3.18	3.38	3.92	2.65	2.85	2.09	2.12	2.06	2.06	3.45

Acknowledgments

The authors would like to recognize Randy Harvey for his invaluable contributions on running and maintaining the facility. Also thanks to Juan Rodriguez for preparing the appendix. This work is sponsored by AFOSR under Mitat Birkan, program manager.

References

1. Oswald, M., Smith, J. J., Branam, R., Hussong, J., Schik, A., Chehroudi, B., Talley, D., "Injection of Fluids into Supercritical Environments", *Combustion Science and Technology*, Vol. 178, No. 1-3, 2006, pp. 49-100.
2. Culick F. E. and Yang, V., "Overview of Combustion Instabilities in Liquid-Propellant Rocket Engines," *Liquid Rocket Engine Combustion Instability*, edited by V. Yang and W. Anderson, Progress in Astronautics and Aeronautics, AIAA, Washington, DC, 1995, pp. 3-38.
3. Muss, J., Chakroborty, S., Leyva, I. A., "Development of the Scorpion LOX/Kerosene engine family", *JANNAF 2005-0356*, 2nd Liquid Propulsion and 1st Spacecraft Propulsion Subcommittee Meeting, Monterey, California, December 5-8, 2005.
4. Marshall, W., Pal, S., Woodward, R., Santoro, R. J., Smith, R., Xia, G., Sankaran, V., Merkle, C. L., "Experimental and Computational Investigation of Combustor Acoustics and Instabilities, Part II: Transverse Modes"; *AIAA 2006-538*

5. Yang, V., Anderson W., editors, *Liquid Rocket Engine Combustion Instability*, Progress in Astronautics and Aeronautics, Vol. 169, 1995
6. Sutton, G. P., *Rocket Propulsion Elements*, Sixth Edition, John Wiley & Sons, Inc., NY, 1992
7. Davis, D. W., Chehroudi, B., "Measurements in an acoustically driven coaxial jet under sub-, near-, and supercritical conditions", *JPP*, Vol. 23, No. 2, March- April 2007
8. Davis, D. W., Chehroudi, B., Sorensen, I., "Measurements in an acoustically driven coaxial jet under supercritical conditions", *AIAA 2005-736*
9. REFPROP, Reference Fluid Thermodynamic and Transport Properties, Software Package, Ver. 7.0, NIST, U.S. Department of Commerce, Gaithersburg, MD, 2002.
10. Otsu, N., "A threshold selection method from gray-level histograms", *IEEE transactions on Systems, Man, and Cybernetics*, Vol. 9, No. 1, 1979, pp. 62-66.
11. Davis, D., "On the behavior of a shear-coaxial jet, spanning sub- to supercritical pressures, with and without an externally imposed transverse acoustic field", Ph.D. Thesis, Dept. of Mechanical Engineering, Penn State University, 2005.
12. Leyva, I. A., Chehroudi, B., Talley, D., "Dark-core analysis of Coaxial Injectors at Sub-, Near-, and Supercritical Conditions in a Transverse Acoustic Field", *54th JANNAF Meeting*, Denver, CO, May 14-18, 2007.

Preliminary Results on Coaxial Jet Spread Angles and the Effects of Variable Phase Transverse Acoustic Fields

Ivett A. Leyva¹, Juan I Rodriguez², Bruce Chehroudi³ and Douglas Talley⁴
Air Force Research Laboratory, Edwards AFB, CA 93524

An experimental study on the jet spreading angle of N₂ shear coaxial jets at sub-, trans-, and supercritical pressures is presented. The jet spreading angle is an important parameter which characterizes the mixing between two flows forming a shear layer. The present results are compared with previous experimental data, CFD results, and theoretical predictions. The angle measurements are made directly from at least 20 backlit images. The shear coaxial injector used here is similar to those used in cryogenic liquid rockets. The chamber pressure ranges from 1.5 to 5.0 MPa to span subcritical to supercritical pressures. The chamber to outer jet density ratio varies from 0.20 to 0.93 and the momentum flux ratio between the outer and the inner jet varies from 0.36 to 30. These ratios are mainly varied by changing the temperature and flow rates of the outer jet. For the range of conditions studied it is found that the tangent of the jet spreading angle is roughly constant and approximately 0.19 with standard deviation of 0.02. The value is lower than those predicted by different theories for 2D mixing layers of variable density for gaseous flows. The second part of the paper focuses on the initial results obtained by combining two piezo-sirens which generate a transverse acoustic field to excite the coaxial jet. The resonant frequency studied is ~3kHz and $\Delta P/P$ varies from 0.7 to 1.3%. These two acoustic sources can have an arbitrary phase between them so the position of the jet with respect to the pressure and velocity fields can be adjusted. The main parameter investigated is the length of the dark inner jet core. The initial results indicate an effect of the phase angle on the dark core length but the differences are statistically significant only in the extreme cases.

Nomenclature

D	=	diameter with subscripts
L	=	axial dark core length
L_t	=	total or curved dark core length
MR	=	outer to inner jet momentum flux ratio
VR	=	outer to inner jet velocity ratio
T	=	temperature
P	=	pressure
Subscripts		
ch	=	chamber
v	=	visual (jet spreading angle)
w	=	vorticity (jet spreading angle)
OJ	=	outer jet
IJ	=	inner jet

¹ Lead, Combustion Group, AFRL/RZSA, Edwards AFB, CA 93524, AIAA Senior Member.

² Graduate Student, UCLA/ AFRL, Edwards AFB, CA 93524, AIAA Student Member.

³ Principal Scientist, ERC Inc., AFRL, Edwards AFB, CA 93524, AIAA Member.

⁴ Sr. Aerospace Engineer, AFRL/RZSA, Edwards AFB, CA 93524, AIAA Member.

Approved for public release; distribution unlimited. PA #07462A.

I. Introduction

COAXIAL jet flows are of great interest to the rocket community because they are widely used in liquid rocket engines LRE's (e.g. Space Shuttle Main Engine (SSME)). A key advantage of coaxial jets is that as the Momentum Flux Ratio (MR) between the outer jet and the inner jet increases mixing between the two jets increases and mixing to certain uniformity can be obtained in relatively short distances from the exit plane. As LRE's have evolved into higher specific impulse designs with chamber pressures reaching supercritical values for some propellants, it is important to characterize coaxial flows at conditions spanning sub to supercritical pressures. The SSME and the Vulcan engine for the Ariane 5 launch vehicles are examples of LRE's designed to operate above the critical pressures of each propellant individually. In a typical application of a coaxial injector for a LOX/LH2 engine, the oxygen is injected at subcritical temperatures in the center jet while the hydrogen is injected at supercritical temperatures, after being used as a coolant for the engine nozzle, in the coaxial jet. A typical velocity ratio between the outer and inner jets is about 10^1 . For these flows, the mixture no longer has a singular critical point but rather there are critical mixing lines that define its thermodynamic state¹. Because of the added complexity introduced when working with mixtures, N_2 is used as the sole working fluid in this study.

The growth of shear layers between two planar flows has been studied for decades since the rate of growth of the shear layer is indicative of the mixing process between the two layers. Of relevance here is the work of Brown and Roshko², who proposed an equation for the growth rate of the shear layer for subsonic two-dimensional incompressible turbulent gas-gas flows. Papamoschou and Roshko³ also proposed an equation for the growth of the visual thickness of the shear layer for sub- to supersonic two-dimensional turbulent mixing layers. Dimotakis⁴ proposed an equation for the vorticity growth rate of a planar freejet. Chehroudi et. al.⁵ performed a comprehensive experimental study of single round jets at sub to supercritical pressures. They also compiled experimental data from different researchers presenting a data set that spans four orders of magnitude in the ratio of the chamber density to the jet density, which is the relevant parameter for single jets ejecting into a quiescent environment. He showed for the first time that for jets at supercritical pressure and temperature, the spreading angle agrees quantitatively with that predicted by the works mentioned above which were derived for incompressible variable-density gas-gas jets. The data from the present study will be compared to the above mentioned body of work.

The second part of the paper is focused on the effects of both the magnitude and phase of the acoustic pressure and velocity field on the coaxial jet flow. So far in the previous experiments performed in this lab there was one acoustic resonator at one end of the test chamber and a non-movable reflective wall at the other end. This meant that the relation of the position of the jet with respect to the acoustic wave profile was fixed. The amplitude of the pressure oscillations could be varied but to achieve the highest ratios of acoustic pressure vs. mean chamber pressure the custom was to run at the highest magnitude possible. By adding a second identical resonator the magnitude and relative position of the jet with respect to the pressure and velocity acoustic field can now be varied. We chose to start this study at subcritical pressures with $MR \sim 1$ and 3 since we found in previous studies by Leyva et. al.^{6,7} that the effects of acoustics on the dark core length were greatest at subcritical pressures and for $1 < MR < 4$. The length of the dark core, both the axial length and the total or curved length are the first metric we studied for this problem.

II. Experimental Setup

These experiments were carried out at the Cryogenic Supercritical Laboratory (EC-4) at the Air Force Research Laboratory (AFRL) at Edwards Air Force Base, CA. An overview of the facility is shown in Fig. 1. The setup with only one acoustic source is shown in Fig. 1A and the new setup with two acoustic sources is shown in Figure 1B. For either configuration, gaseous N_2 is used to supply the inner and outer jet flows and to pressurize the chamber. The outer and inner jets are cooled by two or three heat exchangers (HE's) depending on the plumbing configuration run. The coolant for both the inner and outer jet is liquid nitrogen obtained from a cryogenic tank. One heat exchanger cools the inner jet and the other two cool the outer jet. The temperature (T) of the two jets is controlled by adjusting the flow rate of liquid nitrogen through the HE's. The mass flow rate through the inner and outer jets is measured, before they are cooled, with Porter mass flow meters (122 and 123-DKASVDAA). It was found that it is much easier to measure the flow rates at ambient rather than at cryogenic temperatures. The chamber pressure is

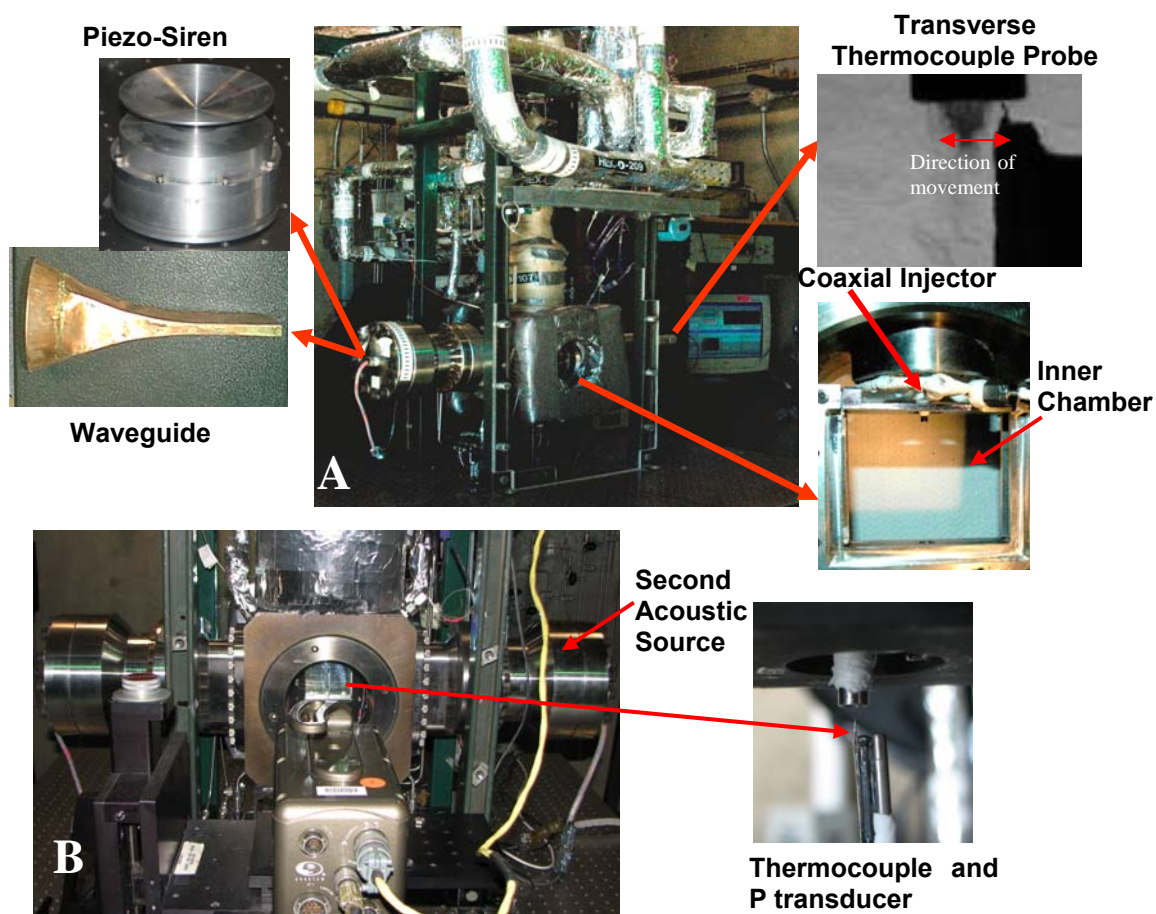


Figure 1. Overview of the Supercritical Flow Facility, EC-4 at AFRL/Edwards used for this study. A. Configuration with one acoustic source. B. Two acoustic sources.

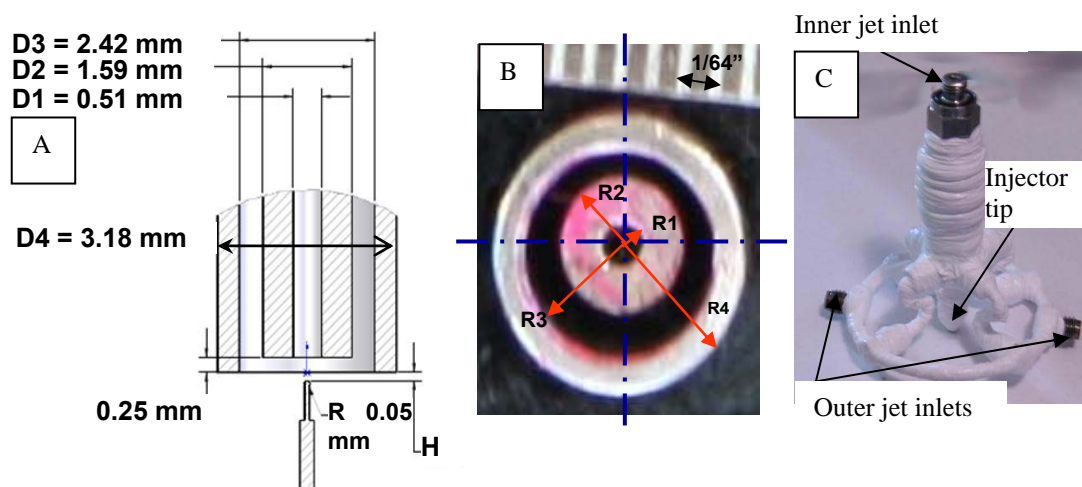


Figure 2. Details on the coaxial injector used for the present study

measured with a Stellar 1500 transducer. To keep the amplitude of the acoustic oscillations to a maximum near the jet, an inner chamber was created (Fig. 1). The inner chamber has nominal height of 6.6cm, width 7.6cm and depth 1.3cm. Details for the coaxial injector used are shown in Fig. 2. The inner diameter of the inner jet, D_1 , is 0.51 mm. The outer jet has an inner diameter, D_2 , of 1.59 mm and outer diameter, D_3 , of 2.42 mm. The length to inside diameter ratio is 100 for the inner jet and 67 for the outer jet (taking as reference the mean width of the annular passage). There is a small bias of about 8% of the mean gap width. The inner jet is recessed by 0.3 mm from the outer jet.

The temperature of the jets is measured with an unshielded type E thermocouple which has a bead diameter of 0.1mm. The accuracy of this thermocouple was checked with an RTD and found to be ± 1 K. With only one acoustic generator present the thermocouple is traversed across the outer and inner jets to obtain a reading as close as possible to the injector exit plane (also seen in Fig. 1A). The average distance from the exit plane, denoted H in Fig. 2 is ~ 0.3 mm. However for the case where two acoustic sources are present the thermocouple is introduced from the bottom of the chamber so it can get as close to the exit plane as possible. In fact, the thermocouple can measure the temperature within the recess of the inner jet. As can be seen from Fig. 1B a Kulite XQC-062 pressure transducer is used to measure the pressure at a sampling frequency of 20kHz. Both the pressure transducer and the thermocouple are moved in the plane perpendicular to the jet axis with a piezo positioning system built by Atto cube which can move a total distance of about 3mm in 1 dimension. Properties such as density, viscosity, and surface tension are computed from the measured flow rates, chamber pressure and jet temperature, using NIST's REFPROP⁸. From this, the Re , We , VR and MR for a given condition can be computed.

The jet is visualized by taking backlit images using a Phantom 7.1 CMOS camera. The images have 128x256 pixels or 128x200 pixels, and each pixel represents an area of about 0.08mmx0.08mm. The framing rate was either 20kHz or 41kHz. The exposure time varies from 1-9 μ s. The jet is backlit using a Newport variable power arc lamp set at 160 or 300W. The acoustic waves are generated using one or two piezo-sirens custom-designed for AFRL by Hersh Acoustical Engineering, Inc. (Fig.1). For these acoustic sources a piezo-ceramic element is externally excited with a sinusoidal wave at the desired driving frequency for the system. This frequency is chosen by manually varying the frequency on a signal generator until the highest amplitudes for the pressure waves are obtained. This signal is amplified and then fed to the piezo-siren. The movement of the piezo element is transmitted to the aluminum cone attached to it, and the cone then produces acoustics waves. To accommodate for the rectangular chamber a waveguide with a catenary contour is used to guide the waves from a circular cross-section to a rectangular cross-section (also shown in Fig.1). The RMS of the acoustic pressure oscillations in the inner chamber ranges from ~ 1.5 to 3 psi at ~ 3.0 kHz.

III. Results and Discussion

A. Outer Jet Spreading Angle

The data for the spreading angle consists of 19 experimental data points spanning chamber pressures from 1.5 to 5.0 MPa. For reference the critical P and T for N_2 are 3.40 MPa, and 126.26 K respectively. The details of the test conditions are presented in the Appendix. A summary of the range of conditions tested is shown in Table 1. From these conditions one can see that at the subcritical pressures, the inner jet temperature is either a few degrees below or at the saturation temperature and the outer jet is a gas, therefore we have a two-phase coaxial flow exiting into a quiescent gas. For the other two pressures, both the inner and the outer jet are in the supercritical region and therefore these are one-phase coaxial flows issuing into a stagnant supercritical fluid. Even though both gas-gas and supercritical-supercritical flows are one-phase flows we want to distinguish between them since in this work we do not have gas-gas coaxial jets, which is what most people have reported in the literature for coaxial jets. The jet spread angle between the outer jet and the chamber was measured directly from the backlit images. At least 20 images were measured manually by two people. It was found that for most cases the jet does not start growing from the exit plane. In fact, for most cases there the jet starts to spread a few D_1 downstream of the exit plane. This is attributed to the recirculation zone created by the thick post of the inner jet. This recirculation zone has been seen experimentally and in the computations performed by Liu et. al.⁹ who modeled two test conditions performed in our

lab. The spreading angle reported here is measured from the point where the jet starts to grow (~2 to 4 D1 downstream of the exit plane) to 10D1. Therefore this can be interpreted as an initial spread angle. Figure 3 shows a typical image and how the spreading angle is measured. Only α_1 and α_4 are visible and measured. The angles α_2 and α_3 although part of the shear layer are not visible in the backlit images. They are indicated to complete a conceptual picture required to compare the measurements with theoretical predictions as will be shown later.

Table 1. Summary of range of conditions for each pressure range

Mean Chamber pressure, P (MPa)	Outer to inner jet Velocity ratio, VR	Outer to inner jet momentum flux ratio, MR	Mean inner jet mass flow rate (mg/s)	Mean Chamber temperature (K)	Mean Inner jet temperature (K)	Mean Outer jet temperature (K)
1.49	3.3 – 27	0.4 – 30	281	235	109	199
3.55	1.4 – 5.9	0.5 – 9.0	289	213	125	145
4.93	0.92 – 4.7	0.6 – 10.	293	229	137	173

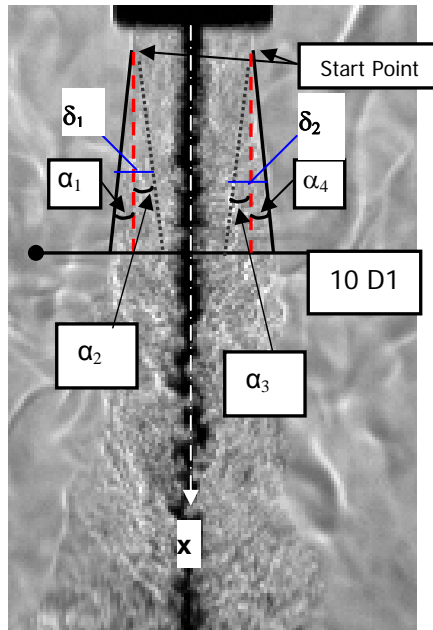


Figure 3. Typical image (from condition sub 7 in the Appendix) showing how the spreading angle is measured

There is very little previous work that we found directly in the area of spreading angles for shear coaxial jets, especially for cases where the exit pressures are much higher than atmospheric like in our case. Therefore, we first looked at the coaxial jet in a simplified form, which is consistent with the few data available for coaxial jets. We treat the outer jet/chamber shear layer as independent of the inner/outer jet shear layer. We then compare the outer jet/chamber shear layer with equation proposed for 2D shear layers and with axisymmetric single jets.

Furthermore, since the outer jet exits into a quiescent atmosphere, we first compare the data to single jets exiting into a quiescent atmosphere. Let's first take a look at how we measure the angles and relate them to theories for the visual growth of the shear layer $\frac{d\delta_v}{dx}$. If we look at Fig. 3 again, we see that for each of the two edges of the shear

layer seen in the backlit images (subscripts 1 and 2), we have for the visual growth of the shear layer δ_v (the v subscript is omitted for simplicity):

$$\frac{d\delta_1}{dx} = \delta'_1 = \tan(\alpha_1) + \tan(\alpha_2) \quad \text{and} \quad (1)$$

$$\frac{d\delta_2}{dx} = \delta'_2 = \tan(\alpha_3) + \tan(\alpha_4) \quad (2)$$

If all the angles are the same, then $\delta'_1 = \delta'_2 = 2 \tan(\alpha_1)$. However, from the experiments we know this is not the case. The approximations we make by not measuring the four angles are as follows. First we can assume that $\alpha_1 \approx \alpha_2$ and $\alpha_3 \approx \alpha_4$ then for small angles we have,

$$\overline{\frac{d\delta}{dx}} \approx \tan(\alpha_1) + \tan(\alpha_4) \quad (3)$$

Where $\overline{\frac{d\delta}{dx}}$ is the mean value of the two measured shear layer thickness derivatives. On the other hand, a lot of literature reports the tangent of the total included angle ($\alpha_1 + \alpha_4$). We start again with equations (1) and (2) and assume all the angles to be small enough such that the approximation $\tan(\alpha) \approx \alpha$ applies. We also assume that $\alpha_2 = R_{12}\alpha_1$ and $\alpha_3 = R_{34}\alpha_4$. Then, accounting for possible asymmetries of the shear layers (for example Abromovich¹⁰ found $R \sim 0.6$ for plane jets exiting into a quiescent atmosphere) we have,

$$2 \overline{\frac{d\delta}{dx}} \approx (1 + R_{12})\alpha_1 + (1 + R_{34})\alpha_4 \quad (4)$$

Since we have not found a theory to describe how R_{12} and R_{34} might differ from each other, for simplicity we assume them to be the same and equal to R since both shear layers have the same mean conditions. We then take the tangent of both sides and we obtain,

$$\tan(\alpha_1 + \alpha_4) \approx \tan\left(\frac{2}{1+R} \overline{\frac{d\delta}{dx}}\right) \approx \tan\left(c \overline{\frac{d\delta}{dx}}\right) \quad (5)$$

Here the only source of uncertainty is the value of R . For $0.6 < R < 1$, $1 < c < 1.25$. For simplicity, if we assume that $R = 1$ then

$$\tan(\alpha_1 + \alpha_4) \approx \tan\left(\overline{\frac{d\delta}{dx}}\right) \quad (6)$$

This equation is equivalent to equation (3) for small angles.

Now let's look at Fig. 4 which is a compilation of experimental data done by Chehroudi et. al.⁵ on single jets with the current data and other data available for coaxial jets added. In this case the tangent of the total jet divergence angle is plotted against the chamber to injectant (single jets) or chamber to outer jet (coaxial jets) density

ratio. The data taken by Chehroudi for single jets in the same AFRL facility is marked by (*) in the legend. The coaxial jet data is labeled as Subcritical, Transcritical and Supercritical P. The first thing to notice is that there is little overlap on the ranges of (ρ_{ch}/ρ_{OJ}) for the coaxial and single jets. Also, the current data is consistently lower than the rest of data. We will look to that in more detail. It is useful to look in detail to some of the theoretical expressions presented in this figure. The first one is the prediction for the jet spreading angle made by Papamoschou and Roshko³ for incompressible variable-density mixing layers. Even though this is for planar jets, Brown and Roshko² argue that the shear layer growth for a planar shear layer is approximately the same as for axisymmetric jets in the near field close to the injector exit plane. In their work³, they proposed,

$$\delta'_v = 0.17 \left(\frac{\Delta U}{U_c} \right) = 0.17 \left(\frac{U_1 - U_2}{U_c} \right) \quad (7)$$

where U_c is a convective velocity given by $U_c = (U_1 \sqrt{\rho_1} + U_2 \sqrt{\rho_2}) / (\sqrt{\rho_1} + \sqrt{\rho_2})$ and the subscripts 1 and 2 refer to the two different mixing layers. That is, the visual shear layers are predicted to grow linearly with the delta U between the jets divided by a convective velocity which takes into account the density of the different jets. The constant 0.17 was obtained from the earlier work of Brown and Roshko². The second equation used is not directly for the visual growth rate but rather for the vorticity growth, δ'_w , derived by Dimotakis⁴,

$$\delta'_w = \varepsilon \left(\frac{1-r}{1-s^{1/2}r} \right) \left[1 + s^{1/2} - \frac{1-s^{1/2}}{1+2.9(1+r)/(1-r)} \right] \quad (8)$$

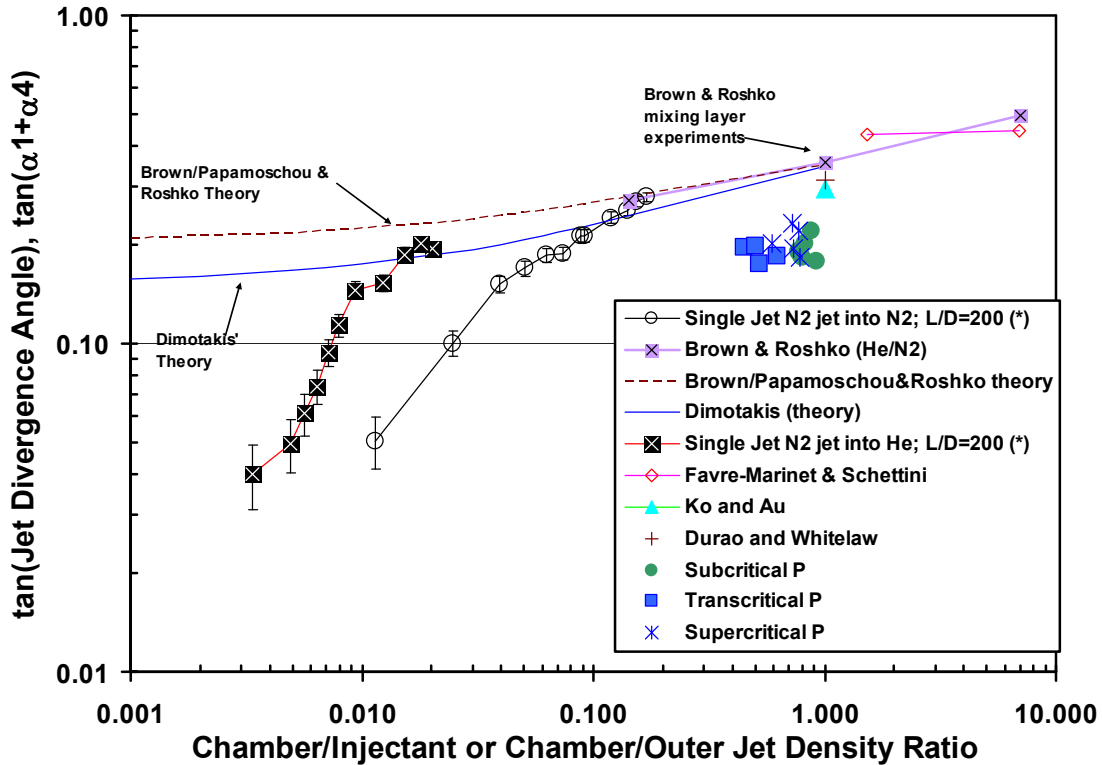


Figure 4. Spreading rate of the shear layer versus the chamber/injectant or chamber/outer jet density ratio for single and coaxial jets compared with different predictions for planar shear layers.

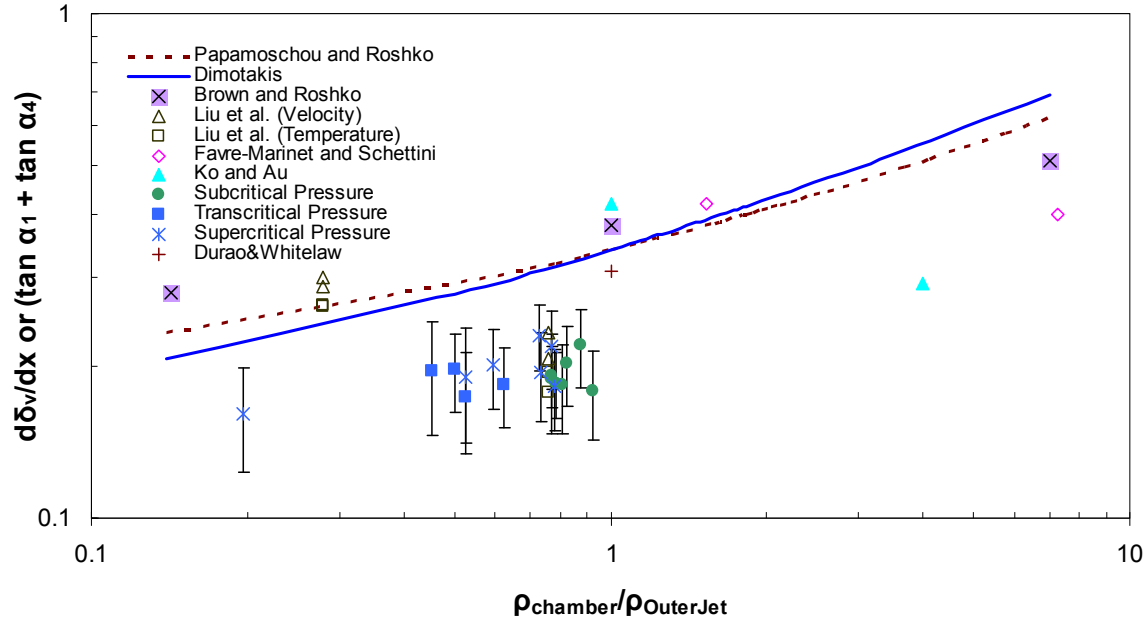


Figure 5. Spreading or growth rate of the shear layer versus the chamber-to-outer jet density ratio for coaxial jets compared with different predictions for planar shear layers with error bars.

where $r = U_2 / U_1$ and $s = \rho_2 / \rho_1$. It has been proposed^{2,3} that $\delta'_v = 2\delta'_w$. For the case of round jets, Chehroudi et.al.⁵ took $\varepsilon = 0.17/2$. Notice again that if U_2 / U_1 is zero δ'_w also becomes a function of ρ_2 / ρ_1 only. Brown and Roshko² also proposed for variable density planar mixing layers:

$$\delta'_v = A \left(\frac{U_1 - U_2}{U_1 + U_2} \right) \quad (9)$$

where A is 0.51, 0.38, and 0.28 for ρ_2 / ρ_1 being 7, 1, and 1/7 respectively. For the case of $U_2 = 0$ (quiescent condition), this reduces to three constants for the different ratios in density.

Now let's look at the present data. Fig.5 shows only coaxial data compared with the same theoretical predictions with error bars. Because the horizontal axis is the ratio of the chamber to the outer jet density, and since the chamber temperature and the outer temperature don't change very much within a given pressure range, then the data points run at sub, trans and supercritical pressures are reasonably well "separated". The data points from Liu et al.⁹ are the results of their CFD analysis and were made from velocity and temperature mean profiles (color contours) found in their paper. The velocity contours included lines of constant velocity which made it easier to approximate the edge of the outer jet. The temperature profiles didn't have such lines so that measurements have larger uncertainty. However, these are presented here since they follow our experimental results closely and are the only data we were able to find so far on coaxial flows at supercritical conditions. The experimental data from Favre-Marinet et. al.¹¹ were made from density profiles in a variable density coaxial jet arrangement. The data from Ko & Au¹² and Durao & Whitelaw¹³ are for gas-gas coaxial jets with density ratio of one and both are velocity based. Branam & Mayer¹⁴ published a study where they compared different techniques to measure the shear layer growth angle for single round jets including supercritical conditions. They compared the results obtained from Raman and shadowgraph measurements with density profiles (50% ρ , 99% ρ), temperature profiles (50% T , 99% T) as well as

computational velocity profiles (50% u , 99% u). They found that the differences between visual measurements and the 99% u , 99% T , and 99% ρ averaged to about 11%, 19% and 13% respectively. As different profiles are being used to estimate the spreading angle this provides a reference to assess the degree of agreement of the collected coaxial jet experimental and computational data with the one obtained here. The data presented here is fairly constant across the range of conditions studied with a mean growth rate value of 0.19 and a standard deviation of 0.02. The differences with other data (except Liu et al.⁹) is more than 50% which is more than the differences expected due to the different measurement techniques use. One difference between these data and the others we compare against is that the thickness of the inner post is unusually large which affects the initial growth of the outer jet due to the large recirculation zone created downstream of the inner jet exit plane (recessed from the outer jet in this case). Also, while the data from other researchers is from gas-gas jets issuing into a gas, our data is liquid/gas at subcritical pressures issuing into a stagnant gas and one-phase at supercritical pressures issuing into a supercritical stagnant fluid. We will run gas-gas-gas conditions next in our lab and will show the results in a later paper.

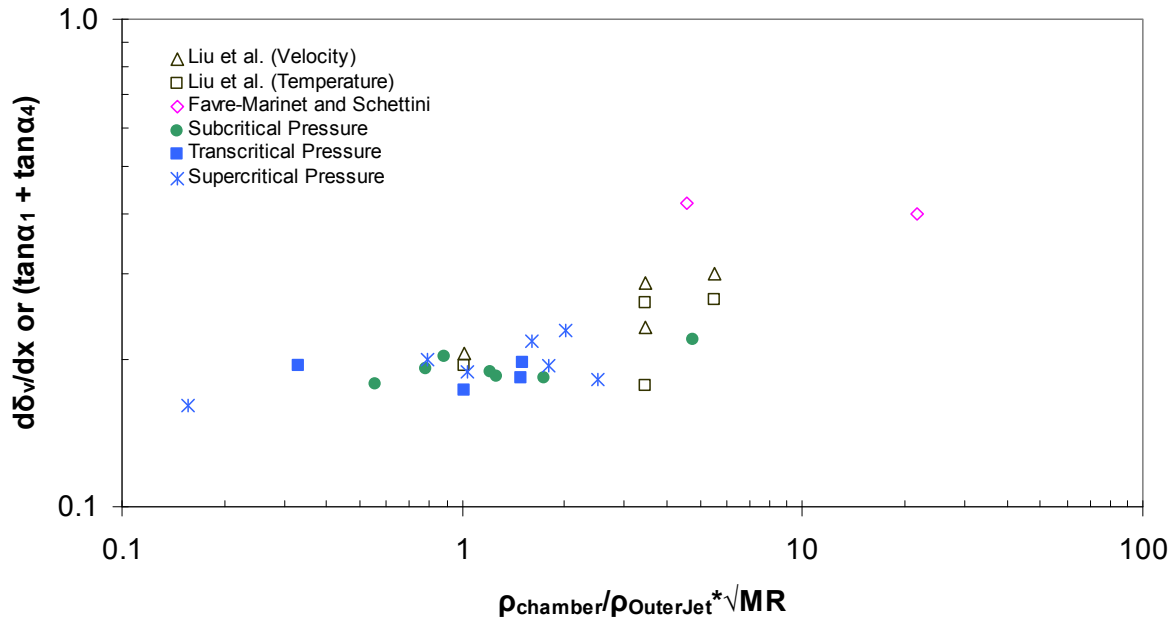


Figure 6. Spreading or growth rate of the shear layer versus the chamber-to-outer jet density ratio* MR for coaxial jets compared with other experimental and CFD data.

Finally, we present the same data in a different light considering the effects of the momentum flux ratio between the inner and outer jets. Figure 6 shows the spreading angle, or $\tan(\alpha_1) + \tan(\alpha_4)$ versus a parameter that includes effects from the outer and inner jet and the chamber, namely the ratio ρ_{ch} / ρ_{OJ} which is the main parameter controlling the shear layer growth into quiescent environment multiplied by the square root (sq. rt.) of MR. MR was chosen because it has been shown before^{6,7,15} to be an important parameter controlling the mixing between the two jets. Also, it has been shown^{6,7,15} that the length of the potential dark core grows approximately as the sq. rt. of the MR. Finally, the sq. rt. preserves the effects of the outer jet density in the proposed variable, which we believe is important for these cases. What stands out in this plot is that no longer are the different chamber P regimes in different regions of the x-axis. In fact, we have conditions at different chamber pressures that have the same value of $\rho_{ch} / \rho_{OJ} * \sqrt{MR}$ and give the same value for $[\tan(\alpha_1) + \tan(\alpha_4)]$. Since all the values for $[\tan(\alpha_1) + \tan(\alpha_4)]$ obtained here are more or less constant we didn't expect to uncover any trends with the new x-variable. However, the new variable has relocated the rest of the data from other researchers in such a way that an

upward trend of the shear layer growth with the variable $\rho_{ch} / \rho_{OJ} * \sqrt{MR}$ seems to be emerging. Needless to say that additional work would be needed to confirm such a trend.

B. Dark Core Length with Two Acoustic Sources On

The second part of this paper concerns preliminary results obtained by transversely exciting the coaxial jet with two identical acoustic wave generating sources whose relative phase can be changed arbitrarily. Referring back to Fig. 1B which shows the two acoustics sources on the chamber, when the two sources have a zero degree phase angle, then the movement of the cones themselves could be described as “towards each other” as presented in Figure 7. At the other extreme, when the two sources are at 180 deg out of phase, then the motion could be seen as “chasing” each other. For all the cases, only the phase of the right resonator is changed with respect to the left resonator. Also, the two acoustic sources are fed with constant voltages throughout the phase changes. As mentioned earlier, we selected to start with two cases in the subcritical pressure regime based on previous experiments^{6,7} which have shown that the greatest effect of acoustics, for the range of conditions studied in our lab, is for subcritical pressures. Within this regime the greatest percentage of reduction of the dark core length when the acoustics were turned on was for $1 < MR < 4$. Therefore, we started with $MR \sim 1$ and $MR \sim 2.6$. Sample images from the case Sub8 ($MR \sim 2.6$) at the different phase angles is presented in Fig. 8. The “no-acoustics” case is the baseline case with both sources off. When the two sources are on and in phase, the injector is located at a pressure antinode (since it is in the middle between the two sources) and the injector sees the least acoustic velocity perturbations. As the figure shows, the acoustic effects start to be visible in terms of the added bending to the inner jet and the growth of spreading angle. Notice that both the inner and outer jet bend with the acoustic field. The bending of the inner jet and outer jets continues to amplify, along with the spreading angle and shortening of the dark core, from 45 deg through 135 deg, reaching the most dramatic results at 135-180 deg. At 180 deg phase difference the dark core length is smallest. The trends reverse as we continue to change the phase angle from 180 deg to 360 deg (0 deg).

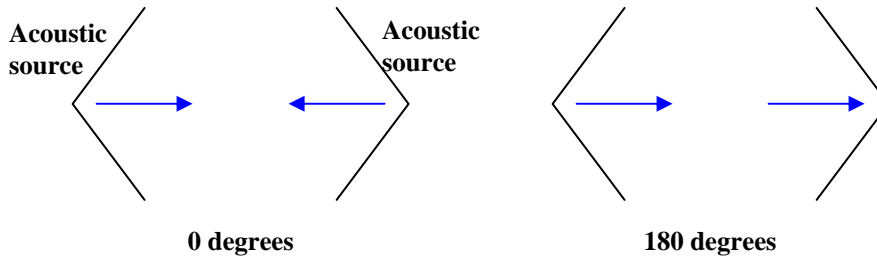


Figure 7. Schematic of the two acoustic sources at with phase angles of 0 and 180 deg between them.

The dark core lengths for cases sub7 ($MR=1.0$) and sub8 ($MR=2.6$) are shown in Figs. 9 and 10. The definitions used and techniques employed to measure the axial and curved dark core length are explained in detail in Leyva et. al.⁷ The dark core lengths are measured from at least 1000 images automatically using a matlab subroutine based on the Otsu¹⁶ technique to find a grayscale threshold which separates the inner core from the rest of the image. The axial length is the projection of the core onto the axial axis and the curved length is the total length of the core which takes into account the curvature produced by the acoustic excitation.

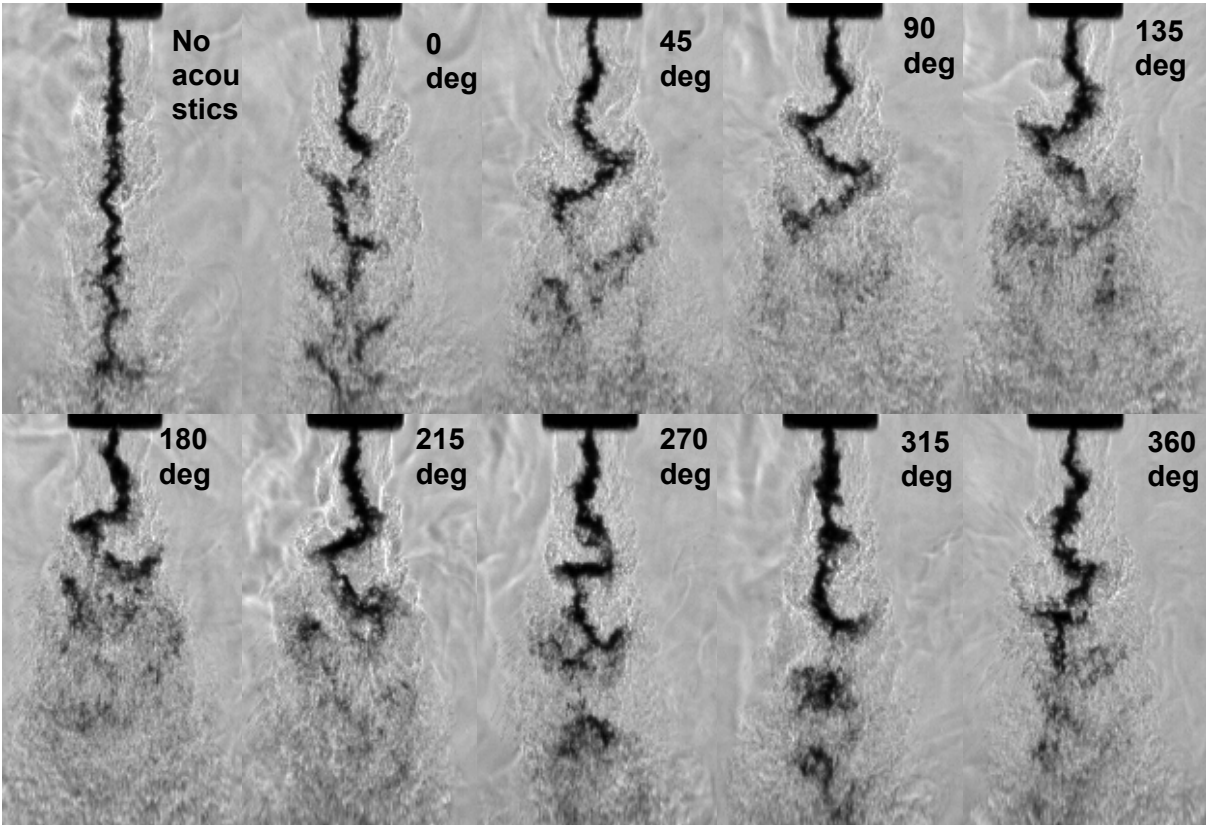


Figure 8. Sample images from Case Sub 8 with different phase angles between the two acoustic sources

As can be noted from Figs. 9 & 10, while there seems to be a periodic variation on the dark core as the phase angle between the two signals changes from 0-360 deg, most of the data falls within the error bars (± 1 standard deviation) and therefore we can't definitely say that such a trend exists. As we would expect the dark core length is longest when there are no acoustic disturbances as also seen in Fig. 8. Next, when one acoustic source is turned on the dark core length decreases as observed in previous studies. For the case of Fig. 10 for the plot of AxialL/D there is a statistical difference between the baseline case with no acoustics and the case with 180 deg phase difference, which also corresponds to the lowest acoustic $\Delta p/p$ measured ($\sim 0.7\%$). Here Δp is the RMS value of the pressure fluctuations.

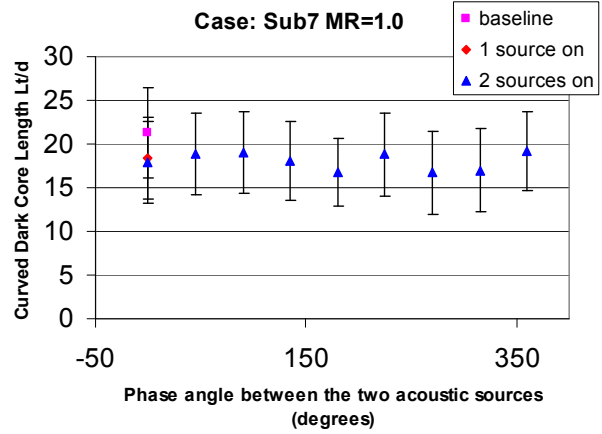
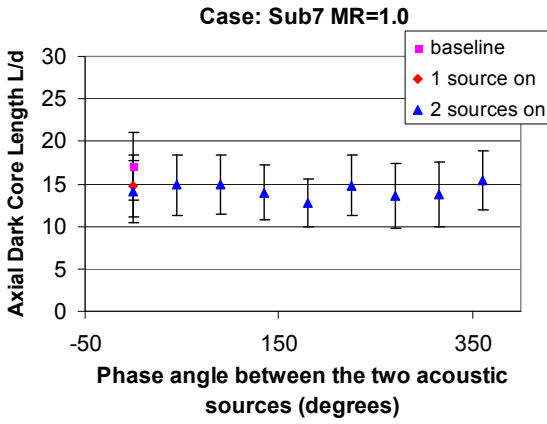


Figure 9. Variation of the axial and curved dark core length for subcritical pressure and $MR=1.0$ as a function of the phase angle between two acoustic resonators.

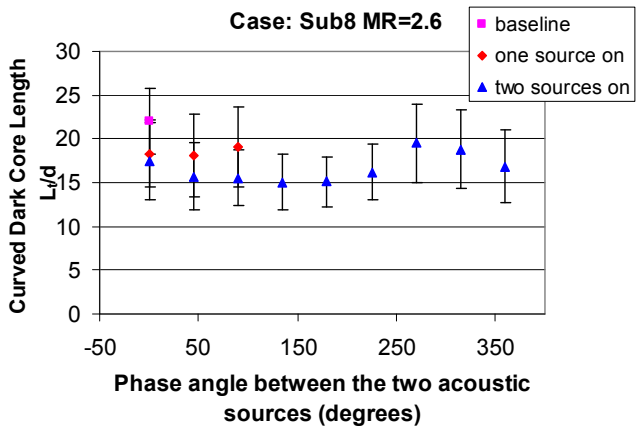
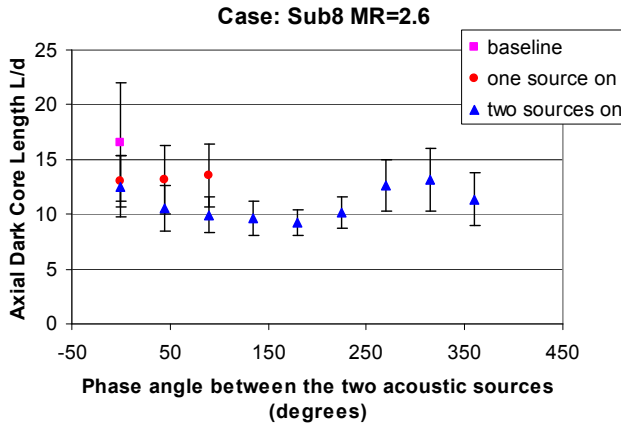


Figure 10. Variation of the axial and curved dark core length for subcritical pressure and $MR=2.6$ as a function of the phase angle between two acoustic resonators

For the same case the maximum dark core occurs at around 315 deg, corresponding to $\Delta p/p \sim 1.2\%$. These changes in $\Delta p/p$ are entirely due to the phase angle since the driving voltage for the two sources is constant throughout the phase sweep. Since the dark core is the longest here, one can say that the acoustics had little impact on the mixing of the two layers. We expect this to be close to a pressure antinodes and therefore to have the weakest acoustic velocity field. This implies, as one would expect that the maximum effect of the acoustic field on the jet mixing is through the velocity field and not the pressure field. This is furthered corroborated by the fact that in the set up with one acoustic resonator the jet was positioned near the pressure node for the same frequency used with two sources. For that case when the acoustics were turned on, we obtained about the same difference in the core

length as the difference observed here between the baseline case and the case at 180 deg. A more thorough study is underway where the pressure will be changed to trans and supercritical values and more MR values will be run.

IV. Conclusions

Extensive experimental data was presented on the growth rate or spreading angle of the outer jet of a coaxial jet flow exiting into a quiescent atmosphere. N_2 was used for both the inner and outer jets and the chamber environment. The chamber pressure varied from 1.5 to 5.0 MPa. When the chamber pressure is subcritical the flow is two-phase (liquid core and gaseous outer jet) and when the pressure is supercritical both jets are in the supercritical regime and we have one-phase flow. It was found that the near-field outer jet spreading angle for all cases was fairly constant (mean=0.19 with standard deviation of 0.02). This value was compared with theoretical predictions obtained for 2D shear layers of variable density flows for gaseous flows and with other experimental data for single jets and coaxial gas-gas jets issuing into a gas. The growth rate or spreading angle for the present data is consistently lower than the theoretical predictions and the other experimental data for coaxial jets. An important difference might be the thickness of the inner jet tube, which produces a big recirculation zone directly downstream of the inner jet exit plane and might have a significant effect on the outer jet spreading angle. The second part of the paper presented preliminary data on the effects of varying the phase angle between two acoustics sources that transversely excite the coaxial jet at subcritical pressures. In effect, what is varying is the magnitude and phase of the velocity and pressure field at the location of the jet. The acoustic frequency is about 3 kHz. The level of the acoustic $\Delta p/p$ was between 0.7 to 1.3 % depending on the phase between the two acoustic sources. It was found that the dark core length is shortest for the lowest amplitudes of $\Delta p/p$. This implies that the maximum enhancement on mixing, and hence decrease on the dark core, corresponds to maximum acoustic velocity fluctuations. An experimental investigation is also underway to thoroughly study these effects.

Appendix

Table A1. Properties of the coaxial jets of the cases presented in this study

	T_{chamber} (K)	ρ_{chamber} (kg/m ³)	P_{chamber} (MPa)	T_{outer} (K)	\dot{m}_{outer} (mg/s)	ρ_{outer} (kg/m ³)	u_{outer} (m/s)	T_{inner} (K)	\dot{m}_{inner} (mg/s)	ρ_{inner} (kg/m ³)	u_{inner} (m/s)	VR	MR	$\tan \alpha_1$ + $\tan \alpha_4$
sub1	252	19.9	1.48	235	395	21.5	7.03	108	280	638	2.17	3.27	0.360	0.18
sub2	242	21.1	1.50	202	787	25.7	11.7	110	280	622	2.22	5.31	1.16	0.20
sub3	242	21.3	1.50	198	1590	26.4	23.1	110	281	622	2.23	10.5	4.64	0.18
sub4	240	21.2	1.49	213	2950	24.2	46.7	110	281	622	2.23	21.1	17.4	0.21
sub5	232	22.1	1.50	206	3940	25.2	59.8	110	280	622	2.22	27.1	29.8	0.22
sub6	213	24.2	1.49	170	1250	31.4	15.3	109	280	630	2.19	7.02	2.45	0.19
sub7	231	22.2	1.50	183	789	28.8	10.5	109	283	630	2.21	4.77	1.04	0.19
sub8	226	21.9	1.45	183	1230	27.8	16.9	109	284	629	2.23	7.63	2.57	0.19
trans1	216	58.7	3.57	138	1410	130	4.14	125	291	482	2.98	1.40	0.530	0.20
trans2	210	60.3	3.54	143	3450	115	11.5	123	292	508	2.84	4.09	3.77	0.17
trans3	215	58.7	3.54	157	4040	94.3	16.4	126	286	442	3.19	5.17	5.72	0.18
trans4	209	60.5	3.54	141	5650	121	17.8	125	287	465	3.05	5.89	9.06	0.20
sup1	245	70.2	4.92	172	2810	118	9.10	133	293	373	3.88	2.36	1.77	0.20
sup2	236	73.8	4.94	195	5750	95.7	23.0	147	295	179	8.12	2.86	4.35	0.22
sup3	225	78.7	4.95	183	5810	107	20.9	138	292	264	5.45	3.86	6.00	0.19
sup4	236	72.9	4.89	188	7050	100	26.9	141	293	214	6.76	4.01	7.55	0.23
sup5	227	77.1	4.93	191	8140	99.0	31.5	141	293	216	6.69	4.74	10.3	0.18
sup6	224	78.8	4.93	132	2580	402	2.45	125	293	535	2.71	0.914	0.628	0.16
sup7	209	86.7	4.96	150	4620	165	10.7	132	294	423	3.42	3.15	3.87	0.19

Acknowledgments

The authors would like to recognize Randy Harvey for his invaluable contributions on running and maintaining the facility. This work is sponsored by AFOSR under Mitat Birkan, program manager.

References

1. Oswald, M., Smith, J. J., Branam, R., Hussong, J., Schik, A., Chehroudi, B., Talley, D., "Injection of Fluids into Supercritical Environments", *Combustion Science and Technology*, Vol. 178, No. 1-3, 2006, pp. 49-100.
2. Brown, G., Roshko, A., "On density effects and large structure in turbulent mixing layers"; *J. Fluid Mech*, Vol. 64 part 4, 1974, pp. 775-816
3. Papamoschou D., Roshko, A., "The compressible turbulent shear layer: an experimental study," *J. Fluid Mech*. Vol. 197, No. 453 1988
4. Dimotakis, P. E., "Two-Dimensional Shear Layer Entrainment", *AIAA Journal*, Vol 24, No. 11, Nov. 1986, pp. 1791-1796
5. Chehroudi, B., Talley, D., Coy, E., "Visual characteristics and initial growth rates of round cryogenic jets at subcritical and supercritical pressure", *Physics of Fluids*, Vol. 14, No. 2, February 2002, pp. 851-861.
6. Leyva, I. A., Chehroudi, B., Talley, D., "Dark-core analysis of Coaxial Injectors at Sub-, Near-, and Supercritical Conditions in a Transverse Acoustic Field", *54th JANNAF Meeting*, Denver, CO, May 14-18, 2007.
7. Leyva, I. A., Chehroudi, B., Talley, D., "Dark-core analysis of Coaxial Injectors at Sub-, Near-, and Supercritical Conditions in a Transverse Acoustic Field", *AIAA-2007-5456*
8. REFPROP, Reference Fluid Thermodynamic and Transport Properties, Software Package, Ver. 7.0, NIST, U.S. Department of Commerce, Gaithersburg, MD, 2002.

9. Liu T., Zong, N., Yang, V., "Dynamics of Shear-Coaxial Cryogenic Nitrogen Jets with Acoustic Excitation under Supercritical Conditions", AIAA 2006-759.
10. Abramovich, G. N., *The Theory of Turbulent Jets*, MIT Press, Cambridge, 1963.
11. Favre-Marinet, M., Camano Schettini, E.B., "The density field of coaxial jets with large velocity ratio and large density differences", *Int. J. of Heat and Mass Transfer*, 44 (2001) pp. 1913-1924
12. Ko, N. W. M. , Au, H., "*Initial region of subsonic coaxial jets*", *J of Fluids Engineering*, June 1981, vol. 103, pp 335-338.
13. Durao, D. and Whitelaw, J. H. Turbulent mixing in the developing region of coaxial jets", *J of Fluids Engineering*, Sept, 1973, pp.467-473 .
14. Branam, R., Mayer, W., "Characterization of Cryogenic Injection at Supercritical Pressure", *JPP* Vol. 19, No. 3, May-June 2003 pp. 342-354
15. Davis, D. W., Chehroudi, B., "Measurements in an acoustically driven coaxial jet under sub-, near-, and supercritical conditions", *JPP*, Vol. 23, No. 2, March- April 2007
16. Otsu, N., "A threshold selection method from gray-level histograms", *IEEE transactions on Systems, Man, and Cybernetics*, Vol. 9, No. 1, 1979, pp. 62-66.

Effects of a Variable-Phase Transverse Acoustic Field on a Coaxial Injector at Subcritical and Near-Critical Conditions

Juan I. Rodriguez*, Ivett A. Leyva, Bruce Chehroudi and Douglas Talley
Air Force Research Laboratory, Edwards AFB, CA 93524 USA

Abstract

An experimental study that focuses on the effects of a variable transverse acoustic field on an N₂ shear coaxial jet is presented. The coaxial jet is exposed to different acoustic conditions by varying the phase between two acoustic sources. The main objective of this investigation is to analyze the effect of transverse acoustic forcing with variable phase on the magnitude of the inner-jet dark-core length. The coaxial jet is exposed to a subcritical and near-critical pressure environment. The measurements are performed on backlit images of the coaxial jet obtained with a high-speed camera. The momentum flux ratio of the outer to the inner jet is varied from 1 to 20 for subcritical conditions and from 0.6 to 5 for near-critical conditions. The resonant frequency of the system is approximately 3 kHz and the maximum pressure variation with respect to total pressure is 3%. It is found that at subcritical pressures the effects of these variable acoustic fields on the length of the dark core achieve a maximum for momentum flux ratios between 1 and 5.

* Corresponding author

Approved for public release; distribution unlimited. PA #08117A.

Introduction

Coaxial injectors such as those used for the J-2 engine and the Space Shuttle Main Engine are of fundamental importance in cryogenic liquid rocket engine (LRE) studies. Due to improvements experienced in performance of LRE's at high mean combustion chamber pressures, the critical value of some propellants has been reached and surpassed. Under these pressures, incidents of high frequency combustion instabilities, potentially causing engine and vehicle damage or destruction, are of critical importance to understand.

Of particular importance in combustion instability is the outer to inner jet velocity ratio. It was found that at high velocity ratios the combustion is more stable [1]. Another important parameter is the mean chamber pressure (p) of the combustion chamber. In recent studies, Marshall et al. [2] evaluated the influence of mass flow rate, mixture ratio, injector and nozzle positions and chamber pressure on the spontaneous excitation of transverse modes. Operating at 1.53 MPa, maximum amplitudes of 4% of the peak-to-peak pressure perturbation (Δp) as a fraction of p were observed. Richecoeur et al. [3] obtained strong coupling between the combustion products from three coaxial CH_4/O_2 injectors and an imposed transverse acoustic field reaching 7% $\Delta p/p$ with a mean chamber pressure of 0.9 MPa. They also observed that combustion is more sensitive to acoustics at low outer jet velocities.

In the present study, both $\Delta p/p$ and momentum flux ratio (MR) are considered to characterize and understand the effects of a variable-phase transverse acoustic field on non-reacting coaxial injectors at conditions below and near the critical pressure of the propellant. The effect of the magnitude and phase of the pressure oscillations on the jet is characterized in this study by examining the behavior of the dark-core length of the inner jet. In previous experiments, the position of the injector with respect to the acoustic field profile was fixed. Only one acoustic driver was used to generate a transverse field and a reflective wall was placed at the other end of the test section. With this configuration, Leyva et al. [4,5] reported that the effects of the externally imposed acoustic field on the dark core length are greatest at subcritical pressures and for MR's between 1 and 4. In the present paper, however, the addition of a second acoustic driver allowed changes of the relative position of the acoustic field with respect to the fixed location of the coaxial jet injector. Preliminary results with this new setup at subcritical pressures were presented in Leyva et al. [6]. Consistent with previous studies [4,5], it was found that the maximum changes in the dark-core length for subcritical pressures were statistically significant for $\text{MR} = 2.6$ but not for $\text{MR} = 1$. The present study extends the range of the MR's

studied for subcritical conditions and introduces results for the (higher) near-critical pressures. The amplitude of the pressure oscillations was maximized to obtain the highest fractional change of the chamber pressure, which was typically between 1 to 3%. The momentum flux ratio of the outer to the inner jet was varied from 1 to 20 for subcritical and from 0.6 to 5 for near-critical conditions.

Experimental Setup

The Cryogenic Supercritical Laboratory (EC-4) facilities of the Air Force Research Laboratory (AFRL) at Edwards Air Force Base, CA were used to perform the experiments. Figure 1 shows the main chamber and the supporting systems. In the current setup, ambient temperature N_2 is used to supply flow to the inner and outer jet and also to pressurize the chamber. To avoid the inherent difficulties in computing the critical lines for mixtures versus having a well characterized critical point for a single element, molecular nitrogen (N_2) was used as the working fluid. The critical temperature of N_2 is 126.2 K and its critical pressure is 3.39 MPa. The central jet of a coaxial jet design entered the combustion chamber at subcritical temperatures and the outer jet was introduced at supercritical temperatures. These conditions resemble typical applications of liquid rocket engine systems. For example, a LOX/LH2 engine features an O_2 center jet at subcritical temperatures and an H_2 outer jet at supercritical temperatures. H_2 is delivered at higher temperatures because it is used as a coolant for the engine nozzle. A typical velocity ratio between the outer and the inner jet is 10 [7].

The inner tube producing the inner jet has an inner diameter, D_1 , of 0.51 mm with length-to-inner-jet-diameter ratio of 100. The inner tube exit plane is recessed by 0.3 mm from the outer tube. The outer annular jet's inner diameter, D_2 , is 1.59 mm with outer diameter, D_3 , of 2.42 mm. For the outer jet, the length-to-mean-width of the annular passage is 67. Both the inner and the outer jets are cooled by heat exchangers (HE's) using liquid nitrogen obtained from a cryogenic tank. One heat exchanger cools the inner jet and other two cool the outer jet. Depending on the setup, one of these HE's can be bypassed to modify the cooling patterns. The mass flow rates of liquid nitrogen through the HE's are regulated in order to control the temperature of the jets. These rates are measured with Porter[®] mass flow meters (122 and 123-DKASVDAA) at ambient conditions to avoid difficulties with mass flow rate measurement at cryogenic temperatures. Also, an inner chamber was built and housed inside the main chamber to maintain the amplitude of the acoustic oscillations to a maximum at the test section. The inner chamber is 6.6 cm high, 7.6 cm wide and 1.3 cm deep (see Fig. 1). The coaxial injector is shown in Fig. 2.

The chamber pressure is measured with a Stellar 1500 transducer. An unshielded type E thermocouple with a bead diameter of 0.1 mm is used to measure the temperature of the jets. The accuracy of this thermocouple was checked with an RTD and found to be ± 1 K. Also, a Kulite® XQC-062 pressure transducer is used to measure the pressure near the location of the thermocouple tip at a sampling frequency of 20 kHz (see bottom right picture in Fig. 1). Both the pressure transducer and the thermocouple are moved in the plane perpendicular to the jet axis with two linear positioning stages built by Attocube Systems AG. Each stage has a range of about 3 mm in 1 dimension with step sizes in the order of 0.01 mm. One stage was placed on top of the other with their axis of movement perpendicular to each other for a total maximum interrogation area of 3 mm by 3 mm. The thermocouple and pressure transducer were fixed to a custom made probe stand mounted on top of the positioning assembly. In turn, the linear stages were placed at the top end of a shaft that rested on a large 4-inch range linear stage built by SETCO™ outside the main chamber. Thus, the temperature probe approaches the coaxial jet from the bottom and it can get arbitrarily close to the exit plane. This thermocouple has even been used to measure the temperature within the recess of the inner jet. NIST's REFPROP® and its thermophysical properties online database [8,9] are used to obtain density, viscosity, and surface tension from the measured flow rates, chamber pressure and jet temperature. From these properties, Re , We , outer to inner jet velocity ratio (VR) and MR for a given condition are then calculated.

The imaging of the coaxial flow was accomplished using a Phantom® 7.1 CMOS camera. The camera can be seen facing the main chamber in the bottom left picture of Figure 1. Backlit images with a resolution of 128x224, 128x256 or 128x304 pixels were obtained, with each pixel representing an area of approximately 0.08 mm by 0.08 mm. The framing rate was 20-25 kHz. The exposure time generally was 1-2 μ s and the number of images saved per run was 1000 on average. The jet was backlit using a Newport® variable power arc lamp set at 160 W. The dark core lengths are measured from 998 images using a MATLAB® subroutine based on the Otsu technique [10] to find a grayscale threshold which helps identify the inner core from the rest of the image (see Fig. 3). Two piezo-sirens custom-designed by Hersh Acoustical Engineering, Inc. were used to generate the transverse acoustic field (see Fig. 1). The principle by which the piezo-sirens work as acoustic drivers is relatively simple, with a piezo element moving an aluminum cone attached to it, which in turn produces acoustics waves. When the two drivers have a zero degree phase angle difference then the movement of the piezo-siren cones is synchronized and they move in opposite directions, that is, towards and away from

each other simultaneously. On the contrary, when the two drivers have a 180-degree phase difference, then the cones move in the same direction. This behavior is represented by the sketches in Fig. 4. A Fluke® signal generator was used to drive the piezo-ceramic element of each piezo-siren with a sinusoidal wave at the preferred driving frequency of the system. The frequency was manually varied using a signal generator until the highest amplitudes of the pressure waves were obtained. These frequencies spanned a range between 2.95 and 3.10 kHz. Then the signals were amplified and fed to the piezo-sirens. The phase between the two elements was modified through each case to expose the coaxial jet to different locations within the acoustic field. The voltage supplied to the two acoustic drivers was the same for all cases and the phase difference was controlled by changing the phase of one acoustic driver with respect to the other using a lead/follower configuration in the signal generator. A waveguide with a catenary contour was used to guide the waves from a circular cross-section at the end of the aluminum cone to the rectangular cross-section of the rectangular inner chamber.

Results and Discussion

The main parameters studied were the curved (or total) length and the axial length of the dark core region of the inner jet as the phase difference between the acoustic drivers was varied. These two parameters are defined due to the sinusoidal shape imposed by the acoustic field. The axial length is the projection of the dark core of the inner jet onto the jet centerline and the curved length is the distance along the curved shape of the core in order to take into account the curvature produced by the acoustic field (see Fig. 3). For a more detailed explanation of the definitions for the axial and curved dark core lengths and the techniques employed to measure them, refer to Leyva et al. [5]. The present study includes the findings of 5 cases at subcritical pressures and 3 cases at near-critical pressures. The effects of the imposed acoustic field on one subcritical case ($P = 1.51$ MPa, $MR = 4.2$) and one near-critical case ($P = 3.55$ MPa, $MR = 2$) are reviewed in detail. The coaxial jet for these two cases is shown in Figs. 5 and 6. Each figure contains two images. The image to the left shows the jet without acoustic forcing ("jet baseline") while the image to the right shows the jet at the phase difference where maximum changes in length were measured when compared to the jet baseline. The effect of the acoustic field on the bending of the jet is clearly visible. The near-critical case definitely shows a more enhanced curvature compared to its baseline but it is not as strong as its subcritical counterpart.

Figs. 7 to 10 show the axial and curved dark core lengths normalized by the inner jet diameter plotted

against the various phase differences between acoustic drivers for the cases pictured in Figs. 5 and 6. A secondary axis includes the measured $\Delta p/p$ at each phase difference. The dark core length in the absence of the acoustic field (both drivers off) is considered as the reference baseline and also shown. For a few phase angles, the dark core length for when only one driver is acting is also indicated. The error bars shown represent $\pm 1\sigma$ of the lengths recorded for a given MR and phase angle difference. For the subcritical case, a statistical difference with respect to the baseline length can be observed for most phase angles. In contrast, for the near-critical condition the error bars for most phase angles are within the error bars of the baseline. Nonetheless, both conditions show a statistically significant reduction of the dark core length under the acoustic field for at least one angle when both drivers are operating. As we would expect, the dark core length is longest when there are no acoustic disturbances. If there is only one driver, the length decreases with respect to the baseline and this length is repeatable (within the error) for different angles, since the acoustic field created by that acoustic driver remains the same at different phase angles if the other acoustic driver is off.

Peak-to-peak pressure perturbations (Δp) generated in the inner chamber by the acoustic waves ranged from 10 to 35 kPa, which translated to different $\Delta p/p$ conditions depending on the mean chamber pressure. In Fig. 7, there is a region where the axial dark core length is reduced to approximately 10D1 from a 15D1 baseline for phase angle differences between 0° and 135° until it starts increasing and it reaches a maximum between 270° and 315° . Interestingly, $\Delta p/p$ has a maximum of 2.9% at 45° and a minimum of 1.5% at 225° . It is important to remember that the changes in $\Delta p/p$ are entirely due to the phase angle since the driving voltage for the two sources is constant throughout the phase sweep experiment. It can be observed that for this case the minimum dark core length occurs at phase angles where there is a maximum in $\Delta p/p$, which corresponds to the pressure antinode of the acoustic field. In contrast, there is a region where the minimum dark core lengths coincide with the location of the pressure node or minimum $\Delta p/p$. These trends are the same observed for the curved dark core length as a function of phase angle difference in Fig 8.

In the near-critical range (Fig. 9), the difference between the baseline case and the minimum axial dark core length was 4D1 with a $\Delta p/p$ range from 0.7% to 0.9% for these measurements. Even though the absolute acoustic field intensity is the same as the subcritical case, the higher near-critical pressure decreases the total relative intensity. Thus the difference between maximum and minimum values of the pressure perturbation is in fact near the minimum resolution of the pressure

transducer. This increases the uncertainty of the measurements in the near-critical regime, making it difficult to quantify the effect of phase angle difference. Nevertheless, it can be seen that at least for one phase angle, the difference between the dark core length with and without acoustic forcing lies outside the error bars, which provides at least one data point where the difference between acoustics and no acoustics can be quantified.

Comparing the two cases that we have been studying in detail, the maximum difference in axial and curved dark core lengths was larger for the subcritical case compared to that of the near critical case by 55% and 28% respectively (see Figs. 7-10). These results show the greater impact the acoustic field had in the subcritical case compared to the near-critical case. This is to be expected due to the higher $\Delta p/p$ attained for the subcritical case.

The difference between the baseline dark core length and the minimum dark core length achieved during the angle sweep normalized by the baseline value ("maximum length change/baseline length") for each of the 8 cases reported in this study is presented in Figs. 11 and 12. This normalized difference in length is plotted as a function of MR. In the near-critical regime the three cases lie within 30-40% with respect to the axial dark core baseline and within 24-32% with respect to the curved dark core baseline. This could be indicative of a weak effect of the acoustics on the jet due to relatively low forcing or a particular trend within this MR range. More extensive studies in the near-critical regime would be needed to reach a definitive conclusion. However, for subcritical pressures, this difference was the largest at a range of momentum flux ratios between 1 and 5. The largest decrease in length of the dark core compared to the case with no acoustics was observed in this regime. These findings support previous experimental results that had shown similar behavior with one acoustic driver configuration [4,5] and preliminary data with two acoustic resonators [6]. A summary of the fluid properties and flow conditions for all 8 cases is shown in Table 1.

Conclusions

The effects of an externally imposed transverse acoustic field with variable relative phase angle on the behavior of a shear coaxial jet are presented in this study. For the detailed analysis of one subcritical case at $MR = 4.2$ and one near-critical case at $MR = 2$, a statistically significant reduction of the inner jet dark core length with acoustic forcing was observed for most phase angles for the former case and at least one phase angle for the latter. In addition, for that particular subcritical condition, the maximum change in dark core length was observed to coincide with the pressure

antinode of the acoustic field, while the minimum change occurred near the pressure node. Similar observations could not be made for the near-critical pressure case due to smaller relative pressure perturbations. Comparing the subcritical condition at $MR = 4.2$ and near-critical condition at $MR = 2$, the difference between the maximum and minimum axial dark core lengths for the subcritical condition was 55% larger than the difference between the maximum and minimum axial dark core lengths for the near-critical condition. This difference was 28% larger when using the curved dark core length definition. In addition, it was confirmed that, for subcritical conditions and acoustic fields with pressure perturbations $\Delta p/p$ as high as 3%, the range of momentum flux ratios that show the greatest impact on dark core length lies between $MR = 1$ and $MR = 5$. Further investigation of the effects of transverse acoustic fields for near-critical and supercritical conditions will be performed in future studies.

Acknowledgements

The authors would like to thank Mr. Randy Harvey and Lt. Jeffrey Graham for their important contributions running and maintaining the facility. This work is sponsored by AFOSR under Mitat Birkan, program manager.

References

1. Hulka, J., Hutt, J. J., *Liquid Rocket Engine Combustion Instability*, AIAA Progress in Astronautics and Aeronautics, Yang, V., Anderson W. E., Eds., 1995, p. 40.
2. Marshall, W., Pal, S., Woodward, R., Santoro, R. J., Smith, R., Xia, G., Sankaran, V., Merkle, C. L., "Experimental and Computational Investigation of Combustor Acoustics and Instabilities, Part II: Transverse Modes," *AIAA-2006-0538*
3. Richecoeur, F., Scoufflaire, P., Ducruix, S., Candel, S., *Journal of Propulsion and Power* 4:790-799 (2006).
4. Leyva, I. A., Chehroudi, B., Talley, D., "Dark-core analysis of Coaxial Injectors at Sub-, Near-, and Supercritical Conditions in a Transverse Acoustic Field", *54th JANNAF Meeting*, Denver, CO, May 14-18, 2007.
5. Leyva, I. A., Chehroudi, B., Talley, D., "Dark-core analysis of Coaxial Injectors at Sub-, Near-, and Supercritical Conditions in a Transverse Acoustic Field", *AIAA-2007-5456*
6. Leyva, I. A., Rodriguez, J. I., Chehroudi, B., Talley, D., "Preliminary Results on Coaxial Jets Spread Angles and the Effects of Variable Phase Transverse Acoustic Fields", *AIAA-2008-0950*
7. Oschwald, M., Smith, J. J., Branam, R., Hussong, J., Schik, A., Chehroudi, B., Talley, D., *Combustion Science and Technology* 1:49-100 (2006)
8. REFPROP, Reference Fluid Thermodynamic and Transport Properties, Software Package, Ver. 7.0, NIST, U.S. Department of Commerce, Gaithersburg, MD, 2002.
9. Thermophysical Properties of Fluid Systems (<http://webbook.nist.gov/chemistry/fluid>), NIST, U.S. Department of Commerce, Gaithersburg, MD, 2005.
10. Otsu, N., *IEEE transactions on Systems, Man, and Cybernetics* 1:62-66 (1979).

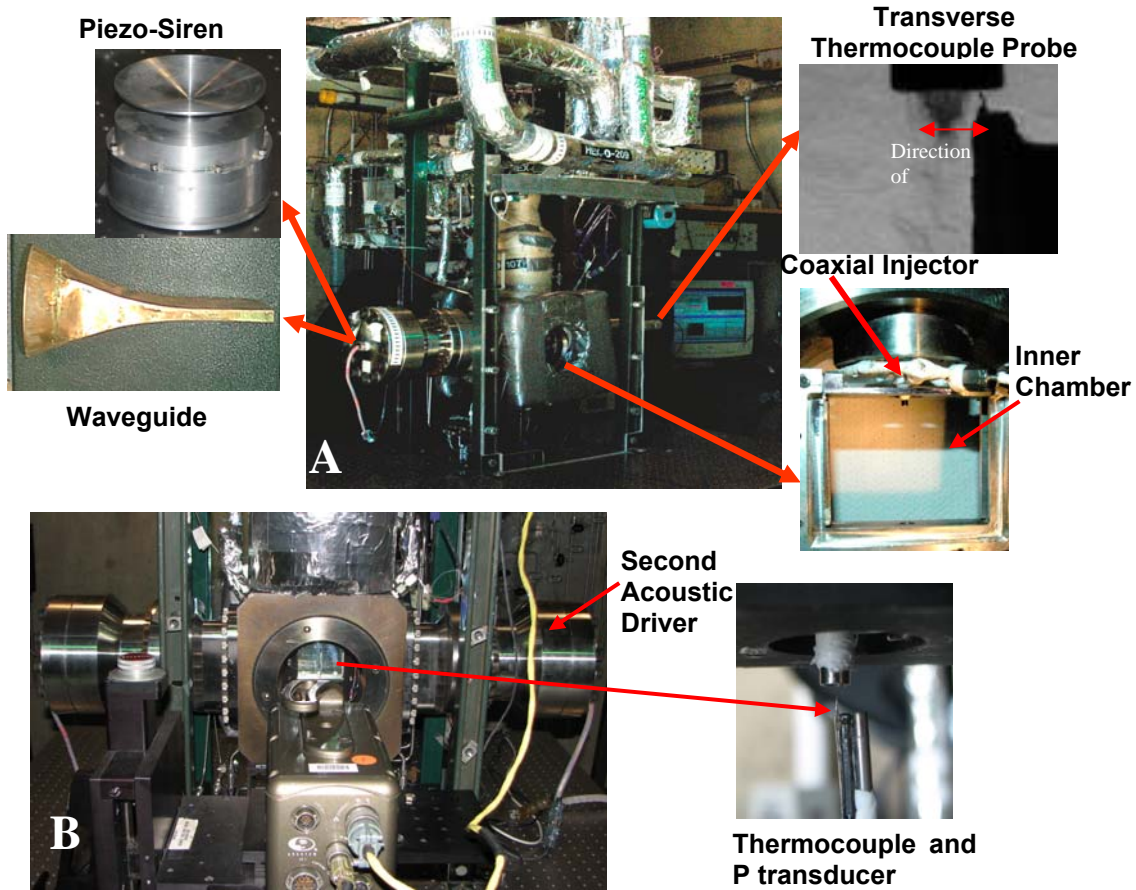


Figure 1. Air Force Research Laboratory's Cryogenic Supercritical Flow Facility, EC-4, at Edwards AFB. The picture labeled "A" shows the facility with only one acoustic driver and a transverse thermocouple. Configuration "B" shows two acoustic drivers, one at each side of the main test section, where the inner chamber shown is located. A thermocouple and a miniature pressure transducer are introduced from the bottom to measure the temperature of the inner and outer jets and also obtain pressure data to characterize the acoustic field.

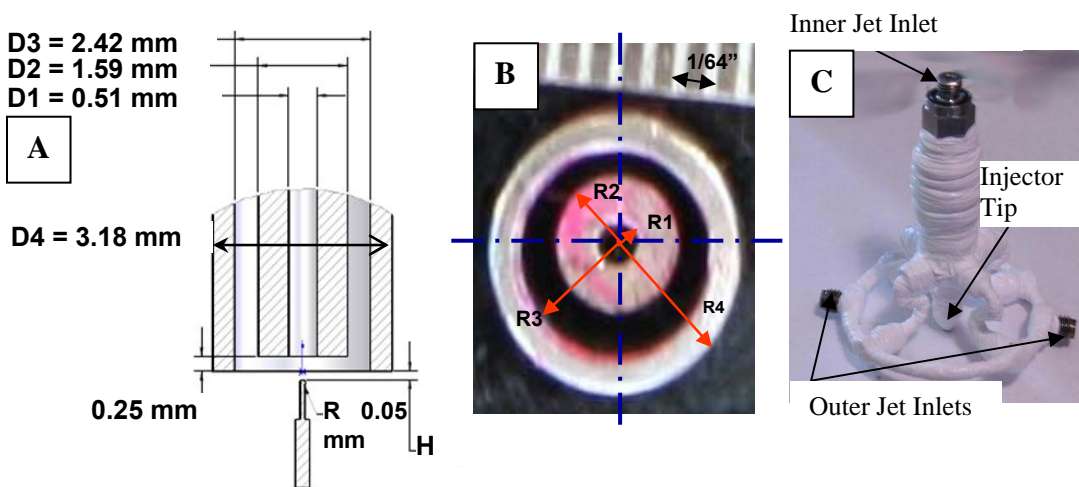


Figure 2. Coaxial injector overview. "A" shows the dimension of the different elements at the tip of the injector. "B" is an actual photograph of the injector tip looking upstream. "C" pictures the injector in its entirety.

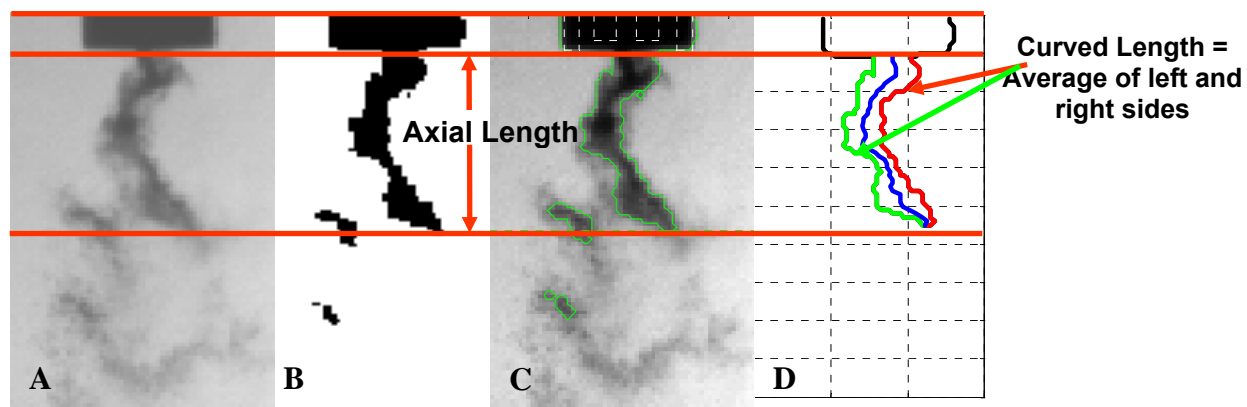


Figure 3. Measuring the dark core length. A. Original image. B. Black and white image after thresholding. C. Contour used to define the axial length. D. Schematic of how the curved length is computed.

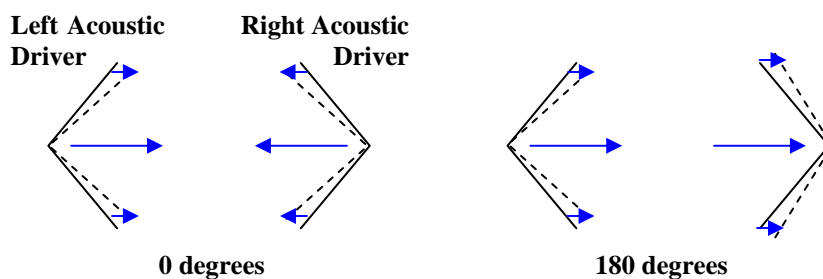


Figure 4. Simplified diagram of the behavior of the two acoustic drivers at a 0° and 180° phase angle difference between them.

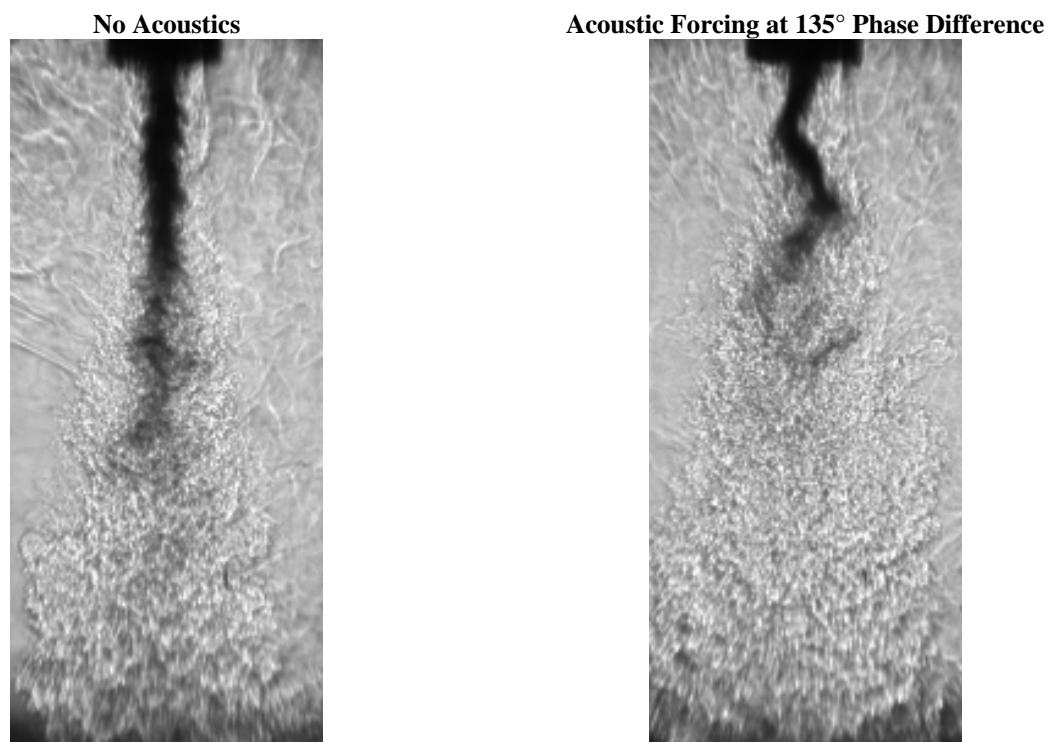


Figure 5. Comparison between a backlit image without acoustic forcing and with forcing at the phase difference (135°) with the maximum effect on dark core length for the subcritical case with $MR = 4.2$ and $P = 1.51$ MPa.

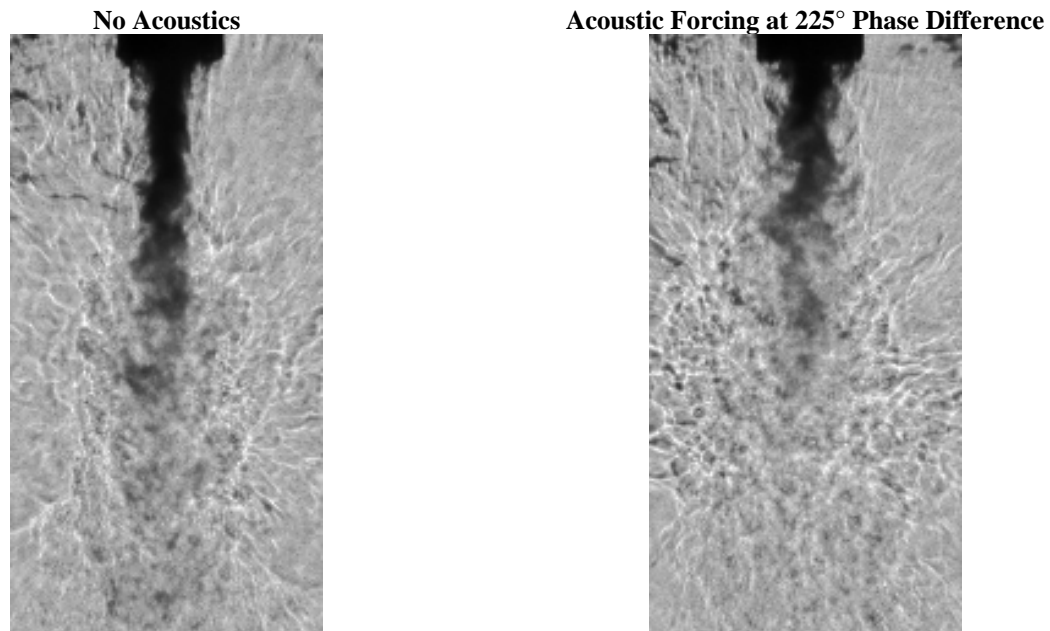


Figure 6. Comparison between a backlit image without acoustic forcing and with forcing at the phase difference (225°) with the maximum effect on dark core length for the near-critical case with $MR = 2$ and $P = 3.55$ MPa.

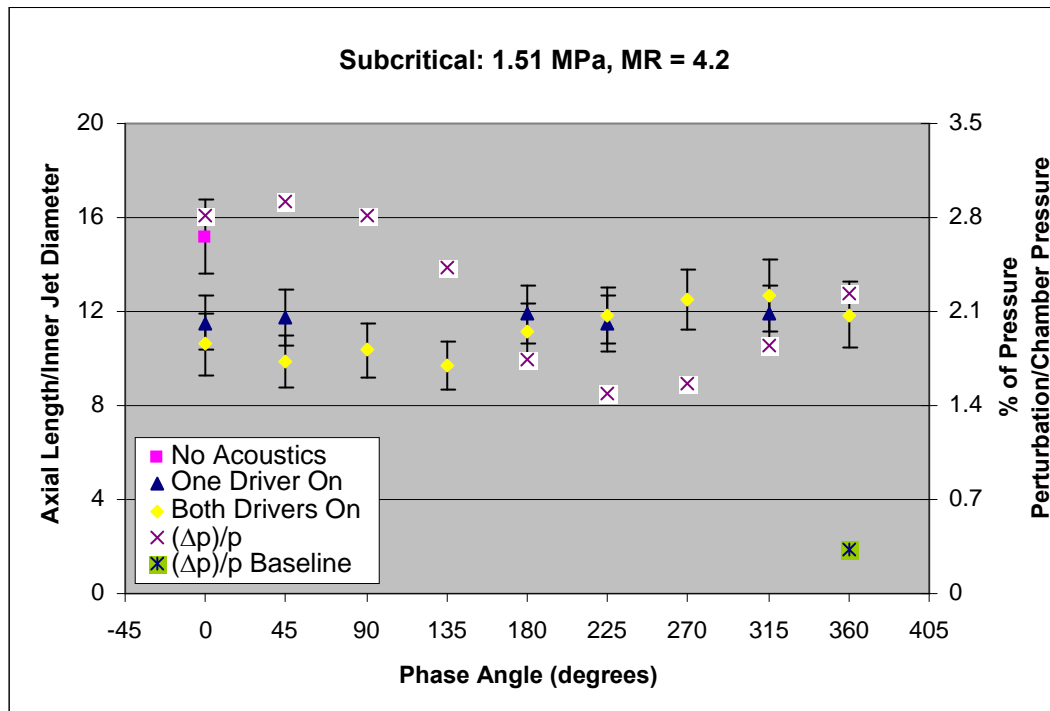


Figure 7. Graph of the axial length normalized by the inner jet diameter for $MR = 4.2$ at the subcritical pressure of 1.51 MPa. The peak-to-peak pressure perturbation as a percentage of the chamber pressure is also plotted on a secondary axis to show the relationship between the strength of the acoustic field and its impact on dark core length.

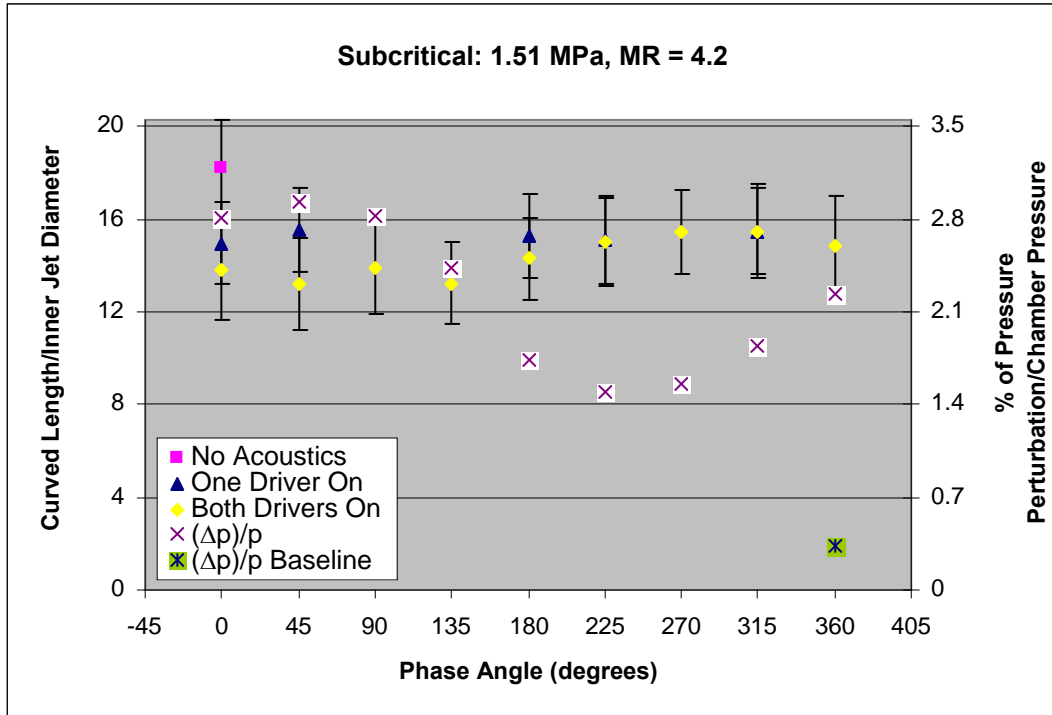


Figure 8. Graph of the curved length normalized by the inner jet diameter for MR = 4.2 at the subcritical pressure of 1.51 MPa. The peak-to-peak pressure perturbation as a percentage of the chamber pressure is also plotted on a secondary axis.

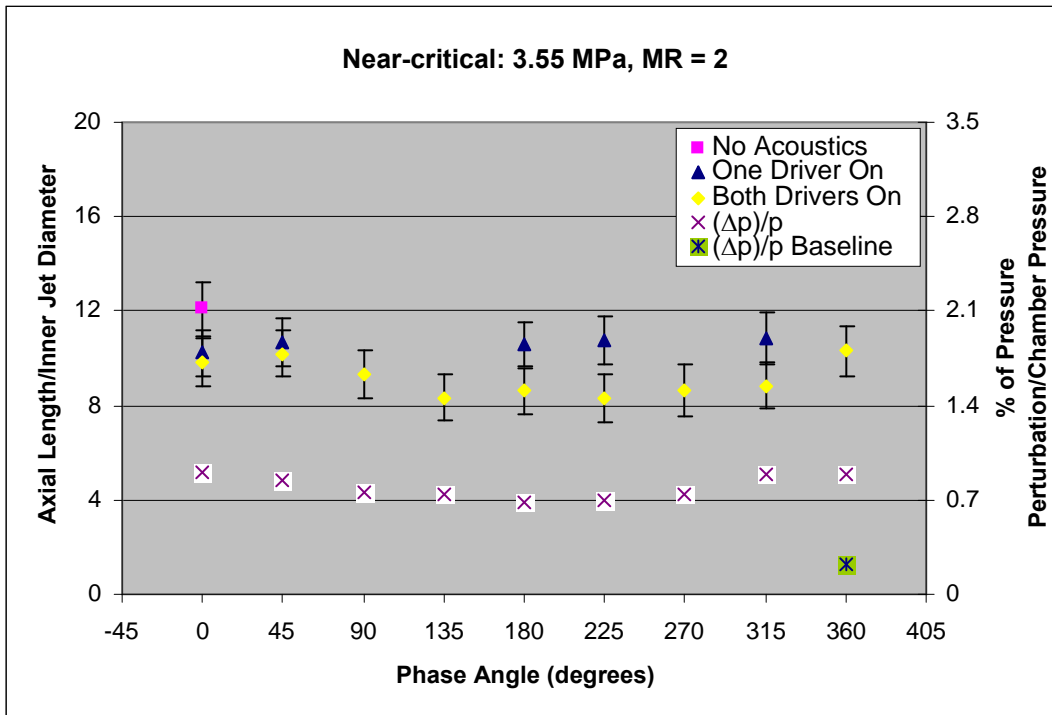


Figure 9. Graph of the axial length normalized by the inner jet diameter for MR = 2 at the near-critical pressure of 3.55 MPa. The peak-to-peak pressure perturbation as a percentage of the chamber pressure is also plotted on a secondary axis to show the relationship between the strength of the acoustic field and its impact on dark core length.

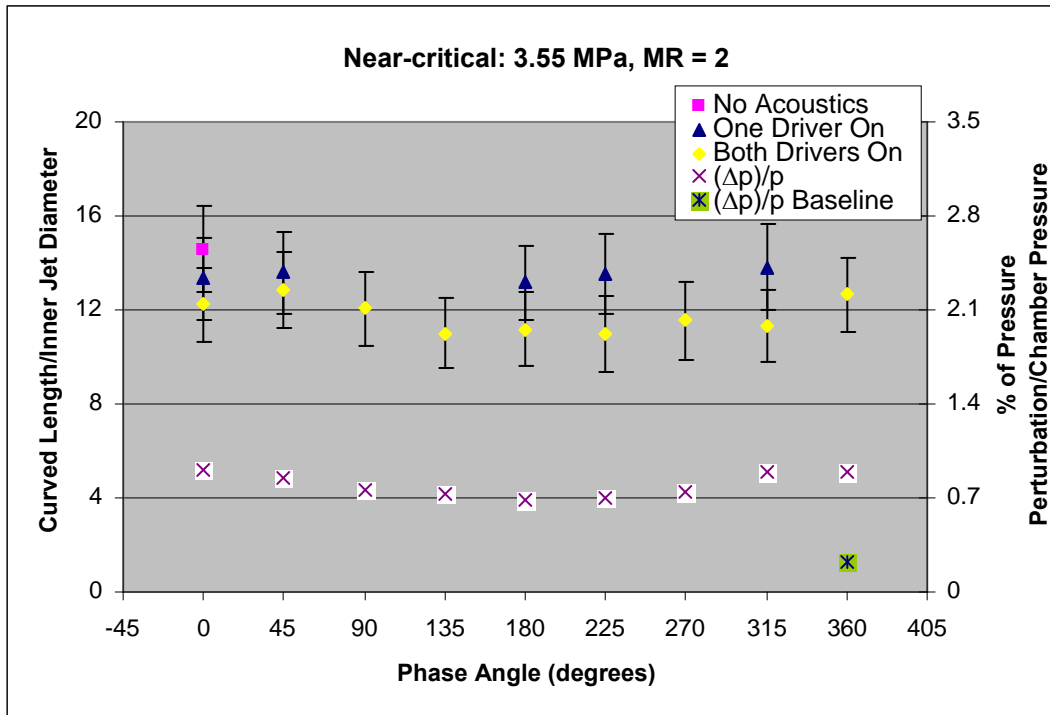


Figure 10. Graph of the curved length normalized by the inner jet diameter for MR = 2 at the near-critical pressure of 3.55 MPa. The peak-to-peak pressure perturbation as a percentage of the chamber pressure is also plotted on a secondary axis.

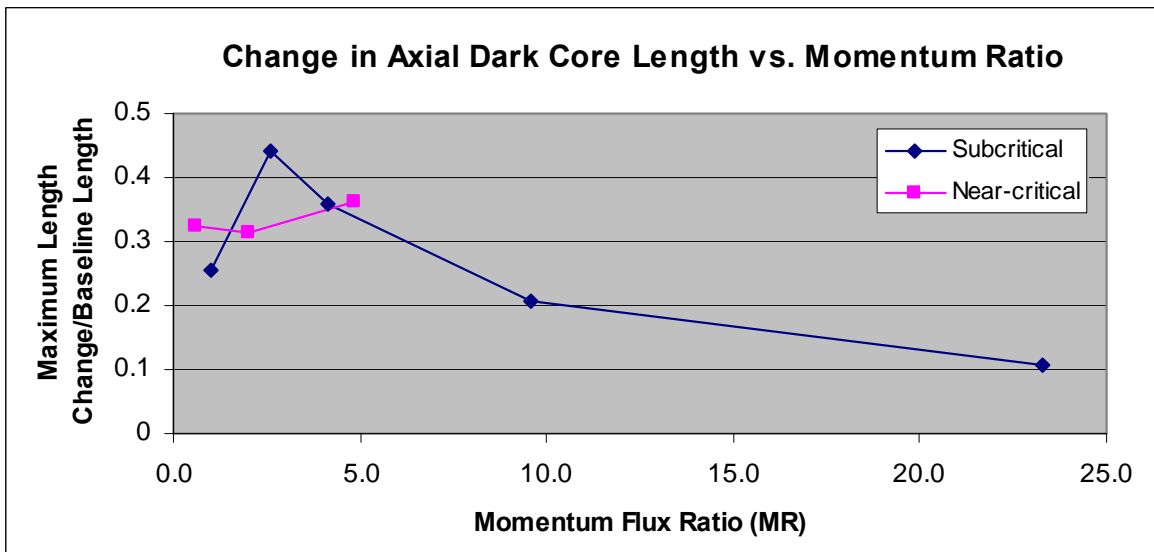


Figure 11. Plot of the maximum axial dark core length change normalized by the axial baseline length observed at each momentum flux ratio.

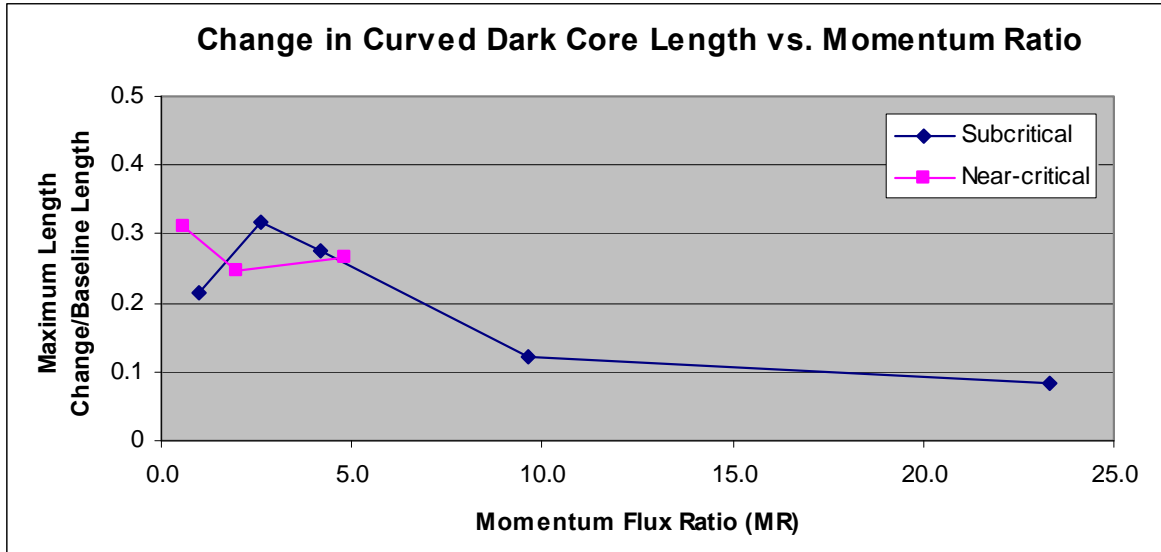


Figure 12. Plot of the maximum curved dark core length change normalized by the curved baseline length observed at each momentum flux ratio.

	T_{chamber} (K)	ρ_{chamber} (kg/m ³)	P_{chamber} (MPa)	T_{outer} (K)	\dot{m}_{outer} (mg/s)	ρ_{outer} (kg/m ³)	u_{outer} (m/s)	T_{inner} (K)	\dot{m}_{inner} (mg/s)	ρ_{inner} (kg/m ³)	u_{inner} (m/s)	VR	MR
SUB													
case1	231	22.2	1.50	183	790	28.8	11	109	283	630	2.2	4.8	1.0
case2	226	21.9	1.45	183	1230	27.8	16.9	109	284	630	2.2	7.6	2.6
case3	226	22.9	1.51	185	1560	28.7	20.9	109	279	630	2.2	9.5	4.2
case4	210	24.9	1.50	182	2400	29.3	31.3	109	279	630	2.2	14	9.6
case5	216	24.1	1.50	191	3640	27.7	50.3	109	279	630	2.2	23	23
NEAR													
case1	223	56.6	3.58	180	1060	75	5.4	123	290	520	2.8	2.0	0.56
case2	223	56	3.55	184	2170	72	12	127	294	400	4	3	2
case3	219	57.6	3.56	194	3080	67	18	125	289	480	3.0	5.9	4.9

Table 1. Summary of the fluid properties and flow conditions for the different cases presented in this study.

Results on Subcritical One-Phase Coaxial Jet Spread Angles and Subcritical to Supercritical Acoustically-Forced Coaxial Jet Dark Core Lengths

Juan I. Rodriguez¹

Department of Mechanical and Aerospace Engineering, UCLA, Los Angeles, CA, 90095

Ivett A. Leyva², Bruce Chehroudi³ and Douglas Talley⁴
AFRL/RZSA, Edwards AFB, CA, 93524

An investigation of the behavior of N₂ gas-gas shear coaxial jet spread angles in conjunction with a comprehensive N₂ shear coaxial jet dark core length analysis is presented. For the one-phase coaxial jet spread angle study, a total of 6 cases, corresponding to different momentum flux ratios (MR's) at subcritical pressures are analyzed and compared to existing data. The measurements are extracted from 20 backlit images. The objective of the second part of this work is to study the effect on the magnitude of the inner jet dark core length of transverse acoustic forcing at subcritical to supercritical pressure environments. The dark core length data comprises MR's from 0.02 to 23 with corresponding velocity ratios from 0.25 to 23. In these acoustically-forced cases, the resonant frequency of the system varied from 2.93 to 3.09 kHz and the maximum root-mean-square pressure variation with respect to total pressure was 4%. When comparing cases with very similar MR's, it was found that the relative acoustic excitation intensities for subcritical pressures were up to eight times stronger than near and supercritical chamber pressures. Despite that fact, the corresponding relative change in length of the dark core did not vary more than 50% between the three pressure regimes.

I. Introduction

One of the mechanisms responsible for inducing combustion instabilities in Liquid Rocket Engines (LRE's) is the interaction of the injector flow with the combustion chamber acoustic modes. Given the widespread use of coaxial injectors in LRE's, such as those used for the J-2 engine and the Space Shuttle Main Engine, understanding the phenomena that could lead to unstable behavior in these propulsion systems is of primary importance. Recent improvements experienced in LRE performance have increased mean combustion chamber pressures over the critical value of some propellants. Therefore, one of the objectives of this work is to perform experiments in the supercritical pressure regime.

Also of interest in LRE studies is the momentum flux ratio (MR) and velocity ratio (VR) between the outer jet and the inner jet. It has been found that combustion is more stable at high velocity ratios¹. Marshall et al.² performed experiments at 1.53 MPa with maximum amplitudes of 4% of the peak-to-peak pressure perturbation ($\Delta p_{\text{peak-to-peak}}$) as a fraction of mean chamber pressure (p_{mean}). They studied the influence of mass flow rate, mixture ratio, injector and nozzle positions and chamber pressure on the spontaneous excitation of the transverse modes of their three-dimensional rectangular chamber. They found that the first mode of the largest dimension of the chamber showed stronger response when the injector was positioned near a pressure antinode location. In another study, Richecoeur et al.³ observed that combustion is more sensitive to acoustics at low outer jet velocities. They obtained strong

¹Graduate Student, UCLA, Los Angeles, CA 90095-1597, AIAA Student Member.

²Lead, Combustion Dev. Group, AFRL/RZSA, 10 E. Saturn Blvd., Edwards AFB, CA 93524, AIAA Sr Member.

³Principal Scientist, ERC Inc., AFRL, Edwards AFB, CA 93524, AIAA Member.

⁴Sr. Aerospace Engineer, AFRL/RZSA, 10 E. Saturn Blvd., Edwards AFB, CA 93524, AIAA Member.

Approved for public release; distribution unlimited. PA #08263A.

coupling between the combustion products from three coaxial CH₄/O₂ injectors and an imposed transverse acoustic field reaching 7% $\Delta p/p$ with a mean chamber pressure of 0.9 MPa.

The first part of this work consists of an analysis of the outer jet angles of a gaseous coaxial jet flow exiting into a gaseous atmosphere. In a thorough experimental analysis, Chehroudi et al.⁴ showed for the first time that the spreading angle growth rate of single round jets at supercritical pressure and temperature agreed quantitatively with theoretical predictions from previous investigations⁵⁻⁷. Chehroudi et al. also compiled experimental data from different researchers which spanned four orders of magnitude in the ratio of the chamber density to the jet density, which is an important parameter for single jets ejecting into a quiescent environment. For coaxial jets at subcritical, nearcritical and supercritical pressures and MR's varying from 0.4 to 30, Leyva et al.⁸ found that the near-field outer jet spreading angle was about constant (11°). This data comprised gas-liquid, supercritical-liquid-like and supercritical-supercritical combinations of the outer and inner jet respectively. The data compared well with CFD simulations completed for two conditions ran in this lab. However, the spreading angles were consistently lower than other experimental data (mostly gas-gas) and theoretical predictions for 2D jet spreading angles and shear layer growth. One of the motivations of this study is to complement this data set with gas-gas data and see if the spreading angles remain about constant.

In this study, a complete set of subcritical to supercritical measurements of the dark core length of a coaxial jet is also presented, building upon data reported previously by the authors^{8,9}. A transverse acoustic field is set up using two acoustic drivers and the phase between them is varied so the coaxial jet can be exposed to different acoustic conditions. The chamber pressure, $\Delta p/p$ and MR are considered to characterize the effects of this transverse acoustic field on the coaxial injector flow. The effect of the magnitude and phase of the pressure oscillations is characterized in this study by examining the behavior of the dark-core length of the inner jet. Leyva et al.^{10,11} used a configuration where the position of the injector with respect to the acoustic field was fixed, since only one acoustic driver was used to generate the transverse acoustic field with a reflective wall placed at the other end of the test section. This study reported that for MR's between 1 and 4 the effects of acoustic forcing on the coaxial jet dark core length were the most significant. The findings of this early configuration were consistent with a later study with two acoustic sources by Leyva et al.⁸ where maximum changes in dark core length for subcritical pressures were statistically significant for an MR of 2.6 but not for an MR of 1. The nearcritical and supercritical data reported in this study will be compared to the subcritical trends mentioned in these previous reports.

II. Experimental setup

The Cryogenic Supercritical Laboratory (EC-4) at the Air Force Research Laboratory (AFRL) at Edwards Air Force Base, CA, was the facility used to conduct the experiments in this study. The main chamber and the supporting systems are shown in Figure 1.

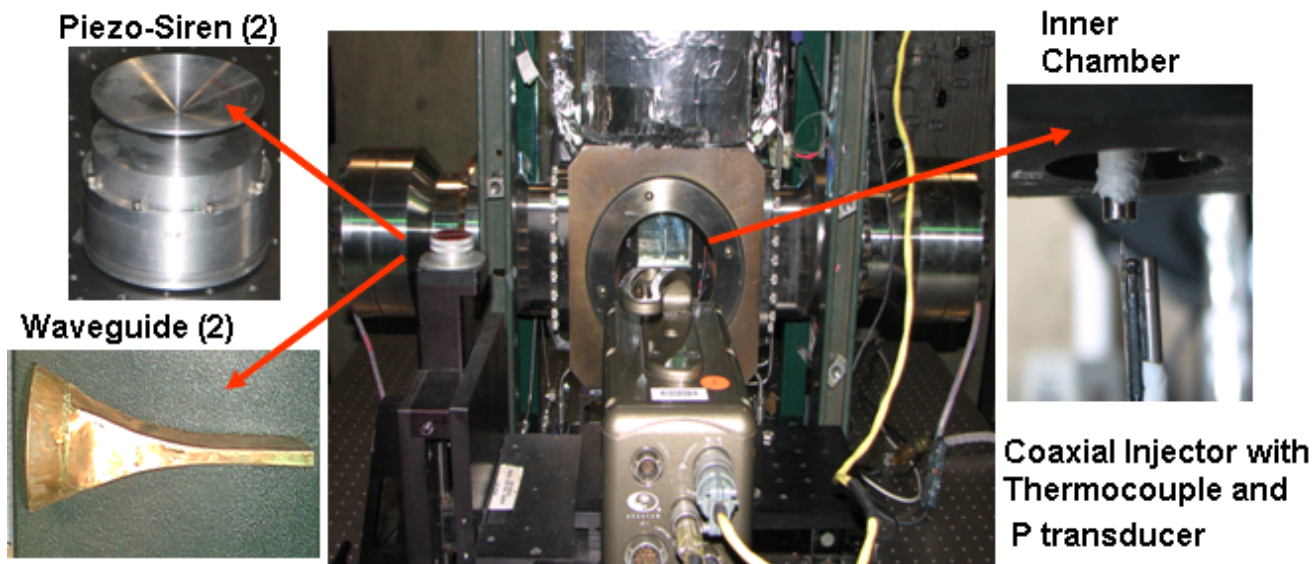


Figure 1. Overview of the experimental apparatus

Ambient temperature N_2 is used to supply the inner and outer jet and also for chamber pressurization. Heat exchangers (HE's) using liquid nitrogen obtained from a cryogenic tank were used to cool the inner and the outer jets. One heat exchanger was used for the inner jet and two others for the outer jet. For the outer jet flow, the option to bypass one of the HE's to modify the cooling pattern is available. In order to control the temperature of the jets, the mass flow rates of liquid nitrogen through the HE's are modified accordingly. To avoid difficulties with mass flow rate measurement at cryogenic temperatures, these rates are measured with Porter® mass flow meters (122 and 123-DKASVDAA) at ambient conditions. Both the inner and the outer jet flow through an injector assembly (see Fig. 2) which exits to an inner chamber built and housed inside the main chamber so that the amplitude of the acoustic oscillations are maximized at the test section. This inner chamber is 6.6 cm high, 7.6 cm wide and 1.3 cm deep (see Fig. 1).

The inner tube making the inner jet has an inner diameter, D_1 , of 0.51 mm with length-to-diameter ratio of 100. The inner jet exit plane is recessed by 0.25 mm from the outer jet. The outer annular jet's inner diameter, D_2 , is 1.59 mm with outer diameter, D_3 , of 2.42 mm. For the outer jet, the length-to-mean-width of the annular passage is 67. Detailed dimensions of the coaxial injector tip are shown in Fig. 2.

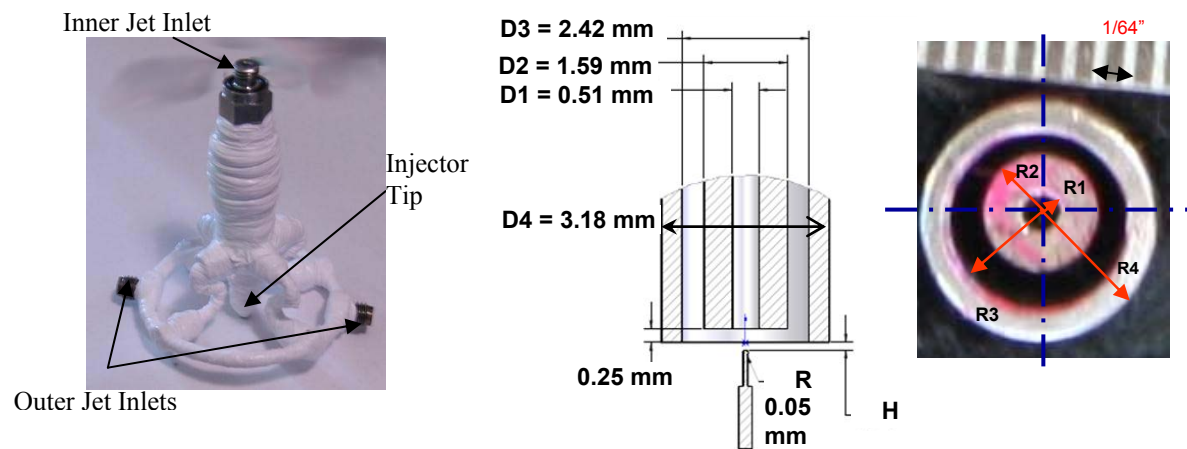


Figure 2. Image and tip geometry of the shear coaxial injector used in this study.

The temperature of the jets was measured using an unshielded type E thermocouple with a bead diameter of 0.1 mm. The accuracy of this thermocouple was checked with an RTD and found to be ± 1 K. The chamber pressure was measured with a Stellar 1500 transducer and a Kulite® XQC-062 pressure transducer was used to measure the pressure near the location of the thermocouple tip at a sampling frequency of 20 kHz (see right picture in Fig. 1). Two linear positioning stages built by Attocube Systems AG were used to move the pressure transducer and the thermocouple in the plane perpendicular to the jet axis. Each stage has a range of about 3 mm in 1 dimension with step sizes in the order of 0.01 mm. One stage was placed on top of the other with their axis of movement perpendicular to each other for a total maximum examination area of 3 mm by 3 mm. The thermocouple and pressure transducer were fixed to a custom made probe stand mounted on top of the positioning assembly. In turn, the linear stages were placed at the top end of a shaft that rested on a large 10-cm range linear stage built by SETCO™ outside the main chamber. Since the temperature probe approached the coaxial jet from the bottom and it had sufficient range, it was capable of getting arbitrarily close to the exit plane of the coaxial jet. In fact, the thermocouple was even been used to measure the temperature within the recess of the inner jet. Non-dimensional quantities such as Re , We , VR and MR for a given condition were calculated using the measured flow rates, the mean chamber pressure and jet temperatures in conjunction with NIST's REFPROP® database^{12,13}. Density, viscosity, and surface tension values were obtained from these properties. For reference, the critical temperature of N_2 is 126.2 K and its critical pressure is 3.39 MPa.

Flow visualization was achieved with a Phantom® 7.1 CMOS camera. The camera can be seen facing the main chamber in the center picture of Fig. 1. Backlit images with a resolution from 128x224 to 196x400 pixels were obtained, with each pixel representing an area of approximately 0.08 mm by 0.08 mm. The framing rate was 20-25 kHz. The number of images saved per run was 1000 on average. The jet was backlit using a Newport® variable power arc lamp set at 160 W. For the analysis of the one-phase subcritical coaxial jet data, the jet spread angle between the outer jet and the chamber was measured directly from 20 backlit images. The spreading angle for this

study was defined to start from the point where the jet starts to grow (approximately 2 to 4 D1 downstream of the exit plane) to 10D1. Therefore this can be interpreted as an initial spread angle. Figure 3 shows a typical image and how the spreading angle is measured. Only α_1 and α_4 are visible and measured. The angles α_2 and α_3 are not visible in the backlit images. They are indicated to complete a conceptual picture of the spreading of the jet.

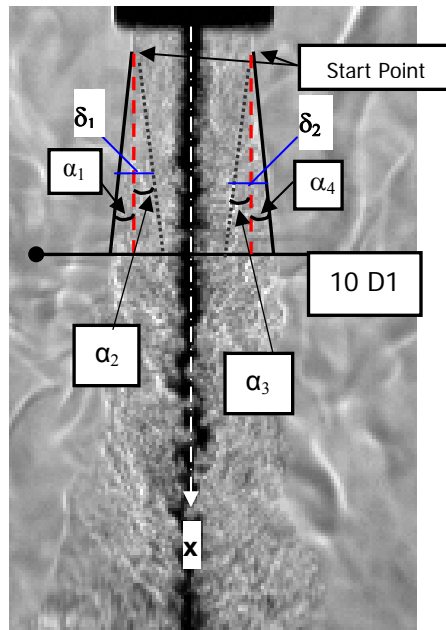


Figure 3. Image showing how spread angles are measured.

The dark core lengths were measured from 998 images using a MATLAB[®] subroutine based on the Otsu technique¹⁴ to find a grayscale threshold which helps distinguish the inner core from the rest of the image (see Fig. 4). More details on how the dark core is defined and measured can be found in previous papers from this group^{10,11}. Essentially, the colder inner jet in our experiments appears as a dark central feature on the images surrounded by a warmer outer jet. The axial dark core length, L_{axial} , is the projection of the inner jet before its first break along the axis parallel to the jet flow. The dark core length is a qualitative indicator of mixing. The shorter it is the faster mixing is occurring between the two jets. The dark core itself as a parameter does not have a unique definition. Different definitions and measuring techniques change its absolute magnitude. Thus, more value is placed on the trends and relative changes seen on the dark core as operating conditions change than on the actual absolute magnitudes.

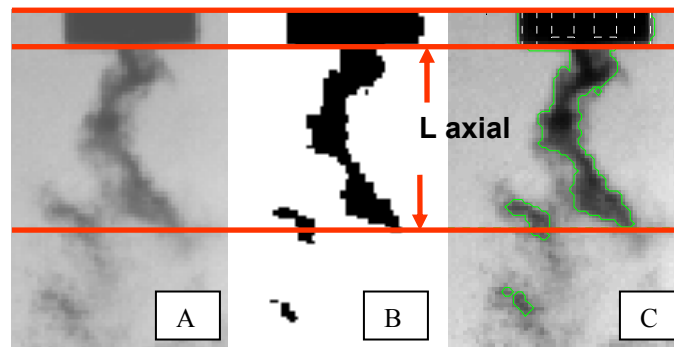


Figure 4. Definition of axial dark core length, L_{axial} . [A] Typical image. [B] Original image after a threshold has been applied to a binary image. [C] Contour from which the axial length is calculated.

The two piezo-sirens used to generate the transverse acoustic field were custom-designed by Hersh Acoustical Engineering, Inc. (see Fig. 1). In principle, a sinusoidal voltage signal moves the piezo element which has an aluminum cone attached to it producing acoustics waves. When the two drivers have a zero degree phase angle difference they move in opposite directions. On the contrary, when the two drivers have a 180-degree phase difference the cones move in the same direction, ‘chasing’ each other. This behavior is represented by the sketches in Fig. 5. A Fluke[®] signal generator was used to drive the piezo-sirens with a sinusoidal wave at a chosen driving frequency and phase angle between them. The frequency was manually varied until the highest amplitudes of the pressure waves were obtained. These frequencies spanned a range between 2.93 and 3.09 kHz. Then the signals were amplified and fed to the piezo-sirens with the voltage supplied to each driver kept constant. A waveguide with a catenary contour was used to guide the waves from a circular cross-section at the end of the aluminum cone to the rectangular cross-section of the inner chamber.

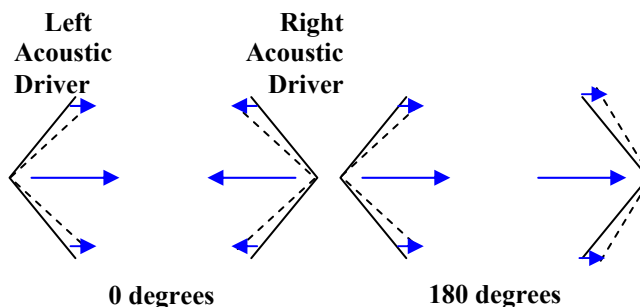


Figure 5. Simplified diagram of the two acoustic drivers at a 0° and 180° phase angle.

III. Results

A. Subcritical One-Phase Outer Jet Spreading Angles.

One of the areas of interest in coaxial jet behavior is the situation where both fuel and oxidizer are injected into the combustion chamber in the gaseous phase. The purpose of this study is to complement previous work⁸ where for subcritical pressures, the inner jet temperature was either a few degrees below or at the saturation temperature, and the outer jet was in the vapor phase, therefore having two-phase flow. For near and supercritical pressures, the inner and the outer jet were mostly both in the supercritical region, and therefore constituted one-phase flows but certainly not gas-gas flows. For a few cases, the inner jet was a few degrees below the critical temperature and therefore had a liquid-like-supercritical combination. Thus, the present work aims to complete this set of coaxial jet spreading angle measurements and make gas-gas data available since it is the most reported type of data in the literature for coaxial jets.

Angle measurements were processed from 6 MR's starting at 0.013 and up to 2.0. To generate these cases, the inner jet mass flow rate was fixed and the outer jet mass flow rate was varied. The temperatures were recorded to obtain the different thermodynamic variables used in the study. A visual inspection of at least 20 randomly-selected images for each case was performed. From each picture a left angle (α_1) and a right angle (α_4) were obtained. These angles were added and a total spread angle was found as shown in Figure 6. In the plot shown, the trend starts with a very low momentum flux ratio (0.013) and a negative spreading angle (- 6°) which indicates that outer jet width is decreasing as it exits the tip of the injector. The next MR is 0.037 and in this case the coaxial jet shows an angle of 5°. The remaining MR's surveyed have angles in the 10-11° range. This behavior is quite similar to previous results with corresponding MR's greater than 0.1 reported by our group for different running conditions⁸ where the outer jet spreading angle was about constant at 11°. These results identify conditions where the behavior of vapor-phase subcritical coaxial jets mimics the observed behavior of previous subcritical two-phase and near and supercritical experiments.

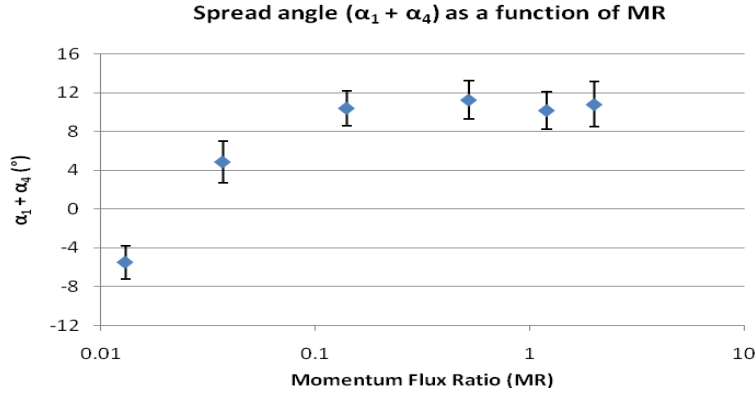


Figure 6. Outer jet spread angle measurements for one-phase coaxial jet at subcritical pressures. The bars indicate one standard deviation above and below the mean spreading angle.

To compare the results from these gas-gas experiments with other available data, a plot of the spreading angle growth rate as a function of the density of the chamber, the density of the outer jet and the momentum flux ratio is shown in Figure 7. The exact variable to which the spreading angle was compared is the ratio of the chamber density to that of the outer jet times the square root of the momentum flux ratio. The reason we incorporated MR to the more widely used chamber to outer jet density ratio is to bring in the effects of the inner jet on the outer jet spreading angle. A square root was used so that the outer jet density would not be cancelled and also because from previous studies^{10,15} it was found this was an important scaling parameter for shear coaxial jets. For $MR > 0.1$ cases it is interesting to notice that the new one-phase subcritical data (orange triangles with error bars) clusters well with previous data from our group (blue triangles) and computational results using the same injector geometry that was used for this study (light green and dark orange squares). Data gathered from other researchers^{5-7,16} and theoretical predictions show larger angles. One of the possible explanations for these larger angles as compared to the shorter angles obtained in our studies could be explained by the injector geometry used. The particular configuration used in our studies, which is the same geometry used by Liu et al.¹⁷, produces a large recirculation zone between the inner jet and the outer jet at the inner jet exit location (see Fig. 2). This recirculation zone does not exist in coaxial jet geometries where the inner jet and the outer jet are separated by a very thin wall or for two-dimensional shear layer mixing studies where the flows mixing at two different velocities are assumed to have wall of negligible thickness between them. The exact mechanism responsible for the smaller outer jet spreading angles is still being understood.

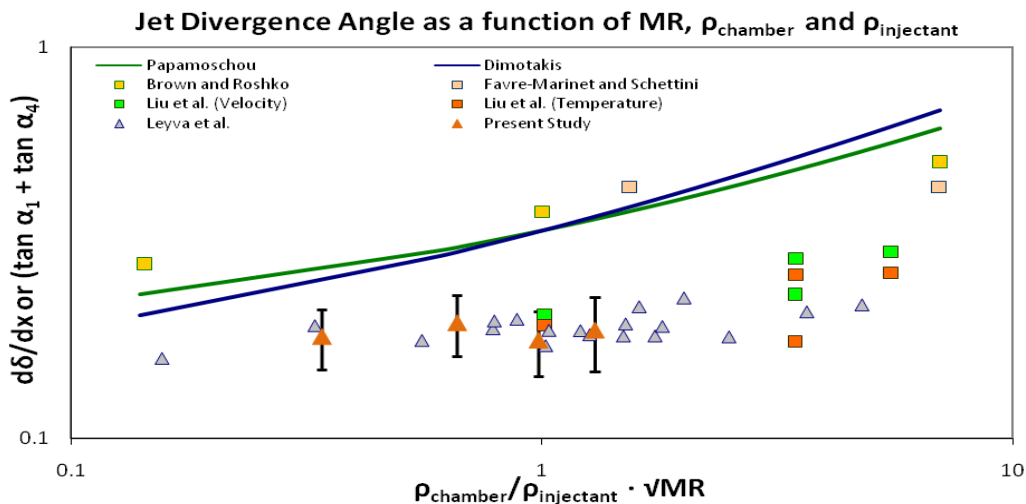


Figure 7. Outer jet spread angle measurements compared to jet divergence angle theoretical predictions and other single jet and coaxial jet spreading angle experimental data. Only cases with $MR > 0.1$ are included.

B. Subcritical to Supercritical Dark Core Length Measurements.

For the second part of this paper, results on the dark core length of the inner jet of a coaxial jet flow at subcritical to supercritical chamber pressures where the flow was exposed to a transverse acoustic field will be presented. The results are drawn from a complete set of data where at least 6 cases are reported for each of the three mean chamber pressure conditions surveyed: subcritical, nearcritical and supercritical. The amplitude of the root-mean-square of the pressure perturbations compared to the mean chamber pressure ranged from 1 to 4 %, the VR varied from 0.25 to 23 and the MR from 0.02 to 23. A complementary analysis on this data will be presented by Leyva et al.¹⁸

Two acoustic sources were used to generate the transverse acoustic field inside the inner chamber of the experimental apparatus. To expose the coaxial jet flow to different acoustic conditions, the phase between the two acoustic sources was varied from 0° to 360° in steps of 45°. A measurement of the root-mean-square values of the pressure fluctuations at each phase angle condition can be observed for a nearcritical case in Figure 8.

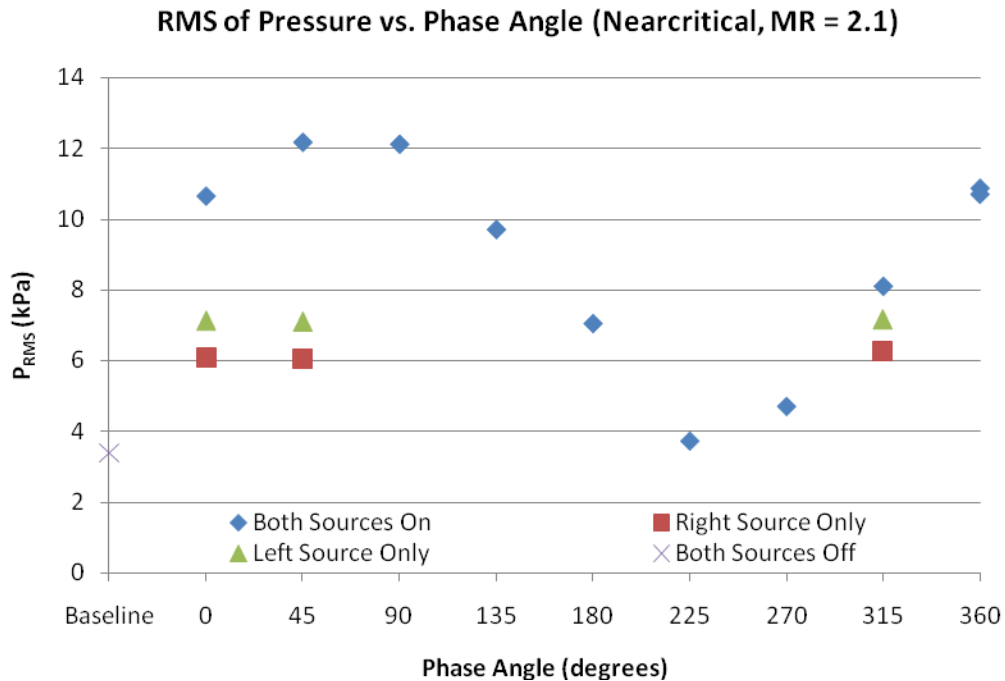


Figure 8. RMS of chamber pressure fluctuations versus phase angle between acoustic sources for the nearcritical case with MR = 2.1.

To have a better understanding of the chamber environment during these tests, the time history of the chamber pressure during different transverse acoustic excitation conditions was plotted on the right column of Figure 9. Each plot on the left column of Figure 9 corresponds to the plot to the right. The image shows how the two acoustic sources combine to expose the jet to different pressure perturbation conditions at the coaxial jet center depending on the phase difference between them. Though ideally a maximum pressure perturbation should be achieved at 0° and the minimum at 180° such as in the supercritical case of Figure 9, maxima were observed as low as 315° (- 45°) such as in the subcritical case for the same figure and as high as 45° such as in the nearcritical case. The search for an explanation for this phenomenon is still ongoing. Though not always at the same phase angles for all cases, the coaxial jet was exposed to different acoustics conditions ranging from minimum to maximum pressure and velocity perturbations. These oscillatory motions affected the jet behavior and the objective of this study was to quantify and understand the effects of these different acoustic conditions on the fluid mechanics of the jet.

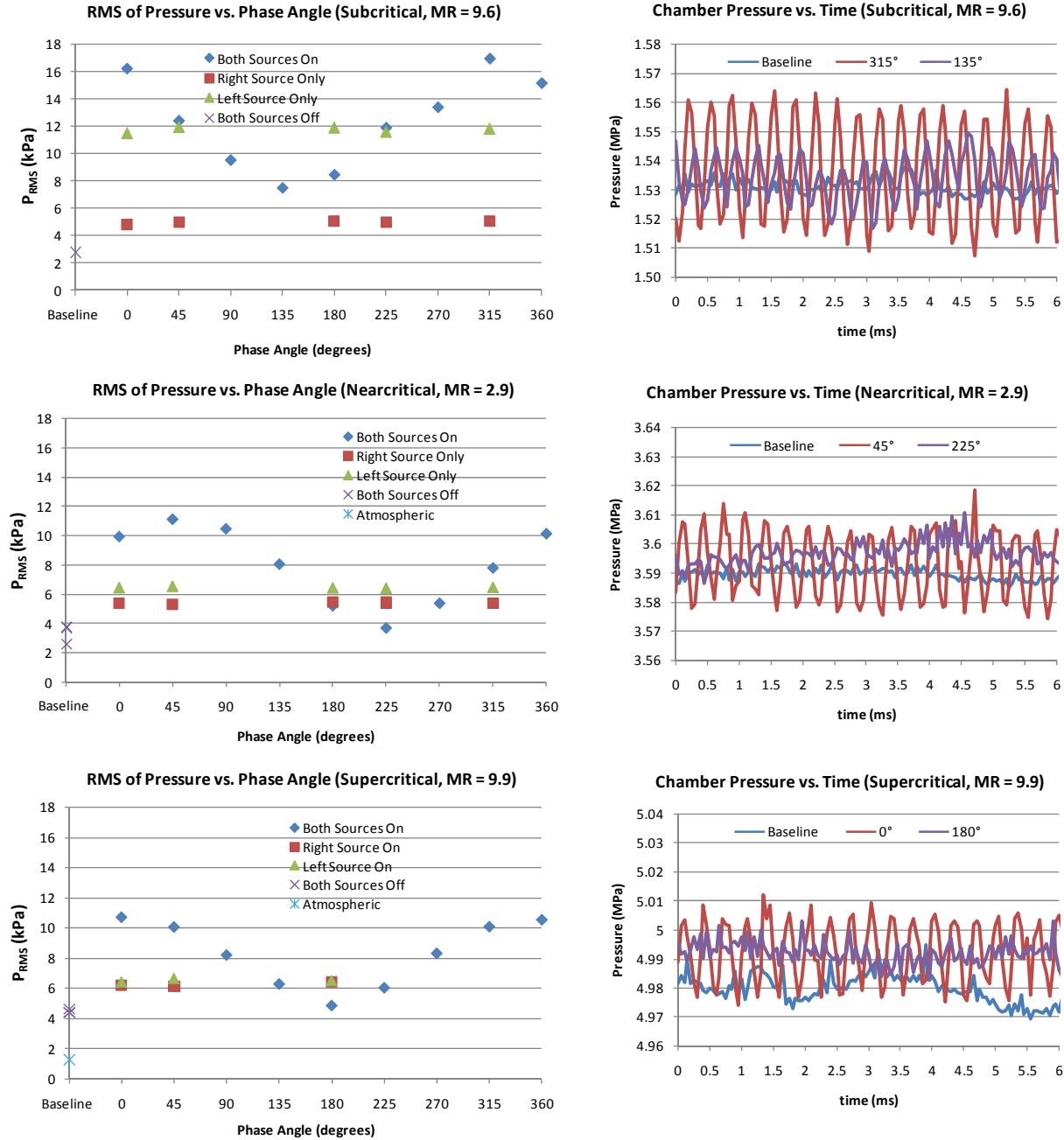


Figure 9. RMS of chamber pressure fluctuations vs. phase angle compared to chamber pressure as a function of time for one particular MR case at each of the three pressure conditions examined this study.

The results of the dark core length change at different MR's and mean chamber pressure conditions are presented next. The ratio of the length of the dark core with acoustics to the length of the dark core with no acoustics ($L_{acoustics}/L_{no\ acoustics}$) and the peak-to-peak pressure perturbation as a percentage of the mean chamber pressure ($\Delta p_{peak-to-peak}/p_{mean}$) both as a function of the phase angle between acoustic sources are shown in Figure 10. In these series of plots, one of the most interesting observations is that for a given momentum flux ratio, the dark core length results from subcritical, nearcritical and supercritical tests do not show much difference among them at each phase angle condition. For instance, despite the relative acoustic excitation intensities varying as much as eight times from subcritical to supercritical chamber pressures, for an MR near 1.0, the change in normalized dark core length ($\langle L_{acoustics}/L_{no\ acoustics} \rangle_{MAX} - \langle L_{acoustics}/L_{no\ acoustics} \rangle_{MIN}$) at any given phase angle was not more than 35% of the value of the minimum normalized dark core length at that phase angle ($\langle L_{acoustics}/L_{no\ acoustics} \rangle_{MIN}$). In fact, still for an MR near

1.0, for most phase angles this change was not higher than 21% (see upper right corner plot in Fig. 10). Momentum flux ratios of 2.5 and 9.5 show similar trends in the change in normalized dark core length at any given phase angle with the largest change ($\langle L_{\text{acoustics}}/L_{\text{no acoustics}} \rangle_{\text{MAX}} - \langle L_{\text{acoustics}}/L_{\text{no acoustics}} \rangle_{\text{MIN}}$) being not higher than 50% of the value of the minimum normalized dark core length ($\langle L_{\text{acoustics}}/L_{\text{no acoustics}} \rangle_{\text{MIN}}$) at that phase angle as can be seen in the mid right and lower right corner plots in Fig. 10. Overall, these results show a very interesting trend which suggests that a normalized dark core length behavior which is independent of mean chamber pressure.

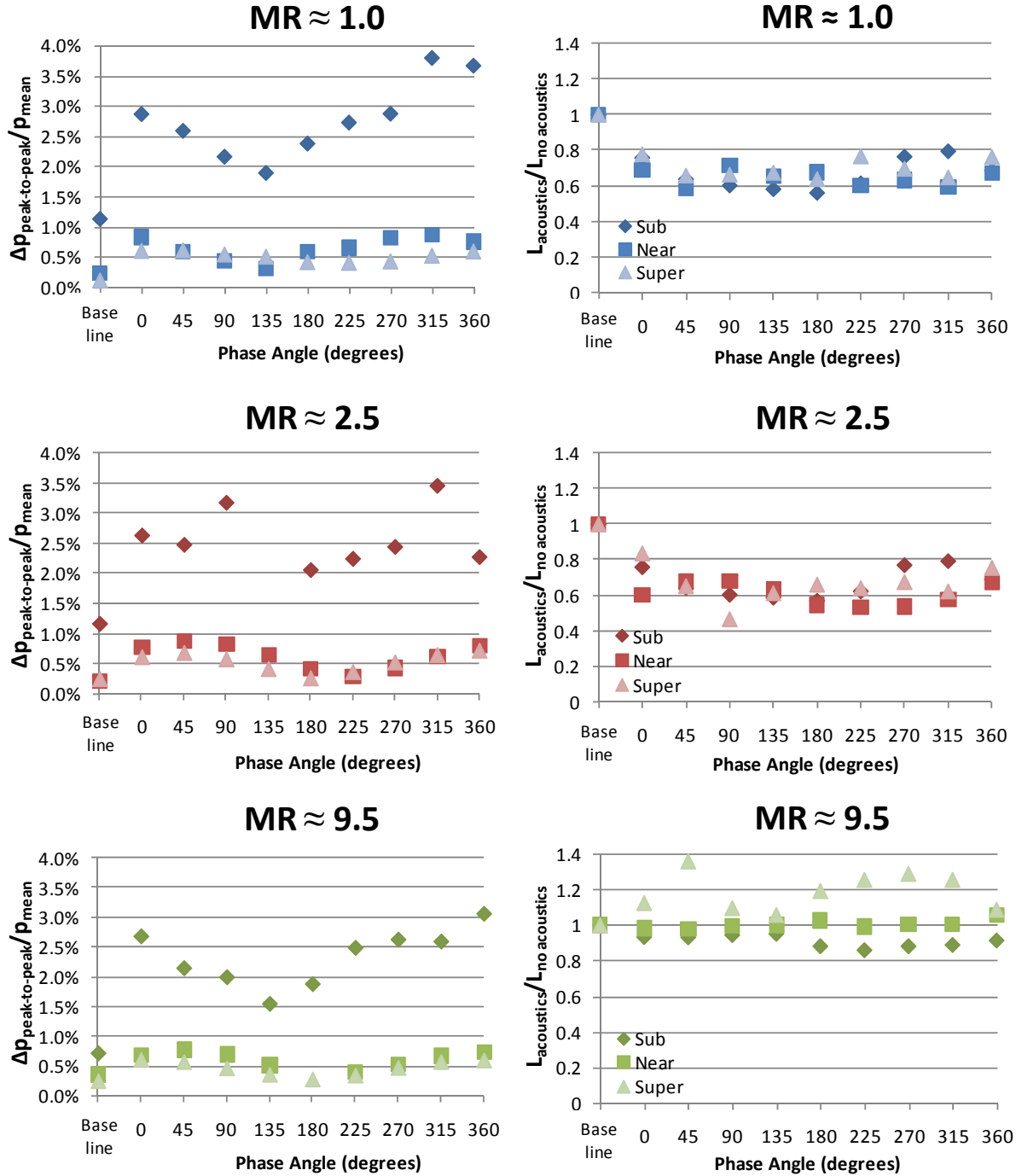


Figure 10. Peak-to-peak pressure perturbation ($\Delta p_{\text{peak-to-peak}}$) as a percentage of the mean chamber pressure (p_{mean}) and dark core length with acoustics ($L_{\text{acoustics}}$) over dark core length without acoustics ($L_{\text{no acoustics}}$) versus phase angle between acoustic sources for sub, near and supercritical pressures at $MR \approx 1.0, 2.5$ and 9.5 .

A plot that compiles all the dark core length data is shown in Figure 11. To make this graph, the difference between the baseline length or the length of the dark core with no acoustics and the length of the dark core with acoustics ($L_{\text{no acoustics}} - L_{\text{acoustics}}$) was found for each phase angle at a given mean chamber pressure and MR and the maximum was selected. This quantity was termed “axial length change” and then the normalized axial length change ($\Delta L_{\text{axial}}/L_{\text{no acoustics}}$) was plotted versus MR for three mean chamber pressures. The overall trend for all pressure conditions shows that at very low MR's (< 0.5) the normalized axial length change drops below 30%. Next, the range of values of MR between 0.5 and 5 shows normalized axial length changes between 30 to 50%. The sole exception is the subcritical case with an MR of 2.6 which has a normalized axial length change of approximately 25%. All the cases with an MR greater than 5 show normalized axial length changes close to 20% or below. Though not in a very clear fashion, this plot confirms earlier statements by our group^{8,9} suggesting a range of MR's in which the acoustic forcing has more influence on injector flow mechanics as suggested by its impact on the axial dark core length of the jet.

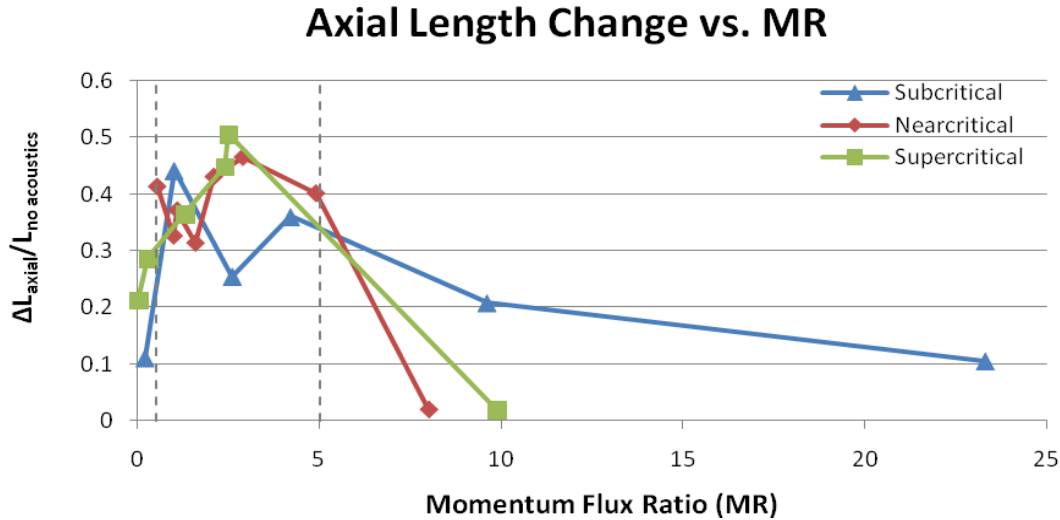


Figure 11. Maximum length change between dark core length without acoustics and dark core length with acoustics (ΔL_{axial}) divided by the dark core length without acoustics ($L_{\text{no acoustics}}$) for each MR case.

IV. Conclusions

This study complemented previous work done at AFRL on shear coaxial jet spreading angles and dark core length measurements from subcritical to supercritical pressures. From the gas-gas coaxial jet experiments, it was found that the outer jet spreading angle remained constant for $MR > 0.1$, in agreement with previous results showing essentially a constant angle for liquid-gas subcritical conditions, and a wide variety of supercritical conditions. In regard to the dark core length analysis for a given momentum flux ratio, the normalized dark core length results from subcritical, nearcritical and supercritical tests did not show much difference among them at each phase angle condition. For instance, despite the relative acoustic excitation intensities varying as much as eight times from subcritical to supercritical chamber pressures, for an MR near 1.0, 2.5, and 9 the change in normalized dark core length at any given phase angle was not more than 50% of the value of the minimum normalized dark core length at that phase angle. In fact, for MR near 1.0, for most phase angles this change was not higher than 21%.

Appendix

A. Case Details for the One-Phase Subcritical Coaxial Jet Spreading Angle Study

	T _{chamber} (K)	P _{chamber} (kg/m ³)	P _{chamber} (MPa)	T _{outer} (K)	\dot{m} _{outer} (mg/s)	P _{outer} (kg/m ³)	u _{outer} (m/s)	T _{inner} (K)	\dot{m} _{inner} (mg/s)	P _{inner} (kg/m ³)	u _{inner} (m/s)	VR	MR	tan $\alpha_1 +$ tan α_4
SUB														
angle1	276	18.0	1.47	250	304	20	5.8	145	281	38	36	0.16	0.013	-0.10
angle2	276	18.8	1.53	254	506	21	9.2	145	281	40	35	0.27	0.037	0.08
angle3	276	18.2	1.48	254	1000	20	19	150	281	36	39	0.50	0.14	0.18
angle4	270	19.2	1.53	245	2000	21	36	155	282	36	39	0.94	0.52	0.20
angle5	270	18.8	1.50	246	3010	21	55	148	282	38	37	1.5	1.2	0.18
angle6	261	20.1	1.54	242	4500	22	78	190	281	28	50	1.6	2.0	0.19

B. Case Details for the Subcritical to Supercritical Coaxial Jet Dark Core Length Study

	T _{chamber} (K)	P _{chamber} (kg/m ³)	P _{chamber} (MPa)	T _{outer} (K)	\dot{m} _{outer} (mg/s)	P _{outer} (kg/m ³)	u _{outer} (m/s)	T _{inner} (K)	\dot{m} _{inner} (mg/s)	P _{inner} (kg/m ³)	u _{inner} (m/s)	Freq. (kHz)	P' _{RMS} (kPa)	VR	MR
SUB															
sub1	233	22.0	1.50	191	310	22.0	4.30	109	279	630	2.2	2.98	21.5	2.0	0.17
sub2	231	22.2	1.50	183	790	28.8	11.0	109	283	630	2.2	3.06	20.1	4.8	1.0
sub3	226	21.9	1.45	183	1230	27.8	16.9	109	284	630	2.2	3.06	17.8	7.6	2.6
sub4	226	22.9	1.51	185	1560	28.7	20.9	109	279	630	2.2	2.96	15.7	9.5	4.2
sub5	210	24.9	1.50	182	2400	29.3	31.3	109	279	630	2.2	3.01	16.9	14	9.6
sub6	216	24.1	1.50	191	3640	27.7	50.3	109	279	630	2.2	3.02	16.3	23	23
NEAR															
near1	223	56.6	3.58	180	1060	75.4	5.38	123	290	520	2.8	3.08	9.04	2.0	0.55
near2	207	62.0	3.57	152	1570	101	5.95	117	289	590	2.4	3.04	10.8	2.5	1.0
near3	228	55.1	3.58	185	1590	72.4	8.40	126	293	440	3.3	3.00	11.8	2.6	1.1
near4	223	56.1	3.55	184	2170	72.3	11.5	127	294	360	4.0	3.01	11.4	2.8	1.6
near5	230	54.2	3.56	199	2120	65.1	12.5	126	292	440	3.3	3.03	12.1	3.8	2.1
near6	229	54.5	3.56	183	2690	73.1	14.1	126	292	420	3.4	3.05	11.1	4.1	2.9
near7	219	57.6	3.56	194	3080	67.4	17.5	125	289	480	3.0	3.06	11.8	5.9	4.9
near8	213	59.6	3.56	192	6460	68.3	36.2	128	295	220	6.6	2.93	9.73	5.5	9.3
SUPER															
super1	231	76.1	4.96	198	292	93.9	1.19	136	291	300	4.8	3.05	8.01	0.25	0.019
super2	231	76.1	4.96	193	997	97.7	3.90	130	292	460	3.1	3.01	10.2	1.2	0.33
super3	221	80.4	4.95	180	2050	109	7.19	128	291	490	2.9	3.01	10.7	2.5	1.3
super4	222	80.1	4.96	182	3110	107	11.1	134	288	360	3.9	3.05	10.1	2.8	2.4
super5	222	80.3	4.97	191	2820	99.5	10.8	131	293	440	3.3	3.09	12.5	3.3	2.5
super6	211	85.8	4.96	187	5820	103	21.6	132	286	410	3.4	3.05	10.7	6.3	9.9

Acknowledgements

The authors would like to thank Lt. Jeff Graham for his valuable help processing the gas-gas coaxial jet angle data, and his assistance with the development of the visualization technique and the installation of the data acquisition system. They also express their appreciation to Mr. Randy Harvey for his invaluable contributions in running and maintaining the facility. This work is sponsored by AFOSR under Mitat Birkan, program manager.

References

1. Hulka, J., Hutt, J. J., *Liquid Rocket Engine Combustion Instability*, AIAA Progress in Astronautics and Aeronautics, Yang, V., Anderson W. E., Eds., 1995, p. 40.
2. Marshall, W., Pal, S., Woodward, R., Santoro, R. J., Smith, R., Xia, G., Sankaran, V., Merkle, C. L., "Experimental and Computational Investigation of Combustor Acoustics and Instabilities, Part II: Transverse Modes," *AIAA-2006-0538*
3. Richecoeur, F., Scoufflaire, P., Ducruix, S., Candel, S., *Journal of Propulsion and Power* 4:790-799 (2006).

4. Chehroudi, B., Talley, D., Coy, E., "Visual characteristics and initial growth rates of round cryogenic jets at subcritical and supercritical pressure", *Physics of Fluids*, Vol. 14, No. 2, February 2002, pp. 851-861.
5. Brown, G., Roshko, A., "On density effects and large structure in turbulent mixing layers"; *J. Fluid Mech.*, Vol. 64 part 4, 1974, pp. 775-816
6. Papamoschou D., Roshko, A., "The compressible turbulent shear layer: an experimental study," *J. Fluid Mech.* Vol. 197, No. 453 1988
7. Dimotakis, P. E., "Two-Dimensional Shear Layer Entrainment", *AIAA Journal*, Vol. 24, No. 11, Nov. 1986, pp. 1791-1796
8. Leyva, I. A., Rodriguez, J. I., Chehroudi, B., Talley, D., "Preliminary Results on Coaxial Jets Spread Angles and the Effects of Variable Phase Transverse Acoustic Fields", *AIAA-2008-0950*
9. Rodriguez, J. I., Leyva, I. A., Chehroudi, B., Talley, D., "Effects of a Variable-Phase Transverse Acoustic Field on a Coaxial Injector at Subcritical and Near-Critical Conditions", *ILASS Americas, 21st Annual Conference on Liquid Atomization and Spray Systems*, Orlando, Florida, May 18-21 2008.
10. Leyva, I. A., Chehroudi, B., Talley, D., "Dark-core analysis of Coaxial Injectors at Sub-, Near-, and Supercritical Conditions in a Transverse Acoustic Field", *AIAA-2007-5456*
11. Leyva, I. A., Chehroudi, B., Talley, D., "Dark-core analysis of Coaxial Injectors at Sub-, Near-, and Supercritical Conditions in a Transverse Acoustic Field", *54th JANNAF Meeting*, Denver, CO, May 14-18, 2007.
12. REFPROP, Reference Fluid Thermodynamic and Transport Properties, Software Package, Ver. 7.0, NIST, U.S. Department of Commerce, Gaithersburg, MD, 2002.
13. Thermophysical Properties of Fluid Systems (<http://webbook.nist.gov/chemistry/fluid>), NIST, U.S. Department of Commerce, Gaithersburg, MD, 2005
14. Otsu, N., *IEEE transactions on Systems, Man, and Cybernetics* 1:62-66 (1979).
15. Davis, D.W., Chehroudi B., "Measurements in an acoustically driven coaxial jet under sub-, near-, and supercritical conditions", *JPP*, Vol. 23, No. 2, March-April 2007
16. Favre-Marinet, M., Camano Schettini, E.B., "The density field of coaxial jets with large velocity ratio and large density differences", *Int. J. of Heat and Mass Transfer*, 44 (2001) pp. 1913-1924
17. Liu T., Zong, N., Yang, V., "Dynamics of Shear-Coaxial Cryogenic Nitrogen Jets with Acoustic Excitation under Supercritical Conditions", *AIAA* 2006-759.
18. Leyva, I. A., Rodriguez, J. I., Chehroudi, B., Talley, D., "Effect of phase angle on coaxial jet behavior spanning sub- to supercritical pressures", *ILASS Europe, 2008*

EFFECT OF PHASE ANGLE ON COAXIAL JET BEHAVIOR SPANNING SUB- TO SUPERCRITICAL PRESSURES

Ivett A Leyva*, Juan Rodriguez°, Bruce Chehroudi+, Douglas Talley*

*AFRL/RZSA Edwards AFB, Ca,
°Graduate Student, UCLA, Los Angeles, Ca
+ ERC, Edwards AFB, Ca

ABSTRACT

This paper describes the effects of phase angle of an acoustic pressure field on a shear coaxial jet. The jet is forced with a transverse acoustic field, made up of two acoustics sources with $p'_{\text{RMS}}/p_{\text{mean}}$ up to 3.1%. The chamber pressure ranges from 1.5 to 5.0 MPa. The momentum flux ratio (MR) between the outer and inner jet varies from 0.02 to 23 and the velocity ratio from 0.25 to 23. The shear coaxial geometry is selected because of its application to liquid rocket engines. The jet was analyzed by taking high speed images and exit-plane temperature measurements. This work continues previous work where the jet was excited with one acoustic source; therefore the jet location was fixed with respect to the acoustic field. For nearcritical pressures, the cases with $\text{MR} < 1$ and $\text{MR} > 9$ were least sensitive to the acoustic field and phase angles. For the cases, $\text{MR} = 1.1$ to 4.9 the trends of L/D qualitatively followed the p' field trends. The maximum L/D was found around the maximum value of p' and viceversa. For these data, it seems like the dark core length is most affected, in terms of its reduction, by high acoustic velocity amplitude and not high pressure amplitudes.

INTRODUCTION

The motivation for this work springs from the problem of combustion instabilities in liquid rocket engines. One of the unit physics problems that can be defined to try to understand the larger problem of combustion instabilities is the problem of the interaction of an acoustic field with a typical rocket injector. We choose to study the effects of a transverse acoustic field vs. a longitudinal field, because the former interactions are some of the most destructive to a rocket engine. Also, we choose to first investigate a shear coaxial injector because they are widely used in liquid rocket engines (LRE's). A key advantage of coaxial jets is that as the Momentum Flux Ratio (MR) between the outer jet and the inner jet increases mixing between the two jets increases so that uniformity can be obtained in relatively short distances from the exit plane. The Space Shuttle Main Engine (SSME) and the Vulcan engine for the Ariane 5 are examples of LRE's designed to operate above the critical pressures of each propellant individually. Hence, in our studies, we vary the chamber pressure from sub to supercritical values. In a typical application of a coaxial injector for a LOX/LH2 engine (e.g SSME), the oxygen is injected at subcritical temperatures in the center jet while the hydrogen is injected at supercritical temperatures, after being used as a coolant for the engine nozzle, in the coaxial jet. For these flows, the mixture no longer has a singular critical point but rather there are critical mixing lines that define its thermodynamic state [1]. Because of the added complexity introduced when working with mixtures, N_2 is used as the sole working fluid in this study. A typical operating velocity ratio (VR) between the outer and inner jets is about 10 arrived at from empirical evidence that injectors operating at these high

VR's were more stable against combustion instabilities [2,3]. Therefore in our studies we vary the VR and MR from less than 1 to as high as our facility allows, which is in the low 20's for both variables.

This paper is focused specifically on the effects of the phase of the acoustic pressure and velocity field on the coaxial jet flow. In previous experiments performed in the same lab there was one acoustic source at one end of the test chamber and a non-movable reflective wall at the other end. This meant that the relation of the position of the jet with respect to the acoustic wave profile was fixed. By adding a second identical resonator the magnitude and relative position of the pressure and velocity acoustic field with respect to the jet are now varied. Preliminary results for a few run conditions were presented before in the papers by Leyva et. al. [4] and Rodriguez et. al. [5]. This paper presents a complete set of data for one geometry. The data includes three chamber pressures and several MR's for each pressure. The axial length of the dark core is the main metric studied in this paper. An analysis of the spreading angle of the inner and outer jet under an acoustic field will be the next metric to be analyzed in a future paper.

EXPERIMENTAL SETUP

The experiments detailed here were performed at the Cryogenic Supercritical Laboratory (EC-4) at the Air Force Research Laboratory (AFRL) at Edwards Air Force Base, CA Figure 1 shows the main chamber and the supporting systems. In the current setup, ambient temperature N_2 is used to supply the inner and outer jet and also to pressurize the chamber. As a note, the critical temperature of N_2 is 126.2 K

Approved for public release; distribution unlimited. PA #08222A.

and its critical pressure is 3.39 MPa. . Both the inner and the outer jets are cooled by heat exchangers (HE's) using liquid nitrogen obtained from a cryogenic tank. One heat exchanger cools the inner jet and other two cool the outer jet. Depending on the setup, one of these HE's can be bypassed to modify the cooling patterns. The mass flow rates of liquid nitrogen through the HE's are regulated in order to control the temperature of the jets. These rates are measured with Porter[®] mass flow meters (122 and 123-DKASVDAA) at ambient conditions to avoid difficulties with mass flow rate measurement at cryogenic temperatures. An inner chamber was built and housed inside the main chamber to maintain the amplitude of the acoustic oscillations to a maximum at the test section. The inner chamber is 6.6 cm high, 7.6 cm wide and 1.3 cm deep (see Fig. 1).

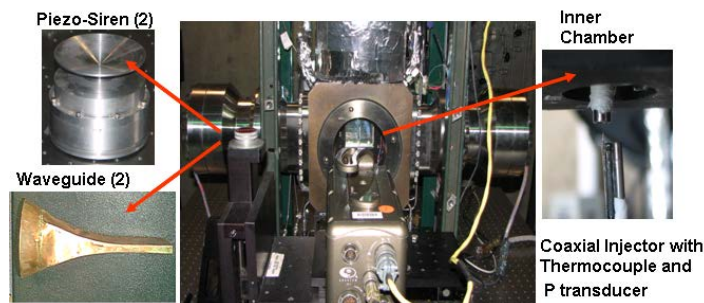


Figure 1. Experimental Setup

The inner tube making the inner jet has an inner diameter, $D1$, of 0.51 mm with length-to-diameter ratio of 100. The inner jet exit plane is recessed by 0.3 mm from the outer jet. The outer annular jet's inner diameter, $D2$, is 1.59 mm with outer diameter, $D3$, of 2.42 mm. For the outer jet, the length-to-mean-width of the annular passage is 67. The coaxial injector is shown in Fig. 2.

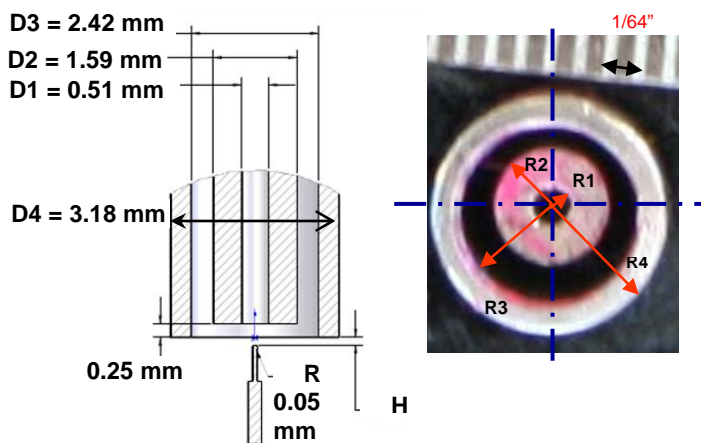


Figure 2. Details on the geometry of the shear coaxial injector used in this study.

The chamber pressure is measured with a Stellar 1500 transducer. An unshielded type E thermocouple with a bead diameter of 0.1 mm is used to measure the temperature of the jets. The accuracy of this thermo-couple was checked with an RTD and found to be ± 1 K. Also, a Kulite[®] XQC-062 pressure transducer is used to measure the pressure near the location of the thermocouple tip at a sampling frequency of 20 kHz (see bottom right picture in Fig. 1). Both the pressure transducer and the thermocouple are moved in the plane perpendicular to the jet axis with two linear positioning stages built by Attocube Systems AG. Each stage has a range

of about 3 mm in 1 dimension with step sizes in the order of 0.01 mm. One stage was placed on top of the other with their axis of movement perpendicular to each other for a total maximum interrogation area of 3 mm by 3 mm. The thermocouple and pressure transducer were fixed to a custom made probe stand mounted on top of the positioning assembly. In turn, the linear stages were placed at the top end of a shaft that rested on a large 4-inch range linear stage built by SETCO[™] outside the main chamber. Thus, the temperature probe approaches the coaxial jet from the bottom and it can get arbitrarily close to the exit plane. This thermocouple has even been used to measure the temperature within the recess of the inner jet.

The density, viscosity, and surface tension from the measured flow rates, chamber pressure and jet temperature are obtained using NIST's REFPROP[®] online database [6,7]. From these properties, Re , We , outer to inner jet velocity ratio (VR) and MR for a given condition are then calculated.

The coaxial flow was visualized using a Phantom[®] 7.1 CMOS camera. The camera can be seen facing the main chamber in the bottom left picture of Figure 1. Backlit images with a resolution from 128x224 to 196x400 pixels were obtained, with each pixel representing an area of approximately 0.08 mm by 0.08 mm. The framing rate was 20-25 kHz. The number of images saved per run was 1000 on average. The jet was backlit using a Newport[®] variable power arc lamp set at 160 W. The dark core lengths are measured from 998 images using a MATLAB[®] subroutine based on the Otsu technique [8] to find a grayscale threshold which helps distinguish the inner core from the rest of the image (see Fig. 3).

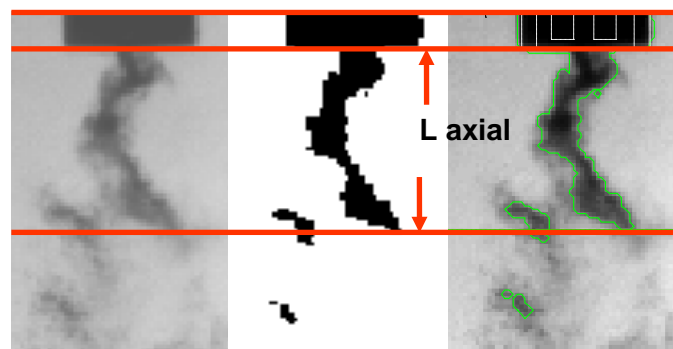


Figure 3. Definition of Axial Dark Core Length, L_{axial} . Leftmost image is a typical image. The middle image shows the original image after it has been thresholded to a binary image. The right image shows the contour from which the axial length is calculated.

The two piezo-sirens used to generate the transverse acoustic field were custom-designed by Hersh Acoustical Engineering, Inc. (see Fig. 1). The principle by which the piezo-sirens work as acoustic drivers is relatively simple. A sinusoidal voltage signal moves a piezo element with an aluminum cone attached to it, which in turn produces acoustics waves. When the two drivers have a zero degree phase angle difference then the movement of the piezo-siren cones is synchronized and they move in opposite directions. On the contrary, when the two drivers have a 180-degree phase difference the cones move in the same direction, or they 'chase' each other. This behavior is represented by the sketches in Fig. 4. A Fluke[®] signal generator was used to drive the piezo-sirens with a sinusoidal wave at a chosen

driving frequency and phase angle between them. The frequency was manually varied until the highest amplitudes of the pressure waves were obtained. These frequencies spanned a range between 2.93 and 3.09 kHz. Then the signals were amplified and fed to the piezo-sirens. The voltage supplied each driver was kept constant. A waveguide with a catenary contour was used to guide the waves from a circular cross-section at the end of the aluminum cone to the rectangular cross-section of the rectangular inner chamber.

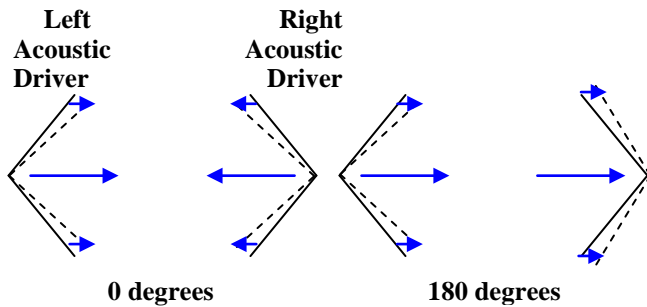


Figure 4. Simplified diagram of the two acoustic drivers at a 0° and 180° phase angle.

RESULTS

A series of runs were made at three nominal chamber pressures to span sub to supercritical chamber pressures. The detailed list of run conditions is shown in Table 1 in the appendix. For each chamber pressure several MR's were taken and for each MR the two acoustic sources were run at phase angles from 0 to 360 deg at intervals of 45 degrees. A qualitative sample of how the jet behaves for the different phase angles is first shown in Fig. 5. Here the first figure shows the jet with no acoustics. In this case, the pressure is subcritical and the inner jet is a liquid within 1 or 2 degrees K of the saturation temperature, and the outer jet is a gas. We can see that the dark core, or inner jet, is longest for the case with no acoustics, or baseline. Immediately when the acoustic field is turned on (0 deg), the jet is affected by the acoustics and the inner core is bent and shortened. We can also see how the outer jet is bent compared to the baseline case but not as dramatically. The bending and shortening of the dark core continues as the phase angle is increased and the minimum dark core length and most bending (qualitatively measured by the horizontal extend of the inner jet travel) are achieved at around 135-180 deg where we expect to have the highest amplitude of the velocity field.

The results on the shortening of the dark core length for all the cases run are compiled in Fig. 6. In this case, the y axis is the axial dark core length non-dimensionalized by the inner diameter of the inner jet, D1. The x-axis represents the phase angle between the two acoustic sources. As a convention, the angle is only changed on the right source with respect to the left source (Fig.1). The leftmost point in every graph corresponds to the case where no acoustics were on. In previous papers [9-10] it was shown that as the MR increases the axial dark core length decreases regardless of the chamber pressure. However, the behavior of the dark core length falls in two branches, one for subcritical pressure in which $L \sim A/MR^{0.2}$ and the other for near and

supercritical pressures where $L \sim B/MR^{0.5}$. The results obtained here for the case of no-acoustics agree with those previous results. Overall, we observe that for the chamber pressures studied here, as MR increases the axial length decreases for all phase angles. For $MR > 9$, $L/D1$ is $< \sim 7$ for the three chamber pressures and phase angles presented here. Also, the absolute (as compared to percentage) variation of the core length with respect to the baseline case as a function of phase angle decreases with MR. In other words, for the cases with the higher MR's the curves become more and more flat. For MR around 1-3 the curves of $L/D1$ show some curvature. For the specific case of subcritical pressures, we observe a grouping in the data. For the case of $MR < 1$ the lengths are longest as mentioned previously. However, for the three cases of $MR=1$ to $MR=4.2$, we see very good agreement among these cases. The L/D values cluster around 9 to 13 and they have about the same shape. Their minimum occurs around 180 deg and their maximum around 315-360 degrees. This is consistent with previous observations that the jet is more affected by high velocity fields than by high pressure fields. Finally, for the cases with $MR > 9$, the data becomes less sensitive to phase angle. For the case of nearcritical pressures, there is a similar grouping on the data, with the two curves for $MR=0.55$ and 1 being longest, then the three curves corresponding to $MR=1.1$ to 2.1 clustering around each other and showing the same curvature. In this case also, the minimum is around 180 deg and the maximum is around the ends of the curve. Note that while the case for $MR=2.9$ follows the same curvature as these three cases, because the values for L/D are lower, it cluster more with the high MR curves. A similar grouping can be observed for the case of supercritical pressure. However for the case of supercritical pressure, the curves for $MR=2.4$ to 9.9 cluster together with low L/D 's. For the case of near and supercritical pressures the dark core length varies by an order of magnitude between the lowest and highest MR's run.

Another way to look at the effect of the phase angle on the dark core length is to look at the ratio of the new dark core with acoustics to the baseline value with no acoustics. The results are shown in Fig. 7. The data is the same as in the previous figure but for each MR, the dark core lengths with acoustics are normalized by the respective baseline value. This is done to see if as the dark core length decreases with MR, its percentage decrease with acoustics also decreases. As it turns out, we see that for all the pressures, when the MR is larger than ~ 9 the change in length for all phase angles varies up to 20%. The biggest percentage reductions are for MR around 1 to 3. This is consistent with previous data reported in papers [9-10] where the maximum effect of a single acoustic source on the axial dark core length was found to be for $\sim 1 < MR < \sim 4$. Plotting the data in this way reveals that while the absolute variation of the dark core length for a given MR is usually greater for subcritical pressures, the percentage change for the MR's explored in this study is about the same for the three pressures studied. That is, the percentage change of the axial dark core length seems to be no greater than 50% for all cases. We also note that the case of supercritical pressures shows the most scatter on the data.

Since we are varying the phase of the acoustic field with respect to the exit of the jet, it is interesting to find out if the dark core length directly responds to the variations of the

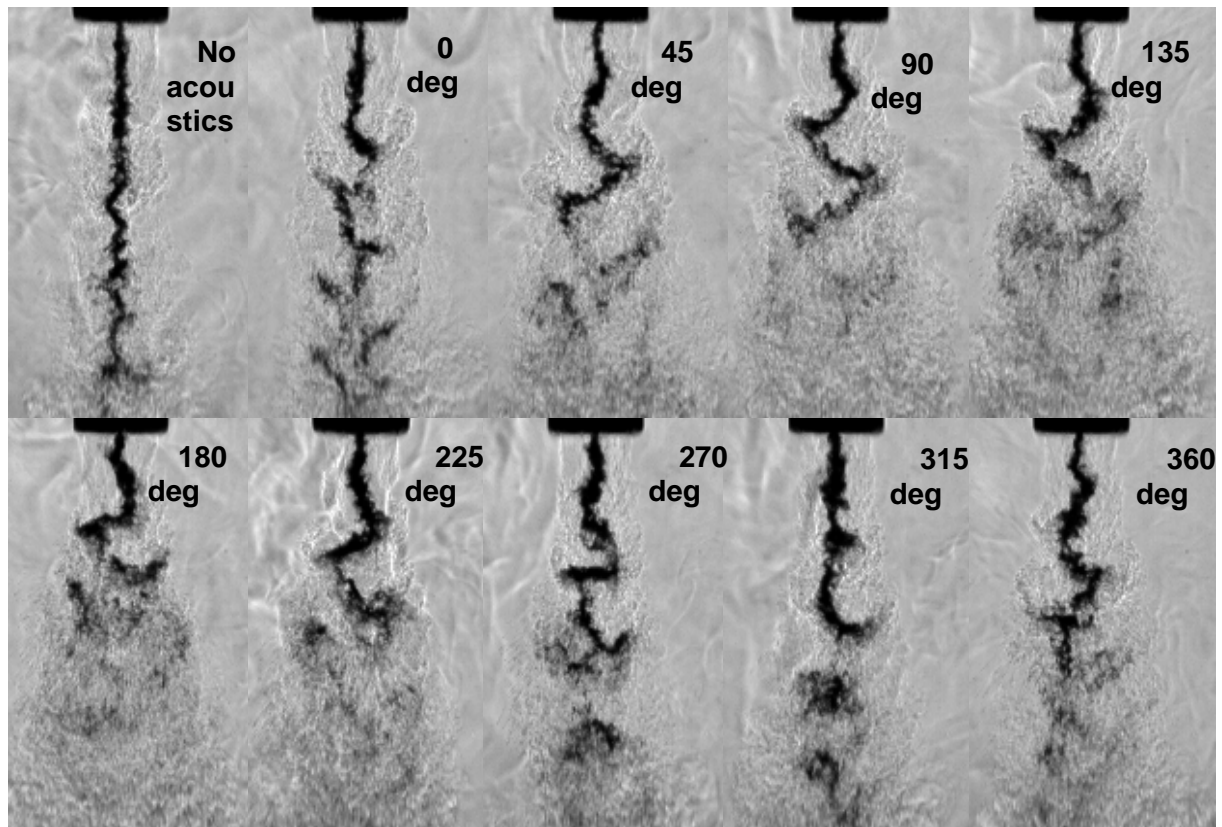


Figure 5. Images of a shear coaxial jet flow for different phase angles between two acoustic sources.

acoustic field. That is, as the acoustic pressure, p' , monotonically increases at the injector location, does the dark core length also monotonically increase or decrease? To answer this question, let's look in detail to a sample of superimposed traces of the acoustic field and the dark core length. We will look in detail to the nearcritical case. The results are shown in Figure 8. In general, the change on the location of the minimum in the p' field is due in part to the different frequencies that drove the acoustic sources. The frequency was chosen to give the max amplitudes in both drivers. The maximum p' amplitudes varied within 0.2 psi for all the cases examined here for the nearcritical pressures.

For the first case, $MR=0.56$, $VR=2.0$ and we can see that even though when the acoustics are turned on the dark core length decrease is statistically significant, the dark core length remains about constant for all the phase angles, except for the last point at 360 deg. This is not surprising since we have seen before that coaxial jets with $MR<1$ do not seem very sensitive to pressure fluctuations. Therefore, qualitatively, the trend of L/D does not follow the trend of p' , which has a minimum at around 135 deg. The inaccuracy of the acoustic pressure are not shown but it is ± 6.9 kPa according to the manufacturer. Therefore, the pressure variations fall within the accuracy of the transducer and the trends although mostly qualitative, agree very well with intuition where we would expect a minimum in acoustic pressure around 180 degrees.

The second case to consider has $MR=1.6$, $VR=2.8$. In this case, the qualitative trends of L/D and p' follow each other. Within the error bars we have a maximum L/D at the same phase angle where we have a maximum in the p' field. This would mean that when the pressure disturbance is maximum, the jet gets disturbed the least. Similarly the minimum L/D happens close to the minimum p' . This also points to the observation that it is the velocity fluctuations that most affect the jet. That is, when u' is highest, hence p , is lowest, the jet gets most decreased and bent. Notice also that p' for 0 deg and 360 deg are very close to each other, as they should be since this represents a full cycle returning to the same point

The following chart in Fig. 8 is for $MR=2.9$ $VR=4.1$. This and the previous chart ($MR=1.6$) are within the range of MR 's where we have previously seen the most effect on the dark core length. In this case, there is not a clear max or min for L/D but the range of max L/D is clustered around the max p' and the range of min L/D is clustered around the min p' . The last chart is for $MR=9.3$ $VR=5.5$. For this high MR , the dark core length has decreased significantly from the other cases. And once again, as it was the case for the low MR , the curve of L/D appears more flat. There does not seem to be a relation between the p' field and L/D . This is consistent with previous observations that for similar p' , for high MR 's the coaxial jet is not as disturbed as for $\sim 1 < MR < \sim 4$.

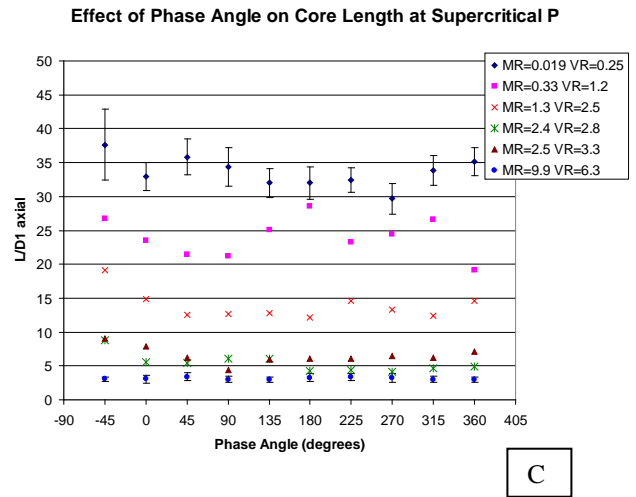
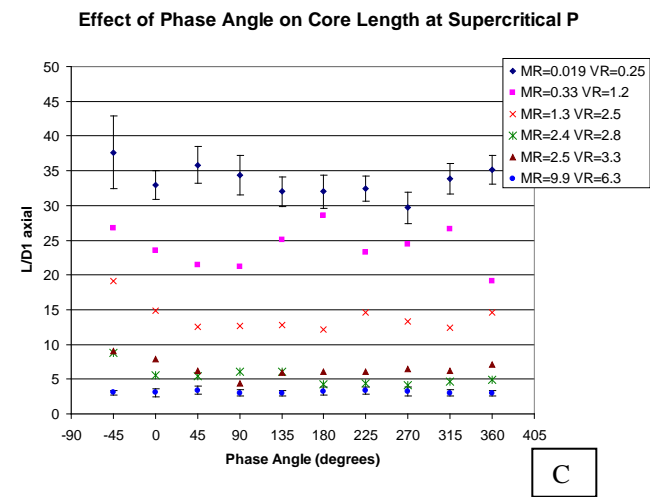
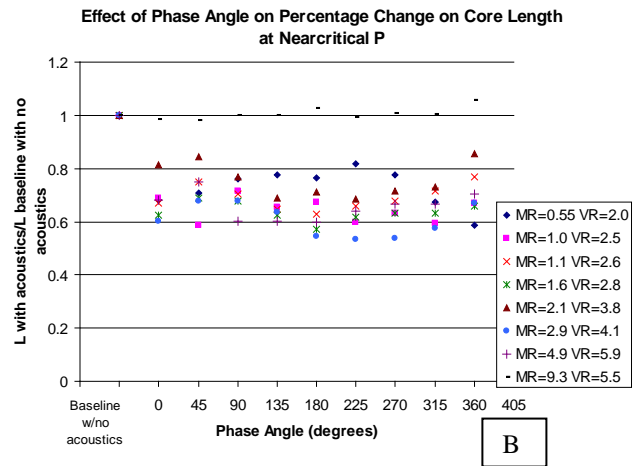
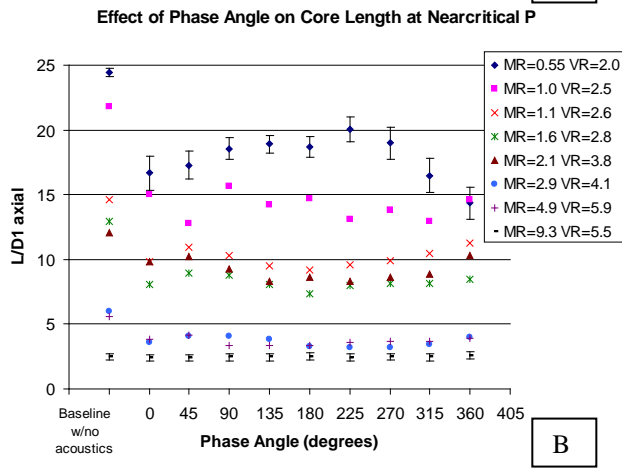
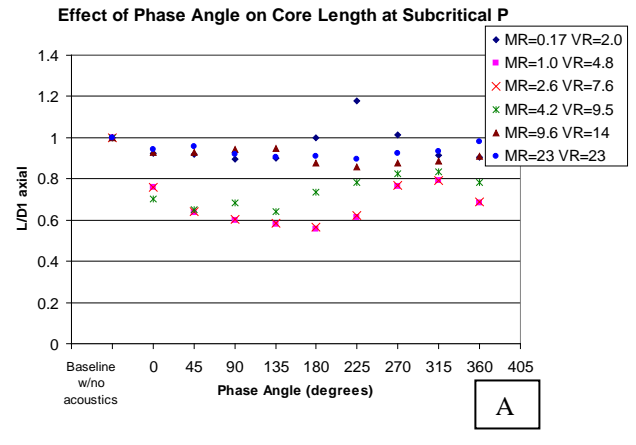
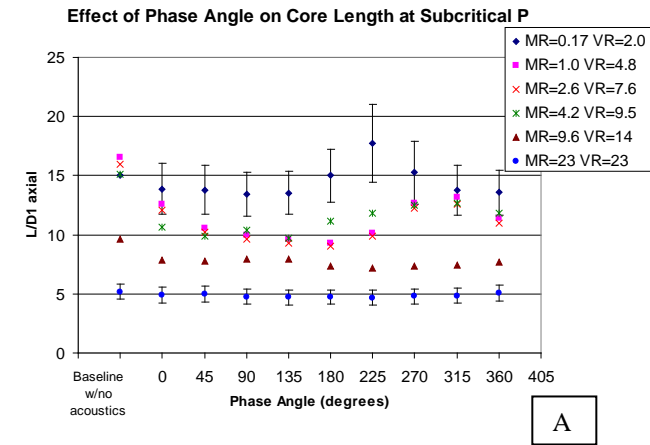


Figure 6. Effect of Phase Angle of the Axial Core Length for [A] Subcritical pressure, [B] Nearcritical pressure and [C] Supercritical pressure

Figure 7. Effect of Phase Angle of the percentage change of the Axial Core Length compared to the baseline case with no acoustics for [A] Subcritical pressure, [B] Nearcritical pressure and [C] Supercritical pressure

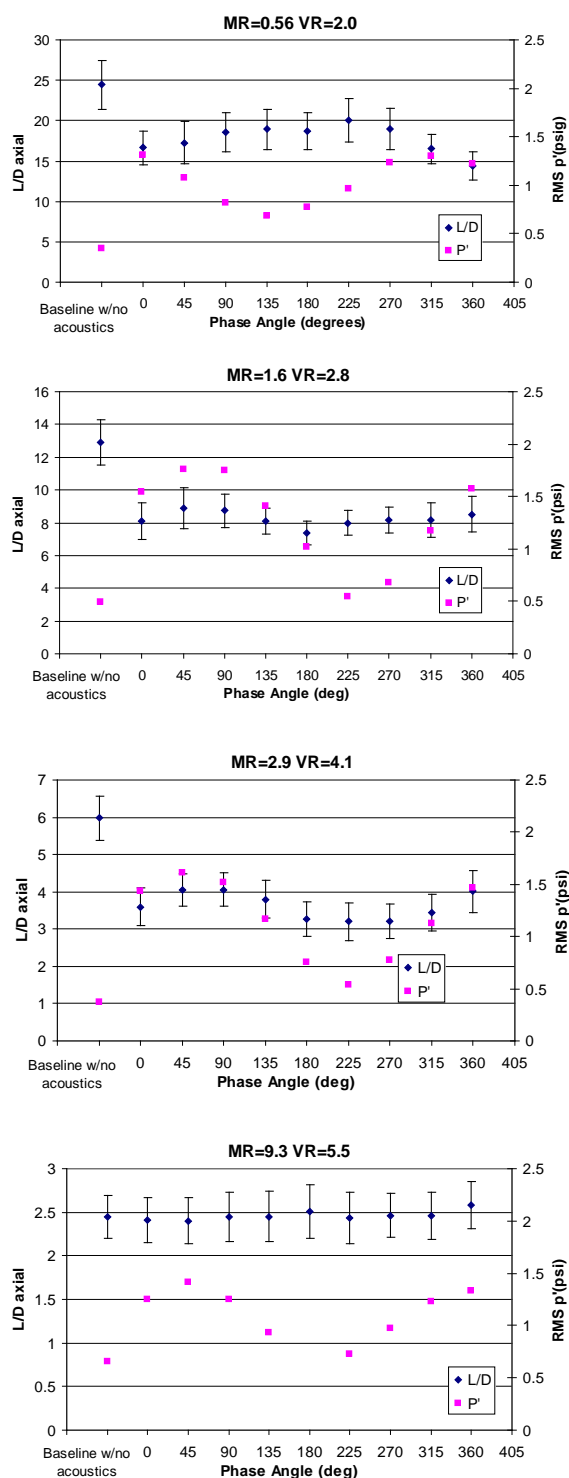


Figure 8. Comparison of acoustic pressure field and dark core length for the case of nearcritical pressures and different MR's

We have seen in the previous observations for the case of nearcritical pressures that the mixing mechanisms are different at different MR's. Once we set a relative momentum flux of the outer jet over the inner one, the interaction of the combined jets differs when it gets affected by a transverse acoustic source according to its MR. When

the MR is high (>9) the recirculation zone that gets set up in the region between the inner and the outer jet, due to the thick lip of the inner jet, becomes more prominent in the images and it starts to be of the same order of magnitude as the dark core itself. For these cases, when the jet is so short, the acoustics at any phase, move the jet back and forth but do not bend it. The contrary happens for low MR's (<1), where the jet is behaving more like a single jet. In these cases, the inner jet barely acquires curvature due to the acoustic field.

SUMMARY

In this paper we showed a complete set of data for a given geometry of a shear coaxial injector being perturbed by a transverse acoustic field. The acoustic field was set up by two acoustic sources. The phase angle of one acoustic source with respect to the other was changed from 0 deg to 360 deg. Three sets of operating chamber pressures spanning sub to supercritical values were chosen. For each chamber pressure an MR scan was done from $MR < 1$ to $MR > 9$. It was found that for the nearcritical pressure condition, the cases with $MR < 1$ and $MR > 9$ were least sensitive to the acoustic field. That is, the percentage variation of the dark core length for these cases was least. Also, the values of L/D were more insensitive to the phase angles. For the cases, $MR = 1.1$ to 4.9 the trends of L/D qualitatively followed the p' field trends. That is, the maximum L/D was found around the maximum value of p' and viceversa. For these data, it seems like the dark core length is most affected, in terms of its reduction, by high acoustic velocity amplitude and not high pressure amplitudes.

NOMENCLATURE

Symbol	Quantity	SI Unit
D	Diameter	mm
P	Pressure	Pa
T	Temperature	T
\dot{m}	Mass flux	mg/s
p'	Acoustic pressure	Pa
ρ	Density	Kg/m ³
MR	Momentum flux ratio between outer and inner jet	Non dimensional
VR	Velocity ratio between outer and inner jet	Non dimensional

ACKNOWLEDGMENTS

The authors would like to thank Mr. Randy Harvey for his invaluable contributions in running and maintaining the facility and to Lt. Jeff Graham for his help with the data acquisition system and visualization technique. This work is sponsored by AFOSR under Mitat Birkan, program manager.

REFERENCES

1. Oschwald, M., Smith, J. J., Branam, R., Hussong, J., Schik, A., Chehroudi, B., Talley, D., "Injection of Fluids into Supercritical Environments", *Combustion Science and Technology*, Vol. 178, No. 1-3, 2006, pp. 49-100.
2. Oschwald, M., Smith, J. J., Branam, R., Hussong, J., Schik, A., Chehroudi, B., Talley, D., *Combustion Science and Technology* 1:49-100 (2006)
3. Hulka, J., Hutt, J. J., *Liquid Rocket Engine Combustion Instability*, AIAA Progress in Astronautics and Aeronautics, Yang, V., Anderson W. E., Eds., 1995, p. 40.
4. Leyva, I. A., Rodriguez, J. I., Chehroudi, B., Talley, D., "Preliminary Results on Coaxial Jets Spread Angles and the Effects of Variable Phase Transverse Acoustic Fields", AIAA-2008-0950
5. Rodriguez, J. I., Leyva, I. A., Chehroudi, B., Talley, D., Effects of a Variable-Phase Transverse Acoustic Field on a Coaxial Injector at Subcritical and Near-Critical Conditions", ILASS Americas, 21st Annual Conference on Liquid Atomization and Spray Systems, Orlando, Florida, May 18-21 2008
6. REFPROP, Reference Fluid Thermodynamic and Transport Properties, Software Package, Ver. 7.0, NIST, U.S. Department of Commerce, Gaithersburg, MD, 2002.
7. Thermophysical Properties of Fluid Systems (<http://webbook.nist.gov/chemistry/fluid>), NIST, U.S. Department of Commerce, Gaithersburg, MD, 2005
8. Otsu, N., *IEEE transactions on Systems, Man, and Cybernetics* 1:62-66 (1979).
9. Leyva, I. A., Chehroudi, B., Talley, D., "Dark-core analysis of Coaxial Injectors at Sub-, Near-, and Supercritical Conditions in a Transverse Acoustic Field", AIAA-2007-5456
10. Leyva, I. A., Chehroudi, B., Talley, D., "Dark-core analysis of Coaxial Injectors at Sub-, Near-, and Supercritical Conditions in a Transverse Acoustic Field", 54th JANNAF Meeting, Denver, CO, May 14-18, 2007.

APPENDIX

Table 1. Run Conditions

	T_{chamber} (K)	ρ_{chamber} (kg/m ³)	P_{chamber} (MPa)	T_{outer} (K)	\dot{m}_{outer} (mg/s)	ρ_{outer_3} (kg/m ³)	u_{outer} (m/s)	T_{inner} (K)	\dot{m}_{inner} (mg/s)	ρ_{inner_3} (kg/m ³)	u_{inner} (m/s)	Freq. (kHz)	$P'_{\text{RMS max}}$ (psi)	VR	MR
SUB															
sub1	233	22.0	1.50	191	310	22.0	4.3	109	279	630	2.2	2.98	3.12	2.0	0.17
sub2	231	22.2	1.50	183	790	28.8	11	109	283	630	2.2	3.06	2.91	4.8	1.0
sub3	226	21.9	1.45	183	1230	27.8	16.9	109	284	630	2.2	3.06	2.58	7.6	2.6
sub4	226	22.9	1.51	185	1560	28.7	20.9	109	279	630	2.2	2.96	2.27	9.5	4.2
sub5	210	24.9	1.50	182	2400	29.3	31.3	109	279	630	2.2	3.01	2.45	14	9.6
sub6	216	24.1	1.50	191	3640	27.7	50.3	109	279	630	2.2	3.02	2.36	23	23
NEAR															
near1	223	56.6	3.58	180	1060	75.4	5.38	123	290	520	2.8	3.08	1.31	2.0	0.55
near2	207	62.0	3.57	152	1570	101	5.95	117	289	590	2.4	3.04	1.56	2.5	1.0
near3	228	55.1	3.58	185	1590	72.4	8.40	126	293	440	3.3	3.00	1.71	2.6	1.1
near4	223	56.1	3.55	184	2170	72.3	11.5	127	294	360	4.0	3.01	1.65	2.8	1.6
near5	230	54.2	3.56	199	2120	65.1	12.5	126	292	440	3.3	3.03	1.76	3.8	2.1
near6	229	54.5	3.56	183	2690	73.1	14.1	126	292	420	3.4	3.05	1.61	4.1	2.9
near7	219	57.6	3.56	194	3080	67.4	17.5	125	289	480	3.0	3.06	1.71	5.9	4.9
near8	213	59.6	3.56	192	6460	68.3	36.2	128	295	220	6.6	2.93	1.41	5.5	9.3
SUPER															
super1	231	76.1	4.96	198	292	93.9	1.19	136	291	300	4.8	3.05	1.16	0.25	0.019
super2	231	76.1	4.96	193	997	97.7	3.90	130	292	460	3.1	3.01	1.48	1.2	0.33
super3	221	80.4	4.95	180	2050	109	7.19	128	291	490	2.9	3.01	1.55	2.5	1.3
super4	222	80.1	4.96	182	3110	107	11.1	134	288	360	3.9	3.05	1.47	2.8	2.4
super5	222	80.3	4.97	191	2820	99.5	10.8	131	293	440	3.3	3.09	1.81	3.3	2.5
super6	211	85.8	4.96	187	5820	103	21.6	132	286	410	3.4	3.05	1.55	6.3	9.9

On the inner jet spread angles of coaxial jets from subcritical to supercritical conditions with preliminary numerical results (Preprint)

Juan I. Rodriguez[†], Jeffrey J. Graham[†], Ivett A. Leyva[‡], Hsin-Yuan Lyu[‡], Douglas Talley^{*}

[†]University of California, Los Angeles, Los Angeles, CA 90095

^{*}Air Force Research Laboratory/RZSA Edwards AFB, CA 93524

[‡]Advatech Pacific, Inc., Redlands, CA 92374

ABSTRACT

A study is performed to analyze the behavior of the inner jet spread angles in a coaxial jet flow configuration similar to those used in liquid rocket engines. These angles are measured from back-lit images. Data is presented for sub-, near-, and supercritical non-reactive N₂ coaxial jets. In the subcritical regime, the effects of an externally-imposed transverse acoustic field are also analyzed. The acoustic field is generated using two piezo-sirens and driven at a frequency of 3.0 ± 0.1 kHz. Pressure oscillations vary from 16 to 22 kPa, peak to peak, at the location of the jet with background pressure of 1.5 MPa. For all cases, by varying the inner and outer jet temperatures and mass flowrates, outer to inner jet velocity ratios from 0.25 to 23 and outer to inner jet momentum flux ratios (J) from 0.02 to 23 are achieved. In the case where no acoustic excitation is applied the angles for the near- and supercritical cases show more spread compared to their subcritical counterparts for $1.0 < J < 2.5$, attaining values up to 18°. However, at higher J values, the spread angles for subcritical pressures are larger than those for near- and supercritical pressures. When acoustics are applied at subcritical pressures, the largest spread angles occur for $2 < J < 10$, reaching values as high as 38°. Also, preliminary numerical results are presented for two supercritical cases with only one acoustic source present.

NOMENCLATURE

$J = \rho_{\text{outer}} u_{\text{outer}}^2 / \rho_{\text{inner}} u_{\text{inner}}^2$, outer to inner jet momentum flux ratio

$VR = u_{\text{outer}} / u_{\text{inner}}$, outer to inner jet velocity ratio

INTRODUCTION

The general problem of mixing between two jets in a coaxial configuration has been studied for several decades. Chigier and Beer [1] provided a very detailed description of the near field in an air-air coaxial jet with different outer to inner velocity ratios, VR (∞ , 2.35, 1.17, 0.235, 0.117, 0.024). They explain the interactions of the recirculation zone setup by the inner jet wall and the subsequent mixing process between the two jets. The lower VR is the less the inner jet is affected by the recirculation zone and the more the outer jet is deflected and entrained by the inner jet. Vice versa when VR is high, the inner jet is more affected by the recirculation zone whose vortices deflect the inner jet toward the annular jet thus getting entrained. Ko et al. and Chan et al. [2-5] have also provided detailed studies of air-air coaxial jets discharging into stationary air. In their research the inner jet post thickness was kept to a minimum. They obtained pressure measurements and hot-wire and microphone spectra. These studies are concerned with the characterization of the flow structures (e.g. vortices) developed at different regions in the coaxial jets and also with similarity of the mean velocity, turbulence intensity and pressure profiles.

In terms of the growth rate of the inner or outer jets in a coaxial configuration, several studies have also been completed by different groups [6-9]. As a point of reference, these results are often compared to the growth of shear layers between two planar flows which has been well characterized by several authors. Brown and Roshko [10], proposed an equation for the growth rate of the shear layer for subsonic two-dimensional incompressible turbulent gas-gas flows. Papamoschou and Roshko [11] later proposed an equation for the growth of the visual thickness of the shear layer for sub- to supersonic two-dimensional turbulent mixing layers. Finally, Dimotakis [12] proposed an equation for the vorticity growth rate of a planar freejet. Chehroudi et al. [13] showed that for single jets at supercritical pressure and temperature, the spreading angle agrees quantitatively with that predicted by the works mentioned above

which were derived for incompressible variable-density gas-gas jets. The data from the present study will be compared to the abovementioned body of work.

The particular interest on coaxial jets in this work springs from their wide application in liquid rocket injectors. For example, the SSME for the Shuttle and the Vulcan engines for the Ariane rocket use coaxial injectors. Furthermore, in this study we greatly expand the region of study as compared to previous results. We study one-phase and two-phase flows in sub to supercritical pressures. We solely use N_2 for the inner and outer jets and the chamber flows. This is to have a single critical point. In previous studies by the same group [14-15] preliminary results were presented for the growth rate of the outer jet. It was found that the spreading angle was fairly constant ($\sim 12^\circ$) for all cases studied, except for the case of gas-gas jets at subcritical pressures with $J < 0.1$ where the angles varied from -4° to 5° .

In the first part of the present study we look at the behavior of the inner jet with and without an externally-imposed transverse acoustic field. On the complex problem of combustion instabilities, which has plagued the development of liquid rocket engines practically since their inception, the interaction of an acoustic field with an injector flow is considered a unit physics problem. Therefore, the intent of this paper is to aid on the understanding of this unit problem. In our experimental setup, we use a rectangular test section and we excite the jet with a transverse acoustic field. A transverse mode on a rectangular chamber would be the equivalent of a tangential mode on a cylindrical chamber which is one of the most dangerous. Thus, in our current experimental configuration we have two acoustic drivers which allow us to change the phase of the acoustic field with respect to the fixed location of the coaxial jet injector. The spread angles that we obtain under acoustic perturbation could perhaps be used by a designer as a measure of the lateral spread expected from a single element under similar conditions. This would aid with designing the separation between elements if one does not want inter-element interactions.

The second part of this paper presents preliminary data on numerical simulations performed for the case of one-phase flows at supercritical conditions with and without acoustic excitation. In these simulations, only one acoustic source is modeled. This condition matches earlier experiments by our group where only one piezo-siren was used to produce an acoustic field within the chamber [16-17]. For this initial numerical study, temperature and species fields were compared with high-speed camera images and axial dark core length results for two experimental cases from the above references.

EXPERIMENTAL SETUP

The experiments in this study were conducted at the Air Force Research Laboratory (AFRL) in Edwards Air Force Base, CA using the Cryogenic Supercritical Laboratory (EC-4) facility. The main chamber and the supporting systems of EC-4 are shown in Figure 1.

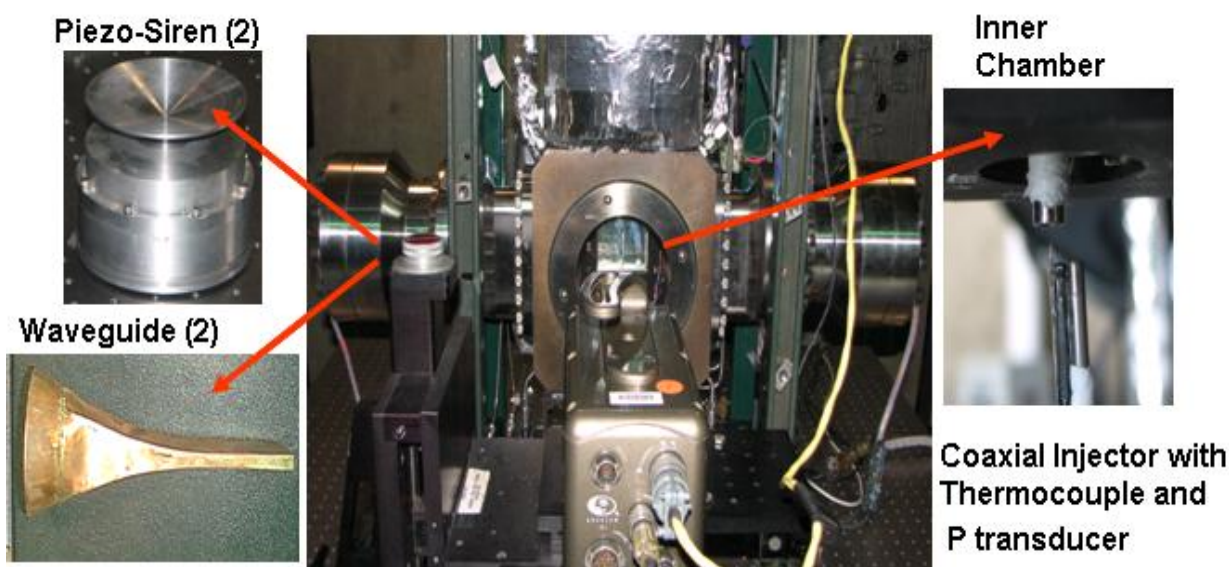


Figure 1. Overview of the experimental apparatus

Ambient temperature N_2 is used to supply the inner and outer jet and also for chamber pressurization. Heat exchangers (HEs) using liquid nitrogen obtained from a cryogenic tank are used to cool the inner and the outer jets. One heat exchanger is used for the inner jet and two others for the outer jet. For the outer jet flow, the option to bypass one of the HEs to modify the cooling pattern is available. The temperature of the jets is controlled by the mass flow rate of liquid N_2 through the HEs. To avoid difficulties with mass flow rate measurement at cryogenic temperatures, these rates are measured with Porter® mass flow meters (122 and 123-DKASVDAA) at ambient temperature. Both the inner and the outer jet flow through an injector assembly, shown in Fig. 2, which exits to an inner chamber built and housed inside the main chamber so that the amplitude of the acoustic oscillations is maximized at the test section. This inner chamber is 6.6 cm high, 7.6 cm wide and 1.3 cm deep (see image on the right in Fig. 1). A detailed image and dimensions of the coaxial injector tip are also found in Fig. 2. The tube housing the inner jet has an inner diameter, D_1 , of 0.51 mm with length-to-diameter ratio of 100. The inner jet exit plane is recessed by 0.25 mm, or $\frac{1}{2} D_1$, from the outer jet. The outer annular jet's inner diameter, D_2 , is 1.59 mm with outer diameter, D_3 , of 2.42 mm. For the outer jet, the length-to-mean-width of the annular passage is 67.

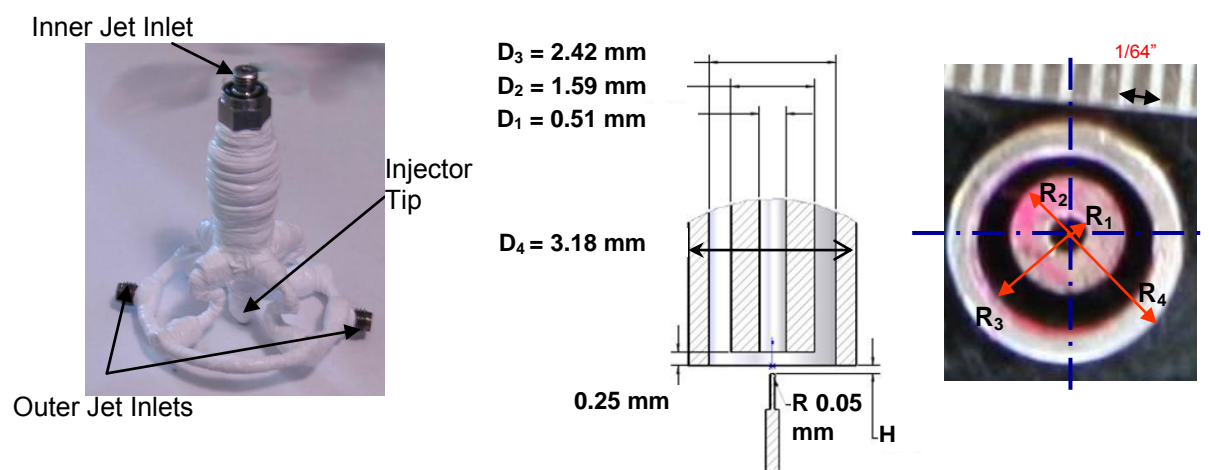


Figure 2. Image and tip geometry of the shear coaxial injector used in this study.

The temperature of the jets was measured using an unshielded type E thermocouple with a bead diameter of 0.1 mm. The accuracy of this thermocouple was checked with an RTD and found to be ± 1 K. The chamber pressure was measured with a Stellar 1500 transducer and a Kulite® XQC-062 pressure transducer. The latter was used to measure the pressure near the location of the thermocouple tip at a sampling frequency of 20 kHz (see rightmost picture in Fig. 1). Two linear positioning stages built by Attocube Systems AG were used to move the pressure transducer and the thermocouple in the plane perpendicular to the jet axis. Each stage has a range of about 3 mm in 1 dimension with step sizes in the order of 0.01 mm. One stage was placed on top of the other with their axis of movement perpendicular to each other for a total maximum examination area of 3 mm by 3 mm. The thermocouple and pressure transducer were fixed to a custom-made probe stand mounted on top of the positioning assembly. In turn, the linear stages were placed at the top end of a shaft that rested on a large 10-cm range linear stage built by SETCO™ outside the main chamber. Since the temperature probe approached the coaxial jet from the bottom and had sufficient range, it was capable of getting arbitrarily close to the exit plane of the coaxial jet. In fact, the thermocouple was even used to measure the temperature within the recess of the inner jet. The values for J and VR for a given condition were calculated using the measured flow rates, the mean chamber pressure and jet temperatures in conjunction with NIST's REFPROP® database [18-19]. Density, viscosity, and surface tension values were obtained from these properties.

Flow visualization was achieved with a Phantom® 7.1 CMOS camera. The camera can be seen facing the main chamber in the center picture of Fig. 1. Backlit images with a resolution from 128x200 to 192x400 pixels were obtained, with each pixel representing an area of approximately 0.08 mm by 0.08 mm. The framing rate was either 20 or 25 kHz. The number of images saved per run was 1000. The jet was backlit using a Newport® variable power arc lamp set at 160 W. The acoustic field for the subcritical

cases was generated using two piezo-sirens custom-designed by Hersh Acoustical Engineering, Inc. (see Fig. 1). An input sinusoidal voltage signal moves the piezoelectric element which has an aluminum cone attached to it producing acoustics waves. When the two drivers have a zero degree phase angle difference they move in opposite directions. Conversely, when the two drivers have a 180-degree phase difference the cones move in the same direction, ‘chasing’ each other. This behavior is represented by the sketches in Fig. 3. A Fluke® signal generator was used to drive the piezo-sirens with a sinusoidal wave at a chosen driving frequency and phase angle between them. The frequency was manually varied until the highest amplitudes of the pressure waves were obtained. These frequencies spanned a range between 2.96 and 3.06 kHz for the subcritical cases reported in this study. Then the signals were amplified and fed to the piezo-sirens keeping the voltage supplied to each driver constant. A waveguide with a catenary contour was used to guide the waves from a circular cross-section at the end of the aluminum cone to the rectangular cross-section of the inner chamber.

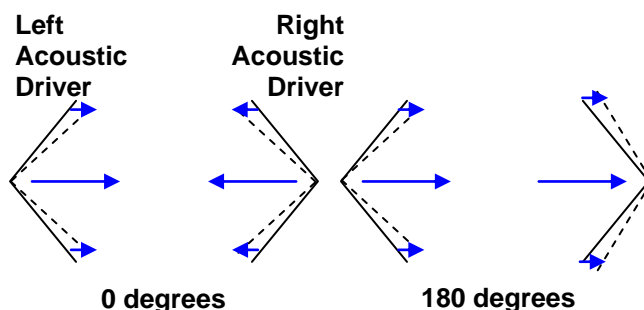


Figure 3. Simplified diagram of the two acoustic drivers at a 0° and 180° phase angle.

EXPERIMENTAL RESULTS AND DISCUSSION

To obtain the inner jet spread angles for a given condition, 998 images such as the one shown in Fig. 4a were used. A raw image is converted to a black and white image using an image processing technique previously described in detail in Leyva et al. [16-17]. From the black and white image, a contour of the dark core is constructed as shown in Fig. 4c. We use the dark core to describe the behavior of the inner jet since for our experiments the inner jet is always colder, thus denser, than the outer jet and appears darker in the backlit images. In order to measure the two angles, first, the locations of the left and right contours were recorded for each image as pictured in Fig. 4d. Then, for each row, the leftmost and rightmost contour points from all 998 images were selected to build a “maximum left contour” and a “maximum right contour” as can be seen in Fig. 5.

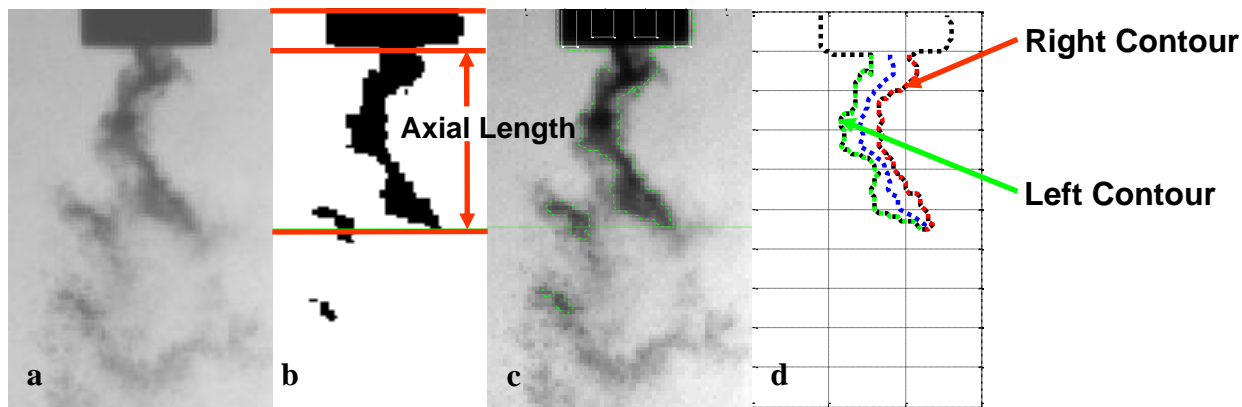


Figure 4a. Raw image from high-speed camera. **4b.** Black and white conversion after image processing. **4c.** Dark core boundary extracted from the processed black and white image. **4d.** Schematic of the left and right contours used in this study.

A linear fit through each contour was used to calculate the left and right spread angles. In Fig. 5 the two angles measured, α_{Left} and α_{Right} , are shown. The linear fit was chosen to start where the contour was the thinnest. This usually took place between $\frac{1}{2} D_1$ (in supercritical cases at high Js, for example) up to $5 D_1$ (for cases at moderate Js) and ended at the mean axial dark core length which is calculated by averaging the extracted axial length (see Fig. 4b) of all 998 images for each case. The axial dark core length is the axial projection of the dark core region connected to the injector and is also carefully explained in Leyva et al. [16-17]. An important reason for not choosing the first row of the contour to start the linear fit but begin a few inner jet diameters downstream was to avoid a recirculation zone that is generated due to the geometry of our injector. This recirculation occurs due to a thick inner jet post which prevents the inner jet and outer jet from coming into contact right away after the inner jet post ends. The recirculation region appears just as dark as the inner jet dark core and biases the measurements. By starting the linear fit where the contour is the thinnest we expect to avoid some of that bias.

Once the limits for the linear fit are chosen, a line is obtained and the angle associated with it is obtained. Both left and right angles computed in this manner are shown in Fig. 5. It is the sum of both left and right angles what is referred to in this study as the “inner jet spread angle”. This computed spread angle represents the region the inner jet traveled during the amount of time it took to record the 998 images. For the case of no acoustics, we call it ‘maximum baseline spread angle’. It is important to note that this ‘maximum baseline spread angle’ will over predict the mean of the spread angles. This is because we find the maximum contour out of all the images and then find a linear fit to the composite contour, instead of fitting a line and finding a spread angle for each image and then taking the average of those individual angles. When acoustics are present, this spreading angle encompasses a region where the inner jet traveled during all acoustic cycles captured in the number of images processed. Thus, for the cases where acoustics are on, this angle is referred to as the ‘maximum acoustic spread angle’.

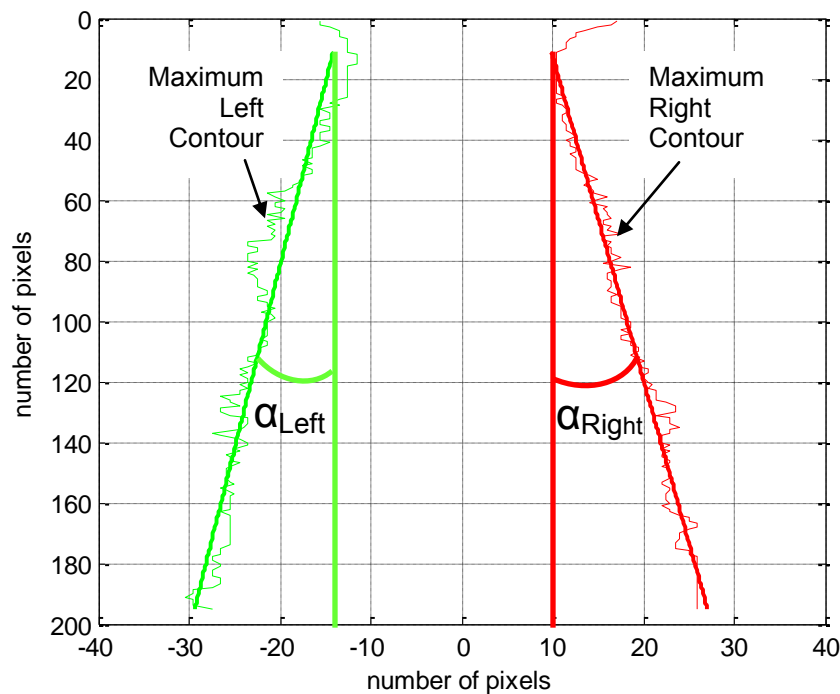


Figure 5. Left and right angles derived using the maximum displacement of the dark core at each row over a sample of 998 images.

Three values for the chamber pressure were selected for this study to span subcritical to supercritical values: 1.5 MPa, 3.6 MPa, and 4.9 MPa. For reference, the critical pressure, P_{cr} , of N_2 is 3.39 MPa and its critical temperature, T_{cr} , is 126.2 K. At subcritical pressures, the inner jet reaches the saturation temperature while for near and supercritical pressures this temperature is kept as close as possible to the critical value.

ANALYSIS OF SUBCRITICAL DATA WITH AND WITHOUT ACOUSTICS

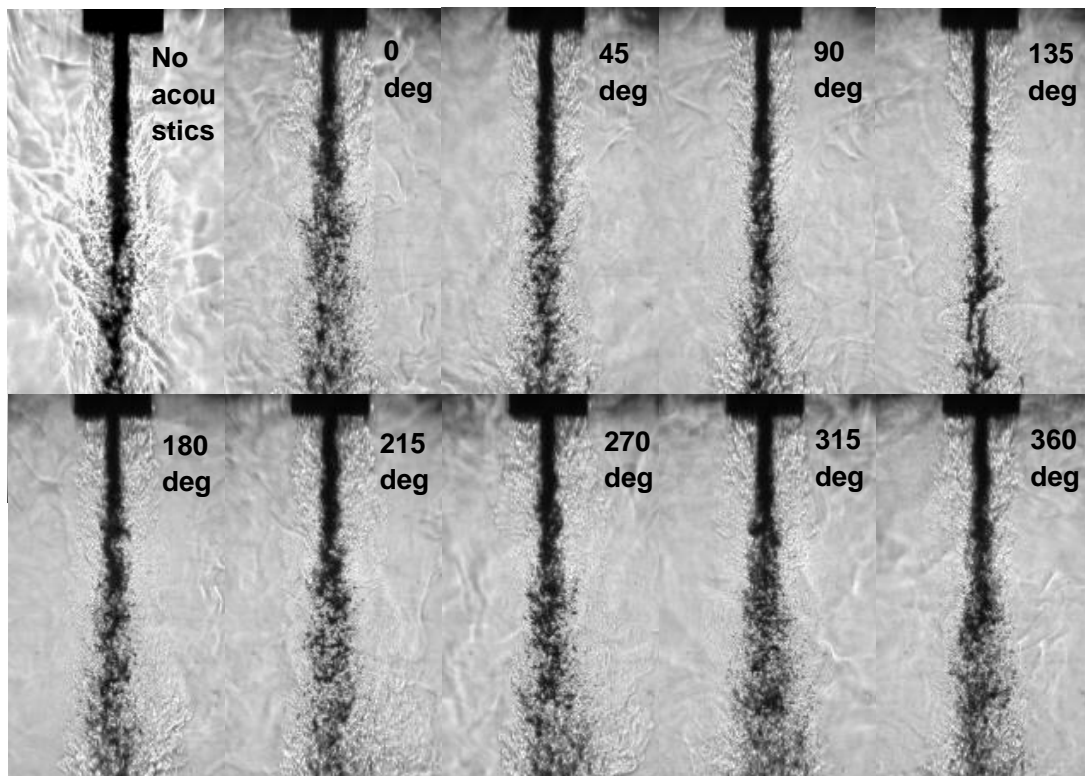


Figure 6. Collection of coaxial jet images at $P_{\text{chamber}} = 1.50 \text{ MPa}$, $J = 0.17$.

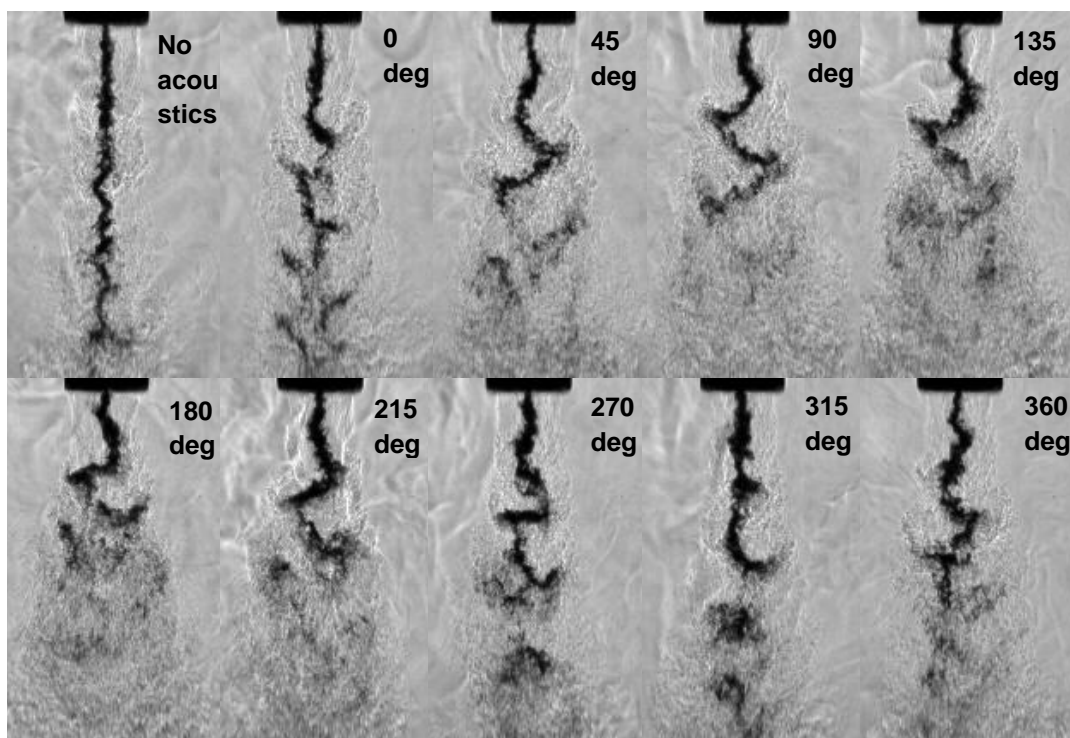


Figure 7. Collection of coaxial jet images at $P_{\text{chamber}} = 1.45 \text{ MPa}$, $J = 2.6$.

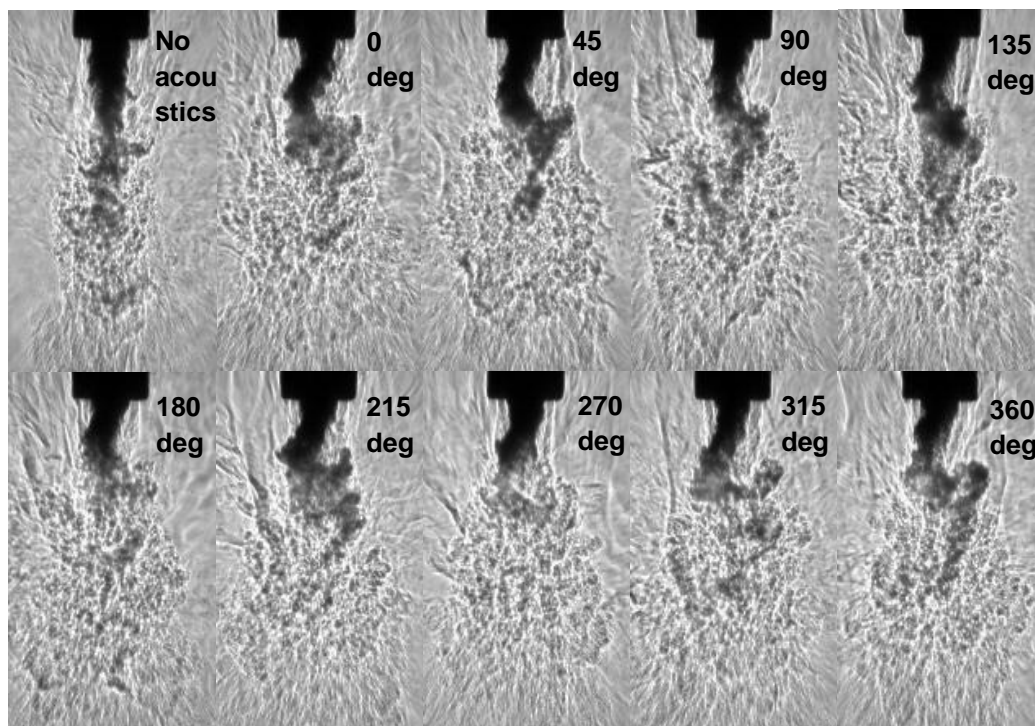


Figure 8. Collection of coaxial jet images at $P_{\text{chamber}} = 1.50 \text{ MPa}$, $J = 9.6$.

A qualitative assessment of the coaxial jet flow at three different subcritical momentum flux ratios under acoustic excitation can be performed with the information shown in Figs. 6 to 8. In these figures the top left image represents the jet with no acoustics, a condition also referred throughout the paper as 'baseline', and the rest are images of the jet under different phase angles between the two piezo-sirens, varying in steps of 45° from 0° to 360° . The acoustic field generated produces maximum amplitudes over the chamber pressure, $\Delta p/p$, between 2.9 and 4.1%. The maximum spread angles, both baseline and acoustic, of all J values studied are compiled in Fig. 9.

At low momentum flux ratios the maximum spread angles are small. The images for $J = 0.17$ in Fig. 6 as well as the upper-left plot in Fig. 9 show this behavior. For this case, the inner jet dominates the behavior of the coaxial jet, entraining and bending the outer jet towards itself. Since the inner jet in this case has a density of 630 kg/m^3 , the outer jet and surrounding plenum have a density of 27.7 and 22.0 kg/m^3 respectively, and both jets have similar mass flow rates around 300 mg/s , the flow surrounding the inner jet is simply not substantial enough to affect its behavior. When the acoustics are turned on, no discernable effect is seen, either visually in Fig. 6 or quantitatively in Fig. 9. This lack of a noticeable effect is also seen in previous observations made in terms of the decrease of the mean axial dark core length when acoustics are turned on [15, 20]. Acoustics in the range studied here do not seem to affect low J coaxial jets, neither by reducing the mean axial dark core length nor by increasing the maximum spread angles of the inner jet.

As we increase J to 1, one can start to observe a slight effect with phase angle (see upper-right plot in Fig. 9). Specifically, the maximum acoustic spread angle tends to achieve its largest value around a phase angle of 180° . This agrees with previous observations [15, 20] that the mean axial dark core length is reduced the most at or near a phase angle of 180° , which corresponds to a velocity antinode (pressure node). At $J=2.6$, the maximum acoustic spread angle increases continuously with phase angle reaching a maximum at a phase angle of 180° as shown in Figs. 7 and the middle-left plot in Fig. 9. In fact, the maximum acoustic spread angle recorded for this case at a phase angle of 180° is the one of highest from all cases at all phase angles. For the $J=4.2$ case, we see a slight peak of the maximum acoustic spread angle at a phase angle of 135° , not far from the phase angle where we would expect the largest value which is 180° . Overall, we can conclude that for this range of J s, we observe the largest maximum acoustic spread angles when the jets are exposed to an acoustic field which has a velocity

antinode at the location of the jet (for our case, the two sources are 180° out of phase). These observations are expected to agree with previously shown results where the highest percentage of shrinkage of mean axial dark core length occurs for the same values of J since the data used to obtain those dark core length measurements is the same used to derive the maximum spread angles in this study [15].

As we move to the case where $J=9.6$, shown in Figs. 8 and the bottom-left plot in Fig. 9, we see a different behavior. In this case the inner jet achieves a uniformly high maximum acoustic spread angle, reaching a value as high as 38° , compared to its 7° maximum baseline spread angle. This large spreading occurs as long as there is a source of acoustic excitation. This behavior is irrespective of the different acoustic conditions produced by the change in phase angle, which produces no statistically relevant change upon its spreading properties. This is surprising since in previous studies [15, 20] we found that for $J=9.6$ the percentage of shrinkage of the mean axial dark core length of the inner jet was smaller than for lower J values suggesting a smaller effect of acoustics on mixing. Also, in the aforementioned studies, we observed the mean axial dark core length change with phase angle whereas here the spread angle seems independent of phase. Finally as J increases to 23, we find a flatter profile of the maximum acoustic spread angle as the phase angle is varied. Also, all the values of maximum spread angles have decreased compared to the case of $J=9.6$. This is in agreement with previous results [15, 20] where it was found that for such high J values, the coaxial jet seems less sensitive to acoustic effects compared to moderate J values.

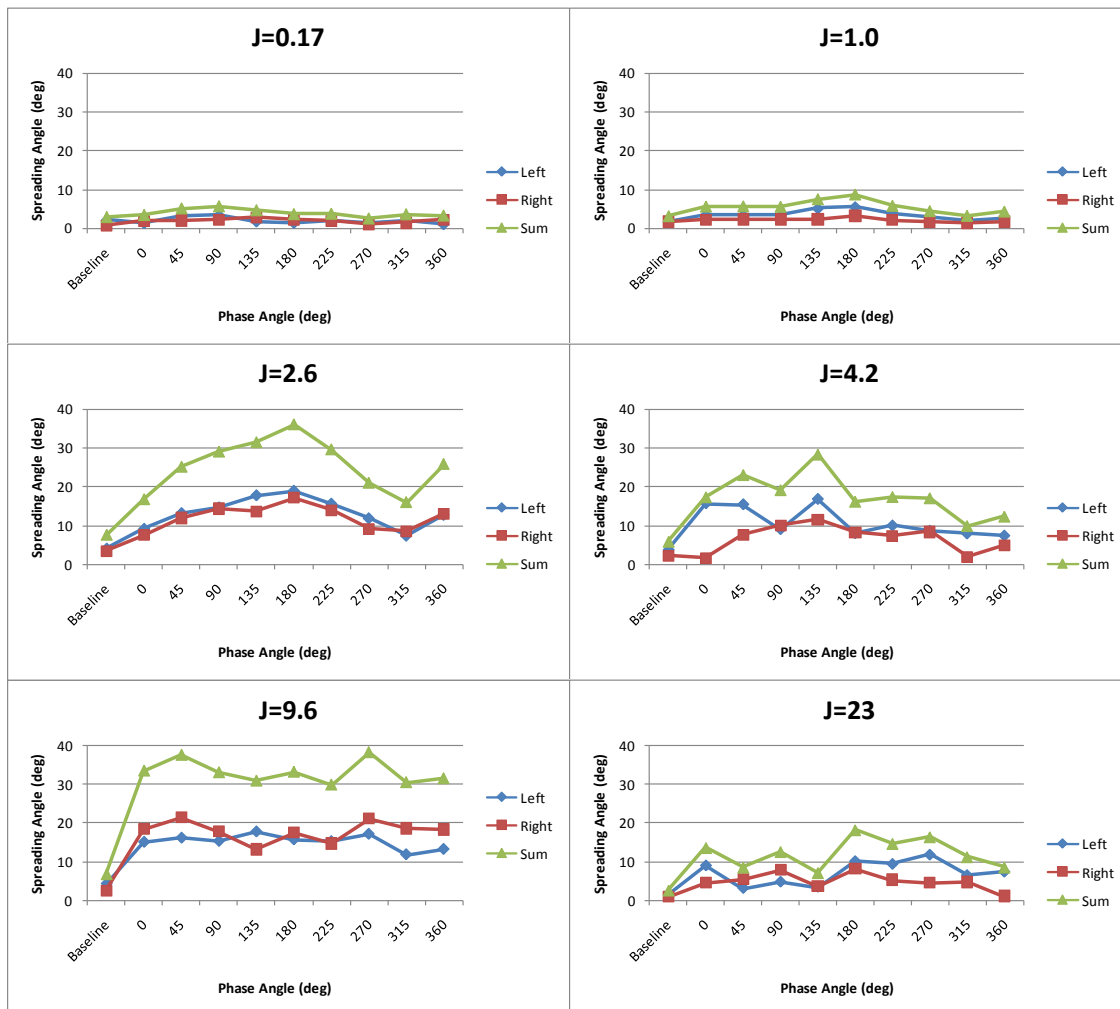


Figure 9. Maximum spread angles as a function of acoustic phase angle for different J s.

ANALYSIS OF SUBCRITICAL TO SUPERCRITICAL DATA WITHOUT ACOUSTICS

Maximum baseline spread angles for all momentum flux ratios at the three pressure regimes were compared. It is important to remind the reader that this 'maximum baseline spread angle' over predicts the average of the spread angles for each image, as explained earlier in this section. However, because the jet is not being exposed to acoustics, the over prediction is expected to be small. The results for these baseline cases show that, for all pressures, as J increases, the maximum baseline spread angle first increases to a maximum value and then decays to similar or lower values than those observed for the lowest J s (see Fig. 10). The maximum baseline spread angles for the near- and supercritical cases show more variation than their subcritical counterparts which seem rather uniform for the J range studied. In addition, near- and supercritical pressures at $1.0 < J < 2.5$ exhibit the largest maximum baseline spread angles, varying from 14° to 18° . At subcritical pressures the maximum baseline spread angles reach a maximum at $J=2.6$. Overall, two distinct trends are observed for the spread angles, one for subcritical (two-phase flow) and one for near and supercritical (one-phase flow) pressures.

Drawing a parallel between dark core lengths and spread angles, a long mean axial dark core length is indicative of slower mixing between the inner and the outer jet which also would result on a smaller maximum baseline spread angle for the inner jet. The trends for $J < 2.5$ show that maximum baseline spread angles are larger for the near- and supercritical cases, support previous findings that, for a given J , the mean axial length of the inner jet dark core is larger for subcritical conditions than for near and supercritical conditions. However, at larger J values, the mean axial dark core lengths for the subcritical cases are larger than for the near- and supercritical cases which are counterintuitive to the results shown by the maximum baseline spread angles.

To put our results in context with the mixing layer growth of other well known flows such two-dimensional (2D) planar shear layers, we compared the current results to the theories given by Papamoschou and Roshko [11] and Dimotakis [12]. It was found that the maximum baseline spread angles measured for the conditions described here are larger than those estimated for 2D shear layers for the same density and velocity ratios. A 2D planar shear layer assumes contact between the inner jet and outer jet immediately after the boundary which separates them ends; however, our injector geometry features a thick inner jet post that creates a recirculation zone and delays the contact between the inner jet and the outer jet, which effectively blurs the discontinuity in velocity between the outer and inner jets. Thus, discrepancies were expected and confirmed by our results, which indicates that the differences between our current geometry and 2D shear layer flows are significant. Analogous theories to those provided by Papamoschou and Roshko [11] and Dimotakis [12] might be needed to better understand the class of flows described here.

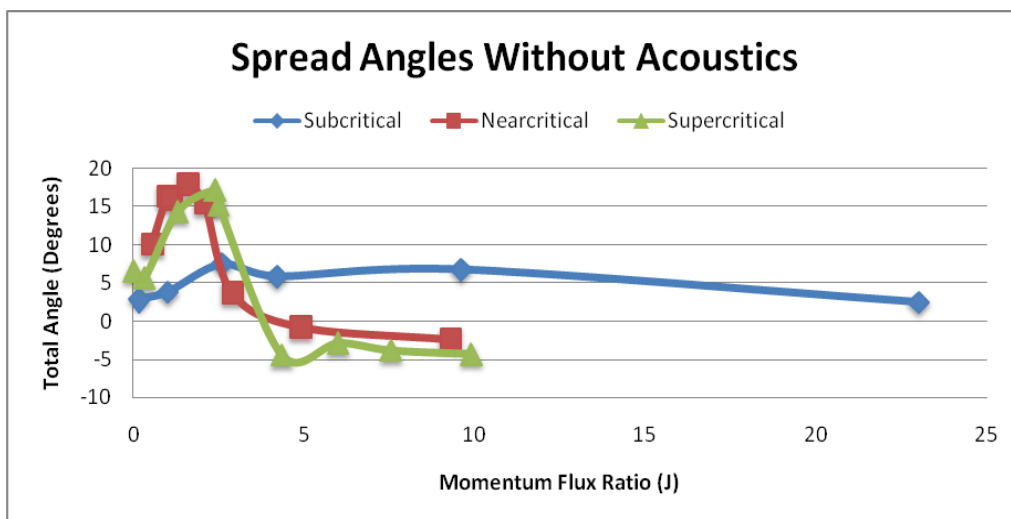


Figure 10. Maximum baseline spread angles as a function of momentum flux ratio for sub-, near-, and supercritical conditions.

NUMERICAL RESULTS AND DISCUSSION

For the second part of the study, CFD++ of the Metacomp Technologies Inc. was used for the numerical simulations. CFD++ is capable of handling multi-physics phenomena encountered in a general fluid problem. For a detailed explanation of CFD++ capabilities please see CFD++ Manual [21]. The computational model considers compressible flow calculations. The 2-equation realizable $k-\epsilon$ model was chosen for the turbulence modeling and a pre-conditioned pressure solver was used in the calculations. Spatial discretization is of second-order with a total variation diminishing limiter. Temporal discretization employs an implicit, dual time-stepping scheme, and a Riemann solver is used for the diffusion control. CFD++ provides an oscillating wall boundary condition, which may be used to simulate an acoustic driving source. Computational evaluation indicated that solutions of an acoustic cycle (about 0.3 ms) could be obtained within five hours of computational time on 48 AMD processors, which perform 64-bit operations.

We started the numerical simulations with a calculation of the acoustic field in a tube with one acoustic source and no jet present. The acoustic field for this simplified geometry has a known analytical solution. This calculation served to validate the acoustic capability of the computational tool, CFD++, used in the program. In addition, adjustments on the numerical settings and grid requirements could be optimized using this unit problem. For example, the longitudinal grid spacing (in the direction of the wave propagation) can be as large as 5 mm for frequencies ranging from 0.1 to 20 times the resonant frequency. Grid sizes in the transverse direction should not exceed 5 times that of the grid sizes in the longitudinal direction. Both the explicit and implicit time integration methods and both the pre-conditioned and non-pre-conditioned methods are effective for the acoustics modeling. The time step of one hundredth of a cycle proves to be acceptable. The unit problem exercise confirmed that the perturbation amplitudes should be small to avoid nonlinear effects. The limiting value of the perturbation amplitude for a linear acoustic wave depends on the acoustic frequency. Increased frequencies for a given amplitude leads to non-linear effects. Similarly, increased amplitudes for a given frequency lead to non-linear behavior.

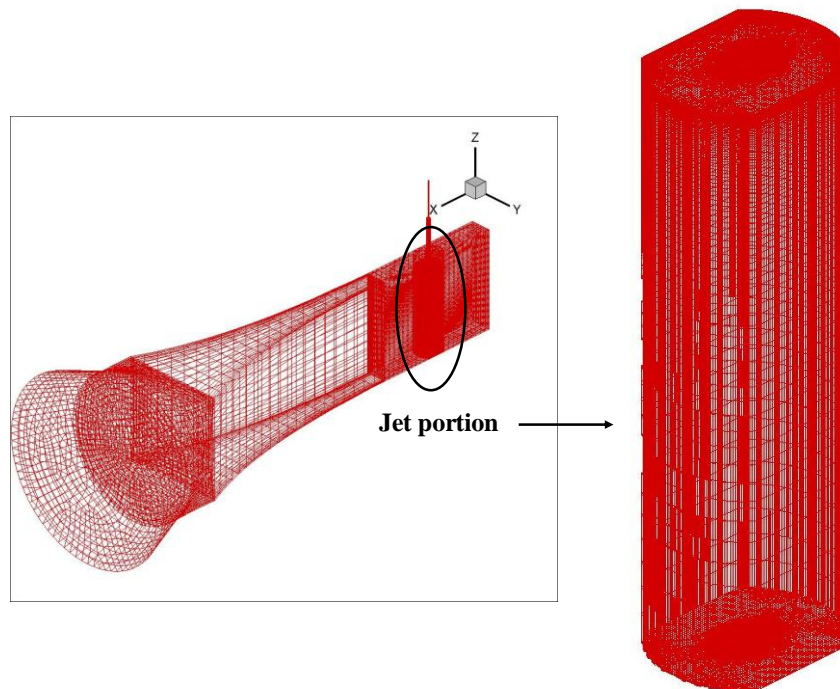


Figure 11. Grid for the Acoustic/Jet Calculations

After the unit problem calculations were complete, the next task was to introduce a jet into the simulation and use the actual 3D experimental geometry (including injector and chamber). We chose to simulate only one acoustic source for several reasons: 1) simplicity, 2) we also have data for that configuration, and 3) we want to understand the problem of one acoustic source well before we proceed to the more complex case of two acoustic sources. This also helped validate the supercritical models of CFD++. Grid issues and boundary condition representations were explored in the current study. A grid-independence analysis was performed and three numerical grids were constructed for the simulation. The grids had similar cell structure with different cell densities. One grid had 1.46 million cells, the other one had 2.06 million cells, and the final one had 3.32 million cells. Hybrid grids including both hexahedrals and tetrahedrals were used for the cells. The jet region required most cells; however, the grid density in the waveguide is sufficient judging from the experience learned in the acoustic unit problem calculations. Numerical tests showed that all three grids give satisfactory results; however, the 2.06-million-grid was used for most of the calculations (see Fig. 11).

The grid was first tested with an acoustic-only calculation (no jet) to examine the pressure mode-shapes. The results are shown in Fig. 12 where the position of the jet is noted with respect to the pressure field. The pressure fluctuations are accentuated as the acoustic field approaches the location of the coaxial jet. The reason for this enhancement in acoustic excitation is greatly due to the geometry that is used. As the waveguide that appears on the bottom left of Figs. 1 and its computer mesh model in Fig. 11 decreases in cross-sectional area, higher pressure fluctuations are possible. For each acoustic/jet calculation, a steady state solution with no acoustics was sought first, and enough iterations were used to assure the residues dropped three orders of magnitude. The velocity perturbation amplitude used in the boundary condition to simulate the acoustic wave was adjusted to match the experimental probing pressure at the jet exit. The flow Courant number was set to be 250. To cope with the near- or supercritical fluids, the Relich-Kwong-Soave equation of the state was used to describe the real gas behavior. In addition, the thermodynamic properties of nitrogen were extracted from the NIST database and curve-fitted into polynomials, illustrated in Fig. 13, which were then used in CFD++. This is because such curve fits were more accurate than the standard equations provided by the CFD++ user interface.

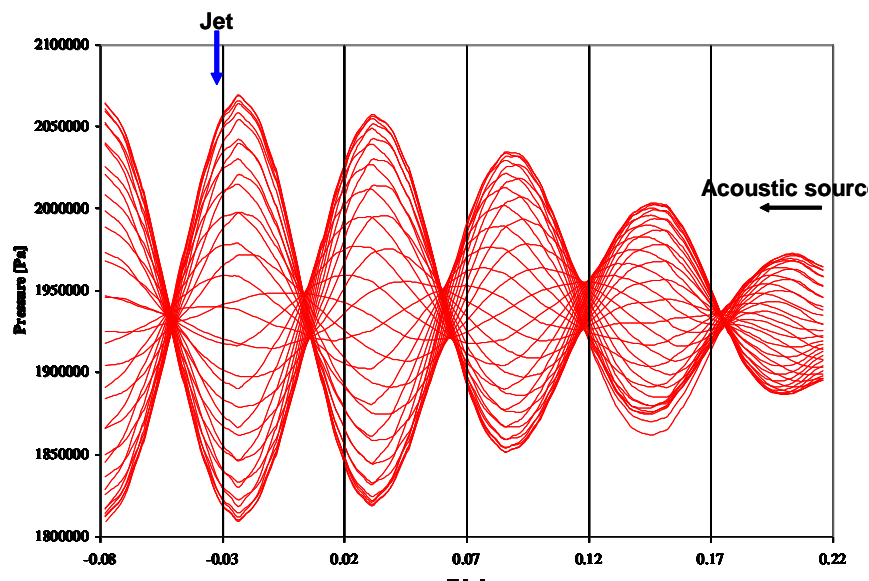


Figure 12. Pressure Mode Shape in the Experimental Geometry

Once the grid was tested, two supercritical cases were analyzed using the numerical model just described. The results are summarized in Table 1 below and shown in Figs. 14 and 15. Case SP2 has $J = 1.3$ and $VR = 1.8$, $P_{\text{chamber}} = 4.93 \text{ MPa}$, $T_{\text{chamber}} = 251 \text{ K}$, $T_{\text{inner jet}} = 137 \text{ K}$, $T_{\text{outer jet}} = 173 \text{ K}$, $\dot{m}_{\text{inner jet}} = 291 \text{ mg/s}$, $\dot{m}_{\text{outer jet}} = 2800 \text{ mg/s}$. The frequency of the acoustic field was 3.11 kHz. SP6 has $J = 3.7$ and $VR = 3.27$,

$P_{\text{chamber}}=4.92\text{MPa}$, $T_{\text{chamber}}=232\text{K}$, $T_{\text{inner jet}}=136\text{K}$, $T_{\text{outer jet}}=185\text{K}$, $\dot{m}_{\text{inner jet}}=295\text{ mg/s}$, $\dot{m}_{\text{outer jet}}=4240\text{ mg/s}$. The acoustic frequency is 3.22 kHz. The reason that preliminary simulations of the coaxial jet experiment started with supercritical cases was the lack of a suitable two-phase model for the working fluid.

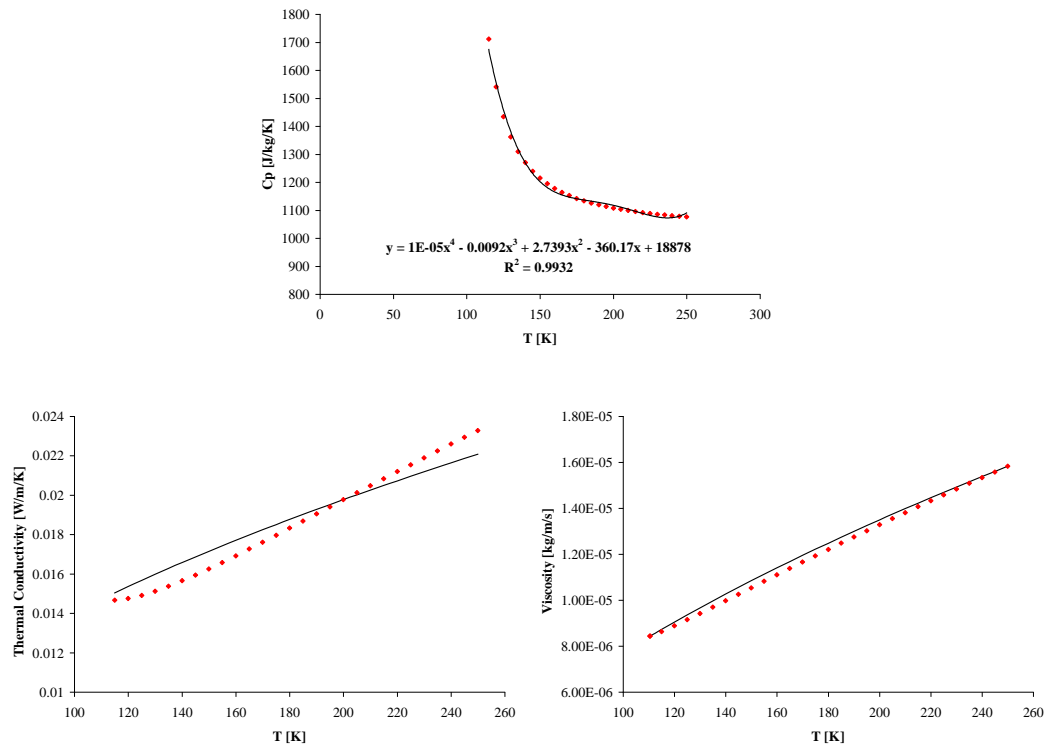


Figure 13. Polynomial curve-fitting of nitrogen transport properties from the NIST database.

The length of the inner jet is defined as the length of the region from the injector exit until an increment of 10% of the temperature difference between the inner and outer jets is achieved. This definition is arbitrary but it intends to capture the cold core of the inner jet. Using the temperature profile shown in the bottom row of Figs. 14 and 15, the numerical results produce a small inner jet core length for the SP6 case which is about one-sixth of that for the SP2 case. Observe that the agreement between the mean axial dark core length (from experimental results) and the numerical simulation for SP2 is encouraging. While the agreement is not as good for the higher J case, we can still see that these preliminary numerical results follow the general trend observed experimentally where the mean axial dark core length of the inner jet decreases with increasing momentum flux ratio.

Table 1. Summary of supercritical cases explored numerically.

Case	Inner Jet Core Length with no acoustics [L/D1] (Based on Temperature)	Pressure Fluctuations [kPa] (Peak-to-Peak at Jet Exit)	Dark Core Length with no acoustics [L/D1] (Experimental Results)
SP2 (J = 1.3)	5.5	~ 14	4.9
SP6 (J = 3.7)	1.0	~ 8.3	3.5

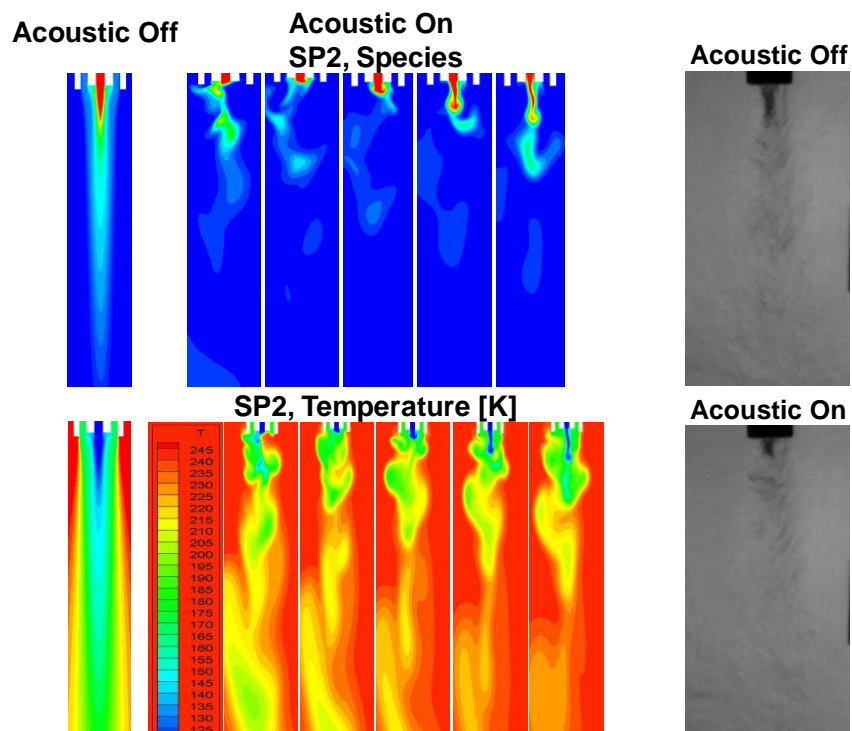


Figure 14. Numerical species concentration and temperature field at different instants and experimental images for condition SP2 with acoustics on and off.

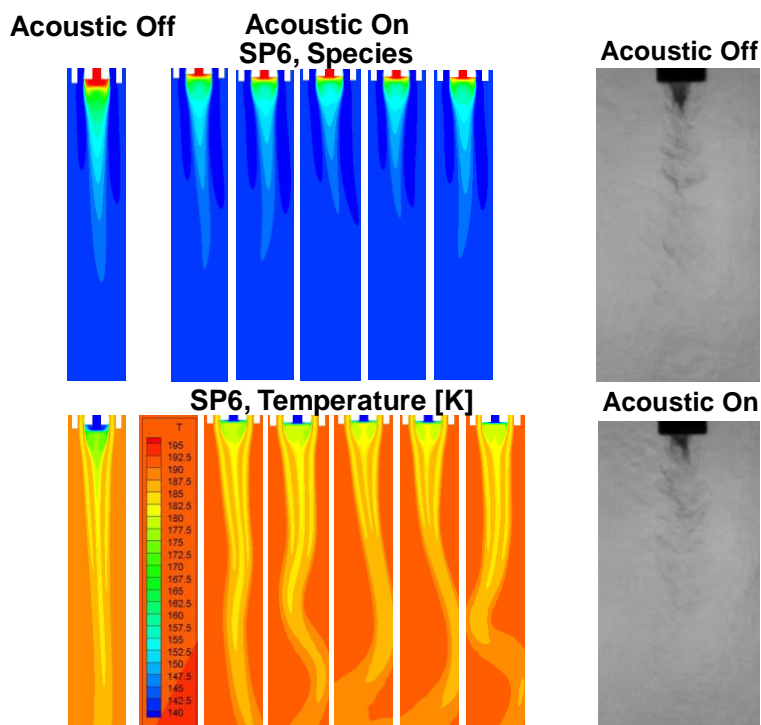


Figure 15. Numerical species concentration and temperature field at different instants and experimental images for condition SP6 with acoustics on and off.

Another trend that is supported by experimental evidence and it is observed in the numerical results is the decrease of the inner jet or dark core length when it is exposed to an external acoustic field. Both cases show a noticeable decrease in the dark core lengths as defined by the species concentration and the temperature field with the presence of acoustics. It is also noteworthy that the baseline conditions for both the SP2 and SP6 cases show very symmetric species and temperature fields, especially if they are compared to their respective behavior when acoustics are modeled. The oscillating patterns observed in both cases when acoustics are present agree very well in a qualitative sense with the type of phenomena observed experimentally when the jets are exposed to these levels of acoustic perturbations.

CONCLUSIONS

The spread angles based on the maximum displacement of the inner jet dark core for a coaxial flow configuration were studied experimentally as a function of the chamber pressure and outer to inner jet momentum flux ratio. The experimental data used for this study had been previously reported in references 14-17, 20. However, previous analysis was mostly concerned with inner jet dark core lengths. The jet is either unexcited or under the influence of a transverse external acoustic field at approximately 3 kHz. When comparing the results with no acoustics at different pressures, the spread angles for the near- and supercritical cases were very similar to each other and showed more variation than their subcritical counterparts over the range of J values studied. We observe two distinct trends for the spread angles, one for subcritical (two-phase flow) and one for near and supercritical (one-phase flow) pressures. For these non-acoustic cases, all spread angles increase with J reaching a maximum around $1 < J < 3$. The largest spread angle recorded for a non-forced case was 18° .

For the cases with acoustic excitation, only subcritical pressures were studied. It was found that acoustics had either no effect or a slight effect on the spread angles for J up to 1. At moderate J 's ($2 < J < 10$) an increase in the spread angle of 30° over the baseline was observed. For $J=2.6$, the spread angle reached a maximum when the phase angle between acoustic resonators was 180° , which corresponds to a velocity antinode, where the highest velocity fluctuations occur. This finding agrees with previous results which also looked at the effect of phase angle on the shrinkage of the inner jet dark core length. For $J = 9.6$, the spread angles show a similar response to the acoustic excitation, regardless of the phase angle between acoustic resonators, which is about 4 to 5 times the value from the non-acoustic baseline behavior. For $J=23$, the absolute acoustic spreading angles decrease but the percentage increase compared to the baseline is still in the order of 4 to 6 times growth.

Preliminary numerical results were presented for two cases at supercritical pressures. The agreement for the dark core length, albeit defined differently for the numerical and experimental cases, was within 10% for one case. Also, the numerical simulations show the experimental trends of decreased dark core length with both increasing J and also when acoustics are present for a given value of J .

ACKNOWLEDGEMENTS

The authors would like to thank Randy Harvey for his very important contributions on running and maintaining the facility. This work is sponsored by AFOSR under Mitat Birkan, program manager.

REFERENCES

1. Chigier, N. A., Beer, J. M., 'The flow region near the nozzle in double concentric jet', Transactions of the American Society of Mechanical Engineers, Journal of Basic Engineering, Vol. 86, pp 797-804, 1964.
2. Ko, N. W. M., Kwan, S. H., 'The initial region of subsonic coaxial jets', JFM, Vol. 73, part 2, pp. 305-332, 1976.
3. Ko, N. W. M., Chan, W. T., 'The inner regions of annular jets', JFM, Vol. 93, pp. 549-584, 1979.
4. Ko, N. W. M., Au, H., 'Coaxial jets of different mean velocity ratios', J. of Sound and Vibration, 1985, 100 (2), pp. 211-232.

5. Chan, W.T., Ko, N. W. M., 'Coherent structures in the outer mixing region of annular jet', JFM, Vol. 89, pp. 515-533, 1978.
6. Mayer W. O. H., Branam, R., 'Atomization characteristics on the surface of a round liquid jet', Exp. in Fluids, 36 (2004), pp. 528-539.
7. Favre-Marinet, M., Camano Schettini, E.B., "The density field of coaxial jets with large velocity ratio and large density differences", Int. J. of Heat and Mass Transfer, 44 (2001), pp. 1913-1924.
8. Ko, N. W. M., Au, H., "Initial region of subsonic coaxial jets", J of Fluids Engineering, June 1981, vol. 103, pp. 335-338.
9. Durao, D. and Whitelaw, J. H. Turbulent mixing in the developing region of coaxial jets", J of Fluids Engineering, Sept. 1973, pp. 467-473.
10. Brown, G., Roshko, A., "On density effects and large structure in turbulent mixing layers"; J. Fluid Mech, Vol. 64 part 4, 1974, pp. 775-816.
11. Papamoschou D., Roshko, A., "The compressible turbulent shear layer:an experimental study," J. Fluid Mech. Vol. 197, No. 453, 1988.
12. Dimotakis, P. E., "Two-Dimensional Shear Layer Entrainment", AIAA Journal, Vol 24, No. 11, Nov. 1986, pp. 1791-1796.
13. Chehroudi, B., Talley, D., Coy, E., "Visual characteristics and initial growth rates of round cryogenic jets at subcritical and supercritical pressure", Physics of Fluids, Vol. 14, No. 2, February 2002, pp. 851-861.
14. Leyva, I. A., Rodriguez, J. I., Chehroudi, B., Talley, D., "Preliminary Results on Coaxial Jets Spread Angles and the Effects of Variable Phase Transverse Acoustic Fields", *AIAA-2008-0950*.
15. Rodriguez, J. I., Leyva, I. A, Chehroudi, B., Talley, D., "Results on Subcritical One-Phase Coaxial Jet Spread Angles and Subcritical to Supercritical Acoustically-Forced Coaxial Jet Dark Core Lengths", *AIAA-2008-4561*.
16. Leyva, I. A., Chehroudi, B., Talley, D., "Dark-core analysis of Coaxial Injectors at Sub-, Near-, and Supercritical Conditions in a Transverse Acoustic Field", 54th JANNAF Meeting, Denver, CO, May 14-18, 2007.
17. Leyva, I. A., Chehroudi, B., Talley, D., "Dark-core analysis of Coaxial Injectors at Sub-, Near-, and Supercritical Conditions in a Transverse Acoustic Field", *AIAA-2007-5456*.
18. REFPROP, Reference Fluid Thermodynamic and Transport Properties, Software Package, Ver. 7.0, NIST, U.S. Department of Commerce, Gaithersburg, MD, 2002.
19. Thermophysical Properties of Fluid Systems (<http://webbook.nist.gov/chemistry/fluid>), NIST, U.S. Department of Commerce, Gaithersburg, MD, 2005.
20. Leyva, I. A., Rodriguez, J., Chehroudi, B., Talley, D., "Effect of Phase Angle on Coaxial Jet Behavior Spanning Sub- To Supercritical Pressures", Paper 14-2, 22nd European Conference on Liquid Atomization and Spray Systems, Como, Italy, September 8-10, 2008.
21. CFD++ User's Manual, Metacomp Technologies Inc, Agoura Hills, CA, 2008.

APPENDIX

A. Data Summary for Subcritical Cases

	T_{chamber} (K)	ρ_{chamber} (kg/m ³)	P_{chamber} (MPa)	T_{outer} (K)	\dot{m}_{outer} (mg/s)	ρ_{outer} (kg/m ³)	u_{outer} (m/s)	T_{inner} (K)	\dot{m}_{inner} (mg/s)	ρ_{inner} (kg/m ³)	u_{inner} (m/s)	Freq. (kHz)	VR
	Spreading Angles											P'_{RMS}	J
	Baseline	$\phi=0^\circ$	$\phi=45^\circ$	$\phi=90^\circ$	$\phi=135^\circ$	$\phi=180^\circ$	$\phi=225^\circ$	$\phi=270^\circ$	$\phi=315^\circ$	$\phi=360^\circ$			
SUB													
sub1	233	22.0	1.50	191	310	27.7	4.30	109	279	630	2.2	2.98	2.0
Left	2.2	1.4	3.0	3.4	1.8	1.5	1.9	1.5	2.1	1.1			
Right	0.8	2.0	2.1	2.2	2.8	2.2	1.9	1.0	1.5	2.2		21.5	0.17
sub2	231	22.2	1.50	183	790	28.8	11.0	109	283	630	2.2	3.06	4.8
Left	1.6	3.5	3.4	3.3	5.2	5.5	3.7	2.8	1.9	2.6			
Right	1.6	2.2	2.4	2.4	2.4	3.2	2.2	1.7	1.4	1.8		20.1	1.0
sub3	226	21.9	1.45	183	1230	27.8	16.9	109	284	630	2.2	3.06	7.6
Left	4.1	9.2	13.2	14.7	17.7	18.9	15.6	11.9	7.4	12.8			
Right	3.4	7.5	11.8	14.3	13.6	17.1	13.9	9.1	8.5	13.0		17.8	2.6
sub4	226	22.9	1.51	185	1560	28.7	20.9	109	279	630	2.2	2.96	9.5
Left	3.8	15.7	15.5	9.1	16.8	8.1	10.0	8.7	8.0	7.4			
Right	2.1	1.6	7.6	10.1	11.5	8.2	7.4	8.4	2.0	4.9		15.7	4.2
sub5	210	24.9	1.50	182	2400	29.3	31.3	109	279	630	2.2	3.01	14
Left	4.2	14.9	16.0	15.2	17.6	15.6	15.1	17.0	11.7	13.1			
Right	2.5	18.4	21.4	17.7	13.2	17.5	14.7	21.0	18.6	18.2		16.9	9.6
sub6	216	24.1	1.50	191	3640	27.7	50.3	109	279	630	2.2	3.02	23
Left	1.5	9.0	3.1	4.8	3.4	10.1	9.4	11.8	6.5	7.4			
Right	0.9	4.5	5.3	7.7	3.6	8.0	5.2	4.5	4.6	1.1		16.3	23

B. Data Summary for Nearcritical Cases

	T_{chamber} (K)	ρ_{chamber} (kg/m ³)	P_{chamber} (MPa)	T_{outer} (K)	\dot{m}_{outer} (mg/s)	ρ_{outer} (kg/m ³)	u_{outer} (m/s)	T_{inner} (K)	\dot{m}_{inner} (mg/s)	ρ_{inner} (kg/m ³)	u_{inner} (m/s)	VR
	Spreading Angles Baseline											J
NEAR												
near1	223	56.6	3.58	180	1060	75.4	5.38	123	290	520	2.8	2.0
Left	4.8											
Right	5.3											0.55
near2	207	62.0	3.57	152	1570	101	5.95	117	289	590	2.4	2.5
Left	7.1											
Right	9.2											1.0
near3	228	55.1	3.58	185	1590	72.4	8.40	126	293	440	3.3	2.6
Left	4.6											
Right	11.4											1.1
near4	223	56.1	3.55	184	2170	72.3	11.5	127	294	360	4.0	2.8
Left	8.9											
Right	9.0											1.6
near5	230	54.2	3.56	199	2120	65.1	12.5	126	292	440	3.3	3.8
Left	2.1											
Right	13.4											2.1
near6	229	54.5	3.56	183	2690	73.1	14.1	126	292	420	3.4	4.1
Left	1.0											
Right	2.7											2.9
near7	219	57.6	3.56	194	3080	67.4	17.5	125	289	480	3.0	5.9
Left	-0.4											
Right	-0.5											4.9
near8	213	59.6	3.56	192	6460	68.3	36.2	128	295	220	6.6	5.5
Left	-4.1											
Right	1.6											9.3

C. Data Summary for Supercritical Cases

	T_{chamber} (K)	ρ_{chamber} (kg/m ³)	P_{chamber} (MPa)	T_{outer} (K)	\dot{m}_{outer} (mg/s)	ρ_{outer} (kg/m ³)	u_{outer} (m/s)	T_{inner} (K)	\dot{m}_{inner} (mg/s)	ρ_{inner} (kg/m ³)	u_{inner} (m/s)	VR
	Spreading Angles											J
	Baseline											
SUPER												
super1	231	76.1	4.96	198	292	93.9	1.19	136	291	300	4.8	0.25
Left	3.5											
Right	3.1											0.019
super2	231	76.1	4.96	193	997	97.7	3.90	130	292	460	3.1	1.2
Left	3.8											
Right	2.0											0.33
super3	221	80.4	4.95	180	2050	109	7.19	128	291	490	2.9	2.5
Left	8.2											
Right	6.3											1.3
super4	222	80.1	4.96	182	3110	107	11.1	134	288	360	3.9	2.8
Left	6.3											
Right	11.0											2.4
super5	222	80.3	4.97	191	2820	99.5	10.8	131	293	440	3.3	3.3
Left	3.5											
Right	11.8											2.5
super6	236	73.79	4.94	195	5753	96	23	147	295	179	8.1	2.9
Left	-2.0											
Right	-2.4											4.4
super7	225	79	4.94	183	5813	107	20.9	138	295	264	5.5	3.9
Left	0.0											
Right	-2.9											6.0
super8	236	73	4.89	188	7055	100	26.9	141	293	214	6.76	4.0
Left	0.0											
Right	-3.8											7.6
super9	211	85.8	4.96	187	5820	103	21.6	132	286	410	3.4	6.3
Left	-3.0											
Right	-1.3											9.9

C. Data Summary for Supercritical Cases

	T_{chamber} (K)	ρ_{chamber} (kg/m ³)	P_{chamber} (MPa)	T_{outer} (K)	\dot{m}_{outer} (mg/s)	ρ_{outer} (kg/m ³)	u_{outer} (m/s)	T_{inner} (K)	\dot{m}_{inner} (mg/s)	ρ_{inner} (kg/m ³)	u_{inner} (m/s)	VR
	Spreading Angles											J
	Baseline											
SUPER												
super1	231	76.1	4.96	198	292	93.9	1.19	136	291	300	4.8	0.25
Left	3.5											
Right	3.1											0.019
super2	231	76.1	4.96	193	997	97.7	3.90	130	292	460	3.1	1.2
Left	3.8											
Right	2.0											0.33
super3	221	80.4	4.95	180	2050	109	7.19	128	291	490	2.9	2.5
Left	8.2											
Right	6.3											1.3
super4	222	80.1	4.96	182	3110	107	11.1	134	288	360	3.9	2.8
Left	6.3											
Right	11.0											2.4
super5	222	80.3	4.97	191	2820	99.5	10.8	131	293	440	3.3	3.3
Left	3.5											
Right	11.8											2.5
super6	236	73.79	4.94	195	5753	96	23	147	295	179	8.1	2.9
Left	-2.0											
Right	-2.4											4.4
super7	225	79	4.94	183	5813	107	20.9	138	295	264	5.5	3.9
Left	0.0											
Right	-2.9											6.0
super8	236	73	4.89	188	7055	100	26.9	141	293	214	6.76	4.0
Left	0.0											
Right	-3.8											7.6
super9	211	85.8	4.96	187	5820	103	21.6	132	286	410	3.4	6.3
Left	-3.0											
Right	-1.3											9.9

UNIVERSITY OF CALIFORNIA

Los Angeles

Acoustic Excitation of Liquid Fuel Droplets and Coaxial Jets

A dissertation submitted in partial satisfaction
of the requirements for the degree
Doctor of Philosophy in Aerospace Engineering

by

Juan Ignacio Rodriguez

2009

Approved for public release; distribution unlimited. PA # 09244.

© Copyright by
Juan Ignacio Rodriguez
2009

The dissertation of Juan Ignacio Rodriguez is approved.

Stanley J. Osher

Jeff D. Eldredge

Ivett A. Leyva

Owen I. Smith, Committee Co-chair

Ann R. Karagozian, Committee Co-chair

University of California, Los Angeles

2009

ii

A mis padres

TABLE OF CONTENTS

List of Figures	vii
List of Tables	xxi
Nomenclature	xxiii
1. Introduction.....	1
1.1 Acoustically Coupled Droplet Combustion	2
1.1.1 Burning of Spherical and Non-spherical Fuel Droplets.....	2
1.1.2 Acoustic Excitation Effects on Condensed Phase Combustion.....	3
1.1.3 Alternative Fuels.....	6
1.2 Acoustic Driving of Coaxial Jets	8
1.2.1 Basic Flow Configuration	8
1.2.2 Motivations and Objectives of Coaxial Jet Study.....	10
1.2.3 Previous Work on Coaxial Jets	14
1.2.4 Dark Core Length	17
1.2.5 Shear Layers and Spreading Angles	20
1.2.6 Stability Analysis of the Coaxial Jet.....	22
1.2.7 Coaxial Jets and Acoustic Excitation.....	25
2. Experimental Setup – Acoustically Coupled Fuel Droplet Combustion	35
2.1 Acoustic Waveguide	35
2.2 Droplet Generation.....	37
2.3 Measurement Methods.....	38
2.4 Experimental Procedure.....	39
2.5 Uncertainty Analysis.....	41

3.	Results – Acoustically Coupled Fuel Droplet Combustion	44
3.1	Baseline Burning Rate Constants.....	44
3.2	Burning Rate Constants under Acoustic Excitation.....	45
3.3	Pressure Node Location Offset	47
3.4	Relation between Acoustic Acceleration and Burning Rate Increase	50
3.5	Fuel Extinction Studies	54
4.	Experimental Setup – Acoustically Excited Coaxial Jet.....	70
4.1	Cryogenic Supercritical Chamber and Coaxial Jet Facility	70
4.2	Original and New Injectors	74
4.3	Measurement Methods.....	75
4.4	Uncertainty Analysis.....	80
5.	Results – Acoustically Excited Coaxial Jet	90
5.1	Quantification of Dark Core Length and Inner and Outer Jet Spreading Angles .	90
5.1.1	Dark Core Length	90
5.1.2	Inner Jet Spreading Angles	92
5.1.3	Outer Jet Spreading Angles	94
5.2	Results with the Original Coaxial Jet Injector Geometry	95
5.2.1	Behavior in the Absence of Acoustic Excitation	95
5.2.2	Dark Core Length Results in the Absence of Acoustic Excitation.....	100
5.2.3	Inner Jet Spreading Angle Results in the Absence of Acoustic Excitation	104
5.2.4	Outer Jet Spreading Angle Results in the Absence of Acoustic Excitation	107
5.2.5	Acoustic Field in the Test Chamber.....	111
5.2.6	Behavior during Exposure to Acoustic Excitation.....	118
5.2.7	Dark Core Length Results in the Presence of Acoustic Excitation	123
5.2.8	Inner Jet Spreading Angle Results in the Presence of Acoustic Excitation	129

5.3	Results with the New Coaxial Jet Injector Geometry	135
5.3.1	Behavior with and without Acoustic Excitation	135
5.3.2	Dark Core Length Results with and without Acoustic Excitation	142
5.3.3	Inner Jet Spreading Angle Results with and without Acoustic Excitation .	149
5.4	Stability of Coaxial Jet Flows	152
6.	Conclusions and Future Work	191
6.1	Acoustically Coupled Droplet Combustion	191
6.2	Acoustic Driving of Coaxial Jets	193
6.2.1	Summary and Conclusions	193
6.2.2	Future Work	197
A.	Detailed Schematic of Coaxial Jet Experimental Facility	200
B.	Coaxial Jet Experimental Procedures	206
C.	Summary of Coaxial Jet Experimental Data.....	228
	References	237

LIST OF FIGURES

Figure 1.1. In microgravity, effect of sound pressure level, SPL, on the mean burning rate constant K normalized by its mean value in the absence of acoustic excitation, K_{unf} , (a) at a pressure antinode, PAN, and (b) at a pressure node, PN. From Dattarajan (14).	28
Figure 1.2. In normal gravity, effect of sound pressure level, SPL, on the mean burning rate constant K normalized by its mean value in the absence of acoustic excitation, K_{unf} , (a) at a pressure antinode, PAN, and (b) at a pressure node, PN. From Dattarajan (14).	29
Figure 1.3. Photographs of a burning droplet in microgravity (a) with no forcing and (b) forced at a pressure node at 770 Hz; and in normal gravity (c) with no forcing and (d) with forcing at a pressure node at 770 Hz. From Dattarajan (14).	30
Figure 1.4. Schematic of coaxial jet flow.	31
Figure 1.5. Schematic of a 2D shear layer spreading angle.	31
Figure 1.6. Schematic of the dark core region and the inner jet spreading angle of a shear coaxial jet.	32
Figure 1.7. Consecutive frames from high-speed shadowgraph movies with the acoustic driver turned off (in rows 1, 3 and 5) and on (in rows 2, 4, and 6) at $\sim 3\text{kHz}$. Time increases from left to right with an interval of $55.6\ \mu\text{s}$ between frames. The first two rows are at a subcritical chamber pressure ($\sim 1.5\ \text{MPa}$), the third and fourth rows are at a near-critical chamber pressure ($\sim 3.5\ \text{MPa}$), and the fifth and sixth rows are	

at a supercritical chamber pressure (~ 4.9 MPa). The light gray lines in the first and second rows connect fluid structures as they evolve in time. Images from Davis and Chehroudi (21).....	33
Figure 1.8. Comparison of dark-core length measurements by Davis and Chehroudi (21) and Leyva et al. (22; 23) with other data available in the literature of core-length vs. momentum flux ratio. Amongst the data reported by others, Eroglu et al. and Woodward are two-phase flows and the rest are single phase. The references for the data are found in Table 1 of Ref. (21). Figure from Leyva et al. (22; 23).	34
Figure 2.1. Experimental setup of the acoustic waveguide and feed droplet system. The tank and microvalve arrangement was used for the tests with methanol, while the syringe pump was used for all other fuels.	42
Figure 2.2. Acoustic characterization of the waveguide as measured by pressure transducers at P1 and P2. From Dattarajan (14). The distance between the speaker and reflector was 62 cm.	43
Figure 2.3. Photograph of a burning fuel droplet showing standoff distance ($d_{standoff}$) and velocity perturbation (u') used to obtain strain rate estimates of the droplet at extinction.....	43
Figure 3.1. Photographs of fuel droplets burning in the absence of acoustic excitation. Backlighting accounts for the light portion of the background observed outside of the flame.....	57
Figure 3.2. Photographs of various fuel droplets burning during acoustic excitation, situated at or near the waveguide center for the “original” locations of the speaker and reflector, based on a measured maximum in P2/P1. Acoustic excitation corresponded to 780 Hz with an amplitude of	

138.6 dB for ethanol, the pure F-T, and the JP-8/F-T fuel blend, and 140.2 dB for methanol.....	57
Figure 3.3. Location of the pressure node relative to the droplet (y) and the droplet relative to the pressure node (y'), based on positioning of the speaker and reflector (S&R). (a) $y = 0$ and $y' = 0$, (b) $y > 0$ and $y' < 0$, where S&R move to the right, and (c) $y < 0$ and $y' > 0$, where S&R move to the left. From Dattarajan (14).....	58
Figure 3.4. Photographs of a burning ethanol droplet with acoustic excitation at 780 Hz (PN) and 138.6 dB. The distances to which the speaker and reflector (S&R) have been moved, relative to their original locations, are indicated.	59
Figure 3.5. Photographs of a burning methanol droplet with acoustic excitation at 540 Hz (PAN) and 139.9 dB. The distances to which the speaker and reflector (S&R) have been moved, relative to their original locations, are indicated.	60
Figure 3.6. Photographs of a burning JP-8/FT fuel droplet with acoustic excitation at 785 Hz (PN) and 138.6 dB. The distances to which the speaker and reflector (S&R) have been moved, relative to their original locations, are indicated.	61
Figure 3.7. For ethanol, measured values of K and d_{eqvs} , and estimated absolute value of g_a as a function of the displacement of the speaker and reflector relative to their original positions, for a 780 Hz PN. The solid line on the K plot represents a fit of the experimental data points, while the solid line on the g_a plot represents the theoretical variation in g_a assuming an average SPL of 138.6 dB. The data points for g_a represent absolute values estimated from the locally measured SPL value.	62

Figure 3.8. For methanol, measured values of K and d_{eqvs} , and estimated absolute value of g_a as a function of the displacement of the speaker and reflector relative to their original positions, for a 540 Hz PAN. The solid line on the K plot represents a fit of the experimental data points, while the solid line on the g_a plot represents the theoretical variation in g_a assuming an average SPL of 139.9 dB. The data points for g_a represent absolute values estimated from the locally measured SPL value. 63

Figure 3.9. For JP-8/F-T fuel, measured values of K and d_{eqvs} , and estimated absolute value of g_a as a function of the displacement of the speaker and reflector relative to their original positions, for a 785 Hz PN. The solid line on the K plot represents a fit of the experimental data points, while the solid line on the g_a plot represents the theoretical variation in g_a assuming an average SPL of 138.6 dB. The data points for g_a represent absolute values estimated from the locally measured SPL value. 64

Figure 3.10. For ethanol, measured values of K and d_{eqvs} , and estimated absolute value of g_a as a function of the displacement of the speaker and reflector relative to their original positions, for a 540 Hz PAN. The solid line on the K plot represents a fit of the experimental data points, while the solid line on the g_a plot represents the theoretical variation in g_a assuming an average SPL of 138.8 dB. The data points for g_a represent absolute values estimated from the locally measured SPL value. 65

Figure 3.11. For ethanol, measured values of K and d_{eqvs} , and estimated absolute value of g_a as a function of the displacement of the speaker and reflector relative to their original positions, for a 290 Hz PN. The solid line on the K plot represents a fit of the experimental data points,

while the solid line on the g_a plot represents the theoretical variation in g_a assuming an average SPL of 137.8 dB. The data points for g_a represent absolute values estimated from the locally measured SPL value. 66

Figure 3.12. For ethanol, measured values of K and d_{eqvs} , and estimated absolute value of g_a as a function of the displacement of the speaker and reflector relative to their original positions, for a 800 Hz PN. The solid line on the K plot represents a fit of the experimental data points, while the solid line on the g_a plot represents the theoretical variation in g_a assuming an average SPL of 138.5 dB. The data points for g_a represent absolute values estimated from the locally measured SPL value. 67

Figure 3.13. Consecutive photographs showing the extinction process of a pure F-T fuel droplet. Images (a) and (b) show the flame before extinction, image (c) shows a “wake” flame and image (d) shows a flameless droplet. The time interval between images is 33.37 ms, with forcing at 141.1 dB or a perturbation pressure of 228 Pa, and maximum velocity perturbation of 0.79 m/s. 68

Figure 3.14. Consecutive photographs showing the extinction process of a JP-8/F-T fuel droplet. Images (a) and (b) show the flame before extinction, image (c) shows a “wake” flame and image (d) shows a flameless droplet. The time interval between images is 33.37 ms, with forcing at 141.3 dB or a perturbation pressure of 233 Pa, and maximum velocity perturbation of 0.82 m/s. 68

Figure 3.15. Consecutive photographs showing the extinction process of an ethanol droplet. Images (a) and (b) show the flame before extinction, images (c) and (d) show a flameless droplet. The time interval between

images is 33.37 ms, with forcing at 142.2 dB or a perturbation pressure of 257 Pa, and maximum velocity perturbation of 0.90 m/s..... 69

Figure 3.16. Consecutive photographs showing the extinction process of a methanol droplet. Images (a) and (b) show the flame before extinction, image (c) shows a “wake” flame and image (d) shows a flameless droplet. The time interval between images is 33.37 ms, with forcing at 143.3 dB or a perturbation pressure of 292 Pa, and maximum velocity perturbation of 1.0 m/s. 69

Figure 4.1. Experimental test chamber and supporting systems of the Experimental Cell 4 at AFRL, Edwards AFB, CA..... 84

Figure 4.2. Chamber section view of the flow schematic for Experimental Cell 4 with the upgrades for the new coaxial injector. For a complete schematic refer to Appendix A..... 84

Figure 4.3. Photograph of the inner chamber within the test chamber in EC 4..... 85

Figure 4.4. (a) First (“original”) coaxial injector used in this study. (b) Exit plane view of the original coaxial injector..... 85

Figure 4.5. (a) Second (“new”) coaxial injector used in this study. (b) Exit plane view of the new coaxial injector. 86

Figure 4.6. Thermocouple and pressure transducer probes near the exit of the coaxial injector. 86

Figure 4.7. (a) Linear positioning stages that moved perpendicular to the vertical axis. (b) Larger view of the positioning stages and the thermocouple and pressure probe they support..... 87

Figure 4.8. (a) Diagonal view of the mechanical stage used to move the thermocouple in the vertical direction inside the main chamber. (b) View of the mechanical stage from above. The bottom of the test chamber can be seen in the upper part of the image.	87
Figure 4.9. High speed camera used in this study.....	88
Figure 4.10. Simplified diagram of the two acoustic drivers at a 0° and 180° phase angle, indicating relative flow perturbation directions.....	88
Figure 4.11. (a) One of two piezo-siren elements used to produce the acoustic field for this study. (b) Waveguide used to transmit the acoustic waves from the piezo-siren to the inner chamber.....	89
Figure 5.1. (a) Raw image from high-speed camera. (b) Dark core boundary extracted from the raw image using the image processing routine. (c) Black and white image after image processing threshold had been applied. (d) Schematic of the left and right contours used in this study to obtain inner jet spreading angles. Figure modified from original by Leyva et al. (22).	157
Figure 5.2. Left and right angles derived using the maximum displacement of the dark core region at each row over a sample of 998 images. From Rodriguez et al. (78).....	157
Figure 5.3. Image showing how outer jet spreading angles are measured. From Leyva et al. (75).	158
Figure 5.4. Collection of coaxial jet images without acoustic forcing at subcritical pressure from lowest to highest J. Original injector geometry.	158
Figure 5.5. Collection of coaxial jet images without acoustic forcing at nearcritical pressure from lowest to highest J. Original injector geometry.	159

Figure 5.6. Collection of coaxial jet images without acoustic forcing at supercritical pressure from lowest to highest J. Original injector geometry.	159
Figure 5.7. Dark core length normalized by the inner jet post inner diameter, L/D_1 , for the subcritical pressure regime. The results shown are for all the cases studied with the original injector geometry.	160
Figure 5.8. Dark core length normalized by the inner jet post inner diameter, L/D_1 , for the nearcritical pressure regime. The results shown are for all the cases studied with the original injector geometry.	160
Figure 5.9. Dark core length normalized by the inner jet post inner diameter, L/D_1 for the supercritical pressure regime. The results shown are for all the cases studied with the original injector geometry.	161
Figure 5.10. Dark core length normalized by the inner jet post inner diameter, L/D_1 for all pressure regimes using the original injector geometry. Results are shown in the $0.02 < J < 10$ range.....	161
Figure 5.11. Dark core length normalized by the inner jet post inner diameter, L/D_1 for all pressure regimes. Results include previous research work using the original injector geometry in the same facility this study was performed (22; 23; 42).	162
Figure 5.12. Spreading angle of the inner jet in degrees for all pressure regimes using the original injector geometry. Dark circular markers are data points from Leyva et al. (22; 23).....	163
Figure 5.13. Single phase coaxial jet images without acoustic excitation at subcritical pressures. Original injector geometry.....	163
Figure 5.14. Outer jet spread angle measurements with original injector geometry for one-phase coaxial jet at subcritical pressures. The bars indicate	

one standard deviation above and below the mean spreading angle. From Rodriguez et al. (79).	164
Figure 5.15. Outer jet spread angle measurements compared to jet divergence angle theoretical predictions and other single jet and coaxial jet spreading angle experimental data. From Rodriguez et al. (79).	164
Figure 5.16. (a) Approximate location during testing of the absolute pressure transducer used to measure the acoustic field inside the inner chamber. (b) Absolute pressure transducers used to quantify the pressure oscillations at three different transversal locations within the inner chamber for tests performed with the original injector. (c) Differential pressure transducers used to quantify the pressure oscillations within the inner chamber for tests performed with the new injector.	165
Figure 5.17. RMS of chamber pressure fluctuations measured at the bottom of the inner chamber versus phase angle between acoustic sources for the nearcritical case with $J = 2.1$ with the original injector geometry. The data with only one acoustic source on was obtained immediately before recording data with both sources on for the corresponding phase angle on which they are plotted. From Rodriguez et al. (79).	165
Figure 5.18. Graphs of the RMS value of the chamber pressure fluctuations at different phase angles between the acoustic sources on the left with chamber pressure as a function of time on the right for one subcritical case, one nearcritical case and one supercritical case with the original injector geometry. From Rodriguez et al. (79).	166
Figure 5.19. Collection of subcritical coaxial jet images at $P_{\text{chamber}} = 1.50 \text{ MPa}$, $J =$ 0.17. Original injector geometry	167

Figure 5.20. Collection of subcritical coaxial jet images at $P_{\text{chamber}} = 1.45$ MPa, $J = 2.6$. Original injector geometry.	167
Figure 5.21. Collection of subcritical coaxial jet images at $P_{\text{chamber}} = 1.50$ MPa, $J = 9.6$. Original injector geometry.	168
Figure 5.22. Collection of subcritical coaxial jet images at $P_{\text{chamber}} = 1.50$ MPa, $J = 23$. Original injector geometry.	168
Figure 5.23. Collection of nearcritical coaxial jet images at $P_{\text{chamber}} = 3.58$ MPa, $J = 0.55$. Original injector geometry.	169
Figure 5.24. Collection of nearcritical coaxial jet images at $P_{\text{chamber}} = 3.56$ MPa, $J = 4.9$. Original injector geometry.	169
Figure 5.25. Collection of nearcritical coaxial jet images at $P_{\text{chamber}} = 3.56$ MPa, $J = 9.3$. Original injector geometry.	170
Figure 5.26. Collection of supercritical coaxial jet images at $P_{\text{chamber}} = 4.96$ MPa, $J = 0.33$. Original injector geometry.	170
Figure 5.27. Collection of supercritical coaxial jet images at $P_{\text{chamber}} = 4.96$ MPa, $J = 2.4$. Original injector geometry.	171
Figure 5.28. Collection of supercritical coaxial jet images at $P_{\text{chamber}} = 4.96$ MPa, $J = 9.9$. Original injector geometry.	171
Figure 5.29. Dark core length with acoustics ($L_{\text{acoustics}}$) over dark core length without acoustics ($L_{\text{no acoustics}}$), shown in diamonds, versus phase angle between acoustic sources for subcritical pressures. The the peak-to-peak pressure perturbation as a percentage of the mean chamber pressure ($\Delta p_{\text{peak-to-peak}}/p_{\text{mean}}$), in squares, is also plotted. Original injector geometry.....	172

Figure 5.30. Dark core length with acoustics ($L_{\text{acoustics}}$) over dark core length without acoustics ($L_{\text{no acoustics}}$), shown in diamonds, versus phase angle between acoustic sources for nearcritical pressures. The the peak-to-peak pressure perturbation as a percentage of the mean chamber pressure ($\Delta p_{\text{peak-to-peak}}/p_{\text{mean}}$), in squares, is also plotted. Original injector geometry.....	173
Figure 5.31. Dark core length with acoustics ($L_{\text{acoustics}}$) over dark core length without acoustics ($L_{\text{no acoustics}}$), shown in diamonds, versus phase angle between acoustic sources for supercritical pressures. The the peak-to-peak pressure perturbation as a percentage of the mean chamber pressure ($\Delta p_{\text{peak-to-peak}}/p_{\text{mean}}$), in squares, is also plotted. Original injector geometry.....	174
Figure 5.32. Peak-to-peak pressure perturbation ($\Delta p_{\text{peak-to-peak}}$) as a percentage of the mean chamber pressure (p_{mean}) and dark core length with acoustics ($L_{\text{acoustics}}$) over dark core length without acoustics ($L_{\text{no acoustics}}$) versus phase angle between acoustic sources for sub, near and supercritical pressures at $J \approx 1.0, 2.5$ and 9.5 for the original injector geometry. From Rodriguez et al. (79).	175
Figure 5.33. Maximum dark core length reduction between dark core length without acoustics and dark core length with acoustics for all phase angles $(L_{\text{no acoustics}} - L_{\text{acoustics}})_{\text{MAX}}$ for a given case divided by the dark core length without acoustics ($L_{\text{no acoustics}}$) as a function of J for all cases obtained with the original injector in this study. From Rodriguez et al. (79).	176
Figure 5.34. Maximum inner spread angles as a function of acoustic phase angle for different J values at subcritical pressures for original injector geometry.....	177

Figure 5.35. Maximum inner spread angles as a function of acoustic phase angle for different J values at nearcritical pressures for original injector geometry.....	178
Figure 5.36. Maximum inner spread angles as a function of acoustic phase angle for different J values at supercritical pressures for original injector geometry.....	179
Figure 5.37. Coaxial jet images with the new injector at subcritical pressure ($P_{\text{chamber}} = 1.48 \text{ MPa}$, $J = 0.089$).	180
Figure 5.38. Coaxial jet images with the new injector at subcritical pressure ($P_{\text{chamber}} = 1.49 \text{ MPa}$, $J = 0.43$).	180
Figure 5.39. Coaxial jet images with the new injector at subcritical pressure ($P_{\text{chamber}} = 1.49 \text{ MPa}$, $J = 2.0$).	181
Figure 5.40. Coaxial jet images with the new injector at subcritical pressure ($P_{\text{chamber}} = 1.49 \text{ MPa}$, $J = 7.8$).	181
Figure 5.41. Coaxial jet images with the new injector at subcritical pressure ($P_{\text{chamber}} = 1.48 \text{ MPa}$, $J = 18$).	182
Figure 5.42. Coaxial jet images with the new injector at nearcritical pressure ($P_{\text{chamber}} = 3.56 \text{ MPa}$, $J = 0.50$).	182
Figure 5.43. Coaxial jet images with the new injector at nearcritical pressure ($P_{\text{chamber}} = 3.58 \text{ MPa}$, $J = 2.2$).	183
Figure 5.44. Coaxial jet images with the new injector at nearcritical pressure ($P_{\text{chamber}} = 3.58 \text{ MPa}$, $J = 9.4$).	183
Figure 5.45. Coaxial jet images with the new injector at nearcritical pressure ($P_{\text{chamber}} = 3.56 \text{ MPa}$, $J = 19$).	184

Figure 5.46. Coaxial jet images with the new injector at supercritical pressure ($P_{\text{chamber}} = 4.95 \text{ MPa}$, $J = 2.6$).	184
Figure 5.47. Dark core length with acoustics ($L_{\text{acoustics}}$) over dark core length without acoustics ($L_{\text{no acoustics}}$), shown in diamonds, versus phase angle between acoustic sources for subcritical pressures. The the peak-to- peak pressure perturbation as a percentage of the mean chamber pressure ($\Delta p_{\text{peak-to-peak}}/p_{\text{mean}}$), in squares, is also plotted. The cases which had their x coordinate marked with an asterisk (*) denote cases that had a dark core length that was longer than the field of view in more than 10% but less than 50% of the images. The ones marked with two asterisks (**) had dark cores larger than the examination window for at least half of the images. New injector geometry.	185
Figure 5.48. Dark core length with acoustics ($L_{\text{acoustics}}$) over dark core length without acoustics ($L_{\text{no acoustics}}$), shown in diamonds, versus phase angle between acoustic sources for pressures above the critical point. The the peak-to-peak pressure perturbation as a percentage of the mean chamber pressure ($\Delta p_{\text{peak-to-peak}}/p_{\text{mean}}$), in squares, is also plotted. See caption of Figure 5.47 for further details. New injector geometry.	186
Figure 5.49. Peak-to-peak pressure perturbation ($\Delta p_{\text{peak-to-peak}}$) as a percentage of the mean chamber pressure (p_{mean}) and dark core length with acoustics ($L_{\text{acoustics}}$) over dark core length without acoustics ($L_{\text{no acoustics}}$) versus phase angle between acoustic sources for sub, near and supercritical pressures at $J \approx 5, 10$ and 20 for the new injector geometry.	187
Figure 5.50. Maximum dark core length reduction between dark core length without acoustics and dark core length with acoustics for all phase angles ($(L_{\text{no acoustics}} - L_{\text{acoustics}})_{\text{MAX}}$ for a given case divided by the dark core length without acoustics ($L_{\text{no acoustics}}$) as a function of J for	

moderate and higher momentum flux ratio cases obtained with the new injector.	188
Figure 5.51. Comparison of the maximum dark core length reduction as a function of momentum flux ratio between the original injector geometry and the new injector geometry.	188
Figure 5.52. Maximum spread angles as a function of acoustic phase angle for different J values at subcritical pressures for the new injector geometry. The cases which had their x coordinate marked with an asterisk (*) denote cases that had a dark core length that was longer than the field of view in more than 10% but less than 50% of the images. The ones marked with two asterisks (**) had dark cores larger than the examination window for at least half of the images.	189
Figure 5.53. Maximum spread angles as a function of acoustic phase angle for different J values at near and supercritical pressures for the new injector geometry. See caption of Figure 5.52 for further details.	190
Figure A.1. Detailed schematic showing the flow path of the experimental setup of this study.	201
Figure A.2. Expanded view of the upper left section of the flow path schematic in Figure A.1.	202
Figure A.3. Expanded view of the upper right section of the flow path schematic in Figure A.1.	203
Figure A.4. Expanded view of the lower left section of the flow path schematic in Figure A.1.	204
Figure A.5. Expanded view of the lower right section of the flow path schematic in Figure A.1.	205

LIST OF TABLES

Table 3.1. Comparison of measured values of burning rate constant K for various fuel droplets, with combustion in the absence of acoustic excitation. Comparison with available established values is also given. †From Smith and Graves (64) and Vielle et al. (65). ‡From Kumagai and Isoda (66), Godsave (67), Wood and Wise (68), Rosser and Peskin (69). §From Wood and Wise (68).	56
Table 3.2. Acoustic conditions of various fuels at extinction. The corresponding sound pressure level in decibels (dB), pressure perturbation in Pascals (Pa), and velocity perturbation in meters per second (m/s) is given. A rough estimate of the strain rate is also shown.....	56
Table C.1. Summary of experimental conditions for tests performed with the original injector including single phase subcritical experimental conditions and results.	229
Table C.2. Summary of two-phase subcritical experimental results for tests performed with the original injector.....	230
Table C.3. Summary of nearcritical experimental results for tests performed with the original injector.	231
Table C.4. Summary of supercritical experimental results for tests performed with the original injector.	232
Table C.5. Summary of experimental conditions for tests performed with the new injector.....	233

Table C.6. Summary of two-phase subcritical experimental results for tests performed with the new injector. See caption of Figure 5.47 for explanation of * and ** markers.	234
Table C.7. Summary of nearcritical experimental results for tests performed with the new injector. See caption of Figure 5.47 for explanation of * and ** markers.	235
Table C.8. Summary of supercritical experimental results for tests performed with the new injector. See caption of Figure 5.47 for explanation of * and ** markers.	236

NOMENCLATURE

Symbols or Abbreviations

α	angle, spreading angle, density coefficient
ϵ	strain rate
g	gravitational acceleration
g_a	acoustic acceleration
\dot{m}	mass flow rate
μ	dynamic viscosity
p	pressure
ρ	density
u	mean velocity
A	area
C	carbon
CFD	computational fluid dynamics
D	diameter
D_{eqvs}	equivalent diameter of a sphere with the same volume
Δ	change
H	hydrogen
HE	heat exchanger
J	outer jet to inner jet momentum flux ratio, $J = \rho_o u_o^2 / \rho_i u_i^2$

K	burning rate constant
L	length, dark core length, distance between S&R; left
LRE	liquid rocket engine
N	nitrogen
O	oxygen
P	pressure
PAN	pressure antinode
PN	pressure node
PT	pressure transducer
R	radius; right
Re	Reynolds number, $Re = \rho uL/\mu$
RMS	root-mean-square, root-mean-square value
RTD	resistance temperature detector
S&R	speaker and reflector
SPL	sound pressure level
T	temperature
TC	thermocouple
VR	outer jet to inner jet velocity ratio, $VR = u_o/u_i$

Subscripts

_{cr}	critical
_i	inner, inner jet, inner wall or post (of coaxial injector)
_o	outer, outer jet, outer wall or post (of coaxial injector), air outside the flame
_s	surrounding products (of droplet combustion)

ACKNOWLEDGMENTS

This work would not have been possible without the help and support of many individuals and groups who directly or indirectly provided the time, knowledge, and/or financial support that I needed to successfully accomplish this endeavor. First and foremost, I would like to sincerely thank my advisor Professor Ann Karagozian who even before I met her encouraged me to pursue graduate studies right away instead of taking a year off school after finishing my undergraduate education. She, since then, has been involved in basically all the research and funding opportunities I have had a chance to take part of as a graduate student. From the NSF funded AGEPS Summer Transition Program, which I started as soon as I arrived to UCLA, and the opportunity to complete the second half of my research work at the Air Force Research Laboratory at Edwards AFB, to the current possibility to perform postdoctoral work overseas at the Laboratoire EM²C at École Centrale Paris in France. I am indebted to her for all her time, support and advice and I truly feel honored to be one of her PhD students.

I would also like to thank my advisor Professor Owen Smith who always gave me helpful and practical research advice when I needed it and for trusting in me twice as his teaching assistant. I also appreciate the help of Dr. Srinivasan Dattarajan whose work I continued during my first years as a graduate student. The support of my lab and classmate Dr. Julieta Davitian throughout our graduate school careers has also been invaluable. To Reinaldo Santos, Alec Pezeshkian, Matthew Sirignano, Hann-Shin Mao, and Sophonias Teshome for their support with my droplet combustion research at its various stages. I would also like to acknowledge the support of the NASA Microgravity Combustion Program, grant NCC3-690, Dr. Ming-Shin Wu and Dr. Kurt Sacksteder, grant monitors, and NASA Dryden/UCLA Flight Systems Research Laboratory, grant NCC4-153, which made possible the completion of this research. Very special thanks to Maj. Gen. Curtis Bedke, Commander of the Air Force Research Laboratory, for supplying the aviation and Fischer-Tropsch synthetic fuels used in this study.

For the second part of my research work, which took place at Edwards, AFB, CA, I would like to especially thank my mentor, Dr. Ivett Leyva, who put an incredible amount of time and effort into preparing me for the type and level of research that I would eventually be in charge of at AFRL. I am also thankful to her for all the work she did so that I could have the opportunity to perform postdoctoral work at École Centrale Paris in France. I share her sincere interest and passion for the work we perform at the Air Force Research Lab. I also deeply appreciate the very valuable discussions and expert advice of Dr. Douglas Talley and Dr. Behrouz Chehroudi from whom I continuously learn how to be a better researcher. I would also like to thank our branch chief at AFRL, Dr. Ingrid Wysong, for her constant support of our work. To Mr. Randy Harvey, Lt. Jeffrey Graham, Mr. Earl Thomas, Mr. David Hill, Mr. Todd Newkirk, Mr. Mark Pilgram, and Mr. Matt Billingsley many sincere thanks for your help supporting my research at Edwards AFB. My acknowledgments would of course be incomplete if I did not thank the Air Force Office of Scientific Research, grant FA 9550-07-1-0156, and Dr. Mitat Birkan, program manager of the supercritical fluids work I performed while at AFRL.

I would like to thank Dean Shirley Hune, Professor Richard Weiss, Dr. Barbara Ige, Professor Oddvar Bendiksen, Dr. Jeffrey Murphy, Dr. Atul Mathur, Ms. Angie Castillo, Ms. Cory Castro and Mr. Abel Lebon and all my professors and instructors from my earliest school years to undergraduate and graduate school for their support, for believing in me and for always helping me improve as a student and as a person. Last, but not least, to my doctoral committee members, Professor Stanley Osher and Professor Jeff Eldredge for their time, patience, and helpful insights.

Also, thank you to all my family and friends: you are who makes it all worth it.

For everyone I have failed to mention in the previous paragraphs who have given their time and effort so that I can accomplish the goal of completing my PhD, I sincerely thank you very, very much.

VITA

1982	Born, San Diego, CA.
1989 - 1997	Attended Instituto Lux Elementary School, Leon, Guanajuato, Mexico.
1997 - 2000	Attended ITESM Campus León High School, Leon, Guanajuato, Mexico.
2000	Participated in MIT's Project Interphase 2000.
2001	Summer Internship, Raytheon Electronic Systems.
2003	Summer Internship, Center for the Advancement of Hispanics in Science and Engineering Education
2004	Undergraduate Teaching Assistantship, Thermal Energy, Aeronautics and Astronautics Department, MIT.
2004	B.S., Aerospace Engineering, MIT.
2004	Summer Internship, MIT Department of Aeronautics and Astronautics
2004	NSF AGEP Fellowship, UCLA Graduate Division.
2005	Winter Teaching Assistantship, Preliminary Design of Aircraft, MAE Department, UCLA.
2005	Spring Teaching Assistantship, Rocket Propulsion, MAE Department, UCLA.
2005	Summer Graduate Research Assistantship, advisory by Professor Ann Karagozian and Professor Owen Smith, Thesis Topic
2005	Fall Teaching Assistantship, Aircraft Propulsion, MAE Department, UCLA.
2006	Winter Graduate Research Assistantship, advisory by Professor Ann Karagozian and Professor Owen Smith, Thesis Topic.
2006	Spring Teaching Assistantship, Rocket Propulsion, MAE Department, UCLA.

- 2006 M.S., Aerospace Engineering, UCLA.
- 2006 Summer Graduate Research Assistantship, advisory by Professor Ann Karagozian and Professor Owen Smith, Thesis Topic.
- 2006 Fall Teaching Assistantship, Aircraft Propulsion, MAE Department, UCLA.
- 2007 Winter Research Assistantship, advisory by Professor Ann Karagozian and Professor Owen Smith, Thesis Topic.
- April 2007 Passed PhD Candidacy Exam.
- 2007 - 2009 Graduate Student Researcher, Air Force Research Laboratory, Propulsion Directorate, Edwards AFB.

PUBLICATIONS AND PRESENTATIONS

Rodriguez, J. I., Graham, J. J., Leyva, I. A., Talley, D., “Effects of Variable Phase Transverse Acoustic Fields on Coaxial Jet Forced Spread Angles”. AIAA Paper No. 2009-0231, 47th AIAA Aerospace Sciences Meeting, Orlando, FL, 5-8 January 2009.

Rodriguez, J. I., Graham, J. J., Leyva, I. A., Lyu, H.-Y., Talley, D., “On the Inner Jet Spread Angles of Coaxial Jets from Subcritical to Supercritical Conditions with Preliminary Numerical Results”. Paper 4D-LPS-II, 55th JANNAF Propulsion/4th Liquid Propulsion Subcommittee Meeting, Orlando, FL, 8-12 December 2008.

Leyva, I. A., Rodriguez, J. I., Chehroudi, B., Talley, D., “Effect of Phase Angle on Coaxial Jet Behavior Spanning Sub- To Supercritical Pressures”. Paper 14-2, 22nd European Conference on Liquid Atomization and Spray Systems, ILASS Europe, Como, Italy. 8-10 September 2008.

Rodriguez, J. I., Leyva, I. A., Chehroudi, B., Talley, D., “Results on Subcritical One-Phase Coaxial Jet Spread Angles and Subcritical to Supercritical Acoustically-Forced Coaxial Jet Dark Core Lengths”. AIAA Paper No. 2008-4561, 44th AIAA/ASME/SAE/SEE Joint Propulsion Conference and Exhibit, Hartford, CT, 20-23 July 2008.

Rodriguez, J. I., Leyva, I. A., Chehroudi, B., Talley, D., “Effects of a Variable-Phase Transverse Acoustic Field on a Coaxial Injector at Subcritical and Near-Critical Conditions”. Paper M32-A-2, 21st Annual Conference on Liquid Atomization and Spray Systems, ILASS Americas, Orlando, FL, 18-21 May 2008.

Rodriguez, J. I., Leyva, I. A., Chehroudi, B., Talley, D., “Preliminary Results on Coaxial Jets Spread Angles and the Effects of Variable Phase Transverse Acoustic Fields”. 2nd Southern California Symposium on Flow Physics, University of California, Los Angeles, Los Angeles, CA, 12 April 2008.

Rodriguez, J., Teshome, S., Mao, H.-S., Pezeshkian, A., Smith, O. I., Karagozian, A. R., “Acoustically Driven Droplet Combustion with Alternative Liquid Fuels”. AIAA Paper No. 2008-1002, 46th AIAA Aerospace Sciences Meeting and Exhibit, Reno, NV, 7-10 January 2008.

Leyva, I. A., Rodriguez, J. I., Chehroudi, B., Talley, D., “Preliminary Results on Coaxial Jets Spread Angles and the Effects of Variable Phase Transverse Acoustic Fields”. AIAA Paper No. 2008-0950, 46th AIAA Aerospace Sciences Meeting and Exhibit, Reno, NV, 7-10 January 2008.

Rodriguez, J., Mao, H.-S., Teshome, S., Pezeshkian, A., Smith, O. I., Karagozian, A. R., “Combustion of Condensed Phase Alternative Fuels in an Acoustic Field”. 60th American Physical Society, Division of Fluid Dynamics Meeting, Salt Lake City, UT, 18-20 November 2007.

Rodriguez, J. I., Smith, O. I., Karagozian, A. R., “Acoustically Coupled Droplet Combustion with Alternative Fuels”. Southern California Symposium on Flow Physics, California Institute of Technology, Pasadena, CA, 7 April 2007.

Rodriguez, J. I., Smith, O. I., Karagozian, A. R., “Acoustically Coupled Droplet Combustion with Alternative Fuels”. Paper G-09, 5th US Combustion Meeting, San Diego, California, 25-28 March 2007.

ABSTRACT OF THE DISSERTATION

Acoustic Excitation of Liquid Fuel Droplets and Coaxial Jets

by

Juan Ignacio Rodriguez

Doctor of Philosophy in Aerospace Engineering

University of California, Los Angeles, 2009

Professor Ann R. Karagozian, Co-chair

Professor Owen I. Smith, Co-chair

This experimental study focuses on two important problems relevant to acoustic coupling with condensed phase transport processes, with special relevance to liquid rocket engine and airbreathing engine combustion instabilities. The first part of this dissertation describes droplet combustion characteristics of various fuels during exposure to external acoustical perturbations. Methanol, ethanol, a liquid synthetic fuel derived from coal gasification via the Fischer-Tropsch process, and a blend of aviation fuel and the synthetic fuel are used. During acoustic excitation, the droplet is situated at or near a pressure node condition, where the droplet experiences the largest velocity perturbations, and at or near a pressure antinode condition, where the droplet is exposed to minimal velocity fluctuations. For unforced conditions, the values of the droplet burning rate constant K of the different fuels are consistent with data in the literature. The location of

xxx

the droplet with respect to a pressure node or antinode also has a measurable effect on droplet burning rates, which are different for different fuels and in some cases are as high as 28% above the unforced burning rate value. Estimates of flame extinction due to acoustic forcing for different fuels are also obtained.

The second part of this work consists of an experimental study on coaxial jet behavior under non-reactive, cryogenic conditions, with direct applications to flow mixing and unstable behavior characterization in liquid rocket engines. These experiments, conducted with nitrogen, span a range of outer to inner jet momentum flux ratios from 0.013 to 23, and explore subcritical, nearcritical and supercritical pressure conditions, with and without acoustic excitation, for two injector geometries. Acoustic forcing at 3 kHz is utilized to maximize the pressure fluctuations within the chamber acting on the jet, reaching maximum values of 4% of the mean chamber pressure. The effect of the magnitude and phase of the acoustic field generated within the chamber on the dark core length and the inner jet spreading angles is presented and the stability of coaxial flows in the current flow regime is discussed with respect to evidence for convective and absolute jet instabilities under different operating conditions.

CHAPTER 1

Introduction

Acoustics play an important role in the performance of combustion systems. There is a strong interest in knowing the response of such reactive systems to acoustic excitation, since the acoustic and combustion processes can couple and enhance instabilities that might lead to the destruction of the combustion device (1). A particular area that is not well understood is the response and behavior of a range of alternative fuels in the environment of an acoustically resonant engine, which can occur in airbreathing engines and other combustion devices. The different reactive time scales associated with different fuels could modify the nature of combustion coupling to acoustic resonances and thus alter the performance of the combustion device. Therefore, it is of interest to investigate the response of various fuels when acoustic disturbances are present.

Such acoustically coupled, condensed phase combustion also occurs in liquid rocket engines (LREs). Combustion instabilities in LREs have been a long-standing challenge, and the fundamental mechanisms underlying such instabilities and the means by which they can be controlled remain largely not well understood. Because supercritical pressures and transcritical (i.e., transitioning from subcritical to supercritical) temperatures are typically found in LREs, it has been of interest to conduct fundamental experiments and numerical simulations in these flow regimes to better

understand acoustic coupling associated with these instabilities. Davis and Chehroudi (2), for example, have explored supercritical coaxial nitrogen jets and have shown that changes in the behavior of the jet as it leaves the injector can be enhanced by acoustic excitation. Since the injectors in LREs feature coaxial jet configurations, the effects of acoustic excitation on mixing and transport, which are flow features that are closely related to the reactive phase of the combustion process, of coaxial jets is a relevant topic. The present study focuses on both burning fuel droplets and coaxial jet behavior in a transverse acoustic field.

1.1 Acoustically Coupled Droplet Combustion

1.1.1 Burning of Spherical and Non-spherical Fuel Droplets

Fuel droplet combustion is a heterogeneous and reactive process. The condensed-phase combustion features of this phenomenon can be obtained from studying the characteristics of its associated diffusion flame. For a quasi-steady, burning spherical droplet, classical studies show that the variation in the diameter of the droplet d with time t follows the “ d^2 ” law (3):

$$d^2(t) = d^2(t = 0) - Kt. \quad (1.1)$$

The burning rate constant K is usually characterized in units of mm^2/s . In microgravity conditions, the observed droplet diameter follows a d^2 type of dependence on time due to a more spherical droplet geometry. One of the many motivations for

microgravity droplet combustion studies is aimed at understanding the applicability of the d^2 law to burning droplets (4).

However, in normal gravity conditions, a suspended droplet cannot maintain a spherical geometry due to surface tension and gravitational forces. Thus, the droplet and its surrounding diffusion flame cannot be assumed to be spherical. To be able to analyze the non-spherical droplets, the equivalent diameter of a sphere with the same volume as the non-spherical droplet d_{eqvs} is obtained via optical means to determine K using equation (1.1) for different burning scenarios (5).

1.1.2 Acoustic Excitation Effects on Condensed Phase Combustion

Several studies show that an increase in heat and mass transfer rates can take place in droplets burning under the effects of an external acoustical field (6; 7; 8; 9). Saito et al. (8; 9) explored how evaporating and burning kerosene droplets reacted when they are placed near a pressure node or antinode associated with standing waves inside a closed acoustic waveguide. This group finds an increase of 2 to 3 times in evaporative and burning rate constants when the droplet is situated at a pressure node (where velocity perturbations are high) compared to little or no change when the droplet is situated at a pressure antinode (where velocity perturbations are small or non-existent).

Some acoustic excitation studies involving droplet combustion have been performed under microgravity conditions. These experiments essentially eliminate natural convection effects and permit an undisturbed analysis of the acoustic forcing effects on the burning droplets. For instance, the work of Okai et al. (10) featured n-

octane droplet combustion in an acoustic field at different amplitudes and frequencies in a microgravity environment. It was observed that for droplets situated at a pressure node location at frequencies over 2 kHz the increase in burning rates is about 40% from the unforced values.

Tanabe et al. (11; 12), exposed a burning n-decane droplet to a pressure node and a location between the pressure node and the pressure antinode of a standing wave inside a duct in a microgravity environment. This research group found that the burning rate of the fuel increased significantly with the magnitude of velocity perturbation. A burning rate increase as high as 85% over the unforced value was observed for velocity perturbations up to 1 m/s. The effects of standing acoustic waves on burning rates and flame deflections are related to acoustic streaming processes, which describe the time-averaged motion induced in a fluid flow by its dominating fluctuating components (13). The concept of an acoustic radiation force, F_R , acting on a sphere of hot gases surrounding the burning droplet is used by Tanabe et al. (11; 12) to interpret their observations. The magnitude and orientation of this acoustic radiation force are presumed to directly affect burning rate constants and the degree of deflection of the flame surrounding the droplet. The expression for the acoustic radiation force is

$$F_R = \alpha(\rho_s - \rho_o)V \frac{\partial(\overline{u'^2})}{\partial x}, \quad (1.2)$$

where ρ_s is the density of the hot combustion products surrounding the diffusion flame, ρ_o is the density of the air outside the flame and the combustion products, V is the volume of a sphere containing the hot combustion products, x is the position of the droplet

measured from the point where the velocity node or antinode is located, and $\overline{u'^2}$ is the mean of the square of the amplitude of the local perturbation velocity, u' , within the waveguide. The coefficient α takes the following form when the density of the combustion products is lower compared to that of the ambient air:

$$\alpha \equiv \frac{3\rho_o}{2(2\rho_s + \rho_o)} . \quad (1.3)$$

The expression for the buoyancy force on an object of density ρ_s and volume V surrounded by a heavier fluid of density ρ_o , has the same form as the expression in equation (1.2). Thus, Tanabe et al. (11; 12) suggest that the acoustic radiation force has an influence on droplet combustion similar to the effect that gravity has on unforced droplet combustion. Their observations of the direction of flame deflection of burning droplets lying away from a pressure node are consistent with this theory.

In an effort to compare the effects of acoustic excitation in normal gravity and microgravity, Dattarajan et al. (14; 15) studied the droplet combustion characteristics of these fuels exposed to different acoustic excitation conditions in a laboratory environment and during free-fall (microgravity) conditions in a NASA drop tower. For these experiments, the droplet was located near a pressure node, where the droplet experiences the greatest effects of velocity perturbations and near a pressure antinode where the droplet is exposed to minimal velocity fluctuations. Results show that droplet burning rates in microgravity increase over 75% when the droplet is located near a pressure antinode and over 200% when the droplet is situated near a pressure node for

sound pressure levels greater than 135 dB compared to the unforced values (see Figure 1.1).

For burning droplets in normal gravity, no appreciable change is observed from the unforced values when the droplet is located near a pressure node and only moderate increases up to 15% are observed when the droplet is located near a pressure node (see Figure 1.2). Overall, the observed flame deformations when the droplet is located to either side of a pressure node or a pressure antinode are consistent with acoustic radiation forces associated with the acoustic field present (see Figure 1.3). When the droplet location is extremely close or coincident with the pressure node, flame oscillations are observed, in contrast to an absence of flame deflection suggested by acoustic radiation forces as in equation (1.2). Moreover, the theoretical acoustic acceleration to which the droplet is exposed when it is moved with respect to a pressure node or a pressure antinode did not completely explain the significant increases in burning rate observed in microgravity. While displacements of the droplet with respect to node or antinode locations are observed to have a measurable effect on droplet burning rates, acoustic accelerations associated with such displacements, as an analogy to gravitational acceleration, do not completely explain the significant increases in burning rate resulting from the excitation in microgravity.

1.1.3 Alternative Fuels

It is of great interest to study the performance and characteristics of potential substitutes to conventional fuels. These alternative sources of fuel are receiving

increasing attention due to sharp fluctuations in crude oil prices and a surge in competition for fossil fuels mostly from emergent economies (16). There is a wide range of options for alternate sources of energy. Some potential fuels, such as liquid hydrogen, have still major technological challenges to address, such as synthesis in sufficient quantity for transportation systems. In the short term, the solution for aircraft propulsion systems involves undoubtedly hydrocarbons. For automotive applications bio-diesel and ethanol have promise as non-fossil fuel derived sources, while synthetic fuels derived from natural gas or coal via the Fischer-Tropsch process (17) show promise as an aviation fuel replacement. To make efficient recommendations for the transition between alternative and conventional fuels for current propulsion systems, it is necessary to understand the differences in combustion and other characteristics of these alternative fuels as compared to conventional fuels. One example is the effect that liquid Fischer-Tropsch synthetic fuel has on the polymer seals of an aircraft engine. The synthetic fuel is found to degrade the seal over time due to its high content of aromatic naphta (18).

In the present study, two alcohols (ethanol and methanol), synthetic fuel (Fischer-Tropsch or F-T), and a blend of aviation fuel (JP-8) and synthetic fuel (F-T) were examined to assess differences and similarities in their combustion characteristics under acoustic excitation. It is interesting to note that this blend of JP-8 and synthetic fuel has been used in a B-52 aircraft during flight tests at Edwards AFB and is currently undergoing exploration at the Air Force Research Laboratory as an alternative aviation fuel (19).

1.2 Acoustic Driving of Coaxial Jets

1.2.1 Basic Flow Configuration

The type of flow analyzed for the second part of this dissertation is a coaxial jet flow. There are two types of coaxial flows depending on the jet dynamics: shear coaxial flows and swirl coaxial flows. In the former, the mean velocity of the outer jet and the mean velocity of the inner jet are parallel. In the latter, either the mean outer jet or the mean inner jet velocity has a tangential or rotational component and it is not parallel to the mean velocity of the other jet. Shear coaxial flows consist of two concentric jets or streams. The stream in the center of this flow configuration has a circular cross section and is referred to as the inner jet. The annular stream which surrounds the center stream is referred to as the outer jet. The boundary between the inner and outer streams is denoted as the inner jet post or tube and the boundary between the outer annular stream and the surrounding environment is denoted as the outer jet post or tube.

This study focuses solely on shear coaxial flows and the schematic in Figure 1.4 is representative of the type of shear coaxial flow investigated. The inner stream has a set of properties that characterize it, such as chemical composition of the fluid, temperature, density and the velocity of the flow. The inner diameter of the inner jet post, D_{ii} , constitutes the diameter of the circular inner jet. From the diameter of the inner jet, the cross sectional area, A_i , can be calculated:

$$A_i = \pi D_{ii}^2 / 4, \quad (1.4)$$

and using the average inner jet velocity, u_i , the mass flow rate, \dot{m}_i , can be found as $\dot{m}_i = \rho_i u_i A_i$, where ρ_i is the density of the inner jet fluid.

The outer stream is characterized by the same set of properties as the inner jet, and the values of the properties of the outer jet are mostly independent from those of the inner jet, the only exception being pressure which is the same for both inner and outer jets. The outer jet cross sectional area is:

$$A_o = \pi D_{oi}^2/4 - \pi D_{io}^2/4, \quad (1.5)$$

and the mass flow rate of the outer jet is given by $\dot{m}_o = \rho_o u_o A_o$, where ρ_o is the density of the outer jet fluid and u_o is the average outer jet velocity.

This basic coaxial jet flow configuration is used in the design of flow injection elements, commonly referred to as injectors, in cryogenic liquid rocket engines or LREs. One of the streams is used for the injection of the fuel and the other stream is used for the injection of the oxidizer. Commonly for cryogenic engines, the inner jet is the oxidizer and the outer jet is the fuel. Both fuel and oxidizer can be referred to as propellants. Examples of both cryogenic and non-cryogenic oxidizer fluids are oxygen, O_2 , hydrogen peroxide, H_2O_2 , and dinitrogen tetroxide, N_2O_4 ; while some fuels include hydrogen, H_2 , kerosene, a hydrocarbon with an approximate chemical formula of $C_{12}H_{26}$, hydrazine, N_2H_4 , monomethylhydrazine, CH_6N_2 and unsymmetrical dimethylhydrazine, $C_2H_8N_2$. Such coaxial flow injectors were used in the J-2 engine which powered the Saturn V

rocket, and are used in the RS-24 engine, also known as the Space Shuttle Main Engine or SSME, and the Vulcain engine that is used to lift the Ariane 5 rocket (20). As LREs evolve into higher specific impulse rocket designs, maximum combustion chamber pressures increase, reaching or surpassing the supercritical pressure values of most propellants. Hence, when propellants are injected into the combustion chamber of an LRE, they mix and the thermodynamic properties of the mixture can deviate significantly from those of the individual propellants. A better understanding of how the propellants behave under these supercritical conditions is of utmost importance.

1.2.2 Motivations and Objectives of Coaxial Jet Study

One of the most important requirements for an injector or a group of injectors in an LRE is to provide homogeneous mixing of the fuel and oxidizer within a short distance from the location where these propellants enter the combustion chamber. Two factors that strongly influence the mixing process are the geometry of the injector and the flow and thermodynamic properties of the propellants as they exit the injector.

The design of the injector plays a very important role in the performance of the device. For a coaxial injector, the thickness of the inner jet post dictates the separation between the inner jet and the outer jet flows after they exit the injector. A thinner post will allow for the fuel and oxidizer streams to come in contact with each other and develop a shear layer as soon as they exit the injector, while a thick inner jet post will delay the contact between the fuel and oxidizer, creating a recirculation region and a different mixing flow pattern between the two streams as they exit the injector. The

thickness of the outer jet post also affects the type of interaction between the outer jet and the mean flow of the combustion chamber.

Another geometry parameter that affects the flow is the axial distance from the end of the inner jet post to the end of the outer jet post; this distance is usually referred to as the inner jet “recess” length (see Figure 1.4) since usually the inner jet post ends before the outer jet post does, leaving no solid boundary between the inner jet and the outer jet for a short distance before both streams leave the coaxial injector exit, which in this case is defined as coincident with the end of the outer jet post.

The other factors that inherently influence the mixing process are the properties of both the inner and the outer jet flows. The local pressure and temperature can be used to find the local density of each jet, which along with their average velocities at the exit of the injector can be used to find parameters such as the outer jet to inner jet velocity ratio, VR , and outer jet to inner jet momentum flux ratio, J . These parameters are defined as follows, respectively: $VR = u_o/u_i$ and $J = \rho_o u_o^2 / \rho_i u_i^2$, and are used to determine which combination of temperatures, pressures and mass flow rates are the most effective to enhance mixing of the propellants as they enter the combustion chamber. For example, empirical evidence from previous experiments at AFRL suggests that as the outer jet to inner jet momentum flux ratio increases, the dark core length, a quantity to be defined in Chapter 5, decreases (21; 22; 23), which constitutes evidence that mixing between the two jets increases at relatively short distances from the exit plane.

Combustion instability constitutes a very challenging phenomenon when working with LREs and its components. Any incidents featuring high-frequency unstable behavior

in the pressure or heat flux in the combustion chamber of an LRE can cause severe engine damage and vehicle destruction. There are several factors that can contribute to high frequency combustion instabilities in LREs and each component of the engine could potentially have a role in the development of these instabilities. In fact, the same factors that affect the mixing process, such as the injector geometry and the outer jet and inner jet flow properties, could have a large influence in the development of such unwanted instabilities (24).

The main motivation of the second part of this work is to study shear coaxial jet flows in order to understand fundamental problems associated with LREs. How propellant fluids come in contact with each other and mix, and how they interact with each other in the combustion chamber when there are strong acoustic fields and resonances present are issues of great interest. It is thus the objective of the present work to analyze the response of a nonreactive coaxial jet when factors such as the injector geometry and the flow properties are varied in a systematic fashion, including exposure to strong acoustic forcing, to obtain a better understanding of the mixing processes of propellants and the high frequency interactions that are most destructive to a rocket engine. The main goal is to gather the knowledge acquired from this study and apply it to the early stages of LRE design so that efficient propellant use is achieved and predisposition to combustion instabilities is assessed and corrective actions are taken.

For the present experimental study, there was only one fluid used to simulate the fuel and oxidizer. The fluid was molecular nitrogen, N_2 , which has a critical temperature, T_{cr} , of 126.2 K and a critical pressure, P_{cr} , of 3.39 MPa. Having only one working species

allowed for a clear boundary between the gas, liquid, and supercritical phases of the fluid, avoiding the added complexity introduced when working with mixtures. Further, having a non-reactive shear coaxial injector flow also allowed the fluid mechanic effects to be isolated from the combustion-related phenomena observed in a reactive combustion chamber.

For instance, in a typical application of a coaxial injector with jets of liquid O_2 /liquid H_2 present, the oxygen is injected at subcritical temperatures through the inner jet and the hydrogen is injected at supercritical temperatures through the outer jet. The temperature of the outer hydrogen jet is higher than that of the inner jet as the hydrogen is used to remove heat from the combustion chamber walls. Therefore in the combustion chamber, since there are at least two species present, there is no single critical point, but instead there are critical mixing lines that define the thermodynamic state of the mixture (25). Hence, the reactive flow increases the difficulty of the thermodynamic analysis by adding more species to the chamber (reactants and products). Thus, this study is comprised of single species flows, either one-phase, when both the inner jet and the outer jet are in a gaseous state or when they both are in a supercritical state, or two-phase flows, when the outer jet is in a gaseous or supercritical state and the inner jet is in a liquid or liquid-like state. This greatly simplifies the analysis of the thermodynamic properties of both the coaxial injector and chamber flows.

Given the connection between this study and LREs, one of the major parameters considered was the mean pressure of the combustion chamber. Both the Space Shuttle and the Ariane 5 launch vehicles have LREs designed to operate above the critical

pressures of each of its propellants individually. Therefore, for this work, experiments were performed at three different mean chamber pressures, a subcritical pressure of 1.5 MPa, a nearcritical pressure of 3.6 MPa and a supercritical pressure of 5.0 MPa. The parameters affecting the interaction between the outer jet and the inner jet, which include their flow properties, were varied by changing the outer jet to inner jet momentum flux ratio, J . Varying J also indirectly modified the velocity ratio, VR . Commonly, the velocity ratio between the outer and inner jets of coaxial injectors in LREs is about 10 or higher. This practice was adopted after empirical evidence showed that injectors operating at these VR s were the most effective in preventing combustion instabilities (26). In this work J was varied from less than 0.02 to over 20, which in turn produced a variation of outer to inner jet velocity ratio in the $0.25 < VR < 23$ range.

1.2.3 Previous Work on Coaxial Jets

To meet the objective of studying the effects of acoustic forcing in a coaxial jet flow configuration, a transverse acoustic field was generated inside the test chamber. A transverse acoustic field was chosen because transverse acoustic modes lead to more destructive instabilities in LREs than longitudinal ones (20; 27). Specifically, this work focused on the effects of varying the pressure and velocity perturbations, by varying the phase difference between the acoustic sources producing the imposed transverse acoustic field, on the coaxial jet flow.

From the information above, it is important to highlight that one of the unique characteristics of this study is the exposure of the coaxial jet flow to the different

conditions found in a transverse acoustic field. To accomplish this, two acoustic sources were used. Each source received a signal at the same frequency and very similar amplitude, only varying the phase between the signals. The objective was to find the effect of the phase difference or phase angle on the coaxial jet, leaving the other acoustic properties the same.

In earlier studies involving acoustic excitation of reactive gaseous $\text{CH}_4/\text{liquid O}_2$ swirl coaxial jets, Marshall et al. (28) performed experiments at a mean chamber pressure of 1.53 MPa with maximum peak-to-peak pressure perturbations ($\Delta p_{\text{peak-to-peak}}$), as a fraction of mean chamber pressure (p_{mean}), of 4%. They studied the influence of mass flow rate, mixture ratio, injector and nozzle positions and chamber pressure on the spontaneous excitation of the transverse modes of their three-dimensional rectangular chamber. They found that the first mode of the largest dimension of the chamber produced a strong response in the jet when the injector was positioned near a velocity node location, where pressure fluctuations were the largest.

In another study, Richecoeur et al. (29) studied an acoustically excited, multiple element, and reactive coaxial injector configuration at elevated but still subcritical pressure conditions, with a mean chamber pressure of 0.9 MPa. Their experiments were performed at conditions where combustion became sensitive to external acoustic oscillations, which corresponded to outer to inner jet momentum flux ratios in the $4.6 < J < 20$ range. They obtained strong coupling between the combustion products from the three coaxial CH_4/O_2 injectors used in the study with pressure amplitude oscillations reaching 7% $\Delta p_{\text{peak-to-peak}}/p_{\text{mean}}$. This strong coupling between acoustics and combustion

was manifested by an enhancement of the flame spread, which is often associated with improved mixing; however, if the acoustic perturbations that enhance mixing result from or lead to combustion instabilities, they are clearly something to avoid. Interestingly, it was also found by a phase analysis study that the flame location (measured indirectly by tracking the emission of OH radicals) and the pressure oscillate in phase at the modulating frequency, a behavior they also observed with their high-speed camera. This indicates that flame enhancement was observed at the equivalent of a pressure antinode location, where pressure perturbations are the highest.

Some of the previous work on coaxial jets has focused on the mixing properties of this concentric flow configuration. For instance, Gutmark et al. (30) concluded in their single phase coaxial vs. free jet experimental studies that in coaxial flow configurations, more of the surrounding fluid is entrained deeper into the inner jet as compared to the free jet case, enhancing the overall mixing process. These researchers also found that the geometry of the injector plays a role as well, with better mixing performance achieved by rectangular injectors as compared to circular ones. Gautam and Gupta (31) reported, in their cryogenic coaxial injector studies at atmospheric pressures, an increase in the evaporation of the inner jet and enhanced mixing with the surrounding flow with increasing outer to inner momentum flux ratio. They also altered the geometry of their injector setup by modifying the recess length between the inner jet and the outer jet exits. They found that larger recess lengths promote higher jet expansion and more entrainment of surrounding gases into the flow. Their shear layer analysis confirms that mixing enhancement and jet expansion are slower at lower J values.

In terms of reactive flows, Zong and Yang (32) also find in their numerical study of high pressure coaxial reactive flow that as J increases, turbulent mixing is enhanced, which reduces the inner jet dark core. One of the earliest studies on the subject, by Chigier and Beér (33), provides a very detailed description of the region near the injector exit in their coaxial jet experiments in which they varied the outer to inner velocity ratio from ∞ to 0.024. They present an explanation for the fluid processes they observe as the inner jet and outer jet leave the injector exit, such as the influence of the recirculation zone between the streams and the mixing process once the flows meet. They observe that at the low VR values the inner jet is less affected by the recirculation zone and is capable of entraining more flow from the outer jet. However, at high VR values, the inner jet gets entrained more by the outer jet because of the way the recirculation zone acts to push the inner jet towards the outer jet.

1.2.4 Dark Core Length

In a coaxial flow configuration, the region whose outer boundaries are composed of the exit plane of the coaxial injector and the contour where the density or the velocity, depending on the definition, start to deviate from its initial value at the exit plane of the injector can be referred to as the potential core of the jet. The previous definition is based on the definition of a jet given by Romiti (34). Given the definition above, both the inner jet and outer jet can have their own potential core regions. The inner or outer potential core length is thus the axial distance from the end of the coaxial injector (either the inner jet or outer jet exit) to the end of their respective potential core region.

Intact surface length, intact core length, liquid intact length, liquid core length, undisturbed jet length, primary and secondary breakup length or simply unbroken, intact or breakup length are other common length scales used in the literature (35; 36; 37; 38; 39; 40) to characterize single and coaxial jets, although some of these variables are almost exclusively applied to the potential region of a single jet or the inner jet of a coaxial flow only. For instance, in a two phase coaxial jet, the term ‘liquid core length’ refers to the length needed for the liquid inner jet to be completely broken into drops and ligaments (37). A similar definition is that of the ‘intact or breakup length’ which refers to the distance between the exit of the injector and the location just before the first drop is formed as the inner jet liquid stream brakes apart from the liquid core (38).

The shape of the core in a two dimensional plane intersecting the axis of symmetry of the coaxial flow configuration resembles a triangle. Thus, for the three dimensional coaxial jet, the potential core has an appearance that is very similar to that of a cone. Thus the words “core” and “cone” are used interchangeably in some of the variable names mentioned above. For this work, the term ‘dark core’ will be used to describe the same variable referred to by the various definitions above. Any term involving the word ‘liquid’ cannot be used exclusively throughout this study since we analyze supercritical inner jets as well. Also, in the supercritical regime, both jets have the same phase, and words such as ‘intact’, ‘undisturbed’ or ‘unbroken’ become more ambiguous. Thus, a ‘dark core region’ based on the flow density, and the corresponding ‘dark core length’ will be precisely defined, discussed and compared to other equivalent potential core measurements in Chapter 5.

Regardless of the name used, such length scales are important parameters to study because, among other considerations, they are related to the degree of mixing that has taken place at a critical distance from the injector exit. The shorter these length scales are, the higher the amount of fluid from the inner jet that has been entrained by the outer jet and mixed with the surroundings.

Given the significance of the dark core length as a qualitative indication of mixing in an LRE, it is important to analyze also the effects that an external acoustic field can have in the behavior of the dark core. External forcing can be introduced in an LRE by means of vibration, especially when the vehicle that the engine will be lifting is being launched. During take-off, high-frequency phenomena within the engine can interact with the combustion processes in the chamber, driving the energy release to unstable and potentially destructive patterns. Analyzing the effects of an acoustic field on the dark core length can lead to an improved understanding of how these acoustic modes couple with the mixing processes taking place in the combustion chamber, thus providing information on potential causes of combustion instabilities in LREs.

Previous experiments performed in the same facility at AFRL in which this study took place (2; 21; 22; 23; 41; 42) feature an acoustic source at one end of the test chamber and a non-movable reflective wall at the other end. This type of acoustic set up only allowed for a fixed position of the jet with respect to the acoustic wave profile for pressure or velocity. By adding a second identical resonator at the location of the reflective surface, the magnitude and relative position of the pressure and velocity acoustic field with respect to the jet could be varied. Therefore, studying the effects of

having the injector positioned at a pressure or velocity node or at positions in between was now possible, and the effects of both the magnitude and gradient of the pressure and acoustic field on the coaxial jet flow could now be carefully analyzed.

1.2.5 Shear Layers and Spreading Angles

The study of the growth of shear layers between two planar flows is relevant because the rate of growth of the shear layer is indicative of the mixing process between the two layers (43; 44; 45; 46; 47). In an idealized 2D shear layer a spreading angle starts to develop at the point where both flows meet. Since the velocity of the particles in the shear layer achieves an intermediate value between the two flows that bound it, the points in the flow where the velocity changes from its original value to a higher or lower one form two lines. The angle between these two lines is the shear layer spreading angle (see Figure 1.5).

One classic shear layer study is described in the work of Brown and Roshko (43), who proposed an equation for the growth rate of a shear layer while studying subsonic two dimensional incompressible turbulent gas-gas flows. Dimotakis (44) in turn proposed an equation for the vorticity growth rate of a planar free jet while Papamoschou and Roshko (45) proposed an equation for the growth of the visual thickness of the shear layers for compressible (subsonic to supersonic) two dimensional turbulent mixing layers. More relevant to the present studies, Chehroudi et al. (46; 47) showed for the first time that the near field spreading angle or growth rate of single round jets at supercritical pressure and temperature agrees quantitatively with experimental data and theoretical

predictions for 2D shear layer growth from the single phase investigations discussed above.

For a single round jet, the spreading angle can also be referred to as the spray angle, spread angle or jet divergence angle (37; 39; 48). It can be defined experimentally using a visual method that averages a sample of images and approximates the left and right contours of the jet as straight lines using the least-squares method (48). In their studies, Chehroudi et al. (46; 47) analyzed the spreading angles of single round jets under pressure conditions spanning from subcritical to supercritical. The study also included experimental data on gas phase variable density jets from different researchers in which the main variable investigated was the ratio of the chamber density to the jet density. This variable is important when considering the interaction between a single jet and a quiescent atmosphere.

For a coaxial flow, the spreading angle of the inner jet can be defined in a similar manner to the spreading angle of a single round jet. One can also consider the spreading angle of the outer jet, for which a different definition is needed since it has an annular shape. The spreading angle of the outer jet is the sum of the angle spanned by a line parallel to one side of the outer jet and the vertical axis of the jet and the angle spanned by a line parallel to the opposite side of the jet and the same vertical axis. In coaxial flows, a shear layer is created when the wall or tube between the inner jet and the outer jet ends (see Figure 1.6).

The development and effect of shear layers in a flow becomes important when analyzing coaxial jet behavior. For the case of a coaxial jet, the inner jet spreading angle

provides an experimental indication of the growth of the shear layer between the inner and outer streams. However, to accurately represent a shear layer, the wall between the inner and outer streams must be very thin. In this work, the spreading angles of both the inner and outer jet with and without exposure to an acoustic field will be defined and analyzed in Chapter 5.

1.2.6 Stability Analysis of the Coaxial Jet

A liquid jet owes its behavior to numerous factors, including the geometry of the orifice from where it is being issued, the properties of the flow when it exits such orifice and the environmental conditions that it encounters as it leaves the exit location. But regardless of how these factors are varied, a liquid jet cannot be prevented from ultimately breaking up at some distance downstream from the exit location. To study the physical reasons for the breakup of a liquid sheet or jet, linear stability analysis is an important tool which predicts the onset of the instability in this class of flows (38). In stability analysis, disturbances should be allowed to grow both temporally and spatially to reach an accurate description of the breakup process. The breakup process leads to two different major regimes, the creation of large drops or fine atomization of the liquid, which are the result of very distinct physical phenomena (37; 38). These two main regimes and others in between are the consequence of how the jet responds to disturbances.

The concept of absolute versus convective instability is also indispensable in stability analysis. One of the characteristics of absolute instability is the spreading of

disturbances both upstream and downstream the flow, in contrast to convective instability where disturbances only travel downstream from the disturbance location (49). Many different effects influence the absolute or convective instability of the inviscid liquid jet flow. Exit conditions, surrounding gas and slip velocity are some of them. For instance, in actual experiments, before the flow leaves the exit orifice, the velocity is zero at the wall due to the no-slip boundary condition and reaches a maximum at the axis; however, according to Scriven and Pigford (50) as the liquid jet flow leaves the exit, the velocity profile does achieve a uniform distribution.

The previous notion was used by Leib and Goldstein (51) in their instability analysis to show that if the Weber number at the orifice exit is less than 3.3 the convectively unstable jet becomes absolutely unstable before the flow has an opportunity to recover a uniform velocity profile. If the Weber number is above 3.3, the jet remains convectively unstable and attains a top-hat distribution. This “velocity relaxation” seems to preclude the disturbance from travelling upstream. The effect of surrounding gas on a liquid jet is also important. When the density ratio is increased by a factor of ten the effect of the ambient air is to increase the spatial growth rate of the disturbances by the same factor since the gas inertial force is an important factor in the enhancement of such growth rate. Likewise, the increase of the relative velocity between the gas and the liquid augments the disturbance growth rate and cut-off wave number, which is the basis for the Kelvin-Helmholtz instability.

The review by Huerre and Monkewitz (49) on local and global instabilities in spatially developing flows classifies open shear flows according with their local/global

and absolute/convective instability features. They point out that flows that are locally convectively unstable everywhere are more prone to external disturbances, which determine the evolution in space of the unsteady flow. These flows, such as mixing layers, are susceptible to acoustic excitation and therefore a certain degree of control can be exercised over their behavior. In contrast, flows that have regions of absolute instability of large enough size are not easily affected by external dynamics. Instead, the source of their absolute instability relies on the temporal growth of the initial perturbations in these absolutely unstable regions of the flow. Wakes and low density jets are examples of these kinds of flows. Finally, flows that are locally convectively unstable but a latent absolute instability is present at some point in the field are referred to as marginally globally stable flows. In these flows, the global mode can be excited if forcing is applied at or near the frequency of the mode, which otherwise would be damped slowly over time. This is the case of homogeneous jets.

Raynal (52) extends the classical stability analysis of two parallel flows with different densities from previous authors to the particular case of coaxial jets with high momentum flux ratios. The main goal of this analysis is to study the main instability that develops at the interface between the liquid and the gas streams. In the particular case of coaxial flows, he points out that a proper model should include the vorticity layers produced by the walls of the nozzle. He also suggests that the gaseous flow sets the velocity and length scales and the liquid flow damps high frequency perturbations and only allows the amplification of large wavelengths. His empirical observations led him to

postulate that the vorticity layer of the gaseous stream is responsible for the instability and not the surface tension between the two fluid streams.

Perrault-Joncas and Maslow (53) performed a linear stability study of a compressible coaxial jet with velocity and temperature profiles characteristic of a turbofan engine exhaust, with outer to inner velocity ratio varying between 0.5 and 0.8. They conclude that there are two primary modes of instability for the velocity profiles they investigate. The secondary mode, associated with the outer stream, is found to have a larger growth rate; however, the two modes seem to behave independently. The outer to inner velocity ratio primarily affects the mode of the inner stream and the diameter ratio has more influence on the mode of the outer stream. They point out that it is simple to diminish the effects of the most unstable outer stream mode by increasing the momentum thickness of the outer stream through changes in the geometry of the flow.

1.2.7 Coaxial Jets and Acoustic Excitation

Previous studies have shown the relevance of changes in the exit area of a coaxial jet injector and the physical processes taking place in the vicinity of the device due to acoustic forcing (54; 55; 56). Richecoeur, et al. (29) found correlation between the intact core-length of the coaxial jet and the enforced acoustic excitation. For several years, Chehroudi and co-workers (41; 47; 57) have investigated supercritical jet flows at high Reynolds numbers, which are of interest to practical applications in propulsion systems.

In recent experiments, Davis and Chehroudi (21) explored large scale acoustic excitation of a liquid(interior)/gaseous(exterior) coaxial nitrogen jet injected into a

gaseous nitrogen chamber at high pressures. Subcritical, near-critical, and supercritical chamber pressures were explored, with acoustic excitation of the jet in the vicinity of the pressure node (or velocity antinode) and with amplitudes as high as 180 dB at pressures up to 5 MPa. As indicated, for example, in Figure 1.7 (from their paper), the strongest effect of acoustic excitation was observed under subcritical pressures, whereby strong jet oscillations and liquid jet spread and breakup were enhanced. The cause of this behavior is not completely understood, but there is the suggestion that the operation of the acoustic driver (operating at constant power for different pressure amplitudes) may be a limitation.

The data by Davis and Chehroudi (21) constitute the first exploration of subcritical conditions in the vicinity of momentum flux ratio $J = 10$. They also have found that there is correlation between the outer to inner jet velocity ratios of the injector and the root-mean-square value of the fluctuations in dark core length of the jet under acoustic excitation. It is thought that an important driving mechanism of the processes leading to combustion instabilities in a rocket engine is inhibited at high outer to inner coaxial jet injector velocity ratios. The present study aims to answer these questions.

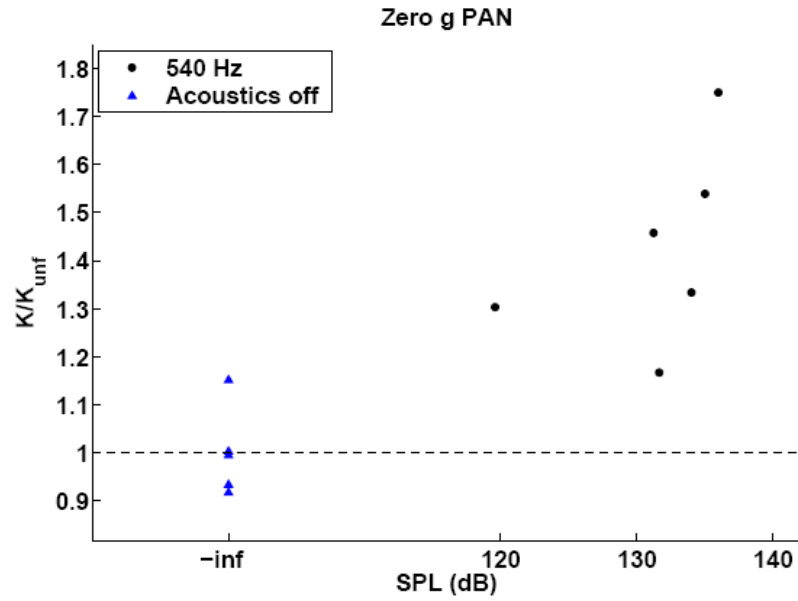
A plot of the normalized dark core length versus J by previous researchers for the different regimes explored in the present study is shown in Figure 1.8. Detailed quantification of the jet dark-core length via high speed shadowgraph movies and image processing was performed by Leyva et al. (22; 23). These experiments with one acoustic source found that the effects of acoustics on the dark core length are statistically significant for outer to inner jet momentum flux ratios in the $1 < J < 4$ range. For subcritical pressures, this range is even larger. In the experiments performed for the

present work the addition of a second acoustic driver allowed changes of the relative position of the acoustic field with respect to the fixed location of the coaxial jet injector, and hence greater variability in the flowfield.

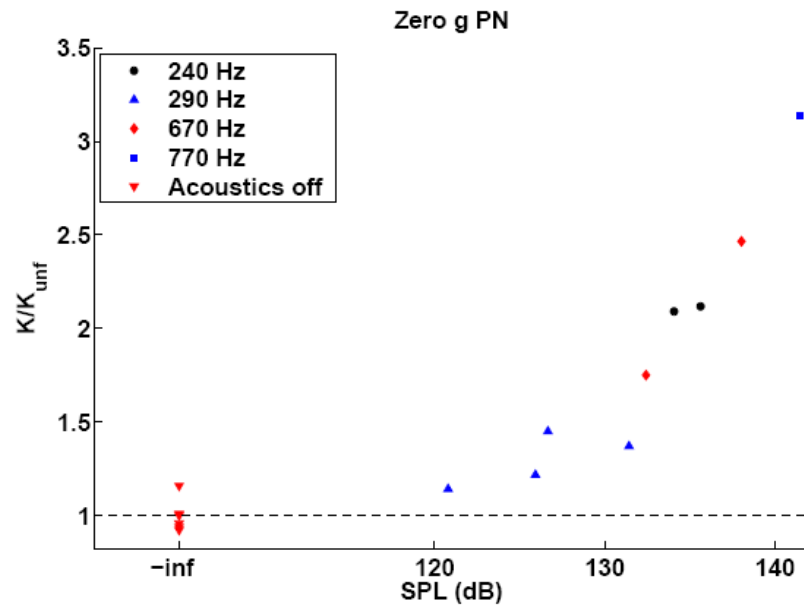
The main focus of the experiments in this thesis was an exploration of the effect of external acoustic excitation on basic condensed phase burning and transport processes. Goals in the droplet combustion experiment consisted of measuring the flame deflection and burning rate constant of different alternative and conventional fuels. Results were compared to previous studies by our research group at UCLA (14; 15) and others (9; 10; 12). Chapter 2 introduces the experimental setup of the droplet combustion experiment and Chapter 3 presents the results.

The other example where condensed phase material is affected by acoustic excitation is in subcritical, transcritical, and supercritical coaxial jets, with useful applications in cryogenic liquid rockets. Understanding the effects of acoustic excitation on mixing and fluid mechanics of subcritical and supercritical jets can provide useful information for improved processes in injector design (26).

In the present study, different responses of the coaxial jet to acoustic excitation for different conditions and properties of the flow will be explored. The experimental setup is described in Chapter 4, and results are provided in Chapter 5. These results can suggest stability behavior in the jet, with the potential to identify convective/absolute and local/global modes and the regimes for which the coaxial jet flow can be assigned any of these instability characteristics.

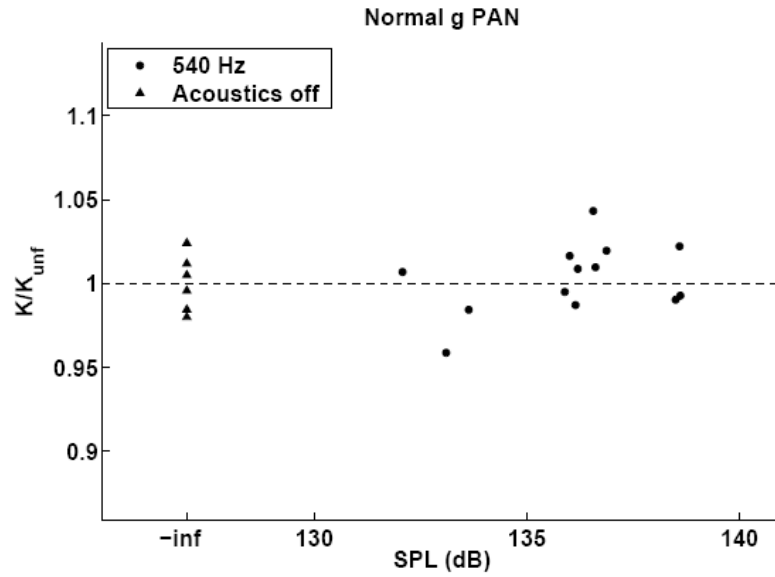


(a)

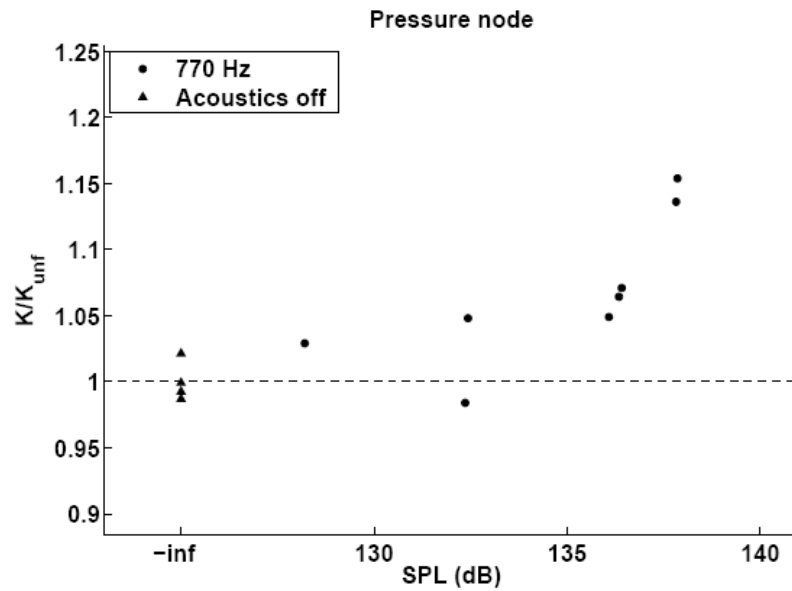


(b)

Figure 1.1. In microgravity, effect of sound pressure level, SPL, on the mean burning rate constant K normalized by its mean value in the absence of acoustic excitation, K_{unf} , (a) at a pressure antinode, PAN, and (b) at a pressure node, PN. From Dattarajan (14).



(a)



(b)

Figure 1.2. In normal gravity, effect of sound pressure level, SPL, on the mean burning rate constant K normalized by its mean value in the absence of acoustic excitation, K_{unf} , (a) at a pressure antinode, PAN, and (b) at a pressure node, PN. From Dattarajan (14).



(a)



(b)



(c)



(d)

Figure 1.3. Photographs of a burning droplet in microgravity (a) with no forcing and (b) forced at a pressure node at 770 Hz; and in normal gravity (c) with no forcing and (d) with forcing at a pressure node at 770 Hz. From Dattarajan (14).

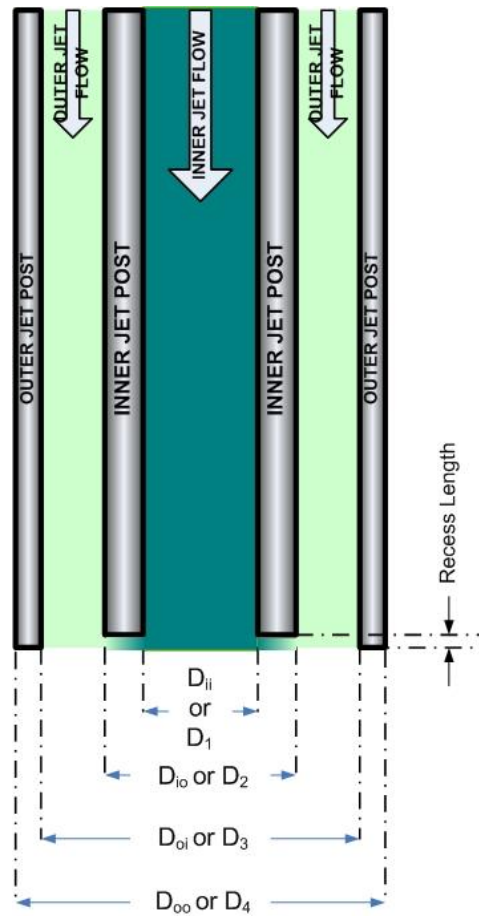


Figure 1.4. Schematic of coaxial jet flow.

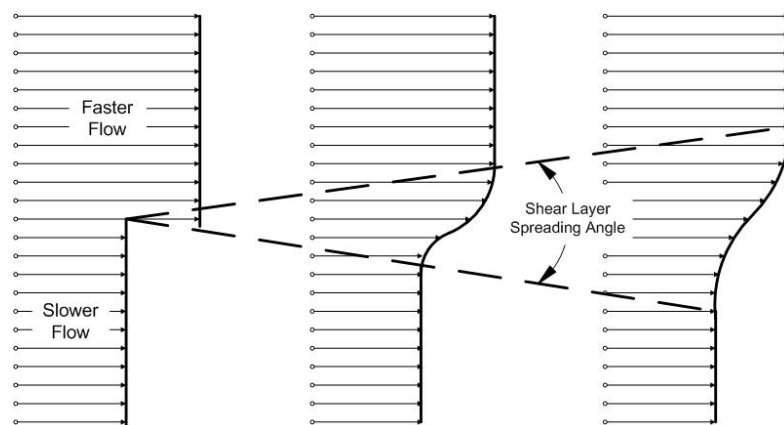


Figure 1.5. Schematic of a 2D shear layer spreading angle.

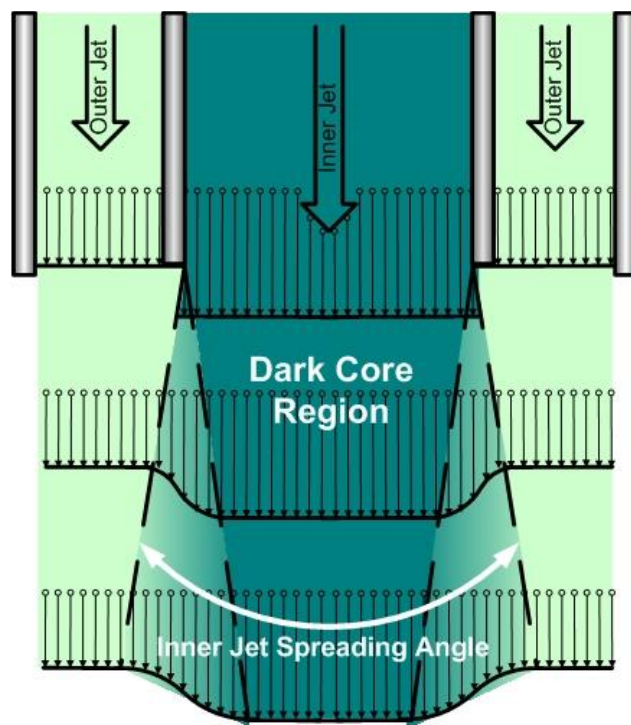


Figure 1.6. Schematic of the dark core region and the inner jet spreading angle of a shear coaxial jet.

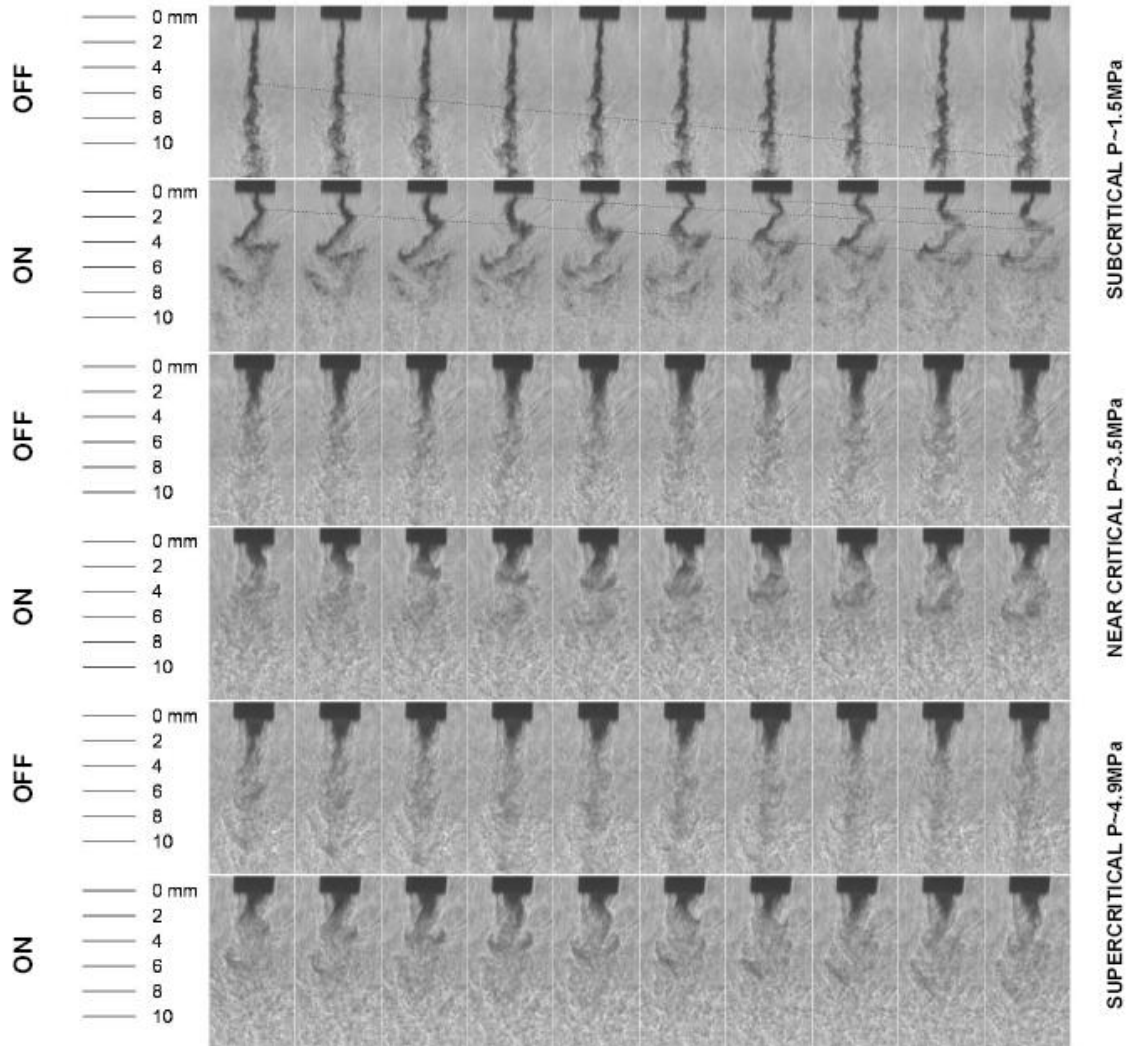


Figure 1.7. Consecutive frames from high-speed shadowgraph movies with the acoustic driver turned off (in rows 1, 3 and 5) and on (in rows 2, 4, and 6) at $\sim 3\text{kHz}$. Time increases from left to right with an interval of $55.6\ \mu\text{s}$ between frames. The first two rows are at a subcritical chamber pressure ($\sim 1.5\text{ MPa}$), the third and fourth rows are at a near-critical chamber pressure ($\sim 3.5\text{ MPa}$), and the fifth and sixth rows are at a supercritical chamber pressure ($\sim 4.9\text{ MPa}$). The light gray lines in the first and second rows connect fluid structures as they evolve in time. Images from Davis and Chehroudi (21).

○ Davis Subcritical P; High T (*)	○ Davis Nearcritical P; High T (*)	○ Davis Supercritical P; High T (*)
✱ Davis Subcritical P; Low T (*)	✱ Davis Nearcritical P; Low T (*)	✱ Eroglu et al. Re=9328
✱ Favre-Marinet DR=0.138 Air	✱ Favre-Marinet DR=0.655 Air	✱ Favre-Marinet DR=0.138 He
✱ Favre-Marinet DR=0.028 He	□ Rehab et al. D3/D1 = 1.37	■ Rehab et al. D3/D1 = 2.29
+ Au and Ko	✱ Woodward KI(aq) - N2	● Woodward KI(aq) - He
◆ Subcritical P, High T	■ Subcritical P, Low T	● Nearcritical P, High T
■ Nearcritical P, Low T	◆ Supercritical P, High T	● Nearcritical P, High T (2)

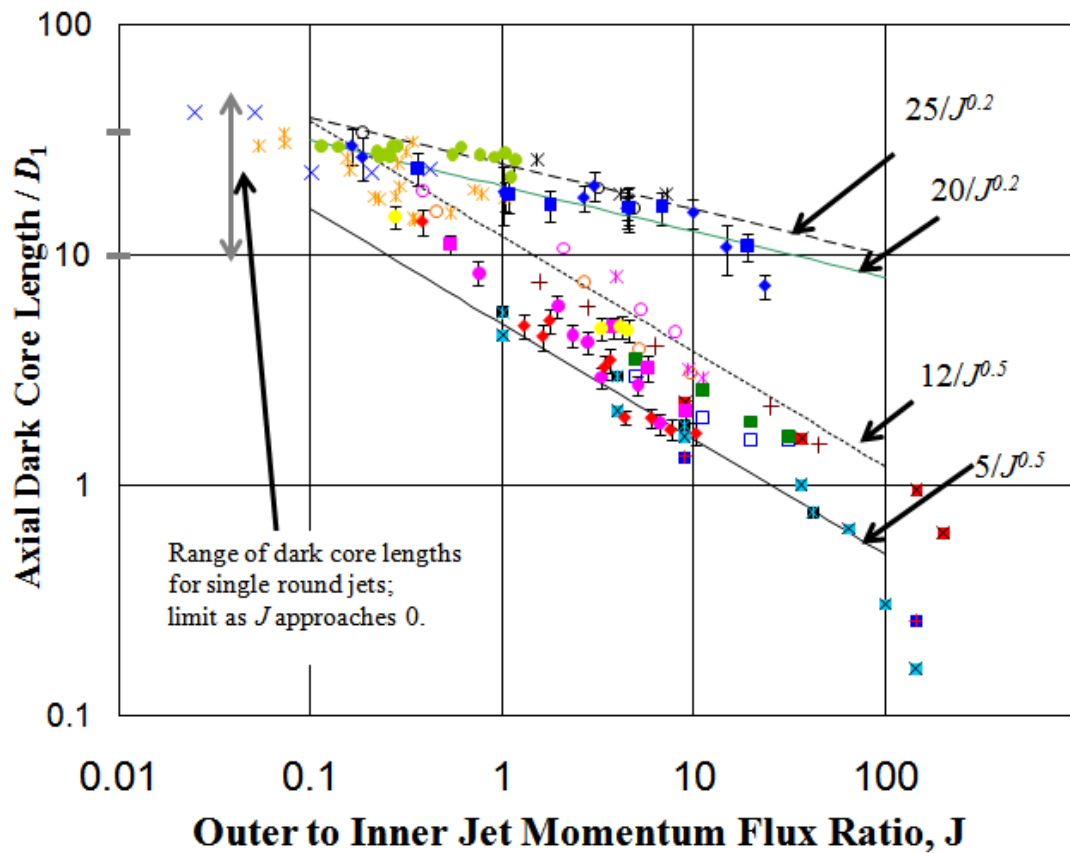


Figure 1.8. Comparison of dark-core length measurements by Davis and Chehroudi (21) and Leyva et al. (22; 23) with other data available in the literature of core-length vs. momentum flux ratio. Amongst the data reported by others, Eroglu et al. and Woodward are two-phase flows and the rest are single phase. The references for the data are found in Table 1 of Ref. (21). Figure from Leyva et al. (22; 23).

CHAPTER 2

Experimental Setup – Acoustically Coupled Fuel

Droplet Combustion

The present studies involving fuel droplet combustion were performed using the same experimental apparatus used by Dattarajan, et al. (14; 15) to analyze the behavior of methanol burning droplets under microgravity and normal gravity conditions. The current setup at UCLA was slightly modified to study the combustion behavior of various liquid alternative fuels in the presence of acoustic disturbances.

2.1 Acoustic Waveguide

In the present experiments, standing acoustic waves were generated by a loudspeaker inside a cylindrical acoustic waveguide. The frequency and amplitude were adjusted with a function generator and a signal amplifier. The continuously fed burning fuel droplet was situated at the center of the waveguide, which operated at atmospheric pressure and room temperature and featured quartz windows situated at either side of the center of the waveguide for optical access.

Figure 2.1 shows a detailed schematic diagram of the experimental device. The aluminum waveguide has an inner diameter of 11.4 cm and a maximum length of 90 cm. An 8-ohm speaker with a maximum power output of 40W and a wave reflector placed at

the opposite end, consisting of a flat aluminum disc, were used to generate the standing waves. The distance L between the speaker and the reflector was fixed using an internal movable rod assembly connected the speaker and reflector. This distance was chosen to be an integral multiple of half the acoustic wavelength, $\frac{1}{2} \lambda = \frac{1}{2} c/f$, where c is the speed of sound in the waveguide and f is the applied frequency of acoustic excitation. The standing waves produced by this configuration allowed the droplet to be exposed to conditions corresponding to either a pressure node or a pressure antinode, depending on the applied frequency f .

In order to assess the response of the burning droplet to different acoustic conditions, the speaker and reflector were moved relative to the droplet, enabling the location of the pressure node or antinode to be moved relative to the droplet as well. For the current experiments, the pressure node was estimated to be at or very close to the burning droplet by moving the fixed speaker and reflector and applying different loudspeaker excitation frequencies so that eventually the local pressure at the location of droplet within the waveguide (at the pressure transducer labeled P1 in Fig. 2.1) was a minimum and the pressure at the end of the waveguide (at P2 in Fig. 2.1) was a maximum. A pressure antinode at the location of the droplet was estimated when the local pressures measured by P1 and P2 were both local maxima.

Figure 2.2 shows a series of pressure transducer measurements in the present device made by Dattarajan et al (14; 15). Based on maxima and minima noted above, pressure nodes were found at 290 Hz and 780 Hz, and a pressure antinode was found at 540 Hz, for the fixed waveguide length of approximately 62 cm.

It is important to note that the position of the droplet at a pressure node or at a pressure antinode was actually approximate here, since the vibrating diaphragm of the speaker and the diameter of the flush-mounted pressure transducer P1, about 1.5 cm, introduced ambiguity in the exact location of the maximum or minimum pressure. Dattarajan, et al. (14; 15) attributed an observed offset between the pressure node or antinode location as estimated by pressure-transducer measurements and the “true” pressure node or antinode, based on flame orientation and the acoustic radiation force F_R (equation (1.2)), to this ambiguity. The nature and magnitude of this offset were explored in the present experiments as well.

2.2 Droplet Generation

The experimental setup featured a 0.38 mm outer diameter hollow glass capillary that was used to suspend the droplet inside the waveguide. This uncommon feature allowed continuous liquid fuel delivery to the droplet. Ethanol and methanol experiments were conducted using a nitrogen-pressurized 300 ml tank, and a filter to eliminate particulate contaminants. The fuel was then diverted to the capillary by a solenoid valve. The volumetric flow rate Q_v of the fuel delivered to the capillary could be altered by changing the duty cycle of the solenoid valve. For the JP-8/F-T blend, due to degradation of internal components of the microvalve, a syringe pump was used instead for controlled fuel delivery to the capillary.

The range of volume flow rates Q_v delivered by the syringe pump matched those used for the alcohol fuels, which were of the order of 1 mm³/s. The volumetric flow rate

Q_v and the droplet size were used to determine the burning rate constant K , as will be described below. A protective shroud was placed above the end of the glass capillary in order to prevent vaporization of the fuel within the glass capillary just above the droplet. Further details on the droplet delivery system may be found in the dissertation of Dattarajan (14).

2.3 Measurement Methods

For the experimental work of Dattarajan, et al. (14; 15), the instantaneous fuel droplet width was examined by back-lighting the droplet and imaging the magnified droplet shadow onto a linear photodiode array. This system was used during microgravity tests along with a closed loop control algorithm that used the width measurements to control fuel delivery to achieve a constant droplet size. The present experiments were only performed in normal gravity, and the droplet width measurements were only monitored and not used for control. A constant volumetric flow rate Q_v was used in each set of experiments, determined from calibration of the microvalve or direct input of the volume flow rate on the syringe pump, and from this information the droplet burning rate K could be determined.

From continuity, for a *spherical* droplet of diameter d , the instantaneous K may be evaluated according to (Dattarajan et al. (14; 15)):

$$K = \frac{4Q_v(t)}{\pi d(t)} - 2d\dot{d}. \quad (2.1)$$

Because of the non-spherical geometry of the droplet in normal gravity tests, video images of the burning droplet were used to determine the cross-sectional area of the oblong droplet. An image processing algorithm in MATLAB, incorporating specially written edge-detection software, was used to estimate the effective volume of the actual oblong droplet. This volume was then equated to that of a spherical droplet of equivalent diameter d_{eqvs} , a procedure also followed by Struk et al. (5) as well as Dattarajan et al. (14; 15) in normal gravity and microgravity droplet combustion experiments. Droplet burning rate constants based on d_{eqvs} in equation (2.1) were then determined, and average K values over time computed. Typically the transient term in equation (2.1) is not large, per the detailed investigation by Dattarajan (14), but it was nevertheless incorporated into the present measurements of K .

2.4 Experimental Procedure

To perform the experiments for droplets burning in the absence of acoustic excitation, fuel was loaded into the tank or the syringe pump, then the valve was calibrated or the syringe pump flowrate was set to the desired constant value. Then an incandescent ignitor was used to ignite the droplet and initiate quasi-steady combustion. A video cassette recorder was used to store the images that a video camera, with optical access to the burning droplet, provided. The video of the burning droplet was later processed by the previously mentioned edge-detection software to obtain an equivalent diameter d_{eqvs} over time. A curve fit for $d_{eqvs}(t)$ as described in Dattarajan (14) is then used to calculate K values according to equation (2.1), K may then be averaged over the

2-3 seconds of data acquisition. After two or three burning cases, the waveguide was purged with air to discard the products of combustion accumulated.

For acoustically excited cases, before droplet combustion commenced, the loudspeaker was turned on and the frequency was adjusted to achieve a P2/P1 maximum for an estimation of a pressure node or a P2/P1 minimum for a pressure antinode. The amplitude was adjusted to the maximum value that could be achieved without having flame extinction.

A different type of test was conceived after observing different extinction conditions for different fuels at high sound pressure levels: a flame extinction study. This study consisted of exposing a burning droplet to increasingly high amplitudes near (but not precisely at) a pressure node until the flame was instantaneously extinguished. These pressure amplitudes at extinction were recorded, and estimates of the velocity perturbation at those amplitudes and the associated strain rates could be approximated.

With the assumption that the flow in the vicinity of the burning droplet may be approximated as stagnation point flow, a rough estimate of the strain rate close to extinction may be obtained in terms of the velocity perturbation u' and the droplet standoff distance (58):

$$\varepsilon = \frac{|u'|}{2d_{standoff}}. \quad (2.2)$$

Estimates of the strain rate using the radius of a porous cylinder instead of the standoff distance have been obtained for counterflow non-premixed flame experiments (59; 60; 61). A photograph depicting $d_{standoff}$ and u' is shown in Figure 2.3. The velocity perturbation u' was obtained from measurements with the pressure transducer P1 in

Figure 2.1. The pressure transducer output in volts (V) was converted to Pascals (Pa) using calibration information from the manufacturer and then the following relation was used to obtain the velocity measurements:

$$u' = \frac{p'}{\rho c}, \quad (2.3)$$

where ρ is the density of the air surrounding the flame and c is the local speed of sound.

2.5 Uncertainty Analysis

The uncertainty analysis of the measurement of the burning rate constant K for the acoustically excited droplet experiment was carried out by Dattarajan (14). For the cases in the present study where the syringe pump was used to deliver the flow to the droplet, the overall uncertainty of the measurement was lower. When the volumetric flow rate, Q_v , was measured using a solenoid valve the precision uncertainty found by Dattarajan was 8-10% (14). However, the syringe pump has an accuracy of $\pm 1\%$. Thus a precision uncertainty of the same magnitude (1%) can be assigned to the syringe pump and a precision error of approximately 10% for the burning rate constant K is obtained instead of the original 13% found by Dattarajan (14) when using the solenoid valve to deliver the flow. In addition, the syringe pump reproducibility of $\pm 0.1\%$ should bring the flow rate bias error indicated by Dattarajan from 10% to less than 1 %.

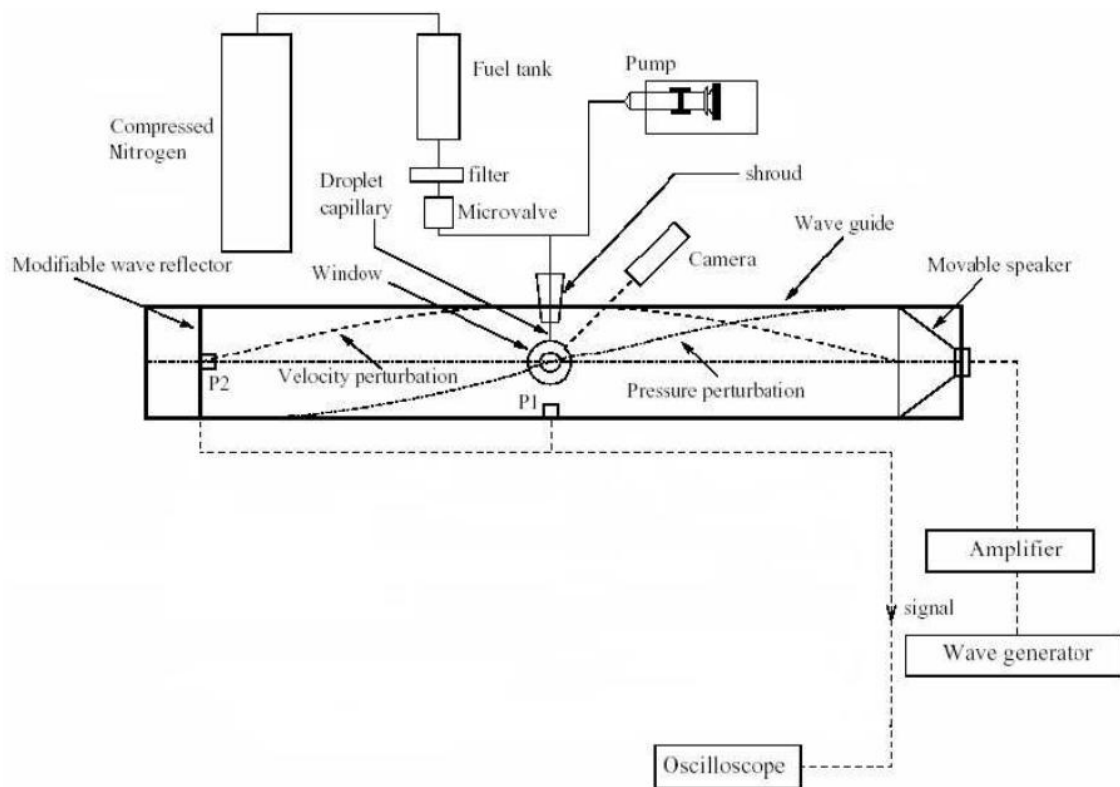


Figure 2.1. Experimental setup of the acoustic waveguide and feed droplet system. The tank and microvalve arrangement was used for the tests with methanol, while the syringe pump was used for all other fuels.

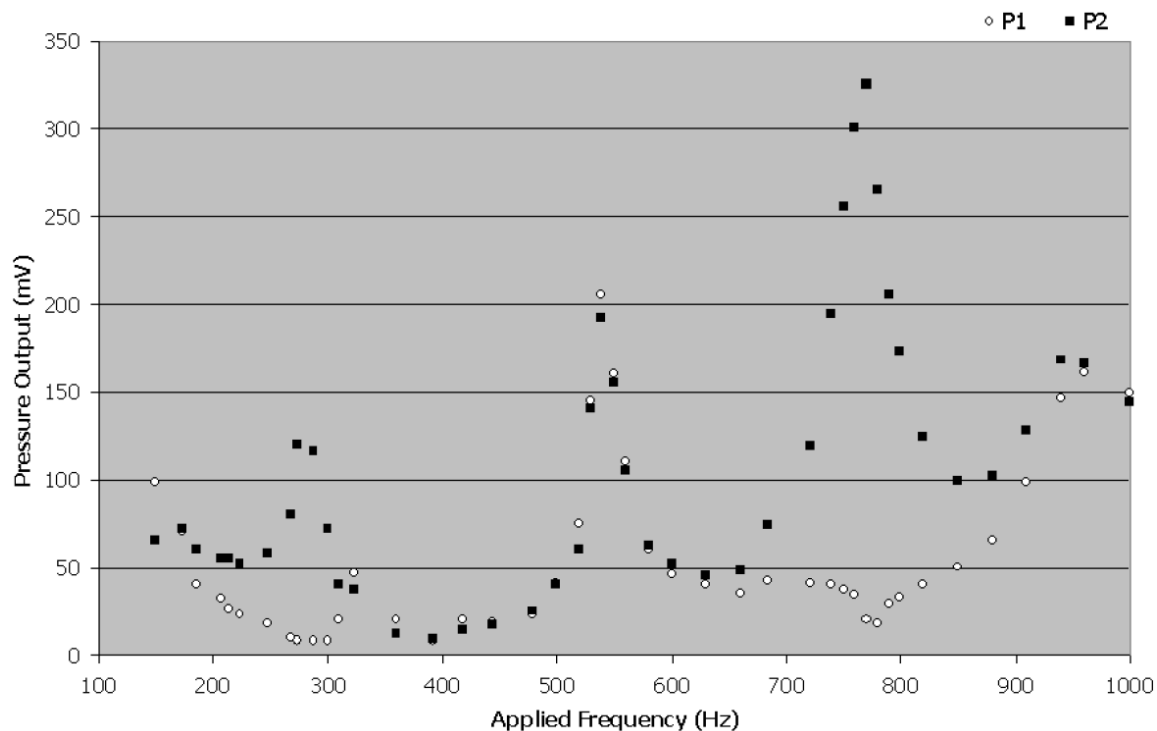


Figure 2.2. Acoustic characterization of the waveguide as measured by pressure transducers at P1 and P2. From Dattarajan (14). The distance between the speaker and reflector was 62 cm.

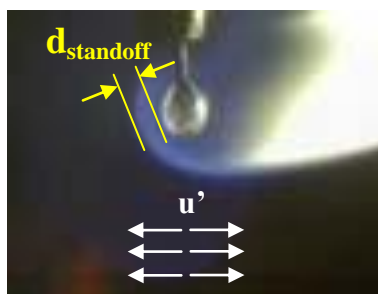


Figure 2.3. Photograph of a burning fuel droplet showing standoff distance ($d_{standoff}$) and velocity perturbation (u') used to obtain strain rate estimates of the droplet at extinction.

CHAPTER 3

Results – Acoustically Coupled Fuel Droplet Combustion

3.1 Baseline Burning Rate Constants

The initial set of experiments took place in the absence of acoustic forcing. The burning rate constants of four alternative liquid fuels, including ethanol, methanol, pure Fischer-Tropsch synthetic fuel and a 50% - 50% blend (by volume) of the F-T and JP-8 aviation fuel was obtained. Representative images of the burning droplets without the effects of acoustic excitation are shown in Figure 3.1. The oblong droplets and surrounding symmetric non-premixed flames burned in a relatively steady fashion when fuel was delivered at a constant volumetric rate. These tests were designed to quantify “baseline” droplet combustion processes for a comparison with the behavior of acoustically coupled burning droplets. K values were obtained from the equivalent diameter, d_{eqvs} , extracted using the edge-detection software and video imaging from the droplet. Instantaneous K values were found to be approximately constant over time for constant volumetric flow rates, as seen for methanol by Dattarajan et al (14; 15).

Table 3.1 shows that K values for methanol and ethanol based on d_{eqvs} were close to available data for fuel droplets burning in normal gravity. K values for the JP-8/F-T

blend were compared to available data for JP-4 fuel and found in agreement. No conclusion could be made for the pure F-T fuel since no burning rate data could be found for this synthetic fuel. Effects such as water adsorption, capillary length and distillation on methanol droplet burning rates were relatively minimal, as documented by Dattarajan (14). Adsorption was minimized in the current configuration due to continuous fuel replenishment and, according to Dattarajan (14), alterations in the capillary length between 2.0 mm and 3.2 mm did not yield significant or systematic changes in K for methanol. Thus, a capillary length of approximately 3.2 mm was used, which isolated the droplet from the shroud while at the same time prevented fuel boiling. Distillation of volatiles was observed to occur with the pure F-T fuel and the JP-8/F-T blend and was often visible within the droplets in video images; it is not likely that this affected the burning rate constant significantly, since the magnitudes of the unforced K values were in the correct range.

3.2 Burning Rate Constants under Acoustic Excitation

The effects of acoustic excitation on droplet burning rates were explored by first placing the estimated pressure node (maximum velocity perturbation) or pressure antinode (no velocity perturbation) near the droplet, by using pressure transducer measurements described previously. The distance between the speaker and reflector, 62 cm, produced pressure nodes at the waveguide center for applied frequencies of around 290 Hz and 780 Hz, and a pressure antinode at a frequency of 540 Hz. This estimates were obtained in the absence of combustion, at room temperature conditions.

As noted in Dattarajan et al. (14; 15), there was some uncertainty in the specific conditions creating a pressure node or antinode at the center of the waveguide where the burning droplet was placed. Because of the relatively large diameter of the pressure transducer P1 (1 cm) compared with the diameter of the droplet (of about 1.6 mm), and the ambiguity introduced by the precise location of the loudspeaker (i.e., with a vibrating membrane), only an approximation for the exact location of the pressure node or antinode near the center of the waveguide could be made using the pressure transducers.

Video images showing a burning droplet that was supposedly located at a pressure node or antinode according to pressure transducer readings showed flames that were actually deflected to one side or the other. According to the theory of Tanabe et al. (11; 12), per eqn. (1.2), this suggests that an actual offset of the droplet from the “true” pressure node or antinode exists. Examples of this phenomenon for all four fuels are shown in Figure 3.2, for droplets burning near the vicinity of a pressure node (determined by a maximum in P2/P1), with forcing at approximately 780 Hz. The acoustic radiation force in equation (1.2) reduces, for a standing wave, to:

$$F_R = (\rho_s - \rho_o)V \left[\mp 4\alpha \left(\frac{I}{z_a} \right) \left(\frac{2\pi f}{c} \right) \sin \left(\frac{2\pi x}{\lambda} \right) \cos \left(\frac{2\pi x}{\lambda} \right) \right]. \quad (3.1)$$

Here c is the speed of sound ($= f\lambda$), z_a the acoustic impedance ($= \rho c$), and I the acoustic intensity. An equivalent acoustic acceleration term, $g_a \equiv \alpha \frac{\partial(\overline{u'^2})}{\partial x}$, is represented by the term in square brackets. A minus sign in the bracketed term corresponds to the case of a pressure node positioned at the center of the waveguide ($x = 0$); and a plus sign corresponds to a pressure antinode at the same location. Therefore, if the droplet is

located to the right ($x > 0$) or left ($x < 0$) of the waveguide center, a finite acoustic radiation force would try to deflect the flame and hot gas zone surrounding the droplet, scaling with frequency as indicated in eqn. (3.1). The observed flame deflection in Figure 3.2 is similar to that observed by Dattarajan et al. (14; 15) for methanol droplet combustion in both microgravity and normal gravity, and is also seen by Tanabe et al. (11; 12) in their microgravity studies with n-decane droplets.

3.3 Pressure Node Location Offset

As noted above, Figure 3.2 shows the flame deflection when the speaker and reflector were placed so that the transducer readings indicated a maximum in P_2/P_1 at the waveguide center. This suggested that there was actually an offset of the burning droplet from the “true” pressure node. To assess the magnitude and the influence of the offset on fuel burning rates, the speaker and reflector were moved systematically to the right or left during these experiments, keeping L constant. Since the droplet and pressure transducer P_1 were each fixed at their original locations, by moving the speaker and reflector, the pressure node or antinode relative to the fixed droplet could be moved. In the present tests, the 780 Hz pressure node with $L \approx 0.62$ m was moved up to 7 cm to the left of the originally estimated pressure node location (slightly more than an eighth of a wavelength), and up to 8 cm to the right. These tests were also conducted for the 540 Hz pressure antinode.

A diagram of the displacements of speaker and reflector is shown in Figure 3.3, where y corresponds to the location of the pressure node (PN) relative to the position of

the droplet, and y' corresponds to the location of the droplet relative to the pressure node. The figure shows that when the speaker and reflector (S&R) were moved substantially to the right, one approaches a condition where the PN was located to the right of the droplet, or the droplet was located to the left of the PN ($y' < 0$ as in Figure 3.3b). In this case, if the droplet was positioned to the left of the PN, the sign of the acoustic radiation force in equation (3.1) would become negative, shifting the flame and hot gases away from the pressure node toward the wave reflector on the left side of the waveguide.

In contrast, when the S&R were moved substantially to the left, so that $y' > 0$ as in Figure 3.3c, the opposite would occur, causing the flame to deflect to the right, away from the PN. For the pressure antinode (PAN) case, e.g., at 540 Hz, the opposite behaviors should take place when the S&R are moved to one side or the other. The flame deflection observed during PN acoustic excitation in Figure 3.2 suggests that the conditions produced by a maximum in P_2/P_1 actually may have placed the droplet to the right of the true PN, with $y' > 0$ and the flame deformation to the right.

To assess this supposition, burning droplets of three fuels (ethanol, methanol, and the fuel blend) were exposed to situations where a pressure node or antinode would lie to either left or right of the droplet. The S&R were moved systematically to the left and to the right in relation to their original positions (e.g., as shown for the PN at 780 Hz in Figure 3.2). Images extracted from video of the burning ethanol droplet situated at different locations relative to the pressure transducer estimated pressure node, for 780 Hz forcing, are shown in Figs. 3.4a-f. These images show that as the speaker and reflector were displaced relative to the burning droplet, the direction of the flame deflection

changed its orientation. This switch occurred when the speaker and reflector were displaced between 2.4 cm (Figure 3.4c) and 4.9 cm (Figure 3.4d) to the right of their original positions, suggesting that the “true” pressure node was likely coincident with the burning droplet for conditions lying between Figs. 3.4c and 3.4d. It can be surmised that in Figs. 3.4a-c, the droplet must have been located to the right of the PN (so that y' or x in eqn. (3.1) was positive), and in Figs. 3.4d-f, the droplet probably was located to the left of the PN (so that y' or x was negative). These characteristic flame shifts were also observed during droplet combustion of methanol (e.g., shown near a PAN at 540 Hz in Figs. 3.5a-f) and for the JP-8/F-T fuel blend (e.g., shown near a PN at 785 Hz as in Figs. 3.6a-f).

While the change in orientation for the alcohols occurred in roughly the same location, when the S&R were displaced between 2.7 cm and 5.2 cm to the right of their original positions, the flame switch location for the JP-8/F-T blend occurred further to the right, when S&R were displaced between 5.1 cm and 6.4 cm in that direction. Further exploration of the phenomena by Sophonias Teshome and Hann-Shin Mao indicated that placing two speakers in the waveguide, rather than a speaker and reflector, made the acoustic field much more symmetric and the flame switch location more repeatable (62). During tests with either configuration, however, an interesting highly unstable flame oscillatory behavior was exhibited when the droplet was positioned very close to the PN. This was also observed by Dattarajan et al. (14; 15) in microgravity.

3.4 Relation between Acoustic Acceleration and Burning Rate Increase

The acoustic radiation force ideas of Tanabe et al. (11; 12) are generally consistent with results obtained in the offset studies presented in the previous section. Flame orientations were consistent with the sign predicted by equation (3.1). The approximate positions of the S&R at which flame switch occurred were quantified for all fuels and excitation conditions. The location of the “true” $x = 0$ location (for a PN or a PAN) was then set at the location of flame switch from the experiments where $x = 0$ was presumed to be coincident with the burning droplet. Once the range for x was determined in this manner, the acoustic acceleration term, g_a , was estimated from the term in square brackets in equation (3.1). Since the relative magnitude of the term α is approximate in any case for each fuel (e.g., for methanol, α is approximately 1.15, but might vary due to temperature dependence, etc.), α was set to unity in the relation for g_a .

Tanabe et al. (11; 12) as well as Dattarajan et al. (14; 15) suggest that a direct correlation between the amplitude of the acoustic radiation force F_R and the droplet burning rate K might exist. In principle, the influence of a vertical buoyancy force in normal gravity conditions could limit the influence of an acoustic radiation force acting horizontally. However, the higher amplitudes of forcing here (over 138 dB) acting perpendicularly to gravity, allowed the influence of the acoustics to have a somewhat greater impact than in previous studies. For example, prior experiments by Dattarajan et al. (14; 15) did not allow strong enough excitation at the 540 Hz PAN to be able to

produce flame distortion in normal gravity, a phenomenon that was always routinely observed at high forcing amplitudes in the present experiments. Hence, at least in terms of magnitude, the correlation between F_R or g_a and K could be studied for several alternative fuels.

Ethanol, methanol, and the JP-8/F-T fuel droplets were exposed to pressure node conditions (at approximately 780 Hz and 290 Hz) and pressure antinode conditions (at approximately 540 Hz). Average burning rate constants based on time averages over a 2-second period were obtained for a range of different droplet positions relative to the waveguide center. Measured average K and d_{eqvs} values for different positions of the speaker and reflector (measured relative to their original position as determined by the magnitude of P2/P1), are plotted in Figure 3.7 for ethanol at the 780 Hz PN, in Figure 3.8 for methanol at the 540 Hz PAN, in Figure 3.9 for the JP-8/F-T blend at a 785 Hz PN, in Figure 3.10 for ethanol at the 540 Hz PAN, in Figure 3.11 for ethanol at the 290 Hz PN, and in Figure 3.12 for ethanol at the 800 Hz PN. The first three figures correspond to the flame photos shown in Figs. 3.4, 3.5 and 3.6, respectively. A value of acoustic acceleration g_a equalling zero is assumed at the position of the S&R where the flame switch occurred, corresponding to the “true” node location at $x = 0$ in equation (3.1). The solid lines on the K plots represent a curve fit of the experimental data. The solid lines on the g_a plots represent the theoretical dependence of the absolute value of g_a on x , assuming an average value of the acoustic intensity I . In reality, however, the sound pressure level and hence I were slightly different for the different conditions explored, and the data points on the plots for g_a represent the more accurately determined values

based on the local I values. In addition to the previous results, data for one pure F-T fuel test is also included in Figure 3.9. For this test, the S&R were located at the pressure transducer estimated pressure node at 785 Hz. A droplet image of this test is shown in Figure 3.2d.

In theory, droplets burning near the “true” pressure node or pressure antinode should have the same burning rate constant K as for the unforced burning droplet. This is due to a zero acoustic radiation force F_R or acoustic acceleration g_a (see equation (3.1)) at the node location. Most of the present results, when compared with unforced values in Table 3.1, suggest that this proposition holds; however, in some cases, such as methanol at the 540 Hz PAN, a reduction in the burning rate constant might be taking place. On the other hand, when the droplet was placed away from the “true” PN or PAN, a general trend of increasing burning rates was observed. The increases were at most about 20% for the alcohol fuels (see Figure 3.10) and the JP-8/F-T blend, and in recent studies, up to 28% for the pure F-T fuel (see Figure 3.9). Although the K value of the pure F-T fuel is not necessarily greater than the K value of the JP-8/F-T blend in the figure, the increase over the unforced value is higher for the pure F-T fuel given its lower unforced burning rate constant value compared to that of the JP-8/F-T fuel (see Table 3.1).

An exception to the previous trends is found at low frequencies, such as ethanol at the 290 Hz PN (see Figure 3.11). There is little discernible trend in the burning rate constant as the location of the speaker and reflector is changed, or actually, one that is somewhat the opposite to the trend in g_a . This behavior could be explained by the low acoustic radiation forces acting on the hot combustion products around the droplet. Since

the acoustic acceleration depends on the frequency applied, its maximum value for this case ($\sim 1.3 \text{ m/s}^2$) is very low compared to the 540 Hz ($\sim 4 \text{ m/s}^2$) and 780 Hz ($\sim 5 \text{ m/s}^2$) cases.

The general consistency between the experimental increases in burning rate constant K and the theoretical increases in acoustic acceleration for $g_a \geq 4 \text{ m/s}^2$ is important and seems to confirm the suppositions of Tanabe et al. (11; 12) and Dattarajan et al. (14; 15) about the relation between K and F_R . Even more significant is the fact that increases were observed for both pressure node and antinode forcing conditions. One important experimental observation is the fact that, as flame deflection increased, the flame front got closer to the droplet. A closer flame front enhances the rate of release or vaporization of reactants due to increased heat transfer between the flame and the droplet. This mechanism could be directly related to the observed increases in K at the conditions mentioned above. This could also explain the lack of a trend in K for the low frequency experiments with ethanol at the 290 Hz, since little or no deflection of the flame was observed in this case.

To our knowledge, investigation of acoustic forcing effects on a burning fuel droplet near a pressure antinode has not been explored to any significant degree in the past and it might provide information on whether enhancement of condensed phase fuel consumption at a pressure antinode could promote or suppress flow instabilities. The similarities in combustion properties for the alcohol fuels and the F-T fuels were remarkable, given their differences in reaction and diffusion time scales.

3.5 Fuel Extinction Studies

In further investigations, fuel droplets were exposed to excitation when situated at a fixed location with respect to a pressure node at 780 Hz. The location was selected so that the theoretical acoustic acceleration was above 2 m/s^2 . Then the droplet was ignited and, after it reached quasi-steady burning conditions, it was exposed to a standing wave of increasing acoustic intensity. The forcing amplitudes at which extinction (flame burnout) was observed were recorded. Photographs of the extinguishing flames for various fuels are shown in Figs. 3.13-3.16. In some cases the flames extinguished near the stagnation region of the droplet but persisted in the wake of the droplet before complete burnout. It was found that the perturbation amplitudes at extinction for the F-T fuel (see Figure 3.13), the JP-8/F-T blend (see Figure 3.14), and ethanol (see Figure 3.15) all corresponded to sound pressure levels close to 141 dB, and velocity perturbations of approximately 0.75 m/s. However, for methanol, the corresponding sound pressure level at extinction was 143 dB, for a velocity perturbation of approximately 1.0 m/s (see Figure 3.16).

Estimated values for the equivalent local strain rate in the vicinity of the droplet were calculated using a rough approximation of the definition for the strain rate as the radial velocity gradient at the flame position by Im and Chen (63). The radial velocity gradient was approximated using equation (2.2) where the velocity perturbation u' is divided by a characteristic length of the flow, in this case twice the flame standoff

distance $2d_{standoff}$, or twice the distance from the flame sheet to the surface of the droplet (see Figure 2.3).

Table 3.2 shows the corresponding velocity perturbations and estimated strain rates for each fuel at extinction. Interestingly, the extinction strain rate associated with methanol and ethanol were higher than the F-T fuel and the JP-8/F-T blend. While these results are only preliminary, requiring further exploration in the new symmetric waveguide configuration utilized by Sophonias Teshome, the extinction strain rates were found to be comparable to those measured in opposed-flow diffusion flame configurations.

Table 3.1. Comparison of measured values of burning rate constant K for various fuel droplets, with combustion in the absence of acoustic excitation. Comparison with available established values is also given. †From Smith and Graves (64) and Vielle et al. (65). ‡From Kumagai and Isoda (66), Godsave (67), Wood and Wise (68), Rosser and Peskin (69). §From Wood and Wise (68).

Fuel	K , present (mm^2/s)	K , established (mm^2/s)
Methanol	0.85 - 0.95	0.86, 0.95 [†]
Ethanol	0.85 - 1.1	0.75 - 0.96 [‡]
JP-8	0.96 - 1.0	0.87, 1.04 (JP-4) [§]
JP-8/F-T	0.78 - 0.90	-
Pure F-T	0.80	-

Table 3.2. Acoustic conditions of various fuels at extinction. The corresponding sound pressure level in decibels (dB), pressure perturbation in Pascals (Pa), and velocity perturbation in meters per second (m/s) is given. A rough estimate of the strain rate is also shown.

Fuel	SPL (dB)	Amplitude (Pa)	Δv (m/s)	ϵ (s^{-1})
Pure F-T	140.4	210	0.73	$3.7 \cdot 10^2$
JP-8/F-T	140.9	222	0.77	$3.7 \cdot 10^2$
Ethanol	141.1	228	0.79	$4 \cdot 10^2$
Methanol	142.9	280	0.98	$4 \cdot 10^2$

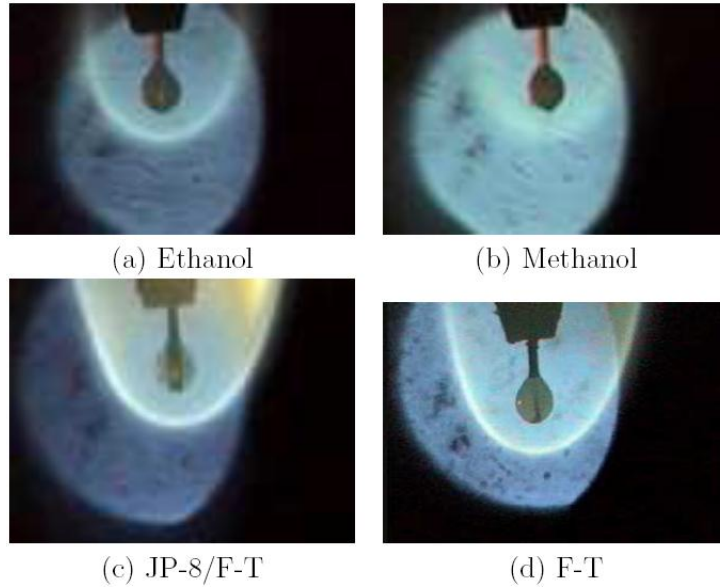


Figure 3.1. Photographs of fuel droplets burning in the absence of acoustic excitation. Backlighting accounts for the light portion of the background observed outside of the flame.

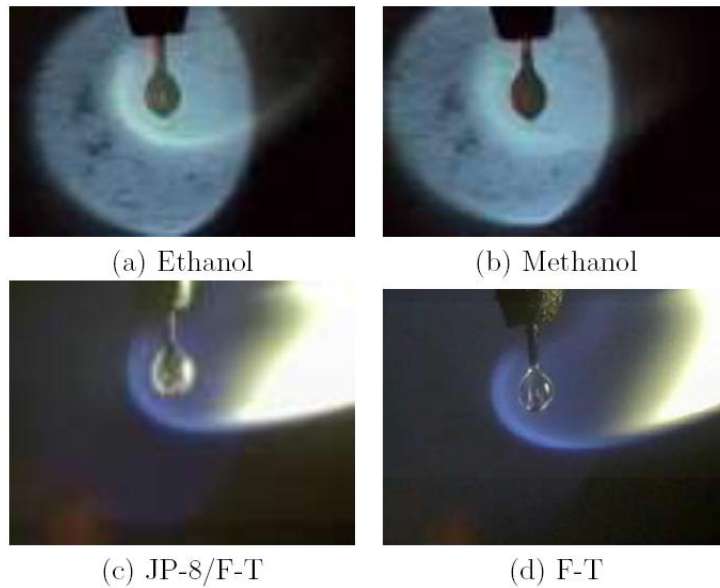
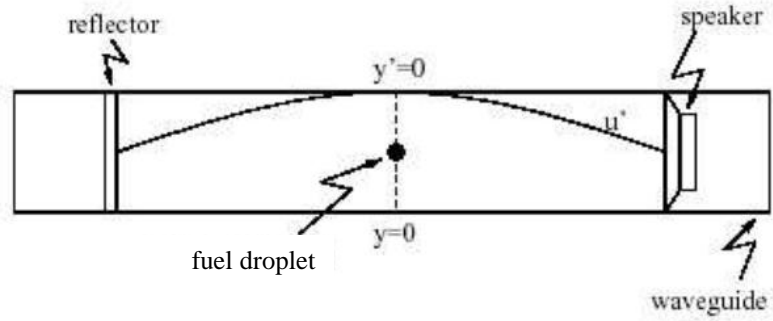
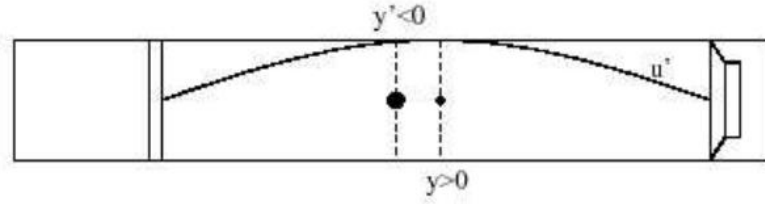


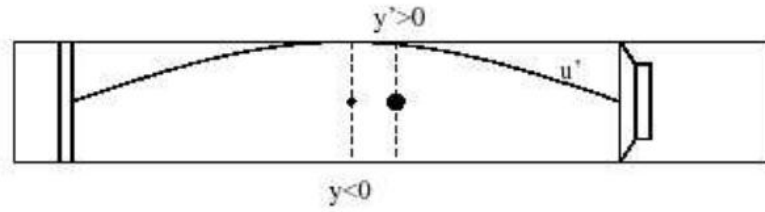
Figure 3.2. Photographs of various fuel droplets burning during acoustic excitation, situated at or near the waveguide center for the “original” locations of the speaker and reflector, based on a measured maximum in P2/P1. Acoustic excitation corresponded to 780 Hz with an amplitude of 138.6 dB for ethanol, the pure F-T, and the JP-8/F-T fuel blend, and 140.2 dB for methanol.



(a)



(b)



(c)

Figure 3.3. Location of the pressure node relative to the droplet (y) and the droplet relative to the pressure node (y'), based on positioning of the speaker and reflector (S&R). (a) $y = 0$ and $y' = 0$, (b) $y > 0$ and $y' < 0$, where S&R move to the right, and (c) $y < 0$ and $y' > 0$, where S&R move to the left. From Dattarajan (14).

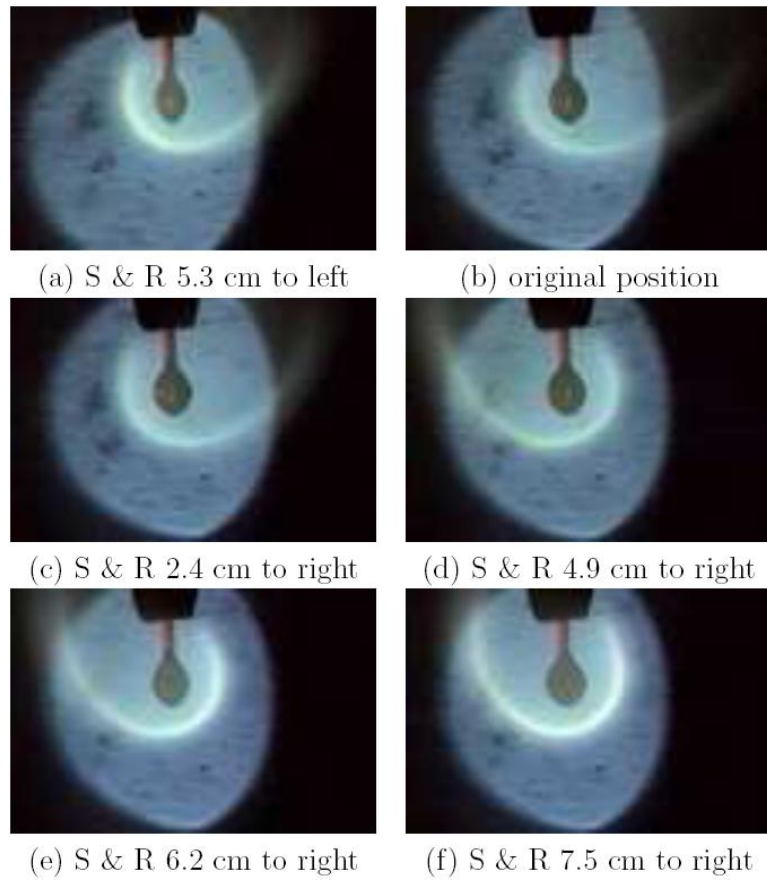


Figure 3.4. Photographs of a burning ethanol droplet with acoustic excitation at 780 Hz (PN) and 138.6 dB. The distances to which the speaker and reflector (S&R) have been moved, relative to their original locations, are indicated.

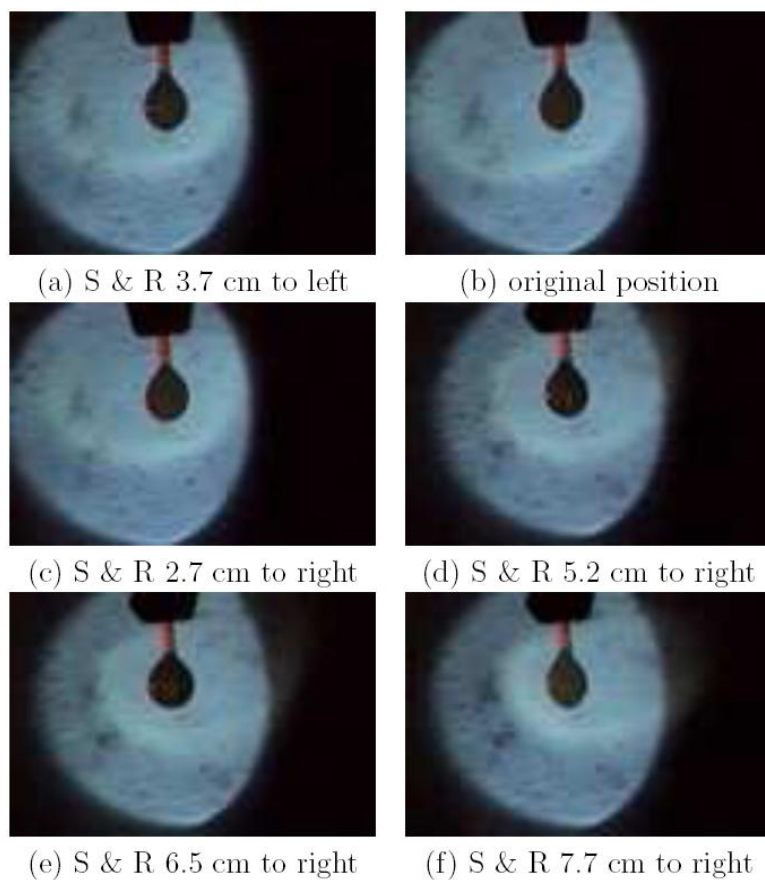


Figure 3.5. Photographs of a burning methanol droplet with acoustic excitation at 540 Hz (PAN) and 139.9 dB. The distances to which the speaker and reflector (S&R) have been moved, relative to their original locations, are indicated.

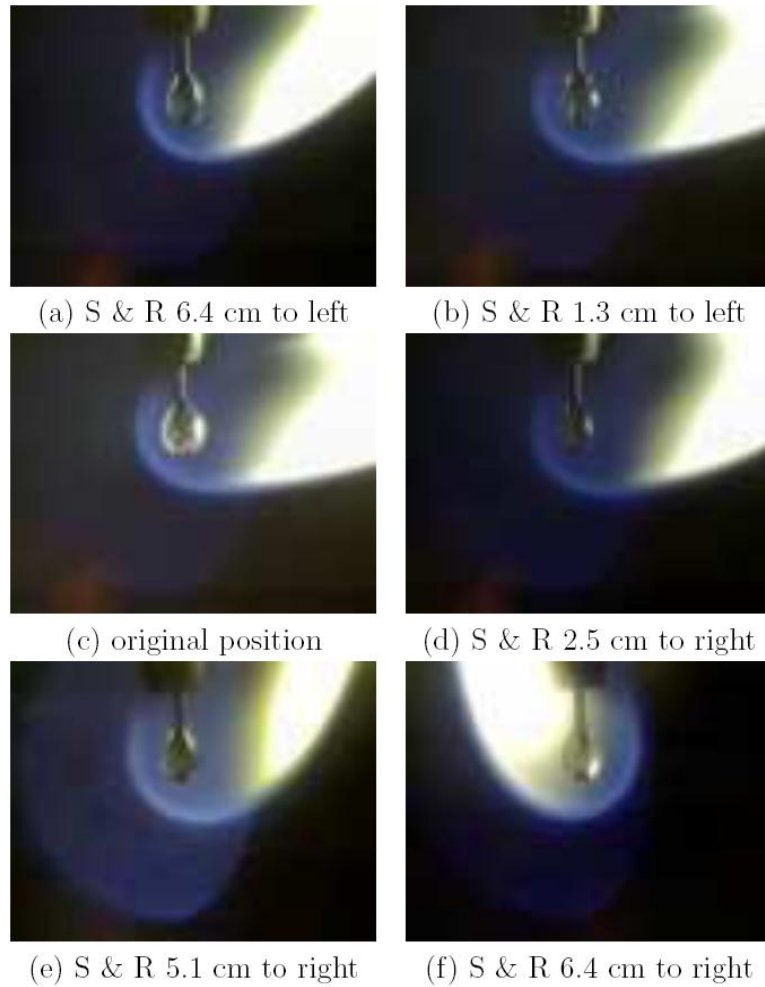


Figure 3.6. Photographs of a burning JP-8/FT fuel droplet with acoustic excitation at 785 Hz (PN) and 138.6 dB. The distances to which the speaker and reflector (S&R) have been moved, relative to their original locations, are indicated.

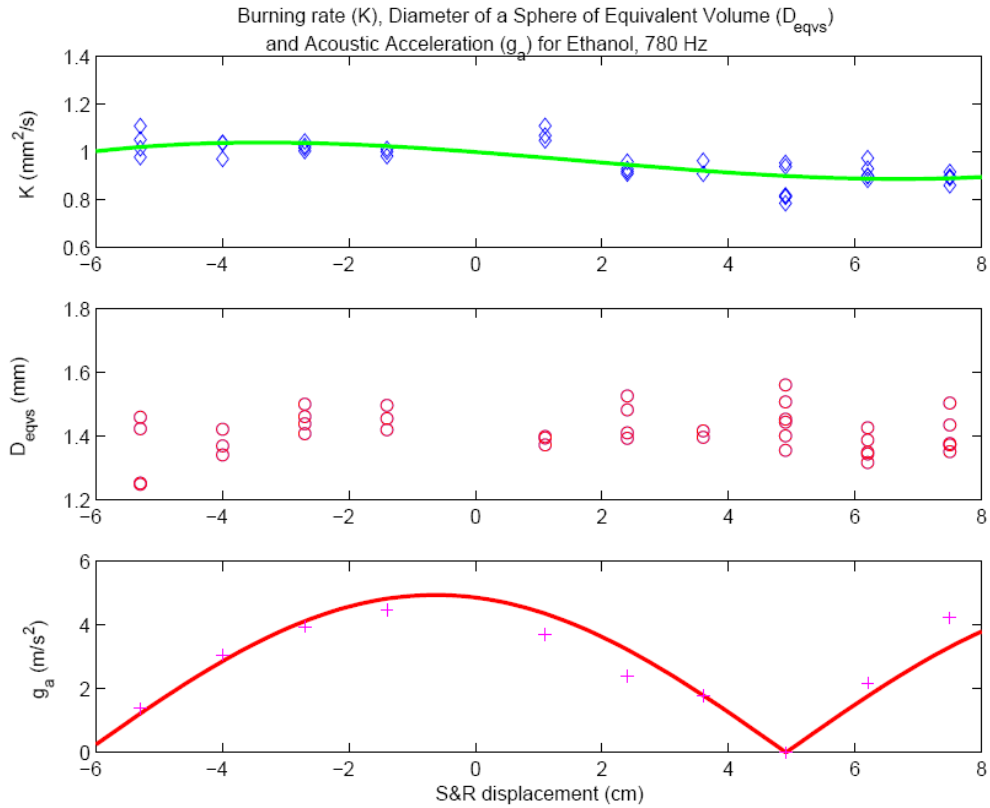


Figure 3.7. For ethanol, measured values of K and d_{eqvs} , and estimated absolute value of g_a as a function of the displacement of the speaker and reflector relative to their original positions, for a 780 Hz PN. The solid line on the K plot represents a fit of the experimental data points, while the solid line on the g_a plot represents the theoretical variation in g_a assuming an average SPL of 138.6 dB. The data points for g_a represent absolute values estimated from the locally measured SPL value.

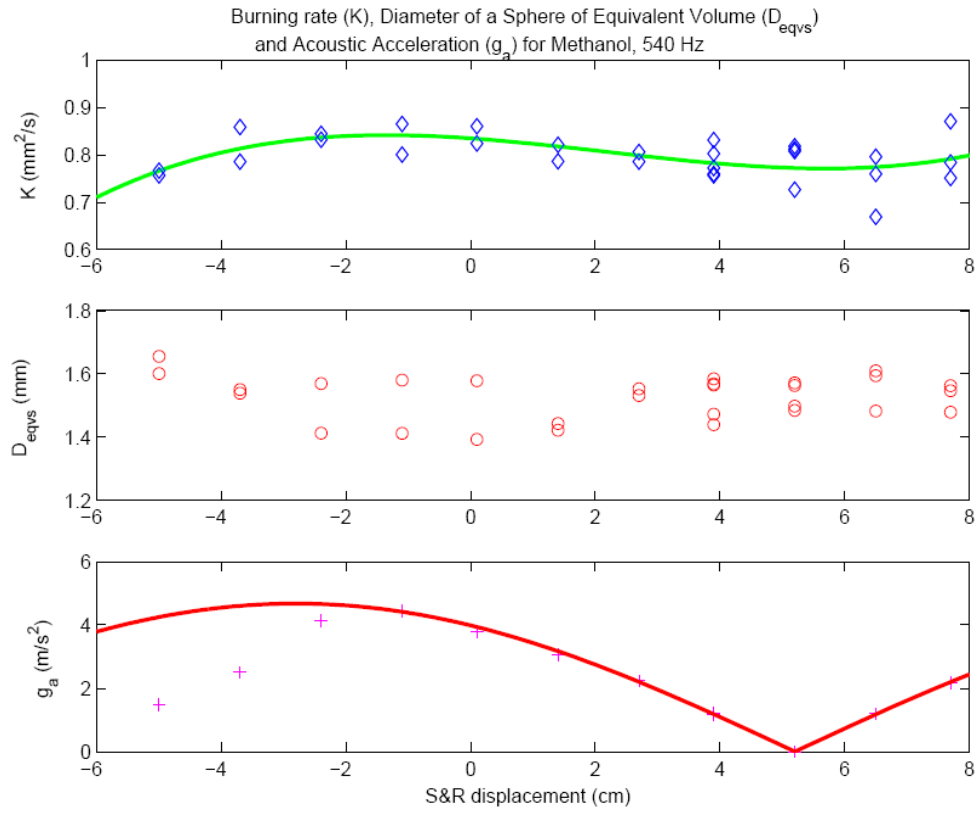


Figure 3.8. For methanol, measured values of K and d_{eqvs} , and estimated absolute value of g_a as a function of the displacement of the speaker and reflector relative to their original positions, for a 540 Hz PAN. The solid line on the K plot represents a fit of the experimental data points, while the solid line on the g_a plot represents the theoretical variation in g_a assuming an average SPL of 139.9 dB. The data points for g_a represent absolute values estimated from the locally measured SPL value.

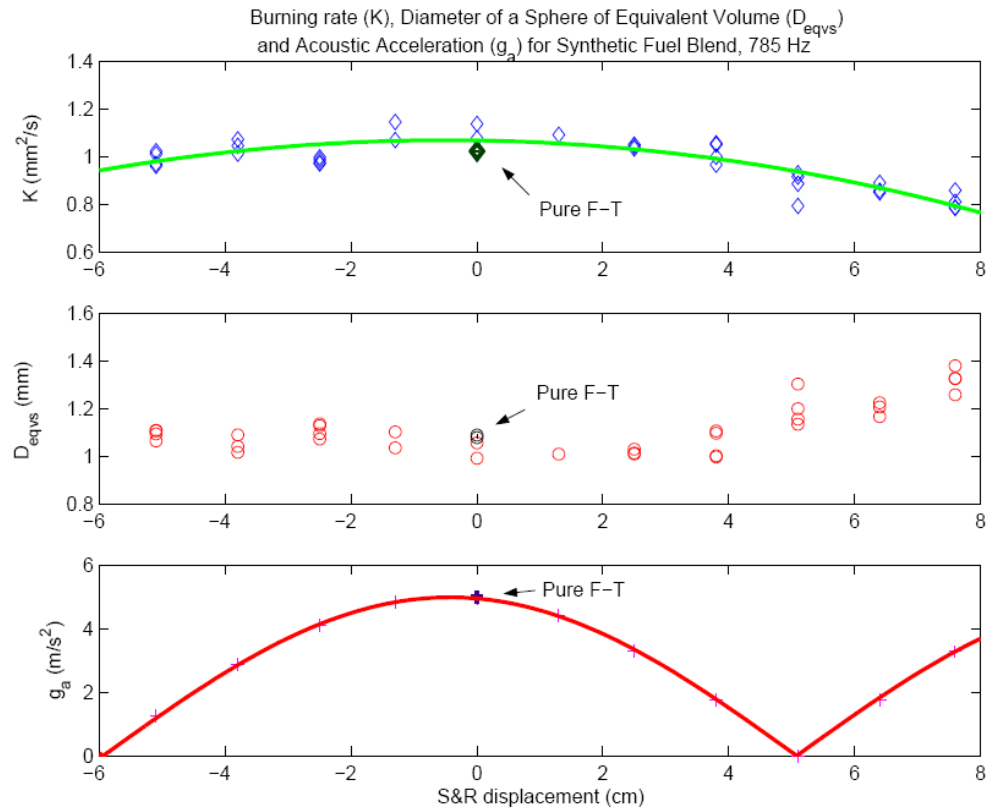


Figure 3.9. For JP-8/F-T fuel, measured values of K and d_{eqvs} , and estimated absolute value of g_a as a function of the displacement of the speaker and reflector relative to their original positions, for a 785 Hz PN. The solid line on the K plot represents a fit of the experimental data points, while the solid line on the g_a plot represents the theoretical variation in g_a assuming an average SPL of 138.6 dB. The data points for g_a represent absolute values estimated from the locally measured SPL value.

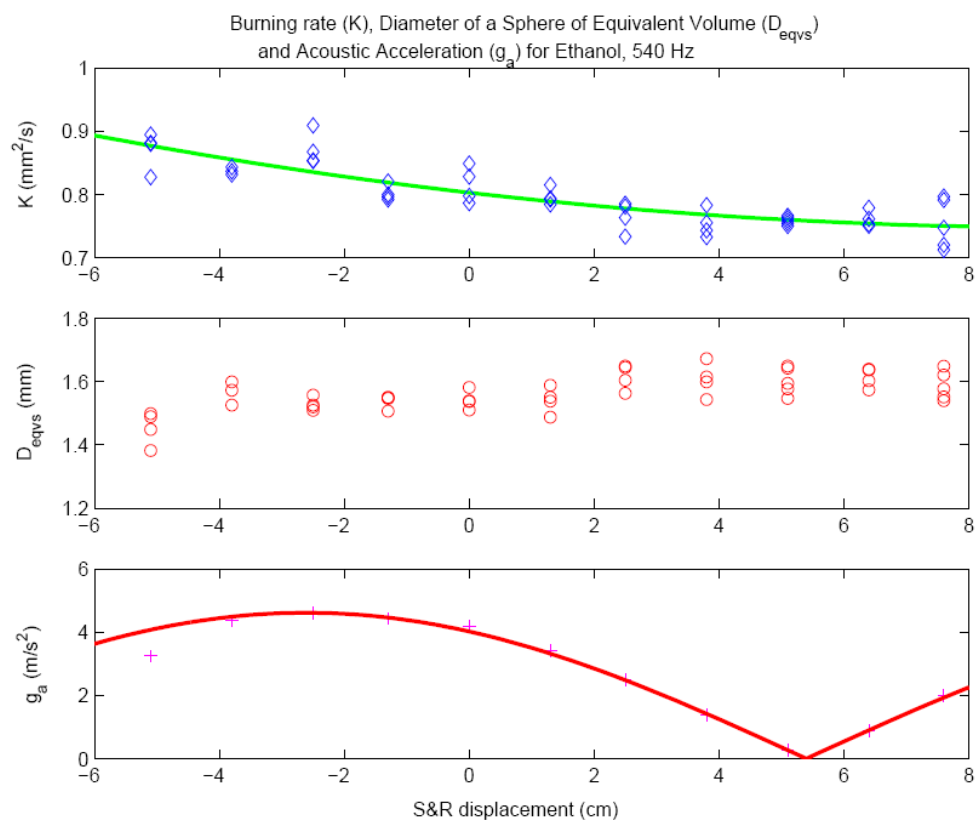


Figure 3.10. For ethanol, measured values of K and d_{eqvs} , and estimated absolute value of g_a as a function of the displacement of the speaker and reflector relative to their original positions, for a 540 Hz PAN. The solid line on the K plot represents a fit of the experimental data points, while the solid line on the g_a plot represents the theoretical variation in g_a assuming an average SPL of 138.8 dB. The data points for g_a represent absolute values estimated from the locally measured SPL value.

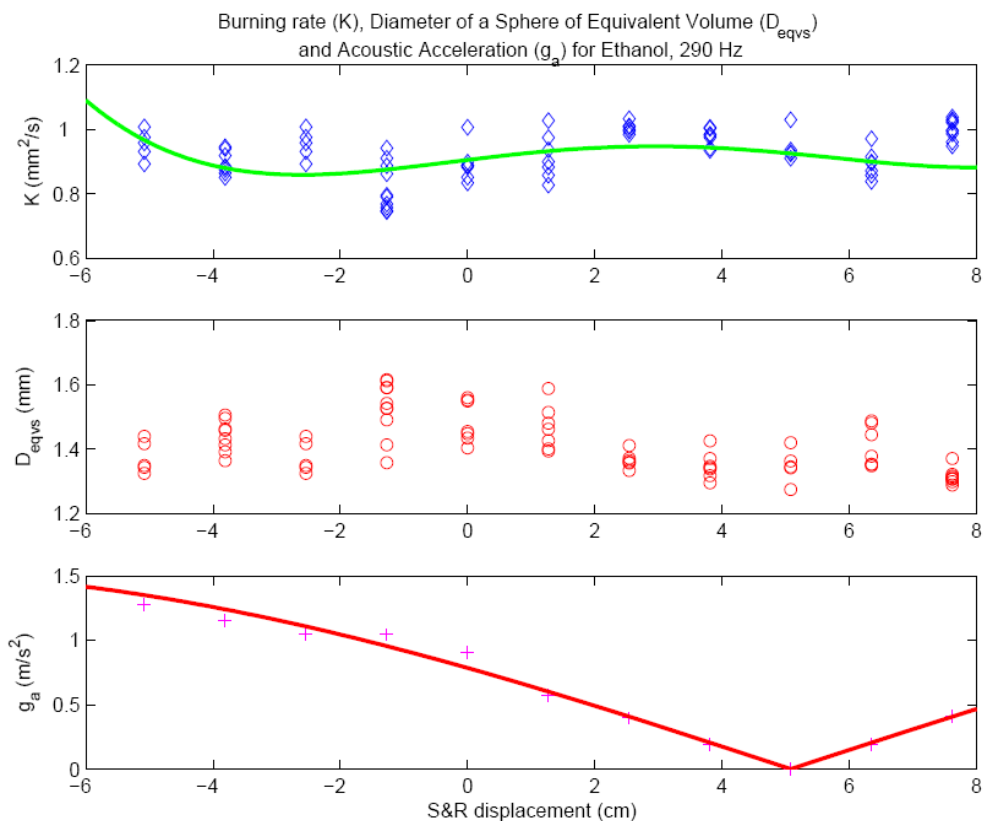


Figure 3.11. For ethanol, measured values of K and d_{eqvs} , and estimated absolute value of g_a as a function of the displacement of the speaker and reflector relative to their original positions, for a 290 Hz PN. The solid line on the K plot represents a fit of the experimental data points, while the solid line on the g_a plot represents the theoretical variation in g_a assuming an average SPL of 137.8 dB. The data points for g_a represent absolute values estimated from the locally measured SPL value.

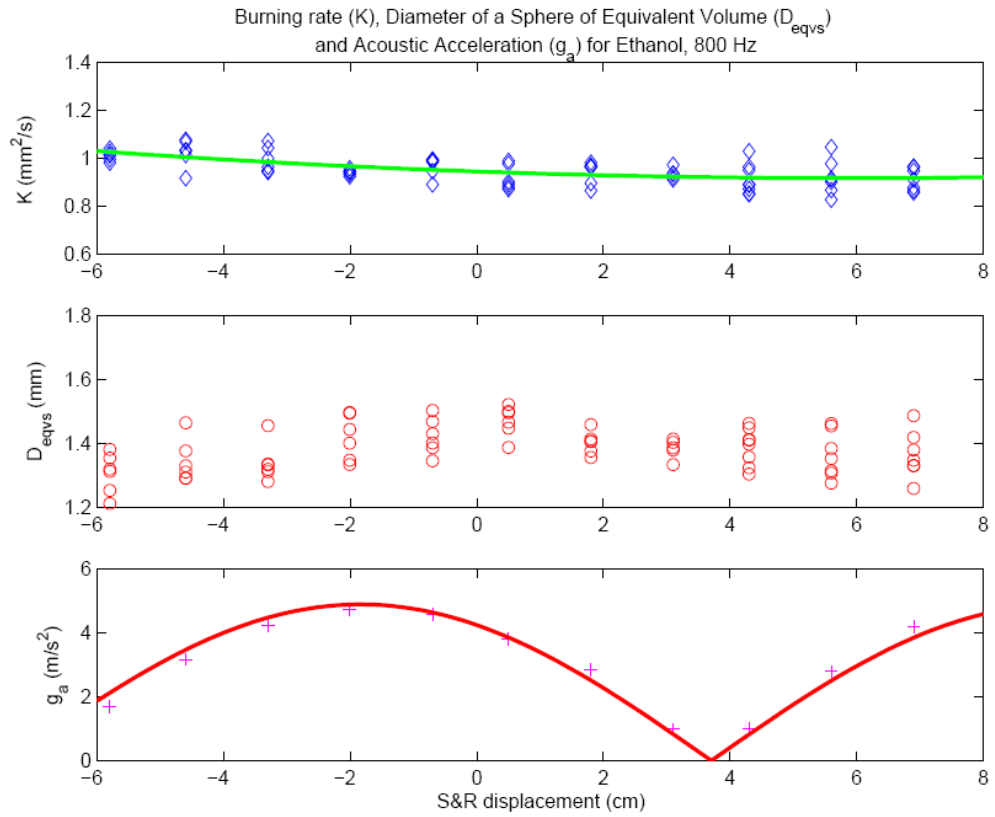


Figure 3.12. For ethanol, measured values of K and d_{eqvs} , and estimated absolute value of g_a as a function of the displacement of the speaker and reflector relative to their original positions, for a 800 Hz PN. The solid line on the K plot represents a fit of the experimental data points, while the solid line on the g_a plot represents the theoretical variation in g_a assuming an average SPL of 138.5 dB. The data points for g_a represent absolute values estimated from the locally measured SPL value.

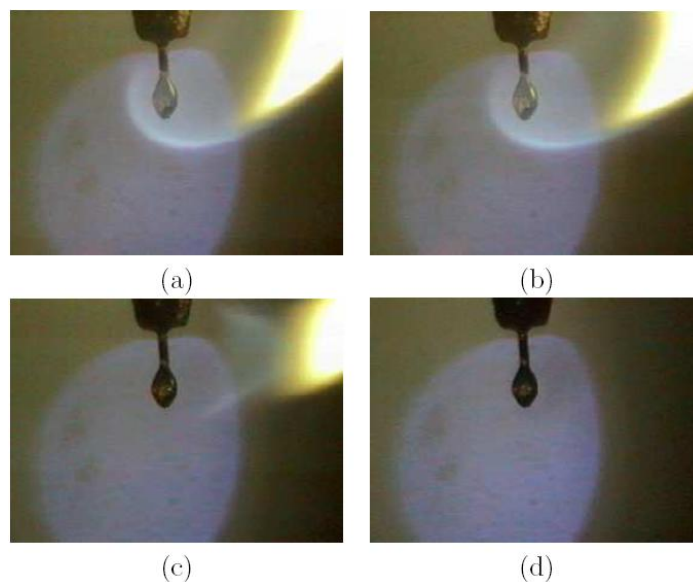


Figure 3.13. Consecutive photographs showing the extinction process of a pure F-T fuel droplet. Images (a) and (b) show the flame before extinction, image (c) shows a “wake” flame and image (d) shows a flameless droplet. The time interval between images is 33.37 ms, with forcing at 141.1 dB or a perturbation pressure of 228 Pa, and maximum velocity perturbation of 0.79 m/s.

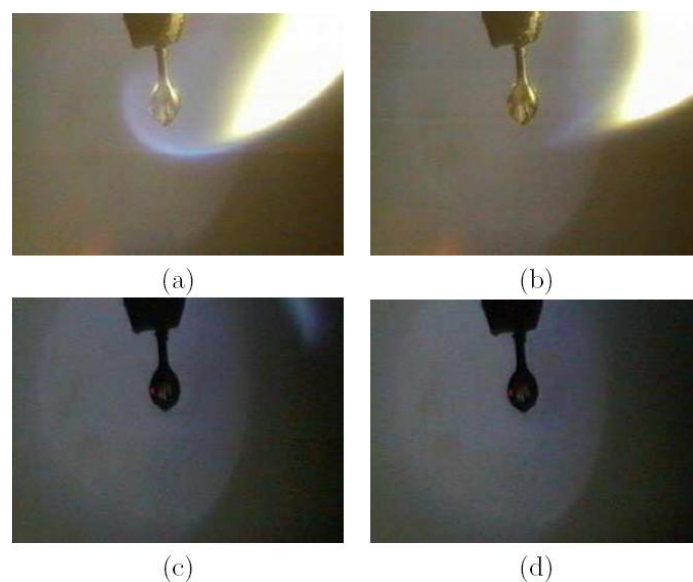


Figure 3.14. Consecutive photographs showing the extinction process of a JP-8/F-T fuel droplet. Images (a) and (b) show the flame before extinction, image (c) shows a “wake” flame and image (d) shows a flameless droplet. The time interval between images is 33.37 ms, with forcing at 141.3 dB or a perturbation pressure of 233 Pa, and maximum velocity perturbation of 0.82 m/s.

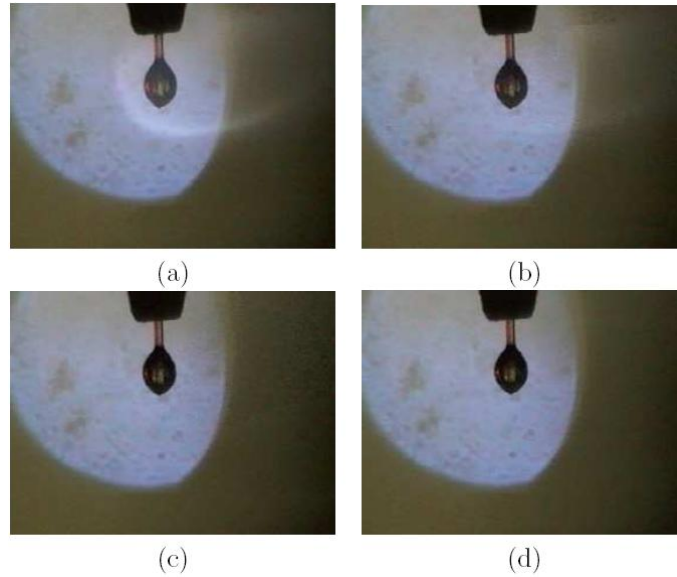


Figure 3.15. Consecutive photographs showing the extinction process of an ethanol droplet. Images (a) and (b) show the flame before extinction, images (c) and (d) show a flameless droplet. The time interval between images is 33.37 ms, with forcing at 142.2 dB or a perturbation pressure of 257 Pa, and maximum velocity perturbation of 0.90 m/s.

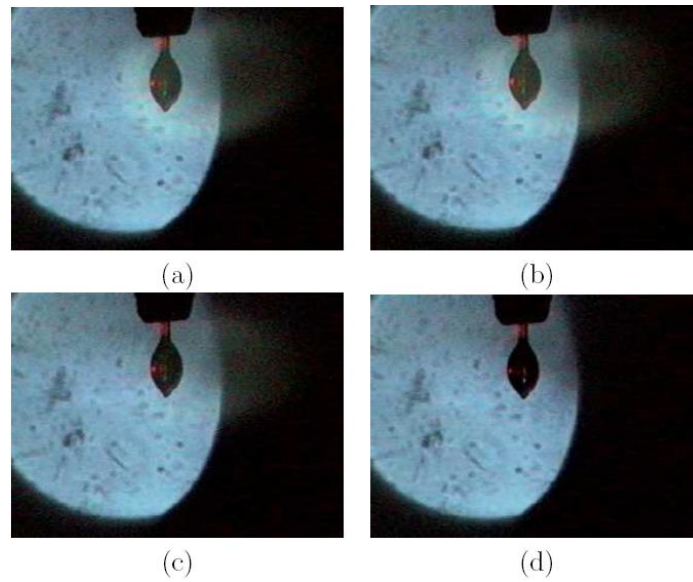


Figure 3.16. Consecutive photographs showing the extinction process of a methanol droplet. Images (a) and (b) show the flame before extinction, image (c) shows a “wake” flame and image (d) shows a flameless droplet. The time interval between images is 33.37 ms, with forcing at 143.3 dB or a perturbation pressure of 292 Pa, and maximum velocity perturbation of 1.0 m/s.

CHAPTER 4

Experimental Setup – Acoustically Excited Coaxial Jet

4.1 Cryogenic Supercritical Chamber and Coaxial Jet Facility

The experimental studies of the acoustically excited coaxial jet were performed at the Air Force Research Laboratory (AFRL) located at Edwards Air Force Base, CA. The Cryogenic Supercritical Laboratory (EC 4) was used to run all the tests. A photograph of the facility is shown in Figure 4.1 and a schematic of the experiment is shown in Figure 4.2. The photograph shows the test chamber in the center and the acoustic drivers on each side. Specific features of the facility such as the inner chamber, which is a smaller chamber within the main test chamber, the coaxial jet injector, and the pressure transducer and thermocouple probe used to obtain measurements very near the exit of the coaxial jet will be discussed in detail below.

The photograph in Figure 4.1 is intended as a visual aid to provide a perspective of the actual facility and the main components of the experimental setup. The chamber flow is exhausted through a vent line located at the center bottom of the chamber. Other diagnostic equipment also is introduced to the chamber from the center bottom. Above the chamber there is a thick insulation that houses the inner jet heat exchanger which cools the nitrogen inner jet as much as possible before it enters the chamber. On top of

the chamber, to the sides of the insulation, there are orifices that allow more probes, such as thermocouples and pressure transducers, to reach inside the test chamber. On the back, towards the right side of the photograph, part of the control panel can be observed, where valves, flow meters and pressure regulators were used to monitor and distribute the right amount of flow to the experimental setup.

The schematic in Figure 4.2 shows how the different flow lines interact with each other in order to produce an inner jet and an outer jet that satisfied testing requirements. The chamber section of the schematic represents the most updated version of the experimental setup. It shows the three differential pressure transducers that were used to measure the pressure fluctuations in three equally spaced locations with one placed just above the location of the coaxial injector exit and the other two to its sides. It also shows the pressure transducer and thermocouple that were brought from the bottom of the chamber to the injector exit inside the inner chamber. The schematic also shows that both the inner jet and outer jet have a pressure transducer and a thermocouple at the coaxial injector location.

The ability to measure the pressure and the temperature of the inner jet and the outer jet just as they enter their corresponding coaxial channel within the injector was only possible with the newly designed coaxial injector (described in section 4.2), since only the new injector featured ports through which pressure transducers and thermocouples could be introduced. This upgrade allowed a better understanding of the effects of acoustics on the flow upstream the injector and how fast the temperature of the inner and outer jets could change as they flow across the injector.

Also shown in the schematic in Figure 4.2 are heat exchangers that allowed the cooling of the inner and outer flows, and the window purge flow that was used to prevent water vapor condensation on the test chamber windows so as to allow proper visualization of the coaxial jet flow. Several thermocouples were used across the heat exchanger and in other locations to keep track of the conditions of the flow in order to maintain the required flow properties for each test.

The flow process started with a high pressure and a low pressure gaseous N_2 supply, ended with a carefully regulated coaxial jet flow inside the test chamber, and consisted of several steps. First, gaseous N_2 was used to supply the inner and outer flows of the coaxial jet and to pressurize the chamber. Then the outer jet was cooled by either one or two heat exchangers (HEs), depending on the test requirements. A third HE was used to decrease the temperature of the inner jet. The coolant that ran through the HEs for both the inner and outer jets consisted of liquid N_2 obtained from a cryogenic pressure vessel located outside EC 4, which had a capacity of 5 m^3 . The temperatures of the two jets were controlled by adjusting the flow rate of liquid N_2 through the HE's. The mass flow rates through the inner and outer jets were measured before they were cooled with Porter mass flow meters (models 122 and 123-DKASVDAA), since it was less cumbersome to measure mass flow rates at ambient temperature than to measure them at cryogenic conditions.

Once the desired mass flow rates for the inner and outer jet were achieved, the mean chamber pressure required for the experiment was adjusted. The chamber pressure was measured with a Stellar 1500 transducer. After the mean chamber pressure was

obtained, the mass flow rates were adjusted for minor changes due to the pressure increase. Finally, the liquid N₂ flow through the HEs was carefully controlled to stabilize the inner and outer jet temperatures to produce the desired outer to inner jet momentum flux ratio for that particular test. For a complete description of the operating procedures of the facility used to perform these studies, refer to Appendix B. To see a summary of the operating conditions achieved for all cases reported in this study, refer to Table C.1 and Table C.5 in Appendix C.

In order to maximize the effect of the available acoustic energy on the jet, an inner chamber was created into which the jet is injected. A photograph of the inner chamber while running a trial test is shown in Figure 4.3. This inner chamber had a nominal height of 6.6 cm, a width of 7.6 cm and a depth of 1.3 cm. The photograph in Figure 4.3 shows a gray object that surrounds the outside of the test chamber. It is foam insulation that was placed between the outside of the test chamber and an acrylic window in order to provide an enclosed space through which gaseous nitrogen at low pressures (10 to 15 kPa) could flow in a continuous fashion, removing all air inside it. The square shape insulation was hollowed at the center to allow visual access of the coaxial jet. Flowing nitrogen through this enclosure prevented water vapor in the ambient air from condensing on the test chamber window, which was a recurrent problem when the chamber was first used for experiments at very low temperatures.

At the center of the photograph, slightly shifted down, we observe the inner chamber. It was bounded by two small acrylic windows in the front and back, and to both sides by the end of the acoustic waveguides, which will be described later in this chapter.

Three round holes can be observed in one of the windows. They show the original location for the three pressure transducers that were flushed with the window to measure the pressure oscillations inside the inner chamber. This configuration was used for tests with the original injector. They were raised to a location between the center and the top of the acrylic windows for the tests performed with the new injector. A description of the “original” and “new” injectors will be given below. At the bottom an aluminum piece served as support for the entire inner chamber and on the top there was a plate that acted as the ‘ceiling’ of the inner chamber. Both the top and bottom pieces had orifices at their centers. The top plate’s orifice allowed the coaxial jet tip to enter the inner chamber and the bottom orifice was used to provide an exit for the flow. It was also used to introduce a thermocouple and pressure transducer to study the properties of the flow near the jet, as can be observed in the photograph as well.

4.2 Original and New Injectors

Two images of the first or “original” coaxial injector used in the majority of these studies are shown in Figs. 4.4a and b. Figure 4.4a presents the full injector and Figure 4.4b shows a plane view of the end where the jets exited. The inner diameter of the inner jet, D_1 , or $2R_1$ as shown in the picture, was 0.51 mm. The outer jet had an inner diameter, D_2 , of 1.59 mm and outer diameter, D_3 , of 2.42 mm. The outer diameter of the injector, D_4 , was 3.18 mm. The length to inner diameter ratio was 100 for the inner jet and 67 for the outer jet (taking as reference one half of the hydraulic diameter, $R_3 - R_2$). The coaxial injector was installed so that the inner and outer jets were concentric and the inner jet exit

plane was recessed by 0.3 mm from the outer jet exit plane. This recess length was chosen to represent one half of D_1 in order to mimic realistic coaxial jet configurations used in industry.

The second or “new” coaxial injector used in these studies is shown in Figs. 4.5a and b. The inner diameter of the inner jet, D_{new1} , or $2R_{\text{new1}}$, was 1.40 mm. The outer jet had an inner diameter, D_{new2} , of 1.65 mm and outer diameter, D_{new3} , of 2.44 mm. The outer diameter of the injector, D_{new4} , was 3.94 mm. The length to inside diameter ratio was 65 for the inner jet and 105 for the outer jet (taking as reference one half of the hydraulic diameter, $R_{\text{new3}} - R_{\text{new2}}$). The injector was installed so that the inner and outer jets were concentric and the inner jet exit plane was recessed by 0.7 mm from the outer jet exit plane, which was chosen to represent one half of D_{new1} , to be able to compare it with the results obtained with the original injector. Notice that the inner post thickness decreased dramatically from the original injector to the new injector. The post thickness of the original injector was 110% of its inner diameter ($1.1D_1$) whereas the post thickness of the new injector is only 9.1% of its inner diameter ($0.091D_{\text{new1}}$).

4.3 Measurement Methods

The temperature of the fluid in the jets was measured with unshielded type E thermocouples with a bead diameter of 0.1 mm. The accuracy of the thermocouples used in the study was checked with an RTD and found to be within ± 1 K. A miniature pressure transducer was placed next to the thermocouple, using a small metallic post as support, and used to measure the pressure at a sampling frequency of 20 kHz. The manufacturer of

the miniature pressure transducers was Kulite Semiconductor Products, Inc. (models CCQ-062-1000A and CCQ-093-750A). These pressure transducers had an absolute pressure range of either 6.9 MPa or 5.2 MPa, respectively. The thermocouple and pressure transducer probe used are shown in Figure 4.6. In this photograph, the upper boundary or ‘ceiling’ of the inner chamber and the tip of the injector discussed above can be clearly seen.

Two linear positioning stages built by Attocube Systems AG were used to move the pressure transducer and the thermocouple in a plane perpendicular to the jet axis. Each stage had a range of 3 mm in 1 dimension with step sizes in the order of 0.01 mm. One stage was placed on top of the other with their axis of movement perpendicular to each other for a total maximum examination area of 3 mm by 3 mm, as shown in Figs. 4.7a and b.

With the configuration described above, the thermocouple tip could easily reach the exit plane of both the outer jet and inner jet. It was even possible to measure the temperature within the recess of the inner jet. During the actual measurements, the thermocouple was placed as close to the exit plane of the outer jet as possible without compromising its integrity as can be seen in Figure 4.6. The thermocouple and pressure transducer were attached to a custom made probe stand, shown in the cone-shaped aluminum part on the top positioning stage in Figure 4.7a. The devices were mounted on top of the linear positioning assembly using a small custom made base (circular base under the bottom positioning stage in Figure 4.7b), which in turn was placed at the top end of a shaft that rested on a large, linear mechanical stage with a 10-cm range built by

SETCO and shown in Figs. 4.8a and b, which allowed the probe to get to the desired interrogation region within the inner chamber.

Properties such as density and viscosity were computed from the measured flow rates, chamber pressure and jet temperature, using the National Institute of Standards and Technology's REFPROP Software (70) and its thermophysical properties online database (71). From these properties, Reynolds number, Re , outer to inner jet velocity ratio, VR , and outer to inner jet momentum flux ratio, J , for a given set of conditions were then calculated. The jet was visualized by taking backlit images using a Phantom v7.1 high-speed camera (see Figure 4.9) capable of recording up to 160,000 frames per second at a resolution of 32 pixels by 32 pixels. For a resolution of 128 pixels by 256 pixels the camera was capable of recording 41,300 pictures per second. The resolution of the images in the present experiments varied from 128 pixels x 224 pixels to 196 pixels x 400 pixels, depending on chamber pressure and outer to inner momentum flux ratio. These in turn determined the size of the visible features of the jet that this study was characterizing. Each pixel represents an approximate area of 0.08 mm x 0.08 mm. Depending on the resolution chosen, the framing rate (frequency at which pictures were recorded) was 20, 25 or 41 kHz.

To focus the camera on the coaxial jet flow an AF Nikkor 35-105 mm lens, a Nikon No. 1 Close-Up lens, and various optical extensions were used. Since focusing on the outer jet structures while at the same time having a clear view of the inner jet was always a difficult process when setting up the camera and related optical equipment, the quality of the coaxial jet images was not always the same. In some cases, to be described

in Chapter 5, the images were blurred and made it more difficult to characterize the inner and outer jet.

The jet was backlit using a Newport variable power arc lamp set at 160 W or 300W. The exposure time generally was 1-2 μ s and the number of images saved per run was 1000 on average. The dark core length and the inner jet spreading angles were measured from 998 images using a MATLAB subroutine based on the Otsu technique (72), which analyzes an image and finds a threshold which helps differentiate the dark core of the inner jet from the rest of the image.

The acoustic waves were generated using two piezo-sirens placed at each end of the chamber, custom-designed for the Air Force Research Laboratory by Hersh Acoustical Engineering, Inc. A Fluke 100 MS/s arbitrary waveform generator (model 292) was used to produce two sinusoidal waves with the same frequency but with a prescribed phase between them. The signals were then sent to two amplifiers, one for each piezo-siren. The amplifiers were a Krohn-Hite (model 7500) and a Trek (model PZD2000A), which amplified the signals and fed them to the piezo-sirens. The amplified signals were in the 200 to 540 V range. The principle by which the piezo-sirens work as acoustic drivers is relatively simple, with a piezo element moving an aluminum cone attached to it, which in turn vibrates to produce acoustic waves. The distance from each cone to the location of the coaxial jet is 44 cm.

The frequency at which the piezo-sirens were driven was chosen by manually varying the frequency on the signal generator until the highest amplitudes of the pressure perturbations were obtained. These pressure perturbations were measured using the three

differential Kulite pressure transducers (model XCQ-093-25D) flushed with the acrylic window of the inner chamber (see Figure 4.3) and shown real time and recorded for further processing using Pacific Instruments PI660 Acquisition and Control Software.

The phase difference, also referred to in this work as phase angle, between the signals sent to the piezo-siren elements was varied to expose the coaxial jet to different effective positions relative to the pressure node or antinode of the generated acoustic field. When the two piezo-siren elements produce waves with a zero degree phase angle between them, the movement of the piezo-siren cones is synchronized and in opposite directions, that is, towards and away from each other. This produces conditions of high pressure perturbations and low velocity fluctuations at the center of the chamber, where the coaxial jet is located. This condition is called a pressure antinode or velocity node. In contrast, when the two drivers present a 180-degree phase difference, then the cones move in the same direction, generating high velocity fluctuations with very small variations in pressure at the jet location. This condition is called a pressure node or velocity antinode. A schematic of this behavior is reproduced in Figure 4.10. The method for creating pressure node and antinode conditions in the chamber differed from that used in the UCLA droplet waveguide, but the effect created was the same.

In these experiments, the voltage supplied to the two acoustic drivers was maintained at the same level for all conditions during each case. Efforts were made to keep the amplitudes of both piezo-siren elements the same. A photograph of one of the piezo-sirens can be seen in Figure 4.11a. Since the experimental setup uses a rectangular test section, the jet was excited with a transverse acoustic field. A transverse mode on a

rectangular chamber would be the equivalent of a tangential mode on a cylindrical chamber, which are the most dangerous for the integrity of such systems and an important reason to analyze its effects on a coaxial jet. To accommodate for the rectangular chamber, a waveguide with a catenary contour was used to transmit the waves from a circular cross-section to a rectangular cross-section as seen in Figure 4.11b. The maximum peak-to-peak acoustic pressure fluctuations generated by the two piezo-ceramic acoustic sources in the inner chamber varied from 7 to 30 kPa (1 to 5 psi) and were produced in the 2.9 to 3.3 kHz range.

4.4 Uncertainty Analysis

It is fundamental, for a useful interpretation of the data, to assess the uncertainty of the measurements for the experiments described in this work. An analysis of the impact that the errors of the measured variables have in the reported quantities is therefore necessary. Of particular interest are those measured quantities that the experimenter identifies as the most sensitive to small changes in experimental conditions or most likely to vary from one experiment to another, increasing the bias error of the measurement, or those quantities that are most difficult to measure with the probes and sensors available to the experimenter, which impact the precision error of the measurement.

The uncertainty of an experimental quantity, u_q , is given by the general formula (73; 74):

$$u_q = \sqrt{\frac{\partial q}{\partial x_1} u_{x_1} + \frac{\partial q}{\partial x_2} u_{x_2} \dots + \frac{\partial q}{\partial x_n} u_{x_n}} . \quad (4.1)$$

The quantities x_1 , x_2 , to x_n are the experimentally measured variables and u_{x_1} , u_{x_2} , to u_{x_n} their corresponding experimental uncertainties. This is the formula used to derive the uncertainties of the experimentally derived quantities shown throughout this study.

For the acoustically excited coaxial injector experiment there were several experimental quantities used to find test parameters such as J or VR. The pressure of the chamber was measured with a precision of $\pm 0.1\%$ of full scale reading. Mass flow meters report $\pm 1\%$ of full scale output. Temperatures were measured within 1 K after calibration with an RTD, which represents less than $\pm 1\%$ of the lowest absolute temperatures recorded (in the vicinity of 105K). The largest source of error appeared when finding the density near the critical temperature of nitrogen, due to the large density gradients occurring at that temperature range. For further details on the uncertainty analysis of the coaxial jet experiment see Davis (42).

For the dark core lengths reported in this study, the quantity L/D_1 was obtained from a sample of 998 images. The number of pixels spanning the width of the outer post of the injector (D_4) was used as the basis to calculate D_1 . The end of the injector was at least 40 pixels for the majority of the cases. The pixel uncertainty was 1 to 2 pixels at each side. That brings a maximum uncertainty of 10% in the calculation of D_1 . The data from each sample were used to create a distribution from which the mean and standard deviation were calculated. This mean value was reported as L/D_1 . The value of the corresponding standard deviation was used to assign an uncertainty value to these

measurements. A 68% confidence level (1σ) was used to report error limits in the length measurements. This means that the dark core length for any given image will stay within those error bars on 68% of the cases. A 95% confidence value could be attained if 1.96σ was used instead.

However, if the uncertainty of the *mean* dark core length and not only of one image is desired, the uncertainty value will decrease by a factor of

$$\sigma_{mean} = \frac{\sigma_{single\ image}}{\sqrt{N}}, \quad (4.2)$$

where N is the number of images from which the mean value is derived (73; 74). In our case $N = 998$ and the uncertainty will decrease by a factor of 31.6. Thus the uncertainty of the mean is only 3.2% that of a single image. Of course, one must be aware that these confidence factors and standard deviation calculations depend on the underlying assumption that the working variable (L/D_1 in our case) assumes a normal distribution as N goes to infinity.

Uncertainties were not reported for the inner jet spreading angles reported in this study since they were based on the measurement of the *maximum* value achieved at each row by all contours. Thus the method searched for the outer most regions of the dark core regardless of the number of images in which they appeared. For most conditions this was a representative method for estimating how much the inner jet will spread during a few milliseconds of operation. If a particular case was found not to accurately depict the observed spreading angle, certain parameters, such as the region of the contour from which the angles were measured, were adjusted to eliminate the sources of inconsistency.

Finally, outer jet spreading angles were extracted from a sample of 20 images. A mean and standard deviation were obtained and the mean reported as the outer jet spreading angle, $\alpha_1 + \alpha_4$. The error bars represent $\pm 1 \sigma$ which gives a 68% confidence that an angle extracted from any image at that condition will remain within the reported error bars. If the uncertainty of the *mean* instead of a single image is desired, its value will only be 22% that of the original uncertainty for one image only per equation (4.2).

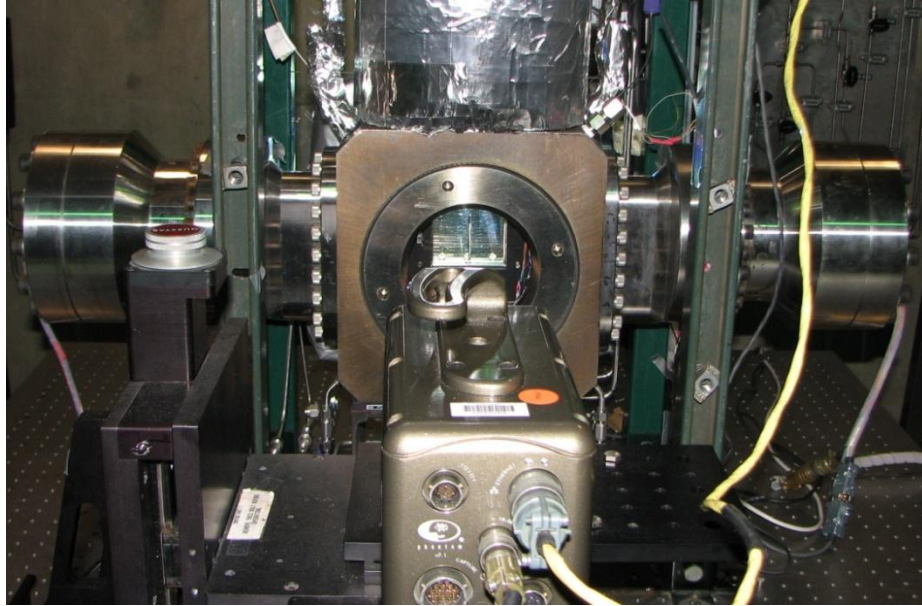


Figure 4.1. Experimental test chamber and supporting systems of the Experimental Cell 4 at AFRL, Edwards AFB, CA.

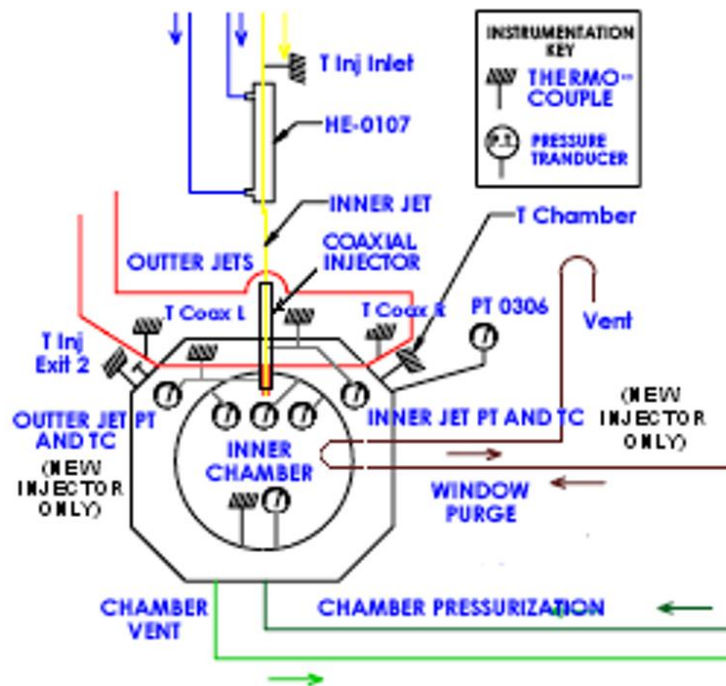


Figure 4.2. Chamber section view of the flow schematic for Experimental Cell 4 with the upgrades for the new coaxial injector. For a complete schematic refer to Appendix A.

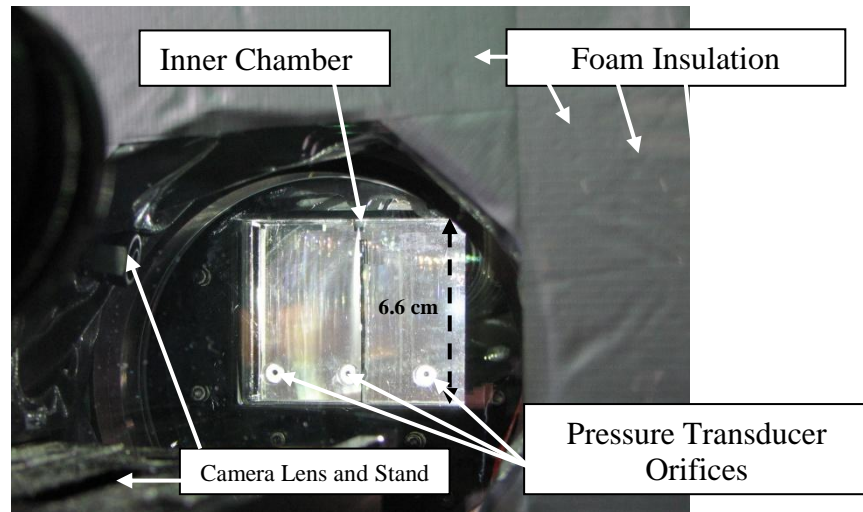


Figure 4.3. Photograph of the inner chamber within the test chamber in EC 4.

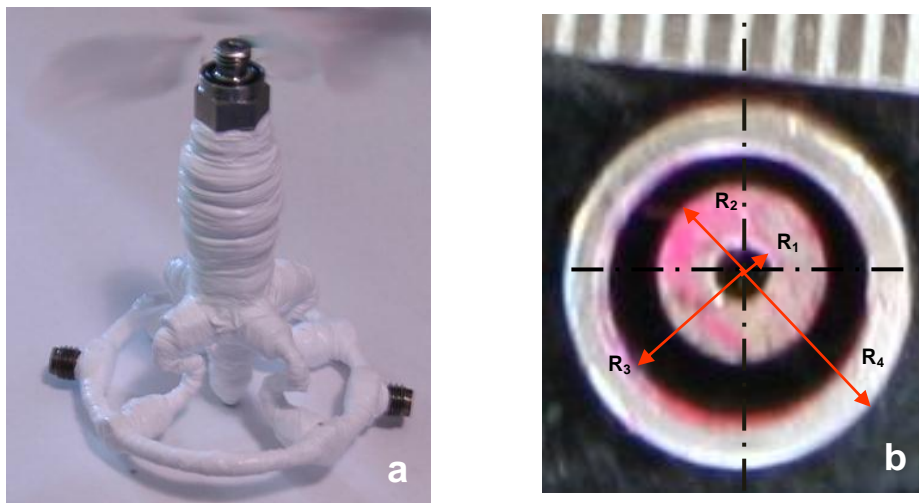


Figure 4.4. (a) First (“original”) coaxial injector used in this study. (b) Exit plane view of the original coaxial injector.

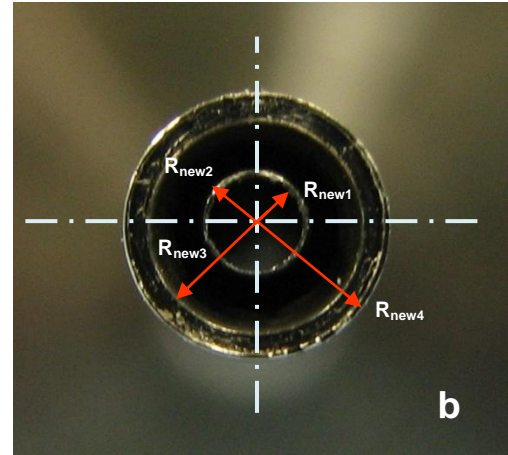
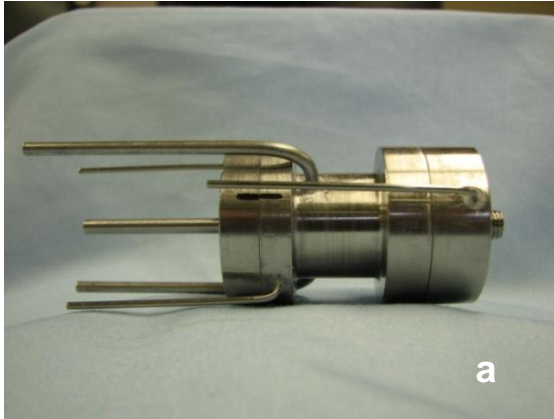


Figure 4.5. (a) Second (“new”) coaxial injector used in this study. (b) Exit plane view of the new coaxial injector.



Figure 4.6. Thermocouple and pressure transducer probes near the exit of the coaxial injector.

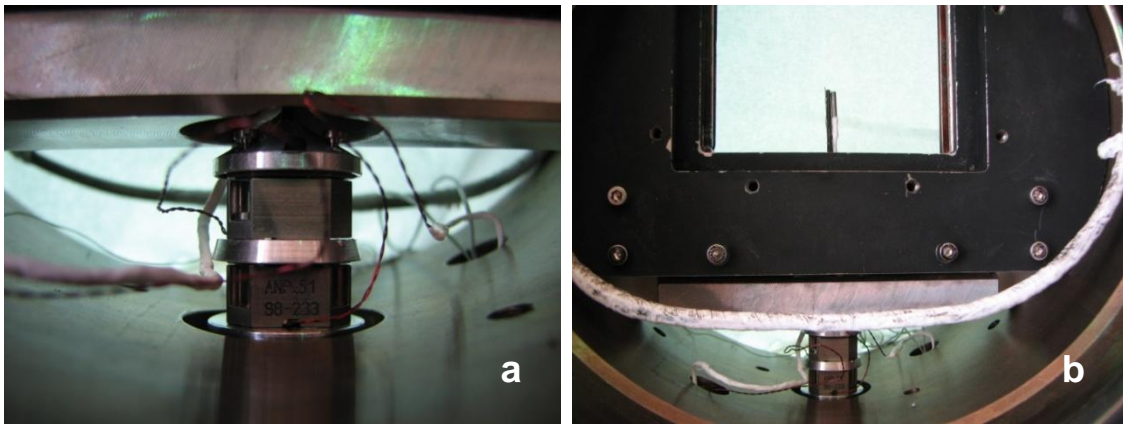


Figure 4.7. (a) Linear positioning stages that moved perpendicular to the vertical axis. (b) Larger view of the positioning stages and the thermocouple and pressure probe they support.

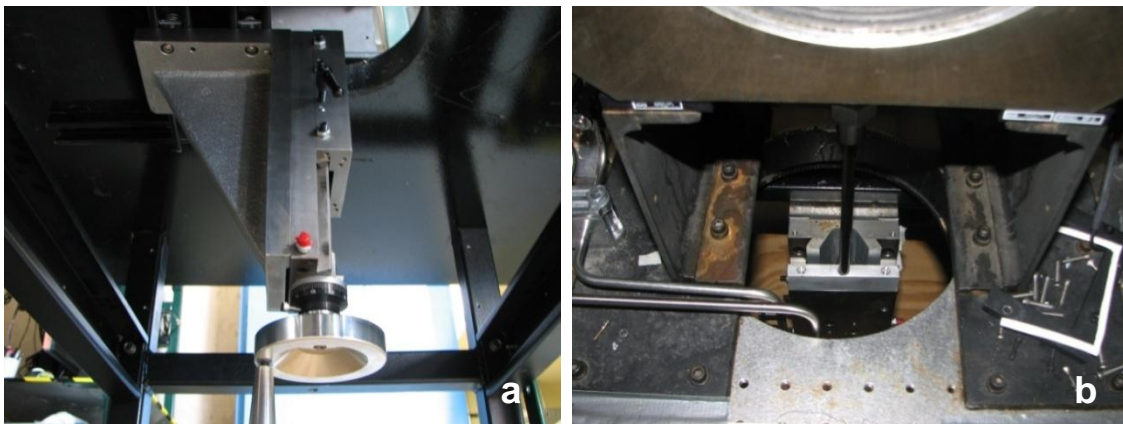


Figure 4.8. (a) Diagonal view of the mechanical stage used to move the thermocouple in the vertical direction inside the main chamber. (b) View of the mechanical stage from above. The bottom of the test chamber can be seen in the upper part of the image.

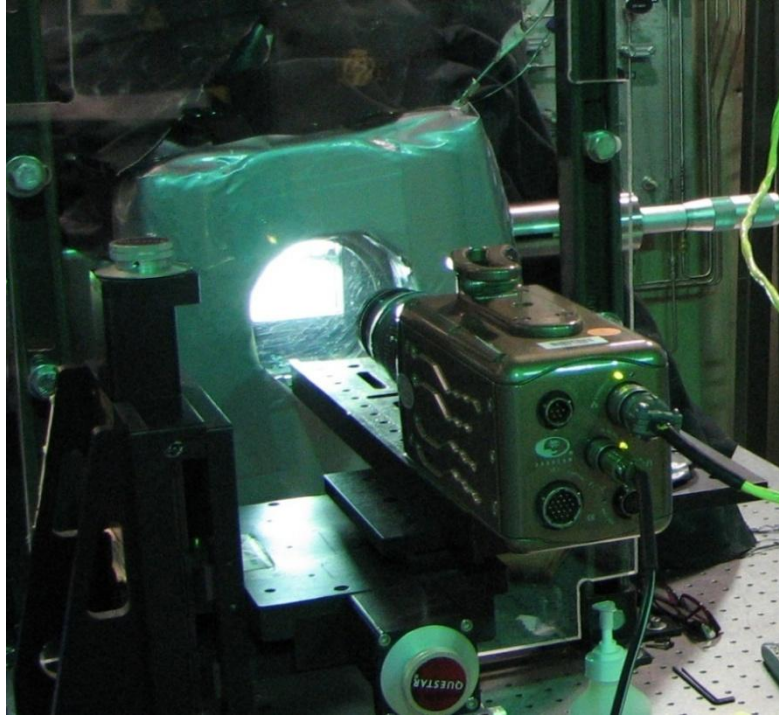


Figure 4.9. High speed camera used in this study.

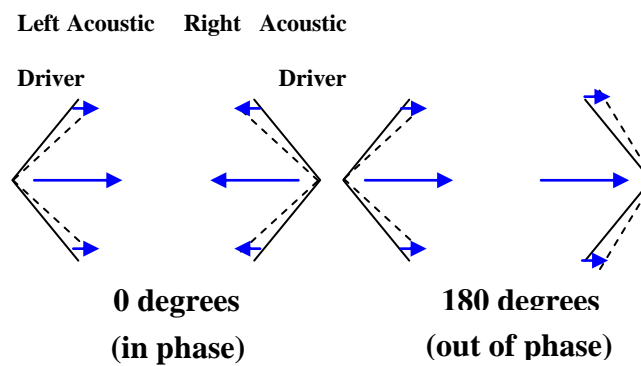


Figure 4.10. Simplified diagram of the two acoustic drivers at a 0° and 180° phase angle, indicating relative flow perturbation directions.

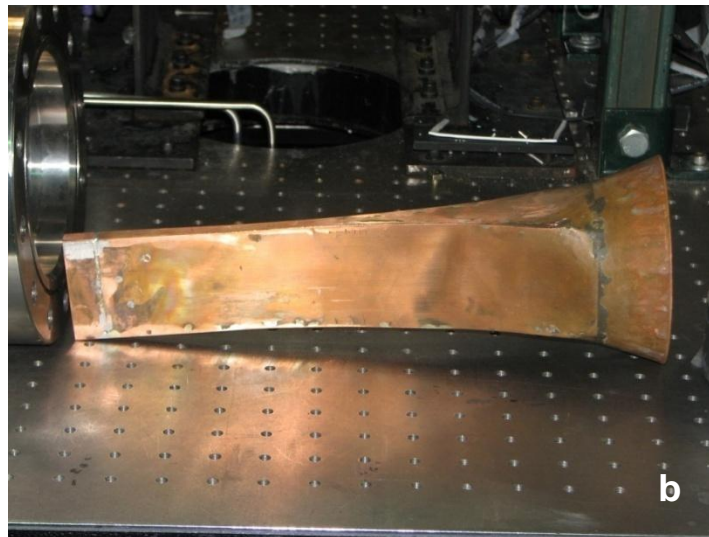
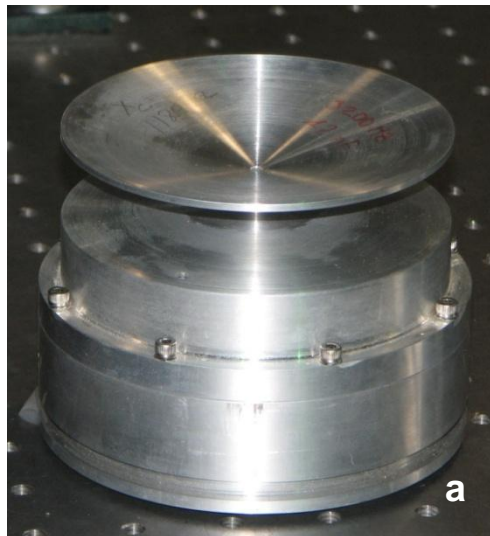


Figure 4.11. (a) One of two piezo-siren elements used to produce the acoustic field for this study. (b) Waveguide used to transmit the acoustic waves from the piezo-siren to the inner chamber.

CHAPTER 5

Results – Acoustically Excited Coaxial Jet

5.1 Quantification of Dark Core Length and Inner and Outer Jet Spreading Angles

The parameters investigated in the present experiments were the mean dark core length of the inner jet, the maximum spreading angle of the inner jet, and the average spreading angle of the outer jet. In this section the method used to quantify each of these parameters will be explained and in subsequent sections the results obtained from applying this method to the experimental data will be presented.

5.1.1 Dark Core Length

The visualization method for the experiments performed for this work consisted of backlit images obtained with a high speed camera. Since the coaxial jet was located between the lens of the camera and the lamp, the denser regions of the inner jet were able to obstruct or deflect the incoming light the most. These denser regions produced dark areas which represented the flow from the inner jet, or the “core” of the coaxial flow. As the denser inner jet flow starts to combine with the less dense flow of the outer jet and the chamber, its ability to obstruct or deflect light diminishes and the flow appears less dark.

When the darkness of the inner jet is reduced below a certain threshold, that region is not considered part of the dark core. It is important to notice that the darker regions, the ones that are above the threshold, are not necessarily connected. It is then possible to find a continuous dark area starting at the exit of the injector and ending a few diameters downstream, then some less dense regions which are not part of the dark core, and then a few disconnected regions or “islands” where the flow is dark enough to go over the threshold.

For this study, the dark core is defined as the continuous dark area starting at the exit of the injector. The dark regions that are not connected with the main “core” that is exiting the injector are not considered part of it, even if their darkness indicates that the fluid in these regions has not been mixed with the outer jet or chamber fluid yet. Once a dark core region was identified, the perimeter of this interconnected area which starts at the exit of the injector was highlighted by a visual processing routine in MATLAB and its projection in the axial direction is reported as the dark core length shown in Figs. 5.1a to c. The width of the inner jet inner post was found (see injector exit region in Figure 5.1b) in pixels and used to normalize the dark core length. The visual processing routine was then used to convert the shadowgraph image to a black and white picture. This method for conversion is based on the Otsu technique (72), which defines edges based on the zeroth and first cumulative moments of the gray-level histogram of the image, and its implementation is described in detail in Leyva et al. (22; 23).

Since the dark core length is an instantaneous measurement, its value changes with each frame analyzed. The mean dark core length is an average of a predetermined

number of images obtained with the high speed camera. In this work, the mean dark core length for each particular condition consisted of an average of 998 images such as the one shown in Figure 5.1a. The average was taken over a period of at least 24 ms (for cases recorded at 41000 frames per second) and at most of 50 ms (for cases recorded at 20000 frames per second). For data with external forcing between 2.9 and 3.1 kHz, the number of acoustic cycles included in the interrogation window varied from 70 to 155 depending on the time periods indicated above. Forcing at these conditions was chosen because it coincided with a multiple of the transverse mode of the chamber, so that the largest possible pressure fluctuations could be obtained.

5.1.2 Inner Jet Spreading Angles

To measure the inner jet spreading angles for a given condition, 998 images such as the one shown in Figure 5.1a were employed. Then, using the process outlined in the previous section to obtain the dark core length, a dark core region was extracted from each image. From the black and white images such as the one shown in Figure 5.1c, a contour of the dark core region was constructed. In order to measure the inner jet spreading angle, the locations of the left and right contours were recorded for each image as seen in Figure 5.1d. Then the leftmost points from each row for the left contours of all 998 images were selected. With this set of points, a “maximum left contour” was obtained. Likewise, the rightmost points from each row for the right contours of all 998 images were selected and a “maximum right contour” was extracted as indicated in Figure 5.2.

A linear fit through each contour was used to calculate the left and right spreading angles. The linear fit was chosen to start where the contour was the thinnest, usually between $\frac{1}{2}D_1$ (in supercritical cases at high J values, for example) and $5D_1$ (for all pressure conditions at moderate J values) and to end at the mean dark core length, which was found using a modified MATLAB routine based on the routine used to extract the dark core length. The reason to omit the first rows of the contour and instead begin the linear fit where the contour was thinner was to avoid a recirculation zone generated at the exit of the original injector used in this work. This recirculation of the flow occurred due to the thick inner jet post which prevented the inner jet and outer jet from coming into contact right away after the inner jet post ended. The recirculation region appeared in the images to be just as dark as the inner jet dark core, and if taken into account it would bias the measurements. Therefore the upper limits of the fit were chosen a few inner jet diameters downstream the exit of the injector.

Once the limits for the linear fit were chosen, the corresponding line was obtained and its associated angle as well. An example of both left and right angles, α_{Left} and α_{Right} , computed in this manner is shown in Figure 5.2. The sum of the left and right angles was referred to as the “maximum inner jet spreading angle”. This computed spreading angle represented the region the inner jet traveled during the time it takes to record the 998 images, which ranged from 24 to 50 milliseconds. Note that this ‘maximum inner jet spreading angle’ over predicted the mean of the spreading angles that could be obtained from each of the 998 frames. This is because the maximum contour out of all the images was found and then the linear fit to the composite contour was obtained, instead of fitting

a line and finding a spread angle for each image and then taking the average of these angles. This was done in purpose to get the maximum spread possible. When acoustics were present, this maximum spreading angle represented the region the inner jet had traveled during all acoustic cycles captured in the number of images processed, which varied from 70 to 155 acoustic cycles as indicated above. It represented the maximum acoustic spreading angle of the inner jet.

5.1.3 Outer Jet Spreading Angles

The outer jet spreading angle was defined to start from the point where the jet started to grow, approximately $2D_1$ to $4D_1$ downstream of the exit plane, and end at a location $10D_1$ downstream of the exit of the injector. Therefore this measure could be interpreted as an outer jet initial spread angle, $\alpha_1 + \alpha_4$. The main difference between the inner jet spreading angle measurement described in the previous subsection and this outer jet spreading angle measurement is the technique used. The outer jet spreading angles were extracted visually from 20 randomly selected images of the total of 998 available. Figure 5.3 shows an image recorded with the high speed camera with labels and arrows indicating how the spreading angle was obtained. Only α_1 and α_4 were visible and measured. The angles α_2 and α_3 were not visible in the images recorded. Regardless, they are indicated in the figure to complete a conceptual picture of the spreading of the outer jet both outside towards the chamber and inside towards the inner jet.

5.2 Results with the Original Coaxial Jet Injector Geometry

5.2.1 Behavior in the Absence of Acoustic Excitation

This section presents the results obtained for the coaxial jet experiment in the absence of acoustic excitation. Images of the jet for different outer to inner momentum flux ratios at each of the three pressure regimes studied are shown and their features discussed. An analysis of the dark core length measurements and spreading angles follows with observations and conclusions offered at the end.

In this work, the coaxial jet images without acoustic excitation provide a baseline to analyze the behavior of the flow when the effects of acoustic forcing are introduced. The results without acoustic excitation also provide information about inherent features of the flow such as naturally occurring instabilities and interaction between the two fluid streams. For reference, the actual distance from the exit of the injector to the bottom of the images varies between 1.5 and 2.0 cm.

The images in Figure 5.4 were obtained at subcritical pressures and show the coaxial jet with the original injector at different outer to inner jet momentum flux ratios. The feature that stands out the most in every image is the length of the dark core region. For $J = 0.17$, the dark core is long and evidence of breakup is only seen towards the end of the image. The relative smoothness of the dark core region at the exit of the injector disappears as the inner jet travels downstream. The core region then develops into shreds of dense fluid that are as dark as the initial dark core region but are not as well connected. Towards the end of the image regions of very

dense fluid can still be observed, though definitely not connected to the inner jet. In this image, the dark core might appear longer than the field of view but video images confirm that the breakup occurs within the visible area of the image. The spreading angle of the outer jet can also be seen.

The images for $J = 1.0$ and 2.6 feature a comparatively thinner and slightly shorter dark core region; however, the inner and the outer jets still behave in a similar manner. The inner jet mass flow rates and temperatures are similar for all cases (see Table C.1) and wider inner jets occur above and below the J values for which these thin inner jets are observed. The $J = 2.6$ case has a feature that was not observed in the previous two cases. The inner jet shows a noticeable jet distortion and spread compared to its initial width. After a few inner diameters downstream the jet broadens and starts breaking up. However, denser flow structures are still convected downstream. Towards the bottom of the image an area with almost no darker regions is observed, unlike the first two, which featured dark structures throughout the image. The boundary of the outer jet is also affected by the spreading behavior of the inner jet and features a wavy pattern; however, the overall angle is still very similar to the previous two conditions.

The next case at $J = 4.2$ shows a thicker, shorter inner jet with a different type of interaction with the outer jet than the previous three. The dark core seems to be entrained by the outer jet right away after it exits the injector region. Gray regions where the denser structures mix with the surrounding outer jet fluid are now noticeable towards the bottom of the image. Both the inner and outer jets shows

similar spread compared to the $J = 2.6$ case. The outer jet contour is also wavy to accommodate for the observed behavior of the inner jet.

The next image corresponds to the $J = 9.6$ case with a very wide inner jet, which is attributed to a recirculation region created at the exit of the injector due to the inner jet post thickness discussed in Chapter 4. With an outer jet momentum flux that is an order of magnitude larger than the inner jet momentum flux, the inner jet is quickly entrained by the outer jet, expanding as it leaves the inner jet. This phenomenon cannot be seen in the image because of the recess of the injector. The inner jet spread is still similar to the previous case as is will be explained in section 5.2.3 and the dark core length is greatly reduced compared to the previous cases. The inner jet also features a transition between the dark core region and progressively lighter regions of the flow downstream, an evidence of mixing between the inner and outer jets. At the exit of the injector a clear coaxial stream and a dark inner stream can be observed. Then, as they flow away from the exit they combine and form blended structures. This behavior is preferred for propellant mixing.

The last image corresponds to a momentum flux ratio of $J = 23$. Such high value for J was only achieved at the subcritical pressure regime. In this image we observe features that are very similar to the $J = 9.3$. This case features a thick dark core region, an even smaller dark core length and inner jet spreading angle. The momentum flux of the outer jet is so strong that the inner jet and outer jet appear very well mixed just a few diameters downstream of the exit of the injector. Since the density and the mass flow rate of the inner jet for all subcritical cases is the same

(see Table C.1), the broadness of the inner jet for the last two cases indicates that the inner jet has slowed down due to recirculation zone effects and the flow has been entrained further into the outer jet.

For the nearcritical pressure regime, images for 8 different momentum flux ratios were obtained. Even though at this pressure regime the flow was single phase, the images still feature a dark core and a lighter outer jet region as can be observed in Figure 5.5. The first image was obtained at $J = 0.55$ and shows a long dark core. A series of structures spreading out from the inner core region are observed near the center and towards the bottom of the image. This could be evidence of a particular instability or just the effect of flow entrainment by the outer jet at low J values for pressures over the critical point. The dark core is long and evidence of strong mixing is only seen towards the bottom. The second and third images show the cases at $J = 1.0$ and 1.1 respectively. The dark core lengths are similar and their dark core regions also spread in a similar fashion. The outer jet is not clear in the image corresponding to case $J = 1.1$ but in the case for $J = 1.0$ it follows the curved pattern of the inner jet. Both images show a region where the inner jet is very well mixed with the outer jet towards the bottom of the image. The first three images show how more homogeneous mixing is accomplished closer to the injector as J increases.

For the case of $J = 1.6$ the dark core length has decreased. The dark core region still shows a wavy contour but it is not as clear as the previous three. The outer jet is clear in this case and shows a very similar spread pattern compared to the outer jets of the subcritical cases. The next image ($J = 2.1$) is not very clear. A dark core region can still

be observed through the top portion of the image. Then a mixed region appears in the bottom half. This image resembles a blurred version of the image for $J = 1.6$, both having very similar dark core lengths.

The next two images in Figure 5.5 ($J = 2.9$ and 4.9) are also very similar and feature short dark core lengths. The spreading angles of the dark core region appear negative and the region where the inner and outer jets become well mixed start around the same location. This more homogeneous flow still shows some undulating structures that are clearly observed in the dark core region of the lower momentum flux ratio images.

The last image in Figure 5.5 shows the nearcritical case with the highest momentum flux ratio recorded ($J = 9.3$). It features a very short dark core. This image presents very clear evidence of the strong effect of the outer jet on the inner jet at high J values. The inner jet flow is completely mixed with its surroundings only a couple of inner jet diameters after it leaves the injector. This effect is desirable in an actual engine for a couple of reasons. First, the propellants will burn more efficiently, and second, any effects of the acoustics on the inner jet will be diminished since its length is very short and there is not much intact dense mass to excite.

The third set of images without acoustic forcing is shown in Figure 5.6. These images correspond to the supercritical pressure regime. The first one features the lowest momentum flux ratio ($J = 0.019$) of all the experimental data presented in this study. This image features a very long and spreading dark core region. It starts very thin at the exit and it expands as it travels downstream. The inner jet did not seem to be affected by the

outer jet, most likely due to the very low outer jet momentum flux compared to that of the inner jet. The dark core in the next image ($J = 0.33$) is also long but its thickness is constant through most of the image until it starts to break up towards the end.

At $J = 1.3$ the inner jet shows again a wavy structure that resembles those found at the lower J values of the nearcritical pressure cases. The outer jet was denser than usual and thus appears darker in the image. In the $J = 2.4$ and 2.5 cases, the dark core length is greatly reduced. Also, the distinction between the inner jet and outer jet is not clear towards the end of the image. This is evidence that strong mixing between the dark core and the outer jet occurred. At the highest momentum flux ratio of the supercritical cases ($J = 9.9$), the same phenomenon that occurred for the highest sub and nearcritical cases was observed. The dark core becomes very thick and extremely short. Mixing is accomplished at a very short distance from the exit of the injector and the spreading angle of the inner jet appears negative.

5.2.2 Dark Core Length Results in the Absence of Acoustic Excitation

The dark core length results for the three different pressure regimes are presented next. The dark core length measurements were performed as described in section 5.1.1. The lengths are normalized by the inner diameter of the inner jet or D_1 . Figure 5.7 shows the behavior of the dark core as a function of the outer to inner jet momentum flux ratio for the subcritical cases. There is a general downward trend that is observed in the graph starting at $26D_1$ for $J = 0.17$ and decreasing to about $17D_1$ to $15D_1$ for J values between 5 and 1. The image also shows that the dark core

lengths have large uncertainties for momentum flux ratio values less than 5. For $J = 9.6$ the value decreases to $8D_1$ and it decays to approximately $5D_1$ for the highest J value.

An effect of having a very long and thin dark core is the existence of regions that do not appear interconnected in some images. At this condition, the routine used to extract the average length interprets some long dark cores as short ones, especially at the lowest J value. At $J = 0.17$, the images generate mostly very long but some short dark cores, which are averaged and reported as a long mean dark core length with a large uncertainty associated to it. A similar effect, which applies to most conditions and cases, takes place when the jet breaks. The dark core length decreases by a few inner jet diameters to the point where the breakup happened. Then the jet starts to “grow” again by a few diameters until it breaks again. This produces a large uncertainty in the dark core length.

In the following plot in Figure 5.8 the dark core lengths for the nearcritical cases are shown. Note that the nearcritical cases follow a very clear trend of decreasing dark core length with increasing J . The only case that seems to be just outside the curve is the $J = 2.1$ case. From Figure 5.5 we observe that the image corresponding to this case is somewhat blurred, most likely due to difficulties adjusting the camera lenses, as described in section 4.3. This could have contributed to a slightly larger length than otherwise expected. The longest dark core of the set is $24D_1$ for $J = 0.55$. Then for $J = 1.0$ and 1.1 the lengths decrease to $15D_1$, with a very good agreement between these two different cases at very similar J values. For $J \approx 2$ they stay in the $15D_1$ to $10D_1$ range. For

$J = 2.9$ and 4.9 the dark core lengths decrease to $6D_1$ and at $J = 9.3$, the highest momentum flux ratio, the dark core length is just one tenth of the value at the lowest J .

The dark core lengths for the supercritical cases (see Figure 5.9) show a similar trend to that found in the nearcritical cases. This is expected since both tests are above the critical pressure of the fluid and constitute single phase flow. Here the dark core length at the lowest momentum flux ratio ($J=0.019$) for the supercritical cases is close to $40D_1$. Then it drops close to $25D_1$ for $J = 0.33$ and reaches a value near $20D_1$ for the $J = 1.3$ case. For the two cases at $J = 2.4$ and 2.5 , a very good agreement, similar to the agreement between $J = 1.0$ and 1.1 in the nearcritical regime, is found, with both dark core lengths being very close to $10D_1$. Finally at $J = 9.9$ the dark core length is very short, $3D_1$, a characteristic that is shared by the highest momentum ratio cases from all three pressure regimes.

A plot showing all dark core length measurements but one obtained with the original injector appears in Figure 5.10. The case not shown is the subcritical case with $J = 23$ which had a value of L/D_1 of 5 and extends off the chart. Figure 5.4 shows that the subcritical dark core lengths span, in a broad sense, the whole image for the 2 cases with the lowest J values and almost all the image for the $J = 2.6$ case. However, the actual breakup of the continuous stream captured by the visual processing routine is occurring halfway along the image for the second and third cases, and it is only clear in the image for the fourth ($J = 4.2$) case. The uncertainty in dark core length for the first three subcritical cases is large compared to the fourth one, since this case features a thicker inner jet and thus breakup location does not fluctuate as much as the first three.

In Figure 5.10 the trend laid out by the sub, near and supercritical cases is quite clear. There is a transition between dark core lengths with L/D_1 greater than 15 when $J < 1$ and dark core lengths with L/D_1 below 8 when $J > 5$. The images shown in Figure 5.5 and Figure 5.6 for near and supercritical cases, respectively, share several features, such as thicker dark core regions and smeared boundaries between the inner and outer streams. The near and supercritical regimes are also single phase, which clearly alters the dynamics of the jet, which explains in part why the boundaries are less clear than those from the subcritical images.

In the subcritical cases, surface tension in the liquid prevents the molecules from drifting towards the gaseous outer jet fluid, making the boundary between both phases sharper. The surface tension maintains the liquid molecules together until shear forces are strong enough to strip away some fluid particles. These are the unconnected structures that are seen in the lower momentum flux ratios. Surface tension thus prevents the jet from mixing. That is a possible explanation to why higher momentum fluxes are needed to reach the same dark core lengths at subcritical conditions in contrast to near and supercritical conditions.

Momentum transfer due to turbulent motion can also be enhanced by the lack of surface tension above the critical pressure and temperature. The particles of heavier fluid are quickly drawn toward the lighter stream due to the large density and velocity gradient in the otherwise homogeneous supercritical flow. For example, the subcritical image (Figure 5.4) for a momentum flux ratio of 23 has a dark core length of $5D_1$, similar to the near and supercritical images (Figs. 5.5 and 5.6) near a momentum flux ratio of 10, which

have dark core lengths between $2D_1$ and $3D_1$. The image for the subcritical condition at $J = 9.6$ also resembles the near and supercritical images in the $2 < J < 3$ range, with dark core lengths around $10D_1$ for all these cases (see Figs. 5.4 to 5.6).

The plot shown in Figure 5.11 shows the results obtained with the original injector with no acoustic excitation gathered over a period of more than 6 years at the Supercritical Cryogenic Laboratory (EC 4) at AFRL in Edwards AFB, CA. For the subcritical data obtained in the present work, the results follow the trend from previous results by Davis (42) and Leyva et al. (22; 23), except at very low supercritical and very high subcritical momentum flux ratios. For the nearcritical results, the present work shows good agreement with the lengths found by Davis. However, the supercritical data only lies close to previous supercritical data by Davis and Leyva at the higher momentum flux ratio case. In the overall sense, the current results fall within the region corresponding to the pressure condition in which they were taken, except for the lowest momentum flux ratio for the supercritical cases. The compiled results in this plot (22; 23; 42) provide a “map” that future researchers using similar coaxial injectors to those employed in this work could use to compare their results in subcritical to supercritical pressure regimes.

5.2.3 Inner Jet Spreading Angle Results in the Absence of Acoustic Excitation

The analysis of the spreading angle provides a measure of how much the inner or outer jet develops in any outward direction that is perpendicular to the axis of motion. In the current experiments, the inner jet spreading angle was easier to identify than the outer jet given the darkness of the inner jet region. Inner and outer jet spreading angles represent a measure of mixing between propellants and how they spread within the chamber. This is useful information for LRE injector design.

In this section we will look at the behavior of the inner jet spreading angles without an externally imposed transverse acoustic field. This study includes inner jet spreading angle results for outer to inner jet momentum flux ratios in the $0.02 < J < 20$ range. The graph in Figure 5.12 shows that the subcritical jets do not spread too much compared to its initial thickness, with all angles below 10° . The maximum spread is observed at $J = 2.6$, consistent with the initial thickness of the inner jets in Figure 5.4 and observing how they spread. The measured changes in spreading angle for the subcritical case could be within the experimental uncertainty; however, more data is required to reach a conclusion. For $J = 4.2$ and 9.6 the spreading is similar but the initial thickness is higher, thus the overall angle is slightly smaller. The smallest angles for the subcritical cases occur at the lowest and highest J values and they are in the 2° to 3° range.

For the near and supercritical cases, the spreading angles reach both higher and lower values than those of the subcritical cases. Starting at the very low J values of 0.019 and 0.33 for the supercritical cases, we observe an initial spread that is comparable to the average value of the angles for the subcritical cases. Looking at the set of supercritical images of Figure 5.6 these low angles correspond to the relative small thickness of these

supercritical jets. Then the cases between $J = 0.5$ and $J = 2.5$ show the largest angles, which vary from 10° to 17° , for both nearcritical and supercritical tests. The dark core regions for these cases show dark core flow structures that oscillate in the transverse direction as the flow travels downstream, which contributes to these large spreads and are likely related to the reduced core length with enhanced mixing. Finally, for values of J near 3 and above, the angles decrease prominently, reaching negative values near 5 and beyond. Previous data by Leyva et al. (22; 23) were used to confirm this trend for supercritical pressures near $J = 5$, since there were no data from the present study near those J values at supercritical pressures. The negative values are the effect of a very thick jet due to the aforementioned circulation zone at the exit of the injector and rapid mixing at very high outer to inner jet momentum flux ratios, which actually make the jet thinner by stripping fluid away from the inner dark core region. These small angles can be observed in the images for the corresponding momentum flux ratios in Figure 5.5 and Figure 5.6.

One important difference between the spreading angles for subcritical cases compared to those for the near and supercritical regimes is the effect of the surface tension of the liquid inner jet and larger density gradients at the boundary between the inner jet and the outer jet for subcritical cases compared to the cases above the critical point. Surface tension forces keep molecules together and could be a factor for the inner jet at subcritical conditions not spreading as much as its nearcritical and supercritical counterparts.

5.2.4 Outer Jet Spreading Angle Results in the Absence of Acoustic Excitation

In this section we analyze the behavior of the outer jet spreading angles without an externally imposed transverse acoustic field. The pressure regime studied is subcritical but the coaxial flow is single phase (gas-gas). The outer to inner jet momentum flux ratios varied from 0.013 to 2.0. The purpose of taking the gas-gas data is to compare the results with the available literature on single phase shear layers and coaxial jets, which is more abundant than two-phase investigations. For subcritical pressures, we generally obtained two phase flow, since the inner jet temperature was either a few degrees below or at the saturation temperature, and the outer jet was in the vapor phase. The experimental procedures were therefore modified to keep the inner jet in a gaseous state. Images of the single phase coaxial jet at subcritical conditions and momentum flux ratios from 0.013 to 2.0 are shown in Figure 5.13.

One of the areas of interest of gas-gas flows in coaxial jet behavior is the situation where both fuel and oxidizer are injected into the combustion chamber in the gaseous phase. For the near and supercritical pressures regimes used for the inner jet spreading angle cases, the inner and the outer jet constituted single phase flows but certainly not in the gaseous state. In order to have a gaseous inner jet and a gaseous outer jet coaxial flow, the flow had to remain at a subcritical pressure and the inner jet had to remain as a gas. To achieve this, the flow of liquid nitrogen through the heat exchanger that cools down the inner jet flow was decreased. This was allowed to provide just enough flow to achieve a density difference between the outer and the inner jet so that the coaxial jet

could be visualized. These single phase tests, to be discussed below, make more complete the outer jet spreading angle measurements and make gas-gas data available for comparison to other researchers. However, since the inner jet flow was not dense enough, it did not appear dark in the backlit images. Thus, a measurement of the dark core length could not be accomplished with the single gaseous phase data.

Outer jet spreading angle measurements in the absence of acoustics were thus the only measure processed from 6 subcritical cases. The momentum flux ratios are low because of the density of the inner jet could not be increased. To generate these cases, the inner jet mass flow rate was fixed and the outer jet mass flow rate was varied. A visual inspection of at least 20 randomly-selected images for each case was performed. From each picture a left angle (α_1) and a right angle (α_4) as described in Figure 5.3 were obtained. These angles were added and a total spread angle was found as shown in Figure 5.14. For these subcritical conditions, the trend starts with a very low J ($= 0.013$) and a negative spreading angle ($- 6^\circ$), which indicates that outer jet width is decreasing as it exits the tip of the injector. The next J is 0.037 and in this case the coaxial jet shows an angle of 5° . The remaining J values surveyed have angles in the 10° to 11° range.

To compare the results from these subcritical gas-gas experiments with other available data, a plot of the spreading angle growth rate as a function of the density of the chamber, the density of the outer jet and the momentum flux ratio is shown in Figure 5.15 which is an extended version of the results compiled in Leyva et al. (75). The plot also includes experimental, numerical and theoretical data from various researchers on spreading angles of coaxial jets and 2D shear layers. The linear fits are derived for the

growth of a 2D shear layer by Dimotakis (44) and Papamoschou and Roshko (45). The expression of Papamoschou and Roshko predicts the visual growth of the shear layer and the formula Dimotakis derives predicts the vorticity growth of the shear layer. However, Dimotakis shows how to convert from vorticity growth to visual growth, which is the quantity that the gas-gas data are compared against. The applicability of these expressions to axisymmetric and coaxial jets is limited to the region very close the exit of the injector where the flow of the outer jet and either the flow of the chamber or the inner jet meet.

The experimental work by Brown and Roshko (43) measured the visual growth of the shear layer formed between two incompressible fluid streams of different densities. The experimental results from Favre-Marinet and Camano Schettini (76) are obtained from coaxial jet experiments where the densities of the inner jet, outer jet, and chamber fluid were different. The data from Liu et al. (77) were extracted from velocity and temperature contour images presented in their paper. An interesting characteristic from their study is that the geometry of their injector is modeled after the original injector analyzed in this study. It is thus not so unexpected to find their results more in agreement with the spreading angles found in this study than the rest of the data discussed so far.

The data by Leyva et al. (75) were obtained using the same facility with the same flow configuration and fluid characteristics used to obtain the one-phase gaseous state data presented in this work, which will explain the very close agreement between their data points and the results of this one-phase gaseous state study for $J > 0.1$. The only

difference is that none of the angles reported by Leyva et al. (75) are one-phase gaseous state coaxial jet flows, which makes the agreement much more interesting.

In the graph in Figure 5.15, the exact variable against which the spreading angle (defined as $d\delta/dx$ or $\tan \alpha_1 + \tan \alpha_4$) is plotted is the ratio of the chamber density to that of the outer jet multiplied by the square root of the outer to inner jet momentum flux ratio. The reason to incorporate outer to inner jet momentum flux ratio as a parameter instead of just the more widely used chamber to outer jet density ratio is to bring in the effects of the inner jet on the outer jet spreading angle. The square root of J was used instead of just J to avoid cancelling outer jet density from the expression.

A very plausible explanation for the larger angles obtained by the analytical formulas from Dimotakis (44) and Papamoschou and Roshko (45), and experimental data from Brown and Roshko (43) and Favre-Marinet and Camano Schettini (76), as compared to the shorter angles obtained for the rest of the data, involves the type of flow modeled and the injector geometry used. The particular injector configuration used in this work, which is the same geometry used by Leyva et al. (75) and Liu et al. (77), produces a relatively large recirculation zone between the inner jet and the outer jet at the inner jet exit location. This recirculation zone does not exist in coaxial jet geometries where the inner jet and the outer jet are separated by a very thin wall or for two-dimensional shear layer mixing studies where the flows mixing at two different velocities are assumed to have a wall of negligible thickness between them. Further studies in the gas-gas regime with the new injector could provide evidence to prove this claim.

5.2.5 Acoustic Field in the Test Chamber

The results of the behavior of the coaxial jet under acoustic forcing are drawn from a complete set of data where at least 6 cases are reported for each of the three mean chamber pressure conditions surveyed: subcritical, nearcritical and supercritical. The peak-to-peak pressure perturbation as a percentage of the mean chamber pressure varied from less than 1 to 4 %, the outer to inner jet velocity ratio ranged from 0.25 to 23 and the outer to inner jet momentum flux ratio ranged from 0.019 to 23.

Two acoustic sources were used to generate the transverse acoustic field inside the inner chamber of the experimental apparatus. To expose the coaxial jet flow to different acoustic conditions, including conditions near or at the pressure node or antinode, the phase between the two acoustic sources was varied from 0° to 360° in steps of 45° . To characterize the acoustic field inside the inner chamber during each test, pressure measurements were obtained from pressure transducers inside the inner chamber. One absolute pressure transducer was located at the bottom of the inner chamber, very close to the orifice through which the flow exited the enclosure, to minimize as much as possible any effects of the probe on the coaxial jet and vice versa (Figure 5.16a). Three absolute pressure transducers were located at the bottom of the inner chamber for the first injector studied (Figure 5.16b) and three differential pressure transducers were located halfway between the middle and the top for the second injector studied (Figure 5.16c).

A measurement of the root-mean-square (RMS) values of the pressure fluctuations at each phase angle condition is shown for a nearcritical case in Figure 5.17.

In the graph, the baseline shows the measurement when there is no acoustic excitation inside the chamber. The positive number in the RMS of the pressure, between 3 and 4 kPa, represents the noise in the measurement. Thus the pressure transducer cannot discern pressure oscillations with an RMS below 3 kPa.

At each phase angle condition, either three or one data sets were obtained. When three data sets were collected, it consisted of data with both acoustic sources on, only the left acoustic source on, and only the right acoustic source on. When only one data set was collected, it consisted of data with both acoustic sources on. The purpose of recording data with only one source on was to compare the results obtained with each acoustic source and verify that their acoustic amplitudes did not change throughout the test. Phase angle is thus not a meaningful quantity for the single source excitation cases and it is indicated to show the order in which this single source excitation cases were taken.

The number of phase angles for which results for one acoustic source were obtained varied depending on the time available to run the tests. Some cases have no results with only one acoustic source on (i.e. only data with both acoustic sources on was recorded) and others have up to five phase angles for which single-source excitation was recorded. The slight differences in the results obtained with either acoustic source throughout the course of any given test may be attributed to the different times at which the measurements were made.

All pressure measurements reported in this study for the original injector were obtained using the pressure transducer at the bottom of the inner chamber shown in Figure 5.16a. The pressure measurements reported for the new injector were obtained

using the center pressure transducer, which was the one closest to the injector exit, of the three shown in Figure 5.16c. The pressure measurements for the new injector are shown, together with dark core length and spreading angle results, in section 5.3.

Results with only one acoustic source on for the case shown in Figure 5.17 were recorded for only three phase angles. In this nearcritical case with $J = 2.1$, the left acoustic source, in triangles, had RMS values of 7.13, 7.10 and 7.17 kPa and the right acoustic source, in squares, had RMS values of 6.07, 6.02 and 6.26 kPa for 0° , 45° and 315° phase difference, respectively. The data verified that the amplitudes of each acoustic source by itself do not vary with phase angle, which is what is expected. Also, though not exactly the same, the left and right source amplitudes are very close. This fact is important when considering the effect of both acoustic sources on. These data points are represented in Figure 5.17 by the diamond-shaped markers, which show a very well defined curve that has the same RMS value at 0° and 360° and it also shows a minimum (at 225°) and a maximum (at 45°) that are separated by a 180° phase difference. The minimum in pressure fluctuations occurs near the 180-degree phase angle and the maximum near the 0-degree phase angle, which is theoretically where the minimum and maximum pressure fluctuations should occur. The minimum pressure fluctuation at 225° also shows an RMS value just slightly over the baseline value, indicating that the two signals cancelled each other almost completely.

The same type of graph shown in Figure 5.17 was plotted on the left side of Figure 5.18 for three other cases. In these graphs, the effect of the phase difference between the two acoustic sources on the coaxial jet at different chamber pressure

conditions can be observed. Higher amplitude forcing and the ability to expose the jet to different effective positions relative to pressure nodes and antinodes are created when there are two acoustic sources operational. The supercritical case with $J = 9.9$, in the bottom graph on the left side of Figure 5.18, shows the ideal acoustic behavior described above where a maximum pressure perturbation was achieved at a 0° phase angle between the acoustic sources and the minimum achieved at a 180° phase angle between them. In the top graph on the left side of Figure 5.18 for the subcritical case with $J = 9.6$, the maximum and minimum pressure perturbation are observed at 315° (-45°) and 135° respectively. Thus, maximum pressure perturbations were observed at $0^\circ \pm 45^\circ$ and minimum pressure perturbations were observed at $180^\circ \pm 45^\circ$ for the three graphs shown on the left side of Figure 5.18.

The reason for the pressure noded and antinodes to be observed at different phase angles for different tests is not fully understood, but a source of error might be the acoustic sources themselves. One possible explanation for this asymmetry is strong crosstalk between speakers. The vibration of one not being completely shielded from the vibration of the other one. This has been observed in strain gauge measurements with only one acoustic source. One of the piezo-sirens has a strain gauge which generates a signal that is carefully monitored to prevent damage to the piezo. It is supposed to only produce a signal when the acoustic source to which the gauge is attached is on. However, a noticeable signal is also recorded when the piezo-siren to which the strain gauge is attached is off and the other piezo-siren is on.

The observed asymmetry could also be explained by the fact that the piezo elements used by the acoustic sources to produce their oscillatory movement are voltage-dependent and capacitance-dependent, the latter also changing with temperature. Very slight through moderate differences in the voltage or capacitance values to each piezo-siren element could delay the signal to one or both sources, which in turn would shift the location of the actual 0° degree phase angle between them. However, minima were observed at 180° apart from the maxima for all three cases, and the relative 0° degree phase angle did not go beyond $\pm 45^\circ$. Therefore, the shift between the expected or ideal phase angle and the actual phase angle was consistent in every case.

To have a better understanding of the chamber environment during these tests, the time history of the chamber pressure for a period of 6 ms during different transverse acoustic excitation conditions is plotted on the right set of graphs of Figure 5.18. The 0 ms point does not indicate the moment when data started to be recorded but it was an arbitrarily chosen point during the time the acoustics were on. The acoustic data shown for different phase angles in these set of graphs refers always to the case when both acoustic sources are on. In these graphs, the conditions where maximum and minimum pressure oscillations were obtained along with the baseline condition with no acoustic sources on are plotted. The top graph on the right, which represents a subcritical case, shows the chamber pressure for the 315° phase angle oscillating consistently between 1.51 and 1.56 MPa, compared with 1.52 to 1.54 MPa which then shifts to 1.53 to 1.55 MPa for the 135° phase angle.

The graphs in Figure 5.18 also include the baseline condition which shows that the pressure stays at 1.53 ± 0.01 MPa. For both the 135° and 315° phase angle conditions one can observe that the pressure follows a wave-like pattern, unlike the baseline condition, and the number of peaks for both phase angles is 18, which corresponds to a frequency of, or very close to, 3kHz for a period of 6 ms. In fact, a wave-like pattern should only be expected for a phase angle of 315° , where the maximum oscillations occur, and for the minimum oscillation condition the signals should cancel as shown in the 225° condition of Figure 5.15. The reason that this does not happen in the top right graph of Figure 5.18 is because the amplitudes of each acoustic source by itself are very different. This can be seen in the top graph on the left side, which shows an RMS value between 11 and 12 kPa for the left acoustic source and a value around 5 kPa for the right acoustic source. Therefore the oscillations reach a minimum at 135° but the signals never cancel because the amplitude of the signal from the right source is smaller than the amplitude of the signal from the left source. Incidentally, the number of peaks in the wave-like signal for the 135° condition is also 18 as expected.

In the middle graph on the right, the chamber pressure history for the nearcritical case is shown. In this case, the condition at 45° presents the maximum oscillations which fluctuate from 3.58 to 3.61 MPa. In contrast, the condition at 225° presents the signal with lowest pressure perturbation. In fact, its behavior is not wave-like but appears more noise-like. Its signal starts at its lowest point around 3.59 and reaches up to 3.61 in the 6 ms period but it is not oscillating between those two extremes but instead drifting from one to the other. The largest oscillations within the 225° condition occur near the 4.5 ms

mark with peak-to-peak amplitudes of 0.01 MPa. In this case, the left and right acoustic sources have values just above and below 6 kPa, which allow for better signal cancellation. The third signal is the baseline, which stays near 3.59 MPa up to the 4 ms point, where it starts going slightly below this value but still very close, showing how little perturbation, if any, the chamber experiences when there are no acoustics present.

Finally, the bottom graph on the right shows a supercritical case where the condition of maximum pressure perturbation took place at 0° , where it is normally expected. The wave-like pattern features 18 peaks with oscillations which range from just under 4.98 MPa to halfway between 5.00 and 5.01 MPa. The minimum pressure oscillations occur at 180° where the oscillations stay between 4.99 and 5.00 MPa for almost the entire 6 ms period. In contrast, the baseline condition performs erratically but does not show any wave-like or high-frequency pattern; its behavior most likely due to a transitional period after adjusting the pressure during testing.

It can be noted that, though sometimes there was some discrepancy in the value of the phase angle at which the minimum and maximum pressure fluctuations occurred for different cases, the coaxial jet was always exposed to a full range of acoustic conditions from a minimum to a maximum in velocity and pressure perturbations. In consequence, an analysis of these different acoustic conditions on the jet behavior could be performed to quantify and understand their effects on the mechanics of the jet by looking at parameters such as the dark core length and the spreading angle of the outer and inner jets.

5.2.6 Behavior during Exposure to Acoustic Excitation

In this section, images of the coaxial jet at each phase angle for three different cases at each of the three pressure regimes studied are shown. The behavior of the jet is described and the important features are highlighted. The baseline images are also included to compare its dynamics with and without acoustic excitation. The first set of images is shown in Figure 5.19. It corresponds to the case where $J = 0.17$ with and without forcing. At this low momentum flux ratio at subcritical pressures the jet is usually thin. The overall behavior of the jet does not change substantially with and without acoustic forcing but an increase in mixing can be observed. For the 0° and 315° conditions the inner jet starts spreading and breaking up into smaller dark core sections that mix with the outer jet towards the middle of the image. In contrast, the 135° and the baseline conditions show very little spread and the core only starts to break up towards the bottom of the image. These images feature the largest dark core lengths of the subcritical tests.

The second set of subcritical images corresponds to a momentum flux ratio of 2.6. The effects of the acoustics in this set of images, shown in Figure 5.20, are very clear. The inner jet dark core bends significantly for every phase angle reaching a maximum at 180° . Mixing improves significantly with large regions where the dark core structures have almost completely blended with their surroundings. This effect is particularly enhanced for phase angles between 45° and 215° . For the rest of the conditions a few dark fluid structures can still be observed throughout the image, but for the phase angle range mentioned the images show very few dark structures beyond certain point near the

center. This sequence of images shows that the effects of high velocity fluctuations (pressure node conditions) due to acoustic forcing are very strong and can make a difference in practical systems operating near this momentum flux ratio.

The next set of images for the subcritical case is shown in Figure 5.21 and corresponds to a momentum flux ratio of 9.6. All the images feature a very thick dark core which differs substantially from the thin dark core regions observed in the previous two sets of images. This thickness is evidence that the high momentum flux of the outer jet is having a strong effect on the inner jet allowing it to expand very rapidly across the recirculation region at the exit of the injector. The recess length of the inner jet hides this phenomenon and we only observe a thick jet emanating from the exit of the injector. Even at this high momentum flux ratio the dark core region is affected by the acoustic forcing as seen by the curvature of the inner jet for all phase angles, an effect that might not be obvious if only the effects of the dark core length are considered.

Finally, the set of images for the subcritical case corresponding to a momentum flux ratio of 23 appears in Figure 5.22. The dark core seems to be even thicker than the case for $J = 9.6$. The shape of the dark core does not seem to vary at all among the images and the only difference is the slight change in curvature at towards the bottom of the dark core for different acoustic conditions, which is evidence of the effects of acoustic excitation even at these high momentum flux ratios. In fact the forcing induces strong oscillations on the already mixed coaxial jet flow towards the middle of the image. However, as pointed out in the previous case, this behavior is not taken into account since only the effects of the dark core length are being considered.

The set of images shown in Figure 5.23 corresponds to the nearcritical case with $J = 0.55$. In this case the inner jet shows an already perturbed behavior with structures emanating from the dark core region in an outward fashion. This could be evidence of the interaction of the denser, faster inner jet flow with the slower and lighter outer jet. However, this oscillating pattern is not enhanced by acoustic forcing as noticed in the rest of the images. In fact, near the 180° phase angle the wavy structures seem to be suppressed. On the other hand, the dark core length provides visual evidence of acoustic forcing. A specific phase angle for which the dark core is shorter cannot be clearly chosen but the general trend is that the dark core region ends sooner for all phase angles compared to the non acoustics condition. Interestingly, acoustic forcing in this case seemed to affect the dark core length and not change the spreading angle. This behavior is opposite to the one observed for the subcritical case with a large momentum flux ratio, where the curvature of the core was affected but not the dark core length.

The next set of images, shown in Figure 5.24 corresponds to the nearcritical case with a momentum flux ratio of 4.9. In these images the effects of acoustics can be noticed on both the dark core length and its spreading behavior. The baseline image shows a thick jet as it exits the injector that eventually gets thinner as it mixes with the surrounding fluid. This effect is not only enhanced for the dark core under acoustic forcing but it actually adds a curvature to the dark core region that was not present in the baseline case. The overall effect of this transversal motion of the jet is a shorter and slightly thinner dark core that shows noticeable bending which enhances mixing even further.

The nearcritical set of images for the test with the highest momentum flux ratio for this pressure regime is shown in Figure 5.25. The baseline case shows an extremely short dark core region that is completely entrained by the outer jet just a few diameters downstream the exit of the injector. The rest of the images with acoustic forcing are quite similar to the baseline case. They feature very short dark core regions and the spreading angle is almost non-existent. If there is an effect of the acoustics on the coaxial jet flow, it takes place after the two streams have completely mixed.

A final set of three different supercritical cases for different momentum flux ratios is presented here. The images in Figure 5.26 show the case for a momentum flux ratio of 0.33. This case features an inner jet region that is not smooth, from which fluid structures emanate right at the exit of the injector, which resembles the momentum flux ratio case $J = 0.55$ of the nearcritical regime. In both cases the difference in velocity and density across the two layers of fluid appear to develop these outward-moving structures. The dark core length of the inner jet under acoustic forcing does not change noticeably. The only clear image that shows a shorter dark core length occurs at 360° whereas the image at 180° shows a dark core length similar to that of the condition with no acoustics. The spreading angle also appears to remain roughly constant. Thus, clear effects of acoustic forcing are not evident here.

The following set of images shown in Figure 5.27 corresponds to the supercritical case at $J = 2.4$ at different acoustic excitation conditions. The dark core length of the baseline is considerably longer than those observed for the cases under acoustic forcing. There is also evidence near the exit of the injector that the inner jet is

being bent by the acoustic field. The curvature that is observed in the jet with acoustics does not appear at all in the baseline image. The spreading and bending associated with the forced conditions produced a well mixed flow earlier than the case without acoustics, which shows a grey region that is very dark towards the bottom of the image, and it does not appear in the rest of the images with acoustics. The closest image to resemble the baseline flow behavior is the condition at 135° and even for that image the dark core length and the spread angle right at the exit are quite different.

The images in Figure 5.28 correspond to a momentum flux ratio of 9.9 at a supercritical pressure. In these images all dark core lengths are very short and therefore look very similar. This case resembles closely the nearcritical case with the momentum flux ratio of 9.3. In both cases the momentum flux of the outer jet is an order of magnitude larger than that of the inner jet. The faster gaseous flow shears off fluid from the thick inner jet very rapidly and leaves a very short dark core region. The only difference that is observed between these two cases is the effect of the acoustics on the spreading angle or bending of the inner jet. The images in this supercritical case do appear to have some curvature due to the effect of acoustics. In particular, the conditions between 135° and 270° feature a short, bent inner jet to the right that is different from the baseline case. Also, some of the images, such as the conditions at 45° and 135° show a gray, less dense structure that continues to show curved features a few diameters downstream; however, their boundaries are difficult to discern.

5.2.7 Dark Core Length Results in the Presence of Acoustic Excitation

The results of the dark core length measurements of the inner jet of the coaxial jet flow are presented in Figs. 5.29 to 5.31. The figures show a series of plots with the dark core length measurements on the vertical axis and the different acoustic conditions on the horizontal axis. A secondary axis shows the amplitude of the pressure oscillations as a fraction of the recorded mean chamber pressure for that case. The first value on the horizontal axis is the baseline measurement without acoustics followed by the measurements of the dark core length with acoustics starting with a 0° phase angle between acoustic sources and then in steps of 45° until a full cycle is achieved at 360° . All the values are normalized by the baseline condition of the case, which is the length of the dark core without acoustics. The error bars show the composite uncertainty of the non-dimensional length variable, $L_{\text{acoustics}}/L_{\text{no acoustics}}$, using one standard deviation as the uncertainty of each measured variable.

The values of the dark core lengths for the tests at subcritical pressures are shown in Figure 5.29. As a reminder, the tests at subcritical pressures represent a two-phase coaxial jet flow, where the inner jet is in liquid state at a temperature below the critical temperature of N_2 , and the outer jet is in a gaseous state at a temperature above the critical temperature of N_2 .

The subcritical tests showed that for $J = 0.17$, the length of the dark core changed noticeably with acoustics. It was shorter or equal to the baseline for all conditions with the exception of the 225° phase angle, where the length was 4% larger, which is not meaningful due to the large uncertainty. The largest dark core also coincided with the

condition of lowest pressure perturbations. The dark core length results for $J = 1.0$ do not show any trend, in contrast with the corresponding acoustic measurements which show a wave-like pattern.

For $J = 2.6$, a sinusoidal-like pattern, similar to the $J = 0.017$ case, is observed in the length. The value goes as high as 80% the baseline value and decreases below 60%. The pressure oscillations seem to follow the pattern, except at a 90° phase angle, so that the lowest pressure oscillations occur at the same conditions as the largest changes in length. For $J = 4.2$, the data shows a clearer trend with smaller uncertainty. It has its lowest length values when acoustic forcing is the largest and vice versa. The pressure data have an evident sinusoidal shape. For $J = 9.6$, there is some change in the length with acoustics, which stays between 80% and 90% of the baseline value. The effects of the outer jet entraining more and more fluid from the inner jet can be seen here. For $J = 23$, the outer jet has even more momentum flux compared to the inner jet, making the dark core very short and irresponsive to the acoustics, the change in length stays between 90% and no change with respect to the baseline value. The large uncertainty in the data did not allow a conclusive statement for most J values but the general trends could still be observed.

The next set of graphs shown in Figure 5.30 show the results for the tests performed at nearcritical pressures. At these pressures, the coaxial jet flow had only one supercritical phase present since both the temperature and pressure of the inner and outer jet, as well as the surrounding environment, was above the critical temperature and pressure of N_2 . The results show that at $J = 0.55$ the change in length of the dark core

varies between 60% and 80% of the baseline value, which indicates a definitively strong effect of the acoustics on the jet. A similar effect is observed at $J = 1.0$ and $J = 1.1$, where most of the lengths obtained under acoustic forcing remain between 60% and 80%, although there are a couple of conditions, 90° and 180° at $J = 1.0$ where the length does not change much with respect to the baseline, and the acoustic data does not have any particular pattern that might account for that behavior.

At $J = 1.6$, the change in length follows very closely the behavior of the pressure perturbations and the dark core lengths remain in a range between 70% and 90% of the baseline values. Then the largest effects of acoustics are observed for $J = 2.1$ and 2.9 . Both cases show an average change of length around 60% with respect to the baseline. Both cases have very similar acoustic fields and dark core length changes. The only difference for the $J = 2.1$ and $J = 2.9$ cases is in the behavior of the conditions at 225° , 270° and 315° , which do not follow a sinusoidal pattern for $J = 2.1$. The effect of the acoustics is also very clear in the $J = 4.9$ case. The length of the dark core changes between 70% and 60% of the baseline value for all conditions except at 45° , where it decreases only to 75% of the baseline value. These results show that at J values near 5, a relatively weak acoustic perturbation, in the order of one percent of the mean acoustic chamber pressure, can reduce noticeably the length of the dark core. For the last case, where $J = 9.3$, the results show that the dark core length hardly changes at different acoustic conditions. At this point, the momentum flux of the outer jet is almost 10 times that of the inner jet and it entrains a large amount of fluid from the inner jet. This results

in a very small dark core region at the exit of the injector, and a very short dark core length that does not get influenced by the acoustic field.

Thus from the nearcritical pressure tests and within the limits imposed by the calculated uncertainty, a significant reduction of the dark core length with respect to its non-forced value is observed during acoustic excitation at moderate J values. This decrease in the length, and therefore enhancement of mixing is achieved in the $1 < J < 5$ range. At higher outer to inner jet momentum flux values the outer jet starts to entrain a significant amount of fluid from the inner jet inhibiting the effects of the acoustic field on the dark core.

The third set of plots in Figure 5.31 presents the values of the dark core lengths for the tests at supercritical pressures. These results also represent single-phase coaxial jet flow since the chamber, the inner jet, and the outer jet are at supercritical temperature and pressure conditions. All the plots show well defined acoustic fields with minima between 180° and 225° . The amplitude of acoustic forcing does not go over 0.75% of the mean chamber pressure. The first two supercritical cases, which are below $J = 1$, show a moderate effect of the acoustics on the dark core. For these cases, most of the dark core lengths with acoustics on fall within the range of 80% to 90% of the baseline length. However, they do not show any trend with phase angle.

For the supercritical case at $J = 1.3$, all the dark core lengths are within 60% to 80% that of the baseline, but no trend is found either. The cases where $J = 2.4$ and 2.5 show a reduction of the dark core that sets the length with acoustics below 60% of the baseline length for some phase angle conditions whereas only one phase angle condition

from both cases presents a dark core length that is over 80% of the baseline length. Finally, similar to the nearcritical case for $J = 9.3$ in Figure 5.30, a supercritical case for which $J = 9.9$ is shown. This test shows a moderate increase of the dark core length with acoustics for half of the conditions. This might be attributed to a short baseline value extracted. However, since the momentum flux of the outer jet is significantly higher than the momentum flux of the inner jet, a very small dark core region at the exit of the injector is expected and effects such as a longer dark core length with acoustics are possible.

From the supercritical pressure tests, within the limits of the uncertainty, a reduction of the dark core length similar to that observed for the nearcritical cases was accomplished. Again, the largest effects on length decrease and mixing enhancement were achieved in the $1 < J < 3$ range. For higher values, the inner jet starts to lose its core in a very rapid fashion to the outer jet which makes very difficult to distinguish the effects of the acoustic field on the dark core.

To assess the effect of the pressure on the coaxial jet flow, dark core length changes at different pressures for a given outer to inner jet momentum flux ratio are presented next. The ratio of the length of the dark core with acoustics to the length of the dark core with no acoustics ($L_{\text{acoustics}}/L_{\text{no acoustics}}$) and the peak-to-peak pressure perturbation as a percentage of the mean chamber pressure ($\Delta p_{\text{peak-to-peak}}/p_{\text{mean}}$) both as a function of the phase angle between acoustic sources are shown in Figure 5.32. Although $\Delta p_{\text{peak-to-peak}}/p_{\text{mean}}$ is not 0% for the baseline conditions, it is still below the rest of the values that correspond to the conditions with acoustic forcing. The quantity shown

represents the noise measured by the pressure transducer. In this series of plots, the uncertainty of the dark core length results is not included, to avoid cluttering of the graphs. The uncertainty values can be obtained from Figs. 5.29 to 5.31.

Despite the relative acoustic excitation intensities varying several times from supercritical to subcritical conditions, the reduction in normalized dark core length ($1 - L_{\text{acoustics}}/L_{\text{no acoustics}}$) at most phase angles for $J \approx 1.0$ ranged from 20% to 40%. Even with the large uncertainties associated with these results, the large amount of data that fall in this region shows that the acoustics have an effect at a value of J close to 1. When the outer to inner jet momentum flux ratio approaches 2.5 a similar trend is observed. The normalized dark core length now has a broader range reaching values as low as 50% of the baseline length and as high as 90% of the baseline length. The large spread could be a consequence of the inherent uncertainty of the measurements but still shows that acoustic forcing produces a clear shortening effect on the dark core length for J values near 2 to 3 as well.

For outer to inner jet momentum flux ratios near 10, the largest reduction in the dark core length ($1 - L_{\text{acoustics}}/L_{\text{no acoustics}}$) is at most 20%, usually at subcritical pressures. Both nearcritical and supercritical cases show little or no reduction in their dark core length, in fact some of the data indicates that the dark core lengths actually increased in some cases. However, this phenomenon is the consequence of very small dark core lengths at these high J values. Also at these conditions and especially true for near and supercritical conditions, the dark core does not show any response to acoustic forcing since most of the flow has been entrained by the outer jet and thus mixed with the rest of

the fluid in the chamber, leaving a short dark core that usually does not show interesting acoustic behavior. Overall, these results show a very interesting trend which suggests that normalized dark core length behavior could be independent of mean chamber pressure; however, the large uncertainties in the measurements still prevent us from a definitive conclusion in this regard.

A plot that compiles all the dark core length data is shown in Figure 5.33. To make this graph, the difference between the baseline length or the average length of the dark core with no acoustics and the average length of the dark core with acoustics ($L_{\text{no acoustics}} - L_{\text{acoustics}}$) was determined for each phase angle at a given p_{mean} and J , and the maximum value was selected. This quantity was termed “maximum dark core length reduction”, ΔL , normalized by the average length of the dark core with no acoustics ($\Delta L/L_{\text{no acoustics}}$), and plotted versus J for all cases. The overall trend for all pressure conditions shows that at very low outer to inner jet momentum flux ratios the normalized maximum dark core length reduction drops below 30%. Next, the range of values of J between 0.5 and 5 shows reductions in normalized dark core length between 30 to 50%. All cases with a J greater than 5 shows that the normalized dark core length decreases at most by 20%. This plot suggests a range of outer to inner jet momentum flux ratios from 0.5 to 5 where acoustic forcing has more influence on the axial dark core length of the coaxial jet and thus in the mixing processes that characterizes it.

5.2.8 Inner Jet Spreading Angle Results in the Presence of Acoustic Excitation

In this section we analyze the behavior of the inner jet spreading angles with an externally imposed transverse acoustic field. The results obtained under acoustic perturbation could perhaps be used by a designer as a measure of the lateral spread expected from one coaxial element under similar conditions. Knowing this would facilitate the selection of a safe distance between injector elements if one wants to avoid any interaction between them. It also gives the designer a good idea of the amount of mixing that it would be expected from these elements under different conditions.

The analysis will focus on the effects of both the magnitude and gradient of the pressure and velocity fields on the coaxial jet flow, specifically on the inner jet spreading angles at subcritical to supercritical pressures. As previously indicated, the relative position of the jet with respect to the pressure and velocity acoustic field is varied by alternating the phase between the two acoustic resonators.

First we will examine the spreading angles at subcritical pressures. At low momentum flux ratios the maximum spread angles are small. The images for $J = 0.17$ in Figure 5.19 as well as the upper-left plot in Figure 5.34 show this behavior. For this case, the inner jet dominates the behavior of the coaxial jet, entraining and bending the outer jet towards itself since the higher density of the inner jet is 20 to 30 times the density of the outer jet and surrounding plenum. With both jets having similar mass flow rates, the flow surrounding the inner jet is simply not substantial enough to affect its behavior. When the acoustics are turned on, no discernable effect is seen, either visually in Figure 5.19 or quantitatively in Figure 5.34.

Acoustics in the range studied here do not seem to strongly affect low J coaxial jets, since they do not seem to produce a significant reduction of the mean axial dark core length or increase of the maximum spreading angles of the inner jet. As J increases to 1, a slight effect is observed with phase angle (see upper-right plot in Figure 5.34). Specifically, the maximum acoustic spread angle tends to achieve its largest value around a phase angle of 180° . This agrees with subcritical results at $J = 2.6$ where the mean axial dark core length is reduced the most at or near a phase angle of 180° , which corresponds to a velocity antinode (pressure node). At $J=2.6$, the maximum acoustic spread angle increases continuously with phase angle reaching a maximum at a phase angle of 180° as shown in Figure 5.20 and the middle-left plot in Figure 5.34. In fact, the maximum acoustic spread angle recorded for this case at a phase angle of 180° is the one of highest from all cases at all phase angles.

For the $J = 4.2$ case, we see a slight peak of the maximum acoustic spread angle at a phase angle of 135° , not far from the phase angle where we would expect the largest value which is 180° . Overall, we can conclude that for this range of J values, we observe the largest maximum acoustic spread angles when the jets are exposed to an acoustic field which has a velocity antinode at the location of the jet (for our case, when the two sources are at a 180° phase angle).

As we move to the case where $J=9.6$, shown in Figure 5.21 and the bottom-left plot in Figure 5.34, we see a different behavior. In this case the inner jet achieves a uniformly high maximum acoustic spread angle, reaching a value as high as 38° , compared to its 7° maximum baseline spread angle. This large spreading occurs as long

as there is a source of acoustic excitation. This behavior is irrespective of the different acoustic conditions produced by the change in phase angle, which produces no statistically relevant change upon its spreading properties. This is surprising since the results from the previous section show that for $J = 9.6$ the percentage of shrinkage of the mean axial dark core length of the inner jet was smaller than for lower J values suggesting a smaller effect of acoustics on mixing. Also, the mean axial dark core length changed with phase angle whereas here the spread angle seems independent of phase. Finally as J increases to 23 shown in Figure 5.22, we find a flatter profile of the maximum acoustic spread angle as the phase angle is varied. Also, all the values of maximum spread angles have decreased compared to the case of $J=9.6$.

The eight nearcritical cases are presented in Figure 5.35 with momentum flux ratio varying from 0.55 to 9.3. The behavior of the jet at $J = 0.55$ (see Figure 5.23) shows a very flat distribution of the spreading angles at different acoustic conditions. Most angles, including the condition with no acoustics present, show a value near 10° . The only exceptions are the spreading angles obtained at a phase angle of 0° and 360° . At these conditions, the dark core bends more than the rest of the cases and the inner jet flow penetrates the outer jet and seems to reach the surrounding media.

The following three cases, $J = 1.0$, 1.1 and 1.6 , show a similar behavior. The values of the spreading angles fall between 10° and 20° and their corresponding baseline spreading angle values are also in that range. For these cases where J is near or less than 1, acoustic forcing has little or no effect on the spreading angles. However, for $J = 2.1$ the

average angles for the acoustic conditions are higher with a baseline value of 15° , which is similar to the lower J cases.

As J is increased to 2.9 and 4.9 a more enhanced behavior is observed. They have average values for the spreading angles under acoustic forcing that are significantly higher than their respective baselines. Both $J = 2.9$ and 4.9 have an average spreading angle with acoustics of over 20° and a baseline smaller than 10° . The effect of acoustics is the highest for these flow conditions. Finally, at $J = 9.3$, all the spreading angles are below 10° with an average below 5° . The reason for this behavior is the very short dark core length of the inner jet, pictured in Figure 5.25, which makes very difficult to capture any effect the acoustics might be having on it. The dark core itself is very straight until it mixes completely with its surroundings just a couple of inner jet diameters downstream the injector exit.

The final set of graphs in Figure 5.36 shows the results for the inner jet spreading angles in the supercritical regime. The first graph on the upper left shows the case for $J = 0.019$. The spreading angle shows a coaxial jet that is very slightly affected by the acoustic field. The baseline image (see Figure 5.6) shows a very long dark core with a large spreading. This large cone might be enhanced near the 180° condition due to large velocity perturbations in the transversal direction but otherwise stays close to the baseline value.

The $J = 0.33$ case also shows no response at all which can be somewhat concluded from the very similar coaxial jet images shown in Figure 5.26. Thus, in the first two cases all but one angle remain below 10° . In the following two cases ($J = 1.3$ and $J = 2.4$) the

spreading angles remain in the 10° to 20° range. The acoustics do not seem to have an effect on the jet. Even if the overall angles are greater, which can be attributed to a higher momentum flux ratio and thus more entrainment of the inner jet fluid by the outer jet irrespective of the acoustic conditions, the angles under acoustic forcing do not appear to be larger than their respective baselines.

The case at $J = 2.5$ shows some angles that increase beyond the spread of the baseline condition. It is the only set that has angles over 20° . This could occur because of dark core bending, which is then translated into curved surfaces that are interpreted as larger spreading angles. In contrast, the case for $J = 9.9$ is shown with different limits for its vertical axis. It starts at negative values to account for some negative angles that appear when the inner jet is immediately entrained into the outer jet as it exits the injector. This produces a ‘thinning’ of the jet (see Figure 5.28) that is processed as a negative angle. Eventually some positive angles are recorded when the jet is exposed to acoustic excitation. Figure 5.28 shows images of the inner jet at a very high momentum ratio for the highest pressure regime. Some of these photographs were noticeably curved towards the right, including the 270° condition which appears as the largest spreading angle (near 10°) for this particular case ($J = 9.9$).

An interesting observation from all cases at the three different pressure regimes is that for some moderate momentum flux ratios in the $1 < J < 5$ range, the inner jet seems to spread the most when it is located at or near a pressure node. This can be seen for the $J = 2.6$ and $J = 4.2$ cases (and slightly in case $J = 1.0$) in Figure 5.34, case $J = 4.9$ in Figure 5.35 and case $J = 2.5$ in Figure 5.36. This is evidence that the maximum velocity

perturbations taking place at this acoustic condition might be enhancing the spreading of the inner jet.

For a detailed summary of all the experimental data obtained with the original injector, refer to Table C.1 to Table C.4 in Appendix C.

5.3 Results with the New Coaxial Jet Injector Geometry

5.3.1 Behavior with and without Acoustic Excitation

As described in Chapter 4 a new injector was designed, built and tested at the Cryogenic Supercritical Laboratory. The following paragraphs will describe sets of images that show the response of the coaxial jet to the same levels of acoustic excitation that were employed for the tests with the original injector. To obtain similar outer to inner momentum flux ratios with the new injector than those obtained with the original injector, the mass flow rate of the inner jet had to be increased by a factor of three. This change in mass flow rate was necessary given the difference in the inner jet inner diameter between D_1 and $D_{1\text{new}}$ (see Figs. 4.4b and 4.5b) between the original and new injectors. The mean velocity of the inner jet with the new injector at the three different pressure regimes remained just under 1 m/s compared with the mean velocity of the original injector which was 2.2 m/s in the subcritical pressure regime and varied between 2.4 m/s and 6.6 m/s for the nearcritical and supercritical regimes (refer to Appendix C, Tables C.1 and C.5)

The first pressure regime to be analyzed with the new injector was the subcritical regime. The images shown in Figure 5.37 correspond to a momentum flux ratio of approximately 0.089. The first image shows the coaxial jet when no acoustics are present. The inner jet can be clearly distinguished from the outer jet and its surroundings. The thickness of the inner jet stays constant throughout the image. The non-dimensional dark core length in this case is longer than $14 L/D_{\text{new}}$, which is expected based on the results from the original injector at similar momentum flux ratios.

The response of the inner jet with acoustic excitation is depicted in the images in Figure 5.37. For the phase angles from 0° to 90° the inner jet bends noticeably too and there is strong atomization taking place near the injector exit. The background flow of the chamber is difficult to notice and the dark core region is somewhat thicker and blurred. The next two images show a perturbed, but straight, inner jet. The images corresponding to a phase difference between 225° and 315° show the liquid stream from the inner jet shortened significantly, with large structures of liquid that have been separated from the inner jet flowing downstream. The last image seems to return to the behavior seen at a 0° phase angle.

It is interesting to notice that the images that show the greatest contrast in the inner jet behavior with acoustics correspond to a phase difference of 135° and 315° , which would correspond to the pressure node and pressure antinode locations. The 135° image shows an inner jet with a fully connected dark core region. In contrast, the 315° image shows the inner jet being completely disintegrated into large liquid structures just a few inner diameters after leaving the exit. A strong response to acoustics at this very low

momentum flux ratio was not expected given the results obtained with the original injector. Also, the effect of the acoustic field on the integrity of the inner jet is something that was not observed with the original injector before.

A possible cause of this phenomenon is the change in geometry from the original injector to the new injector. As discussed previously, the original injector featured a very thick inner jet post which created a large recirculation zone between the inner jet and the outer jet at the exit of the injector. This recirculation zone could have damped the pressure and velocity fluctuations, which instead of affecting the inner jet directly, modified the dynamics of the recirculation zone (42) which in turn altered the dynamics of the inner jet at the exit. That would explain the smooth back-and-forth oscillations of the inner jet that were characteristic of “strong evidence of acoustic excitation” with the original injector. However, without such a large recirculation zone, the pressure and velocity fluctuations could be having a direct impact on the inner jet flow and that might explain the very strong atomization taking place right at the exit of the injector for every acoustic condition regardless of phase angle.

The group of images in Figure 5.38 shows the coaxial jet at a subcritical pressure of 1.49 MPa and a momentum flux ratio of 0.43. The baseline condition has a dark core that spans the whole length of the image; however, compared with the same condition in Figure 5.37, this dark core region is not as smooth and features fluid structures from the inner jet moving outwards to the outer jet. This shreds of fluid that seem to be shed away from the inner jet might be evidence of instability at this momentum flux ratio, since this

behavior was also observed in the original injector at nearcritical and subcritical pressures for similar momentum flux ratios (see Figs. 5.23 and 5.26).

There is also a striking response of the coaxial jet to acoustic excitation in this case. The flow at 0° and 45° shows an inner jet that starts shearing off fluid outwards just as it exits the injector and is convected downstream, as the fluid travels away from the inner jet, it starts slowing down. It seems to “wrap around” the fluid in the dark core assuming the shape of an inverted mushroom. The excitation is so violent that the dark core is fully mixed by the time the flow reaches the center of the picture and the spreading angle is very large. This is an “expanding” effect. However, as the phase angle varies from 135° to 180° a different behavior takes place. The inner jet is widened at the exit but as it reaches the center of the image it gets very thin, just to spread out again in an hourglass shape fashion. This effect seems to “compress” or “pinch” the inner jet flow. These two effects are separated by 180° , with the relaxing effect taking place near the pressure antinode location and the compressing effect near the pressure node location. The conditions at 90° and 225° show a transition between these two different responses and the last two images (315° and 360°) show the same behavior as the first two images described in this paragraph (0° and 45°).

The set of images in Figure 5.39 show the coaxial jet behavior at a subcritical pressure of 1.49 MPa and momentum flux ratio of 2.0. The baseline condition shows a dark core region that does not extend the whole length of the image, in contrast with the previous two cases. In the first few inner jet diameters after the exit of the injector the dark core region is thick and connected, then it starts being sheared apart

by the outer jet and becomes thinner with shreds of flow extending from the core towards the end. At the bottom of the image only a very thin dark core region, which is most likely unconnected from the main core, remains. In comparison, the response of the coaxial jet to acoustics for this J value is very similar to the response to the previous value of $J = 0.43$. The only noticeable difference is that the images at 135° and 180° do not show an hourglass shape but instead they seem to show similar dynamics to the baseline condition and even a longer dark core region.

The following subcritical case, shown in Figure 5.40, features a momentum flux ratio of 7.8. The high momentum flux of the outer jet is capable of entraining enough flow from the inner jet to end the dark core region towards the middle of the image, and in the bottom portion only a few dark spots are observed with mostly mixed flow. The behavior with acoustics is similar to the “expanding” case for $J = 0.43$ and 2.0, although the structures are clearer for this case. Again, at 0° and 360° phase angle the structures are periodic, extend outward and wrap around forming eddies and near 180° phase angle the image is very similar to the case with no acoustics.

The last of the subcritical cases presented here is shown in Figure 5.41. It features a baseline that has the shortest dark core of all the five subcritical cases with the new injector, as it would be expected for this case at a momentum flux ratio of 18. In this case the effect of the acoustics are still visible with a very short dark core at a 0° and 360° phase angle and longer dark cores near the 180° phase angle. The no acoustics case does not show eddies and similar structures that extend outwards from the inner jet and seem to bend up but they are very clear in almost all the images showing acoustic excitation

conditions. For the new injector, acoustic effects are noticed in the dynamics of the dark core at subcritical pressures for momentum flux ratios near 20, since the dark core is still long enough to interact with the acoustic field, unlike the original injector where the effects of acoustics could not be adequately quantified by measuring the short dark core region from the images at these high J values.

The following paragraphs describe four sets of images that show the coaxial jet with the new injector exposed to nearcritical pressures. For the new injector tests, the heat exchangers were improved to increase cooling efficiency. The result led to inner jet temperatures below the critical temperature of nitrogen. In consequence all the following cases features two phase flow, with the inner jet being in a liquid-like phase (nearcritical pressure but below critical temperature) at the exit and the outer jet and surrounding chamber fluid in a supercritical state.

The first set of nearcritical images corresponds to a momentum flux ratio of 0.50 (see Figure 5.42). The baseline case shows a slightly spreading, thick inner jet dark core that extends for the entire image. The outer jet is smooth at the exit and follows the dynamics of the inner jet. The acoustic conditions are not too different from the baseline. Some of the images show a thinner inner jet (90° and 180°) but the most interesting effect is that there is no similar spreading in the acoustic cases. An interesting condition took place at the 315° phase angle which corresponded to the maximum pressure perturbation for this case as seen in Figure 5.48. The inner jet was completely obliterated by the acoustic field and the dark core was completely dispersed across the region at the exit of the injector depicted by the image. This could be an indication that there exists a

threshold amplitude that was surpassed at the 315° phase angle condition for this particular injector geometry; an amplitude above which the thin shear layer between the inner jet and outer jet cannot damp the pressure and velocity fluctuations and the liquid inner jet becomes rapidly mixed with its surroundings.

The images shown in Figure 5.43 show a nearcritical case with a momentum flux ratio of 2.2. The images are similar to the nearcritical case $J = 0.50$ in Figure 5.42. For this J value, an even more uniform behavior across all conditions, including the baseline, is observed. All images feature a steady spread of the inner jet dark core and evidence of mixing towards the bottom of the picture where gray areas can be observed between the darker inner jet and the outer jet. In this case, the coaxial jet had no noticeable response to acoustic excitation.

The coaxial jet at a momentum flux ratio of 9.4 for the nearcritical pressure regime is shown in Figure 5.44. It behaves in a similar fashion to its subcritical counterpart with $J = 7.8$ in Figure 5.40 but the structures that shed from the dark core are not as pronounced, with the most noticeable ones taking place at the 45° phase angle condition. This nearcritical case appears to have the shortest dark core length from all the different cases with the new injector. In the 360° condition one can observe a very short dark core that is quickly entrained by the outer jet and thus a gray region downstream that eventually mixes with its surroundings. In fact, all the images show this transition but they do so over longer distances from the injector exit.

A nearcritical case with momentum flux ratio of 19 is presented next in Figure 5.45. It features the shortest dark core of all nearcritical cases, as it is expected for the

case with the highest momentum flux ratio, whether using the original or new injector. Unlike the first two nearcritical cases shown, and only slightly perceived in the third one, a noticeable effect of the acoustics on the coaxial jet is observed on the length of the dark core when compared between the baseline condition and the rest of the images at different phase angles. It seems that for this particular geometry, very high momentum flux ratios are needed to shorten the jet to an adequate length so that the pressure and velocity perturbations can interact with it and display visible acoustic phenomena.

The last set of images presented here from the new injector tests show the coaxial jet at a momentum flux ratio of 2.6 at supercritical pressures in Figure 5.46. The behavior is basically the same as the one observed for its nearcritical counterpart in Figure 5.43. It has a slightly spreading inner jet angle with some structures shearing of the dark core towards the bottom of some images. The gray region between the inner jet and the outer jet indicates that mixing is taking place at the boundary between the two streams. At this condition there is no observed response to acoustics at any phase angle.

5.3.2 Dark Core Length Results with and without Acoustic Excitation

The results of the dark core length measurements of the inner jet of the coaxial jet flow with the new injector are presented in Figs. 5.47 and 5.48. The figures show a series of plots with the dark core length measurements on the vertical axis and the different acoustic conditions on the horizontal axis. A secondary axis shows the amplitude of the pressure oscillations as a fraction of the recorded mean chamber pressure for that case. The first value on the horizontal axis is the baseline measurement without acoustics

followed by the measurements of the dark core length with acoustics starting with a 0° phase angle between acoustic sources and then in steps of 45° until a full cycle is achieved at 360° . All the values are normalized by the baseline condition of the case, which is the length of the dark core without acoustics. The error bars show the composite uncertainty of the non-dimensional length variable, $L_{\text{acoustics}}/L_{\text{no acoustics}}$, using one standard deviation as the uncertainty of each measured variable.

In some cases, particularly the ones with lower momentum flux ratios, the dark core extended beyond the vertical length of the examination window used for these tests at some or all phase angles. In order to highlight those acoustic conditions, zero, one or two asterisks were placed next the phase angles on the horizontal axis labels. No asterisks indicate that less than 10% of the images had a dark core length that extended beyond the field of view. One asterisk means that between 10% and 50% of the images had dark cores that were longer than the field of view and two asterisks mean that the dark core was longer than the field of view in 50% or more of the images used to extract its length. The values of the dark core lengths for the tests at subcritical pressures are shown in Figure 5.47. These tests at subcritical pressures represent a two-phase coaxial jet flow, where the inner jet is in liquid state at a temperature below the critical temperature of N_2 , and the outer jet is in a gaseous state at a temperature above the critical temperature of N_2 . The dark core length for the coaxial jet obtained with the new injector was analyzed using a new routine in MATLAB based on the one used to analyze the cases with the original injector so that inner jet spreading angles could be measured even if the dark

core length was not quantifiable, since the previous routine was not designed to process images with dark cores that extended beyond the field of view.

The behavior of the case with J equal to 0.089 had very long dark cores even when acoustic excitation was applied. The only condition that showed a short core length was the 315° phase angle. Images from this case can be seen in Figure 5.37. In the following two cases, with $J = 0.43$ and 2.0 the dark core length was measurable for half of the phase angles. The conditions for which the dark core was too long were those near the pressure node as indicated by the pressure data shown in the plots. Of relevance here is the dark core reduction at the rest of the conditions (see Figs. 5.38 and 5.39). These cases show dark core lengths between 50% and 60% that of the baseline for the phase angles away from the pressure node. The reduction in dark core length for the acoustic cases is actually larger since the length of the baseline cases was limited by the examination window. This means that the baselines of both cases are in fact longer and the relative dark core lengths at the acoustic conditions away from the pressure antinode are smaller.

For the next two plots in Figure 5.47, for J equal to 3.4 and 5.2, the same trend with phase angle can be observed. Most dark core lengths away from the pressure node show a 60% reduction compared to the dark core length of the baseline condition for both cases. The dark core length then increases as the phase angle approaches the pressure node location, where it reaches a maximum. In fact, the dark core length for the cases between $J = 0.43$ and 5.2 show the same qualitative behavior. Also, the plots for $J = 0.43$ and 2.0 appear as truncated versions of the ones for $J = 3.4$ and 5.2. Whether the

qualitative behavior between these 4 cases is the same is uncertain but the fact that the dark core lengths in the baseline cases for $J = 0.43$ and 2.0 are longer indicate that the qualitative results shown in their respective plots are conservative and could potentially match the reduction seen for the following two cases at $J = 3.4$ and 5.2 .

The last three plots in Figure 5.47 show the reduction in the dark core length for $J = 7.8, 12$ and 18 . Images for two of these cases are shown in Figs. 5.40 and 5.41. These plots show a smaller reduction in dark core length compared to the baseline case than the reduction in the lower momentum flux ratio cases. The dark core lengths for the higher J value cases were reduced between 58% and 93% of their corresponding baseline. Considering all the different conditions, the dark core length reduction in the $J = 7.8$ case was not as large as the reduction in the $J = 12$ and 18 cases. This effect might be due to transitional behavior between low and moderate momentum flux ratio cases and the high momentum flux ratio cases.

The general trend observed in these measurements consists of longer dark cores near the pressure node and very short ones near the pressure antinode. The reason for this behavior is not well understood and in fact is contrary to what was expected from experiments with the original injector. One of the possible explanations might involve the lack of recirculation zone in the new injector. The recirculation zone could be responsible for the bending of the jet at high velocity fluctuations but in the case of the new injector this recirculation zone is non-existent and the bending does not take place, thus a straight dark core is observed.

The following set of plots in Figure 5.48 show the behavior of the dark core length for the cases obtained when the pressure was above the critical point. The lower four momentum flux ratio cases have flat profiles, indicating that the dark core lengths were always as long as the baseline case. In fact, all conditions for these four momentum flux ratios showed dark cores longer than the field of view, explaining the results. Images for three of these four cases can be seen in Figs. 5.42, 5.43 and 5.46. Pressure profiles show that the coaxial jet was exposed to maxima and minima in pressure perturbations ranging from 0.2% to 1% of the mean chamber pressure; however, no effect on the dark core was seen. There were some instances, as in the 315° condition for the nearcritical case with $J = 0.50$ (see Figure 5.42), where the acoustic excitation modified significantly the mechanics of the jet. Dark core lengths and spreading angles were not reported for such cases because the jet behavior departed significantly from the rest of the conditions. This behavior was observed at various J values near the pressure antinode condition at sufficiently high acoustic amplitudes. The nature of this phenomena is believed to be due to the lack of recirculation zone near the injector exit allowing high pressure fluctuations to interact with the inner jet leading to a violent disintegration of the dark core.

The results of the remaining three nearcritical cases; however, show very interesting trends that match those of the subcritical results of the new injector. For instance, the nearcritical case with $J = 4.6$ shows a very large reduction in the dark core for conditions near the pressure antinode, with the value of the dark core length with acoustics close to 40% that of the baseline condition. In fact, this percentage could be

even lower because the dark core length was underestimated for the baseline of this case, similar to the results for the $J = 2.0$ subcritical case. As the pressure node condition is approached, the dark core increases its length, reaching a maximum near a 180° phase angle. This behavior was also observed for the subcritical cases with momentum flux ratios of 3.4 and 5.2 (see Figure 5.47).

The nearcritical case at $J = 9.4$ followed the same trend as the $J = 4.6$ case and reached a maximum near the pressure node. The greatest reduction of the dark core happened at the pressure antinode and was almost 50% of the dark core length of the baseline. This behavior is similar to the subcritical case at $J = 12$. Finally, the nearcritical case at $J = 19$ had a smaller reduction in the dark core length, with the minimum dark core length consisting of two-thirds of the baseline length and being located again at the pressure antinode location. The maximum dark core length with acoustics was obtained for a phase angle of 180° , very close to the pressure node indicated by the pressure measurements.

A comparison of the dark core length behavior for a given momentum flux ratio between the subcritical and nearcritical pressure regimes is shown in Figure 5.49. A remarkable feature of these plots is the agreement in the relative dark core lengths between subcritical and nearcritical cases. For a J value close to 5, the maximum pressure oscillations normalized by the mean chamber pressure are almost twice as much for the subcritical case compared to that of the nearcritical case. In contrast, for J near 20, the relative acoustic forcing is almost the same. Nonetheless, for each momentum flux ratio, the maxima and minima in normalized dark core length between subcritical and

nearcritical pressures are very similar, regardless of the relative pressure oscillation. Therefore, the relative effect of the acoustics on the dark core length with the new injector for similar momentum flux ratios agrees with the results obtained with the original injector (see Figure 5.32). Given the differences between the inner jet characteristics of the original and the new injector (inner post thickness, inner jet diameter, inner jet velocity and temperature), the agreement in dark core length results for the same J values indicates that this parameter could in fact reduce the data for a given geometry regardless of its characteristics. Further evidence of this observation could have important repercussions in shear coaxial injector design.

A plot of the difference between the shortest dark core length for a given case and its corresponding baseline is shown in Figure 5.50. This graph shows agreement between subcritical and nearcritical cases with $J > 3$ with the new injector. Except for the subcritical case with $J = 7.8$, all cases follow a trend that steadily decreases from over 60% change for moderate momentum flux ratio cases to under 40% for high momentum flux ratio cases. The low value of this maximum change in dark core length for the subcritical case with $J = 7.8$ could point to a transitional behavior between momentum flux ratio cases up to 5 and cases at J values near 10 and above. Further tests in the $5 < J < 10$ range will be needed to assess whether the results obtained from the $J = 7.8$ case are an isolated phenomenon or the indication of a transition region between moderate and high momentum flux ratio jets.

When the results of both injectors are compared, (see Figure 5.51) two very distinct trends can be observed for each injector. If the subcritical, $J = 7.8$ case with the

new injector is neglected, it seems that the new injector allows for a larger reduction in dark core length for any given outer to inner jet momentum flux ratio. There could be various mechanisms that will enhance the reduction with the new injector, chief among them the lack of a recirculation zone that dampens the effect of the acoustics on the inner jet. If the conclusions from these results and those from Figs. 5.32 and 5.49 are combined, it seems that the geometry of the coaxial injector has a larger effect than the chamber pressure when analyzing the effects of acoustic perturbations (and therefore acoustic instabilities) on the dynamics of a coaxial jet.

5.3.3 Inner Jet Spreading Angle Results with and without Acoustic Excitation

The spreading angle results for the new injector identify certain trends observed qualitatively in the images obtained from the high-speed camera. One of the most important features of the new injector is the tendency of the inner jet to decrease its size significantly at moderate momentum flux ratios and display a very exotic behavior with structures that are shed perpendicularly from the direction of flow with very strong atomization at the exit of the injector at or near the pressure antinode. In contrast, at the pressure node location the jet becomes very long and sometimes surpasses the length of the baseline. The large velocity fluctuations might cancel the effect of the outer jet on the inner jet allowing it to extend past its no acoustics length. The spreading angles are able to capture this behavior as it can be

seen at the pressure node locations in most subcritical and some nearcritical plots at various momentum flux ratios (see Figs. 5.52 and 5.53).

The first set of plots show the spreading angles for the subcritical cases in Figure 5.52. Despite having long dark core lengths, spreading angles from the low momentum flux ratio were measured successfully, showing very interesting behavior. For instance, for the first two subcritical cases show peaks at phase angles of 45° and 315° , close to pressure antinode locations. These spreading angles go as high as 25° for $J = 0.089$ and 15° for $J = 0.43$. They also show a minimum spreading angle of 0° near a phase angle of 135° , which is the location of the pressure node for these cases. Overall, the lowest momentum flux ratio ($J = 0.089$) shows a trend of decreasing spreading angle as the pressure node is approached. The second plot, which corresponds to a J equal to 0.43, does not show a trend but some response to the varying acoustic field can be observed from the results of some conditions near the pressure and velocity nodes.

Compared to the rest of the cases, the spreading angles for $J = 2.0$ show a weak response to acoustics. The minimum angle at 225° does not quite coincide with the pressure node at 135° . The rest of the spreading angles do not vary much (between 4° and 10°) and do not follow a discernable trend. In contrast, the spreading angles for $J = 3.4$ and 5.2 show an enhanced response to the acoustic field. It is easy to differentiate the baseline and the angles near a pressure node from the rest for these two cases. The minimum spreading angle near 5° in both instances coincides with the location of the pressure node at a phase angle of 225° . The next smallest are those near the pressure node

and the baseline cases. The rest of the spreading angles for those cases are higher than the minimum by approximately 10° .

The following case is similar in behavior to $J = 2.0$ since the angles do not show any response to the applied acoustic field. All angles for $J = 7.8$ vary between 3° and 6° with the maximum spreading angle happening at the baseline condition. In contrast, the spreading angles for the highest two momentum flux ratios behave quite similarly to the lowest two cases. They both have minima near their respective pressure nodes with a spreading angle of 5° for $J = 12$ and 7° for $J = 18$. As the phase angle changes toward a pressure antinode, the spreading angles increase reaching values over 15° for $J = 12$ and close to 25° for $J = 18$, indicating a strong response of the coaxial jet to the imposed acoustic field.

In contrast to the rich behavior observed in the range of subcritical cases, the long and straight dark core lengths of the first four lower momentum flux ratio cases of the cases above the critical point shown in Figure 5.53 produced results that did not show any response to the imposed acoustic field. The trend lines in these cases were almost horizontal with spreading angles for all phases ranging from 5° to 10° for almost all conditions. At moderate momentum flux ratios the trends did not improve much. For $J = 4.6$ and 9.4 the spreading angles varied from 2° to 11° and no clear response to phase angle variation or pressure node or antinode conditions was observed. The only case above the critical point that showed a clear response to the externally imposed acoustic field was $J = 19$. For this case, the smallest spreading angle was 5° at a phase angle of 180° and then 8° for a phase angle of 225° with one

condition at and the other near the pressure node location. The next smallest spreading angle was the baseline with 10° . The rest of the spreading angles were all higher than 15° . The trend formed by these angles was a coarse sinusoidal shape, showing the only clear response by the spreading angles to the acoustic field for a nearcritical or supercritical case with the new injector.

For a detailed summary of all the experimental data obtained with the original injector, refer to Table C.5 to Table C.8 in Appendix C.

5.4 Stability of Coaxial Jet Flows

The purpose of this section is to present a qualitative analysis of the stability characteristics of the coaxial jet flow presented in this study. In the present work two type of flow conditions were observed. One of them is the flow of a liquid with a coaxial gas stream around it. This flow was obtained at subcritical conditions. The second one was the flow of a jet supercritical fluid with high density surrounded by a coaxial stream of supercritical flow at a lower density. The latter was obtained when the pressure of the system was raised over the critical pressure of the fluid used in the experiments. This observation is important because instabilities might behave in a different manner when the surface tension varies greatly. For instance, Leib and Goldstein (51) report that Weber number impact the onset of absolute instability, a substance in its subcritical liquid phase can present a very different stability behavior than its corresponding supercritical phase.

As mentioned in Chapter 1, previous researchers point out that geometry, momentum thickness and the effects of the vorticity layer could affect the stability

characteristics of a flow. In these experiments both the momentum thickness of the gaseous flow and the shear layer between the two coaxial streams seem to play an important role in the development of instabilities, since one of the mechanisms which might be dampening (or perhaps enhancing) these instabilities is the large recirculation region that is created between the inner and outer streams right at the exit of the original injector. It is difficult to say that the recirculation region aids or dampens the instability, since Figure 5.34 shows that both $J = 2.6$ and $J = 9.6$ are greatly affected by acoustics; however, Figure 5.20, shows a very thin inner jet at $J = 2.6$ which seems not to feel any recirculation zone at all whereas Figure 5.21 shows a very thick jet at $J = 9.6$ that quickly expands into the recirculation zone due to the large momentum flux of the outer jet.

Overall, in the experimental results obtained using the original injector geometry at subcritical pressures (see Figs. 5.33 and 5.34), there seems to be a range of momentum flux ratios between 2 and 10 for which the coaxial jet responds very well to acoustics. This provides evidence of a convectively unstable coaxial jet flow at these conditions, which could act as a noise amplifier. In the case of nearcritical and supercritical pressures (Figs. 5.33, 5.35 and 5.36) the range of momentum flux ratios for which the jet responds better to acoustics seems to be smaller ($2 < J < 5$). However, there is some evidence from this work (see Figure 5.28) that even at higher momentum flux ratios for supercritical pressures the coaxial jet responds to acoustics. The response for this supercritical case is not as clear at this higher momentum ratio case as compared to its subcritical case counterpart because the

supercritical dark core is quickly combined with the outer jet and surrounding fluid as it exits the injector. However, the mixed jet flowing downstream, which has a dark grey color in the images, presents the same oscillatory behavior.

This observation would effectively extend the range in which coaxial jet flows can be characterized as convectively unstable at conditions above the critical pressure of the fluid. Further support for this claim is provided by the fact that acoustic forcing at this pressure regime produces maximum peak-to-peak pressure perturbations that are less than one percent of the mean pressure chamber but still are able to generate a response in the coaxial jet. It is just difficult to characterize this response of the coaxial jet to acoustics using the inner jet due to the size of its dark core region at these high momentum flux ratios.

In the tests conducted with the new injector, a completely different response to acoustics was observed. The same level of acoustic forcing applied to the original injector geometry was used in the new injector cases. The subcritical cases (Figs. 5.37 to 5.41) showed a strong response to the applied acoustic field, with visible differences between the pressure antinode or velocity node location (315° , 360° and 0° conditions) and the pressure node or velocity antinode location (135° and 180° conditions). In contrast, the nearcritical cases and the subcritical case showed mostly a weak or no response to acoustics (Figs. 5.42 to 5.46). The only cases that showed some level of excitation were those with a momentum flux ratio near or above 10.

Aside from those high momentum flux ratios, the only other instance in which the coaxial jet with the new geometry showed response to acoustic excitation was

observed at the 315° condition for a J value near 0.5 in the nearcritical regime. This was a particularly violent reaction of the inner jet as it can be observed in Figure 5.42 where dark core particles covered the entire image for that particular condition. A possible explanation for this effect is that there exists an amplitude threshold beyond which the inner jet becomes highly unstable, and that for this particular case the 315° condition was the closest one to the pressure antinode, which reaches the highest pressure perturbations. Thus, the larger pressure oscillations might have surpassed this excitation threshold and produced such a dramatic effect on the dark core behavior of the inner jet.

The results with the new injector geometry show that at the current forcing conditions the coaxial jet shows a strong response to all the momentum flux ratios at subcritical pressures (see Figs. 5.37 to 5.41). The new geometry could be extending the convective instability range of the flow to reach both higher and lower momentum flux ratios as compared to the original injector. One can argue that the thinner shear layer between the inner jet and the outer jet without a recirculation region allows more energy from the acoustic forcing to reach the inner jet and disturb it. However, the nearcritical and supercritical regimes seem to have no significant response to acoustic forcing (see Figs. 5.42 to 5.46), when one would expect at least a small range of moderate J values for which the nearcritical and supercritical regimes would show an effect. One potential cause for this lack of response is the need for higher acoustic amplitudes. It is possible that the near and supercritical cases were not being forced at sufficiently high relative amplitudes to

visibly excite the coaxial jet. Further testing with the new injector will be necessary to support this claim.

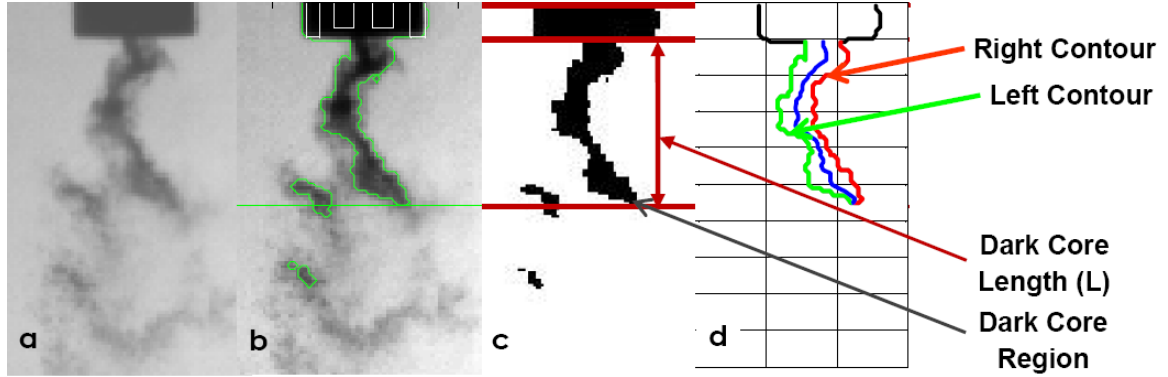


Figure 5.1. (a) Raw image from high-speed camera. (b) Dark core boundary extracted from the raw image using the image processing routine. (c) Black and white image after image processing threshold had been applied. (d) Schematic of the left and right contours used in this study to obtain inner jet spreading angles. Figure modified from original by Leyva et al. (22).

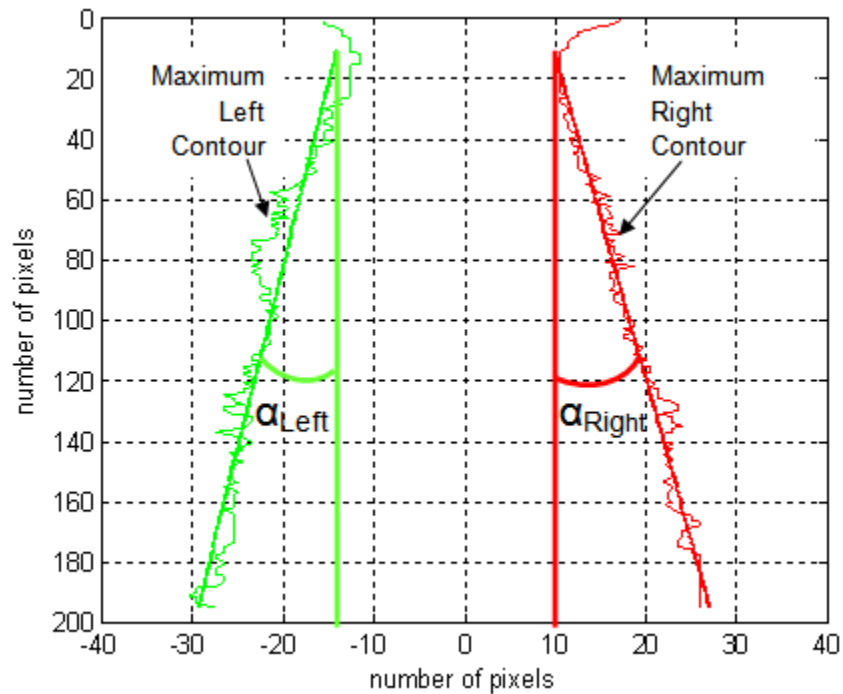


Figure 5.2. Left and right angles derived using the maximum displacement of the dark core region at each row over a sample of 998 images. From Rodriguez et al. (78).

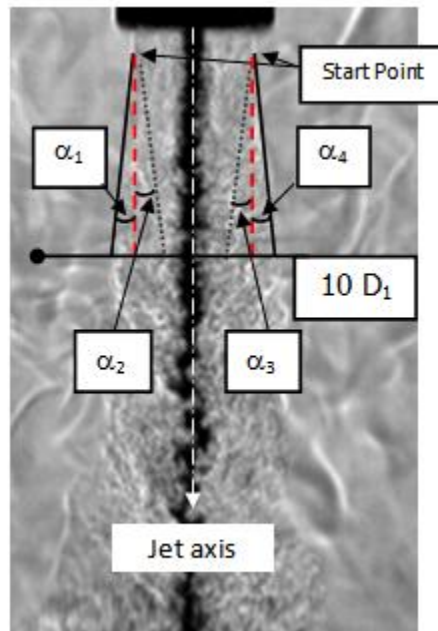


Figure 5.3. Image showing how outer jet spreading angles are measured. From Leyva et al. (75).

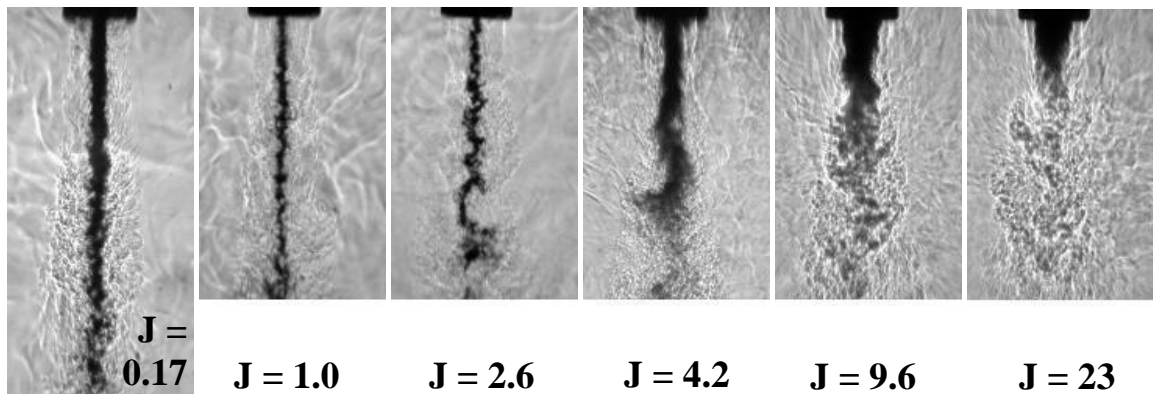


Figure 5.4. Collection of coaxial jet images without acoustic forcing at subcritical pressure from lowest to highest J . Original injector geometry.

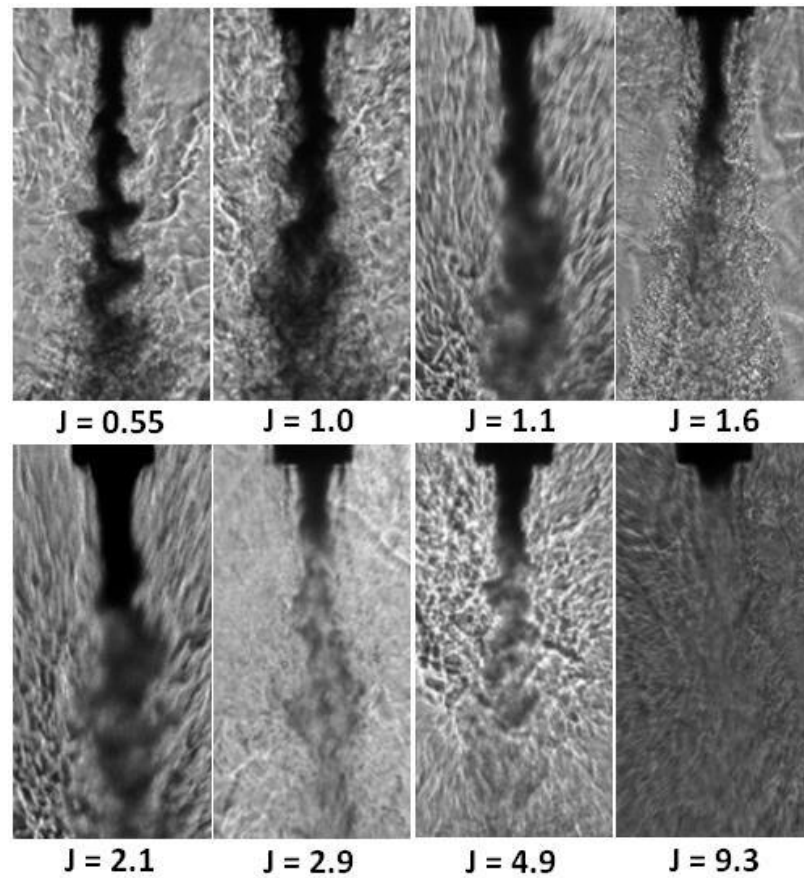


Figure 5.5. Collection of coaxial jet images without acoustic forcing at nearcritical pressure from lowest to highest J . Original injector geometry.

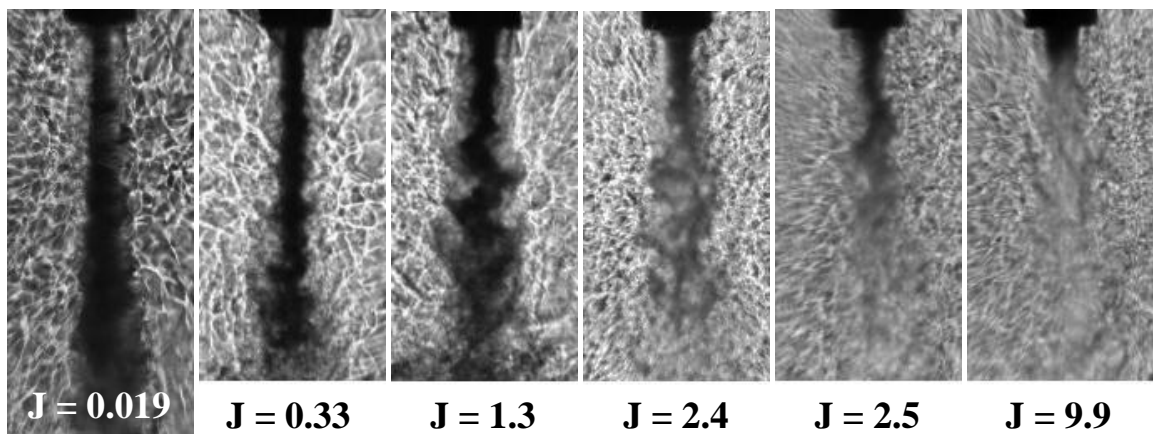


Figure 5.6. Collection of coaxial jet images without acoustic forcing at supercritical pressure from lowest to highest J . Original injector geometry.

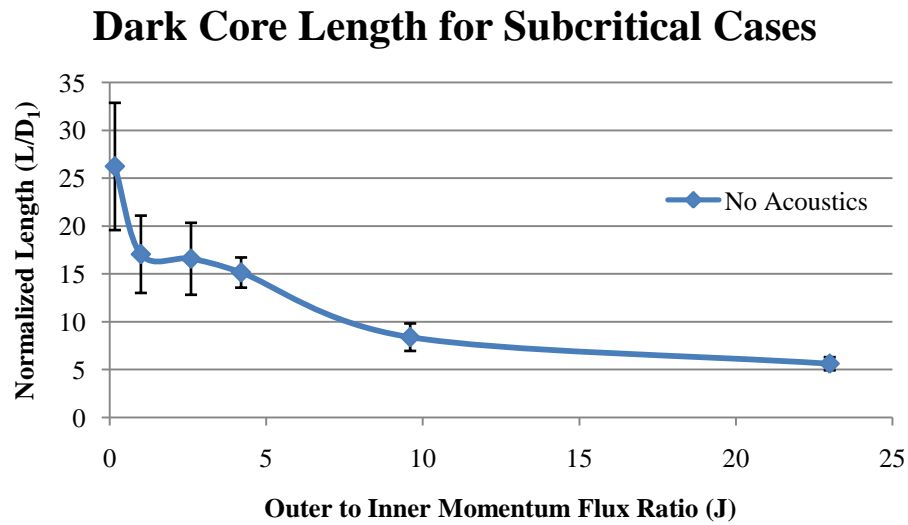


Figure 5.7. Dark core length normalized by the inner jet post inner diameter, L/D_1 , for the subcritical pressure regime. The results shown are for all the cases studied with the original injector geometry.

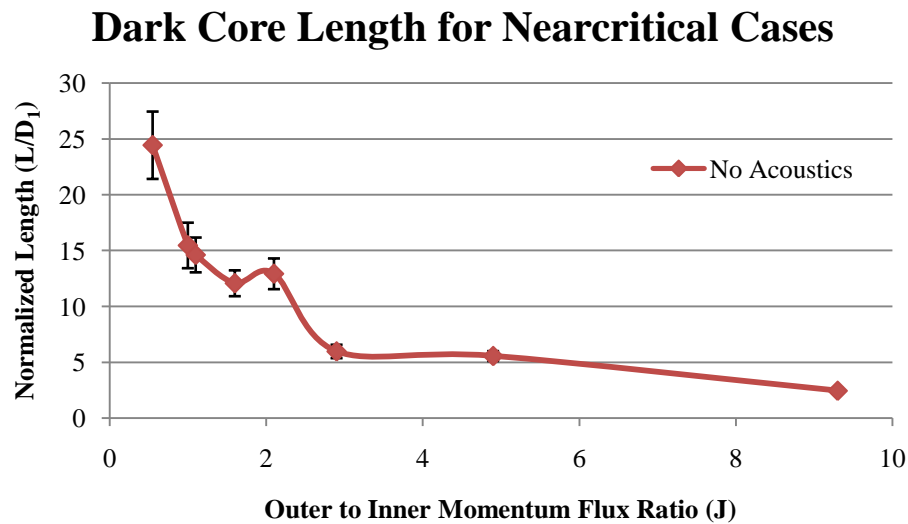


Figure 5.8. Dark core length normalized by the inner jet post inner diameter, L/D_1 , for the nearcritical pressure regime. The results shown are for all the cases studied with the original injector geometry.

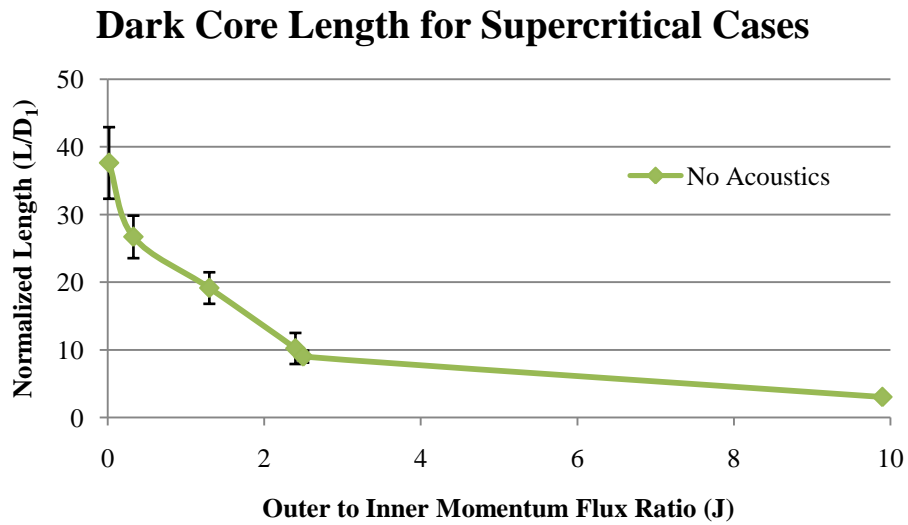


Figure 5.9. Dark core length normalized by the inner jet post inner diameter, L/D_1 for the supercritical pressure regime. The results shown are for all the cases studied with the original injector geometry.

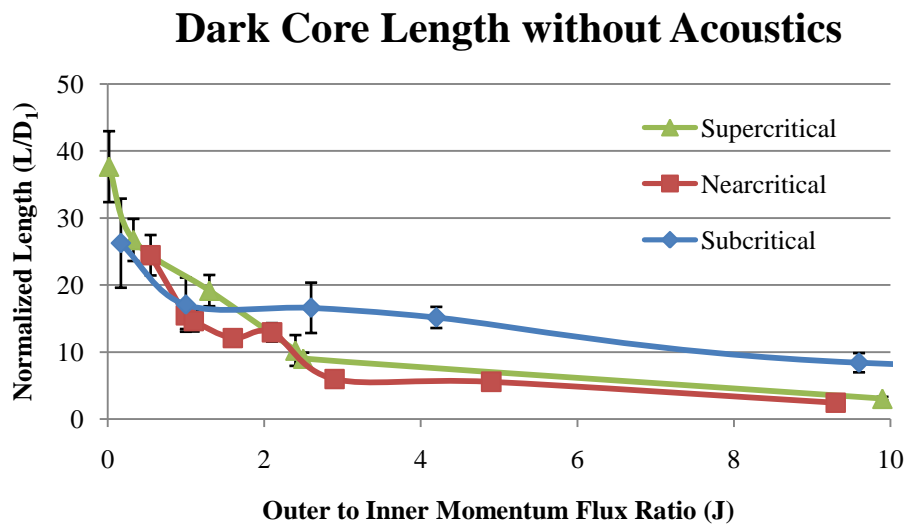


Figure 5.10. Dark core length normalized by the inner jet post inner diameter, L/D_1 for all pressure regimes using the original injector geometry. Results are shown in the $0.02 < J < 10$ range.

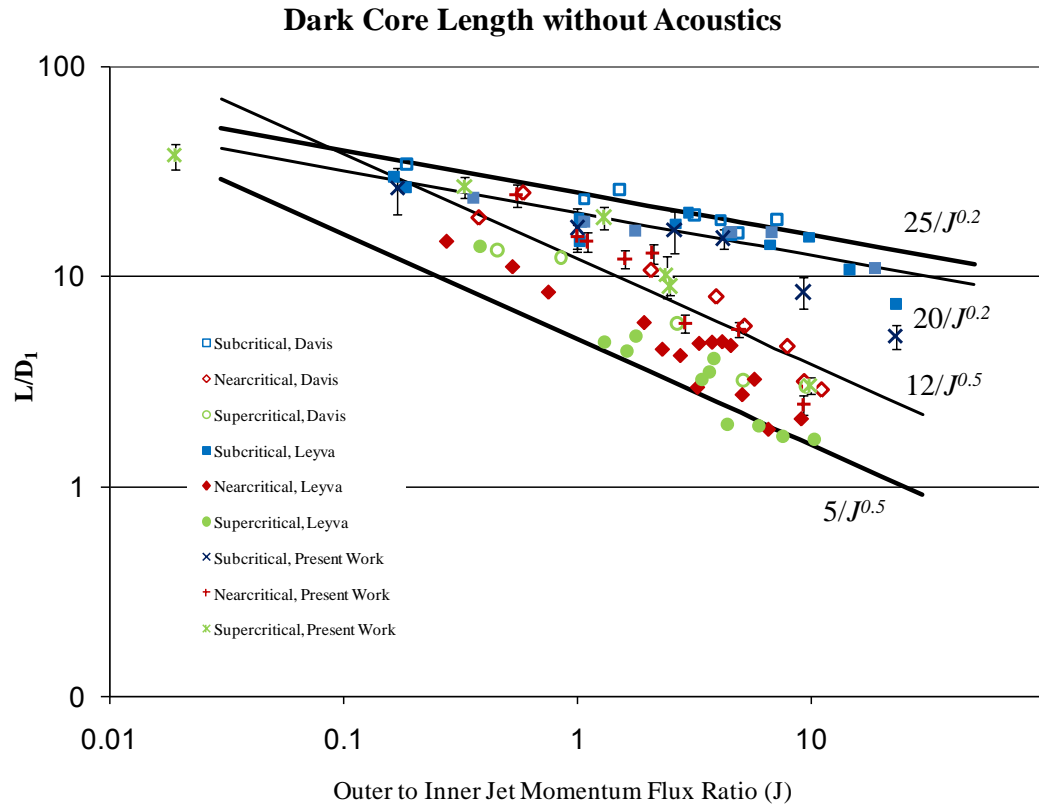


Figure 5.11. Dark core length normalized by the inner jet post inner diameter, L/D_1 for all pressure regimes. Results include previous research work using the original injector geometry in the same facility this study was performed (22; 23; 42).

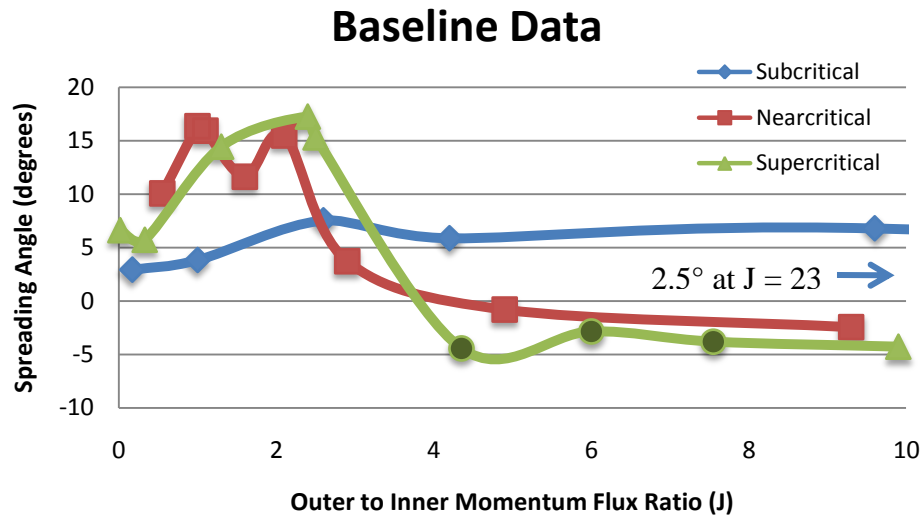


Figure 5.12. Spreading angle of the inner jet in degrees for all pressure regimes using the original injector geometry. Dark circular markers are data points from Leyva et al. (22; 23).

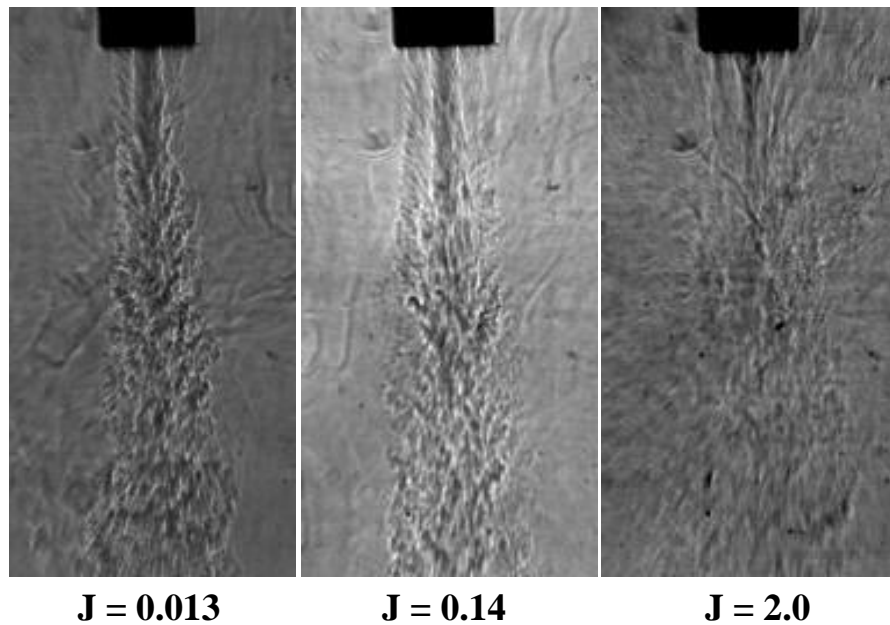


Figure 5.13. Single phase coaxial jet images without acoustic excitation at subcritical pressures. Original injector geometry.

Single Phase Outer Jet Spreading Angle ($\alpha_1 + \alpha_4$) vs. J for Subcritical Pressures

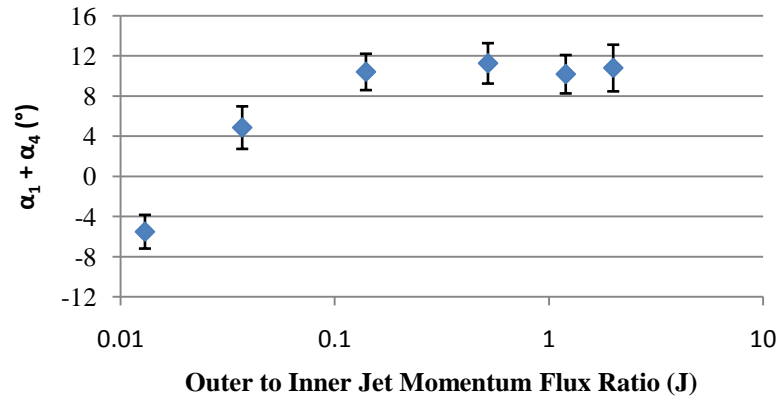


Figure 5.14. Outer jet spread angle measurements with original injector geometry for one-phase coaxial jet at subcritical pressures. The bars indicate one standard deviation above and below the mean spreading angle. From Rodriguez et al. (79).

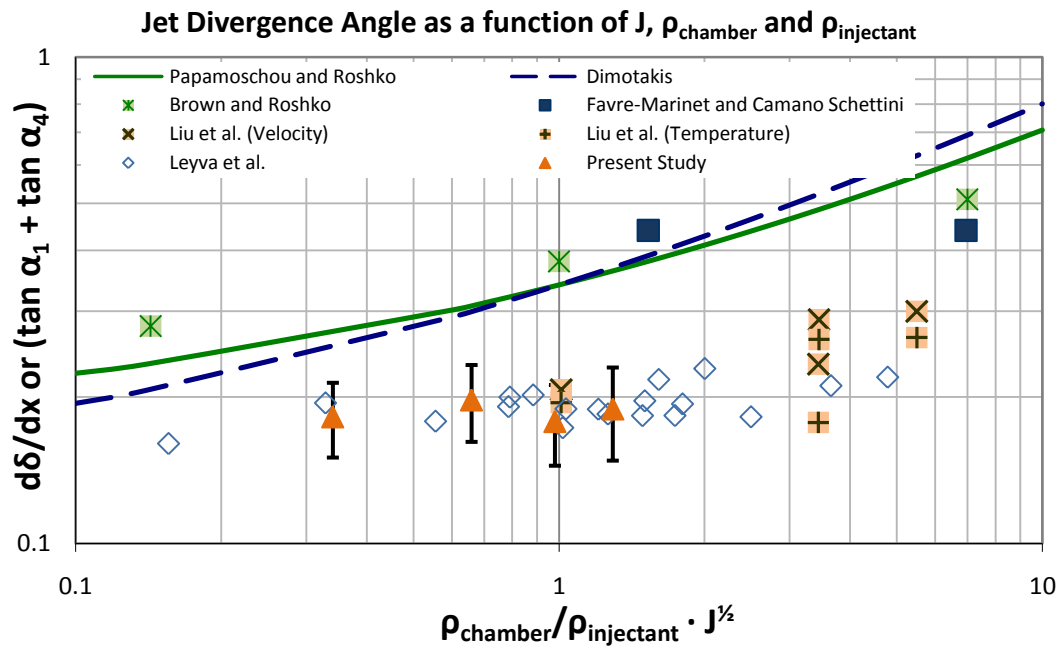


Figure 5.15. Outer jet spread angle measurements compared to jet divergence angle theoretical predictions and other single jet and coaxial jet spreading angle experimental data. From Rodriguez et al. (79).

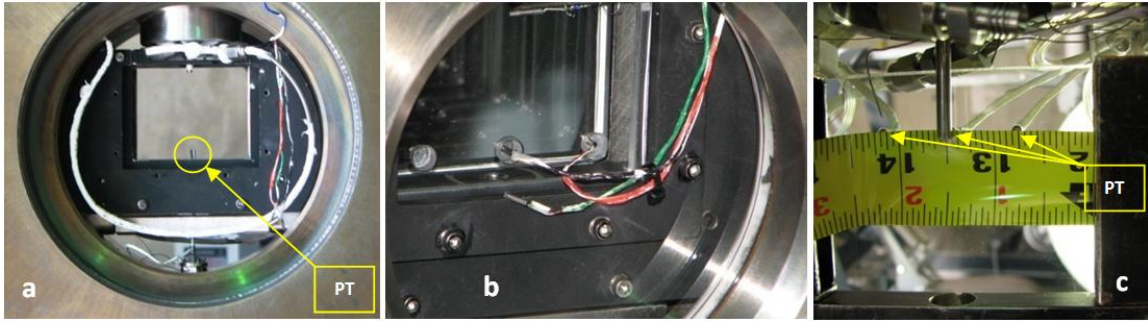


Figure 5.16. (a) Approximate location during testing of the absolute pressure transducer used to measure the acoustic field inside the inner chamber. (b) Absolute pressure transducers used to quantify the pressure oscillations at three different transversal locations within the inner chamber for tests performed with the original injector. (c) Differential pressure transducers used to quantify the pressure oscillations within the inner chamber for tests performed with the new injector.

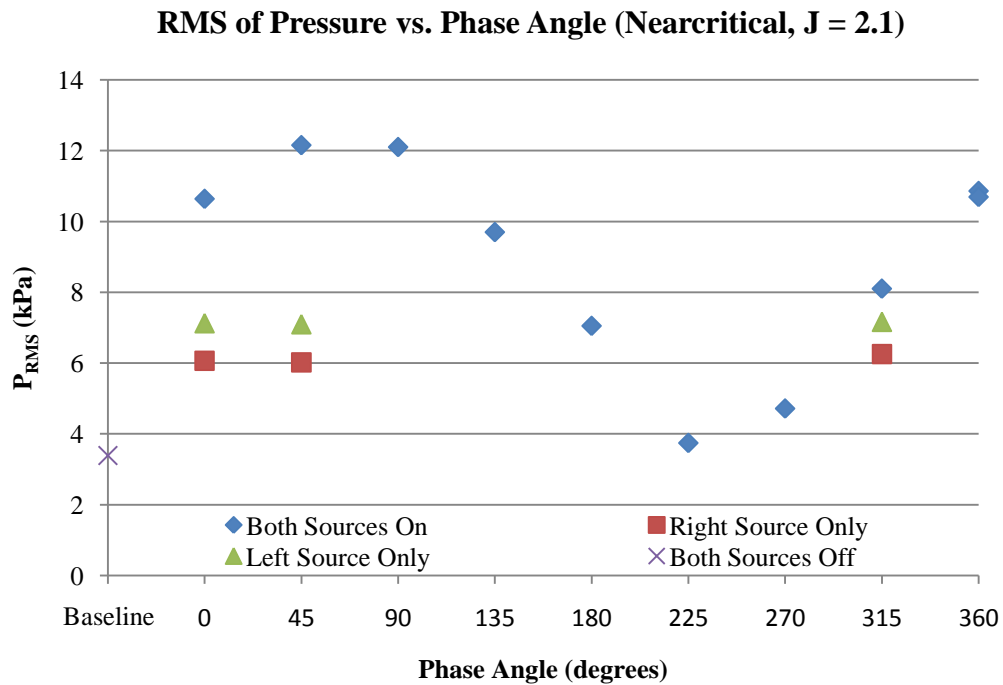


Figure 5.17. RMS of chamber pressure fluctuations measured at the bottom of the inner chamber versus phase angle between acoustic sources for the nearcritical case with $J = 2.1$ with the original injector geometry. The data with only one acoustic source on was obtained immediately before recording data with both sources on for the corresponding phase angle on which they are plotted. From Rodriguez et al. (79).

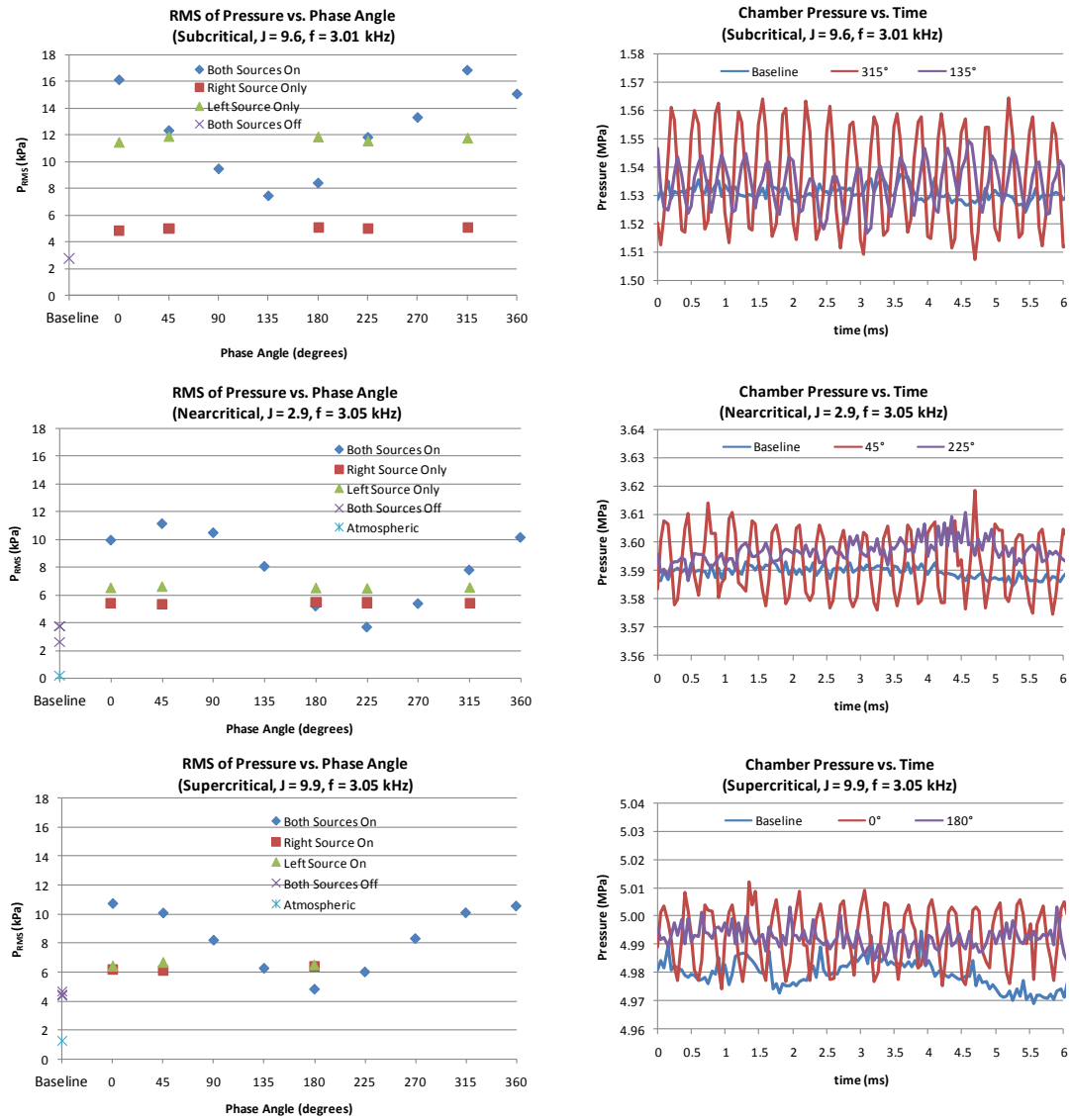


Figure 5.18. Graphs of the RMS value of the chamber pressure fluctuations at different phase angles between the acoustic sources on the left with chamber pressure as a function of time on the right for one subcritical case, one nearcritical case and one supercritical case with the original injector geometry. From Rodriguez et al. (79).

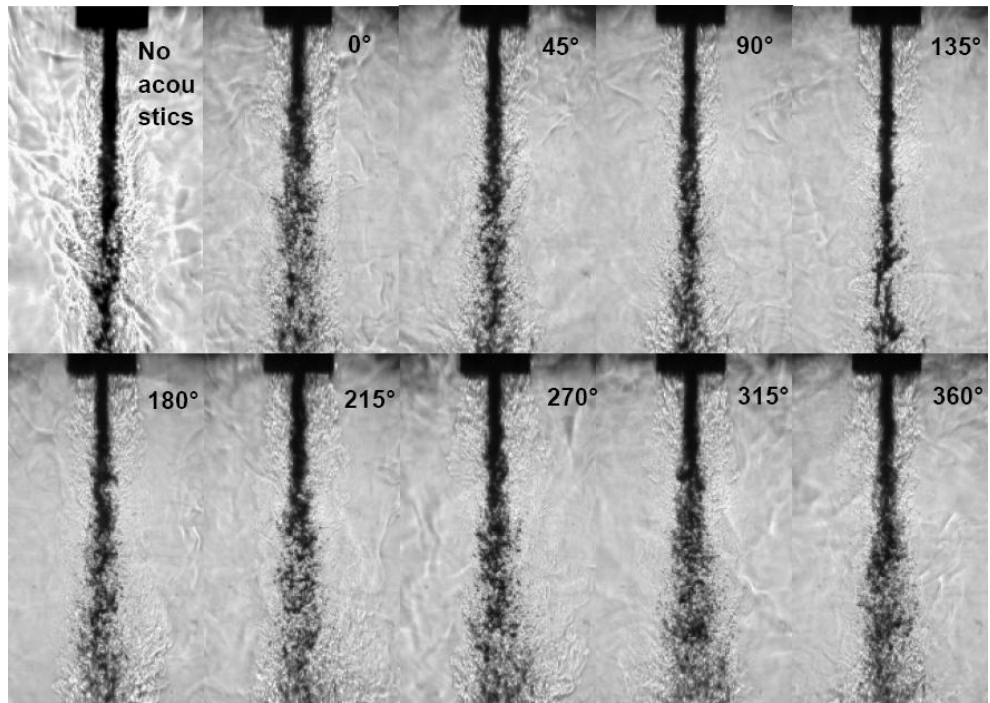


Figure 5.19. Collection of subcritical coaxial jet images at $P_{\text{chamber}} = 1.50 \text{ MPa}$, $J = 0.17$. Original injector geometry

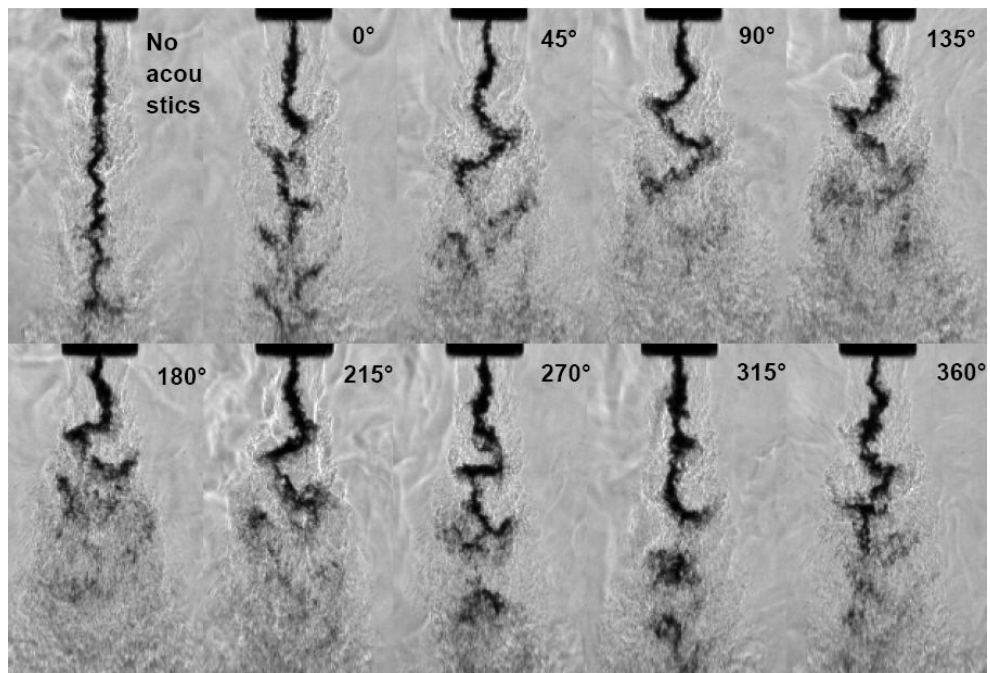


Figure 5.20. Collection of subcritical coaxial jet images at $P_{\text{chamber}} = 1.45 \text{ MPa}$, $J = 2.6$. Original injector geometry.

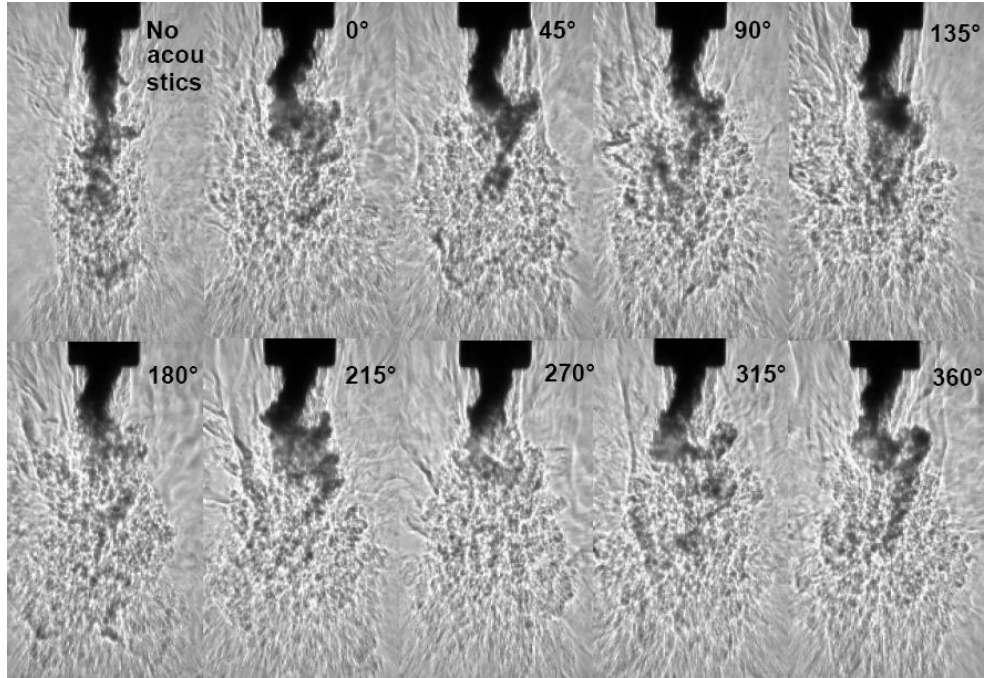


Figure 5.21. Collection of subcritical coaxial jet images at $P_{\text{chamber}} = 1.50 \text{ MPa}$, $J = 9.6$. Original injector geometry.

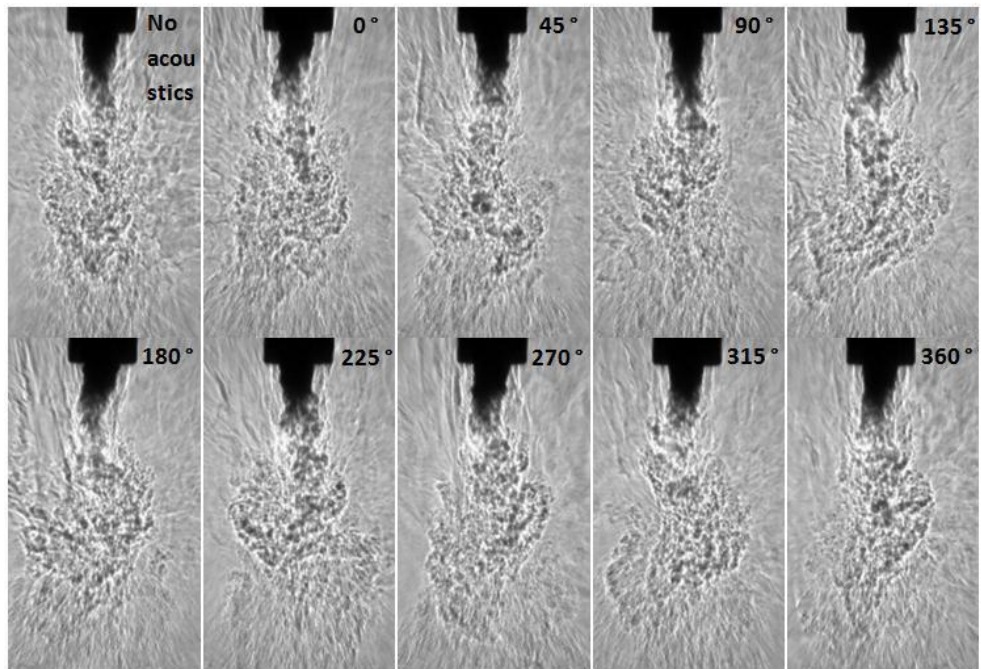


Figure 5.22. Collection of subcritical coaxial jet images at $P_{\text{chamber}} = 1.50 \text{ MPa}$, $J = 23$. Original injector geometry.

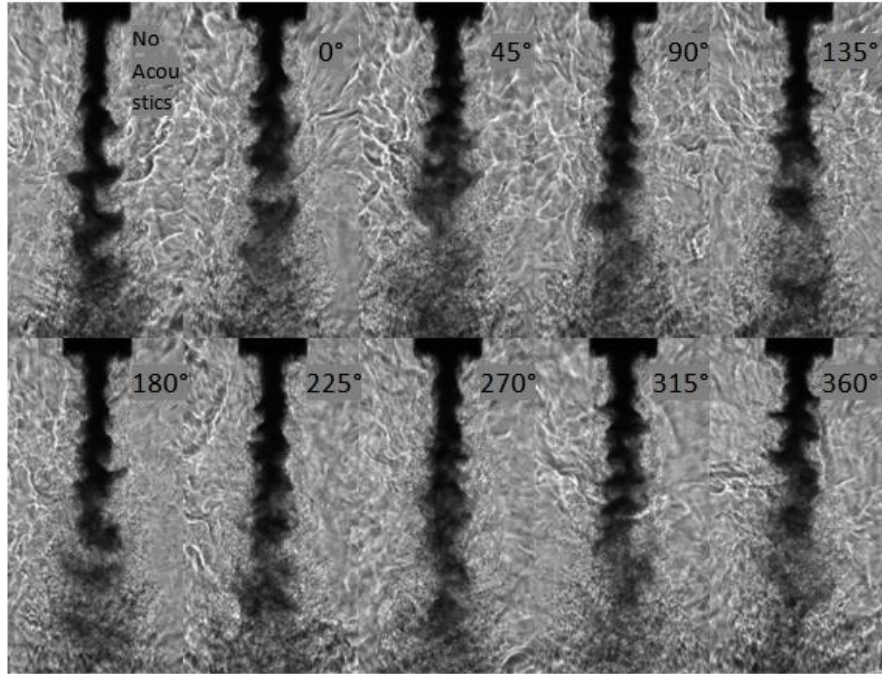


Figure 5.23. Collection of nearcritical coaxial jet images at $P_{\text{chamber}} = 3.58 \text{ MPa}$, $J = 0.55$. Original injector geometry.

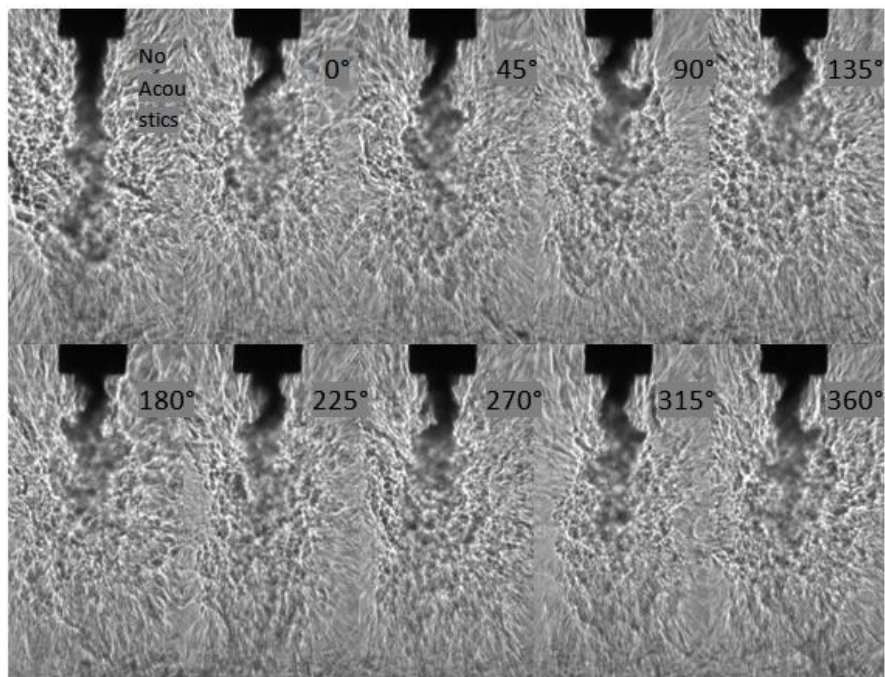


Figure 5.24. Collection of nearcritical coaxial jet images at $P_{\text{chamber}} = 3.56 \text{ MPa}$, $J = 4.9$. Original injector geometry.

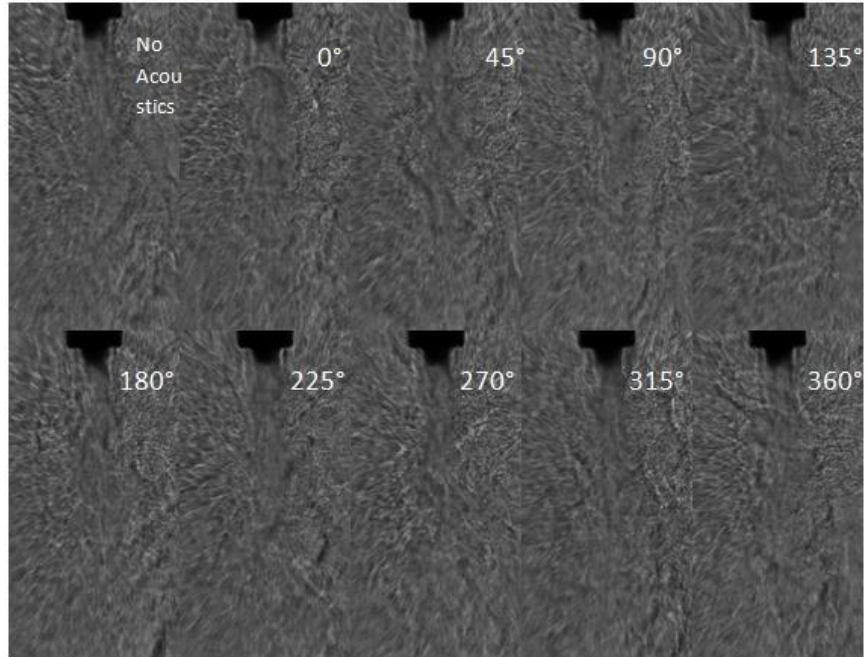


Figure 5.25. Collection of nearcritical coaxial jet images at $P_{\text{chamber}} = 3.56 \text{ MPa}$, $J = 9.3$. Original injector geometry.

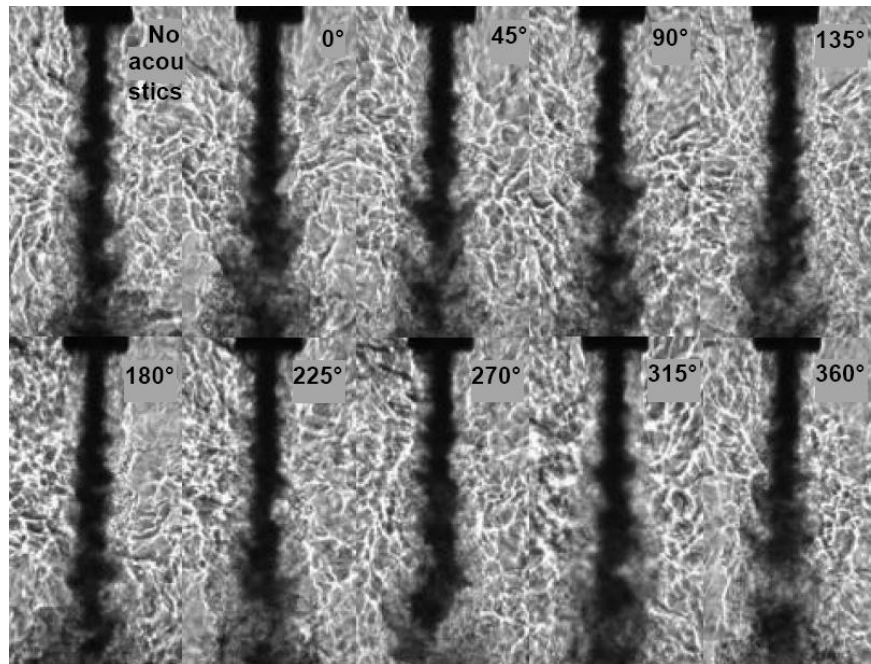


Figure 5.26. Collection of supercritical coaxial jet images at $P_{\text{chamber}} = 4.96 \text{ MPa}$, $J = 0.33$. Original injector geometry.

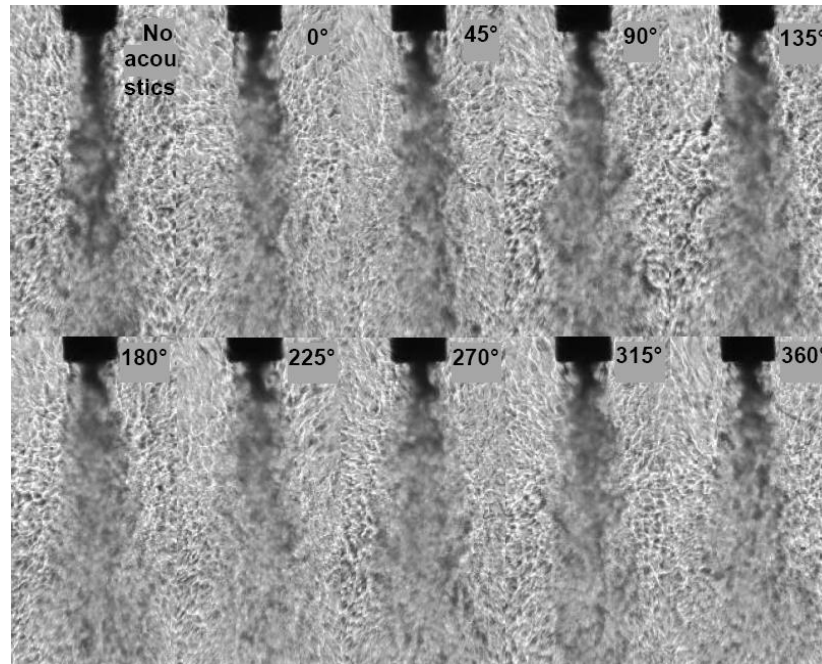


Figure 5.27. Collection of supercritical coaxial jet images at $P_{\text{chamber}} = 4.96$ MPa, $J = 2.4$. Original injector geometry.

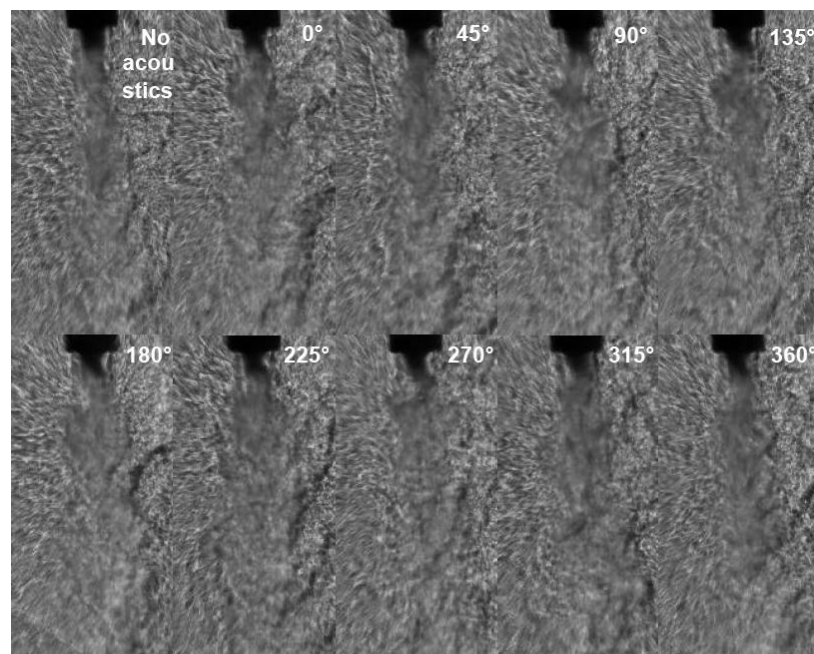


Figure 5.28. Collection of supercritical coaxial jet images at $P_{\text{chamber}} = 4.96$ MPa, $J = 9.9$. Original injector geometry.

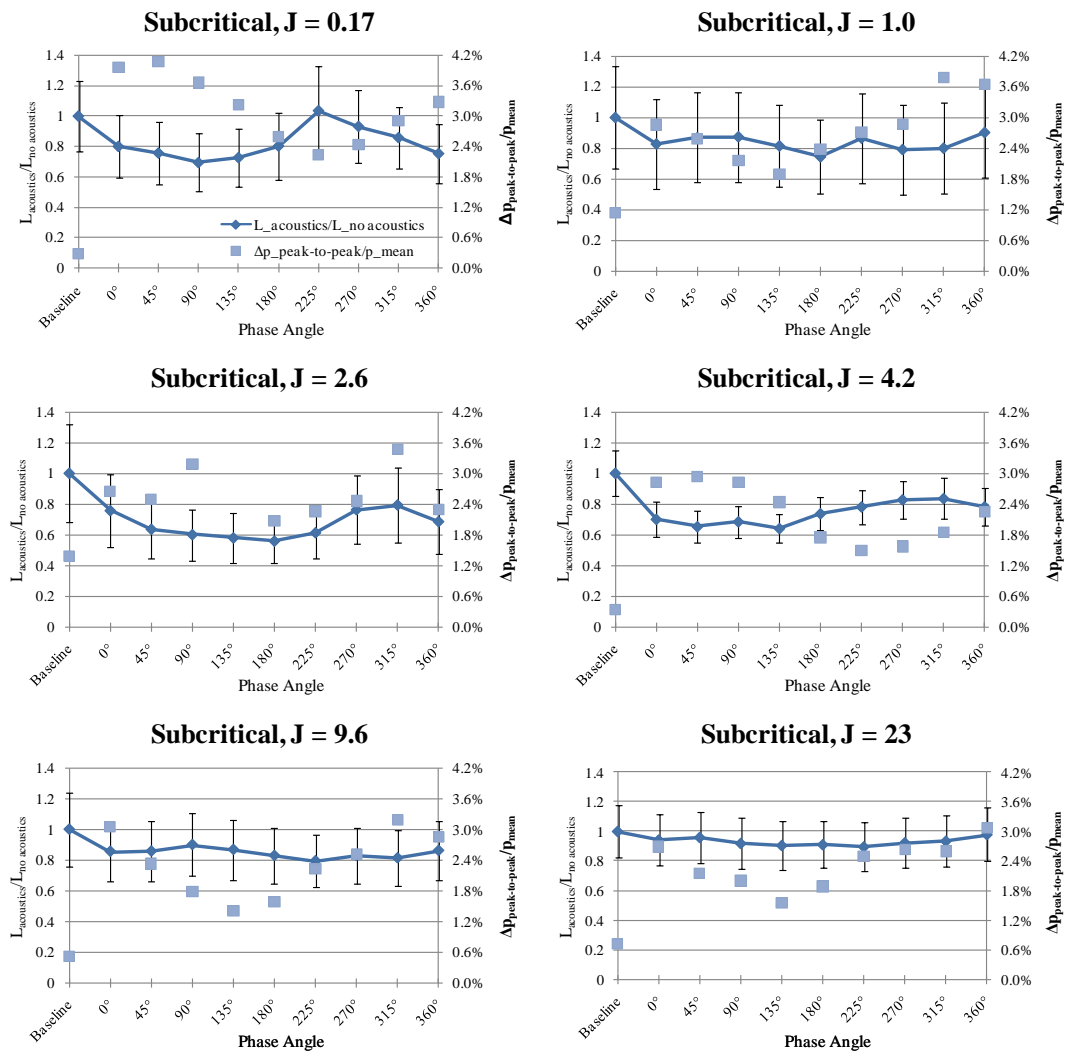


Figure 5.29. Dark core length with acoustics ($L_{\text{acoustics}}$) over dark core length without acoustics ($L_{\text{no acoustics}}$), shown in diamonds, versus phase angle between acoustic sources for subcritical pressures. The the peak-to-peak pressure perturbation as a percentage of the mean chamber pressure ($\Delta p_{\text{peak-to-peak}}/p_{\text{mean}}$), in squares, is also plotted. Original injector geometry.

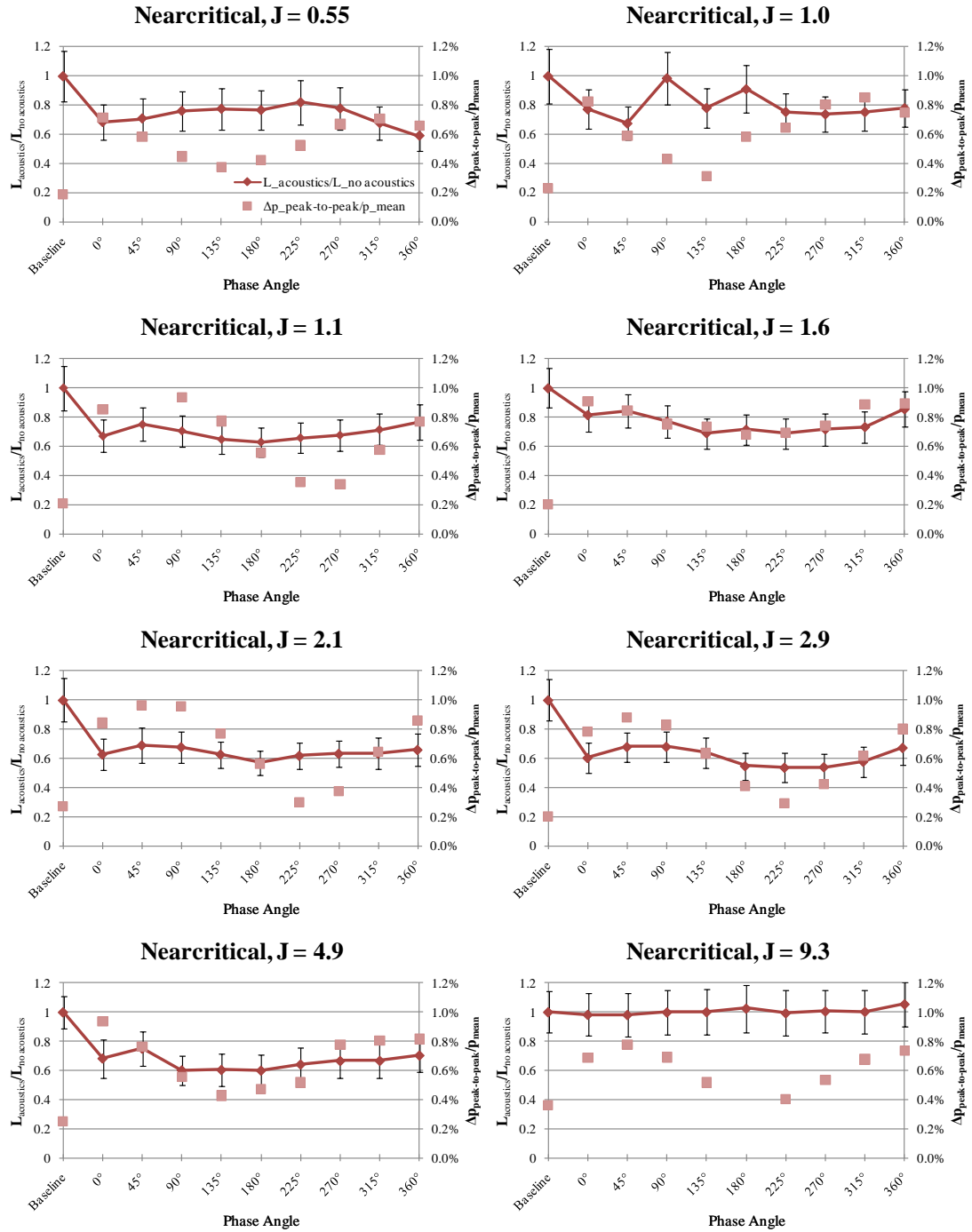


Figure 5.30. Dark core length with acoustics ($L_{\text{acoustics}}$) over dark core length without acoustics ($L_{\text{no acoustics}}$), shown in diamonds, versus phase angle between acoustic sources for nearcritical pressures. The the peak-to-peak pressure perturbation as a percentage of the mean chamber pressure ($\Delta p_{\text{peak-to-peak}}/p_{\text{mean}}$), in squares, is also plotted. Original injector geometry.

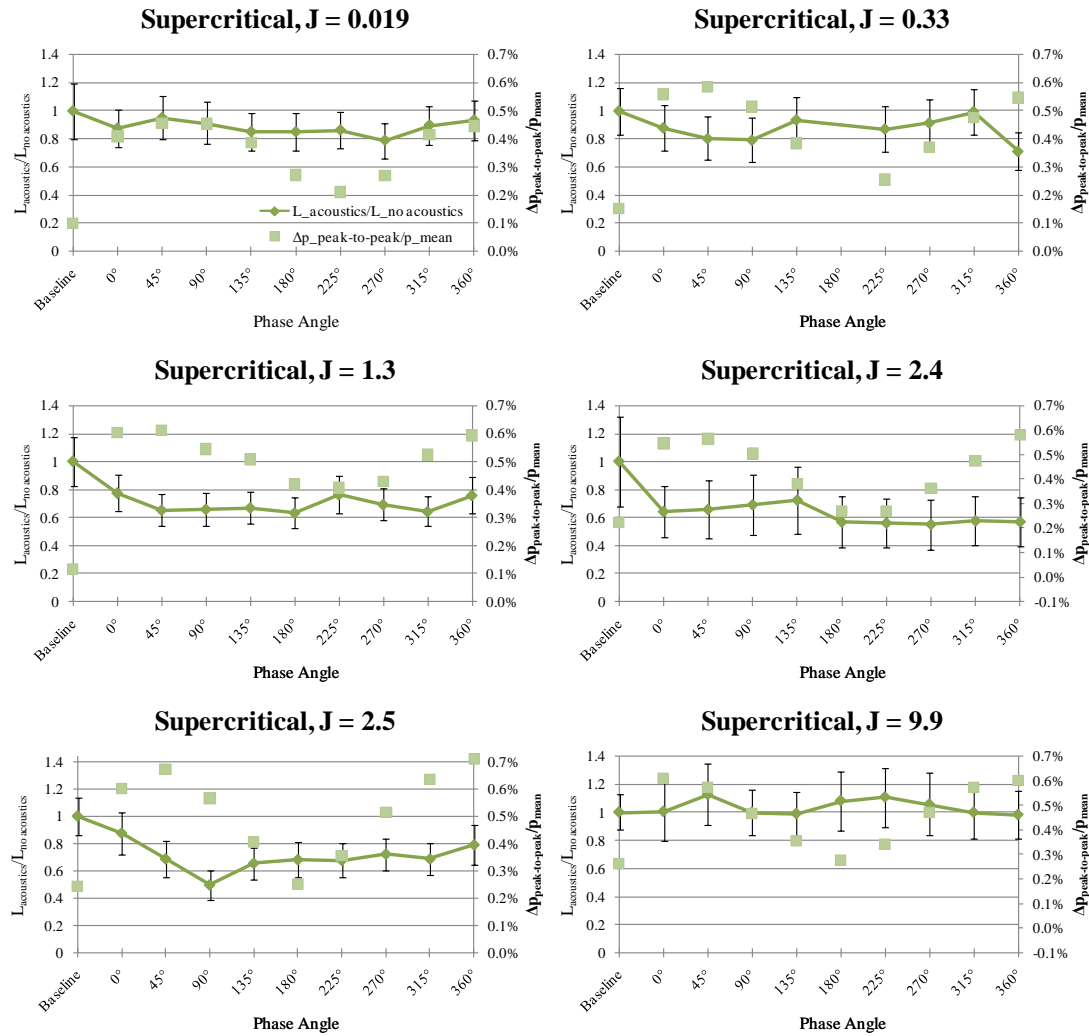


Figure 5.31. Dark core length with acoustics ($L_{\text{acoustics}}$) over dark core length without acoustics ($L_{\text{no acoustics}}$), shown in diamonds, versus phase angle between acoustic sources for supercritical pressures. The the peak-to-peak pressure perturbation as a percentage of the mean chamber pressure ($\Delta p_{\text{peak-to-peak}}/p_{\text{mean}}$), in squares, is also plotted. Original injector geometry.

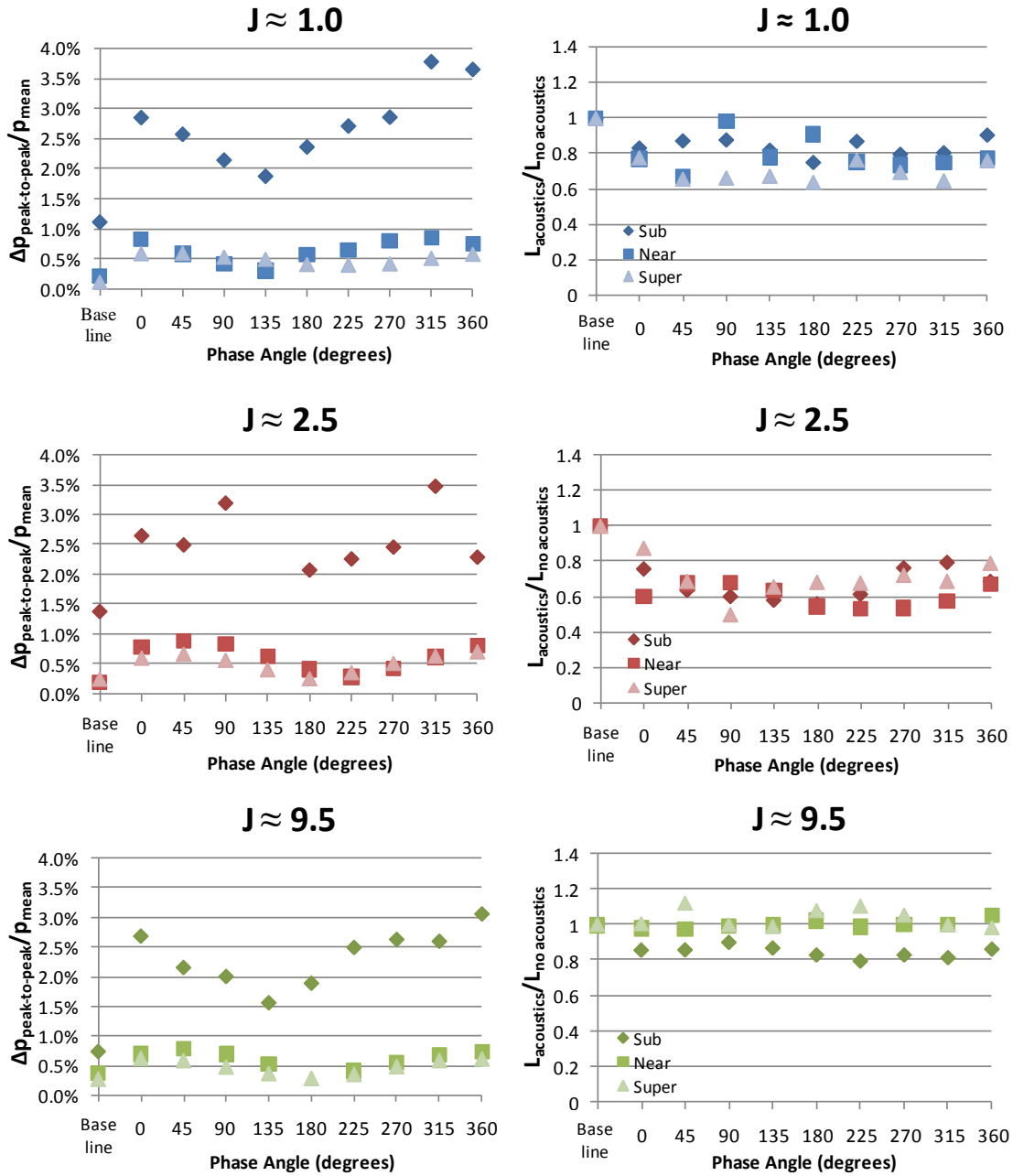


Figure 5.32. Peak-to-peak pressure perturbation ($\Delta p_{\text{peak-to-peak}}$) as a percentage of the mean chamber pressure (p_{mean}) and dark core length with acoustics ($L_{\text{acoustics}}$) over dark core length without acoustics ($L_{\text{no acoustics}}$) versus phase angle between acoustic sources for sub, near and supercritical pressures at $J \approx 1.0$, 2.5 and 9.5 for the original injector geometry. From Rodriguez et al. (79).

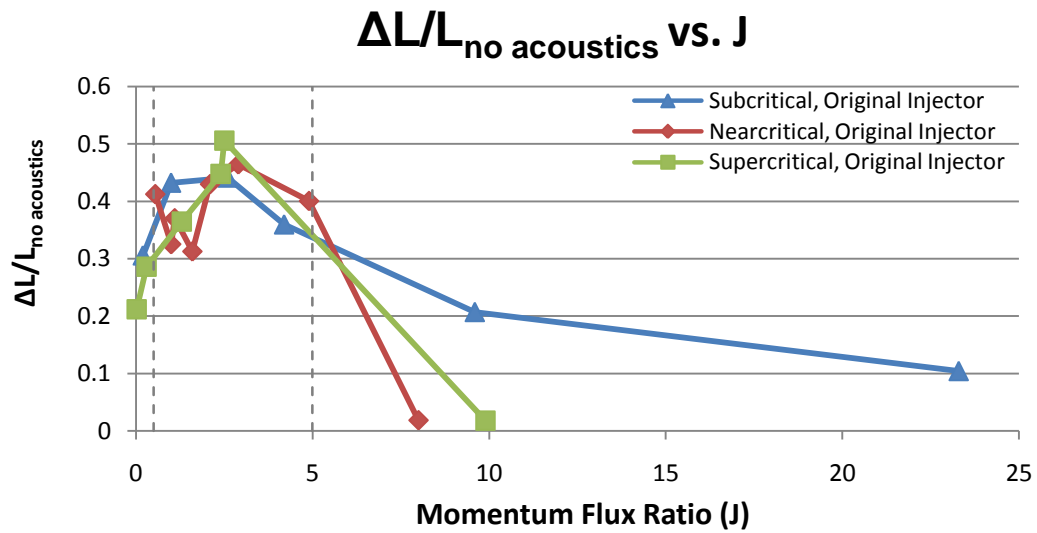


Figure 5.33. Maximum dark core length reduction between dark core length without acoustics and dark core length with acoustics for all phase angles $(L_{\text{no acoustics}} - L_{\text{acoustics}})_{\text{MAX}}$ for a given case divided by the dark core length without acoustics $(L_{\text{no acoustics}})$ as a function of J for all cases obtained with the original injector in this study. From Rodriguez et al. (79).

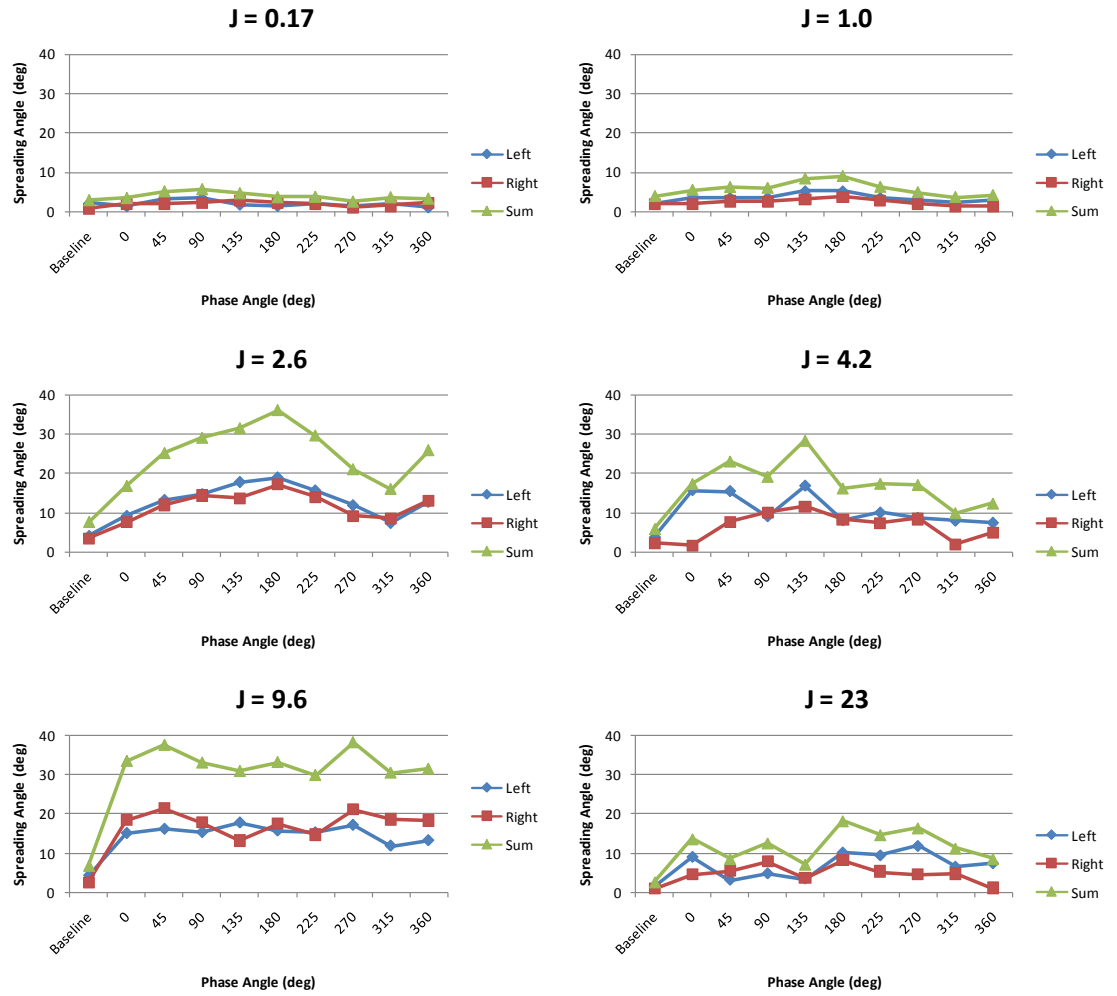


Figure 5.34. Maximum inner spread angles as a function of acoustic phase angle for different J values at subcritical pressures for original injector geometry.

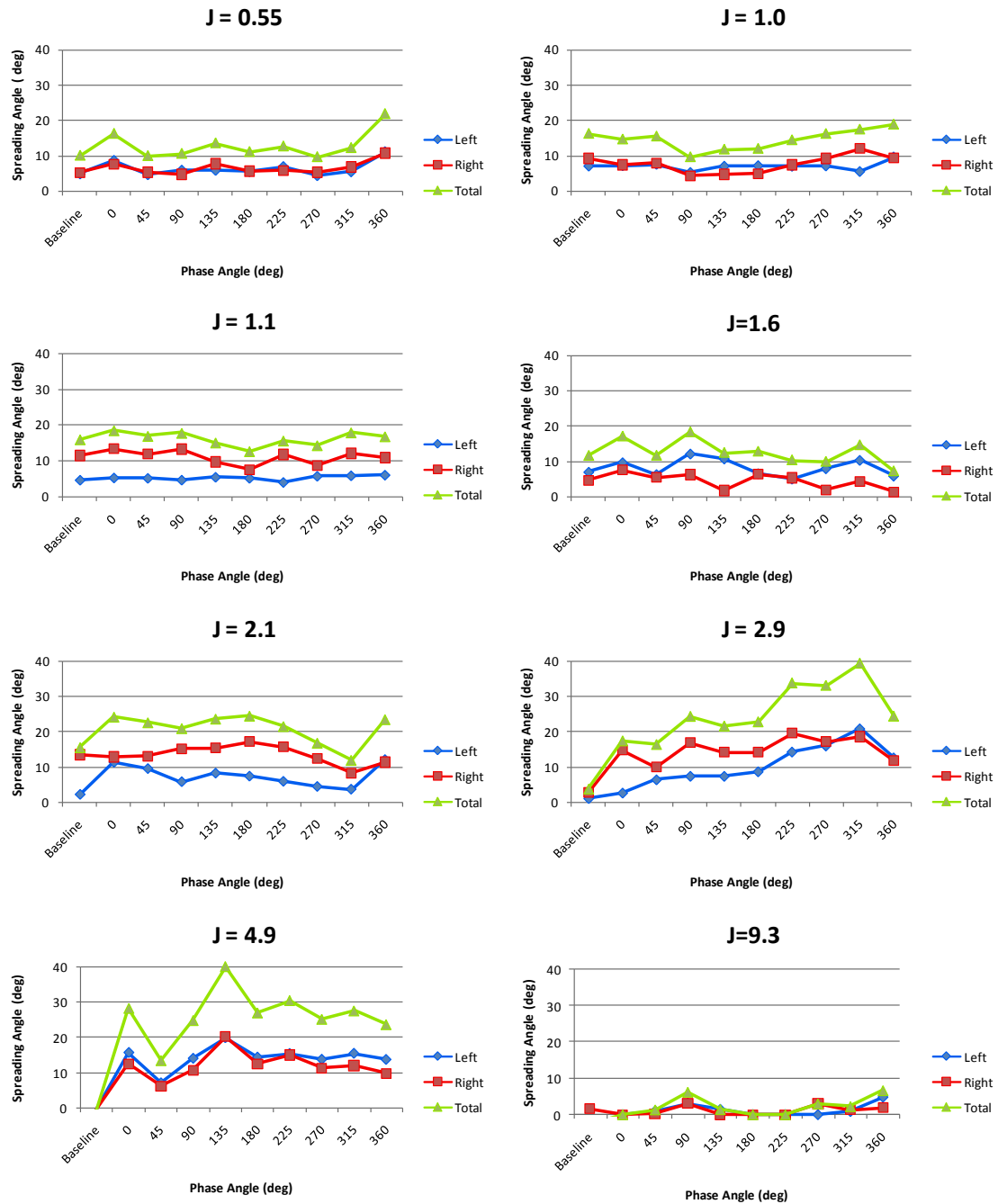


Figure 5.35. Maximum inner spread angles as a function of acoustic phase angle for different J values at nearcritical pressures for original injector geometry.

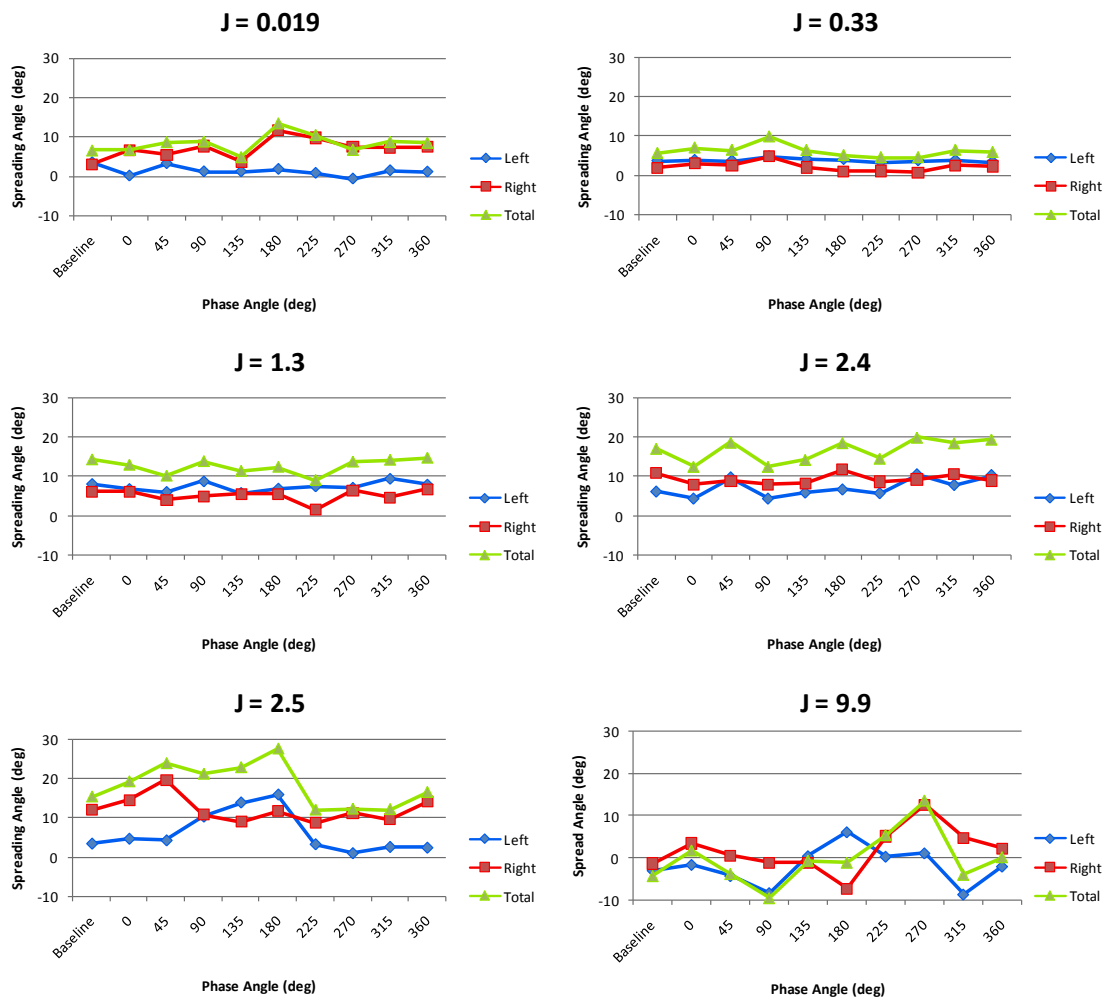


Figure 5.36. Maximum inner spread angles as a function of acoustic phase angle for different J values at supercritical pressures for original injector geometry.

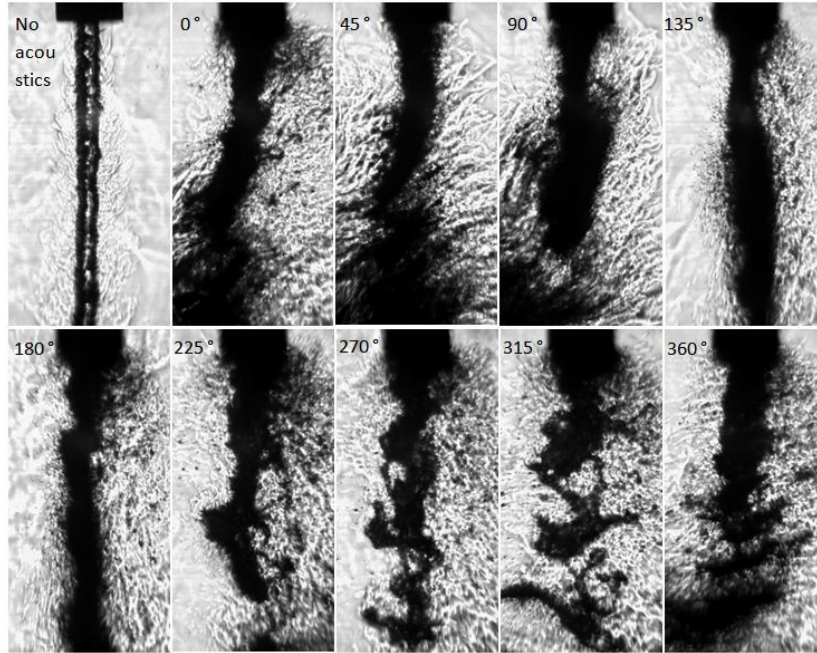


Figure 5.37. Coaxial jet images with the new injector at subcritical pressure ($P_{\text{chamber}} = 1.48 \text{ MPa}$, $J = 0.089$).

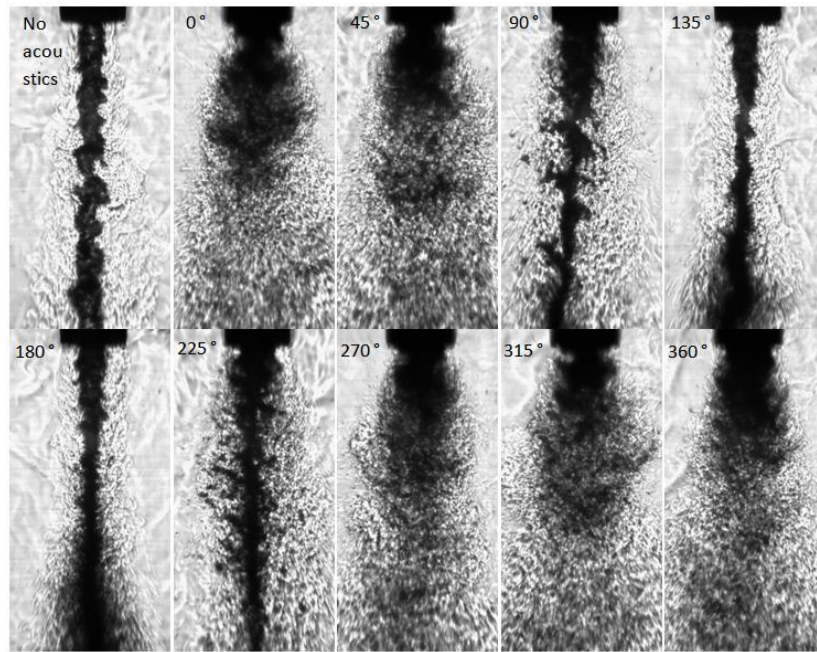


Figure 5.38. Coaxial jet images with the new injector at subcritical pressure ($P_{\text{chamber}} = 1.49 \text{ MPa}$, $J = 0.43$).

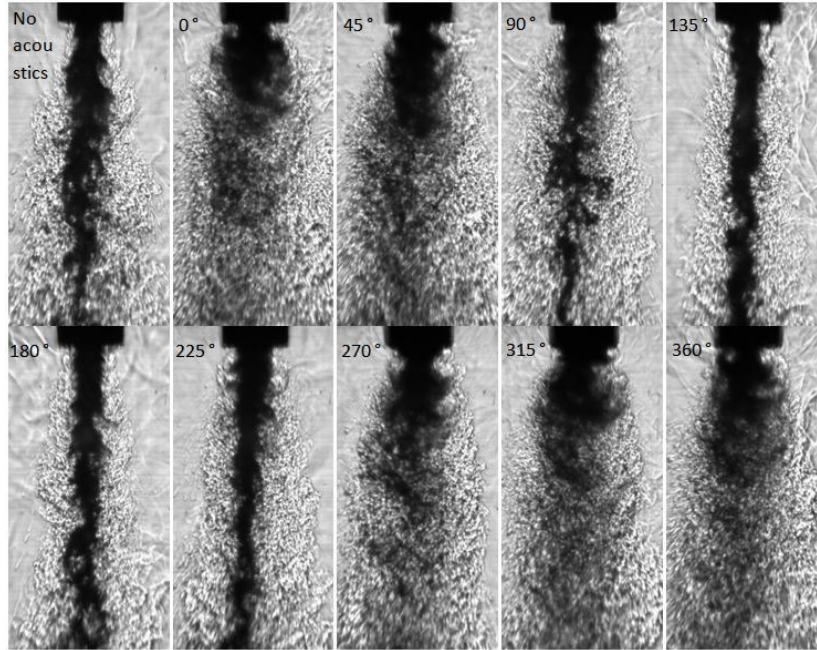


Figure 5.39. Coaxial jet images with the new injector at subcritical pressure ($P_{\text{chamber}} = 1.49 \text{ MPa}$, $J = 2.0$).

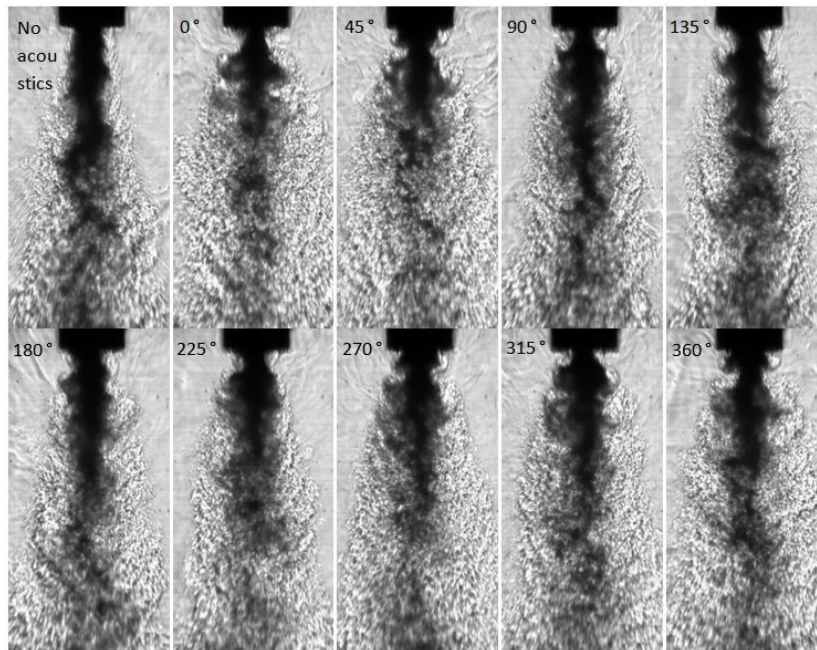


Figure 5.40. Coaxial jet images with the new injector at subcritical pressure ($P_{\text{chamber}} = 1.49 \text{ MPa}$, $J = 7.8$).

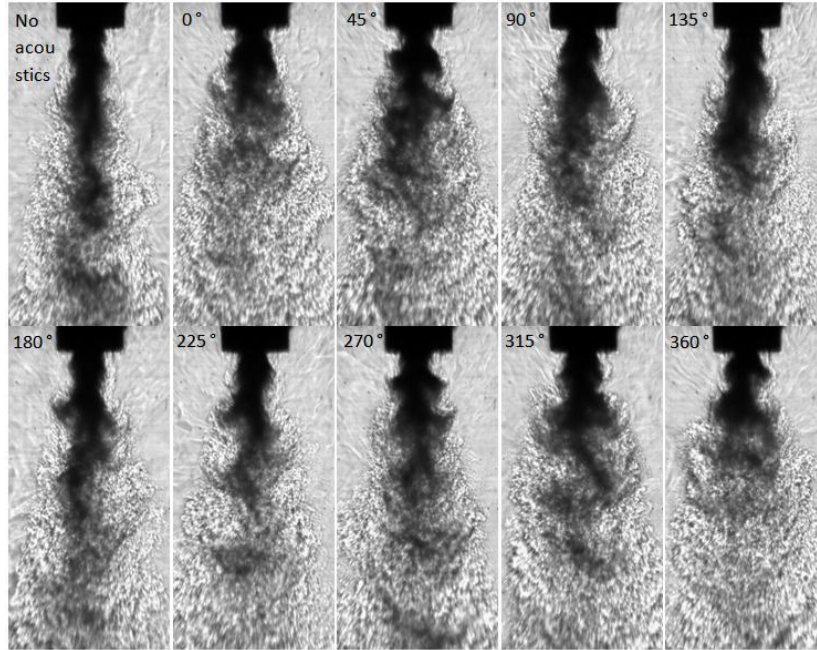


Figure 5.41. Coaxial jet images with the new injector at subcritical pressure ($P_{\text{chamber}} = 1.48 \text{ MPa}$, $J = 18$).

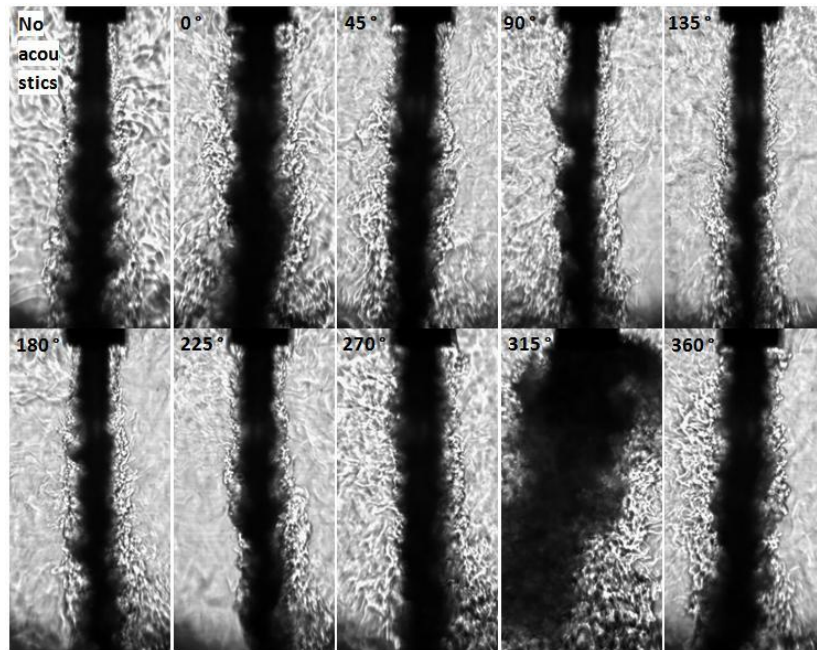


Figure 5.42. Coaxial jet images with the new injector at nearcritical pressure ($P_{\text{chamber}} = 3.56 \text{ MPa}$, $J = 0.50$).

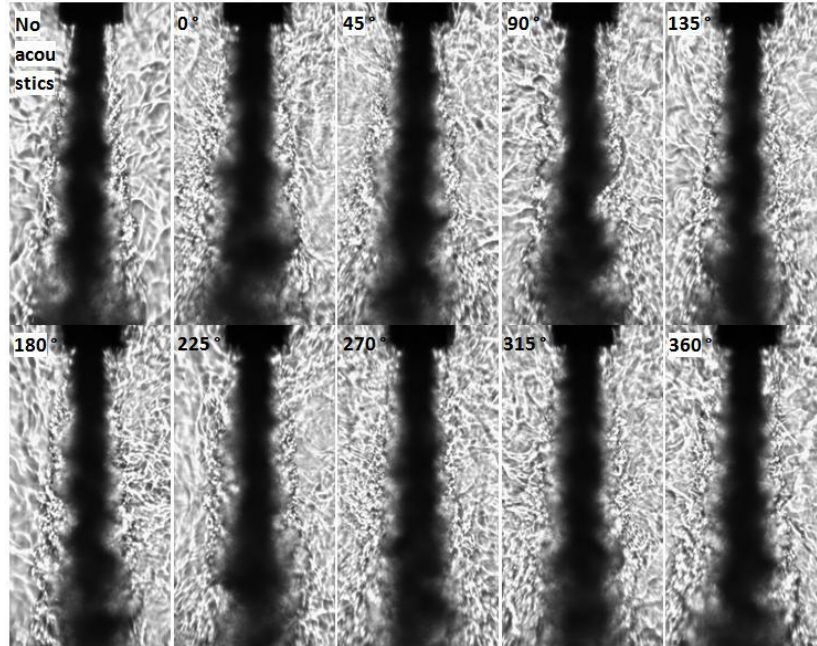


Figure 5.43. Coaxial jet images with the new injector at nearcritical pressure ($P_{\text{chamber}} = 3.58 \text{ MPa}$, $J = 2.2$).

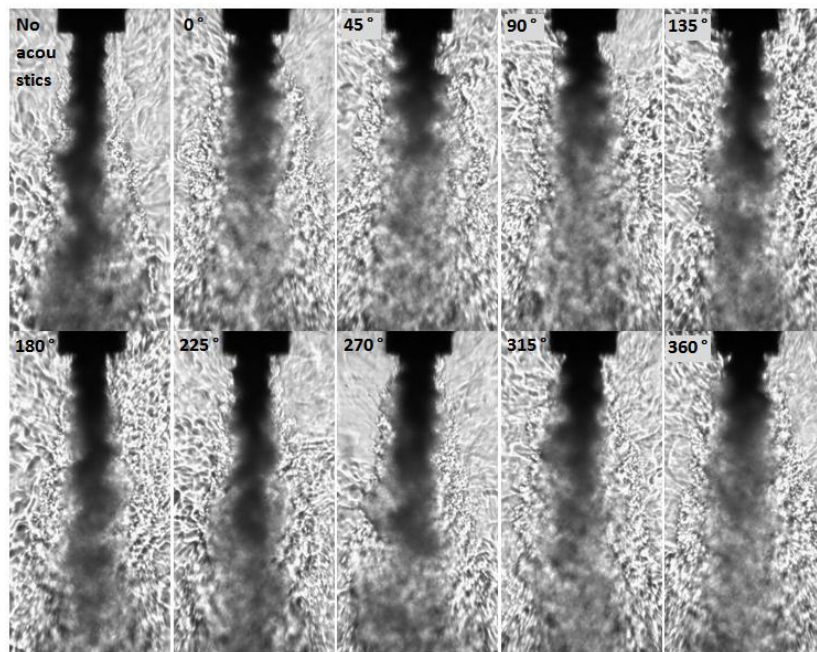


Figure 5.44. Coaxial jet images with the new injector at nearcritical pressure ($P_{\text{chamber}} = 3.58 \text{ MPa}$, $J = 9.4$).

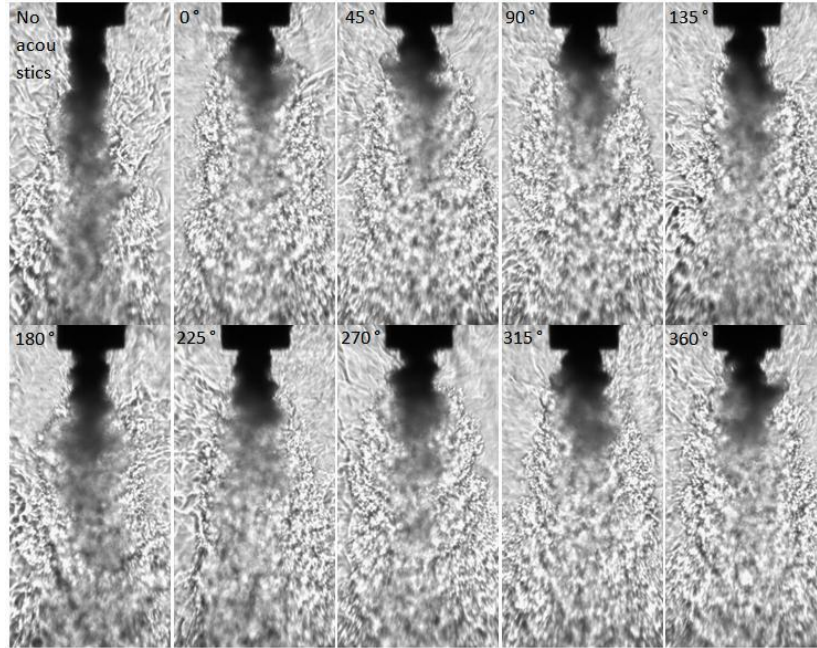


Figure 5.45. Coaxial jet images with the new injector at nearcritical pressure ($P_{\text{chamber}} = 3.56 \text{ MPa}$, $J = 19$).

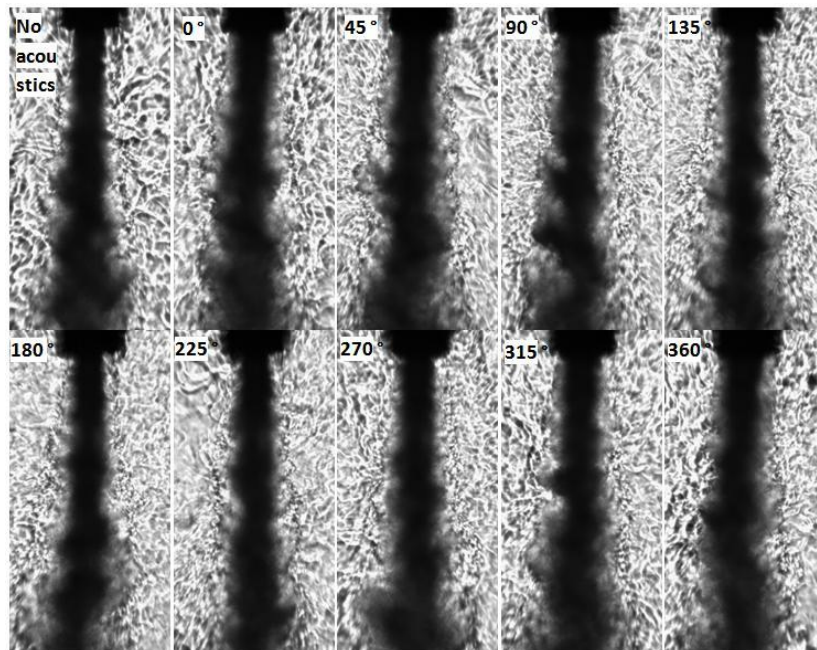


Figure 5.46. Coaxial jet images with the new injector at supercritical pressure ($P_{\text{chamber}} = 4.95 \text{ MPa}$, $J = 2.6$).

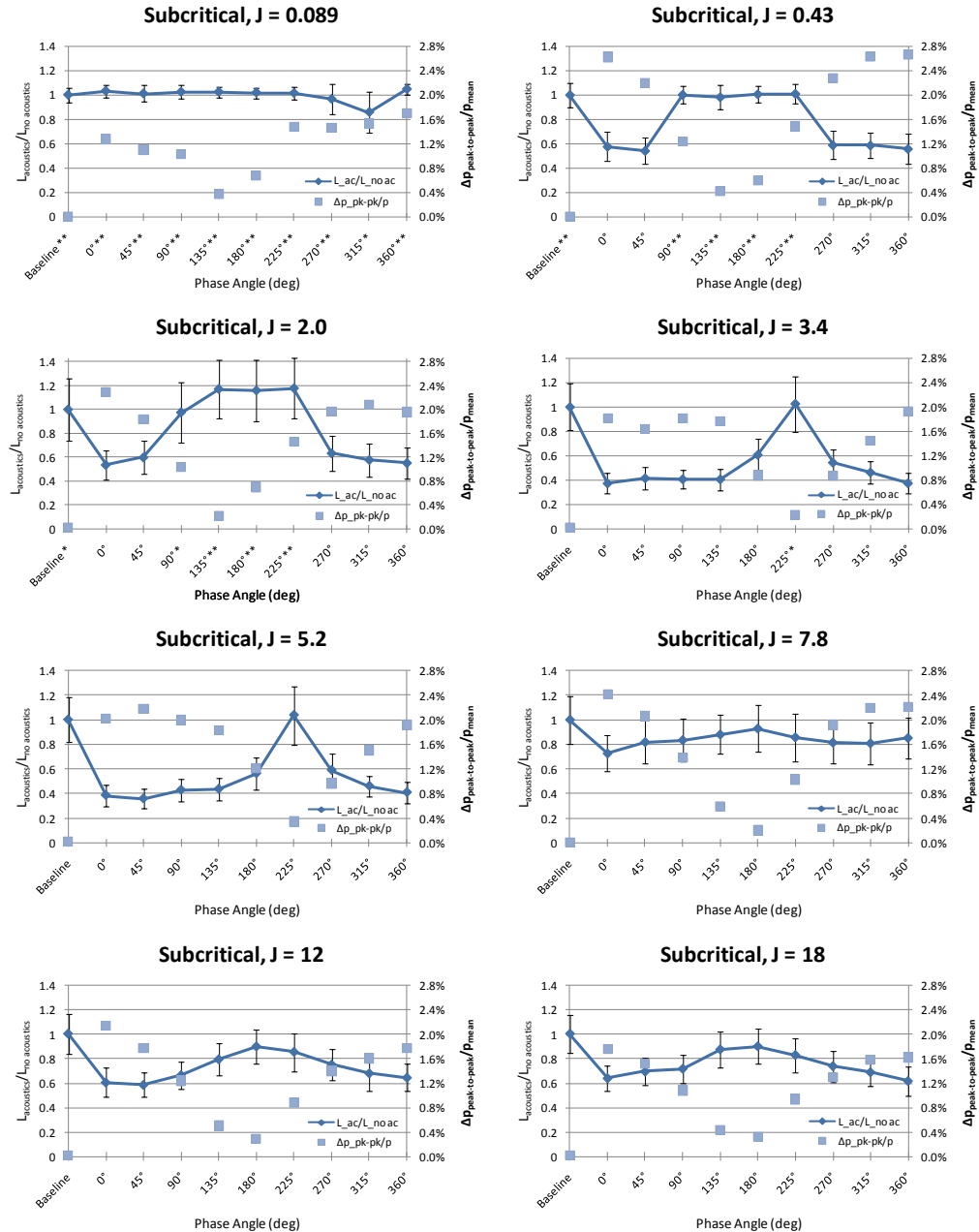


Figure 5.47. Dark core length with acoustics ($L_{\text{acoustics}}$) over dark core length without acoustics ($L_{\text{no acoustics}}$), shown in diamonds, versus phase angle between acoustic sources for subcritical pressures. The the peak-to-peak pressure perturbation as a percentage of the mean chamber pressure ($\Delta p_{\text{peak-to-peak}}/p_{\text{mean}}$), in squares, is also plotted. The cases which had their x coordinate marked with an asterisk (*) denote cases that had a dark core length that was longer than the field of view in more than 10% but less than 50% of the images. The ones marked with two asterisks (**) had dark cores larger than the examination window for at least half of the images. New injector geometry.

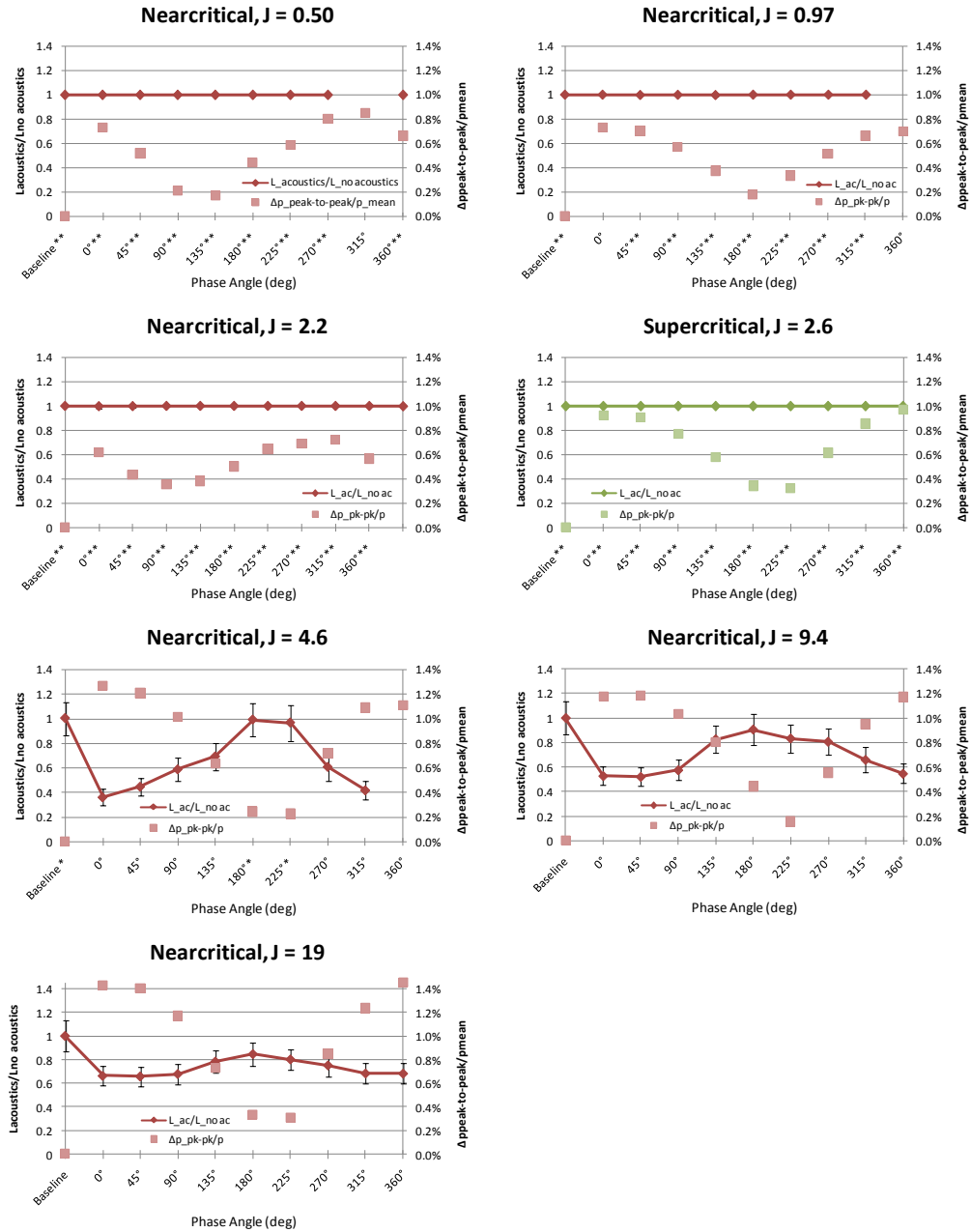


Figure 5.48. Dark core length with acoustics ($L_{\text{acoustics}}$) over dark core length without acoustics ($L_{\text{no acoustics}}$), shown in diamonds, versus phase angle between acoustic sources for pressures above the critical point. The the peak-to-peak pressure perturbation as a percentage of the mean chamber pressure ($\Delta p_{\text{peak-to-peak}}/p_{\text{mean}}$), in squares, is also plotted. See caption of Figure 5.47 for further details. New injector geometry.

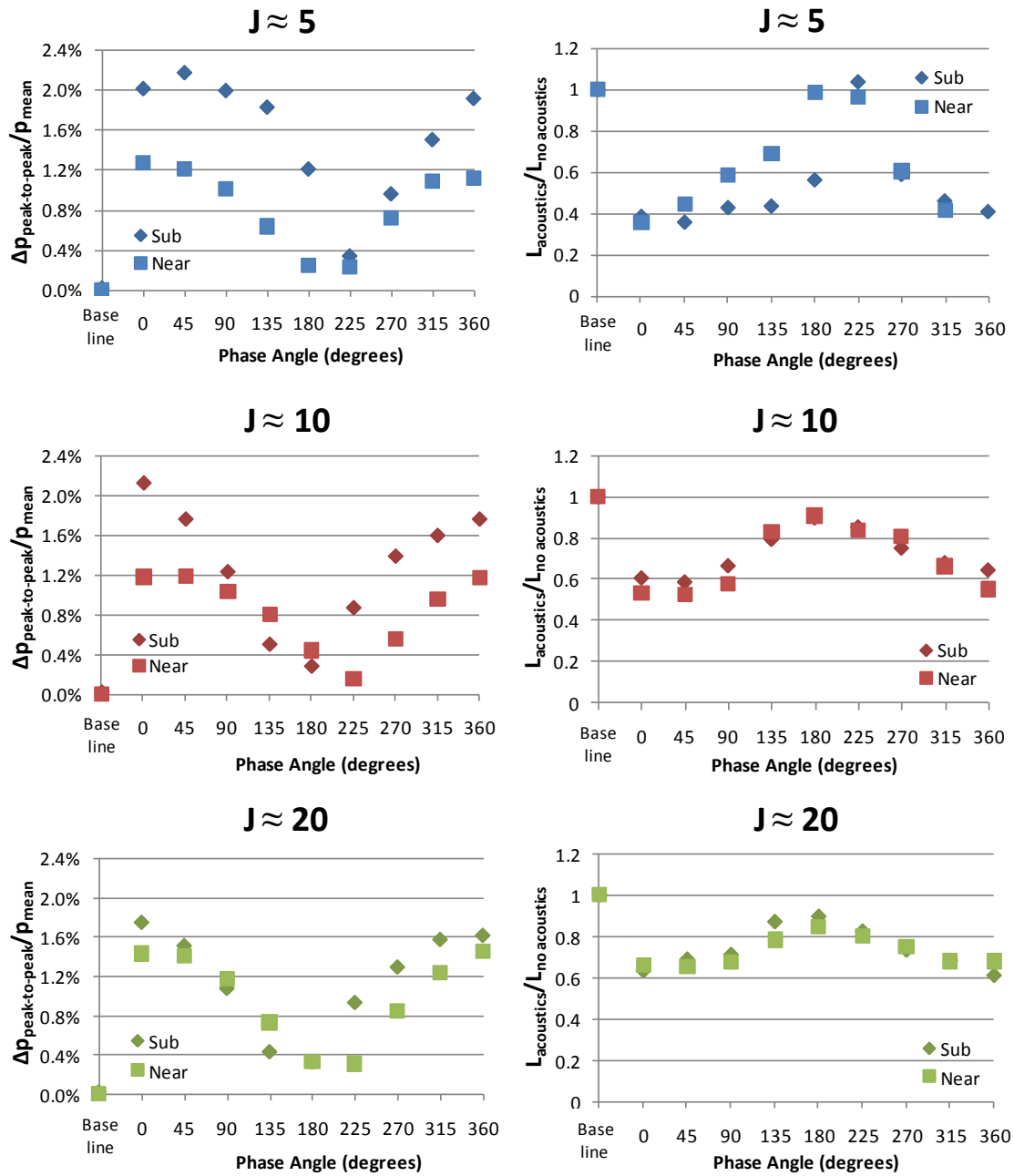


Figure 5.49. Peak-to-peak pressure perturbation ($\Delta p_{\text{peak-to-peak}}$) as a percentage of the mean chamber pressure (p_{mean}) and dark core length with acoustics ($L_{\text{acoustics}}$) over dark core length without acoustics ($L_{\text{no acoustics}}$) versus phase angle between acoustic sources for sub, near and supercritical pressures at $J \approx 5, 10$ and 20 for the new injector geometry.

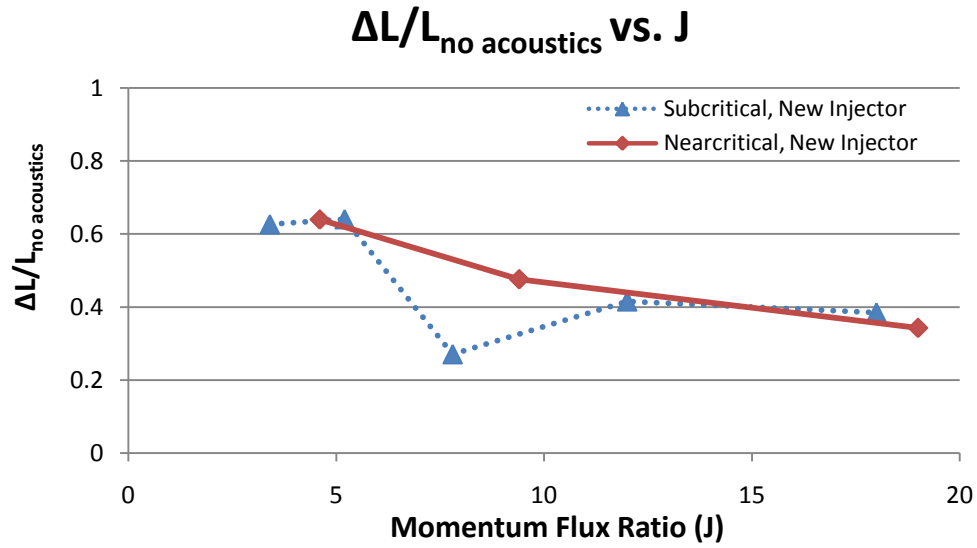


Figure 5.50. Maximum dark core length reduction between dark core length without acoustics and dark core length with acoustics for all phase angles $(L_{no\ acoustics} - L_{acoustics})_{MAX}$ for a given case divided by the dark core length without acoustics ($L_{no\ acoustics}$) as a function of J for moderate and higher momentum flux ratio cases obtained with the new injector.

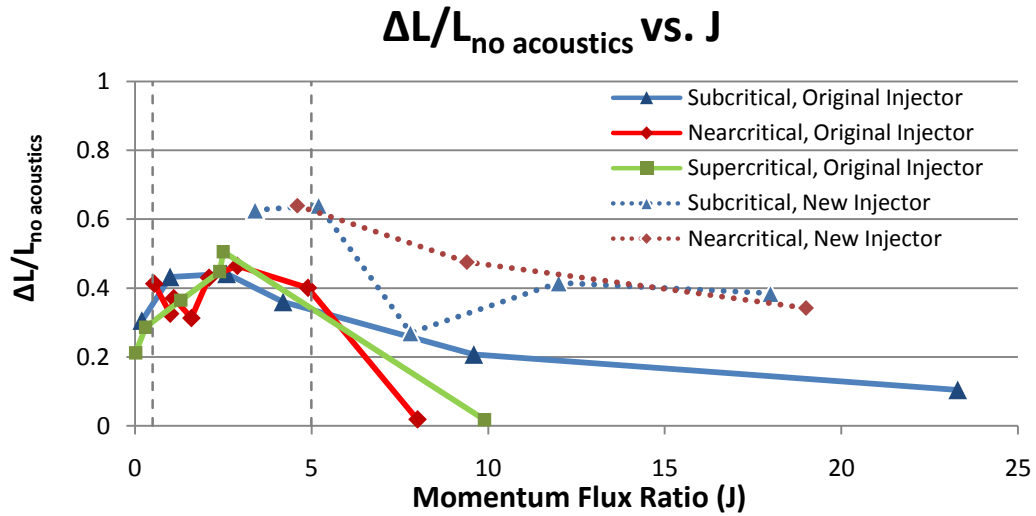


Figure 5.51. Comparison of the maximum dark core length reduction as a function of momentum flux ratio between the original injector geometry and the new injector geometry.

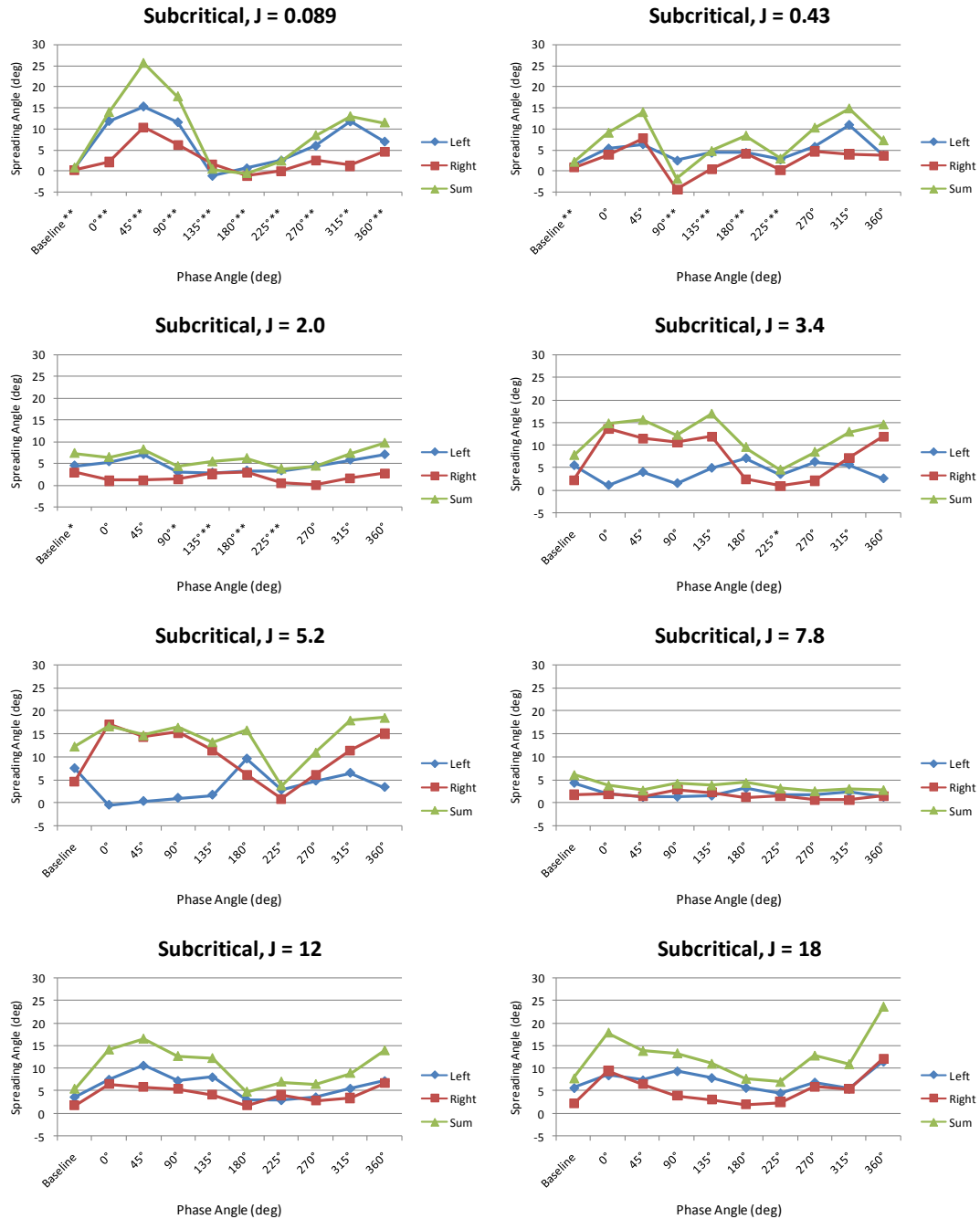


Figure 5.52. Maximum spread angles as a function of acoustic phase angle for different J values at subcritical pressures for the new injector geometry. The cases which had their x coordinate marked with an asterisk (*) denote cases that had a dark core length that was longer than the field of view in more than 10% but less than 50% of the images. The ones marked with two asterisks (**) had dark cores larger than the examination window for at least half of the images.

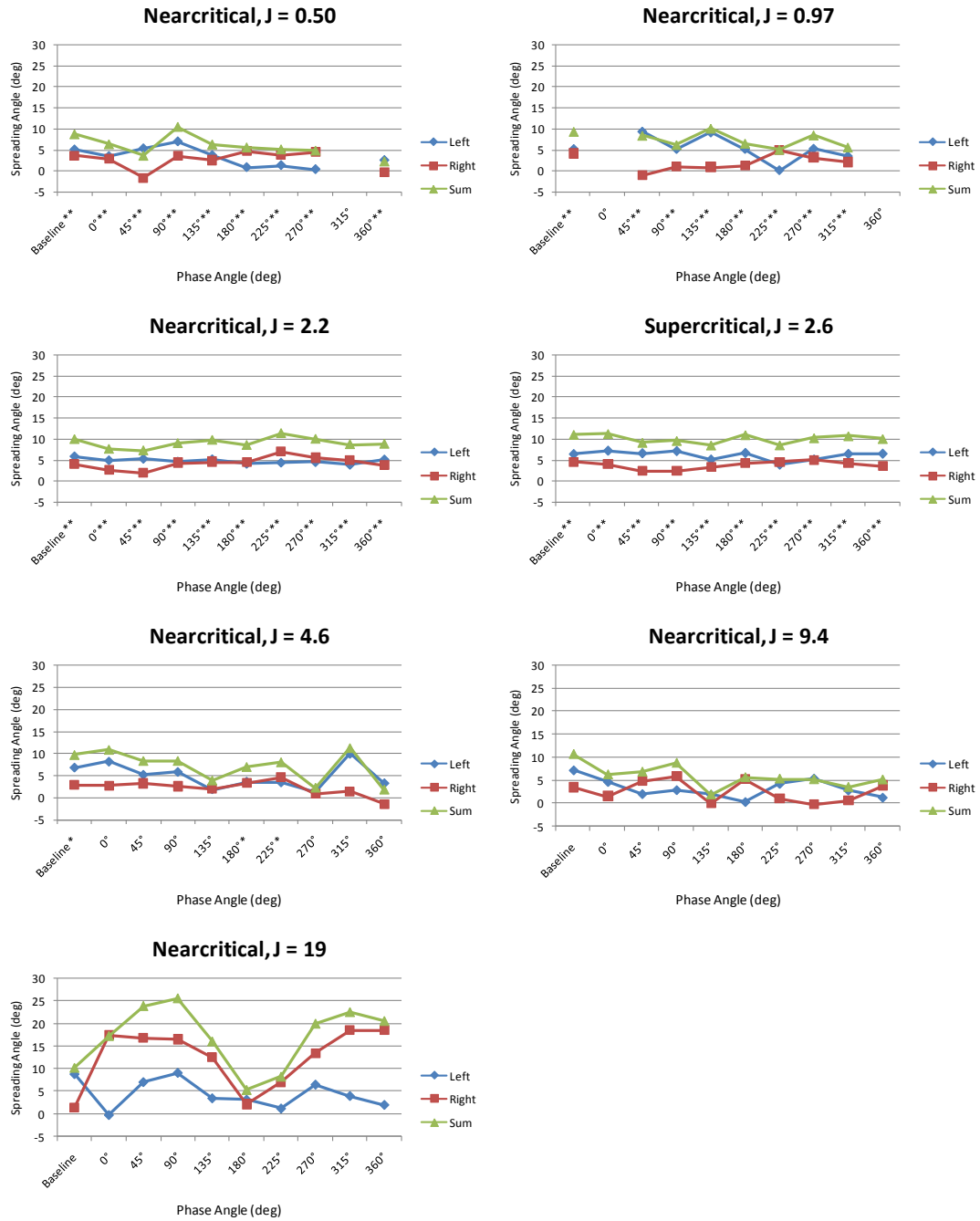


Figure 5.53. Maximum spread angles as a function of acoustic phase angle for different J values at near and supercritical pressures for the new injector geometry. See caption of Figure 5.52 for further details.

CHAPTER 6

Conclusions and Future Work

With the motivation being an improved understanding of fundamental acoustic coupling with condensed-phase combustion and mixing relevant to Liquid Rocket Engines, the present dissertation has described experimental studies on relevant phenomena in both droplet combustion and in coaxial, cryogenic jets. Both sets of experiments have elucidated important phenomenological features of this coupling.

6.1 Acoustically Coupled Droplet Combustion

The present experiments quantified changes that can occur in mean burning rate constants and flame structures associated with a single burning fuel droplet during acoustic excitation for several different fuels and for a range of excitation conditions. The effects of the acoustic excitation with the droplet placed in the vicinity of a pressure node and a pressure antinode have confirmed noticeable increases in burning rates for different alternative fuels. Effective acoustic accelerations, estimated to be on the order of $g_a \approx 2 \text{ m/s}^2$ or less, were observed to have an effect on flame deformation and droplet burning rates. Despite the fact that natural convection is predominant in a normal gravity environment, these acoustic excitation levels had a noticeable effect on the combustion behavior of the droplet. For instance, at sufficiently high acoustic intensities, strong flame deflection and distortion were routinely observed for burning droplets away from the

pressure node or pressure antinode. Thus, the current configuration provides a useful setup for a systematic testing of the response of different fuels during combustion to an acoustically resonant environment. Increases in burning rate, changes in ignition and extinction phenomena and altered flame response can be quantified and were explored for different condensed phase fuels.

During acoustic excitation of droplets situated in the vicinity of a pressure node or antinode, flame orientation was consistent with the sign of an acoustic radiation force acting on the burning system, per the theory proposed by Tanabe, et al (11; 12). This type of acoustic excitation created conditions where the flame deflection switched, depending on the relative location of the droplet. It is noted that later droplet experiments by Teshome et al. (80) in our group, in which two speakers at either end of the waveguide were incorporated, a more symmetric acoustic field was created, and hence somewhat greater consistency with the theory of Tanabe was observed. Yet, in the present experiments, increases in burning rates were observed as the droplet was moved further from the pressure node or antinode for high amplitude acoustic excitation, consistent with the theory. Moreover, the degree of increase in droplet burning rate was slightly different for different fuels, in some cases as high as 20% above the unforced burning rate. With respect to the preliminary estimates of extinction strain rates, it appeared that the Fischer-Tropsch and aviation fuels, JP-8 and Jet A, tended to have lower extinction strain rates, of the order 300 s^{-1} , than did the alcohol fuels (ethanol and methanol, of the order 400 s^{-1}).

It is important to note, however, that for some conditions, the differences were within the uncertainty of the rough estimation of strain rate. Further studies of extinction

phenomena have been ongoing, examined by Sophonias Teshome at the Energy and Propulsion Research Laboratory at UCLA. His findings were recently presented at the 61st Annual Meeting of the APS Division of Fluid Dynamics in San Antonio, Texas (80).

6.2 Acoustic Driving of Coaxial Jets

6.2.1 Summary and Conclusions

This study complemented previous work done at AFRL on shear coaxial jet spreading angles and dark core length measurements from subcritical to supercritical pressures. With a second acoustic source to generate a variable phase acoustic field, the present study aims to understand the effect of such variable acoustic field on the behavior of shear coaxial injectors. The coaxial jet was exposed to pressure node (velocity antinode) conditions, where pressure perturbations are small and velocity perturbations large; to pressure antinode (velocity node) conditions, where pressure fluctuations are large and velocity fluctuations are small; and other acoustic conditions in between by carefully varying the phase angle between the two acoustic sources. Acoustic forcing at 3 kHz was utilized to maximize the pressure fluctuations within the chamber, reaching maximum values between 1 to 4% of the mean chamber pressure.

The second objective of this study was to look at the effect of geometry on shear coaxial injector flows. Two geometries were studied. The original injector had a large recirculation zone with a post thickness 1.1 times the size of its inner diameter. The new injector had an inner jet post just one tenth the size of its inner diameter with minimum

recirculation expected. This study spanned a range of outer to inner jet momentum flux ratios from 0.019 to 23, obtaining results for at least 6 different J values at each pressure condition.

First, for the original injector, which had been used in previous studies at AFRL, the results showed the largest reduction of dark core length with acoustic excitation in the $1 < J < 5$ range for all pressure regimes and up to 10 for the subcritical regime. This agrees with previous results (22; 23). The effect of acoustics at lower or higher momentum flux ratios did not have significant effects on the behavior of the dark core length. This observation was supported by analyzing the behavior of the inner jet spreading angle for all conditions. Also, the single phase gas-gas coaxial jet experiments found that the outer jet spreading angle remains constant for $J > 0.1$, in agreement with previous results showing essentially a constant angle for liquid-gas subcritical conditions, and a wide variety of supercritical conditions (75).

Second, a new coaxial injector design was tested. There was a qualitative enhancement in mixing and atomization of the inner jet dark core with the surrounding outer jet and chamber obtained with this new injector. The new injector data extended the range at which acoustics had a noticeable effect on the coaxial flow to momentum flux ratios as low as 0.1 in the subcritical pressure regime when compared to the original injector. Testing at nearcritical and supercritical pressures showed a measureable response for J equal to 5 or greater. The quantitative analysis of the data for the new injector showed that the longest dark cores with acoustic excitation were observed at or near the pressure node location both at subcritical and supercritical conditions. The new

injector thus provided evidence that different geometries for coaxial injectors of similar size could have an impact on the dynamics of a coaxial jet.

The fact that the results for the new injector show that the normalized dark core lengths ($L_{\text{acoustics}}/L_{\text{no acoustics}}$) for the different phase angle conditions at subcritical and nearcritical cases agree remarkably well for a given outer to inner jet momentum flux ratio is evidence of similarity between the dynamics of the original and new injector. The maximum reduction of the dark core length between the baseline condition and a condition with the acoustics on, regardless of phase angle, also had good agreement between the original and the new injector. Both injectors showed the same large effect on the dark core at moderate J values and as the momentum flux ratio is increased the maximum reduction decreases. These results were found to be independent of the relative acoustic pressure the coaxial jets were exposed to.

A noticeable difference between the original and new injector results was found. In general, phase angle had a weak effect on most results obtained with the original injector geometry. On the cases that the effect was clear, being at a pressure node shortened the dark core length the most. In contrast, the results with the new injector showed a clear phase angle effect with the longest dark cores occurring at the pressure node.

Third, the results in this study showed that the relative acoustic pressure did not seem to severely affect the behavior of the dark core length for different pressures at the same outer to inner momentum flux ratio. This finding supports the possibility that only a small perturbation, equal or smaller than the relative amplitudes used in this study, is

needed to achieve the same large reductions of the dark core length obtained with the largest perturbations. If the previous proposition is true, even small pressure perturbations could have a large impact on the stability behavior of LRE injectors and other applications of coaxial flows.

Relevant to the previous finding is the discussion on stability of liquid jets and coaxial flows presented in this study. Using local/global and convective/absolute instability concepts the response of the two coaxial jet geometries to acoustic excitation was roughly assessed. It is very possible that there exists a range of values of the momentum flux ratio or a similar parameter for which the coaxial jet behaves as a convectively unstable flow, given the response of the coaxial jet to the acoustic forcing outlined above.

Finally, given the discrepancy in the dark core length behavior at the pressure node and antinode and the qualitative differences observed between the two injectors, it is possible that a different non-dimensional number not used in this study exists which can reduce the data from the original and new injector in a more ordered fashion. However, from an overall perspective, the momentum flux ratio, J , has proven to be a very good parameter to systematically describe the relative change in dark core lengths and spreading angles for acoustically excited coaxial injector flows. Also, by analyzing coaxial injectors with a very large and a very small inner jet post thickness we have covered both ends of the spectrum of practical applications in coaxial jet flows.

6.2.2 Future Work

Testing at the Supercritical Cryogenic Experimental Cell EC 4 at AFRL in Edwards, AFB will continue with the new coaxial injector design presented in this dissertation. Other parameters and regimes such as outer jet spreading angles and single phase subcritical (gas-gas) conditions could also be explored. A quantitative investigation of the instability of the coaxial jet with the current geometry is recommended to identify parameters that might lead to weaker or stronger response of the flow to acoustic excitation

Preliminary work has been started to study the effects of the recess length between the inner jet and the outer jet posts. All the cases presented in this thesis with both the original and new injector had a recess length of one half the inner diameter of the inner jet post ($1/2 D_{ii}$ as shown in Figure 1.4). A systematic study will be performed to look at the effect of this distance on the coaxial jet dynamics. Data will be gathered when there is no recess and both posts are “flushed”, and at other recess lengths.

CFD simulations that model exact or similar conditions and geometries have been available from other groups closely related to our experimental research. An effort to develop a computer model readily available to the group at AFRL in Edwards, AFB has been underway. If fully implemented, this project could evolve into a very successful experimental design tool for new injectors and flow models and provide supporting evidence to experiments performed at the Supercritical Cryogenic Facility.

A method to obtain instantaneous velocity measurements at the exit of the injector would aid in understanding the flow behavior where the two coaxial streams meet and the

effect of the acoustics on the trajectory of fluid particles. However, given the current configuration of the facility, this diagnostics method might be very difficult to implement.

Using a different fluid, such as helium, for either the inner or outer jet would increase the range of conditions that can be tested in EC 4 and provide experimental cold flow data with different species at the unique conditions this facility offers such as supercritical pressures and variable phase transversal acoustic excitation to be available for the research community.

Finally, a plan to construct a new supercritical chamber at AFRL in Edwards, AFB that will study reactive flows under the effects of acoustic excitation is in progress. It is currently at its preliminary stages and when it is finished it will have the capability to test many of the injector configurations that have been tested with the current, non-reactive facility. The versatility to test the behavior of a coaxial injector both in a non-reactive and a reactive environment will give the researcher the possibility to understand which acoustic effects are due to the fluid mechanics of the flow alone and which are enhanced by the energy release and combustion processes of the propellants in a Liquid Rocket Engine.

APPENDICES

The appendices consist of three sections. Appendix A presents a detailed schematic of the flow system used in the experiments performed at the Supercritical Cryogenic Facility EC 4 at AFRL in Edwards AFB, CA. It shows the version that was used for the tests with the original injector. Figure 4.2 in Chapter 4 shows the upgrades performed when the new injector was installed. Appendix B lists the standard operating procedures that were followed in the EC 4 facility for every test. Appendix C provides a summary of the coaxial jet experimental data presented in this dissertation.

APPENDIX A

Detailed Schematic of Coaxial Jet Experimental Facility

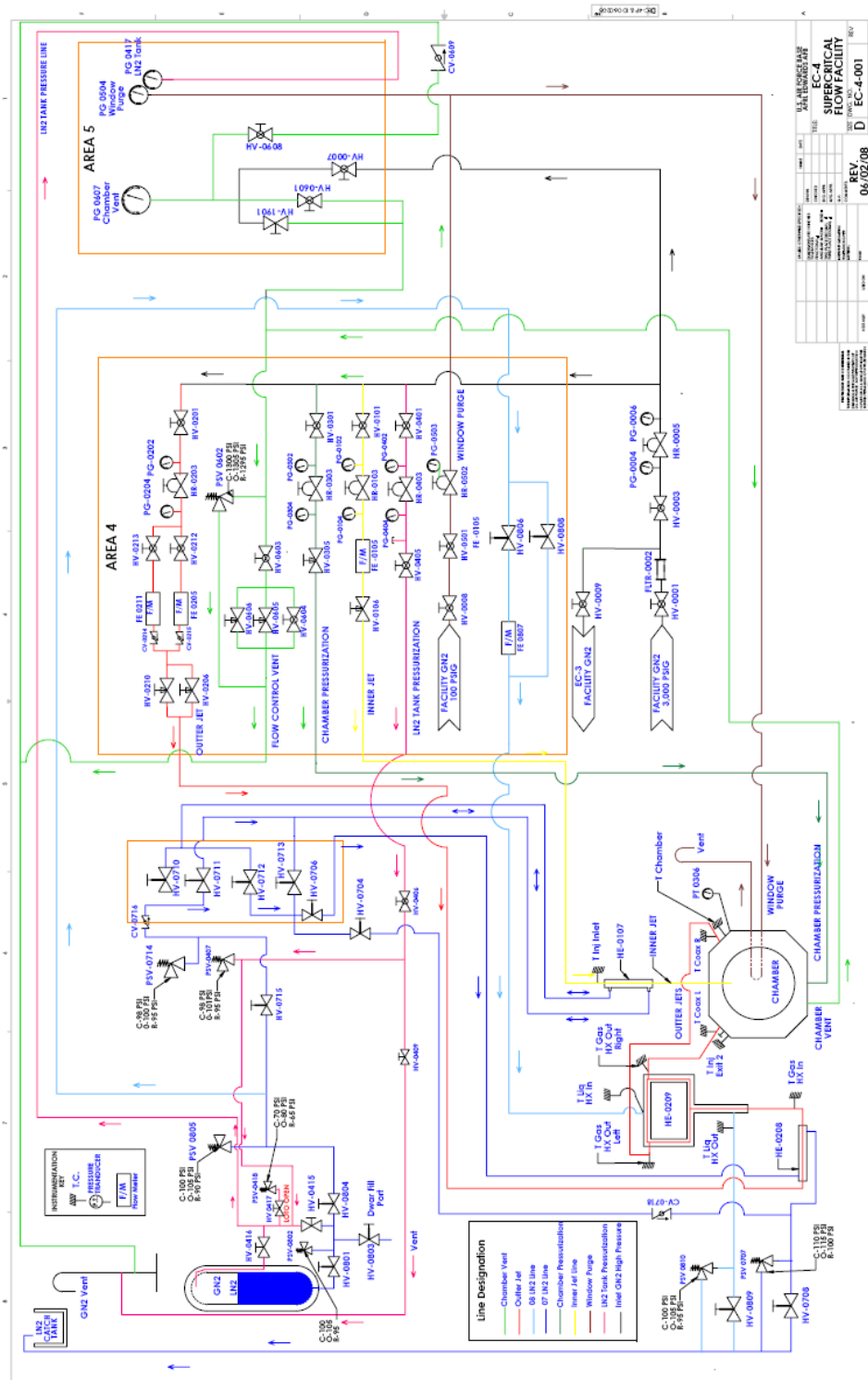


Figure A.1. Detailed schematic showing the flow path of the experimental setup of this study.

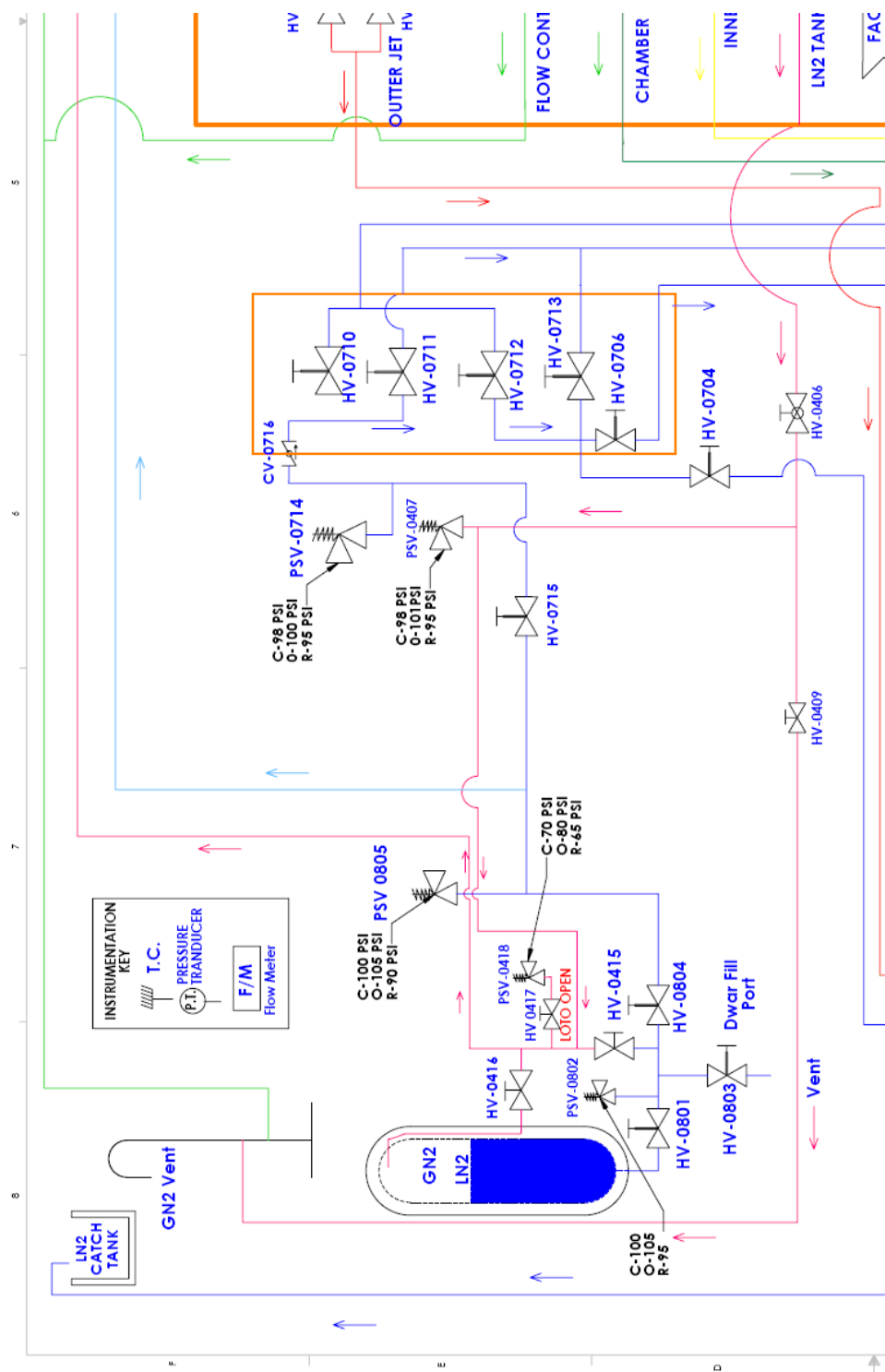


Figure A.2. Expanded view of the upper left section of the flow path schematic in Figure A.1.

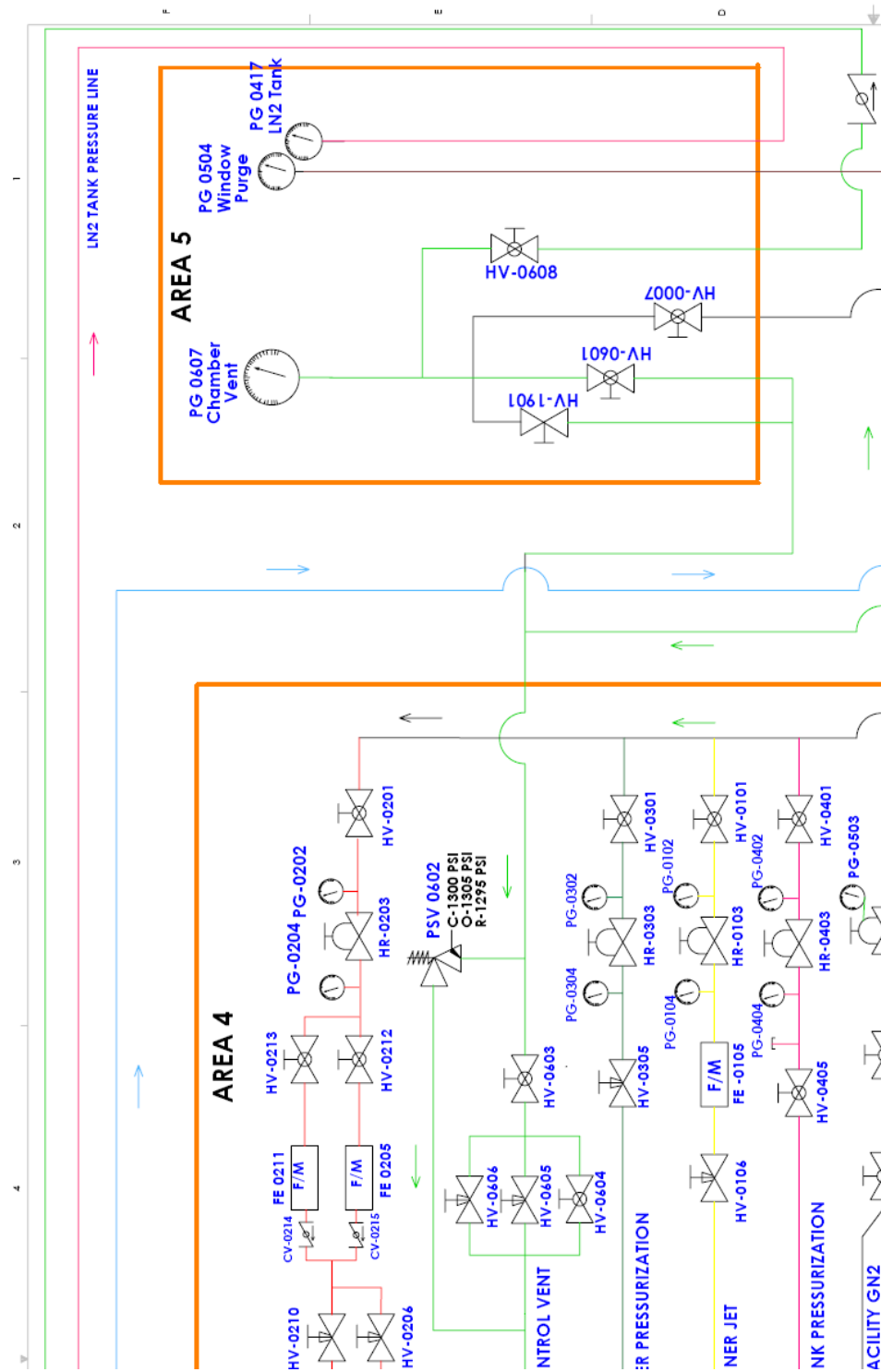


Figure A.3. Expanded view of the upper right section of the flow path schematic in Figure A.1.

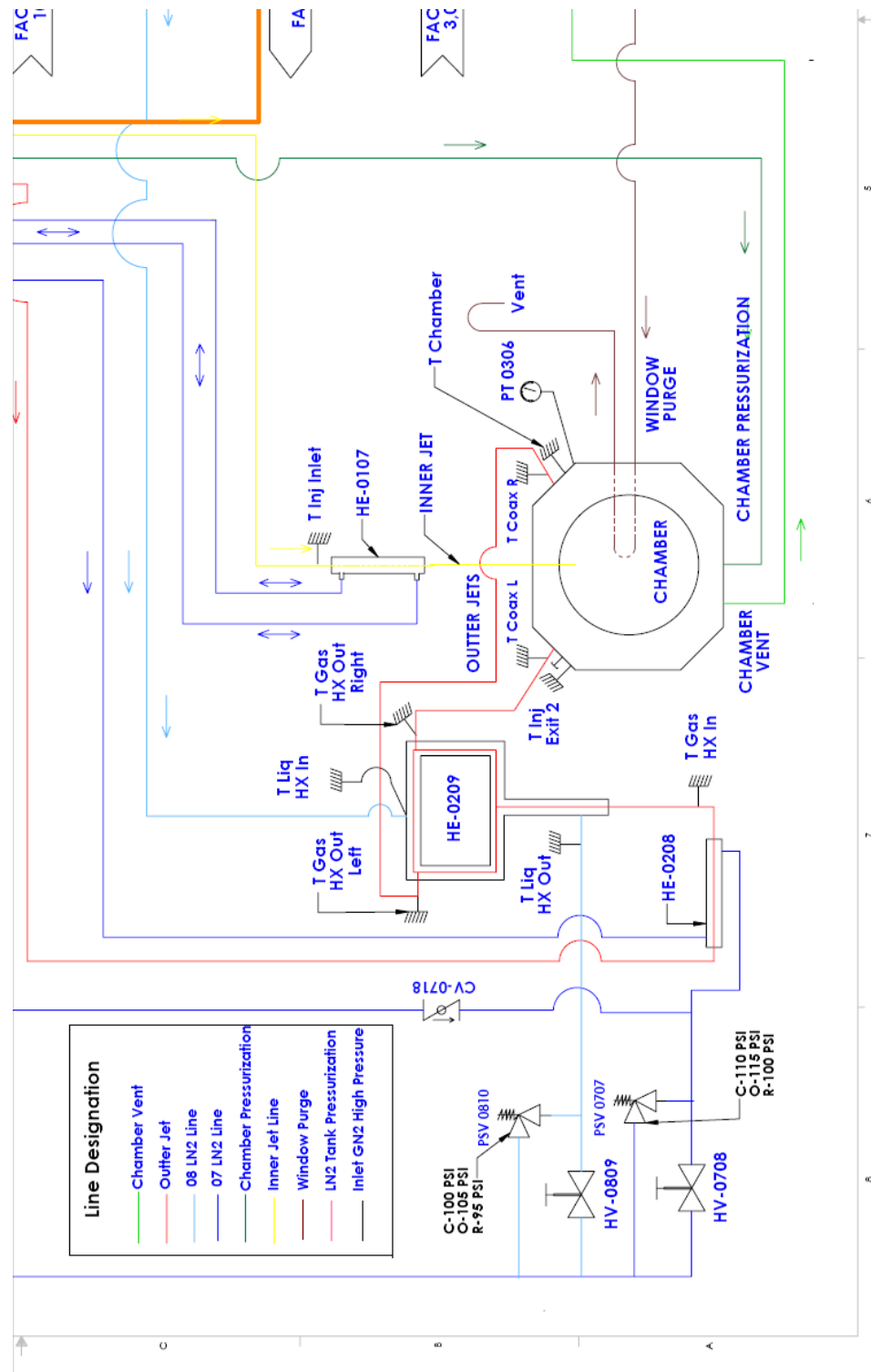


Figure A.4. Expanded view of the lower left section of the flow path schematic in Figure A.1.

APPENDIX B

Coaxial Jet Experimental Procedures

**BUILDING 8451
EXPERIMENTAL CELL, EC-4
AIR FORCE RESEARCH LABORATORY
EDWARDS AFB, CA**

PROCEDURE: SOP-RZSA-EC4-0001
REVISION: 2.4
DATE REVISED: September 4, 2008
No. OF PAGES: 23

**BUILDING 8451
EXPERIMENTAL CELL, EC-4
OPERATIONS**

PROCEDURE TITLE

**SUPERCRITICAL COLD FLOW
OPERATIONS using LN2/GN2**

PREPARED BY:

Ivett Leyva, Principal Investigator, RZSA

DATE

REVIEWED BY:

Doug Talley, Program Manager, RZSA

DATE

COORDINATED BY:

Randy Harvey, Red Crew Leader, ERC

DATE

Tim Auyeung, System Safety Engineer, Det 7/SES

DATE

APPROVED BY:

David Campbell, Program Manager, ERC

DATE

Ingrid Wysong, Branch Chief, RZSA

DATE

Debra Fuller, Branch Chief, Det 7/SE

DATE

Revision	Notes	Prepared By
0	- Initial procedure written	D. Davis, 24 June 2004
1	- Added more details on the operation of the facility - Deleted Dewar steps and LN2 mass flow meter	I. Leyva, 12 May 2006
2	- Modified procedures to account for a different arrangement of hand valves	J. Rodriguez, 30 July 2007
2.1	- Slight modifications to order of instructions in general procedure	J. Rodriguez, 31 July 2007
2.2	- Minor changes in preparation steps before pressurization	J. Rodriguez, 22 August 2007
2.3	- Slight modifications to instructions - Added explanatory notes to some steps	J. Rodriguez, 10 October 2007
2.4	- Modified procedures to account for rearrangement of flow elements	J. Rodriguez, 4 September 2008

PERSONNEL

EXPERIMENTAL CELL EC-4

DATE

AEROPHYSICS BRANCH, BLDG 8451

WORK

AUTHORIZATION#

The following personnel are designated as test team members, and are charted to perform their assignment as follows:

Test Conductor (TC) – Responsible for the timely performance of the test as written and for overall facility and test safety. This includes coordinating and directing the activities of the Red Crew and other test support teams. TC is responsible for coordinating all pretest activities and outside support required, including (but not limited to) security, fire, medical, and safety. TC is responsible for initialing completion on each step of the master test procedure and ensuring all test goals are met and all critical data is acquired. Has authority to perform real-time redlines on test procedures as required to ensure test requirements and goals are met. All safety-related redlines will be coordinated and approved by AFRL and/or ERC Safety.

Name _____ Signature _____

Red Crew Leader (RCL) – Responsible for directing the activities of Red Crew members. Reports directly to the TC and ensures all Red Crew tasks are completed. Responsible for ensuring all RCM's have all required certifications and training. Responsible for ensuring all required equipment is available, accessible, and serviceable.

Name _____ Signature _____

Other Test Team Members – Responsible for performing ancillary duties in support of test, support of anomaly resolution, and other necessary activities.

Name _____ Signature _____

Name _____ Signature _____

ALL TEST TEAM MEMBERS – Responsible for the safe performance of the test. Have read and understood all portions of the test procedure. Any Test Team Member can declare an emergency or unsafe condition.

1.

ABBREVIATIONS AND ACRONYMS

CPR	- Cardiopulmonary Resuscitation
CV	- Check Valve
EC	- Experimental Cell
ER	- Engineering Request
FE	- Flow Element
FLTR	- Filter
FLX	- Flexible Line
FOD	- Foreign Object Debris
GN2	- Gaseous Nitrogen
HE	- Heat Exchanger
He	- Helium
HR	- Hand Regulator
HV	- Hand Valve
LN2	- Liquid Nitrogen
N2	- Nitrogen
PC	- Chamber Pressure
PG	- Pressure Gauge
PI	- Principal Investigator
PM	- Program Manager
PPE	- Personal Protective Equipment
PSV	- Pressure Safety Valve
PT	- Pressure Transducer
QA	- Quality Assurance
RCL	- Red Crew Leader
RD	- Rupture Disk
SCF	- Supercritical Facility
SOCC	- Site Operations Control Center
SOP	- Standard Operating Procedure
TC	- Test Conductor
TOP	- Test Operation Procedure

_____ 2.		TEST DESCRIPTION AND OBJECTIVES
_____ 2.1.		PURPOSE
		This procedure performs a stand-alone operation of the EXPERIMENTAL CELL, EC-4. This procedure may be used in conjunction with other Test Operation Procedures (TOP) or Work Authorizations (WA) as required to support operations or checkouts.
_____ 2.2.		SCOPE
		This procedure will verify proper configuration before operation including purges and valve configuration and sequential steps to perform the Supercritical Cold Flow (SCF) Operation. Securing the SCF post operation and emergency shutdown are also included in the procedure.
_____ 3.		DOCUMENTATION
		The completion of each applicable event shall be verified by marking to the left of the item number by the TC. Deviations from these procedures will be coordinated with the Test Engineer, TC, RCL
_____ 3.1.		APPLICABLE DOCUMENTS
		AFRL/PR OI 91-202, Environmental, Safety, and Occupational Health (ESOH) Programs, 7 Aug 2000. Space & Missile Propulsion Division, Chemical Hygiene Plan (CHP), Bldg 8451.
_____ 3.2.		REFERENCE DOCUMENTS: NONE
_____ 3.3.		SPECIFICATIONS
		Nitrogen Purge Gas: Pressurizing agent, nitrogen, Grade B, Type I, Spec. Mil-P-27401. Water: Facility domestic water supply
_____ 3.4.		DRAWINGS
		EC4-001, EC-4 Supercritical Facility

4.

4.1.

4.2.

4.3.

4.4.

TEST REQUIREMENTS AND RESTRICTIONS

TRAINING

The following training is required for personnel using these procedures:

CPR & First Aid

Initial HAZCOM

Job Site HAZCOM

High Pressure

Cryogenics

Lock-Out/Tag-Out

Noise

MAXIMUM PERSONNEL ALLOWED IN EC-4:

Five (5): Workers – (3) (RCL and TC),
Supervision – (1) (PI, PM, etc.),
Casual (Bio, Safety, QA, etc) – (1)

LIST OF EQUIPMENT

Vapor Detection Equipment: two (2) portable oxygen sensors (one for each worker in the cell).

Mechanics Tool Kit, Torque Wrench, Caliper, Digital Thermometer and Multimeter.

Ensure all tools associated with this experiment/test/operation are accounted for prior to initiating system/item test. Assure all trash, debris, and FOD is picked up from around the test stand.

METEOROLOGICAL LIMITATIONS/ RESTRICTIONS

A. No hazardous operations will be started when thunderstorms are within 25 nautical miles (28.75 miles) of AFRL unless the operation can meet the requirements for stopping the operation for lightning within 10 nautical miles. Operations in progress may be completed if it is safe to do so; however supervisors must assess individual operations to determine the appropriate action.

B. All hazardous operations will be stopped when thunderstorms are within 10 nautical miles (11.5 miles) of AFRL. The operation should be secured and personnel evacuated to Bldg 8451 and remain indoors.

C. All outside work must stop when thunderstorms are within 5 nautical miles (5.75 miles) of AFRL and all personnel must seek safety in Bldg 8451 until the lightning warning is cancelled.

_____ 5.	SAFETY REQUIREMENTS
_____ 5.1.	<p>TEST HAZARDS:</p> <p>Nitrogen gas (GN2) is used for pressurization of the chamber and production of the supercritical jet in the chamber. Nitrogen gas can cause asphyxiation hazards to personnel working in EC-4. Oxygen deficiency monitors will be used to warn personnel working in EC-4 of the hazard.</p> <p>Liquid nitrogen (LN2) is used for temperature conditioning of the supercritical jet in the chamber. This presents a cryogenic hazard to test crew working inside and outside EC-4. LN2 will also convert to GN2.</p> <p>The Acoustic test can produce hazardous noise levels (>120 dB). Personnel are required to wear ear muffs to reduce exposure.</p>
_____ 5.2.	<p>PERSONNEL PROTECTIVE CLOTHING REQUIREMENTS</p> <p>Test PPE: Lab coat or coveralls, safety goggles, safety shoes, and ear muffs (noise protection as required).</p> <p>Cryogenic PPE: Cryogenic gloves.</p>
_____ 5.3.	<p>TEST AREA ACCESS DURING OPERATIONS</p> <p>EC-4 GREEN: Normal test preparation activities. There are no pressure or chemical hazards in the test cell. The RCL will limit access to the affected operational area of interest.</p> <p>EC-4 AMBER: Hazardous chemicals in the test cell. No pressure or flows (static condition). RCL will monitor the Test Cell entrance, and prevent access to the cell. Personnel will not be allowed access to the test area unless cleared by the RCL and TC.</p> <p>EC-4 RED Hazardous test operations including propellant chill downs and purging operations. The TC will maintain access control to the area. Personnel will not be allowed access to EC-4 unless cleared by the TC.</p>

_____ 6.		EXPLOSIVE LIMITS: NONE
_____ 7.		EMERGENCY PROCEDURES In the event of a major nitrogen leak or other emergency that jeopardizes the safety of the operators or other personnel perform Section 20 emergency procedures at the end of this document.
_____ 8.		SPECIAL INSTRUCTIONS Red Crew Member shall notify Test Engineer of any leaks from the system. Any lines, which require maintenance or re-torquing, should be coordinated with Test Engineering to maintain SCF system cleanliness. Work must be authorized in order to break into clean and sealed systems.
_____ 9.		PRETEST PREPARATIONS
_____ 9.1.	ALL	DON Test PPE listed in step 5.2
_____ 9.2.	RCL	Verify portable oxygen sensors are operational and calibrated.
_____ 9.3.	RCL	Turn ON or Verify ON EC-4 Air Handler ventilation system.
_____ 9.4.	RCL	Turn OFF Air Handler.
_____ 9.5.	ALL	UNLOCK EC-4 outside door.
_____ 9.6.	ALL	NOTE any potential hazards in and outside EC-4
_____ 9.7.	ALL	Verify GREEN, AMBER, and RED lights are functional and return to GREEN.
_____ 9.8.	TC	If Acoustic Testing Verify Gain or Turn Gain on Amplifier to the ZERO position.
_____ 9.9.	TC	If Acoustic Testing, Turn ON Amplifier to allow warm up as per ER_____
_____ 9.10.	RCL	If Acoustic Testing, POST "HEARING PROTECTION REQUIRED" signs on the outside of the doors to EC-4, Room 19, foam door and adjacent hallway.
_____ 9.11.	TC	Turn on Data Acquisition System and System Electronics.
_____ 9.12.	RCL	Position "DO NOT ENTER" sign on exterior door near LN2 catch tank.
_____ 9.13.	RCL	Position "DO NOT ENTER" signs in rooms 39 and 41.
_____ 9.14.	RCL	Place chain in front of entrance to horseshoe.

_____10.		INITIAL SETUP
_____10.1.	RCL	OPEN / Verify OPEN HV-0001 (EC-3, EC-4 Primary Facility Isolation Valve) - Area 3
_____10.2.	RCL	CLOSE / Verify CLOSED HV-0003 (EC-4 Secondary Facility Isolation Valve) - Area 3
_____10.3.	RCL	CLOSE / Verify CLOSED HV-0008 (EC-4 Low Pressure Facility Isolation Valve) - Area 3
_____10.4.	RCL	CLOSE / Verify CLOSED HV-0009 (EC-3 Secondary Facility Isolation Valve) - Area 3
_____10.5.	RCL	CLOSE / Verify CLOSED HV-0406 (Tank GN2 Pressurization Isolation Valve) - Area 2
_____10.6.	RCL	CLOSE / Verify CLOSED HV-0409 (Dewar Pressurization Vent Isolation Valve) - Area 2
_____10.7.	RCL	OPEN / Verify OPEN HV-0715 (Direct LN2 Supply Valve) - Area 2
_____10.8.	RCL	CLOSE / Verify CLOSED HV-0801 (Tank LN2 Isolation Valve) – Area1
_____10.9.	RCL	OPEN / Verify OPEN HV-0803 (Local Dewar Fill Isolation Valve) – Area1
_____10.10.	RCL	CLOSE / Verify CLOSED HV-0804 (Tank-Dewar Separation Valve) – Area 1
_____10.11.	RCL	CLOSE / Verify CLOSED HV-0415 (Vacuum Jacketed Line Purge Valve) – Area 1 NOTE: In case the LN₂ line needs to be broken, moisture could get in. This valve permits purging of the line after it is reconnected
_____10.12.	RCL	CLOSE / Verify CLOSED HV-0416 (Tank GN2 Pressurization Valve) – Area 1
_____10.13.	RCL	CLOSE / Verify CLOSED HV-1901 (He System Isolation Valve) - Area 5
_____10.14.	RCL	CLOSE / Verify CLOSED HV-0601 (PC Vent PG Isolation Valve) - Area 5
_____10.15.	RCL	OPEN / Verify OPEN HV-0608 (Gauge Vent Valve) - Area 5
_____10.16.	RCL	CLOSE / Verify CLOSED HV-0007 (Upstream Regulator Pressure Valve) - Area 5
_____10.17.	RCL	OPEN / Verify OPEN HV-0603 (Chamber Pressure Build Valve) - Area 4

_____10.18.	RCL	OPEN / Verify OPEN HV-0604 (Primary Chamber Pressure Vent Valve) - Area 4
_____10.19.	RCL	CLOSE / Verify CLOSED HV-0605 (Secondary Chamber Pressure Vent Valve) - Area 4
_____10.20.	RCL	CLOSE / Verify CLOSED HV-0606 (Tertiary Chamber Pressure Vent Valve) - Area 4
_____10.21.	RCL	CLOSE / Verify CLOSED HV-0708 (Heat Exchanger LN2 Throttle Vent Valve) – ceiling between Area 4 & Area 5
_____10.22.	RCL	CLOSE / Verify CLOSED HV-0809 (Coax Heat Exchanger LN2 Throttle Vent Valve) – ceiling between Area 4 & Area 5
_____10.23.	RCL	OPEN / Verify OPEN HV-0704 (Heat Exchanger LN2 Bypass Valve) – Area 3
_____10.24.	RCL	CLOSE / Verify CLOSED HV-0706 (Heat Exchanger Flow Valve) – Area 3
_____10.25.	RCL	CLOSE / Verify CLOSED HV-0710 (Primary Co-Flow Valve) – Area 4
_____10.26.	RCL	OPEN / Verify OPEN HV-0711 (Primary Counter Flow Valve) – Area 4
_____10.27.	RCL	OPEN / Verify OPEN HV-0712 (Secondary Counter Flow Valve) – Area 4
_____10.28.	RCL	CLOSE / Verify CLOSED HV-0713 (Secondary Co-Flow Valve) – Area 4
_____10.29.	RCL	CLOSE / Verify CLOSED HV-0806 (Coax LN2 Flow Meter Isolation Valve) – Area 4
_____10.30.	RCL	OPEN / Verify OPEN HV-0808 (Coax LN2 Flow Meter Bypass Valve) – Area 4
_____10.31.	RCL	Verify PG-0607 (Chamber Pressure Gauge) reads 0 psig– Area 5
_____10.32.	RCL	Verify PG-0004 (EC-4 System Inlet Pressure Gauge) reads 0 psig – Area 5
_____10.33.	RCL	DECREASE FULLY / Verify FULLY DECREASED HR-0005 (EC-4 Facility Pressure Regulator) – Area 5
_____10.34.	RCL	Verify PG-0006 (EC-4 System Outlet Pressure Gauge) reads 0 psig – Area 5
_____10.35.	RCL	CLOSE / Verify CLOSED HV-0101 (Center Jet GN2 Isolation Valve) – Area 4

_____10.36.	RCL	Verify PG-0102 (Center Jet GN2 System Inlet Pressure Gauge) reads 0 psig – Area 4
_____10.37.	RCL	DECREASE FULLY / Verify FULLY DECREASED HR-0103 (Center Jet GN2 Pressure Regulator) – Area 4
_____10.38.	RCL	Verify PG-0104 (Center Jet GN2 Regulated Pressure Gauge) reads 0 psig – Area 4
_____10.39.	RCL	CLOSE / Verify CLOSED HV-0106 (Center Jet GN2 Throttle Valve) – Area 4
_____10.40.	RCL	CLOSE / Verify CLOSED HV-0201 (Coax Jet GN2 Isolation Valve) – Area 4
_____10.41.	RCL	Verify PG-0202 (Coax Jet GN2 System Inlet Pressure Gauge) reads 0 psig – Area 4
_____10.42.	RCL	DECREASE FULLY / Verify FULLY DECREASED HR-0203 (Coax Jet GN2 Pressure Regulator) – Area 4
_____10.43.	RCL	Verify PG-0204 (Coax Jet GN2 Regulated Pressure Gauge) reads 0 psig – Area 4
_____10.44.	RCL	CLOSE / Verify CLOSED HV-0212 (Outer Jet Low Flow Isolation Valve) – Area 4
_____10.45.	RCL	CLOSE / Verify CLOSED HV-0213 (Outer Jet High Flow Isolation Valve) – Area 4
_____10.46.	RCL	CLOSE / Verify CLOSED HV-0206 (fine Coax Jet GN2 Throttle Valve) – Area 4
_____10.47.	RCL	CLOSE/ Verify CLOSED HV-0210 (coarse Coax Jet GN2 Throttle valve) – Area 4
_____10.48.	RCL	CLOSE / Verify CLOSED HV-0301 (Chamber Pressurization Isolation Valve) – Area 4
_____10.49.	RCL	Verify PG-0302 (Chamber Pressurization System Inlet Pressure Gauge) reads 0 psig – Area 4
_____10.50.	RCL	DECREASE FULLY / Verify FULLY DECREASED HR-0303 (Chamber Pressurization Regulator) – Area 4
_____10.51.	RCL	Verify PG-0304 (Chamber Pressure Regulated Pressure Gauge) reads 0 psig – Area 4
_____10.52.	RCL	CLOSE / Verify CLOSED HV-0305 (Chamber Pressurization Throttle Valve) – Area 4
_____10.53.	RCL	CLOSE / Verify CLOSED HV-0401 (Dewar and Tank Pressurization Isolation Valve) – Area 4

_____ 10.54.	RCL	Verify PG-0402 (Dewar and Tank GN2 System Inlet Pressure Gauge) reads 0 psig – Area 4
_____ 10.55.	RCL	DECREASE FULLY / Verify FULLY DECREASED HR-0403 (Dewar and Tank GN2 Pressure Regulator) – Area 4
_____ 10.56.	RCL	Verify PG-0404 (Dewar and Tank Pressurization Pressure Gauge) reads 0 psig – Area 4
_____ 10.57.	RCL	CLOSE / Verify CLOSED HV-0405 (Dewar LN2 Supply Dewar Tank Isolation Valve) – Area 4
_____ 10.58.	RCL	CLOSE / Verify CLOSED HV-0501 (Window Purge Isolation Valve) – Area 4
_____ 10.59.	RCL	Verify PG-0504 (Window Purge Pressure Gauge) reads 0 psig – Area 5
_____ 10.60.	RCL	DECREASE FULLY / Verify FULLY DECREASED HR-0502 (Window Purge Pressure Regulator) – Area 4
_____ 10.61.	RCL	Verify PG-0417 (LN2 Tank Pressure Gauge) reads 0 psig – Area 5 If not: A – OPEN HV-0409 – Area 2 B – CLOSE HV-0409 – Area 2

_____ 11.		WINDOW PURGE
_____ 11.1.	TC	Notify SOCC via hotline in EC-1, EC-2 or EC-3 control room that EC-4 is going into a RED condition for SCF testing.
_____ 11.2.	ALL	Verify all personnel are wearing Test PPE
_____ 11.3.	RCL	Change EC-4 light to RED
_____ 11.4.	TC	Record Time _____
_____ 11.5.	RCL	Verify window purge apparatus is in satisfactory condition.
_____ 11.6.	RCL	OPEN HV-0008 (EC-4 Low Pressure Facility Isolation Valve) – Area 3
_____ 11.7.	RCL	OPEN HV-0501 (Window Purge Isolation Valve) – Area 4 CAUTION: Do NOT Increase HR-0502 so that PG-0504 reads greater than 5 psig as it will damage PG-0504
_____ 11.8.	RCL	INCREASE HR-0502 (Window Purge Pressure Regulator) until PG-0504 (Window Purge Pressure Gauge) reads 1.5 psig +/- 0.5 psig – Area 4
_____ 11.9.	RCL	Permit window purge to continue according to ER _____

_____ 12.		FACILITY GN2 SETUP
_____ 12.1.	RCL	<i>Slowly</i> OPEN HV-0003 (EC-4 Facility Isolation Valve) – Area 3
_____ 12.2.	RCL	Verify PG-0004 (EC-4 System Inlet Pressure Gauge) reads a pressure greater than 2000 psig – Area 4 _____
_____ 12.3.	RCL	OPEN HV-0007 (Upstream Regulator Pressure Valve) – Area 5
_____ 12.4.	RCL	CLOSE HV-0608 (Gauge Vent Valve) – Area 5
_____ 12.5.	RCL	INCREASE HR-0005 (EC-4 Facility Pressure Regulator) until PG-0607 (Chamber Pressure Gauge) reads 2000 psig +/- 50 psig – Area 5
		NOTE: Open and quickly close HV-0608 to check if PG-0607 actually reads 2000 psig
_____ 12.6.	RCL	CLOSE HV-0007 (Upstream Regulator Pressure Valve) – Area 5
_____ 12.7.	RCL	<i>Slowly</i> OPEN HV-0608 (Gauge Vent Valve) – Area 5
_____ 12.8.	RCL	Verify PG-0607 (Chamber Pressure Gauge) reads 0 psig – Area 5
_____ 12.9.	RCL	CLOSE HV-0608 (Gauge Vent Valve) – Area 5
_____ 12.10.	RCL	OPEN HV-0601 (PC Vent PG Isolation Valve) – Area 5
_____ 12.11.	RCL	Verify PG-0607 (Chamber Pressure Gauge) reads 0 psig – Area 5
_____ 12.12.	RCL	Turn ON Air Handler

_____ 13.		CHAMBER PURGE
_____ 13.1.	TC	Record Time _____
_____ 13.2.	TC	Record zero values for Pressure Transducer (Agilent Ch. 103), Incoming Mass Flow Meter (Agilent Ch. 104) and Outgoing Mass Flow Meter (Agilent Ch. 102).
_____ 13.3.	RCL	<i>Slowly</i> OPEN HV-0301 (Chamber Pressurization Isolation Valve) – Area 4
_____ 13.4.	RCL	Verify PG-0302 (Chamber Pressurization System Inlet Pressure Gauge) reads 2000 psig +/- 150 psig – Area 4 _____
_____ 13.5.	RCL	INCREASE HR-0303 (Chamber Pressure GN2 Pressure Regulator) until PG-0304 (Chamber Pressure Regulated Pressure Gauge) reads _____ psig +/-100 psig as per ER – Area 4
_____ 13.6.	RCL	OPEN HV-0305 (Chamber Pressurization Throttle Valve) as per ER _____ – Area 4 NOTE: Perform next 3 steps in quick succession
_____ 13.7.	RCL	CLOSE HV-0603 (Chamber Pressure Build Valve) – Area 4
_____ 13.8.	RCL	Verify PG-0607 (Chamber Pressure Gauge) indicates that PC is increasing to indicate purge is flowing. – Area 5
_____ 13.9.	RCL	OPEN HV-0603 (Chamber Pressure Build Valve) – Area 4
_____ 13.10.	RCL	Go to Chamber Pressurization Section if taking ambient T measurements with no flows
_____ 14.		CENTER JET PURGE
_____ 14.1.	RCL	<i>Slowly</i> OPEN HV-0101 (Center Jet GN2 Isolation Valve) – Area 4
_____ 14.2.	RCL	Verify PG-0102 (Center Jet GN2 System Inlet Pressure Gauge) reads 2000 psig +/- 150 psig – Area 4 _____
_____ 14.3.	RCL	INCREASE HR-0103 (Center Jet GN2 Pressure Regulator) until PG-0104 (Center Jet GN2 Regulated Pressure Gauge) reads _____ psig +/-100 psig as per ER – Area 4
_____ 14.4.	RCL	OPEN HV-0106 (Center Jet GN2 Throttle Valve) as per ER _____ – Area 4 NOTE: Check chamber pressure periodically Ch. 103 in Agilent (at least every 500 mg/s)
_____ 14.5.	TC	Verify FE-0105 (Center Jet GN2 Flow Meter) indicates purge is flowing NOTE: Ch. 104 in Agilent

_____15.		COAXIAL JET PURGE
_____15.1.	RCL	<i>Slowly</i> OPEN HV-0201 (Coax Jet GN2 Isolation Valve) – Area 4
_____15.2.	RCL	Verify PG-0202 (Coax Jet GN2 System Inlet Pressure Gauge) reads 2000 psig +/- 150 psig – Area 4 _____
_____15.3.	RCL	Open HV-0212 (Outer Jet Low Flow Isolation Valve) for use with FE-0205 (flow rate up to 3500 mg/s) or HV-0213 (Outer Jet High Flow Isolation Valve) for use with FE-0211 (higher flow rates) as per ER _____
_____15.4.	RCL	INCREASE HR-0203 (Coax Jet GN2 Pressure Regulator) until PG-0204 (Coax Jet GN2 Regulated Pressure Gauge) reads _____ psig +/-100 psig as per ER – Area 4 NOTE: 1100 psig is the high limit for PG-0204. The calibration curve available does not go beyond this pressure.
_____15.5.	RCL	OPEN HV-0206 (Coax Jet GN2 Throttle Valve) as per ER _____ – Area 4 NOTE: Check chamber pressure periodically Ch. 103 in Agilent (at least every 500 mg/s).
_____15.6.	TC	Verify FE-0205 (Coax Jet GN2 Flow Meter) indicates purge is flowing NOTE: Ch. 102 in Agilent.

_____16.		CHAMBER PRESSURIZATION
_____16.1.	RCL	OPEN HV-0605 (Secondary Chamber Pressure Vent Valve) – Area 4
_____16.2.	RCL	OPEN HV-0606 (Tertiary Chamber Pressure Vent Valve) 7 turns – Area 4
_____16.3.	RCL	CLOSE HV-0604 (Primary Chamber Pressure Vent Valve) – Area 4
_____16.4.	RCL	ADJUST HV-0605 (Secondary Chamber Pressure Vent Valve) and HV-0606 (Tertiary Chamber Pressure Vent Valve) until PG-0607 (Chamber Pressure Gauge) reads INITIAL CHAMBER PRESSURE as per ER _____ – Area 4
_____16.5.	RCL	Wait for required time to elapse from step 13.1 as per ER _____
_____16.6.	RCL	IF taking measurements at room temperature A - Take measurements B - Reduce chamber pressure after measurements C - Return to “Center Jet Purge” section

_____17.		SYSTEM CHILL DOWN
_____17.1.	TC	Verify Red Crew has donned Cryogenic PPE as outlined in Step 5.2
_____17.2.	RCL	CLOSE HV-0803 (Local Dewar Fill Isolation Valve) – Area 1
_____17.3.	RCL	OPEN HV-0801 (Tank LN2 Isolation Valve) – Area 1
_____17.4.	RCL	OPEN HV-0804 (Tank-Dewar Separation Valve) – Area 1
_____17.5.	RCL	OPEN HV-0416 (pressurize tank with GN2) – Area 1
_____17.6.	RCL	Remove Cryogenic PPE and don Test PPE as listed in Step 5.2
_____17.7.	RCL	<i>Slowly</i> OPEN HV-0401 (Dewar and Tank Pressurization Isolation Valve) – Area 4
_____17.8.	RCL	Verify PG-0402 (Dewar and Tank GN2 System Inlet Pressure Gauge) reads 2000 psig +/-150 psig – Area 4 _____
_____17.9.	RCL	Increase HR-0403 (Dewar and Tank GN2 Pressure Regulator) until PG-0404 (Dewar and Tank Pressurization Pressure Gauge) reads as per ER – Area 4 _____
_____17.10.	RCL	OPEN HV-0405 (Dewar LN2 Supply Dewar Tank Isolation Valve) – Area 4
_____17.11.	RCL	OPEN HV-0406 (Tank GN2 Pressurization Isolation Valve) – Area 2
_____17.12.	TC	Record Time _____
_____17.13.	RCL	OPEN HV-0809 (Coax Heat Exchanger LN2 Throttle Vent Valve) as per ER _____ ceiling between Area 4 & 5 NOTE: Rotate valve ¼ of a turn and wait 10 minutes
_____17.14.	RCL	OPEN HV-0708 (Heat Exchanger LN2 Throttle Vent Valve) as per ER _____ ceiling between Area 4 & 5 NOTE: Rotate valve ¼ of a turn and wait 10 minutes
_____17.15.	ALL	Wait Required time for chill down as per ER _____

_____18.		TESTING
_____18.1.	RCL	If acoustic testing, place foam door into position
_____18.2.	TC	Verify all personnel are wearing ear muffs if acoustic testing.
_____18.3.	RCL	Adjust HR-0103 (Center Jet GN2 Pressure Regulator) to maintain desired flow rates NOTE: Ch. 104 in Agilent
_____18.4.	RCL	Adjust HR-0203 (Coax Jet GN2 Pressure Regulator) to maintain desired flow rates NOTE: Ch. 102 in Agilent
_____18.5.	RCL	Adjust HV-0606 (Tertiary Chamber Pressure Vent Valve) and HV-0605 (Secondary Chamber Pressure Vent Valve) to maintain desired pressure chamber NOTE: Ch. 103 in Agilent
_____18.6.	TC	Direct RCL to operate system as per test needs
_____18.7.	RCL	OPERATE System as directed by test conductor

_____ 19.	RCL	SHUT DOWN
_____ 19.1.	RCL	CLOSE HV-0003 (EC-4 Secondary Facility Isolation Valve) – Area 2
_____ 19.2.	RCL	CLOSE HV-0008 (EC-4 Low Pressure Facility Isolation Valve) – Area 2
_____ 19.3.	RCL	Turn off air handler
_____ 19.4.	RCL	DON Cryogenic PPE
_____ 19.5.	RCL	CLOSE HV-0801 (Tank LN2 Isolation Valve) – Area 1
_____ 19.6.	RCL	CLOSE HV-0416 (Tank GN2 Pressurization Isolation Valve) – Area 1
_____ 19.7.	RCL	REMOVE Cryogenic PPE
_____ 19.8.	RCL	OPEN HV-0409 (Dewar Pressurization Vent Isolation Valve) – Area 2
_____ 19.9.	RCL	Wait for PG-0004 (EC-4 System Inlet Pressure Gauge) to read 0 psig – Area 5
_____ 19.10.	RCL	Fully DECREASE HR-0005 (EC-4 Facility Pressure Regulator) – Area 5
_____ 19.11.	RCL	Verify PG-0006 (EC-4 System Regulated Pressure Gauge) reads 0 psig – Area 5
_____ 19.12.	RCL	Verify PG-0102 (Center Jet GN2 System Inlet Pressure Gauge) reads 0 psig – Area 4
_____ 19.13.	RCL	CLOSE HV-0101 (Center Jet GN2 Isolation Valve) – Area 4
_____ 19.14.	RCL	Fully DECREASE HR-0103 (Center Jet GN2 Pressure Regulator) – Area 4
_____ 19.15.	RCL	Verify PG-0104 (Center Jet GN2 Regulated Pressure Gauge) reads 0 psig – Area 4
_____ 19.16.	RCL	CLOSE HV-0106 (Center Jet GN2 Throttle Valve) – Area 4
_____ 19.17.	RCL	Verify PG-0202 (Coax Jet GN2 System Inlet Pressure Gauge) reads 0 psig – Area 4
_____ 19.18.	RCL	CLOSE HV-0201 (Coax Jet GN2 Isolation Valve) – Area 4
_____ 19.19.	RCL	Fully DECREASE HR-0203 (Coax Jet GN2 Pressure Regulator) – Area 4
_____ 19.20.	RCL	Verify PG-0204 (Coax Jet GN2 Regulated Pressure Gauge) reads 0 psig – Area 4
_____ 19.21.	RCL	CLOSE HV-0212 (Outer Jet Low Flow Isolation Valve) – Area 4

_____19.22.	RCL	CLOSE HV-0213 (Outer Jet High Flow Isolation Valve) – Area 4
_____19.23.	RCL	CLOSE HV-0206 (coarse Coax Jet GN2 Throttle Valve) – Area 4
_____19.24.	RCL	CLOSE HV-0210 (fine Coax Jet GN2 Throttle Valve) – Area 4
_____19.25.	RCL	Verify PG-0302 (Chamber Pressurization System Inlet Pressure Gauge) reads 0 psig – Area 4
_____19.26.	RCL	CLOSE HV-0301 (Chamber Pressurization Isolation Valve) – Area 4
_____19.27.	RCL	Fully DECREASE HR-0303 (Chamber Pressurization Regulator) – Area 4
_____19.28.	RCL	Verify PG-0304 (Chamber Pressure Regulated Pressure Gauge) reads zero psig () – Area 4
_____19.29.	RCL	CLOSE HV-0305 (Chamber Pressurization Throttle Valve) – Area 4
_____19.30.	RCL	Verify PG-0402 (Dewar and Tank GN2 System Inlet Pressure Gauge) read 0 psig – Area 4 NOTE: Current readout sticks
_____19.31.	RCL	CLOSE HV-0401 (Dewar and Tank Pressurization Isolation Valve) – Area 4
_____19.32.	RCL	Fully DECREASE HR-0403 (Dewar and Tank GN2 Pressure Regulator) – Area 4
_____19.33.	RCL	Verify PG-0404 (Dewar and Tank Pressurization Pressure Gauge) reads 0 psig – Area 4
_____19.34.	RCL	OPEN HV-0405 (Dewar LN2 Supply Dewar Tank Isolation Valve) – Area 4
_____19.35.	RCL	OPEN/Verify OPEN HV-0406 (Tank GN2 Pressurization Isolation Valve) – Area 2
_____19.36.	RCL	Verify PG-0504 (Window Purge Pressure Gauge) reads 0 psig – Area 5
_____19.37.	RCL	CLOSE HV-0501 (Window Purge Isolation Valve) – Area 4
_____19.38.	RCL	Fully DECREASE HR-0502 (Window Purge Pressure Regulator) – Area 4
_____19.39.	RCL	OPEN HV-0608 (Gauge Vent Valve) – Area 5
_____19.40.	RCL	Verify PG-0607 (Chamber Pressure Gauge) reads 0 psig – Area 5
_____19.41.	RCL	CLOSE HV-0601 (PC Vent PG Isolation Valve) – Area 5

_____ 19.42.	RCL	OPEN / Verify OPEN HV-0603 (Chamber Pressure Build Valve) – Area 4
_____ 19.43.	RCL	OPEN HV-0604 (Primary Chamber Pressure Vent Valve) – Area 4
_____ 19.44.	RCL	CLOSE HV-0605 (Secondary Chamber Pressure Vent Valve) – Area 4
_____ 19.45.	RCL	CLOSE HV-0606 (Tertiary Chamber Pressure Vent Valve) – Area 4
_____ 19.46.	RCL	OPEN HV-0708 (Heat Exchanger LN2 Throttle Vent Valve) – ceiling between Area 4&5
_____ 19.47.	RCL	OPEN HV-0809 (Coax Heat Exchanger LN2 Throttle Vent Valve) – ceiling between Area 4&5
_____ 19.48.	RCL	OPEN / Verify OPEN HV-0715 (Direct LN2 Supply Valve) - Area 2
_____ 19.49.	RCL	Don Cryogenic PPE
_____ 19.50.	RCL	CLOSE HV-0804 (Tank-Dewar Separation Valve) – Area 1
_____ 19.51.	RCL	OPEN HV-0803 (Local Dewar Fill Isolation Valve - vent trapped LN2 between 0801 and 0804) - Area 1
_____ 19.52.	RCL	Remove Cryogenic PPE
_____ 19.53.	RCL	Verify PG-0417 (LN2 Tank Pressure Gauge) reads 0 psig – Area 5
_____ 19.54.	TC	Notify SOCC EC-4 is going back to green condition
_____ 19.55.	ALL	Turn off portable O ₂ sensors
_____ 19.56.	RCL	Turn EC-4 lights back to green
_____ 19.57.	RCL	Remove “DO NOT ENTER” and “HEARING PROTECTION REQUIRED” signs
_____ 19.58.	RCL	Remove chain from entrance to horseshoe

_____20.	RCL	EMERGENCY PROCEDURE (GN₂ or LN₂ line leak or burst)
		IF OXYGEN DEFICIENCY MONITORS ALARMS:
_____20.1.	ALL	Exit the facility to a safe zone given in safety brief.
_____20.2.	TC	Contact SOCC 5-5632 and report the emergency. Have SOCC contact the Fire Dept. 5-5181
_____20.3.	TC	Contact the Facility Manager and isolate the cell or area.
		IF POSSIBLE AND WHEN SAFE, DO THE FOLLOWING:
_____20.4.	RCL	CLOSE HV-0001 (EC-3, EC-4 Primary Facility Isolation Valve)
_____20.5.	RCL	CLOSE HV-0701 (LN2 Isolation Valve)
_____20.6.	RCL	CLOSE HV-0801 (Tank LN2 Isolation Valve)
		NOTE: WHEN SAFE TO DO SO COMPLETE THE STEPS OF THE "SHUT DOWN" SECTION 19

APPENDIX C

Summary of Coaxial Jet Experimental Data

Table C.1. Summary of experimental conditions for tests performed with the original injector including single phase subcritical experimental conditions and results.

	T_{chamber} (K)	ρ_{chamber} (kg/m ³)	P_{chamber} (MPa)	T_{outlet} (K)	\dot{m}_{outlet} (mg/s)	P_{outlet} (kg/m ²)	u_{outlet} (m/s)	Re_{outlet} (10 ⁴)	T_{inner} (K)	\dot{m}_{inner} (mg/s)	ρ_{inner} (kg/m ³)	u_{inner} (m/s)	Re_{inner} (10 ⁴)	L/D_1 (baseline)	Freq. (kHz)	$P'_{\text{RMS max}}$ (kPa)	VR	J
SUB																		
sub1	233	22.0	1.50	191	310	27.6	4.30	0.768	109	279	630	2.2	1.2	26.2	2.98	21.5	2.0	0.17
sub2	231	22.2	1.50	183	790	28.8	11.0	2.02	109	283	630	2.2	1.2	17.1	3.06	20.1	4.8	1.0
sub3	226	21.9	1.45	183	1230	27.8	16.9	3.16	109	284	630	2.2	1.2	16.6	3.06	17.8	7.6	2.6
sub4	226	22.9	1.51	185	1560	28.7	20.9	3.96	109	279	630	2.2	1.2	15.2	2.96	15.7	9.5	4.2
sub5	210	24.9	1.50	182	2400	29.3	31.3	6.18	109	279	630	2.2	1.2	8.40	3.01	16.9	14	9.6
sub6	216	24.1	1.50	191	3640	27.7	50.3	9.02	109	279	630	2.2	1.2	5.63	3.02	16.3	23	23
NEAR																		
near1	223	56.6	3.58	180	1060	75.4	5.38	2.58	123	290	520	2.8	2.0	24.4	3.08	9.04	2.0	0.55
near2	227	62.0	3.57	152	1570	101	5.95	4.16	117	289	590	2.4	1.5	15.5	3.04	10.8	2.5	1.0
near3	228	55.1	3.58	185	1590	72.4	8.40	3.80	126	293	440	3.3	2.5	14.6	3.00	11.8	2.6	1.1
near4	223	56.1	3.55	184	2170	72.3	11.5	5.21	127	294	360	4.0	3.4	12.1	3.01	11.4	2.8	1.6
near5	230	54.2	3.56	199	2120	65.1	12.5	4.84	126	292	440	3.3	2.5	12.9	3.03	12.1	3.8	2.1
near6	229	54.5	3.56	183	2690	73.1	14.1	6.48	126	292	420	3.4	2.5	5.98	3.05	11.1	4.1	2.9
near7	219	57.6	3.56	194	3080	67.4	17.5	7.15	125	289	480	3.0	2.2	5.56	3.06	11.8	5.9	4.9
near8	213	59.6	3.56	192	6460	68.3	36.2	15.1	128	295	220	6.6	5.2	2.45	2.93	9.73	5.5	9.3
SUPER																		
super1	231	76.1	4.96	198	292	93.9	1.19	0.642	136	291	300	4.8	3.9	37.7	3.05	8.01	0.25	0.019
super2	231	76.1	4.96	193	997	97.7	3.90	2.22	130	292	460	3.1	2.4	26.7	3.01	10.2	1.2	0.33
super3	221	80.4	4.95	180	2050	109	7.19	4.72	128	291	490	2.9	2.1	19.2	3.01	10.7	2.5	1.3
super4	222	80.1	4.96	182	3110	107	11.1	7.13	134	288	360	3.9	3.3	10.2	3.05	10.1	2.8	2.4
super5	222	80.3	4.97	191	2820	99.5	10.8	6.32	131	293	440	3.3	2.6	9.02	3.09	12.5	3.3	2.5
super6	211	85.8	4.96	187	5820	103	21.6	13.2	132	286	410	3.4	2.7	3.04	3.05	10.7	6.3	9.9
SUB																		
angle1	276	18.0	1.47	250	304	20	5.8	0.61	145	281	38	36	6.8	0.16	0.013	-0.10		
angle2	276	18.8	1.53	254	506	21	9.2	1.0	145	281	40	35	6.8	0.27	0.037	0.08		
angle3	276	18.2	1.48	254	1000	20	19	2.0	150	281	36	39	6.6	0.50	0.14	0.18		
angle4	270	19.2	1.53	245	2000	21	36	4.1	155	282	36	39	6.5	0.94	0.52	0.20		
angle5	270	18.8	1.50	246	3010	21	55	6.1	148	282	38	37	6.7	1.5	1.2	0.18		
angle6	261	20.1	1.54	242	4500	22	78	9.3	190	281	28	50	5.5	1.6	2.0	0.19		

Table C.2. Summary of two-phase subcritical experimental results for tests performed with the original injector.

SUBCRITICAL

J = 0.17					J = 1.0				
	L/D ₁	STD L/D ₁	$\Delta p_{\text{peak-to-peak}}/p_{\text{mean}}$	$\alpha_{\text{Left}} + \alpha_{\text{Right}} (^{\circ})$		L/D ₁	STD L/D ₁	$\Delta p_{\text{peak-to-peak}}/p_{\text{mean}}$	$\alpha_{\text{Left}} + \alpha_{\text{Right}} (^{\circ})$
Baseline	26.2	6.6	0.28%	2.9	Baseline	17.1	4.0	1.13%	3.8
0°	21.0	4.6	3.96%	3.5	0°	14.1	3.7	2.86%	5.4
45°	19.9	3.4	4.06%	5.1	45°	14.8	3.5	2.58%	6.1
90°	18.2	3.0	3.65%	5.7	90°	14.9	3.5	2.16%	5.9
135°	19.1	3.1	3.22%	4.7	135°	13.9	3.2	1.89%	8.3
180°	21.1	3.4	2.58%	3.7	180°	12.7	2.8	2.37%	9.0
225°	27.2	5.2	2.23%	3.8	225°	14.8	3.6	2.72%	6.2
270°	24.5	4.7	2.44%	2.6	270°	13.5	3.8	2.86%	4.8
315°	22.5	4.7	2.91%	3.6	315°	13.7	3.8	3.78%	3.6
360°	19.8	3.4	3.27%	3.3	360°	15.4	3.5	3.65%	4.1

J = 2.6					J = 4.2				
	L/D ₁	STD L/D ₁	$\Delta p_{\text{peak-to-peak}}/p_{\text{mean}}$	$\alpha_{\text{Left}} + \alpha_{\text{Right}} (^{\circ})$		L/D ₁	STD L/D ₁	$\Delta p_{\text{peak-to-peak}}/p_{\text{mean}}$	$\alpha_{\text{Left}} + \alpha_{\text{Right}} (^{\circ})$
Baseline	16.6	3.8	1.37%	7.5	Baseline	15.2	1.6	0.33%	5.9
0°	12.6	2.8	2.64%	16.7	0°	10.6	1.3	2.81%	17.4
45°	10.5	2.1	2.49%	25.1	45°	9.9	1.1	2.93%	23.1
90°	10.0	1.6	3.19%	28.9	90°	10.4	1.1	2.82%	19.2
135°	9.6	1.5	n/a	31.4	135°	9.7	1.0	2.43%	28.4
180°	9.3	1.2	2.07%	36.0	180°	11.2	1.1	1.74%	16.2
225°	10.2	1.5	2.25%	29.5	225°	11.8	1.2	1.49%	17.4
270°	12.7	2.3	2.45%	20.9	270°	12.5	1.3	1.56%	17.1
315°	13.2	2.8	3.47%	15.9	315°	12.7	1.5	1.85%	9.9
360°	11.4	2.4	2.28%	25.8	360°	11.8	1.4	2.24%	12.4

J = 9.6					J = 23				
	L/D ₁	STD L/D ₁	$\Delta p_{\text{peak-to-peak}}/p_{\text{mean}}$	$\alpha_{\text{Left}} + \alpha_{\text{Right}} (^{\circ})$		L/D ₁	STD L/D ₁	$\Delta p_{\text{peak-to-peak}}/p_{\text{mean}}$	$\alpha_{\text{Left}} + \alpha_{\text{Right}} (^{\circ})$
Baseline	8.4	1.4	0.52%	6.8	Baseline	5.6	0.7	0.72%	2.5
0°	7.2	1.1	3.04%	33.3	0°	5.2	0.7	2.69%	13.5
45°	7.2	1.1	2.33%	37.4	45°	5.4	0.7	2.15%	8.4
90°	7.6	1.1	1.79%	32.9	90°	5.0	0.7	2.00%	12.5
135°	7.3	1.1	1.41%	30.8	135°	5.0	0.7	1.55%	7.0
180°	7.0	1.0	1.59%	33.0	180°	5.0	0.6	1.88%	18.1
225°	6.7	0.9	2.23%	29.8	225°	4.9	0.7	2.49%	14.6
270°	7.0	0.9	2.51%	38.0	270°	5.1	0.7	2.63%	16.3
315°	6.8	1.0	3.18%	30.4	315°	5.1	0.7	2.60%	11.1
360°	7.2	1.1	2.84%	31.4	360°	5.4	0.7	3.06%	8.4

Table C.3. Summary of nearcritical experimental results for tests performed with the original injector.

NEARCRITICAL

J = 0.55					J = 1.0				
	L/D ₁	STD L/D ₁	$\Delta p_{\text{peak-to-peak}}/p_{\text{mean}}$	$\alpha_{\text{Left}} + \alpha_{\text{Right}} (^{\circ})$		L/D ₁	STD L/D ₁	$\Delta p_{\text{peak-to-peak}}/p_{\text{mean}}$	$\alpha_{\text{Left}} + \alpha_{\text{Right}} (^{\circ})$
Baseline	24.4	3.0	0.19%	10.1	Baseline	15.5	2.0	0.23%	16.3
0°	16.7	2.1	0.72%	16.2	0°	11.9	1.3	0.83%	14.7
45°	17.3	2.6	0.59%	10.0	45°	10.4	1.1	0.59%	15.6
90°	18.6	2.4	0.45%	10.6	90°	15.3	1.9	0.43%	9.6
135°	18.9	2.5	0.37%	13.6	135°	12.1	1.4	0.31%	11.8
180°	18.7	2.3	0.42%	11.1	180°	14.1	1.7	0.58%	12.1
225°	20.0	2.7	0.52%	12.7	225°	11.7	1.2	0.65%	14.5
270°	19.0	2.6	0.67%	9.6	270°	11.4	1.2	0.81%	16.3
315°	16.5	1.9	0.71%	12.2	315°	11.6	1.3	0.85%	17.6
360°	14.4	1.8	0.66%	21.8	360°	12.1	1.2	0.75%	19.0

J = 1.1					J = 1.6				
	L/D ₁	STD L/D ₁	$\Delta p_{\text{peak-to-peak}}/p_{\text{mean}}$	$\alpha_{\text{Left}} + \alpha_{\text{Right}} (^{\circ})$		L/D ₁	STD L/D ₁	$\Delta p_{\text{peak-to-peak}}/p_{\text{mean}}$	$\alpha_{\text{Left}} + \alpha_{\text{Right}} (^{\circ})$
Baseline	14.6	1.6	0.21%	15.9	Baseline	12.1	1.2	0.20%	11.6
0°	9.8	1.2	0.85%	18.5	0°	9.8	1.0	0.91%	17.2
45°	11.0	1.2	n/a	16.9	45°	10.2	1.0	0.84%	11.7
90°	10.3	1.1	0.93%	17.7	90°	9.3	1.0	0.75%	18.4
135°	9.5	1.1	0.77%	15.0	135°	8.3	1.0	0.73%	12.5
180°	9.2	1.1	0.55%	12.6	180°	8.6	1.0	0.68%	12.8
225°	9.6	1.1	0.35%	15.6	225°	8.3	1.0	0.69%	10.4
270°	9.9	1.2	0.34%	14.3	270°	8.6	1.1	0.74%	9.9
315°	10.4	1.1	0.57%	17.9	315°	8.8	1.0	0.89%	14.7
360°	11.2	1.3	0.77%	16.8	360°	10.3	1.1	0.89%	7.2

J = 2.1					J = 2.9				
	L/D ₁	STD L/D ₁	$\Delta p_{\text{peak-to-peak}}/p_{\text{mean}}$	$\alpha_{\text{Left}} + \alpha_{\text{Right}} (^{\circ})$		L/D ₁	STD L/D ₁	$\Delta p_{\text{peak-to-peak}}/p_{\text{mean}}$	$\alpha_{\text{Left}} + \alpha_{\text{Right}} (^{\circ})$
Baseline	12.9	1.4	0.27%	15.5	Baseline	6.0	0.6	0.21%	3.7
0°	8.1	1.1	0.84%	24.2	0°	3.6	0.5	0.79%	17.3
45°	8.9	1.2	0.97%	22.6	45°	4.1	0.4	0.88%	16.3
90°	8.7	1.0	0.96%	20.9	90°	4.1	0.5	0.83%	24.2
135°	8.1	0.8	0.77%	23.6	135°	3.8	0.5	0.64%	21.5
180°	7.4	0.7	0.56%	24.5	180°	3.3	0.5	0.41%	22.7
225°	8.0	0.8	0.30%	21.5	225°	3.2	0.5	0.29%	33.7
270°	8.2	0.8	0.37%	16.8	270°	3.2	0.5	0.43%	33.0
315°	8.2	1.1	0.64%	11.9	315°	3.4	0.5	0.62%	39.3
360°	8.5	1.1	0.86%	23.5	360°	4.0	0.6	0.80%	24.3

J = 4.9					J = 9.3				
	L/D ₁	STD L/D ₁	$\Delta p_{\text{peak-to-peak}}/p_{\text{mean}}$	$\alpha_{\text{Left}} + \alpha_{\text{Right}} (^{\circ})$		L/D ₁	STD L/D ₁	$\Delta p_{\text{peak-to-peak}}/p_{\text{mean}}$	$\alpha_{\text{Left}} + \alpha_{\text{Right}} (^{\circ})$
Baseline	5.6	0.4	0.25%	-0.8	Baseline	2.4	0.2	0.36%	-2.4
0°	3.8	0.7	0.94%	28.2	0°	2.4	0.3	0.68%	0.0
45°	4.2	0.6	0.76%	13.4	45°	2.4	0.3	0.77%	1.4
90°	3.3	0.5	0.56%	24.8	90°	2.4	0.3	0.69%	6.2
135°	3.4	0.6	0.43%	40.0	135°	2.5	0.3	0.51%	1.4
180°	3.3	0.5	0.47%	26.9	180°	2.5	0.3	n/a	0.0
225°	3.6	0.6	0.52%	30.4	225°	2.4	0.3	0.40%	0.0
270°	3.7	0.6	0.78%	25.1	270°	2.5	0.3	0.53%	3.0
315°	3.7	0.6	0.81%	27.5	315°	2.5	0.3	0.67%	2.3
360°	3.9	0.5	0.82%	23.6	360°	2.6	0.3	0.73%	6.7

Table C.4. Summary of supercritical experimental results for tests performed with the original injector.

SUPERCritical

J = 0.019					J = 0.33				
	L/D ₁	STD L/D ₁	$\Delta p_{\text{peak-to-peak}}/p_{\text{mean}}$	$\alpha_{\text{Left}} + \alpha_{\text{Right}} (^{\circ})$		L/D ₁	STD L/D ₁	$\Delta p_{\text{peak-to-peak}}/p_{\text{mean}}$	$\alpha_{\text{Left}} + \alpha_{\text{Right}} (^{\circ})$
Baseline	37.7	5.3	0.10%	6.6	Baseline	26.7	3.1	0.15%	5.7
0°	33.0	2.1	0.41%	6.8	0°	23.5	3.4	0.56%	7.1
45°	35.8	2.6	0.46%	8.7	45°	21.5	3.3	0.58%	6.5
90°	34.4	2.8	0.46%	8.9	90°	21.2	3.5	0.51%	9.9
135°	32.0	2.1	0.39%	4.9	135°	25.0	3.1	0.38%	6.5
180°	32.0	2.4	0.27%	13.5	180°	n/a	n/a	n/a	5.2
225°	32.5	1.8	0.21%	10.6	225°	23.3	3.3	0.26%	4.7
270°	29.7	2.3	0.27%	6.8	270°	24.4	3.3	0.37%	4.7
315°	33.8	2.2	0.42%	8.8	315°	26.6	3.0	0.48%	6.6
360°	35.2	2.0	0.45%	8.6	360°	19.1	2.8	0.55%	6.0

J = 1.3					J = 2.4				
	L/D ₁	STD L/D ₁	$\Delta p_{\text{peak-to-peak}}/p_{\text{mean}}$	$\alpha_{\text{Left}} + \alpha_{\text{Right}} (^{\circ})$		L/D ₁	STD L/D ₁	$\Delta p_{\text{peak-to-peak}}/p_{\text{mean}}$	$\alpha_{\text{Left}} + \alpha_{\text{Right}} (^{\circ})$
Baseline	19.2	2.3	0.12%	14.4	Baseline	10.2	2.3	0.22%	17.2
0°	14.9	1.7	0.60%	13.0	0°	6.6	1.2	0.55%	12.6
45°	12.5	1.5	0.61%	10.2	45°	6.7	1.5	0.56%	18.8
90°	12.7	1.6	0.54%	14.0	90°	7.1	1.5	0.50%	12.6
135°	12.9	1.5	0.51%	11.5	135°	7.4	1.8	0.38%	14.4
180°	12.2	1.5	0.42%	12.5	180°	5.8	1.3	0.27%	18.7
225°	14.6	1.9	0.41%	9.1	225°	5.7	1.2	0.27%	14.7
270°	13.3	1.4	0.43%	13.9	270°	5.6	1.3	0.36%	20.1
315°	12.4	1.4	0.52%	14.3	315°	5.9	1.2	0.47%	18.6
360°	14.5	1.7	0.59%	14.9	360°	5.8	1.2	0.58%	19.6

J = 2.5					J = 9.9				
	L/D ₁	STD L/D ₁	$\Delta p_{\text{peak-to-peak}}/p_{\text{mean}}$	$\alpha_{\text{Left}} + \alpha_{\text{Right}} (^{\circ})$		L/D ₁	STD L/D ₁	$\Delta p_{\text{peak-to-peak}}/p_{\text{mean}}$	$\alpha_{\text{Left}} + \alpha_{\text{Right}} (^{\circ})$
Baseline	9.0	0.9	0.25%	15.3	Baseline	3.0	0.3	0.26%	-4.3
0°	7.9	1.2	0.60%	19.2	0°	3.1	0.6	0.61%	1.8
45°	6.2	1.0	0.67%	23.8	45°	3.4	0.6	0.57%	-3.8
90°	4.5	0.8	0.57%	21.1	90°	3.0	0.4	0.47%	-9.5
135°	5.9	0.9	0.41%	22.8	135°	3.0	0.4	0.36%	-0.6
180°	6.1	1.0	0.25%	27.6	180°	3.3	0.6	0.27%	-1.1
225°	6.1	1.0	0.36%	11.9	225°	3.4	0.6	0.34%	5.5
270°	6.5	0.9	0.51%	12.2	270°	3.2	0.6	0.47%	13.7
315°	6.2	0.8	0.64%	12.1	315°	3.0	0.5	0.57%	-4.0
360°	7.1	1.1	0.71%	16.5	360°	3.0	0.4	0.60%	0.2

Table C.5. Summary of experimental conditions for tests performed with the new injector.

	T_{chamber} (K)	ρ_{chamber} (kg/m ³)	P_{chamber} (MPa)	T_{outlet} (K)	\dot{m}_{outlet} (mg/s)	ρ_{outlet} (kg/m ³)	U_{outlet} (m/s)	Re_{outlet} (10 ⁴)	T_{inner} (K)	\dot{m}_{inner} (mg/s)	ρ_{inner} (kg/m ³)	U_{inner} (m/s)	Re_{inner} (10 ⁴)	L/D_1 (baseline)	Freq. (kHz)	$P_{\text{rms max}}$ (kPa)	VR	J
SUB																		
subnew1	235	22	1.48	199	90	26	1.4	0.21	105	920	660	0.91	1.3	13+	3.01	8.86	1.5	0.089
subnew2	237	22	1.49	197	200	26	3.0	0.47	106	925	655	0.92	1.3	13+	2.96	14.0	3.3	0.43
subnew3	246	21	1.49	195	450	27	6.6	1.1	109	925	630	0.96	1.5	11+	2.97	12.1	6.9	2.0
subnew4	224	23	1.49	189	600	28	8.5	1.5	110	925	620	0.97	1.5	10.4	3.04	10.2	8.7	3.4
subnew5	217	24	1.49	184	750	29	10	1.9	110	925	620	0.97	1.5	9.29	3.02	11.5	11	5.2
subnew6	228	22	1.49	193	880	27	13	2.1	108	925	640	0.94	1.4	8.08	2.96	12.7	14	7.8
subnew7	222	23	1.49	194	1100	27	16	2.6	108	925	640	0.94	1.4	7.63	2.92	11.2	17	12
subnew8	217	24	1.48	201	1300	26	20	3.0	109	925	630	0.96	1.5	7.26	2.90	9.16	21	18
NEAR																		
nearnew1	228	55	3.56	213	330	60	2.2	0.70	109	925	650	0.93	1.3	14+	2.98	10.8	2.3	0.50
nearnew2	226	55	3.56	209	460	61	3.0	1.0	109	925	650	0.93	1.3	14+	3.06	9.17	3.2	0.97
nearnew3	230	54	3.58	198	730	66	4.3	1.6	108	925	655	0.92	1.3	13+	3.00	9.12	4.7	2.2
nearnew4	216	59	3.58	199	1030	65	6.3	2.3	109	925	650	0.93	1.3	13+	3.11	16.0	6.7	4.6
nearnew5	214	59	3.58	203	1460	63	9.2	3.2	109	925	650	0.93	1.3	7.01	3.07	15.0	9.9	9.4
nearnew6	215	59	3.56	207	2060	62	13	4.5	111	925	635	0.95	1.4	3.55	3.09	18.3	14	19
SUPER																		
supernew1	219	81	4.95	212	890	85	4.1	1.8	111	925	650	0.93	1.4	13+	3.11	17.0	4.4	2.6

Table C.6. Summary of subcritical experimental results for tests performed with the new injector. See caption of Figure 5.47 for explanation of * and ** markers.

SUBCRITICAL

J = 0.089					J = 0.43				
	L/D ₁	STD L/D ₁	$\Delta p_{\text{peak-to-peak}}/p_{\text{mean}}$	$\alpha_{\text{Left}} + \alpha_{\text{Right}} (^{\circ})$		L/D ₁	STD L/D ₁	$\Delta p_{\text{peak-to-peak}}/p_{\text{mean}}$	$\alpha_{\text{Left}} + \alpha_{\text{Right}} (^{\circ})$
Baseline**	+13	n/a	0.02%	0.8	Baseline**	+13	n/a	0.01%	2.2
0°**	+13	n/a	1.27%	14.0	0°	7.6	1.5	2.63%	9.1
45°**	+13	n/a	1.10%	25.7	45°	7.1	1.3	2.20%	14.0
90°**	+13	n/a	1.03%	17.7	90°**	+13	n/a	1.24%	-1.9
135°**	+13	n/a	0.38%	0.5	135°**	+13	n/a	0.42%	4.8
180°**	+13	n/a	0.68%	-0.5	180°**	+13	n/a	0.60%	8.4
225°**	+12	n/a	1.47%	2.4	225°**	+13	n/a	1.49%	2.9
270°**	+11	n/a	1.46%	8.5	270°	7.7	1.4	2.28%	10.3
315°**	n/a	n/a	1.53%	13.0	315°	7.7	1.3	2.64%	14.9
360°**	+13	n/a	1.69%	11.5	360°	7.3	1.5	2.66%	7.3

J = 2.0					J = 3.4				
	L/D ₁	STD L/D ₁	$\Delta p_{\text{peak-to-peak}}/p_{\text{mean}}$	$\alpha_{\text{Left}} + \alpha_{\text{Right}} (^{\circ})$		L/D ₁	STD L/D ₁	$\Delta p_{\text{peak-to-peak}}/p_{\text{mean}}$	$\alpha_{\text{Left}} + \alpha_{\text{Right}} (^{\circ})$
Baseline*	+11	2.0	0.03%	7.3	Baseline	10.4	1.4	0.03%	7.8
0°	5.8	0.8	2.30%	6.4	0°	3.9	0.7	1.82%	14.9
45°	6.5	0.9	1.84%	8.2	45°	4.3	0.7	1.64%	15.6
90°*	+11	1.9	1.04%	4.3	90°	4.2	0.6	1.82%	12.3
135°**	+13	n/a	0.22%	5.4	135°	4.2	0.7	1.77%	17.0
180°**	+13	n/a	0.70%	6.1	180°	6.3	1.1	0.88%	9.6
225°**	+13	n/a	1.46%	3.7	225°*	+11	1.9	0.24%	4.6
270°	6.9	0.9	1.97%	4.4	270°	5.6	0.8	0.87%	8.6
315°	6.3	1.0	2.08%	7.3	315°	4.8	0.7	1.46%	13.0
360°	6.0	0.9	1.96%	9.7	360°	3.9	0.7	1.93%	14.6

J = 5.2					J = 7.8				
	L/D ₁	STD L/D ₁	$\Delta p_{\text{peak-to-peak}}/p_{\text{mean}}$	$\alpha_{\text{Left}} + \alpha_{\text{Right}} (^{\circ})$		L/D ₁	STD L/D ₁	$\Delta p_{\text{peak-to-peak}}/p_{\text{mean}}$	$\alpha_{\text{Left}} + \alpha_{\text{Right}} (^{\circ})$
Baseline	9.3	1.2	0.03%	12.3	Baseline	8.1	1.1	0.02%	6.2
0°	3.6	0.7	2.01%	16.7	0°	5.9	0.9	2.41%	3.9
45°	3.3	0.6	2.17%	14.7	45°	6.6	1.1	2.06%	2.8
90°	4.0	0.7	1.99%	16.4	90°	6.8	1.1	1.39%	4.3
135°	4.1	0.7	1.83%	13.2	135°	7.1	0.8	0.60%	3.9
180°	5.2	1.0	1.21%	15.8	180°	7.5	1.2	0.21%	4.4
225°	9.6	1.8	0.35%	3.8	225°	6.9	1.2	1.03%	3.2
270°	5.5	1.1	0.97%	11.0	270°	6.6	1.0	1.92%	2.6
315°	4.3	0.6	1.51%	18.0	315°	6.6	1.0	2.20%	3.1
360°	3.8	0.6	1.92%	18.6	360°	6.9	1.0	2.21%	2.9

J = 12					J = 18				
	L/D ₁	STD L/D ₁	$\Delta p_{\text{peak-to-peak}}/p_{\text{mean}}$	$\alpha_{\text{Left}} + \alpha_{\text{Right}} (^{\circ})$		L/D ₁	STD L/D ₁	$\Delta p_{\text{peak-to-peak}}/p_{\text{mean}}$	$\alpha_{\text{Left}} + \alpha_{\text{Right}} (^{\circ})$
Baseline	7.6	0.9	0.03%	5.5	Baseline	7.3	0.8	0.02%	7.8
0°	4.6	0.8	2.13%	14.1	0°	4.6	0.6	1.75%	17.9
45°	4.5	0.6	1.77%	16.5	45°	5.0	0.6	1.51%	13.8
90°	5.1	0.6	1.24%	12.7	90°	5.2	0.6	1.08%	13.3
135°	6.0	0.8	0.51%	12.2	135°	6.3	0.8	0.43%	11.0
180°	6.8	0.7	0.29%	4.8	180°	6.5	0.8	0.33%	7.7
225°	6.5	0.9	0.88%	7.0	225°	6.0	0.8	0.93%	7.0
270°	5.7	0.7	1.39%	6.5	270°	5.3	0.7	1.29%	12.8
315°	5.2	0.9	1.60%	8.9	315°	5.0	0.6	1.57%	10.9
360°	4.9	0.6	1.77%	14.0	360°	4.5	0.7	1.62%	23.6

Table C.7. Summary of nearcritical experimental results for tests performed with the new injector. See caption of Figure 5.47 for explanation of * and ** markers.

NEARCRITICAL

J = 0.50					J = 0.97				
	L/D ₁	STD L/D ₁	$\Delta p_{\text{peak-to-peak}}/p_{\text{mean}}$	$\alpha_{\text{Left}} + \alpha_{\text{Right}} (^{\circ})$		L/D ₁	STD L/D ₁	$\Delta p_{\text{peak-to-peak}}/p_{\text{mean}}$	$\alpha_{\text{Left}} + \alpha_{\text{Right}} (^{\circ})$
Baseline**	+14	n/a	0.01%	8.8	Baseline**	+14	n/a	0.01%	9.3
0°**	+14	n/a	0.73%	6.4	0°	n/a	n/a	0.73%	n/a
45°**	+14	n/a	0.52%	3.7	45°**	+14	n/a	0.70%	8.4
90°**	+14	n/a	0.21%	10.5	90°**	+14	n/a	0.57%	6.2
135°**	+14	n/a	0.17%	6.3	135°**	+14	n/a	0.37%	10.1
180°**	+14	n/a	0.45%	5.6	180°**	+14	n/a	0.18%	6.5
225°**	+14	n/a	0.59%	5.2	225°**	+14	n/a	0.34%	5.0
270°**	+14	n/a	0.81%	4.9	270°**	+14	n/a	0.52%	8.5
315°	n/a	n/a	0.85%	n/a	315°**	+14	n/a	0.66%	5.6
360°**	+14	n/a	0.67%	2.3	360°	n/a	n/a	0.70%	n/a

J = 2.2					J = 4.6				
	L/D ₁	STD L/D ₁	$\Delta p_{\text{peak-to-peak}}/p_{\text{mean}}$	$\alpha_{\text{Left}} + \alpha_{\text{Right}} (^{\circ})$		L/D ₁	STD L/D ₁	$\Delta p_{\text{peak-to-peak}}/p_{\text{mean}}$	$\alpha_{\text{Left}} + \alpha_{\text{Right}} (^{\circ})$
Baseline**	+13	n/a	0.01%	10.0	Baseline*	+13	1.2	0.01%	9.7
0°**	+13	n/a	0.62%	7.7	0°	4.6	0.7	1.26%	10.9
45°**	+13	n/a	0.44%	7.3	45°	5.7	0.7	1.21%	8.3
90°**	+13	n/a	0.36%	9.0	90°	7.4	0.9	1.01%	8.4
135°**	+13	n/a	0.38%	9.8	135°	8.8	1.1	0.64%	3.9
180°**	+13	n/a	0.50%	8.6	180°*	+13	1.2	0.25%	7.0
225°**	+13	n/a	0.64%	11.5	225°*	+12	1.5	0.23%	8.0
270°**	+13	n/a	0.69%	10.1	270°	7.7	1.3	0.72%	2.2
315°**	+13	n/a	0.72%	8.8	315°	5.3	0.8	1.09%	11.3
360°**	+13	n/a	0.57%	8.9	360°	n/a	n/a	1.11%	1.8

J = 9.4					J = 19				
	L/D ₁	STD L/D ₁	$\Delta p_{\text{peak-to-peak}}/p_{\text{mean}}$	$\alpha_{\text{Left}} + \alpha_{\text{Right}} (^{\circ})$		L/D ₁	STD L/D ₁	$\Delta p_{\text{peak-to-peak}}/p_{\text{mean}}$	$\alpha_{\text{Left}} + \alpha_{\text{Right}} (^{\circ})$
Baseline	7.0	0.7	0.01%	10.7	Baseline	3.6	0.3	0.01%	10.2
0°	3.7	0.4	1.18%	6.2	0°	2.4	0.2	1.43%	17.2
45°	3.7	0.4	1.18%	6.8	45°	2.3	0.2	1.40%	23.8
90°	4.0	0.4	1.04%	8.8	90°	2.4	0.2	1.17%	25.5
135°	5.8	0.6	0.81%	1.9	135°	2.8	0.2	0.73%	16.0
180°	6.4	0.6	0.44%	5.6	180°	3.0	0.2	0.33%	5.3
225°	5.8	0.6	0.16%	5.3	225°	2.8	0.2	0.31%	8.3
270°	5.7	0.6	0.56%	5.2	270°	2.7	0.2	0.85%	19.9
315°	4.6	0.5	0.95%	3.5	315°	2.4	0.2	1.23%	22.5
360°	3.8	0.4	1.17%	5.1	360°	2.4	0.2	1.45%	20.5

Table C.8. Summary of supercritical experimental results for tests performed with the new injector. See caption of Figure 5.47 for explanation of * and ** markers.

SUPERCritical				
J = 2.6				
	L/D ₁	STD L/D ₁	$\Delta p_{\text{peak-to-peak}}/p_{\text{mean}}$	$\alpha_{\text{Left}} + \alpha_{\text{Right}} (^{\circ})$
Baseline**	+13	n/a	0.01%	11.0
0°**	+13	n/a	0.92%	11.2
45°**	+13	n/a	0.91%	9.1
90°**	+13	n/a	0.77%	9.6
135°**	+13	n/a	0.58%	8.5
180°**	+13	n/a	0.34%	11.0
225°**	+13	n/a	0.32%	8.5
270°**	+13	n/a	0.62%	10.2
315°**	+13	n/a	0.85%	10.7
360°**	+13	n/a	0.97%	10.1

REFERENCES

1. McManus, K. R., Poinso, T., Candel, S. M., "A Review of Active Control of Combustion Instabilities", *Prog. Energy Comb. Sci.*, Vol. 19, No. 1, pp. 1-29, 1993.
2. Davis, D. W., Chehroudi, B., "Measurements in an Acoustically Driven Coaxial Jet under Sub-, Near-, and Supercritical Conditions", *J. Propul. Power*, Vol. 23, pp. 364-374, 2007.
3. Law, C. K., "Recent Advances in Droplet Vaporization and Combustion", *Prog. Energy Comb. Sci.*, Vol. 8, p. 171, 1982.
4. Law, C. K., Faeth, G. M., "Opportunities and Challenges of Combustion in Microgravity", *Prog. Energy Comb. Sci.*, Vol. 20, pp. 65-113, 1994.
5. Struk, P. M., Ackerman, M., Nayagam, V., Dietrich, D. L., "On Calculating Burning Rates during Fibre Supported Droplet Combustion", *Micrograv. Sci. Technology*, Vol. XI, No. 4, pp. 144-151, 1998.
6. Blaszczyk, J., "Acoustically Disturbed Fuel Droplet Combustion", *Fuel*, Vol. 70, pp. 1023-1025, 1991.
7. Sujith, R. I., Waldherr, G. A., Jagoda, J. I., Zinn, B. T., "Experimental Investigation of the Evaporation of Droplets in Axial Acoustic Fields", *J. Propul. Power*, Vol. 16, pp. 278-285, 2000.
8. Saito, M., Sato, M., Suzuki, I., "Evaporation and Combustion of a Single Fuel Droplet in Acoustic Fields", *Fuel*, Vol. 73, pp. 349-353, 1994.
9. Saito, M., Hoshikawa, M., Sato, M., "Enhancement of Evaporation/Combustion Rate Coefficient of a Single Fuel Droplet by Acoustic Oscillation", *Fuel*, Vol. 75, pp. 669-674, 1996.
10. Okai, K., Moriue, O., Araki, M., Tsue, M., Kono, M., Sato, J., Dietrich, D. L., Williams, F. A., "Combustion of Single Droplets and Droplet Pairs in a

- Vibrating Field Under Microgravity”, *Symposium (International) on Combustion*, Vol. 28, pp. 977-983, 2000.
11. Tanabe, M., Morita, T., Aoki, K., Satoh, K., Fujimori, T., Sato, J., “Influence of Standing Sound Waves on Droplet Combustion”, *Symposium (International) on Combustion*, Vol. 28, pp. 1007-1013, 2000.
 12. Tanabe, M., Kuwahara, T., Satoh, K., Fujimori, T., Sato, J., Kono, M., “Droplet Combustion in Standing Sound Waves”, *Proc. Combustion Inst.*, Vol. 30, pp. 1957-1964, 2005.
 13. Rayleigh, Lord, “On the Circulation of Air Observed in Kundt’s Tubes, and on Some Allied Acoustical Problems”, *Phil. Trans. Roy. Soc.*, Vol. 175, pp. 1-21, 1884.
 14. Dattarajan, S., “Acoustically Excited Droplet Combustion in Normal Gravity and Microgravity”, Ph. D. Dissertation, Department of Mechanical and Aerospace Engineering, UCLA, 2004.
 15. Dattarajan, S., Lutomirski, A., Lobbia, R., Smith, O. I., Karagozian, A. R., “Acoustic Excitation of Droplet Combustion in Microgravity and Normal Gravity”, *Comb. and Flame*, Vol. 144, pp. 299-317, 2006.
 16. Karagozian, A. R., Dahm, W. J. A., Glasgow, E., Howe, R., Kroo, I., Murray, R., Shyu, H., “Technology Options for Improved Air Vehicle Fuel Efficiency”, *Air Force Scientific Advisory Board*, SAB-TR-06-04, May 2006.
 17. Fischer, F., **The Conversion of Coal**, Ernst Benn, Ltd., 1925.
 18. Harrison, W., “OSD Clean Fuel Initiative and Air Force Fuels”, 12 December 2005, Presented to the Air Force Scientific Advisory Board.
 19. Department of the Air Force, “B-52 Flight Uses Synthetic Fuel in All Eight Engines”, *Air Force AIM Points*, December 2006. <http://www.af.mil/news/story.asp?storyID=123035568>.
 20. Vingert, L., Gicquel, P., Lourme, D., Ménoret, L., “Coaxial Injector Atomization”, *Liquid Rocket Engine Combustion Instability*, Progress in Astronautics and Aeronautics, AIAA, Anderson, V., Yang, W., eds., pp. 145-190, 1995.

21. Davis, D. W., Chehroudi, B., "Shear-Coaxial Jets from a Rocket-Like Injector in a Transverse Acoustic Field at High Pressures", *44th AIAA Aerospace Sciences Meeting and Exhibit*, Reno, NV, 9-12 January 2006.
22. Leyva, I. A., Chehroudi, B., Talley, D., "Dark-Core Analysis of Coaxial Injectors at Sub-, Near-, and Supercritical Conditions in a Transverse Acoustic Field", *54th JANNAF Meeting*, Denver, CO, 14-18 May 2007.
23. Leyva, I. A., Chehroudi, B., Talley, D., "Dark-Core Analysis of Coaxial Injectors at Sub-, Near-, and Supercritical Conditions in a Transverse Acoustic Field", *43rd AIAA/ASME/SAE/ASEE Joint Propulsion Conference and Exhibit*, Cincinnati, OH, 8-11 July 2007.
24. Harje, D. T., Reardon, F. H., eds., *Liquid Propellant Rocket Combustion Instability*, NASA SP-194, pp. 17-19, 1972.
25. van Konynenburg, P. H., Scott, R. L., "Critical Lines and Phase Equilibria in Binary van der Waals Mixtures", *Phil. Trans. R. Soc. London*, Vol. 298, p. 495, 1980.
26. Oschwald, M., Smith, J. J., Branam, R., Hussong, J., Schik, A., Chehroudi, B., Talley, D., "Injection of Fluids into Supercritical Environments", *Combust. Sci. and Tech.*, Vol. 178, pp. 49-100, January 2006.
27. Sutton, G. P., **Rocket Propulsion Elements**, 6th Ed., John Wiley & Sons, Inc., New York, 1992.
28. Marshall, W., Pal, S., Woodward, R., Santoro, R. J., Smith, R., Xia, G., Sankaran, V., Merkle, C. L., "Experimental and Computational Investigation of Combustor Acoustics and Instabilities, Part II: Transverse Modes", *44th AIAA Aerospace Sciences Meeting and Exhibit*, Reno, NV, 9-12 January 2006.
29. Richecoeur, F., Scoufflaire, P., Ducruix, S., Candel, S., "Interactions Between Propellant Jets and Acoustic Modes in Liquid Rocket Engines: Experiments and Simulations", *42nd AIAA/ASME/SAE/ASEE Joint Propulsion Conference and Exhibit*, Sacramento, CA, 9-12 July 2006.
30. Gutmark, E., Schadow, K. C., Wilson, K. J., "Mixing Enhancement in Coaxial Supersonic Jets", *20th AIAA Fluid Dynamics, Plasma Dynamics and Lasers Conference*, Buffalo, NY, 12-14 June 1989.

31. Gautam, V., Gupta, A. K., "Simulation of Flow and Mixing from a Cryogenic Rocket Injector", *J. Propul. Power*, Vol. 23, pp. 123-130, 2007.
32. Zong, N., Yang, V., "A Numerical Study of High-Pressure Oxygen/Methane Mixing and Combustion of a Shear Coaxial Injector", *43rd AIAA Aerospace Sciences Meeting and Exhibit*, Reno, NV, 10-13 January 2005.
33. Chigier, N. A., Beér, J. M., "The Flow Region Near the Nozzle in Double Concentric Jet", *Journal of Basic Engineering*, Vol. 86, pp. 797-804, 1964.
34. Romiti, A., **Fluid Dynamics of Jet Amplifiers**, Springer-Verlag, Udine, 1970.
35. Reitz, R. D., Bracco, F. V., "Mechanisms of Breakup of Round Liquid Jets", *Encyclopedia of Fluid Mechanics*, Cheremisinoff, N. P., ed., Vol. 3, pp. 233-249, 1986.
36. Ghafourian, A., Mahalingam, S., Dindi, H., Daily, J. W., "A Review of Atomization in Liquid Rocket Engines", *29th AIAA Aerospace Sciences Meeting*, Reno, NV, 7-10 January 1991.
37. Lasheras, J. C., Hopfinger, E. J., "Liquid Jet Instability and Atomization in a Coaxial Gas Stream", *Annu. Rev. Fluid Mech.*, Vol. 32, pp. 275-308, 2000.
38. Lin, S. P., **Breakup of Liquid Sheets and Jets**, Cambridge University Press, Cambridge, 2003.
39. Mayer, W. O. H., Branam, R., "Atomization Characteristics on the Surface of a Round Liquid Jet", *Experiments in Fluids*, Vol. 36, pp. 528-539, 2004.
40. Srinivasan, V., Salazar, A., Saito, K., "Investigation of the Primary Breakup of Round Turbulent Liquid Jets Using LES/VOF Technique", *36th AIAA Fluid Dynamics Conference and Exhibit*, San Francisco, CA, 5-8 June 2006.
41. Davis, D. W., Chehroudi, B., "The effects of Pressure and Acoustic Field on a Cryogenic Coaxial Jet", *42nd AIAA Aerospace Sciences Meeting and Exhibit*, Reno, NV, 5-8 January 2004.
42. Davis, D. W., "On the Behavior of a Shear-Coaxial Jet, Spanning Sub- to Supercritical Pressures, with and without an Externally Imposed Transverse

Acoustic Field”, Ph. D. Dissertation, Department of Mechanical and Nuclear Engineering, Pennsylvania State University, 2006.

43. Brown, G., Roshko, A., “On Density Effects and Large Structure in Turbulent Mixing Layers”. *J. Fluid Mech.*, Vol. 64, No. 4, p. 775-816, 1974.
44. Dimotakis, P. E., “Two-Dimensional Shear-Layer Entrainment”, *AIAA Journal*, Vol. 21, p. 1791, 1986.
45. Papamoschou, D., Roshko, A., “The Compressible Turbulent Shear Layer: An Experimental Study”, *J. Fluid Mech.*, Vol. 197, p. 453, 1988.
46. Chehroudi, B., Talley, D., Coy, E., “Initial Growth Rate and Visual Characteristics of a Round Jet into a Sub- to Supercritical Environment of Relevance to Rocket, Gas Turbine, and Diesel Engines”, *37th AIAA Aerospace Sciences Meeting and Exhibit*, Reno, NV, 11-14 January 1999.
47. Chehroudi, B., Talley, D., Coy, E., “Fractal Geometry and Growth Rate Changes of Cryogenic Jets near the Critical Point”, *35th AIAA/ASME/SAE/ASEE Joint Propulsion Conference and Exhibit*, Los Angeles, CA, 20-24 June 1999.
48. Mayer, W., Telaar, J., Branam, R., Schneider, G., “Characterization of Cryogenic Injection at Supercritical Pressure”, *37th AIAA/ASME/ASEE Joint Propulsion Conference and Exhibit*, Salt Lake City, UT, 9-11 July 2001.
49. Huerre, P., Monkewitz, P. A., “Local and Global Instabilities in Spatially Developing Flows”, *Annu. Rev. Fluid Mech.*, Vol. 22, pp. 473-537, 1990.
50. Scriven, L. E., Pigford, R. L., “Fluid Dynamics and Diffusion Calculation for Laminar Liquid Jets”, *AIChE Journal*, Vol. 5, pp. 397-402, 1959.
51. Leib, S. J., Goldstein, M. E., “Convective and Absolute Instability of a Viscous Liquid Jet”, *Phys. Fluids*, Vol. 29, pp. 952-954, 1986.
52. Raynal, L., “Instabilité et entrainement à l’interface d’une couche de mélange liquide-gaz”, Thèse de Doctorat, Université Joseph Fourier, Grenoble, 1997.
53. Perrault-Joncas, D., Maslowe, S. A., “Linear Stability of a Compressible Coaxial Jet with Continuous Velocity and Temperature Profiles”, *Phys. Fluids*, Vol. 20, 2008.

54. Heidmann, M. F., "Oxygen Jet Behavior during Combustion Instability", *NASA TN D-2725*, 1965.
55. Miesse, C. C., "The Effect of Ambient Pressure Oscillations on the Disintegration and Dispersion of a Liquid Jet", *Jet Propulsion*, Vol. 25, pp. 525-530, 1955.
56. Buffum, F. G., Williams, F. A., "Response of Turbulent Liquid Jets to Transverse Acoustic Fields", *Heat Transfer and Fluid Mechanics Institute*, pp. 247-276, 1967.
57. Chehroudi, B., Cohn, R., Talley, D. G., "Cryogenic Shear Layers: Experiments and Initial Growth Rates of Round Cryogenic Jets at Subcritical and Supercritical Pressures", *International Journal of Heat and Fluid Flow*, Vol. 23, pp. 554-563, 2002.
58. Kent, J. H., Williams, F. A., "Extinction of Laminar Diffusion Flames for Liquid Fuels", *Symposium (International) on Combustion*, Vol. 15, pp. 315-325, 1975.
59. Tsuji, H., Yamaoka, I., "The Structure of Counterflow Diffusion Flames in the Forward Stagnation Region of a Porous Cylinder", *Symposium (International) on Combustion*, Vol. 12, pp. 997-1005, 1968.
60. Tsuji, H., Yamaoka, I., "Structure Analysis of Counterflow Diffusion Flames in the Forward Stagnation Region of a Porous Cylinder", *Symposium (International) on Combustion*, Vol. 13, pp. 723-731, 1970.
61. Correa, S. M., "Effect of Compressibility on Strain in Forward Stagnation Region", *J. Propulsion*, Vol. 6, No. 1, pp. 93-96, January-February 1990.
62. Rodriguez, J., Teshome, S., Mao, H.-S., Pezeshkian, A., Smith, O. I., Karagozian, A. R., "Acoustically Driven Droplet Combustion with Alternative Liquid Fuels", *46th AIAA Aerospace Sciences Meeting and Exhibit*, Reno, NV, 7-10 January 2008.
63. Im, H. G., Chen, J. H., "Effects of Flow Transients on the Burning Velocity of Laminar Hydrogen/Air Premixed Flames", *Symposium (International) on Combustion*, Vol. 28, pp. 1833-1840, 2000.

64. Smith, A. L., Graves, C. C., “Drop Burning Rates of Hydrocarbon and Nonhydrocarbon Fuels”, *NACA RME 57, F11*, 1957.
65. Vielle, B., Chauveau, C., Chesneau, X., Odeide, A., Gökalp, I., “High Pressure Droplet Burning Experiments in Microgravity”, *Symposium (International) on Combustion*, Vol. 26, pp. 1259-1265, 1996.
66. Kumagai, S., Isoda, H., “Combustion of Fuel Droplets in a Falling Chamber”, *Symposium (International) on Combustion*, Vol. 6, pp. 726-731, 1957.
67. Godsave, G. A. E., “Studies of the Combustion of Drops in a Fuel Spray – The Burning of Single Drops of Fuel”, *Symposium (International) on Combustion*, Vol. 4, pp. 818-830, 1953.
68. Wood, B. J., Wise, H., “Measurements of the Burning Constant of a Fuel Drop”, *J. Applied Physics*, Vol. 28, p. 1068, 1957.
69. Rosser, Jr., W. A., Peskin, R. L., “A Study of Decomposition Burning”, *Comb. and Flame*, Vol. 10 p. 152, 1966.
70. REFPROP, Reference Fluid Thermodynamic and Transport Properties, Software Application Ver. 7.0, NIST, Gaithersburg, MD, U. S. Department of Commerce, 2002.
71. Thermophysical Properties of Fluid Systems, Online Database, NIST, U. S. Department of Commerce, 2005. <http://webbook.nist.gov/chemistry/fluid>.
72. Otsu, N., “A Threshold Selection Method from Gray-Level Histograms”, *IEEE Transactions on Systems, Man and Cybernetics*, Vol. 9, pp. 62-66.
73. Taylor, J. R., **An Introduction to Error Analysis**, University Science Books, Mill Valley, 1982.
74. Coleman, H. W., Steele, Jr., W. G., **Experimentation and Uncertainty Analysis for Engineers**, Wiley Interscience 1989.
75. Leyva, I. A., Rodriguez, J. I., Chehroudi, B., Talley, D., “Preliminary Results on Coaxial Jet Spread Angles and the Effects of Variable Phase Transverse Acoustic Fields”, *46th AIAA Aerospace Sciences Meeting and Exhibit*, Reno, NV, 7-10 January 2008.

76. Favre-Marinet, M., Camano Schettini, E. B., "The Density Field of Coaxial Jets with Large Velocity Ratio and Large Density Differences", *Int. J. of Heat and Mass Transfer*, Vol. 44, pp. 1913-1924, 2001.
77. Liu, T., Zong, N., Yang, V., "Dynamics of Shear-Coaxial Cryogenic Nitrogen Jets with Acoustic Excitation under Supercritical Conditions", *44th AIAA Aerospace Sciences Meeting and Exhibit*, Reno, NV, 9-12 January 2006.
78. Rodriguez, J. I., Graham, J. J., Leyva, I. A., Lyu, H.-Y., Talley, D., "On the Inner Jet Spread Angles of Coaxial Jets from Subcritical to Supercritical Conditions with Preliminary Numerical Results", *6th MS 4th LP and 3rd SP Joint Subcommittee Meeting*, Orlando, FL, 8-12 December 2008.
79. Rodriguez, J. I., Leyva, I. A., Chehroudi, B., Talley, D., "Results on Subcritical One-Phase Coaxial Jet Spread Angles and Subcritical to Supercritical Acoustically-Forced Coaxial Jet Dark Core Lengths", *44th AIAA/ASME/SAE/ASEE Joint Propulsion Conference and Exhibit*, Hartford, CT, 21-23 July 2008.
80. Teshome, S., Pezeshkian, A., Smith, O., Karagozian, A., "Influence of Standing Acoustic Waves on Combustion of Alternative Fuels", *61st Annual Meeting of the APS Division of Fluid Dynamics*, San Antonio, TX, 23-25 November 2008.

On the Effect of a Transverse Acoustic Field on a Flush Shear Coaxial Injector

Jeffrey J. Graham¹, Ivett A. Leyva², Juan I. Rodriguez³, Douglas Talley⁴
Air Force Research Laboratory, Edwards AFB, CA 93524

An experimental study on the effects of an externally-imposed transverse acoustic field in a flush shear coaxial jet is presented. In this case the inner jet recess is zero and both the inner and outer jet exit planes coincide. Since recess is a design variable used when designing new injectors, this study complements previous studies from this group where the injector geometries included a recess. The shear coaxial injector used here is similar to those used in cryogenic liquid rockets. By using N₂ as the working fluid, the chemistry effects are separated from the fluid mechanic effects of a transverse acoustic field on coaxial jets. The acoustic field is generated by two piezo-sirens whose resonant frequency is ~3kHz. The acoustic pressures generated are about 0.2-0.8% the value of the chamber pressure. The phase angle between these two sources is varied at 45 degree intervals. Two values of pressures are studied, 1.5 MPa (Reduced Pressure, Pr=0.44) where the flow is subcritical and 3.6 MPa (Pr=1.06) where the pressure is nearcritical. The outer to inner jet velocity ratio varies from ~1.5 to 17 and the outer to inner jet momentum flux ratio (J) varies from ~0.09 to 20. These ratios are mainly varied by changing the temperature and flow rates of the outer jet. At least 3000 backlit images were taken at 20 kHz for each run. These images are the main analysis tool to study the jet behavior. The most dramatic effects resulting in about 90% reduction of the length of the inner jet core were obtained at nearcritical conditions for the J=1.7 and 3.5 cases.

I. Introduction

OWING to their ubiquity in modern rocket engine design, the sheer coaxial injector has been subjected to intense scrutiny. Its use in the Ariane V rocket Vulcain engine, Atlas V rocket RS-68 engine, and Space Shuttle Main Engine has given it prominence in the field of rocket injectors, making it a strong candidate for use in the next generation of cryogenic engines. It is precisely this potential for use in safer, more efficient, and less expensive launch systems that has made a well-grounded understanding of its operational parameters a necessity to avoid unexpected behavior such as combustion instabilities.

In this paper, we are concerned primarily with the position of the inner jet post with respect to the exit plane of the outer jet. For cryogenic rocket engines, LOX is usually injected in the center post and hydrogen is injected into the outer jet. Kendrick *et al* [1], in their LOX/GH₂ experiments on shear coaxial jets, observed that a recessed internal LOX post contributed to a more rapid flame expansion. They proposed a simple model which indicates that, in a hot fire experiment, a small amount of combustion takes place within the injector recess, and the momentum flux ratio $J = \frac{\rho_g v_g^2}{\rho_l v_l^2}$ between the outer (gas) and the inner jets (liquid) is effectively increased, improving primary atomization. Sasaki *et al* [2] noticed an increase in combustion efficiency with increased outer to inner jet velocity ratio (achieved by only changing the outer jet area) for a fixed mixture ratio in non-recessed swirl injectors. For certain geometries, there was an increase of combustion performance with recess for a given velocity ratio. Subsequently, Juniper and Candel [3] showed that a recessed inner post has a larger region of absolute instability

¹ 1st Lt, AFRL/RZSA, Edwards AFB, CA 93524

² Lead, Combustion Group, AFRL/RZSA, Edwards AFB, CA 93524

³ Post Doctoral Researcher, UCLA/AFRL, Edwards AFB, CA 93524

⁴ Senior Scientist, AFRL/RZSA, Edwards, AFB, CA 93524

Approved for public release; distribution unlimited.

than a flush injector, following from self-sustained wake-like flow instabilities that are seen only intermittently in the flush case. Lux and Haidn [4] found in their LOX/methane experiments that a recessed LOX post leads to more rapid flame expansion and lesser combustion roughness. More recently, Moser and Saffell [5] using GOX/methane have noted that increasing the depth of recess improves combustion efficiency by less than one percent for one diameter of recess, and on average 4.5 percent for two injector diameters of recess, indicating that the amount of distance afforded to the jets to mix within the duct of the outer jet wall is a significant factor in shear coaxial injector performance. However they found that changing L^* (chamber volume/nozzle throat area) had a bigger effect on the combustion efficiency.

Furthermore, it is well known that the combustion chamber is an acoustically active environment. Glogowski *et al* [6] have indicated that using a tapered inner jet post in a shear coaxial injector resulted on a transition to resonance characterized by a “whistling noise” and significant modification of the spray. Moreover, by spectral analysis, they showed that the system experienced coupled pressure fluctuations between the chamber and the fuel plenum which were higher at higher frequencies.

At the Air Force Research Laboratory (AFRL) non-reactive cryogenic experiments have been performed using a shear coaxial injector, with and without transverse acoustic forcing. The experiments from Davis and Chehroudi [7], along with data from other researchers they compiled, showed that the inner jet dark core (related to the intact core or potential core) depends on J with a relation of the form $AJ^{-n} + B$, where n is 0.2 for two phase flows (subcritical pressures) and 0.5 for one phase flows (near and supercritical pressures). Since the dark core is a qualitative indicator of mixing, with better mixing achieved with shorter dark cores, then mixing efficiency increases as the velocity ratio and J values increase. Leyva *et al* [8] continued work in this vein by characterizing the behavior of coaxial jets for a wide range of velocity ranges and J values with high speed backlit images (20-40 kHz). They found that there is an optimum range of J from about 1 to 5 for which acoustics has a statistically significant decrease on the dark core length of the inner jet for all pressures studied. The range is even larger for subcritical pressures. Both of those studies were completed with a fixed phase angle of the acoustic field with respect to the jet location since only one acoustic source was used and the geometry of the experiment was fixed. Rodriguez *et al* [9] modified the phase angle of the acoustic excitation at the jet location using twin acoustic sources. Their results have shown that acoustic excitation can result in much more rapid mixing than for a similar non-acoustic case, and moreover that this occurs primarily for a range of J values between one and four. For part of that work the same injector as the one being used here was used except that in that case the inner jet was recessed about one half of the inner jet diameter.

Little work, however, has been done on the effect of recess on the interaction of an externally imposed acoustic oscillation with the flow field of coaxial injectors. This research is necessary, however, because recess is a variable that engine designers use to fabricate new injectors.

II. Experimental Setup

The experimental studies reported in this paper were performed at the Air Force Research Laboratory (AFRL) located at Edwards Air Force Base, CA, in the Cryogenic Supercritical Laboratory, EC-4. An overview of the test section is shown in Figure 1. Gaseous N_2 is used to supply the inner and outer jet flows and to pressurize the chamber. The outer and inner jets are cooled by LN_2 in heat exchangers (HE's) immediately preceding entry to the chamber; one HE was used for each jet to allow independent temperature (T) control. This was effected by adjusting the flow rate of liquid nitrogen through the HEs. The mass flow rate through the inner and outer jets was measured with Porter mass flow meters (122 and 123-DKASVDAA) prior to cooling, since it was found that it is much easier to measure the flow rates at ambient rather than at cryogenic temperatures. The chamber pressure is measured with a Stellar 1500 transducer. To keep the amplitude of the acoustic oscillations to a maximum near the jet, an inner chamber was created (Figure 1). This inner chamber has a nominal height of 6.6cm, a width of 7.6cm and a depth of 1.3cm. The dimensions of the injector are given in Figure 2A. For all the cases presented here the inner jet was flush with the outer jet.

Acoustic Drivers

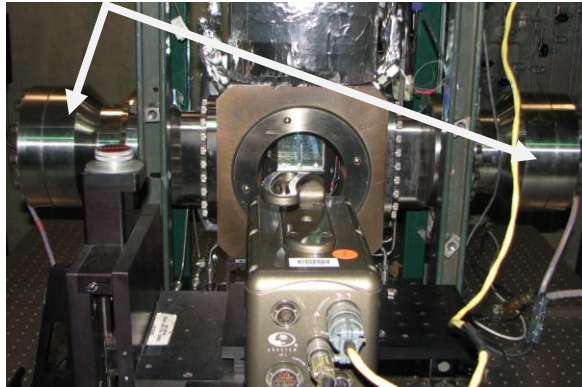


Figure 1. Overview of the Main Chamber of the Supercritical Flow Facility, EC-4 at AFRL/Edwards.

Images of the injector and its placement within the chamber are shown in Figures 2a and 2b, respectively. The temperature of the jets is measured with an unshielded type E thermocouple which has a bead diameter of 0.1mm and an accuracy of ± 1 K as checked with an RTD. A Kulite XQC-062 pressure transducer is placed next to the thermocouple and used to measure the pressure at a sampling frequency of 20 kHz. Both the pressure transducer and the thermocouple are moved in a volume around the jet with a piezoelectric positioning system built by Attocube Systems which can move in an area 3mm by 6 mm with step sizes in the order of 0.01mm. Vertical motion is achieved with a fine hand-screw. For temperature profile measurements, the average distance from the exit plane is ~ 0.3 mm, though the system has the ability to insert the thermocouple into the recess of the injector if so desired. Properties such as density, viscosity, and surface tension are computed from the measured flow rates, chamber pressure and jet temperature, using NIST's REFPROP [10]. From this, the velocity ratio (VR) and J for a given condition can be computed.

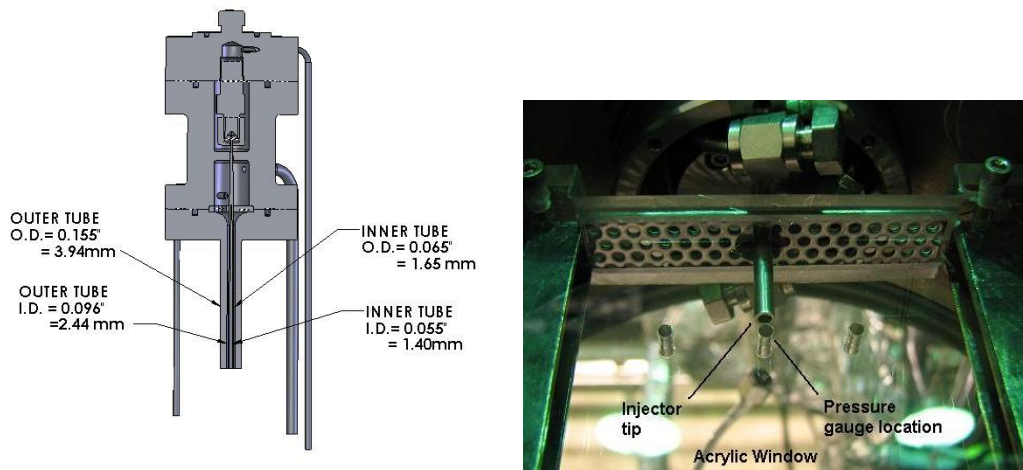


Figure 2. A. Injector Cut-Away. B. Injector Placement

The jet is visualized by taking backlit images using a Phantom 7.1 CMOS camera. The resolution of the images varies from 128x384 to 160x496, with most at the latter, depending on chamber pressure and J, which in turn determines the size of the visible features of the jet under scrutiny. The framing rate was 20 kHz. The jet is backlit using a Newport arc lamp set at 160 W. The acoustic waves are generated using two piezo-sirens custom made for AFRL by Hersh Acoustical Engineering, Inc. (Figure 1). These are operated by providing a sinusoidal signal from a function generator amplified to high voltage for use as the driving potential. These piezo sirens have a resonant

frequency of approximately 3 kHz. The specific frequency to use for each run is found empirically by scanning a frequency range from about 2.9 to 3.1 kHz and choosing the frequency that has the most effect on the jet. The distance between the two acoustic sources is about 67 cm and for a nominal driving frequency of 3 kHz, there are about 7 wavelengths in this length. However, even the outer diameter of the outer jet is very small compared to the characteristic wavelength so we operate in the long wavelength limit. To accommodate for the rectangular chamber a waveguide with a catenary contour is used to guide the waves from a circular cross-section to a rectangular cross-section. The max RMS sound acoustic pressure in the inner chamber ranges from 4.3 to 14.0 kPa.

III. Experimental Results

A total of 8 conditions were run at subcritical pressure corresponding to a reduced pressure, Pr , of about 0.44, where $Pr = \text{Chamber pressure} / \text{Critical pressure of } N_2$. For that case, we have two phase flows since the inner jet is at the saturation temperature or a few degrees below and the outer jet is in the vapor phase. A set of 4 conditions were run at nearcritical pressure ($Pr=1.06$). In this case the jet flow is one phase since both fluids are slightly above the critical pressure. The inner jet temperature is below the critical temperature (liquid-like state) and the outer jet is above the critical temperature. For reference, the critical temperature, T_{cr} , for N_2 is 126.3K and the critical pressure, P_{cr} is 3.4 MPa. For each condition run one or two baseline cases were taken with the acoustics turned off. Then, a series of cases were taken where the phase angle between the two acoustic sources (Figure 1) was varied from 0 to 360 degrees in increments of 45 degrees. This is to capture the full span of acoustic conditions at the jet location, from a pressure antinode to a pressure node. At 0 degrees, the two acoustic sources are in phase and move towards each other as shown in Figure 3. For this case, there is a pressure antinode (velocity node) at the center of the two sources, in other words at the injector location. At 180 degrees, the two sources move away from each other forming a pressure node (velocity antinode) at the injector location.

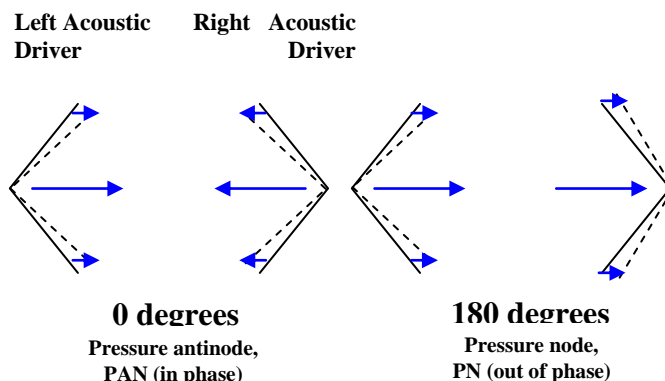


Figure 3. Simplified diagram of the two acoustic drivers at a 0° and 180° phase angle

In what follows, some of the most interesting cases are presented in the form of image collages. For each collage, ten instantaneous back-lit images are shown, each corresponding to a different phase angle tested. The first case to be analyzed is for $Pr=0.44$ with $J=0.09$ (

Figure 4). This is the limit of a single jet since the outer jet is moving so slowly compared to the inner jet. In the images the inner jet appears darker than the outer jet since it is colder and denser and thus the light from the lamp gets obstructed or deflected the most. For the baseline case, the inner jet does not break within the field of view. Despite the smooth appearance of the inner jet, it is turbulent at $Re \sim 10^3$. This case shows a great effect from acoustics. In the phases around 0 to 45 and 270 to 360 degrees, the jet is violently destroyed by the acoustics and large sections of the liquid jet as well as big droplets and ligaments are noticeable after the first break of the jet. In fact, for the case of 45 degrees we can see discrete droplets and their trails. This behavior contrasts sharply with the cases 135, 180, and to some extent 225 degrees, where the pressure gradient is small, and the local velocity oscillation is relatively large. In those cases, though the jet moves within the plenum, it moves as a whole, and

therefore they have longer dark cores. The 180 degree excitation is particularly interesting in this regard—for some distance down the jet, it looks very nearly like the baseline case. However, necking is observed and downstream of the neck there is much finer atomization of the jet. Finally note that for all cases except for 180 degrees, there is a toroidal vortex formed at the exit plane of the jet.

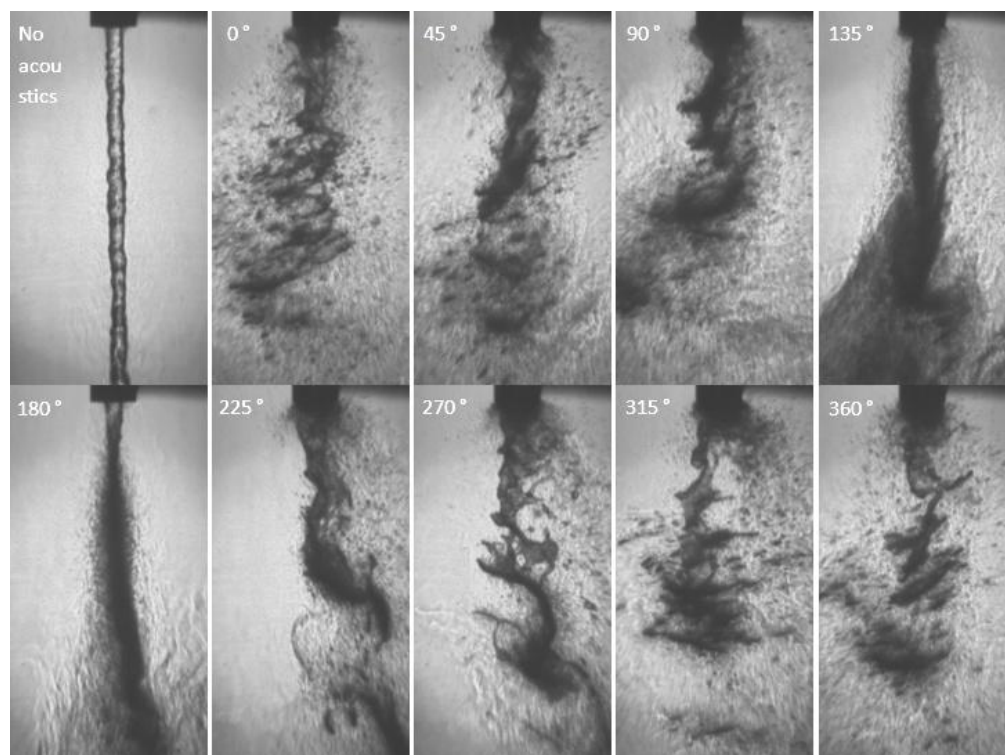


Figure 4. Collection of subcritical coaxial jet images for $Pr = 0.44$, $J = 0.09$.

The next case was obtained at the same pressure but with $J=1.93$ (Figure 5). Comparing the baseline with the previous case, one can see that the inner jet is thicker and it breaks down within the field of view. This widening of the inner jet is typical of higher J values. The jet shows more pronounced disturbances in the surface. Also, one can observe a range of droplet sizes as we move downstream from the exit plane. In the baseline case, it is possible to see a glimmer of light through the jet itself, reminiscent of the $J=0.09$ case. Especially noteworthy is, again, the difference between the 0 and 360 degree conditions and those more toward the 180 degrees. In all conditions except 180 degrees there are clear images of vortices forming on the surface of the inner jet. Certainly, the inner jet does break down in a similar fashion to the $J=0.09$ case down the centerline, but only after a sufficient length to allow for mixing. One further point is that, as the flow rates for the inner jet in both cases were very close, only the change in the outer jet can account for this particular change in spray behavior. At 45 and 90 degrees there is a region downstream from the first vortical structure with very fine droplets. At 180 degrees, where we have a pressure node at the jet location, no toroidal vortex formation is observed. The jet is being moved as a whole. Conditions 135 and, to some extent, 225 degrees are particularly notable insofar as they show a transition from one behavior to the other.

For the following case of $J=7.9$ (Figure 6), changes are occurring more with respect to intensity rather than fundamental form. In the $J=7.9$ case the outer jet has sped up and is carrying considerably more momentum, such that it blows along the surface of the inner jet and generates surface disturbances. Furthermore, the annular vortices of the boundary are significantly more pronounced in the 0 through 90 degree cases—the presence of a strong black protrusion from the center jet indicates that mass from the inner jet is being pulled away quite strongly in these cases. At the other phase angles mass is still being pulled from the inner jet to some extent, but not nearly as much, and the vortex appears to involve mass mostly from the outer boundaries of the inner jet as well as the outer jet. For the 180 degree condition, and the 225 degree to a lesser extent, the vortices do not form as strongly. There are a few, to be sure, but they lack the symmetry and persistence of the previously discussed conditions.

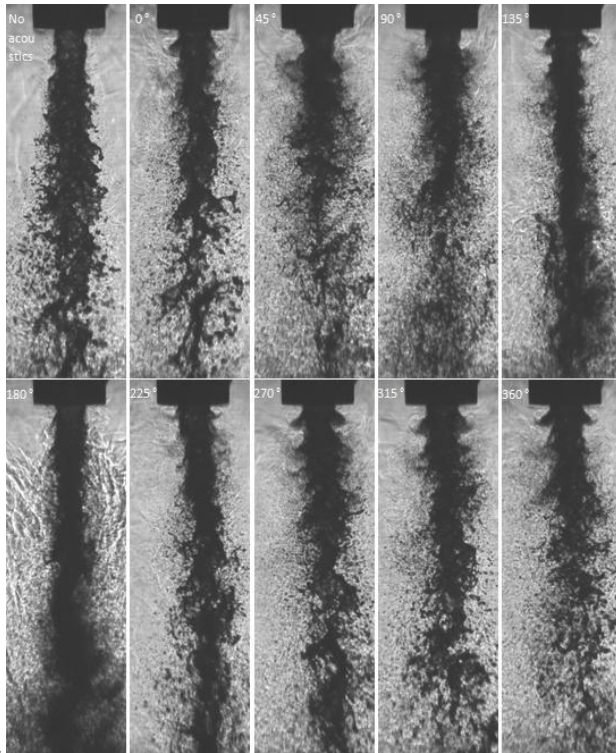


Figure 5. Collection of subcritical coaxial jet images for $Pr = 0.44$, $J = 1.93$

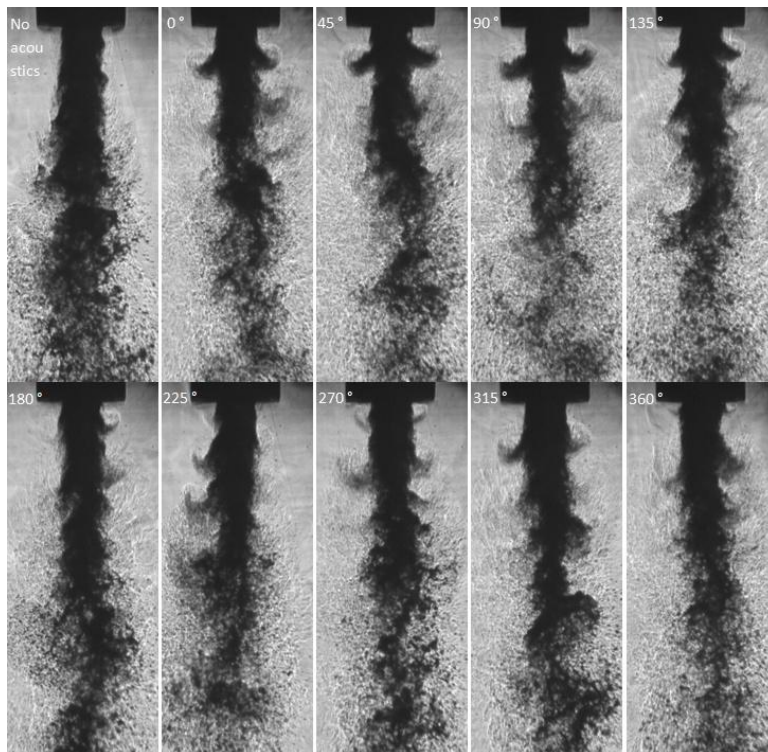


Figure 6. Collection of subcritical coaxial jet images for $Pr = 0.44$, $J = 7.9$

The last subcritical case to be analyzed is that of $J=18$ (Figure 7). Here one can see how the dramatically larger velocity of the outer jet as compared to the inner jet manifests itself. Observe how the vortices which have appeared in prior cases, though still present, appear more thoroughly stretched vertically, and develop further down from the injector exit plane. The outer jet, besides being a key component in the formation of the vortices, is pulling them downstream considerably faster than if they convected downstream at the inner jet velocity. This does not appear to be happening in the 180 degree condition. The baseline condition shows the formation of spray generally in the vertical axis, with some, not particularly strong, expansion to the left and the right, while all the acoustically driven cases show stronger fragmentation earlier. One final point: on the 180 degree excitation, there are what appear to be pulses of inner core matter protruding out at regular intervals and at alternating vertical position, serving as a dramatic illustration of the effects that the alternating velocity of the surrounding plenum have on the jet as it emerges in to the chamber.

Next we will explore the cases taken at nearcritical pressures ($Pr=1.06$). The first two cases to be discussed have $J=1.7$ (Figure 8) and 3.5 (Figure 9). These are very dramatic cases illustrating the effects of both acoustics and phase angle. Owing to their striking similarity, they are discussed simultaneously here. The most noteworthy occurrence in these cases is the total annihilation of the inner jet dark core at conditions 90 degrees and below or 270 degrees and above at $J=1.7$. Similarly, though not as dramatic, the inner jet dark core was greatly reduced in the $J=3.5$ case. At $J=1.7$, for phase angles of 90 and 135 degrees, there are two, or three vortical structures that are closely spaced and then collapse in to a well-mixed jet. At $J=3.5$, there are two or three vortical structures that are much more widely spaced. A natural inference is that the increase in spacing follows from the increased outer jet velocity. The greatest effect is a at the pressure antinode (0 degrees) like in previous cases where the pressure fluctuations are maximum. Close to the pressure node (180 or 225 degrees), where the velocity fluctuations are the largest the jet remains the longest, or least affected. Also the vortical structures are not as prominent as for the rest of the cases.

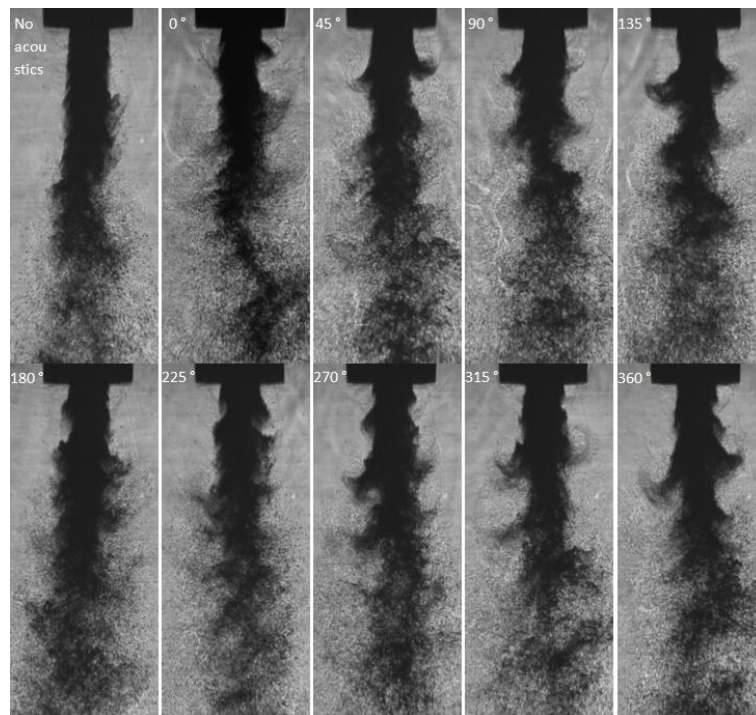


Figure 7. Collection of subcritical coaxial jet images for $Pr = 0.44$, $J = 18$

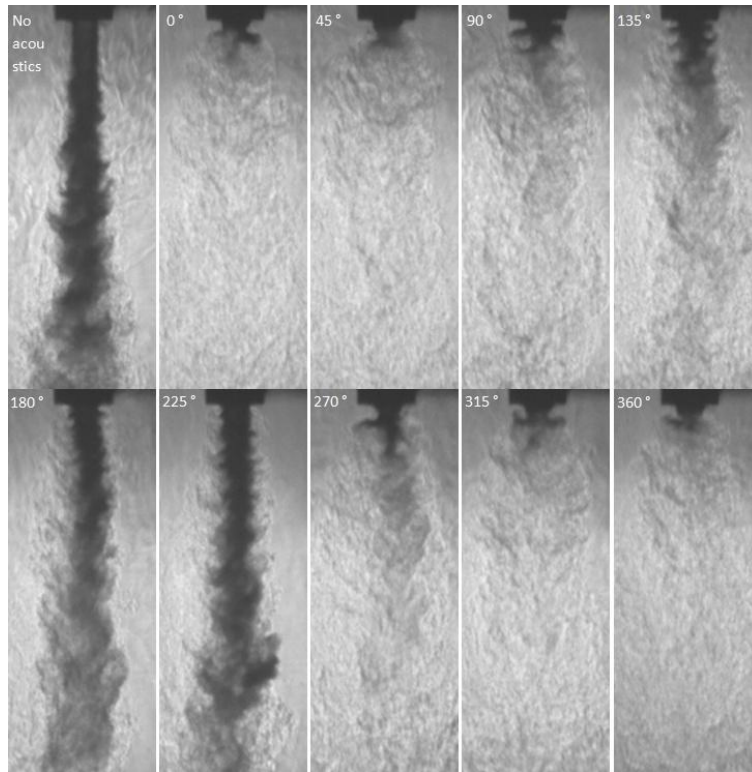


Figure 8. Collection of nearcritical coaxial jet images for $Pr = 1.04$, $J = 1.7$

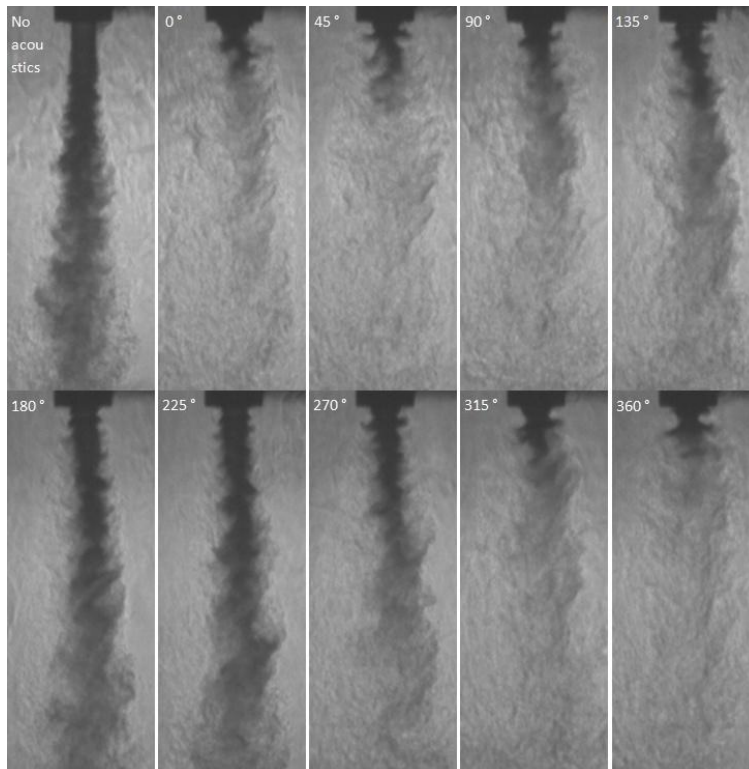


Figure 9. Collection of nearcritical coaxial jet images for $Pr = 1.04$, $J = 3.5$

For $J=10$ case (Figure 10), the acoustics have less of an effect, similar to what the subcritical cases showed at the largest momentum flux ratios. The toroidal vortices are still apparent though. The baseline condition is longer than the rest, implying that acoustics do affect mixing, but the effect is not linked to the phase angle. In the baseline condition, the primary mixing mechanism between the two jets is the velocity gradient, or shear, between them. The acoustics, however, drive the outer jet into the inner jet by pressure or velocity gradients, and then strong mixing occurs for certain conditions. The large vortical structures prompted by the acoustics act as mixing enhancements for the jet. The last case corresponds to $J=20$ (Figure 11). This case corroborates the points made in the $J=10$ case. The inner jet dark core for the baseline is significantly longer than for the conditions with acoustics on; but the perturbed dark cores are about equal regardless of the phase angle. Therefore, once excited, the system collapses into one basic mixing regime. Since they are shorter than the $J=10$ case, their mixing is more rapid, and the chief difference between the two is the momentum flux of the outer jet. Consequently, in this high J regime, all the perturbations introduced appear to collapse the system, assuming an inner jet dark core length based primarily on J .

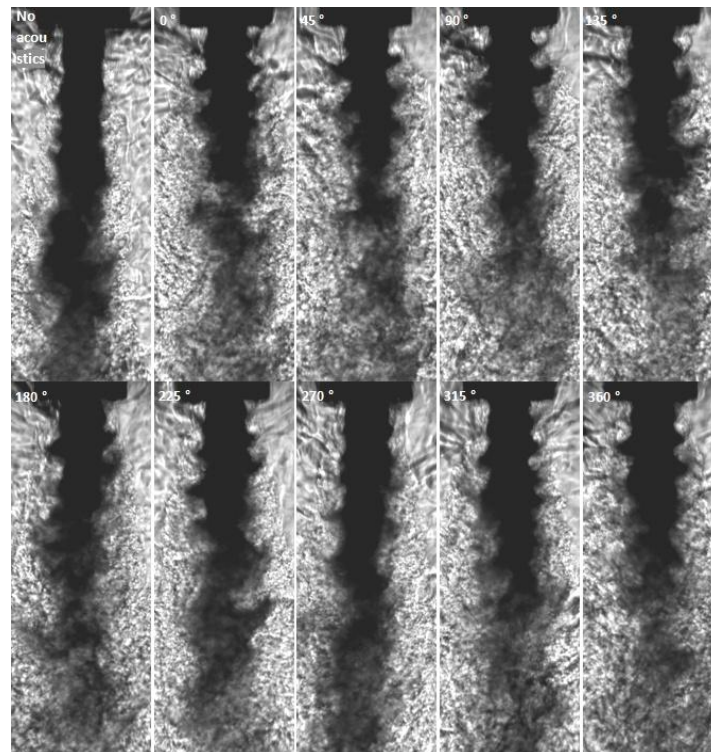


Figure 10. Collection of subcritical coaxial jet images for $Pr = 1.04$, $J = 10$

Next, we put the aforementioned results together in the form of plots of the dark core length at the various phase angles normalized by the dark core length at the baseline condition. A detailed explanation of the definition and calculation of the dark core length is presented in Leyva et al [8]. Figure 12 shows the subcritical pressure results. In here we can see that for the two lower J values, 0.09 and 0.36, the largest reduction is for a pressure antinode and the jet is less reduced close to the pressure node. The case for $J=1.93$ is very interesting since it would seem like the jet is actually getting longer at the pressure node. This should be taken with a word of caution. The way the dark core length is calculated is solely based on thresholding the image to black and white pixels depending on the distribution of the brightness of the image. That is, the routine cannot distinguish very well between a continuous dark core and an agglomeration of very fine droplets, which is more likely what is happening here. For the $J=1.93$ case there is very fine atomization occurring close to the pressure node, which makes the dark core appear longer. As the J value increases the reduction decreases and the dependence with phase angle also ceases. For the cases with nearcritical pressures (Figure 13), the results are qualitatively the same, except that we do not have a case with $J=1.93$ so we cannot make a direct comparison with the similar case in the subcritical regime. Also

note that for $J=1.6$ and 3.47 cases there are dramatic reductions on the dark core length at the pressure antinode. Finally, for the $J=20$ case there does not seem to be a dependence on the phase angle.

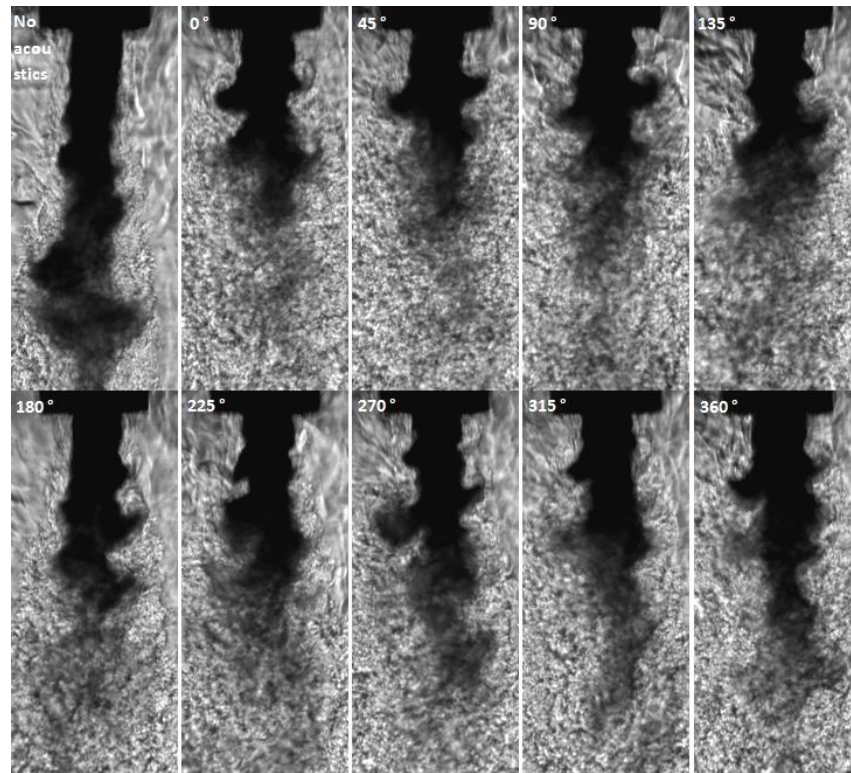


Figure 11. Collection of subcritical coaxial jet images for $Pr = 1.04$, $J = 20$.

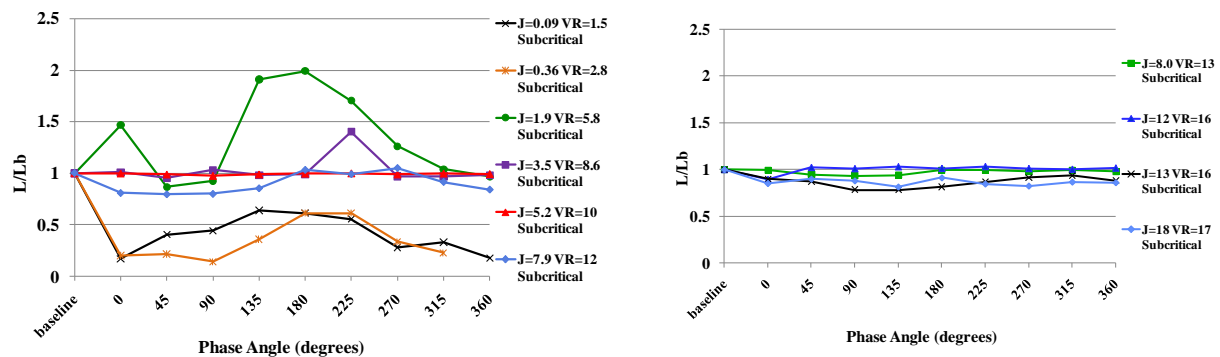


Figure 12. Normalized Inner Jet Dark Core Length as a Function of Phase Angle for Subcritical Pressure.

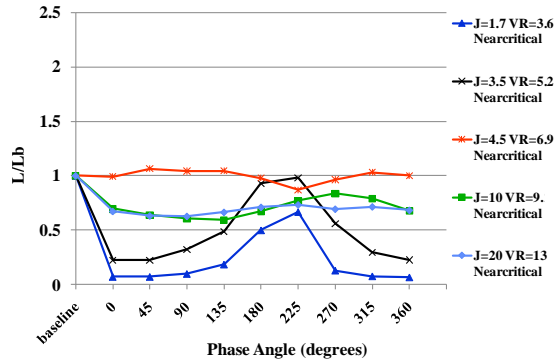


Figure 13. Normalized Inner Jet Dark Core Length as a Function of Phase Angle for Nearcritical Pressure.

IV. Conclusions

An experimental study was carried out to explore the effects of a transverse acoustic field on a flush shear coaxial injector. The magnitude of the acoustic pressure was 0.2-0.8% of the mean chamber pressure. Two chamber pressures were studied, 1.5 MPa ($Pr=0.44$) and 3.6 MPa ($Pr=1.06$). The outer to inner jet velocity ratio varies from ~ 1.5 to 17 and the outer to inner jet momentum flux ratio (J) varies from ~ 0.09 to 20. It was found that for the single jet limit in the case of subcritical pressures the jet was destroyed by the acoustics when it was located close to a pressure antinode. At the other extreme, at a pressure node, the jet exhibited necking and fine vaporization downstream of the neck. For $J < 8$ the jet responded to the phase of the acoustic field with the largest reduction around the pressure antinode except for the case with $J=5.2$ which has a lower acoustic excitation. Large vortical structures emanating from the inner jet and enhancing the mixing between the two jets were evident for these cases, except for the case of pressure nodes, where such structures were much less conspicuous. For the case of $J=18$, the effect of acoustics had become independent of phase angle. While there was still a reduction on the core length, it was about the same for all conditions. The vortical structures were still evident for this case but less pronounced than in lower J values.

The most dramatic effects were found for the nearcritical pressure for $J=1.7$ and 3.5. For those cases, the reduction of the dark core at the pressure antinode was about 90% of the baseline condition. For those cases, one can still see vortical structures but they involve the whole inner jet flow, and downstream of the first one or two vortical structures one can no longer distinguish the inner jet. Complete mixing seems to have been achieved. As the J value increased up to 20, the effect diminished quantitatively but remained the same qualitatively.

Acknowledgements

The authors would like to express their appreciation to Mr. Randy Harvey for his invaluable contributions in running and maintaining the facility. This work is sponsored by AFOSR under Mitat Birkan, program manager.

Appendix

Table 1. Run Conditions

	T_{chamber} (K)	ρ_{chamber} (kg/m ³)	P_{chamber} (MPa)	T_{outer} (K)	\dot{m}_{outer} (mg/s)	ρ_{outer} (kg/m ³)	u_{outer} (m/s)	T_{inner} (K)	\dot{m}_{inner} (mg/s)	ρ_{inner} (kg/m ³)	u_{inner} (m/s)	Freq. (kHz)	Baseline L/D1	VR	P _{rms} max (kPa)	J
SUB																
sub1	248	20	1.49	207	89.8	25	1.4	106	920	688	0.87	3.04	35+	1.5	6.7	0.09
sub2	244	21	1.50	187	192	28	2.7	111	916	619	0.97	3.02	35+	2.8	7.3	0.36
sub3	208	25	1.50	150	525	37	5.6	106	942	646	0.94	2.96	6.9	5.8	7.8	1.9
sub4	251	20	1.49	180	605	29	8.1	109	914	630	0.95	2.95	7.2	8.6	6.6	3.5
sub5	240	21	1.49	177	747	30	9.8	109	913	630	0.95	3.05	6.9	10	7.3	5.2
sub6	223	23	1.50	164	999	33	12	109	944	630	0.98	3.04	7.2	13	5.4	7.9
sub7	240	21	1.49	182	911	29	12	109	913	630	0.95	3.04	7.0	13	4.4	8.0
sub8	221	23	1.50	170	1178	32	15	109	913	635	0.94	3.04	6.6	16	6.7	12.3
sub9	215	24	1.51	167	1250	33	15	109	945	630	0.98	2.96	6.9	16	4.6	12.5
sub10	198	25	1.50	150	1590	37	17	109	947	630	0.98	3.06	7.0	17	8.6	18
NEAR																
near1	216	59	3.57	176	730	78	3.7	120	938	556	1.0	3.09	21	3.6	14.0	1.7
near2	210	61	3.57	186	1035	72	5.7	122	936	530	1.2	3.06	11	5.2	7.6	3.5
near3	228	55	3.58	209	994	61	6.1	112	927	629	1.0	3.02	15.3	6.9	4.3	4.5
near4	255	48	3.57	181	1699	74	9	112	942	629	0.98	2.98	9.1	9.2	5.5	10
near5	202	64	3.57	183	2397	73	13	113	945	621	0.98	3.05	9.2	13	6.2	20

References

1. Kendrick, D., Herding, G., Scouflaire, P., Rolon, C., and Candel, S., "Effects of a recess on cryogenic flame stabilization", *Combustion and Flame* 118:327-339 (1999).
2. Sasaki, M., Sakamoto, H., Takahashi, M., Tomita, T., Tamura, H., "Comparative study of recessed and non-recessed swirl coaxial injectors," AIAA-1997-2907-657, 1997.
3. Juniper, M.P., and Candel, SM. "The stability of ducted compound flows and the consequences for the geometry of coaxial injectors," *Journal of Fluid Mechanics* (2003), vol 482, 257-269.
4. Lux, J. and Haidn, O. "Effect of Recess in High-Pressure Liquid Oxygen/Methane Coaxial Injection and Combustion", *Journal of Propulsion and Power*, Vol. 25, No. 1, Jan-Feb 2009.
5. Moser, M.D. and Saffell, R.J., "GOX/Methane Injector Effects on Combustion Efficiency", AIAA 2008-4952.
6. Glogowski, M. et al. "Shear Coaxial Injector Stability Mechanisms", AIAA-1994-2774.
7. Davis, D. W., Chehroudi, B., "Measurements in an Acoustically Driven Coaxial Jet under Sub-, Near-, and Supercritical Conditions". *J. Propul. Power*, Vol. 23, pp. 364-374, 2007.
8. Leyva, I. A., Rodriguez, J.I., Chehroudi, B., Talley, D., "Preliminary Results On The Effect Of Phase Angle On Coaxial Jet Behavior Spanning Sub- To Supercritical Pressures," ILASS 08-A142, 2008.

9. Rodriguez, J.I., Leyva, I. A., Graham, J., Talley, D., "Mixing enhancement of liquid rocket engine injector flow," AIAA-2009-5143.
10. Thermophysical Properties of Fluid Systems, Online Database, NIST, U. S. Department of Commerce, 2005.
<http://webbook.nist.gov/chemistry/fluid>.

Mixing Enhancement of Liquid Rocket Engine Injector Flow

Juan I. Rodriguez¹

Department of Mechanical and Aerospace Engineering, UCLA, Los Angeles, CA, 90095

Ivett A. Leyva², Jeffrey J. Graham³ and Douglas Talley⁴

AFRL/RZSA, Edwards AFB, CA, 93524

An investigation of the mixing enhancement behavior of N₂ shear coaxial jets between two injector geometries is presented. A total of 20 cases with one injector geometry and 15 with the other, corresponding to different momentum flux ratios (J values) at subcritical, nearcritical and supercritical pressures are analyzed and compared. The measurements are extracted from 998 backlit images for each data point. Acoustic excitation is used to analyze the response of the system to velocity and pressure perturbations. The frequency of the system varied from 2.90 to 3.11 kHz and the maximum peak-to-peak pressure perturbation as a percentage of the mean chamber pressure was 4%. It was found that the geometry differences between the two injectors had a large impact on their behavior. The qualitative response of one of the injectors to acoustics at low J values in the subcritical regime was completely different to the other. In contrast, when comparing cases with very similar J values for different pressures, it was found that the normalized dark core length between these cases remains close regardless of phase angle for the two injectors despite the fact that the relative acoustic excitation intensities for subcritical pressures were up to eight times stronger than those at near and supercritical chamber pressures..

I. Introduction

Mixing enhancement is an important design parameter when considering Liquid Rocket Engine (LRE) performance. Thorough mixing of the inner and outer jet streams in a coaxial injector could lead to an increase of the total energy release from the propellants. To characterize mixing, several variables could be considered. However, for the purposes of this study, both the qualitative response of the coaxial jet and the length of the inner jet dark core will be the chosen parameters to assess mixing between the inner and the outer jets in two different coaxial jet configurations. For instance, a shorter inner jet dark core means that mixing with its surroundings takes place faster than compared to a longer one at the same flow conditions. In previous studies, Gutmark et al.¹ concluded in their coaxial vs. free jet studies that in coaxial flow configurations more of the surrounding fluid is entrained deeper into the inner jet as compared to the free jet case, enhancing the overall mixing process. These researchers also found that the geometry of the injector plays a role as well, with better mixing performance achieved by rectangular injectors compared to circular ones. Gautam and Gupta² reported in their cryogenic coaxial injector studies at atmospheric pressures an increase in the evaporation of the inner jet and enhanced mixing with the surrounding flow with increasing outer to inner momentum flux ratio (J). They also change the geometry of their injector setup by modifying the recess length between the inner jet and the outer jet exits. They found that larger recess lengths promote higher jet expansion and more entrainment of surrounding gases into the flow. Their shear layer analysis confirms that mixing and jet expansion are slower at lower J values. Zong and Yang³ also find in their numerical study of high pressure coaxial reactive flow that as J increases, turbulent mixing is enhanced whereas the inner jet dark core is reduced. Finally, Richecoeur et al.⁴ studied an acoustically excited, multiple element, reactive coaxial injector configuration at elevated but still subcritical pressure conditions. They found that conditions where combustion became sensitive to external oscillations happened at lower J values. The strong coupling between acoustics and combustion showed an enhancement of the

¹Research Associate, UCLA, Los Angeles, CA 90095-1597, AIAA Member.

²Lead, Combustion Dev. Group, AFRL/RZSA, 10 E. Saturn Blvd., Edwards AFB, CA 93524, AIAA Sr. Member.

³Combustion Scientist, 1st Lt., AFRL, Edwards AFB, CA 93524, AIAA Member.

⁴Sr. Aerospace Engineer, AFRL/RZSA, 10 E. Saturn Blvd., Edwards AFB, CA 93524, AIAA Member.

Approved for public release; distribution unlimited. PA #09319.

flame spread at a pressure antinode location, where pressure perturbations are the highest, which might be associated with improved mixing.

Therefore, the overall objective of our study is to provide an analysis of mixing enhancement in a coaxial injector flow, which is a type of injector extensively used in LREs. Two different coaxial injector geometries will be studied and in addition to varying J and the chamber pressure, acoustic forcing is used to generate different velocity and pressure perturbation conditions at the location of the jet. These transversal pressure and velocity fields are generated with two piezo-siren elements that produce high amplitude acoustics. The phase between them can be adjusted so the position of the jet with respect to the generated pressure and velocity fields can be varied. The resonant frequency is around 3 kHz and pressure perturbations can reach values as high as 4% of the chamber pressure. The experimental study is conducted at three different pressure regimes ranging from 1.5 to 5.0 MPa; thus the reduced pressure, P_r , which is the ratio of the chamber pressure to the critical pressure, varied from 0.45 to 1.5. J varied from 0.019 to 23. The effect of having a relatively thick versus a thin wall between the inner and outer jet flows in a coaxial jet configuration will be studied. Similar outer to inner jet momentum flux ratios between the two geometries were maintained, as well as similar inner and outer jet densities and velocity ratios. However, the outer to inner jet mass flow ratios were very different for a given J value due to the change in geometry. Very recent results from our research group show that a thicker post could create a recirculation zone that prevents or at least delays unstable behavior of the inner jet in certain flow regimes^{5,6}.

II. Experimental setup

The experimental work presented in this study was performed at the Air Force Research Laboratory, Edwards Air Force Base, CA. The Cryogenic Supercritical Laboratory (EC-4) was used to run all tests. A photograph of the facility is shown in Fig. 1.a and a schematic of the experiment is shown in Fig. 1.b. The photograph shows the test chamber in the center and the acoustic drivers on each side. The chamber flow exits through a vent line located at the center bottom of the chamber. Above the chamber there is a thick insulation that houses the inner jet heat exchanger which cools the nitrogen inner jet as much as possible before it enters the chamber. On top of the chamber, to the sides of the insulation, there are orifices that allow more probes, such as thermocouples and pressure transducers, to reach inside the test chamber.

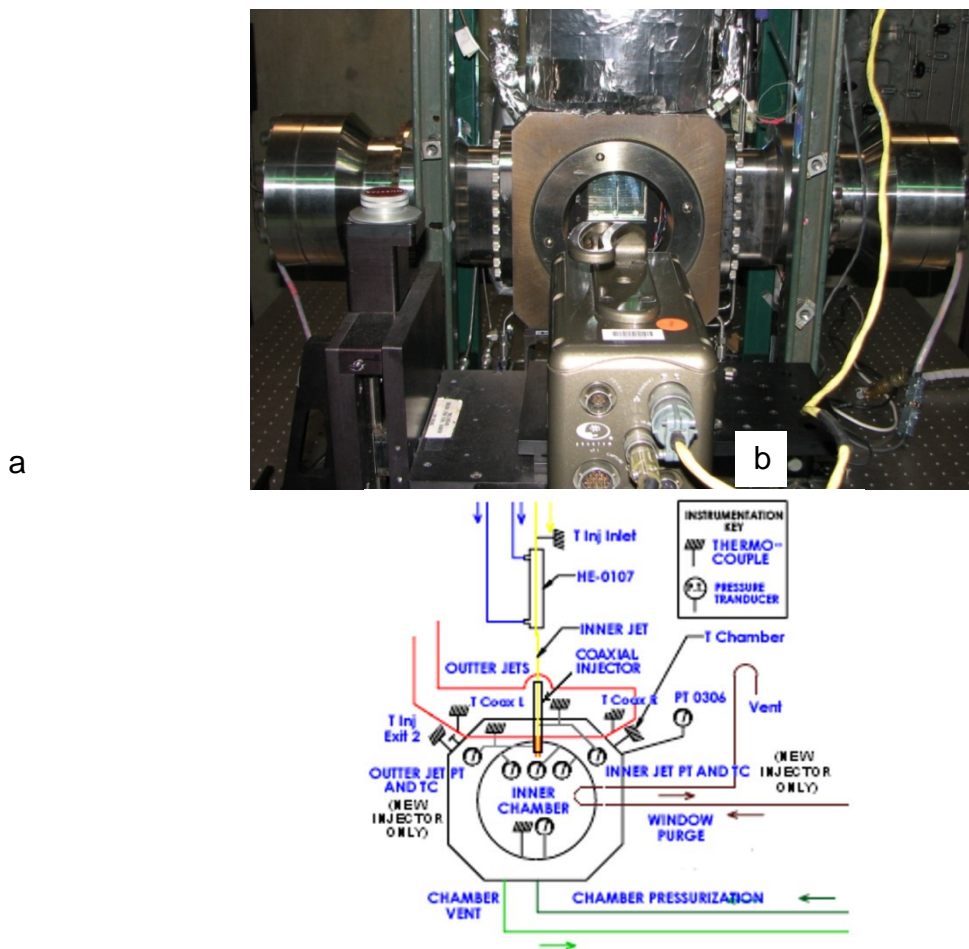


Figure 1a. Experimental test chamber and supporting systems of the Experimental Cell 4 at AFRL, Edwards AFB, CA. b. Chamber section view of the flow schematic for Experimental Cell 4.

The chamber section of the schematic in Fig. 1.b represents the most updated version of the experimental setup. It shows the three differential pressure transducers that were used to measure the pressure fluctuations in three equally spaced locations with one placed just above the location of the coaxial injector exit and the other two to its sides. It also shows the pressure transducer and thermocouple that were brought from the bottom of the chamber to the injector exit inside the inner chamber. The schematic also shows that both the inner jet and outer jet have a pressure transducer and a thermocouple at the coaxial injector location. Also shown in the schematic in Fig. 1.b are heat exchangers that allowed the cooling of the inner and outer flows, and the window purge flow that was used to prevent water vapor condensation on the test chamber windows so as to allow proper visualization of the coaxial jet flow. Several thermocouples were used across the heat exchanger and in other locations to keep track of the conditions of the flow in order to maintain the required flow properties for each test. To run one of these tests, gaseous N_2 was used to supply the inner and outer flows of the coaxial jet and to pressurize the chamber. Then the outer jet was cooled by either one or two heat exchangers (HEs), depending on the test requirements. A third HE was used to decrease the temperature of the inner jet. The coolant that ran through the HEs for both the inner and outer jets consisted of liquid N_2 obtained from a cryogenic pressure vessel located outside EC-4, which had a capacity of 5 m^3 . The temperatures of the two jets were controlled by adjusting the flow rate of liquid N_2 through the HE's. The mass flow rates through the inner and outer jets were measured before they were cooled with Porter mass flow meters (models 122 and 123-DKASVDAA), since it was less cumbersome to measure mass flow rates at ambient temperature than to measure them at cryogenic conditions.

Once the desired mass flow rates for the inner and outer jet were achieved, the mean chamber pressure required for the experiment was adjusted. The chamber pressure was measured with a Stellar 1500 transducer. After the mean chamber pressure was obtained, the mass flow rates were adjusted for minor changes due to the pressure

increase. Finally, the liquid N₂ flow through the HEs was carefully controlled to stabilize the inner and outer jet temperatures to produce the desired outer to inner jet momentum flux ratio for that particular test. To see a summary of the operating conditions achieved for all cases reported in this study, refer to the Appendix. In order to maximize the effect of the available acoustic energy on the jet, an inner chamber was created into which the jet is injected. This inner chamber had a nominal height of 6.6 cm, a width of 7.6 cm and a depth of 1.3 cm. At the bottom of the inner chamber an aluminum piece served as support and on the top there was a plate that acted as the ‘ceiling’. Both the top and bottom pieces had orifices at their centers. The top plate’s orifice allowed the coaxial jet tip to enter the inner chamber and the bottom orifice was used to provide an exit for the flow. It was also used to introduce a thermocouple and pressure transducer to study the properties of the flow near the jet.

Two images of the first or “original” coaxial injector used in these studies are shown in Figs. 2.a and b. Fig. 2.a presents the full injector and Fig. 2.b shows a plane view of the end where the jets exited. The inner diameter of the inner jet, D_1 , or $2R_1$ as shown in the picture, was 0.51 mm. The outer jet had an inner diameter, D_2 , of 1.59 mm and outer diameter, D_3 , of 2.42 mm. The outer diameter of the injector, D_4 , was 3.18 mm. The length to inner diameter ratio was 100 for the inner jet and 67 for the outer jet (taking as reference one half of the hydraulic diameter, $R_3 - R_2$). The coaxial injector was installed so that the inner and outer jets were nominally concentric and the inner jet exit plane was recessed by 0.3 mm from the outer jet exit plane. This recess length was chosen to represent one half of D_1 in order to mimic realistic coaxial jet configurations used in industry.

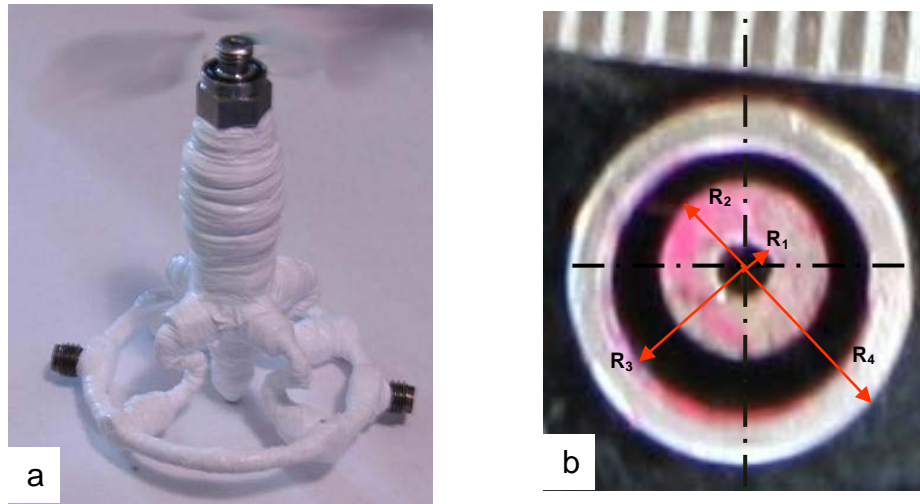


Figure 2.a. First (“original”) coaxial injector used in this study. b. Exit plane view of the original coaxial injector.

The second or “new” coaxial injector used in these studies is shown in Figs. 3.a and b. The inner diameter of the inner jet, D_{new1} , or $2R_{new1}$, was 1.40 mm. The outer jet had an inner diameter, D_{new2} , of 1.65 mm and outer diameter, D_{new3} , of 2.44 mm. The outer diameter of the injector, D_{new4} , was 3.94 mm. The length to inside diameter ratio was 65 for the inner jet and 105 for the outer jet (taking as reference one half of the hydraulic diameter, $R_{new3} - R_{new2}$). The injector was installed so that the inner and outer jets were nominally concentric and the inner jet exit plane was recessed by 0.7 mm from the outer jet exit plane, which was chosen to represent one half of D_{new1} , to be able to compare it with the results obtained with the original injector. Note that the inner post thickness decreased dramatically from the original injector to the new injector. The post thickness of the original injector was 110% of its inner diameter ($1.1D_1$) whereas the post thickness of the new injector is only 9.1% of its inner diameter ($0.091D_{new1}$).

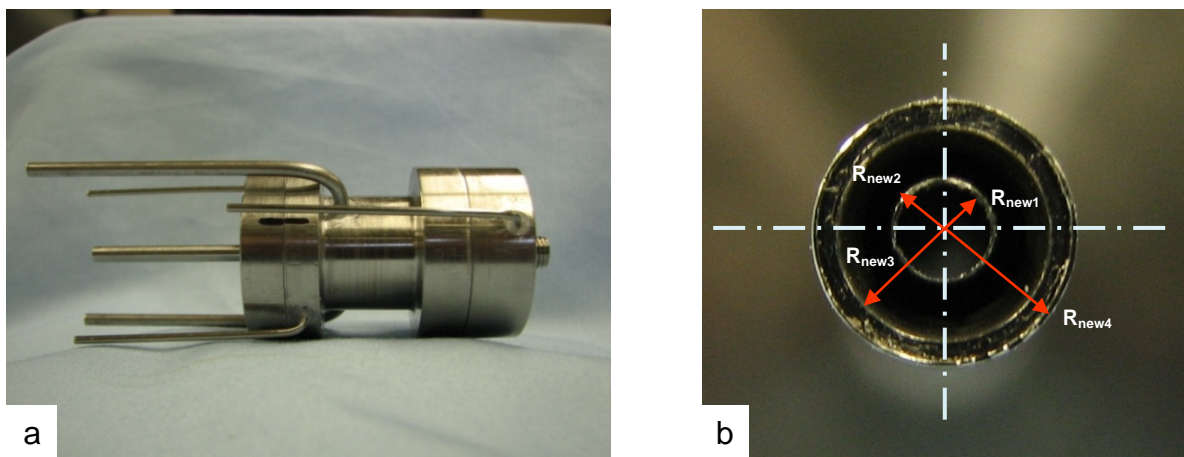


Figure 3.a. Second (“new”) coaxial injector used in this study. b. Exit plane view of the new coaxial injector.

The temperature of the fluid in the jets was measured with unshielded type E thermocouples with a bead diameter of 0.1 mm. The accuracy of the thermocouples used in the study was checked with an RTD and found to be within ± 1 K. A miniature pressure transducer was placed next to the thermocouple, using a small metallic post as support, and used to measure the pressure at a sampling frequency of 20 kHz. The manufacturer of the miniature pressure transducers was Kulite Semiconductor Products, Inc. (models CCQ-062-1000A and CCQ-093-750A). These pressure transducers had an absolute pressure range of either 6.9 MPa or 5.2 MPa, respectively. The thermocouple and pressure transducer probe used are shown in Fig. 4. In this photograph, the upper boundary or ‘ceiling’ of the inner chamber and the tip of the injector discussed above can be clearly seen.



Figure 4. Thermocouple and pressure transducer probes near the exit of the coaxial injector.

Two linear positioning stages built by Attocube Systems AG were used to move the pressure transducer and the thermocouple in a plane perpendicular to the jet axis. Each stage had a range of 3 mm in 1 dimension with step sizes in the order of 0.01 mm. One stage was placed on top of the other with their axis of movement perpendicular to each other for a total maximum examination area of 3 mm by 3 mm. With the configuration described above, the thermocouple tip could easily reach the exit plane of both the outer jet and inner jet. It was further possible to measure the temperature within the recess of the inner jet. The thermocouple and pressure transducer were attached to a custom made probe stand which in turn was affixed to the top of the linear positioning assembly using a small custom made base placed at the top end of a shaft that rested on a large, linear mechanical

stage. The 10-cm range stage built by SETCO allowed the probe to get to the desired interrogation region within the inner chamber.

Properties such as density and viscosity were computed from the measured flow rates, chamber pressure and jet temperature, using the National Institute of Standards and Technology's REFPROP Software and its thermophysical properties online database^{7,8}. From these properties, Reynolds number, Re , outer to inner jet velocity ratio, VR , and outer to inner jet momentum flux ratio, J , for a given set of conditions were then calculated. The jet was visualized by taking backlit images using a Phantom v7.1 high-speed camera capable of recording up to 160,000 frames per second at a resolution of 32 pixels by 32 pixels. For a resolution of 128 pixels by 256 pixels the camera was capable of recording 41,300 pictures per second. The resolution of the images in the present experiments varied from 128 pixels x 224 pixels to 196 pixels x 400 pixels, depending on chamber pressure and outer to inner momentum flux ratio. These in turn determined the size of the visible features of the jet that this study was characterizing. Each pixel represents an approximate area of 0.08 mm x 0.08 mm. Depending on the resolution chosen, the framing rate (frequency at which pictures were recorded) was 20, 25 or 41 kHz.

To focus the camera on the coaxial jet flow an AF Nikkor 35-105 mm lens, a Nikon No. 1 Close-Up lens, and various optical extensions were used. Since focusing on the outer jet structures while at the same time having a clear view of the inner jet was always a difficult process when setting up the camera and related optical equipment, the quality of the coaxial jet images was not always the same. The jet was backlit using a Newport variable power arc lamp set at 160W or 300W. The exposure time was generally 1-2 μ s and the number of images saved per run was 1000 on average. The dark core length and the inner jet spreading angles were measured from 998 images using a MATLAB subroutine based on the Otsu technique⁹, which analyzes an image and finds a threshold which helps differentiate the dark core of the inner jet from the rest of the image.

The acoustic waves were generated using two piezo-sirens placed at each end of the chamber, custom-designed for the Air Force Research Laboratory by Hersh Acoustical Engineering, Inc. A Fluke 100 MS/s arbitrary waveform generator (model 292) was used to produce two sinusoidal waves with the same frequency but with a prescribed phase between them. The signals were then sent to two amplifiers, one for each piezo-siren. The amplifiers were a Krohn-Hite model 7500 and a Trek model PZD2000A, which amplified the signals and fed them to the piezo-sirens. The amplified signals were in the 200 to 540 V range. The principle by which the piezo-sirens work as acoustic drivers is relatively simple, with a piezo element moving an aluminum cone attached to it, which in turn vibrates to produce acoustic waves. The distance from each cone to the location of the coaxial jet is 44 cm. The frequency at which the piezo-sirens were driven was chosen by manually varying the frequency on the signal generator until the highest amplitudes of the pressure perturbations were obtained. These pressure perturbations were measured using the three differential Kulite pressure transducers (model XCQ-093-25D) flushed with the acrylic window of the inner chamber and recorded for further processing using Pacific Instruments PI660 Acquisition and Control Software.

The phase difference, also referred to in this work as phase angle, between the signals sent to the piezo-siren elements was varied to expose the coaxial jet to different effective positions relative to the pressure node or antinode of the generated acoustic field. When the two piezo-siren elements produce waves with a zero degree phase angle between them, the movement of the piezo-siren cones is synchronized and in opposite directions, that is, towards and away from each other. This produces conditions of high pressure perturbations and low velocity fluctuations at the center of the chamber, where the coaxial jet is located. This condition is called a pressure antinode or velocity node. In contrast, when the two drivers present a 180-degree phase difference, then the cones move in the same direction, generating high velocity fluctuations with very small variations in pressure at the jet location. This condition is called a pressure node or velocity antinode. A schematic of this behavior is reproduced in Fig 5.

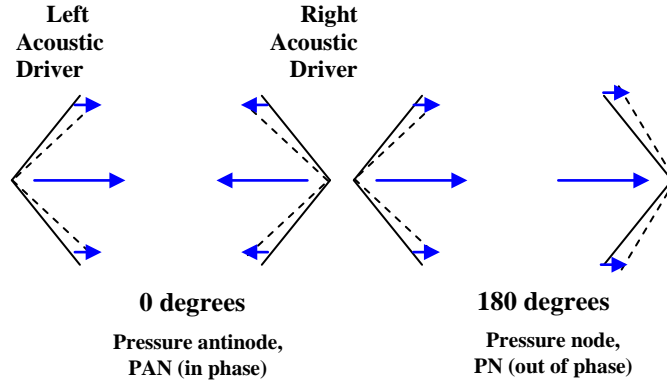


Figure 5. Simplified diagram of the two acoustic drivers at a 0° and 180° phase angle, indicating relative flow perturbation directions.

In these experiments, the voltage supplied to the two acoustic drivers was maintained at the same level for all conditions during each case. The amplitudes of both piezo-siren elements were nominally the same. The piezo-sirens can be seen at both sides of the chamber in the photograph shown in Fig. 1.a. Since the experimental setup uses a rectangular test section, the jet was excited with a transverse acoustic field. A transverse mode on a rectangular chamber would be the equivalent of a tangential mode on a cylindrical chamber, which are the most dangerous for the integrity of such systems and an important reason to analyze its effects on a coaxial jet. To accommodate for the rectangular chamber, a waveguide with a catenary contour was used to transmit the waves from a circular cross-section to a rectangular cross-section. The maximum root-mean-square acoustic pressure fluctuations generated by the two piezo-ceramic acoustic sources in the inner chamber varied from 8.0 to 22 kPa and were produced in the 2.9 to 3.1 kHz range.

III. Results

To assess the effects of geometry on the behavior of the jet and mixing, the results of the original injector were compared to those with the new injector. The next sets of images show the response of the coaxial jet with the original and new injector at similar pressures and J values with the same levels of acoustic excitation. In the cases described in this study, the location of the pressure node (PN) and antinode (PAN) were not always at 180° and 0° respectively. It varied between 135° to 225° for the pressure node and 315° to 45° for the pressure antinode. This is probably due to cross-talk between the acoustic sources. To obtain similar outer to inner momentum flux ratios with the new injector to those obtained with the original injector, the mass flow rate of the inner jet had to be increased by a factor of three, which meant that the ratio of the mass flow rates between the two jets for a given J value was not the same. This change in mass flow rate was necessary given the difference in the inner jet inner diameter between D_1 and D_{new1} (see Figs. 2 and 3) between the original and new injectors. The first set of images is shown in Fig. 6.a. It corresponds to the case where $J = 0.17$ with the original injector. At this low momentum flux ratio at subcritical pressures ($Pr = 0.45$) the jet is usually thin. The overall behavior of the jet does not change substantially with and without acoustic forcing but an increase in mixing can be observed. For the 0° and 315° conditions (PAN) the inner jet starts spreading and breaking up into smaller dark core sections that mix with the outer jet towards the middle of the image. In contrast, the 135° (PN) and the baseline conditions show very little spread and the core only starts to break up towards the bottom of the image.

The images shown in Fig. 6.b correspond to a momentum flux ratio of approximately 0.089 with the new injector. The first image on the top left shows the coaxial jet when no acoustics are present. The inner jet can be clearly distinguished from the outer jet and its surroundings. The thickness of the inner jet stays constant throughout the image and it is longer than the available field of view with a non-dimensional dark core length of at least 14 L/D_{new1} and most likely significantly longer based on the results from the original injector at similar momentum flux ratios. For the phase angles from 0° to 90° the inner jet bends noticeably too and there is strong atomization taking place near the injector exit. The background flow of the chamber is difficult to notice and the dark core region is somewhat thicker and blurred. The next two images show a **perturbed**, but straight, inner jet. The images

corresponding to a phase difference between 225° and 315° show the liquid stream from the inner jet shortened significantly, with large structures of liquid that have been separated from the inner jet flowing downstream. The last image seems to return to the behavior seen at a 0° phase angle.

It is interesting to notice that the images that show the greatest contrast in the inner jet behavior with acoustics correspond to phase differences of 135° and 315° , which would correspond to the pressure node and pressure antinode locations respectively. In all phase angle conditions, the effect of the acoustic field on the integrity of the inner jet is something that was not observed with the original injector before, especially at these low momentum flux ratios. A possible cause of this phenomenon is the change in geometry from the original injector to the new injector which resulted in two main differences. First, the original injector featured a very thick inner jet post which created a large recirculation zone between the inner jet and the outer jet at the exit of the injector. This recirculation zone could have modified the effect of the pressure and velocity fluctuations, because instead of interacting with the inner jet directly, they modified the dynamics of the recirculation zone¹⁰ which in turn altered the dynamics of the coaxial jet at the exit. That would explain the smooth back-and-forth oscillations of the inner jet that were characteristic of “strong evidence of acoustic excitation” with the original injector. However, without such a large recirculation zone, the pressure and velocity fluctuations could be having a direct impact on the inner jet flow and that might explain the very strong atomization taking place right at the exit of the injector for every acoustic condition regardless of phase angle. Secondly, the outer to inner mass flow ratio was very different between the two injectors, being much lower for the new injector. Thus the potential effect of the outer jet in the response of the inner jet was expected to be different as well. .

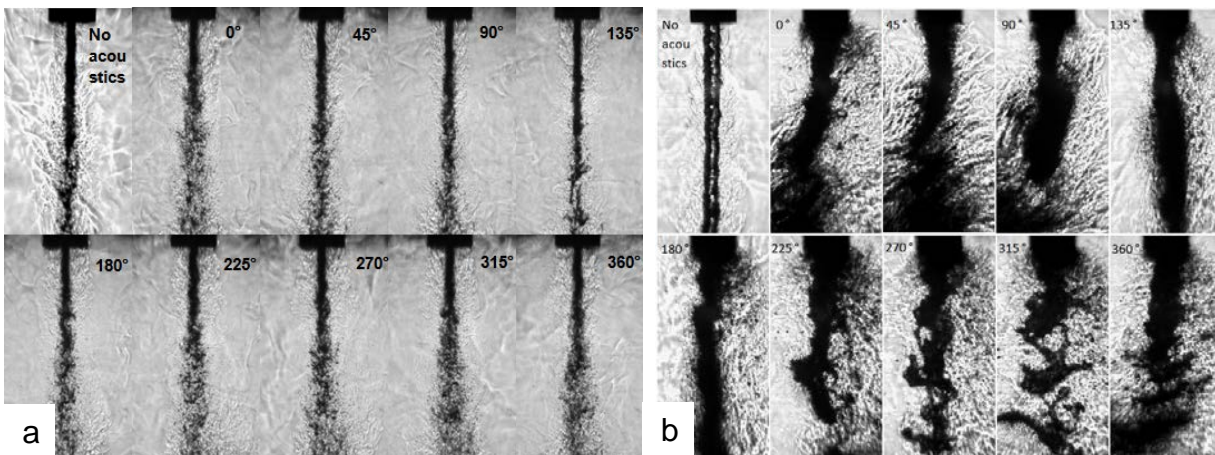


Figure 6.a. Collection of subcritical coaxial jet images at $P_{\text{chamber}} = 1.50$ MPa, $J = 0.17$ with original injector geometry. b. Images with $P_{\text{chamber}} = 1.48$ MPa, $J = 0.089$ with new injector geometry.

The second set of subcritical images corresponds to a momentum flux ratio between 2 and 3. The effects of the acoustics in this set of images with the original injector, shown in Fig. 7.a, are very clear. The inner jet dark core bends significantly for every phase angle reaching an apparent maximum dark core length reduction and increased bending at 180° (PN). Mixing changes significantly and large regions where the dark core structures have almost completely blended with their surroundings are seen. This effect is particularly enhanced for phase angles between 45° and 215° . For the rest of the conditions a few dark fluid structures can still be observed throughout the image, but for the phase angle range mentioned the images show very few dark structures beyond certain point near the center. This sequence of images shows that the effects of high velocity fluctuations (PN) due to acoustic forcing are very strong and can make a difference in practical systems operating near this momentum flux ratio with the original geometry. The set of images in Fig. 7.b show the coaxial jet behavior at a subcritical pressure of 1.49 MPa and momentum flux ratio of 2.0 for the new injector. The baseline condition shows a wide dark core region that does not extend the whole length of the image, in contrast with the $J = 0.089$ case. In the first few inner jet diameters after the exit of the injector the dark core region is thick and connected, then it starts being sheared apart by the outer jet and becomes thinner with ligaments extending from the core outward. At the bottom of the image only a very thin dark core region, which is most likely unconnected from the main core, remains. The acoustics have the largest impact at the 0° and 360° conditions (PAN). The images at 135° , 180° and 225° do not show the extreme atomization near the

injector exit observed at the PAN, but instead they show similar dynamics to the baseline condition and even a longer dark core region. The image at 90° shows a transition between the most noticeable acoustic effects near the pressure antinode and the baseline conditions. The original and new injector show that the effect of acoustics at this J value is significant but its particular manifestation can vary significantly with coaxial jet geometry, as it can be concluded by the acoustic condition at which they manifest their largest deviation from the baseline (i.e. PN for the original injector geometry and PAN for the new injector geometry).

Another example of this claim is the presence of large periodic vortical structures in the new injector case in contrast with the bending of the inner jet flow in the case of the original injector. Unlike the original injector where the large effects of acoustics were manifested by the complete motion of the outer and inner jets, the acoustic field near the pressure antinode for the case with the new injector produced substantial atomization at the injector exit. The large vortical structures involving the inner jet flow were ejected in an inverted mushroom-like fashion at the excitation frequency (~3 kHz). Up to the current experiments with the new injector (featuring a very thin inner jet post), this phenomenon had not been observed by our group, with only very small shedding from the inner jet having been seen. Also, the new injector case shows the interesting effect of having a very similar structure to that of the baseline condition at the PN location (135°, 180° and 225°) whereas no such similarity is found on the original injector.

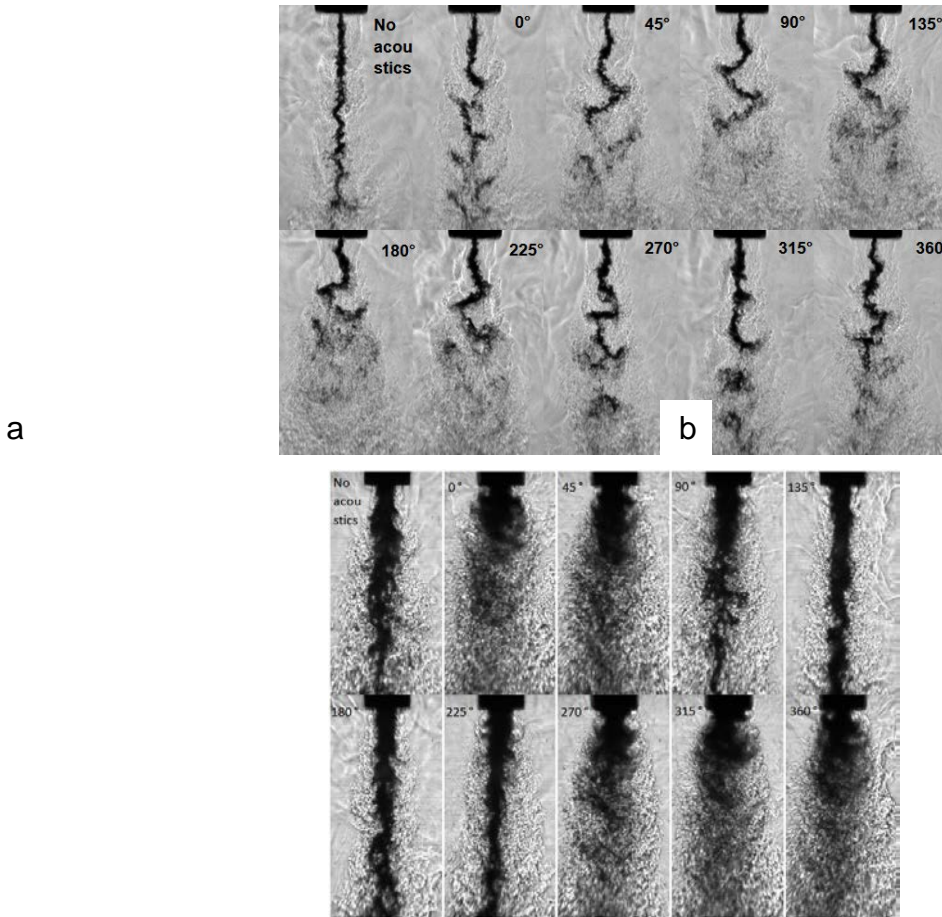


Figure 7.a. Collection of subcritical coaxial jet images at $P_{\text{chamber}} = 1.45 \text{ MPa}$, $J = 2.6$ with original injector geometry. **b.** Images at $P_{\text{chamber}} = 1.49 \text{ MPa}$, $J = 2.0$ with new injector geometry.

The next set of images for the subcritical case with the original injector is shown in Fig. 8.a and corresponds to a momentum flux ratio of 9.6. All the images feature a very thick dark core which differs substantially from the thin dark core regions observed in the previous two sets of images with the original injector. This thickness is evidence that the high momentum flux of the outer jet is having a strong effect on the inner jet,

mixing more in the recirculation zone and allowing it to expand very rapidly at the exit of the injector. The recess length of the inner jet hides this phenomenon and we only observe a thick jet emanating from the exit. Even at this high momentum flux ratio the dark core region is affected by the acoustic forcing as seen by the curvature of the inner jet for all phase angles; an effect that might not be obvious if only the effects of the dark core length are considered. For the original injector, the acoustics again have a “bending” effect on the dark core. In contrast, the images in Fig. 8.b, which feature a momentum flux ratio of 7.8 with the new injector, are affected by the acoustic field in a different manner. First, note that the normalized dark core lengths for the baseline cases are within 4% of each other (see Appendix), even though the absolute length of the dark core is larger for the new geometry. The acoustics seem to induce a periodic “pulsation” of the inner jet, which consists of vortices being shed from the exit plane (seen in Figure 8.b), but the centerline of the jet remains approximately straight, that is, no bending. The behavior with acoustics at each condition is similar to the $J = 2.0$ case in Fig. 7.b, although the structures are clearer and less atomization takes place at the exit for this case. Again, with the new injector at the 0° and 360° phase angles (PAN) the vortical structures are periodic, extend outward and wrap around. Near the 180° phase angle (PN) the image is similar to the case with no acoustics. Last, it is worthwhile to point out that the percentage reduction of the dark core with acoustics for any angle for both geometries was very similar but the manner in which the dark core was reduced was very different as explained above.

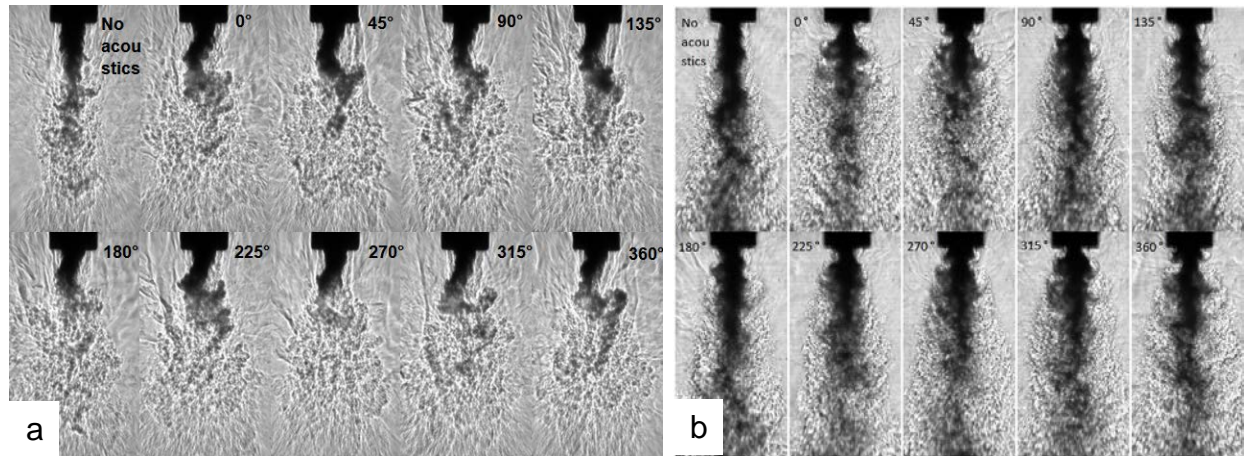


Figure 8.a. Collection of subcritical coaxial jet images at $P_{\text{chamber}} = 1.50$ MPa, $J = 9.6$ with original injector geometry. **b.** Images at $P_{\text{chamber}} = 1.49$ MPa, $J = 7.8$ with the new injector geometry.

The last set of images for a subcritical case with the original injector corresponds to a momentum flux ratio of 23. Fig. 9.a shows a dark core that does not seem to vary at all among the images and the only difference is a slight change in curvature towards the bottom of the dark core for different acoustic conditions. However, the mixed flow downstream behaves in a similar manner to the dark core for lower J values: the mixed flow is bent. This is more noticeable near the 180° condition (PN). The new injector case is shown in Fig. 9.b. In this case the effect of the acoustics are still visible with a very short dark core at a 0° and 360° phase angle (PAN) and longer dark cores near the 180° phase angle (PN). For the new injector, acoustic effects are noticed in the dynamics of the dark core at subcritical pressures for momentum flux ratios near 20, since the dark core is still long enough to interact with the acoustic field. In contrast, for the original injector, the slight effects of acoustics on the coaxial jet could not be adequately quantified by measuring the short dark core region from the images at these high J values.

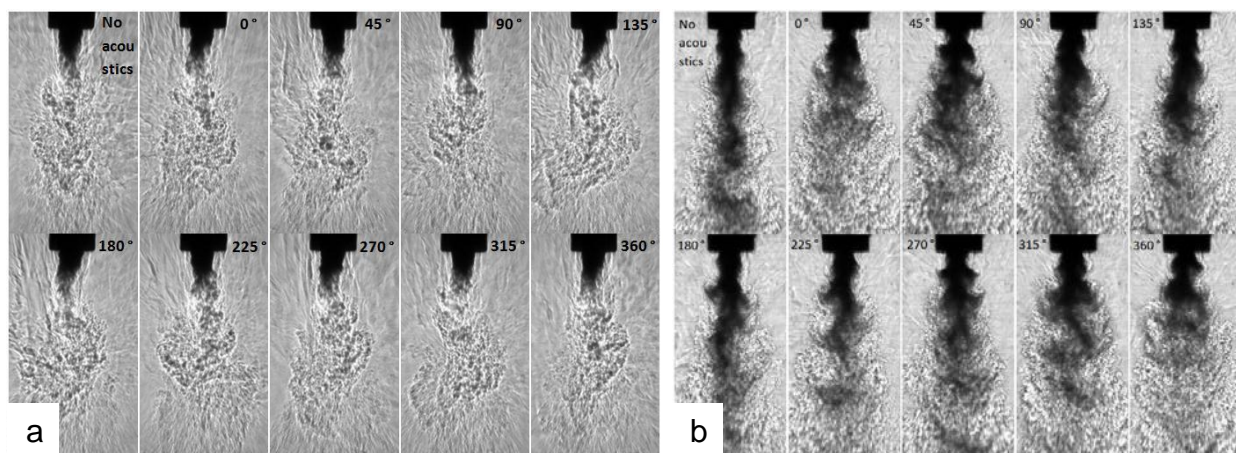


Figure 9.a. Collection of subcritical coaxial jet images at $P_{\text{chamber}} = 1.50$ MPa, $J = 23$ with original injector geometry. **b.** Images at $P_{\text{chamber}} = 1.48$ MPa, $J = 18$ with the new injector geometry.

The next figure shows a nearcritical case where the momentum flux ratio is near 10. The case with the original injector is shown in Fig. 10.a. In this set of images, the dark core is extremely short, and the effects of the acoustics, are only noticeable by the slight back and forth movement of the lower part of the inner jet dark core. No dependence on the phase angle is observed. On the other hand, Fig. 10.b shows a dark core reduced by imposing an acoustic field. The longest dark core is seen at the conditions with no acoustics followed by the condition at 180° (PN). As the phase difference approaches 0° or 360° the effects of acoustics are more evident, with a shortening of the dark core and periodic smaller vortical structures emanating from the exit of the injector. These vortices are shed at the driving frequency.

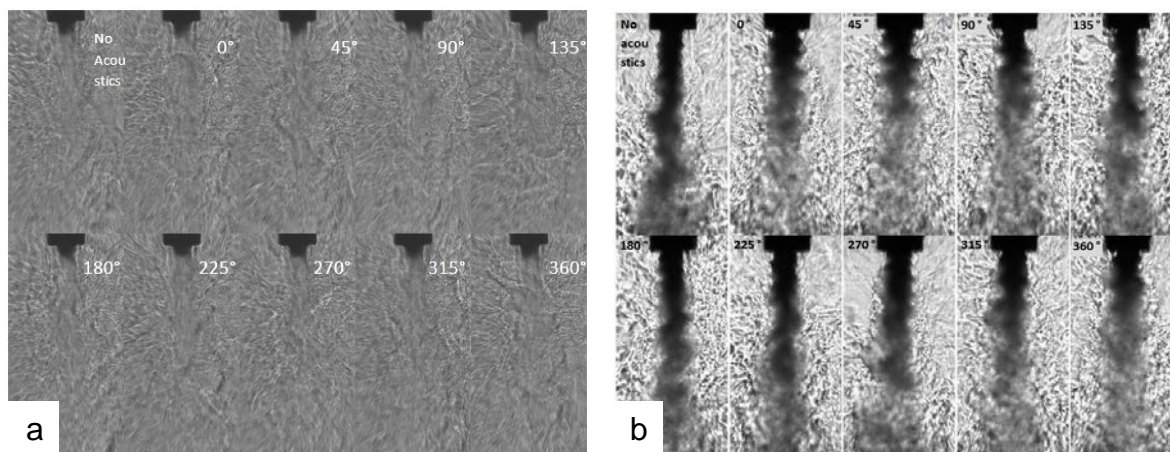


Figure 10.a. Collection of nearcritical coaxial jet images at $P_{\text{chamber}} = 3.56$ MPa, $J = 9.3$ with original injector geometry. **b.** Images at $P_{\text{chamber}} = 3.58$ MPa, $J = 9.4$ with the new injector geometry.

A comparison of two supercritical cases is presented in Fig. 11. The momentum flux ratio is approximately 2.5. The first set of images in Fig. 11.a represent the case with the original injector. The dark core lengths with acoustics are all shorter than the baseline condition. Another effect of the acoustics is a slight bending of the inner jet dark core. In these images, the transition between a very dark inner jet and a completely mixed coaxial jet can be observed. In contrast, the supercritical case with the new injector in Fig. 11.b features a very long dark core, which was not captured in its entirety by the camera. Acoustics did not seem to have any effect on the visible portion of the jet and all conditions show very similar images. This makes us believe that the effect of the acoustics on the dark

core for the region very close to the exit ($< 10 D_{new1}$) was not significant, unless the acoustic amplitude was not high enough to excite the coaxial jet as seen in other cases.

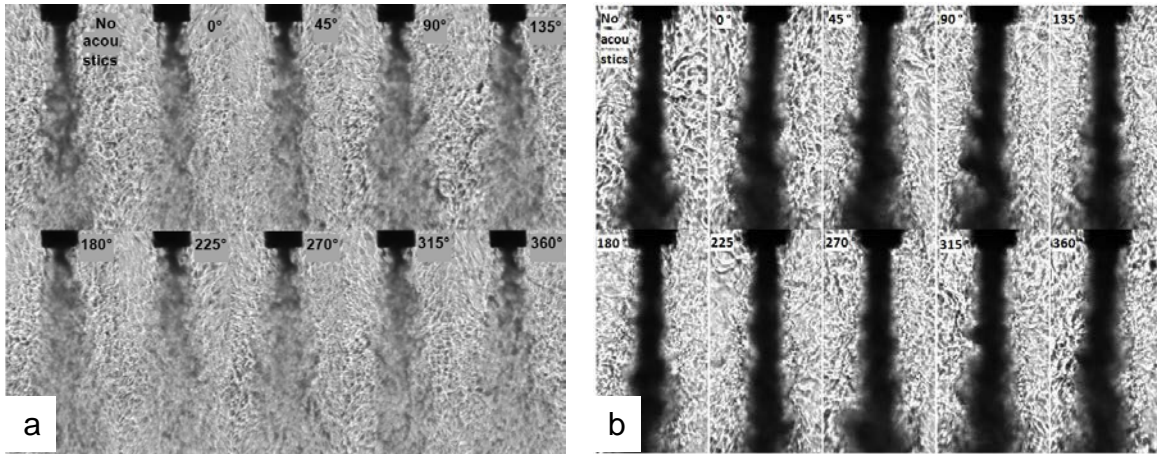


Figure 11.a. Collection of supercritical coaxial jet images at $P_{chamber} = 4.96$ MPa, $J = 2.4$ with original injector geometry. **b.** Images at $P_{chamber} = 4.95$ MPa, $J = 2.6$ with the new injector geometry.

The results of the dark core length measurements of the inner jet of the coaxial jet with the original and new injector geometries are presented next. The following figures show a series of plots with the dark core length measurements on the vertical axis and the different acoustic conditions on the horizontal axis. A secondary axis shows the peak amplitude of the pressure oscillations as a fraction of the recorded mean chamber pressure for that case. The first value on the horizontal axis is the baseline measurement without acoustics followed by the measurements of the dark core length with acoustics starting with a 0° phase angle between acoustic sources and then in steps of 45° until a full cycle is achieved at 360° . All the values are normalized by the baseline condition of the case, which is the length of the dark core without acoustics. The error bars show the composite uncertainty of the non-dimensional length variable, $L_{acoustics}/L_{no\ acoustics}$, using one standard deviation as the uncertainty of each measured variable. The subcritical tests with the original injector in Fig. 12 showed that, for $J = 0.17$, the largest dark core coincided with the condition of lowest pressure perturbations. The dark core length results for $J = 1.0$ do not show any trend, in contrast with the corresponding acoustic measurements which show a wave-like pattern. For $J = 2.6$, the lowest pressure oscillations produced the largest variation in length. For $J = 4.2$, the largest length values occur near but not at the conditions where acoustic forcing is the lowest. For $J = 9.6$ and 23 , the outer jet has even more momentum flux compared to the inner jet, making the dark core very short and less responsive to the acoustics ($\sim 15\%$ reduction) regardless of the phase angle. For these cases, a clear trend linking the longest dark cores and a particular condition in the acoustic field could not be identified.

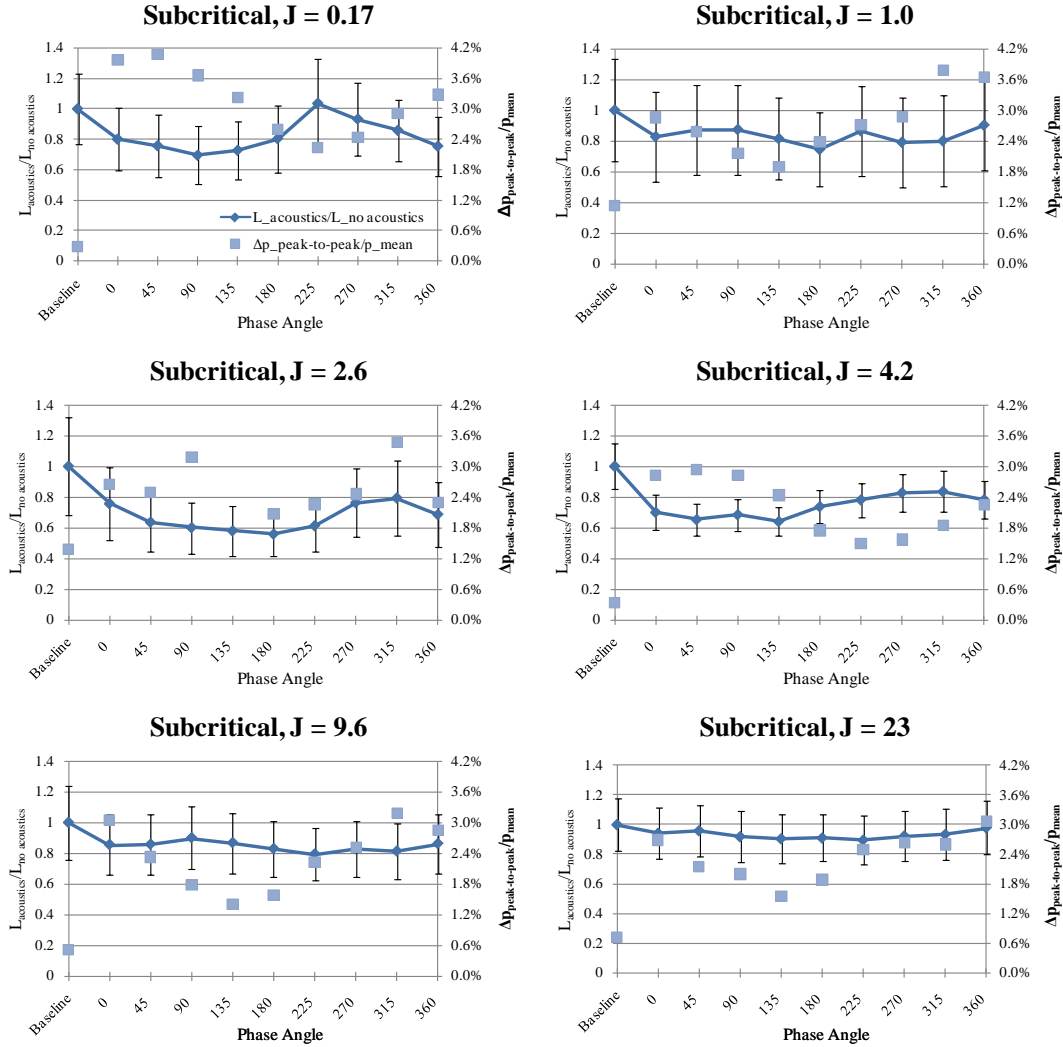


Figure 12. Dark core length with acoustics ($L_{\text{acoustics}}$) over dark core length without acoustics ($L_{\text{no acoustics}}$), shown in diamonds, versus phase angle between acoustic sources for subcritical pressures. The the peak-to-peak pressure perturbation as a percentage of the mean chamber pressure ($\Delta p_{\text{peak-to-peak}}/p_{\text{mean}}$), in squares, is also plotted. Original injector geometry.

The values of the dark core lengths with the new injector for the tests at subcritical pressures are shown in Fig. 13. As the J value of the case decreased, at some or all conditions as explained in the caption of the figure, the dark core length was longer than the image obtained from the camera. Thus, accurate dark core measurements could not be obtained for those conditions. However, a semi-quantitative analysis can still be made for some of those cases. For instance, the cases with $J = 0.43$ and 2.0 had dark core lengths that were measurable for half of the phase angles. The conditions for which the dark core was too long were those near the pressure node as indicated by the pressure data shown in the plots. The conclusion can be made that for these cases the longest dark core lengths were close to the condition with the lowest pressure perturbations. For the next two plots in Fig. 13, for J equal to 3.4 and 5.2 , the same trend with phase angle can be observed. The last three plots in Fig. 13 show the reduction in the dark core length for $J = 7.8, 12$ and 18 . These plots show longer dark core lengths at the location of the pressure node.

The general trend observed in these measurements consists of longer dark cores near the pressure node and very short ones near the pressure antinode. One of the possible explanations for this effect might involve the lack of recirculation zone in the new injector. The recirculation zone could be responsible for the bending of the jet at high velocity fluctuations but in the case of the new injector this recirculation zone is practically non-existent; the bending does not take place, and a straight dark core is observed.

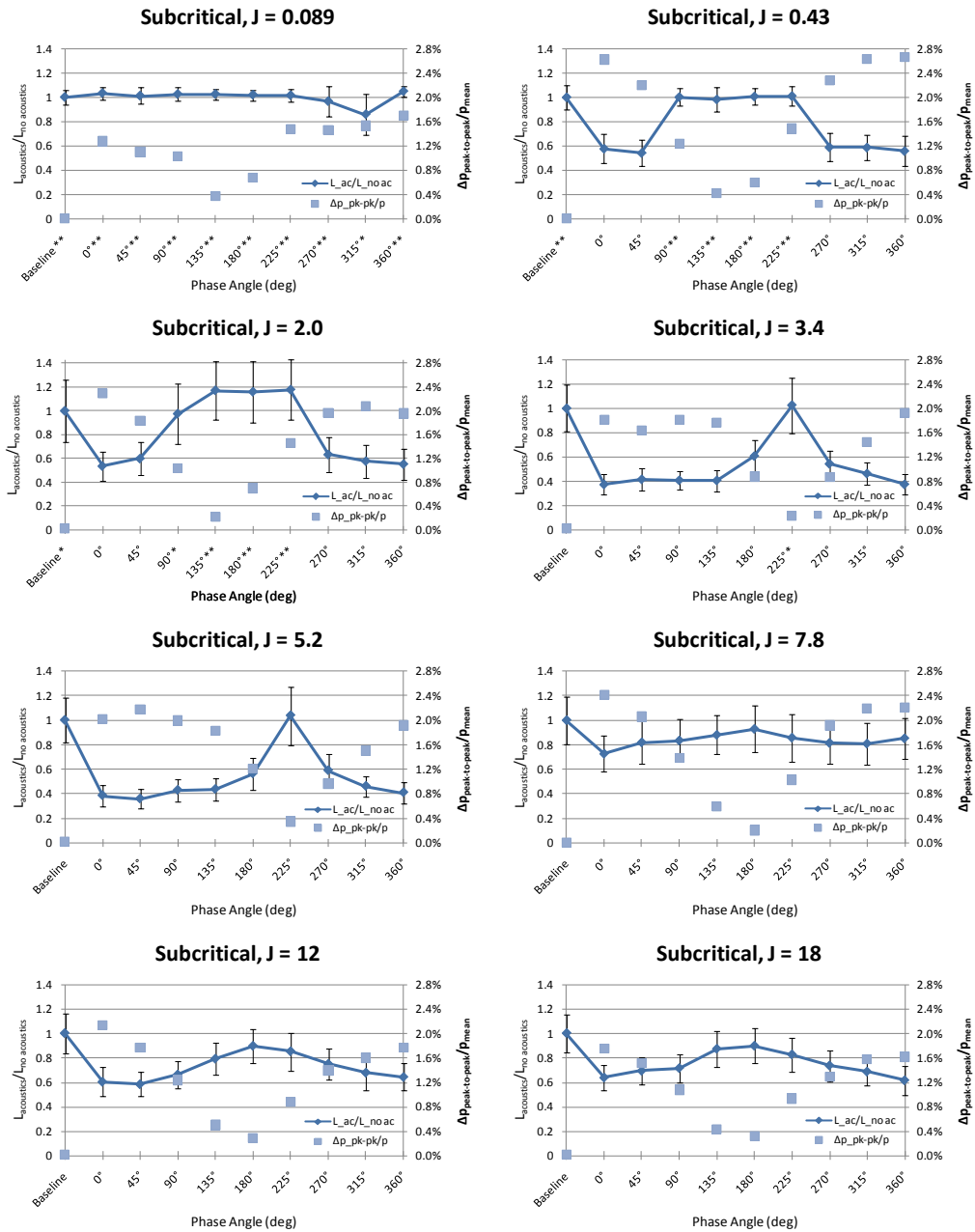


Figure 13. Dark core length with acoustics (L_{ac}) over dark core length without acoustics ($L_{no\ ac}$), shown in diamonds, versus phase angle between acoustic sources for subcritical pressures. The the peak-to-peak pressure perturbation as a percentage of the mean chamber pressure ($\Delta p_{peak-to-peak}/p_{mean}$), in squares, is also plotted. The cases which had their x coordinate marked with an asterisk (*) but less than 50% of the images. The ones marked with two asterisks (**) had dark cores larger than the examination window for at least half of the images. New injector geometry.

The next set of graphs shown in Figs. 14 and 15 show the results for the tests performed at nearcritical and supercritical pressures with the original injector. At these pressures, the coaxial jet flow had only one supercritical phase present since both the temperature and pressure of the inner and outer jet, as well as the surrounding environment, was above the critical temperature and pressure of N_2 .

For some nearcritical cases with the original injector (see Fig. 14), the dark core seems to be the shortest when the pressure perturbations are a minimum or conversely when the velocity fluctuations are largest. Also, within the limits imposed by the calculated uncertainty, a significant reduction of the dark core length with respect to its non-forced value is observed during acoustic excitation at moderate J values. This decrease in the length, and therefore enhancement of mixing, is achieved in the $1 < J < 5$ range. At higher outer to inner jet momentum flux values the outer jet starts to entrain a significant amount of fluid from the inner jet resulting in short dark core lengths which makes quantifying the effects of the acoustic field more difficult.

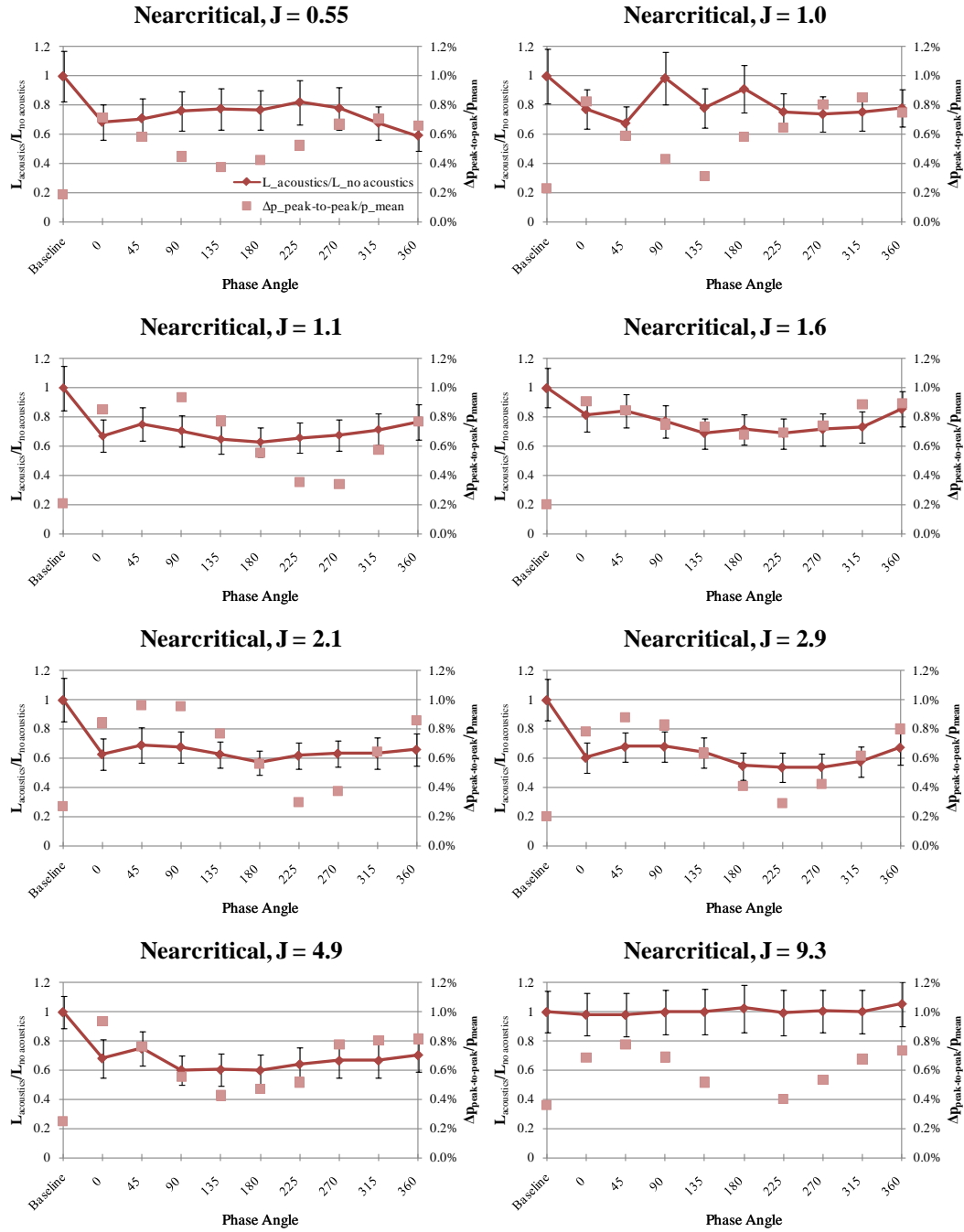


Figure 14. Dark core length with acoustics ($L_{\text{acoustics}}$) over dark core length without acoustics ($L_{\text{no acoustics}}$), shown in diamonds, versus phase angle between acoustic sources for nearcritical pressures. The the peak-to-

peak pressure perturbation as a percentage of the mean chamber pressure ($\Delta p_{\text{peak-to-peak}}/p_{\text{mean}}$), in squares, is also plotted. Original injector geometry.

The set of plots in Fig. 15 presents the values of the dark core lengths for the tests at supercritical pressures with the original injector. These results also represent single-phase coaxial jet flow since the chamber, the inner jet, and the outer jet are at supercritical temperature and pressure conditions. In these cases, the amplitude of acoustic forcing does not go over 0.75% of the mean chamber pressure. From the supercritical pressure tests, within the limits of the uncertainty, a reduction of the dark core length similar to that observed for the nearcritical cases was accomplished. Again, the largest effects on length decrease and mixing enhancement were achieved in the $1 < J < 3$ range. For higher values, the inner jet starts to lose its core in a very rapid fashion to the outer jet which makes very difficult to distinguish the effects of the acoustic field on the dark core. Overall, it was difficult to see a trend between the location of the pressure node and the maximum length of the dark core, as observed in previous subcritical and nearcritical cases with the original injector.

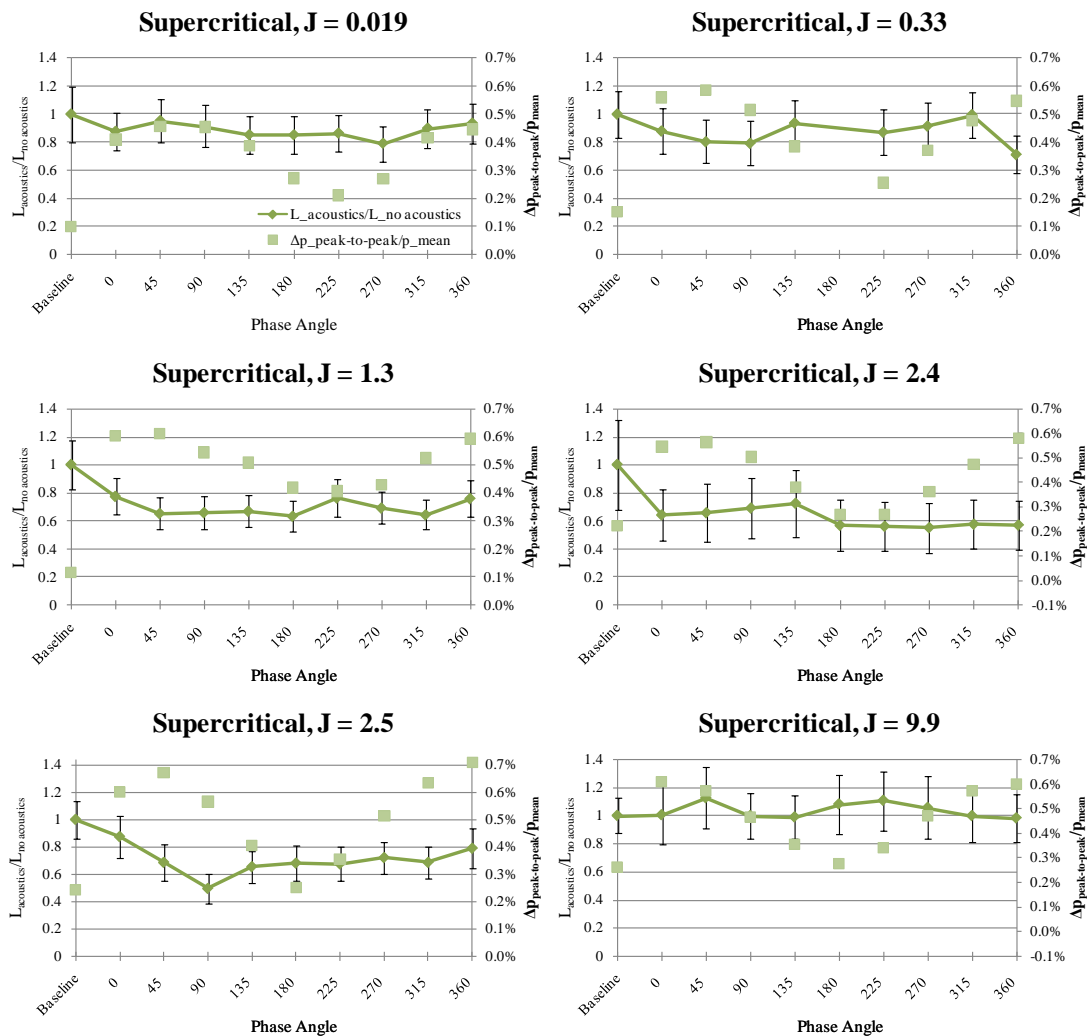


Figure 15. Dark core length with acoustics ($L_{\text{acoustics}}$) over dark core length without acoustics ($L_{\text{no acoustics}}$), shown in diamonds, versus phase angle between acoustic sources for supercritical pressures. The the peak-to-peak pressure perturbation as a percentage of the mean chamber pressure ($\Delta p_{\text{peak-to-peak}}/p_{\text{mean}}$), in squares, is also plotted. Original injector geometry.

The following set of plots in Fig. 16 show the behavior of the dark core length for the cases obtained when the pressure was above the critical point with the new injector. All conditions for the lower four momentum flux

ratio cases showed dark cores that were longer than the field of view and no effect on the dark core could be seen. Pressure profiles show that the coaxial jet was exposed to pressure perturbations ranging from 0.2% to 1% of the mean chamber pressure. There were some instances, as in the 315° condition for the nearcritical case with $J = 0.50$ and the 360° condition for the case with $J = 4.6$ where the acoustic excitation modified significantly the mechanics of the jet. Dark core lengths are not reported for such cases because the jet behavior departed significantly from the rest of the conditions. The behavior was observed near the pressure antinode condition at sufficiently high acoustic amplitudes. The nature of this phenomena is believed to be due to the lack of recirculation zone near the injector exit allowing high pressure fluctuations to interact with the inner jet leading to a violent disintegration of the dark core.

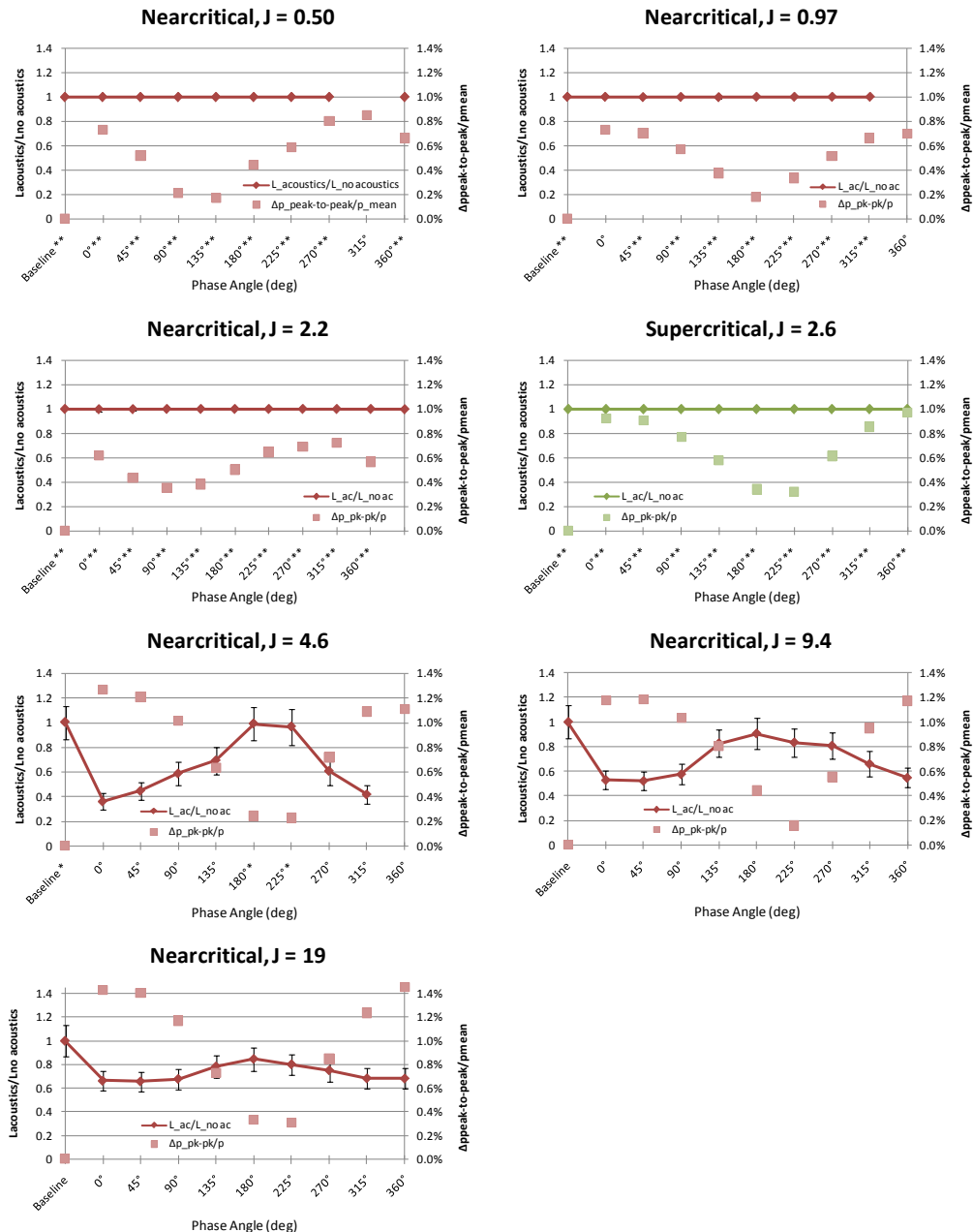


Figure 16. Dark core length with acoustics ($L_{\text{acoustics}}$) over dark core length without acoustics ($L_{\text{no acoustics}}$), shown in diamonds, versus phase angle between acoustic sources for pressures above the critical point. The

the peak-to-peak pressure perturbation as a percentage of the mean chamber pressure ($\Delta p_{\text{peak-to-peak}}/p_{\text{mean}}$), in squares, is also plotted. See caption of Fig. 13 for further details. New injector geometry.

The results of the last three nearcritical cases in Fig. 16, however, show very interesting trends that match those of the subcritical results of the new injector in Fig. 13. For instance, the nearcritical case with $J = 4.6$ shows that, as the pressure node condition is approached, the dark core increases its length, reaching a maximum near a 180° phase angle. This behavior was also observed for the subcritical cases with momentum flux ratios of 3.4 and 5.2 (see Fig. 13). For the nearcritical case at $J = 9.4$ the dark core length reached a maximum near the pressure node. Finally, the nearcritical case at $J = 19$ had its maximum dark core length with acoustics at a phase angle of 180° , very close to the pressure node indicated by the pressure measurements.

The dark core length changes at different pressures for a given outer to inner jet momentum flux ratio are presented next. The ratio of the length of the dark core with acoustics to the length of the dark core with no acoustics ($L_{\text{acoustics}}/L_{\text{no acoustics}}$) and the peak-to-peak pressure perturbation as a percentage of the mean chamber pressure ($\Delta p_{\text{peak-to-peak}}/p_{\text{mean}}$) both as a function of the phase angle between acoustic sources are shown in Figs. 17 and 18.

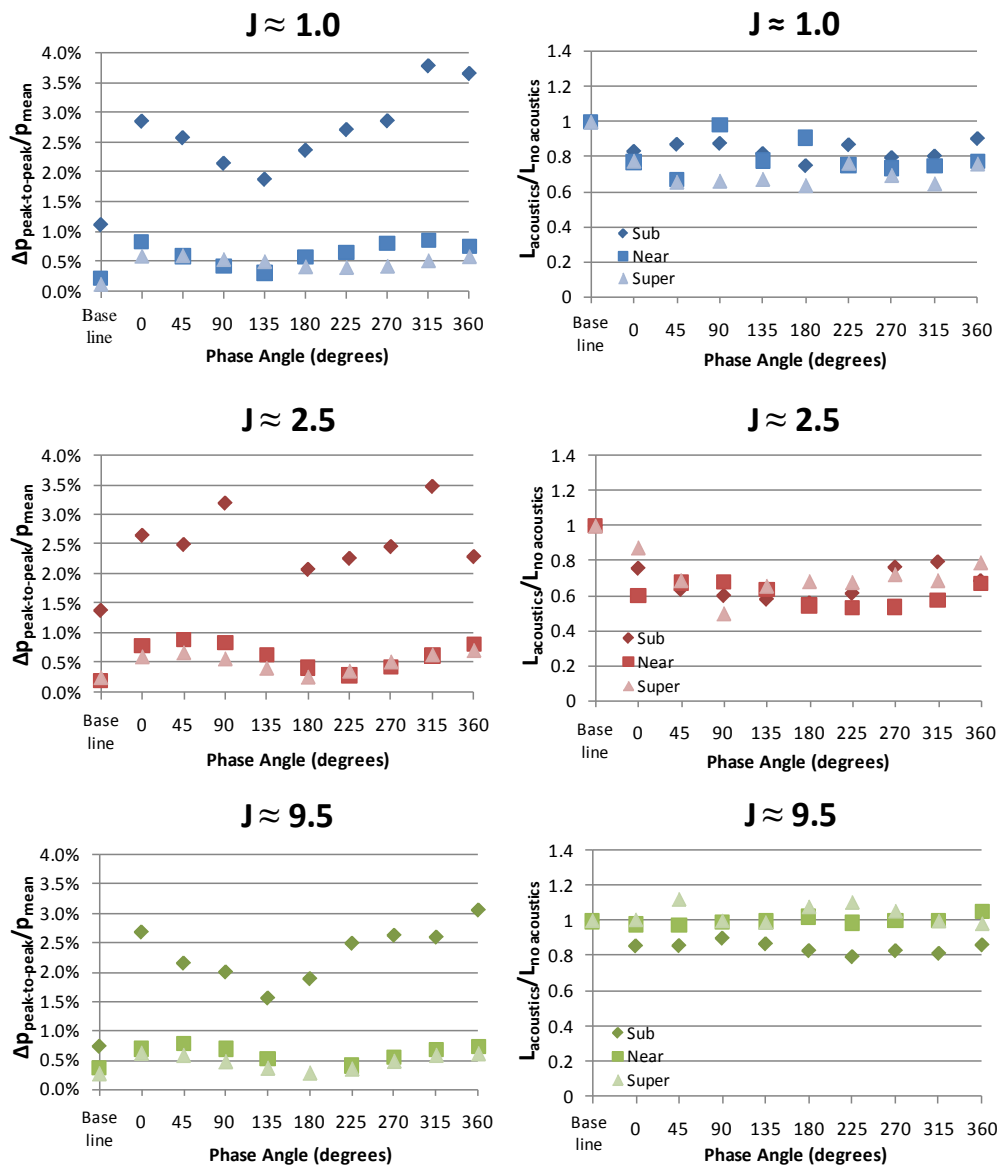


Figure 17. Peak-to-peak pressure perturbation ($\Delta p_{\text{peak-to-peak}}$) as a percentage of the mean chamber pressure

(p_{mean}) and dark core length with acoustics ($L_{\text{acoustics}}$) over dark core length without acoustics ($L_{\text{no acoustics}}$) versus phase angle between acoustic sources for sub, near and supercritical pressures at $J \approx 1.0, 2.5$ and 9.5 for the original injector geometry. From Rodriguez et al.¹¹

In Fig. 17 we observe the results for the original injector. Despite the relative acoustic excitation intensities varying several times from supercritical to subcritical conditions, the reduction in normalized dark core length ($1 - L_{\text{acoustics}}/L_{\text{no acoustics}}$) at most phase angles for $J \approx 1.0$ ranged from 20% to 40%. When the outer to inner jet momentum flux ratio approaches 2.5 a similar trend is observed. The normalized dark core length now has a broader range reaching values as low as 50% of the baseline length and as high as 90% of the baseline length. The large spread could be a consequence of the inherent uncertainty of the measurements but still shows that acoustic forcing produces a clear shortening effect on the dark core length for J values near 2 to 3 as well. For outer to inner jet momentum flux ratios near 10, the largest reduction in the dark core length ($1 - L_{\text{acoustics}}/L_{\text{no acoustics}}$) is at most 20%, at subcritical pressures. Both nearcritical and supercritical cases show little or no reduction in their dark core length, in fact some of the data indicates that the dark core lengths actually increased in some cases. However, this phenomenon is the consequence of very small dark core lengths at these high J values.

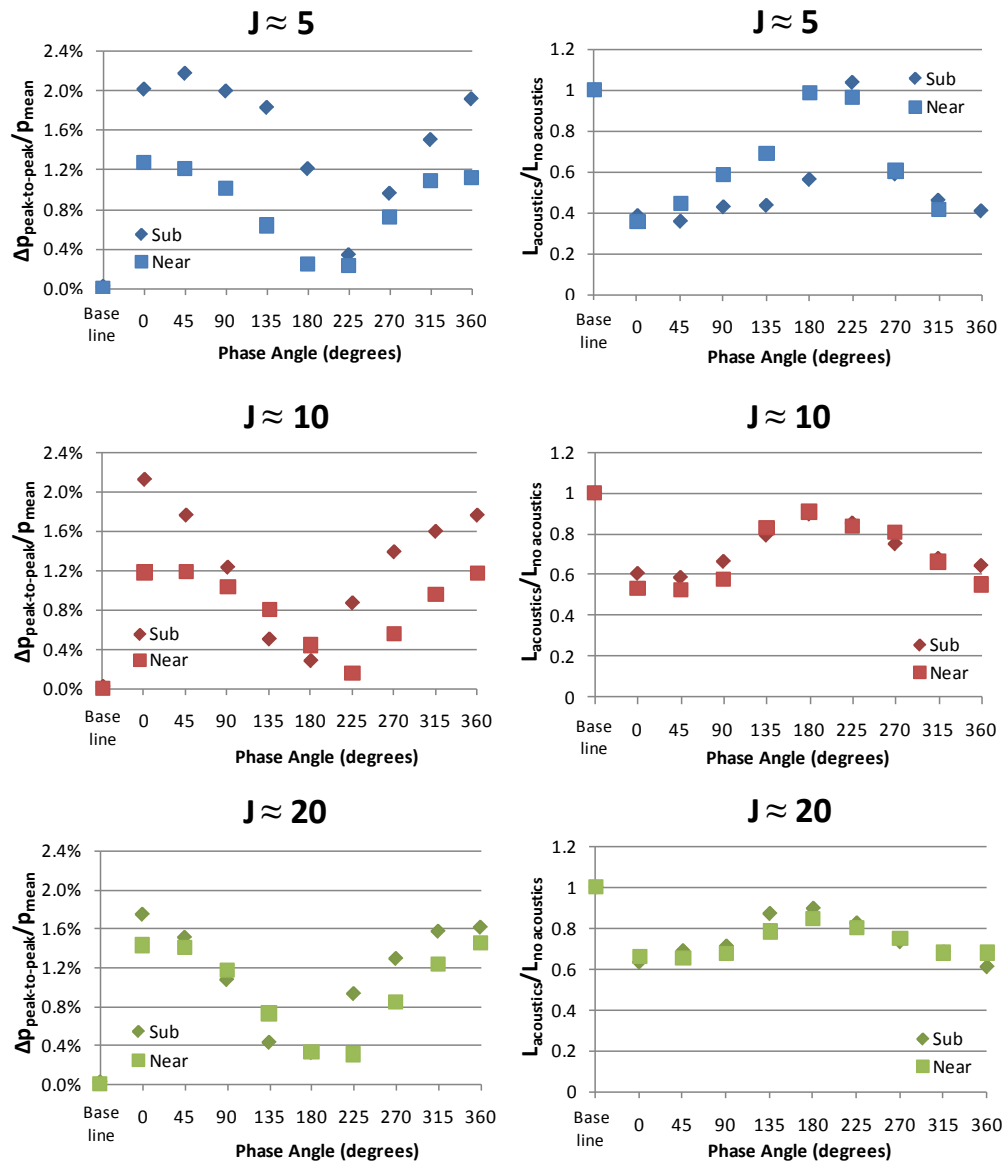


Figure 18. Peak-to-peak pressure perturbation ($\Delta p_{\text{peak-to-peak}}$) as a percentage of the mean chamber pressure (p_{mean}) and dark core length with acoustics ($L_{\text{acoustics}}$) over dark core length without acoustics ($L_{\text{no acoustics}}$) versus phase angle between acoustic sources for sub, near and supercritical pressures at $J \approx 5, 10$ and 20 for the new injector geometry. From Rodriguez¹².

Also at these conditions and especially true for near and supercritical conditions, the dark core does not show any response to acoustic forcing since most of the flow has been entrained by the outer jet and thus mixed with the rest of the fluid in the chamber, leaving a short dark core that usually does not show interesting acoustic behavior. Overall, these results with the original injector geometry show a very interesting trend which suggests that normalized dark core length behavior could be independent of mean chamber pressure; however, the large uncertainties in the measurements still prevent us from a definitive conclusion in this regard.

Similar results for the new injector are shown in Fig. 18 above. A remarkable feature of these plots is the agreement in the normalized dark core lengths between subcritical and nearcritical cases. As previously explained, data for lower J values are not available since the dark core length was longer than the acquired image. For a J value close to 5, the maximum pressure oscillations normalized by the mean chamber pressure are almost twice as much for the subcritical case compared to that of the nearcritical case. In contrast, for J near 20, the normalized acoustic forcing is almost the same. Nonetheless, for each momentum flux ratio, the maxima and minima in normalized dark core length between subcritical and nearcritical pressures are very similar, regardless of the normalized pressure oscillation values. Therefore, the results on the dark core length seen with the new injector in Fig. 18 agree with the results obtained with the original injector in Fig. 17 in so far as the normalized dark core length is the same despite large differences in acoustic forcing amplitude. Given the differences between the inner jet characteristics of the original and the new injector (inner post thickness, inner jet diameter, inner jet velocity and temperature), the agreement in dark core length results for the same J values indicates that this parameter could in fact reduce the data for a given geometry regardless of its characteristics. Further evidence of this observation could have important repercussions in shear coaxial injector design.

IV. Conclusions

In this study two coaxial injector geometries were tested at three different pressure regimes. The “new” injector geometry featured a larger cross-sectional area for the inner jet and thinner wall between the inner and outer jet flows than the “original” injector geometry, resulting in a significantly smaller recirculation zone at the location where the inner and outer jets meet near the exit of the injector. Qualitatively, there was an enhancement in mixing and atomization of the inner jet dark core with the surrounding outer jet and chamber with the new injector when comparing both geometries.

The data obtained with the new injector extended the range at which acoustics had a noticeable effect on the coaxial flow to momentum flux ratios as low as 0.1 in the subcritical pressure regime. Testing at nearcritical and supercritical pressures showed a measureable response for J equal to 5 or greater. The quantitative analysis of the data for the new injector showed that the longest dark cores with acoustic excitation were observed at or near the pressure node location both at subcritical and supercritical conditions. The new injector thus provided evidence that different geometries for coaxial injectors of similar size could have an impact on the dynamics of a coaxial jet.

The fact that the results for the new injector show that the normalized dark core lengths ($L_{\text{acoustics}}/L_{\text{no acoustics}}$) for the different phase angle conditions at sub, near and supercritical cases agree remarkably well for a given outer to inner jet momentum flux ratio is evidence of similarity between the dynamics of the original and new injector. Both injectors showed the same large effect on the dark core at moderate J values and as the momentum flux ratio is increased the maximum reduction decreases. The comparison between the two geometries showed that acoustics can promote mixing enhancement through different mechanisms.

The results in this study showed that the relative acoustic pressure did not seem to severely affect the behavior of the dark core length for different pressures at the same outer to inner momentum flux ratio. This finding supports the possibility that only a small perturbation, equal or smaller than the relative amplitudes used in this study, is needed to achieve the same large reductions of the dark core length, and thus mixing enhancement, obtained with the largest perturbations. If the previous proposition is true, even small pressure perturbations could have a large impact on the stability behavior of LRE injectors and other applications of coaxial flows.

Appendix

A. Case Details for the Original Injector Tests

	T _{chamber} (K)	ρ _{chamber} (kg/m ³)	P _{chamber} (MPa)	T _{outer} (K)	\dot{m} _{outer} (mg/s)	ρ _{outer} (kg/m ³)	u _{outer} (m/s)	Re _{outer} (10 ⁴)	T _{inner} (K)	\dot{m} _{inner} (mg/s)	ρ _{inner} (kg/m ³)	u _{inner} (m/s)	Re _{inner} (10 ⁴)	L/D ₁ (baseline)	Freq. (kHz)	P' _{RMS max} (kPa)	VR	J
SUB																		
sub1	233	22.0	1.50	191	310	27.6	4.30	0.768	109	279	630	2.2	1.2	26.2	2.98	21.5	2.0	0.17
sub2	231	22.2	1.50	183	790	28.8	11.0	2.02	109	283	630	2.2	1.2	17.1	3.06	20.1	4.8	1.0
sub3	226	21.9	1.45	183	1230	27.8	16.9	3.16	109	284	630	2.2	1.2	16.6	3.06	17.8	7.6	2.6
sub4	226	22.9	1.51	185	1560	28.7	20.9	3.96	109	279	630	2.2	1.2	15.2	2.96	15.7	9.5	4.2
sub5	210	24.9	1.50	182	2400	29.3	31.3	6.18	109	279	630	2.2	1.2	8.40	3.01	16.9	14	9.6
sub6	216	24.1	1.50	191	3640	27.7	50.3	9.02	109	279	630	2.2	1.2	5.63	3.02	16.3	23	23
NEAR																		
near1	223	56.6	3.58	180	1060	75.4	5.38	2.58	123	290	520	2.8	2.0	24.4	3.08	9.04	2.0	0.55
near2	207	62.0	3.57	152	1570	101	5.95	4.16	117	289	590	2.4	1.5	15.5	3.04	10.8	2.5	1.0
near3	228	55.1	3.58	185	1590	72.4	8.40	3.80	126	293	440	3.3	2.5	14.6	3.00	11.8	2.6	1.1
near4	223	56.1	3.55	184	2170	72.3	11.5	5.21	127	294	360	4.0	3.4	12.1	3.01	11.4	2.8	1.6
near5	230	54.2	3.56	199	2120	65.1	12.5	4.84	126	292	440	3.3	2.5	12.9	3.03	12.1	3.8	2.1
near6	229	54.5	3.56	183	2690	73.1	14.1	6.48	126	292	420	3.4	2.5	5.98	3.05	11.1	4.1	2.9
near7	219	57.6	3.56	194	3080	67.4	17.5	7.15	125	289	480	3.0	2.2	5.56	3.06	11.8	5.9	4.9
near8	213	59.6	3.56	192	6460	68.3	36.2	15.1	128	295	220	6.6	5.2	2.45	2.93	9.73	5.5	9.3
SUPER																		
super1	231	76.1	4.96	198	292	93.9	1.19	0.642	136	291	300	4.8	3.9	37.7	3.05	8.01	0.25	0.019
super2	231	76.1	4.96	193	997	97.7	3.90	2.22	130	292	460	3.1	2.4	26.7	3.01	10.2	1.2	0.33
super3	221	80.4	4.95	180	2050	109	7.19	4.72	128	291	490	2.9	2.1	19.2	3.01	10.7	2.5	1.3
super4	222	80.1	4.96	182	3110	107	11.1	7.13	134	288	360	3.9	3.3	10.2	3.05	10.1	2.8	2.4
super5	222	80.3	4.97	191	2820	99.5	10.8	6.32	131	293	440	3.3	2.6	9.02	3.09	12.5	3.3	2.5
super6	211	85.8	4.96	187	5820	103	21.6	13.2	132	286	410	3.4	2.7	3.04	3.05	10.7	6.3	9.9

B. Case Details for the New Injector Tests

	T _{chamber} (K)	ρ _{chamber} (kg/m ³)	P _{chamber} (MPa)	T _{outer} (K)	\dot{m} _{outer} (mg/s)	ρ _{outer} (kg/m ³)	u _{outer} (m/s)	Re _{outer} (10 ⁴)	T _{inner} (K)	\dot{m} _{inner} (mg/s)	ρ _{inner} (kg/m ³)	u _{inner} (m/s)	Re _{inner} (10 ⁴)	L/D ₁ (baseline)	Freq. (kHz)	P' _{RMS max} (kPa)	VR	J
SUB																		
subnew1	235	22	1.48	199	90	26	1.4	0.21	105	920	660	0.91	1.3	13+	3.01	8.86	1.5	0.089
subnew2	237	22	1.49	197	200	26	3.0	0.47	106	925	655	0.92	1.3	13+	2.96	14.0	3.3	0.43
subnew3	246	21	1.49	195	450	27	6.6	1.1	109	925	630	0.96	1.5	11+	2.97	12.1	6.9	2.0
subnew4	224	23	1.49	189	600	28	8.5	1.5	110	925	620	0.97	1.5	10.4	3.04	10.2	8.7	3.4
subnew5	217	24	1.49	184	750	29	10	1.9	110	925	620	0.97	1.5	9.29	3.02	11.5	11	5.2
subnew6	228	22	1.49	193	880	27	13	2.1	108	925	640	0.94	1.4	8.08	2.96	12.7	14	7.8
subnew7	222	23	1.49	194	1100	27	16	2.6	108	925	640	0.94	1.4	7.63	2.92	11.2	17	12
subnew8	217	24	1.48	201	1300	26	20	3.0	109	925	630	0.96	1.5	7.26	2.90	9.16	21	18
NEAR																		
nearnew1	228	55	3.56	213	330	60	2.2	0.70	109	925	650	0.93	1.3	14+	2.98	10.8	2.3	0.50
nearnew2	226	55	3.56	209	460	61	3.0	1.0	109	925	650	0.93	1.3	14+	3.06	9.17	3.2	0.97
nearnew3	230	54	3.58	198	730	66	4.3	1.6	108	925	655	0.92	1.3	13+	3.00	9.12	4.7	2.2
nearnew4	216	59	3.58	199	1030	65	6.3	2.3	109	925	650	0.93	1.3	13+	3.11	16.0	6.7	4.6
nearnew5	214	59	3.58	203	1460	63	9.2	3.2	109	925	650	0.93	1.3	7.01	3.07	15.0	9.9	9.4
nearnew6	215	59	3.56	207	2060	62	13	4.5	111	925	635	0.95	1.4	3.55	3.09	18.3	14	19
SUPER																		
supernew1	219	81	4.95	212	890	85	4.1	1.8	111	925	650	0.93	1.4	13+	3.11	17.0	4.4	2.6

Acknowledgements

The authors would like to express their appreciation to Mr. Randy Harvey for his invaluable contributions in running and maintaining the facility. This work is sponsored by AFOSR under Mitat Birkan, program manager.

References

1. Gutmark, E., Schadow, K. C., Wilson, K. J., "Mixing Enhancement in Coaxial Supersonic Jets", *AIAA-89-1812*.
2. Gautam, V., Gupta, A. K., "Simulation of Flow and Mixing from a Cryogenic Rocket Injector", *Journal of Propulsion and Power*, Vol. 23, No. 1, 2007, pp. 123-130.
3. Zong, N., Yang, V., "A Numerical Study of High-Pressure Oxygen/Methane Mixing and Combustion of a Shear Coaxial Injector", *AIAA-2005-0152*.
4. Richecoeur, F., Scouflaire, P., Ducruix, S., Candel, S., "High-Frequency Transverse Acoustic Coupling in a Multiple-Injector Cryogenic Combustor", *Journal of Propulsion and Power*, Vol. 22, No. 4, 2006, pp. 790-799.
5. Leyva, I. A., Chehroudi, B., Talley, D., "Dark-Core Analysis of Coaxial Injectors at Sub-, Near-, and Supercritical Conditions in a Transverse Acoustic Field", *54th JANNAF Meeting*, Denver, CO, May 14-18, 2007.
6. Leyva, I. A., Chehroudi, B., Talley, D., "Dark-Core Analysis of Coaxial Injectors at Sub-, Near-, and Supercritical Conditions in a Transverse Acoustic Field", *AIAA-2007-5456*.
7. REFPROP, Reference Fluid Thermodynamic and Transport Properties, Software Application Ver. 7.0, NIST, Gaithersburg, MD, U. S. Department of Commerce, 2002.
8. Thermophysical Properties of Fluid Systems, Online Database, NIST, U. S. Department of Commerce, 2005. <http://webbook.nist.gov/chemistry/fluid>.
9. Otsu, N., "A Threshold Selection Method from Gray-Level Histograms", *IEEE Transactions on Systems, Man and Cybernetics*, Vol. 9, pp. 62-66.
10. Davis, D. W., "On the Behavior of a Shear-Coaxial Jet, Spanning Sub- to Supercritical Pressures, with and without an Externally Imposed Transverse Acoustic Field", Ph. D. Dissertation, Department of Mechanical and Nuclear Engineering, Pennsylvania State University, 2006.
11. Rodriguez, J. I., Leyva, I. A., Chehroudi, B., Talley, D., "Results on Subcritical One-Phase Coaxial Jet Spread Angles and Subcritical to Supercritical Acoustically-Forced Coaxial Jet Dark Core Lengths", *44th AIAA/ASME/SAE/ASEE Joint Propulsion Conference and Exhibit*, Hartford, CT, 21-23 July 2008.
12. Rodriguez, J. I., "Acoustic Excitation of Liquid Fuel Droplets and Coaxial Jets", Ph. D. Dissertation, Department of Mechanical and Aerospace Engineering, UCLA, 2009.

Effect of Phase Angle of Transverse Acoustics on Shear Coaxial Jets for Two Geometries

Juan I. Rodriguez†, Ivett A. Leyva‡, Douglas Talley‡

†UCLA/AFRL, Edwards AFB, CA 93524 USA

‡Air Force Research Laboratory, Edwards AFB, CA 93524 USA

Motivation

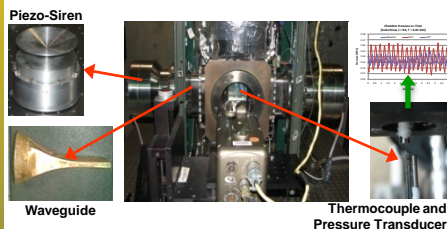
Reduce combustion instabilities

Characterize mixing enhancement

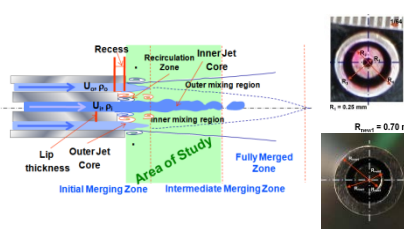
Objective

Characterize the behavior of a shear coaxial jet under the effects of a transverse acoustic field for two different injector geometries. Acoustic Instabilities are known to affect the development of liquid rocket engines, which often feature shear coaxial injectors.

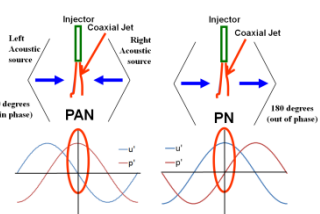
Experimental Setup



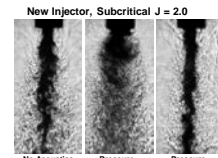
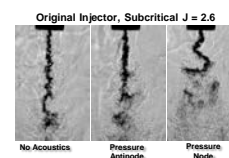
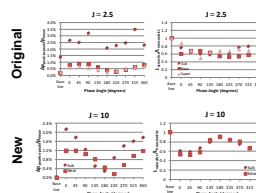
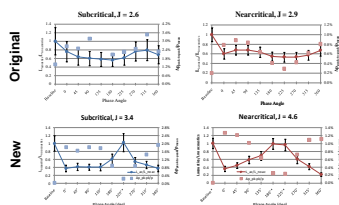
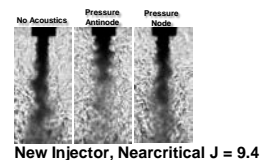
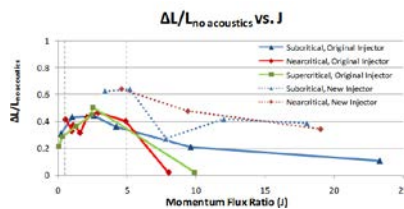
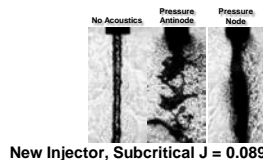
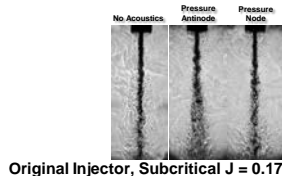
Two Shear Coaxial Injectors



Transverse Acoustic Field

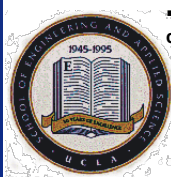


Effect on Dark Core Length



Conclusions

- Largest reduction of dark core length with acoustic excitation in the $1 < J < 5$ range for all pressure regimes and up to 10 for the subcritical regime with original injector.
- New injector data extended the range to as low as 0.1 in the subcritical pressure regime when compared to the original injector. Nearcritical and supercritical pressures showed a response for $J \geq 5$.
- With the original injector being at a pressure node the dark core length was shortened the most.
- New injector showed a clear phase angle effect with the longest dark cores occurring at the pressure node.
- Relative acoustic pressure did not affect the behavior of the dark core length for different pressures at the same J .
 - There might be a range of values of the momentum flux ratio or a similar parameter for which the coaxial jet behaves as a convectively unstable flow.



Mixing under Transcritical Coaxial Injection Conditions: Experiments and Simulations

Thomas Schmitt[†], Juan Rodriguez[†], Sébastien Candell[†]
and Ivett Leyva[‡]

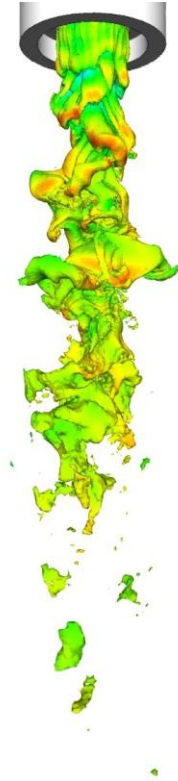
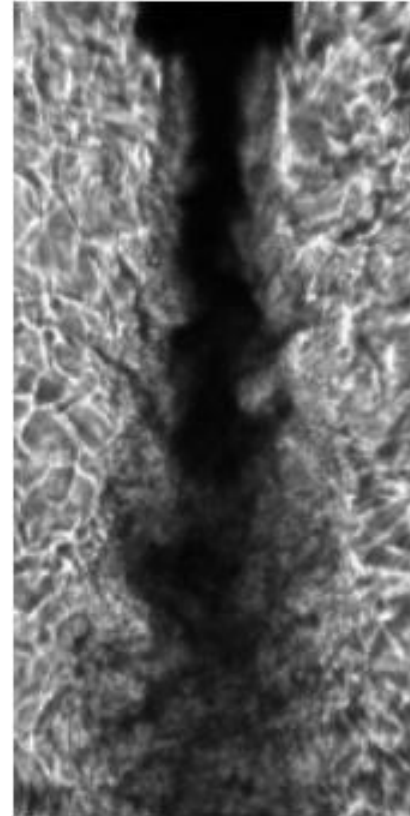
[†]EM2C Laboratory, École Centrale Paris, Châtenay-Malabry,
France

[‡]Air Force Research Laboratory, Edwards AFB, USA

8th EuroMech Fluid Mechanics Conference
13 September 2010

Motivation & Objectives

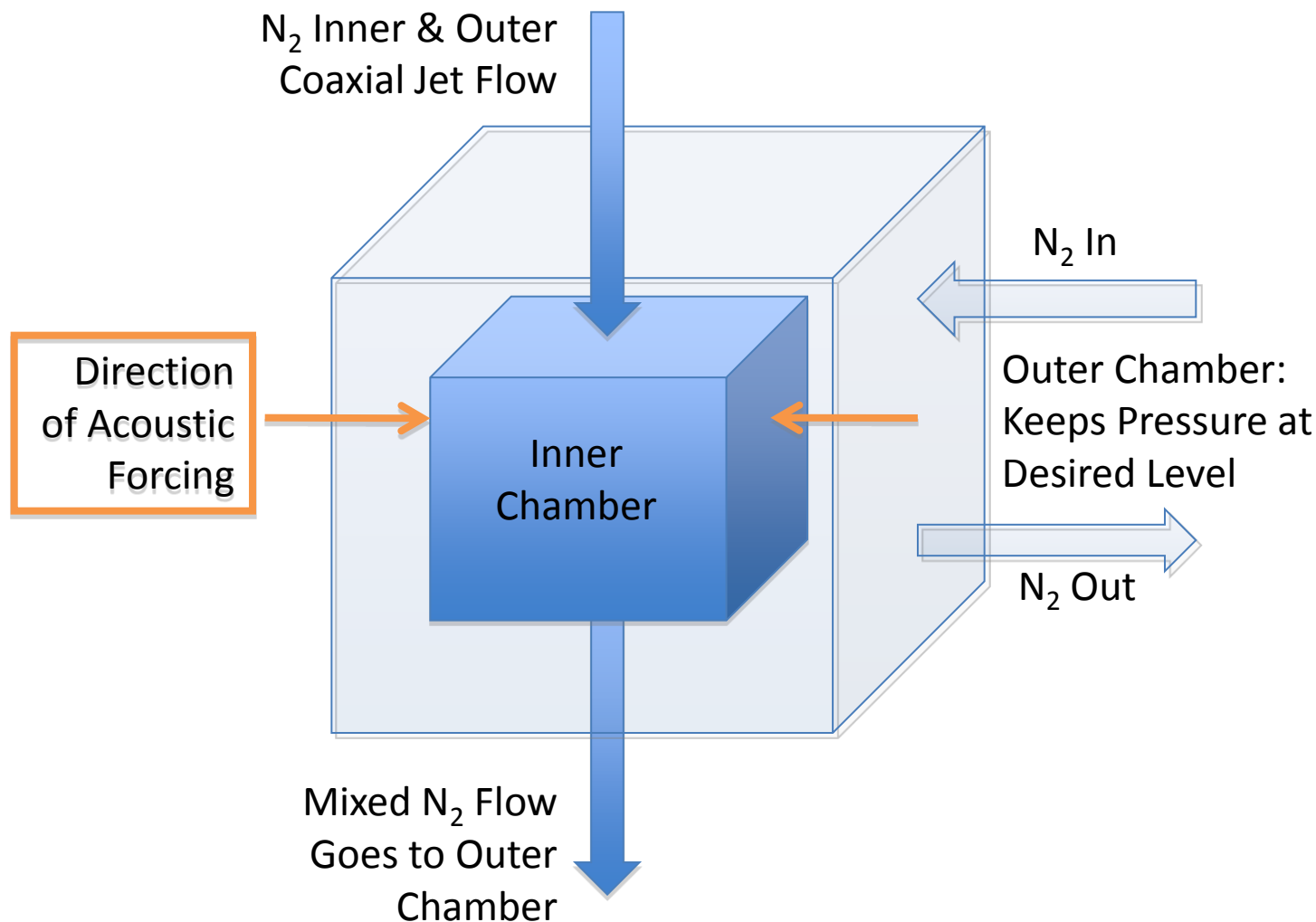
- Mixing at transcritical conditions. Highly important for Liquid Rocket Engines.
 - Temperature below critical point
 - Pressure above critical value
- We study the behavior of a coaxial injector with nitrogen as the working fluid.
 - Inner flow is in the transcritical regime
 - Outer flow is at a higher, supercritical temperature.
- Simulations and Experiments
 - Experimental work performed at Edwards
 - Modeling with LES approach at EM2C



Coaxial Jet Images. Left: Experiment. Right: Simulation.

- Parameters of interest to us are:
 - Momentum flux ratio, J
 - Densities and velocities.

Experimental Setup



A-771

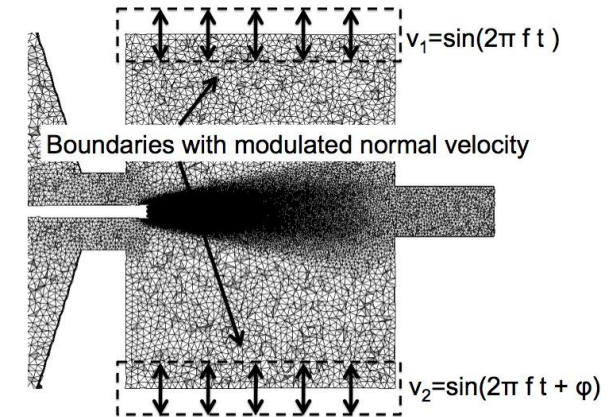
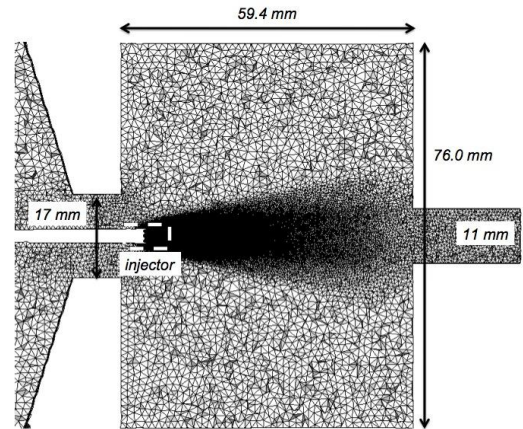
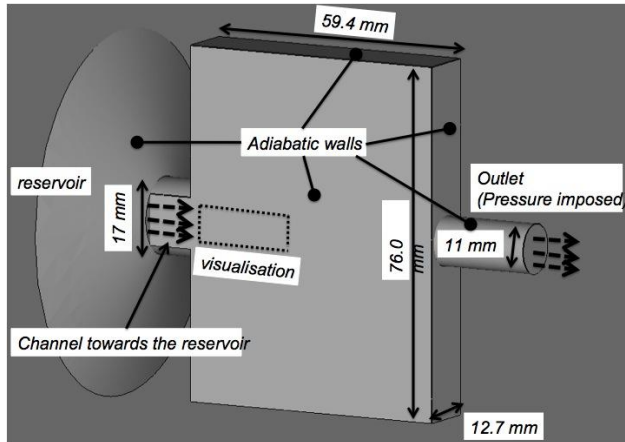
- Favre-Averaged Navier-Stokes equations
 - Fluid viscosity and heat diffusion coefficient follow Chung *et al.* method
 - Low pressure SGS model used (WALE)

$$\begin{aligned}\frac{\partial \bar{\rho}}{\partial t} + \frac{\partial \bar{\rho} \tilde{u}_j}{\partial x_j} &= 0 \\ \frac{\partial \bar{\rho} \tilde{u}_i}{\partial t} + \frac{\partial \bar{\rho} \tilde{u}_j \tilde{u}_i}{\partial x_j} &= -\frac{\partial \bar{P}}{\partial x_i} + \frac{\partial \bar{\tau}_{ij}}{\partial x_j} - \frac{\partial \tau_{ij}^t}{\partial x_j} \\ \frac{\partial \bar{\rho} \tilde{E}}{\partial t} + \frac{\partial \bar{\rho} \tilde{E} \tilde{u}_j}{\partial x_j} + \frac{\partial \bar{P} \tilde{u}_j}{\partial x_j} &= -\frac{\partial \bar{q}_j}{\partial x_j} - \frac{\partial q_j^t}{\partial x_j} + \frac{\partial \tilde{u}_i \bar{\tau}_{ij}}{\partial x_j} + \bar{\dot{\omega}}_T\end{aligned}$$

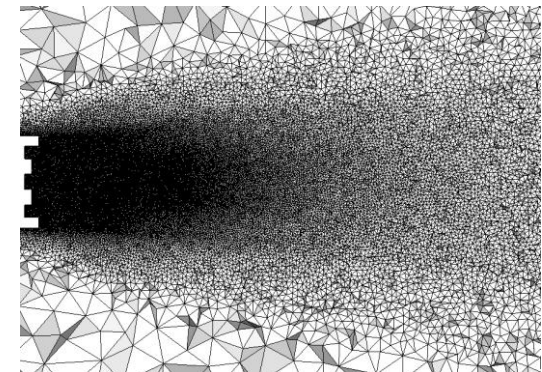
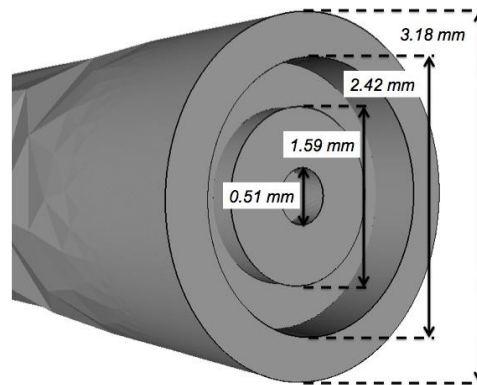
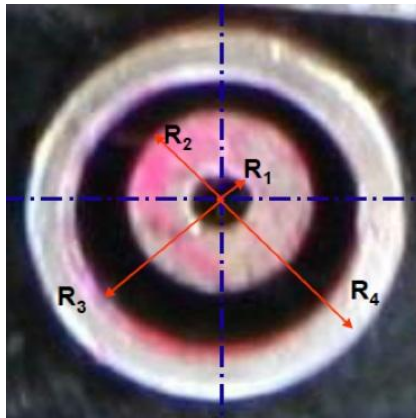
- Thermodynamics
 - Peng-Robinson equation of state

$$P = \frac{\rho r T}{1 - \rho b} - \frac{\rho^2 a(T)}{1 + 2\rho b - \rho^2 b^2}$$

Modeling



The first image shows a 3D visualization of the reservoir. The second shows a longitudinal cut of the mesh and the third the same cut with the imposed acoustic boundary conditions.

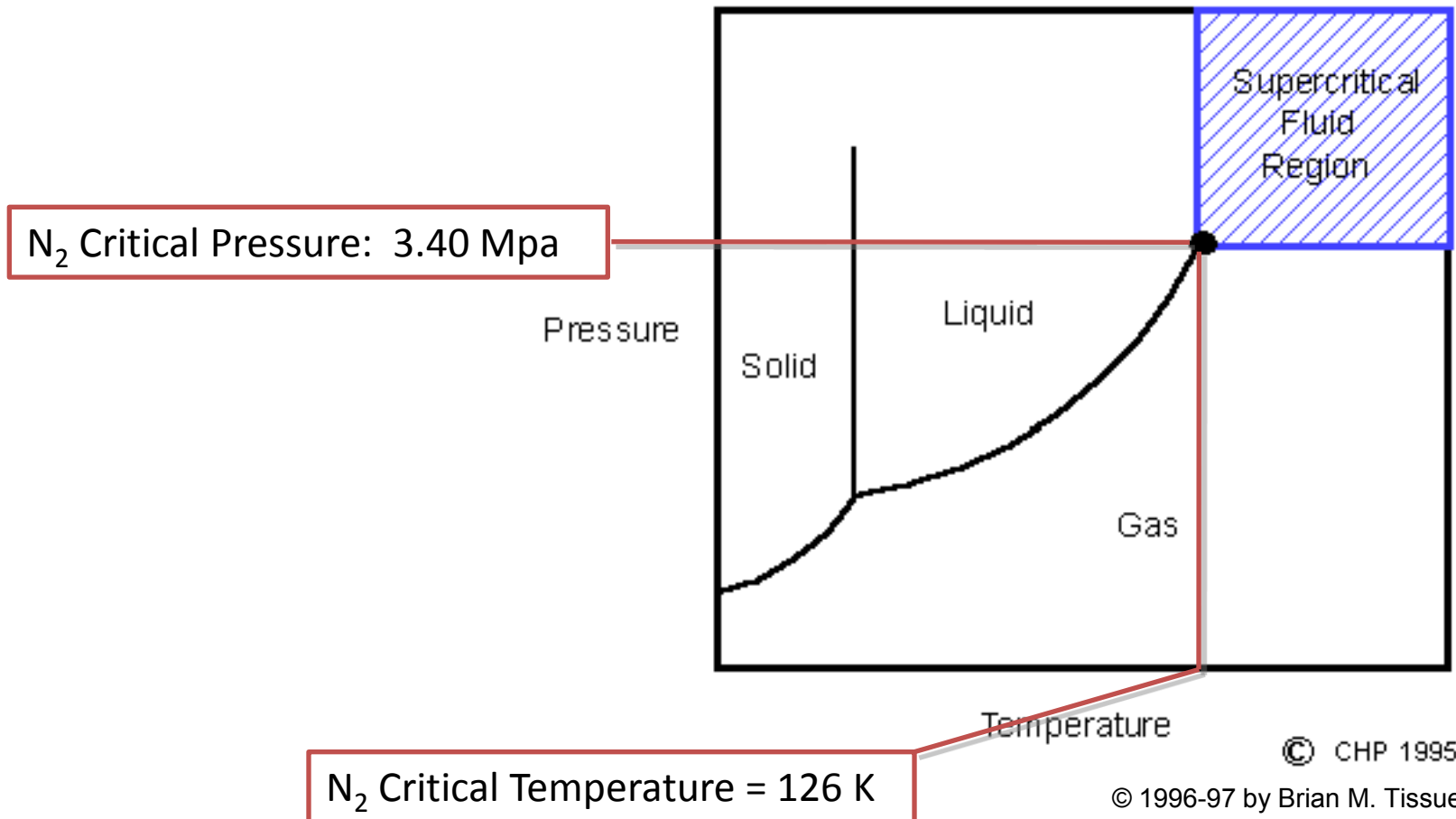


First and second images shows a picture and a 3D view of the injector used in the study. The third shows the mesh detail near the injector.

A-773

Phase Diagram

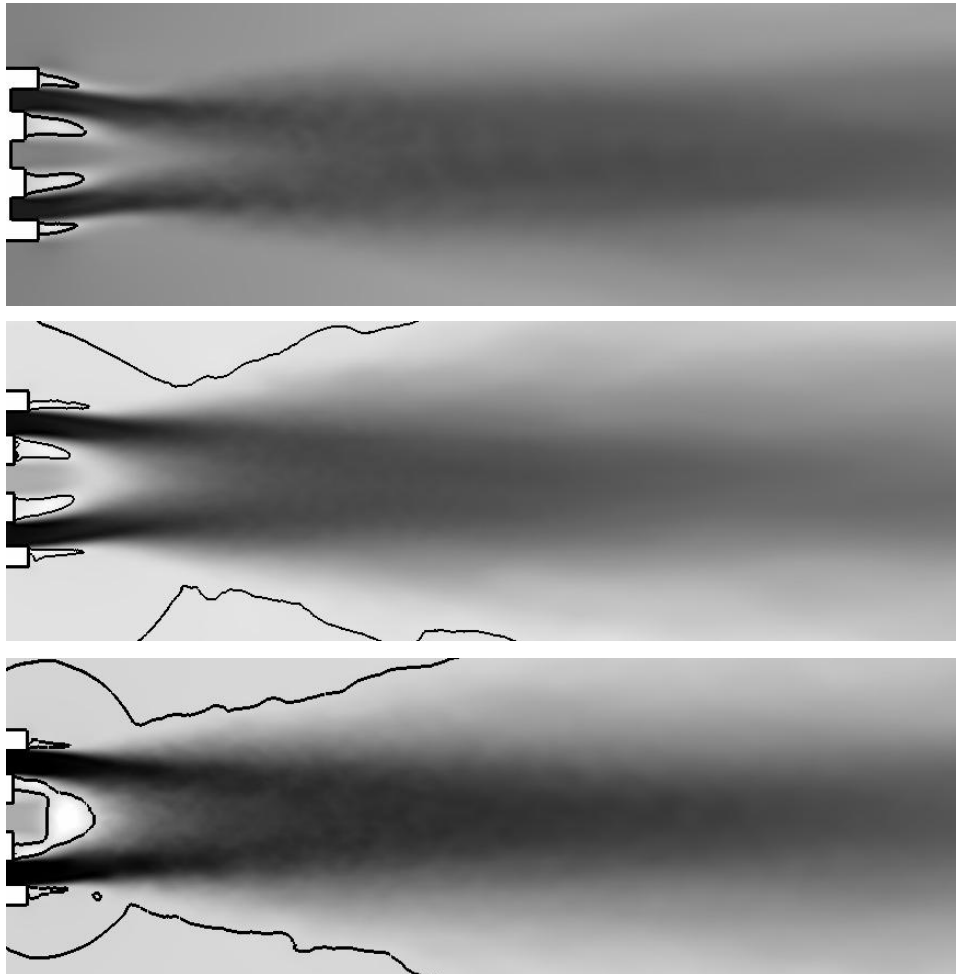
Phase Diagram



© CHP 1995

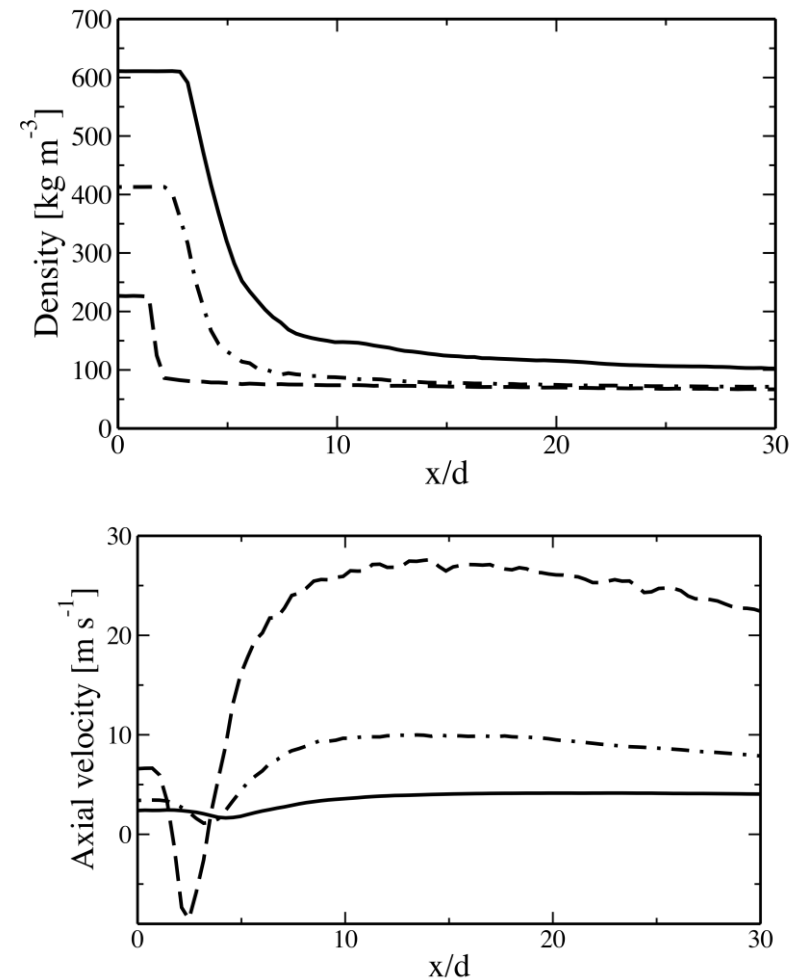
© 1996-97 by Brian M. Tissue

Results



Longitudinal slice of axial velocity. White: minimum; black: maximum. Dark line indicates iso-contour of zero axial velocity. Top: $J = 1.1$; middle: $J = 3.0$; bottom: $J = 9.3$.

A-775

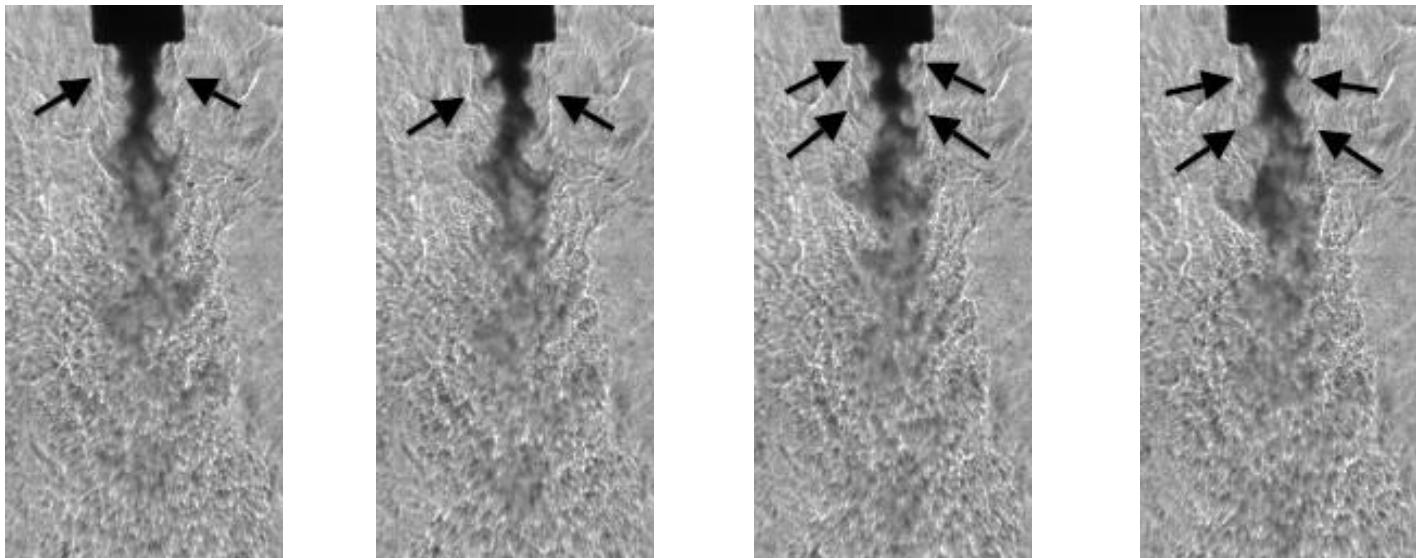


Top: centerline profile of density; bottom: centerline profile of velocity. Dark line: $J = 1.1$; dash point line: $J = 3.0$; dashed line: $J = 9.3$.

Results

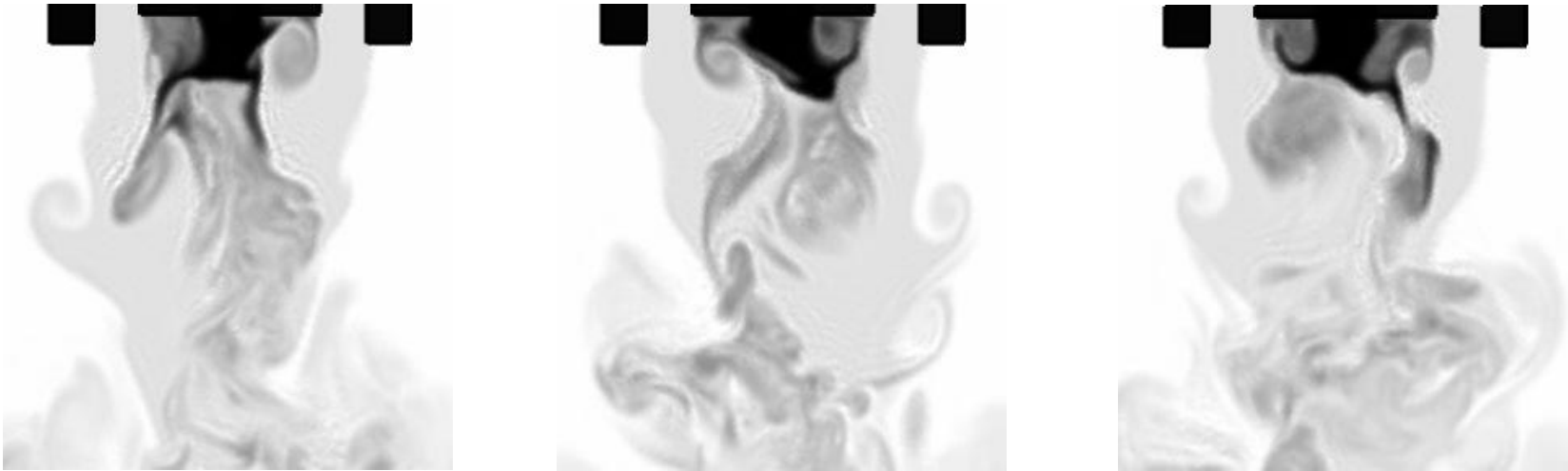


Instantaneous images of the simulation of an acoustic case with the injector at a pressure antinode for a $J = 3.0$

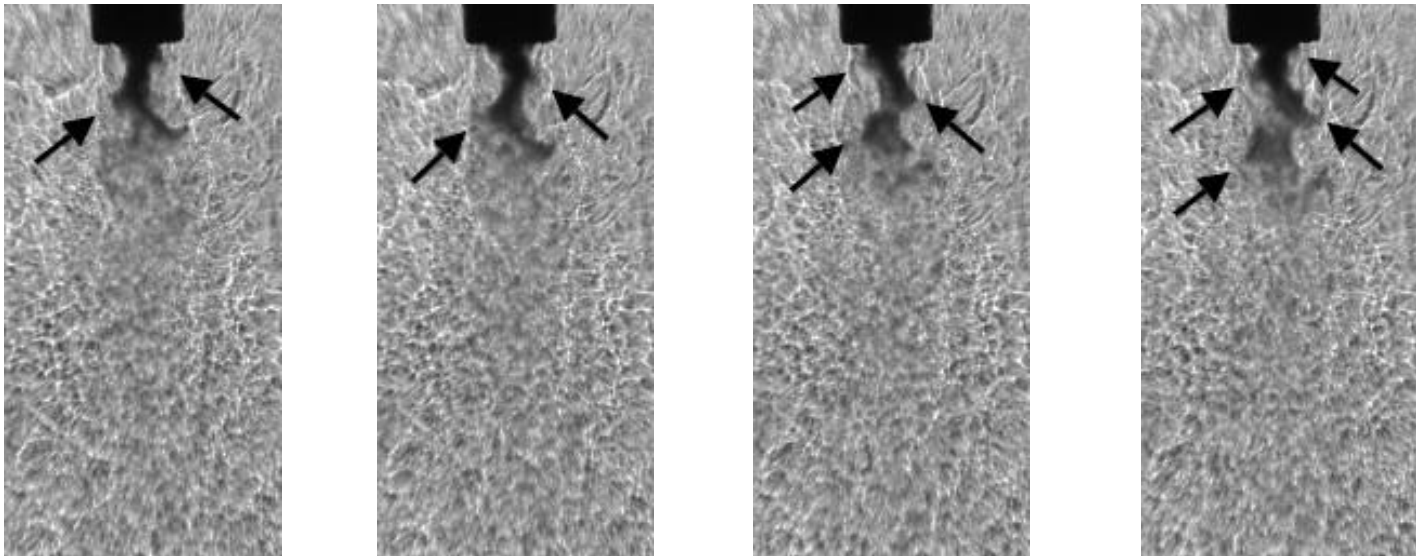


Instantaneous images of an experimental acoustic case with the injector at a pressure antinode for a $J = 2.9$

Results



Instantaneous images of the simulation of an acoustic case with the injector at a pressure node for a $J = 3.0$



Instantaneous images of an experimental acoustic case with the injector at a pressure node for a $J = 2.9$

Conclusions



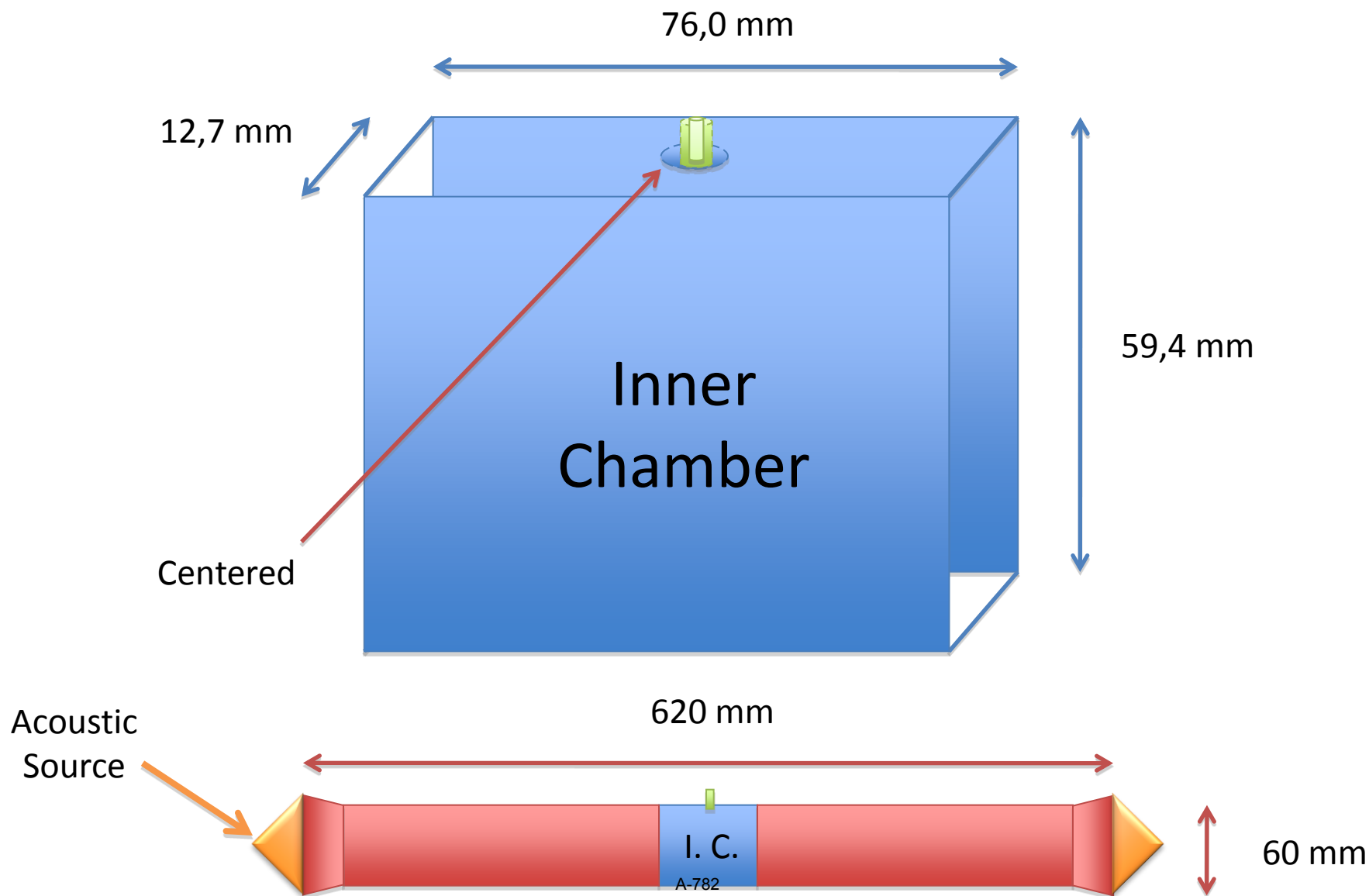
- An LES model has been developed for transcritical coaxial jet simulations with nitrogen at very low temperatures and pressures near the critical point.
 - The model has been able to reproduce experimentally-observed behavior.
 - Comparison with observed experimental features such as recirculation zones is very encouraging.
 - New features, such as points where the axial velocity of the flow is zero or negative, can now be analyzed using simulations.

- Direct Numerical Simulation
 - Use to model mixing between the higher temperature, supercritical, lower density nitrogen outer jet and the lower temperature, transcritical, higher density nitrogen inner jet.

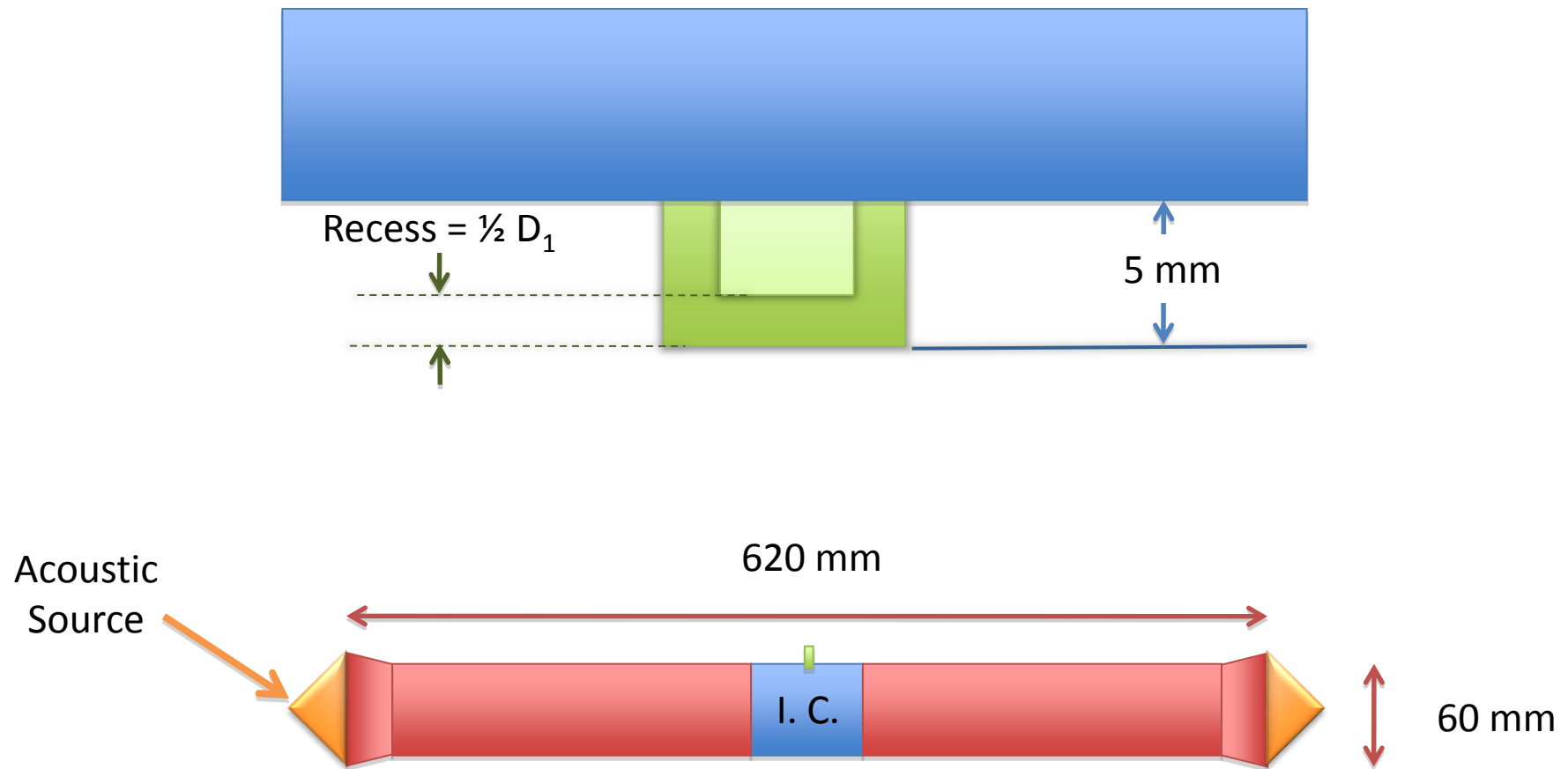
Thank You

Backup Slides

Experimental Setup



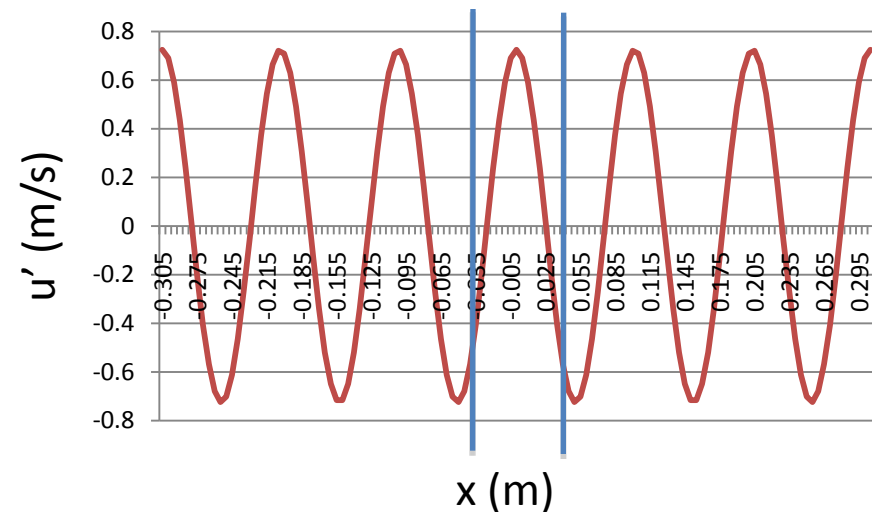
Experimental Setup



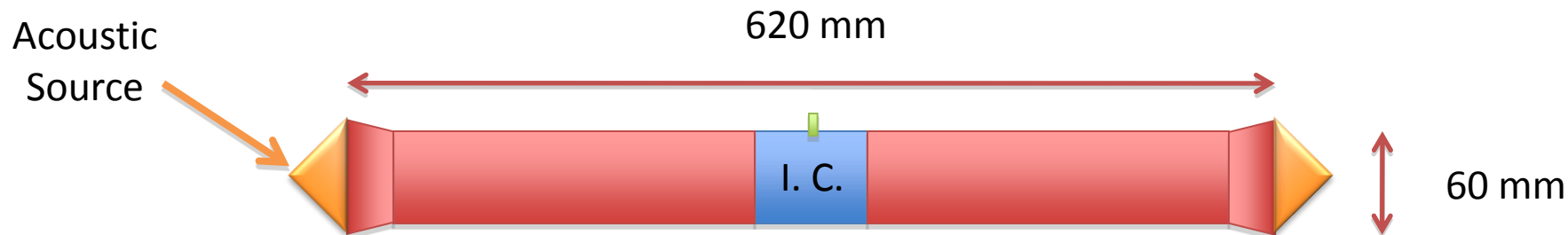
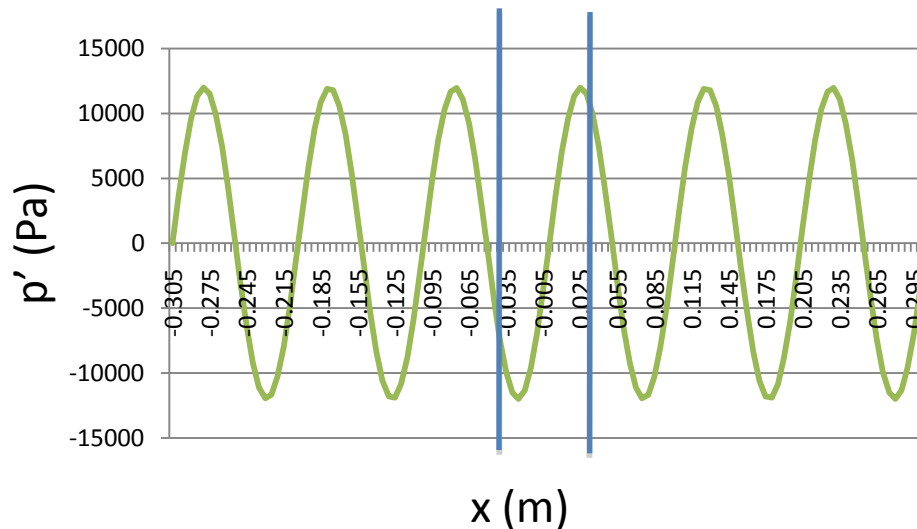
A-783

Experimental Setup

velocity



pressure



- Solver used: AVBP
 - Adapted Numerical Scheme
 - Taylor-Galerking weighted residual central distribution scheme TTG4A
 - Requires a particular stabilization procedure due to large density gradients and highly non-linear thermodynamic relations
 - Artificial viscosity is added for unresolved gradients
- Adapted Boundary Conditions
 - Treated with wave decomposition method NSCBC

Physical Hypothesis for the Combustion Instability in Cryogenic Liquid Rocket Engines

Bruce Chehroudi

Advanced Technology Consultants, Laguna Niguel, California 92677

DOI: 10.2514/1.38451

In this work, the author would like to portray a sketch of a fluid dynamical picture to describe the coupling nature/strength between the chamber acoustics and the injectors. This new perspective is achieved through a physically intuitive argument combined with previously published test results for two popular injector designs, namely, coaxial and impinging jets. For the impinging jet injectors, it is shown that the dynamic behavior of the dark-core (or breakup) zone for each jet, their lengths and thicknesses, has a profound impact on injector sensitivity to disturbances in its surrounding. This information is used to offer a possible explanation for the trends seen on the Hewitt stability plot in impinging jet injectors.

Nomenclature

d_j	=	jet diameter from a hole
d_n	=	hole diameter of the injector
$L_{C, Pth}$	=	average liquid core length
P_{th}	=	threshold chamber pressure
P_{ch}	=	chamber pressure
ρ_l	=	liquid density
ρ_g	=	gas density
T_{ch}	=	chamber temperature
V	=	average liquid jet exit velocity
θ	=	impinging jet included half-angle

Introduction

ACOUSTIC combustion instability has been one of the most complex phenomena in liquid rocket engines, and therefore difficult to fully understand, control, and predict particularly in the design of high-power rockets. The difficulty arises from the emergence of oscillatory combustion with rapidly increasing and large pressure amplitudes. This leads to local burnout of the combustion chamber walls and injector plates, which is caused through extreme heat transfer rates by high-frequency pressure and gas velocity fluctuations, see Harje and Reardon [1] and Yang and Anderson [2]. It is thought that resonance acoustic modes of the thrust chamber, amongst them the transverse modes being the most troublesome, are excited through the energy provided by the combustion. The amplification process is thought to include a feedback of information from the acoustic field to the injector or near-injector phenomena, which in turn tends to reinforce the combustion-to-acoustic-field energy transfer processes. The energy transfer reasoning alone is the widely cited general principle by Rayleigh [3]. In essence, he made a phasing argument and stated that the interaction between the combustion heat release and the acoustic field is the strongest if heat is added in a region of space and at the time when the acoustic amplitude is the highest. Although this view has been useful to understand a part of the big picture, evidences gathered by past investigations attributed combustion instability to a complex interaction of the external acoustic field with the fuel injection or near-injector processes as a feedback mechanism, thereby leading to incidences of instability in rocket engines. See, for example, Heidemann and Groeneweg [4], Anderson et al. [5], and Hulka and Hutt [6]. For this

and other reasons, controlled studies have been conducted probing into the effects of acoustic waves on gaseous and liquid jets from a variety of injector hole designs. A series of investigations concentrated on disturbances induced from within the injection system. They considered the effects of acoustic fields on many phenomena such as flow structure, vortex pairing, and shear layer growth rate in the initial region of the jet (for example, see a short review article by Kiwata et al. [7]). More relevant to the work reported here, are a few reports and articles on gaseous and (in particular) liquid jets under the influence of external (transverse and longitudinal) acoustic fields. These have been reviewed in Chehroudi and Talley [8] and Davis and Chehroudi [9].

In this paper, however, the author would like to propose a physical picture based on experimental results and intuitive arguments to describe a possible coupling nature/strength between the chamber acoustics and injectors or near-injector processes in cryogenic liquid rocket engines.

Discussion

In the following, key conclusions from the work the author and his coworkers have conducted in the past are briefly reviewed to set the stage for when they are used later in the paper. These observations/conclusions are critical to the arguments made here. For a detailed discussion of these results, the reader is referred to the cited references.

In Davis and Chehroudi's [9,10] experimental work on a cryogenic nonfired coaxial injector at sub and supercritical pressures, we have offered a plausible explanation of why in temperature ramping stability rating exercises an engine becomes unstable. In such tests, which are usually conducted in LOX/H₂ cryogenic liquid rocket engines (LRE), we proposed that a progressive reduction of the propellant (H₂) temperature decreases the outer-to-inner jet velocity ratio for shear coaxial injectors and hence pushes the engine into an unstable operating zone. This velocity ratio was found to be a key parameter defining the stability of the engine, see Hulka and Hutt [6]. Moreover, in Davis and Chehroudi [9,10], where an externally-imposed acoustic field is used to simulate certain key aspects of their interaction in real engines, it is shown that at subcritical conditions the dark-core length root mean square (rms) fluctuation values were much higher than those at near-critical and supercritical conditions by a factor of 4 to 6 at all velocity ratios. Also, as the outer-to-inner jet velocity ratio declines, the rms value increases from 1–2 to values of about 7–8 inner jet hole diameters at subcritical pressures. Taking the rms of the dense core as a reflection of mass fluctuations to a first-order approximation, combined with the measurements of a core dominant oscillation frequency consistent with the imposed acoustic field's resonant mode frequency, it was then suggested that a connection to rocket combustion instability could be obtained from

Received 8 May 2008; revision received 13 April 2010; accepted for publication 27 June 2010. This material is declared a work of the U.S. Government and is not subject to copyright protection in the United States. Copies of this paper may be made for personal or internal use, on condition that the copier pay the \$10.00 per-copy fee to the Copyright Clearance Center, Inc., 222 Rosewood Drive, Danvers, MA 01923; include the code 0748-4658/10 and \$10.00 in correspondence with the CCC.
Approved for public release; distribution unlimited. PA #08190A.

these data through examination of the rms of the dark-core length fluctuations. Decreases in the dark-core length fluctuation levels (quantified through the rms) were then interpreted as the reduced intrinsic sensitivity of the jet. We then stated the possibility that decreases in the dark-core length fluctuation levels could weaken a key feedback mechanism for the self-excitation process that is believed to drive the combustion instability in cryogenic LRE. This was offered as a possible explanation for the combustion stability improvements experienced in production engines under higher outer-to-inner jet velocity ratios. The effect of temperature ramping was linked to its impact on the outer-to-inner velocity ratio and hence was also explained. More details can be found in Davis and Chehroudi [9,10], Davis [11], and Leyva et al. [12]. In other words, the dynamic behavior of the dark-core, specifically its axial length, is considered to be the primary culprit for coaxial jet injectors.

It is noted here that measured mean intact or dark-core length for space shuttle main engine (SSME)-like momentum flux ratios by Woodward et al. [13] in a LOX/GH₂ fired single-element rocket engine agrees with those of Davis and Chehroudi's [9,10] non-reacting case. And, in addition, existence of the dark-core length fluctuations has also been reported by Woodward et al. [13]. In a recent work published by Yang et al. [14], they performed tests in a fired single-element rocket equipped with a coaxial LOX/CH₄ injector. Measurements of the dark core length indicated an increasing trend in the level of fluctuations when the outer-to-inner velocity ratio was decreased and the core oscillation spectra showed more high-frequency contents in jet oscillation at lower velocity ratios. These results are consistent with the Davis and Chehroudi's [9,10] conclusions cited above.

Interestingly, results published in a LOX/GH₂ (i.e., liquid oxygen/gaseous hydrogen) single-element coaxial jet fired-engine work by Smith et al. [15] also are consistent with the Davis and Chehroudi's view described above that high rms values for the dark-core length, specifically at subcritical and low velocity ratios, may lead to or cause combustion instability. In their work, Smith et al. swept the engine from the ignition period into three consecutive steady-state phases of supercritical (phase 1), near-critical (phase 2), and subcritical (phase 3) chamber pressures, each sufficiently long for adequate measurements and allowing 2–4 s of transition in between phases. The intention was to investigate effects of the chamber reduced pressure (Chamber/Critical pressures) on the engine combustion instability. Under all conditions tested, the peak-to-peak pressure remained less than 3% and 2% of the mean chamber pressure for phases 1 and 2, respectively. For phase 3, however, conditions led to unstable combustion. In fact, under all test conditions they investigated, no instability could be triggered when operating above or very near to the critical point of oxygen. In another test, referred to as *V-test*, chamber pressure was adjusted through propellant flow rate regulation while maintaining a constant fuel-to-oxidizer (F/O) ratio. During this test, under no conditions combustion instability was seen as long as chamber pressure was above the critical point of the oxygen, yet an unstable operating mode was triggered as soon as reduced pressure reached less than unity, see Fig. 1. More important, they showed significantly different appearances of the liquid oxygen core in different phases. Above and near the critical point of oxygen (phases 1 and 2) the oxygen core flow appeared very steady (implying low rms) with surface perturbations reducing as chamber pressure approached critical point. They also reported that below the critical point of oxygen, the LOX jet experienced "increased oscillation and general unsteadiness," implying high rms values. The initially undisturbed flow became unsteady at approximately 15–20 liquid oxygen (LOX) jet diameters downstream from the injector exit plane. Therefore, very low rms values of the dark-core length at near- and supercritical conditions and high rms values at subcritical pressures, both measured by Davis and Chehroudi [9,10] in their nonreacting experimental setup, are consistent with the fired-engine experimental observations by Smith et al. [15]. Hence, their reported unstable combustion behavior at subcritical pressures with high core unsteadiness correlates with Davis and Chehroudi's high rms values at subcritical conditions, interpreted as conditions leading to highly sensitive dark-core dynamic response to its surrounding. Note that

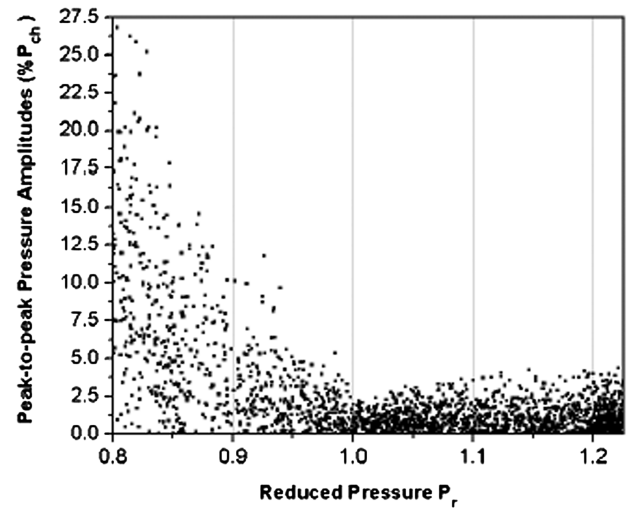


Fig. 1 Peak-to-peak chamber pressure oscillations for the *V* test, showing a minimum value at a chamber pressure equal to the critical point of the oxygen (Smith et al. [15]).

although velocity ratio declines somewhat during each *V*-test from supercritical to subcritical pressures, rms values for the supercritical (and near-critical) test phase still remains well below the subcritical phase because of large differences in the rms values between these two test phases indicated before.

It should be indicated here that the observed instability frequency reported by Smith et al. [15] was at about 40 Hz, much lower than typical acoustic instabilities. The reason for this was not clearly explained by the authors. Nevertheless, the result is consistent with the statement that a jet under subcritical conditions is more sensitive to environmental disturbances than at supercritical conditions. The intuition here comes from the fact that at subcritical pressures well-defined liquid gas boundaries exist, leading to strong acoustic impact, whereas such boundaries are not sharply defined at supercritical pressures and hence lower acoustic impact is expected. The author has investigated a frequency range of 1–5 KHz and found his conclusions to be valid. Therefore, although extension to lower frequencies may appear intuitive, they are not measured.

One is then tempted to expand the same idea explained above for coaxial jets to impinging jet injectors such as like-on-like, or LOL, type. In other words, considering the dynamics of the dark core as the underlying culprit contributing to instability. Before doing so, however, attention is drawn to an intact core (or dark core) length proposed by Chehroudi et al. [16], being equal to $(d_j)^* C^* (\rho_l/\rho_g)^{1/2}$. The constant C is between 3.3 to 11 and a recommended

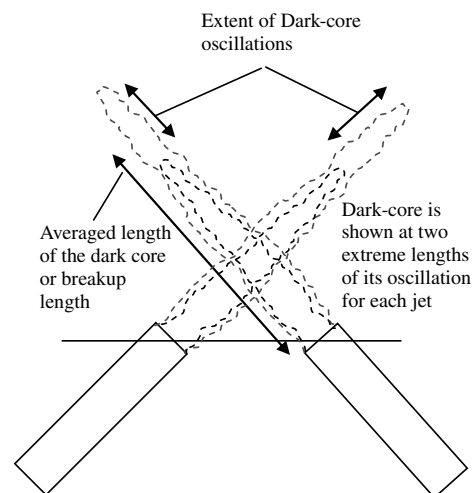


Fig. 2 Shows the dark-core (or breakup) lengths of individual jets of an impinging injector for a situation when the average length is much larger than the distance from each hole to the impinging point.

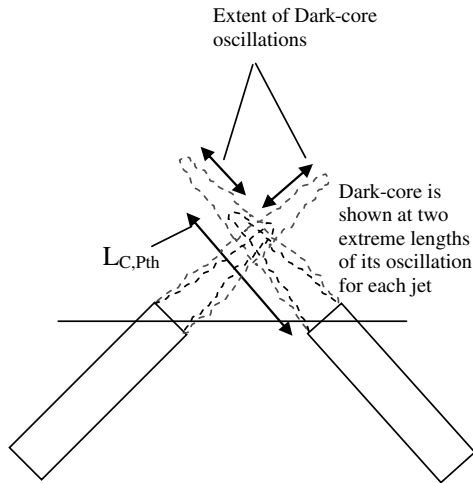


Fig. 3 Shows the dark-core (or breakup) lengths of individual jets of an impinging injector for a situation when the average length is of the same order as the distance from each hole to the impinging point.

value of 7.15 is given. The following questions are then posed in expanding the idea to impinging jets. Conceptualizing that each individual circular jet of an impinging injector possesses a dark-core (or breakup zone) with its averaged length changing according to the Chehroudi et al. [16] equation and each having a certain rms level of fluctuations, what would be the implication of a situation when the averaged core length approaches the same order of magnitude as the distance from the exit hole to the impinging point? Under what conditions such a scenario could happen? Is it possible to have such a situation in a practical rocket engine? Historically, it was Heidemann and Groeneweg [4] who, based on tests on a radially injected subscale rocket model, first suggested that the breakup of the jet before the impingement point may be an important contributing factor to engine instability. We will revisit this below.

Figures 2 and 3 schematically show the two scenarios that would intuitively exhibit completely different dynamic behaviors as a system. Figure 2 shows the dark-core length for a case where this length is larger than the preimpingement distance. In actual operation, however, a liquid sheet is formed which breaks up at a distance from the impinging point. Under the scenario shown in this figure, a robust and steady sheet is expected as a result of impingement, being relatively insensitive to its environmental disturbances. Figure 3 shows the case where the average dark-core length is shorter than the preimpingement distance. In addition, the averaged jet cross section at the impingement point is substantially reduced, being smaller than the hole diameter. In actual operation, however, under this scenario, a highly unsteady liquid sheet is expected as a result of the impingement, being highly sensitive to its environmental disturbances.

Let us now consider a startup event when the chamber pressure begins from an atmospheric value (~ 100 kPa) to where a steady high pressure and temperature condition is established. The mean core length will then change according to the Chehroudi et al. [16] equation and, under supercritical chamber pressures, could even reach a negligibly small value (see Davis and Chehroudi [9,10]). Hence, one would expect that the nature of the impingement continuously changes in time as chamber pressure increases. Therefore, at a certain chamber pressure (call it a threshold P_{th}), the averaged unimpinged core length, $L_{C,Pth}$, becomes short enough, say, of the same order as the distance from the exit holes to the impingement point, to be of importance in dominating the dynamic behavior of the injector unit, see Fig. 3. Considering the high rms levels of the core length fluctuations for each jet of an impinging injector, one can then intuitively regard this system, at the dark core length equal to $L_{C,Pth}$, as highly unpredictable and, more to the point, being very sensitive to, and responsive to, ambient disturbances. This is especially so for impingement targeting when a wiggly shape is superimposed under an externally imposed acoustic field. In a sense, the feedback link or coupling between the environment, or the acoustic field, and the

injector becomes very strong, somewhat similar to the effect of the velocity ratio seen on the sensitivity of the coaxial injector dark-core length to its environmental acoustic disturbances. This way, one has the dark core dynamic characteristics as a common underlying factor affecting the instability. Hence, a sketch of a unified physical picture emerges for the feedback linkage between the chamber acoustics and the injector through the dynamics of the dark core or the breakup zone of the liquid propellants. Although the dark-core length reaches and passes the $L_{C,Pth}$ value, that is, becomes shorter than the $L_{C,Pth}$, at high chamber pressures approaching supercritical conditions, it could also become sufficiently close to it if the engine operating pressure range includes the P_{th} value. There are host of other ways that the $L_{C,Pth}$ can be reached and are discussed later in this paper.

Note that under the situation described in Fig. 3, there are two factors contributing to impinging jet injector hypersensitivity. First, the fact that the average length of the dark-core is now too short for a robust impingement, and the second is that the mean jet cross section at the impingement point is sufficiently reduced from its nominal value of injector hole diameter for good targeting. For example, Chehroudi and Talley [8] showed pinching of a single round LN₂ jet (into GN₂ ambient) at as close a distance as five (5) jet diameters when an acoustic field is externally imposed. The effect was relatively more dramatic at subcritical chamber pressures and substantially subdued at supercritical values. At the same time, the breakup length was affected as well. Both effects though could happen independently would reinforce the hypersensitivity of an impinging jet injector unit. Note that changes in the dark core (or breakup zone) length and thickness occur both through changes in mean values of thermofluid parameters, such as chamber pressure P_{ch} , chamber temperature T_{ch} , velocity, etc., for example, when engine thrust level is varied, as well as through level of their fluctuations (depending on the frequency, of course).

On the other hand, let us now look at the Hewitt correlation as shown in Fig. 4, see Anderson et al. [5]. This correlation suggests that for LOL impinging injectors (and certain similar class), as one decreases the dn/V value from an stable operating condition, engine will be eventually pushed into an unstable operating mode at a certain critical dn/V value $[(dn/V)_c]$. This is shown by an arrow in Fig. 4. Here, dn is the injector hole diameter and V is the injection velocity for the impinging jet injector. There have been a few proposed mechanisms, such as jet atomization frequency (Anderson et al. [5]), flame straining/extinction (Kim and Williams [17]), and fuel jet aerodynamic excitation (Chao and Heister [18]) attempting to offer explanations of the trend seen in Hewitt correlation. Although none has been fully proven as an established fact and a combined effect of several mechanisms can be in play, the author's hypothesis is a new perspective to the list. An attempt to decrease the dn/V ratio implies either reduction of the dn or an increase of the V or both. Generally speaking, an increase in V tends to shorten the dark-core (or breakup) length (stronger interaction through enhanced aerodynamic interaction) in the first, second, wind-induced liquid jet breakup regimes, using the terminology proposed by Reitz and Bracco [19]. This is shown in Figs. 5 along with the corresponding terms used by

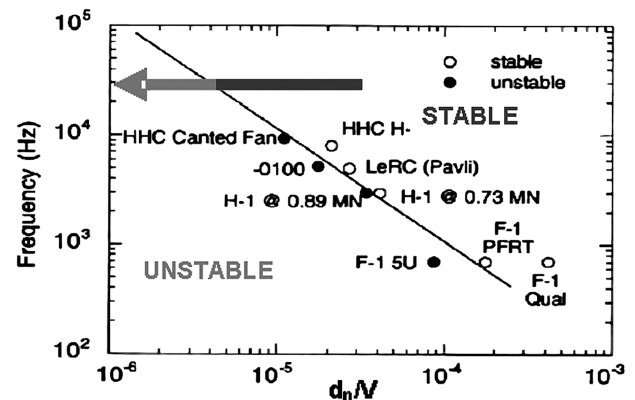


Fig. 4 Shows the Hewitt correlation (Anderson et al. [5]).

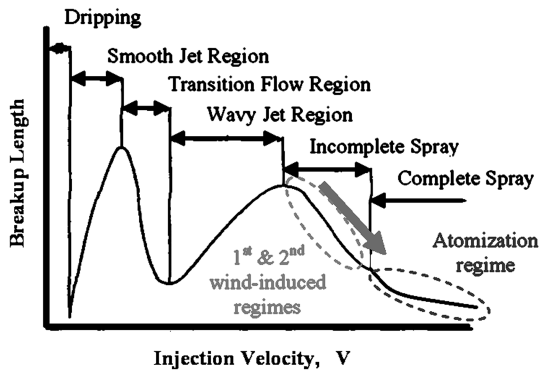


Fig. 5 Mean breakup length of a circular jet as a function of the injection velocity, V . Note the decline of the breakup length with injection velocity in the region of interest (Hiroyasu [20]).

Hiroyasu [20]. Note that the terms *breakup* and *dark-core* lengths were interchangeably used here although strictly speaking, the former is for the first and second wind-induced, and the latter is used for the atomization regimes (dark core or intact core). With injection velocities in the order of 20 m/s or higher, typical for rocket

operation, a jet is in the first, second wind-induced breakup regimes at lower pressures and in the (full) atomization regime at sufficiently high pressures. In the former cases (i.e., the wind-induced), the length is affected both by injection relative velocity and density ratio, whereas in the latter, the density ratio is more dominant (see Fig. 5). Hence, reduction in the dark core (or breakup) length is expected when V is increased in Hewitt stability parameter as shown in Fig. 5. Also, in an operating engine, increases in V (higher thrust) will be followed by higher chamber pressures, which impact the dark core length even more dramatically. At the same time, a reduction in the dn (or dj) also reduces the dark-core length according to Chehroudi's equation, see Fig. 5. Note that the dj in Chehroudi equation is the exit jet diameter and intended to capture inner-nozzle effects, such as hydraulic flip and cavitation, to a certain degree, whereas the dn in the Hewitt is a fixed hole diameter for a given design because the actual jet exit diameter is not usually known (measured or measurable) in real engine chamber environments. Nevertheless, reduction of the dn/V through changes in either dn or V leads to shortening of the mean dark-core (or breakup) length for each jet in an impinging jet injector. Then, it is quite possible that as dn/V is reduced in an engine, the mean dark core length reaches a critical value ($L_{C, Pth}$) where one intuitively expects inherently high sensitivity for an impinging jet system to environmental acoustic field. Here, the author is hypothesizing that the Hewitt stable-to-unstable transition point (or line) as dn/V reduces is at or near where the distance from the holes exit plane of the impinging injector to the impinging point (i.e., preimpingement length) reaches a critical value $L_{C, Pth}$, creating a situation somewhat similar to what is shown in Fig. 3.

Although larger values were also used, according to Ryan et al. [21], the preimpingement length (along the jet) is typically 3.5–11.5 hole diameters. For example, for the Lunar Module Ascent (LMA) injector, it is about 6–8 hole diameters (Chemical Propulsion Information Agency 245 and 246 [22]). Measurements published by both Chehroudi et al. [23] and Oschwald et al. [24] indicate that the mean dark core length of a single liquid nitrogen jet at moderate to high chamber pressures progressively shortens, for example, from 12 to a value of about 7 hole diameters, see Fig. 6. The two injectors had hole lengths of 40 and 100 times larger than their diameters. Hence, under normal operation, it is expected to provide a longer dark-core (breakup) length as compared with those used in rocket engines. In addition, considering that the data in Fig. 6 is for injection into the room temperature, entrainment of hot gases in thrust chambers is expected to shorten this core length even more due to enhanced evaporation. This may, in part, be a reason for the general finding that displacement of the combustion zone closer to the injector face increases susceptibility for combustion instability, see Oefelein and Yang [25]. Considering high rms values of the dark core (or breakup) length, this suggests feasibility of conditions that the preimpingement and dark core lengths are sufficiently close to cause hypersensitivity and high responsiveness to environmental oscillations and

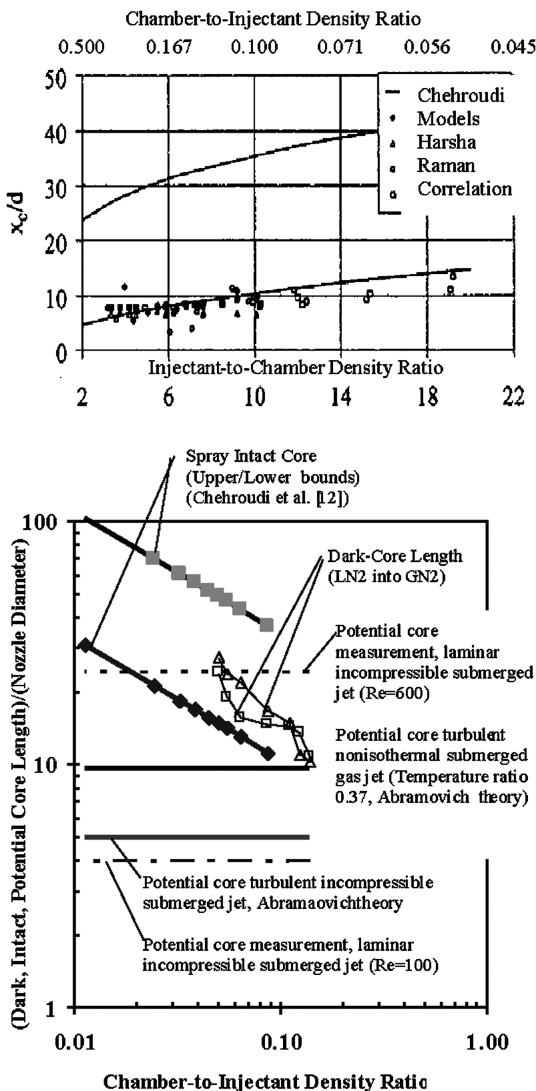


Fig. 6 Comparison of the mean dark-core length measurements for LN_2 jet injection into GN_2 at room temperature from sub up to supercritical pressures. Also, shown are boundaries using Chehroudi's (intact) core equation (solid diamond and square symbols). The horizontal axis of the two plots are inverse of each other (Chehroudi et al. [23] and Oschwald et al. [24]).

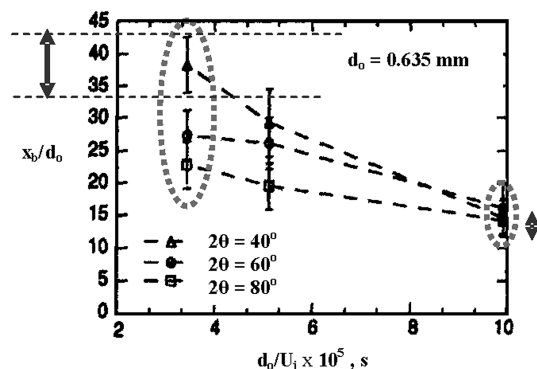


Fig. 7 Shows sheet breakup length as a function of instability parameter at three different impingement included angles. Much higher sensitivity of the sheet breakup length is seen with included angle (2θ) at low dn/V ($=d_0/U_j$, in the original article) values (Anderson et al. [5]).

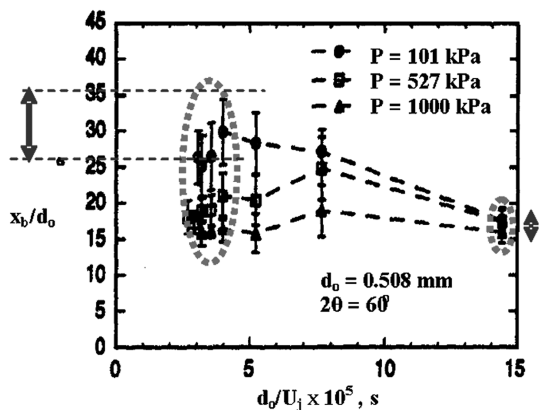


Fig. 8 Shows sheet breakup length as a function of instability parameter at three different chamber pressures. Much higher sensitivity of the sheet breakup length is seen with chamber pressure at low dn/V ($=d_o/U_j$, in the original article) values (Anderson et al. [5]).

disturbances. For example, with a rms (or standards deviation) value of 4 hole diameters, assuming normal distribution, the instantaneous dark-core length is between ± 8 hole diameters of its mean value 95% of the time. With mean core length of 12 hole diameters, it will penetrate into or have overlap with the preimpingement length region. Importance of the preimpingement length and its impact on the characteristics of the impinging jet injector has also been reported by Ryan et al. [21]. One reads in this work, "Variations of pre-impingement length had a measurable effect on (sheet) breakup length and drop size, pointing to the importance of the jet condition before impingement."

Although performed under steady conditions, the higher sensitivity of the impinging jet injector can also be discerned/inferred in Figs. 7 and 8 taken from the work of Anderson et al. [5], where large differences between the sheet breakup lengths for different pressures and impinging jets included angles 2θ are clearly seen at low values of the dn/V stability parameter. For example, Fig. 8 strongly suggests higher sensitivity of the injector when dn/V is reduced through increase in V . This is simply deduced by the enlarged size of the scatter bounds at any given pressure and sensitivity to pressure changes at low dn/V values. Although strictly speaking one should have its frequency response (amplitude and phase) measured, the

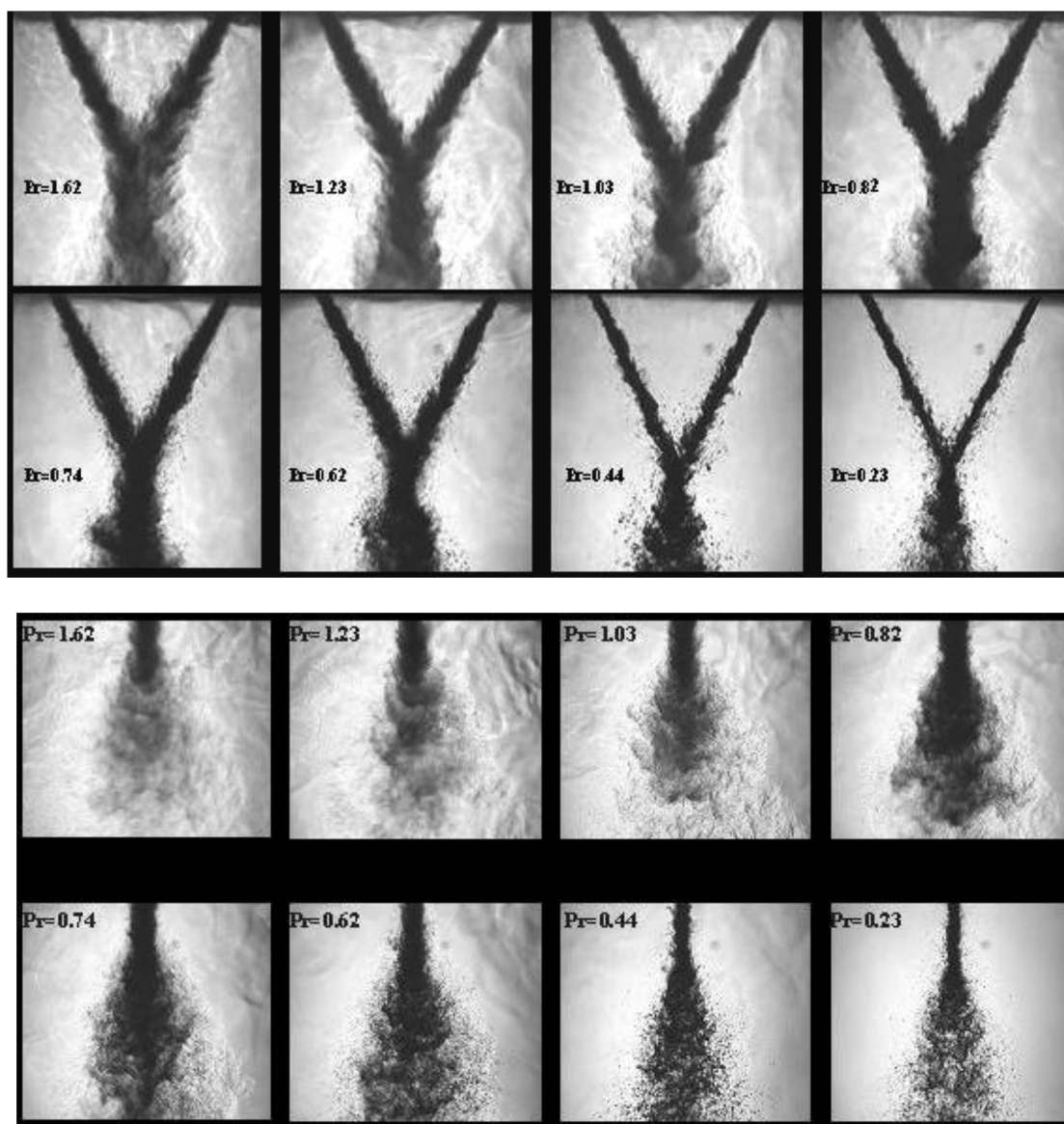


Fig. 9 Instant images of sub-, near-, and supercritical impinging jets for LN2 into GN2 (room temperature) injection by Chehroudi. Last two rows show the same injector in the first two rows but viewed at 90 deg angle. $P_{ch} = 0.8, 1.5, 2.1, 2.5, 2.8, 3.5, 4.2, 5.5$ MPa; from lower right to upper left, ($P_{ch} = 100, 200, 300, 350, 400, 500, 600, 800$ psig). (For nitrogen: $P_{critical} = 3.39$ MPa; $T_{critical} = 126.2$ K). ($Re = 25,000$ to $70,000$; hole $L/d_h \sim 100$; no cavitation; injection velocity: 10–15 m/s). Pr is the reduced chamber pressure.

author takes these results as indicating a high probability and a strong suggestion for injector hypersensitivity. On the other hand, accepting the proposed hypothesis (see Fig. 3), then one expects a higher level of unsteadiness and sensitivity on the sheet breakup length. Examination of the results in Figs. 7 and 8 is reinforcing. This sheet breakup-length enhanced sensitivity seen in Figs. 7 and 8 is in agreement with the similar trend derived by the hypothesis. This is because it implies elevated sensitivity when the mean length of each (or one of the) circular jet's dark-core zone reaches a critical value ($L_{C,Ph}$), namely the same order as the distance from the hole exit plane to the impinging point. In addition, at a given pressure or included angle the data scatter band shown in Figs. 7 and 8 is also largest at low dn/V values, again and consistently suggesting a more erratic/chaotic dynamic behavior. This is in congruence with the sensitivity trend predictions of the proposed hypothesis. An individual, unaware of the hypothesis proposed here, seeking the causes of this hypersensitivity in Figs. 7 and 8, would also consider searching features arising from each jet and also hole geometrical designs of the impinging jet injector as one top and potential candidate.

Considering what was discussed for the coaxial jet injector, one implication of the hypothesis is that an impinging jet injector engine should be more stable at sufficiently high pressures, such as supercritical conditions. This is because not only the rms of the core length fluctuations declines substantially, but also the length of the core may become adequately shorter than the preimpingement length depending on the geometrical dimensions of the impinger. The changes in the dark-core (breakup) length can also be inferred by examination of Fig. 9, showing a progressive increase in chamber pressure up to a supercritical condition for liquid nitrogen injection into gaseous nitrogen environment with no externally-imposed acoustic field. The long preimpingement length seen along the jet is expected due to L/dn of about 100 which was intentionally designed

to obtain a fully developed condition at the hole exit plane and also to accentuate the effects of chamber pressure on the nature of the impingement. Obviously, shorter dark core is achieved for lower (injector hole) L/dn values used in LRE. Not only the dark core length of each individual jet is reduced as supercritical pressures are approached (as before and expected), but the jet also thickens. The impinger is expected to pass through a situation described in Fig. 3 as chamber pressure is increased. Hypersensitivity is anticipated at that condition according to the hypothesis. Progressive increase of chamber pressure beyond this point sufficiently thickens each jet and shortens the dark core length to a situation where the two dark-core lengths are shorter than the preimpingement distance and a gaslike jet is impinging another gaslike jet with enlarged cross-section areas. Based on the hypothesis proposed here and given that rms of the dark core is much lower at supercritical than subcritical conditions, a more robust (targeting and mixing) and less sensitive impinging jet system would be expected at supercritical chamber pressures. However, it is likely that the dynamic behavior of the potential core plays a somewhat similar role under this latter gaslike condition.

An example is given here to show the feasibility of unexpected dramatic and/or gradual changes in the dark core (or breakup) length leading to a situation described in Fig. 3. The breakup length has been shown to be sensitive to events inside the injector as injection velocity or chamber conditions are changed. For instance, Tamaki et al. [26] recently showed that when cavitation occurs and, if bubbles collapse inside the injector, leading to higher hole exit-plane turbulence levels, it will enhance jet-breakup/atomization and causes a sudden decrease of the breakup length, see Fig. 10. On the other hand when a hydraulic flip is seen, it leads into a sudden increase, or decrease when it disappears, of the breakup length. This is just an example to show that when conditions change causing increases in V in the dn/V stability parameter, it is quite possible that either a gradual or sudden reduction of the dark core (or breakup) length is experienced,

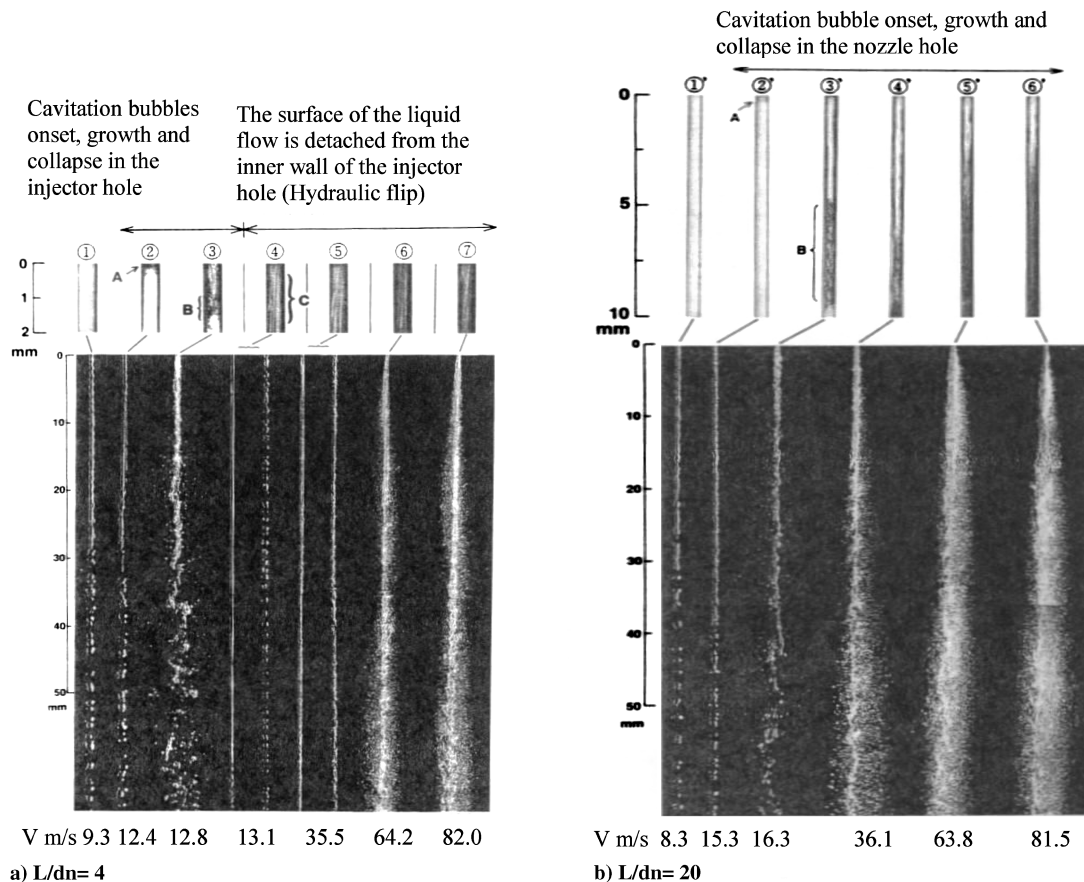


Fig. 10 Internal flow in the nozzle hole and disintegration behavior of the liquid jets (effects of L/dn). The breakup length measured by the Hiroyasu's group as a function of injection velocity is shown. V is injector velocity (Tamaki et al. [26]).

leading to a situation described by the hypothesis causing hypersensitivity of the injector unit to chamber acoustic field oscillations. Obviously, the cavitation and hydraulic flip phenomena depend on the type of the propellant used, injector internal geometry, and operating conditions, compounded by drastic changes in its onset and behavior under transient/unsteady or oscillating operation, which is rarely characterized. Hence, the cavitation state inside the hole under unsteady conditions is unknown and just recently being addresses by the research community. Therefore, not only pre-impingement length and the jet dark-core (breakup) length can approach each other at sufficiently high pressures and velocities, but there are other phenomena, such as cavitation, hydraulic flip, etc., that can act in such a way to bring about injector hypersensitivity of the same nature as that described in Fig. 3.

The hypothesis proposed here has the advantage, simplicity and the beauty as well, of unifying the possible cause of the combustion stability irrespective of the design of the injector at least for the two popular cryogenic impinging and coaxial cases as described above. What remains, amongst others, is to closely examine the historical data on the dynamic characteristics of the dark-core (or breakup) length and width for the circular jets forming the impinging injector for the propellant of interest and under the realistic thrust chamber conditions (which is quite rare or nonexistent) to further substantiate that a critical value, $L_{C,Ph}$, is reached when the onset of instability is detected in an engine. Also, dynamic characterization of each jet forming the impinging injector and when the two jets meet, in the presence of an externally imposed acoustic field, is highly desirable to assess sensitivity of the dark-core or breakup length of the jet to relevant design and operating variables.

Conclusions

In summary, an attempt has been made to portray a fluid dynamical perspective and link a hypothesis proposed here to observations made in cold flow injector studies, subscale fired engines, and full-scale production engines with an aim to offer a sketch of a theory being consistent with most observations pertaining to combustion instability.

Based on the author's previous work on intrinsic sensitivity of the dark-core length in a coaxial jet-like injector in cold sub- and supercritical conditions, it is proposed that a similar phenomenon pertaining to the dark core in impinging jet injectors is to be considered, attempting to offer underlying fluid mechanical reasons for the injector-caused combustion instabilities in LRE. The basic premise here is that when an important dynamic feature, such as the dark-core or breakup zone, of an injector design becomes sufficiently sensitive to thermofluid parameters of its environment, it is highly likely that this could strengthen the feedback link thought to be critical in the amplification process and hence push the system into an unstable operating state. Evidences cited suggest that the enhanced sensitivity of impinging jet injectors to their environment occurs when the mean dark-core or break up length of one or both jets forming the impingement reaches a critical value, being of the same order as the preimpingement length. Feasibility of such a scenario is explored by comparing the range of preimpingement length values for engines and some recently measured dark-core lengths for cryogenic jets at density ratios of interest. It is then hypothesized that the stable-unstable transition boundary in the Hewitt stability plot is when the core length of one or more of the jets of the impinging jet injector becomes comparable to the preimpingement distance. This proposed hypothesis is able to offer a consistent explanation of why an engine design based on impinging jets becomes unstable when Hewitt stability parameter (dn/V) is decreased. While work is needed to make a transition from a hypothesis to an established fact, there is sufficient published information in favor of the hypothesis to make it a strong possibility amongst others previously proposed. Finally, the readers are cautioned that as some atomization results from cold studies are linked to fired sub- and full-scale engines, more targeted investigations guided by the hypothesis on the dynamic behavior of the dark-core length and width in cold and fired coaxial and impinging jet injectors are justified and highly recommended.

Acknowledgments

This work is sponsored by the U.S. Air Force Office of Scientific Research under Mitat Birkan, program manager. The author would like to thank Jay Levin and Doug Talley, U.S. Air Force Research Laboratory, for their continued support of the author's activities in supercritical and combustion instability areas. Additionally, Jennie Paton at U.S. Air Force Research Laboratory library is especially thanked for her valuable efforts on literature search and acquisition. The author also thanks the reviewers for constructive suggestions. Also, constructive comments by Forman A. Williams, Robert Santoro, William A. Sirignano, and Vigor Yang are greatly appreciated.

References

- [1] Harje, T. D., and Reardon, H. F., "Liquid Propellant Rocket Combustion Instability," NASA Rept. NASA SP-194, 1972.
- [2] Yang, V., and Anderson, W. E. (eds.), *Liquid Rocket Engine Combustion Instability*, AIAA Progress in Astronautics and Aeronautics, Vol. 169, AIAA, Washington, D.C., 1995, p. 577.
- [3] Rayleigh, Lord, "The Explanation of Certain Acoustical Phenomena," *Nature*, Vol. 18, No. 455, 1878, pp. 319–321.
- [4] Heidemann, M. F., and Groeneweg, J. F., "Analysis of the Dynamic Response of Liquid Jet Atomization to Acoustic Oscillations," NASA Technical Rept. NASA TN D-5339, 1969.
- [5] Anderson, W. E., Ryan, H. M., and Santoro, R. J., "Combustion Instability Mechanisms in Liquid Rocket Engines Using Impinging Jet Injectors," *31st AIAA/ASME/SAE/ASEE Joint Propulsion Conference and Exhibit*, AIAA Paper 95-2357, 1995.
- [6] Hulka, J., and Hutt, J. J., "Instability Phenomena in Liquid Oxygen/Hydrogen Propellant Rocket Engines," *Liquid Rocket Engine Combustion Instability*, edited by V. Yang, and W. E. Anderson, AIAA Progress in Astronautics and Aeronautics, AIAA, Washington, D.C., 1995, pp. 39–71.
- [7] Kiwata, T., Okajima, A., and Ueno, H., "Effects of Excitation on Plane and Coaxial Jets," *Proceedings of the 3rd Joint ASME/JSME Fluid Engineering Conference*, American Society of Mechanical Engineers, Fairfield, NJ, 1999.
- [8] Chehroudi, B., and Talley, D., "Interaction of Acoustic Waves with a Cryogenic Nitrogen Jet at Sub- and Supercritical Pressures," *40th AIAA Aerospace Sciences Meeting & Exhibit*, AIAA Paper 2002-0342, 2002.
- [9] Davis, D. W., and Chehroudi, B., "Shear-Coaxial Jets from a Rocket-Like Injector in a Transverse Acoustic Field at High Pressures," *44th AIAA Aerospace Sciences Meeting and Exhibit*, AIAA Paper No. 2006-0758, 2006.
- [10] Davis, D. W., and Chehroudi, B., "Measurements in an Acoustically-Driven Coaxial Jet under Supercritical Conditions," *Journal of Propulsion and Power*, Vol. 23, No. 2, 2007 pp. 364–374. doi:10.2514/1.19340
- [11] Davis, D. W., "On the Behavior of a Shear-Coaxial Jet, Spanning Sub- to Super-critical Pressures, With and Without an Externally Imposed Transverse Acoustic Field," Ph.D. Thesis, Department of Mechanical and Nuclear Engineering, The Pennsylvania State Univ., 2006.
- [12] Leyva, I., Chehroudi, B., and Talley, D., "Dark Core Analysis of Coaxial Injectors at Sub-, Near-, and Supercritical Conditions in a Transverse Acoustic Field," *43rd AIAA/ASME/SAE/ASEE Joint Propulsion Conference and Exhibit*, AIAA Paper 2007-5456, Cincinnati, OH, July 8–11, 2007.
- [13] Woodward, R. D., Sibtos, P., Farhangi, S., Jensen, G. E., and Santoro, R. J., "LOX/GH2 Shear Coaxial Injector Atomization Studies: Effect of Recess and Non-Concentricity," *45th AIAA Aerospace Sciences Meeting and Exhibit*, AIAA Paper 2007-571, 2007.
- [14] Yang, B., Francesco, C., Wang, L., and Oschwald, M., "Experimental Investigation of reactive Liquid Oxygen/CH4 Coaxial Sprays," *Journal of Propulsion and Power*, Vol. 23, No. 4 2007, pp. 763–771. doi:10.2514/1.26538
- [15] Smith, J. J., Bechle, M., Suslov, D., Oschwald, M., Haiden, O. J., and Schneider, G. M., "High Pressure LOX/H2 Combustion and Flame Dynamics Preliminary Results," *40th AIAA/ASME/SAE/ASEE Joint Propulsion Conference & Exhibit*, AIAA Paper 2004-3376, 2004.
- [16] Chehroudi, B., Chen, S. H., Bracco, F. V., and Onuma, Y., "On the Intact Core of Full-Cone Sprays, Society of Automotive Engineers," *1985 Congress and Exposition*, Society of Automotive Engineers Paper 850126, 1985.
- [17] Kim, J. S., and Williams, F. A., "Acoustic-Instability Boundaries in

- Liquid Propellant Rockets: Theoretical Explanation of Empirical Correlation," *Journal of Propulsion and Power*, Vol. 12, No. 3, 1996, pp. 621–624.
doi:10.2514/3.24081
- [18] Chao, C-C., and Heister, S. D., "Contributions of Atomization to F-1 Engine Combustion Instabilities," *Engineering Analysis with Boundary Elements*, Vol. 28, No. 9, 2004, pp. 1045–1053.
doi:10.1016/j.enganabound.2004.04.003
- [19] Reitz, R. D., and Bracco, F. V., "Mechanisms of Breakup of Round Liquid Jets," *The Encyclopedia of Fluid Mechanics*, Vol. 3, edited by N. Chermisnoff, Gulf Publishing, New Jersey, 1986, pp. 233–249, Chap. 10.
- [20] Hiroyasu, "Spray Breakup Mechanism from the Hole-Type Nozzle and its Applications," *Atomization and Sprays*, Vol. 10, Nos. 3–5, 2000, pp. 511–527.
- [21] Ryan, H. M., Anderson, W. E., Pal, S., and Santoro, R. J., "Atomization Characteristics of Impinging Liquid Jets," *31st Aerospace Sciences Meeting and Exhibit*, AIAA Paper 93-0230, 1993.
- [22] JANNAF Rocket Engine Performance Methodology Sample Cases, CPIA Publication 245 and 246 supplements, Johns Hopkins Univ., Applied Physics Lab., April 1975.
- [23] Chehroudi, B., Talley, D., Mayer, W., Branam, R., Smith, J. J., Schik, A., and Oschwald, M., "Understanding Injection Into High Pressure Supercritical Environment," *Fifth International Symposium on Liquid Space Propulsion, Long Life Combustion Devices Technology*, NASA Marshall Space Flight Center, Chattanooga, TN, 2003.
- [24] Oschwald, M., Smith, J. J., Branam, R., Hussong, J. R., Schik, A., Chehroudi, B., and Talley, D., "Injection of Fluids into Supercritical Environments," *Combustion Science and Technology*, Vol. 178, Nos. 1–3, Jan. 2006, pp. 49–100(52).
doi:10.1080/00102200500292464
- [25] Oefelein, J. C., and Yang, V., "Comprehensive Review of Liquid Propellant Combustion Instabilities in F-1 Engines," *Journal of Propulsion and Power*, Vol. 9, No. 5, Sept–Oct., 1993, pp. 657–677.
doi:10.2514/3.23674
- [26] Tamaki, N., Shimizu, M., Nishida, K., and Hiroyasu, H., "Effects of Cavitation and Internal Flow on Atomization of a Liquid Jet," *Atomization and Sprays*, Vol. 8, No. 2, 1998, pp. 179–197.

V. Yang
Past Editor-in-Chief

Non-Reacting Shear Coaxial Jets in an Acoustic Field

Current and former students and staff researchers:

Sophonias Teshome, Juan Rodriguez, Jeff Graham

Advisors:

Ivett A Leyva, Doug Talley, Ann Karagozian

Air Force Research Lab, UCLA

15-16 June 2011

London, UK



Distribution A: Approved for Public Release; Distribution Unlimited. PA #11108.



Statement of need

- **Modern rockets operate at supercritical pressures with respect to the propellants**
 - **Need to understand mixing beyond liquid, gas states**
- **Shear coaxial injectors are a common choice for cryogenic liquid rocket engines**
- **Interactions of transverse acoustics with injector's own modes and mixing needs to be understood for combustion instability**
 - **Need to understand differences in response to pressure and velocity nodes**
- **Understand what non-dimensional numbers capture the mixing of typical injectors**
- **Characterize how geometry affects mixing**



Distribution A: Approved for Public Release; Distribution Unlimited



Relevant physics of shear coaxial jets

1. Transverse Acoustic mode from chamber/siren

- $f=f(c, \text{geometry})$

2. Acoustic modes for outer and inner jets

- $f \sim c/2L$ – 2 speeds of sound up and downstream

3. Wake resulting from inner post thickness

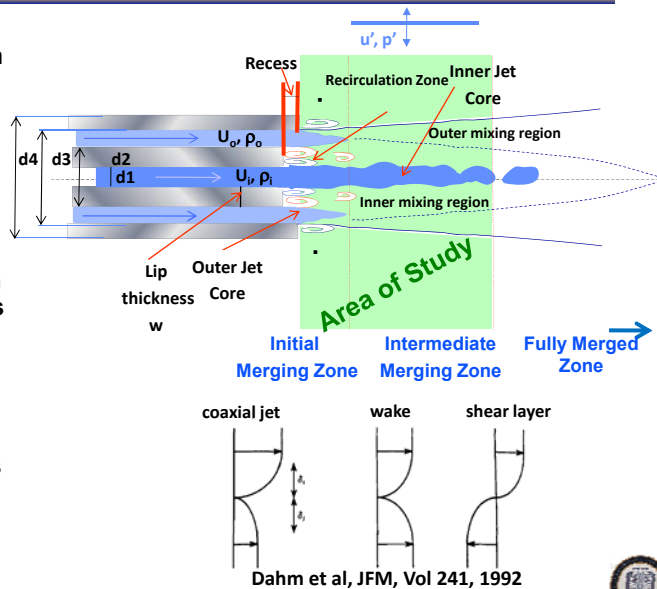
- $St=fw/U_{ch}$

4. Shear layer instabilities

- $St_0=f_0/U_{ch}$

5. Jet preferred modes

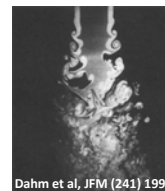
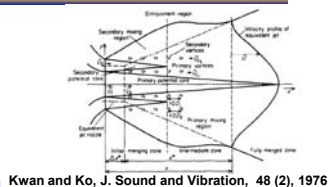
- $St=fD_{ij}/U_{ij}$



Distribution A: Approved for Public Release; Distribution Unlimited

Highlights from previous work on jet instabilities 1/2

- Michalke, 1964
 - Linear stability theory for inviscid instability of the hyperbolic tangent velocity profile, $St_0 \sim f_0/U \sim 0.033$
- Crow and Champagne, 1971
 - Single jet preferred mode, $St_0 = f_0/U \sim 0.3$
- Gutmark and Ho, 1983
 - Collects previous results on jet preferred mode, St_0 has a range from $\sim 0.24-0.64$
- Ko et al, 1976-1989
 - Some of earliest detailed description of near field mixing for coaxial jets
- Boldman et al, 1975
 - Experimental and theoretical analysis for mixing of two streams with different velocities – points out different vortex interactions
- Wicker and Eaton, 1994
 - Forces inner and outer jets independently – observes vortex growth
- Dahm et al, 1992
 - Points out importance of layer thickness and velocity defect on shear layers, seminal pictures of different instabilities

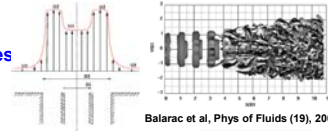


Distribution A: Approved for Public Release; Distribution Unlimited

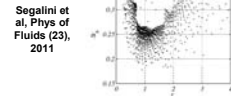
Highlights from previous work 2/2

5

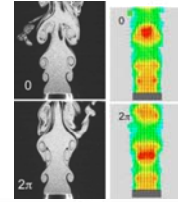
- Balarac, da Silva, Metais et al (2003, 2007)
 - DNS analysis of coaxial jets - same density, top-hat profiles
 - Consider two shear layers, study effect of R
 - Consider axisymmetric and azimuthal excitation
- Buresti, Talamelli, Petagna (1994, 1998)
 - Air jets, same density, top-hat profile, $St_{do}=fd_o/U_{o_j}\sim 0.3$ to 1, function of x/D_j
- Segalini, Talamelli, et al (2006, 2011)
 - Air jets, same density, top-hat profile, $St_{b(lip)}=fb(lip)/U_{average}$
- Birbaud, Ducruix, Durox, Candel (2006-2007)
 - Single air jets, low Re, laminar, top-hat profile, subjected to acoustic modulation
 - Systematic study of effect of modulation in terms of St_d , St_θ
- Tshohas, Canino, Heister (2004, 2009)
 - 2D unsteady CFD for LOX/H₂ elements but non-reacting
 - Unforced behavior, found $St_{lip}=fd_{lox}/U_{lox}\sim 0.10-0.25$
- Richecoeur et al (Candel's group), 2006
 - Forced transverse acoustic excitation of flames



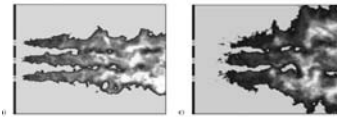
Balarac et al, Phys of Fluids (19), 2007



Segalini et al, Phys of Fluids (23), 2011



Birbaud et al, Phys of Fluids (19), 2007



Richecoeur et al, JPP (22) No 4, 2006



Distribution A: Approved for Public Release; Distribution Unlimited



Relevant variables for cold-flow studies

6

Geometry	Acoustics	Recess	Phase	VR	J	Coupling
Single Jet	On/Off	N/A	v' max	N/A		No
LAR_thickLip (injector 1)	Off P' max U' max	1/2D1	2-phase P<Pc P>Pc T>Tc T<Tc	0.1-20 0.1-20		No
SAR_thinLip (injector 2)		1/2D1 D1 0				Yes& No
SAR_thickLip (injector 3)		0				
LAR_thinLip (injector 4)		0				

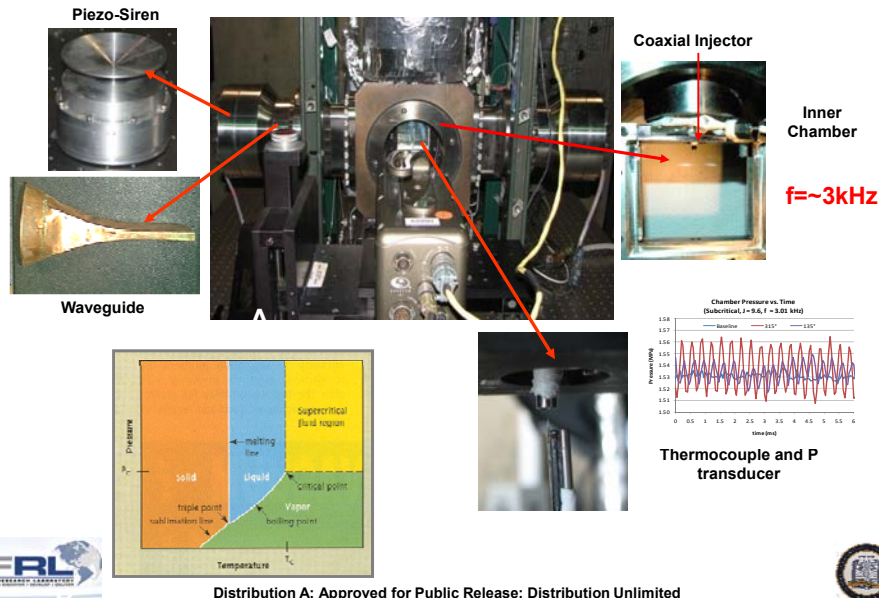


Distribution A: Approved for Public Release; Distribution Unlimited



Experimental setup – EC-4

7

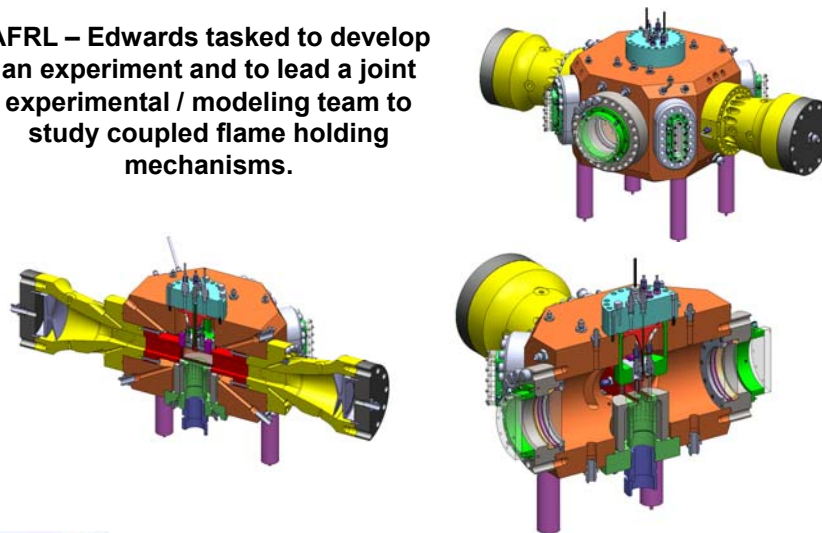


Distribution A: Approved for Public Release; Distribution Unlimited

New Combustion Chamber

8

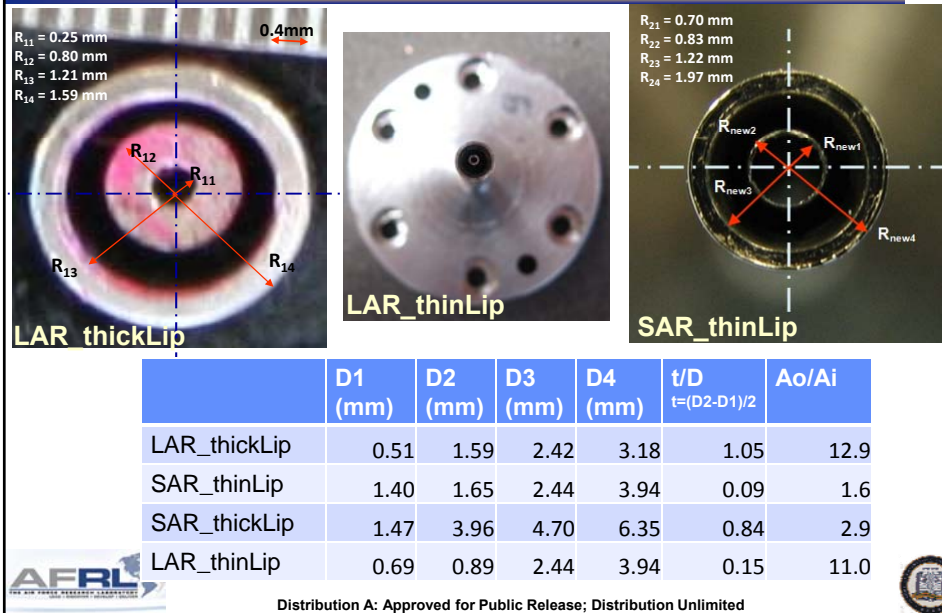
AFRL – Edwards tasked to develop an experiment and to lead a joint experimental / modeling team to study coupled flame holding mechanisms.



Distribution A: Approved for Public Release; Distribution Unlimited

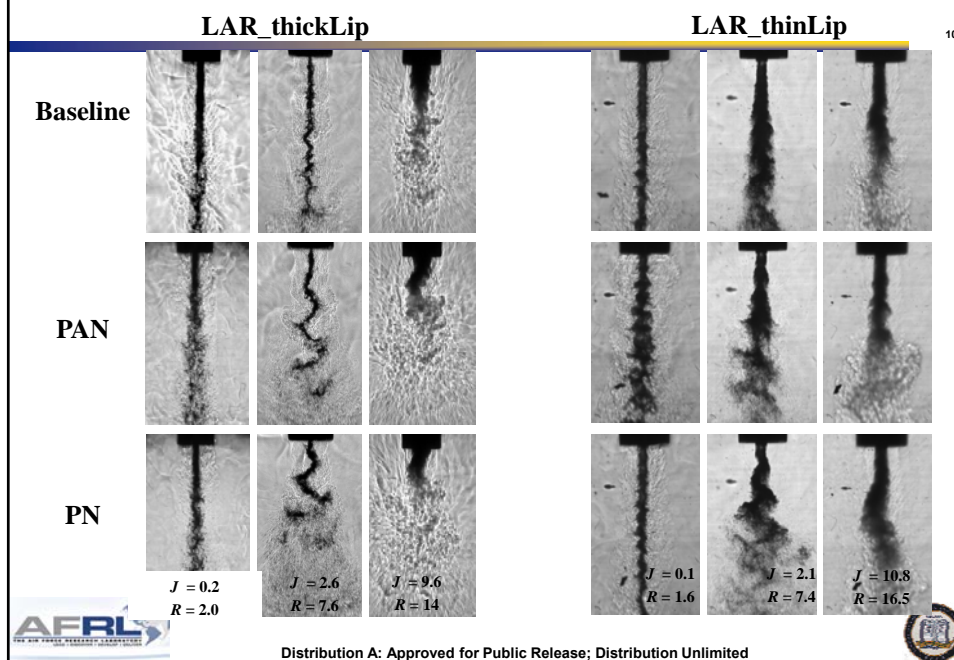
Geometries for present study

9

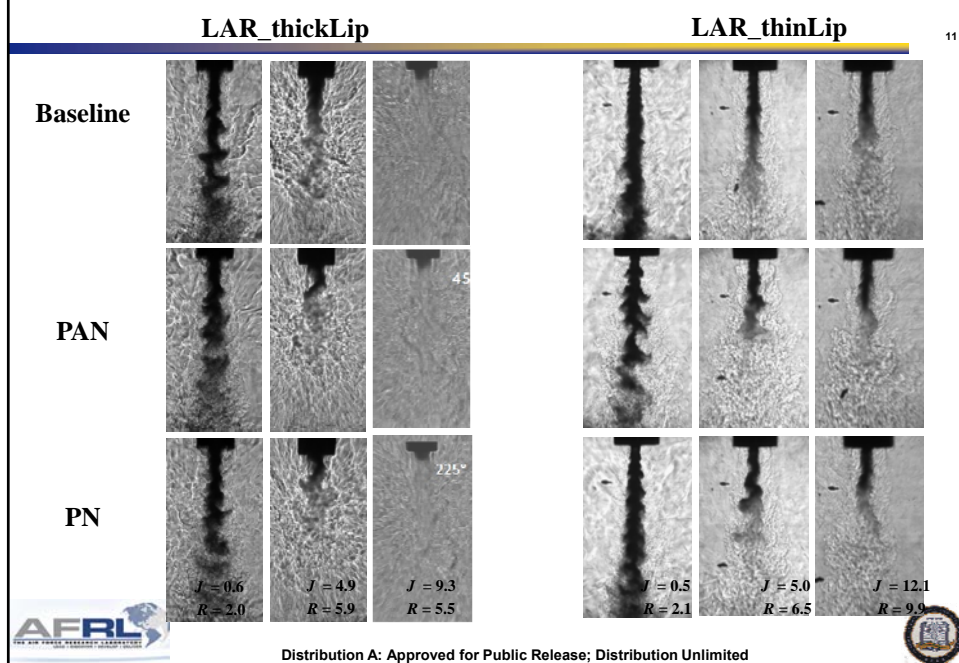


Sub-Critical Pressure: Two Geometries

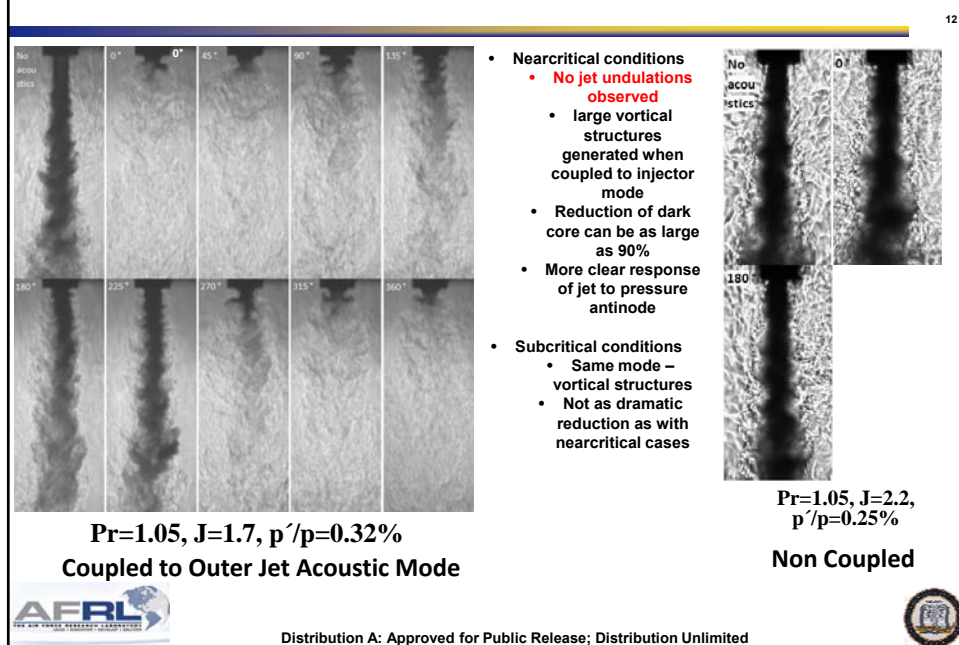
10



Near-Critical Pressure: Two geometries

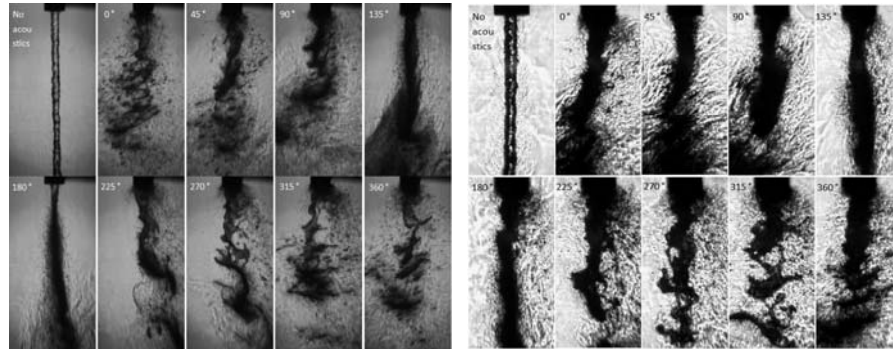


SAR_thinLip



Effect of Recess: SAR_ThinLip; Pr=0.45, J~0.09

13



Flush inner post, $J=0.09$, $p'/p=0.45\%$

Recessed inner post, $J=0.089$, $p'/p=0.60\%$

Qualitatively similar at very low J values



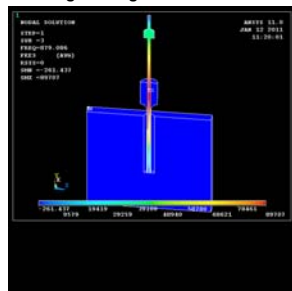
Distribution A: Approved for Public Release; Distribution Unlimited



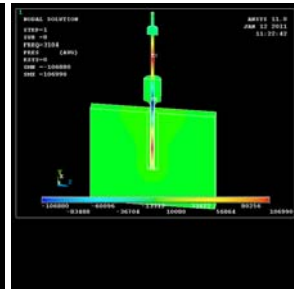
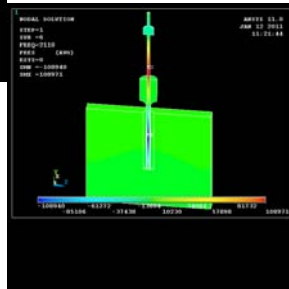
Acoustic Analysis for Injectors

14

In collaboration
with Jeff Muss and
Rory Davis, Sierra
Engineering



Have more accurately
computed the acoustic
modes for the inner and
outer jets for constant and
linearly varying
temperatures for
subcritical and
supercritical pressures

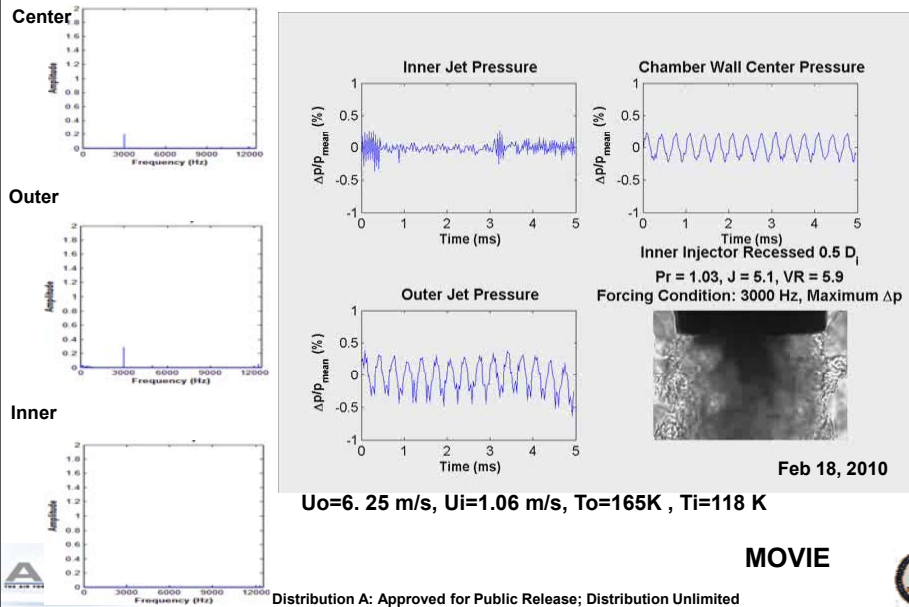


Distribution A: Approved for Public Release; Distribution Unlimited



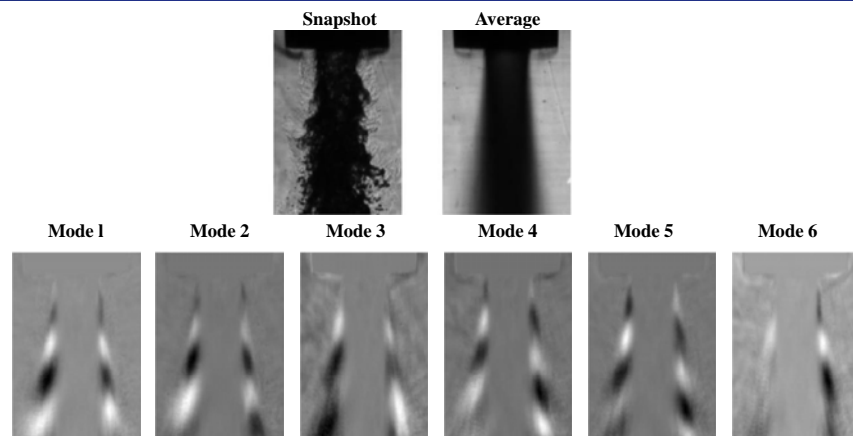
Synchronized p' and images: Pr=1.03, J=5.1, VR=5.9

15



Case I: Baseline Flow

16



Case	P_R	$T_{R,OJ}$	$T_{R,IJ}$	R	J	f (kHz)
I	0.44	1.19	0.84	5.8	2.0	2.96

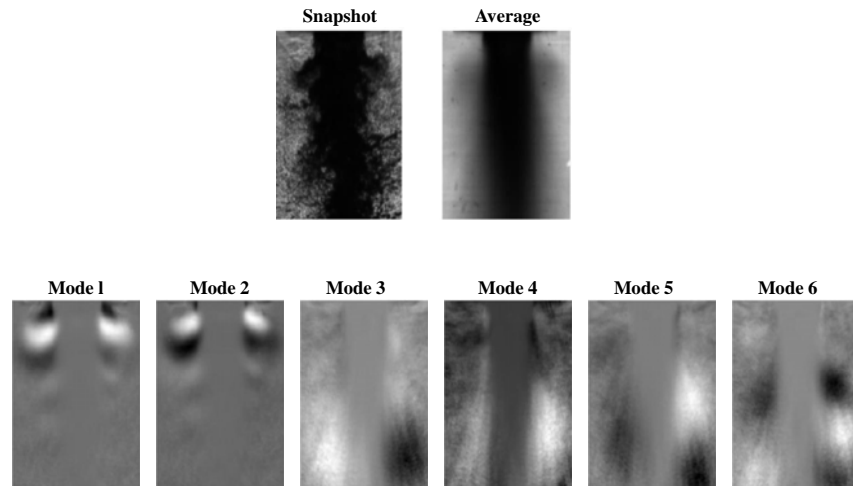


Distribution A: Approved for Public Release; Distribution Unlimited



Case I: Acoustically Forced Flow

17



Distribution A: Approved for Public Release; Distribution Unlimited

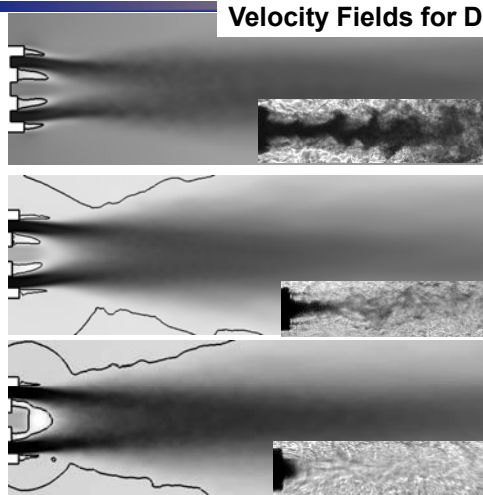


Collaboration with ECP: Thomas Schmitt, Juan Rodriguez
(AFRL post-doc), Sebastien Candel, Ivett Leyva

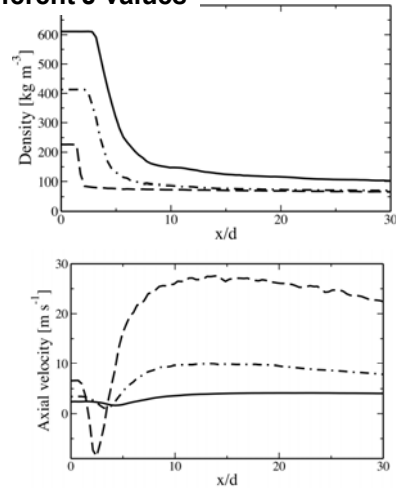


18

Velocity Fields for Different J values



Longitudinal slice of axial velocity. White: minimum; black: maximum.
Dark line indicates iso-contour of zero axial velocity. Top: $J = 1.1$; middle: $J = 3.0$; bottom: $J = 9.3$.



Top: centerline profile of density; bottom: centerline profile of velocity. Dark line: $J = 1.1$; dash point line: $J = 3.0$; dashed line: $J = 9.3$.



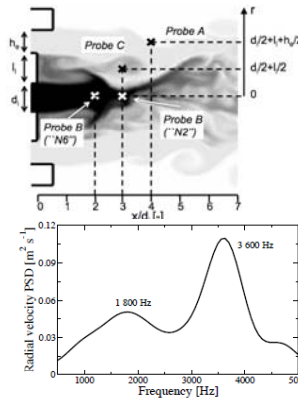
Distribution A: Approved for Public Release; Distribution Unlimited

Fundamental frequencies for baseline conditions

19

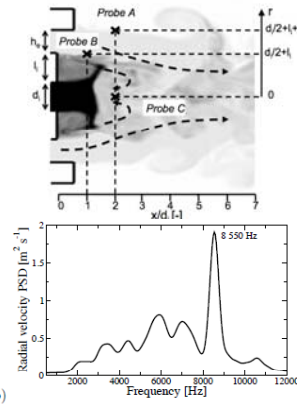
Case "N6"
($J=3.05$)
Density
distribution
(white: 60
 kg/m^3 ;
black: 410
 kg/m^3 ;
logarithmic
scale).

OUTER
JET
 $J=1.05$



Case "N8"
($J=9.3$)
Density
distribution
(white: 60 kg/m^3 ;
black: maximum;
logarithmic
scale).

OUTER
JET
 $J=3.05$



Case	St^* (probe A)	St^l (probe B)	St^l (probe C)
N2	0.25	0.34	0.15
N6	0.25	0.26	0.14



Found relevant St numbers for our configurations

Distribution A: Approved for Public Release; Distribution Unlimited



Conclusions

20

- For LARthickLip
 - Found bending mode with largest effect at velocity antinodes
 - The reduction on the dark core length was greatest for a medium J range
 - For near critical pressures, the collaboration with ECP determined relevant St for our injector configuration and was able to capture qualitative behavior of natural and excited jets
- For SARthinLip
 - Did not see undulation mode for conditions studied
 - Saw vortex roll-up and puffing occurring over entire J range (0.09-21) tested – most predominantly at pressure nodes and most likely associated with acoustic mode of outer jet
 - Vortex roll up and puffing is independent of injector recess configuration
- For LARthinLip
 - Sees both undulation and vortex roll-up modes depending on the acoustic frequency
- Synchronized measurements for p' and jet images - correlate structures observed to p' amplitudes
- Initial POD analysis recovers features seen in movies – next will be to compute convective velocities of structures observed



Distribution A: Approved for Public Release; Distribution Unlimited



BACKUP MATERIAL

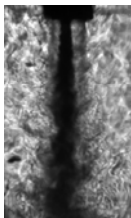


Distribution A: Approved for Public Release; Distribution Unlimited

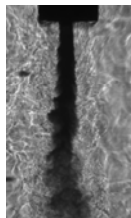


Effect of R on L/D for a given J

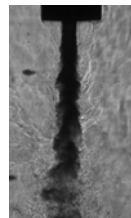
Injector IV: **Constant J , Varying R**



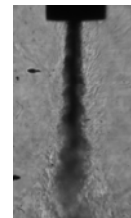
$J = 2.0$
 $R = 3.0$
 $L/D_1 = 17.9$



$J = 2.0$
 $R = 3.5$
 $L/D_1 = 12.1$



$J = 2.0$
 $R = 4.0$
 $L/D_1 = 11.6$



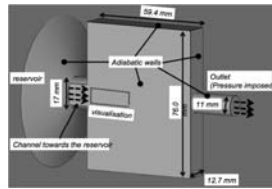
$J = 2.1$
 $R = 4.3$
 $L/D_1 = 10.1$



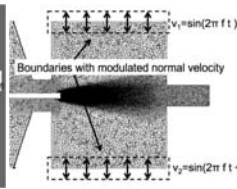
Distribution A: Approved for Public Release; Distribution Unlimited



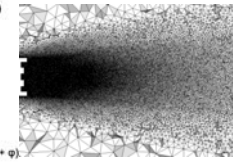
Collaboration with ECP: Grid and Mesh



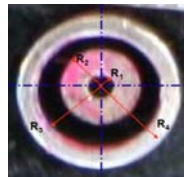
3D visualization of reservoir



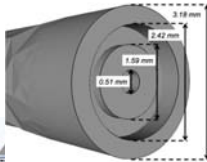
Longitudinal cut of domain with the BC's



Mesh detail near the injector



Experimental Injector



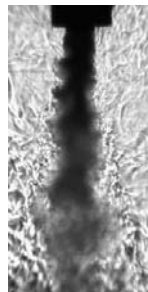
CFD Injector

- **Solver: AVBP – state of the art LES code**
 - With real fluid properties to tackle supercritical fluids
- **Mesh: 2 100 000 nodes/10 000 000 tetrahedra**
 - Highly refined near the injector (0.032 mm on a distance of 10 inner jet diameters)
- **CPU hours on Europe SuperComputer Center: 100,000**

Distribution A: Approved for Public Release; Distribution Unlimited



Effect of Temperature on L/D for a given J

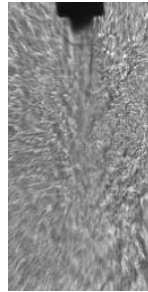


J = 9.4 R=9.9

109K/203K

Ui=0.93/9.2m/s

SAR_thinLip



J = 9.4 R=9.9

128K/192K

Ui=6.6 /36.2m/s

LAR_thickLip



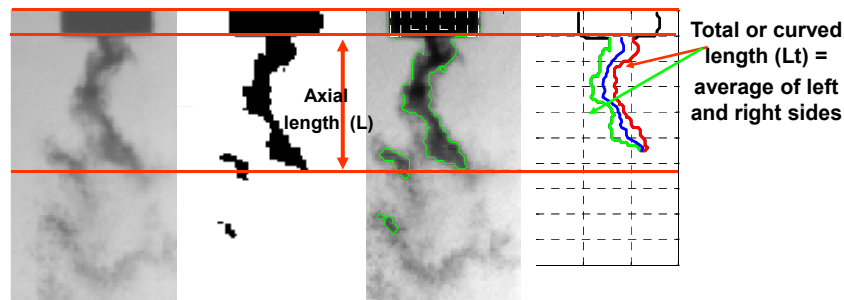
Flow Structure Comparison

25

Date & Case	F_r (kHz)	P_r (MPa)	T_{max} (K)	T_{min} (K)	u_{max} (m/s)	u_{min} (m/s)	density ratio	VR	λ	σ_j mode match	P_{core}/P_r (%)	P_{core}/P_{core} (%)	P_{core}/P_{core} (%)	Structure Type	
Graham $R_{max} = 0$															
ShC1 04May09 c1	3.04	1.49	207	106	1.4	0.87	0.036	1.5	0.09	Y up	0.68	13.47	187.21	large ij vortex roll up (puffs), intermittent penetration of ij	
ShC2 04May09 c2	2.96	1.5	180	110	5.7	0.97	0.040	2.8	0.78	Y down	0.68	10.16	198.33	med ij vortex roll up @ ~2800 Hz, no penetration of ij	
ShC3 23Apr09 c2	2.96	1.5	150	106	5.6	0.94	0.057	5.8	1.03	Y up	1.06	21.24	60.55	large ij vortex roll up at ~2857 Hz	
ShC7 22Apr09 c1	3.04	1.49	188	110	14	0.98	0.045	14.5	0.00	Y up/down	0.81	3.75	81.47	large ij vortex roll up @ ~2857 Hz	
ShC8 23Apr09 c1	3.04	1.5	170	109	15	0.94	0.050	16.0	0.25	N	1.13	3.37	55.84	large ij vortex roll up @ ~2857 Hz, @ tips ij vortices	
ShC9 22Apr09 c2	2.96	1.5	187	110	17.4	0.99	0.095	17.5	0.90	Y up	1.31	1.96	39.22	large ij vortex roll up downstream, large ij roll up at exit	
ShC10 23Apr09 c3	3.06	1.5	178	110	21.51	0.99	0.048	21.5	21.03	N	0.56	13.32	5.15	med ij vortex roll up downstream	
NC1 05May09 c2	3.09	3.57	176	120	5.7	1.0	0.140	5.6	1.92	Y up	0.85	4.96	72.69	large ij vortex roll up, pinched off	
NC2 05May09 c3	3.06	3.57	186	122	5.7	1.2	0.136	5.2	3.07	Y up/down	0.66	2.36	64.30	large ij vortex roll up	
NC3 30Apr09 c1	3.02	3.58	209	112	6.1	1.0	0.097	6.0	3.92	N	0.20	14.63	30.67	minimal ij disturbance	
NC4 27Apr09 c2	2.98	3.57	181	112	9	0.98	0.118	9.2	9.92	Y up/down	0.33	5.29	96.91	large ij vortex roll up	
NC5 27Apr09 c3	3.05	3.57	183	113	13	0.98	0.118	13.0	20.69	Y up	0.31	13.95	51.82	large ij vortex roll up downstream	
Rodriguez $R_{max} = 0.50$															
ShC1 06Nov08 c1	3.01	1.48	199	105	1.4	0.9	0.040	1.5	0.09	Y down	0.38	3.29	326.90	large ij vortex roll up (puffs), intact core flow	
ShC2 07Nov08 c1	2.96	1.49	197	106	3	0.9	0.039	1.3	0.43	Y down	0.62	4.30	155.04	large ij vortex roll up (puffs), no intact core	
ShC3 10Nov08 c1	2.97	1.49	193	109	6.6	1.0	0.042	6.9	2.01	Y up/down	0.58	3.77	117.85	large ij vortex roll up	
ShC4 10Nov08 c2	3.04	1.49	189	110	8.5	0.97	0.045	8.7	1.40	Y up/down	0.85	1.40	65.43	large ij vortex roll up, pinched off	
ShC5 10Nov08 c3	3.02	1.49	184	110	10	0.97	0.043	11.0	5.20	Y up/down	1.18	2.01	49.59	large ij vortex roll up	
ShC6 12Nov08 c1	2.96	1.49	193	108	13.0	0.9	0.040	14.0	1.80	Y down	0.61	1.18	113.80	large ij vortex roll up	
ShC7 12Nov08 c2	2.92	1.49	194	108	16	0.9	0.042	17.0	12.00	Y down	0.59	1.09	107.52	large ij vortex roll up	
ShC8 12Nov08 c3	2.9	1.48	201	109	20	1.0	0.041	21.0	18.00	N	0.51	4.89	102.90	large ij vortex roll up downstream	
NC1 18Nov08 c1	2.98	3.56	213	109	2.2	0.93	0.095	2.3	0.50	N	0.75	21.49	72.45	minimal ij disturbance (small pulsing)	
NC2 18Nov08 c2	3.06	3.56	209	109	3	0.93	0.095	3.2	0.97	Y up	0.55	10.69	55.31	minimal ij disturbance (small pulsing)	
NC3 30Dec08 c1	3	3.58	198	108	4.3	0.92	0.100	4.7	2.01	Y down	0.21	9.83	96.60	small ij shedding	
NC4 30Dec08 c3	3.11	3.58	199	109	6.3	0.93	0.102	6.7	1.60	Y up/down	0.35	5.57	105.82	med ij vortex roll up, no vortex growth	
NC5 30Dec08 c4	3.07	3.58	203	109	9.2	0.93	0.096	9.9	9.40	Y up/down	0.41	3.13	87.66	large ij vortex roll up downstream	
NC6 30Dec08 c5	3.09	3.56	207	111	13	0.95	0.097	14.0	19.00	Y down	0.42	2.83	86.32	med ij vortex roll up	
ShC1 30Dec08 c2	3.11	4.95	212	111	4.1	0.93	0.134	4.4	2.60	Y up	0.40	17.18	53.55	small ij vortex roll up	
Teshome $R_{max} = 0.5$															
NC 23-Mar-10 c1	3.10	3.51	160	121	3.33	1.09	0.164	3.1	1.53	N	0.77	5.54	20.15	small ij vortex roll up	
NC 18-Feb-10	3.02	3.40	165	118	6.26	1.08	0.146	5.9	1.07	N	0.19	17.14	169.82	med ij vortex roll up, @ amplification	
NC 26-Mar-10	3.05	3.52	184	129	32.97	8.50	0.389	3.9	5.86	Y up/down	0.69	19.31	43.52	laterally undulating jet, ejection of mass, ij vortex roll up downstream	
Teshome $R_{max} = 0.625$															
NC 03-Aug-10 c1	3.09	4	3.56	158	126	2.5	2.23	0.207	1.1	0.26	N	0.60	7.93	18.18	small structures shed from the U at exit plane
NC 22-Jul-10 c1	3.1	3.52	148	123	3.39	1.93	0.203	1.8	0.63	N	0.31	37.60	14.59	not so organized structures shed from ij exit plane	
NC 30-June-10 c1	3.02	3.49	161	117	21.3	3.56	0.150	6.0	5.56	N	0.38	4.44	9.80	minimal ij disturbance	
NC 21-June-10 c1	3.08	3.52	191	130	4.74	1.26	0.393	3.8	8.66	Y up/down	0.24	42.63	35.90	large ij vortex roll up	
NC 05-May-10 c1	3.13	3.80	193	130	34.51	8.59	0.375	4.0	6.05	Y down				laterally undulating, ij disturbance	

Dark-Core Length

26



$P = 1.50$ MPa ; $P_r = 0.44$; $VR = 7.50$; $J = 2.64$; acoustic field on

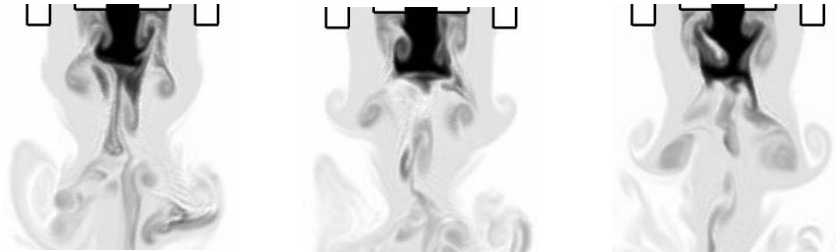
- Threshold Images based on Otsu's method (N. Otsu, "A Threshold Selection Method from Gray-Level Histograms," IEEE Transactions on Systems, Man, and Cybernetics, vol. 9, no. 1, pp. 62-66, 1979.)
- Accounts for variability from image to image (including d1 the parameter by which the jet is normalized)

Distribution A: Approved for Public Release; Distribution Unlimited

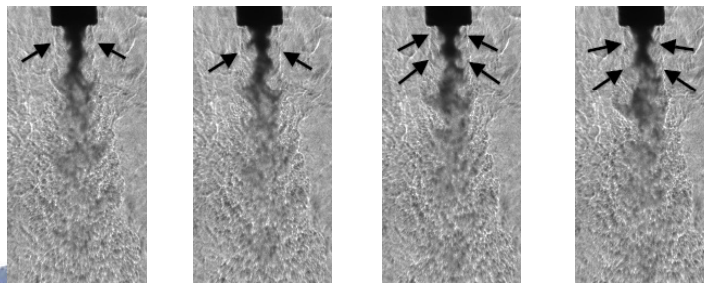
Acoustic Forcing Results



27



Instantaneous images of the simulation of an acoustic case with the injector at a pressure antinode for a $J = 3.0$

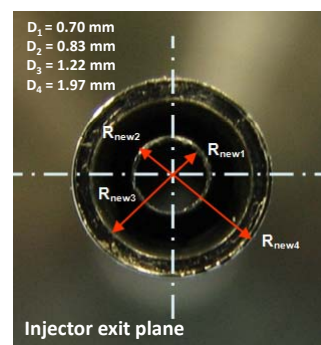
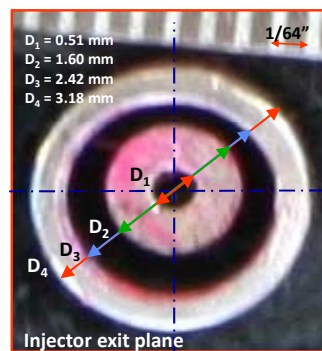


Instantaneous images of an experimental acoustic case with the injector at a pressure antinode for a $J = 2.9$

Distribution A: Approved for public release; distribution unlimited



28

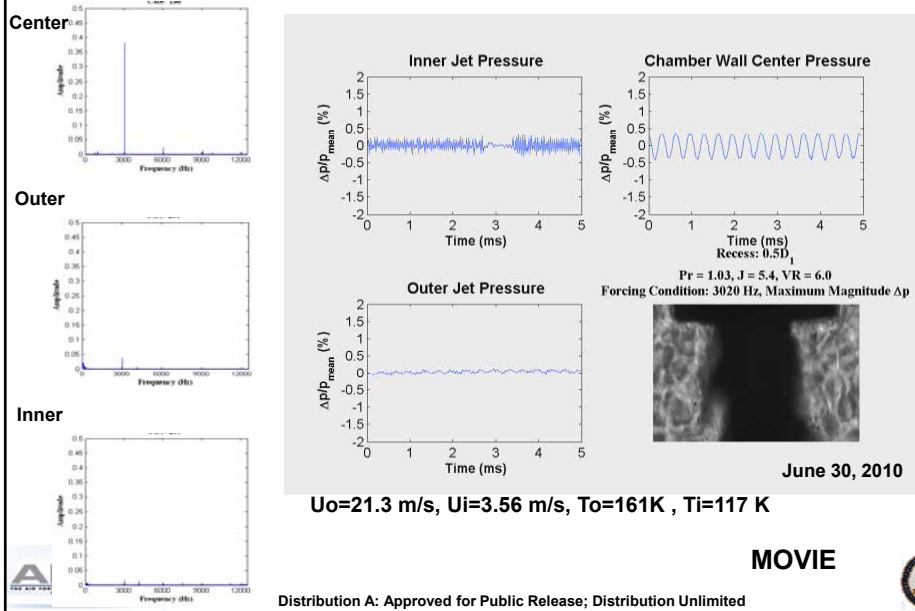


Distribution A: Approved for Public Release; Distribution Unlimited



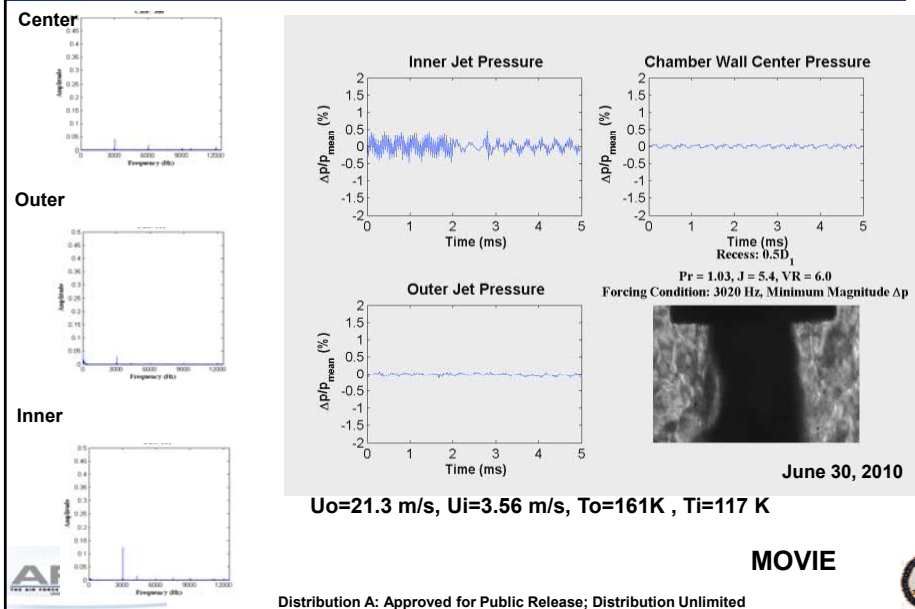
Synchronized p' and images: Pr=1.03, J=5.4, VR=6.0

29



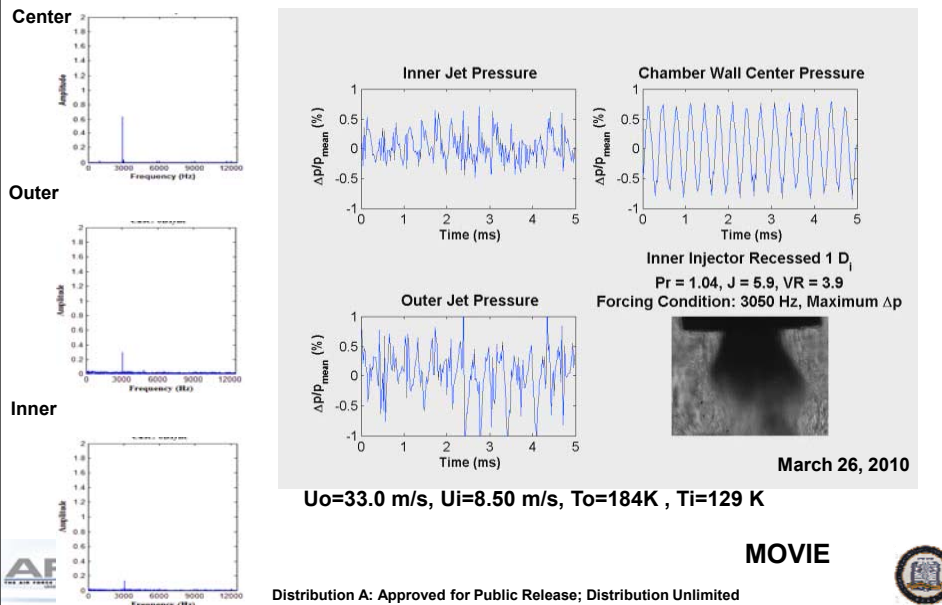
Synchronized p' and images: Pr=1.03, J=5.4, VR=6.0

30



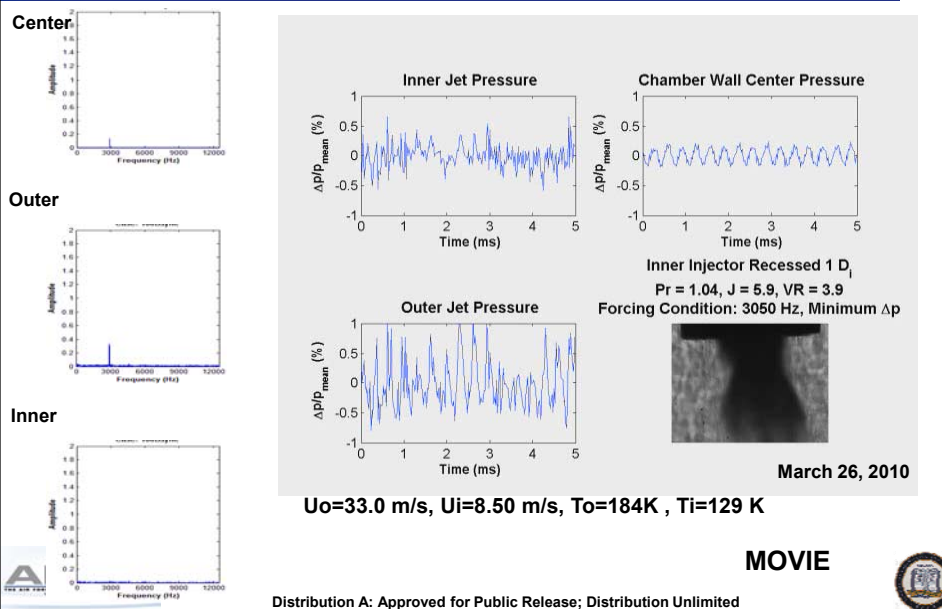
Synchronized p' and images: Pr=1.03, J=5.9, VR=3.9

31



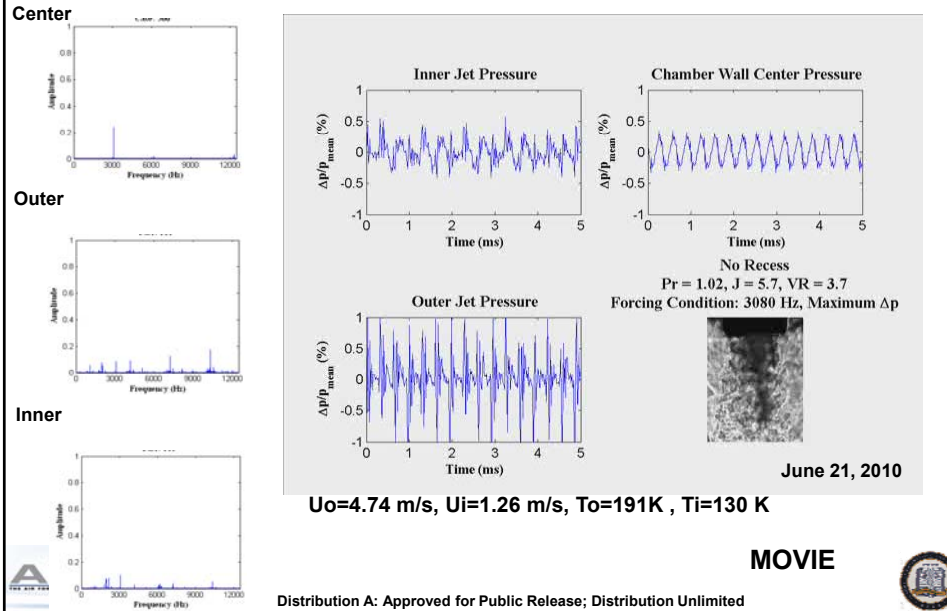
Synchronized p' and images: Pr=1.03, J=5.9, VR=3.9

32



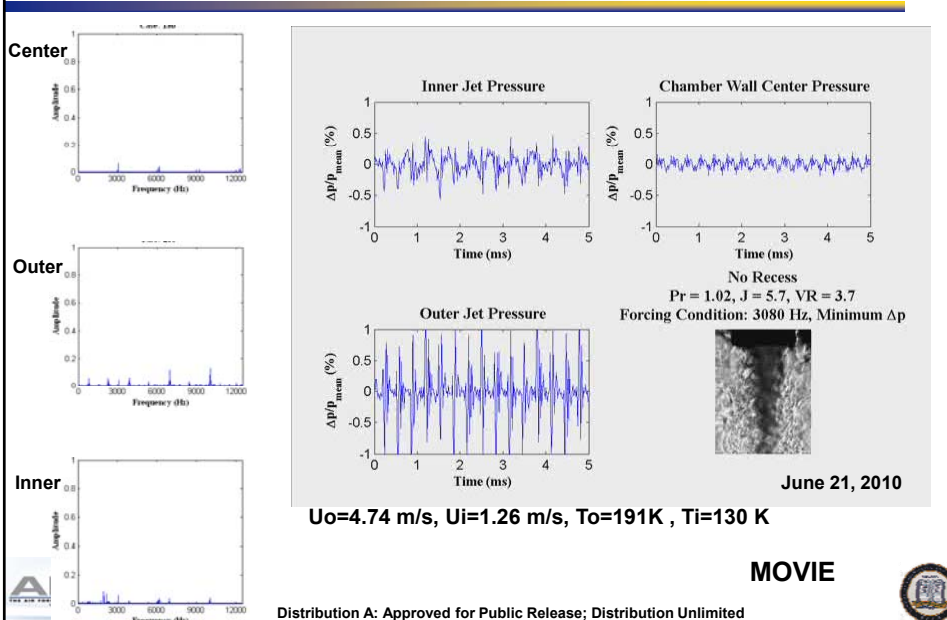
Synchronized p' and images: Pr=1.02, J=5.7, VR=3.8

33



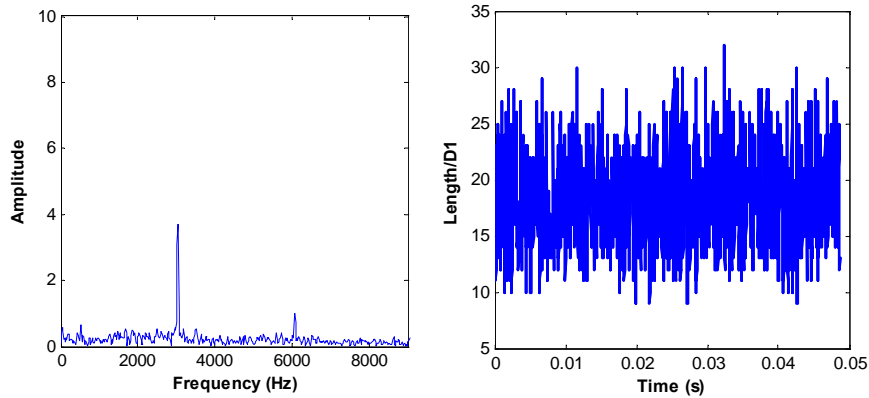
Synchronized p' and images: Pr=1.02, J=5.7, VR=3.8

34



Typical FFT of Dark Core Length

35



Sampling Frequency=41kHz, Driving frequency=3.05kHz,
Pch=3.5MPa; Pr=1.03; VR=2.68, MR=2.27,



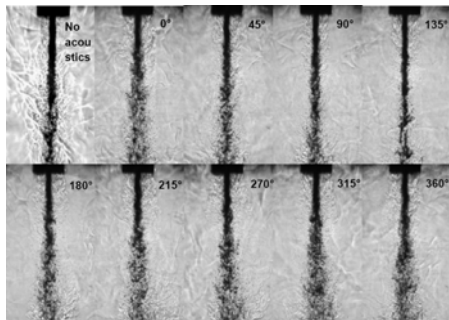
Distribution A: Approved for Public Release; Distribution Unlimited



Subcritical Low J

36

$P_{\text{chamber}} = 1.5 \text{ MPa (Pr = 0.44)}$



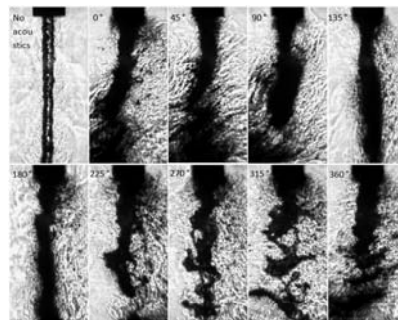
$J = 0.17$

VR =

$\Delta p_{\text{peak-to-peak}} / p_{\text{chamber}} =$

$\dot{m}_{\text{outer}} / \dot{m}_{\text{inner}} =$

thick inner post injector



$J = 0.089$ with thin inner post injector

Negligible effect vs. violent destruction of the jet



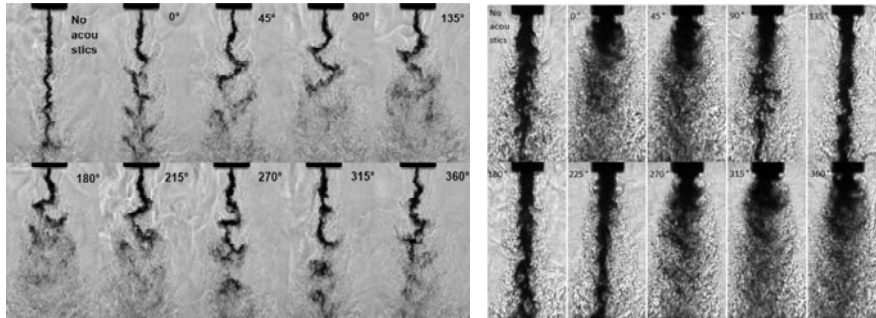
Distribution A: Approved for Public Release; Distribution Unlimited



Subcritical Moderate J

37

$$P_{\text{chamber}} = 1.5 \text{ MPa (Pr = 0.44)}$$



J = 2.6 with thick inner post injector

J = 2.0 with thin inner post injector

Bending vs. vortical structures with fine atomization



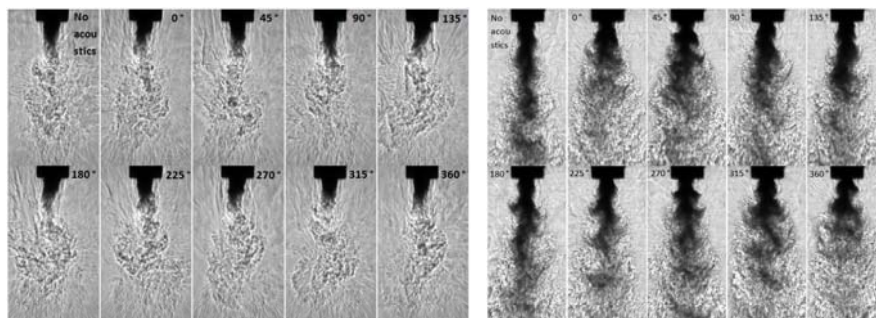
Distribution A: Approved for Public Release; Distribution Unlimited



Subcritical Large J

38

$$P_{\text{chamber}} = 1.5 \text{ MPa (Pr = 0.44)}$$



J = 23 with thick inner post injector

J = 18 with thin inner post injector

Two different mixing mechanisms for similar large J values



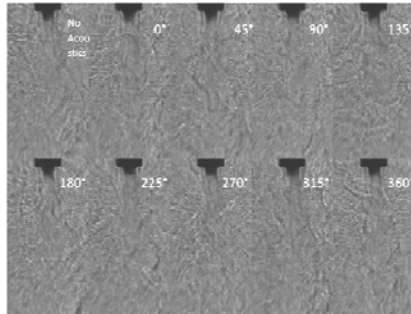
Distribution A: Approved for Public Release; Distribution Unlimited



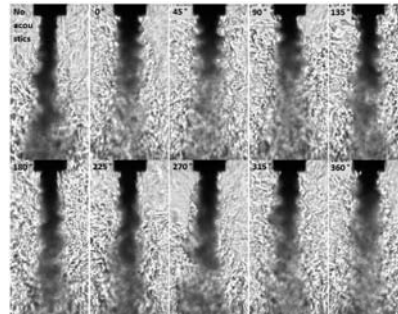
Nearcritical Large J

39

$$P_{\text{chamber}} = 3.6 \text{ MPa (Pr = 1.1)}$$



J = 9.3 with thick inner post injector



J = 9.4 with thin inner post injector

Longer dark core lengths and hence visible effect of acoustics for thin inner post geometry



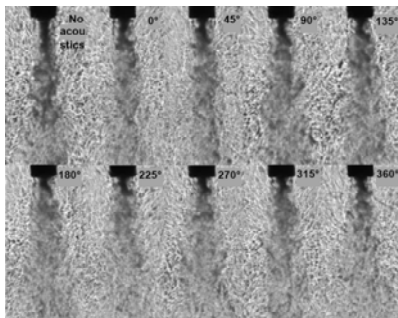
Distribution A: Approved for Public Release; Distribution Unlimited



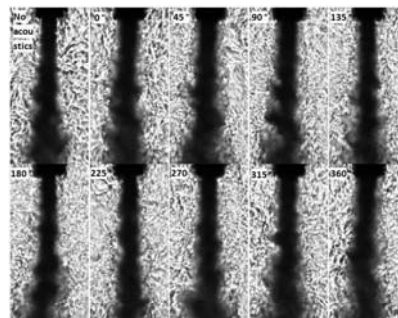
Supercritical Moderate J

40

$$P_{\text{chamber}} = 5.0 \text{ MPa (Pr = 1.5)}$$



J = 2.4 with thick inner post injector



J = 2.6 with thin inner post injector

Large dark core lengths for the thin post geometry prevent us from observing acoustic effects, if any



Distribution A: Approved for Public Release; Distribution Unlimited



thick inner post injector

41

	T _{chamber} (K)	P _{chamber} (kg/m ³)	P _{chamber} (MPa)	T _{outer} (K)	\dot{m} outer (mg/s)	P _{outer} (kg/m ³)	U _{outer} (m/s)	Re _{outer} (10 ⁴)	T _{inner} (K)	\dot{m} inner (mg/s)	P _{inner} (kg/m ³)	U _{inner} (m/s)	Re _{inner} (10 ⁴)	L/D ₁ (baseline)	Freq. (kHz)	P _{test max} (kPa)	VR	J
SUB																		
sub1	233	22.0	1.50	191	310	27.6	4.30	0.768	109	279	630	2.2	1.2	26.2	2.98	21.5	2.0	0.17
sub2	231	22.2	1.50	183	790	28.8	11.0	2.02	109	283	630	2.2	1.2	17.1	3.06	20.1	4.8	1.0
sub3	226	21.9	1.45	183	1230	27.8	16.9	3.16	109	284	630	2.2	1.2	16.6	3.06	17.8	7.6	2.6
sub4	226	22.9	1.51	185	1560	28.7	20.9	3.96	109	279	630	2.2	1.2	15.2	2.96	15.7	9.5	4.2
sub5	210	24.9	1.50	182	2400	29.3	31.3	6.18	109	279	630	2.2	1.2	8.40	3.01	16.9	14	9.6
sub6	216	24.1	1.50	191	3640	27.7	50.3	9.02	109	279	630	2.2	1.2	5.63	3.02	16.3	23	23
NEAR																		
near1	223	56.6	3.58	180	1060	75.4	5.38	2.58	123	290	520	2.8	2.0	24.4	3.08	9.04	2.0	0.55
near2	207	62.0	3.57	152	1570	101	5.95	4.16	117	289	590	2.4	1.5	15.5	3.04	10.8	2.5	1.0
near3	228	55.1	3.58	185	1590	72.4	8.40	3.80	126	293	440	3.3	2.5	14.6	3.00	11.8	2.6	1.1
near4	223	56.1	3.55	184	2170	72.3	11.5	5.21	127	294	360	4.0	3.4	12.1	3.01	11.4	2.8	1.6
near5	230	54.2	3.56	199	2120	65.1	12.5	4.94	126	292	440	3.3	2.5	12.9	3.03	12.1	3.8	2.1
near6	229	54.5	3.56	183	2690	73.1	14.1	6.46	126	292	420	3.4	2.5	5.98	3.05	11.1	4.1	2.8
near7	219	57.6	3.56	194	3080	67.4	17.5	7.15	125	289	480	3.0	2.2	5.56	3.06	11.8	5.9	4.9
near8	213	59.6	3.56	192	6460	68.3	36.2	15.1	128	295	220	6.6	5.2	2.45	2.93	9.73	5.5	9.3
SUPER																		
super1	231	76.1	4.96	198	292	93.9	1.19	0.642	136	291	300	4.8	3.9	37.7	3.05	8.01	0.25	0.019
super2	231	76.1	4.96	193	997	97.7	3.90	2.22	130	292	460	3.1	2.4	26.7	3.01	10.2	1.2	0.33
super3	221	80.4	4.95	180	2050	109	7.19	4.72	128	291	490	2.9	2.1	19.2	3.01	10.7	2.5	1.3
super4	222	80.1	4.96	182	3110	107	11.1	7.13	134	288	360	3.9	3.3	10.2	3.05	10.1	2.8	2.4
super5	222	80.3	4.97	191	2820	99.5	10.8	6.32	131	293	440	3.3	2.6	9.02	3.09	12.5	3.3	2.5
super6	211	85.8	4.96	187	5820	103	21.6	13.2	132	286	410	3.4	2.7	3.04	3.05	10.7	6.3	9.9



Distribution A: Approved for Public Release; Distribution Unlimited



New Injector

42

	T _{chamber} (K)	P _{chamber} (kg/m ³)	P _{chamber} (MPa)	T _{outer} (K)	\dot{m} outer (mg/s)	P _{outer} (kg/m ³)	U _{outer} (m/s)	Re _{outer} (10 ⁴)	T _{inner} (K)	\dot{m} inner (mg/s)	P _{inner} (kg/m ³)	U _{inner} (m/s)	Re _{inner} (10 ⁴)	L/D ₁ (baseline)	Freq. (kHz)	P _{test max} (kPa)	VR	J
SUB																		
subnew1	235	22	1.48	199	90	26	1.4	0.21	105	920	660	0.91	1.3	13+	3.01	8.86	1.5	0.089
subnew2	237	22	1.49	197	200	26	3.0	0.47	106	925	655	0.92	1.3	13+	2.96	14.0	3.3	0.43
subnew3	246	21	1.49	195	450	27	6.6	1.1	109	925	630	0.96	1.5	11+	2.97	12.1	6.9	2.0
subnew4	224	23	1.49	189	600	28	8.5	1.5	110	925	620	0.97	1.5	10.4	3.04	10.2	8.7	3.4
subnew5	217	24	1.49	184	750	29	10	1.9	110	925	620	0.97	1.5	9.29	3.02	11.5	11	5.2
subnew6	228	22	1.49	193	880	27	13	2.1	108	925	640	0.94	1.4	8.08	2.96	12.7	14	7.8
subnew7	222	23	1.49	194	1100	27	16	2.6	108	925	640	0.94	1.4	7.63	2.92	11.2	17	12
subnew8	217	24	1.48	201	1300	26	20	3.0	109	925	630	0.96	1.5	7.26	2.90	9.16	21	18
NEAR																		
nearnew1	228	55	3.56	213	330	60	2.2	0.70	109	925	650	0.93	1.3	14+	2.98	10.8	2.3	0.50
nearnew2	226	55	3.56	209	460	61	3.0	1.0	109	925	650	0.93	1.3	14+	3.06	9.17	3.2	0.97
nearnew3	230	54	3.58	198	730	66	4.3	1.6	108	925	655	0.92	1.3	13+	3.00	9.12	4.7	2.2
nearnew4	216	59	3.58	199	1030	65	6.3	2.3	109	925	650	0.93	1.3	13+	3.11	16.0	6.7	4.6
nearnew5	214	59	3.58	203	1460	63	9.2	3.2	109	925	650	0.93	1.3	7.01	3.07	15.0	9.9	9.4
nearnew6	215	59	3.56	207	2060	62	13	4.5	111	925	635	0.95	1.4	3.55	3.09	18.3	14	19
SUPER																		
supernew1	219	81	4.95	212	890	85	4.1	1.8	111	925	650	0.93	1.4	13+	3.11	17.0	4.4	2.6



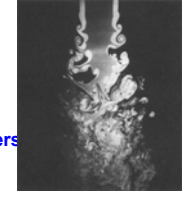
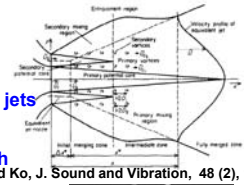
Distribution A: Approved for Public Release; Distribution Unlimited



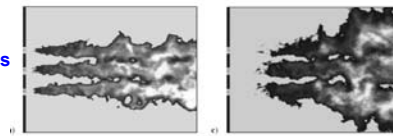
Highlights from previous work 1/2

43

- Crow and Champagne, 1971
 - Single jet preferred mode, $St=fd/U \sim 0.3$
- Ko et al, 1976-1989
 - Some of earliest detailed description of near field mixing for coaxial jets
- Boldman et al, 1975
 - Experimental and theoretical analysis for mixing of two streams with different velocities – points out different vortex interactions
- Gutmark and Ho, 1983
 - Collects previous results on jet preferred mode, St has a range from ~ 0.24 - 0.64
- Dahm et al, 1992
 - Points out importance of layer thickness and velocity defect on shear layers
- Villiermeaux 1998
 - Inner jet core length expression, $L/D_1 = 6/J^{0.5}$
- Richecoeur et al (Candel's group), 2006
 - Forced transverse acoustic excitation of flames



Dahm et al, JFM (241) 1992



Richecoeur et al, JPP (22) No 4, 2006



Distribution A: Approved for Public Release; Distribution Unlimited



Short Thick post behavior families

44

	Baseline	Max Δp	Min Δp		Subcritical conditions			
					• Acoustics undulate inner jet like in Heldmann's experiments consistent with being driven by an imposed velocity field			
					• Reductions of core of more than 20% for $0.2 < J < 10$			
					Near and supercritical conditions			
					• Less undulation on inner jet but same mode			
					• Not a clear effect of phase on the reduction of the dark core length			
					• Max reduction of inner jet occurred at $1 < J < 5$			

Conditions of Interest

45

Run Date	T _{chamber} (K)	$\rho_{chamber}$ (kg/m ³)	P _{chamber} (MPa)	T _{outer} (K)	M _{outer} (mg/s)	ρ_{outer} (kg/m ³)	u _{outer} (m/s)	Re _{outer} (10 ⁴)	T _{inner} (K)	M _{inner} (mg/s)	ρ_{inner} (kg/m ³)	u _{inner} (m/s)	Re _{inner} (10 ⁴)	Freq. (kHz)	VR	J	Recess
2010_02_18	233	52	3.49	165	1330	84	6.25	3.3	118	938	576	1.06	1.8	3.00	5.9	5.1	D1
2010_03_26	201	63	3.52	184	5976	72	32.97	17	129	2408	185	8.50	14	3.05	3.9	5.9	D1
2010_06_21 case1	234	53	3.54	191	814	68	4.74	1.9	130	333	175	1.26	2.4	3.08	3.8	5.5	0.5D1
2010_06_30 case1	174	78	3.51	161	4732	88	21.3	12	117	3199	586	3.56	6.0	3.02	6.0	5.4	0.5D1

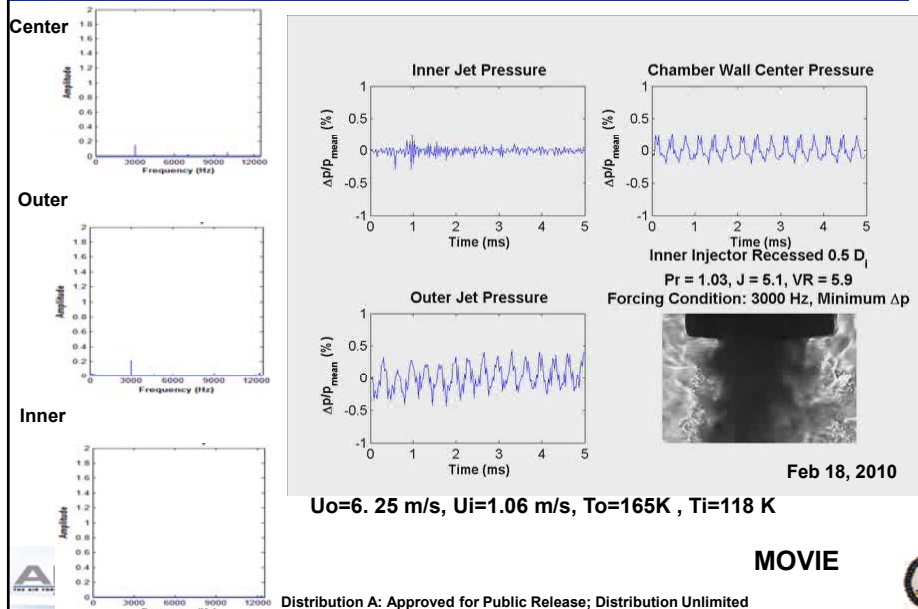


Distribution A: Approved for Public Release; Distribution Unlimited



Synchronized p' and images: Pr=1.03, J=5.1, VR=5.9

46

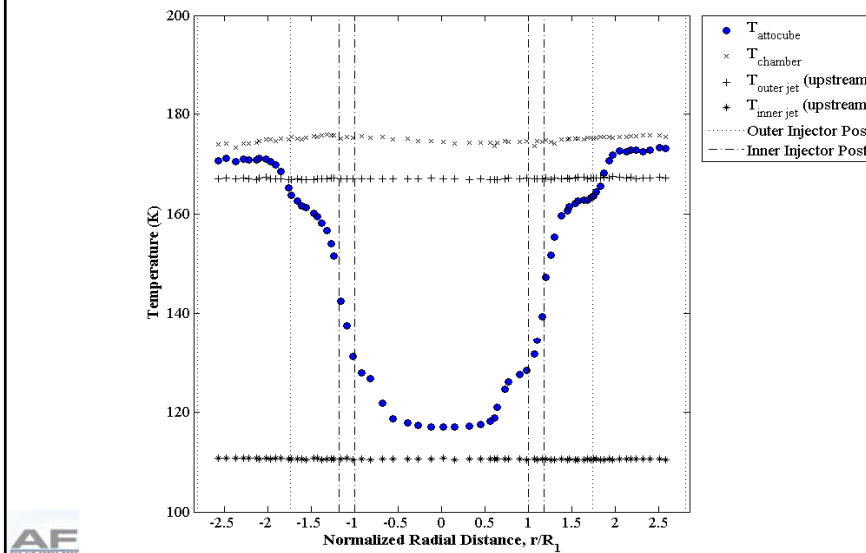


Distribution A: Approved for Public Release; Distribution Unlimited



Jet Temperature Profiles

47



Shear Coaxial Jets Subjected to an External Acoustic Field

Ivett A. Leyva^{*}, Doug Talley^{*}, Sophonias Teshome⁺, Juan Rodriguez[^], Jeffrey Graham^{*}

^{*}Air Force Research Laboratory, Edwards AFB, California, USA

⁺UCLA, Los Angeles, CA, USA

[^]Ecole Centrale Paris, Châtenay-Malabry, France

1 Introduction

Shear coaxial injectors are a common design choice for boost and upper stage cryogenic rocket engines where the propellants are liquid oxygen and hydrogen. The liquid oxygen is generally introduced as the inner jet and hydrogen is introduced in the coaxial or outer jet. Mixing between the inner and outer jet happens through the shear layer that develops in the interface of the two propellants; the faster the shear layer grows the faster mixing occurs. To provide good mixing, shear coaxial jets depend on a large difference in the velocities and momentum fluxes of the two streams, which is easily achieved in rocket engines. High performance for rocket engines is also coupled to higher chamber pressures. For example, the F-1 engine for the Saturn V operated at 6.7 MPa [1] while the SSME engine operates at 19.3 MPa [2]. One consequence of operating at higher pressures is that the propellants are injected at pressures greater than their individual critical pressures. In the case of hydrogen it usually is injected at higher than its critical temperature, so it is considered a supercritical fluid, whereas oxygen usually is injected at lower than its critical temperature, so it is considered a liquid-like or transcritical fluid. What happens to the mixing processes in a shear coaxial injector as the working fluids cross into the supercritical regime is the first topic of this paper. The second topic is how the mixing reacts to external acoustics. The interest on knowing the response to acoustics arises from the ever present concern of developing combustion instabilities on a new engine design or new operating conditions. The results presented here are solely concerned with all-nitrogen shear coaxial injectors exiting into a nitrogen atmosphere. This choice allows us to have a single critical point making it easy to know exactly the thermodynamic state of the inner and outer jets and the chamber. Being non-reacting allows us to focus on the fluid mechanics instabilities of a coaxial jet and their response to external acoustics.

2 Experimental Setup

The Cryogenic Supercritical Laboratory (EC-4) at the Air Force Research Laboratory, Edwards Air Force Base, CA, where the experiments are performed, is shown in Fig. 1A. A schematic of the facility and the experiment is shown in Fig. 1B. The photograph shows the test chamber in the center, one acoustic driver on each side and a high speed camera on the front. The injector flow is from top to bottom. The maximum chamber pressure is 13.8 MPa. The lowest tested temperature is about 95 K. Nominal injector flow rates are in the order of g/s. This is a non-reacting facility using only N₂ for the pressurizing gas and for the injector flows. In order to maximize the effect of the available acoustic energy on the jet, a rectangular inner chamber was created into which the injector flow exits and the acoustic waves are directed (Fig. 1B). The inner chamber has a height of 6.6 cm, a width of 7.6 cm and a depth of 1.3 cm. The top of the inner chamber consists of a perforated plate to allow the outer and inner chambers to get their pressures equalized. Both the top and bottom pieces have an orifice at the center. The top plate's orifice allows the coaxial injector tip to enter the inner chamber and the bottom orifice provides an exit for the flow. The bottom hole is also used to introduce a thermocouple and high speed pressure transducer to study the properties of the flow near the jet exit plane. The front and back sides to the inner chamber are plexiglass for flow visualization. On the back plexiglass panel, there are three Kulite high speed pressure transducers, equally spaced, just above the exit plane of the coaxial injector to measure the acoustic pressure field. The outer and inner jets are cooled by

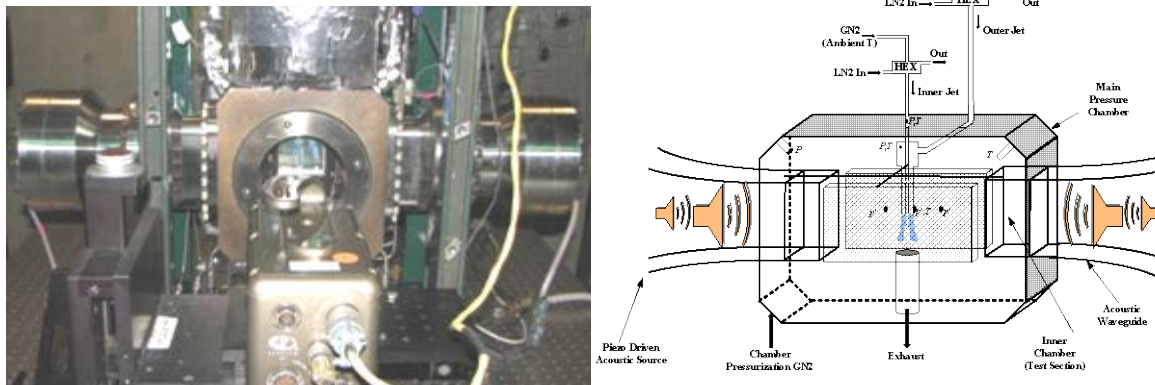


Figure 1. A: Experimental test chamber and supporting systems of the Experimental Cell 4 at AFRL, Edwards AFB, CA. B: Chamber section view of the flow schematic for Experimental Cell 4.

independent heat exchangers (HEs) using liquid N_2 (LN2) as the coolant. The temperatures of the two jets are controlled by the flow rate of LN2 through the HE's. The mass flow rates for the inner and outer jets are measured with Porter mass flow meters (models 122 and 123-DKASVDAA) before they are cooled, since it is easier to measure mass flow rates at ambient temperature than at cryogenic conditions. The two acoustic sources are nominally identical and use a piezosiren to generate acoustic waves at frequencies of about 3kHz and 5.2kHz. A waveguide is used to guide the acoustic waves from a round cross section at the source to a rectangular cross-section at the inner chamber.

3 Injector Geometry and Measurement Techniques

Two injector geometries will be discussed in this paper. Pictures of two representative geometries are shown in Fig. 2. The injector on the left has a thick inner jet post ($t/d=1.06$) and the one on the right has a thin post ($t/d=0.089$). Together, they give us a practical upper and lower limit for the inner jet thickness. For the thick post injector, the L/D was 100 for the inner jet and 34 for the outer jet (taking as reference the hydraulic diameter). The same ratios were 65 and 55 respectively for the thin post injector. The inner and outer injector flows are designed to be fully developed turbulent. For the cases studied the inner jet can be flushed or recessed with respect to the outer jet.

The flows are characterized with different measurements aside from static pressure and flow rates. Temperature profiles of the inner and outer jets are taken at the exit plane of the injector with an unshielded type E thermocouple with a bead diameter of 0.1 mm. The thin post injector is equipped with high speed pressure transducers and thermocouples in both the inner and outer jet reservoirs. Three high speed pressure transducers are also placed at the exit plane of the injector. Finally, a Phantom 7.1 high speed camera is used to obtain backlit movies at frame rates of 20-40kHz. The sizes of the images presented here vary from 128×224 to 196×400 pixels. Each pixel represents an area of approximately 0.08×0.08 mm.

4 Baseline measurements without acoustics

Studies of non-reacting shear coaxial mixing date back to the 60's with the pioneering paper of Chigier and Beer [3] using air-air coaxial jets at atmospheric pressure. They concluded that the inner jet potential core decreased as the outer to inner velocity ratio increased. The potential core is associated with the inner jet volume not entrained into the shear layer formed between the inner and outer jets. Ko et al [4-6], also studying air jets, have made a wealth of contributions since the 70's

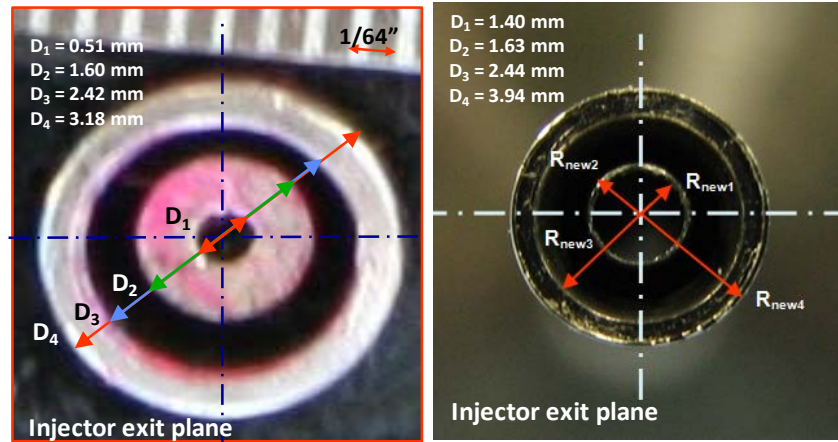


Figure 2. Geometries of two injectors tested. Left: thick post injector. Right: thin post injector.

describing the observed structures and mixing phenomena, pertaining mainly to the near field. Dahm et al [7], using water coaxial jets, investigated the vortical structures formed in the shear layers as a function of the velocity ratio and pointed out the effect of the different types of vortical structures on the inner jet core length. Villermeaux [8] and other researchers cited on the review article by Lasheras and Hopfinger [9] deduced that for shear coaxial jets, the momentum flux ratio defined as $J = \frac{\rho_o u_o^2}{\rho_i u_i^2}$, where o refers to outer and i to inner jet, is a dominant non-dimensional parameter characterizing mixing. As J increases the mixing becomes more efficient and the inner jet is entrained by the outer jet within a shorter distance.

Figure 3 shows a compilation of available data on coaxial jets presented by Davis [10] with more recent results added for from Leyva et al. [11]. The dark core, intact core, or potential core length is plotted as a function of J. As Davis [10] points out, two branches emerge from the data. The upper branch corresponds to two phase flows and the lower one to single phase flows which include gas-gas, supercritical-supercritical, and supercritical-transcritical. It is evident that both branches scale with J, but because of the large bands where the data falls, further analysis is underway to investigate if incorporating other non-dimensional parameters, such as velocity ratio can collapse the experimental data even further.

5 Effects of Acoustics on Thick Post Injector

The general trends of the behavior of the thick post injector are shown in Fig. 4. The set of images on the left correspond to a subcritical pressure where the inner jet is liquid and the outer jet is vapor, and the set of images on the right correspond to a supercritical pressure. The momentum flux ratio J spans about two orders of magnitude. The top row corresponds to cases without acoustic excitation. The middle row corresponds to cases with acoustics on where the jet is in a pressure antinode. The bottom row corresponds to cases with acoustics on where the jet is in a pressure node.

Attention may be directed first to the subcritical cases on the left side of Fig. 4. As previously reported [10-11] and can be seen in Fig. 4, the dark core decreases as J increases. However, we can also see that at high J values, the inner jet appears to be much thicker at the exit plane. This is because, above certain critical value of J, a recirculation bubble is established downstream of the inner jet, much like Villermeaux [12] had observed in water jets. Also observe that acoustics shorten the inner jet at the lower value of J without undulation. However, undulation becomes prominent at J=2.6 and J=9.6. Undulation of the jet is almost intuitive as we think of the transverse acoustic field imposing a lateral

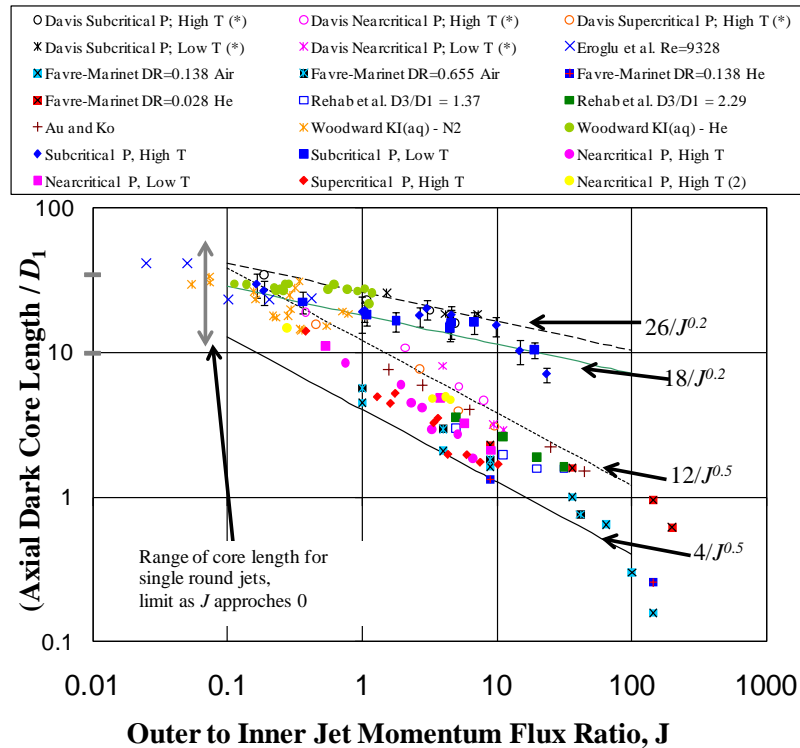


Figure 3. Scaling of Length of Inner Jet Dark Core Length for Shear Coaxial Jets with Momentum Flux Ratio,

force on the jet, the direction of which oscillates as the acoustic cycle proceeds. The effects look more dramatic for the middle value of J since the dark core for that case has enough length to sustain several undulations before it breaks. The undulation effect is greatest at a velocity antinode and moderate J values. Attention may be directed next to the supercritical cases on the right side of Fig. 4. The set of images on the right correspond to supercritical pressures. The trends are qualitatively similar to the subcritical cases, with the caveat that the dark core is shorter for a given value of J (see also Fig. 3) and so the undulations are not as pronounced for mid values of J . Also, the natural inner jet instabilities for the baseline cases are more prominent for the higher pressure case. Finally, the inner jet is so short for the supercritical case $J=9.3$ that the acoustics have the effect of bending the core from left/right as the cycle proceeds. A more detailed analysis will be presented for this geometry and compared with a similar analysis for the thin post injector.

6 Cycle-to-cycle and averaged analysis of coaxial jets

By synchronizing the movie frames and the high speed transducers we can obtain cycle-to-cycle information on how the jet reacts to the acoustic field. Fig. 5 shows a snapshot of the backlit images together with the pressure measured at the inner and outer jet reservoirs and directly behind the coaxial injector. By comparing the relative amplitude of the signals we can assess whether the acoustics are being damped or amplified at the injector reservoirs, which is particularly useful when trying to understand coupling of the post modes with the external acoustics. Also, one can examine the behavior of the jet at pressure nodes and antinodes. FFT's of the different signals are also performed to determine characteristic frequencies for the system. This type of analysis will be presented for the thin post injector and at least one more new geometry.

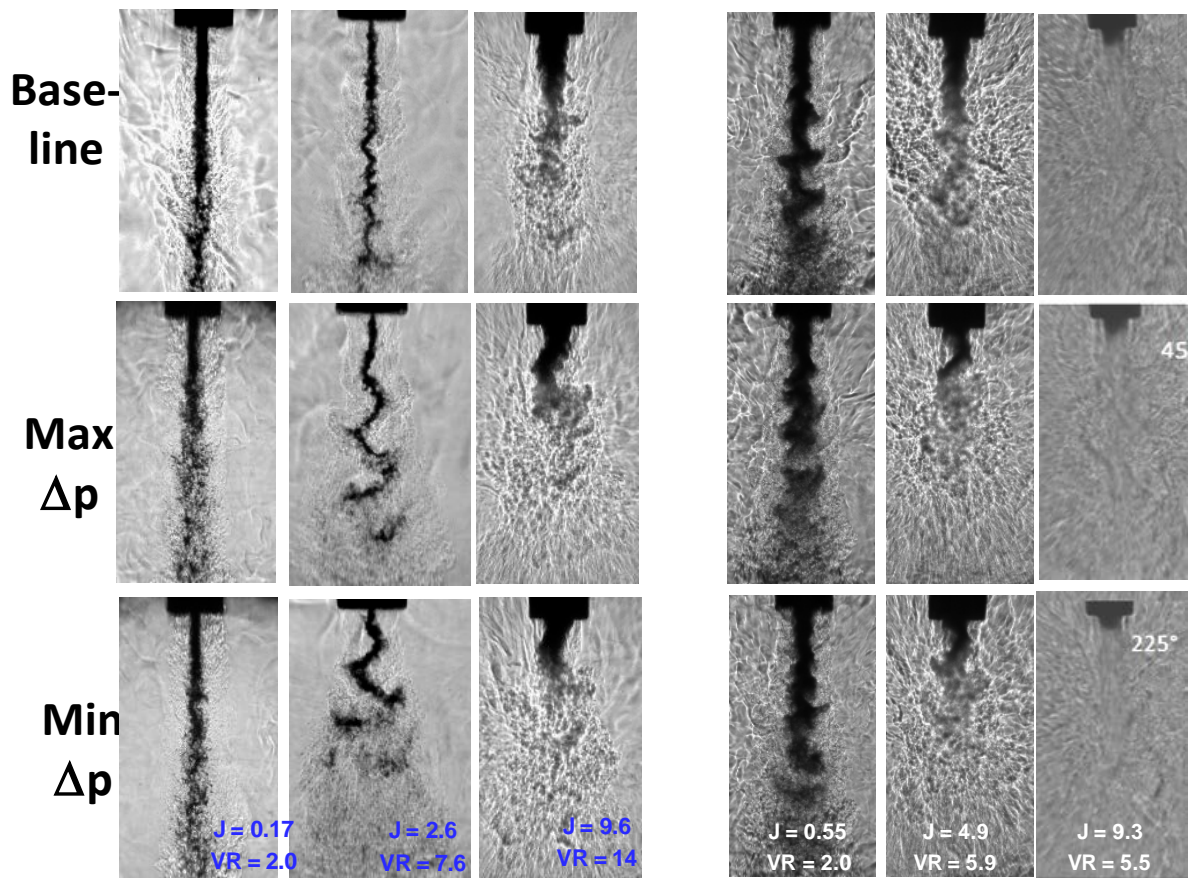


Figure 4. Behavior of shear coaxial jets at baseline conditions (without acoustics) and exposed to acoustic pressure nodes and antinodes. Left: Subcritical pressure ($Pr=0.45$). Right: Supercritical pressure ($Pr=1.05$).

Finally, very careful measurements of the exit plane temperature for a range of conditions will be presented. Fig. 6 shows a sample. The differences on the reservoir and exit plane temperatures for the inner and outer jets are indicative of the heat transfer taking place along the injector and can be assessed as a function of J and velocity ratio. The growth of the shear layer between the inner and outer jet can also be studied by looking at these temperature profiles.

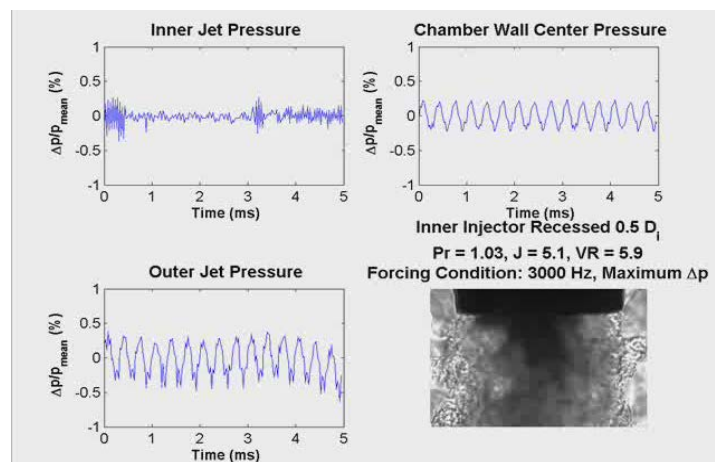


Figure 5. Inner jet dark core length as a function of the momentum flux ratio for tor.

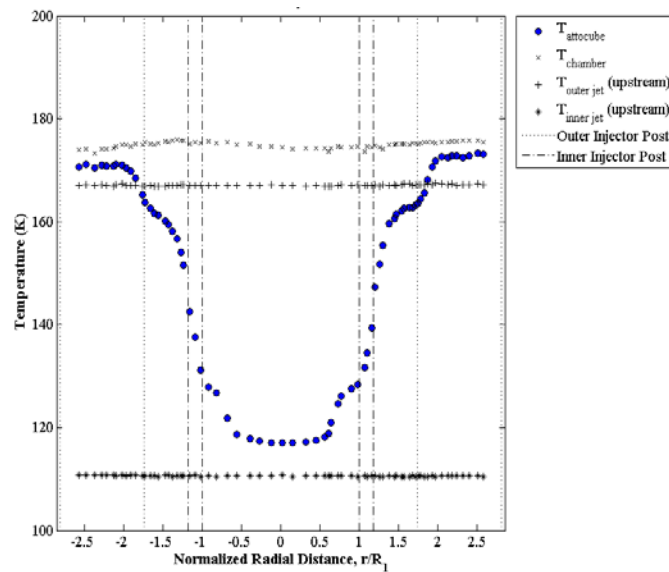


Figure 6. Various temperature profiles measured in and around the injector.

References

- [1] http://history.msfc.nasa.gov/saturn_apollo/documents/F-1_Engine.pdf
- [2] JPP Vol. 18, No. 2, March–April 2002
- [3] Chigier, NA and Beer JM. (1964). The flow region near the nozzle in double concentric jets. Trans. ASME 86D, J. of Basic Engineering. 4:797-804.
- [4] Kwan, ASH and Ko, NWM. (1976). Coherent structures in subsonic coaxial jets. J of Sound and Vibration. 48(2):203-219.
- [5] Ko, NWM and Au, H. (1985). Coaxial jets on different mean velocity ratios. J of Sound and Vibration. 100(2):211-232.
- [6] Kwan, ASH and Ko, NWM. (1977). Covariance measurements in the initial region of coaxial jets. J of Sound and Vibration. 52(4):567-578.
- [7] Dahm, W., Frieler, C., Tryggvason, G. (1992). Vortex Structure and Dynamics in the Near Field of a Coaxial Jet. J. of Fluid Mechanics. 241:371-402.
- [8] Lasheras, JC, Villiermaux, E and Hopfinger EJ. (1998). Break-up and atomization of a round water jet by a high-speed annular air jet. J. of Fluid Mechanics. 357:351–379.
- [9] Villiermaux, E. and Rehab, H. (2000). Mixing in coaxial jets. J. of Fluid Mechanics. 425:161–185.
- [10] Davis, DW. (2006). On the Behavior of a Shear-Coaxial Jet, Spanning Sub- to Supercritical Pressures, With and Without an Externally Imposed Transverse Acoustic Field. Ph. D. Dissertation: Dept. of Mech. and Nuclear Engineering, Pennsylvania State University.
- [11] Leyva, I. A., Chehroudi, B., Talley, D. (2007). Dark-Core Analysis of Coaxial Injectors at Sub-, Near-, and Supercritical Conditions in a Transverse Acoustic Field. AIAA 2007- 5456.
- [12] Villiermaux, E., Rehab, H., and Hopfinger, E. J. (1994). Breakup Regimes and Self-Sustained Pulsations in Coaxial Jets. Meccanica. 29:393-401.

PROPER ORTHOGONAL DECOMPOSITION ANALYSIS OF SHEAR-COAXIAL INJECTOR FLOWS WITH AND WITHOUT TRANSVERSE ACOUSTIC FORCING

S. Teshome[†], I. A. Leyva[‡], D. Talley[‡]

[†]University of California, Los Angeles, Los Angeles, CA

[‡]Air Force Research Laboratory, Edwards AFB, CA

ABSTRACT

This experimental study investigated the response of dynamic flow structures of cryogenic coaxial nitrogen jets to pressure perturbations due to transverse acoustic forcing at a pressure antinode (PAN). The role of injector exit geometry on the flow response was examined using two shear coaxial injectors with different outer-to-inner jet area ratios. Flow conditions spanning subcritical (reduced pressure of 0.44) to supercritical (reduced pressure of 1.05) chamber pressures, varying outer-to-inner jet momentum flux ratios (0.5 – 20), and acoustic pressure antinode at the jet axis location were considered. A basic application of proper orthogonal decomposition on the intensity fluctuation of high-speed images enabled the extraction of the spatial and temporal characteristics of the dominant flow structures that existed in the flow field during exposure to acoustic forcing. Regardless of injector geometry or pressure regime, low outer-to-inner momentum flux ratio flows were found to be responsive to acoustic pressure antinode forcing. With increasing momentum flux ratio, however, the flow response to forcing depended on the injector geometry.

NOMENCLATURE

A	area
D	diameter
f	frequency
J	outer jet-to-inner jet momentum flux ratio, $\rho_2 U_2^2 / \rho_1 U_1^2$
m	no. of columns of pixels in a single image frame
\dot{m}	mass flow rate
N	no. of image frames
n	no. of rows of pixels in a single image frame
P	pressure
Pr	reduced pressure, P/P_{cr}
R	outer-to-inner jet velocity ratio, U_2/U_1
Re	Reynolds number
S	outer-to-inner jet density ratio, ρ_2/ρ_1
T	temperature
U	flow velocity

GREEK SYMBOLS

θ	shear-layer momentum thickness
ρ	density

SUBSCRIPTS

1,2	pertaining to the inner jet, outer jet, respectively
F	acoustically forced

I. INTRODUCTION

Coaxial injectors have proven to be one of the most effective and simple means of delivering propellants in combustion devices such as in liquid rocket engines (LREs). Their application in LREs was seen as early as the development of the J-2 engine and as recent as the space shuttle main engine (SSME). Combustion instability is a phenomenon that has, in severe instances, led to the demise of LREs. It is primarily a result of feedback interactions

between unsteady combustion rates and pressure fluctuations from acoustic modes in the combustion chamber. Since injector flows are directly involved in processes that take place inside combustors, it is crucial to understand how they contribute to, as well as how they are affected by, these unsteady physical mechanisms that lead to combustion instabilities. However, a successful understanding at a fundamental level of these interactions between injector flows and chamber phenomena can only be achieved by first isolating the fluid dynamics aspect from the reactive flow processes, and studying the coupling of non-reactive injector flow instabilities with external pressure perturbations.

Shear-coaxial jets consist of a circular core or inner jet and an annular or outer jet. In the near field region, where the potential cores of both the inner and outer jets exist, two shear-layers exist: an inner shear layer between the inner and outer jet flow, and an outer shear layer between the outer jet and the ambient fluid. Detailed descriptions and characteristics of the different flow regimes in coaxial jets are given, for example, in [1]. The development of instabilities in the individual shear layers, and the interaction between the two shear layers has a direct impact on the eventual instability characteristics of the entire flow field. Several studies [2-5] investigate the existence and behavior of large-scale vortex structures in the near-field region of single-phase similar or different density coaxial jets. It was shown that for outer jet velocity (U_2) to inner jet velocity (U_1) ratios exceeding unity ($R = U_2/U_1 > 1$), coherent structures in the outer shear layer dominate those in the inner shear layer.

The influence of these coherent structures on the overall dynamics of the flow field calls for an understanding of the factors leading to their formation. Detailed studies on the development and growth of natural instabilities in a single circular jet [6] or a single circular jet with coflow [7] reveal two of the most significant natural modes of instability: the axisymmetric and the first azimuthal or helical modes. These modes have comparable amplification rates over most of the core region downstream of the exit, with the helical mode eventually dominating the flow field farther downstream. It is shown [1] that the development of the outer shear layer of a coaxial jet behaves as the shear layer of a single jet, while the development of the inner shear layer behaves as that of a single jet issuing into an external flow. Thus, the axisymmetric and helical modes of instability along with natural as well as externally imposed flow conditions, such as pressure or velocity perturbations, that affect their development may be used to assess the stability of the coaxial jet.

The present study continues the series of experimental studies done in the same facility [8-14], which looked at the behavior of shear-coaxial N_2 jets at elevated pressures with and without the presence of a transverse acoustic field. It examines the baseline flow characteristics of two injectors with similar inner jet post thickness to diameter ratio, but different outer jet to inner jet area ratios, for different momentum flux ratios. It also investigates the flow response to a pressure antinode forcing condition, where the coaxial jet is exposed to the maximum local pressure fluctuations in a transverse acoustic field. Unlike previous studies in the current facility, the present study applies a proper orthogonal decomposition (POD) analysis (see Section II) to reduce the information obtained from a set of high-speed back-lit images in order to characterize the spatial and temporal behavior of dominant flow structures in the inner shear layer of the baseline and acoustically forced flows. Using this novel approach, the goal is to gain a better understanding of the evolution of flow instabilities, and underline the critical differences in the flow stability characteristics brought about as a result of simple design alterations in the shear-coaxial injector.

II. EXPERIMENTAL SETUP AND METHODOLOGY

These experiments were carried out at the Air Force Research Laboratory (AFRL), Edwards, test cell EC-4. Figure 1 shows a schematic of the experimental facility. The chamber was designed to operate at pressures spanning subcritical to supercritical pressures of N_2 , whose critical pressure is 3.4 MPa, and critical temperature is 126 K.

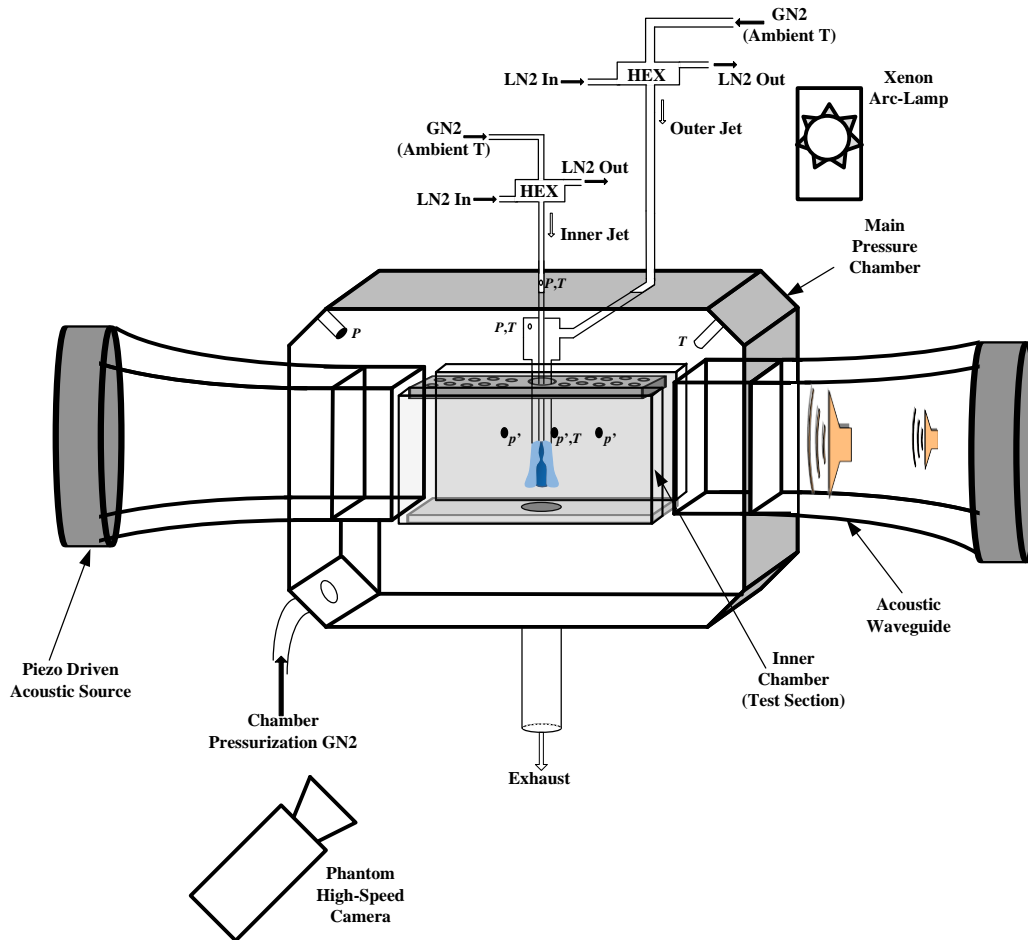


Figure 1. Experimental Facility Schematic

The inner and outer jets as well as the chamber pressurization flows were supplied by ambient temperature, high pressure facility GN2 lines. Counter-flow heat exchangers using LN2 as the coolant fluid were used to cool the test fluids down to the desired temperatures. An unshielded Omega type-E thermocouple with a bead diameter of 0.25 mm was mounted on top of two linear positioning stages and placed near the injector to measure the radial temperature profile of the coaxial jet within one inner jet diameter from the exit plane. Porter mass flow meters (model 123-DKASVDAA) were used to measure the inner and outer jet flow rates, which were controlled via metering valves. The jets issued into the test section (Figure 1) of the inner chamber halfway between the two piezo-sirens located at opposite ends of the chamber. Each piezo-siren was fitted with a waveguide that transitioned from a circular cross-section to a rectangular one. The inner chamber was used to maximize the amplitude of acoustic oscillations generated by the piezo-sirens. However, both the inner and main chambers were maintained at the same static pressure, which was measured with a Stellar ST1500 pressure transducer. The momentum flux ratio ($J = \rho_2 U_2^2 / \rho_1 U_1^2$), velocity ratio ($R = U_2 / U_1$), and other flow conditions were determined based on thermophysical properties evaluated at the measured chamber pressure, and jet exit temperatures. Kulite absolute (CCQ-093) and differential (XCQ-093, XCE-093) pressure transducers were also used for making high-speed acoustic pressure measurements. These pressure transducers were placed along the inner chamber wall, where one transducer was located directly behind the jet, and two others inside the injector plenums.

The acoustic wave signals were generated using a Fluke 292 arbitrary waveform generator. A Trek PZD2000A high-voltage amplifier amplified continuous sine wave signals from the waveform generator before being input into each piezo-siren. The resulting acoustic waves from each piezo-siren were traveling waves that propagated transversely along the waveguide. Depending on the phase difference between the signals applied to each piezo-siren, a pressure antinode (PAN) condition, where the perturbation in pressure was maximum, or a pressure node (PN) condition, where the perturbation in pressure was minimum, can be created. Thus, using signals

that were in-phase (0° phase difference), a PAN condition was established at the center of the waveguide, where the coaxial jets were situated.

Figure 2 shows a schematic of the injector exit with dimensional nomenclature, and Table 1 provides a summary of the injector exit dimensions under consideration. Both injectors were characterized by small lip thickness to inner diameter ratio t/D_1 , but one had a large outer-to-inner jet cross-sectional area ratio (LAR), while the other had a small area ratio (SAR).

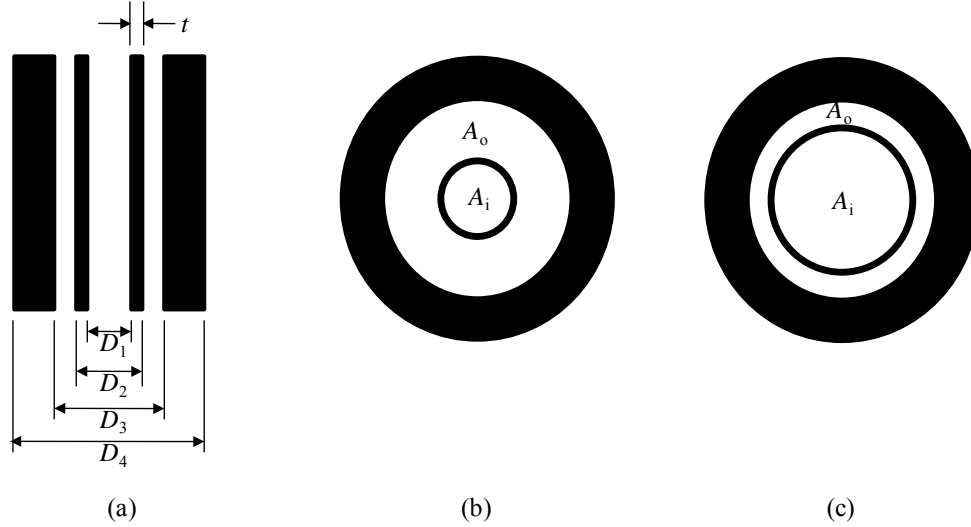


Figure 2. Injector geometry schematic: (a) axial cross-sectional view, (b) LAR exit configuration, (c) SAR exit configuration

Table 1. Injector Exit Dimensions (mm)

Injector	t	D_1	t/D_1	D_2	D_3	D_4	A_o/A_i
LAR	0.09	0.70	0.13	0.89	2.44	3.94	10.6
SAR	0.13	1.40	0.09	1.65	2.44	3.94	1.65

Proper orthogonal decomposition (POD) of the high-speed images has proven to provide a powerful means for extracting relevant qualitative and quantitative information from an otherwise complicated and noise-ridden set of image data [15-17]. A xenon arc lamp was used to provide a back-lit image of the coaxial jet, which was visualized using a high speed Phantom v7.1 CMOS camera at framing rates exceeding 20 kHz. The decomposition was achieved by first arranging all the pixel intensity values of all frames into a single array, whereby the pixel intensities from one frame occupied one row of the data array. Thus, a set of N consecutive frames, each of which had an n by m pixel resolution, constituted an N by $n \times m$ data array. The temporal mean of the data array was subtracted in order to eliminate the DC component of the intensity values. The method of singular value decomposition was implemented in MATLAB[®] using a built-in subroutine to represent the data array of intensity fluctuations as a matrix product of an N by N array of temporal amplitude coefficients and an N by $n \times m$ array of right singular column vectors, also known as proper orthogonal modes. The matrix product of the left singular vectors and the diagonal matrix of singular values formed the matrix of column vectors of the temporal amplitude coefficients. These modes were arranged in decreasing order of significance as dictated by the magnitude of the singular values of the decomposition.

III. RESULTS AND DISCUSSION

The experiments done under subcritical (reduced pressure, $Pr = 0.44$) pressure conditions were such that the inner jet was in liquid phase, while the outer jet was in gas phase at temperatures well above the saturation

temperature of N_2 . Under nearcritical (reduced pressure, $Pr = 1.05$) conditions, the inner jet temperatures were below the critical temperature, while that of the outer jet were well above the critical temperature, thereby resulting in a supercritical outer fluid. A test matrix containing all the flow conditions and parameters is given in Table 2 in the Appendix. As previously noted, for coaxial jets of different densities, J is one of the governing parameters of coaxial jet mixing. However, for a set of test conditions in a particular pressure regime, the outer-to-inner jet density ratio ($S = \rho_2/\rho_1$) was held approximately constant while R was varied. Thus, the variation in J in these studies resulted mainly due the variation in R only.

The remainder of this section will focus on results pertaining to the coaxial jet without any acoustic forcing and with acoustic forcing that created a PAN condition inside the acoustic waveguide where the jets were situated.

BASELINE (NO ACOUSTICS)

As the name implies, this condition merely reflects a state of the coaxial jet flow without any type of external flow disturbances present. It provides information on the main characteristics of the natural flow disturbances, as well as a basis condition against which an acoustically forced flow response can be compared.

Figure 3(a) shows a snapshot image for $J = 0.5$ at $Pr = 0.44$ using LAR. It shows a single frame out of a set of images recorded at 25,000 fps. Characteristic of low J flow [10,11,14], it shows a long dark-core region spanning the region up to $20D_1$ downstream of the injector exit. It also has a relatively small spread angle, which is indicative of the slow spatial shear-layer development. These features are also evident in Figure 3(b), which is a temporal mean of each individual pixel over 1,000 frames. A distinct difference between the snapshot and average images can be clearly seen by the absence of any discrete flow structures emanating from the dark-core at the jet interface boundary in the average image. These structures, which appear to be at least spatially periodic in Figure 3(a), start forming by about $10D_1$. It is to be noted that the inner jet tube was not perfectly flush, but sticks out by about $0.2D_1$. This allowed for direct visual confirmation that inner jet injector tube was not disturbed by turbulent flow disturbances in the outer jet.

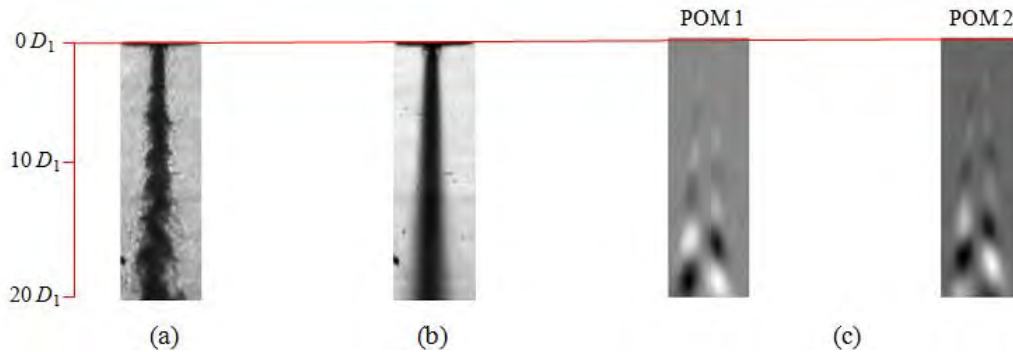


Figure 3. Baseline LAR flow at $Pr = 0.44$, $J = 0.5$: (a) snapshot image, (b) average image, (c) proper orthogonal mode (POM).

Figure 3(c) shows the first two proper orthogonal modes (POM) of the decomposition. As described in the previous section, since only the fluctuation in intensity level was considered, the background fluid and the relatively uniform portion of the inner jet flow were subtracted out, thus depicted by a gray region to indicate a mean level in a gray-scaled image. On the other hand, the lighter and darker lobes represent, respectively, the presence and absence of flow structures emanating from the dense inner jet. Their spatial arrangement is indicative of the symmetry or antisymmetry of the flow structures formed in the inner shear layer. That is, at any given axial location, the presence of two similar lobes adjacent to each other indicates the presence of flow structures associated with axisymmetric instabilities in the shear layer. Meanwhile, opposite adjacent lobes indicate antisymmetry, which in an axisymmetric flow geometry represents flow structures associated with helical instabilities. This is a viable assumption since under no external disturbances that can impose a preferential direction of oscillation of the shear-layer region, the only manner of propagation of the antisymmetric structures must be in the form of a helical disturbance. Hence, viewing

the jet from two perpendicular lines of sight should reveal indistinguishable features for a baseline coaxial jet, as was shown for some flow conditions in [8].

The singular values of all modes of the decomposition are shown in Figure 4. POMs 1 and 2 in Figure 3(c) whose singular values correspond to modes 1 and 2, respectively, are seen to be the two most dominant flow structures. Moreover, the monotonically decreasing magnitude of the singular values with increasing mode numbers, and more than an order of magnitude difference between the highest and lowest modes implies that the more important flow dynamics were captured by the lower mode numbers. This is actually a direct outcome of a POD procedure, which orders the singular values, and their corresponding POMs, in order of decreasing importance.

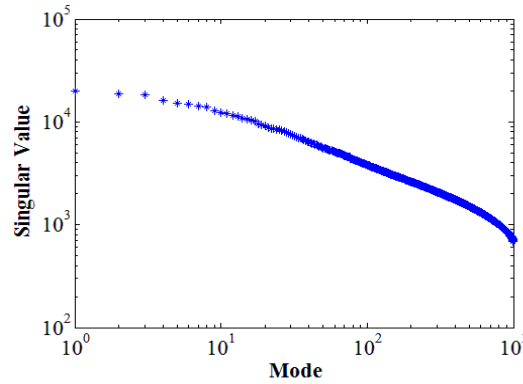


Figure 4. Baseline LAR flow at $Pr = 0.44$, $J = 0.5$: singular values.

The temporal characteristics of these dominant POMs were represented in the form of power spectral density of the temporal amplitude coefficients of the POD, and are shown in the plots in Figures 5(a, b). The peaks located at the low end of the spectra were associated with the disturbance frequencies of the lobes identified in their respective POMs. Furthermore, a time-sequence of images of each individual POM revealed a progression of changes in the lobe pattern similar to that of a standing wave. That is, with every passing period associated with the characteristic peak frequencies, a light lobe turned dark, and vice-versa. On the other hand, a time-sequence of images of a superposition of the two POMs revealed a continuous propagation of the lobes traveling downstream of the injector exit.

This outcome is analogous to a simply demonstrable result that the superposition of two standing one-dimensional waves is a traveling wave, as long as the two standing waves are $\pm 90^\circ$ out-of-phase both temporally and spatially. In a similar manner, the cross-power spectral density (CPSD) of the temporal amplitude coefficients can be used to check the existence of a phase difference of $\pm 90^\circ$ at the frequencies near the peak of a CPSD magnitude spectrum. Figures 5(c, d) show the CPSD magnitude and phase plots of POMs 1 and 2. The phase plot shows that the temporal requirement to form a propagating disturbance was satisfied by structures whose frequencies were associated with a -90° phase difference. It can thus be concluded that the frequencies associated with the peak in the CPSD magnitude plot were the characteristic frequencies of the propagating disturbances seen in the time sequence of the superposed POMs. A similar analysis demonstrating the spatial requirement for forming a propagating disturbance has not been done in the current study. However, it should be sufficient to check that the two POMs have similar lobe pattern, and together with the temporal requirement, form what are known as conjugate modes [16]. Hereafter, images of POMs presented will be the superposition of conjugate modes.

Figures 6(a-d) show the snapshot, average, and POM images for increasing J values at $Pr = 0.44$ using LAR. Figures 7(a-d) show similar images at $Pr = 1.05$. The decreasing dark-core lengths with increasing J are evident from both the snapshot and average images in both pressure regimes. In fact, it decreased from over $20D_1$ at $J = 0.5$ [Figures 3(a, b)] to less than $10D_1$ at $J = 20$ [Figure 6(d)], resulting in about 50% decrease at $Pr = 0.44$. The percent reduction was larger than 50% at $Pr = 1.05$ even at $J = 12$. This difference in the reduction is partly attributable to the transcritical state of the inner jet at $Pr = 1.05$, and the associated distinct physical properties, namely an almost non-existent surface tension and large momentum diffusivity. In either case, however, the dark-core length decrease very well signifies an increased rate of shear-layer growth, and thus enhanced mixing with

increasing J for this geometry. Although the end of the dark-core is not coincident with the end of the potential core, it is nevertheless a good

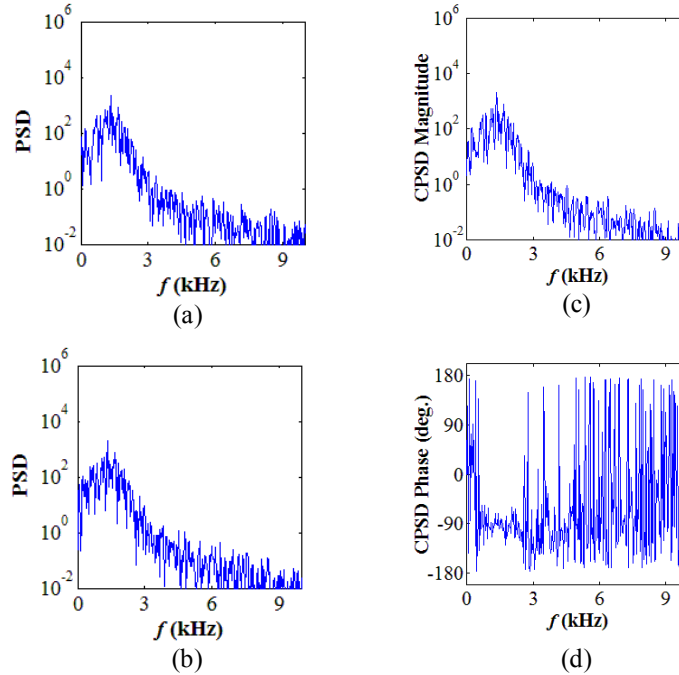


Figure 5. Baseline LAR flow at $Pr = 0.44$, $J = 0.5$: power spectral density (PSD) of the temporal amplitude coefficients of the decomposition corresponding to (a) POM 1, (b) POM 2, and cross-power spectral density (CPSD) (c) magnitude, (d) phase.

The location downstream of the injector exit, where the helical disturbances begin to dominate the inner shear layer region also decreased with increasing J . This is in accordance with the well known progression of development of shear-layer instabilities in axisymmetric single or coaxial jets [6,7]. In the region close to the jet exit, where the shear-layer momentum thickness is very small compared to the jet diameter ($D/\theta \gg 1$), all modes of instability have been shown to have the same growth rates, with the axisymmetric and helical instability growth rates remain significant and comparable while that of the others become negligible. At the end of the potential core, however, the growth rate of helical instabilities becomes the most prevalent. Therefore, what the POMs show may well be the helical mode of instability of the jet.

Figures 6(e-h) and Figures 7(e-h) show the corresponding CPSD magnitude spectra for increasing J values at $Pr = 0.44$ and $Pr = 1.05$, respectively. Clearly, the peak frequencies became broader and moved to higher frequencies as J increased. This behavior was in line with analytical results [7] that with increasing coflow velocity, the region of unstable frequencies becomes broader and that the peak of the spatial growth rates shift to higher frequencies. Another notable outcome from these spectra was that the peak frequencies were not dependent on R or J , but on the magnitude of the outer jet velocity. Despite the significant rise in R or J from Figure 6(g) to Figure 6(h), the peak for the latter sat at a slightly lower frequency than the former, since as shown in Table 2 in the Appendix, the magnitude of the outer velocity was smaller. However, further investigation will need to be done to generalize this outcome.

As described earlier, the only distinguishing design feature between LAR and SAR was A_o/A_i , where it was almost an order of magnitude smaller for the latter. Figures 8(a-d) and Figures 9(a, b) show similar snapshot, average and POM images for SAR at $Pr = 0.44$ and $Pr = 1.05$, respectively. At $Pr = 0.44$, it is evident that increasing J had a weaker influence on the dark-core length unlike for LAR. Due to the small hydraulic radius of the outer jet of SAR, the potential core of the outer jet was relatively short. Thus, an effective entrainment of the inner jet by the outer jet was limited to a relatively shorter distance from the exit plane. The influence of J on the dark-core length at $Pr = 1.05$ was more significant again due to the severely reduced to non-existent surface tension at the inner jet boundary.

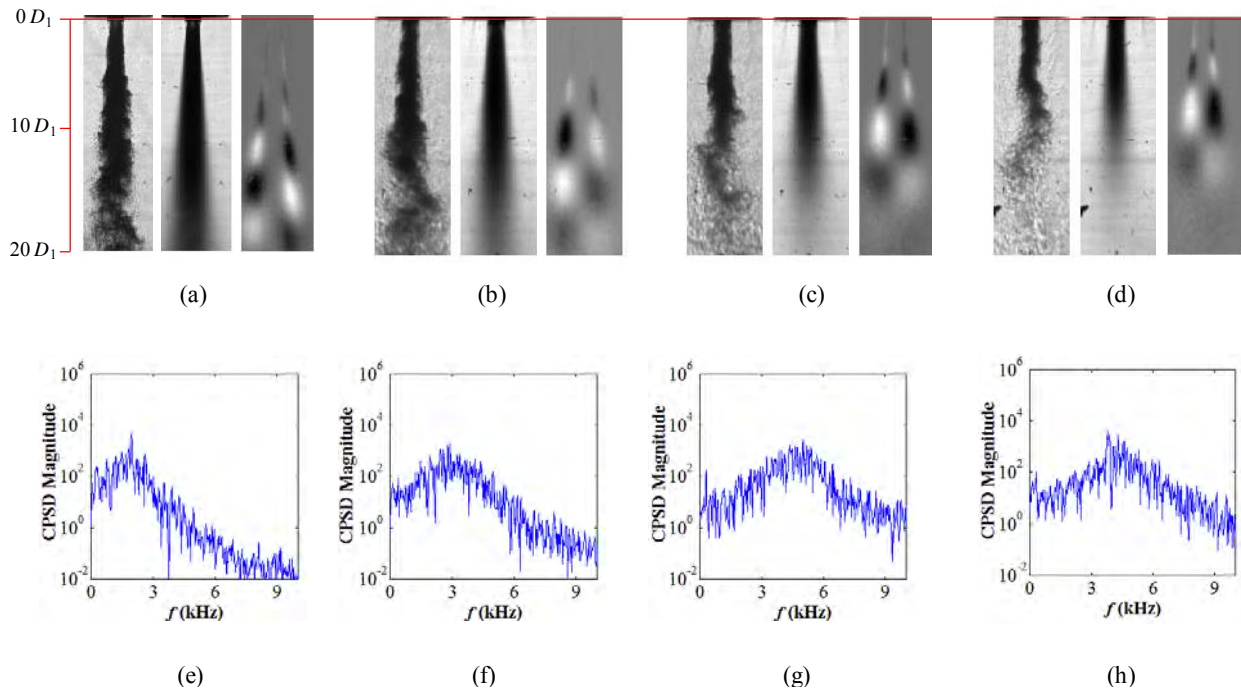


Figure 6. Baseline LAR flow at $Pr = 0.44$: snapshot, average, POM images for J (a) 2.1, (b) 5.2, (c) 11, (d) 20, and CPSPD magnitude for J (e) 2.1, (f) 5.2, (g) 11, (h) 20.

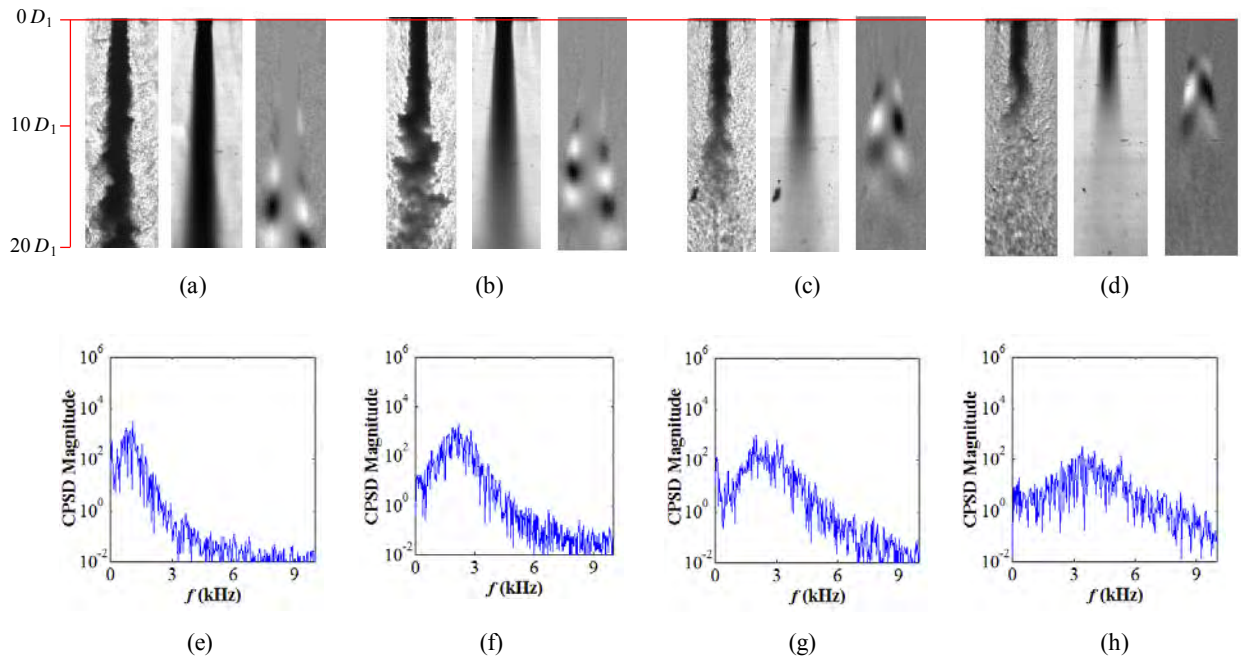


Figure 7. Baseline LAR flow at $Pr = 1.05$: snapshot, average, POM images for J (a) 0.5, (b) 1.9, (c) 5.0, (d) 12, and CPSPD magnitude for J (e) 0.5, (f) 1.9, (g) 5.0, (h) 12.

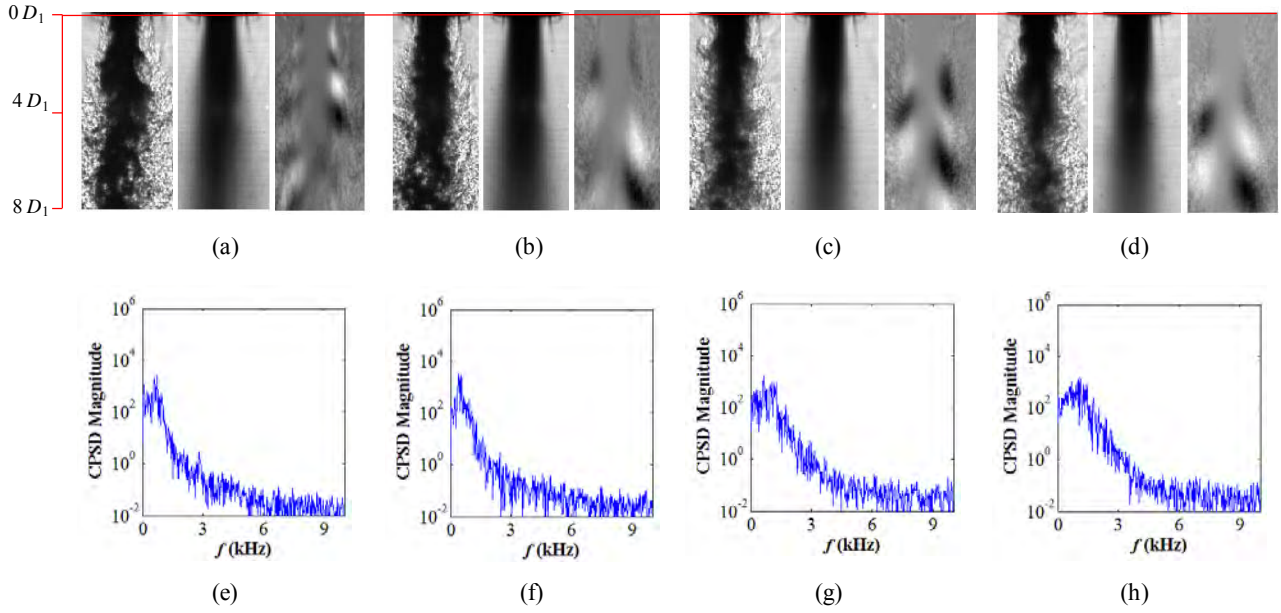


Figure 8. Baseline SAR flow at $Pr = 0.44$: snapshot, average, POM images for J (a) 2.0, (b) 5.2, (c) 12, (d) 17, and CPSD magnitude for J (e) 2.0, (f) 5.2, (g) 12, (h) 17.

The CPSD magnitude spectra in Figures 8(e-h) and Figures 9(c, d) show that the peak frequencies appear to be unaffected with increasing J values. This was in contradiction to the expected shift to higher frequencies and broadening of the range of peak frequencies as demonstrated by [7] for an increasing coflow velocity. The reason behind this may again be explained by how soon the inner and outer jets attain a single jet behavior, thereby rendering the effect of coflow nonexistent.

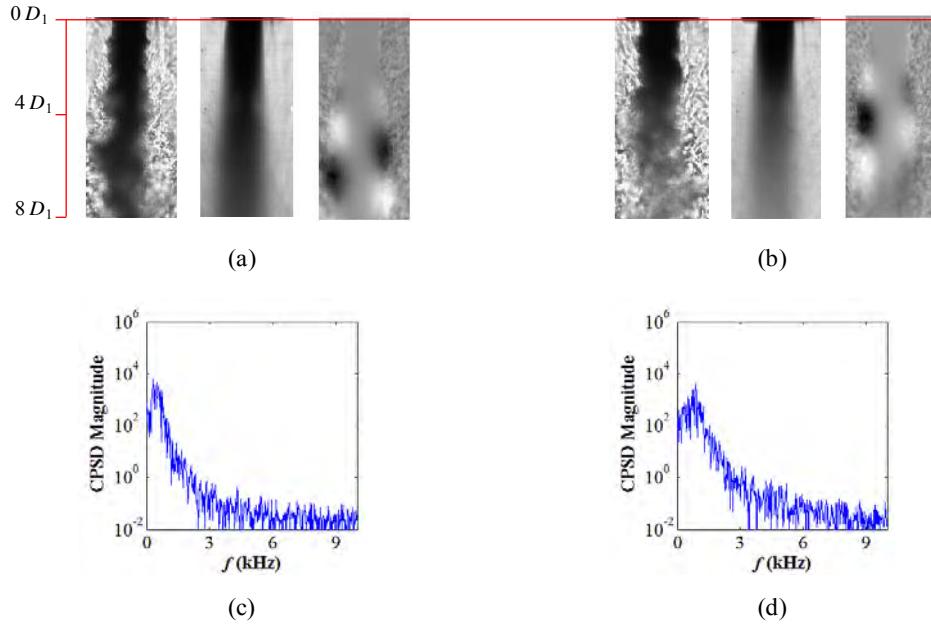


Figure 9. Baseline SAR flow at $Pr = 1.05$: snapshot, average, POM images for J (a) 9.4, (b) 19, and CPSD magnitude for J (c) 9.4, (d) 19.

ACOUSTICALLY FORCED (PAN)

The PAN condition established a region of locally maximum pressure fluctuation in the vicinity of the coaxial jets so that the velocity fluctuation was minimum or non-existent in the ideal case. As pressure is a scalar physical quantity, PAN can essentially be regarded as a condition that creates a symmetric fluctuation in pressure about the jet center plane that is normal to the transverse direction of propagation of the acoustic waves.

Figure 10 shows the flow response under PAN condition for the same case in Figure 3 without acoustics. The snapshot image in Figure 10(a) clearly depicts a series of orderly structures formed along almost the entire inner jet column. They appear to have started forming near the injector exit, and grew as they propagated farther downstream due to the entrainment effect of the outer jet. This planar view of the structures depicts them as varicose instability structures in a planar jet. As a matter of fact, varicose instability plays a similar role in planar jets as does axisymmetric instability in round jets [21]. The POMs shown in Figure 10(c) give further evidence of the symmetric structures that started forming immediately downstream of the injector exit, and spread as they traveled downstream.

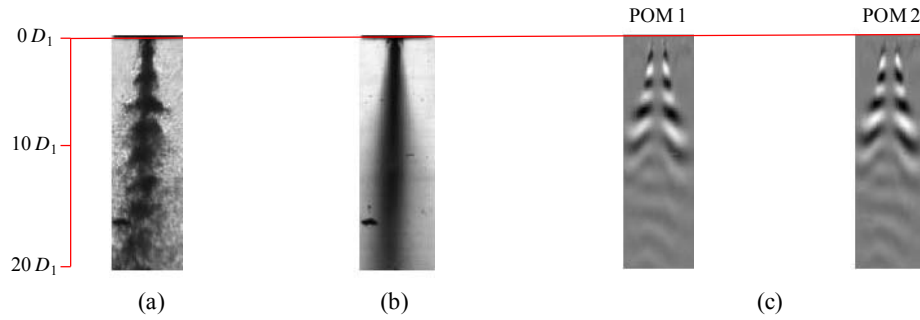


Figure 10. PAN forced ($f_F = 3.14$ kHz) LAR flow at $Pr = 0.44$, $J = 0.5$: (a) snapshot image, (b) average image, (c) proper orthogonal mode (POM).

The dark-core length and inner-jet spread angles also underwent noticeable changes under this forcing condition. The dark-core is visibly shorter ($< 20D_1$). As Figure 10(b) more vividly shows, on average, the dark-core flow pervades more of the flow field than it did in Figure 3(b), hence, indicating an enhanced mixing between the two flows.

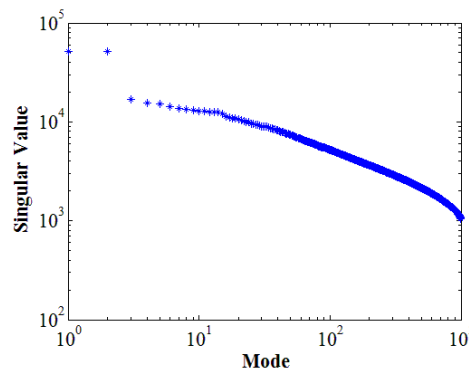


Figure 11. PAN forced ($f_F = 3.14$ kHz) LAR flow at $Pr = 0.44$, $J = 0.5$: singular values

Another unique nature of the flow response to PAN forcing is depicted in Figures 11 and 12(a, b). Figure 11 shows that the flow response to PAN forcing represented by POMs 1 and 2 in Figure 10(c) was the dominant type of response. The relative magnitudes of all other modes were similar to those for the baseline shown in Figure 4. Moreover, the spectral plots in Figures 12(a, b) associated with POMs 1 and 2 indicate that the orderly structures had a characteristic frequency that was identical to the forcing acoustic frequency, f_F . This may seem to be

a trivial outcome of external forcing, yet it does tell a lot about the nature of the flow stability as will be discussed below. Figure 12(c) shows the CPSD magnitude of the forced conjugate modes overlaid with the one for the baseline conjugate modes in Figure 5(c). It shows that f_F completely overtook the baseline characteristic frequencies, which are no longer visible in the spectra of the PAN condition.

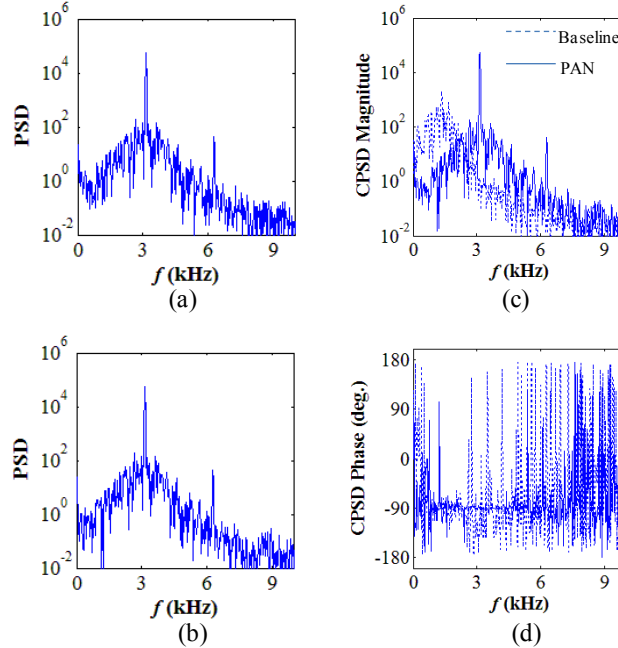


Figure 12. PAN forced ($f_F = 3.14$ kHz) LAR flow at $Pr = 0.44$, $J = 0.5$: power spectral density (PSD) of the temporal amplitude coefficients of the decomposition corresponding to (a) POM 1, (b) POM 2, and cross-power spectral density (CPSD) (c) magnitude, (d) phase.

Figures 13 and Figures 14 present the forced counterparts to the baseline cases at $Pr = 0.44$ and $Pr = 1.05$, respectively, presented in Figures 6 and 7 for varying J values using LAR. Similar to the forced case of $J = 0.5$ at $Pr = 0.44$, the forced lower J cases underwent noticeable reductions in their dark-core lengths while it became less and less so with increasing J as shown in Figures 13(a-d) and 14(a-d). In addition, for a similar J , it can be qualitatively argued that the $Pr = 1.05$ cases underwent a larger reduction in dark-core length compared to their $Pr = 0.44$ counterparts. The same argument involving surface tension or the lack there of can be made here as to why the $Pr = 1.05$ cases were more influenced by forcing.

The lobe patterns visible in the POMs also showed a peculiar transition with increasing J at both Pr conditions. Considering $Pr = 0.44$, for example, the lower J values [Figures 10(c) and 13(a)] showed a symmetric lobe pattern due to PAN forcing, whereas with increasing J , the symmetry became more skewed, and eventually turned into an antisymmetric pattern identical to the baseline cases. As noted earlier, antisymmetric pattern is the two-dimensional representation of a helical disturbance. The same trend was observed at $Pr = 1.05$. Thus, for the LAR geometry, it can be concluded that the dominant flow response to PAN forcing at low J is in the form of amplified symmetric disturbances, while that at higher J transitions to helical disturbances identical to those present in flows without acoustic forcing.

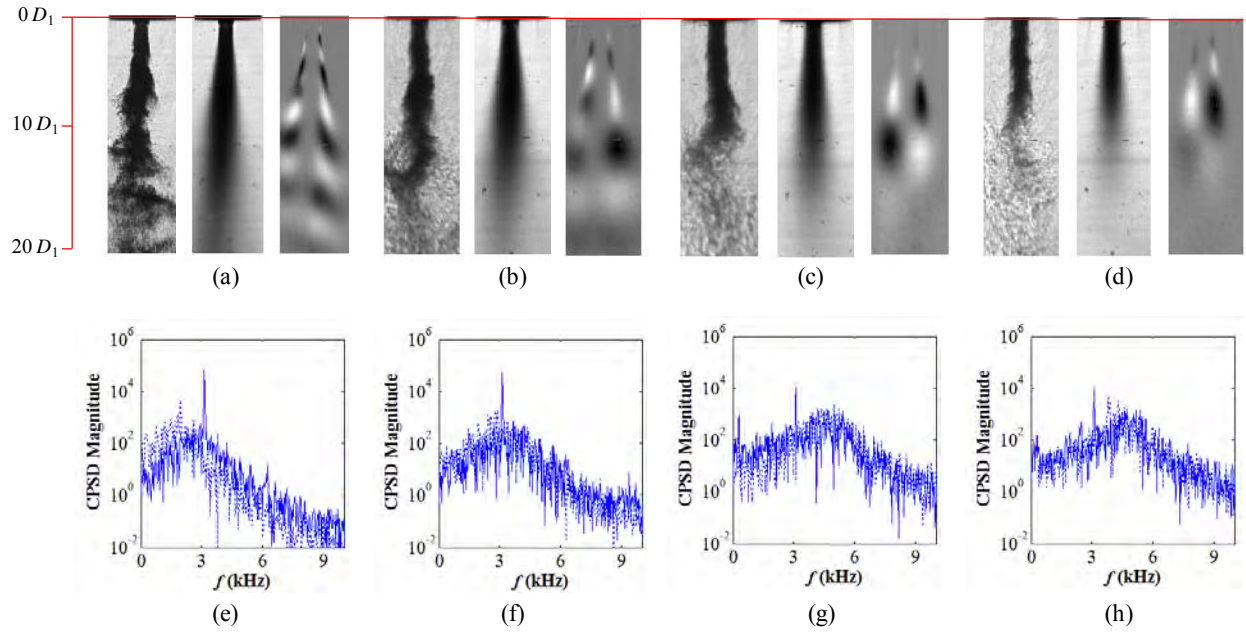


Figure 13. PAN forced LAR flow at $Pr = 0.44$: snapshot, average, POM images and CPSD magnitudes for J (a),(e) 2.1 ($f_F = 3.12$ kHz); (b),(f) 5.2 ($f_F = 3.12$ kHz); (c),(g) 11 ($f_F = 3.10$ kHz); (d),(h) 20 ($f_F = 3.11$ kHz). (..... Baseline, ——— PAN)

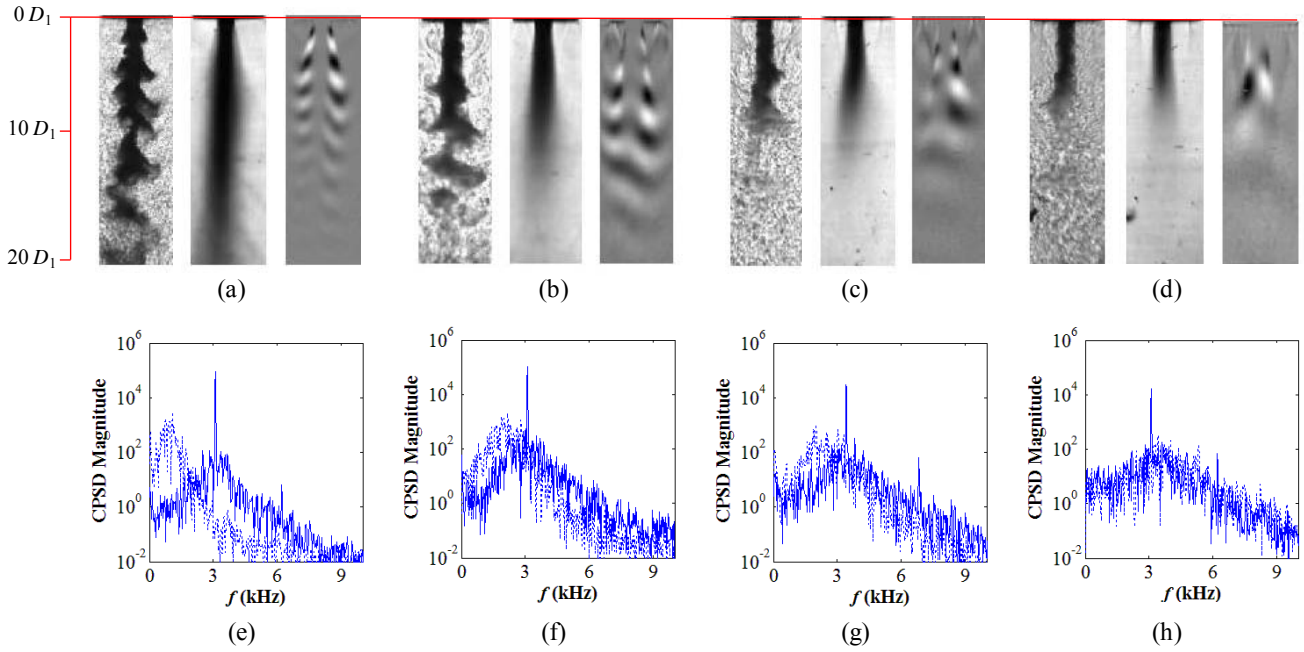


Figure 14. PAN forced LAR flow at $Pr = 1.05$: snapshot, average, POM images and CPSD magnitude for J (a) 0.5 ($f_F = 3.10$ kHz), (b) 1.9 ($f_F = 3.10$ kHz), (c) 5.0 ($f_F = 3.41$ kHz), (d) 12 ($f_F = 3.10$ kHz). (..... Baseline, ——— PAN)

The temporal characteristics of the flow response to the acoustic forcing are shown in the spectral plots in Figures 13(e-h) and Figures 14(e-h) overlaid with the baseline spectra. Again considering $Pr = 0.44$, the spectral content of the lower J values [Figures 11(c) and 13(e)] was such that during forcing, a peak in the magnitude at f_F completely took over the low peak frequencies of the baseline flows. As J increased, the significance of the peak at f_F relative to the baseline peak frequencies became more and more diminished, and the forced spectra began retaining more of the baseline spectra, as clearly evident in the highest J attained (due to limitations of the experiment for the specified jet temperatures) in Figure 13(h). In other words, the spectral energy contained at f_F for lower J values was less so at higher J values. A similar trend in the spectra was also seen at $Pr = 1.05$, despite the highest attainable J was not as high as that for $Pr = 0.44$.

The nature of the flow response to an external disturbance depending on the flow condition, namely J , may be used to characterize the state of stability of the flow. Previous works [18,19,20] on flow stability characterize convectively unstable flows as noise amplifiers; that is, they are prone to external flow disturbances such as acoustic disturbances used in this study. Their spectral characteristics are such that when exposed to external forcing, their natural instabilities are completely removed and replaced by instabilities whose frequency match those of the forcing frequency [22]. Absolutely unstable flows, on the other hand, are characterized as naturally self-excited flows that do not respond well to external disturbances. Their spectra preserve the natural instabilities with or without a coexisting frequency content associated with the forcing frequency. These and the flow responses observed at both $Pr = 0.44$ and $Pr = 1.05$ may be used to argue that LAR flows may be characterized as convectively unstable for low J flows, and transition into absolutely unstable flows with increasing J values.

The response of SAR flows to PAN forcing were drastically different from that of LAR as shown in Figures 15 and Figures 16. At $Pr = 0.44$ and for lower J values ($J = 2.0, 5.2$), strong symmetric disturbances annihilate the inner jet flow, thus severely limiting the dark-core region to within $2-3D_1$. The corresponding CPSD magnitude spectra also reveal local peaks around subharmonic frequencies ($0.5f_F$), which indicate vortex merging processes. For the higher J values ($J = 12, 17$), although symmetric disturbances were not as strong as in the lower J cases, they nevertheless were still prevalent as evident in the POM images and the CPSD magnitude spectra. At $Pr = 1.05$, symmetric disturbances were again prevalent even for the highest J . However, as their spectra reveals, disturbances at the subharmonic frequencies were the most dominant indicating that vortex merging prevailed in the flow field.

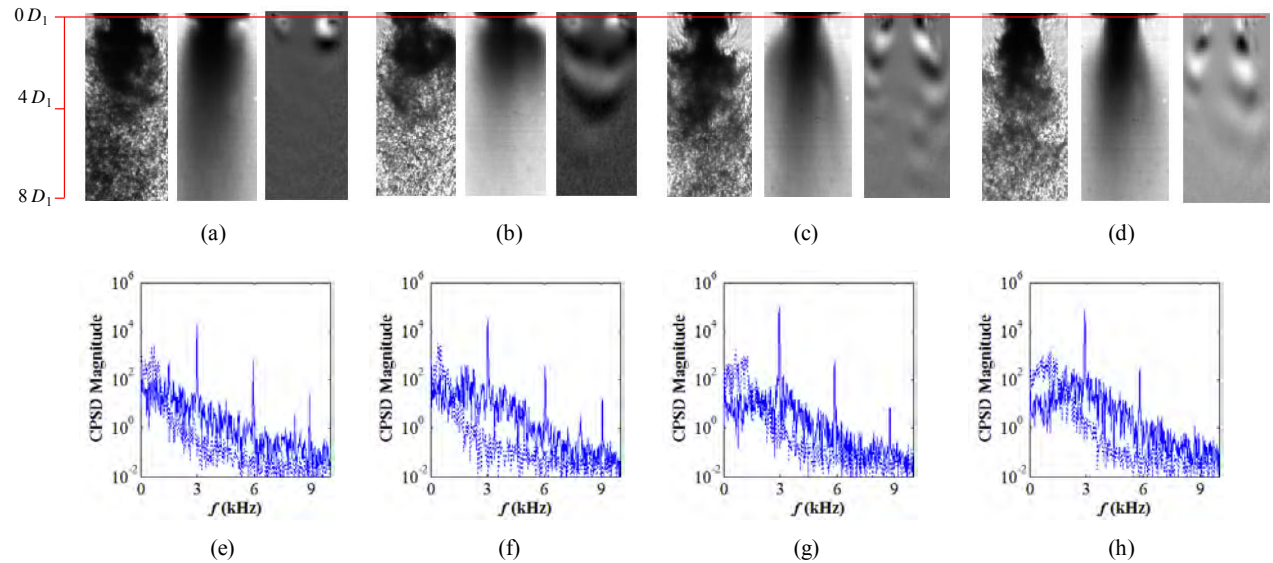


Figure 15. PAN forced SAR flow at $Pr = 0.44$: snapshot, average, POM images and CPSD magnitude for J (a),(e) 2.0 ($f_F = 2.97$ kHz); (b),(f) 5.2 ($f_F = 3.02$ kHz); (c),(g) 12 ($f_F = 2.92$ kHz); (d),(h) 17 ($f_F = 2.90$ kHz). (..... Baseline, ——— PAN)

As the spectra in Figures 15(e-f) and Figures 16(c, d) also reveal, the flow showed strong response to external forcing regardless of the J value. This was again evident by the lack of any remnants of the low-frequency peaks present in the forced spectra. Accordingly, SAR flows depicted the behavior of convectively unstable flows per the discussion for LAR.

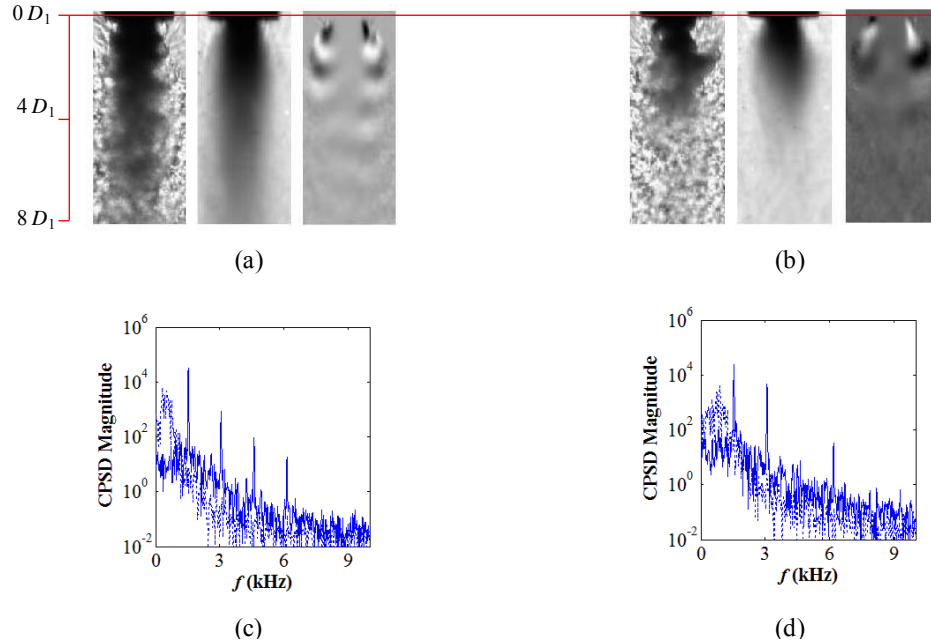


Figure 16. PAN forced SAR flow at $Pr = 1.05$: snapshot, average, POM images and CPSD magnitude for J (a),(c) 9.4 ($f_F = 3.07$ kHz); (b),(d) 19 ($f_F = 3.09$ kHz). (..... Baseline, ——— PAN)

From a practical standpoint, it is crucial to ensure that the injector flow under non-design operating conditions behave as closely as possible to that under design operating conditions. Flow disturbances that arise as a result of acoustic instabilities due to excitation of the combustion chamber acoustic modes are typical instances of non-design operating conditions. Although special cases of the chamber acoustic behavior can be modeled and incorporated in the design considerations, a great many other unpredictable scenarios exist. Hence, the best approach is to implement a robust design that guarantees predictable flow behavior for a given set of flow conditions regardless of any externally imposed disturbances. In light of this argument, LAR would be considered a preferable design configuration solely on the fact that it has been shown to be less sensitive to external disturbances at high J values.

CONCLUSION

This study examined the dynamic behavior of flow structures that develop in the inner shear layer of shear-coaxial nonreactive jets with and without the present of transverse acoustic forcing. A proper orthogonal decomposition of pixel intensity fluctuation data revealed both the spatial and temporal characteristics of these flow structures for subcritical and nearcritical pressure regimes and a range of J values using two injector exit geometries.

The large outer-to-inner jet area ratio (LAR) injector baseline flows exhibited helical instabilities at far enough downstream locations regardless of J . The frequencies of the flow structures associated with these helical instabilities shifted to higher frequencies with increasing magnitudes of jet velocities. Pressure antinode (PAN) acoustic forcing of low J LAR flows showed strong response by forming symmetric structures whose frequencies were identical with the forcing frequencies. Magnitude spectral plots also showed large peaks at the forcing frequencies and the baseline flow peak frequencies were completely removed from the forced spectra. With

increasing J , however, the response to forcing became gradually weaker, and the broad baseline peak frequencies coexisted with the peaks at the forcing frequency.

The small outer-to-inner jet area ratio (SAR) injector baseline flows also exhibited helical instabilities. However, unlike LAR, the frequencies of the flow structures did not show significant shift to higher frequencies with increasing jet velocities. In addition, regardless of J , they showed strong response to PAN forcing. Thus, due to their readily responsiveness to external acoustic forcing, SAR flows may be regarded as a class of flows that display convectively unstable behavior. On the contrary, LAR flows displayed a transition from convectively unstable to absolutely unstable flow behavior with increasing J . This makes LAR flows at large enough J more desirable from a design standpoint since they behave in a predictable manner despite externally imposed disturbances such as those that arise due to the excitation of combustion chamber acoustic modes.

Acknowledgements: The authors would like to thank Mr. Randy Harvey for his invaluable contributions in running and maintaining the experimental facility. They appreciate Dr. Juan Rodriguez for providing the image data for the SAR injector. They also would like to thank Mr. Brian Newkirk, Mr. David Hill, and Mr. John Hasier for providing technical assistance while running the experiments. This work is sponsored by AFOSR under Dr. Mitat Birkan, program manager.

REFERENCES

- [1] Ko, N. W. M. and Kwan, S. H. 1976 The initial region of subsonic coaxial jet. *J. Fluid Mech.* **73**, 305-332.
- [2] Dahm, W. J. A., Frieler, C.E., and Tryggvason, G. 1992 Vortex structure and dynamics in the near field of a coaxial jet. *J. Fluid Mech.* **241**, 371-402.
- [3] Wicker, R.B. and Eaton, J.K. 1994 Near Field of a Coaxial Jet With and Without Axial Excitation. *AIAA Journal* **32**, 542-546.
- [4] Balarac, G., Métais, O. and Lesieur, M. 2007 Mixing enhancement in coaxial jets through inflow forcing: A numerical study. *Phys. Fluids* **19**, 075102.
- [5] Gladnick, P. G., Enotiadis, A. C., LaRue, J. C. and Samuelsen, G. S. 1990 Near-field characteristics of a turbulent coflowing jet. *AIAA Journal* **28**, 1405-1414.
- [6] Cohen, J. and Wygnanski, L. 1987 The Evolution of Instabilities in an Axisymmetric Jet, Part I. Linear Growth of Disturbances Near the Nozzle. *J. Fluid Mech.* **176**, 191-219.
- [7] Michalke, A. and Hermann, G. 1982 On the inviscid instability of a circular jet with external flow. *J. Fluid Mech.* **114**, 343-359.
- [8] Davis, D.W., "On the behavior of a shear-coaxial jet, spanning sub- to supercritical pressures, with and without an externally imposed transverse acoustic field. Ph.D. Thesis," Penn State University, 2005.
- [9] Davis, D.W. and Chehroudi, B. 2007 Measurements in an Acoustically Driven Coaxial Jet under Sub-, Near-, and Supercritical Conditions. *J. Propulsion and Power* **23**, 2.
- [10] Leyva, I. A., Chehroudi, B., Talley, D., "Dark-core analysis of coaxial injectors at sub-, near-, and supercritical conditions in a transverse acoustic field", *54th JANNAF Meeting*, Denver, CO, May 14-18, 2007
- [11] Leyva, I.A., Chehroudi, B. and Talley, D., "Dark-core analysis of coaxial injectors at sub-, near-, and supercritical pressures in a transverse acoustic field". *43rd AIAA/ASME/SAE/ASEE Joint Propulsion Conference and Exhibit*, AIAA 2007-5456.

- [12] Leyva, I.A., Rodriguez, J.I., Chehroudi, B. and Talley, D. Preliminary, “Results on Coaxial Jet Spread Angles and the Effects of Variable Phase Transverse Acoustic Fields. *46th AIAA Aerospace Sciences Meeting and Exhibit*, AIAA 2008-950.
- [13] Rodriguez, J. I., Graham, J. J., Leyva, I. A., Lyu, H.-Y., Talley, D., “On the Inner Jet Spread Angles of Coaxial Jets from Subcritical to Supercritical Conditions with Preliminary Numerical Results”, *55th JANNAF Propulsion/4th Liquid Propulsion Subcommittee Meeting*, Orlando, FL, December 8-12, 2008.
- [14] Rodriguez, J. I., “Acoustic Excitation of Liquid Fuel Droplets and Coaxial Jets,” Ph.D. Thesis, University of California, Los Angeles, 2009.
- [15] Chatterjee, A. 2000 An introduction to the proper orthogonal decomposition. *Current Science* **78**, 7.
- [16] Arienti, M, and Soteriou, M.C. 2009 Time-resolved proper orthogonal decomposition of liquid jet dynamics. *Phys. Fluids* **21**, 112104.
- [17] Narayanan, V., Lightfoot, M.D.A, Schumaker, S.A. Schumaker, Danczyk, S.A., and Eilers, B., “Use of Proper Orthogonal Decomposition Towards Time-resolved Image Analysis of Sprays,” *ILASS Americas, 23rd Annual Conference on Liquid Atomization and Spray Systems*, Ventura, CA, May 2011
- [18] Huerre, P. and Monkewitz, P.A. 1990 Local and Global Instabilities in Spatially Developing Flows. *Annu. Rev. Fluid Mech.* **22**, 473-537
- [19] Huerre P. 2000. Open shear flow instabilities. In *Perspectives in Fluid Dynamics*, ed. G.K. Batchelor, H.K. Moffatt, M.G. Worster, pp. 159–229. Cambridge, UK: Cambridge Univ.
- [20] Jendoubi, S. and Strykowski, P.J. 1994 Absolute and convective instability of axisymmetric jets with external flow. *Phys. Fluids* **6**, 3000.
- [21] Sevilla, A., Gordillo, J. M. and Martínez-Bazán, Ç. 2002 The effect of the diameter ratio on the absolute and convective instability of free coflowing jets. *Phys. Fluids* **14**, 3028.
- [22] Megerian, S., Davitian, J., Alves, L. S. de B. & Karagozian, A. R. 2007 Transverse jet shear-layer instabilities. Part 1. Experimental studies. *J. Fluid Mech.* **593**, 93–129.

APPENDIX

Table 2. Summary of flow conditions and parameters

$Pr = 0.44$, LAR

J	R	T_{chamber} (K)	ρ_{chamber} (kg/m ³)	P_{chamber} (MPa)	T_{outer} (K)	\dot{m}_{outer} (mg/s)	ρ_{outer} (kg/m ³)	u_{outer} (m/s)	Re_{outer} (10 ⁴)	T_{inner} (K)	\dot{m}_{inner} (mg/s)	ρ_{inner} (kg/m ³)	u_{inner} (m/s)	Re_{inner} (10 ⁴)
0.5	3.5	217	24	1.50	204	1106	26	10.7	3.1	110	727	622	3.0	2.4
2.1	7.4	220	23	1.50	205	2212	25	21.5	6.3	107	725	646	2.9	2.1
5.2	11	221	23	1.50	203	3531	26	33.9	10	108	733	639	3.0	2.2
11	17	216	24	1.51	204	4991	26	47.9	14	107	722	646	2.9	2.1
20	22	220	23	1.50	204	4633	26	44.8	13	110	482	622	2.0	1.6

$Pr = 1.05$, LAR

J	R	T_{chamber} (K)	ρ_{chamber} (kg/m ³)	P_{chamber} (MPa)	T_{outer} (K)	\dot{m}_{outer} (mg/s)	ρ_{outer} (kg/m ³)	u_{outer} (m/s)	Re_{outer} (10 ⁴)	T_{inner} (K)	\dot{m}_{inner} (mg/s)	ρ_{inner} (kg/m ³)	u_{inner} (m/s)	Re_{inner} (10 ⁴)
0.5	2.1	223	56	3.56	199	1742	65	6.6	4.8	115	724	605	3.1	2.5
1.9	4.1	221	57	3.56	200	3479	65	13.3	9.6	118	724	577	3.3	2.8
5.0	6.5	223	57	3.58	203	4189	64	16.2	11	122	511	531	2.5	2.4
12	9.9	223	56	3.57	208	6217	62	24.9	17	124	482	497	2.5	2.5

$Pr = 0.44$, SAR

J	R	T_{chamber} (K)	ρ_{chamber} (kg/m ³)	P_{chamber} (MPa)	T_{outer} (K)	\dot{m}_{outer} (mg/s)	ρ_{outer} (kg/m ³)	u_{outer} (m/s)	Re_{outer} (10 ⁴)	T_{inner} (K)	\dot{m}_{inner} (mg/s)	ρ_{inner} (kg/m ³)	u_{inner} (m/s)	Re_{inner} (10 ⁴)
2.0	6.9	246	21	1.49	195	450	27	6.6	1.1	109	925	630	0.96	1.5
5.2	11	217	24	1.49	184	750	29	10	1.9	110	925	620	0.97	1.5
12	17	222	23	1.49	194	1100	27	16	2.6	108	925	640	0.94	1.4
17	20	217	24	1.48	194	1300	27	19.3	3.1	108	925	638	0.95	1.4

$Pr = 1.05$, SAR

J	R	T_{chamber} (K)	ρ_{chamber} (kg/m ³)	P_{chamber} (MPa)	T_{outer} (K)	\dot{m}_{outer} (mg/s)	ρ_{outer} (kg/m ³)	u_{outer} (m/s)	Re_{outer} (10 ⁴)	T_{inner} (K)	\dot{m}_{inner} (mg/s)	ρ_{inner} (kg/m ³)	u_{inner} (m/s)	Re_{inner} (10 ⁴)
9.4	9.9	214	59	3.58	203	1460	63	9.2	3.2	109	925	650	0.93	1.3
19	14	215	59	3.56	207	2060	62	13	4.5	111	925	635	0.95	1.4

Cryogenic High-Pressure Shear-Coaxial Jets Exposed to Transverse Acoustic Forcing

Sophonias Teshome*

Department of Mechanical and Aerospace Engineering, UCLA, Los Angeles, CA 90095-1597

Ivett A. Leyva[†] and Douglas Talley[‡]

Air Force Research Laboratory, Edwards AFB, CA

Ann R. Karagozian[§]

Department of Mechanical and Aerospace Engineering, UCLA, Los Angeles, CA 90095-1597

This experimental study investigated the mixing characteristics and response of dynamic flow structures of cryogenic coaxial nitrogen jets to pressure perturbations due to transverse acoustic forcing at a pressure antinode (PAN). The role of injector exit geometry was examined using two shear-coaxial injectors with different outer-to-inner jet area ratios. Flow conditions for varying outer to inner jet momentum flux ratios (0.5 - 20), and acoustic pressure antinode at the jet axis location, under subcritical chamber pressures (reduced pressure of 0.44) were considered. Dark-core length measurements of the dense inner jet were used to indicate the extent of mixing under different flow conditions and injector geometries. A basic application of proper orthogonal decomposition on the intensity fluctuation of high-speed images enabled the extraction of the spatial and temporal characteristics of the dominant flow structures that existed in the flow field during exposure to acoustic forcing. Regardless of injector geometry or pressure regime, low outer to inner momentum flux ratio flows were found to be responsive to acoustic pressure antinode forcing. With increasing momentum flux ratio, however, the flow response to forcing depended on the injector geometry.

Nomenclature

A	area
a	vector of time-dependent amplitude coefficients
B	matrix of image pixel intensities
D	diameter
f	frequency
J	outer to inner jet momentum flux ratio, $\rho_o U_o^2 / \rho_i U_i^2$
L	dark-core length
m	no. of columns of pixels in a single image frame
\dot{m}	mass flow rate
N	no. of image frames
n	no. of rows of pixels in a single image frame
P	pressure
P_r	reduced pressure, P/P_{cr}
Q	matrix of column vectors, a
R	outer to inner jet velocity ratio, U_o/U_i

*Graduate Student Researcher, AIAA Student Member.

[†]Senior Aerospace Engineer, AIAA Member.

[‡]Principal Research Scientist, AIAA Member.

[§]Professor, AIAA Fellow.

Re	Reynolds number
S	outer to inner jet density ratio, ρ_o/ρ_i
T	temperature
U	jet velocity
\mathbf{V}	matrix of column vectors, ϕ
λ	wavelength of period flow structures
ϕ	proper orthogonal mode
ρ	density

Subscript

B	baseline or no acoustic forcing
F	acoustically forced
i	pertaining to the inner jet
o	pertaining to the outer jet
s	pertaining to periodic flow structures

I. Introduction

Coaxial injectors have proven to be one of the most effective and simple means of delivering propellants in combustion devices such as in liquid rocket engines (LREs). Their application in LREs in the United States was seen as early as the development of the J-2 engine and as recently as the space shuttle main engine (SSME). Combustion instability is a phenomenon that can destroy an LRE in less than a second. It is primarily a result of feedback interactions between unsteady combustion rates and pressure fluctuations from acoustic modes in the combustion chamber. Since injector flows are directly involved in processes that take place inside combustors, it is crucial to understand how they contribute to, as well as how they are affected by, these unsteady physical mechanisms that lead to combustion instabilities. However, a successful understanding at a fundamental level of these interactions between injector flows and chamber phenomena can be aided by first isolating the fluid dynamics aspect from the reactive flow processes, and studying the coupling of non-reactive injector flow instabilities with external pressure perturbations.

Shear-coaxial jets consist of a circular core or inner jet and an annular or outer jet. In the near field region, where the potential cores of both the inner and outer jets exist, two shear-layers exist: an inner shear layer between the inner and outer jet flow, and an outer shear layer between the outer jet and the ambient fluid.¹ The development of instabilities in the individual shear layer, and the interaction between the two shear layers has a direct impact on the eventual instability characteristics of the entire flow field. Several studies²⁻⁴ investigate the existence and behavior of vortex structures in the near-field region of single-phase similar or different density coaxial jets. It is shown that for outer jet velocity (U_o) to inner jet velocity (U_i) ratios exceeding unity ($R = U_o/U_i > 1$), coherent structures in the outer shear layer dominate those in the inner shear layer.

The influence of these coherent structures on the overall dynamics of the flow field calls for an understanding of the factors leading to their formation. Detailed studies on the development and growth of natural instabilities in a single circular jet⁶ or a single circular jet with coflow⁷ reveal two of the most significant natural modes of instability: the axisymmetric and the first azimuthal or helical modes. These modes have comparable amplification rates over most of the core region downstream of the exit, with the helical mode eventually dominating the flow field farther downstream. It is shown¹ that the development of the outer shear layer of a coaxial jet behaves as the shear layer of a single jet, while the development of the inner shear layer behaves as that of a single jet issuing into an external coflow. Thus, the axisymmetric and helical modes of instability, along with natural as well as externally imposed flow conditions such as pressure or velocity perturbations, affecting their development, may be used to assess the stability of the coaxial jet.

Of equal importance in the application of coaxial jets is the mixing between the inner jet, usually the oxidizer, and the outer jet, the fuel. Since the growth and development of the shear layers is directly related to the mixing of the two jets, one way of quantifying the degree of mixing is to determine the inner jet potential core length.^{1,8-10} The inner jet potential core ends once the inner shear layer converges on the jet axis. The current study does not involve detailed velocity profile measurements, but takes advantage of the dark images of back-lit dense inner jets, thus obtaining measurement of the dark-core length,^{13,14,17} which

is related to the inner jet potential core length.

The present study continues the series of experimental studies done in the same facility,^{11–17} which have examined the behavior of shear-coaxial N₂ jets at elevated pressures with and without the presence of a transverse acoustic field. It examines the baseline flow characteristics of two injectors with similar inner jet post thickness to diameter ratio, but different outer to inner jet area ratios, for different momentum flux ratios. The present study also investigates the flow response to a pressure antinode forcing condition, where the coaxial jet is exposed to the maximum local pressure fluctuations in a transverse acoustic field. Dark-core length measurements are made to survey the effect of varying momentum flux ratios and that of the presence of acoustic forcing on the mixing behavior of the two jets. Unlike previous studies in the current facility, the present study applies a proper orthogonal decomposition (POD) analysis (see next section) to reduce the information obtained from a set of high-speed back-lit images in order to characterize the spatial and temporal behavior of dominant flow structures in the inner shear layer of the baseline and acoustically forced flows. Using this new approach, the goal is to gain a better understanding of the evolution of flow instabilities, and underline the critical differences in the flow stability characteristics brought about as a result of simple design alterations in the shear-coaxial injector.

II. Experimental Set-Up and Methods

These experiments were carried out at the Air Force Research Laboratory (AFRL), Edwards, test cell EC-4. Figure 1 shows a schematic of the experimental facility. The chamber was designed to operate at pressures spanning subcritical to supercritical pressures of N₂, whose critical pressure is 3.4 MPa, and critical temperature is 126 K.

The inner and outer jets as well as the chamber pressurization flows were supplied by ambient temperature, high pressure N₂ lines. Counter-flow heat exchangers using liquid nitrogen as the coolant fluid were used to cool the test fluids down to the desired temperatures. An unshielded Omega type-E thermocouple with a bead diameter of 0.25 mm was mounted on top of two linear positioning stages and placed near the injector to measure the radial temperature profile of the coaxial jet within one inner jet diameter from the exit plane. Porter mass flow meters (model 123-DKASVDAA) were used to measure the inner and outer jet flow rates, which were controlled via metering valves. The jets issued into the test section (Figure 1) of the inner chamber halfway between the two piezo-sirens located at opposite ends of the chamber. Each piezo-siren was fitted with a waveguide that transitioned from a circular cross-section to a rectangular one. The inner chamber was used to maximize the amplitude of acoustic oscillations generated by the piezo-sirens. However, both the inner and main chambers were maintained at the same static pressure, which was measured with a Stellar ST1500 pressure transducer. The outer to inner jet momentum flux ratio ($J = \rho_o U_o^2 / \rho_i U_i^2$), velocity ratio ($R = U_o / U_i$), and other flow conditions were determined based on thermophysical properties evaluated at the measured chamber pressure, and jet exit temperatures. Kulite absolute (CCQ-093) and differential (XCQ-093, XCE-093) pressure transducers were also used for making high-speed acoustic pressure measurements. These pressure transducers were placed along the inner chamber wall, where one transducer was located directly behind the jet, and two others inside the injector plenums.

The acoustic wave signals were generated using a Fluke 292 arbitrary waveform generator. A Trek PZD2000A high-voltage amplifier amplified continuous sine wave signals from the waveform generator before being input into each piezo-siren. The resulting acoustic waves from each piezo-siren were traveling waves that propagated transversely along the waveguide. Depending on the phase difference between the signals applied to each piezo-siren, a pressure antinode (PAN) condition, where the perturbation in pressure was maximum, or a pressure node (PN) condition, where the perturbation in pressure was minimum, could be created at the center of the chamber. Thus, using signals that were in-phase (0° phase difference), a PAN condition was established at the center of the waveguide, where the coaxial jets were situated.

Figure 2 shows a schematic of the injector exit with dimensional nomenclature, and Table II provides a summary of the injector exit dimensions under consideration. Both injectors were characterized by small lip thickness to inner diameter ratio t/D_1 , but one had a large outer to inner jet cross-sectional area ratio (LAR), while the other had a small area ratio (SAR).

One of the main parameters used for assessing the effect of varying J values and the impact of the external acoustic field on the coaxial jet mixing was the “dark-core” length of the inner jet measured from high-speed back-lit images. A xenon arc lamp was used to provide a back-lit image of the coaxial jet, which was visualized using a high speed Phantom v7.1 CMOS camera at framing rates exceeding 20 kHz. A detailed

Table 1. Injector exit dimensions (mm)

Injector	t	D_1	t/D_1	D_2	D_3	D_4	A_o/A_i
LAR	0.09	0.70	0.13	0.89	2.44	3.94	10.6
SAR	0.13	1.4	0.09	1.65	2.44	3.94	1.65

discussion of how the dark-core length is defined and measured had previously been reported¹³ and only a brief description will be given here. The original images (Figure 3a) were first converted, or thresholded, to a black and white image using the MATLAB subroutine “im2bw” (Figure 3b). The threshold level was determined using the MATLAB subroutine “graythresh”. This subroutine uses Otsu’s method¹⁸ and it is based on the zeroth and first cumulative moments of the gray-level histogram. Once a black and white image was obtained, the length of the jet was finally determined by drawing a contour around the black and white image and measuring the axial length of the longest contour attached to the injector as shown in Figure 3c.

Proper orthogonal decomposition (POD) of the high-speed images has proven to be a powerful means for extracting relevant qualitative and quantitative information from an otherwise complicated and noise-ridden set of image data. Thus, a pixel intensity data matrix, \mathbf{B} for a set of images may be represented^{19–21} as

$$\mathbf{B} = \sum_{k=1}^M a_k(t) \phi_k(x) \quad (1)$$

where a_k are vectors of temporal amplitude coefficients, ϕ_k are vectors of proper orthogonal modes, k is the mode number, and M is the number of modes. The decomposition was achieved by first arranging all the pixel intensity values of all frames into a single data array, whereby the pixel intensities from one frame occupied one row of the data array. Thus, a set of N consecutive frames, each of which had an n by m pixel resolution, constituted an N by $n \times m$ data array. The temporal mean of the data array was subtracted in order to eliminate the DC component of the intensity values resulting in a matrix $\tilde{\mathbf{B}}$ of intensity fluctuations. The method of singular value decomposition was implemented in MATLAB using a built-in subroutine to represent the matrix of intensity fluctuations as

$$\tilde{\mathbf{B}} = \mathbf{Q} \mathbf{V}^T \quad (2)$$

where \mathbf{Q} is an N by N matrix composed of column vectors a_k , and \mathbf{V} is an N by $n \times m$ matrix composed of column vectors ϕ_k from Equation 1. The matrix \mathbf{Q} is the product of an orthogonal matrix of left singular vectors and a diagonal matrix of singular values of $\tilde{\mathbf{B}}$. The different modes were arranged in decreasing order of significance as dictated by the magnitude of the singular values of the decomposition.

In order to identify the existence of conjugate mode pairs,²⁰ which have a temporal phase difference of $\pm 90^\circ$ and also have similar ϕ_k , the cross-power spectral density of their amplitude coefficients, a_k and b_k was computed as

$$\text{CPSD} = \sum_{s=0}^{N-1} \text{corr}(a_k, b_k) e^{-i\omega s} \quad (3)$$

Here, $\text{corr}(a_k, b_k)$ represents the cross-correlation of a_k and b_k .

III. Results

All the experimental data presented here were obtained under subcritical (reduced pressure, $P_r = 0.44$) pressure conditions: the inner jet was in the liquid phase, while the outer jet was in the gas phase at temperatures well above the saturation temperature of N_2 . Tables of flow conditions and parameters are given in the Appendix. As previously noted, for coaxial jets of different densities, J is one of the governing parameters of coaxial jet mixing. However, for all test cases, the outer to inner jet density ratio ($S = \rho_o/\rho_i$) was held approximately constant while R was varied. Thus, the variation in J in these studies resulted mainly due the variation in R only.

III.A. Characterization of Dark-Core Lengths

The back-lit images were a result of non-uniform density in the coaxial jet flow field due to the difference in temperature of the inner and outer jets. Thus, the denser inner or core jet appears dark, hence the term “dark-core”. Accordingly, the length of dark-core downstream of the injector exit was used as an indicator of the extent of mixing between the inner and outer jets. In addition, although the end of a dark-core is not coincident with the end of a potential core, it was nevertheless a good indicator of the extent of growth of the inner shear layer. The variation in the dark-core lengths with J will now be discussed for the two exit geometries.

Figures 4a and 4b show baseline flow (without acoustics) snapshot images for various J values using LAR and SAR injectors, respectively. The snapshots represent a single frame out of a set of images recorded at 25,000 fps for the LAR injector and 20,000 fps for the SAR injector. The LAR injector flows showed a significant reduction in the dark-core lengths with increasing J . This was a direct outcome of the enhanced growth rate of the inner shear layer, which, in turn, resulted from the increased momentum flux defect between the inner and outer jets. In contrast, increasing J had a weaker influence on the dark-core length for the SAR injector. Due to the small hydraulic radius of the outer jet of the SAR injector, an effective entrainment of the inner jet fluid by the outer jet was limited to a relatively shorter distance from the exit plane resulting in longer dark-core lengths compared with the LAR injector for the same flow conditions.

Dark-core lengths were measured for a set of 1,000 image frames using the method described earlier. The measured mean dark-core lengths for each injector normalized by the respective D_1 are shown in Figure 5a with error bars denoting uncertainty in measurement from a single image. It should be noted that for such a large sample size, the uncertainties in the mean, given by the standard deviation of the mean ($\sigma_{mean} = \sigma/\sqrt{1000}$), of the measured dark-core lengths were negligible. It is clearly evident that the LAR injector flow underwent a significant change in the dark-core length with increasing J . For J values less than 1, since the dark-core exceeds the field of view of the image, the mean L_B/D_1 were inconclusive, and thus, were not reported. The measured L_B/D_1 of the SAR injector¹⁷ flow confirmed the trend in the axial dark-core length already observed in the images.

The L_B/D_1 data in Figure 5a were replotted in Figure 5b, in which the data set for each injector was fitted with a power curve-fit of the form CJ^r , where C and r are constants. It was found that $L_B/D_1 \propto J^{-0.36}$ for LAR injector flows and $L_B/D_1 \propto J^{-0.20}$ for SAR injector flows, thereby, yielding a quantitative variation of L_B/D_1 with J for each flow geometry. Included in Figure 5b is also a set of L_B/D_1 measurements¹⁷ for an exit geometry with large area ratio, similar to the LAR injector, but one with large t/D_1 ($t = 0.53, D_1 = 0.51, t/D_1 = 1.05, D_2 = 1.59, D_3 = 2.42, D_4 = 3.18, A_o/A_i = 12.9$). The results revealed that the dependence of L_B/D_1 on J was similar to that of the LAR injector. This may imply that the area ratio is a more important governing factor than t/D_1 when it comes to the variation with J of the extent of mixing of coaxial jets. However, more investigation must be done before generalizing this observation.

Figures 6a and 6b show acoustically forced flow (PAN condition) snapshot images for various J values at $P_r = 0.44$ using the LAR and SAR injectors, respectively. For both injectors, forcing frequencies were within 5-10% of the resonant frequency of the outer jet injector tube. In addition, the peak-to-peak pressure perturbations were under 3% of the chamber pressure. The LAR injector flows under a PAN condition exhibited a response that gradually seemed to be subdued at higher J values. That is, the dark-core lengths at lower J values appeared to be noticeably shorter than their baseline counterparts, while at high J , they appeared indistinguishable from the corresponding baseline cases. On the other hand, the SAR injector flows under PAN condition resulted in flows that were significantly altered from the corresponding baseline cases regardless of J values.

These observations were further investigated using a plot of forced dark-core lengths, L , normalized by the corresponding baseline dark-core length, L_B , as shown in Figure 7. The forced LAR injector flow dark-core length was around 80% of that of the baseline at the lowest J , and showed a trend that gradually approached the baseline dark-core lengths with increasing J . On the contrary, SAR flows had dark-core lengths that were well below 80% that of baseline, hence, indicating a larger impact of the PAN condition.

III.B. Characterization of Dominant Flow Structures

Application of POD on the pixel intensity fluctuations in the high speed images, revealed spatial and temporal characteristics of the dominant periodic flow structures present in the coaxial jet flow. Figure 8a shows a

snapshot image for $J = 0.5$ using the LAR injector. It shows a single frame out of a set of images recorded at 25,000 fps. A distinct difference between the snapshot and average images can be clearly seen by the absence of any discrete flow structures emanating from the dark-core at the jet interface boundary in the average image. These structures, which appear to be at least spatially periodic in Figure 8a, start forming by about $10D_1$. It is to be noted that the inner jet tube was not perfectly flush, but sticks out by about $0.2D_1$. This allowed for direct visual confirmation that the inner jet injector tube was not oscillating due to turbulent flow disturbances in the outer jet.

Figure 8c shows the first two proper orthogonal modes (POM) of the decomposition. As described in the previous section, since only the fluctuation in intensity level was considered, the background fluid and the relatively uniform portion of the inner jet flow were subtracted out, thus depicted by a gray region to indicate a mean level in a gray-scaled image. On the other hand, the lighter and darker lobes represent, respectively, the presence and absence of flow structures emanating from the dense inner jet. Their spatial arrangement is indicative of the symmetry or antisymmetry of the flow structures formed in the inner shear layer. That is, at any given axial location, the presence of two similar lobes adjacent to each other indicates the presence of flow structures associated with axisymmetric instabilities in the shear layer. Meanwhile, opposite adjacent lobes indicate antisymmetry, which in axisymmetric flow geometries represents flow structures associated with helical instabilities. This is a viable assumption since under no external disturbances that can impose a preferential direction of oscillation to the shear-layer region, the only manner of propagation for the antisymmetric structures must be in the form of a helical disturbance. Hence, viewing the jet from two perpendicular lines of sight should reveal indistinguishable features for a baseline coaxial jet, as previously shown for some flow conditions.¹¹

The singular values of all modes of the decomposition are shown in Figure 9. POMs 1 and 2 in Figure 8c, whose singular values correspond to modes 1 and 2, respectively, are seen to be the two most dominant flow structures. Moreover, the monotonically decreasing magnitude of the singular values with increasing mode numbers, and more than an order of magnitude difference between the highest and lowest modes implies that the more important flow dynamics were captured by the lower mode numbers. This is a direct outcome of a POD procedure, which orders the singular values, and their corresponding POMs, in order of decreasing importance.

The temporal characteristics of these dominant POMs were represented in the form of power spectral density of the temporal amplitude coefficients of the POD, and are shown in the plots in Figures 10a and 10b. The peaks located at the low end of the spectra were associated with the disturbance frequencies of the lobes identified in their respective POMs. Furthermore, a time-sequence of images of each individual POM revealed a progression of changes in the lobe pattern similar to that of a standing wave. That is, with every passing period associated with the characteristic peak frequencies, a light lobe turned dark, and vice-versa. On the other hand, a time-sequence of images of a superposition of the two POMs revealed a continuous propagation of the lobes traveling downstream of the injector exit.

This outcome is analogous to a simply demonstrable result that the superposition of two standing one-dimensional waves is a traveling wave, as long as the two standing waves are $\pm 90^\circ$ out-of-phase both temporally and spatially. In a similar manner, the cross-power spectral density (CPSD) of the temporal amplitude coefficients can be used to check the existence of a phase difference of $\pm 90^\circ$ at the frequencies near the peak of a CPSD magnitude spectrum. Figures 10c and 10d show the CPSD magnitude and phase plots of POMs 1 and 2. The phase plot shows that the temporal requirement to form a propagating disturbance was satisfied by structures whose frequencies were associated with a -90° phase difference. It can thus be concluded that the frequencies associated with the peak in the CPSD magnitude plot were the characteristic frequencies of the propagating disturbances seen in the time sequence of the superposed POMs. A similar analysis demonstrating the spatial requirement for forming a propagating disturbance has not been done in the current study. However, it should be sufficient to check that the two POMs have a similar lobe pattern. Hereafter, images of POMs presented will be the superposition of conjugate modes.

The location downstream of the injector exit, where the helical disturbances begin to dominate the inner shear layer region also decreased with increasing J . This is in accordance with the well known progression of development of shear-layer instabilities in axisymmetric single or coaxial jets.^{6,7} In the region close to the jet exit, where the shear-layer momentum thickness is very small compared to the jet diameter ($D/\theta \gg 1$), all modes of instability have been shown to have the same growth rates, with the axisymmetric and helical instability growth rates remain significant and comparable while that of the others become negligible. At the end of the potential core, however, the growth rate of helical instabilities becomes the most prevalent.

Therefore, what the POMs show may well be the helical mode of instability of the jet.

Figures 11a-d and Figures 12a-d show the snapshot, average, and POM images for LAR and SAR injector flows, respectively, for increasing J values. Figures 11e-h and Figures 12e-h show the corresponding CPSD magnitude spectra. Clearly, the LAR injector flows had dominant structures with peak frequencies that became broader and moved to higher frequencies as J increased. Unlike a single jet with a coflowing ambient fluid, the coaxial jet configuration in this study had finite area ratio due to the finite diameter outer jet. Nevertheless, the behavior of the instability peak frequencies was in line with analytical results⁷ that with increasing coflow velocity, the region of unstable frequencies becomes broader and that the peak of the spatial growth rates shift to higher frequencies. On the contrary, as the CPSD magnitude spectra for the SAR injector flows show, the peak frequencies were unaffected by increasing J . This contradiction to the expected behavior⁷ may again be explained by how soon the inner and outer jets attain a single jet behavior, thereby rendering the effect of coflow nonexistent.

Another notable outcome from the spectra in Figures 11e-h was that the peak frequencies were not dependent on R or J , but on the magnitude of the outer jet velocity. Despite the significant rise in R or J from Figure 11g-h, the peak for the latter sat at a slightly lower frequency. In order to investigate this, downstream convection velocities, U_s , of the dominant periodic structures depicted in the POM images were estimated based on the relation $U_s = \lambda f_s$, where λ is the wavelength measured from the images, and f_s is the characteristic frequency. The frequency, f_s , was obtained from the frequency that corresponded to the maximum CPSD magnitude that was closest to a CPSD phase of $\pm 90^\circ$ as illustrated in Figure 10c and 10d. The estimated U_s along with exit velocity of the inner jet, outer jet, and their mean are shown in Figure 13a for the LAR injector and Figure 13b for the SAR injector. For uniform density coaxial jets, the inner shear layer convection velocity may be approximated by the mean velocity. On the other hand, for variable density jets, as it is the case in this study, the shear-layer velocity is less than the mean velocity when the high-velocity jet is less dense.²² The estimated values of U_s for both the LAR and SAR injector flows depict this. However, U_s for LAR flow appear to closely depend on the magnitude of U_o more than those for SAR flow do. This may be an indication that in the LAR geometry, the outer jet velocity governed the dynamics of the inner shear layer structures. However, further investigation will need to be done to generalize this outcome.

The PAN condition established a region of locally maximum pressure fluctuation in the vicinity of the coaxial jets so that the velocity fluctuation was minimum or non-existent in the ideal case. As pressure is a scalar physical quantity, PAN can essentially be regarded as a condition that creates a symmetric fluctuation in pressure about the jet center plane that is normal to the transverse direction of propagation of the acoustic waves.

Figure 14 shows the flow response under PAN condition for the same case in Figure 8 without acoustics. The snapshot image in Figure 14a clearly depicts a series of orderly structures formed along almost the entire inner jet column. They appear to have started forming near the injector exit, and grew as they propagated farther downstream due to the entrainment effect of the outer jet. This planar view of the structures depicts them as varicose instability structures in a planar jet. As a matter of fact, varicose instability plays a similar role in planar jets as does axisymmetric instability in round jets.²⁶ The POMs shown in Figure 14c give further evidence of the dominant symmetric structures that started forming immediately downstream of the injector exit, and spread as they traveled downstream.

Another unique nature of the flow response to PAN forcing is depicted in Figures 15, 16a and 16b. Figure 15 shows that the flow response to PAN forcing represented by POMs 1 and 2 in Figure 8c was the dominant type of response. The relative magnitudes of all other modes were similar to those for the baseline shown in Figure 9. Moreover, the spectral plots in Figures 16a and 16b associated with POMs 1 and 2 indicate that the orderly structures had a characteristic frequency that was identical to the forcing acoustic frequency, f_F . This may seem to be a trivial outcome of external forcing, yet it does tell a lot about the nature of the flow stability as will be discussed below. Figure 16c shows the CPSD magnitude of the forced conjugate modes overlaid with the one for the baseline conjugate modes in Figure 10c. It shows that f_F completely overtook the baseline characteristic frequencies, which are no longer visible in the spectra of the PAN condition.

Figures 17 and 18 present the forced counterparts to the baseline cases presented in Figures 11 and 12 for the LAR and SAR injector flows, respectively. The lobe patterns visible in the POMs of the LAR flows showed a peculiar transition with increasing J . The lower J values (Figures 14c and 17a) showed a symmetric lobe pattern due to PAN forcing, whereas with increasing J , the symmetry became more skewed, and eventually turned into an antisymmetric pattern identical to the baseline cases. As noted earlier,

antisymmetric pattern is the two-dimensional representation of a helical disturbance. Thus, for the LAR geometry, it can be concluded that the dominant flow response to PAN forcing at low J was in the form of amplified symmetric disturbances, while that at higher J , it transitioned to helical disturbances identical to those present in flows without acoustic forcing.

The temporal characteristics of the flow response to the acoustic forcing are shown in the spectral plots in Figures 17e-h and 18e-h overlaid with the baseline spectra. The spectral content of the lower J values (Figures 16c and 17e) was such that during forcing, a peak in the magnitude at f_F completely took over the low peak frequencies of the baseline flows. As J increased, the significance of the peak at f_F relative to the baseline peak frequencies became more and more diminished, and the forced spectra began retaining more of the baseline spectra, as clearly evident in the highest J attained in Figure 17h. In other words, the spectral energy contained at f_F for lower J values was less so at higher J values.

The response of the SAR injector flows to PAN forcing were drastically different from that of the LAR injector as shown in Figures 18. For lower J values ($J = 2.0, 5.2$), strong symmetric disturbances annihilate the inner jet flow. For higher J values ($J = 12, 17$), although symmetric disturbances were not as strong as in the lower J cases, they nevertheless were still prevalent as evident in the POM images and the spectra. As a matter of fact, the spectra showed strong response to external forcing regardless of the J value. This was again evident by the lack of any remnants of the low-frequency peaks present in the baseline spectra.

From a practical standpoint, it is crucial to ensure that the injector flow under non-design operating conditions behave as closely as possible to that under design operating conditions. Flow disturbances that arise as a result of acoustic instabilities due to excitation of the combustion chamber acoustic modes are typical instances of non-design operating conditions. Although special cases of the chamber acoustic behavior can be modeled and incorporated in the design considerations, a great many other unpredictable scenarios exist. Hence, the best approach is to implement a robust design that renders more predictable flow behavior for a given set of flow conditions regardless of any externally imposed disturbances. In light of this argument, LAR would be considered a preferable design configuration solely on the fact that it has been shown to be less sensitive to external disturbances at high J values.

IV. Conclusions

This experimental study examined the mixing behavior as well as the dominant periodic flow structures that develop in the inner shear layer of nonreactive shear-coaxial jets with and without the presence of transverse acoustic forcing. Flow conditions in subcritical pressure regime and spanning a range of outer to inner jet momentum flux ratios, J , were investigated using two injector geometries. It was found that increasing J reduced the dark-core lengths of the large outer to inner jet area ratio (LAR) injector baseline flows more than the small outer to inner jet area ratio (SAR) injector baseline flows. This was indicative of more enhanced mixing of the inner and outer jets with increasing J for the LAR injector flows than for the SAR injector flows. Moreover, it was found that the dark-core lengths of the SAR injector flows were significantly shorter under PAN forcing for a given J than those of the LAR injector flows. Thus, this outcome showed that J was not the only parameter governing the coaxial jet mixing, but geometry as well.

A proper orthogonal decomposition of pixel intensity fluctuation data revealed both the spatial and temporal characteristics of the inner shear layer flow structures. The LAR injector baseline flows exhibited helical instabilities at far enough downstream locations regardless of J . The frequencies of the flow structures associated with these helical instabilities shifted to higher frequencies with increasing magnitudes of the outer jet velocities. Pressure antinode (PAN) acoustic forcing of low J LAR injector flows showed strong response by forming symmetric structures whose frequencies were identical with the forcing frequencies. Magnitude spectral plots also showed large peaks at the forcing frequencies and the baseline flow peak frequencies were completely removed from the forced spectra. With increasing J , however, the response to forcing became gradually weaker, and the broad baseline peak frequencies coexisted with the peaks at the forcing frequency.

The SAR injector baseline flows also exhibited helical instabilities. However, unlike the LAR injector flows, the frequencies of the flow structures did not show significant shift to higher frequencies with increasing jet velocities. In addition, regardless of J , they showed strong response to PAN forcing. Thus, due to their readily responsive nature to external acoustic forcing, SAR injector flows may be regarded as a class of flows that display convectively unstable behavior. On the contrary, LAR injector flows appeared to display a transition from convectively unstable to absolutely unstable flow behavior with increasing J . This makes LAR injector flows at large enough J more desirable from a design standpoint since they behave in a

predictable manner despite externally imposed disturbances such as those that arise due to the excitation of combustion chamber acoustic modes.

For a given geometry, the nature of the flow response to an external disturbance depending on the flow condition, namely J , may be used to characterize the state of stability of the flow. Previous works²³⁻²⁵ on flow stability characterize convectively unstable flows as noise amplifiers; that is, they are prone to external flow disturbances such as acoustic disturbances as used in this study. Their spectral characteristics are such that when exposed to external forcing, their natural instabilities are completely removed and replaced by instabilities whose frequency match those of the forcing frequency.²⁷ Absolutely unstable flows, on the other hand, are characterized as naturally self-excited flows that do not respond well to external disturbances. Their spectra preserve the natural instabilities with or without a coexisting frequency content associated with the forcing frequency. These and the flow responses observed may be used to argue that the LAR flows can be characterized as convectively unstable for low J flows, and transition into absolutely unstable flows with increasing J values, while the SAR flows depicted the behavior of convectively unstable flows. However, this characterization deserves further exploration in future studies.

Acknowledgments

The authors would like to thank Mr. Randy Harvey for his invaluable contributions in running and maintaining the experimental facility. They express their appreciation to Dr. Juan Rodriguez for providing the image data for the SAR injector. They also would like to thank Mr. Brian Newkirk, Mr. David Hill, Mr. Earl Thomas and Mr. John Hasier for providing technical assistance while running the experiments. This work is sponsored by AFOSR under Dr. Mitat Birkan, program manager.

References

- ¹Ko, N. W. M. and Kwan, S. H. 1976 The initial region of subsonic coaxial jet. *J. Fluid Mech.* 73, 305-332.
- ²Dahm, W. J. A., Frieler, C.E., and Tryggvason, G. 1992 Vortex structure and dynamics in the near field of a coaxial jet. *J. Fluid Mech.* 241, 371-402.
- ³Wicker, R.B. and Eaton, J.K. 1994 Near Field of a Coaxial Jet With and Without Axial Excitation. *AIAA Journal* 32, 542-546.
- ⁴Balarac, G., Mtais, O. and Lesieur, M. 2007 Mixing enhancement in coaxial jets through inflow forcing: A numerical study. *Phys. Fluids* 19, 075102.
- ⁵Gladnick, P. G., Enotiadis, A. C., LaRue, J. C. and Samuelsen, G. S. 1990 Near-field characteristics of a turbulent coflowing jet. *AIAA Journal* 28, 1405-1414.
- ⁶Cohen, J. and Wygnanski, L. 1987 The Evolution of Instabilities in an Axisymmetric Jet, Part I. Linear Growth of Disturbances Near the Nozzle. *J. Fluid Mech.* 176, 191-219.
- ⁷Michalke, A. and Hermann, G. 1982 On the inviscid instability of a circular jet with external flow. *J. Fluid Mech.* 114, 343-359.
- ⁸Mayer, W. and Krülle, G. 1995 Rocket Engine Coaxial Injector Liquid-Gas Interface Flow Phenomena. *J. Propulsion and Power* 11, 3.
- ⁹Villermaux, E., Rehab, H. and Hopfinger, E.J. 1994 Breakup Regimes and Self-Sustained Pulsations in Coaxial Jets. *Meccanica* 29, 393-401.
- ¹⁰Rehab, H., Villermaux, E. and Hopfinger, E.J. 1997 Flow regimes of large-velocity-ratio coaxial jets. *J. Fluid Mech.* 345, 357-381.
- ¹¹Davis, D.W., "On the behavior of a shear-coaxial jet, spanning sub- to supercritical pressures, with and without an externally imposed transverse acoustic field. Ph.D. Thesis," Penn State University, 2005.
- ¹²Davis, D.W. and Chehroudi, B. 2007 Measurements in an Acoustically Driven Coaxial Jet under Sub-, Near-, and Supercritical Conditions. *J. Propulsion and Power* 23, 2.
- ¹³Leyva, I. A., Chehroudi, B., Talley, D., "Dark-core analysis of coaxial injectors at sub-, near-, and supercritical conditions in a transverse acoustic field", *54th JANNAF Meeting*, Denver, CO, May 14-18, 2007.
- ¹⁴Leyva, I.A., Chehroudi, B. and Talley, D., "Dark-core analysis of coaxial injectors at sub-, near-, and supercritical pressures in a transverse acoustic field". *43rd AIAA/ASME/SAE/ASEE Joint Propulsion Conference and Exhibit*, AIAA 2007-5456.
- ¹⁵Leyva, I.A., Rodriguez, J.I., Chehroudi, B. and Talley, D. Preliminary, "Results on Coaxial Jet Spread Angles and the Effects of Variable Phase Transverse Acoustic Fields. *46th AIAA Aerospace Sciences Meeting and Exhibit*, AIAA 2008-950.
- ¹⁶Rodriguez, J. I., Graham, J. J., Leyva, I. A., Lyu, H.-Y., Talley, D., "On the Inner Jet Spread Angles of Coaxial Jets from Subcritical to Supercritical Conditions with Preliminary Numerical Results", *55th JANNAF Propulsion/4th Liquid Propulsion Subcommittee Meeting*, Orlando, FL, December 8-12, 2008.
- ¹⁷Rodriguez, J. I., "Acoustic Excitation of Liquid Fuel Droplets and Coaxial Jets," Ph.D. Thesis, University of California, Los Angeles, 2009.
- ¹⁸Otsu, N. 1979 A threshold selection method from gray-level histograms. *IEEE transactions on Systems, Man, and Cybernetics* 9, 62-66.

- ¹⁹Chatterjee, A. 2000 An introduction to the proper orthogonal decomposition. *Current Science* 78, 7.
- ²⁰Arienti, M, and Soteriou, M.C. 2009 Time-resolved proper orthogonal decomposition of liquid jet dynamics. *Phys. Fluids* 21, 112104.
- ²¹Narayanan, V., Lightfoot, M.D.A, Schumaker, S.A., Danczyk, S.A., and Eilers, B., "Use of Proper Orthogonal Decomposition Towards Time-resolved Image Analysis of Sprays," ILASS Americas, *23rd Annual Conference on Liquid Atomization and Spray Systems*, Ventura, CA, May 2011
- ²²Dimotakis, P.E. 1986 Two-Dimensional Shear-Layer Entrainment. *AIAA Journal* 24, 11.
- ²³Huerre, P. and Monkewitz, P.A. 1990 Local and Global Instabilities in Spatially Developing Flows. *Annu. Rev. Fluid Mech.* 22, 473-537
- ²⁴Huerre P. 2000. Open shear flow instabilities. In *Perspectives in Fluid Dynamics*, ed. G.K. Batchelor, H.K. Moffatt, M.G. Worster, pp. 159-229. Cambridge, UK: Cambridge Univ.
- ²⁵Jendoubi, S. and Strykowski, P.J. 1994 Absolute and convective instability of axisymmetric jets with external flow. *Phys. Fluids* 6, 3000.
- ²⁶Sevilla, A., Gordillo, J. M. and Martnez-Bazn, . 2002 The effect of the diameter ratio on the absolute and convective instability of free coflowing jets. *Phys. Fluids* 14, 3028.
- ²⁷Megerian, S., Davitian, J., Alves, L. S. de B. and Karagozian, A. R. 2007 Transverse jet shear-layer instabilities. Part 1. Experimental studies. *J. Fluid Mech.* 593, 93-129.

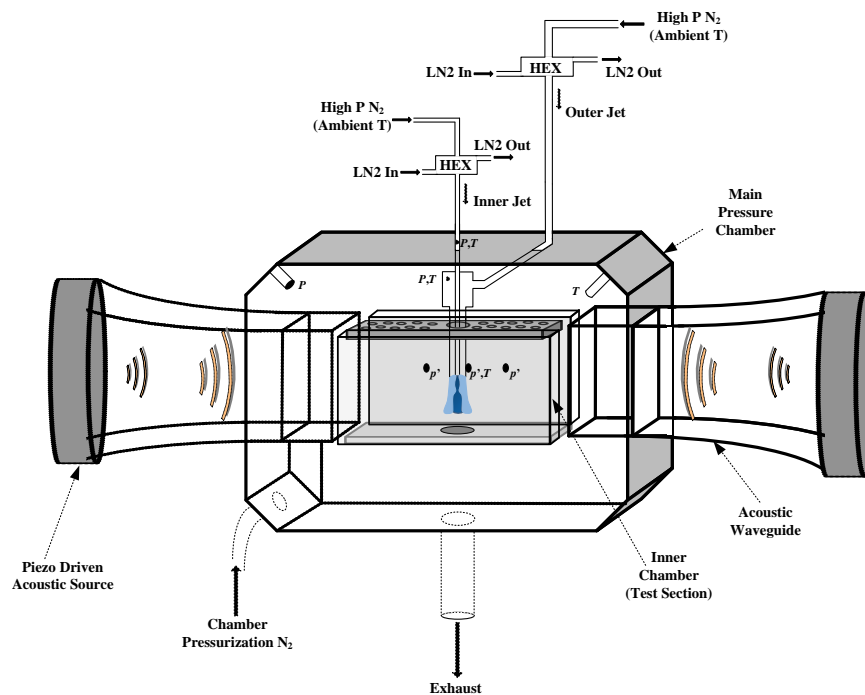


Figure 1. A schematic of the chamber and peripheral lines.

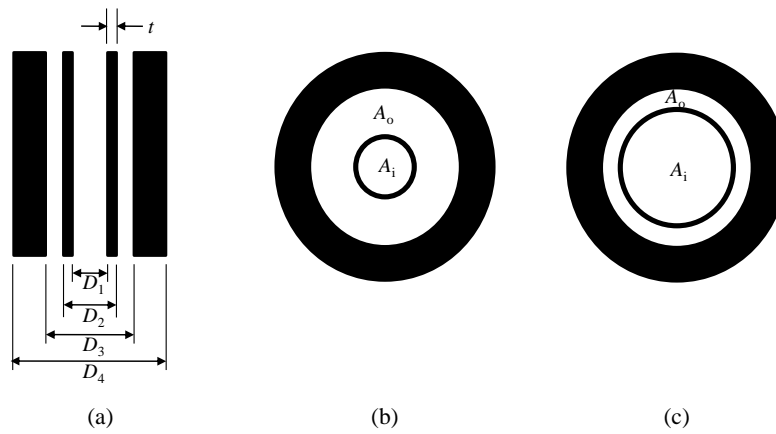


Figure 2. Injector geometry schematic: (a) axial cross-sectional view, (b) LAR exit configuration, (c) SAR exit configuration.

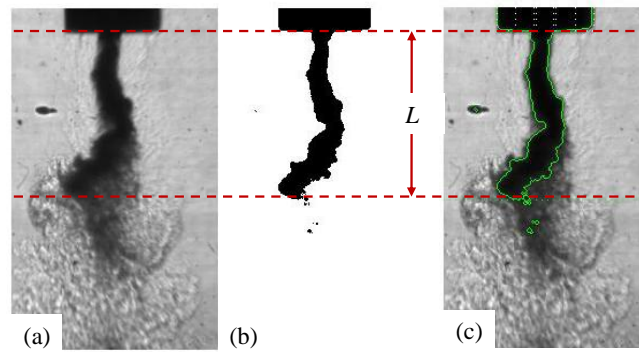
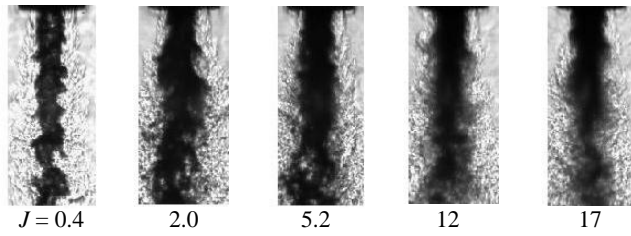
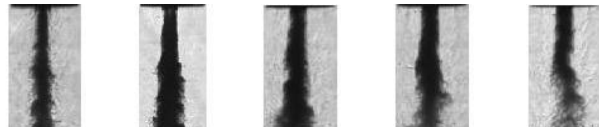


Figure 3. Measurement of dark-core length: (a) original image (b) black and white image after thresholding (c) Contour used to define the dark-core length (L).



$J = 0.4$

2.0

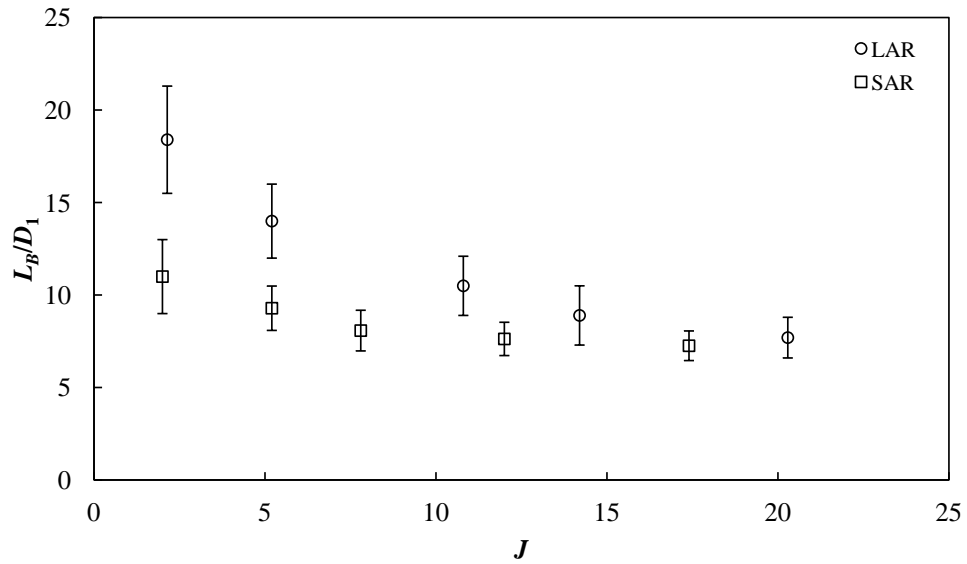
5.2

12

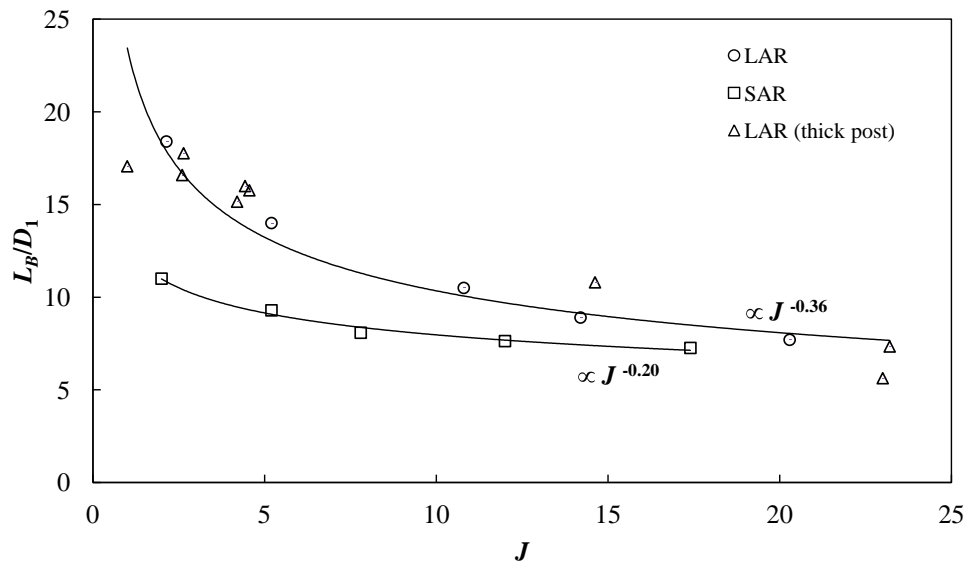
17

(b)

Figure 4. Back-lit images of baseline (a) LAR injector flows, and (b) SAR injector flows at $P_r = 0.44$.



(a)



(b)

Figure 5. Normalized dark-core lengths (L_B/D_1) for baseline flow at $P_r = 0.44$: (a) LAR and SAR injector flows with uncertainties in individual L_B/D_1 measurements, and (b) power-fit for LAR, SAR, and LAR (with thick inner jet post¹⁷).

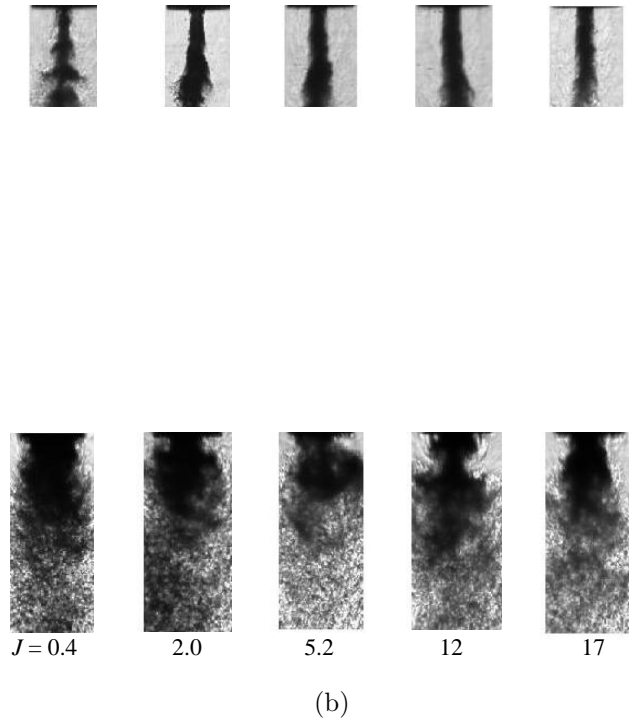


Figure 6. Back-lit images of PAN (a) LAR injector flows, and (b) SAR injector flows at $P_r = 0.44$.

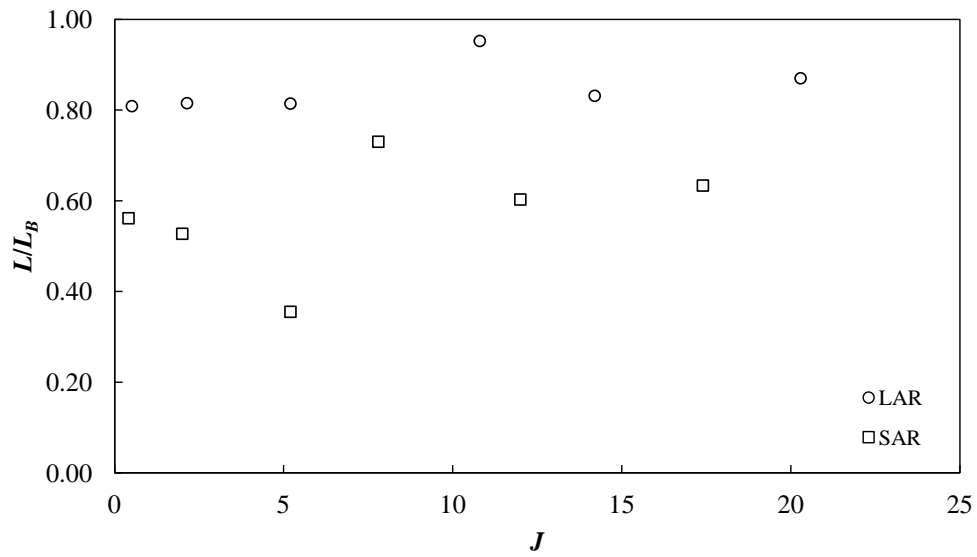


Figure 7. Dark-core lengths L normalized by baseline flow dark-core lengths L_B for PAN flow at $P_r = 0.44$.

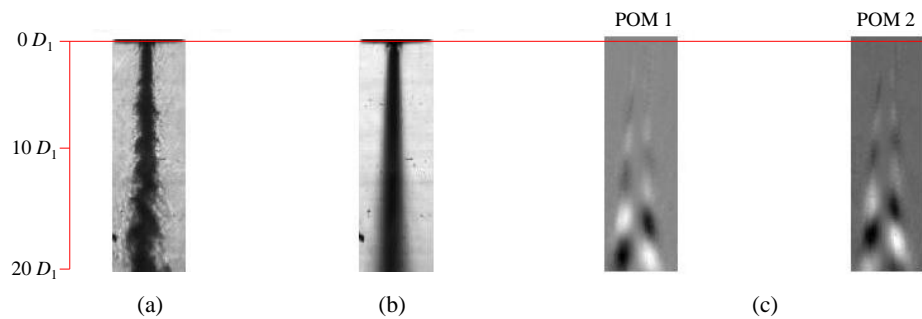


Figure 8. Baseline LAR injector flow at $P_r = 0.44$, $J = 0.5$: (a) snapshot image, (b) average image, (c) proper orthogonal mode (POM).

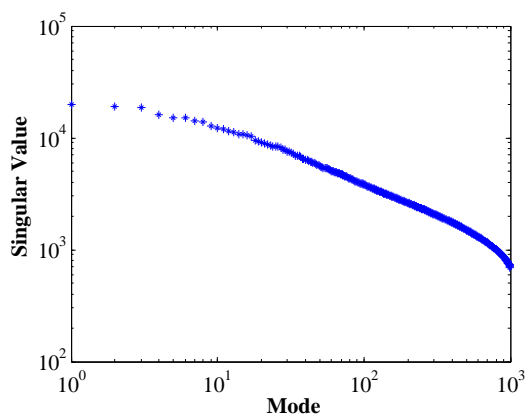


Figure 9. Singular values for baseline LAR injector flow at $P_r = 0.44$, $J = 0.5$.

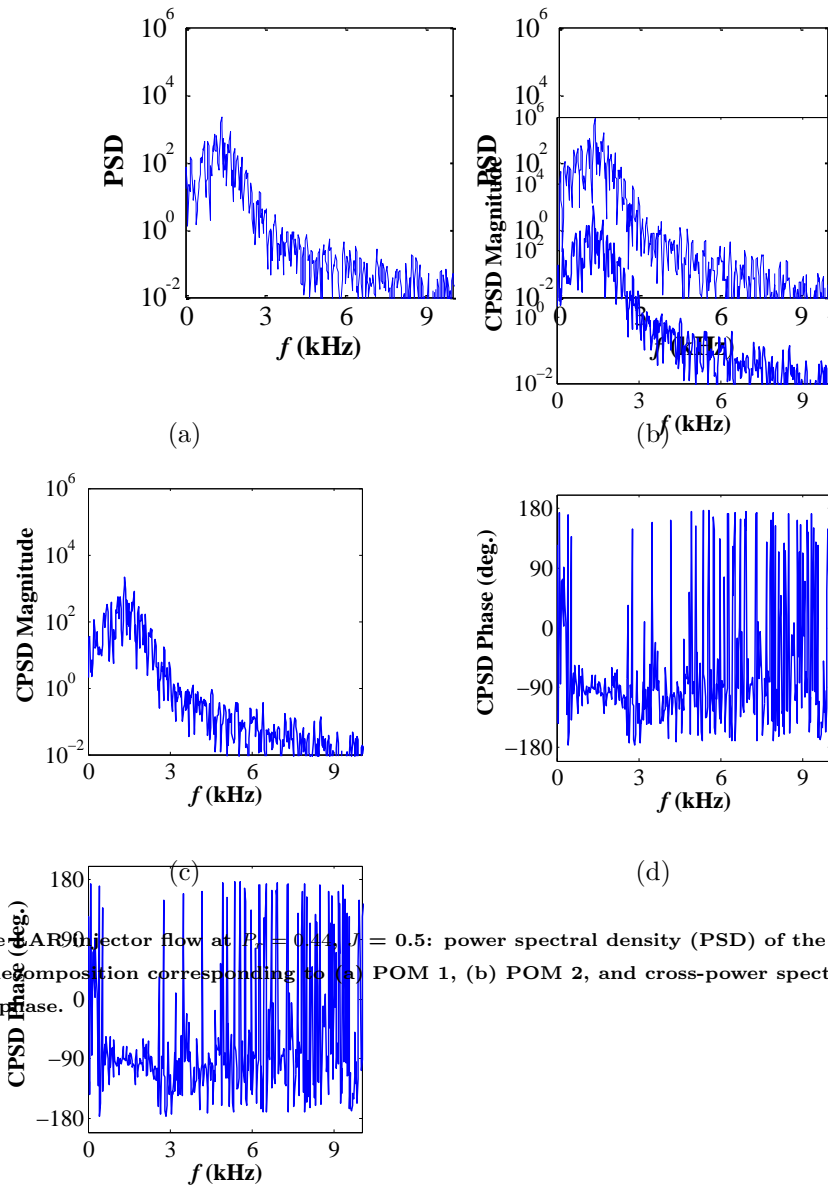
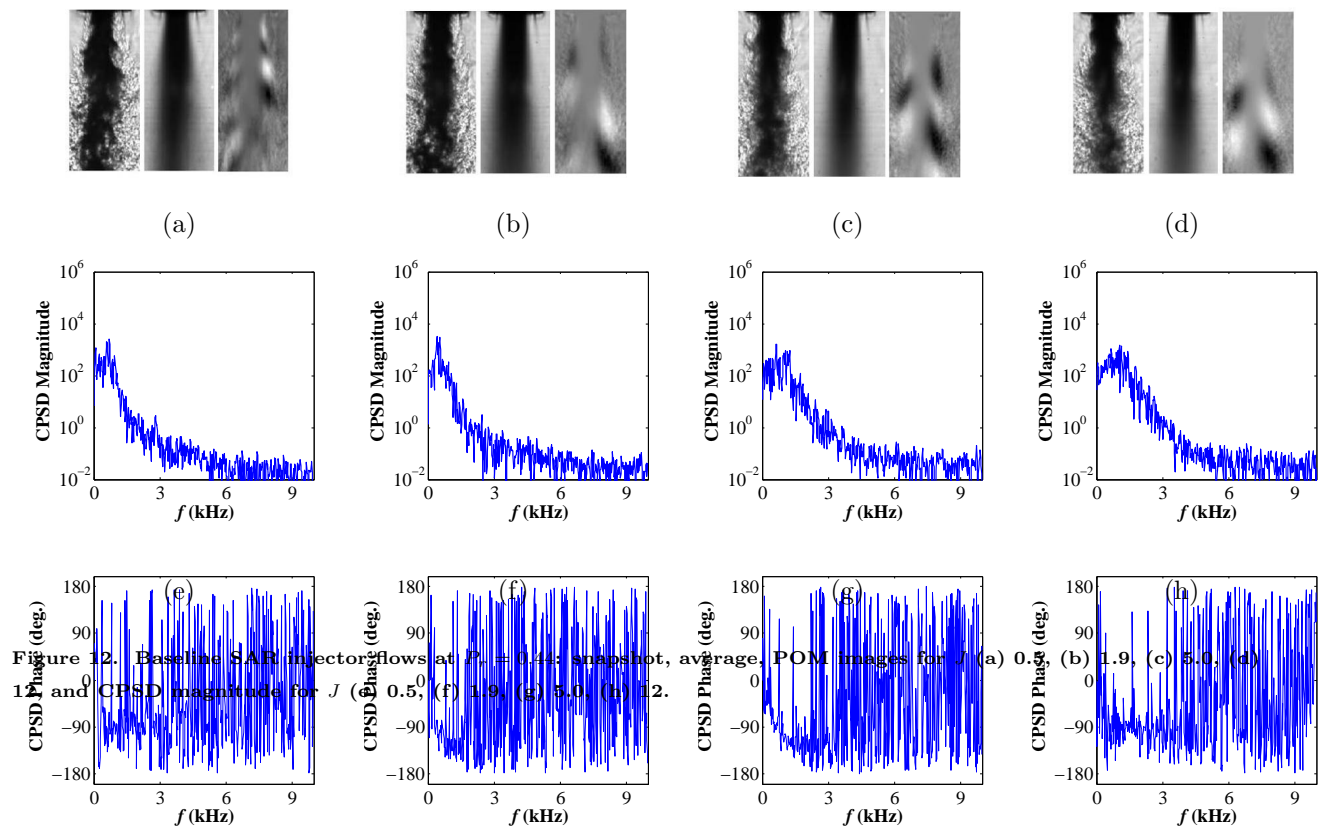
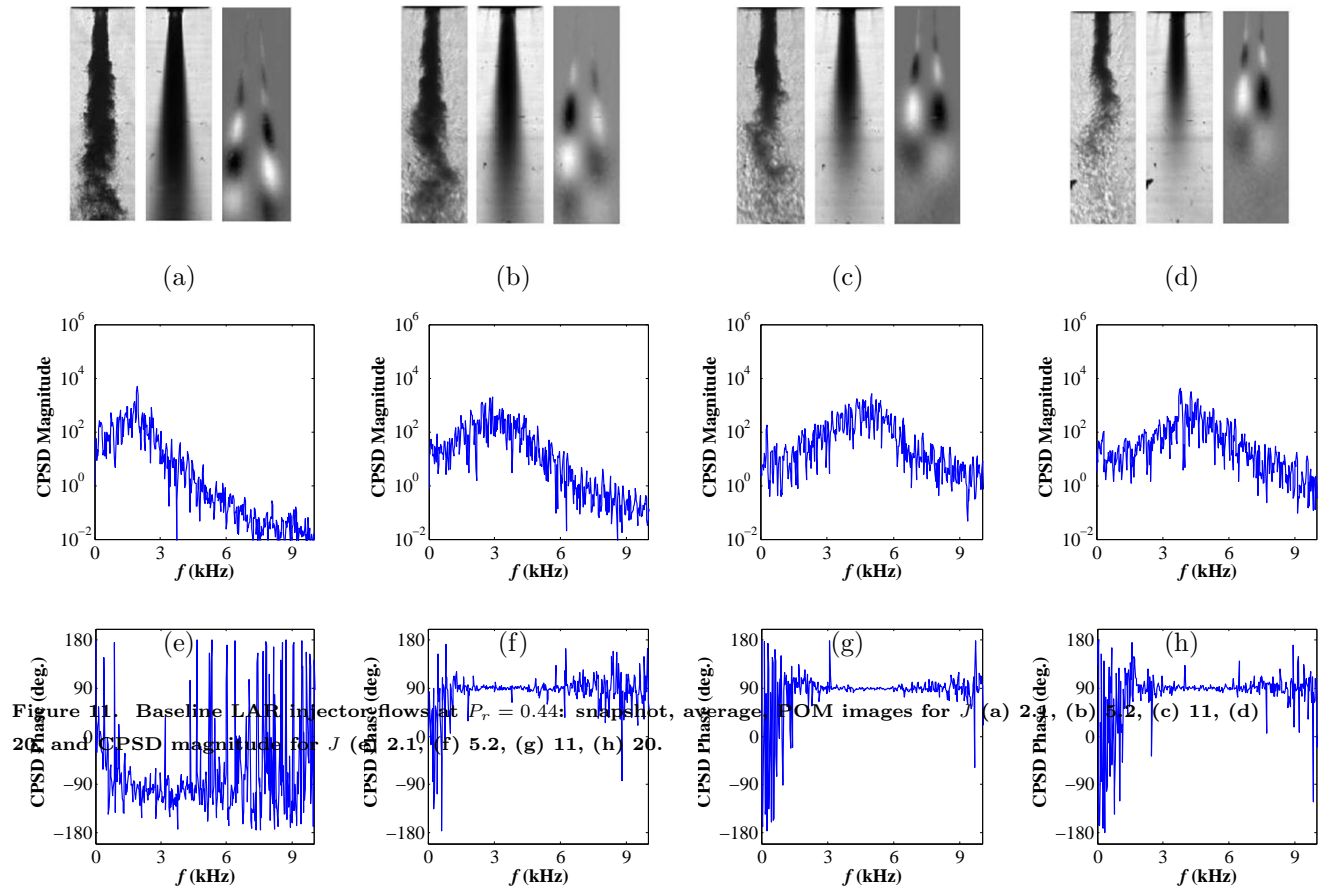
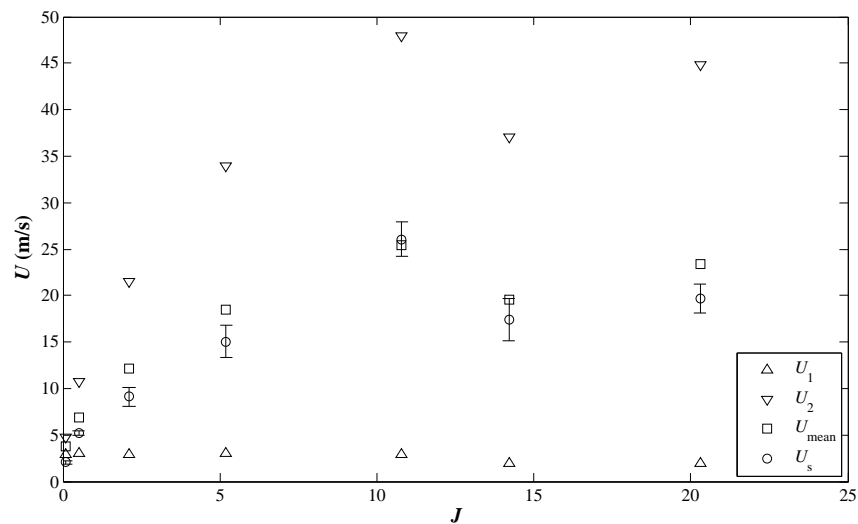
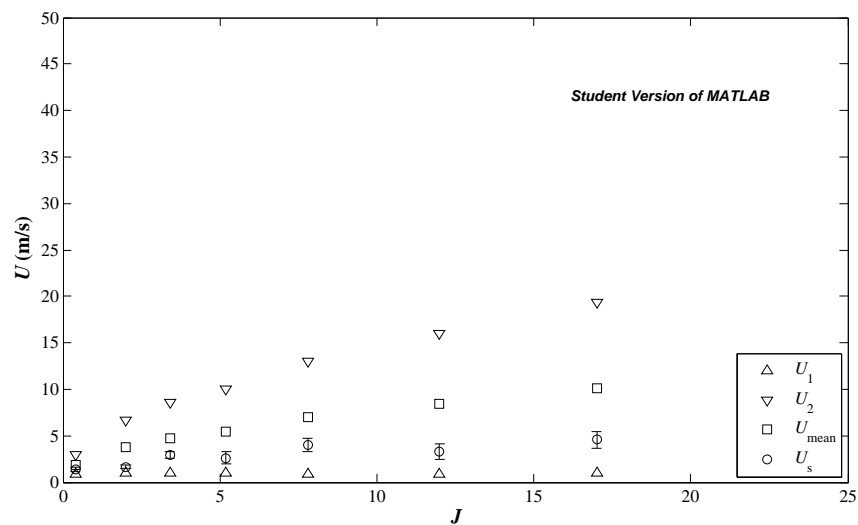


Figure 10. Baseline AR90 injector flow at $P_{inj} = 0.42$, $f = 0.5$: power spectral density (PSD) of the temporal amplitude coefficients of the decomposition corresponding to (a) POM 1, (b) POM 2, and cross-power spectral density (CPSD), (c) magnitude, (d) phase.





(a)



(b)

Figure 13. Baseline velocities for (a) LAR injector flows, and (b) SAR injector flows at $P_r = 0.44$.

Student Version of MATLAB

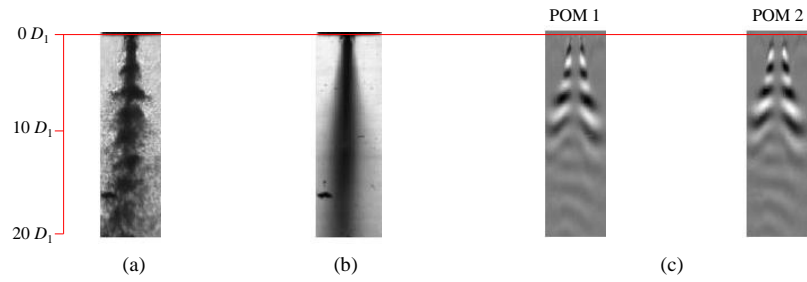


Figure 14. PAN forced ($f_F = 3.14$ kHz) LAR injector flow at $P_r = 0.44$, $J = 0.5$: (a) snapshot image, (b) average image, (c) proper orthogonal mode (POM).

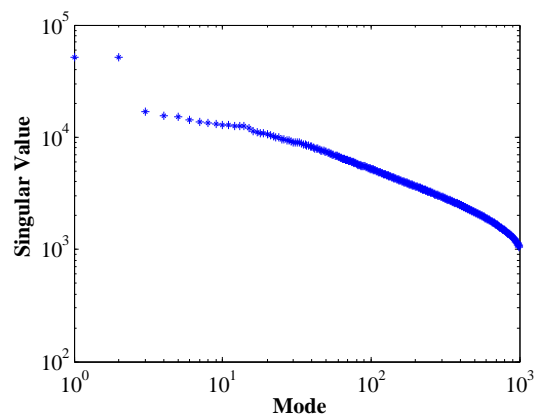


Figure 15. Singular values for PAN forced ($f_F = 3.14$ kHz) LAR injector flow at $P_r = 0.44$, $J = 0.5$.

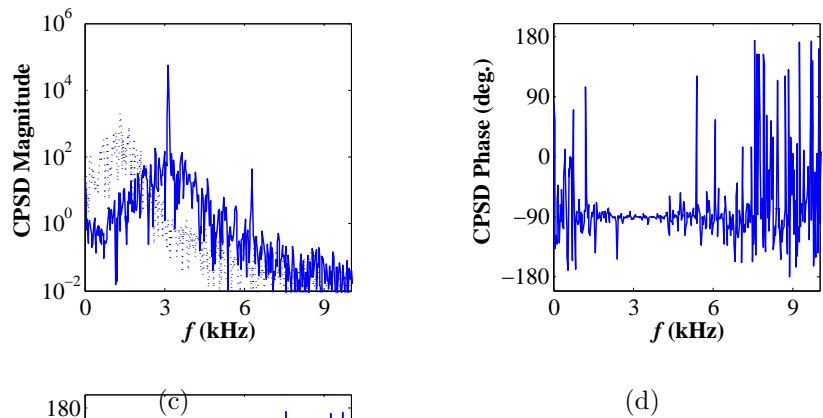
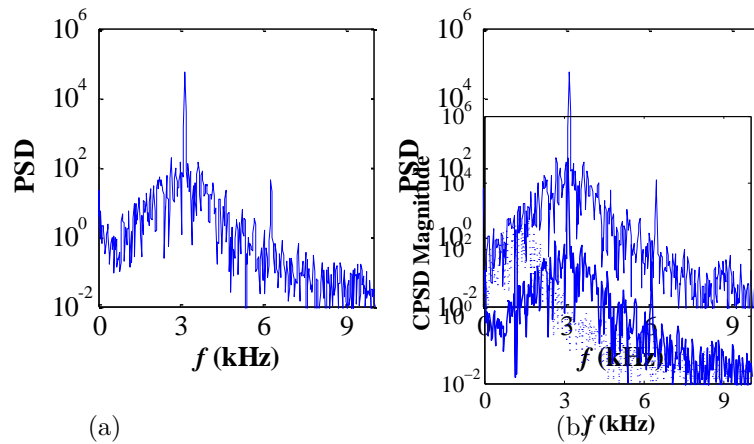
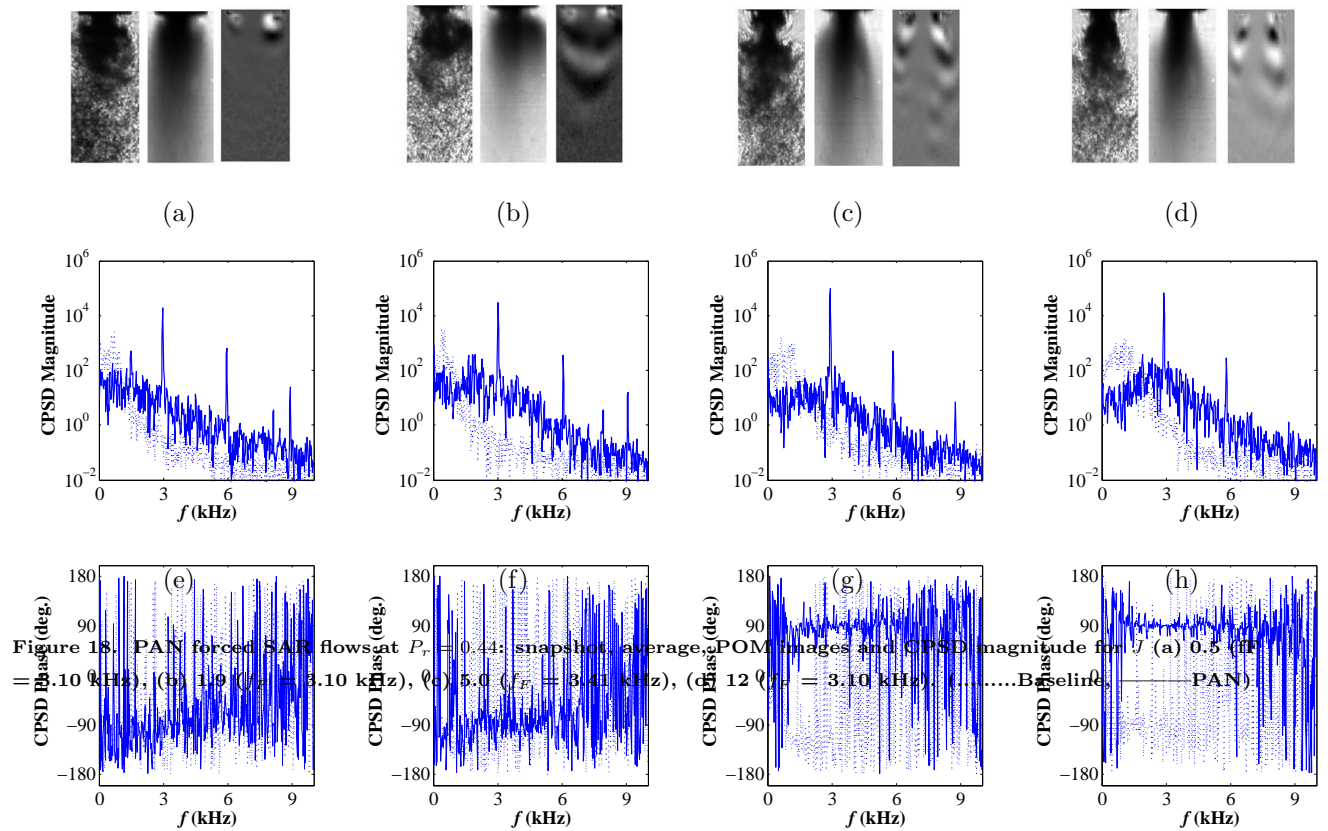
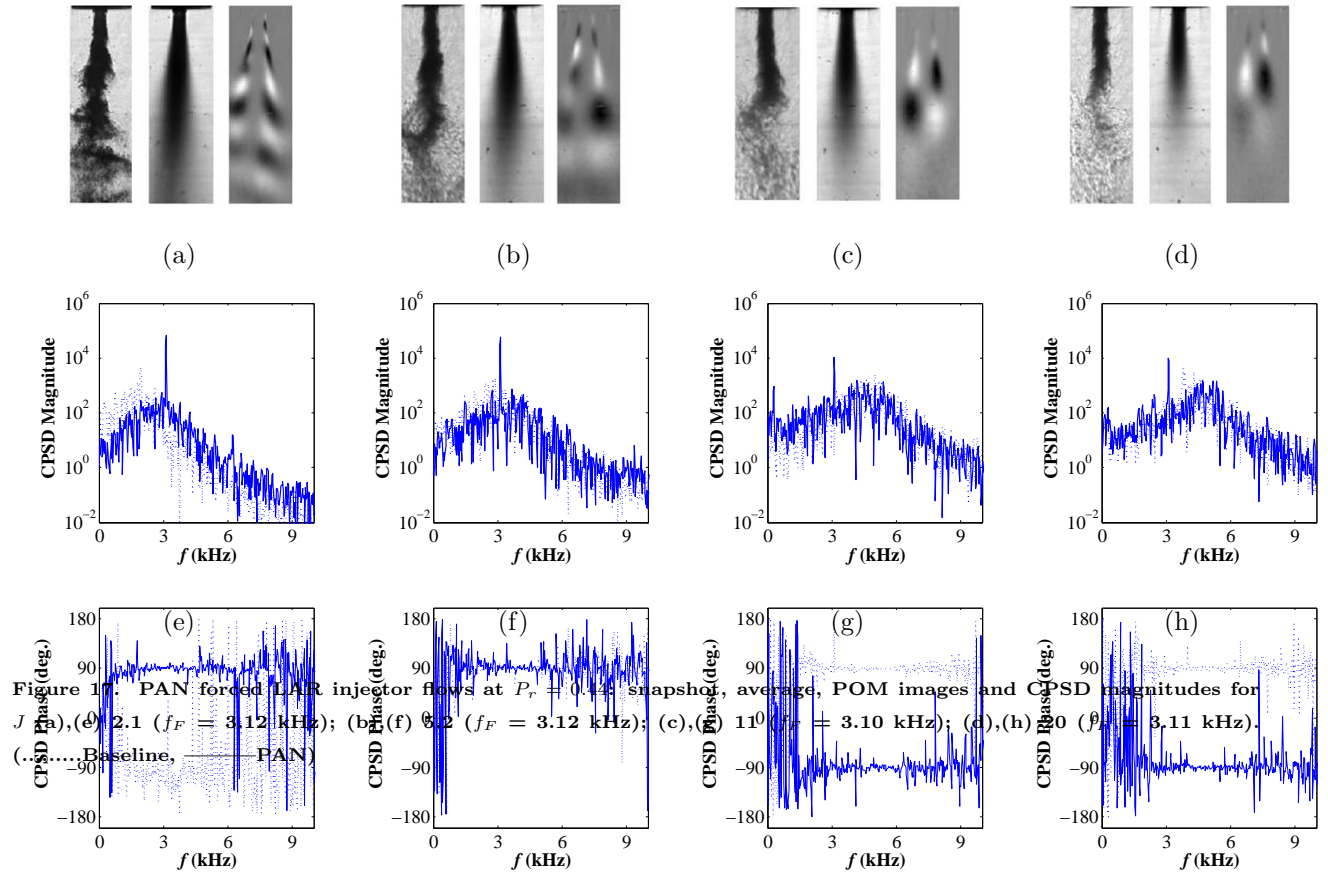


Figure 16. PAN forced (90 = 3.14 kHz) LAR injector flow at $P_r = 0.44$, $J = 0.5$: power spectral density (PSD) of the temporal amplitude coefficients of the decomposition corresponding to (a) POM 1, (b) POM 2, and cross-power spectral density (CPSD) (c) magnitude, (d) phase. (.....Baseline, —PAN)

Student Version of MATLAB

Student Version of MATLAB



$J \mid R \mid T_{\text{chamber}} \mid \rho_{\text{chamber}} \mid P_{\text{chamber}} \mid T_o \mid \dot{m}_o \mid \rho_o \mid U_o \mid \text{Re}_o \mid T_i \mid \dot{m}_i \mid \rho_i \mid U_i \mid \text{Re}_i$

J	R	T_{chamber} (K)	ρ_{chamber} (kg/m ³)	P_{chamber} (MPa)	T_o (K)	\dot{m}_o (mg/s)	ρ_o (kg/m ³)	U_o (m/s)	Re_o (10 ⁴)	T_i (K)	\dot{m}_i (mg/s)	ρ_i (kg/m ³)	U_i (m/s)	Re_i (10 ⁴)
2.0	6.9	246	21	1.49	195	450	27	6.6	1.1	109	925	630	0.96	1.5
5.2	11	217	24	1.49	184	750	29	10	1.9	110	925	620	0.97	1.5
12	17	222	23	1.49	194	1100	27	16	2.6	108	925	640	0.94	1.4
17	20	217	24	1.48	194	1300	27	19.3	3.1	108	925	638	0.95	1.4

UNIVERSITY OF CALIFORNIA

Los Angeles

**Droplet Combustion and Non-Reactive
Shear-Coaxial Jets with Transverse Acoustic
Excitation**

A dissertation submitted in partial satisfaction
of the requirements for the degree
Doctor of Philosophy in Mechanical Engineering

by

Sophonias Teshome

2012

Approved for public release; distribution unlimited. PA #12667.

© Copyright by
Sophonias Teshome
2012

ABSTRACT OF THE DISSERTATION

**Droplet Combustion and Non-Reactive
Shear-Coaxial Jets with Transverse Acoustic
Excitation**

by

Sophonias Teshome

Doctor of Philosophy in Mechanical Engineering

University of California, Los Angeles, 2012

Professor Ann R. Karagozian, Co-chair

Professor Owen I. Smith, Co-chair

This experimental study focused on the coupling of transverse acoustic flow perturbations with two different fundamental phenomena that take place in combustion chambers: droplet combustion, and injection of non-reactive shear-coaxial jets.

The study on fuel droplet combustion characteristics examined the response and behavior of various burning fuel droplets during exposure to external acoustical perturbations. These liquid fuels included ethanol, methanol, aviation fuel (JP-8), liquid synthetic fuel derived from natural gas, and a blend of JP-8 and synfuel. The study examined combustion during acoustic excitation conditions in a closed waveguide in which the droplet was situated at or near a pressure node, where the droplet experienced the greatest effects of velocity perturbations. A two-speaker configuration provided the means to produce a fairly symmetric acoustic field in the waveguide. In the absence of acoustic excitation, values of the measured droplet burning rate constant, K , were generally consistent with available values for the different fuels explored. During acoustic excitation of a burning droplet situated in the vicinity of a pressure node, the flame

orientation was consistent with the sign of an acoustic radiation force acting on the burning system, creating conditions where the flame deflection switched, depending on the relative location of the droplet with respect to the pressure node. The acceleration associated with the acoustic radiation force was estimated by measuring the degree of deflection that the flame underwent relative to an unforced flame. Although overall there were no significant variations in the measured K values with changing acoustic excitation, in some cases, locally increased K values were observed to be associated with larger measured acoustic accelerations. This study also examined the extinction characteristics and made preliminary estimations of the extinction strain rates of the different fuels.

The non-reactive flow study investigated the mixing behavior and characteristics of dynamic flow structures of shear-coaxial nitrogen jets under varying flow conditions, with and without the presence of pressure and velocity perturbations due to acoustic forcing transverse to the flow direction. The role of injector geometry was examined using two shear-coaxial injectors with different outer to inner jet area ratios, A_o/A_i , and different inner jet post thickness to inner jet diameter ratios, t/D_1 . Flow conditions under chamber pressures spanning high subcritical pressures (reduced pressure or chamber to critical pressure ratio, P_r , of 0.44) to nearcritical pressures ($P_r = 1.05$), with varying outer to inner jet momentum flux ratios ($J = 0.1 - 21$), and maximum or minimum amplitude in the pressure perturbation at the jet axis location were considered. The inner and outer jet temperatures were independently controlled so that the inner and outer flows were in liquid and gaseous states at $P_r = 0.44$, respectively, and in transcritical and supercritical states at $P_r = 1.05$, respectively. Back-lighting the coaxial jets resulted in a silhouette of the dense inner jet, which appeared as a dark column. This distinguished it from the outer jet, and thus, enabled high speed images to capture its flow dynamics. Dark-core length pertains to the axial length of the unmixed portion of the inner flow; such measurements were used to indicate the extent of mixing under the different flow

conditions and injector geometries. In general, for baseline flows at both P_r values, the dark-core length to inner jet diameter ratio, L_B/D_1 , decreased with increasing J and t/D_1 , and with decreasing A_o/A_i . During a maximum pressure perturbation forcing condition, the ratio of forced to baseline flow dark-core length, which stayed constant, around unity, for $J < 10$ for the small A_o/A_i , large t/D_1 injector flows, also underlined the influence of geometry on the mixing and response to external pressure disturbances. A basic application of proper orthogonal decomposition on the intensity fluctuation of the high-speed images enabled the extraction of the spatial and temporal characteristics of the dominant flow structures that existed in the flow field during exposure to acoustic forcing. With increasing J , the flow response to forcing depended on the injector geometry. A comparison of the spatio-temporal characteristics of the baseline flows and their corresponding acoustically forced flows revealed that for the $J > 5$ flows of the large A_o/A_i , small t/D_1 injector, the baseline flow behavior was retained in the forced flow, thereby indicating a flow regime with strong instabilities and which was less sensitive to external pressure disturbances. On the other hand, the $J > 5$ flows of the small A_o/A_i , large t/D_1 injector showed strong response at the forcing frequency.

The dissertation of Sophonias Teshome is approved.

Russel E. Caflisch

Xiaolin Zhong

Ivett A. Leyva

Owen I. Smith, Committee Co-chair

Ann R. Karagozian, Committee Co-chair

University of California, Los Angeles

2012

To my parents

TABLE OF CONTENTS

1	Introduction	1
1.1	Fuel Droplet Combustion	2
1.1.1	Alternative Fuels	2
1.1.2	Related Works in Droplet Combustion	3
1.1.3	Effects of Acoustics on Droplet Combustion	4
1.1.4	Objectives	8
1.2	Shear-Coaxial Jets	9
1.2.1	Near-Field Mixing of Same and Different Density Shear-Coaxial Jets	10
1.2.2	Stability Consideration of Coaxial Jets	14
1.2.3	Transverse Acoustic Excitation of Coaxial Jets	17
1.2.4	Objectives	20
2	Droplet Combustion: Experimental Set-up and Methods	24
2.1	Acoustic Waveguide	24
2.2	Droplet Generation and Ignition	27
2.3	Measurement Methods	28
2.3.1	Burning Rate Constant	28
2.3.2	Acoustic Acceleration	28
2.3.3	Extinction Strain Rate Estimation	29
2.4	Experimental Procedure	30

2.5	Measurement Uncertainties	31
2.5.1	Precision Uncertainty	31
2.5.2	Bias Uncertainty	32
3	Droplet Combustion: Results and Discussion	39
3.1	Baseline Burning Rate Constants	39
3.2	Flame Alterations under Acoustic Excitation	40
3.3	Effect of Acoustic Acceleration on Burning Rate Constants	44
3.4	Fuel Extinction Studies	45
4	Shear-Coaxial Jets: Experimental Set-Up and Methods	68
4.1	High Pressure Chamber and Flow Facility	69
4.2	Shear-Coaxial Injectors	70
4.3	Inner Chamber: Acoustic Waveguide and Characterization	72
4.4	Measurement of Physical Properties	73
4.5	Jet Visualization	74
4.6	Measurement of Dark-Core Length	74
4.7	Proper Orthogonal Decomposition of Pixel Intensity Data Array	75
4.8	Measurement Uncertainty	79
5	Shear-Coaxial Jets: Results and Discussion	90
5.1	Shear-Coaxial Jets without Acoustic Forcing	91
5.1.1	Qualitative Characteristics of Baseline Flows	91
5.1.2	Baseline Dark-Core Length Measurements	94
5.1.3	Characterization of Dominant Dynamic Flow Structures	97

5.2	Transverse Acoustic Forcing of Shear-Coaxial Jets	134
5.2.1	Qualitative Characteristics of Acoustically Forced Flows	135
5.2.2	Acoustically Forced Dark-Core Length Measurements	140
5.2.3	Characterization of Dominant Dynamic Flow Structures	142
6	Summary, Conclusions and Recommendations for Future Work . . .	189
6.1	Droplet Combustion	189
6.2	Non-Reactive Shear-Coaxial Jets	190
6.3	Future Work	194
A Shear-Coaxial Jets Experimental Facility:		
	Piping and Instrumentation Diagram	196
B Shear-Coaxial Jets Experiment:		
	Standard Operating Procedures	202
C Shear-Coaxial Jets Experiment:		
	Summary Tables of Flow Conditions	227
	References	231

LIST OF FIGURES

2.1	Experimental setup of the acoustic waveguide and droplet feed system. .	33
2.2	Acoustic characterization of the waveguide (S&R configuration) as measured by pressure transducers at P1 and P2. Local maxima for both pressure transducers corresponds to a pressure antinode location. A local minimum at P1 and maximum at P2 corresponds to a pressure node. The distance between the speaker and reflector is approximately 62 cm. . . .	34
2.3	Measurements of relative local perturbation velocity (made by the hot wire anemometer) and the relative local perturbation pressure (made by the pressure transducer), both at the geometric center of the waveguide, for the Speaker-Reflector configuration (S&R). The displacement of the speaker and reflector is indicated on the abscissa, relative to their original locations as determined from the geometric center of the waveguide. Positive displacement refers to the S&R moved to the right. Results are shown for acoustic excitation at an applied frequency of: (a) 784 Hz (for a pressure node condition) and (b) 544 Hz (for a pressure antinode condition).	35

2.4	Measurements of relative local perturbation velocity (made by the hot wire anemometer) and the relative local perturbation pressure (made by the pressure transducer P1), both at the geometric center of the waveguide, for the two Speaker configuration (S&S). The displacement of the two speakers is indicated on the abscissa, relative to their original locations as determined from the geometric center of the waveguide and a maximum or minimum in the pressure transducer. Positive displacement refers to the S&S moved to the right. Results are shown for acoustic excitation at an applied frequency of: (a) 784 Hz (for a pressure node condition) and (b) 544 Hz (for a pressure antinode condition).	36
2.5	Ethanol droplet burning with and without acoustic excitation or forcing. In the absence of acoustic forcing, the flame orientation is only influenced by force of buoyancy F_B , while with acoustic excitation, both F_B and acoustic radiation force F_R affect its orientation: (a) Unforced flame orientation (b) Forced flame orientation	37
2.6	A schematic of the flow and relevant parameters used in estimating extinction strain rate. The flame assumes a nearly horizontal orientation at the instant before extinction.	38
3.1	Images of various fuel droplets burning in the absence of acoustic excitation.	48

3.2	Schematic showing the relative displacement between a pressure node (velocity antinode) and the droplet. <i>Top</i> : Location of the speakers in the waveguide relative to a velocity antinode (pressure node) situated at $x' = 0$, with the droplet located at $x = 0$ relative to the velocity antinode. <i>Middle</i> : Location of velocity antinode at $x' > 0$ relative to the droplet (and of the droplet at $x < 0$ relative to the velocity antinode), resulting from displacement of the speakers to the right as compared with the original condition. <i>Bottom</i> : Location of velocity antinode at $x' < 0$ relative to the droplet (and of the droplet at $x > 0$ relative to the velocity antinode), resulting from displacement of the speakers to the left as compared with the original condition.	49
3.3	Photographs of a burning ethanol droplet with acoustic excitation at an applied frequency of 784 Hz (for a pressure node condition). The positions of the two speakers (“S&S”) are indicated, relative to their original locations as determined from the geometric waveguide center and minimum in measured pressures. “S&S X cm to left” refers to the case where the speakers were moved by X cm to the left as compared with their original positions, etc. The true pressure node was likely coincident with the droplet located between cases (c) and (d), very close to the pressure node.	50

- 3.4 Photographs of a burning JP-8 droplet with acoustic excitation at an applied frequency of 784 Hz (for a pressure node condition). The positions of the two speakers (“S&S”) are indicated, relative to their original locations as determined from the geometric waveguide center and minimum in measured pressures. “S&S X cm to left” refers to the case where the speakers were moved by X cm to the left as compared with their original positions, etc. The true pressure node was likely coincident with the droplet located between cases (c) and (d), very close to the pressure node. 51
- 3.5 Photographs of a burning JP-8/FT blend droplet with acoustic excitation at an applied frequency of 784 Hz (for a pressure node condition). The positions of the two speakers (“S&S”) are indicated, relative to their original locations as determined from the geometric waveguide center and minimum in measured pressures. “S&S X cm to left” refers to the case where the speakers were moved by X cm to the left as compared with their original positions, etc. The true pressure node was likely coincident with the droplet located between cases (c) and (d), very close to the pressure node. 52
- 3.6 Photographs of a burning FT droplet with acoustic excitation at an applied frequency of 784 Hz (for a pressure node condition). The positions of the two speakers (“S&S”) are indicated, relative to their original locations as determined from the geometric waveguide center and minimum in measured pressures. “S&S X cm to left” refers to the case where the speakers were moved by X cm to the left as compared with their original positions, etc. The true pressure node was likely coincident with the droplet located between cases (c) and (d), very close to the pressure node. 53

- 3.7 Photographs of a burning ethanol droplet with acoustic excitation at an applied frequency of 1340 Hz (for a pressure node condition). The positions of the two speakers (“S&S”) are indicated, relative to their original locations as determined from the geometric waveguide center and minimum in measured pressures. “S&S X cm to left” refers to the case where the speakers were moved by X cm to the left as compared with their original positions, etc. The true pressure node was likely coincident with the droplet located between cases (c) and (d), very close to the pressure node. 54
- 3.8 Photographs of a burning JP-8 droplet with acoustic excitation at an applied frequency of 1340 Hz (for a pressure node condition). The positions of the two speakers (“S&S”) are indicated, relative to their original locations as determined from the geometric waveguide center and minimum in measured pressures. “S&S X cm to left” refers to the case where the speakers were moved by X cm to the left as compared with their original positions, etc. The true pressure node was likely coincident with the droplet located between cases (c) and (d), very close to the pressure node. 55
- 3.9 Photographs of a burning FT droplet with acoustic excitation at an applied frequency of 1340 Hz (for a pressure node condition). The positions of the two speakers (“S&S”) are indicated, relative to their original locations as determined from the geometric waveguide center and minimum in measured pressures. “S&S X cm to left” refers to the case where the speakers were moved by X cm to the left as compared with their original positions, etc. The true pressure node was likely coincident with the droplet located between cases (c) and (d), very close to the pressure node. 56

3.10	Pressure perturbations, estimated theoretical and actual acoustic accelerations g_a , and average burning rate constant K as a function of the displacement of the speakers with respect to the original position (0 cm) for the ethanol droplet burning in the vicinity of a pressure node at a frequency of approximately 784 Hz.	57
3.11	Pressure perturbations, estimated theoretical and actual acoustic accelerations g_a , and average burning rate constant K as a function of the displacement of the speakers with respect to the original position (0 cm) for the JP-8 droplet burning in the vicinity of a pressure node at a frequency of approximately 784 Hz.	58
3.12	Pressure perturbations, estimated theoretical and actual acoustic accelerations g_a , and average burning rate constant K as a function of the displacement of the speakers with respect to the original position (0 cm) for the JP-8/FT blend droplet burning in the vicinity of a pressure node at a frequency of approximately 784 Hz.	59
3.13	Pressure perturbations, estimated theoretical and actual acoustic accelerations g_a , and average burning rate constant K as a function of the displacement of the speakers with respect to the original position (0 cm) for the FT droplet burning in the vicinity of a pressure node at a frequency of approximately 784 Hz.	60
3.14	Pressure perturbations, estimated theoretical and actual acoustic accelerations g_a , and average burning rate constant K as a function of the displacement of the speakers with respect to the original position (0 cm) for the ethanol droplet burning in the vicinity of a pressure node at a frequency of approximately 1340 Hz.	61

3.15	Pressure perturbations, estimated theoretical and actual acoustic accelerations g_a , and average burning rate constant K as a function of the displacement of the speakers with respect to the original position (0 cm) for the JP-8 droplet burning in the vicinity of a pressure node at a frequency of approximately 1340 Hz.	62
3.16	Pressure perturbations, estimated theoretical and actual acoustic accelerations g_a , and average burning rate constant K as a function of the displacement of the speakers with respect to the original position (0 cm) for the FT droplet burning in the vicinity of a pressure node at a frequency of approximately 1340 Hz.	63
3.17	A sequence of images showing the extinction process of the flame surrounding an ethanol fuel droplet. The time span between the consecutive images was approximately 33 ms. The sound pressure level was 142.3 dB, and the estimated strain rate at extinction for this case was 350 s^{-1} . . .	64
3.18	A sequence of images showing the extinction process of the flame surrounding a JP-8 fuel droplet. The time span between the consecutive images was approximately 33 ms. The sound pressure level was 140.8 dB, and the estimated strain rate at extinction for this case was 250 s^{-1} . . .	65
3.19	A sequence of images showing the extinction process of the flame surrounding a JP-8/FT fuel blend droplet. The time span between the consecutive images was approximately 33 ms. The sound pressure level was 141.3 dB, and the estimated strain rate at extinction for this case was 260 s^{-1}	66

3.20	A sequence of images showing the extinction process of the flame surrounding an FT fuel droplet. The time span between the consecutive images was approximately 33 ms. The sound pressure level was 141.9 dB, and the estimated strain rate at extinction for this case was 330 s^{-1}	67
4.1	A schematic of the chamber and peripheral lines.	82
4.2	A schematic of the shear-coaxial injector assembly (expanded view of A : See Figure 4.3).	83
4.3	A schematic of the shear-coaxial injector exit.	83
4.4	Pictures of the acoustic elements. Acoustic waves generated by the piezosiren enter the end of the waveguide of circular cross-section and propagate down to the test-section of rectangular cross-section	84
4.5	Back-lit images of baseline LAR-thin injector flows at $J = 0.1$ where the chamber pressure, and the chamber, outer jet and inner jet temperatures were: (a) 1.5 MPa, 243 K, 198 K, 107 K, and (b) 3.57 MPa, 252 K, 195 K, 114 K, respectively.	84
4.6	Measurement of dark-core length: (a) original image (b) black and white image after thresholding (c) contour used to define the dark-core length (L).	85
4.7	Illustration of (a) how pixel intensity values from a single image are arranged into a row vector; (b) the construction of A , data matrix of pixel intensities.	85
4.8	PN forced ($f_F = 3.12\text{ kHz}$) LAR-thin injector flow at $P_r = 0.44$, $J = 5.2$: (a) a snapshot image captured at 25 kHz; (b) a time-averaged image from 1000 consecutive images.	86

4.9	Singular values for PN forced ($f_F = 3.12$ kHz) LAR-thin injector flow at $P_r = 0.44$, $J = 5.2$	86
4.10	Proper orthogonal mode (POM) image and power spectral density (PSD) of the temporal amplitude coefficients for PN forced ($f_F = 3.12$ kHz) LAR-thin injector flow at $P_r = 0.44$, $J = 5.2$: mode-1 (a) POM, (b) PSD; mode-2 (c) POM (d) PSD.	87
4.11	A time sequence of POM images for PN forced ($f_F = 3.12$ kHz) LAR-thin injector flow at $P_r = 0.44$, $J = 5.2$: (a) mode-1 only, (b) superposition of mode-1 and mode-2.	88
4.12	Cross-power spectral density (CPSD) of mode-1 and mode-2 for PN forced ($f_F = 3.12$ kHz) LAR-thin injector flow at $P_r = 0.44$, $J = 5.2$: (a) magnitude, (b) phase.	89
5.1	Back-lit images of the LAR-thin injector baseline flow at $P_r = 0.44$ and varying J . The image framing rate was 25 kHz. At subcritical chamber pressure, the inner jet was in the liquid state while the outer jet was in the gaseous state. Table C.1 gives a summary of the flow conditions. . . .	105
5.2	Back-lit images of the LAR-thin injector baseline flow at $P_r = 1.05$ and varying J . The image framing rate was 25 kHz. At nearcritical chamber pressure, the inner jet was a transcritical fluid while the outer jet was a supercritical fluid. Table C.1 gives a summary of the flow conditions. . .	106
5.3	Back-lit images of the SAR-thick injector baseline flow at $P_r = 0.44$ and varying J . The image framing rate was 25 kHz. At subcritical chamber pressure, the inner jet was in the liquid state while the outer jet was in the gaseous state. Table C.2 gives a summary of the flow conditions. . . .	107

5.4	Back-lit images of the SAR-thick injector baseline flow at $P_r = 1.05$ and varying J . The image framing rate was 25 kHz. At nearcritical chamber pressure, the inner jet was in a transcritical fluid while the outer jet was a supercritical fluid. Table C.2 gives a summary of the flow conditions.	108
5.5	Measurements of the LAR-thin injector baseline flows dark-core lengths, L_B normalized by the inside diameter of the inner injector, D_1 . The vertical error bars represent the uncertainty in a single measurement to within 2σ of the mean for 1000 measurements. The horizontal error bars represent the bias errors in the measurement of J . The large errors at higher J values were mainly due to the large relative uncertainties ($\delta\dot{m}_i/\dot{m}_i$) in the low inner jet flowrate measurements.	109
5.6	Measurements of the SAR-thick injector baseline flows dark-core lengths, L_B normalized by the inside diameter of the inner injector, D_1 . The vertical error bars represent the uncertainty in a single measurement to within 2σ of the mean for 1000 measurements. The horizontal error bars represent the bias errors in the measurement of J .	110
5.7	A power-law curve-fit to the L_B/D_1 data plotted in Figures 5.6 and 5.5. The variation of L_B/D_1 with J was similar for both injector flows in the same pressure regime. In addition, the SAR-thick injector L_B/D_1 were consistently lower than the LAR-thin injector, and those at $P_r = 1.05$ were lower than at $P_r = 0.44$.	111
5.8	Measured L_B/D_1 at $P_r = 0.44$ using different injector configurations including those used by Rodriguez, Graham <i>et al.</i> , and Leyva <i>et al.</i> . The dimensions of the LAR-thick and SAR-thin injectors are given in Table 1.2.	112

5.9	Measured L_B/D_1 (a) without adjustment and (b) with adjustment to $T_i = 109$ K, at $P_r = 1.05$ using different injector configurations including those used by Rodriguez, Graham <i>et al.</i> , and Leyva <i>et al.</i> . The dimensions of the LAR-thick and SAR-thin injectors are given in Table 1.2.	113
5.10	Measured L_B/D_1 for the different injectors at $P_r = 0.44$ plotted versus $G = c_1 J^{c_2} (t/D_1)^{c_3} (A_o/A_i)^{c_4}$, where the constants were obtained using non-linear regression, and whose values are listed in Table 5.1. The linear fit with about unit slope indicated that the model was a good representation of the dependance of L_B/D_1 on J and the injector geometry. . . .	114
5.11	Measured L_B/D_1 for the different injectors at $P_r = 1.05$ plotted versus $G = c_1 J^{c_2} (t/D_1)^{c_3} (A_o/A_i)^{c_4}$, where the constants were obtained using non-linear regression, and whose values are listed in Table 5.1. The linear fit with about unit slope indicated that the model was a good representation of the dependance of L_B/D_1 on J and the injector geometry. . . .	115
5.12	See caption on page 119.	116
5.12	See caption on page 119.	117
5.12	See caption on page 119.	118
5.12	A back-lit image of the LAR-thin injector baseline flow at $P_r = 0.44$ similar to those in Figure 5.1, a time-averaged image and an image of the superposed conjugate proper orthogonal modes (POMs) are shown for each J . The averaged image consisted of 1000 frames sampled at 25 kHz. The corresponding plots are the cross-power spectral density (CPSD) magnitude of the time-dependent amplitude coefficients of the conjugate modes. The peaks in the spectra are the characteristic frequencies of the periodic flow structures identified in the POM images.	119
5.13	See caption on page 122.	120

5.13	See caption on page 122.	121
5.13	A back-lit image of the LAR-thin injector baseline flow at $P_r = 1.05$ similar to those in Figure 5.2, a time-averaged image and an image of the superposed conjugate proper orthogonal modes (POMs) are shown for each J . The averaged image consisted of 1000 frames sampled at 25 kHz. The corresponding plots are the cross-power spectral density (CPSD) magnitude of the time-dependent amplitude coefficients of the conjugate modes. The peaks in the spectra are the characteristic frequencies of the periodic flow structures identified in the POM images.	122
5.14	See caption on page 126.	123
5.14	See caption on page 126.	124
5.14	See caption on page 126.	125
5.14	A back-lit image of the SAR-thick injector baseline flow at $P_r = 0.44$ similar to those in Figure 5.3, a time-averaged image and an image of the superposed conjugate proper orthogonal modes (POMs) are shown for each J . The averaged image consisted of 500 frames sampled at 25 kHz. The corresponding plots are the cross-power spectral density (CPSD) magnitude of the time-dependent amplitude coefficients of the conjugate modes. The peaks in the spectra are the characteristic frequencies of the periodic flow structures identified in the POM images.	126
5.15	See caption on page 130.	127
5.15	See caption on page 130.	128
5.15	See caption on page 130.	129

5.15	A back-lit image of the SAR-thick injector baseline flow at $P_r = 1.05$ similar to those in Figure 5.4, a time-averaged image and an image of the superposed conjugate proper orthogonal modes (POMs) are shown for each J . The averaged image consisted of 500 frames sampled at 25 kHz. The corresponding plots are the cross-power spectral density (CPSD) magnitude of the time-dependent amplitude coefficients of the conjugate modes. The peaks in the spectra are the characteristic frequencies of the periodic flow structures identified in the POM images.	130
5.16	Plots of the outer jet exit velocities, U_o , inner jet exit velocities, U_i , their corresponding mean velocities, U_{mean} , and the estimated convection velocities of the dominant flow structures, U_s for the LAR-thin and SAR-thick injector flows at $P_r = 0.44$. It can be seen that the LAR-thin injector outer jet flow had more influence on the inner shear layer flow than did the SAR-thick outer jet flow.	131
5.17	Plots of the outer jet exit velocities, U_o , inner jet exit velocities, U_i , their corresponding mean velocities, U_{mean} , and the estimated convection velocities of the dominant flow structures, U_s for the LAR-thin and SAR-thick injector flows at $P_r = 1.05$. Again, it is clear that the LAR-thin injector outer jet flow had more influence on the inner shear layer flow than did the SAR-thick outer jet flow.	132
5.18	Comparison of Strouhal numbers, St_{D_1} , of the inner shear layer periodic flow structures based on the inner jet exit diameter, and the mean of the outer and inner jet exit velocities. All St_{D_1} for the LAR-thin and SAR-thick injector flows at both P_r remained within 10% of 0.1 for the different J values.	133
5.19	See caption on page 150.	148

5.19	See caption on page 150.	149
5.19	Back-lit images of the LAR-thin injector PAN flow at $P_r = 0.44$ and varying J . The image framing rate was 25 kHz. Table C.3 gives a summary of the acoustic forcing frequencies and amplitudes.	150
5.20	See caption on page 152.	151
5.20	Back-lit images of the LAR-thin injector PAN flow at $P_r = 1.05$ and varying J . The image framing rate was 25 kHz. Table C.3 gives a summary of the acoustic forcing frequencies and amplitudes.	152
5.21	A time-sequence of images during PAN forcing ($f_F = 3.14$ kHz) of the $J = 0.5$ LAR-thin injector flow at $P_r = 0.44$. The images were captured at $40 \mu s$ intervals, and show formation of the outer shear-layer vortices, which grow and dominate the inner shear layer and inner jet flow dynamics.	153
5.22	A time-sequence of images during PAN forcing ($f_F = 3.11$ kHz) of the $J = 14$ LAR-thin injector flow at $P_r = 0.44$. The images were captured at $40 \mu s$ intervals. Unlike the $J = 0.5$ flow in Figure 5.21, the large convection speed of the shear-layer vortices prevented their interaction with the inner shear layer.	154
5.23	Synchronized acoustic pressure perturbation measurements during PAN forcing ($f_F = 3.14$ kHz) of the $J = 0.5$ LAR-thin injector flow at $P_r = 0.44$. The numbers next to the data points refer to the amplitudes measured corresponding to the image numbers in Figure 5.21.	155
5.24	Synchronized acoustic pressure perturbation measurements during PAN forcing ($f_F = 3.11$ kHz) of the $J = 14$ LAR-thin injector flow at $P_r = 0.44$. The numbers next to the data points refer to the amplitudes measured corresponding to the image numbers in Figure 5.22.	155

5.25	See caption on page 158.	156
5.25	See caption on page 158.	157
5.25	Back-lit images of the SAR-thick injector PAN flow at $P_r = 0.44$ and varying J . The image framing rate was 25 kHz. Table C.4 gives a summary of the acoustic forcing frequencies and amplitudes.	158
5.26	See caption on page 161.	159
5.26	See caption on page 161.	160
5.26	Back-lit images of the LAR-thin injector PAN flow at $P_r = 1.05$ and varying J . The image framing rate was 25 kHz. Table C.4 gives a summary of the acoustic forcing frequencies and amplitudes.	161
5.27	Measurements of the PAN forced flow dark-core length, L_{PAN} normalized by the corresponding baseline flow dark-core length, L_B	161
5.28	Measurements of the PN forced flow dark-core length, L_{PN} normalized by the corresponding baseline flow dark-core length, L_B	162
5.29	A back-lit image of the LAR-thin injector forced ($f_F = 3.13$ kHz) flows at $P_r = 0.44$ similar to that in Figure 5.19, a time-averaged image and an image of the superposed conjugate proper orthogonal modes (POMs). The averaged image consisted of 1000 frames sampled at 25 kHz. The corresponding plots are the cross-power spectral density (CPSD) magnitude of the time-dependent amplitude coefficients of the conjugate modes. The peak characteristic frequencies of the periodic flow structures were identical to f_F . For the purpose of comparison, the baseline spectra are shown in dots. Under both the PAN and PN forcing conditions, the forced spectra were completely different from that of the baseline. (.....Baseline, ——Forced)	163

5.30	A back-lit image of the LAR-thin injector forced ($f_F = 3.14$ kHz) flows at $P_r = 0.44$ similar to that in Figure 5.19, a time-averaged image and an image of the superposed conjugate proper orthogonal modes (POMs). The averaged image consisted of 1000 frames sampled at 25 kHz. The corresponding plots are the cross-power spectral density (CPSD) magnitude of the time-dependent amplitude coefficients of the conjugate modes. The peak characteristic frequencies of the periodic flow structures were identical to f_F . For the purpose of comparison, the baseline spectra are shown in dots. Under both the PAN and PN forcing conditions, the forced spectra were completely different from that of the baseline. (.....Baseline, ——Forced)	164
5.31	A back-lit image of the LAR-thin injector forced ($f_F = 3.12$ kHz) flows at $P_r = 0.44$ similar to that in Figure 5.19, a time-averaged image and an image of the superposed conjugate proper orthogonal modes (POMs). The averaged image consisted of 1000 frames sampled at 25 kHz. The corresponding plots are the cross-power spectral density (CPSD) magnitude of the time-dependent amplitude coefficients of the conjugate modes. The peak characteristic frequencies of the periodic flow structures were identical to f_F . For the purpose of comparison, the baseline spectra are shown in dots. Under both the PAN and PN forcing conditions, the forced spectra were still different from that of the baseline. (.....Baseline, ——Forced)	165

5.32	A back-lit image of the LAR-thin injector forced ($f_F = 3.12$ kHz) flows at $P_r = 0.44$ similar to that in Figure 5.19, a time-averaged image and an image of the superposed conjugate proper orthogonal modes (POMs). The averaged image consisted of 1000 frames sampled at 25 kHz. The corresponding plots are the cross-power spectral density (CPSD) magnitude of the time-dependent amplitude coefficients of the conjugate modes. The peak characteristic frequencies of the periodic flow structures were identical to f_F . For the purpose of comparison, the baseline spectra are shown in dots. (.....Baseline, ———Forced)	166
5.33	A back-lit image of the LAR-thin injector forced ($f_F = 3.10$ kHz) flows at $P_r = 0.44$ similar to that in Figure 5.19, a time-averaged image and an image of the superposed conjugate proper orthogonal modes (POMs). The averaged image consisted of 1000 frames sampled at 25 kHz. The corresponding plots are the cross-power spectral density (CPSD) magnitude of the time-dependent amplitude coefficients of the conjugate modes. The peak characteristic frequencies of the periodic flow structures were identical to f_F . For the purpose of comparison, the baseline spectra are shown in dots. Under the PAN forcing condition, the forced spectrum retained the baseline spectrum. (.....Baseline, ———Forced)	167

- 5.34 A back-lit image of the LAR-thin injector forced ($f_F = 3.11$ kHz) flows at $P_r = 0.44$ similar to that in Figure 5.19, a time-averaged image and an image of the superposed conjugate proper orthogonal modes (POMs). The averaged image consisted of 1000 frames sampled at 25 kHz. The corresponding plots are the cross-power spectral density (CPSD) magnitude of the time-dependent amplitude coefficients of the conjugate modes. The peak characteristic frequencies of the periodic flow structures were identical to f_F . For the purpose of comparison, the baseline spectra are shown in dots. Under the PAN forcing condition, the forced spectrum retained the baseline spectrum. (.....Baseline, ——Forced) 168
- 5.35 A back-lit image of the LAR-thin injector forced ($f_F = 3.11$ kHz) flows at $P_r = 0.44$ similar to that in Figure 5.19, a time-averaged image and an image of the superposed conjugate proper orthogonal modes (POMs). The averaged image consisted of 1000 frames sampled at 25 kHz. The corresponding plots are the cross-power spectral density (CPSD) magnitude of the time-dependent amplitude coefficients of the conjugate modes. The peak characteristic frequencies of the periodic flow structures were identical to f_F . For the purpose of comparison, the baseline spectra are shown in dots. Under the PAN forcing condition, the forced spectrum retained the baseline spectrum. (.....Baseline, ——Forced) 169

- 5.36 A back-lit image of the LAR-thin injector forced ($f_F = 3.10$ kHz) flows at $P_r = 1.05$ similar to that in Figure 5.20, a time-averaged image and an image of the superposed conjugate proper orthogonal modes (POMs). The averaged image consisted of 1000 frames sampled at 25 kHz. The corresponding plots are the cross-power spectral density (CPSD) magnitude of the time-dependent amplitude coefficients of the conjugate modes. The peak characteristic frequencies of the periodic flow structures were identical to f_F . For the purpose of comparison, the baseline spectra are shown in dots. Under both the PAN and PN forcing conditions, the forced spectra were completely different from that of the baseline. (.....Baseline, ——Forced) 170
- 5.37 A back-lit image of the LAR-thin injector forced ($f_F = 3.10$ kHz) flows at $P_r = 1.05$ similar to that in Figure 5.20, a time-averaged image and an image of the superposed conjugate proper orthogonal modes (POMs). The averaged image consisted of 1000 frames sampled at 25 kHz. The corresponding plots are the cross-power spectral density (CPSD) magnitude of the time-dependent amplitude coefficients of the conjugate modes. The peak characteristic frequencies of the periodic flow structures were identical to f_F . For the purpose of comparison, the baseline spectra are shown in dots. Under the PAN forcing condition, the forced spectrum was completely different from that of the baseline. (.....Baseline, ——Forced) 171

- 5.38 A back-lit image of the LAR-thin injector forced ($f_F = 3.41$ kHz) flows at $P_r = 1.05$ similar to that in Figure 5.20, a time-averaged image and an image of the superposed conjugate proper orthogonal modes (POMs). The averaged image consisted of 1000 frames sampled at 25 kHz. The corresponding plots are the cross-power spectral density (CPSD) magnitude of the time-dependent amplitude coefficients of the conjugate modes. The peak characteristic frequencies of the periodic flow structures were identical to f_F . For the purpose of comparison, the baseline spectra are shown in dots. Under both the PAN and PN forcing conditions, the forced spectra were completely different from that of the baseline. (.....Baseline, ——Forced) 172
- 5.39 A back-lit image of the LAR-thin injector forced ($f_F = 3.10$ kHz) flows at $P_r = 1.05$ similar to that in Figure 5.20, a time-averaged image and an image of the superposed conjugate proper orthogonal modes (POMs). The averaged image consisted of 1000 frames sampled at 25 kHz. The corresponding plots are the cross-power spectral density (CPSD) magnitude of the time-dependent amplitude coefficients of the conjugate modes. The peak characteristic frequencies of the periodic flow structures were identical to f_F . For the purpose of comparison, the baseline spectra are shown in dots. Under the PAN forcing condition, the forced spectrum retained the baseline spectrum. (.....Baseline, ——Forced) 173

- 5.40 A back-lit image of the LAR-thin injector forced ($f_F = 3.10$ kHz) flows at $P_r = 1.05$ similar to that in Figure 5.20, a time-averaged image and an image of the superposed conjugate proper orthogonal modes (POMs). The averaged image consisted of 1000 frames sampled at 25 kHz. The corresponding plots are the cross-power spectral density (CPSD) magnitude of the time-dependent amplitude coefficients of the conjugate modes. The peak characteristic frequencies of the periodic flow structures were identical to f_F . For the purpose of comparison, the baseline spectra are shown in dots. Under the PAN forcing condition, the forced spectrum retained the baseline spectrum. (.....Baseline, ——Forced) 174
- 5.41 A back-lit image of the SAR-thick injector forced ($f_F = 3.10$ kHz) flows at $P_r = 0.44$ shown in Figure 5.25, a time-averaged image and an image of the superposed conjugate proper orthogonal modes (POMs). The averaged image consisted of 500 frames sampled at 25 kHz. The corresponding plots are the cross-power spectral density (CPSD) magnitude of the time-dependent amplitude coefficients of the conjugate modes. The low frequency peak associated with the periodic flow structures was not identical to f_F . For the purpose of comparison, the baseline spectra are shown with dots. (.....Baseline, ——Forced) 175

- 5.42 A back-lit image of the SAR-thick injector forced ($f_F = 3.04$ kHz) flows at $P_r = 0.44$ shown in Figure 5.25, a time-averaged image and an image of the superposed conjugate proper orthogonal modes (POMs). The averaged image consisted of 500 frames sampled at 25 kHz. The corresponding plots are the cross-power spectral density (CPSD) magnitude of the time-dependent amplitude coefficients of the conjugate modes. The low frequency peak associated with the periodic flow structures was not identical to f_F . For the purpose of comparison, the baseline spectra are shown with dots. (.....Baseline, ———Forced) 176
- 5.43 A back-lit image of the SAR-thick injector forced ($f_F = 3.07$ kHz) flows at $P_r = 0.44$ shown in Figure 5.25, a time-averaged image and an image of the superposed conjugate proper orthogonal modes (POMs). The averaged image consisted of 500 frames sampled at 25 kHz. The corresponding plots are the cross-power spectral density (CPSD) magnitude of the time-dependent amplitude coefficients of the conjugate modes. The low frequency peaks associated with the periodic flow structures was not identical to f_F . For the purpose of comparison, the baseline spectra are shown with dots. (.....Baseline, ———Forced) 177

5.44	A back-lit image of the SAR-thick injector forced ($f_F = 3.11$ kHz) flows at $P_r = 0.44$ shown in Figure 5.25, a time-averaged image and an image of the superposed conjugate proper orthogonal modes (POMs). The averaged image consisted of 500 frames sampled at 25 kHz. The corresponding plots are the cross-power spectral density (CPSD) magnitude of the time-dependent amplitude coefficients of the conjugate modes. The peak frequencies of the periodic flow structures were identical to f_F . For the purpose of comparison, the baseline spectra are shown with dots. (.....Baseline, ———Forced)	178
5.45	A back-lit image of the SAR-thick injector forced ($f_F = 3.11$ kHz) flows at $P_r = 0.44$ shown in Figure 5.25, a time-averaged image and an image of the superposed conjugate proper orthogonal modes (POMs). The averaged image consisted of 500 frames sampled at 25 kHz. The corresponding plots are the cross-power spectral density (CPSD) magnitude of the time-dependent amplitude coefficients of the conjugate modes. The peak frequencies of the periodic flow structures were identical to f_F . For the purpose of comparison, the baseline spectra are shown with dots. (.....Baseline, ———Forced)	179

5.46	A back-lit image of the SAR-thick injector forced ($f_F = 3.04$ kHz) flows at $P_r = 0.44$ shown in Figure 5.25, a time-averaged image and an image of the superposed conjugate proper orthogonal modes (POMs). The averaged image consisted of 500 frames sampled at 25 kHz. The corresponding plots are the cross-power spectral density (CPSD) magnitude of the time-dependent amplitude coefficients of the conjugate modes. The peak frequencies of the periodic flow structures were identical to f_F . For the purpose of comparison, the baseline spectra are shown with dots. (.....Baseline, ———Forced)	180
5.47	A back-lit image of the SAR-thick injector forced ($f_F = 3.11$ kHz) flows at $P_r = 0.44$ shown in Figure 5.25, a time-averaged image and an image of the superposed conjugate proper orthogonal modes (POMs). The averaged image consisted of 500 frames sampled at 25 kHz. The corresponding plots are the cross-power spectral density (CPSD) magnitude of the time-dependent amplitude coefficients of the conjugate modes. The peak frequencies of the periodic flow structures were identical to f_F . For the purpose of comparison, the baseline spectra are shown with dots. (.....Baseline, ———Forced)	181

- 5.48 A back-lit image of the SAR-thick injector forced ($f_F = 3.12$ kHz) flows at $P_r = 1.05$ shown in Figure 5.26, a time-averaged image and an image of the superposed conjugate proper orthogonal modes (POMs). The averaged image consisted of 500 frames sampled at 25 kHz. The corresponding plots are the cross-power spectral density (CPSD) magnitude of the time-dependent amplitude coefficients of the conjugate modes. The low frequency peak associated with the periodic flow structures was not identical to f_F . For the purpose of comparison, the baseline spectra are shown with dots. (.....Baseline, ———Forced) 182
- 5.49 A back-lit image of the SAR-thick injector forced ($f_F = 3.00$ kHz) flows at $P_r = 1.05$ shown in Figure 5.26, a time-averaged image and an image of the superposed conjugate proper orthogonal modes (POMs). The averaged image consisted of 500 frames sampled at 25 kHz. The corresponding plots are the cross-power spectral density (CPSD) magnitude of the time-dependent amplitude coefficients of the conjugate modes. The low frequency peaks associated with the periodic flow structures were not identical to f_F . For the purpose of comparison, the baseline spectra are shown with dots. (.....Baseline, ———Forced) 183

5.50	A back-lit image of the SAR-thick injector forced ($f_F = 3.04$ kHz) flows at $P_r = 1.05$ shown in Figure 5.26, a time-averaged image and an image of the superposed conjugate proper orthogonal modes (POMs). The averaged image consisted of 500 frames sampled at 25 kHz. The corresponding plots are the cross-power spectral density (CPSD) magnitude of the time-dependent amplitude coefficients of the conjugate modes. The low frequency peaks associated with the periodic flow structures were not identical to f_F . For the purpose of comparison, the baseline spectra are shown with dots. (.....Baseline, ———Forced)	184
5.51	A back-lit image of the SAR-thick injector forced ($f_F = 3.08$ kHz) flows at $P_r = 1.05$ shown in Figure 5.26, a time-averaged image and an image of the superposed conjugate proper orthogonal modes (POMs). The averaged image consisted of 500 frames sampled at 25 kHz. The corresponding plots are the cross-power spectral density (CPSD) magnitude of the time-dependent amplitude coefficients of the conjugate modes. The peak frequencies of the periodic flow structures were identical to f_F . For the purpose of comparison, the baseline spectra are shown with dots. (.....Baseline, ———Forced)	185

5.52	A back-lit image of the SAR-thick injector forced ($f_F = 3.11$ kHz) flows at $P_r = 1.05$ shown in Figure 5.26, a time-averaged image and an image of the superposed conjugate proper orthogonal modes (POMs). The averaged image consisted of 500 frames sampled at 25 kHz. The corresponding plots are the cross-power spectral density (CPSD) magnitude of the time-dependent amplitude coefficients of the conjugate modes. The peak frequencies of the periodic flow structures were identical to f_F . For the purpose of comparison, the baseline spectra are shown with dots. (.....Baseline, ———Forced)	186
5.53	A back-lit image of the SAR-thick injector forced ($f_F = 3.05$ kHz) flows at $P_r = 1.05$ shown in Figure 5.26, a time-averaged image and an image of the superposed conjugate proper orthogonal modes (POMs). The averaged image consisted of 500 frames sampled at 25 kHz. The corresponding plots are the cross-power spectral density (CPSD) magnitude of the time-dependent amplitude coefficients of the conjugate modes. The peak frequencies of the periodic flow structures were identical to f_F . For the purpose of comparison, the baseline spectra are shown with dots. (.....Baseline, ———Forced)	187

5.54	A back-lit image of the SAR-thick injector forced ($f_F = 3.12$ kHz) flows at $P_r = 1.05$ shown in Figure 5.26, a time-averaged image and an image of the superposed conjugate proper orthogonal modes (POMs). The averaged image consisted of 500 frames sampled at 25 kHz. The corresponding plots are the cross-power spectral density (CPSD) magnitude of the time-dependent amplitude coefficients of the conjugate modes. The peak frequencies of the periodic flow structures were identical to f_F . For the purpose of comparison, the baseline spectra are shown with dots. (.....Baseline, ———Forced)	188
A.1	Experimental facility piping and instrumentation diagram.	197
A.2	Expanded view of section A in Figure A.1.	198
A.3	Expanded view of section B in Figure A.1.	199
A.4	Expanded view of section C in Figure A.1.	200
A.5	Expanded view of section D in Figure A.1.	201

LIST OF TABLES

1.1	Summary of flow conditions used in the literature	22
1.2	Summary of injector exit dimensions (schematic shown in Figure 4.3) used in the literature	23
3.1	Comparison of measured values of burning rate constant K for various fuel droplets in the absence of acoustic excitation. Comparisons with available established values for K are also given.	47
3.2	Acoustic conditions of various fuels at extinction. The corresponding sound pressure levels in decibels (dB) and rough estimates of the strain rates are also shown.	47
4.1	Injector exit dimensions (mm)	72
5.1	Values of the constants in Equation 5.4 obtained from non-linear regres- sion of the L_B/D_1 data.	98
C.1	Summary table of flow conditions for the LAR-thin injector.	228
C.2	Summary table of flow conditions for the SAR-thick injector.	229
C.3	Summary table of acoustic forcing conditions and dark-core length mea- surements for the LAR-thin injector.	230
C.4	Summary table of acoustic forcing conditions and dark-core length mea- surements for the SAR-thick injector.	230

NOMENCLATURE

Symbols

\mathbf{A}	matrix of image pixel intensities
A	area
a	vector of time-dependent amplitude coefficients
c	speed of sound
D	injector diameter, jet diameter
d	droplet diameter
f	acoustic frequency
F_R	acoustic radiation force
g_a	acoustic acceleration
g_o	gravitational acceleration
I	acoustic intensity
J	outer to inner jet momentum flux ratio, $\rho_o U_o^2 / \rho_i U_i^2$
K	burning rate constant
L	distance between speakers, dark-core length
M	momentum flux
\dot{m}	mass flowrate
P	pressure
p'	pressure perturbation
P_r	reduced pressure, P/P_{cr}
Q	volume flowrate
R	outer to inner jet velocity ratio, U_o/U_i
r	droplet radius
Re	Reynolds number
S	outer to inner jet density ratio, ρ_o/ρ_i

T	temperature
t	time, inner jet injector post thickness
U	flow velocity
u'	velocity perturbation
V	volume
x	displacement of droplet relative to PN
x'	displacement of PN relative to droplet
z	impedance

Greek Symbols

α	density difference correction factor
δX	uncertainty in quantity X
ϵ	strain rate
θ	flame deflection angle
λ	acoustic wavelength
ϕ	proper orthogonal mode
ρ	density
σ	standard deviation
ψ	streamfunction

Subscripts

1	inner jet injector inside diameter
2	inner jet injector outside diameter
3	outer jet injector inside diameter
4	outer jet injector outside diameter
a	acoustic
c	chamber
cr	critical
eqvs	equivalent volume of a sphere
exp	experimental
f	flame
i	inner jet
o	ambient air surrounding droplet, outer jet
p	hot combustion products
th	theoretical
v	volumetric
∞	ambient flow, bulk flow

ACKNOWLEDGMENTS

First of all, I thank God for providing me with the much needed spiritual sustenance and discipline in dealing with different challenges and experiences. I also thank Him for all the good people, who have played significant roles and helped me chart my course in life.

It was a privilege to have Professor Ann Karagozian and Professor Owen Smith as my class instructors and research advisors. Among other things, they have taught me the value of organized and systematic thinking as part of the key tools to approaching complex problems. I want to sincerely thank Professor Karagozian for her unrelenting effort to find me the necessary support to go through graduate school. The inputs from Professor Xiaolin Zhong and Professor Russel Caflisch are very much appreciated. I would like to recognize current and former lab colleagues including Juliett, Juan, Chris, Dan, Cory, Lord, Jeff, Kevin, Hann-Shin, Alec, Ian, James and Vishal for their contributions to the droplet combustion study. I also thank Professor Karagozian and Professor Smith for giving me the option to go out to AFRL at Edwards AFB, and do part of my research work with an outstanding group of people.

I want to express my appreciation to Dr. Ivett Leyva and Dr. Douglas Talley for granting me the opportunity to join the EC-4 team at AFRL, for providing me support, and lending me their expert advice on so many aspects of the non-reactive shear-coaxial jets study. I especially want to thank Dr. Leyva for all the extra hours of discussions, which provided me with the technical guidance that I needed to complete my work. Mr. Randy Harvey's expertise was invaluable to the proper operation of the experimental facility. The timely completion of the experimental work would not have been possible without Mr. Harvey's continuous support even during the holiday seasons. I truly enjoyed the time I spent working with him while gaining hands-on experience and a good sense of humor. I also would like to extend my appreciation

to Dr. Juan Rodriguez, Mr. John Hasier, Mr. Jeffrey Wegener, Mr. Chad Eberhart, Mr. Foster Beasley, Mr. Edgar Felix, Mr. David Hill, Mr. Earl Thomas, Mr. Todd Newkirk, Dr. Alireza Badakhshan, Dr. Ananda Himansu, and Mr. Matthew Billingsley for the helpful discussions and technical assistance. I was able to have timely access to some key literature only because of the resourcefulness of Ms. Jennie Paton and Ms. Vicki Polzin. The shear-coaxial jet experimental work was sponsored by the Air Force Office of Scientific Research, grant FA9550-08-1-0048, under Dr. Mitat Birkan, program manager, and by subcontract RS111000-1 via ERC, Inc. from the Air Force Research Laboratory at Edwards AFB.

I would not have reached this point if it was not for my parents' selfless effort to ensure my sister and I had the best upbringing that a child could possibly have. Their unconditional love, support and the sense of discipline that they instilled in me has been essential to my success. Thank you Abbaba and Emmama for all your sacrifices. Fiona, thank you for being such a loving and supportive sister, who has been a great role model since our early childhood. I am lucky to have a loving and caring extended family, including Gashe, Nini, Babi, Koke, Sele, and Yirga, who also played monumental roles in my upbringing and my academic success. My friends, Negede and Wondwossen, have been nothing less than brothers to me with their constant show of support, advice and encouragement in my personal and academic ventures. I am also lucky to have such good friends and fellow students as Anson, Sergey, Maziar, Poyan and Albert with whom I have enjoyed sharing knowledge and experiences.

It is a great blessing to have my beloved Sifirwork in my life, and I am grateful for all her love and support. I look forward to learning so much more from her in the years to come.

VITA

2003	High School Diploma, Van Nuys High School, Van Nuys, CA
2005	Member, Tau Beta Pi Engineering Honor Society, CA Epsilon
2006	Scholarship, Pratt & Whitney Rocketdyne
2007	B.Sc., Aerospace Engineering, UCLA
2007-2008	Fellowship, Mechanical and Aerospace Engineering (MAE) Department, UCLA
2007-2009	Graduate Research Assistanship, advisory by Professor Karagozian and Professor Smith, Thesis Topic
2008	Teaching Assistantship, Intermediate Fluid Mechanics, Winter Quarter, MAE Department, UCLA
2009	Teaching Assistantship, Combustion Systems, Winter Quarter, MAE Department, UCLA
2009	Teaching Assistantship, Elementary Fluid Mechanics, Spring Quarter, MAE Department, UCLA
2009	M.Sc., Mechanical Engineering, UCLA
2009-2012	Graduate Student Researcher, Air Force Research Laboratory, Edwards AFB

PUBLICATIONS AND PRESENTATIONS

S. Teshome, I.A. Leyva, D. Talley, and A.R. Karagozian. “Cryogenic High-Pressure Shear-Coaxial Jets Exposed to Transverse Acoustic Forcing,” *Paper AIAA-2012-1265*, 50th AIAA Aerospace Sciences Meeting & Exhibit, January 2012

S. Teshome, I.A. Leyva, and D. Talley. “Proper Orthogonal Decomposition Analysis of Shear-Coaxial Injector Flows with and without Transverse Acoustic Forcing,” JANNAF 6th Liquid Propulsion Subcommittee Meeting, December 2011

Ivett A. Leyva, Doug Talley, Sophonias Teshome, Juan Rodriguez, and Jeffrey Graham. Shear-Coaxial Jets Subjected to an External Acoustic Field. Invited paper presented at the 23rd International Colloquium on the Dynamics of Explosions and Reactive Systems, UC Irvine, July 2011

S. Teshome, A. Pezeshkian, O.I. Smith, and A.R. Karagozian. “Droplet Combustion in the Presence of Altered Acceleration Fields via Acoustic Excitation,” Fall Technical Meeting of the Western States Section of the Combustion Institute, October 2009

S. Teshome, A. Pezeshkian, O.I. Smith, and A.R. Karagozian. Influence of Standing Acoustic Waves on Combustion of Alternative Liquid Fuels. APS/DFD Meeting Presentation, November 2008

J.I. Rodriguez, S. Teshome, H.S. Mao, A. Pezeshkian, O.I. Smith, and A.R. Karagozian. “Acoustically driven droplet combustion with alternative liquid fuels,” 46th AIAA Aerospace Sciences Meeting & Exhibit, *Paper AIAA-2008-1002*, January 2008

CHAPTER 1

Introduction

The present experimental studies focus on condensed phase combustion processes and non-reactive shear injection flows in the presence of transverse acoustic excitation. Combustion in the presence of and with coupling to acoustic instabilities is widely known to occur in airbreathing as well as rocket engines, particularly in the latter, where large scale combustion instabilities in liquid rocket engines (LREs) can lead to strong vehicle vibrations, as occurs in the “pogo” instability, or in catastrophic failure. The ability to understand the implications of combustion coupled acoustic instabilities on burning rates and other combustion processes such as localized extinction is critical for the operation and design of current and future engine systems. As a means of contributing to this understanding, the experimental studies presented consists of two independent investigations. The first set of studies, conducted in the UCLA Energy and Propulsion Research Laboratory, explores the combustion of alternative liquid fuel droplets while exposed to acoustic excitation in a cylindrical acoustic waveguide. The second set of studies, conducted in an experimental facility at the Air Force Research Laboratory in Edwards AFB, CA, explores cryogenic, non-reactive shear-coaxial jets in a high pressure chamber with and without the presence of acoustic excitation.

1.1 Fuel Droplet Combustion

1.1.1 Alternative Fuels

A rapid increase in worldwide demand for fossil fuels and fluctuating prices of crude oil has enhanced the search for alternative sources of fuels for transportation systems and power generation. Associated with this increase in the consumption of fossil fuels is the alarming rise of environmentally harmful emissions, including carbon dioxide and nitrogen oxides. This being the case, however, the near term feasible solutions for replacement fuels mainly involve hydrocarbons [1].

Among the different types of fuels under consideration for automotive applications, alcohols and biodiesel are receiving the most attention. Alcohol fuels such as methanol and ethanol exhibit favorable combustion characteristics such as clean burning and higher octane performance over gasoline [2]. However, realization of these features of pure alcohols require significant design changes to the present engines to attain higher compression ratio than that used for gasoline. Moreover, the mass production and distribution costs do not make pure alcohols the ideal substitutes for gasoline. Blends of gasoline and alcohol fuels, on the other hand, require only minimal to none engine modifications and less production costs while delivering some of the beneficial features of alcohol fuels. At the present, many gas stations around the world provide a blend of gasoline and 10% ethanol (E10), which is certified to be used in gasoline engines without any modification, whereas a blend of gasoline and 85% ethanol (E85) is only certified to be used in flexible fuel vehicles (FFVs) with engines specifically designed for this fuel.

As for possible aviation fuel replacements, liquid synthetic fuels derived from natural gas or coal gasification via the Fischer-Tropsch (FT) [3] process show the most promise. In 2006, flight tests using a 50-50% by volume blend of JP-8 and FT fuel in a B-52H aircraft were conducted at Edwards Air Force Base, and later the Air Force certified the

blend fuel to be used in this aircraft [4, 5]. Similar flight tests have been conducted using the C-17 Globemaster III, the KC-135 tanker, and others, until the entire Air Force fleet is certified for this alternative fuel blend.

With the potential to use such alternative fuels comes the need to understand, from a fundamental perspective, the performance of such fuels in a typical engine environment. One arena that is not particularly understood is the performance and response of these fuels when the combustion environment is itself acoustically resonant. The differing reactive, diffusive, and convective time scales associated with combustion processes when one changes from one fuel to another could alter the coupling to acoustic resonances and ultimately alter the combustion performance of the device. Thus, it is of interest to examine at a fundamental level the differing behaviors of various fuels when combustion is coupled to acoustic instabilities.

1.1.2 Related Works in Droplet Combustion

Spray injection systems commonly employed in internal combustion and gas turbine engines involve a dilute spray of fuel droplets with the combustion of individual droplets that make up the spray [6, 7]. For non-dilute sprays, on the other hand, the flame structures can surround the entire spray field. Despite the complexity that is present in an actual fuel spray combustion where interaction between neighboring burning droplets has a significant impact on the combustion characteristic of the ensemble, studying the fundamental character of a single isolated burning fuel droplet is important to the whole understanding of spray combustion. Fuel droplet combustion is a heterogeneous and reactive process whereby the droplet evaporates and acts as a source of fuel vapor that reacts with an oxidizer, typically air, to form a diffusion flame front surrounding the droplet. The fuel droplet is also commonly used as a fundamental model for condensed-phase combustion processes in general [8].

For a quasi-steady burning spherical droplet in a quiescent oxidizing environment, classical studies have shown that the variation in the diameter of the droplet d varies linearly with time t following the d^2 -Law [9, 10]:

$$d^2(t) = d^2(t = 0) - Kt \quad (1.1)$$

The d^2 -Law has been shown to be applicable to essentially spherical burning droplets in a microgravity environment [8], and approximately valid for burning droplets in a gravitational environment, even under non-quiescent conditions [11, 12].

In a microgravity environment, the burning droplet maintains a spherical geometry, thus enabling a direct application of the d^2 -Law to obtain the burning rate constant K . Such an environment also allows the study of fundamental droplet combustion phenomena, which would otherwise be difficult, if at all possible, to study in a normal gravity environment, where buoyant motions complicate the flowfield around the droplet [8].

In normal gravity conditions, a suspended burning droplet can no longer maintain a spherical geometry due to gravitational and surface tension forces. In order to determine K using Equation 1.1, the non-spherical droplet diameter is determined by equating the effective volume of the actual droplet to the volume of a spherical droplet of diameter d_{eqvs} as done by Struk *et. al* [13].

1.1.3 Effects of Acoustics on Droplet Combustion

Several experimental studies have shown that there can be an increase in the burning rate constant of droplets under the influence of an external acoustical field. This effect is mainly thought to occur as a result of steepening reactant species concentration and temperature gradients, which in turn, lead to increased mass and heat transfer rates at the droplet surface [11, 14, 15]. Saito *et. al* [14, 15], examine the effects of acoustic waves on single evaporating and burning kerosene droplets in 1g, observing that when

the fuel droplet is situated at or near a pressure node (velocity antinode), there can be a two to three-fold increase in evaporative or burning rate constants, while if the droplet is located at a pressure antinode, there is no change in the evaporation and combustion rates. Other experiments have involved acoustical excitation of burning droplets in microgravity, where the absence of natural convection arising from buoyancy force allows isolation of the influence of acoustic radiation forces. Okai *et. al* [16], investigate the effect of the amplitude and frequency on the disturbance of n-octane single droplets and droplet pairs. At a forcing frequency of 2000 Hz and under conditions where the droplets lie at the pressure node of the standing acoustic wave, the burning rate constants increase monotonically with increasing acoustic intensity until the flame extinguishes.

Microgravity droplet burning experiments of Tanabe *et al.* [17, 18] present further evidence of the enhancing effect of acoustics on burning rates. Their studies involve a burning n-decane droplet situated at a pressure node, or between a pressure node and antinode of a standing acoustic wave. They observe significant increases in the burning rate constant as the amplitude of the velocity perturbation is increased, resulting in burning rate constants that are almost double that for a quiescent or an unforced value. In addition, these researchers observe characteristic flame distortions whereby the flame is consistently deflected toward the pressure node when the droplet is situated between a node and antinode. They interpret burning rate increases and flame deflections in terms of the phenomenon of acoustic streaming, a term which they used to describe the time-averaged motion that is induced in a fluid flow dominated by its fluctuating components [19], such as one which occurs in the presence of standing acoustic waves. Tanabe *et al.* explain the cause of flame deflection in terms of the magnitude and direction of an acoustic radiation force F_R , a body force, acting on the sphere of hot gases surrounding the burning droplet. They propose an expression for this force as

$$F_R = \alpha(\rho_p - \rho_o)V \frac{\partial \overline{u'^2}}{\partial x} \quad (1.2)$$

where ρ_p is the density of the hot combustion products situated about the diffusion flame and the droplet, ρ_o is the density of ambient air surrounding the flame, V is the volume of the sphere containing the hot products, x is the displacement of the droplet from the pressure node or antinode location, and $\overline{u'^2}$ is the mean of the square of the amplitude of the local perturbation velocity, u' , inside the waveguide. The coefficient α takes the form

$$\alpha \equiv \frac{3\rho_o}{2(2\rho_p + \rho_o)} \quad (1.3)$$

The acoustic radiation force in Equation 1.2 has the same form as the net buoyant force acting on an object of density ρ_p and volume V submerged in a fluid of density ρ_o . This led Tanabe *et al.* to propose that the influence of the acoustic radiation force on the droplet combustion and flame deformation is similar to that of a gravitational force. The observed flame deflections are consistent with this theory when the droplet is situated away from a pressure node or antinode. They even state that when the droplet is situated precisely at the pressure node, there is no droplet deflection, but there is limited evidence for this.

Recent studies at UCLA and at NASA Glenn Research Center by Dattarajan *et al.* [20, 21] have focused on methanol droplet combustion characteristics during exposure to external acoustical perturbations in both normal gravity and microgravity. The waveguide used in these experiments consisted of a cylindrical tube bounded at one end by a loudspeaker and at the other end by a reflector plate. Emphasis is placed on excitation conditions in which the droplet is situated at or near a velocity antinode (pressure node), where the droplet experiences the greatest effects of velocity perturbations, or at a velocity node (pressure antinode), where the droplet is exposed to minimal velocity fluctuations. In microgravity, for sound pressure levels exceeding about 135 dB, droplet burning rates are seen to increase by over 75% and 200% for droplets situated near pressure antinode and pressure node locations, respectively. In contrast, in normal gravity, acoustic excitation of droplets situated near abpressure node produce only very

moderate increases in burning rate (about 11-15% higher during 138 dB forcing than for non-acoustically excited, burning droplets) and produce no significant change in burning rate near a pressure antinode for pressure perturbations in the same range of sound pressure level. Observed flame deformation for droplets situated to one side or the other of pressure nodes or antinodes in microgravity are generally consistent with the notion of acoustic radiation forces per Equation 1.2, yet both velocity and pressure perturbations are seen to affect flame behavior, even when the droplet appears to be situated precisely at or extremely close to node or antinode locations. While displacements of the droplet with respect to node or antinode locations are observed to have a measurable effect on droplet burning rates, acoustic accelerations associated with such displacements, as an analogy to gravitational acceleration, do not completely explain the significant increases in burning rate resulting from the excitation in microgravity.

Further experimental investigations by Rodriguez [22] using the same apparatus from the Dattarajan *et al.* studies, explore the combustion behavior of methanol, ethanol, pure FT, and JP-8/FT blend fuel droplet combustion in the presence of acoustic disturbances in normal gravity. The droplet is placed both near and at successively increasing displacements away from a pressure node or antinode. This is accomplished by moving the speaker and reflector to the left or right within the waveguide, maintaining the distance between the two. A general trend of increasing burning rate constants is observed when the droplet is further away from the node or antinode, with increases of up to 20% in the burning rate constant of the alcohol fuels. Extinction studies of the burning fuel droplets are also conducted by exposing them to increasing acoustic intensities. At sufficiently high forcing amplitudes, flame extinction (blow-out) is observed, and the extinction strain rates for the different fuels are roughly estimated based on velocity perturbation amplitudes.

Other several studies of the flame extinction phenomena associated with burning

droplets use porous spheres wetted with fuel [23, 24]. In these studies, the point of extinction is marked by the condition in which the leading half of the sphere is no longer inside the flame envelope, but where the flame is stabilized in the wake region of the sphere. The extinction velocities show an increase with increasing sphere diameters. For droplet sizes encountered in industrial fuel sprays, Agnoston *et al.* [24] predict an extinction velocity of about 0.5 m/s.

1.1.4 Objectives

The present experimental study continues to explore alternative and conventional fuel droplet combustion with transverse acoustic excitation. The alternative fuels considered are ethanol, methanol, pure FT and JP-8/FT blend, while the conventional fuel is JP-8. Thus, the main goals are:

1. to assess the flame response to acoustic excitation in the vicinity of a pressure node condition and compare to the theoretical predictions of the acoustic radiation force theory.
2. to compare the trends between the theoretical acoustic acceleration, $g_a = \alpha \frac{\partial \overline{u'^2}}{\partial x}$ from Equation 1.2, and the experimentally estimated acoustic acceleration profiles.
3. to quantify the burning rate constants with and without acoustic excitation, and examine any variation with changing acoustic acceleration.
4. to estimate and compare flame extinction conditions between the different fuels.

1.2 Shear-Coaxial Jets

Shear-coaxial injectors have proven to be one of the most effective and simple means of delivering propellants in combustion devices such as in liquid rocket engines (LREs). Their application in LREs in the United States was seen as early as the development of the J-2 engine for the Saturn I and Saturn V launch vehicles, and as recently as the space shuttle main engine (SSME), both of which utilized liquid hydrogen (LH_2) and liquid oxygen (LOX) as propellants. While LREs are one of the most commonly used types of rocket engines, there are nevertheless critical technical challenges associated with them, namely combustion instabilities.

Combustion instability is a phenomenon that can destroy an LRE in less than a second. It is primarily a result of feedback interactions between unsteady combustion rates and pressure fluctuations from acoustic modes in the combustion chamber (Harje and Reardon [25], Schadow *et al.* [26]). This feedback cycle may be described as one where pressure fluctuations in the combustion chamber enhance injector flow perturbations, which in turn give rise to unsteady combustion heat release rates. The by-product of unsteady heat production is density fluctuation, or equivalently pressure and velocity fluctuation, which can become so large as to destroy the engine. Although LOX/hydrocarbon LREs are most susceptible to combustion instabilities, LOX/ LH_2 engines are also known to experience such problems.

Since injector flows are directly involved in the flow processes that take place inside combustors, it is crucial to understand how they contribute to, as well as how they are affected by, these unsteady physical mechanisms that lead to combustion instabilities. However, a successful understanding at a fundamental level of these interactions between injector flows and chamber phenomena can be aided by first isolating the fluid dynamics aspect from the reactive flow processes, and studying the coupling of non-reactive coaxial injector flow instabilities with external pressure perturbations.

1.2.1 Near-Field Mixing of Same and Different Density Shear-Coaxial Jets

Shear-coaxial jets consist of a circular core or inner jet and an annular or outer jet. In the near-field region, where the potential cores of both the inner and outer jets exist, two shear-layers exist: an inner shear layer between the inner and outer jets, and an outer shear layer between the outer jet and the ambient fluid. As such, the mixing of the coaxial jets primarily depends on the development of the inner shear layer, which is governed by their velocity ratio, for same density jets, or their momentum flux ratio, for different density jets, as well as their exit area ratio and inner jet post thickness. However, the dynamics of the inner shear layer is also influenced by the development and dynamics of the outer shear layer.

Several extensive studies explore the effect of outer to inner jet velocity ratio, $R \equiv U_o/U_i$ (Chigier and Beer [27], Forstall and Shapiro [28], Ko and Kwan [29], Wicker and Eator [30], Villiermaux *et al.* [31]) and outer to inner nozzle exit area ratio, A_o/A_i , (Champagne and Wygnanski [32], Rehab *et al.* [33]) on the potential core length of the inner jet and the near-field flow structure of isodensity coaxial jets. Chigier and Beer [27] present one of the pioneering experimental works on uniform density coaxial jets by making detailed velocity and static pressure measurements of fully developed turbulent coaxial air jets issuing into stationary air. A summary of the exit configuration of the injection elements used in their and other works is given in Table 1.1. They investigate R values ranging from infinite to 0.024 in order to span the limiting cases of an annular jet to an axisymmetric single jet, respectively. For $R = 2.35$, they measure an inner potential core length of about half the inner jet nozzle diameter, D_1 , and report that the outer jet completely absorbs the inner jet by $3D_1$, where reverse flow occurs. This reverse flow occurs due to the lack of sufficient entrainment fluid with increasing outer jet mass flow. In the other extreme, for $R = 0.085$, they show that inner jet completely absorbs the outer jet within one hydraulic diameter of the annular nozzle.

Unlike the fully developed turbulent flow exit velocity profile in the Chigier and Beer [27] study, a majority of the studies done on shear-coaxial jets has been on top-hat exit velocity profiles, which are attained using contraction nozzles. Champagne and Wygnanski [32] present one of such studies where they investigate the effect of varying both velocity ratio, R ($0 < R < 10$), and area ratio, A_o/A_i (1.28, 2.94), on coaxial air jets. Hot-wire anemometer measurements reveal that the outer potential core length is independent of R as confirmed by Au and Ko [34], and is about 8 times the annular gap width. However, the outer potential core length is shown to increase with A_o/A_i . The inner jet potential core length, on the other hand, is strongly dependent on both R and A_o/A_i . For $0 < R < 1$, the inner potential core length is longer than that for a single jet since the presence of the outer jet creates a decreased shear between the inner jet and the surrounding. For $R > 1$, the inner core length decreases with R . The dependence of the core length with A_o/A_i is due to the fact that the pressure gradient, which exists between the inner jet flow and the ambient fluid, is smaller with thicker outer jets, thereby, inducing less convergence of the jets towards the centerline. Champagne and Wygnanski [32] conclude that for a fixed A_o/A_i , R should be greater than one for enhanced mixing between the inner and outer jets.

Further studies on the near-field region of coaxial air jets by Ko and Kwan [29] reveal that in the initial merging zone, the region upstream of the end of the outer jet potential core, there is good agreement between the outer jet mean velocity profile and that of a single jet. Their study examines three velocity ratios, $R = 0.37, 0.5, 0.7$, where they made detailed velocity measurements using a constant temperature hot-wire anemometer and pressure measurements using a microphone. The agreement between their velocity profiles reaffirms the notion that the outer jet behaves similar to a single jet. The inner jet behaves more like a single jet discharging into a coflowing ambient fluid (equivalent to an infinite diameter outer jet). The authors, however, do not make a clear distinction between a coflowing ambient fluid and a finite diameter outer jet flow.

The existence of an “outer shear layer” in the latter plays a key role in the mixing and stability characteristics of the inner jet (Sevilla *et al.* [35]). Ko and Kwan [29] also indicate the presence of vortical or coherent flow structures by identifying peaks in the overall pressure profile measured in the inner and outer shear layers. The dominance of the vortices in the inner and outer shear layers are found to depend with R , whereby, the vortices in the outer shear layer become more dominant with increasing R .

While these observations hold for lower outer to inner jet velocity ratios, $R < 1$, studies in the velocity ratio regime $1 < R < 6.7$ (Ko and Au [36], Au and Ko [34]) also reveal the presence of coherent structures in inner and outer shear layers. The coherent structures in the outer shear layer form outward rolling vortices similar to those for the $R < 1$ flows, resembling the same single jet behavior independent of R . The nature of the vortex structures that form in the inner shear layer is dependent on R . For $R > 2$, shear layer vortices, which the authors label as “coflowing-wake-vortices”, form with a mean sense of rotation opposite to that of the outer shear layer dominate the flow region. Dahm *et al.* [37] identify these vortices as shear-layer type of instabilities, which occur when a large velocity jump across the interface of the two jets exists. As R approaches one ($R < 1.25$), negligible or no velocity jump across the interface exists, resulting in more dominant “alternate-shedding” or wake-like vortices. These give clear evidence that velocity ratio has a major impact on the dynamics and interaction of vortex structures in the two shear layers, thus affecting the potential core length, or equivalently the extent of mixing of the two jets.

Rehab *et al.* [33, 38] and Villiermaux *et al.* [31] conducted similar investigations using same density coaxial water jets. They show that increasing the outer to inner nozzle diameter ratio results in a longer outer potential core, delaying the pinching of the inner jet after the outer potential core ends. Although the inverse proportionality between the inner potential core length to inner jet diameter ratio, L_p/D_1 , and R is

preserved regardless of the diameter ratio, the constant of proportionality, however, is altered (Rehab *et al.* [33, 38]). In addition, Rehab *et al.* [33] show that a top-hat exit velocity profile results in a longer inner potential core length than a fully developed turbulent flow velocity profile. This is the case since the jet momentum in the latter is less and velocity gradient exists across the entire cross-section of the jet rather than just the edges as in a top-hat profile.

A vast majority of shear-coaxial jet studies have a uniform density flow field with an outer to inner jet density ratio of one ($S = 1$). When that no longer holds, the effect of S on the coaxial jet mixing characteristics comes into play in addition to R . Thus, the effect of both density and velocity ratios may be captured in the outer to inner jet momentum flux ratio, $J \equiv SR^2$. The work by Gladnick *et al.* [39], which studies the near-field evolution of the velocity field of an inner CFC-12 jet with an outer air jet, deals with different density coaxial jets. However, it does not discuss the effects of varying S on the shear layer growth and consequently on the potential core length of the inner jet.

Favre-Marinet *et al.* [40, 41] make a systematic exploration of varying S for low-speed, high-density inner jets and high-speed, low-density outer jets using air-air, He-air, air-SF₆, and He-SF₆, where air and He are used as the outer jets in each coaxial jet pair. For isodensity air-air jets, the inner potential core length varies as $J^{-1/2}$ or equivalently as R^{-1} . This is in agreement with the R^{-1} dependence for coaxial water jets (Rehab *et al.* [33, 38]). Reducing the density ratio to $S \approx 0.2$ using air-SF₆ jets results in a shorter inner potential core length for a given J . This may be attributed to the increased shear layer growth rate due to the enhanced entrainment velocity of the inner jet by the outer jet. Favre-Marinet *et al.* [40] propose the relation $V_E/U_i \propto (J^{1/2} - S^{1/2})/(1 + S^{1/2})$ for the normalized entrainment velocity based on the estimation for the convection velocity of the vortical structures in a two-dimensional mixing layer (Dimotakis [42]). As this relation shows, lower density ratios translate into increased shear layer growth rates,

and hence, shorter core length. However, they find this is only valid up to density ratios of about an order of magnitude below isodensity cases. Larger density differences, such as with He-SF₆ ($S = 0.028$), the potential core length is slightly increased relative to the isodensity case of the same J . Although Favre-Marinet *et al.* [40, 41] do not put forth an explanation as to why this happens, this phenomenon might be attributed to the considerable reduction in the momentum diffusivity of the inner fluid leading to a relatively retarded growth of the inner shear layer.

Other studies involving different density or two-phase coaxial jets include those by Eroglu *et al.* [43], Lasheras *et al.* [44], Davis and Chehroudi [45], Leyva *et al.* [46], and Rodriguez [22]. Lasheras *et al.* [44] examine the break-up and atomization of an inner water jet by a high-speed outer air jet. They found that for high Weber number and high Reynolds number flows, J is the dominant parameter. The liquid intact length, break-up length or cone length, defined as the distance from the exit to where the liquid fraction is close to 1 along the axis, is found to vary as $J^{-1/2}$. This is again in agreement with the dependence of isodensity coaxial air and coaxial water jets (Rehab *et al.* [33, 38], Favre-Marinet *et al.* [40]).

1.2.2 Stability Consideration of Coaxial Jets

The influence of the coherent shear layer flow structures on the overall dynamics of the flow field calls for an understanding of the factors leading to their formation. Detailed studies on the development and growth of natural instabilities in a single circular jet (Cohen and Wygnanski [47]) or a single circular jet with coflow (Michalke and Hermann [48]) reveal two of the most significant natural modes of instability: the axisymmetric mode and the first azimuthal or helical mode. These modes have comparable amplification rates over most of the core region downstream of the exit, with the helical mode eventually dominating the flow field farther downstream. As Ko and Kwan [29] show,

the development of the outer shear layer of a coaxial jet behaves as the shear layer of a single jet, while the development of the inner shear layer behaves as that of a single jet issuing into an external coflow. Thus, the axisymmetric and helical modes of instability, along with natural as well as externally imposed flow conditions such as pressure or velocity perturbations that can affect their development, may be used to assess the stability of the coaxial jet.

The theoretical and experimental investigation of Cohen and Wygnanski [47] on the evolution of instabilities in a single, axisymmetric jet shows that very close to the nozzle exit, where the jet diameter to the shear layer momentum thickness ratio is very large ($D/\theta \gg 1$), the axisymmetric and all azimuthal modes of instability have the same amplification rates. As the shear layer grows, all azimuthal modes except the first (helical) mode become negligible within two jet diameters from the exit, while the amplification rate of the axisymmetric mode dominates at high frequencies and that of the helical mode at low frequencies. Near the end of the potential core and beyond, the helical mode dominates at all frequencies, and is shown to govern the evolution of the fully developed axisymmetric jet. External excitation of the axisymmetric and helical mode also reveals that the amplitude of the excited mode can be an order of magnitude larger than the unexcited mode.

The linear, inviscid instability analysis of a circular jet issuing into a coflowing ambient fluid of the same density by Michalke and Hermann [48] examines the effect of the presence of a coflow on the natural instabilities of a single jet. For zero coflow velocity, they also find that the helical mode is more unstable than the axisymmetric mode at large enough downstream location from the exit. A finite coflow velocity shows a stabilizing effect on the jet since the spatial growth rate decreases at all frequencies. Increasing the coflow velocity increases the region of unstable frequencies, and results in a shift of the peak of the spatial growth rates to higher frequencies.

In lieu of a coflow with an infinite cross-stream extent, a coaxial jet configuration has a finite diameter coflow, so that outer to inner jet diameter ratio comes into play in determining the stability characteristics of the flow (Sevilla *et al.* [35], Perrault-Joncas and Maslowe [49]). Sevilla *et al.* [35] investigate the effect of outer to inner jet diameter ratio as well as S on the convective and absolute instability of coaxial jets with $S \geq 1$, $R \leq 1$. They consider how the variation in these parameters factors into the transition from a convectively unstable flow to an absolutely unstable flow. When $R = 1$, increasing the diameter ratio, equivalent to pushing the outer shear layer farther out from the jets' interface, reduces the critical outer to inner jet density ratio, S , at which transition to an absolutely unstable flow occurs, thereby inhibiting absolute instability. In addition, for a diameter ratio larger than 1.03, unlike the axisymmetric mode, the helical mode stays in the convectively unstable regime for all $S > 1$. For $R < 1$, the transition from a convectively to absolutely unstable flow may be due to instabilities in the inner or outer shear layers. They show that the transition to absolutely unstable flow due to inner shear layer instabilities is only possible for very small outer jet velocities (approximately $R < 0.3$), and the transition due to the outer shear layer instability occurs at larger R for a given S and diameter ratio. For a given R , increasing the diameter ratio again reduces the range of S for which the flow is absolutely unstable.

The effect of inner nozzle wall thickness is discussed in the linear instability analysis of isodensity coaxial jets by Talamelli and Gavarini [50]. Their analysis shows that the absolutely unstable flow region may be enlarged by reducing the shear-layer thickness at the jet exit for a given R . In addition, the range of R for which an absolute instability occurs decreases with increasing shear-layer thickness. As a thicker wall delays the development of a shear layer, it may be the case that thick-walled nozzles are more likely to promote absolutely unstable flows.

1.2.3 Transverse Acoustic Excitation of Coaxial Jets

The earliest investigations of the effect of ambient pressure oscillations on free jets includes those by Miesse [51], Newman [52], and Heidmann and Groeneweg [53]. Miesse's experimental study examines how transverse ambient pressure oscillations, generated from a sound source directed perpendicular to the flow axis, alters the disintegration and dispersion behavior of a liquid jet. The results show that acoustic forcing decreases the length of liquid stream, and affected the dispersion pattern in a way so that increasing the frequency of pressure oscillation results in decreased dispersion. Transverse waves also prove to aid in the mixing of parallel streams.

Newman [52] explores how the jet break-up is affected under pressure antinode and velocity antinode conditions in a transverse acoustic field. His results show that both pressure and velocity oscillations are equally effective in promoting jet break-up although they have entirely different mechanisms. A pressure antinode condition induces periodic variation in the flowrate, which in turn, promotes break-up by inducing cyclic thickenings in the jet column. A velocity antinode condition, on the other hand, produces lateral displacement of the jet column due to transverse motion of the ambient fluid, thereby, again producing surface irregularities on the jet. His results, however, show pressure oscillations are more effective than velocity oscillations at higher chamber pressure, and both appear less effective in breaking up the jet than at lower chamber pressure.

A majority of the studies done on acoustically excited coaxial jets involve in-flow, axial or longitudinal forcing, where the acoustic source is placed upstream of the nozzle exit. Wicker and Eaton [30] study the effect of the outer jet on the near-field dynamics of the inner jet with axial excitation of each jet independently for $0.55 < R < 1.45$. Axial forcing of the outer jet show formation of periodic axisymmetric vortex rings at the forcing frequency. For $R > 1$, vortex structures in the outer shear layer completely

controlled the inner flow within $4D_1$. Forcing the inner jet flow alone does not have a significant effect on the development of structures in the outer shear layer. However, both forcing types result in a reduction of the inner potential core.

Balarac *et al.* [54] analyze numerically the mixing behavior of isodensity coaxial jets when a pure axisymmetric forcing is applied to the outer shear layer. Their analysis shows that strongly axisymmetric vortex rings in the outer shear layer undergo rapid amplification inducing a similar amplification of the inner shear layer rings. Stream-wise vortices also appear earlier compared to the natural case. Moreover, this forcing condition reduces both the inner and outer potential core lengths.

In the interest of gaining a better understanding of how acoustic instabilities play a role in combustion instabilities that occur in liquid rocket engine combustion chambers Richecoeur *et al.* [55] investigate the interaction of transverse acoustic waves with multiple shear-coaxial injector cold flows. The nonreactive flow experimental study uses liquid oxygen inner jets and gaseous nitrogen outer jets flowing out of five shear-coaxial injectors in a 3 MPa pressure chamber. Forcing at the first transverse mode of the chamber, at a frequency of 585 Hz, produces measurably shorter jets, whose dark-core regions are as much as 17% shorter than that of the unforced jet. The sinusoidal undulation of the jet due to velocity fluctuation aids in breaking up the jet into filaments, which enhances primary atomization and increases the vaporization rate of the inner oxygen jet.

The dependence of flame-acoustic interactions on density ratio ($1 < S^{-1} < 16$) and velocity ratio ($3.02 < R < 5.27$) is discussed by Ghosh *et al.* [56], and in more detail by Ghosh [57], where they use a planar shear-coaxial injector with an inner gaseous oxygen jet and two outer gaseous hydrogen jets to produce two diffusion flames fronts. Acoustic drivers produce transverse acoustic waves in a chamber at atmospheric pressure. An acoustic frequency of 1.15 kHz used in these experiments is comparable to the high

frequency or screeching instabilities that are known to be the most destructive form of instability. Reducing the density gradient (as $S^{-1} \rightarrow 1$) shows a greater resistance to flame-acoustic coupling. This is attributed to the reduced effect of the baroclinic torque due to the density gradient across the flame front and the imposed acoustic pressure perturbation. For the narrow range of R considered in this study, negligible changes in the flame-acoustic interactions are observed.

Earlier studies in the present AFRL experimental facility by Davis [58], Leyva *et al.* [46], and Rodriguez [22] study shear-coaxial nitrogen jets in a high pressure, cryogenic flow facility. With chamber pressures spanning subcritical to supercritical pressures, these studies investigate cryogenic inner nitrogen jets with less dense outer nitrogen jets with and without the presence of a transverse acoustic field. They make dark-core length measurements of the denser inner jet flow for a range of J values. Davis [58] uses an injector with a large outer to inner jet area ratio, and a large inner post thickness to diameter ratio (see Table 1.2). He reports shorter dark-core length measurements at nearcritical and supercritical pressures than at subcritical chamber pressure. This is in agreement with reports by Favre-Marinet *et al.* [40] in that at the elevated chamber pressures, S is on the order of 0.1 or larger. The normalized dark-core lengths under subcritical pressure are found to vary as $J^{-0.2}$, while they vary as $J^{-0.5}$ under near- and supercritical pressures. The mean dark-core length also shortens with acoustic forcing.

Rodriguez [22] continues the study with the same injector as Davis [58] and another injector with a small outer to inner jet area ratio and a small post thickness to diameter ratio. Transverse acoustic forcing using two acoustic sources enabled exposure of the coaxial jet flow to various portions of a standing acoustic field including pressure antinode and pressure node conditions. During acoustic forcing, both injector types show maximum reduction in their dark-core lengths relative to the baseline cases at lower momentum flux ratios ($1 < J < 5$) in all chamber pressure regimes. However, Ro-

driguez [22] reports that the large area ratio injector flow attains the largest reduction of dark-core length at or near a pressure node (velocity antinode) condition, while the small area ratio injector flow does so at or near a pressure antinode condition.

1.2.4 Objectives

The present work continues the series of experimental studies done in the same facility, which have examined the behavior of shear-coaxial N₂ jets at elevated chamber pressures spanning subcritical to supercritical pressure with and without the presence of a transverse acoustic field. As stated earlier, Davis [58], Davis and Chehroudi [45], Leyva *et al.* [46], and part of the study by Rodriguez [22] uses a shear-coaxial injector with a large outer to inner jet area ratio, A_o/A_i (see Table 1.2), and a large inner jet injector post thickness to inside diameter ratio, t/D_1 . As stated earlier, the study by Rodriguez [22] also uses an injector with a small A_o/A_i and small t/D_1 . The magnitude of A_o/A_i is one of the factors that dictate the interaction between the outer and inner shear layers; that is, larger A_o/A_i delays their interaction, therefore, limiting the influence of outer shear layer structures on the development of the inner shear layer. Moreover, the flow recirculation region that is established for a configuration with a large t/D_1 creates a delayed onset and growth of the inner shear layer region. In consideration of such geometric influences, the present study investigates two other injector exit configurations: a large A_o/A_i with a small t/D_1 and a small A_o/A_i with a large t/D_1 . It also employs different methods of analyzing high-speed image data to examine differences among various flow conditions.

Therefore, the main objectives of this study are:

1. to measure baseline flow dark-core lengths of the inner jets from high-speed back-lit images in order to characterize the mixing behavior using the two injectors under subcritical (reduced pressure, $P_r = 0.44$) and nearcritical ($P_r = 1.05$) chamber

pressure conditions for a range of J values. Here, the reduced pressure is defined as the ratio of the chamber pressure to the critical pressure of nitrogen ($P_r \equiv P_c/P_{cr}$).

2. to identify the dependence of baseline flow dark-core lengths on J , and injector geometric parameters, t/D_1 and A_o/A_i .
3. to evaluate the flow response to pressure antinode and pressure node acoustic forcing conditions by comparing the forced flow dark-core lengths to their baseline counterparts.
4. to apply a proper orthogonal decomposition (POD) analysis to extract coherent, periodic flow structures captured in the high-speed images. This will aid in characterizing the spatial and temporal behavior of the dominant flow structures in the inner shear layer of the baseline and acoustically forced flows. Using this approach, a better understanding may be gained of the critical differences and evolution of flow instability characteristics brought about as a result of simple design alterations in the shear-coaxial injector.

Table 1.1: Summary of flow conditions used in the literature

Ref.	Author(s)	Outer-Inner Jet	R or J	Exit Flow*
[27]	Chigier & Beer	Air-Air	$0.024 < R < \infty$	FDTF
[32]	Champagne & Wygnanski	Air-Air	$0 < R < 10$	TH
[29]	Ko & Kwan	Air-Air	$R = 0.37, 0.5, 0.7$	TH
[36, 34]	Ko & Au, Au & Ko	Air-Air	$1 < R < 6.7$	TH
[37]	Dahm <i>et al.</i>	Water-Water	$0.59 < R < 4.16$	TH
[33]	Rehab <i>et al.</i>	Water	$1 < R < 8$	TH
[38]	Rehab <i>et al.</i>	Water-Water	$1 < R < 8$	FDTF
[38]	Rehab <i>et al.</i>	Water-Water	$1 < R < 8$	TH
[39]	Gladnick <i>et al.</i>	Air-CFC12	$R = 0.64, 1, 2$	FDTF
[40]	Favre-Marinet <i>et al.</i>	Air,He,SF ₆ **	$1 < J < 200$	TH
[43]	Eroglu <i>et al.</i>	Air-Water	$10 < R < 164$	FDTF
[44]	Lasheras <i>et al.</i>	Air-Water	$2.5 < J < 40$	FDTF
[45]	Davis & Chehroudi	N ₂ -N ₂ ***	$0.2 < J < 11.2$	FDTF
[46]	Leyva <i>et al.</i>	N ₂ -N ₂ ***	$0.2 < J < 23$	FDTF
[22]	Rodriguez	N ₂ -N ₂ ***	$0.1 < J < 23$	FDTF
[30]	Wicker & Eaton	Air-Air	$0.55 < R < 1.45$	TH
[55]	Richecoeur <i>et al.</i>	N ₂ -LOx	$5 < J < 12$	FDTF
-	Present Work	N ₂ -N ₂ ***	$0.1 < J < 21$	FDTF

* Fully developed turbulent flow (FDTF) or top-hat (TH) velocity profile

** Air-Air, He-Air, Air-SF₆, He-SF₆

*** Inner jet is denser: liquid or transcritical fluid

Table 1.2: Summary of injector exit dimensions (schematic shown in Figure 4.3) used in the literature

Ref.	t (mm)	D_1 (mm)	D_2 (mm)	D_3 (mm)	t/D_1	A_o/A_i or D_3/D_1^*
[27]	19.5	25	64	97	0.78	8.5
[32]	-	25.4	-	-	-	1.28, 2.94
[29]	0.78	21	22.6	40	0.04	2.67
[36, 34]	1	20	22	40	0.05	2.73
[37]	1.27	53.3	55.9	76.4	0.02	0.94 or 1.4*
[33]	-	20	-	27	-	1.82
[38]	-	-	-	-	-	1.37*, 2.29*
[38]	-	-	-	-	-	1.35*
[39]	0.7	18	19.4	56	0.04	8.5 or 3.1*
[40]	0.2	20	20.4	27	0.01	1.53*
[43]	0.15	0.971	1.262	10.36	0.15	112.1 or 10.7*
[44]	0.2	3.8	4.2	5.6	0.05	0.95 or 1.47*
[45]	0.53	0.51	1.59	2.42	1.05	12.9
[46]	0.53	0.51	1.59	2.42	1.05	12.9
[22]	0.53, 0.13	0.51, 1.40	1.59, 1.65	2.42, 2.44	1.05, 0.09	12.9, 1.65
[30]	-	20	-	60	-	8 or 3*
[55]	0.3	5.78	-	7	-	1.21*
-	0.09, 1.24	0.7, 1.47	0.89, 3.96	2.44, 4.70	0.13, 0.84	10.6, 2.9

CHAPTER 2

Droplet Combustion: Experimental Set-up and Methods

The present studies were performed using the same experimental apparatus, with some modifications, used by Dattarajan [21] to analyze the behavior of methanol burning droplets under microgravity and normal gravity conditions, and later on by Rodriguez [22] to study the combustion behavior of methanol and various liquid alternative fuels in the presence of acoustic disturbances under normal gravity conditions.

2.1 Acoustic Waveguide

In the present experiments, standing acoustic waves were generated by two loudspeakers placed at either end of a closed cylindrical waveguide, which operated at background atmospheric pressure and at room temperature. The frequency and amplitude of the acoustic drivers were controlled via a function generator and amplifier. Prior experiments by Dattarajan [21] and by Rodriguez [22] used a speaker and reflector, as will be discussed below. A continuously fed, burning fuel droplet was situated at the center of the waveguide. A detailed schematic diagram of the experimental apparatus is shown in Figure 4.1. The waveguide was constructed of aluminum, with an inner diameter of 11.4 cm and a maximum length of 90 cm. Quartz windows were situated at either side of the center of the waveguide to provide optical access. A woofer type 8- Ω loudspeaker with a maximum power output of 40 W was placed at each end of the waveguide. A

rod assembly connecting the two speakers was used to fix the distance between them to a distance L as they were both moved to the left or to the right. Accordingly, to create a standing acoustic wave in the waveguide, the applied frequency f , of acoustic excitation was chosen such that L was an integral multiple of half the acoustic wavelength, $\frac{1}{2}\lambda = \frac{1}{2}c/f$, where c is the speed of sound in the waveguide.

The standing acoustic waves generated by this configuration allowed the droplet to be exposed to either a pressure node (PN) or pressure antinode (PAN) condition or an intermediate condition, depending on the applied f and positions of the speakers. In order to examine the response of the burning droplet to different acoustic conditions, the speakers were moved relative to the droplet to produce a relative displacement between the droplet and the PN or PAN. At the location of the droplet at the waveguide center, a flush-mounted pressure transducer with a sensitivity rating of 73 mV/kPa revealed approximate PN and PAN conditions based on minima and maxima of the local pressures, respectively. It is important to note that the length L and the position of the droplet relative to a PN or PAN were approximate, since the loudspeaker consisted of a vibrating diaphragm as opposed to a solid wall, and the diameter of the pressure transducer, about 1 cm, introduced ambiguity in the precise location of the minimum and maximum pressure.

The experimental apparatus used by Dattarajan [21], and later on by Rodriguez [22], employed a configuration whereby a speaker was placed at one end of the waveguide, and a wave reflector, consisting of a flat aluminum disc, was placed at the opposite end. A pressure transducer was placed within the reflector plate to provide additional data for determination of standing wave conditions. A sample plot of the variation in pressure measurements at the center and end of the waveguide for a fixed length L and different forcing frequencies is shown in Figure 2.2.

In order to compare the actual acoustic perturbation fields in the waveguide for the

speaker and reflector (S&R) configuration with the present two-speaker (S&S) configuration, hot wire anemometry in addition to pressure transducer measurements were used. A single component hot wire anemometer (Dantec StreamLine with a 55P15 probe), placed at the location of the droplet, measured velocity perturbations at the waveguide center. Such velocity perturbations were measured for acoustic excitation with the S&R and with the S&S situated at different locations but with a constant waveguide length L . Simultaneously, the pressure at the center of the waveguide was measured using the pressure transducer. Symmetry in both velocity and pressure perturbations would be expected as one moved the S&R or S&S to the left and right about the geometric center, with a maximum in velocity and minimum in pressure expected about the center for the PN case, and the reverse expected for the PAN conditions.

Figures 2.3ab show the measured pressure and velocity perturbations for the S&R configuration (with their movement at a constant waveguide length) at applied frequencies of 784 Hz (PN condition) and 544 Hz (PAN condition), respectively. The speakers were operated 180° out-of-phase at 784 Hz, and in-phase at 544 Hz. Figures 2.4ab show similar profiles, but for the S&S configuration. Clearly, the S&R configuration produced an asymmetry in the velocity field about the waveguide center for the pressure node condition, albeit with a relatively symmetric pressure field (Fig. 2.3a), while the S&S configuration under these conditions produced symmetric variation in pressure as well as velocity (Fig. 2.4a). The S&R configuration produced an asymmetry in both the velocity field and pressure field for the pressure antinode condition (Fig. 2.3b), while the S&S configuration under these conditions produced symmetric measurements (Fig. 2.4b).

It is not known why the asymmetry should be so pronounced when the S&R are moved to the right for the PN case and when they are moved to the left for the PAN case, but proximity of the reflector to a peak pressure location could have caused this behavior. In any event, the improved symmetry with the two-speaker configuration led

us to use this system in the subsequent experiments.

2.2 Droplet Generation and Ignition

The fuel delivery system consisted of a hollow borosilicate glass capillary and a KDS Model 100 syringe pump. The fuel droplet was suspended within the waveguide from the tip of the glass capillary of approximately 0.37 mm outer diameter. An unusual feature of the present experiments was that the liquid fuel could be continuously delivered during the droplet combustion. The syringe pump provided a controlled fuel delivery to the capillary. The volume flowrates Q_v and the droplet size were used to determine the burning rate constant K , as will be described below. A protective copper shroud was placed above the end of the glass capillary in order to prevent vaporization of the fuel within the glass capillary just above the droplet. As described in [20], the distance between the end of the shroud and the end of the tip of the capillary was fixed at 3.2 mm, a regime for which the droplet burning rate constant did not depend on this length.

The droplet was ignited by means of a resistive heating Ni-Cr wire mounted on a push-type solenoid. A TattleTale Model 8 data logger/controller board was used to synchronize the extension of the solenoid arm and the passage of current in the ignitor wires. This mechanism created an efficient means for igniting the droplet remotely without having to open, manually ignite, and close the waveguide, thus avoiding the risk of over-heating the capillary by reducing the time span between ignition and the start of data acquisition.

2.3 Measurement Methods

2.3.1 Burning Rate Constant

From continuity for a *spherical* droplet of diameter d , the instantaneous burning rate constant K may be evaluated according to:

$$K = \frac{4Q_v}{\pi d(t)} - 2d\dot{d} \quad (2.1)$$

A direct input of the volume flowrate Q_v on the syringe pump provided a constant rate of fuel delivery to the burning droplet. It can be noted that the preceding equation for K reduces to that of a typical “non-fed” burning droplet (the “d-squared law” described in Turns [10]) when $Q_v = 0$. Since the burning droplet in the present experiments was not always completely spherical, digitized video images of the burning droplet were used to determine an equivalent diameter of a sphere. An image processing MATLAB® algorithm incorporating custom written edge-detection routine [21] was used, so that the effective volume of the actual oblong droplet could be estimated and equated to that of a spherical droplet of equivalent diameter d_{eqvs} , as done by Struk, *et al.* [13]. Droplet burning rate constants based on d_{eqvs} in (2.1) were then determined, and time-averaged K values were computed.

2.3.2 Acoustic Acceleration

In the absence of acoustic excitation, the net force acting on the hot products of density ρ_p surrounding the burning droplet would be only the buoyancy force, $F_B = (\rho_p - \rho_o) V g_o$, which resulted in a vertically oriented, symmetric flame as shown in Figure 2.5a. Here, g_o is normal gravitational acceleration on the earth’s surface, 9.81 m/s^2 , ρ_o is the density of the surrounding (cooler) air, and V is the volume of the hot gases.

With acoustic excitation, the flame orientation was such that it became aligned

with the resultant force due to buoyancy and an analogous acoustic radiation force, $F_R = (\rho_p - \rho_o) V g_a$, where g_a is the acoustic acceleration. A sample deflected flame is shown in Figure 2.5b. According to the theory suggested by Tanabe, *et al* [18], based on the work of Nyborg [59], the acoustic acceleration g_a depends on the relative position of the droplet with respect to the PN or PAN. The actual acoustic acceleration at the location of the droplet could be estimated from the measured deflection angle, θ , and the gravitational acceleration:

$$g_a = g_o \tan \theta \quad (2.2)$$

The degree of flame deflection θ was estimated by measuring the inclination of the major axis of an ellipse, which was used to approximate the visible flame boundary, with respect to a vertical line as shown in Figures 2.5ab.

2.3.3 Extinction Strain Rate Estimation

A schematic showing the different parameters used in estimating the strain rate experienced by the flame in the vicinity of the droplet stagnation point is shown in Figure 2.6. The strain rate associated with extreme acoustic forcing conditions that induced extinction was estimated based on Oseen's solution for flow over a sphere. The streamfunction for this flow is given as [60]

$$\psi = \frac{U_\infty r_o^2}{4} \left[2 \left(\frac{r}{r_o} \right)^2 - 3 \left(\frac{r}{r_o} \right) + \left(\frac{r_o}{r} \right) \right] \sin^2 \theta \quad (2.3)$$

The resulting extension strain rate is

$$\epsilon_{\theta\theta} = \frac{3U_\infty}{4r} \left[2 \left(\frac{r_o}{r} \right)^3 - \left(\frac{r_o}{r} \right) \right] \cos \theta \approx -\frac{3U_\infty}{4r} \left(\frac{r_o}{r} \right) \cos \theta \quad (2.4)$$

where the radius of the droplet equivalent to a sphere radius of r_o is less than r . Here, U_∞ is the effective bulk flow velocity in the vicinity of the droplet. In the stagnation region ($\theta \rightarrow \pi$), where the flame front is located at a distance r_f (as shown in Figure

2.6), the strain rate was estimated to be

$$\epsilon \approx \frac{3U_{\infty}r_o}{4r_f^2} \quad (2.5)$$

The bulk flow velocity U_{∞} was estimated based on the assumption that the kinetic energy of the hot gases is equal to the work done on these gases by the resultant force due to buoyancy and acoustic radiation forces. Thus, the velocity U_{∞} of the hot gases was estimated as

$$U_{\infty} = \sqrt{2gH \frac{T_f - T_{\infty}}{T_{\infty}}} \quad (2.6)$$

where g is the resultant acceleration, $H = 2r_f$, and T_f is the stoichiometric, constant pressure, adiabatic flame temperature.

2.4 Experimental Procedure

The pre-experimental set-up involved loading the fuel on the syringe pump, connecting the syringe with the glass capillary via a rubber tube, and eliminating any trapped air pockets out of the fuel line. The acoustic waveguide was also purged of combustion products from a prior experiment. After the fuel was introduced, the ignitor was used to ignite the fuel droplet and the value of Q_v was adjusted until a quasi-steady burning was attained. For all fuels under investigation, this value of Q_v was determined to be $0.9 \pm 0.05 \text{ mm}^3/\text{s}$. A video camera was used to capture images of the burning droplet, and to store these images on a video cassette. These video images were later digitized and processed by the edge detection software to obtain an equivalent diameter d_{eqvs} and calculate K values according to Equation 2.1.

For cases with acoustic excitation, the S&S were displaced so that the droplet was situated at some desired location with respect to the PN or PAN. At each such displacements of the S&S, three to four sets of burning droplet video and pressure transducer data were acquired. Then, the waveguide was purged with air to remove the combustion

products accumulated. When conducting later extinction experiments, the S&S were set at a displacement where the flame surrounding the burning droplet experienced the maximum deflection. Then, the amplitude of forcing was systematically increased until flame extinction was achieved.

2.5 Measurement Uncertainties

2.5.1 Precision Uncertainty

The sources of the precision uncertainties in the measured values of the burning rate constant K computed using Equation 2.1 were those associated with the equivalent volume of a sphere diameter d_{eqvs} and the flowrate Q_v . The method of determining d_{eqvs} employed in the present experiments was identical to those used previously by Dattarajan, *et al.* [21]. Accordingly, the precision uncertainty in d_{eqvs} of 10% determined by Dattarajan based on an uncertainty in edge detection of 5 pixels at both edges of the droplet out of an average droplet width of 50 pixels was applied. On the other hand, the uncertainty in Q_v was based on the precision uncertainty of the syringe pump. Hence, the manufacturer's reproducibility rating of the syringe pump at $\pm 0.1\%$ was taken as the precision uncertainty in Q_v . Since this precision uncertainty in Q_v is very small compared to that in d_{eqvs} , it was not accounted for.

Therefore, applying the propagation of precision uncertainties proposed by Mills and Chang [61], the precision uncertainty in the burning rate constant K was computed as

$$\begin{aligned}\Delta K &= \sqrt{\left(\frac{4\Delta Q_v}{\pi d(t)}\right)^2 + \left(\frac{\partial K}{\partial d}\Delta d\right)^2} \\ &\approx \sqrt{\left(\frac{-4Q_v\Delta d}{\pi d}\right)^2}\end{aligned}\tag{2.7}$$

$$\begin{aligned}
&= \frac{4Q_v}{\pi d} \left(\frac{\Delta d}{d} \right) \\
&= \frac{4Q_v}{\pi d} (0.1) \\
&\approx 0.1K
\end{aligned}$$

In this analysis, the transient term in Equation 2.1 was determined from data to be negligible. The measured K values displayed in subsequent sections were averaged over 60 points. Thus, the precision uncertainty in the average K values was estimated to be $10\%/\sqrt{60} \approx 1.3\%$.

2.5.2 Bias Uncertainty

The source of bias uncertainties in the measured values of K was mainly attributed to those associated with Q_v . The syringe pump manufacturer rates the accuracy at $\pm 1\%$. This gave a bias uncertainty in K to be of the order 1%.

As pointed out by Dattarajan, *et al.* [21], a possible overestimation of the size of the actual droplet diameter might have occurred depending on the number of pixels that defined the droplet edge. However, based on repeated measurements of known actual sizes such as the the outer diameter of the tip of the shroud or the glass capillary, the uncertainty introduced due to the pixel representation was deemed insignificant.

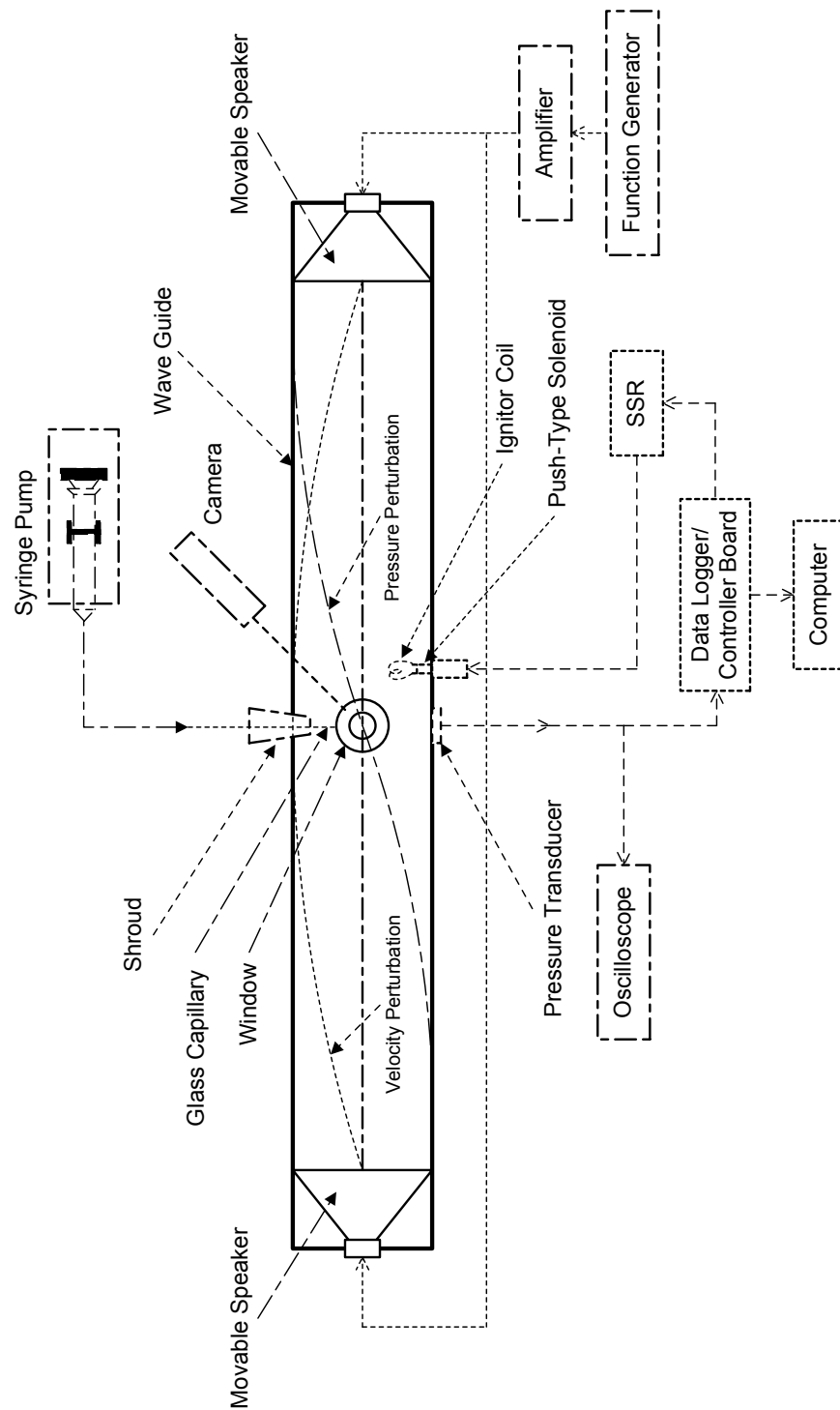


Figure 2.1: Experimental setup of the acoustic waveguide and droplet feed system.

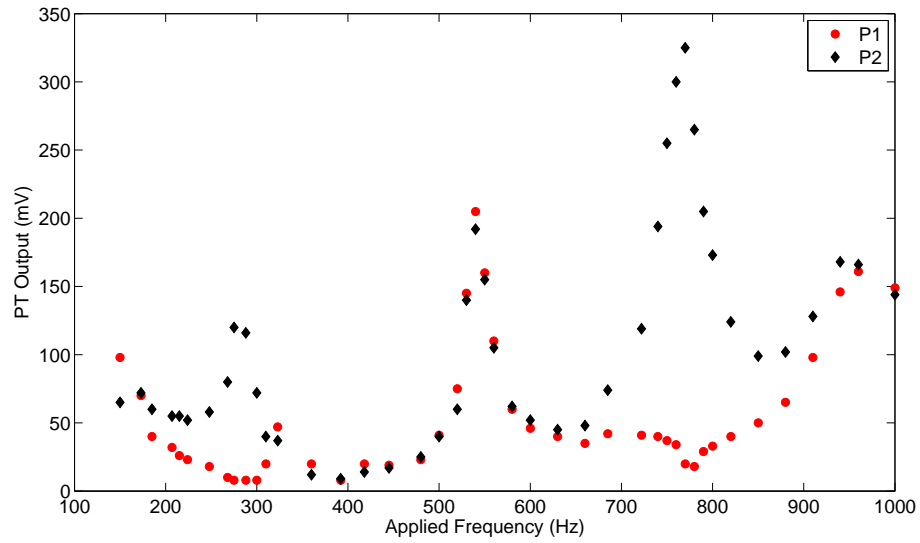
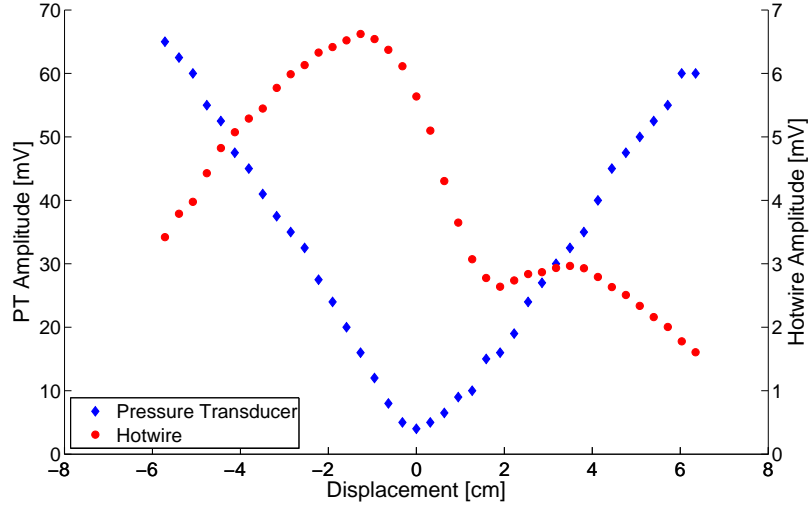
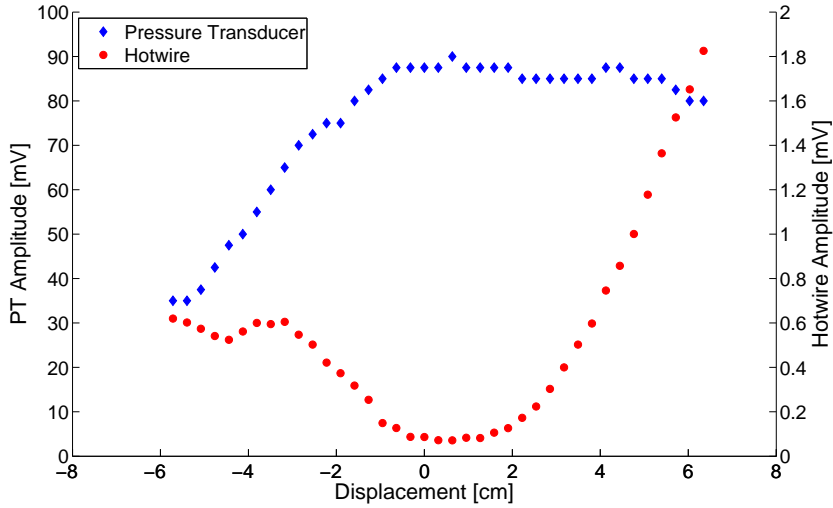


Figure 2.2: Acoustic characterization of the waveguide (S&R configuration) as measured by pressure transducers at P1 and P2. Local maxima for both pressure transducers corresponds to a pressure antinode location. A local minimum at P1 and maximum at P2 corresponds to a pressure node. The distance between the speaker and reflector is approximately 62 cm (Dattarajan, *et. al* [20])

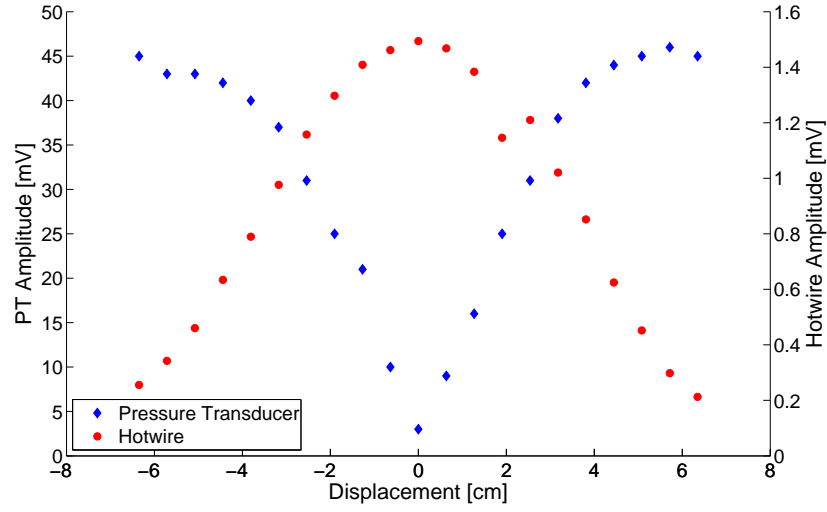


(a) 784 Hz PN

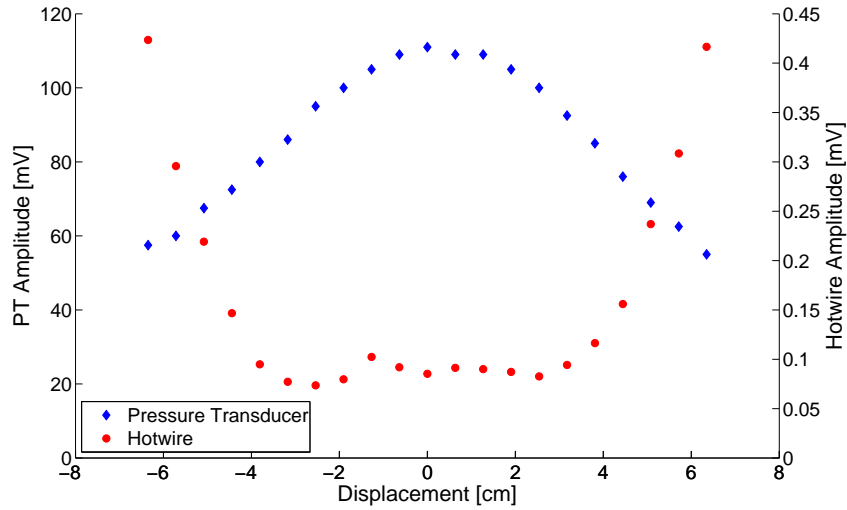


(b) 544 Hz PAN

Figure 2.3: Measurements of relative local perturbation velocity (made by the hot wire anemometer) and the relative local perturbation pressure (made by the pressure transducer), both at the geometric center of the waveguide, for the Speaker-Reflector configuration (S&R). The displacement of the speaker and reflector is indicated on the abscissa, relative to their original locations as determined from the geometric center of the waveguide. Positive displacement refers to the S&R moved to the right. Results are shown for acoustic excitation at an applied frequency of: (a) 784 Hz (for a pressure node condition) and (b) 544 Hz (for a pressure antinode condition).

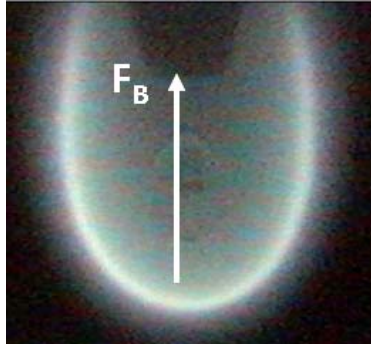


(a) 784 Hz PN

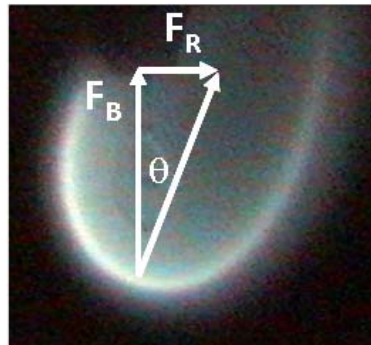


(b) 544 Hz PAN

Figure 2.4: Measurements of relative local perturbation velocity (made by the hot wire anemometer) and the relative local perturbation pressure (made by the pressure transducer P1), both at the geometric center of the waveguide, for the two Speaker configuration (S&S). The displacement of the two speakers is indicated on the abscissa, relative to their original locations as determined from the geometric center of the waveguide and a maximum or minimum in the pressure transducer. Positive displacement refers to the S&S moved to the right. Results are shown for acoustic excitation at an applied frequency of: (a) 784 Hz (for a pressure node condition) and (b) 544 Hz (for a pressure antinode condition).



(a)



(b)

Figure 2.5: Ethanol droplet burning with and without acoustic excitation or forcing. In the absence of acoustic forcing, the flame orientation is only influenced by force of buoyancy F_B , while with acoustic excitation, both F_B and acoustic radiation force F_R affect its orientation: (a) Unforced flame orientation (b) Forced flame orientation

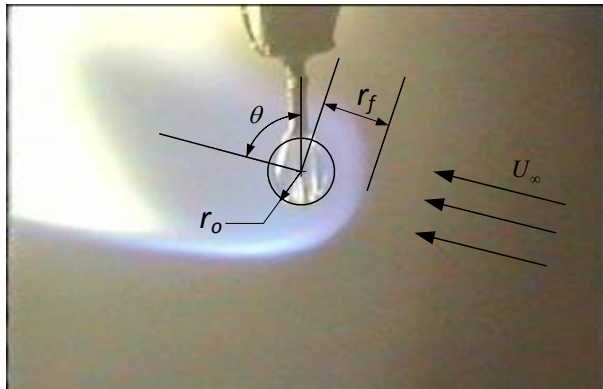


Figure 2.6: A schematic of the flow and relevant parameters used in estimating extinction strain rate. The flame assumes a nearly horizontal orientation at the instant before extinction.

CHAPTER 3

Droplet Combustion: Results and Discussion

3.1 Baseline Burning Rate Constants

Fuel droplet combustion experiments were first conducted in the absence of acoustic excitation. Images of some of the burning fuel droplets without acoustic forcing are shown in Figure 3.1. The effects of gravitational and surface tension forces gave the droplets a characteristic oblong shape. The symmetric but rather elongated diffusion flames surrounding the droplets were also a result of buoyancy force acting on the hot species. For the hydrocarbon fuels, the presence of soot gave the flame an orange or yellow appearance.

These studies were designed to evaluate “baseline” droplet combustion features for comparison with droplets burning in the presence of acoustic excitation. Determination of the droplet diameter d_{eqvs} via video imaging allowed for extraction of K values that were roughly constant over time for constant fuel flowrates. Average K values based on d_{eqvs} were close to available data for various fuel droplets burning in normal gravity, as indicated in Table 3.1.

It should be noted that in the present experiments, the potential influence of water absorption on the alcohol droplet burning rates was likely reduced or eliminated, since there was continual replenishment of the droplet with fresh fuel via continuous delivery through the capillary. Dattarajan [21] has shown that alterations in the capillary length between 2.0 mm and 3.2 mm did not yield significant or systematic changes in K . A

capillary length of 3.2 ± 0.2 mm was thus selected for these experiments since this produced a minimal influence of the shroud on droplet and flame characteristics, while simultaneously preventing fuel boiling in the capillary.

3.2 Flame Alterations under Acoustic Excitation

The influence of acoustic excitation or forcing on the combustion of the fuel droplets was explored by causing the pressure node to be situated at various locations relative to the location of the droplet. With the distance between the two speakers fixed to approximately 62 cm, forcing frequencies of approximately 784 Hz and 1340 Hz produced a standing wave with a pressure node at the waveguide center, as verified from pressure transducer measurements. Such estimates of the standing wave were obtained within the waveguide in the absence of combustion, at room temperature.

For a standing wave, the acoustic radiation force equation can be expressed per the analysis of Tanabe, *et al.* [17, 18], as

$$F_R = (\rho_p - \rho_o)V \left[\mp 4\alpha \left(\frac{I}{z_a} \right) \left(\frac{2\pi f}{c} \right) \sin \left(\frac{2\pi x}{\lambda} \right) \cos \left(\frac{2\pi x}{\lambda} \right) \right]. \quad (3.1)$$

Here I represents the acoustic intensity, which depends on the maximum sound pressure level inside the waveguide, $z_a = \rho c$ represents the acoustic impedance, and c represents the speed of sound ($= f\lambda$). The term in square brackets represents an equivalent acoustic acceleration term, $g_a \equiv \alpha \frac{\partial u'^2}{\partial x}$, for a condition where a standing wave is present in the waveguide. The coefficient α defined in Equation (1.3) was approximated to be equal to one in subsequent analyses. The minus sign in the bracketed term corresponds to the case where a pressure node or velocity antinode was positioned at the center of the waveguide ($x = 0$); the plus sign corresponds to a pressure antinode or velocity node at that location. Thus, if the droplet were situated to the right ($x > 0$) or left ($x < 0$) of the waveguide center, the flame and hot gas zone surrounding the droplet would experience a

nonzero acoustic acceleration g_a , which in turn would result in a finite acoustic radiation force that deflected the flame in a direction opposite to that of g_a . These phenomena were observed for n-decane droplet combustion in microgravity by Tanabe, *et al.* [17, 18], for methanol droplet combustion in microgravity and normal gravity by Dattarajan, *et al.* [20, 21], and in normal gravity for several fuels by Rodriguez [22]. It is noted that the latter two sets of experiments were conducted in the present waveguide but with a speaker-reflector configuration.

A schematic diagram of the displacements of the two speakers is shown in Figure 3.2, where x' corresponds to the location of the pressure node (PN) relative to the position of the droplet, and x corresponds to the location of the droplet relative to the PN. Hence, during an acoustic forcing that produced a PN at the waveguide center, when the two speakers (“S&S”) were moved substantially to the right, one approached a condition where the PN lay to the right of the droplet, or the droplet lay to the left of the PN ($x < 0$). In this case, if the droplet lay to the left of the PN, then the sign of the acoustic radiation force in Equation 3.1 would become negative, shifting the flame and hot gases toward the left side of the waveguide, away from the PN. On the other hand, when the S&S were moved substantially to the left, so that $x > 0$, the opposite would occur, causing the flame to deflect to the right, away from the PN. For the case of a standing wave with an established pressure antinode (PAN) in the waveguide, the opposite behaviors should take place when the S&R or S&S are moved. In general, the direction of the acoustic radiation force was oriented towards the nearest PAN.

The influence of relative droplet-node displacements on the flame surrounding a burning fuel droplet was explored using different fuels. Figures 3.3-3.6 show images captured from video of the burning droplets of the different fuels during acoustic forcing. Images of a burning ethanol droplet at different locations relative to the estimated pressure node location, which coincides with the waveguide center and is designated as

the location of 0 cm displacement, are shown in Figures 3.3a-f. It can be seen from these images that when the speakers were displaced to the left, resulting in a left displacement of the PN relative to the droplet (so that $x' < 0$), or equivalently, a right displacement of the droplet relative to the PN (so that $x > 0$), the flames were deflected to the right, away from the PN location or towards the PAN. This observation was consistent with the direction of the acoustic radiation force as predicted in the above discussion. However, a switch in the direction of the flame deflection occurred between the original location (0 cm) and 0.6 cm (Figure 3.3d) to the right of the original or PN location. Thus, in Figures 3.3d-f, the droplet probably lay slightly to the left of the PN (so that $x < 0$). Similar types of flame shifts were observed during exposure of a burning JP-8, JP-8/FT fuel blend, and pure FT droplets near a PN at 784 Hz forcing frequency, as shown in Figures 3.4a-f, 3.5a-f, and 3.6a-f, respectively.

The location of the flame switch, however, was consistently offset by up to 0.5 cm, or 1 cm in some cases, from the PN location. Plots of local (at the droplet location) pressure measurements taken for a range of speaker displacements during a 784 Hz forcing frequency are shown in Figures 3.3-3.6. These pressure profiles show that a minimum in the pressure perturbations occurred at the waveguide center. This being the case, the locations of the flame switch were nevertheless observed to occur anywhere between 0.5 cm to 1 cm displacement of the speakers to the right of the PN. Similar plots of pressure measurements (Figures 3.7-3.9) during a 1340 Hz forcing frequency show a PN situated at about 0.5 cm to the left of the waveguide center. Despite this, the flame switch locations corresponding to these cases were still within 1 cm to the right of the PN location. One possible cause for this offset of the flame switch location, which did not show any quantifiable dependency on the fuel type, may be attributable to the uncertainties in the precise location of the PN. This is mainly due to the fact that the pressure transducer diaphragm has a diameter of about 1 cm, thus giving rise to a measurement uncertainty in the location of the PN of about 0.5 cm.

The idea of acoustic acceleration in the vicinity of the burning droplet, related to the acoustic radiation force in Equation 3.1 was explored experimentally. The fuel droplet burning in the absence of acoustic forcing did so under the sole influence of gravitational acceleration, g_o , which gave rise to the buoyancy force, resulting in the characteristic vertically symmetric, yet elongated flame structure. When acoustics was imposed on the burning droplet, the flame was deflected from its original vertically symmetric orientation to one where it aligned itself with the resultant force due to buoyancy and an analogous acoustic radiation force. As shown in Figure 2.5, the actual acoustic accelerations, $g_{a,exp}$, were quantified based on the geometry of the angular deflection of the flames using the relation given in Equation 2.2. The theoretical acoustic accelerations, $g_{a,th}$, were computed based on Equation 3.1, where the “true” PN location ($x = 0$) was set at the flame switch location. Plots comparing the $g_{a,exp}$ and $g_{a,th}$ profiles for the different 784 Hz cases are shown in Figures 3.3 - 3.6, and similar plots for the 1340 Hz cases are shown in Figures 3.7 - 3.9. It is evident that the direction of $g_{a,exp}$, depicted by its sign, was consistent with the $g_{a,th}$. However, the magnitudes of $g_{a,exp}$ showed a rather large deviation from the theoretical estimation.

In theory, the magnitude of the acoustic radiation force is the largest at a midpoint location between a node and antinode (or equivalently, $\lambda/8$ from a node or antinode), since that is where $\frac{\partial u^2}{\partial x}$ is maximized [18]. Farther away from this midpoint, the gradient term decreases finally reaching zero at a node or antinode, thus resulting in a zero acoustic acceleration. This theoretical scenario should be reflected with maximum flame deflections at the halfway location between a node and antinode, and no deflection at a node or antinode. On the other hand, experimental observations showed a steep profile of the acoustic acceleration as shown in Figures 3.10-3.16, whereby the flame deflections were rather steep in the immediate region of the PN, and became less deflected farther from the PN.

3.3 Effect of Acoustic Acceleration on Burning Rate Constants

Average burning rate constants based on time averages over the period of experimentation that lasted 2 seconds were obtained for various fuels for pressure node conditions and for a range of different positions of the speakers. Sample K values for different positions of the speakers are plotted in Figures 3.10, 3.11, 3.12, and 3.13 for ethanol, pure JP-8, JP-8/FT blend, and pure FT, respectively. A 784 Hz (PN) forcing was employed, and the positions of the speakers relative to their original locations are plotted on the abscissa. On the upper plots of these figures, the local pressure measured at the center of the wageguide is compared with the theoretical values for different speaker positions. The middle plots show the acoustic acceleration $g_{a,exp}$ measured from the flame deflection as compared with the theoretical $g_{a,th}$ from Equation 3.1. Placed on the bottom plots are measured K values as well as the estimates of the magnitudes of the theoretical and experimental acoustic accelerations at different speaker displacements. Similar plots are shown for the 1340 Hz (PN) forcing condition for ethanol, pure JP-8, and pure FT in Figures 3.14, 3.15, and 3.16, respectively.

The pressure measurements were generally consistent with theory, except in some cases for the amplitude. As discussed previously, it is evident from the plots for the 784 Hz cases that the magnitude of the actual acoustic acceleration, $g_{a,exp}$, increased as the speakers' displacement approached the flame switch location, which coincides with the supposed "true" PN location. Although the flame switch near the zero displacement indicated the same qualitative behavior for g_a as in the theory, the magnitudes of the flame deflection near the zero location were considerably larger than suggested by theory. Accordingly, variations in the K values were observed to follow more closely the magnitudes of $g_{a,exp}$ rather than the theory. These effects were more pronounced in the ethanol (Figure 3.10) and pure JP-8 (Figure 3.11) cases, where the K values near the PN increased by up to 15% above the lower limit of the unforced K values for these

fuels. The trends in K values obtained for the 1340 Hz case did not show as large a variation from the unforced. There was nevertheless a general trend in K that followed the magnitude $g_{a,exp}$ more closely than the theory.

Dattarajan's [21] studies on the combustion of methanol fuel droplet combustion in microgravity revealed significant increases in K values (up to 200%) while the droplet was placed at or near a PN. Similar studies in normal gravity, however, showed a severe limitation on the effects of acoustics on the K values (11-15% increase). In the present studies, the same limitations were observed despite significant changes in the acoustic accelerations.

3.4 Fuel Extinction Studies

An exploration of the extinction phenomenon was performed whereby burning droplets in the absence of acoustic forcing were abruptly exposed to successively increasing acoustic intensities. At high enough acoustic intensities, extinction (flame blowout) occurred. Sample sets of consecutive image frames showing the extinction process of ethanol, pure JP-8, JP-8/FT fuel blend, and pure FT are shown in Figures 3.17, 3.18, 3.19 and 3.20, respectively. It can be seen that the instant before extinction, the acoustic radiation force acting on the hot products was the dominant force as was evident in the extreme degree of deflection that the flames underwent. Under such conditions, it was estimated that the hot gases experience magnitudes of $g_{a,exp}$ that were up to eight fold that of g_o .

The flame extinction strain rates on the stagnation side of the droplets were estimated for some of the fuels under consideration. The preliminary results including the extinction sound pressure levels (SPLs) are shown in Table 3.2. As given in Equation 2.5, the strain rate is directly proportional to the droplet radius, and bulk flow velocity induced in the vicinity of the droplet due to the action of the acoustic radiation force on the hot gases, and inversely proportional to the flame standoff distance. The bulk flow

velocity, in turn, is proportional to the acoustic acceleration and flame temperature. In the current estimations, this velocity was found to be on the order 1 m/s. In general, extinction occurs when the reaction time scale becomes very long or the diffusion time scale becomes very short. Thus, the effect of increased acoustic intensities was in decreasing the diffusion time scale so that the finite rate chemical kinetics could no longer maintain the temperature that could sustain the reaction. This argument may be used to explain why fuels with higher flame temperature are harder to extinguish than those with relatively lower ones. Current limits on the knowledge of a complete thermochemical data for the hydrocarbon fuels rendered rather crude flame extinction strain rate estimates for those fuels. However, based on just SPL of extinction, it was observed that the alcohols and pure FT had slightly larger resistance to extinction.

Table 3.1: Comparison of measured values of burning rate constant K for various fuel droplets in the absence of acoustic excitation. Comparisons with available established values for K are also given.

Fuel	K , present (mm^2/s)	K , established (mm^2/s)
Ethanol	0.78-0.88	0.81-0.86
Methanol	0.83-0.95	0.85-1.2
JP-8	0.88-1.05	0.87,1.04 (JP-4)
JP-8/FT	0.78-0.90	-
Pure FT	0.80	-

Table 3.2: Acoustic conditions of various fuels at extinction. The corresponding sound pressure levels in decibels (dB) and rough estimates of the strain rates are also shown.

Fuel	SPL (dB)	Strain Rate (s^{-1})
Ethanol	142.3 ± 0.6	350
Methanol	142.0 ± 0.6	-
JP-8	140.8 ± 0.7	250
JP-8/FT	141.3 ± 0.5	260
Pure FT	141.9 ± 0.4	330

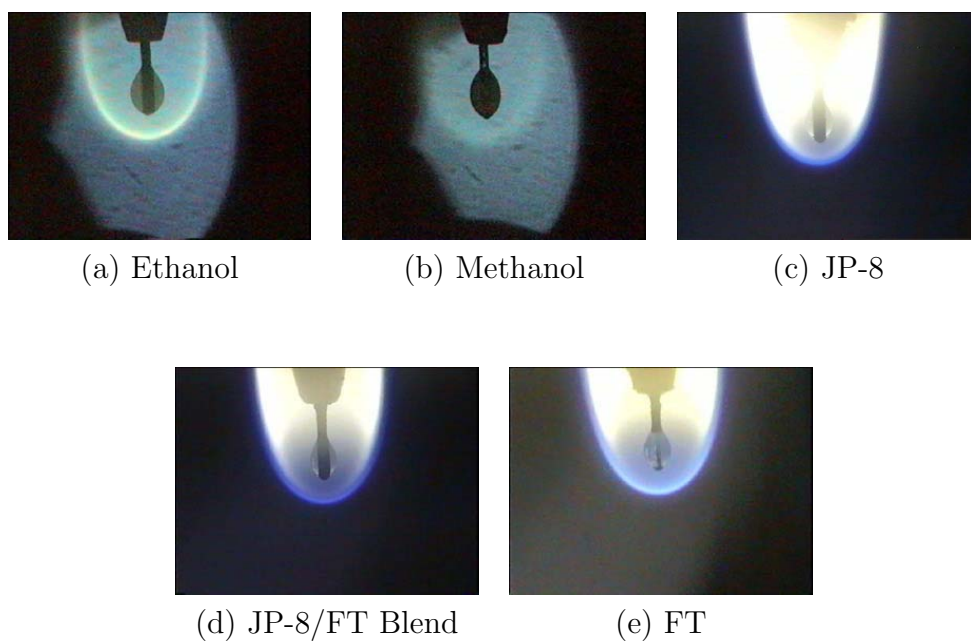


Figure 3.1: Images of various fuel droplets burning in the absence of acoustic excitation.

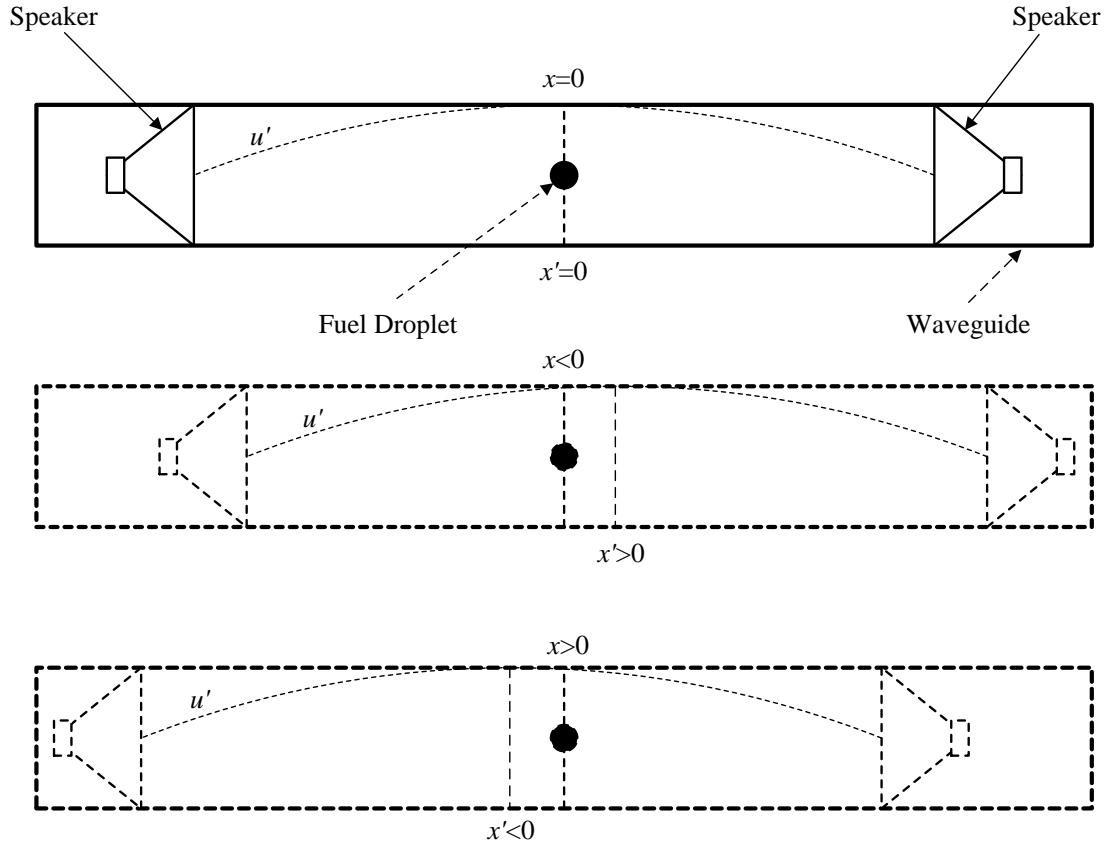


Figure 3.2: Schematic showing the relative displacement between a pressure node (velocity antinode) and the droplet. *Top*: Location of the speakers in the waveguide relative to a velocity antinode (pressure node) situated at $x' = 0$, with the droplet located at $x = 0$ relative to the velocity antinode. *Middle*: Location of velocity antinode at $x' > 0$ relative to the droplet (and of the droplet at $x < 0$ relative to the velocity antinode), resulting from displacement of the speakers to the right as compared with the original condition. *Bottom*: Location of velocity antinode at $x' < 0$ relative to the droplet (and of the droplet at $x > 0$ relative to the velocity antinode), resulting from displacement of the speakers to the left as compared with the original condition.

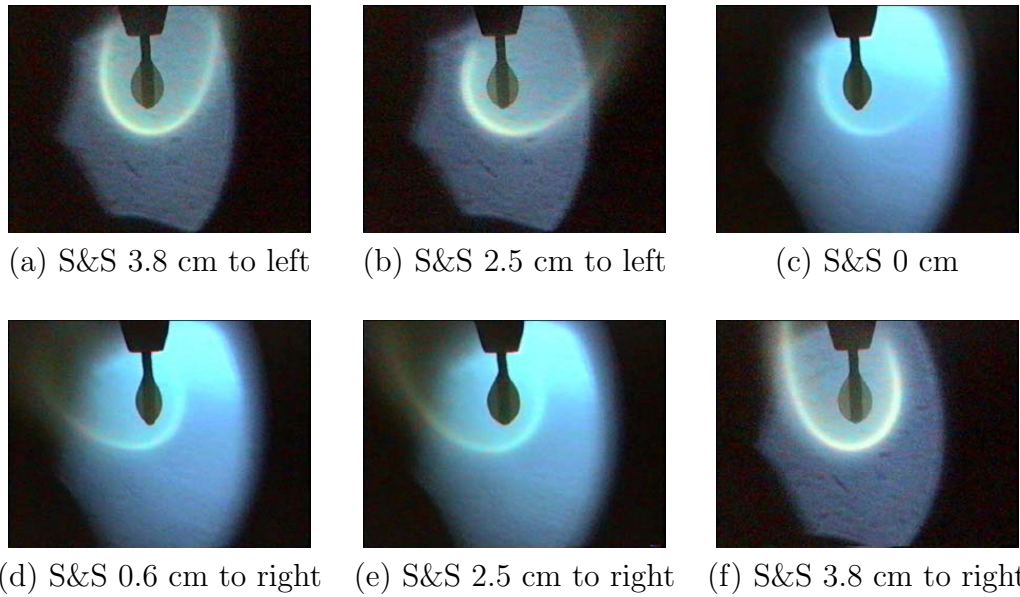


Figure 3.3: Photographs of a burning ethanol droplet with acoustic excitation at an applied frequency of 784 Hz (for a pressure node condition). The positions of the two speakers (“S&S”) are indicated, relative to their original locations as determined from the geometric waveguide center and minimum in measured pressures. “S&S X cm to left” refers to the case where the speakers were moved by X cm to the left as compared with their original positions, etc. The true pressure node was likely coincident with the droplet located between cases (c) and (d), very close to the pressure node.

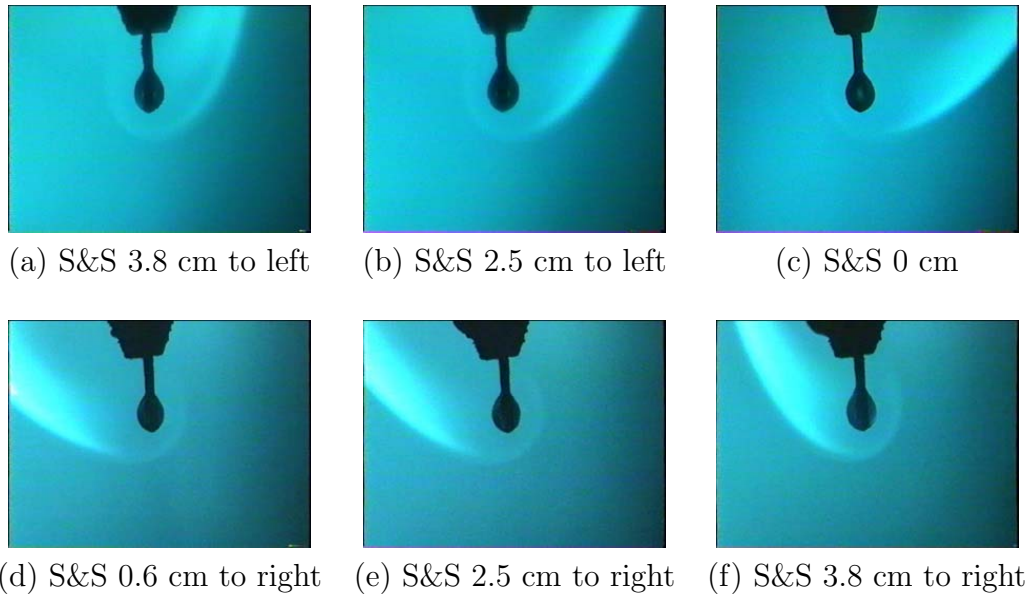


Figure 3.4: Photographs of a burning JP-8 droplet with acoustic excitation at an applied frequency of 784 Hz (for a pressure node condition). The positions of the two speakers (“S&S”) are indicated, relative to their original locations as determined from the geometric waveguide center and minimum in measured pressures. “S&S X cm to left” refers to the case where the speakers were moved by X cm to the left as compared with their original positions, etc. The true pressure node was likely coincident with the droplet located between cases (c) and (d), very close to the pressure node.

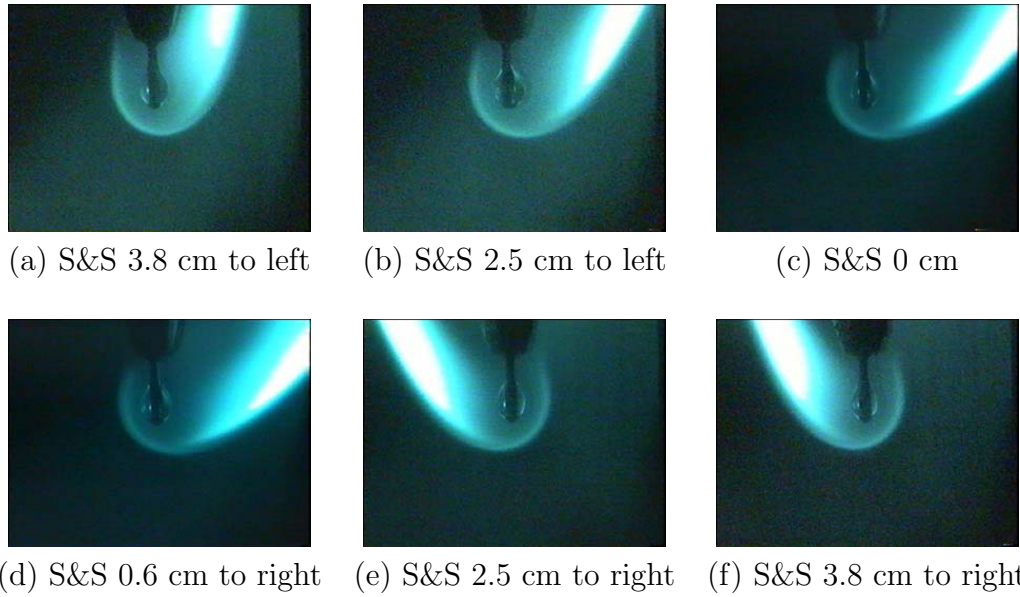


Figure 3.5: Photographs of a burning JP-8/FT blend droplet with acoustic excitation at an applied frequency of 784 Hz (for a pressure node condition). The positions of the two speakers (“S&S”) are indicated, relative to their original locations as determined from the geometric waveguide center and minimum in measured pressures. “S&S X cm to left” refers to the case where the speakers were moved by X cm to the left as compared with their original positions, etc. The true pressure node was likely coincident with the droplet located between cases (c) and (d), very close to the pressure node.

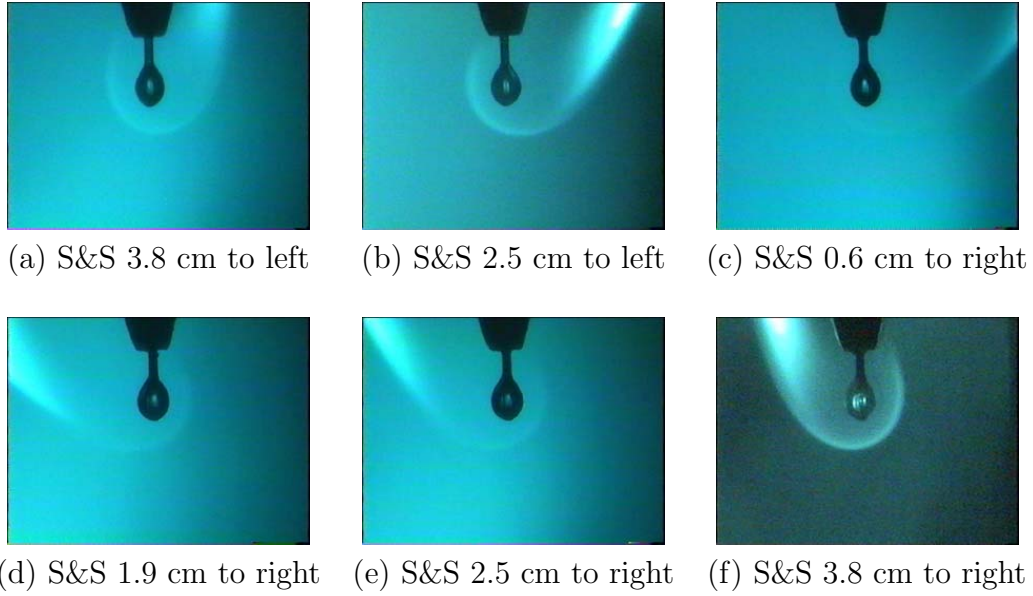


Figure 3.6: Photographs of a burning FT droplet with acoustic excitation at an applied frequency of 784 Hz (for a pressure node condition). The positions of the two speakers (“S&S”) are indicated, relative to their original locations as determined from the geometric waveguide center and minimum in measured pressures. “S&S X cm to left” refers to the case where the speakers were moved by X cm to the left as compared with their original positions, etc. The true pressure node was likely coincident with the droplet located between cases (c) and (d), very close to the pressure node.

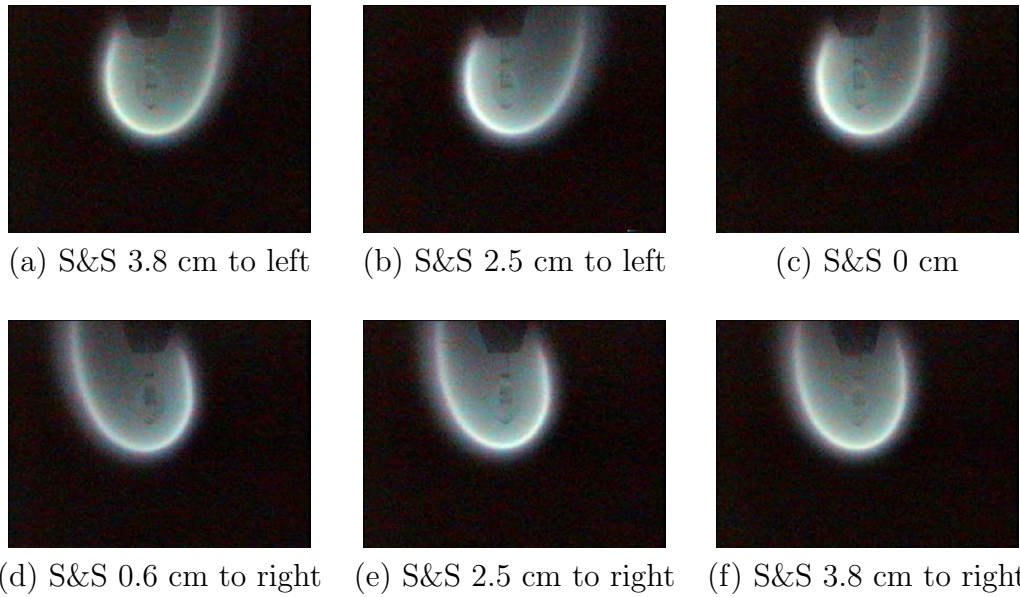


Figure 3.7: Photographs of a burning ethanol droplet with acoustic excitation at an applied frequency of 1340 Hz (for a pressure node condition). The positions of the two speakers (“S&S”) are indicated, relative to their original locations as determined from the geometric waveguide center and minimum in measured pressures. “S&S X cm to left” refers to the case where the speakers were moved by X cm to the left as compared with their original positions, etc. The true pressure node was likely coincident with the droplet located between cases (c) and (d), very close to the pressure node.

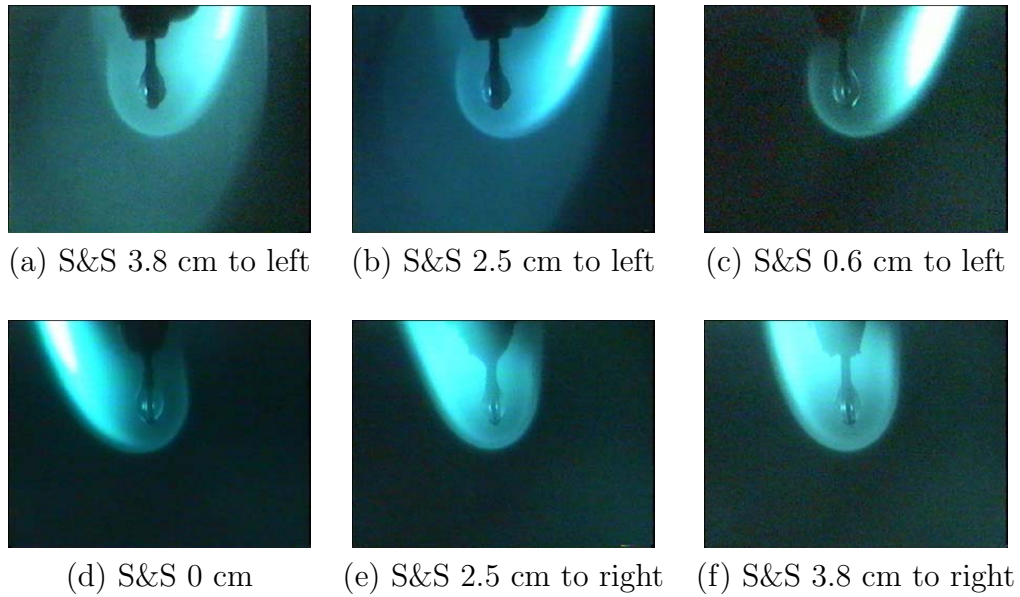


Figure 3.8: Photographs of a burning JP-8 droplet with acoustic excitation at an applied frequency of 1340 Hz (for a pressure node condition). The positions of the two speakers (“S&S”) are indicated, relative to their original locations as determined from the geometric waveguide center and minimum in measured pressures. “S&S X cm to left” refers to the case where the speakers were moved by X cm to the left as compared with their original positions, etc. The true pressure node was likely coincident with the droplet located between cases (c) and (d), very close to the pressure node.

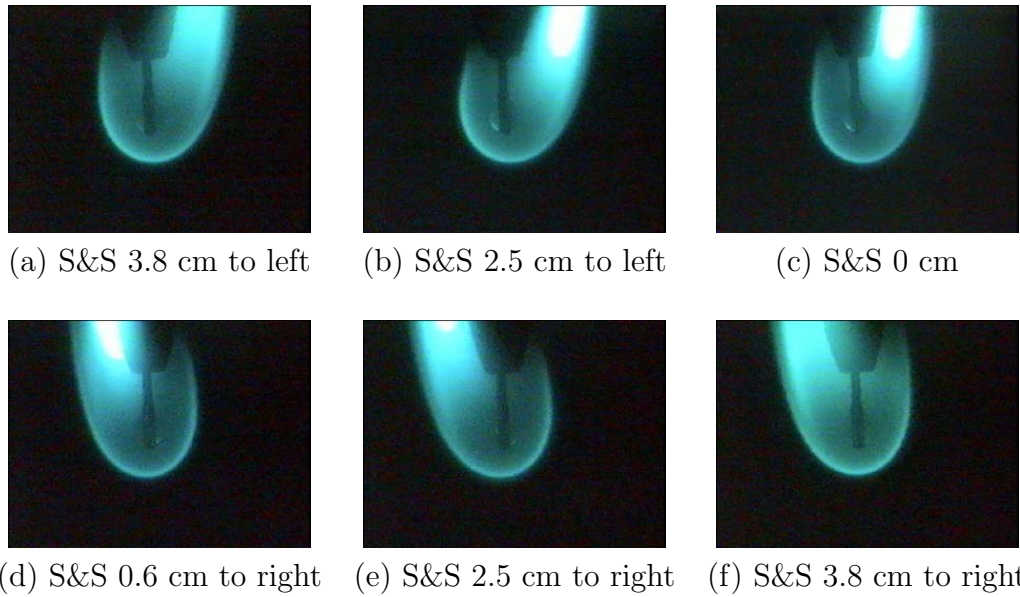


Figure 3.9: Photographs of a burning FT droplet with acoustic excitation at an applied frequency of 1340 Hz (for a pressure node condition). The positions of the two speakers (“S&S”) are indicated, relative to their original locations as determined from the geometric waveguide center and minimum in measured pressures. “S&S X cm to left” refers to the case where the speakers were moved by X cm to the left as compared with their original positions, etc. The true pressure node was likely coincident with the droplet located between cases (c) and (d), very close to the pressure node.

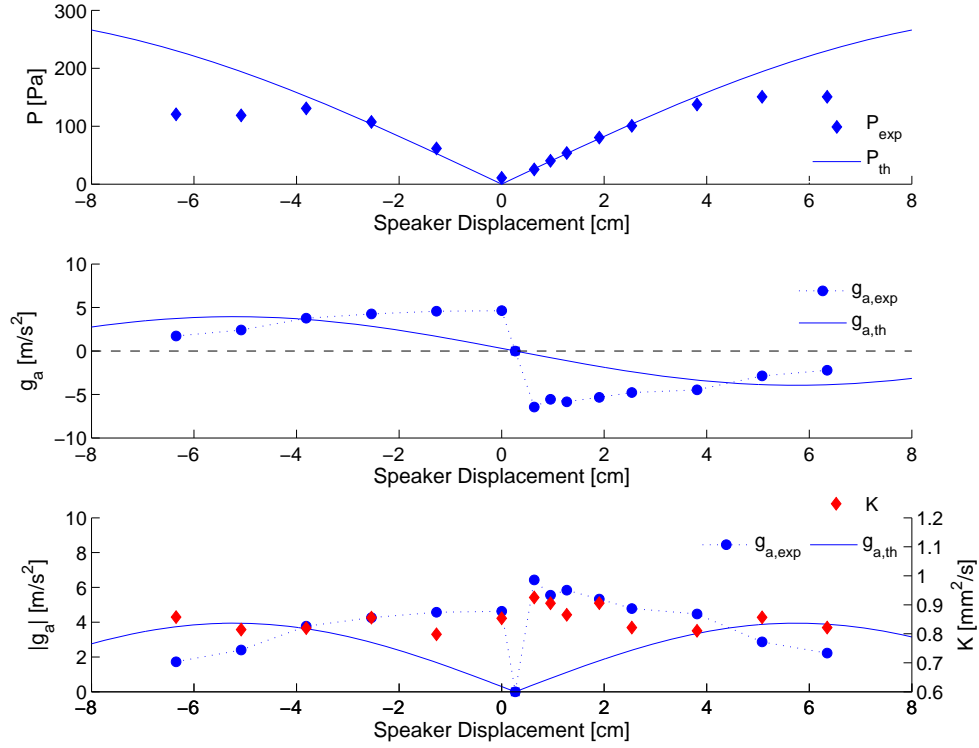


Figure 3.10: Pressure perturbations, estimated theoretical and actual acoustic accelerations g_a , and average burning rate constant K as a function of the displacement of the speakers with respect to the original position (0 cm) for the ethanol droplet burning in the vicinity of a pressure node at a frequency of approximately 784 Hz.

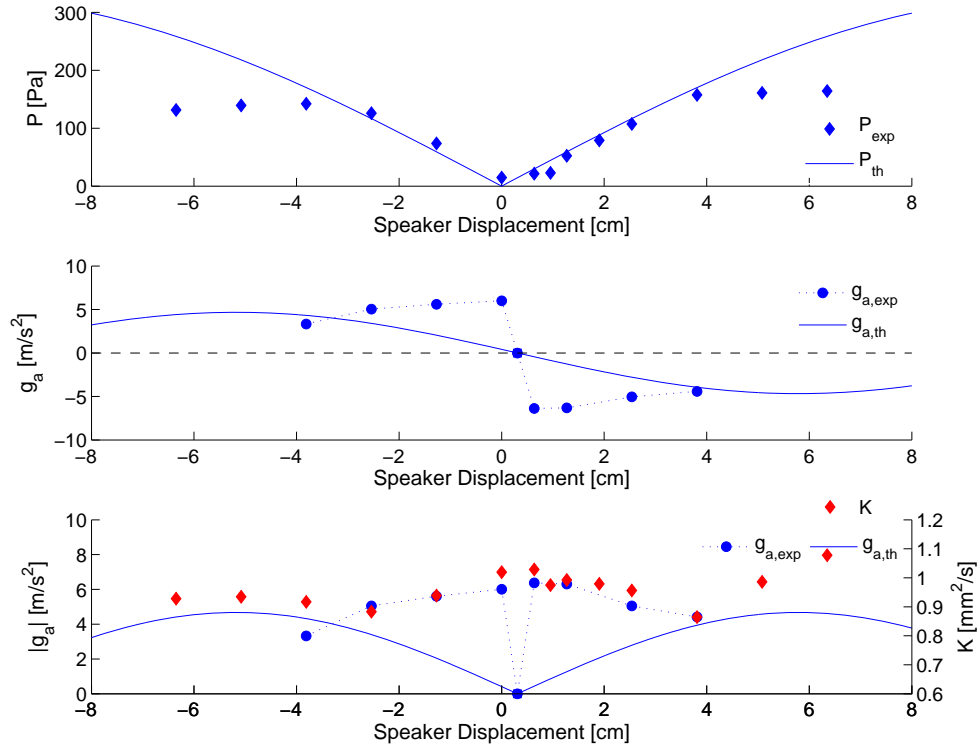


Figure 3.11: Pressure perturbations, estimated theoretical and actual acoustic accelerations g_a , and average burning rate constant K as a function of the displacement of the speakers with respect to the original position (0 cm) for the JP-8 droplet burning in the vicinity of a pressure node at a frequency of approximately 784 Hz.

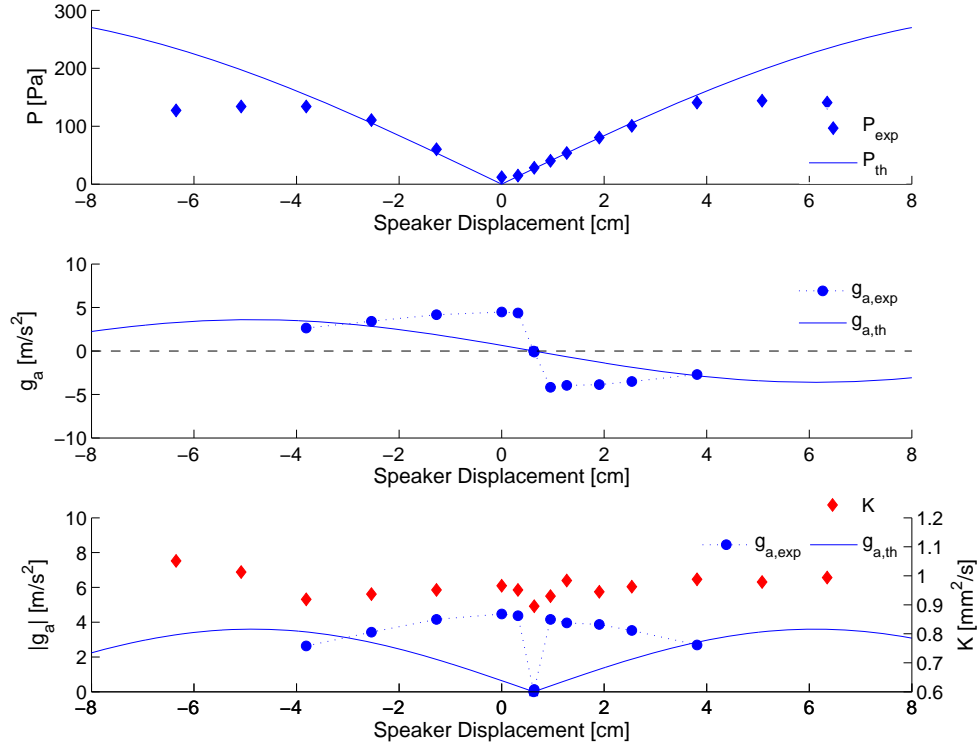


Figure 3.12: Pressure perturbations, estimated theoretical and actual acoustic accelerations g_a , and average burning rate constant K as a function of the displacement of the speakers with respect to the original position (0 cm) for the JP-8/FT blend droplet burning in the vicinity of a pressure node at a frequency of approximately 784 Hz.

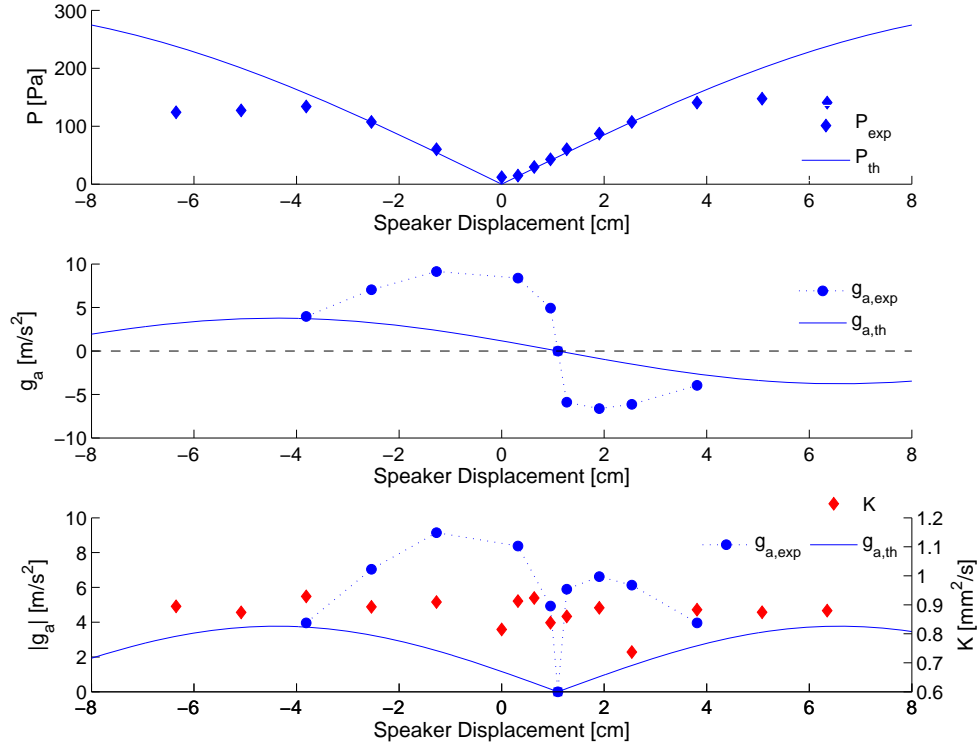


Figure 3.13: Pressure perturbations, estimated theoretical and actual acoustic accelerations g_a , and average burning rate constant K as a function of the displacement of the speakers with respect to the original position (0 cm) for the FT droplet burning in the vicinity of a pressure node at a frequency of approximately 784 Hz.

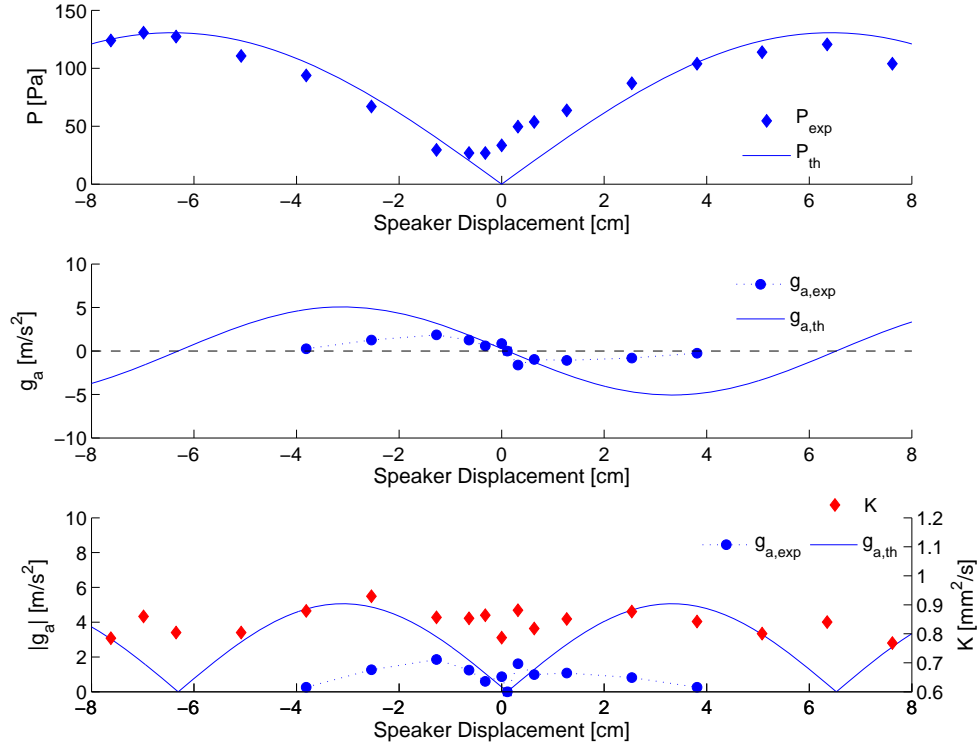


Figure 3.14: Pressure perturbations, estimated theoretical and actual acoustic accelerations g_a , and average burning rate constant K as a function of the displacement of the speakers with respect to the original position (0 cm) for the ethanol droplet burning in the vicinity of a pressure node at a frequency of approximately 1340 Hz.

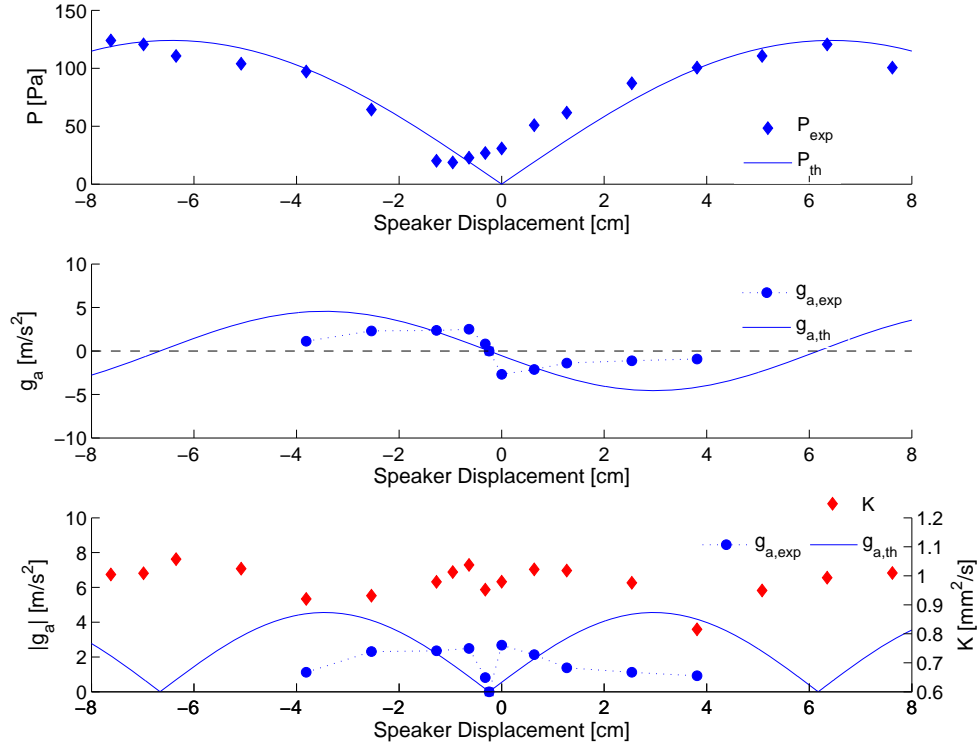


Figure 3.15: Pressure perturbations, estimated theoretical and actual acoustic accelerations g_a , and average burning rate constant K as a function of the displacement of the speakers with respect to the original position (0 cm) for the JP-8 droplet burning in the vicinity of a pressure node at a frequency of approximately 1340 Hz.

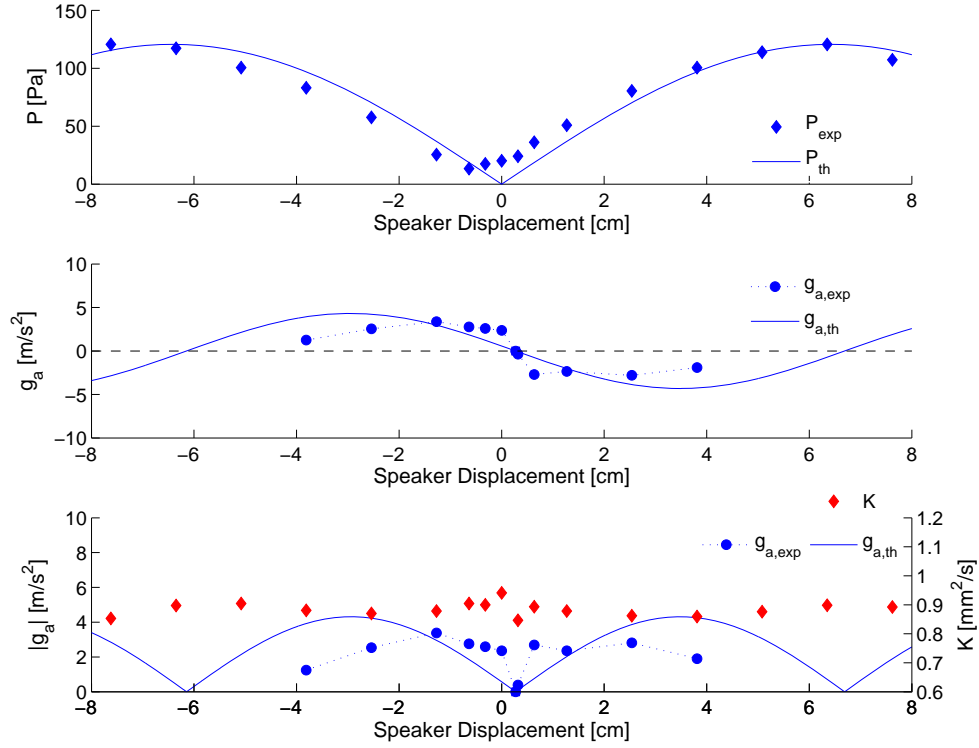


Figure 3.16: Pressure perturbations, estimated theoretical and actual acoustic accelerations g_a , and average burning rate constant K as a function of the displacement of the speakers with respect to the original position (0 cm) for the FT droplet burning in the vicinity of a pressure node at a frequency of approximately 1340 Hz.

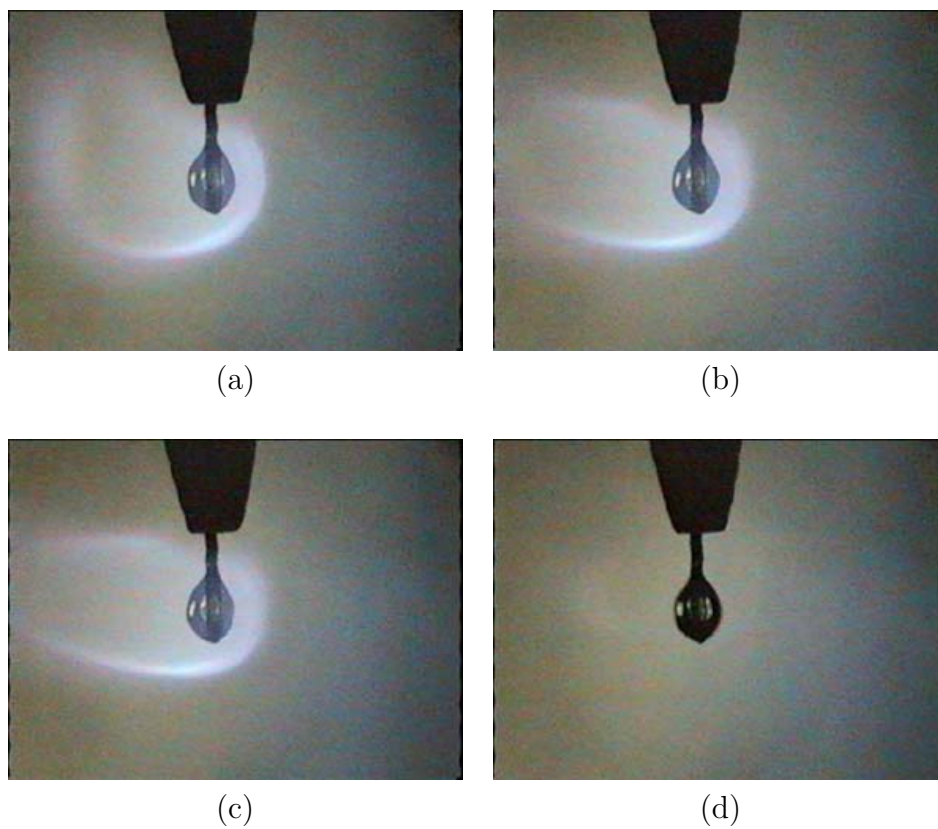


Figure 3.17: A sequence of images showing the extinction process of the flame surrounding an ethanol fuel droplet. The time span between the consecutive images was approximately 33 ms. The sound pressure level was 142.3 dB, and the estimated strain rate at extinction for this case was 350 s^{-1} .

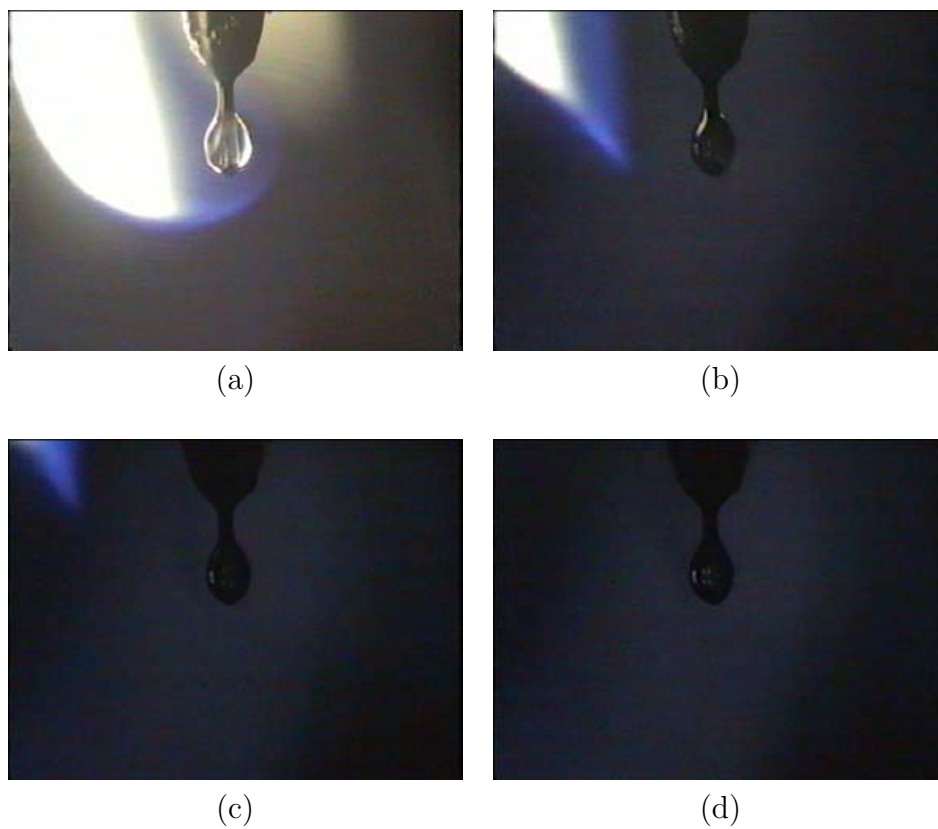


Figure 3.18: A sequence of images showing the extinction process of the flame surrounding a JP-8 fuel droplet. The time span between the consecutive images was approximately 33 ms. The sound pressure level was 140.8 dB, and the estimated strain rate at extinction for this case was 250 s^{-1} .

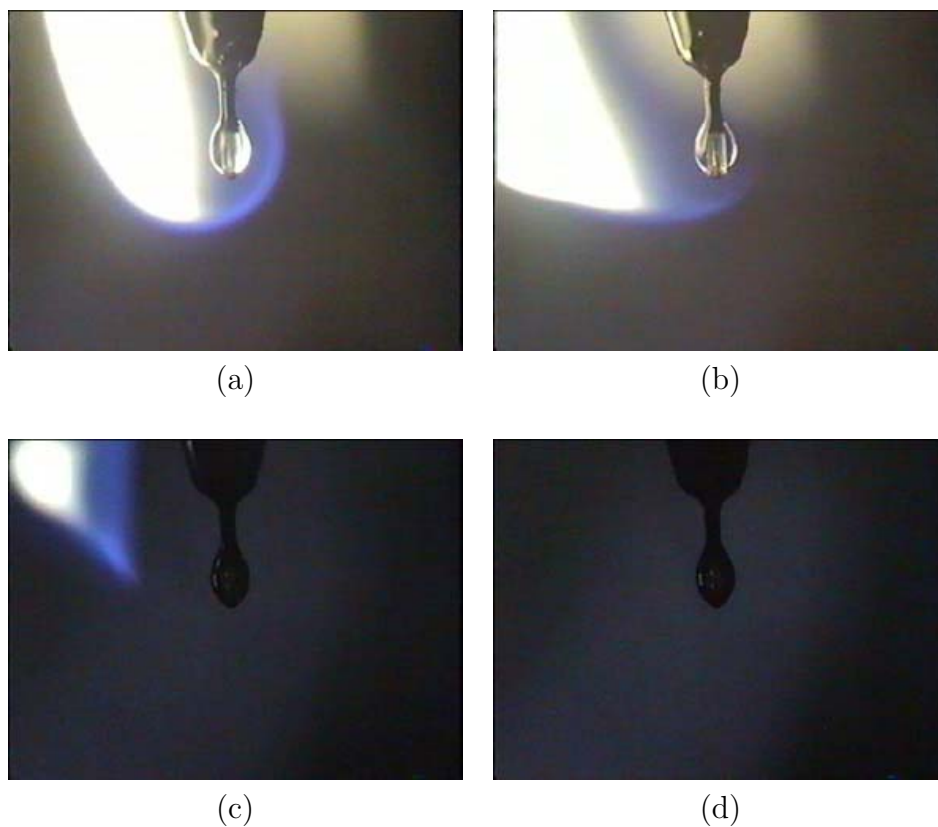


Figure 3.19: A sequence of images showing the extinction process of the flame surrounding a JP-8/FT fuel blend droplet. The time span between the consecutive images was approximately 33 ms. The sound pressure level was 141.3 dB, and the estimated strain rate at extinction for this case was 260 s^{-1} .

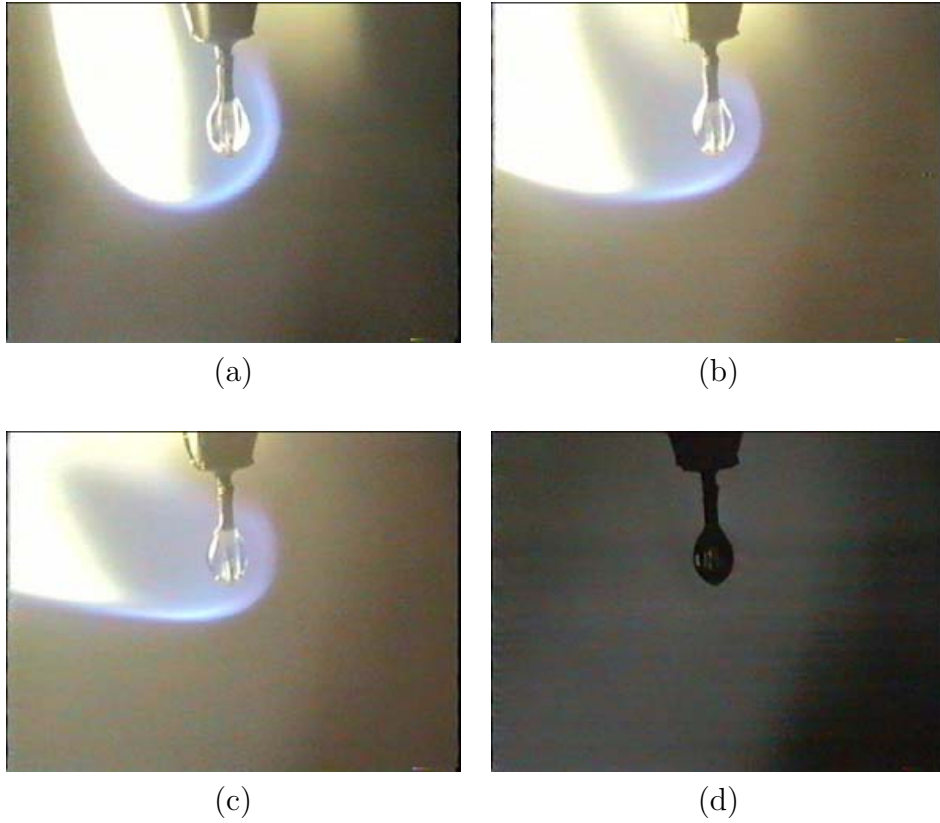


Figure 3.20: A sequence of images showing the extinction process of the flame surrounding an FT fuel droplet. The time span between the consecutive images was approximately 33 ms. The sound pressure level was 141.9 dB, and the estimated strain rate at extinction for this case was 330 s^{-1} .

CHAPTER 4

Shear-Coaxial Jets: Experimental Set-Up and Methods

The experiments in the non-reactive shear-coaxial study were conducted in the cryogenic supercritical flow facility (EC-4) at the Air Force Research Laboratory located at Edwards Air Force Base, CA. This facility was primarily designed to study non-reactive flows under different pressure (at or well above standard atmosphere) and temperature (at or well below room temperature) conditions. Accordingly, it is equipped with a high-pressure supply line of ambient temperature N_2 , which was used as both the pressurizing and test fluid. In addition, liquid nitrogen (LN2) was used as the chilling fluid for achieving the desired test fluid temperature. A detailed set of standard operating procedures (SOP) for using this facility are given in Appendix B.

In the following subsections, a brief description of the major components of the high pressure chamber and flow facility will be given followed by the main test articles, which are the shear-coaxial injectors. An overview of the acoustics generation and image visualization techniques are then discussed. A detailed discussion of the analysis method of the acquired high-speed image data are presented. Finally, the inherent experimental errors, and their propagation to the resulting uncertainties in the reported measured quantities are discussed.

4.1 High Pressure Chamber and Flow Facility

A schematic of the experimental facility is shown in Figure 4.1. The main pressure chamber, which is made of 304 stainless steel, was designed to operate at pressures up to 13.8 MPa (136 atm). It had four optical access ports on its lateral faces, two of which were used for installing the acoustic waveguides. The remaining two ports on opposite faces (not shown in Figure 4.1) measure 12 cm in diameter and were closed with Sapphire windows. It had additional holes and ports on the top and bottom faces for providing access to chamber pressurization and vent lines, test fluid inlets, and different instrumentation cables.

The chamber was mainly pressurized with ambient temperature N_2 tapped off from a high-pressure supply line. A pressure regulator reduced the incoming high-pressure gas, which was then flown to the chamber via a metering valve as shown in the chamber pressurization line in the piping and instrumentation diagram in Figure A.1 in Appendix A. A controlled rate of pressure build-up was then attained by adjusting the coarse and fine thread metering valves placed on the chamber vent line. This resulted in a continuous purging of the chamber. A ball valve placed on a bypass vent line remained closed during normal operating conditions, and was fully opened to completely vent the system.

Although flowing an ambient temperature high-pressure N_2 was the primary means of pressurizing the chamber, the inner and outer jet flows issued from the injector also contributed to pressurizing the chamber. Similar to the chamber pressurization flow, the inner jet flow was tapped off from the high-pressure supply line, and reduced to a calibrated inlet pressure of a Porter mass flow meter (a 200 slpm model 123-DKASVDAA). A fine thread metering valve placed downstream of the mass flow meter was used to adjust to the desired testing mass flowrate. Temperature conditioning of the inner jet was achieved using a simple heat exchanger whereby the warm inner jet flowed through a 1/8

inch coiled 316 stainless steel tube placed in a one inch tube flowing LN2. The plumbing was arranged so that either a coflow or counterflow arrangement was possible. Due to the desired low inner jet temperatures, and its enhanced heat transfer characteristics, the counterflow arrangement was used in all of the present experiments.

The outer jet flow set-up was identical to that of the inner jet with only minor differences. Since some of the test cases required relatively large outer jet mass flowrates, a 500 slpm mass flow meter of the same Porter model was used. In addition, both a coarse and fine thread metering valves were used. A two-step chill-down of the outer jet was possible using a coflow (HE-0208 in Figure A.1) followed by a counterflow (HE-0209) concentric tube heat exchanger. The former utilized LN2 that was already used to chill-down the inner jet flow, and was used for prechilling the outer jet flow before passing on to the main (counterflow) heat exchanger. The prechiller was used only for test cases that required enhanced cooling of the outer jet flow.

As mentioned above, LN2 stored in a 2,850 L supply tank was used to chill-down the inner and outer jet flows to the desired testing temperatures. The ullage pressure of the tank was maintained at a constant pressure of about 410 ± 30 kPa. For a constant inner and outer jet mass flowrates, the heat transfer was controlled by adjusting the LN2 flowrate using needle valves placed downstream of the heat exchangers on the LN2 exhaust line.

4.2 Shear-Coaxial Injectors

The shear-coaxial injector consisted of concentric straight tubes, where the inner jet flowed through the center tube while the outer jet flowed through the annulus. All injector parts were made of 316 stainless steel. A schematic of a section view of the entire injector assembly is shown in Figure 4.2.

The inner jet was introduced through the top inlet hole of the assembly, and enters a small plenum, which served as a settling chamber for the inner jet flow. An Omega EMQSS-020E, Type E, unshielded, 0.5 mm sheath diameter thermocouple inside the plenum measured the injector inlet temperature. A Kulite XCE-093-50D differential pressure transducer placed at the plenum wall provided measurements of any flow disturbances in the upstream section of the injector. The inner jet fluid then exited the injector down through a 7.6 cm straight tube connected to the plenum.

The outer jet was introduced into a settling chamber through two ports located on the side of the assembly. A Kulite CCQ-093-750A absolute pressure transducer and a similar thermocouple as for the inner jet were also used for the outer jet. The outer jet fluid was then led down a funnel section to a 4.3 cm long straight tube, which constituted the outer jet injector. Since the inner jet tube passed through the entire outer jet injector section of the assembly, it created an annular tube configuration. Hence, heat transfer between the inner (core) jet and outer (annular) jet took place from the outer jet plenum to the injector exit.

As discussed in Section 1.2.4, two parameters were varied for the two types of injectors considered in this study: the ratio of the inner jet tube thickness to the inner jet tube I.D., and the outer jet to inner jet cross-sectional area ratio. Figure 4.3 shows a schematic, and Table 4.1 below gives a summary of the dimensions of the injector exit. The injector with the large area ratio (LAR) and thin inner tube post was labeled ‘LAR-thin’ while the injector with the small area ratio (SAR) and thick post was labeled ‘SAR-thick’.

In order to ensure that a fully-developed turbulent flow emerged at the injector exit, the inner and outer jet Re were determined based on the typical entrance length estimation for turbulent flows as given by $X_E/D = 4.4Re^{1/6}$ [62]. The LAR-thin injector had an X_E/D of 109 for the inner jet, and 29 for the outer jet, where D for the outer

Table 4.1: Injector exit dimensions (mm)

Injector	D_1	D_2	D_3	D_4	t/D_1	A_o/A_i
LAR-thin	0.70	0.89	2.44	3.94	0.13	10.6
SAR-thick	1.47	3.96	4.70	6.35	0.84	2.90

jet is the hydraulic diameter of the annulus. The SAR-thin had an X_E/D of 52 and 62 for the inner and outer jets, respectively.

4.3 Inner Chamber: Acoustic Waveguide and Characterization

The inner chamber consisted of an acoustic waveguide attached to each side of a rectangular test section as shown in Figure 4.1. In order to provide optical access for backlighting and camera view, the front and back walls of the test section was made of 1.3 cm thick acrylic pieces. Three Kulite XCQ-093-50D differential pressure transducers were placed flush with the inside face of the back acrylic wall on the far side of the camera. One pressure transducer was placed at the same transverse location as the injector while the other two were located equidistant on either side of the center. A solid piece of stainless steel plate covered the bottom of the test section with an exhaust hole in the middle, while a perforated plate with a hole for inserting the injector tube covered the top of the test section. The size of the perforations were much smaller than the wavelengths of the acoustic waves generated during testing, and provided a means for maintaining pressure equilibrium between the inner and main sections of the pressure chamber.

The acoustic waveguide was contoured so as to provide a smooth transition from the circular cross-section of the acoustic sources to the rectangular cross-section of the test section. These acoustic sources, known as piezo-sirens, were custom-designed and

built by Hersh Acoustical Engineering, Inc. They can generate sound pressure levels exceeding 180 dB near their design operating frequency of 3 kHz. Since the experiments were conducted at elevated chamber pressures, as high as 36 atmospheres, these piezo-sirens provided the ideal means for generating acoustic waves in the high density medium. Pictures of one of the two piezo-siren elements and acoustic waveguides are shown in Figures 4.4a and 4.4b.

A 2-channel Fluke 292 waveform generator supplied continuous sine wave signals, which were amplified via Trek PZD2000A high-voltage amplifiers, to each piezo-siren. The waveform generators output signals were locked in frequency. However, their phase difference was varied in order to create a pressure antinode (PAN) and pressure node (PN) conditions at the injector location as measured by the center pressure transducer.

4.4 Measurement of Physical Properties

The physical parameters of the coaxial jet flow, namely J , were determined based on the injector exit flow properties. The jet exit temperatures were measured using an Omega EMQSS-010E, Type E, unshielded, 0.25 mm sheath diameter thermocouple mounted on a pair of linear positioners, and placed within a distance D_1 downstream of the injector exit plane. Two linear positioning stages ANPx51 manufactured by Attocube Systems AG provided a 3 mm back-and-forth, and a 6 mm transverse range of motions with a resolution on the order of microns. This enabled the measurement of the jet exit temperature profile, from which the inner jet and outer jet core temperatures were extracted. With knowledge of two state properties, the exit T and P , all other thermophysical properties of the jet were evaluated using NIST REFPROP [63] tables.

All of the instrumentation (pressure transducer, thermocouple, and mass flow meter) data recordings were synchronized with the image frame recordings. Pacific Instruments PI 6013, 6017, 6030 and 6030HF data acquisition boards with the PI 660 Acquisition

and Control Software were used for all data acquisition and recording tasks.

4.5 Jet Visualization

The primary means of studying the coaxial jet flow dynamics was provided by back-lit high speed images. A variable power Newport model 66986 that ran a 300 W Xe lamp, and emitted a collimated beam in the near ultraviolet spectrum, was used as the back-light source. Differences in the refractive index of the jets and the surrounding medium provided the necessary distinction between the fluids of interest. The denser inner jet, due to its low temperature, appeared as a dark column of fluid as viewed by the high-speed camera on the opposite side of the light source. The less dense outer jet was also in many cases distinguishable from the relatively warmer, and hence, even less dense ambient N_2 in the chamber. Examples of such back-lit images of the coaxial jet stream are shown in Figure 4.5 for a subcritical and nearcritical flow using the LAR-thin injector.

Phantom v7.1 and v710 high-speed cameras were used to capture the fast dynamical processes inherent to an unforced coaxial jet flow as well as those present during a high frequency acoustic forcing. Image framing rates of 25 kHz were used in order to avoid aliasing of up to the fourth harmonic of the forcing frequency. An external trigger was used to start recording the image frames, which were synchronized to the Kulite dynamic pressure transducer recordings at the sample rate of 25 kHz using an IRIG-B timecode.

4.6 Measurement of Dark-Core Length

The measurements reported as the “dark-core length” in this document refer to the axial length of the dark-core. Accordingly, the goal was to identify the longest contour line that outlined the dark-core structure attached to the injector body. In order to do this,

first each image with an 8-bit depth grayscale was converted to a binary image using the *im2bw* subroutine after obtaining a thresholding constant derived from the *graythresh* subroutine, both of which are found in the MATLAB[®] image processing toolbox. The thresholding was done based on Otsu's method [64]. Then, the dark regions in the binary image whose contour lines were connected to that of the injector body, also a dark region, were identified. This ensured that the dark structures considered were part of the unbroken portion of the inner jet starting from the injector exit. Finally, the contour line with the maximum continuous length represented the boundary of the dark-core that was sought for. Figure 4.6 shows the major steps involved in identifying the dark-core contour line. An automated routine repeated the above steps for 1000 image frames.

The dark-core length was computed by measuring the distance in pixels from the bottom of the injector to the largest row pixel on the dark-core contour line. The injector body width (the outer injector's outer diameter, D_4) in pixels was used as a scaling factor for converting the dark-core length in pixels to millimeters. The standard deviation of the mean for the sample of 1000 images was also computed.

4.7 Proper Orthogonal Decomposition of Pixel Intensity Data Array

Proper orthogonal decomposition (POD), also known as Principal Component Analysis (PCA), has proven to be a powerful means for extracting relevant qualitative and quantitative information from an otherwise complicated and noise-ridden measurement data. Berkooz *et al.* [65] and Chatterjee [66] give an in-depth discussion on the fundamentals of POD. Arienti and Soteriou [67] show its application to high-speed image analysis,

where a pixel intensity data matrix, \mathbf{A} , for a set of images is represented as

$$\mathbf{A} = \sum_{k=1}^N a_k(t) \phi_k(x) \quad (4.1)$$

where a_k are vectors of temporal amplitude coefficients, ϕ_k are vectors of proper orthogonal modes, k is the mode number, and N is the number of modes.

In a similar manner, in the present study, POD was used to extract the most dominant and periodic coherent flow structures in the recorded high-speed image frames. However, in order to implement this method, the pixel intensities, which are the measured parameters used to identify the flow structures, had to be arranged into a single aggregate data array for all image frames. This was achieved by first forming a row vector consisting of all pixel intensity values of each image frame (of resolution n rows by m columns) in order of increasing columns, followed by increasing rows as depicted in Figure 4.7a. Then, all such row vectors were combined for a sequence of N image frames, resulting in a matrix \mathbf{A} consisting of N rows by $M(=n \times m)$ columns of intensity values as shown in Figure 4.7b. Thus, \mathbf{A} is an array of N sets of M pixel intensities in a single frame.

Furthermore, as the goal was to identify periodic coherent structures, the intensity fluctuations need only be considered. Thus, the temporal mean of each pixel intensity was subtracted resulting in a matrix of intensity fluctuations $\tilde{\mathbf{A}}$. That is,

$$\tilde{\mathbf{A}}_{ij} = \mathbf{A}_{ij} - \frac{1}{N} \sum_i \mathbf{A}_{ij} \quad (4.2)$$

where $i = 1 \dots N$, $j = 1 \dots M$. Figure 4.8a shows a single image frame, and Figure 4.8b shows the corresponding averaged image for $N = 10^3$ frames.

Typically, $\tilde{\mathbf{A}}$ is a rectangular matrix where $N < M$. A singular value decomposition (SVD) can be readily computed for a non-square matrix as opposed to eigenvalue decomposition, which can only be applied to a square matrix. The geometric interpretation of

SVD as well as its relation to eigenvalue decomposition is discussed in Chatterjee [66]. The SVD of $\tilde{\mathbf{A}}$, represented as

$$\tilde{\mathbf{A}} = \mathbf{U}\mathbf{S}\mathbf{V}^T, \quad (4.3)$$

was computed in MATLAB[®] resulting in an $N \times N$ orthogonal matrix \mathbf{U} , an $N \times M$ diagonal matrix of singular values \mathbf{S} , and an $M \times M$ orthogonal matrix \mathbf{V} . However, since $N \ll M$, only the first N diagonal elements of \mathbf{S} and the first N columns of \mathbf{V} are non-zero. Accordingly, it was computationally more efficient to reduce \mathbf{S} and \mathbf{V} to an $N \times N$ and $M \times N$ matrices, respectively.

By convention, since the singular values are arranged in descending order of magnitude, the columns of \mathbf{U} and \mathbf{V} , which represent an orthonormal bases set of the column and row space of $\tilde{\mathbf{A}}$, respectively, were arranged in a corresponding manner. Furthermore, each column of $\mathbf{Q} = \mathbf{U}\mathbf{S}$, equivalent to $a_k(t)$ in Equation 4.1, is a vector of time-dependent amplitude coefficients, while the columns of \mathbf{V} are the proper orthogonal modes. The first column of \mathbf{Q} may thus be interpreted as containing the temporal characteristic of the coherent flow structure of the first (most) dominant mode, and the first column of \mathbf{V} as containing the spatial distribution of the first mode, and so on, for subsequent columns. Figure 4.9 shows a plot of the singular values for all $N = 10^3$ modes of a baseline flow.

The spatial distribution of mode-1, corresponding to the mode with the maximum singular value in Figure 4.9, was constructed from the first column of \mathbf{V} as shown in Figure 4.10a; this is called the proper orthogonal mode (POM) image. As stated earlier, because only the fluctuation in intensity levels were considered, the background fluid and the relatively uniform portion of the inner jet flow were subtracted out, and thus, were depicted by a gray region to indicate a mean level in a gray-scaled image. Lobes of dark and light regions indicate locations where fluid (emanating from the dense inner jet flow) was present and absent, respectively. Moreover, at a given downstream loca-

tion, the presence of identical adjacent lobe regions indicates the formation of symmetric structures about the inner jet, while a dark region next to a light one indicates asymmetry. The spatial distributions of subsequent modes could be constructed similarly from the remaining columns of \mathbf{V} .

The frequency content of these coherent lobe structures were obtained from the power spectral density (PSD) plots of each column of \mathbf{Q} . Figure 4.10b shows one such plot for mode-1 obtained from the first column of \mathbf{Q} . It represents how the magnitude of the intensity fluctuation is distributed with frequency. A peak in the spectrum denotes a recurring flow structure that originates from the inner jet flow with the associated peak frequency. Similarly, the POM image and PSD plot for mode-2 are shown in Figures 4.10c and 4.10d, respectively.

The product of a column vector in \mathbf{Q} with a corresponding row vector in \mathbf{V}^T gave the time progression of the spatial distribution represented by a single mode, such as in Figure 4.10a for mode-1. Figure 4.11a shows a time sequence of frames of images represented by mode-1. This sequence reveals that the dynamics captured by mode-1 merely represent a standing wave type of progression in time of the flow structures. However, it can easily be shown in 1-D waves that the superposition of two standing waves $\psi_1 = B \cos(kx)e^{i\omega t}$ and $\psi_2 = B \cos(kx - \phi)e^{i(\omega t - \phi)}$ with similar amplitude and frequency, and a spatial and temporal phase difference $\phi = \pm 90^\circ$ will be a traveling wave. That is,

$$\begin{aligned}\psi &= \psi_1 + \psi_2 \\ &= B (\cos(kx) - i \sin(kx)) e^{i\omega t} \\ &= B e^{i(kx - \omega t)}\end{aligned}\tag{4.4}$$

Arienti and Soteriou [67] define conjugate mode pairs as any two modes whose cross-power spectra magnitude peaks near a phase of $\pm 90^\circ$, such as the one shown in Figure

4.12 for mode-1 and mode-2, and are represented by similar lobe patterns. The cross-power spectral density of a conjugate mode pair with temporal amplitude coefficients, a_k and b_k was computed as

$$\text{CPSD} = \sum_{s=0}^{N-1} \text{corr}(a_k, b_k) e^{-i\omega s} \quad (4.5)$$

where $\text{corr}(a_k, b_k)$ represents the cross-correlation of a_k and b_k . Therefore, the superposition of the two modes resulted in a lobe pattern that convected downstream as time progressed. Figure 4.11b shows a time sequence of frames for the superposition of mode-1 and mode-2. It is distinguished from Figure 4.11a in that the coherent flow structures are convected downstream with each time step.

4.8 Measurement Uncertainty

As do all measured quantities, the measurement results reported in this document have an inherent uncertainty in them. These uncertainties arise both from the systematic or bias error associated with the measurement devices or the repeatability of individual measurements commonly known as precision errors. It is important to realize the limitation of a measurement on how accurately it represents the true value, and even more importantly, to keep track of how that measurement uncertainty propagates to other parameters that are defined by the measured quantities. Thus, error propagation was performed on the measured physical parameters with significant sources of error in order to determine the appropriate degree of accuracy with which to report other dependent physical quantities.

These dependent quantities mainly pertain to the calculated jet exit velocities, velocity ratios, and momentum flux ratios, which depend on the measured mass flowrates, exit area, and density, which, in turn, depends on the measured exit temperature and static pressure. The precision errors in all of the high frequency data samples acquired during

the mass flowrate, temperature and pressure measurements were significantly smaller than the bias errors of the measurement devices. Hence, only bias error propagation was considered.

The jet exit velocities were determined using the relation

$$U_k = \frac{\dot{m}_k}{\rho_k A_k}, \quad (4.6)$$

where $k \equiv i, o$ for the inner and outer jet flows, respectively. Following the standard rule of error propagation for a function of several variables [68], the uncertainty in the calculated jet velocities was determined as

$$\delta U_k = U_k \sqrt{\left(\frac{\delta \dot{m}_k}{\dot{m}_k}\right)^2 + \left(\frac{\delta \rho_k}{\rho_k}\right)^2 + \left(\frac{\delta A_k}{A_k}\right)^2} \quad (4.7)$$

Similarly, the uncertainty in the momentum flux, $M_k \equiv \frac{\dot{m}_k^2}{\rho_k A_k}$, was

$$\delta M_k = M_k \sqrt{4 \left(\frac{\delta \dot{m}_k}{\dot{m}_k}\right)^2 + \left(\frac{\delta \rho_k}{\rho_k}\right)^2 + \left(\frac{\delta A_k}{A_k}\right)^2} \quad (4.8)$$

Vendor calibration reports provided the measurement uncertainties for the mass flow meters and the pressure transducer. The Porter mass flow meters had an accuracy of $\pm 1.0\%$ full scale, and the Stellar absolute pressure transducer was accurate to within $\pm 0.02\%$ full scale. Accordingly, the uncertainties in the measured mass flowrates were ± 36 mg/s and ± 97 mg/s for the inner and outer jets, respectively, while that for the chamber pressure was ± 0.004 MPa. The uncertainty in the thermocouple measurements determined based on a calibration using an RTD [58, 22] were ± 1 K.

As stated previously, the exit jet densities were evaluated, based on the measured exit temperatures and chamber pressure, using NIST REFPROP [63] tables. According to [61], as long as the error from a particular source is significantly smaller than all other sources of error, it is ignored. Since density has a much weaker dependence on pressure than on temperature, the uncertainty in density due to pressure variation was ignored. Thus, for the purpose of measurement error analysis in this study, $\rho(p, T) \approx \rho(T)$.

Finally, the uncertainties in the momentum flux ratio and velocity ratio were determined as

$$\delta J = J \sqrt{\left(\frac{\delta M_o}{M_o}\right)^2 + \left(\frac{\delta M_i}{M_i}\right)^2} \quad (4.9)$$

and

$$\delta R = R \sqrt{\left(\frac{\delta U_o}{U_o}\right)^2 + \left(\frac{\delta U_i}{U_i}\right)^2}, \quad (4.10)$$

respectively.

The precision uncertainty in the L/D_1 values reported was as the standard deviation, σ , for a total of 1000 measurements. That is, one standard deviation represented uncertainty in the L/D_1 measurement from a single image. It should be noted that for such a large sample size, the uncertainties in the mean, given by the standard deviation of the mean ($\sigma_{mean} = \sigma/\sqrt{1000}$), of the measured dark-core lengths were negligible.

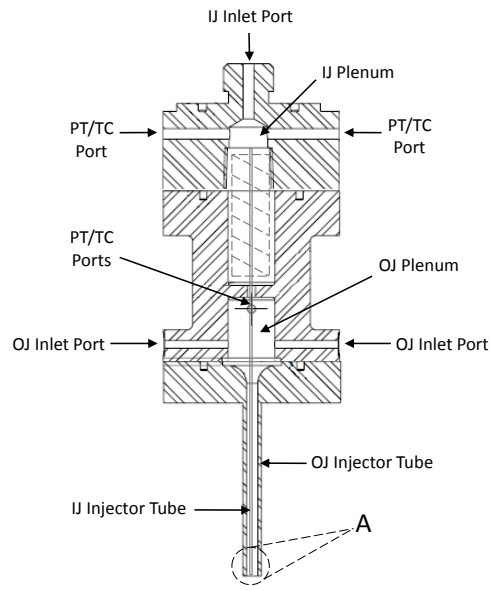


Figure 4.2: A schematic of the shear-coaxial injector assembly (expanded view of **A**: See Figure 4.3).

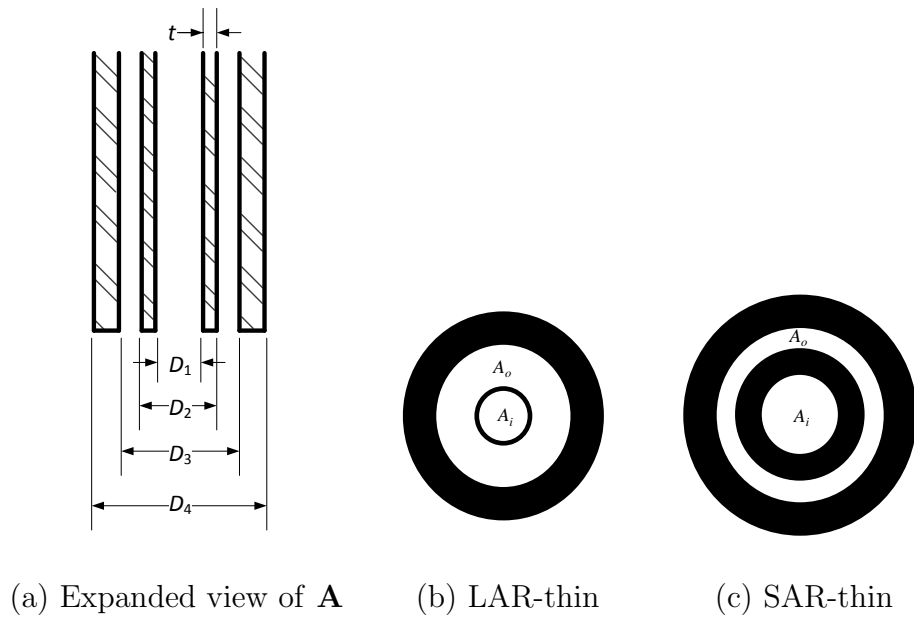


Figure 4.3: A schematic of the shear-coaxial injector exit.

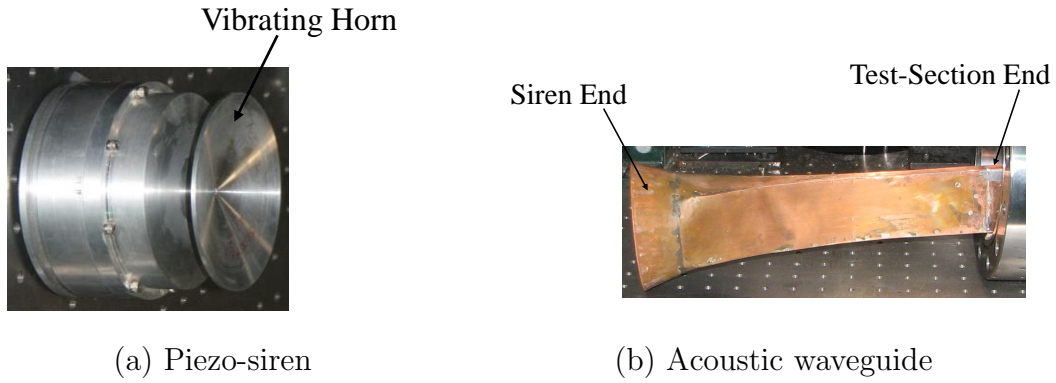


Figure 4.4: Pictures of the acoustic elements. Acoustic waves generated by the piezosiren enter the end of the waveguide of circular cross-section and propagate down to the test-section of rectangular cross-section .

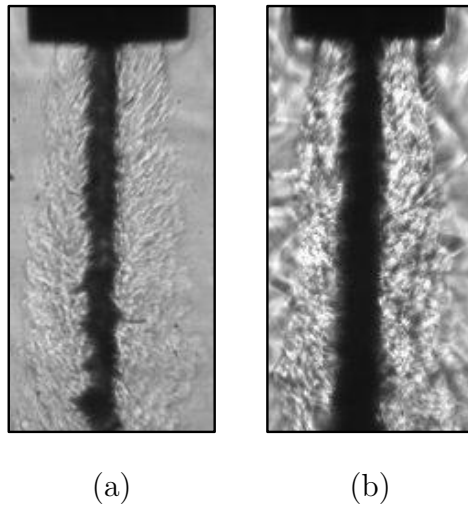
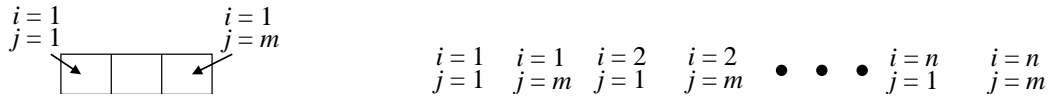
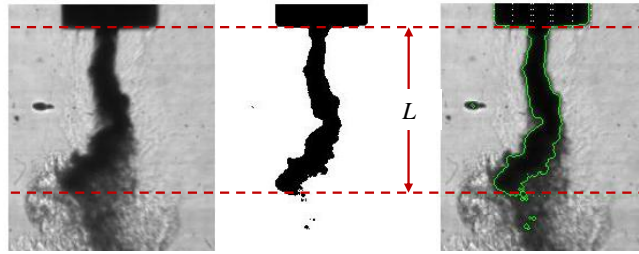


Figure 4.5: Back-lit images of baseline LAR-thin injector flows at $J = 0.1$ where the chamber pressure, and the chamber, outer jet and inner jet temperatures were: (a) 1.5 MPa, 243 K, 198 K, 107 K, and (b) 3.57 MPa, 252 K, 195 K, 114 K, respectively.



$$\mathbf{A} = \left(\begin{array}{c} \begin{array}{c} \updownarrow \\ \text{\textit{N time steps}} \end{array} \\ \begin{array}{c} \leftarrow \text{\textit{M pixels}} \rightarrow \end{array} \end{array} \right)$$

(b)

Figure 4.7: Illustration of (a) how pixel intensity values from a single image are arranged into a row vector; (b) the construction of \mathbf{A} , data matrix of pixel intensities.

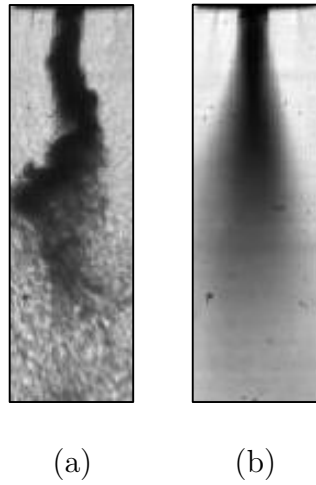


Figure 4.8: PN forced ($f_F = 3.12$ kHz) LAR-thin injector flow at $P_r = 0.44$, $J = 5.2$: (a) a snapshot image captured at 25 kHz; (b) a time-averaged image from 1000 consecutive images.

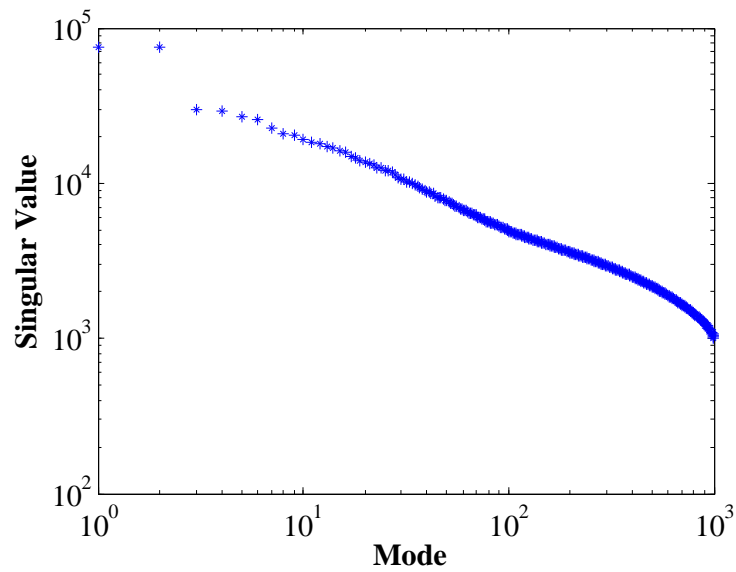


Figure 4.9: Singular values for PN forced ($f_F = 3.12$ kHz) LAR-thin injector flow at $P_r = 0.44$, $J = 5.2$.

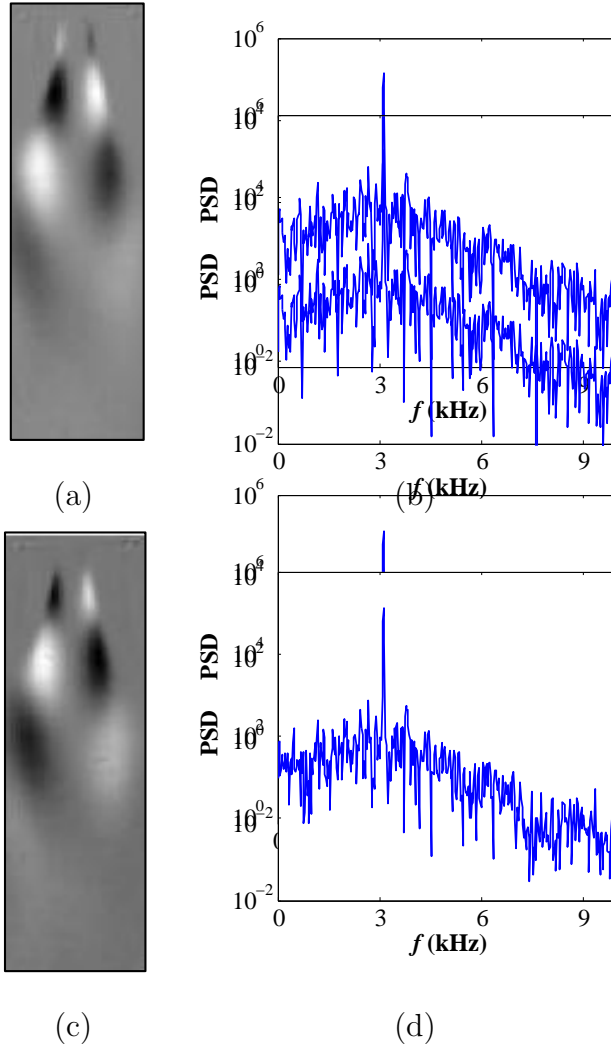


Figure 4.10: Proper orthogonal mode (POM) image and power spectral density (PSD) of the temporal amplitude coefficients for PN forced ($f_F = 3.12$ kHz) LAR-thin injector flow at $P_r = 0.44$, $J = 5.2$: mode-1 (a) POM, (b) PSD; mode-2 (c) POM (d) PSD.

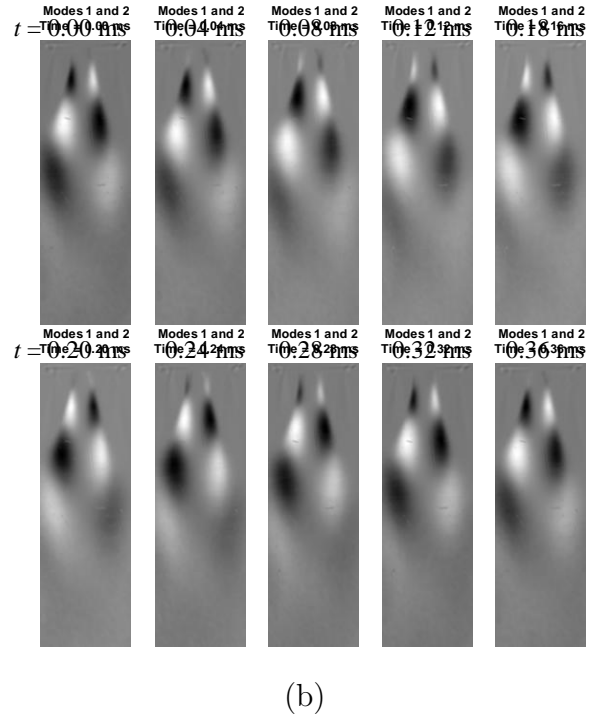
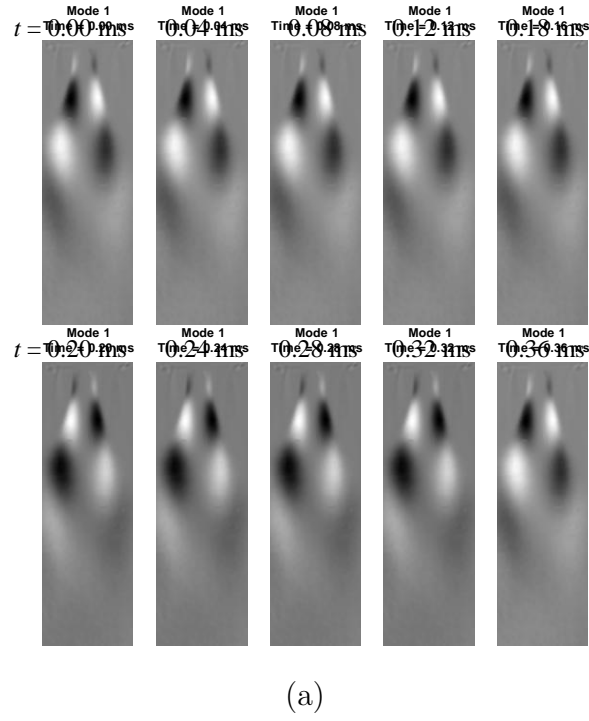
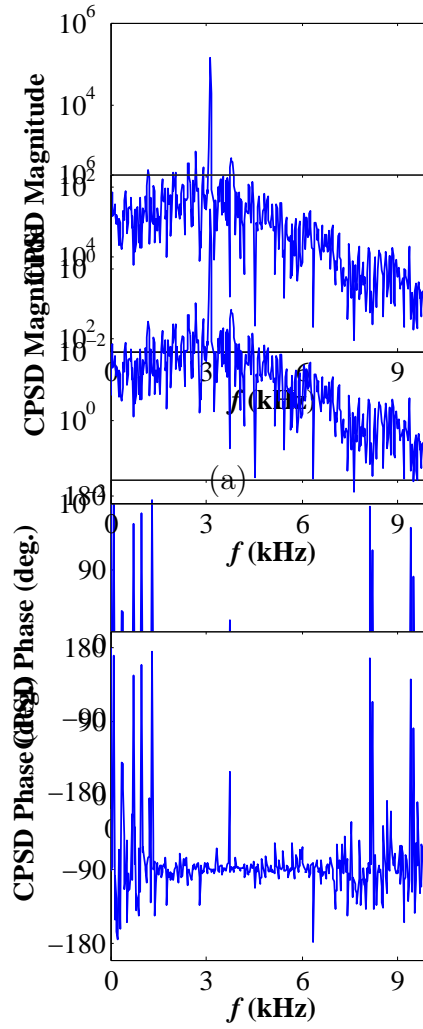


Figure 4.11: A time sequence of POM images for PN forced ($f_F = 3.12$ kHz) LAR-thin injector flow at $P_r = 0.44$, $J = 5.2$: (a) mode-1 only, (b) superposition of mode-1 and mode-2.



(b)

Student Version of MATLAB

Figure 4.12: Cross-power spectral density (CPSD) of mode-1 and mode-2 for PN forced ($f_F = 3.12$ kHz) LAR-thin injector flow at $P_r = 0.44$, $J = 5.2$; (a) magnitude, (b) phase.

Student Version of MATLAB

CHAPTER 5

Shear-Coaxial Jets: Results and Discussion

The experiments done under subcritical (reduced pressure, $P_r = 0.44$) conditions were such that the inner jet was in the liquid phase, while the outer jet was in the gas phase at temperatures well above the saturation temperature of N_2 . Under nearcritical (reduced pressure, $P_r = 1.05$) conditions, the inner jet was a transcritical fluid at temperatures below the critical temperature, while the outer jet was a supercritical fluid at temperatures well above the critical temperature. A summary of all the flow conditions and parameters is given in Tables C.1 and C.2 in the Appendix. As previously noted, for coaxial jets of different densities, the outer to inner jet momentum flux ratio, J , is one of the governing parameters of coaxial jet mixing. In the present work, for a set of test conditions in a particular pressure regime, the outer-to-inner jet density ratio ($S = \rho_o/\rho_i$) was held approximately constant while R was varied. Thus, the variation in J in these studies resulted mainly due the variation in R .

Although the goal was to maintain constant inner jet flow conditions, small changes were necessary to achieve subcooled or subcritical inner jet exit temperatures at higher J values. This was due to the enhancement in heat transfer between the coaxial jets while flowing down the concentric injector tubes. This was especially challenging with the LAR-thin inner jet flow because the ratio of outer to inner jet volume per unit tube length was considerably larger for this injector. Thus, the LAR-thin injector inner jet temperature was much more sensitive to the outer jet flowrate. Since a liquid inner jet was desired at the exit, maintaining a low exit inner jet temperature required lowering

the outer jet mass flowrate. This can be explained by considering a simple energy balance, assuming small changes in the specific heat constants, between the coflowing jets inside the injector as follows:

$$\text{Injector : } T_{i,\text{exit}} = T_{i,\text{inlet}} + \frac{(\dot{m}c_p\Delta T)_o}{(\dot{m}c_p)_i}. \quad (5.1)$$

As Equation 5.1 shows, lowering the outer jet mass flowrate enabled to reduce the heat gained by the inner jet. However, in order to achieve the desired high J , the inner jet mass flowrate also had to be reduced. In addition, a reduction in the inner jet mass flowrate also assisted in lowering the injector inlet temperature of the inner jet. This may be deduced from Equation 5.2, which shows a similar simple energy balance between the inner jet fluid and the coolant LN2 flowing the the heat exchanger:

$$\text{Heat Exchanger : } T_{i,\text{exit}} = T_{i,\text{inlet}} - \frac{(\dot{m}c_p\Delta T)_{\text{LN2}}}{(\dot{m}c_p)_i}. \quad (5.2)$$

5.1 Shear-Coaxial Jets without Acoustic Forcing

5.1.1 Qualitative Characteristics of Baseline Flows

As mentioned previously, the high-speed images were obtained at framing rates that exceeded three times the highest frequency of the dominant baseline flow structures. Although the overall flow dynamics cannot be captured in a single snapshot image, this section will give a brief account of the general observable behavior of the coaxial jets for the two injector configurations with varying J at the different chamber pressure regimes. Since the back-lit images only revealed the dense inner jet flow, the discussion will be limited to the dark-core flow region and the identifiable flow structures on its periphery. It is to be noted that the inner jet tube for the LAR-thin injector was not perfectly flush, but stuck out by about $0.2D_1$. This allowed for direct visual confirmation that

the inner jet injector tube was not oscillating due to turbulent flow disturbances in the outer jet.

Figure 5.1 shows the baseline LAR-thin injector flows of various momentum flux ratios at $Pr = 0.44$. At $J = 0.1$, the presence of the very low momentum outer jet flow had minimal impact on the development of the liquid inner jet flow. The low aerodynamic Weber number ([69] $We_o \equiv \rho_o(U_o - U_i)^2 D_1 / \sigma \approx 21$) for this low J flow enabled the inner jet to maintain coherence for over $20D_1$ downstream of the exit, which is about where the field of view in the image ends. Although small periodic surface wrinkles started forming about $10D_1$ downstream of the exit, they were not large enough to disrupt the continuity of the jet. As the outer jet flowrate was increased resulting in $J = 0.5$, the dark-core region of the inner jet flow still stayed intact for over $20D_1$. However, surface instabilities were enhanced and occurred earlier than the lower J case. As J increased to higher than one, the dark-core region could no longer remain intact within the field of view, and broke up into fine droplet spray. The presence of a larger shear force at the jets' interface also aided in the formation of a fine mist of droplets on the periphery of the inner jet flow. Enhanced entrainment of the inner jet flow into the outer flow was evident in the increased spread of the inner jet. Higher J values aided in the break-up and dispersion of the inner jet and rapid mixing with outer jet at closer distances to the injector exit. Accordingly the dark-core length became shorter with increasing J . However, a much more gradual decrease in the size of the dark-core region was seen over the range of higher momentum flux ratios, $J = 11 - 20$, than at the lower ones.

As Figure 5.2 shows, similar trends in the dark-core lengths were seen at $Pr = 1.05$ with increasing J . The dark-core again remained intact for the entire length of the image for the two lowest J flows ($J = 0.1, 0.5$). However, both flows showed increased spread as evident in the wider inner flow relative to the corresponding flows at $Pr = 0.44$.

Despite being below the critical temperature at the exit, the lack of discrete structures and droplets emanating from the inner jet was due to the diminishing cohesive surface tension force as the critical point was approached, and its absence in the supercritical fluid regime. Since the temperature of the inner jet at the interface was supercritical, hence a supercritical fluid, the periphery of the inner jet did not form a well defined boundary like a liquid would. For $J = 1.9 - 12$, further decrease in the dark-core region was observed as J increased. The dark-core regions were also shorter compared to the flows with similar J values at $P_r = 0.44$.

Figure 5.3 shows the baseline SAR-thick injector flows at $P_r = 0.44$ and for J values similar to those of the LAR-thin flows. At $J = 0.1$, just as with the LAR-thin flow, the inner jet stayed intact and undisturbed along the entire field of view of about $13D_1$ in length. In contrast to the LAR-thin injector flow, the thick inner injector post created a unique flow field, whereby for this low J case, the low momentum outer jet fluid formed an axisymmetric recirculation zone just below the thick post and surrounding the inner jet flow. The sense of rotation of the recirculating flow was such that a local counterflow condition existed at the interface of the inner jet and the recirculation zone. At $J = 0.5$, there was a significant presence of surface irregularities that formed ligaments just a few diameters D_1 downstream of the exit, and subsequently broke down and dispersed into droplets. Yet, the dark-core region still remained intact for the entire field of view. The recirculation zone also consisted of the outer jet fluid with small traces of droplets that came off the surface of the inner flow.

When the momentum flux ratio was increased to $J = 2.1$, higher entrainment by the outer flow caused most of the recirculation zone to be filled with the lower momentum inner jet fluid. The presence of the dense, dark fluid in the recirculation zone created a perception of “necking” in the dark-core flow. Further downstream, the dark-core could no longer maintain its coherence and was fully dispersed into droplets. By $J = 5.7$, the

recirculation zone was completely filled with the inner jet fluid. The remaining inner jet fluid underwent increased dispersion resulting in a shorter dark-core. Together with the recirculation flow, the inner jet started forming a conical dark-core region. The shape of the conical dark-core region became well defined by $J = 10$, and the dark-core length was significantly reduced. Increasing to $J = 15$ and $J = 21$ showed relatively small decreases in the dark-core length.

Figure 5.4 shows the corresponding baseline SAR-thick injector flows at $P_r = 1.05$. At $J = 0.1$, the inner jet showed greater spread than its counterpart at the lower chamber pressure. It, nevertheless, maintain a long, intact dark-core region. The slightly darker fluid in the recirculation zone was evidence that the denser inner jet fluid was also present. An even more diffused inner jet flow at $J = 0.5$ resulted in a shorter dark-core region compared to the $P_r = 0.44$. At $J = 2.1$, the recirculation zone was fully filled with inner jet fluid, and a similar “necking” in the dark-core region was observed. Further increase in J resulted in shorter conical dark-core regions. Beyond $J = 9.2$, relatively small changes in the dark-core lengths were observed with increasing J . Moreover, the recirculation zone grew until and stayed constant beyond $J = 9.2$.

5.1.2 Baseline Dark-Core Length Measurements

The high-speed images showed that the back-lit coaxial jets created a silhouette of the relatively high density inner jet that formed a dark-core flow region in the images. As noted earlier, the axial length of the intact dark-core region was used to gauge the extent of mixing between the outer and inner jets. In an analogous manner, the length of an inner velocity potential core has been used to mark the extent of the inner shear-layer growth in coaxial jets. Thus, a dark-core length and a potential-core length may be considered as two different physical parameters that describe different aspects of flow processes pertinent to mixing of coaxial jets.

The baseline flow dark-core lengths, L_B were measured and normalized by D_1 , and plotted versus J for the LAR-thin and SAR-thick injectors as shown in Figures 5.5 and 5.6, respectively. The dark-core lengths for the two lowest J flows ($J = 0.1$ and $J = 0.5$) were omitted since their dark-core region exceeded the field of view. Also included in these plots are the measurement uncertainties in single measurements of L_B/D_1 , and the uncertainties in the reported J values. The rather large uncertainties in the higher J values, especially for the LAR-thin injector flows, were due to the large relative uncertainties in the inner jet mass flowrates in Equation 4.8. This was because lower inner jet mass flowrates were used in order to attain the desired flow temperatures as already discussed at the beginning of this chapter. On the other hand, the uncertainties in the L_B/D_1 for both injectors showed statistically significant decrease for lower J values, and relatively small differences for higher ones.

Figure 5.7 shows a power-law curve-fit of the form $c_1 J^{c_2}$, where c_1 and c_2 are constants, through each data set of L_B/D_1 for each injector at $P_r = 0.44$ and $P_r = 1.05$. It can be seen that at $P_r = 1.05$, the variation of L_B/D_1 with J was similar for both injectors, and was also in agreement with that obtained by Davis [58] and Rodriguez [22] using a different injector configuration, for which they reported $c_2 \approx 0.5$. In terms of the labeling convention used for the present work's injectors, Davis used a LAR-thick injector and Rodriguez used both a LAR-thick and SAR-thin injector. On the other hand, at $P_r = 0.44$, although both the LAR-thin and SAR-thick injectors again had comparable variation of L_B/D_1 with J , they did not agree well with the $c_2 \approx 0.2$ reported by Davis and Rodriguez. It was also shown that for a given J , the SAR-thick injector flows had consistently lower L_B/D_1 under both pressure regimes, and that for each injector and a given J , the L_B/D_1 at $P_r = 1.05$ was lower than that at $P_r = 0.44$. In general, it may be deduced that for a specific J baseline flow, the SAR-thick injector at elevated pressures had the most enhanced mixing.

A revision of the L_B/D_1 data that Rodriguez [22] and Leyva *et al.* [46] obtained using a LAR-thick injector, and Rodriguez [22] and Graham *et al.* [70] obtained using a SAR-thin injector were compared with the L_B/D_1 data from the LAR-thin and SAR-thin as shown in Figures 5.8 and 5.9 at $P_r = 0.44$ and $P_r = 1.05$, respectively. The dimensions for these injectors are given in Table 1.2. Leyva *et al.* and Rodriguez introduced a $0.5D_1$ recess in the inner injector tube unlike Graham *et al.* and the present study, which used flushed outer and inner injector tube exits. However, at $P_r = 0.44$, there was negligible differences in L_B/D_1 between the flushed and recessed configurations of the SAR-thin injector. Moreover, for low J flows, the SAR-thick and SAR-thin injectors showed comparable L_B/D_1 , which were significantly lower than that of the LAR-thin and LAR-thick injectors. This was in agreement with observations by Champagne and Wygnanski [32] and Gladnick *et al.* [39] that the potential core length is longer for larger area ratio. The large difference in L_B/D_1 between the LAR-thin and LAR-thick injectors may be attributed to the presence of the recirculation zone behind the thick inner tube post of the LAR-thick injector that entrained a significant portion of the inner jet fluid for $J \approx 2$ and higher. For high J , the data for all injectors appeared to asymptote to the same L_B/D_1 . However, due to experimental limitations, high enough J were not attainable to verify this trend.

At $P_r = 1.44$, challenges with conditioning the inner jet temperatures resulted in a wide range of inner jet exit temperatures for a given J using the different injectors. In order to mitigate the impact of the resulting large differences in the inner jet exit densities on the measured L_B/D_1 , each measured L_B/D_1 (shown in Figure 5.9a) was scaled by the ratio of a chosen reference inner jet density (at $T_i = 109$ K) to the actual inner jet density:

$$\left(\frac{L_B}{D_1}\right)_{\text{adjusted}} = \frac{L_B}{D_1} \frac{\rho|_{T=109K}}{\rho}. \quad (5.3)$$

As Figure 5.9b shows, for the low J flows, again the SAR-thick injector had the lowest L_B/D_1 . The agreement between the SAR-thin injector's flushed and recessed data at $P_r = 0.44$ was not upheld at the elevated pressures. The flushed cases had consistently higher L_B/D_1 . On the overall, L_B/D_1 showed less separation for a given J compared with those at $P_r = 0.44$. They also appeared to approach an asymptotic L_B/D_1 at high enough J .

The wide variation in the measured L_B/D_1 of the different injectors, especially for lower J flows, was an evidence that J is not the only governing parameter, but also the injector geometry, namely t/D_1 and A_o/A_i . To estimate the dependence of L_B/D_1 on J and these geometric parameters, a functional dependence of the following form was assumed:

$$\frac{L_B}{D_1} = c_1 J^{c_2} \left(\frac{t}{D_1} \right)^{c_3} \left(\frac{A_o}{A_i} \right)^{c_4}. \quad (5.4)$$

All of the L_B/D_1 at each P_r was used in a non-linear regression analysis used to estimate the constants $c_1 - c_4$, whose converged values are listed in Table 5.1. The results of the regression are given in Figures 5.10 and 5.11 for $P_r = 0.44$ and $P_r = 1.05$, respectively, in which L_B/D_1 was plotted versus G (the right-hand-side of Equation 5.4). The regression constants revealed that L_B/D_1 increased with A_o/A_i , as expected, while it decreased with J and t/D_1 at both pressure regimes. They also revealed a stronger dependence on A_o/A_i at $P_r = 0.44$ than at $P_r = 1.05$. The reason as to why this was the case is yet to be determined.

5.1.3 Characterization of Dominant Dynamic Flow Structures

Application of POD on the pixel intensity fluctuations in the high speed images, revealed spatial and temporal characteristics of the dominant periodic flow structures present in the coaxial jet flow. Figures 5.12a-g show snapshot images of the LAR-thin injector flow

Table 5.1: Values of the constants in Equation 5.4 obtained from non-linear regression of the L_B/D_1 data.

P_r	c_1	c_2	c_3	c_4
0.44	9	-0.34	-0.15	0.30
1.05	11	-0.43	-0.12	0.15

at $Pr = 0.44$ along with time-averaged images of 1,000 consecutive images acquired at 25,000 frames per second, images of the proper orthogonal mode (POM) of the conjugate modes, and the corresponding cross-power spectral density (CPSD) magnitude plots. The images shown span a distance of about $20D_1$ downstream of the injector exit plane. For $J = 0.1$, the average image shows a relatively undisturbed dark-core flow for over $20D_1$. In contrast to the snapshot image, the average image was characterized by the absence of any discrete flow structures emanating from the dark-core at the outer-inner jet interface.

As described in Section 4.7, the POM image represented fluctuations in intensities with dark and light shades, which indicated a local periodic presence and absence, respectively, of dense fluid structures. Regions which showed no change in intensity over a span of 1,000 image frames, such as near the axis of the inner jet flow and the outer jet flow, were depicted in gray as a means to represent the DC component or the reference mean on an 8-bit grayscale. Accordingly, the majority of the field of view in the POM image of Figure 5.12a shows the absence of any significant dynamic dense fluid structures except in the inner shear-layer region far downstream of the injector exit.

Also shown in Figure 5.12a is the CPSD magnitude of the conjugate mode pair corresponding to the POM image. The low frequency peak in the spectrum indicated the temporal periodicity of the dark and light lobes in the POM images around that frequency. It has been shown that the superposition of a conjugate pair represents down-

stream propagating flow structures in time, per the discussion in Section 4.7. Therefore, the information conveyed in the POM image and the CPSD magnitude spectrum was that the $J = 0.1$ flow had spatially and temporally periodic dominant flow structures as shown in the dark and light lobes, and spectral peaks, respectively. The staggered or antisymmetric arrangement of the lobes in the POM image suggests that the flow structures were propagating as a helical disturbance. This may be a strong claim to make based on a planar view of an axisymmetric flow. However, in the absence of external disturbances that can impose a preferred direction of flow oscillation, it may be argued that the only manner of propagation for the periodic antisymmetric structures must be in the form of a helical disturbance. Hence, viewing the jet from two perpendicular lines of sight should reveal indistinguishable features for a baseline coaxial jet, as Davis [58] previously showed for some flow conditions .

Figure 5.12b shows the same set of images and spectral plot for the $J = 0.5$ case. Compared to that for $J = 0.1$, the average image shows a noticeable spread with increasing downstream distance. The dominant periodic structures in the POM image were also comparably larger and started forming a few diameters upstream of those for $J = 0.1$. Their antisymmetric arrangement again was an indication of the propagation of helical disturbances. The low frequency peak in the CPSD magnitude spectrum was the characteristic frequency associated with these structures. It was broader and shifted slightly to a higher frequency.

As the momentum flux ratio increased to $J = 2.1$, the average image in Figure 5.12c shows that the inner jet spread also continued to increase. The dominant flow structures were antisymmetric as the two lower J cases, but their inception moved farther upstream. Their CPSD magnitude spectral peak was relatively broader and situated at a higher frequency. Figures 5.12d,e for $J = 5.2, 11$ also show similar trends seen with increasing J .

For reasons described at the beginning of this chapter, the jet flowrates were lower

for $J = 14$ than for $J = 11$. As Figure 5.12f shows, the inception point of the antisymmetric structures was relatively unchanged. However, the broad peak in the magnitude spectrum shifted back to lower frequencies. Thus, the peak frequency in the CPSD magnitude spectrum, which is the characteristic frequency of the dominant flow structures identified, was clearly also dependent on the magnitude of the outer jet flowrate and not only on J . The next higher J case shown in Figure 5.12g for the same inner jet flowrate, but increased outer jet flowrate, confirmed the increasing trend of the peak frequency with increasing outer flowrate.

Figures 5.13a-e show similar snapshot, average and POM images along with the CPSD magnitude for the LAR-thin injector flows at $Pr = 1.05$. At this elevated pressure, the outer to inner jet density ratio, S , was larger by almost three times that of the subcritical pressure cases. This difference may have brought about a difference in the development of the shear-layer disturbances under the two pressure conditions. For the low momentum flux ratio of $J = 0.5$, however, no significant differences were discernable between the two pressure regimes. The inner jet spread depicted in the average image in Figure 5.13a was comparable to that of the $Pr = 0.44$. In addition, the onset of antisymmetric structures, and the CPSD magnitude spectrum were also comparable. For the $J = 0.5$ flow at $Pr = 1.05$, however, the peak frequency was slightly lower perhaps partly due to the lower outer jet flowrate.

As the momentum flux ratio increased, the onset of the dominant antisymmetric structures moved farther upstream as the dark-core length was reduced. However, compared to that of the $Pr = 0.44$ cases, the onset of these antisymmetric structures was relatively closer to the end of the dark-core as shown in Figures 5.12b-e. In other words, helical disturbances had a slightly delayed start under the higher chamber pressure conditions, where S was larger. These disturbances appeared to penetrate deeper towards the jet axis and also appeared to have shorter wavelength compared to those of compa-

rable J at $Pr = 1.05$. On the other hand, in a manner that was observed at $Pr = 0.44$, the peaks in the magnitude spectra shifted to higher frequencies with increasing J due to increasing outer jet flowrates.

Similarly, Figures 5.14a-g show snapshot images of the SAR-thick injector flow at $Pr = 0.44$ along with a time-averaged image of 500 consecutive images acquired at 25,000 frames per second, POM images of the conjugate modes, and the corresponding CPSD magnitude plots. The images shown span a distance of about $8D_1$ downstream of the injector exit plane. For $J = 0.1$, the average image in Figures 5.14a shows a relatively undisturbed dark-core flow for over $8D_1$. However, the POM image shows weak but symmetric flow disturbances propagating along the inner jet surface. Based on the same argument used to suggest that antisymmetric structures represented helical disturbances in baseline flows due to the absence of directional bias, it may be argued that the symmetric flow structures represented axisymmetric disturbances. A possible cause for the axisymmetric disturbances to dominate over the helical disturbances may have been the presence of the axisymmetric, recirculating low momentum outer jet flow just below the inner post and surrounding a region of about $1D_1$ just downstream of the inner jet exit. The peak in the CPSD magnitude associated with these disturbances was at a low frequency, similar to the LAR-thin injector flow with the same J and Pr .

For $J = 0.5$, the average image in Figure 5.14b shows a sudden spread in the dark-core at the location where the recirculation zone ends. Due to entrainment of the outer jet by the inner jet at low J , once it exited the injector, the outer flow was forced to converge towards the jets' axis while tracing the outer edge of the recirculation zone. It thus impinged on the inner jet at an angle, and the reattached outer jet flowed parallel to the inner jet. This impinging flow may have been the cause for the sudden spread at the reattachment point visible in the average image. The POM image does not clearly identify whether symmetric or antisymmetric disturbances exist. The peak frequency in

the magnitude spectrum still stayed at lower frequencies.

As J increased, the snapshot and average images show the recirculation zone filled with the dense inner jet fluid. This implied that the higher momentum outer jet fluid entrained more of the inner jet fluid, while the reverse happened for low J flows. The apparent “necking” in the dark-core flows profile that was described earlier, and is clearly visible in the average images, also became less severe with increasing J as less of the outer jet was pulled towards the center. For $J = 2.1$, the POM image in Figure 5.14c shows distinct antisymmetric structures denoting the presence of helical disturbances, and the CPSD magnitude shows a low frequency peak. The higher momentum flux ratio cases, $J = 5.7 - 21$, in Figure 5.14d-g also show antisymmetric structures. However, unlike the LAR-thin flows, the peaks in the magnitude spectra stayed at low frequencies.

At $P_r = 1.05$, the average images in Figures 5.15a,b for $J = 0.1$ and $J = 0.5$ show that the recirculation zone was filled with dark fluid, unlike their counterparts at $P_r = 0.44$, implying relatively more inner jet fluid was entrained into the recirculation zone. The antisymmetric structures in the POM images were not well-defined, and had low characteristic frequencies denoted by the low frequency peaks in the magnitude spectra. As J increased, antisymmetric structures became the dominant form of disturbances as the POM images in Figures 5.15c-g show. Similar to the SAR-thick flows at $P_r = 0.44$, the peaks in the magnitude spectra stayed at low frequencies.

Clearly, one of the main differences between the two injectors’ baseline flows was the spectral nature of the dominant periodic antisymmetric structures with increasing J . The LAR-thin injector flows had structures with peak frequencies that became broader and moved to higher frequencies as J increased. Unlike a single jet with a coflowing ambient fluid, the coaxial jet configuration in this study had finite area ratio due to the finite diameter outer jet. Nevertheless, the behavior of the instability peak frequencies agreed with analogous analytical results of Michalke and Hermann [48] that with

increasing coflow velocity, the region of unstable frequencies becomes broader and that the peak of the spatial growth rates shift to higher frequencies. On the contrary, as the CPSD magnitude spectra for the SAR injector flows show, the peak frequencies were unaffected by increasing J . This contradiction with the LAR-thin flow behavior may be explained by how soon the inner and outer jets attained a single jet behavior, thereby rendering the effect of coflow nonexistent.

Another notable outcome from the spectra was that the peak frequencies for the LAR-thin injector flows were not only dependent on R or J , but on the magnitude of the outer jet flowrate while the peaks for the SAR-thick injector flows were relatively insensitive to the changing outer jet flowrates. Note that at constant density and a fixed injector exit area, the effects of varying the jet mass flowrates may be regarded as equivalent to the effects of varying jet velocities. In order to investigate this, downstream convection velocities, U_s , of the dominant periodic structures depicted in the POM images were estimated based on the relation $U_s = \lambda f_s$, where λ is the wavelength measured from the images, and f_s is the characteristic frequency. The frequency, f_s , was obtained from the frequency that corresponded to the maximum CPSD magnitude that was closest to a CPSD phase of $\pm 90^\circ$ as illustrated in Figure 4.12. The estimated U_s along with exit velocity of the inner jet, outer jet, and their mean are shown in Figures 5.16 and 5.17 for the two injectors at $P_r = 0.44$ and $P_r = 1.05$, respectively. For uniform density coaxial jets, the inner shear layer convection velocity may be approximated by the mean velocity. On the other hand, for variable density jets, as it is the case in this study, the shear-layer velocity is less than the mean velocity when the high-velocity jet is less dense [42]. The estimated values of U_s for both the LAR and SAR injector flows depict this. However, U_s for the LAR-thin injector flow appeared to closely depend on the magnitude of U_o more than those for SAR-thick injector flow did. This may be an indication that in the LAR-thin geometry, the outer jet governed the dynamics of the inner shear layer structures. However, further investigation will need to be done to

generalize this outcome.

The Strouhal numbers of the periodic flow structures were also estimated based on D_1 , and the mean of the outer and inner jet exit velocities as $St_{D_1} = 2f_s D_1 / (U_o + U_i)$. Figure 5.18 shows St_{D_1} for varying J of the LAR-thin and SAR-thick injector flows at both P_r . It can be seen that all St_{D_1} values were within 10% of about 0.1 for the range of J explored. The absence of significant variation in St_{D_1} may suggest the lack of transition in the flow instability regime. The literature shows that St based on the shear-layer thickness and shear layer convection velocity undergoes a dramatic increase as a convectively unstable flow transitions to a globally unstable flow; future experiments could investigate this potential transition in more detail.

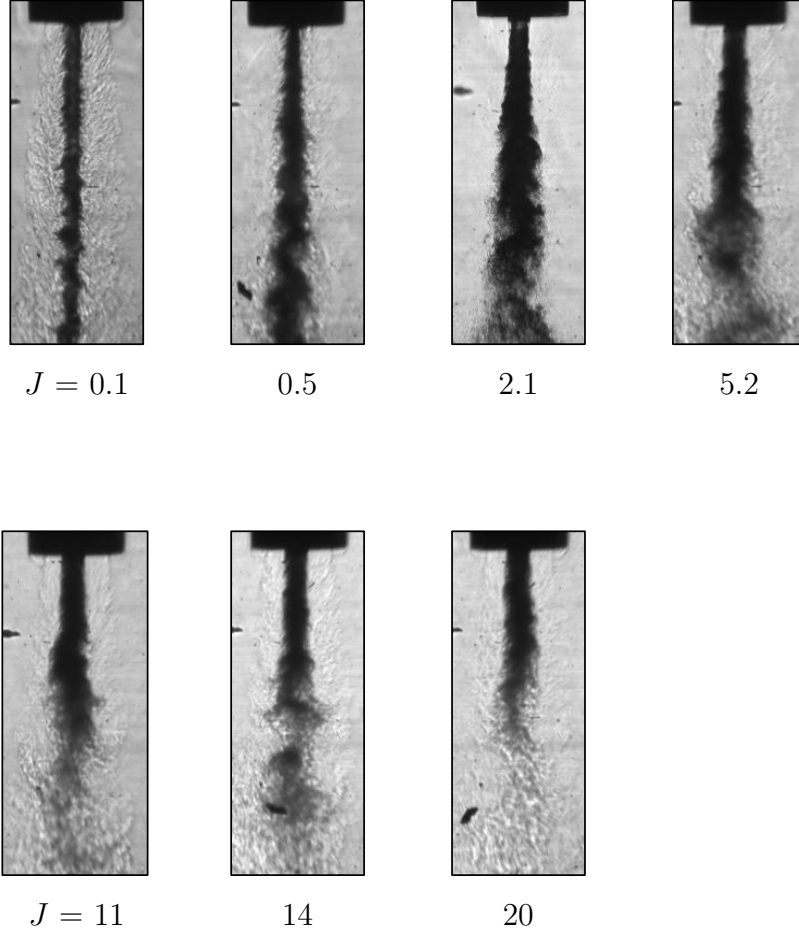


Figure 5.1: Back-lit images of the LAR-thin injector baseline flow at $P_r = 0.44$ and varying J . The image framing rate was 25 kHz. At subcritical chamber pressure, the inner jet was in the liquid state while the outer jet was in the gaseous state. Table C.1 gives a summary of the flow conditions.

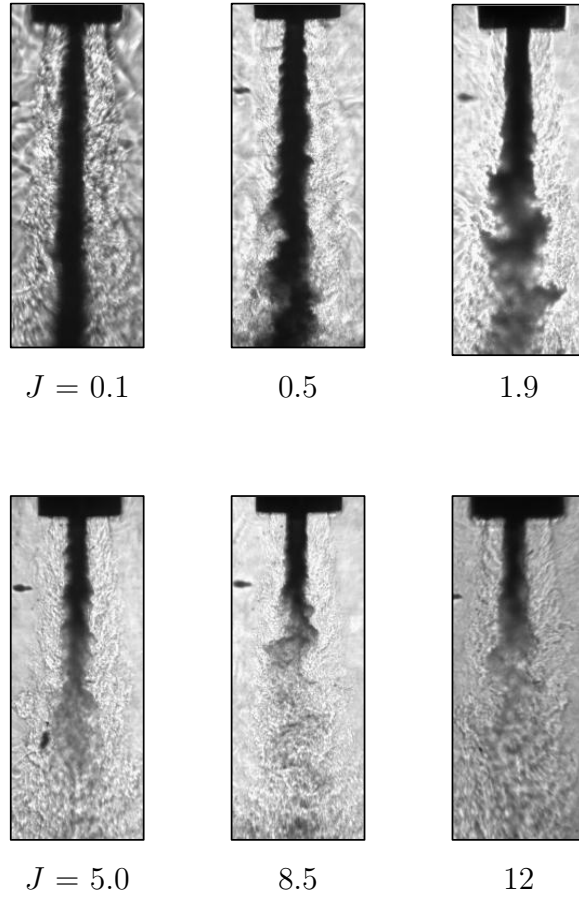


Figure 5.2: Back-lit images of the LAR-thin injector baseline flow at $P_r = 1.05$ and varying J . The image framing rate was 25 kHz. At nearcritical chamber pressure, the inner jet was a transcritical fluid while the outer jet was a supercritical fluid. Table C.1 gives a summary of the flow conditions.

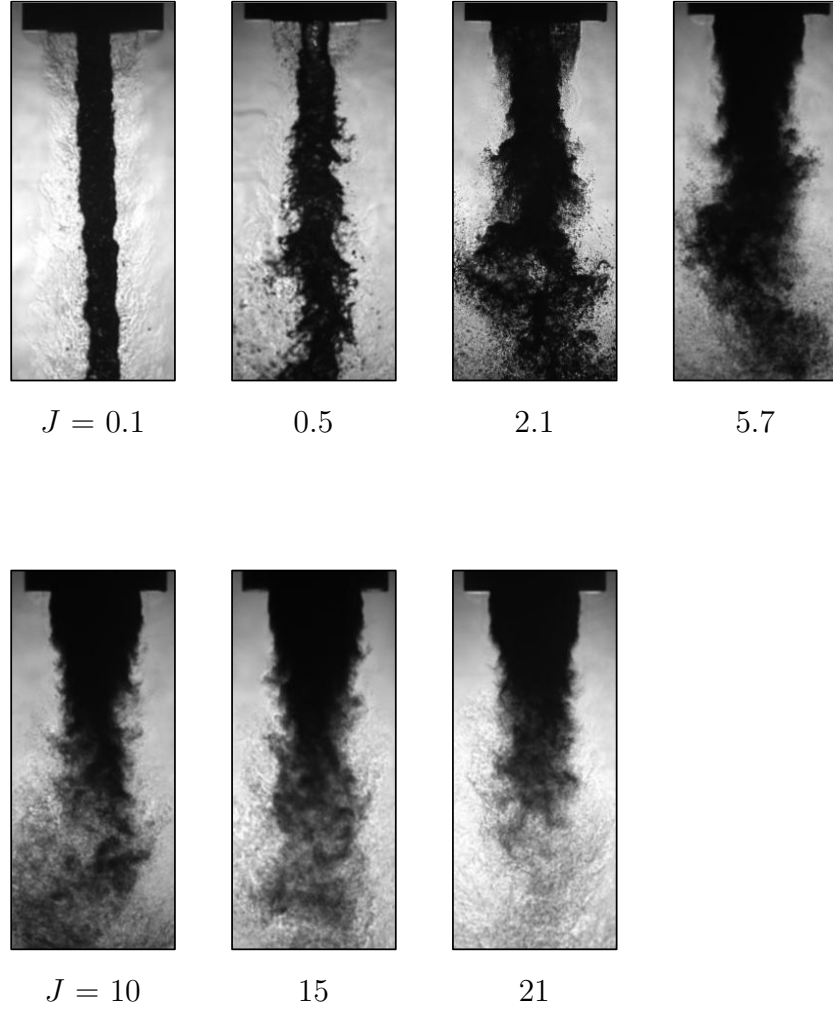


Figure 5.3: Back-lit images of the SAR-thick injector baseline flow at $P_r = 0.44$ and varying J . The image framing rate was 25 kHz. At subcritical chamber pressure, the inner jet was in the liquid state while the outer jet was in the gaseous state. Table C.2 gives a summary of the flow conditions.

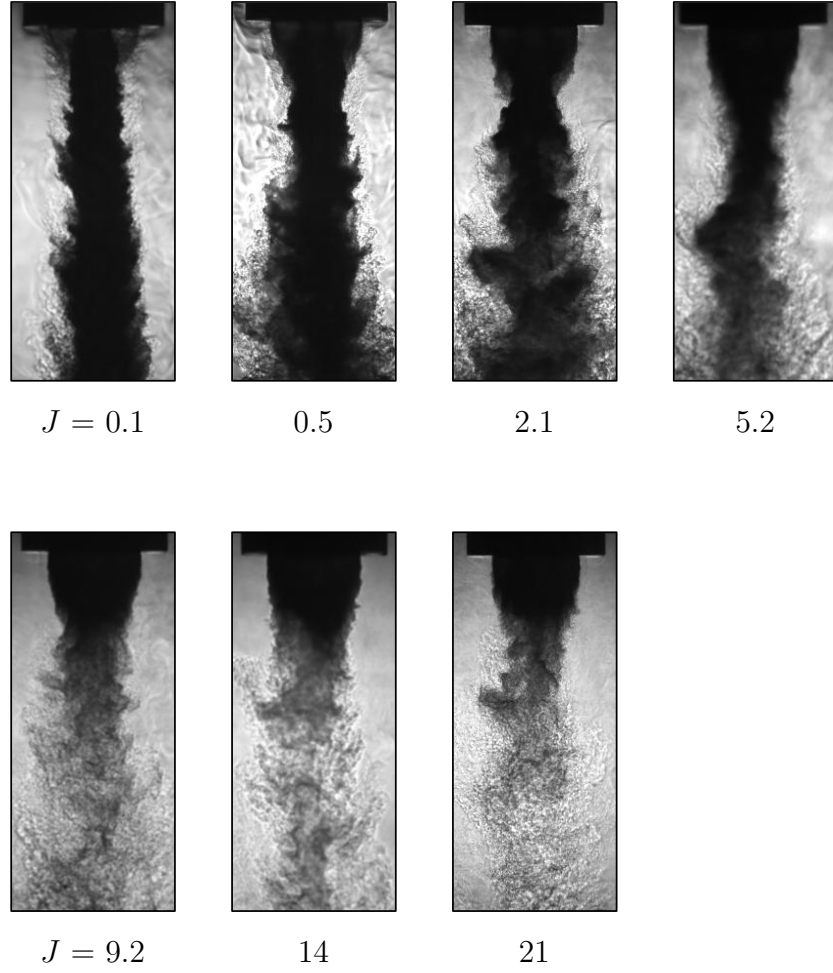


Figure 5.4: Back-lit images of the SAR-thick injector baseline flow at $P_r = 1.05$ and varying J . The image framing rate was 25 kHz. At nearcritical chamber pressure, the inner jet was in a transcritical fluid while the outer jet was a supercritical fluid. Table C.2 gives a summary of the flow conditions.

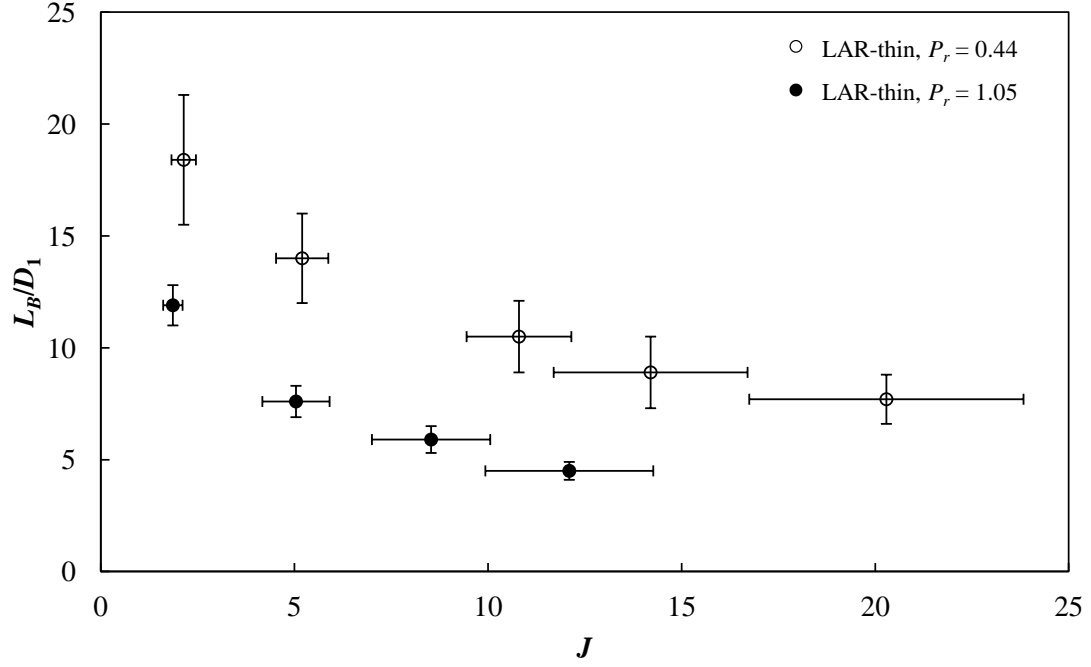


Figure 5.5: Measurements of the LAR-thin injector baseline flows dark-core lengths, L_B normalized by the inside diameter of the inner injector, D_1 . The vertical error bars represent the uncertainty in a single measurement to within 2σ of the mean for 1000 measurements. The horizontal error bars represent the bias errors in the measurement of J . The large errors at higher J values were mainly due to the large relative uncertainties ($\delta\dot{m}_i/\dot{m}_i$) in the low inner jet flowrate measurements.

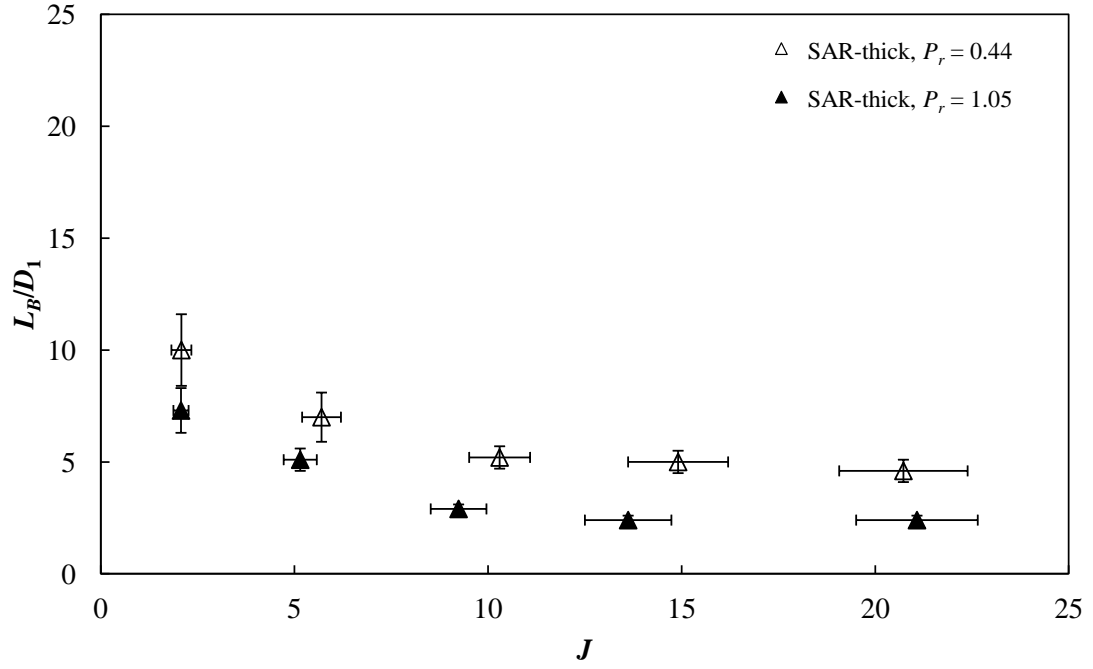


Figure 5.6: Measurements of the SAR-thick injector baseline flows dark-core lengths, L_B normalized by the inside diameter of the inner injector, D_1 . The vertical error bars represent the uncertainty in a single measurement to within 2σ of the mean for 1000 measurements. The horizontal error bars represent the bias errors in the measurement of J .

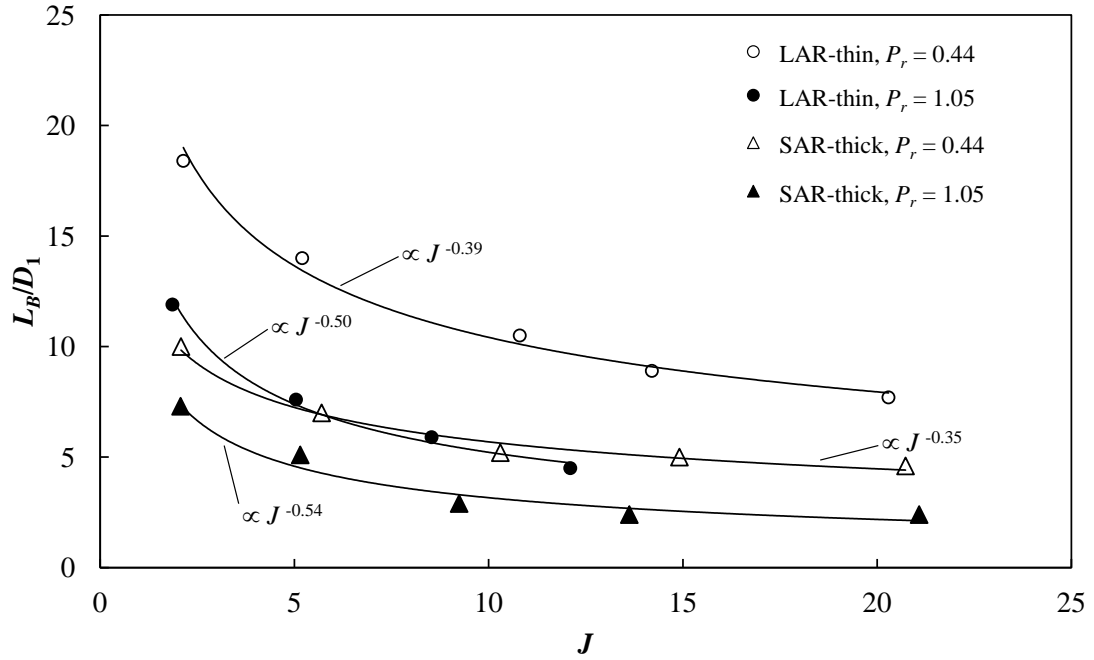


Figure 5.7: A power-law curve-fit to the L_B/D_1 data plotted in Figures 5.6 and 5.5. The variation of L_B/D_1 with J was similar for both injector flows in the same pressure regime. In addition, the SAR-thick injector L_B/D_1 were consistently lower than the LAR-thin injector, and those at $P_r = 1.05$ were lower than at $P_r = 0.44$.

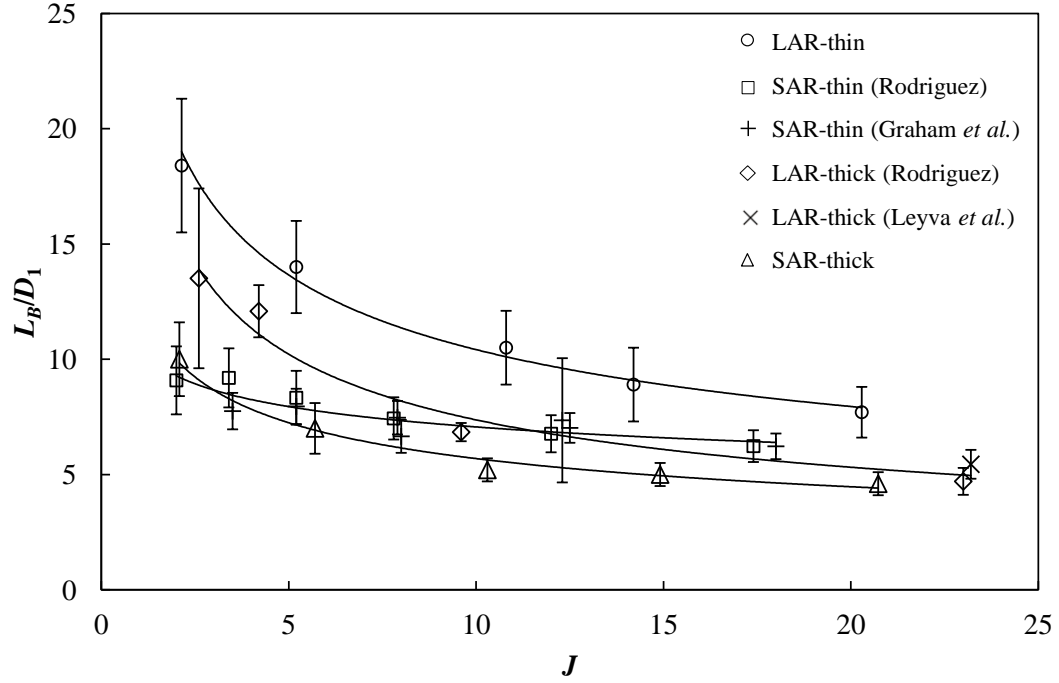


Figure 5.8: Measured L_B/D_1 at $P_r = 0.44$ using different injector configurations including those used by Rodriguez [22], Graham *et al.* [70], and Leyva *et al.* [46]. The dimensions of the LAR-thick and SAR-thin injectors are given in Table 1.2.

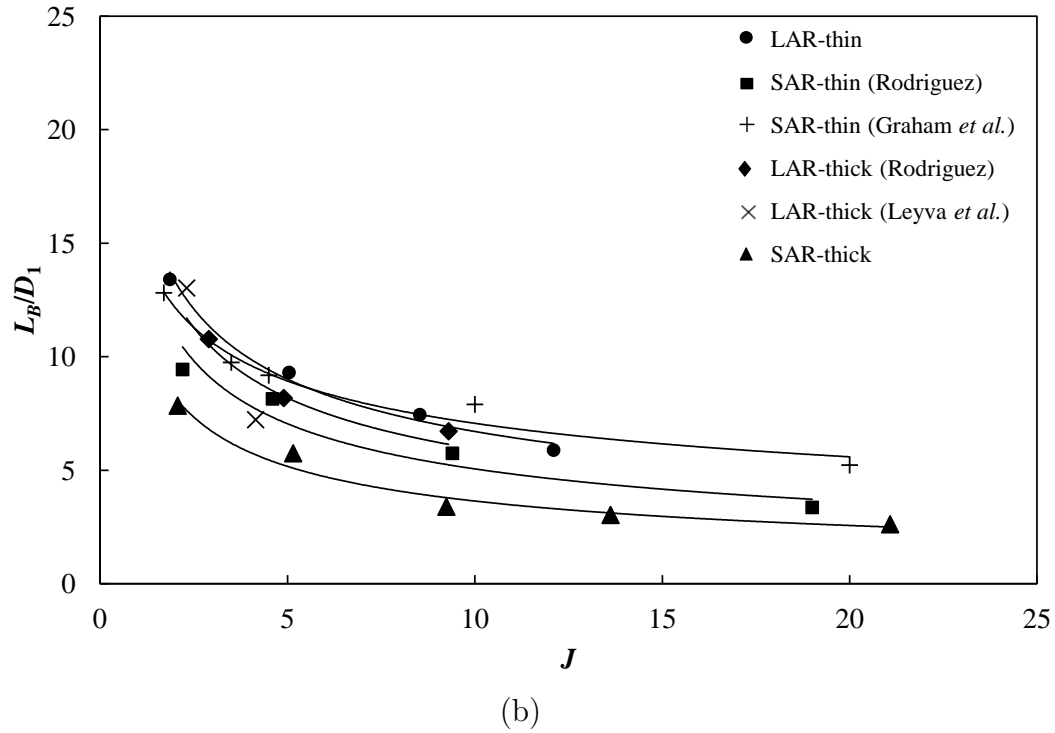
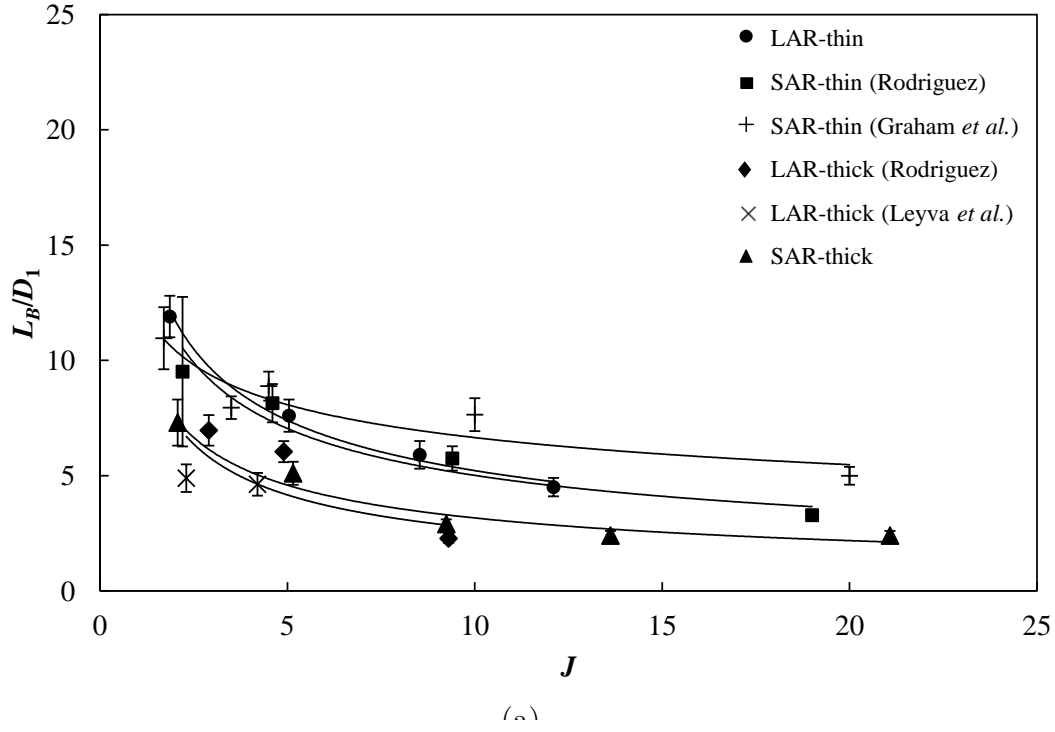


Figure 5.9: Measured L_B/D_1 (a) without adjustment and (b) with adjustment to $T_i = 109$ K, at $P_r = 1.05$ using different injector configurations including those used by Rodriguez [22], Graham *et al.* [70], and Leyva *et al.* [46]. The dimensions of the LAR-thick and SAR-thin injectors are given in Table 1.2.

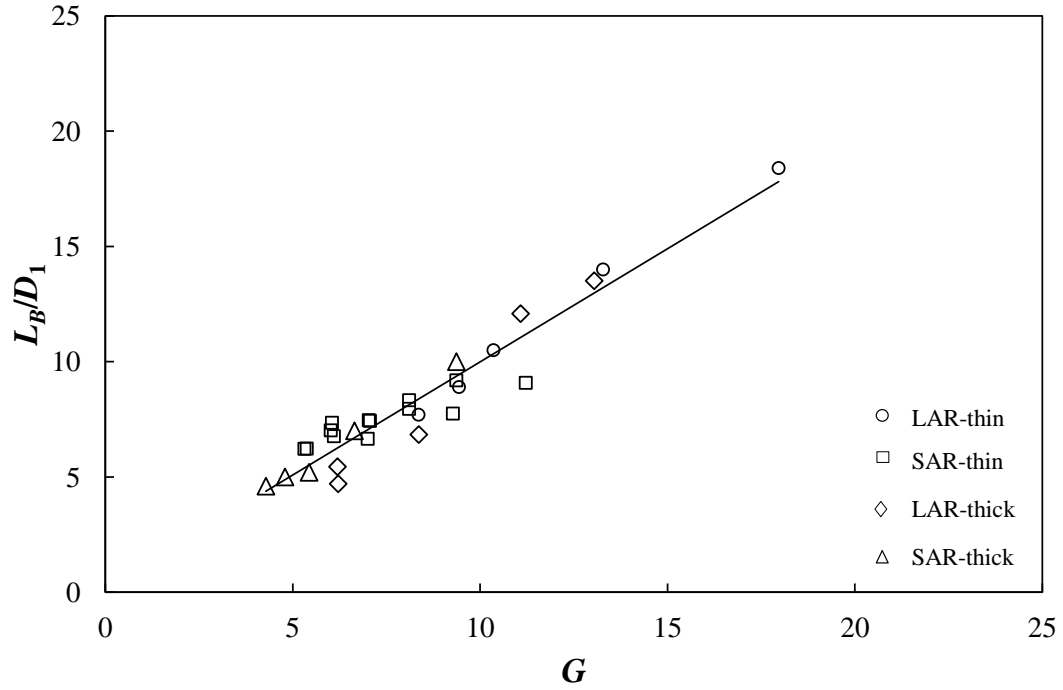


Figure 5.10: Measured L_B/D_1 for the different injectors at $P_r = 0.44$ plotted versus $G = c_1 J^{c_2} (t/D_1)^{c_3} (A_o/A_i)^{c_4}$, where the constants were obtained using non-linear regression, and whose values are listed in Table 5.1. The linear fit with about unit slope indicated that the model was a good representation of the dependance of L_B/D_1 on J and the injector geometry.

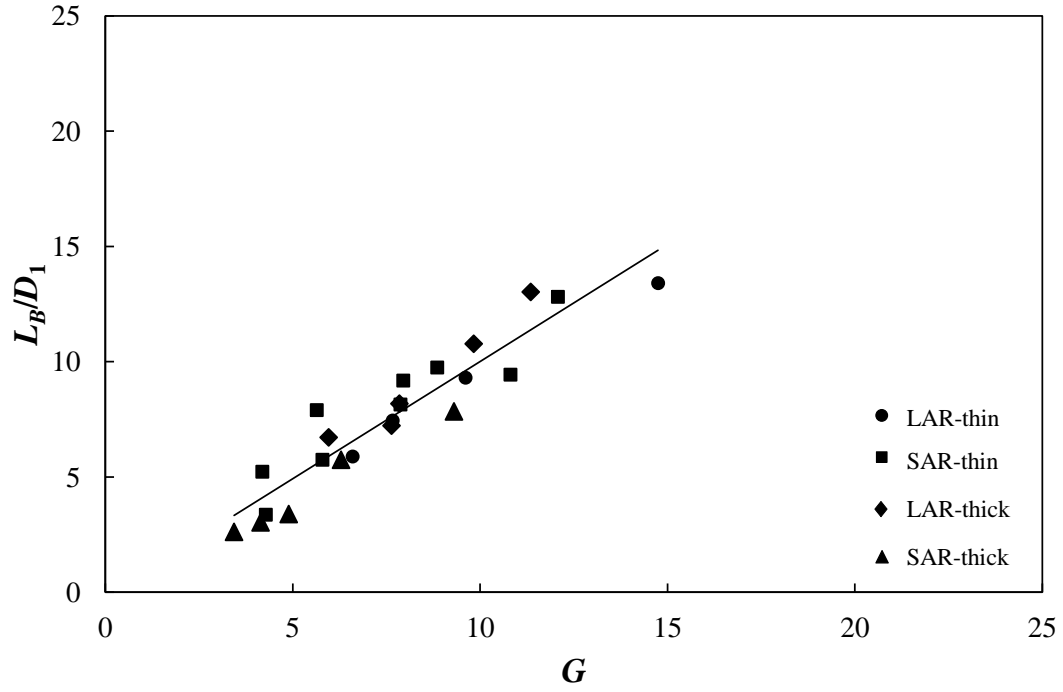


Figure 5.11: Measured L_B/D_1 for the different injectors at $P_r = 1.05$ plotted versus $G = c_1 J^{c_2} (t/D_1)^{c_3} (A_o/A_i)^{c_4}$, where the constants were obtained using non-linear regression, and whose values are listed in Table 5.1. The linear fit with about unit slope indicated that the model was a good representation of the dependance of L_B/D_1 on J and the injector geometry.

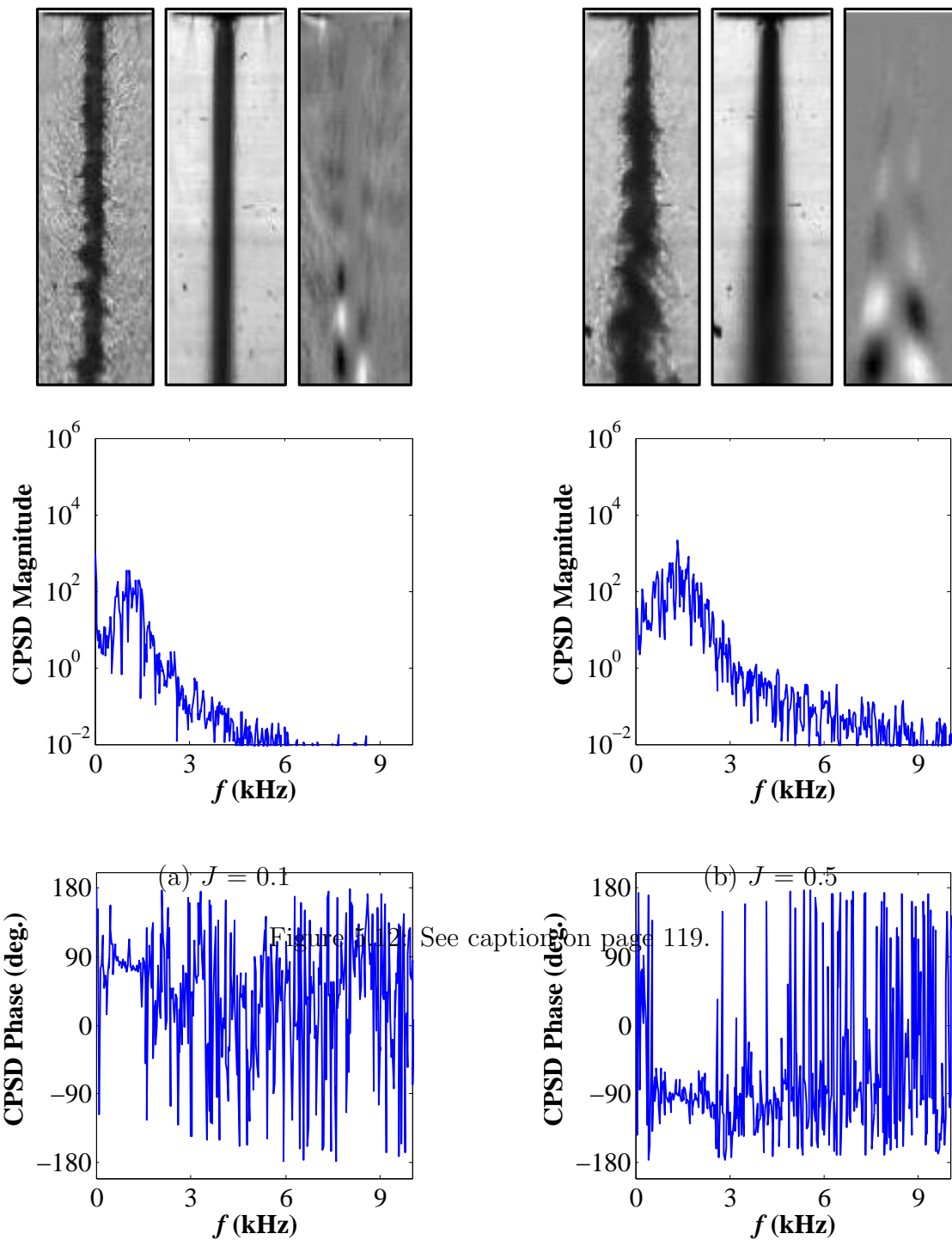
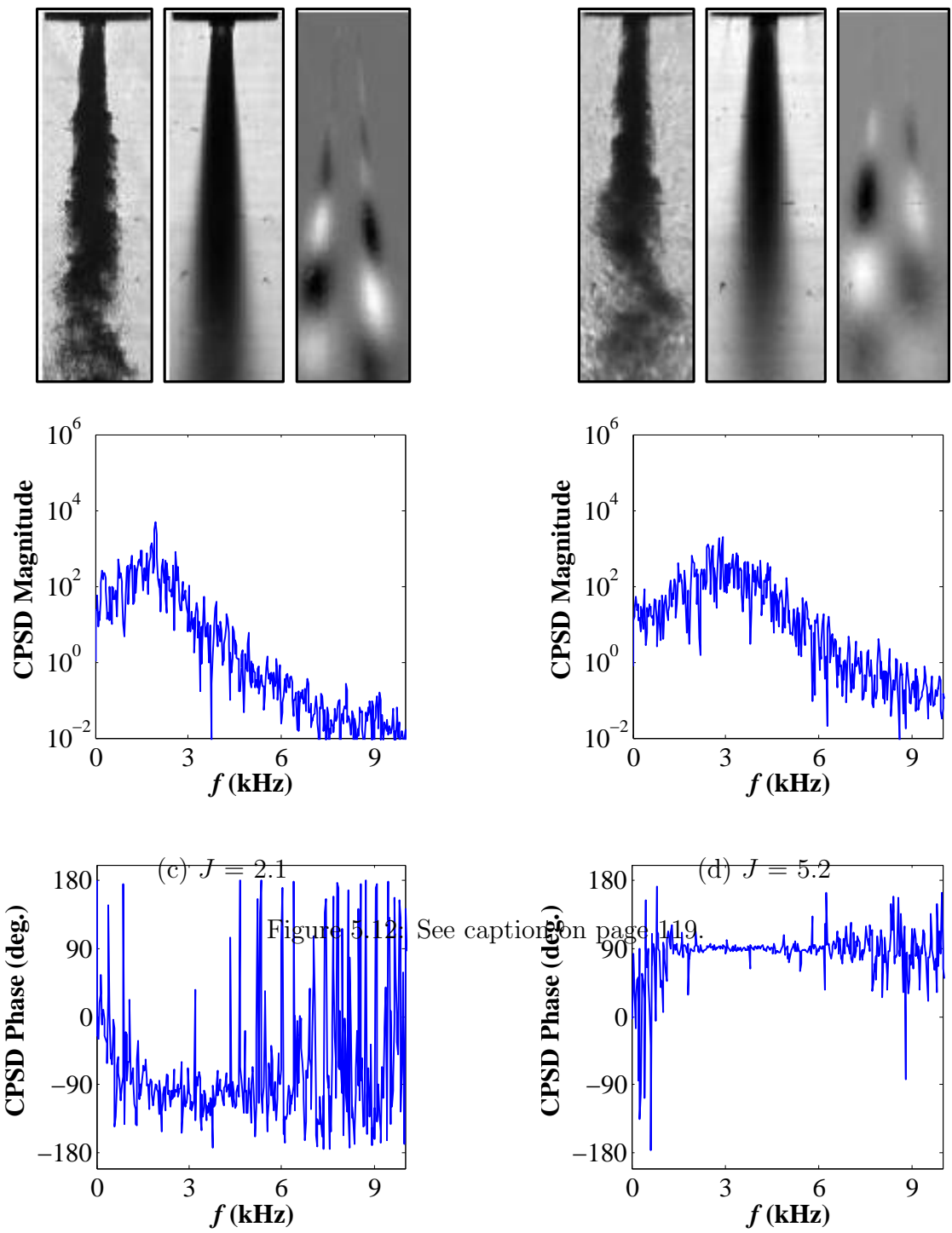


Figure 5.12: See caption on page 119.



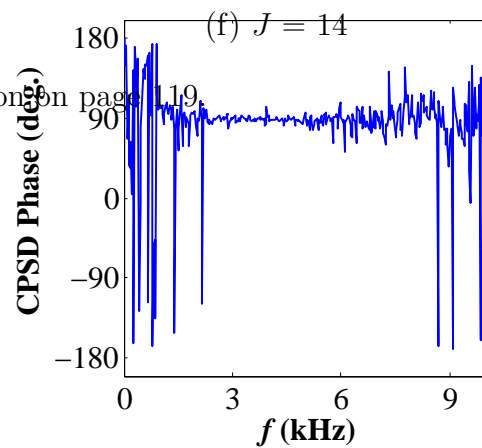
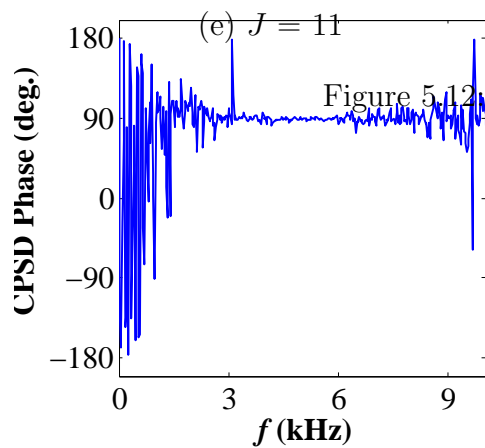
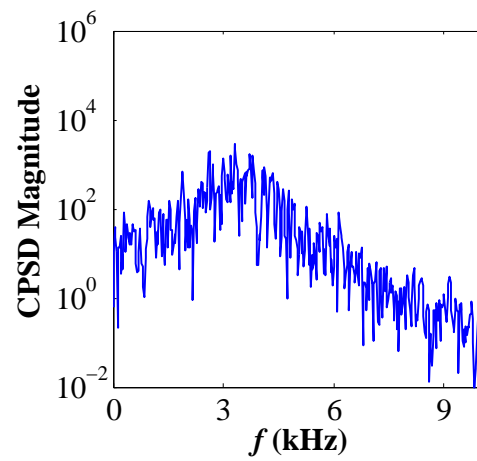
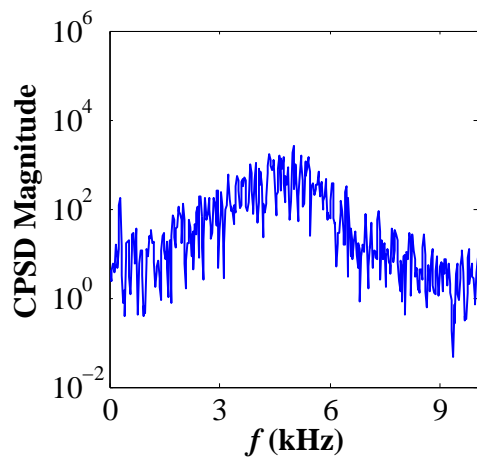
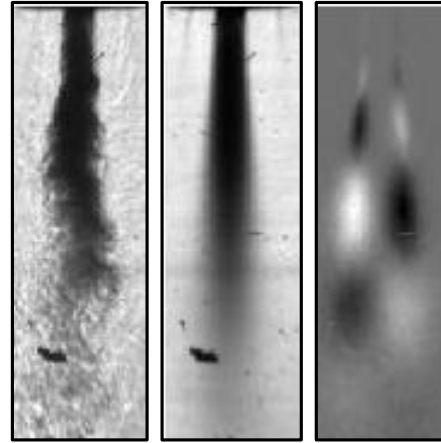
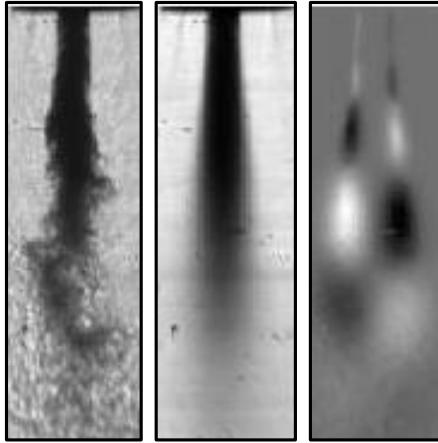


Figure 5.12: See caption on page 119.

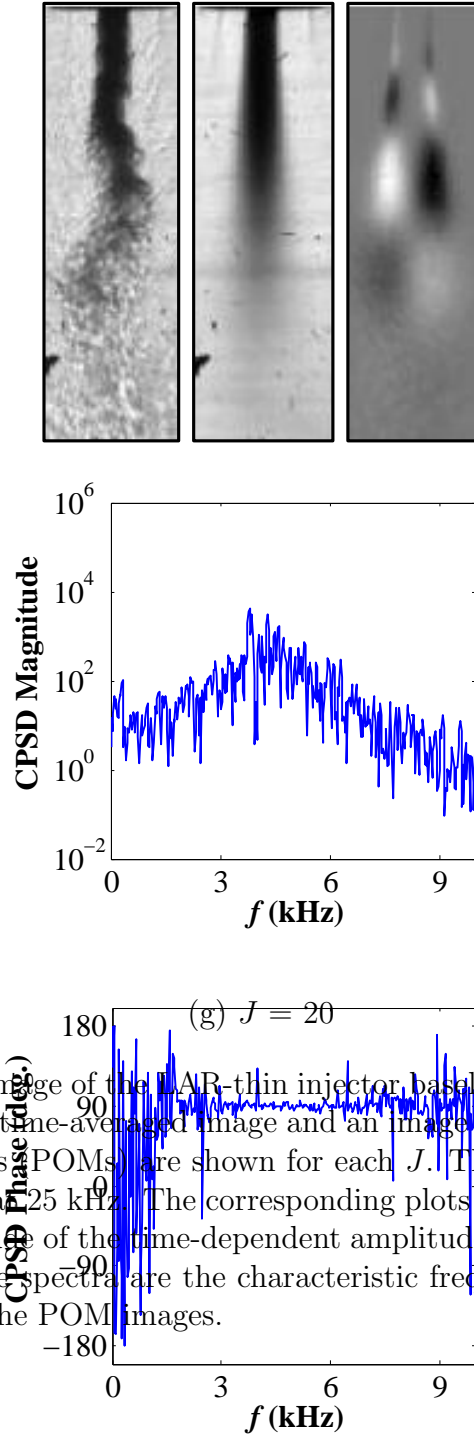


Figure 5.12: A back-lit image of the LAR-thin injector baseline flow at $P_r = 0.44$ similar to those in Figure 5.1, a time-averaged image and an image of the superposed conjugate proper orthogonal modes (POMs) are shown for each J . The averaged image consisted of 1000 frames sampled at 25 kHz. The corresponding plots are the cross-power spectral density (CPSD) magnitude of the time-dependent amplitude coefficients of the conjugate modes. The peaks in the spectra are the characteristic frequencies of the periodic flow structures identified in the POM images.

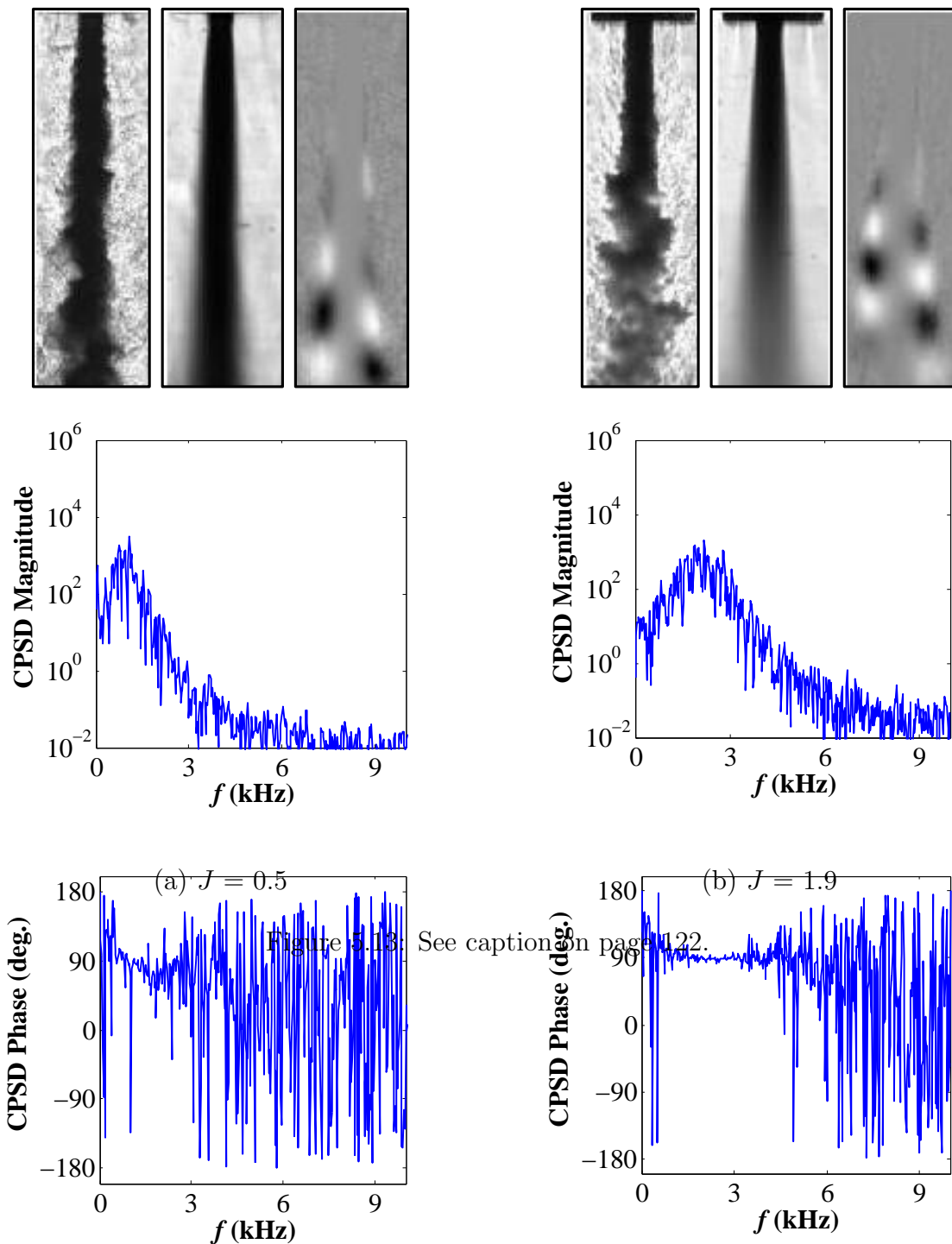


Figure 5.13: See caption on page 422.

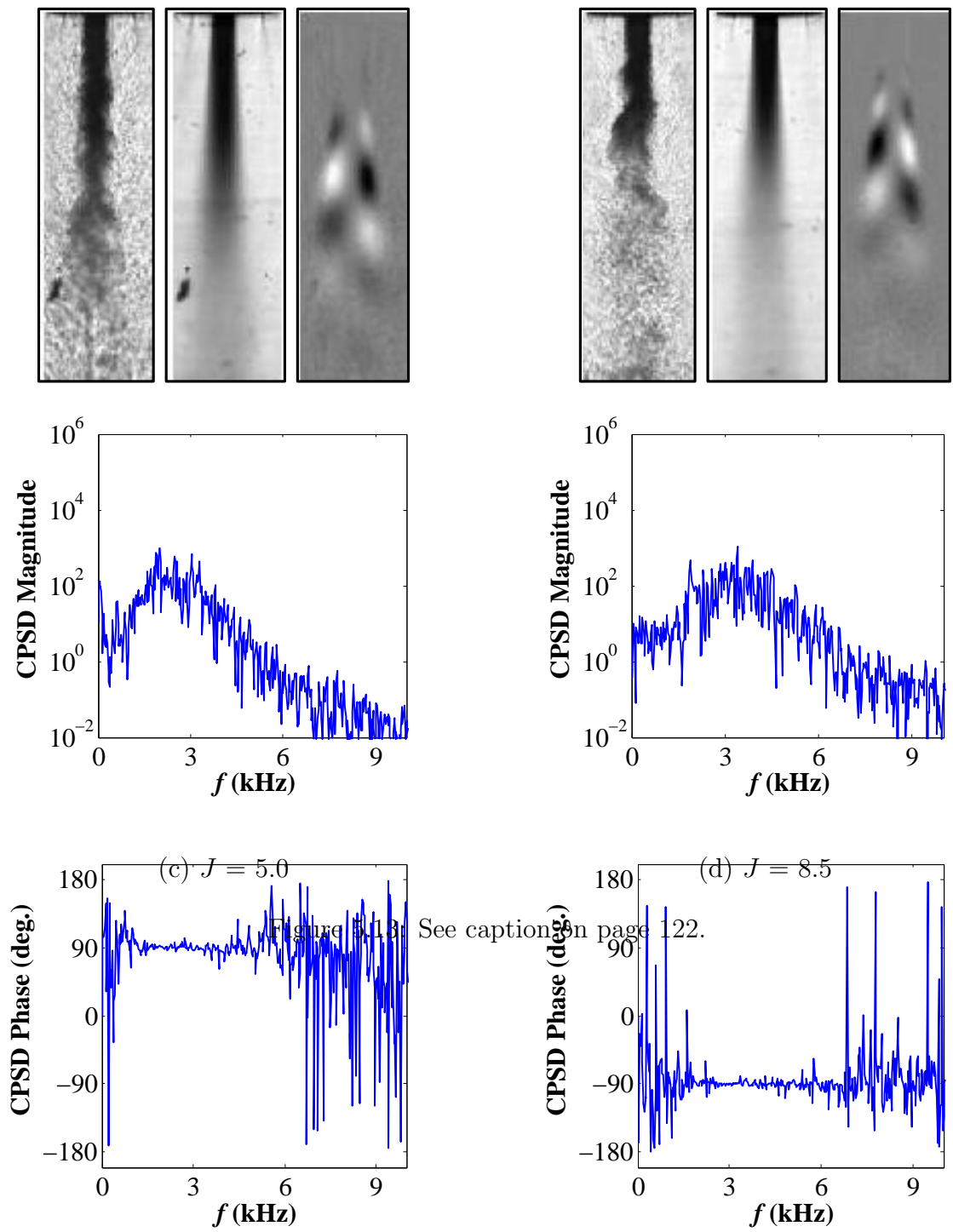
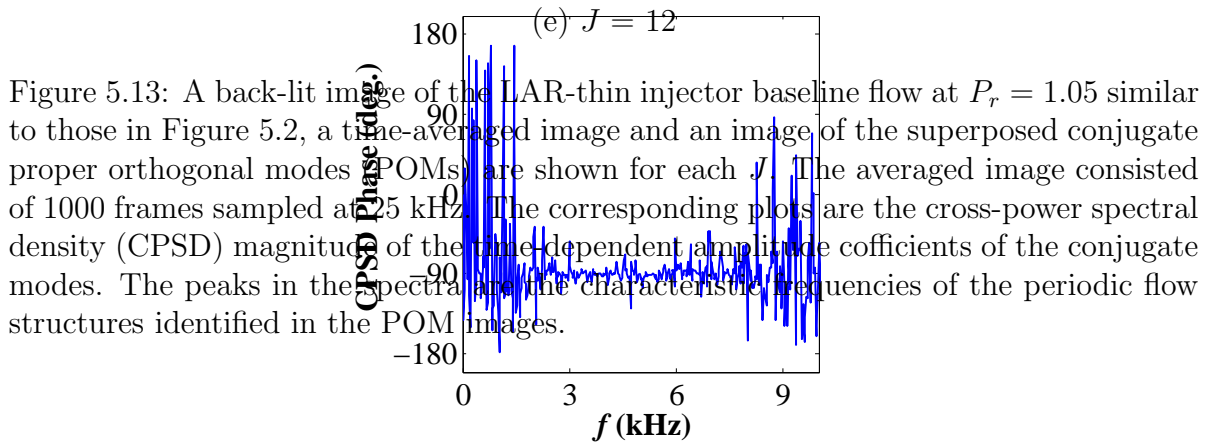
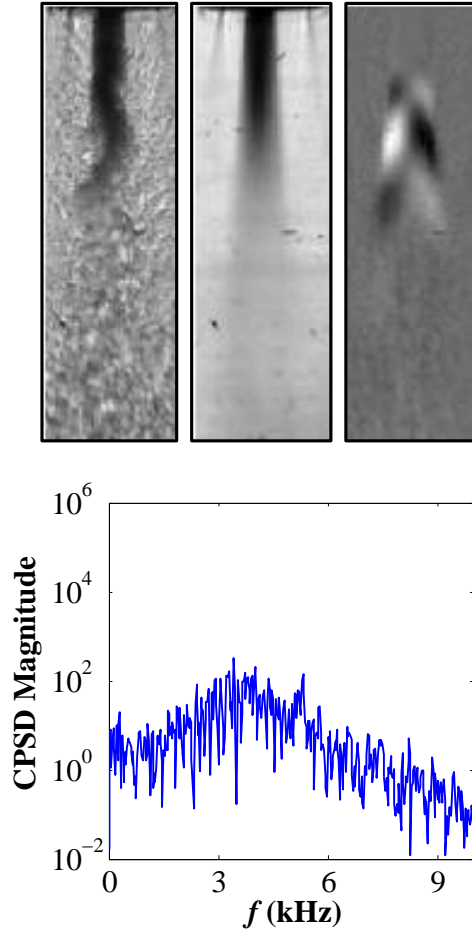


Figure 5.13: See caption on page 122.



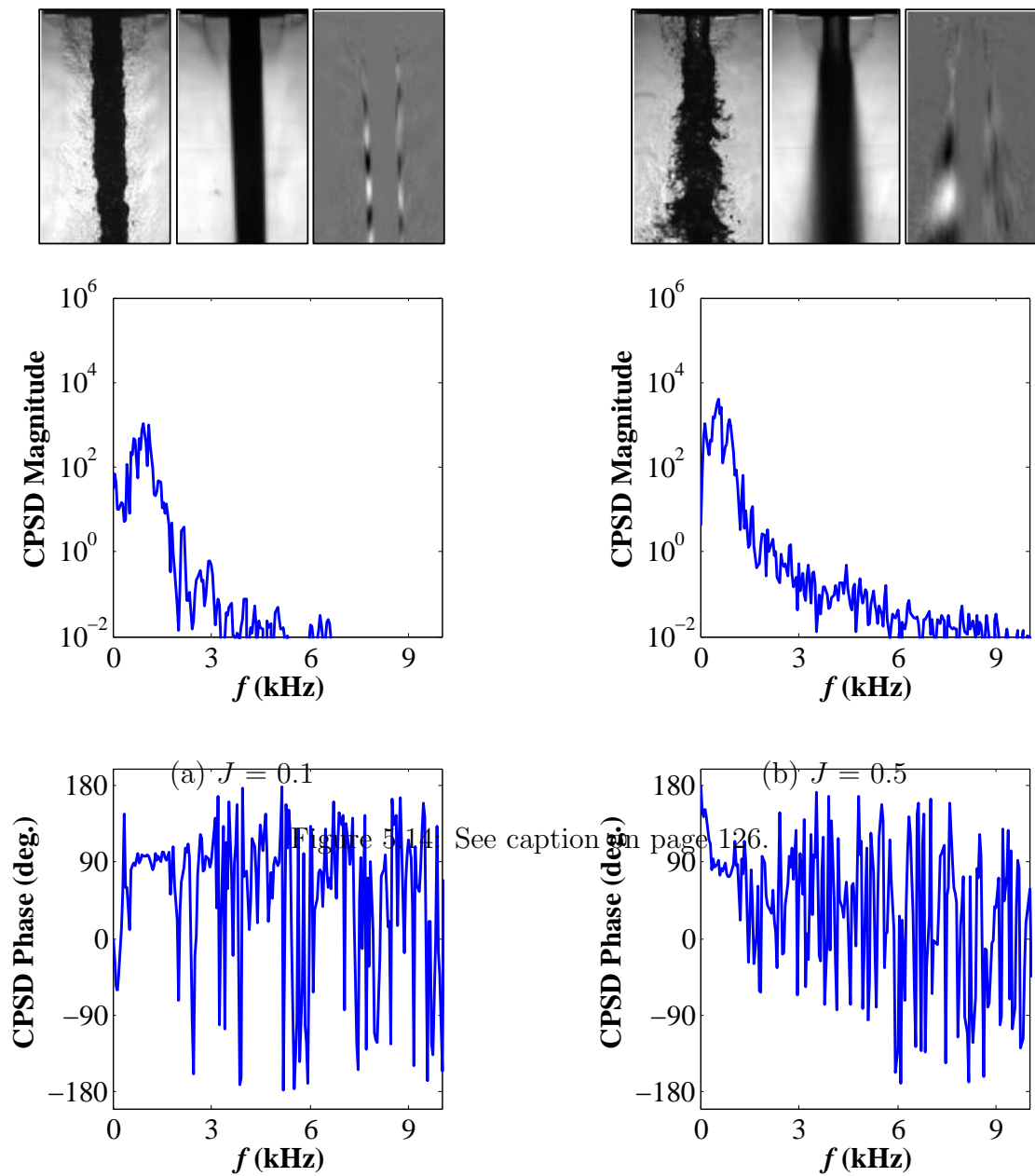
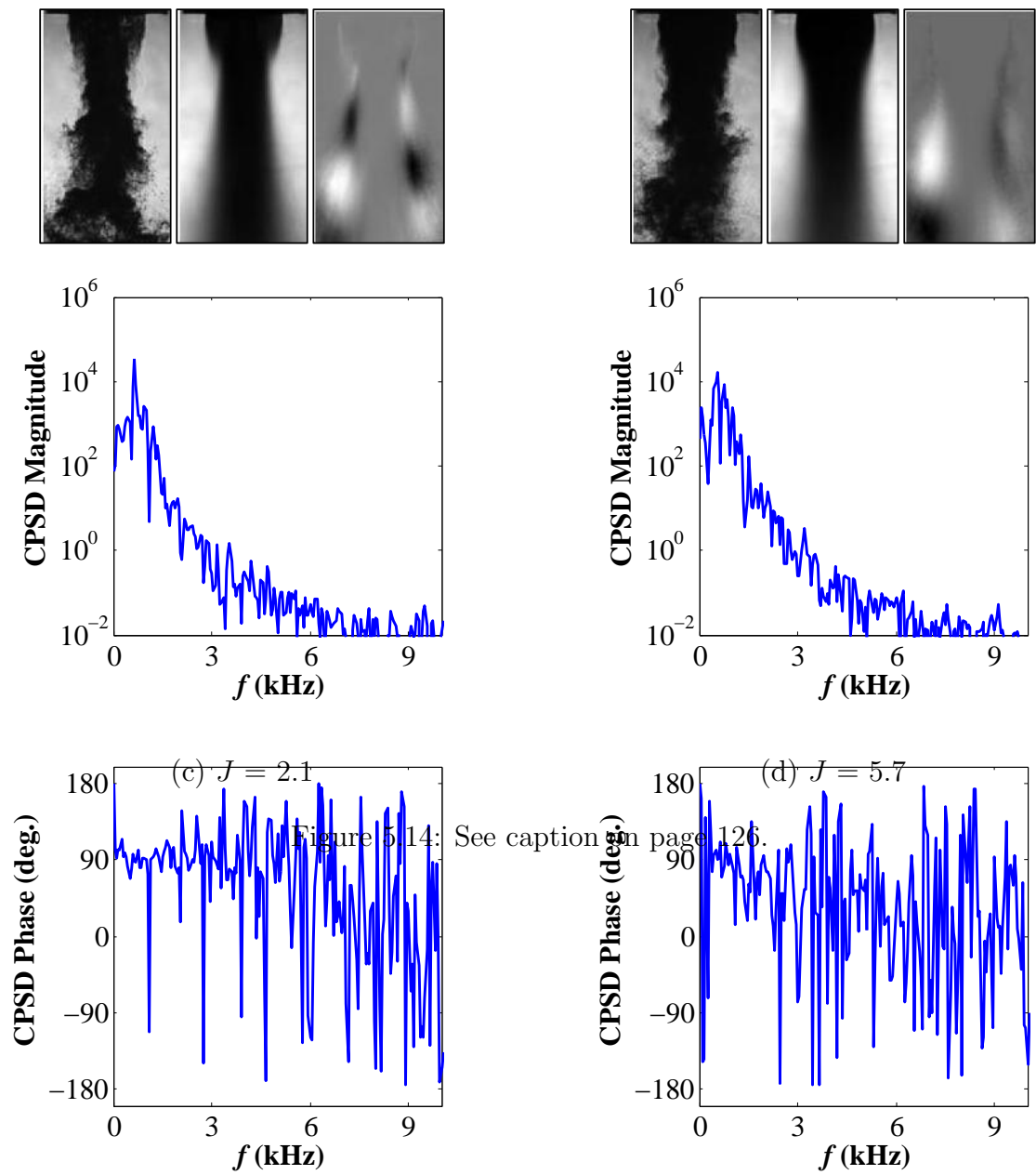
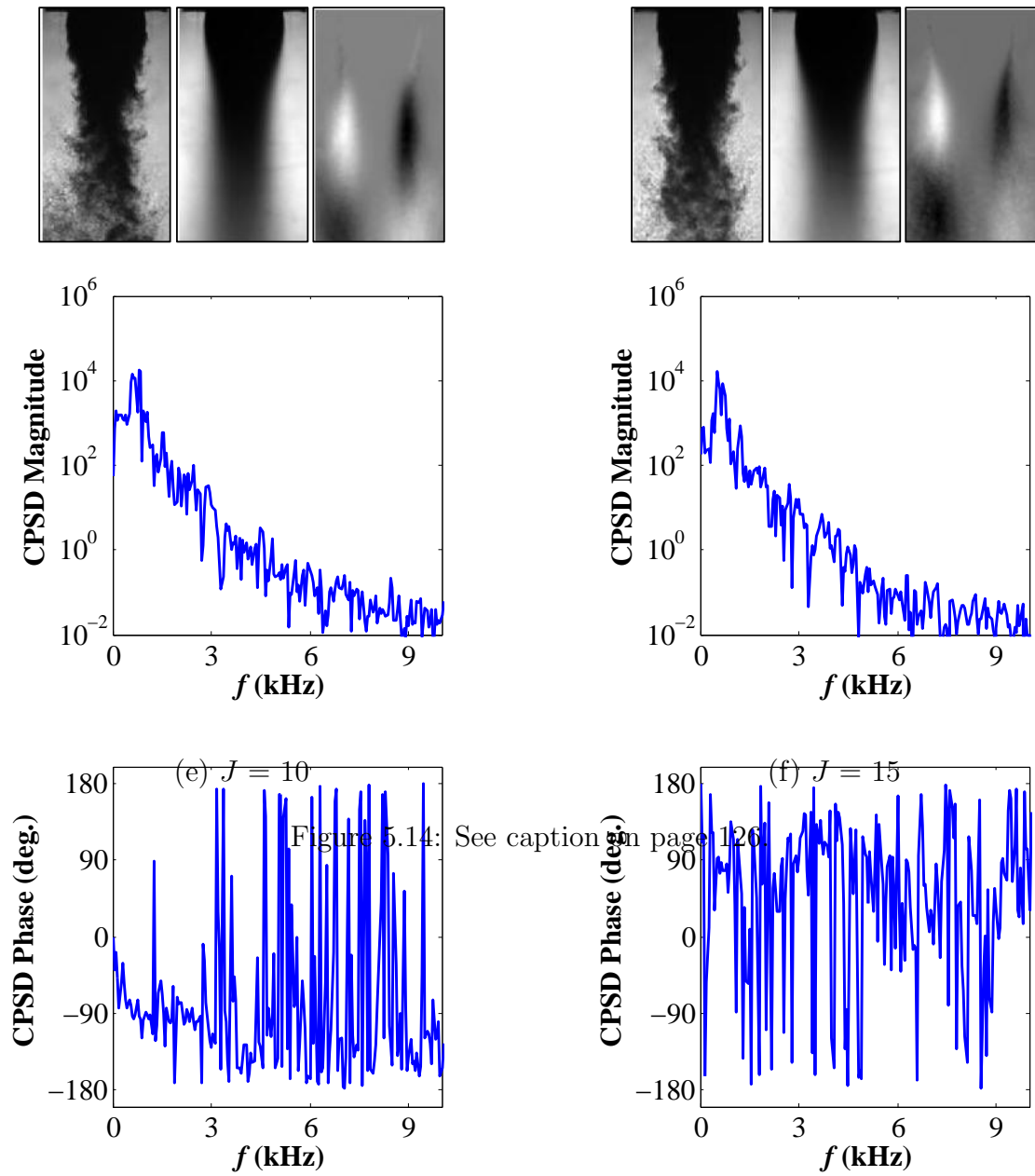


Figure 5.14: See caption on page 126.





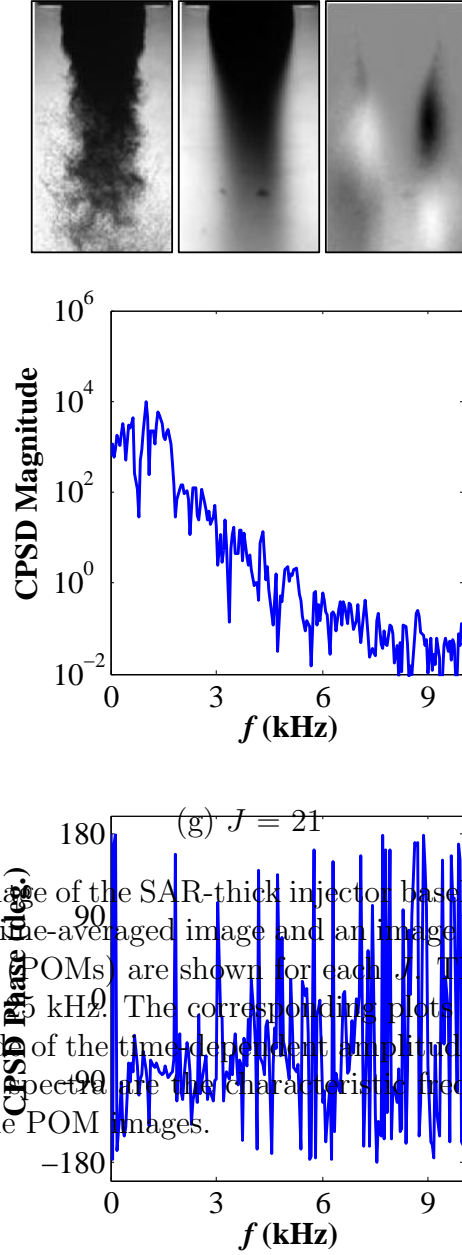
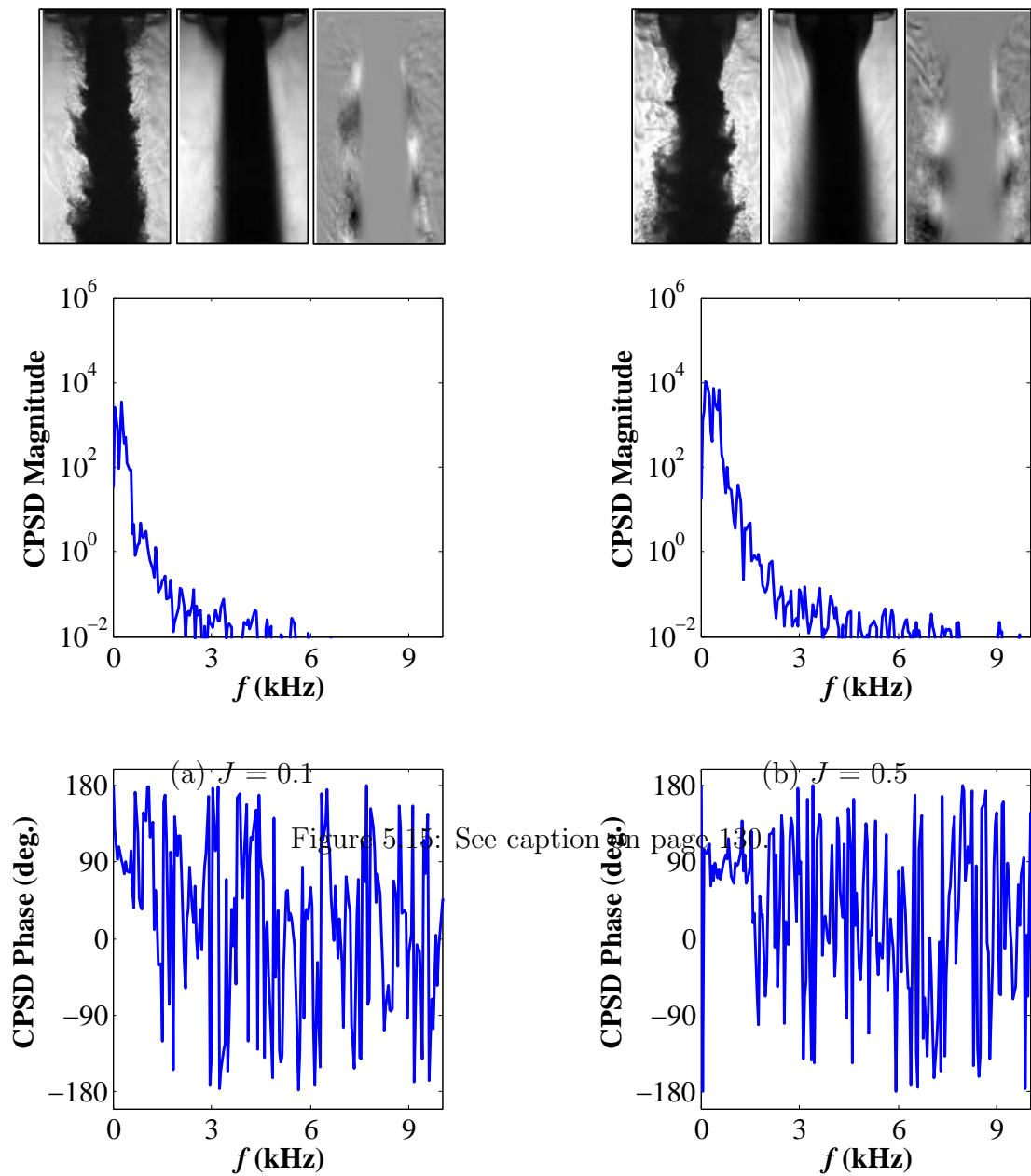
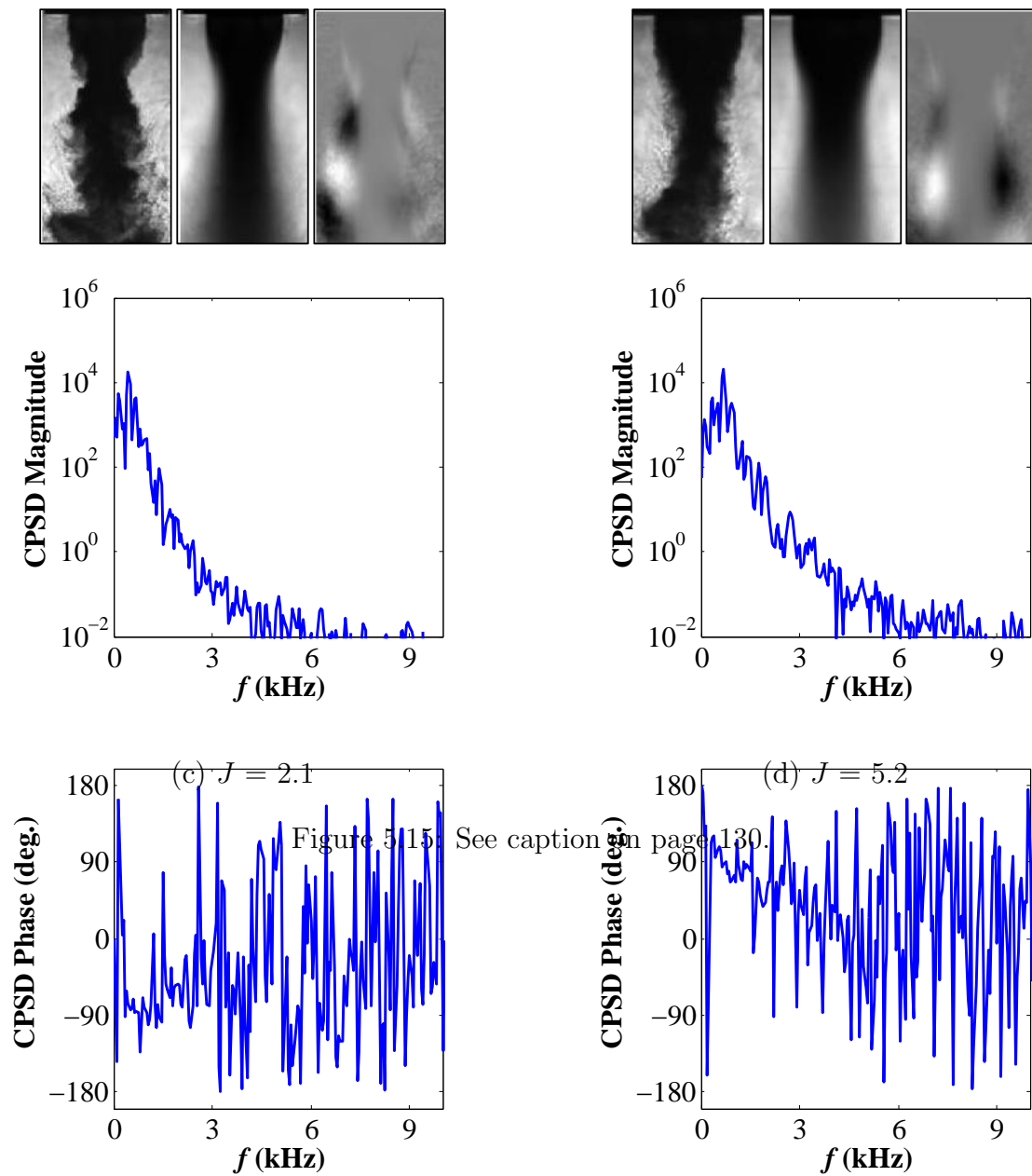


Figure 5.14: A back-lit image of the SAR-thick injector baseline flow at $P_r = 0.44$ similar to those in Figure 5.3, a time-averaged image and an image of the superposed conjugate proper orthogonal modes (POMs) are shown for each J . The averaged image consisted of 500 frames sampled at 10 kHz. The corresponding plots are the cross-power spectral density (CPSD) magnitude of the time-dependent amplitude coefficients of the conjugate modes. The peaks in the spectra are the characteristic frequencies of the periodic flow structures identified in the POM images.





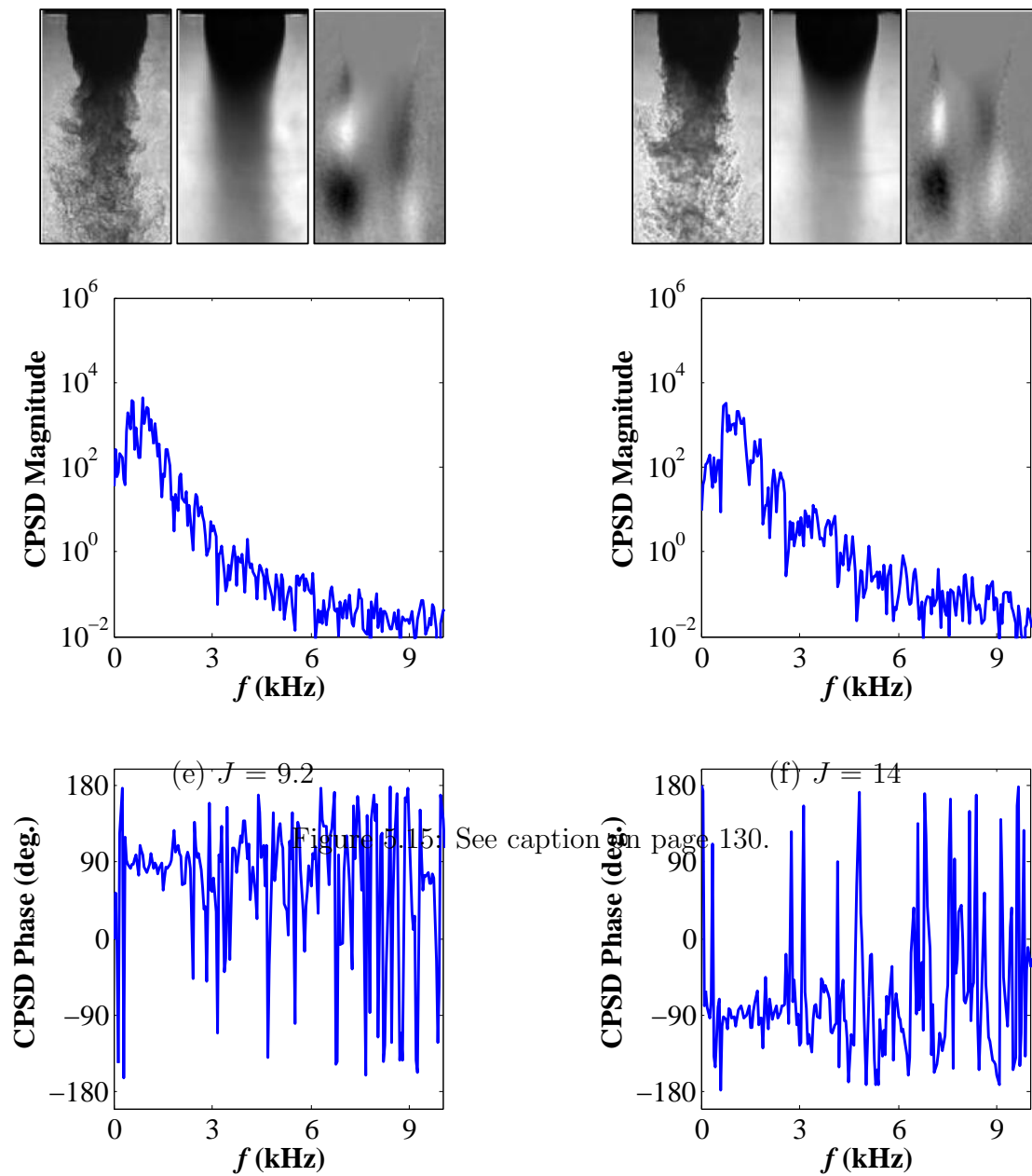


Figure 5.15: See caption on page 130.

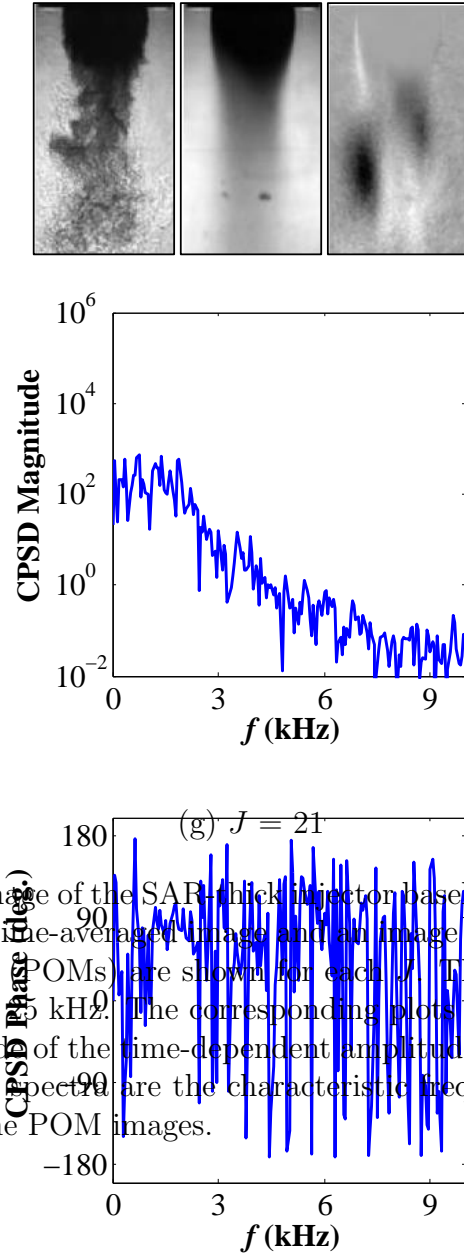
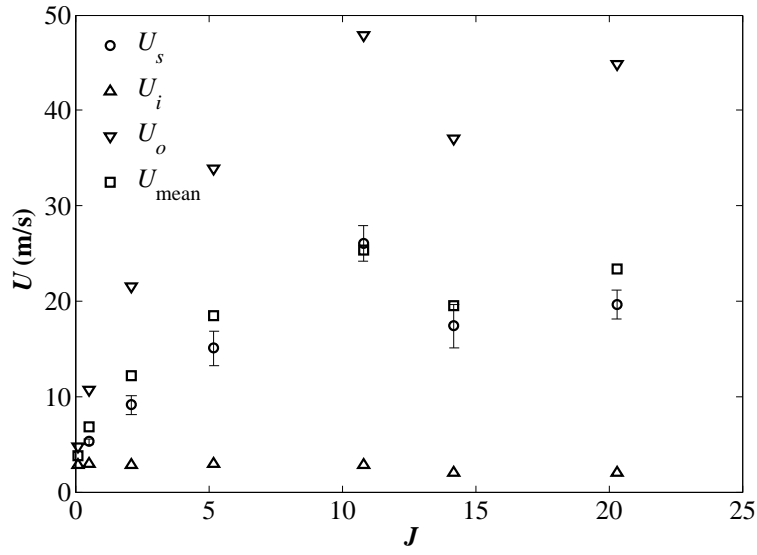
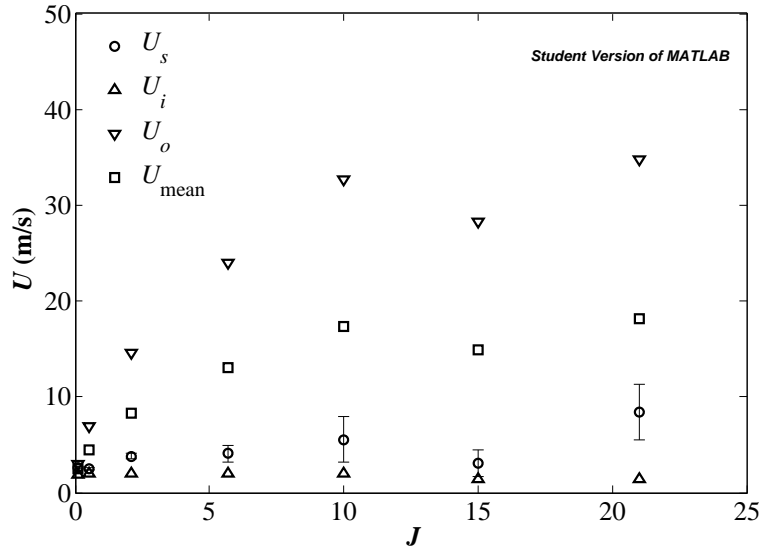


Figure 5.15: A back-lit image of the SAR-chick injector baseline flow at $P_r = 1.05$ similar to those in Figure 5.4, a time-averaged image and an image of the superposed conjugate proper orthogonal modes (POMs) are shown for each J . The averaged image consisted of 500 frames sampled at 15 kHz. The corresponding plots are the cross-power spectral density (CPSD) magnitude of the time-dependent amplitude coefficients of the conjugate modes. The peaks in the spectra are the characteristic frequencies of the periodic flow structures identified in the POM images.

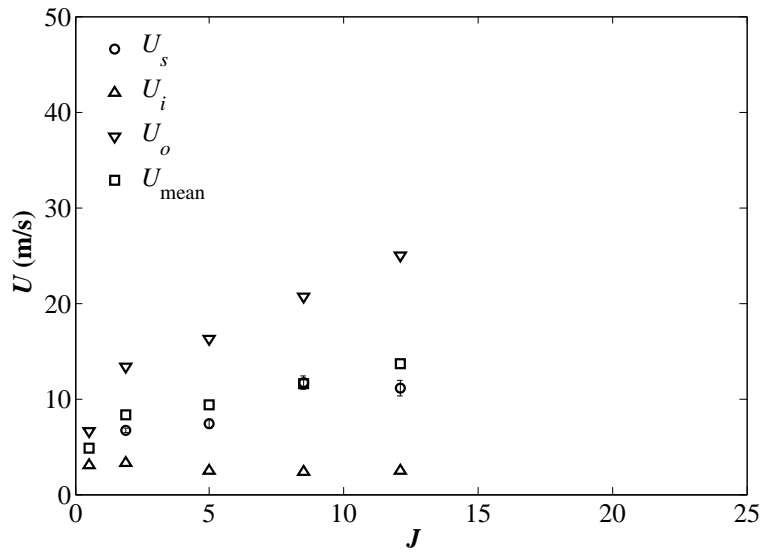


(a) LAR-thin

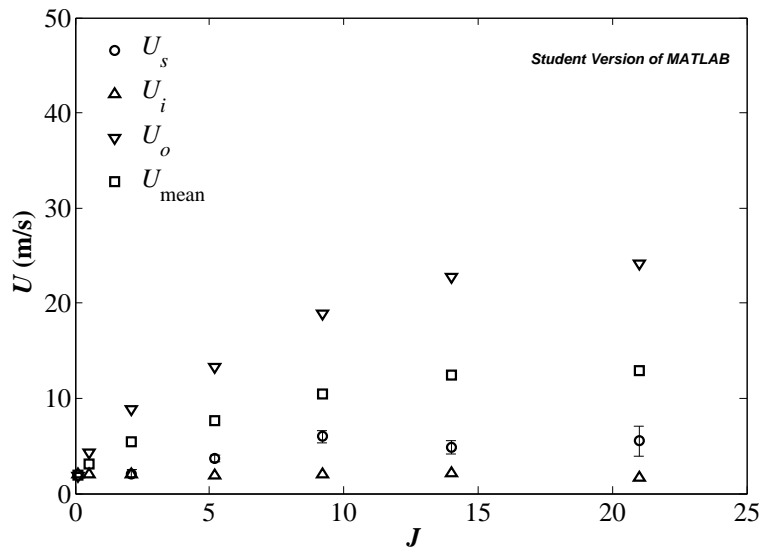


(b) SAR-thick

Figure 5.16: Plots of the outer jet exit velocities, U_o , inner jet exit velocities, U_i , their corresponding mean velocities, U_{mean} , and the estimated convection velocities of the dominant flow structures, U_s for the LAR-thin and SAR-thick injector flows at $P_r = 0.44$. It can be seen that the LAR-thin injector outer jet flow had more influence on the inner shear layer flow than did the SAR-thick outer jet flow.



(a) LAR-thin



(b) SAR-thick

Figure 5.17: Plots of the outer jet exit velocities, U_o , inner jet exit velocities, U_i , their corresponding mean velocities, U_{mean} , and the estimated convection velocities of the dominant flow structures, U_s for the LAR-thin and SAR-thick injector flows at $P_r = 1.05$. Again, it is clear that the LAR-thin injector outer jet flow had more influence on the inner shear layer flow than did the SAR-thick outer jet flow.

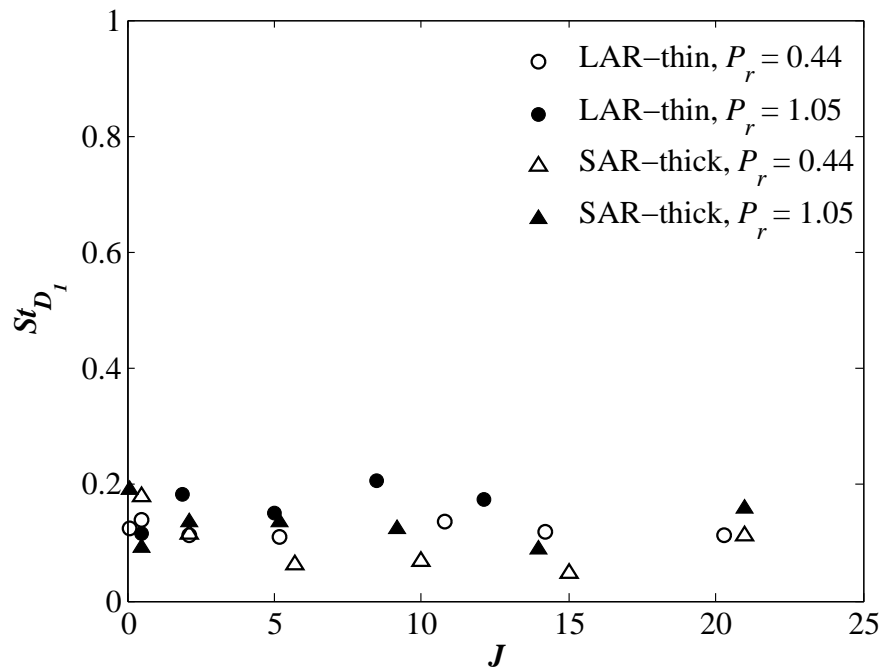


Figure 5.18: Comparison of Strouhal numbers, St_{D_1} , of the inner shear layer periodic flow structures based on the inner jet exit diameter, and the mean of the outer and inner jet exit velocities. All St_{D_1} for the LAR-thin and SAR-thick injector flows at both P_r remained within 10% of 0.1 for the different J values.

Student Version of MATLAB

5.2 Transverse Acoustic Forcing of Shear-Coaxial Jets

As described in Section 4.3, two types of transverse acoustic forcing conditions were investigated: a pressure antinode (PAN) and a pressure node (PN) at the coaxial jet location. A PAN condition created a region of locally maximum pressure fluctuation in the vicinity of the coaxial jets so that the velocity fluctuation was minimum or non-existent in the ideal case. As pressure is a scalar physical quantity, a PAN can essentially be regarded as a condition that created a symmetric pressure fluctuation about the jet center plane that was normal to the transverse direction of propagation of the acoustic waves. On the other hand, a PN condition created a region of locally maximum velocity fluctuation, or a locally minimum pressure fluctuation, where the fluid in this vicinity was displaced in the transverse direction, perpendicular to the jet axis and the line of sight of the jet.

The maximum peak-to-peak pressure perturbation, p'_{pk-pk} , amplitude attained in the present experiments were well below 5% of the mean chamber pressure, P_c , where 5% is considered to be the threshold for the onset of rough combustion (Sutton [71]). On average, slightly higher p'_{pk-pk}/P_c were attainable at $P_r = 0.44$ than at $P_r = 1.05$ because of the higher chamber fluid density in the latter. Most PAN forcing conditions had $p'_{pk-pk}/P_c = 1.00\% - 1.50\%$ at $P_r = 0.44$, and $p'_{pk-pk}/P_c = 0.70\% - 1.20\%$ at $P_r = 1.05$. Ideally, PN forcing conditions should not have produced pressure perturbations larger than what was measured under baseline flow conditions, which was $p'_{pk-pk}/P_c \leq 0.02\%$. However, a lot of factors prevent the complete cancelation of the pressure waves at the coaxial jet location including imperfect match between the individual traveling waves, the presence of access holes and flow obstructions such as the injector tube, which can produce additional reflected running waves. Thus, most PN forcing conditions had $p'_{pk-pk}/P_c = 0.05\% - 0.30\%$.

The forcing frequencies applied for all forcing conditions, except one anomalous case

forced at 3.41 kHz, were in the 3.00 - 3.12 kHz range since the frequency response of the piezosirens were maximum in that frequency range. For both injectors, these forcing frequencies were within 5-10% of the fundamental resonance frequency of the outer jet injector tube. In actual combustion chambers, these kilohertz range frequencies constitute what are known as screeching or screaming instabilities, which are associated with the most destructive type of combustion instability.

5.2.1 Qualitative Characteristics of Acoustically Forced Flows

The impact of the PAN and PN forcing on the mixing characteristics and on the natural development of flow instabilities was found to depend on flow parameters, namely the momentum flux ratio, as well as the injector geometry. Figures 5.19a-g show snapshot images of the LAR-thin injector flows at $P_r = 0.44$ under the PAN and PN forcing conditions. The corresponding baseline flow images are also shown for reference. For $J = 0.1$, Figure 5.19a shows that the PAN forcing produced uniformly spaced bulges on either side of the planar view of the inner jet. Unlike baseline flow conditions, since transverse forcing introduced a bias to the flow in the vicinity of the coaxial jet, it would no longer be valid to generalize the observed behavior in the planar view to an axisymmetric flow behavior. Thus, the most that can be deduced from the observable response of the $J = 0.1$ jet is that the PAN forcing produced periodic disturbances of the flow that were symmetric about a plane perpendicular to the transverse direction and passing through the jet center. In planar jet configurations, such a symmetric disturbances in the shear-layer vortex sheets is commonly known as a varicose mode of disturbance (Yu and Monkewitz [72]). The resulting waves of instability were evenly spaced closer to the exit, but merged and formed disorderly structures farther downstream. The dark-core length was also notably shorter than that of the baseline flow. In contrast, the PN forcing condition imposed periodic transverse displacements of the inner shear layer,

resulting in a sinuous mode of disturbance that became more prominent with increasing downstream distance.

The $J = 0.5$ LAR-thin injector flows in Figure 5.19b showed similar responses to the PAN and PN forcing conditions as $J = 0.1$. The evenly spaced and growing surface waves on the inner jet formed during the PAN forcing could be seen until the end of the dark-core region. The PN forcing also produced a prominent sinuous disturbance of the inner jet. Both forcing conditions promoted the disintegration of the inner jet, thereby, leading to enhanced mixing of the outer and inner jets.

For $J = 2.1$, although the presence of a varicose mode of disturbance during the PAN forcing was discernable in the image, the growth of the resulting symmetric structures was relatively subdued. Yet, the PN forcing still imposed a significant sinuous disturbance on the inner jet. With increasing J , the effect of acoustic forcing gradually subsided. For $J = 5.2$, varicose disturbances were barely visible during the PAN forcing while sinuous disturbance during the PN forcing was still present. For the higher momentum flux ratio flows, $J = 11 - 20$ shown in Figures 5.19e-g, the flows under the PAN forcing were virtually similar to the corresponding baseline flows. Meanwhile, although the sinuous disturbances of the inner jet were considerably reduced compared to the lower J flows, their presence was still evident in the images. It is worth noting that while the undulations in the inner jet began close to the injector exit for low J , it was merely limited to the end of the dark-core at higher J values.

Figures 5.20a-f show a similar set of images of the LAR-thin injector flows at $P_r = 1.05$. The PN forcing cases were only obtained for the $J = 0.5$ and $J = 5.0$ flows. Similar to the observations at $P_r = 0.44$, the PAN forcing conditions imposed strong varicose disturbances on the inner shear layer that subsided with increasing J . The periodic disturbance structures formed during PAN forcing of the $J = 0.1$ shown in Figure 5.20a were not distinctly visible. The absence of such discrete flow structures may be due to

the negligible surface tension at $P_r = 1.05$.

For $J = 0.5$ and $J = 1.9$, the familiar symmetric structures were clearly visible during the PAN forcing as shown in Figures 5.20b and 5.20c, respectively. As the momentum flux ratio increased to $J = 5.0$ and higher, the inner shear layer became progressively less vulnerable to the varicose mode of disturbance during the PAN forcing. The PN forcing condition for $J = 0.5$ showed very small sinuous disturbances while that for $J = 5.0$ showed stronger undulations. This may be since the latter case had a better defined PN condition whose p'_{pk-pk}/P_c was closer to zero.

In general, under both chamber pressure conditions, the dynamics of the inner jet of the LAR-thin flow configuration became less and less sensitive to acoustic forcing with increasing J values. This was especially true with PAN forcing. To elaborate on the mechanism and to illustrate how the effect of a PAN forcing on the dynamics of the inner jet depended on J , a sequence of 15 images at $40 \mu s$ intervals are shown in Figures 5.21 and 5.22 for the $J = 0.5$ and $J = 14$ flows, respectively, at $P_r = 0.44$. The raw images were enhanced to create some contrast between the outer jet and the ambient fluid. Figures 5.23 and 5.24 show a time series plot of the normalized local pressure perturbation amplitudes at the instant that each corresponding image frame was recorded during the PAN acoustic forcings at 3.14 kHz and 3.11 kHz, respectively. Thus, the sets of images represent a period of about one and a half acoustic cycles. It must be emphasized that both flow conditions had similar amplitudes of forcing and forcing frequencies that were within about 9% of the longitudinal resonance mode of the outer jet injector.

Based on the pressure perturbation amplitudes in Figure 5.23, for example, images 2-5 and 10-13 in Figure 5.21 show the compression cycles while images 6-9 show the expansion cycle. At the onset of each compression cycle, a large vortex structure was formed in the outer shear layer. As it was being convected downstream, it grew and

entrained fluid from the inner shear layer along with part of the inner jet. Thus, inner shear-layer vortices were formed at the same frequency as did the outer shear-layer vortices, which were in turn, formed at the acoustic forcing frequency. However, for the higher J flow shown in Figure 5.22, where the outer jet velocities were considerably larger, the outer shear-layer vortex convection time scales became much smaller than their formation and growth time scales. Accordingly, for higher J flows under comparable PAN forcing conditions, the interaction between the outer shear-layer vortices and the inner shear layer could no longer be initiated and sustained near the jet exit, therefore, leaving the inner jets relatively undisturbed for longer distances downstream with increasing J . In addition to the increased convection speed, the large outer to inner jet area ratio also played a role in delaying the interaction between the outer and inner shear layers because it dictated the size that the outer shear-layer vortices had to grow to before being able to interact with the inner shear layer.

Similar snapshot images of the acoustically forced SAR-thick injector flows at $P_r = 0.44$ and $P_r = 1.05$ are shown in Figures 5.25a-g and Figures 5.26a-g, respectively. Despite showing response to acoustic forcing to some extent for all J values, coherent and periodic flow structures were only formed at higher J . For the $J = 0.1$ and $J = 0.5$ flows, vortical structures were only observed in the recirculation zone, while no organized flow structures developed in the inner shear layer and the inner jet. This was in contradiction with the response seen with the LAR-thin injector flows, which exhibited strong response at lower J in the form of periodic structures due to varicose or sinuous disturbances, and gradually subdued response with increasing J .

For the lowest J SAR-thick injector flow at $P_r = 0.44$ shown in Figure 5.25a, PAN forcing resulted in the formation of random ligament structures on the surface of the inner jet that grew with increasing downstream distance. The portion of the inner jet closer to the recirculation zone appeared relatively undisturbed. One possible reason for

this may be because the fluid in the recirculation zone shielded the inner jet from being overcome by the outer shear-layer vortices. In the case of PN forcing, again the portion of the inner jet closer to the recirculation zone was relatively undisturbed, while farther downstream, it formed a dispersion of fine droplets.

The PAN forcing of the $J = 0.5$ flow in Figure 5.25b caused the outer shear-layer vortices to entrain fluid in the recirculation zone, but was unable to form coherent structures on the inner jet surface. However, increased spread was observed in the initial region of the inner jet, and also resulted in break-up and scattering of the ligament structures into fine droplets. On the other hand, PN forcing was less dispersive with no apparent sinuous disturbance in the inner jet.

As discussed previously, for $J = 0.1$ and $J = 0.5$, the sense of rotation of the fluid inside the recirculation zone was such that a counterflow existed at the inner jet boundary. When the momentum flux ratio increased to $J = 2.1$, the fluid inside the recirculation zone mainly consisted of the lower momentum inner jet fluid, and the sense of rotation was such that a counterflow existed at the inside boundary of the outer jet. Thus, for $J = 2.1$ and higher, the outer shear-layer vortices had the same sense of rotation as the fluid in the recirculation zone, unlike for lower J flows. One would then expect that coupling between these flow regions during varicose disturbances due to the PAN forcing may induce symmetric flow structures on the inner jet surface. However, as Figure 5.25c shows, besides imparting a merely irregular and dispersive flow pattern, the PAN forcing did not result in a periodic, varicose type of disturbance pattern on the inner jet. The PN forcing did not form any coherent sinuous motion of the jet as well.

Interestingly, as Figures 5.25d-g show, the next higher and subsequent J values exhibited the expected symmetric flow disturbances during the PAN forcing. They appeared to start just beyond the end of the recirculation zone, rolled-up and entrained the inner jet fluid further downstream. In addition, for the higher J flows, the dark-core

region of the inner jet was too stubby to manifest any appreciable sinuous disturbance during the PN forcing.

At $Pr = 1.05$, acoustic forcing of the low momentum flux ratio flows, $J = 0.1$ and $J = 0.5$, in Figures 5.26a and 5.26b also exhibited weak response. This may be partly attributed to the relatively low forcing amplitudes that were achieved for those conditions. Although during the PAN forcing the outer shear layer dynamics dominated the flow in the recirculation zone, it had minimal impact on the inner jet, which appeared to be reasonably comparable to the corresponding baseline cases. The flow also had subdued response to the PN forcing.

As J increased and the sense of rotation in the recirculation zone reversed, the effect of the PAN forcing became more and more prominent. For $J = 2.1$ shown in Figure 5.26c, the PAN forcing induced what appeared to be organized, periodic structures forming along the inner jet. Its effect became increasingly pronounced for $J = 5.2 - 21$, where the symmetric outer shear-layer vortex roll-ups dominated the inner jet flow dynamics. The growing impact of the PN forcing was also seen for this range of J values, with alternate vortex roll-ups instead of symmetric ones.

5.2.2 Acoustically Forced Dark-Core Length Measurements

The dark-core lengths of the acoustically forced flows were measured and normalized by their corresponding baseline flows as shown in Figures 5.27 and 5.28 for the PAN and PN forcing conditions, respectively. Since the $J = 0.1$ and $J = 0.5$ flows had dark-core regions that exceeded the image border, they were excluded from these plots. The normalized PAN forcing dark-core lengths, L_{PAN}/L_B and PN forcing dark-core lengths, L_{PN}/L_B , gave a measure of the effect of each forcing condition relative to the baseline flow.

As Figures 5.27 shows, the overall trend in L_{PAN}/L_B for the LAR-thin injector

flows was that it approached one with increasing J . This implied that the PAN forcing condition had less impact on the dark-core lengths at higher J . However, the effect of the PAN forcing seemed to have depended on the outer jet flowrate as well as J . This may be seen in the reduction of L_{PAN}/L_B at $P_r = 0.44$, as the momentum flux ratio increased from $J = 11$ to $J = 14$ while the outer and inner jet flowrates were reduced (Table C.1). When the momentum flux ratio was raised to $J = 21$ with further increase in the outer jet flowrate while holding the inner jet flowrate constant, L_{PAN}/L_B also increased. This again underlined the role that the outer jet flowrate played in diminishing the impact of the PAN forcing. At $P_r = 1.05$, a similar monotonic increase in L_{PAN}/L_B with J can be seen. Furthermore, for a given J and comparable forcing conditions, L_{PAN}/L_B at $P_r = 1.05$ were lower than those at $P_r = 0.44$ as can be seen for $J \approx 2, 5$.

On the other hand, the effect of the PAN forcing on the SAR-thick injector flows was seen at higher J values. At $P_r = 0.44$, the dark-core lengths stayed relatively unchanged from that of the baseline until $J = 11$, beyond which it decreased with J . It showed a similar trend at $P_r = 1.05$ except that the dark-core region got longer at $J = 9.2$ and $J = 14$ before decreasing to below that of the baseline at $J = 21$. Thus, for the SAR-thick injector flows, the outer jet flow in the recirculation zone at low J played a major role in dampening the disturbances due to the PAN forcing.

The response to the PN forcing of the LAR-thin injector flows at $P_r = 0.44$ was similar to the PAN forcing as shown in Figure 5.28. The dark-core lengths approached that of the baseline with increasing J , and decreased as the jet flowrates were reduced. Unlike the PAN forcing cases, the SAR-thick injector flows showed relatively low L_{PN}/L_B that monotonically increased towards one as J increased, with an exception of the $J = 2.1$ flow at $P_r = 1.05$. Thus, these results showed that the flow in the recirculation zone was not as effective in diminishing the effect of the PN forcing condition on the SAR-thick injector flow mixing.

5.2.3 Characterization of Dominant Dynamic Flow Structures

Application of POD on the high speed images of the acoustically forced flows was used to further draw contrast between the flow response to the PAN and PN forcing conditions, and the corresponding baseline conditions for the two injector configurations. Similar to the analysis results presented for the baseline flow in Section 5.1.3, time-averaged images, POM images of the conjugate modes, and the corresponding CPSD magnitude plots were used to reveal and describe the key differences. For ease of comparison, the baseline spectra are included in the CPSD magnitude plots and are shown with dotted lines.

Figures 5.29a and 5.29b show the results for the LAR-thin injector $J = 0.1$ flow during the PAN and PN forcing conditions, respectively, at $P_r = 0.44$. Unlike the baseline flow, the average image for the PAN forcing showed a more diffuse dark-core flow. In addition, as was already observed in the snapshot images, the POM images identified adjacent dark lobes, which started forming immediately downstream of the injector exit, indicating the presence of symmetric flow structures due to the varicose mode of disturbance. The dominant sharp peak in the magnitude spectrum denoted the characteristic frequency of these symmetric structures, and it was identical to the acoustic forcing frequency. The baseline flow spectral characteristic, shown in dotted line, was clearly absent from the forced flow spectrum. That is, the dominant inner shear-layer flow dynamics was completely altered during PAN forcing. In the case of the PN forcing condition, antisymmetric structures shown in the POM image indicated the presence of sinusoid disturbances as opposed to the helical disturbances in baseline flows, since the PN forcing imposed a bias in the transverse direction. The corresponding magnitude spectrum again had a sharp peak frequency identical to the acoustic forcing frequency, and it can be seen that the low frequency peak of the baseline flow was also removed from this spectrum.

The next two higher momentum flux ratio flows, $J = 0.5$ and $J = 2.1$, also exhibited similar responses to the PAN and PN forcing conditions. The POM images in Figures 5.30a and 5.31a show the formation of symmetric structures due to the PAN forcing condition. As discussed earlier, with increasing J , the outer shear-layer vortices attained larger convection speed due to the increasing outer jet mass flowrate. Since the observed symmetric structures were a direct outcome of the interaction of the outer shear-layer vortices with the inner shear layer, this increased convection speed was apparent in the stretching of the dark and light lobes in the POM images. The magnitude spectra also had dominant sharp peaks at the forcing frequency without any significant remnant of the baseline spectral characteristic. For the PN forcing conditions in Figures 5.30b and 5.31b, the sinusoidal disturbances were depicted with antisymmetric structures in the POM images. The apparent stretch in the dark lobes with increasing J again showed the corresponding increases in the disturbance propagation speed. The sharp dominant peaks at the forcing frequencies also indicated strong response to the PN forcing.

When the momentum flux ratio further increased to $J = 5.2$, the identified dominant structures during the PAN forcing condition were mainly antisymmetric as shown in Figure 5.32a. Although it cannot be deduced without further evidence that these antisymmetric structures represented helical disturbances as in baseline flow conditions, it can nevertheless be argued that unlike the PN forcing condition, which set-up a velocity antinode at the jet location, PAN forcing did not induce a net motion in the transverse direction. Thus, these antisymmetric structures may very well have represented helical disturbances. Moreover, despite still having a dominant peak at the forcing frequency in the magnitude spectrum, the $J = 5.2$ flow retained some of the baseline flow spectral behavior, in contrast to the lower J flows. The PN forcing condition, on the other hand, continued imposing strong sinusoidal disturbances as shown in the POM image in Figure 5.32b. As with the PAN forcing condition, the magnitude spectrum had a dominant peak at the forcing frequency but also retained the baseline spectral characteristic.

At the higher momentum flux ratios, $J = 11$, 14 , and 20 , the diminishing impact of the PAN forcing became more evident in the baseline flow types of antisymmetric structures, and even more importantly, in their spectral behavior as shown in Figures 5.33a, 5.34a, and 5.35a, respectively. The magnitude spectra still clearly show a peak at the forcing frequency. However, the broad characteristic peaks in the baseline spectra were retained, and were also relatively significant in amplitude. The PN forcing conditions in Figures 5.33b, 5.34b, and 5.35b also exhibited this retentive behavior although they still had a relatively strong peak at the forcing frequency.

At $P_r = 1.05$, the LAR-thin injector flows during the PAN forcing condition again showed a trend where a gradual shift occurred from flows with symmetric structures and spectral characteristic dominated by the forcing frequency to those with antisymmetric structures and spectra that retained the baseline flow characteristic with increasing J . Accordingly, the lower momentum flux ratio flows, $J = 0.5$ and $J = 1.9$, formed symmetric structures in response to PAN forcing as shown in Figures 5.36a and 5.37. Their magnitude spectra also showed single dominant peaks at frequencies identical to the forcing frequencies, and none of their baseline spectral characteristics were retained. As the momentum flux ratio increased to $J = 5.0$, only antisymmetric structures were sustained as shown in Figure 5.38a. However, its spectral characteristic was still distinct from that of the baseline. For the higher momentum flux ratio flows, $J = 8.5$ and $J = 12$, although their spectra still had dominant peaks at the forcing frequency, the baseline spectral characteristics were also retained as shown in Figures 5.39 and 5.40. The PN forcing conditions for only the $J = 0.5$ in Figure 5.36b and $J = 5.0$ in Figure 5.38b were obtained. It can be seen that both flow conditions exhibited the expected sinusoid disturbances and dominant peaks at the forcing frequencies.

As discussed earlier, one of the distinguishing features of the SAR-thick injector flows was the presence of a flow recirculation zone. This created a delay in the interaction

between the inner jet and the outer shear layer. Moreover, it was observed that for low momentum flux ratio flows, such as $J = 0.1$ and $J = 0.5$, the recirculation zone was filled with the outer jet fluid that had an opposite sense of rotation from the outer shear-layer vortices during the PAN forcing. Thus, this prevented the outer shear-layer vortices from dominating the dynamics of the inner shear layer. In light of this, for the $J = 0.1$ flow during the PAN forcing at $P_r = 0.44$, the POM image exhibited antisymmetric structures with low characteristic frequency as shown in Figure 5.41. The resulting behavior of the dominant flow structures was indeed different from the corresponding baseline case shown in Figure 5.14a. However, unlike the LAR-thin flows, there was no response at the forcing frequency.

The $J = 0.5$ and $J = 2.1$ flows also exhibited similar behavior during PAN forcing as shown in Figures 5.42 and 5.43a, respectively. Based on the snapshot images as well as the POM images, the dominant flow disturbance structures during the PAN forcing were clearly distinct from their baseline counterparts. However, as their magnitude spectra show, none of these flow structures had characteristic frequencies identical to the forcing frequencies. This again shows that the low J , SAR-thick injector inner jet flow dynamics was insensitive to the PAN acoustic forcing. Moreover, as Figure 5.43b shows, the $J = 2.1$ flow during the PN forcing also showed a similar spectral behavior. The PN forcing cases for the $J = 0.1$ and $J = 0.5$ were not reported because conjugate modes could not be identified.

When the momentum flux ratio increased to $J = 5.7$, symmetric disturbance structures appeared downstream of the recirculation zone as shown in the POM images for the PAN forcing condition in Figure 5.44a. A dominant peak at the forcing frequency was identified in the magnitude spectrum. A dominant peak was also identified in the spectrum during the PN forcing condition as shown in Figure 5.44b. Its corresponding POM image shows initially antisymmetric structures due to the sinusoid disturbances,

but appeared symmetric further downstream.

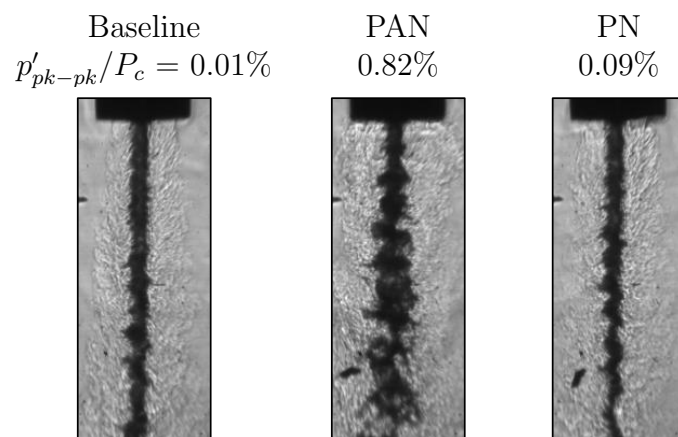
The POM images in Figures 5.45a, 5.46a, and 5.47a, for the $J = 10$, $J = 15$, and $J = 21$ flows, respectively, show similar symmetric structures during the PAN forcing condition. Their magnitude spectra had dominant peaks at the forcing frequency as well, thus providing further evidence that the SAR-thick flows were more responsive to the PAN forcing at higher J . A unique feature of the $J = 21$ flow was that initially symmetric structures gradually became antisymmetric further downstream perhaps due to the dominant nature of helical instabilities at such a high J . Meanwhile, the POM images in Figures 5.45b, 5.46b, and 5.47b for these high J flows showed the expected antisymmetric structures due to the periodic transverse displacements during the PN forcing condition. The spectra also show distinct peaks at the forcing frequencies.

Likewise at $P_r = 1.05$, the low J flows showed subdued response to the PAN forcing while the higher J flows formed symmetric structures with characteristic frequencies identical to the forcing frequencies. Accordingly, the POM images and magnitude spectra in Figures 5.48, 5.49a, and 5.50a for the $J = 0.1$, $J = 0.5$, and $J = 2.1$ flows, respectively, show neither the symmetric structures nor dominant peak frequencies at the forcing frequency. On the contrary, the $J = 5.2$ and higher flows exhibited the familiar symmetric structures with strong responses at the forcing frequencies. Similarly, the higher J flows showed stronger response to the PN forcing condition as evident in the antisymmetric structures seen in the POM images, and the dominant peaks at the forcing frequencies in the magnitude spectra shown in Figures 5.51b, 5.52b, 5.53b, and 5.54b.

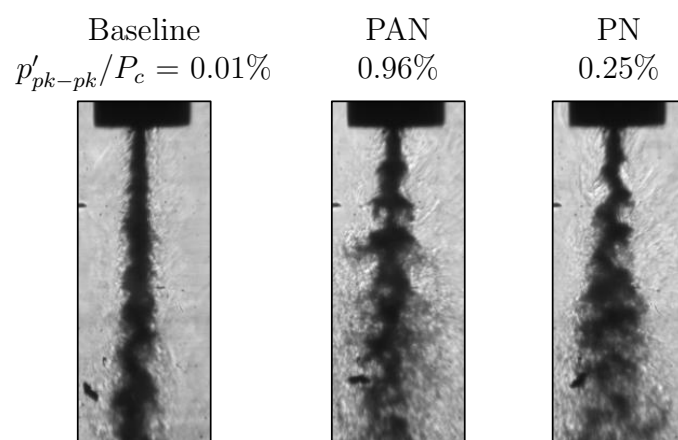
Thus, this distinction between the SAR-thick and the LAR-thin injector flows in their response to transverse acoustic forcing was a direct consequence of different injector geometries. As noted earlier, one of the distinguishing features of the SAR-thick injector flows was the presence of a region of recirculating flow behind the thick inner tube

post. In low J flows, this recirculation zone inhibited the influence of the outer shear-layer vortices on the inner flow unlike the LAR-thin injector flows under similar forcing conditions. With increasing J , the SAR-thick injector flows became responsive to the imposed acoustic forcing while the LAR-thin injector flows became less susceptible.

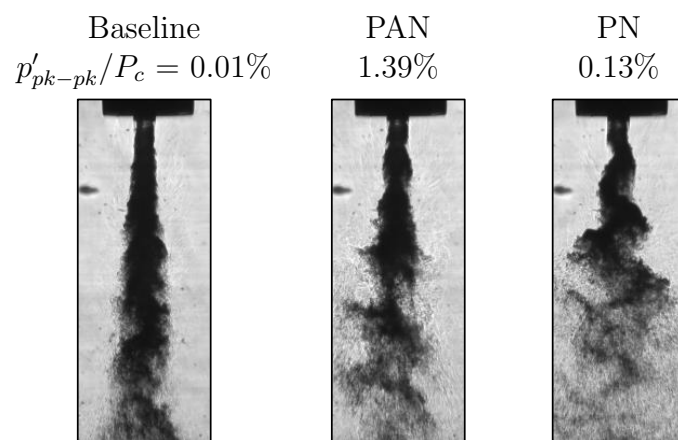
From a practical standpoint, it is crucial to ensure that the injector flow under non-design operating conditions behave as closely as possible to that under design operating conditions. Flow disturbances that arise as a result of acoustic instabilities due to excitation of the combustion chamber acoustic modes are typical instances of non-design operating conditions. Although special cases of the chamber acoustic behavior can be modeled and incorporated in the design considerations, a great many other unpredictable scenarios exist. Hence, the best approach would be to implement a robust design that renders a more predictable flow behavior for a given set of flow conditions regardless of any externally imposed disturbances. In light of this argument, the LAR-thin injector, for instance, may be considered to be a preferable design configuration based on the fact that it has been shown to be less sensitive to external disturbances for high J values.



(a) $J = 0.1$, $f_F = 3.13$ kHz

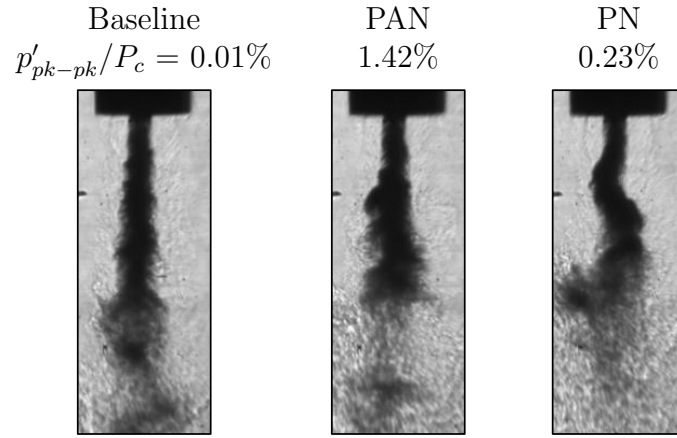


(b) $J = 0.5$, $f_F = 3.14$ kHz

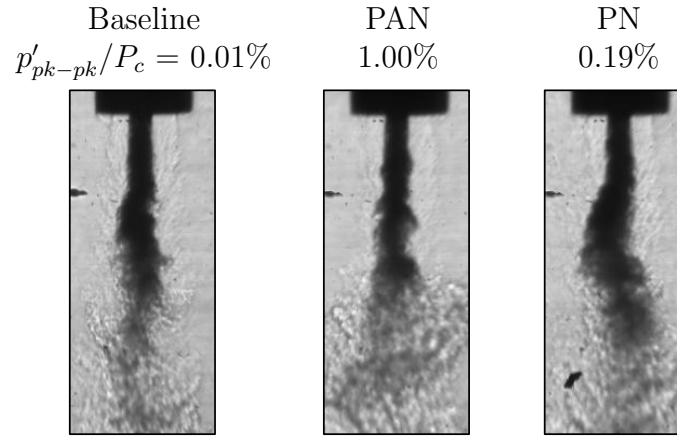


(c) $J = 2.1$, $f_F = 3.12$ kHz

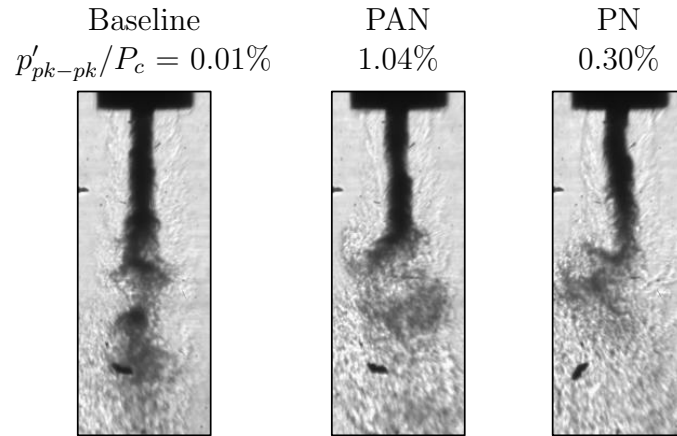
Figure 5.19: See caption on page 150.



(d) $J = 5.2$, $f_F = 3.12$ kHz



(e) $J = 11$, $f_F = 3.10$ kHz



(f) $J = 14$, $f_F = 3.11$ kHz

Figure 5.19: See caption on page 150.

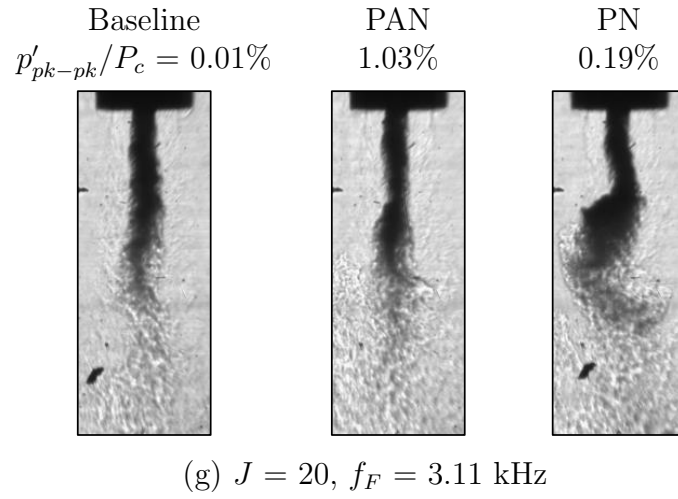
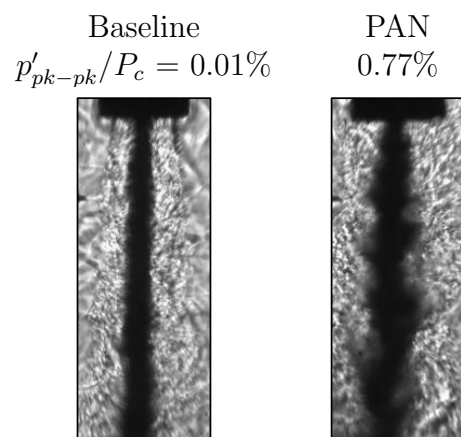
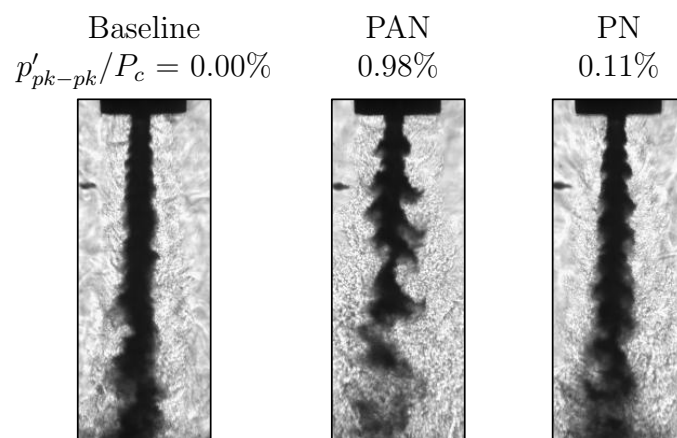


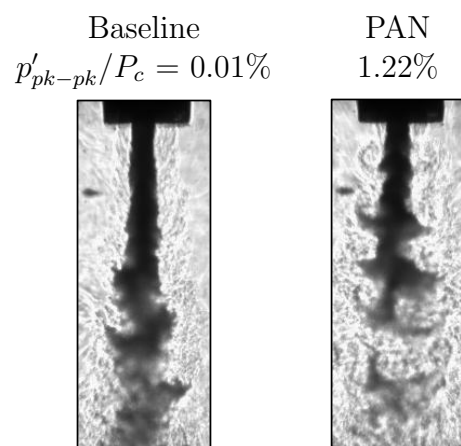
Figure 5.19: Back-lit images of the LAR-thin injector PAN flow at $P_r = 0.44$ and varying J . The image framing rate was 25 kHz. Table C.3 gives a summary of the acoustic forcing frequencies and amplitudes.



(a) $J = 0.1$, $f_F = 3.16$ kHz

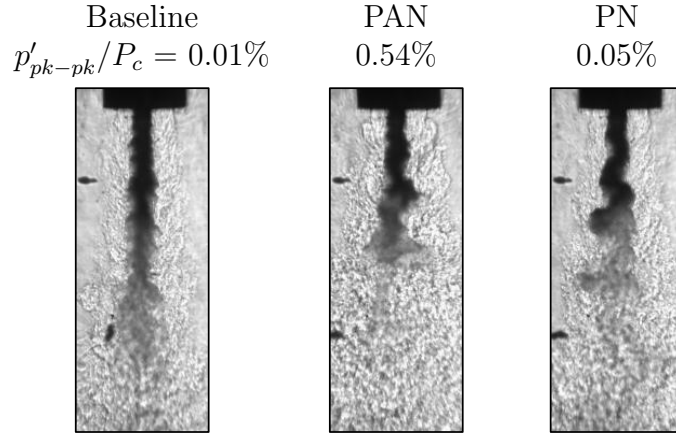


(b) $J = 0.5$, $f_F = 3.10$ kHz

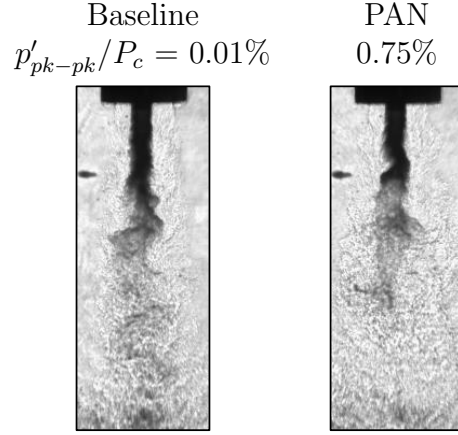


(c) $J = 1.9$, $f_F = 3.10$ kHz

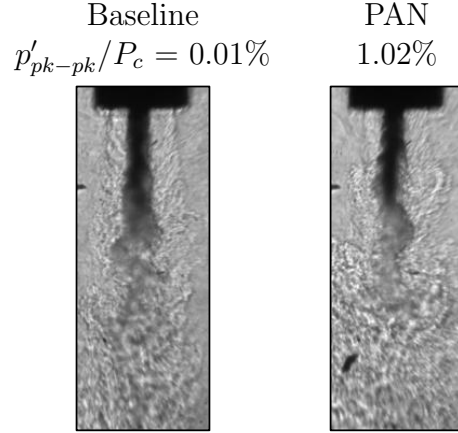
Figure 5.20: See caption on page 152.



(d) $J = 5.0$, $f_F = 3.41$ kHz



(e) $J = 8.5$, $f_F = 3.10$ kHz



(f) $J = 12$, $f_F = 3.10$ kHz

Figure 5.20: Back-lit images of the LAR-thin injector PAN flow at $P_r = 1.05$ and varying J . The image framing rate was 25 kHz. Table C.3 gives a summary of the acoustic forcing frequencies and amplitudes.

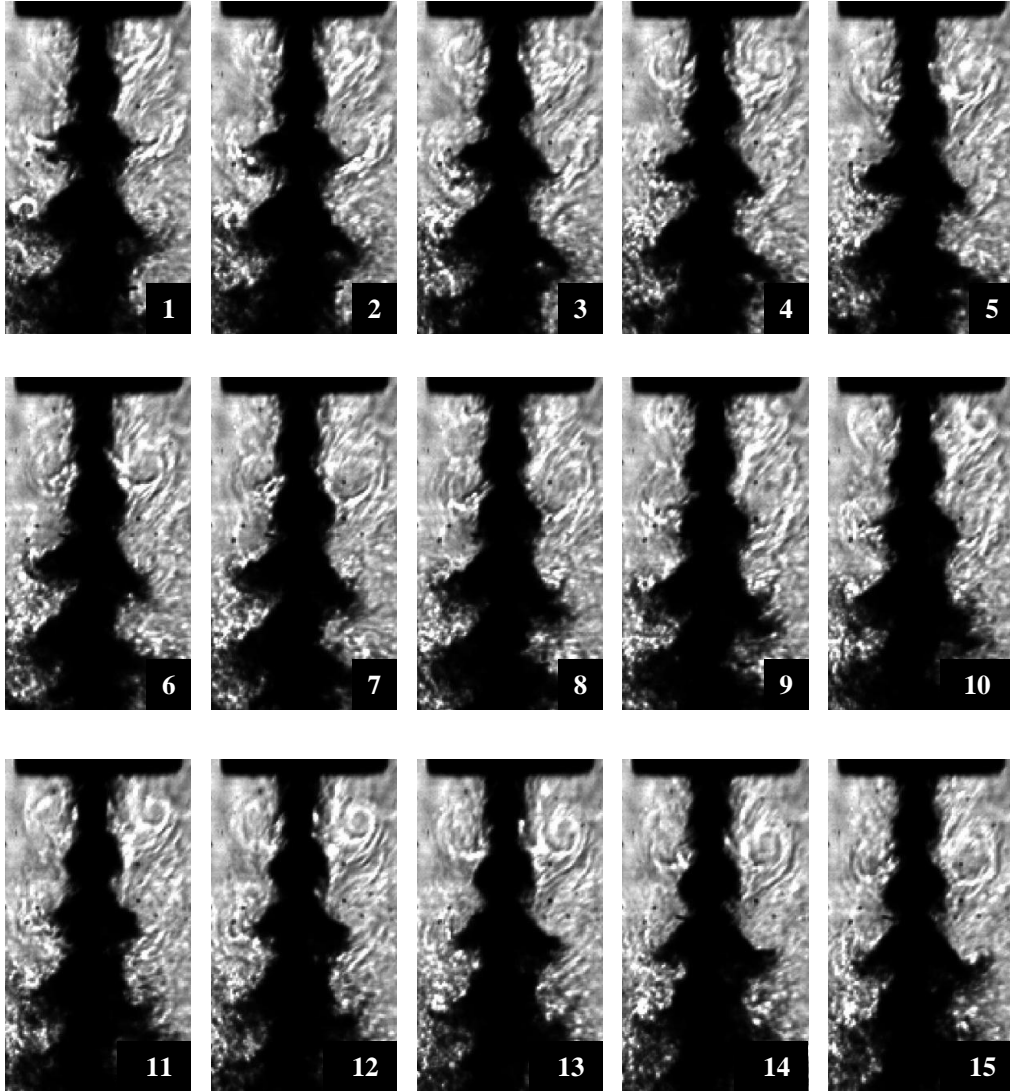


Figure 5.21: A time-sequence of images during PAN forcing ($f_F = 3.14$ kHz) of the $J = 0.5$ LAR-thin injector flow at $P_r = 0.44$. The images were captured at $40 \mu s$ intervals, and show formation of the outer shear-layer vortices, which grow and dominate the inner shear layer and inner jet flow dynamics.

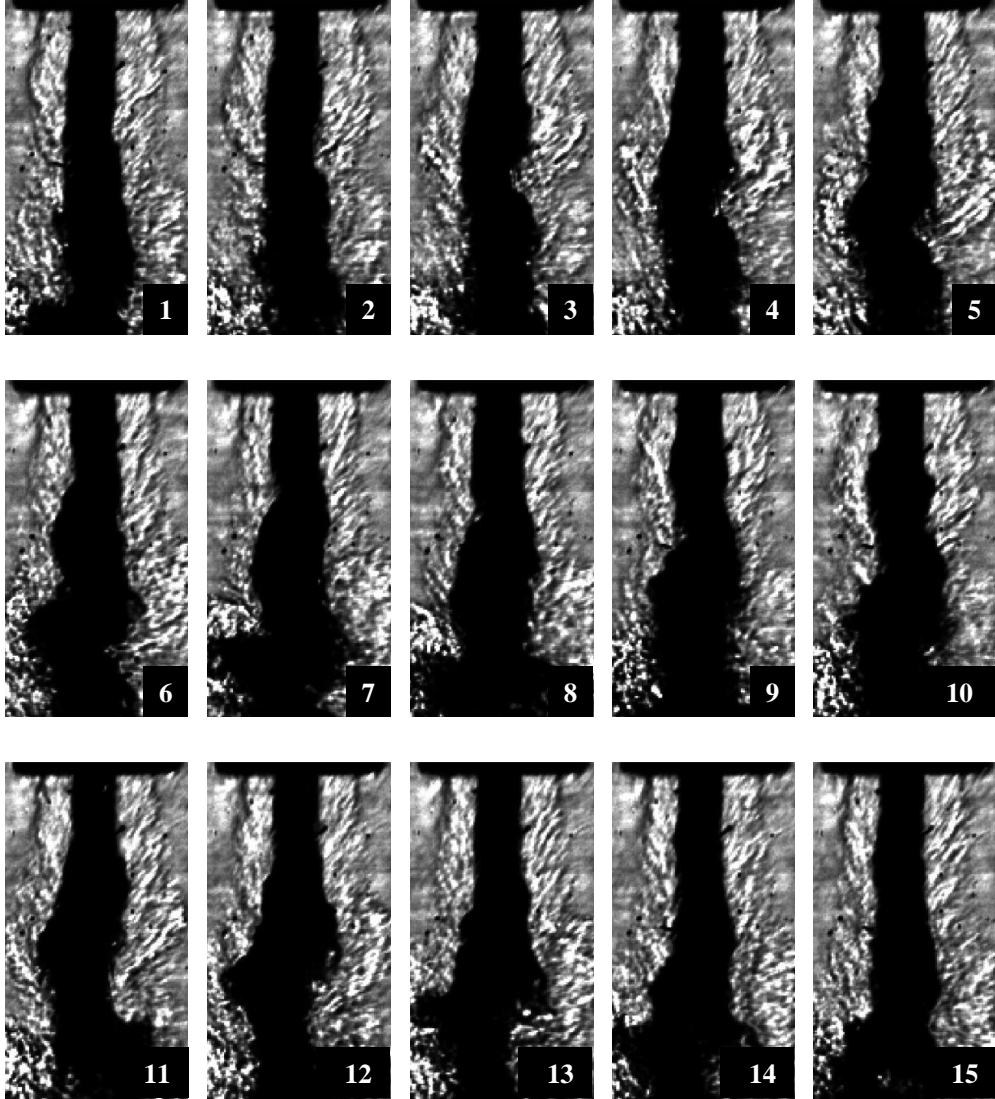


Figure 5.22: A time-sequence of images during PAN forcing ($f_F = 3.11$ kHz) of the $J = 14$ LAR-thin injector flow at $P_r = 0.44$. The images were captured at $40 \mu s$ intervals. Unlike the $J = 0.5$ flow in Figure 5.21, the large convection speed of the shear-layer vortices prevented their interaction with the inner shear layer.

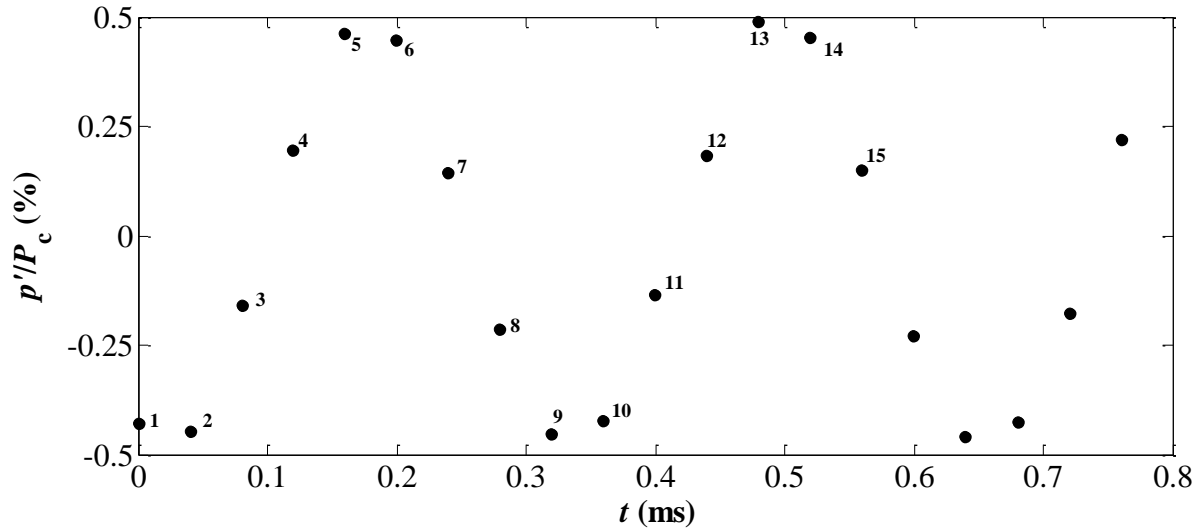


Figure 5.23: Synchronized acoustic pressure perturbation measurements during PAN forcing ($f_F = 3.14$ kHz) of the $J = 0.5$ LAR-thin injector flow at $P_r = 0.44$. The numbers next to the data points refer to the amplitudes measured corresponding to the image numbers in Figure 5.21.

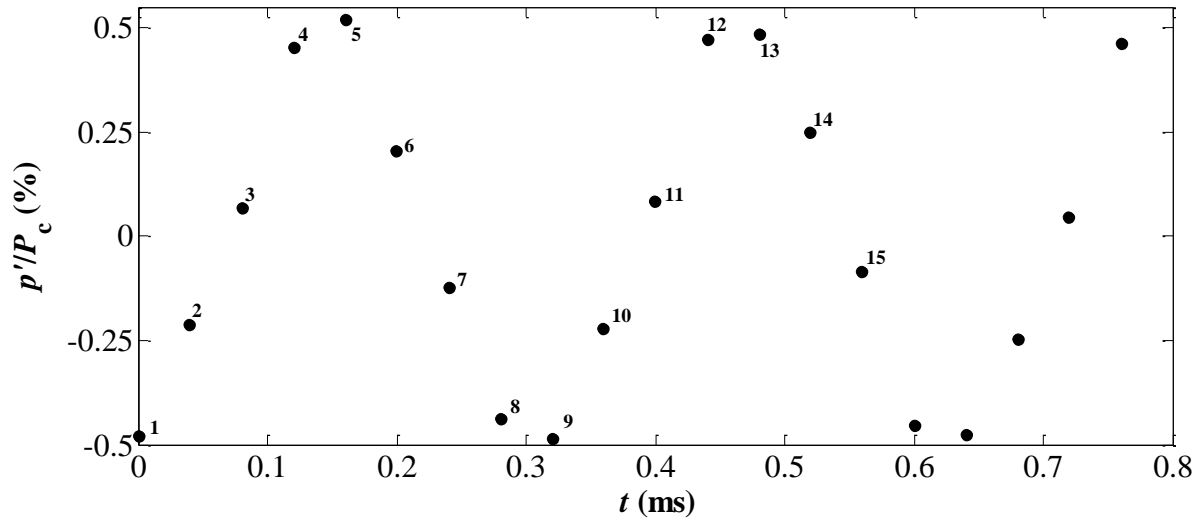
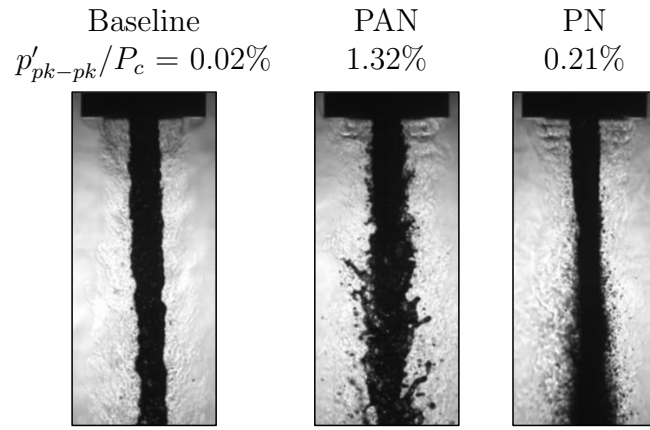
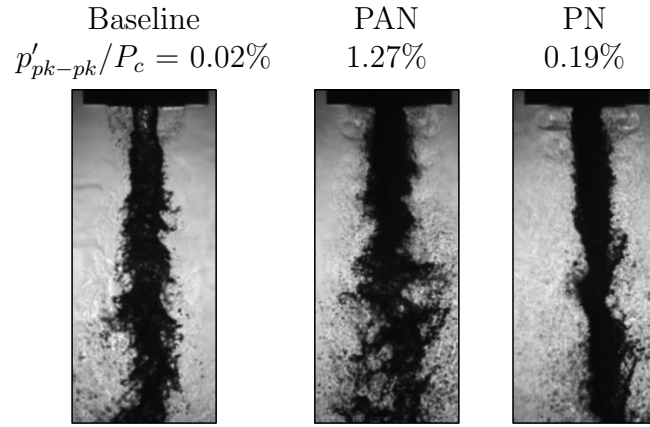


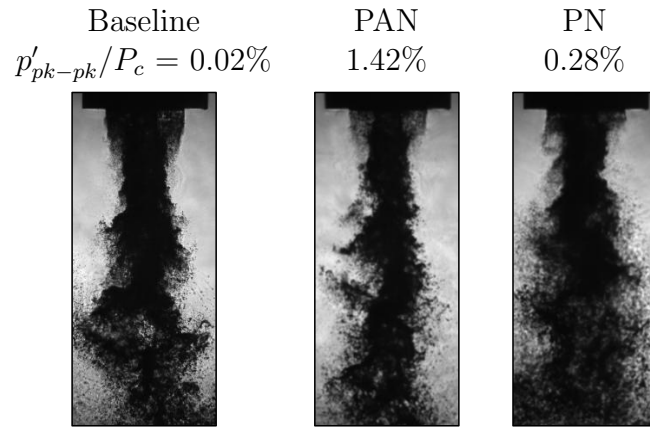
Figure 5.24: Synchronized acoustic pressure perturbation measurements during PAN forcing ($f_F = 3.11$ kHz) of the $J = 14$ LAR-thin injector flow at $P_r = 0.44$. The numbers next to the data points refer to the amplitudes measured corresponding to the image numbers in Figure 5.22.



(a) $J = 0.1$, $f_F = 3.10$ kHz

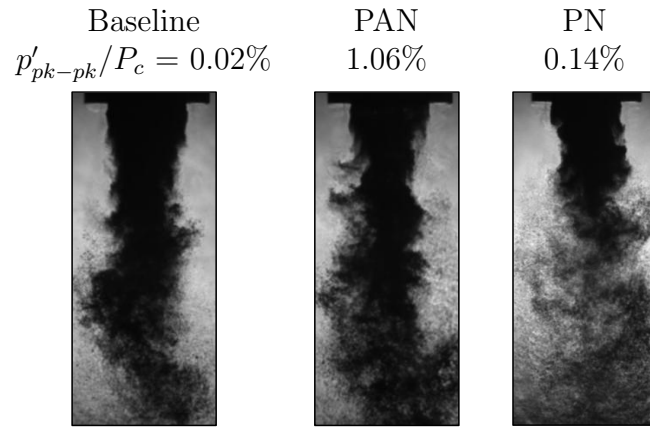


(b) $J = 0.5$, $f_F = 3.04$ kHz

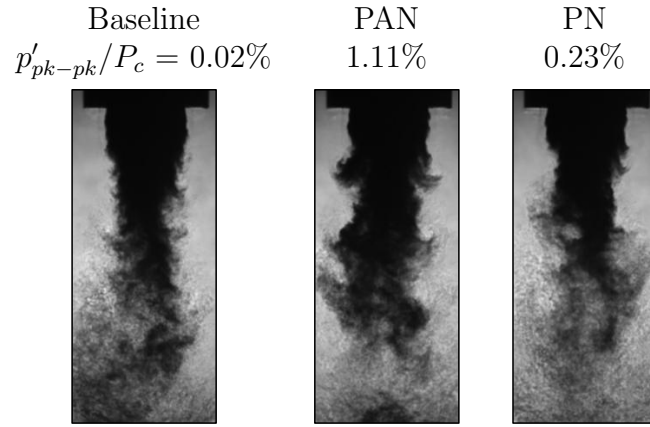


(c) $J = 2.1$, $f_F = 3.07$ kHz

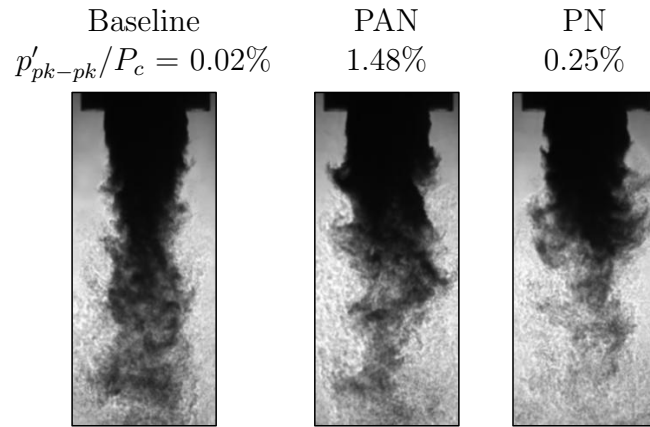
Figure 5.25: See caption on page 158.



(d) $J = 5.7$, $f_F = 3.11$ kHz



(e) $J = 10$, $f_F = 3.11$ kHz



(f) $J = 15$, $f_F = 3.04$ kHz

Figure 5.25: See caption on page 158.

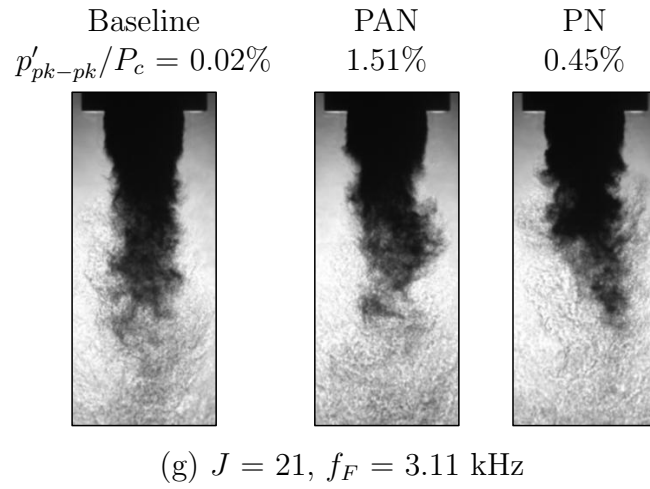
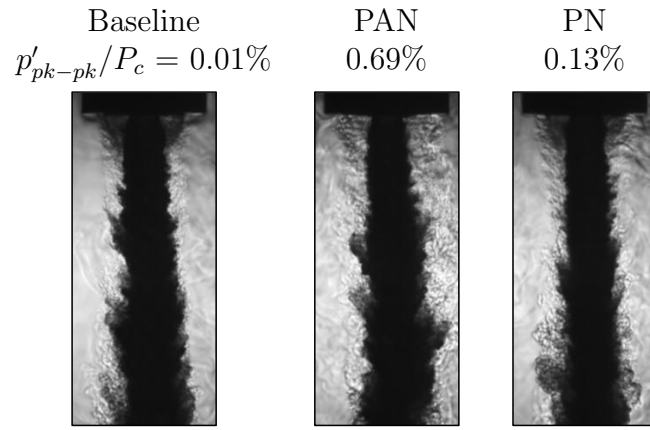
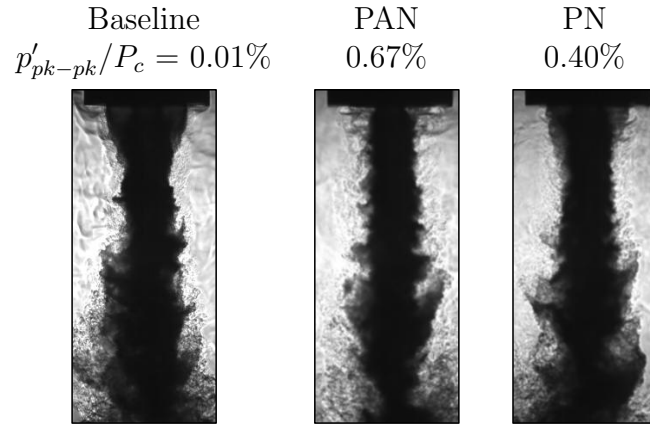


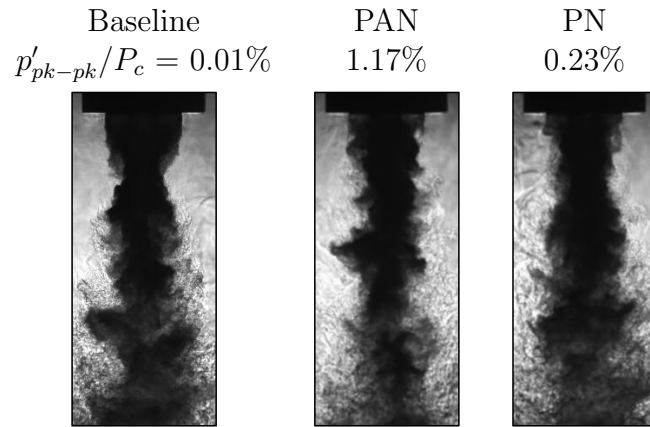
Figure 5.25: Back-lit images of the SAR-thick injector PAN flow at $P_r = 0.44$ and varying J . The image framing rate was 25 kHz. Table C.4 gives a summary of the acoustic forcing frequencies and amplitudes.



(a) $J = 0.1$, $f_F = 3.12$ kHz

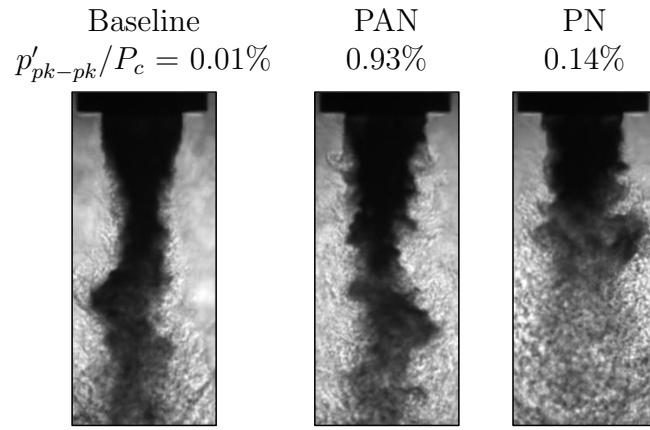


(b) $J = 0.5$, $f_F = 3.00$ kHz

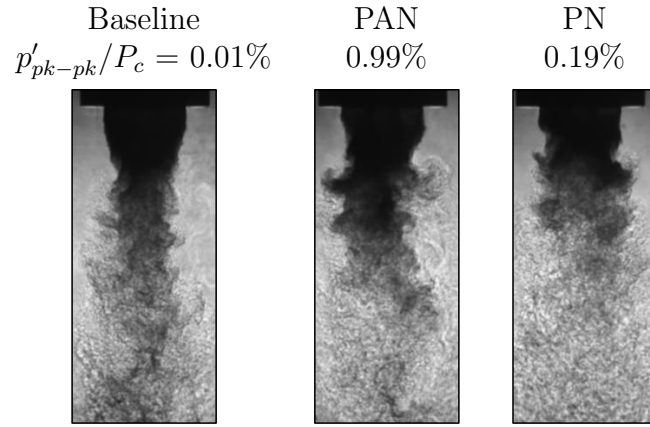


(c) $J = 2.1$, $f_F = 3.04$ kHz

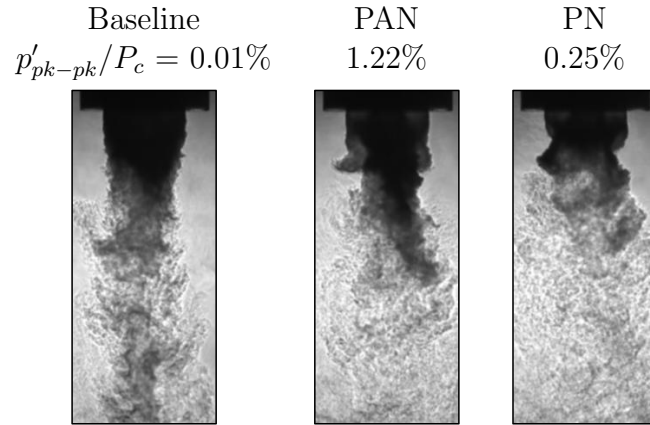
Figure 5.26: See caption on page 161.



(d) $J = 5.2$, $f_F = 3.08$ kHz



(e) $J = 9.2$, $f_F = 3.11$ kHz



(f) $J = 14$, $f_F = 3.04$ kHz

Figure 5.26: See caption on page 161.

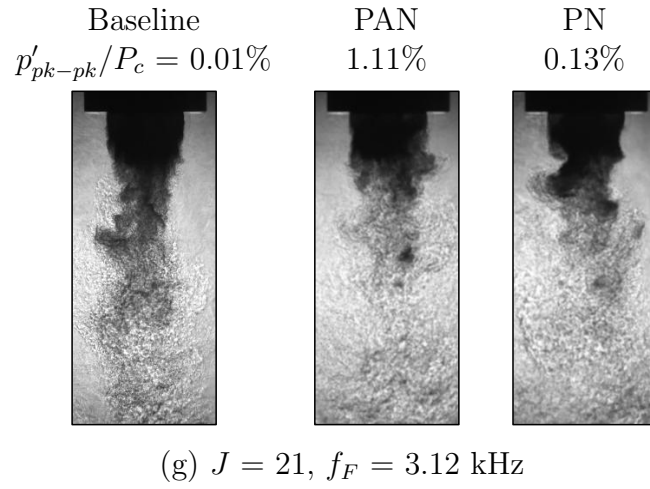


Figure 5.26: Back-lit images of the LAR-thin injector PAN flow at $P_r = 1.05$ and varying J . The image framing rate was 25 kHz. Table C.4 gives a summary of the acoustic forcing frequencies and amplitudes.

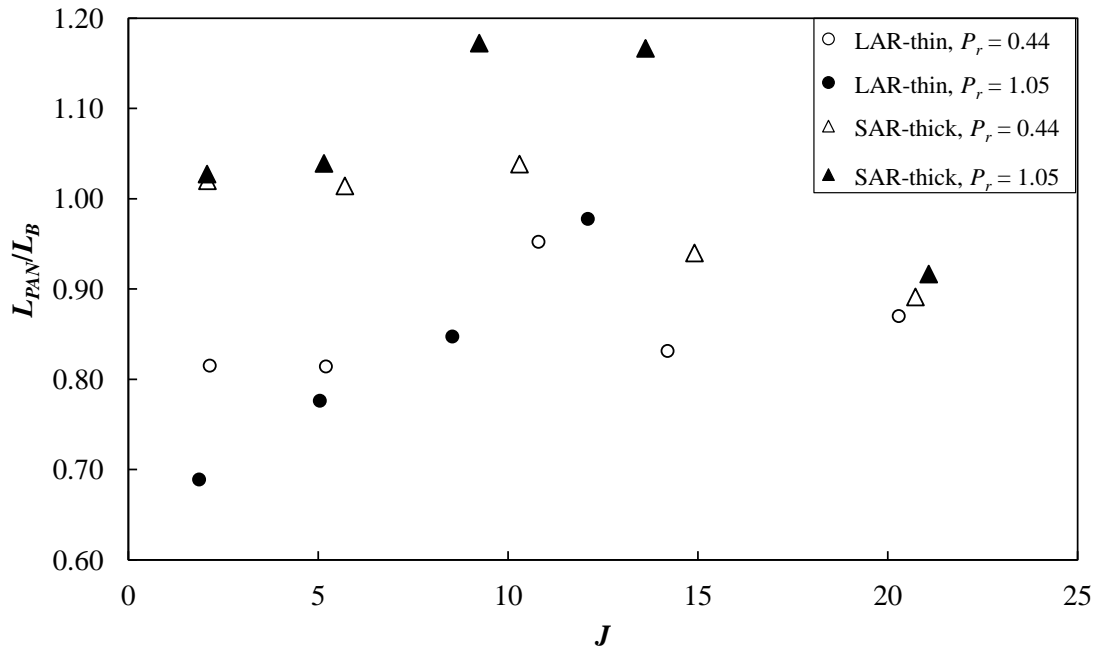


Figure 5.27: Measurements of the PAN forced flow dark-core length, L_{PAN} normalized by the corresponding baseline flow dark-core length, L_B .

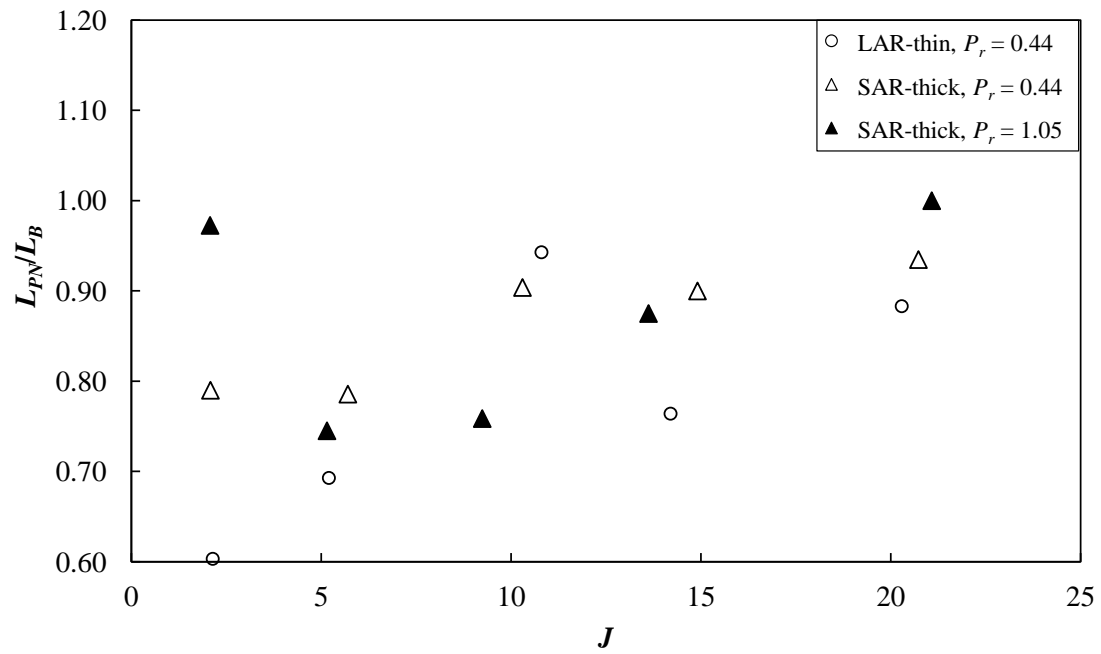


Figure 5.28: Measurements of the PN forced flow dark-core length, L_{PN} normalized by the corresponding baseline flow dark-core length, L_B .

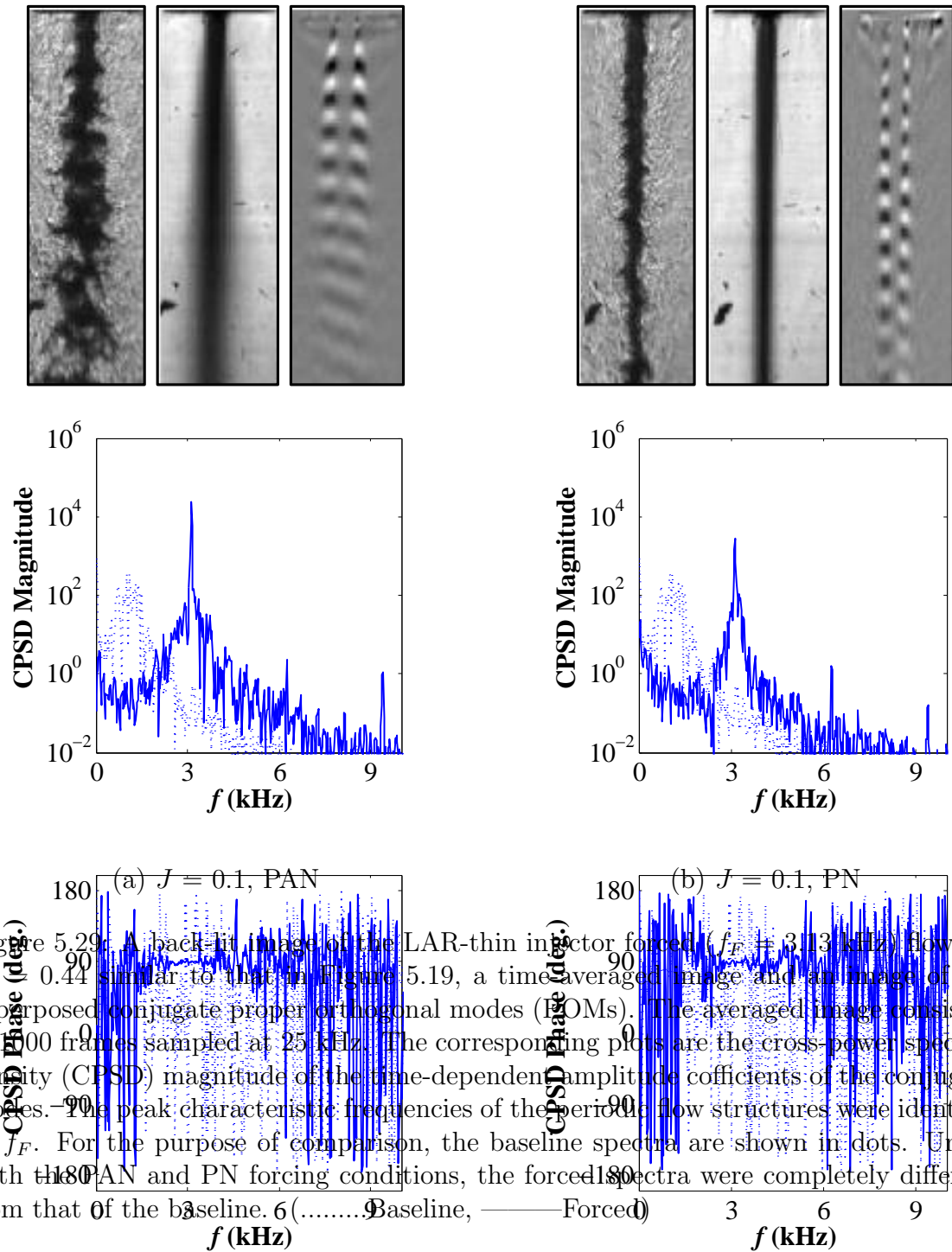


Figure 5.29: (a) $J = 0.1$, PAN (b) $J = 0.1$, PN. A back-fit image of the LAR-thin injector forced ($f_F = 3.13$ kHz) flows at $P_r = 0.44$ similar to that in Figure 5.19, a time-averaged image and an image of the superposed conjugate proper orthogonal modes (POMs). The averaged image consisted of 1000 frames sampled at 25 kHz. The corresponding plots are the cross-power spectral density (CPSD) magnitude of the time-dependent amplitude coefficients of the conjugate modes. The peak characteristic frequencies of the periodic flow structures were identical to f_F . For the purpose of comparison, the baseline spectra are shown in dots. Under both the PAN and PN forcing conditions, the forced spectra were completely different from that of the baseline. (..... Baseline, — Forced)

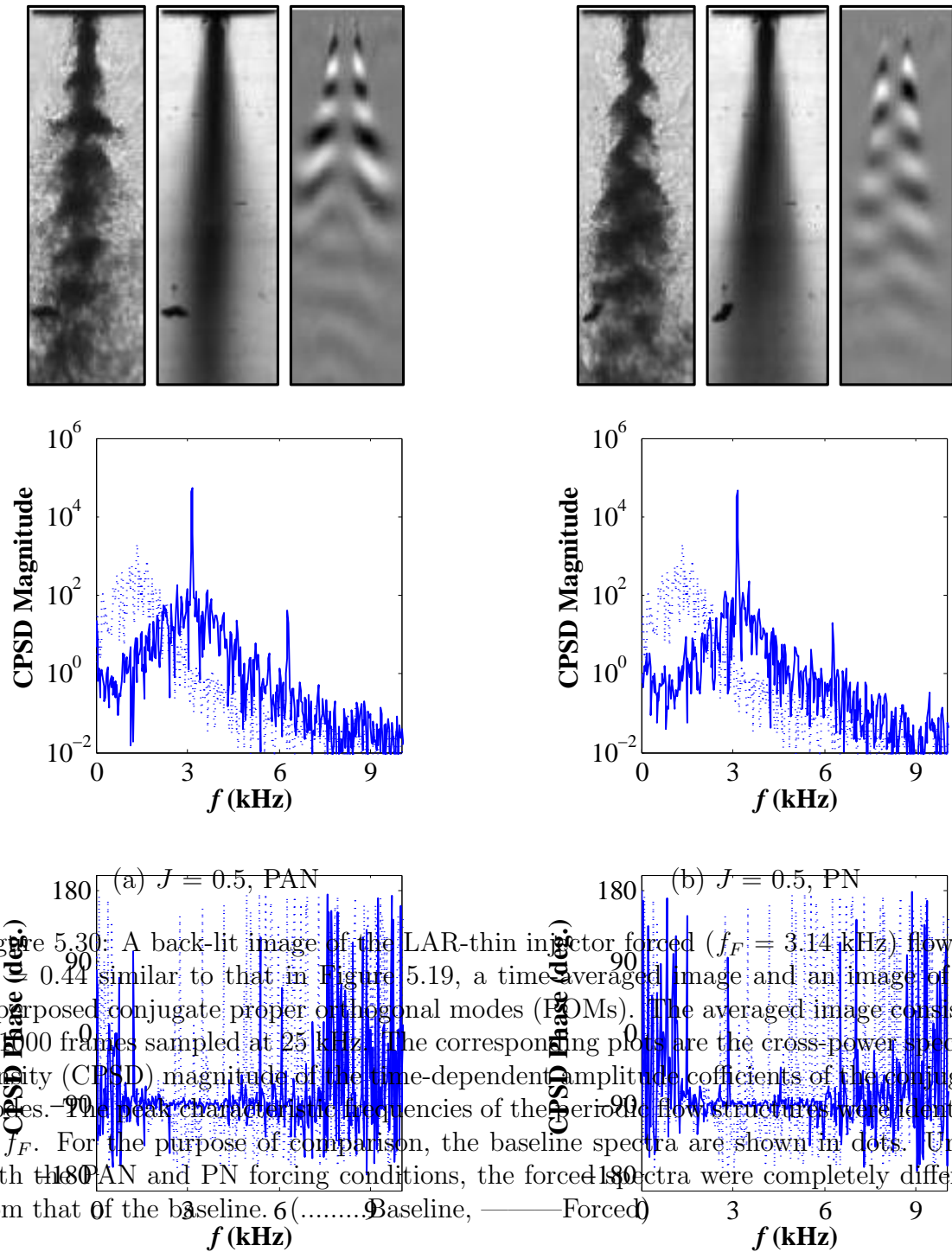


Figure 5.30: A back-lit image of the LAR-thin injector forced ($f_F = 3.14$ kHz) flows at $P_r = 0.44$ similar to that in Figure 5.19, a time-averaged image and an image of the superposed conjugate proper orthogonal modes (POMs). The averaged image consisted of 1000 frames sampled at 25 kHz. The corresponding plots are the cross-power spectral density (CPSD) magnitude of the time-dependent amplitude coefficients of the conjugate modes. The peak characteristic frequencies of the periodic flow structures were identical to f_F . For the purpose of comparison, the baseline spectra are shown in dots. Under both the PAN and PN forcing conditions, the forced spectra were completely different from that of the baseline. (..... Baseline, — Forced)

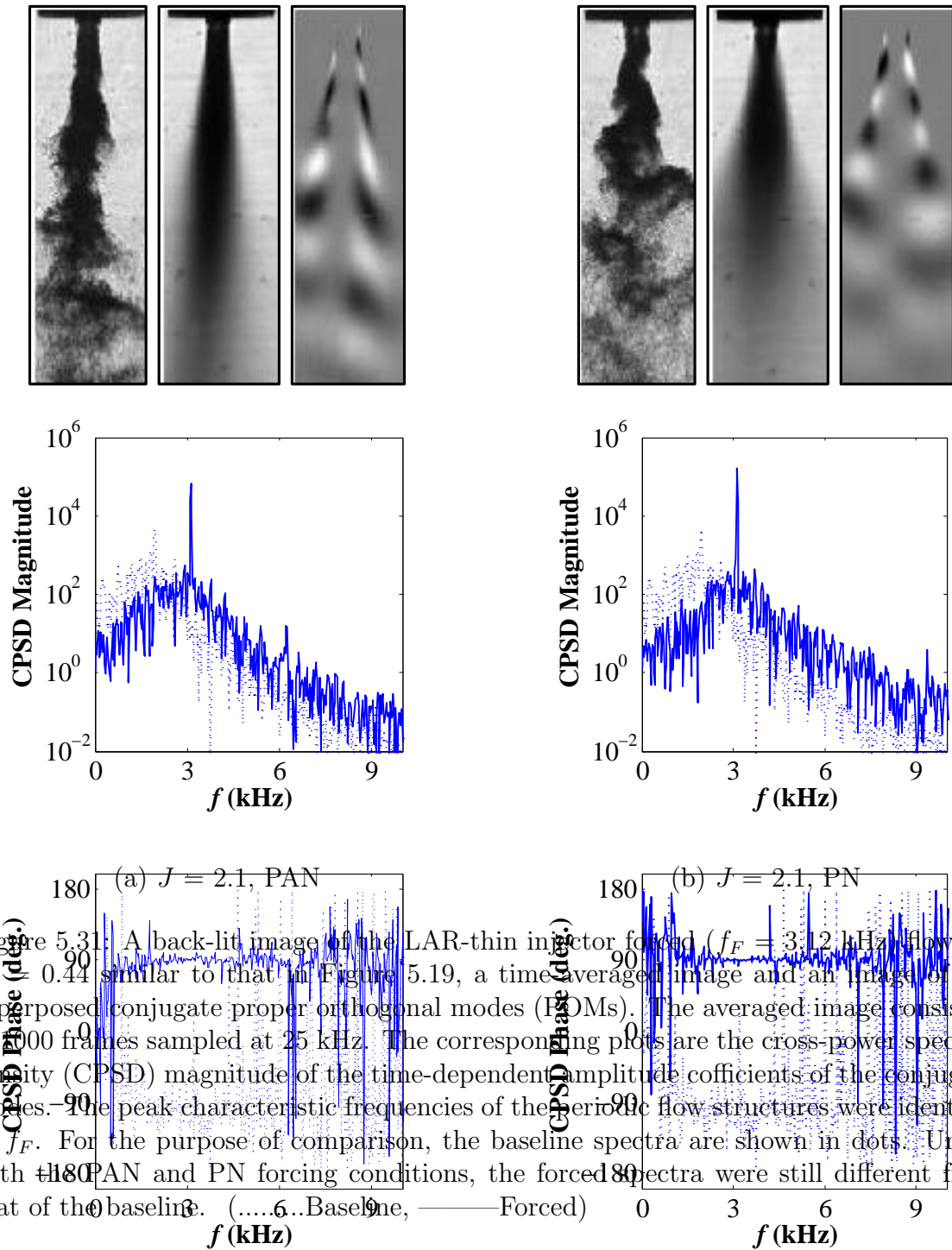
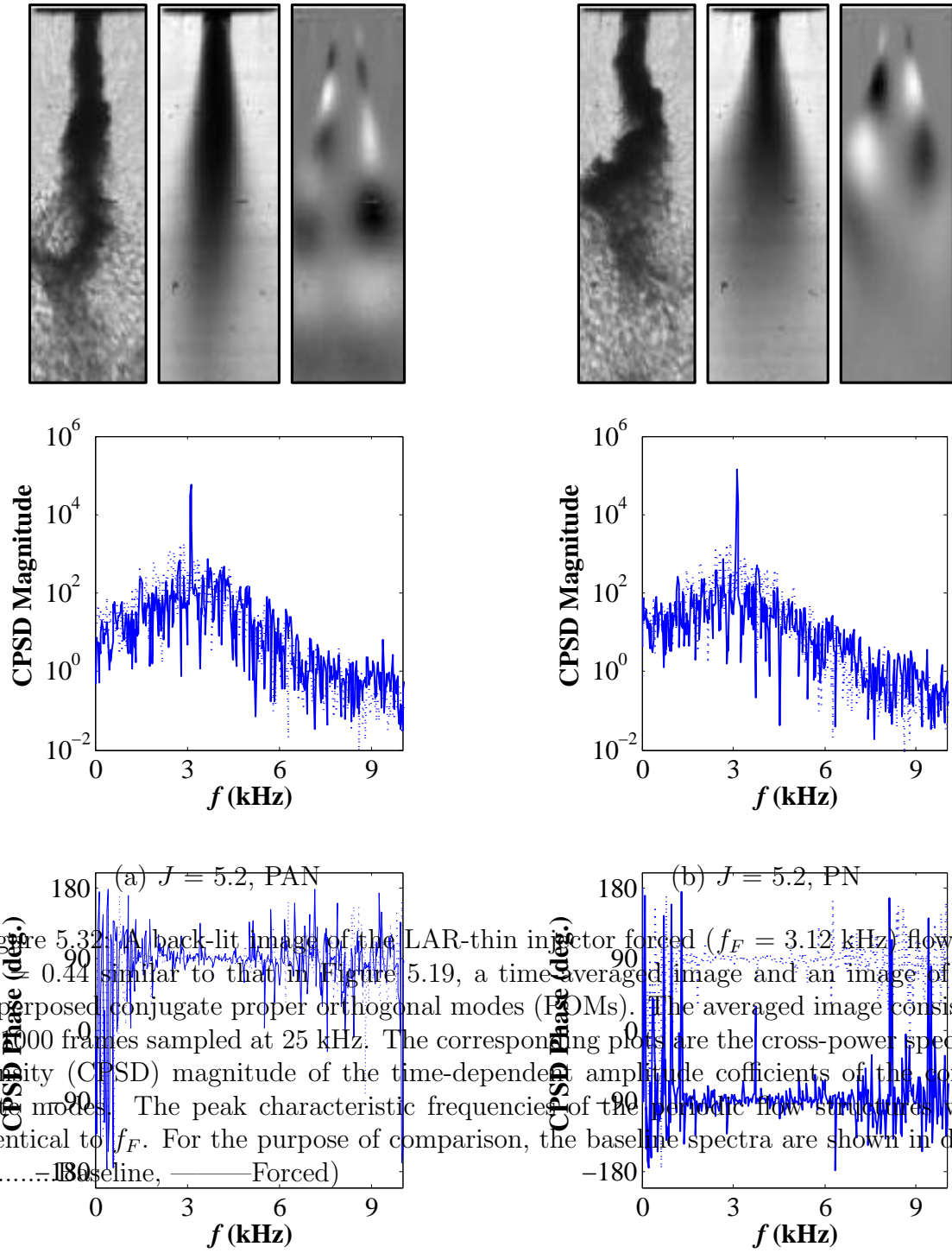


Figure 5.31: A back-lit image of the LAR-thin injector forced ($f_F = 3.12$ kHz) flows at $P_r = 0.44$ similar to that in Figure 5.19, a time-averaged image and an image of the superposed conjugate proper orthogonal modes (POMs). The averaged image consisted of 1000 frames sampled at 25 kHz. The corresponding plots are the cross-power spectral density (CPSD) magnitude of the time-dependent amplitude coefficients of the conjugate modes. The peak characteristic frequencies of the periodic flow structures were identical to f_F . For the purpose of comparison, the baseline spectra are shown in dots. Under both PAN and PN forcing conditions, the forced spectra were still different from that of the baseline. (..... Baseline, — Forced)



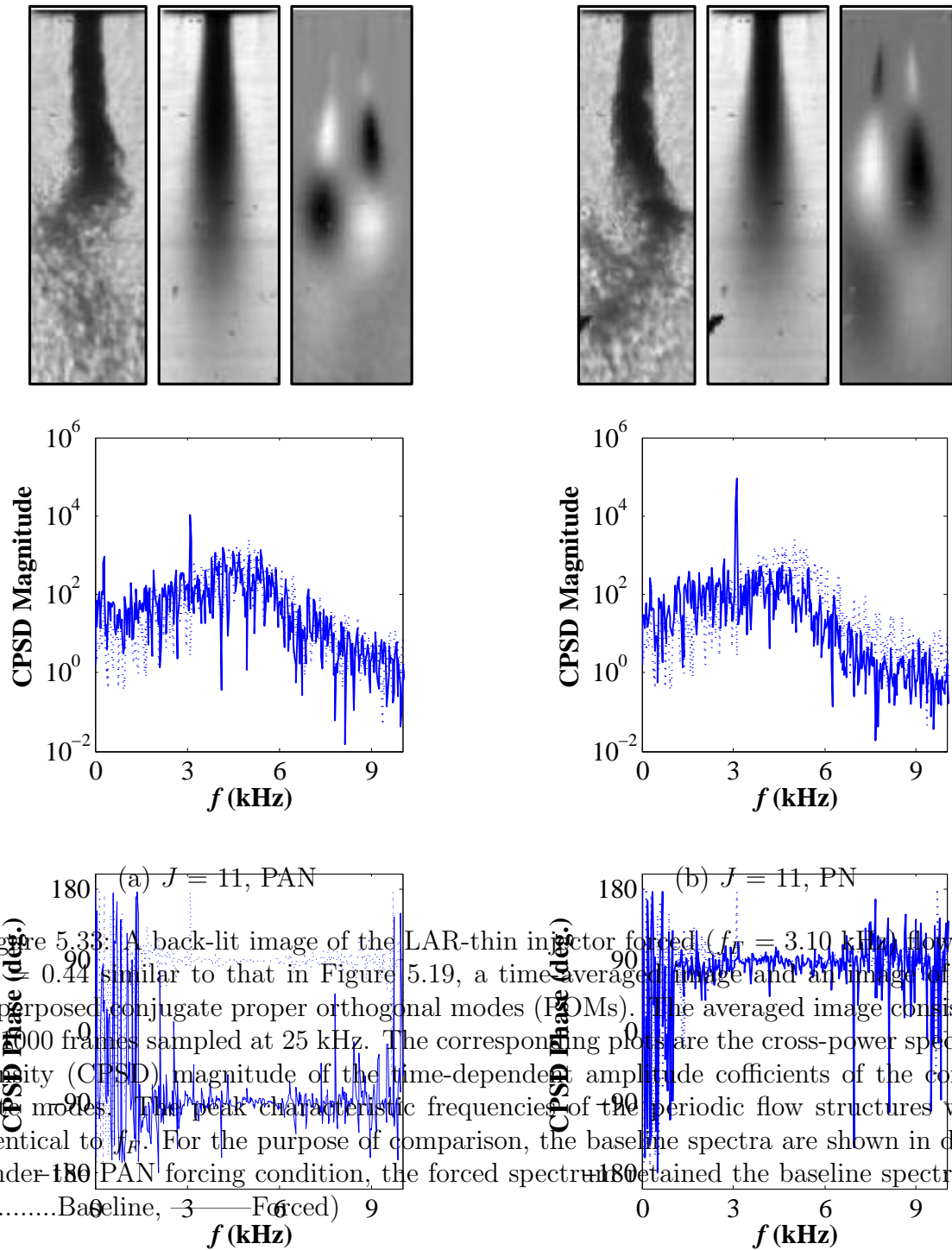
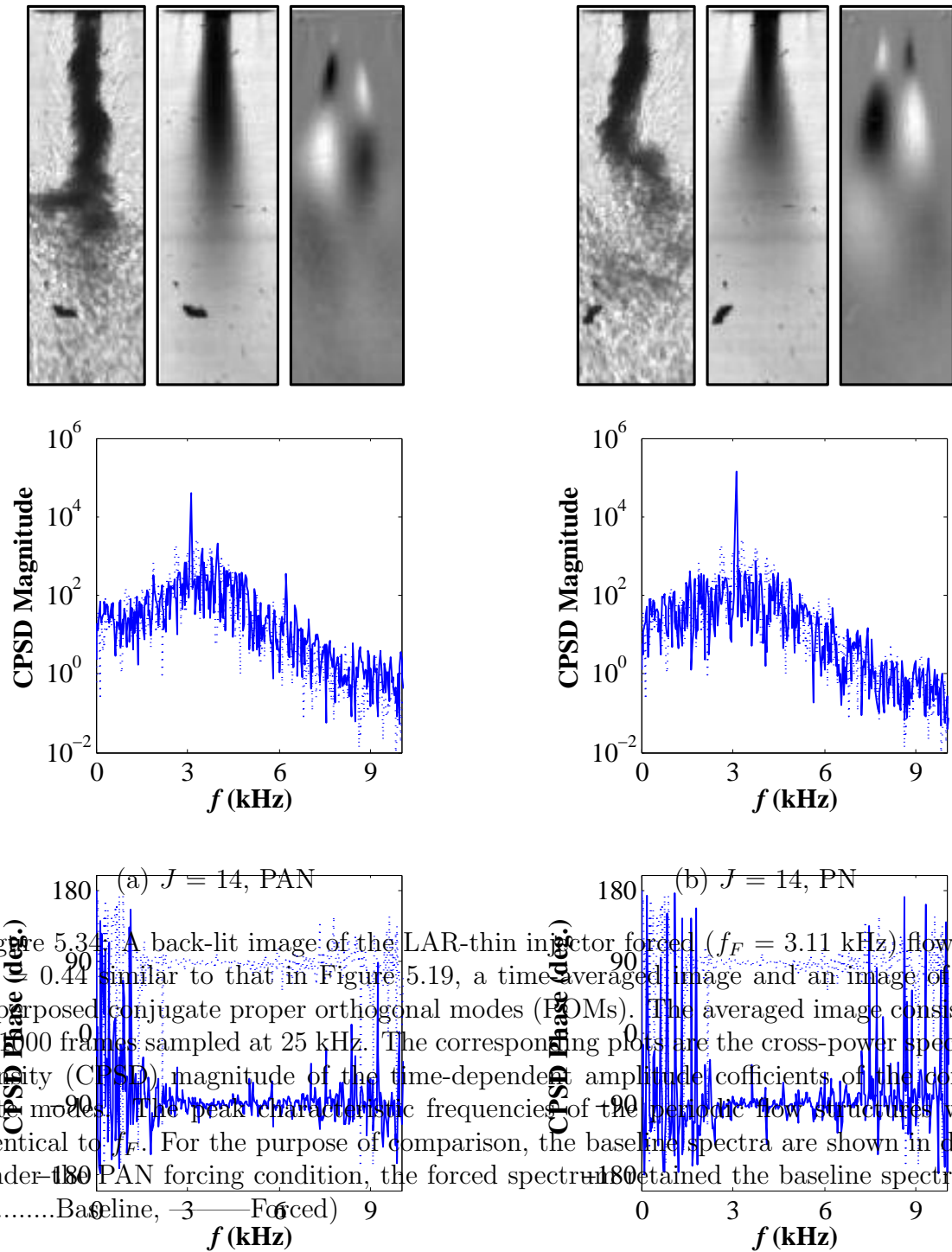
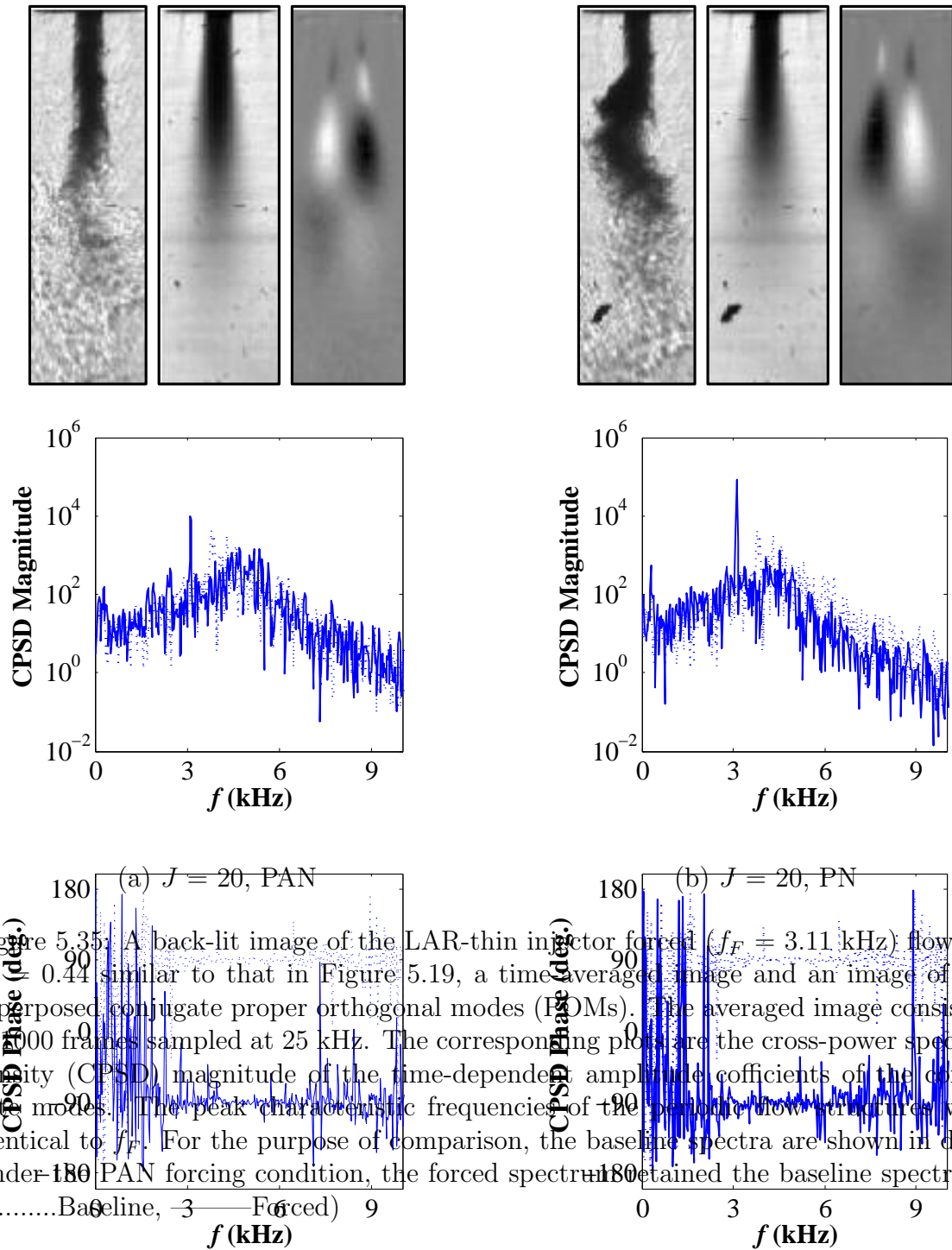


Figure 5.33: A back-lit image of the LAR-thin injector forced ($f_f = 3.10$ kHz) flows at $P_r = 0.44$ similar to that in Figure 5.19, a time-averaged image and an image of the superposed conjugate proper orthogonal modes (POMs). The averaged image consisted of 1000 frames sampled at 25 kHz. The corresponding plots are the cross-power spectral density (CPSD) magnitude of the time-dependent amplitude coefficients of the conjugate modes. The peak characteristic frequencies of the periodic flow structures were identical to f_f . For the purpose of comparison, the baseline spectra are shown in dots. Under PAN forcing condition, the forced spectrum retained the baseline spectrum. (.....Baseline, — Forced)





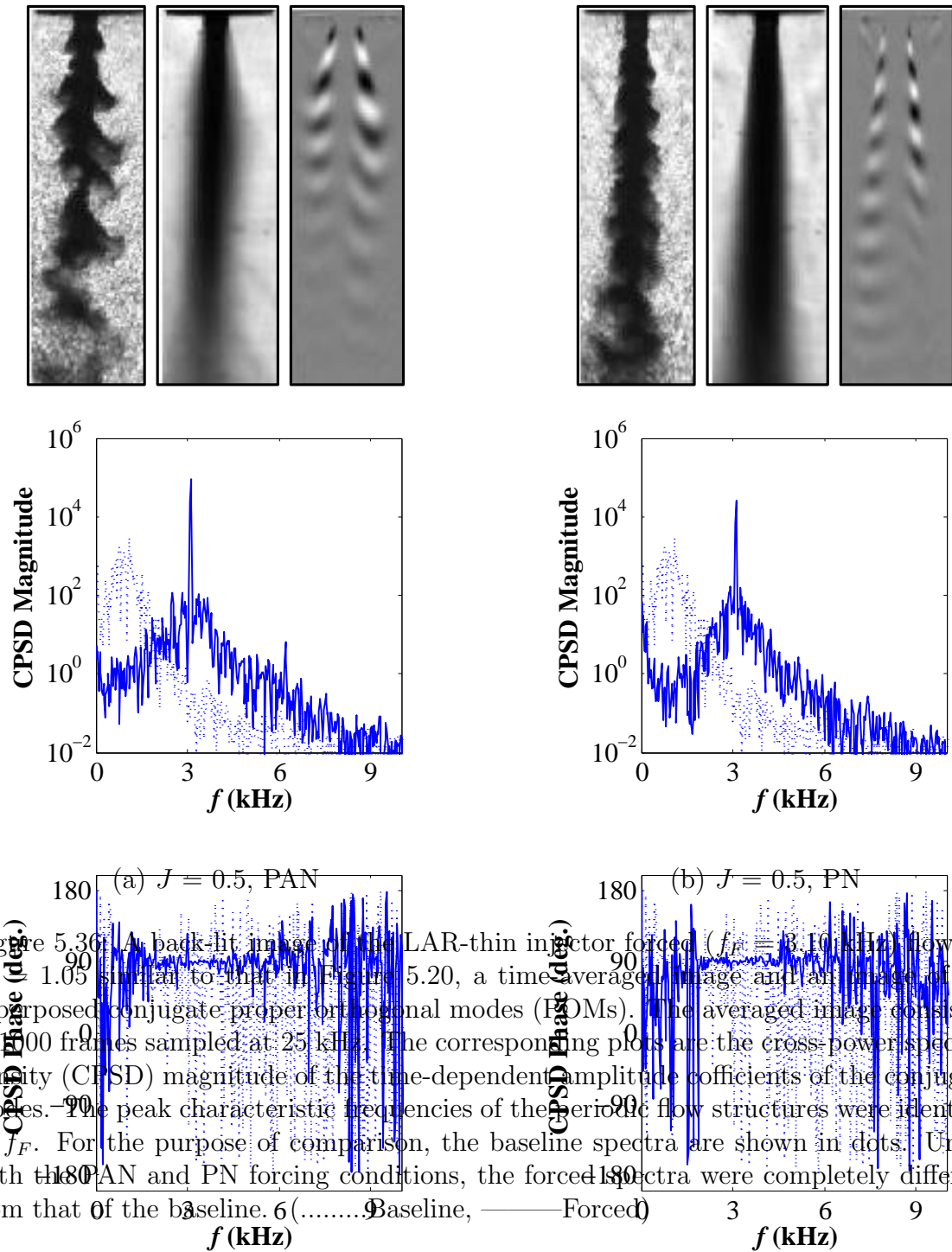


Figure 5.36: (a) A back-lit image of the LAR-thin injector forced ($f_F = 3.10$ kHz) flows at $P_r = 1.05$ similar to that in Figure 5.20, a time-averaged image and an image of the superposed conjugate proper orthogonal modes (POMs). The averaged image consisted of 1000 frames sampled at 25 kHz. The corresponding plots are the cross-power spectral density (CPSD) magnitude of the time-dependent amplitude coefficients of the conjugate modes. The peak characteristic frequencies of the periodic flow structures were identical to f_F . For the purpose of comparison, the baseline spectra are shown in dots. Under both the PAN and PN forcing conditions, the forced spectra were completely different from that of the baseline. (..... Baseline, — Forced)

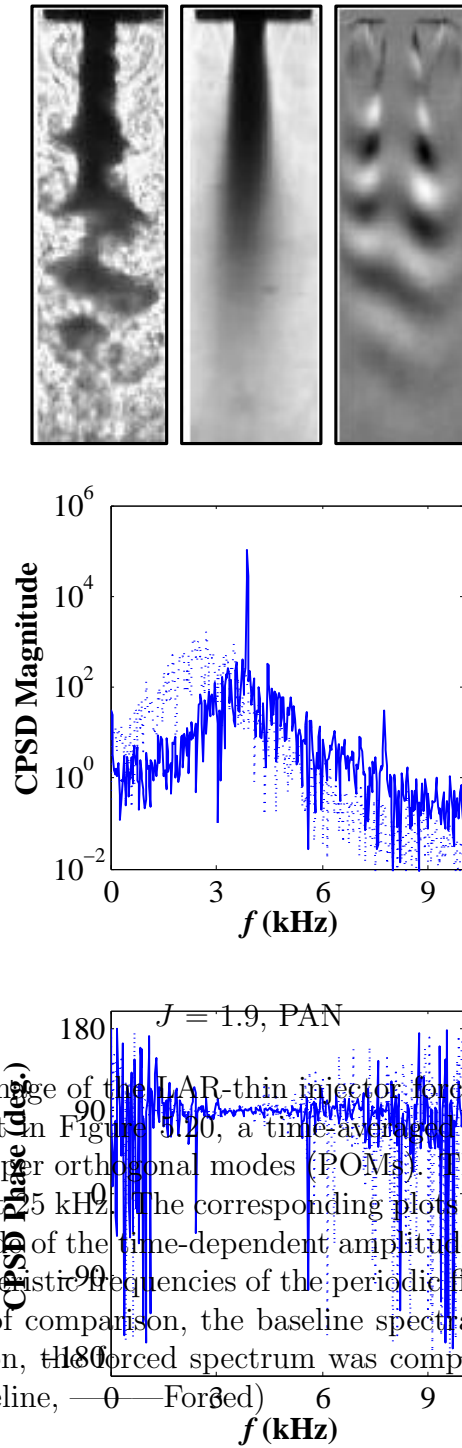


Figure 5.37: A back-lit image of the LAR-thin injector forced ($f_F = 3.10$ kHz) flows at $P_r = 1.05$ similar to that in Figure 5.20, a time-averaged image and an image of the superposed conjugate proper orthogonal modes (POMs). The averaged image consisted of 1000 frames sampled at 5 kHz. The corresponding plots are the cross-power spectral density (CPSD) magnitude of the time-dependent amplitude coefficients of the conjugate modes. The peak characteristic frequencies of the periodic flow structures were identical to f_F . For the purpose of comparison, the baseline spectra are shown in dots. Under the PAN forcing condition, the forced spectrum was completely different from that of the baseline. (.....Baseline, — Forced)

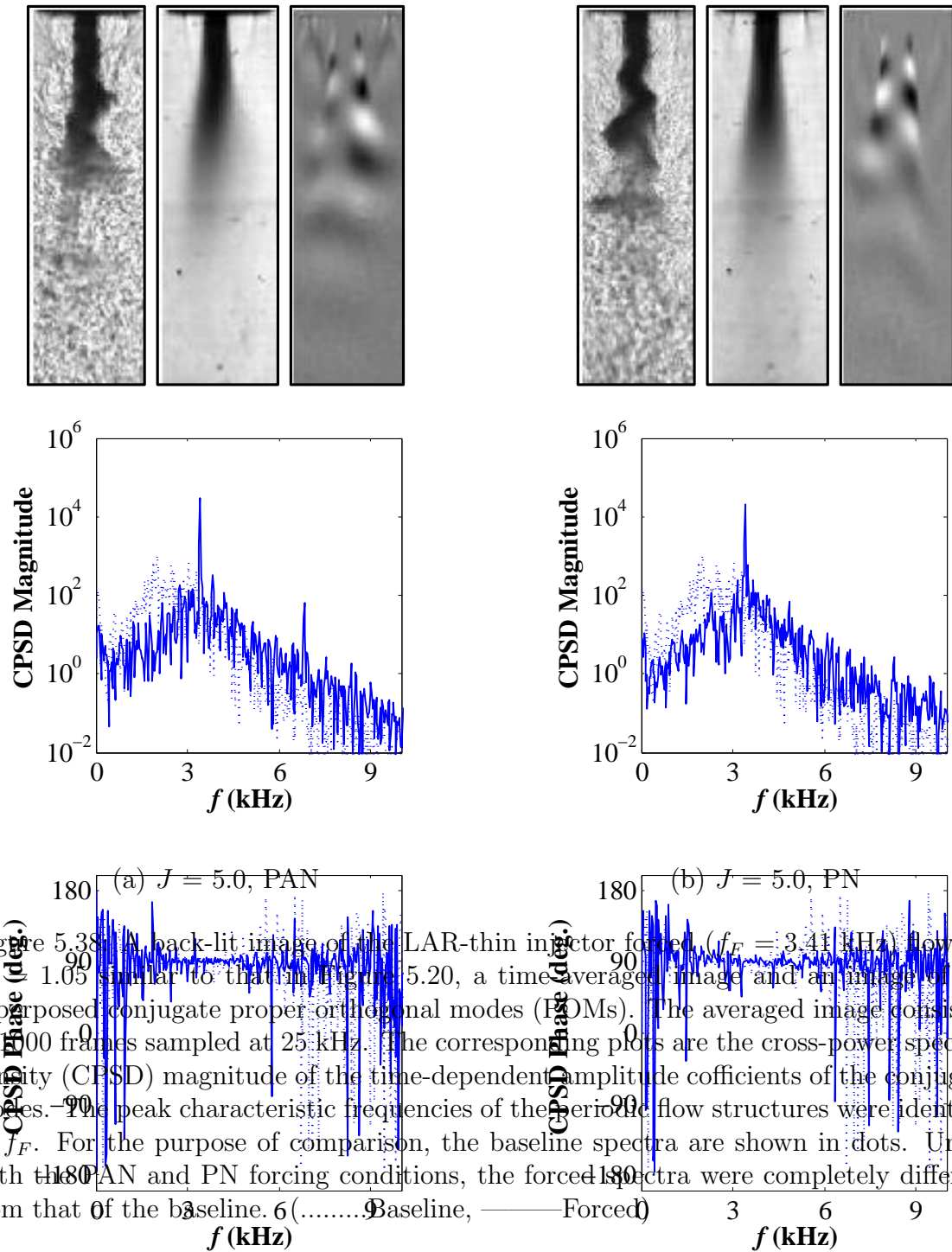


Figure 5.38: (a) A back-lit image of the LAR-thin injector forced, ($f_F = 3.41$ kHz) flows at $P_r = 1.05$ similar to that in Figure 5.20, a time-averaged image and an image of the superposed conjugate proper orthogonal modes (POMs). The averaged image consisted of 1000 frames sampled at 25 kHz. The corresponding plots are the cross-power spectral density (CPSD) magnitude of the time-dependent amplitude coefficients of the conjugate modes. The peak characteristic frequencies of the periodic flow structures were identical to f_F . For the purpose of comparison, the baseline spectra are shown in dots. Under both the PAN and PN forcing conditions, the forced spectra were completely different from that of the baseline. (..... Baseline, — Forced)

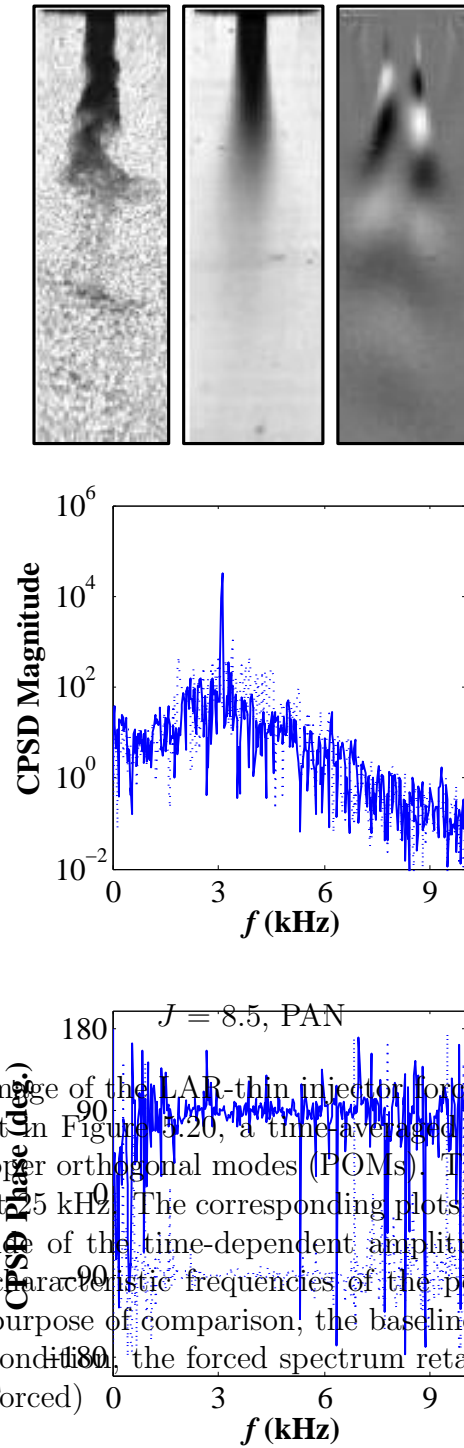


Figure 5.39: A back-lit image of the LAR-thin injector forced ($f_F = 3.10$ kHz) flows at $P_r = 1.05$ similar to that in Figure 5.20, a time-averaged image and an image of the superposed conjugate proper orthogonal modes (POMs). The averaged image consisted of 1000 frames sampled at 15 kHz. The corresponding plots are the cross-power spectral density (CPSD) magnitude of the time-dependent amplitude coefficients of the conjugate modes. The peak characteristic frequencies of the periodic flow structures were identical to f_F . For the purpose of comparison, the baseline spectra are shown in dots. Under the PAN forcing condition, the forced spectrum retained the baseline spectrum. (.....Baseline, — Forced)

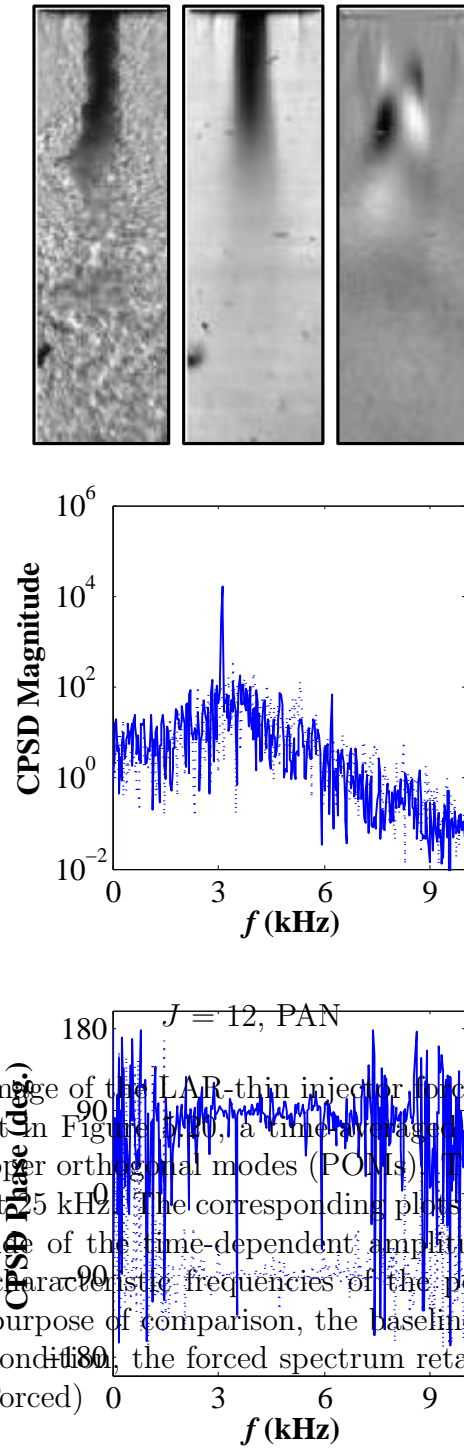


Figure 5.40: A back-lit image of the LAR-thin injector forced ($f_F = 3.10$ kHz) flows at $P_r = 1.05$ similar to that in Figure 5.20, a time-averaged image and an image of the superposed conjugate proper orthogonal modes (POMs). The averaged image consisted of 1000 frames sampled at 5 kHz. The corresponding plots are the cross-power spectral density (CPSD) magnitude of the time-dependent amplitude coefficients of the conjugate modes. The peak characteristic frequencies of the periodic flow structures were identical to f_F . For the purpose of comparison, the baseline spectra are shown in dots. Under the PAN forcing condition, the forced spectrum retained the baseline spectrum. (.....Baseline, — Forced)

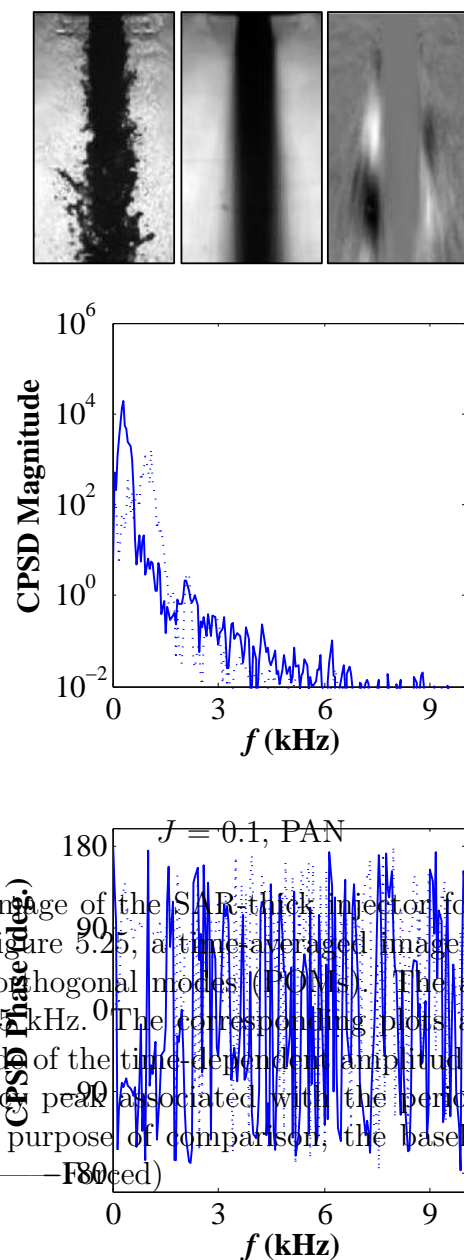


Figure 5.41: A back-lit image of the SAR-thick injector forced ($f_F = 3.10$ kHz) flows at $P_r = 0.44$ shown in Figure 5.25, a time-averaged image and an image of the superposed conjugate proper orthogonal modes (POMs). The averaged image consisted of 500 frames sampled at 25 kHz. The corresponding plots are the cross-power spectral density (CPSD) magnitude of the time-dependent amplitude coefficients of the conjugate modes. The low frequency peak associated with the periodic flow structures was not identical to f_F . For the purpose of comparison, the baseline spectra are shown with dots. (.....Baseline, — Forced)

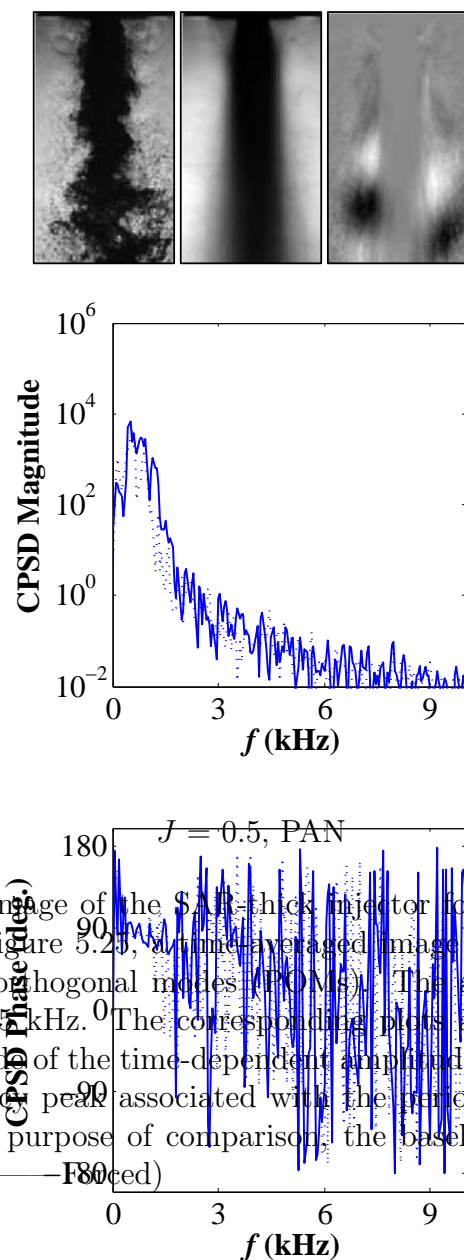


Figure 5.42: A back-lit image of the SAR-thick injector forced ($f_F = 3.04$ kHz) flows at $P_r = 0.44$ shown in Figure 5.25, a time-averaged image and an image of the superposed conjugate proper orthogonal modes (POMs). The averaged image consisted of 500 frames sampled at 25 kHz. The corresponding plots are the cross-power spectral density (CPSD) magnitude of the time-dependent amplitude coefficients of the conjugate modes. The low frequency peak associated with the periodic flow structures was not identical to f_F . For the purpose of comparison, the baseline spectra are shown with dots. (.....Baseline, (—) Forced)

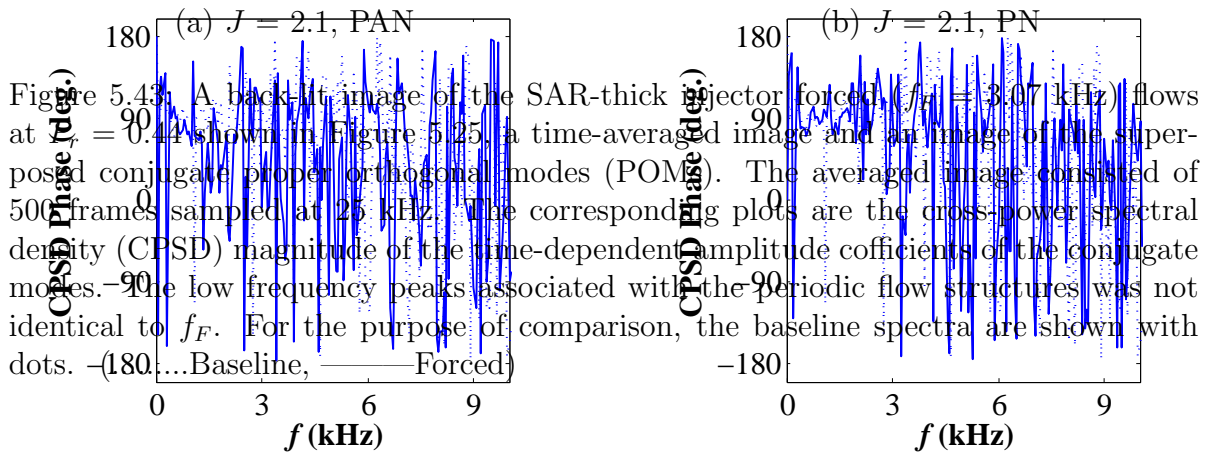
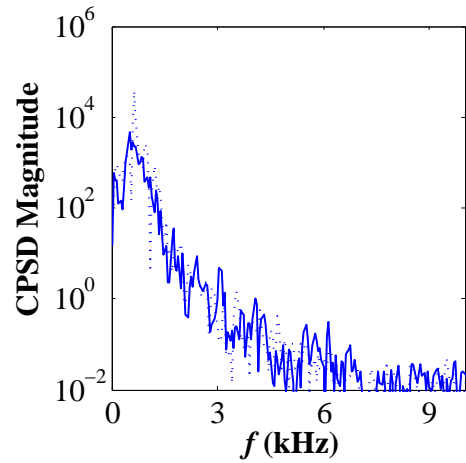
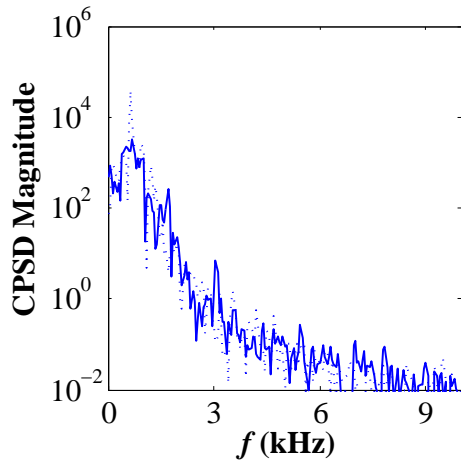
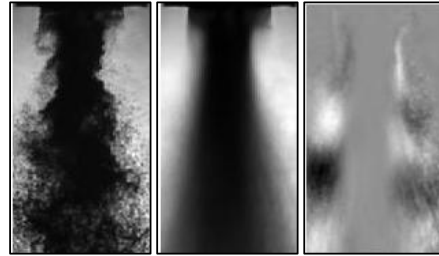
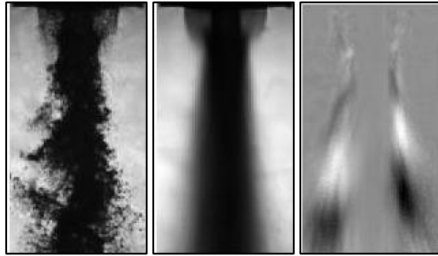
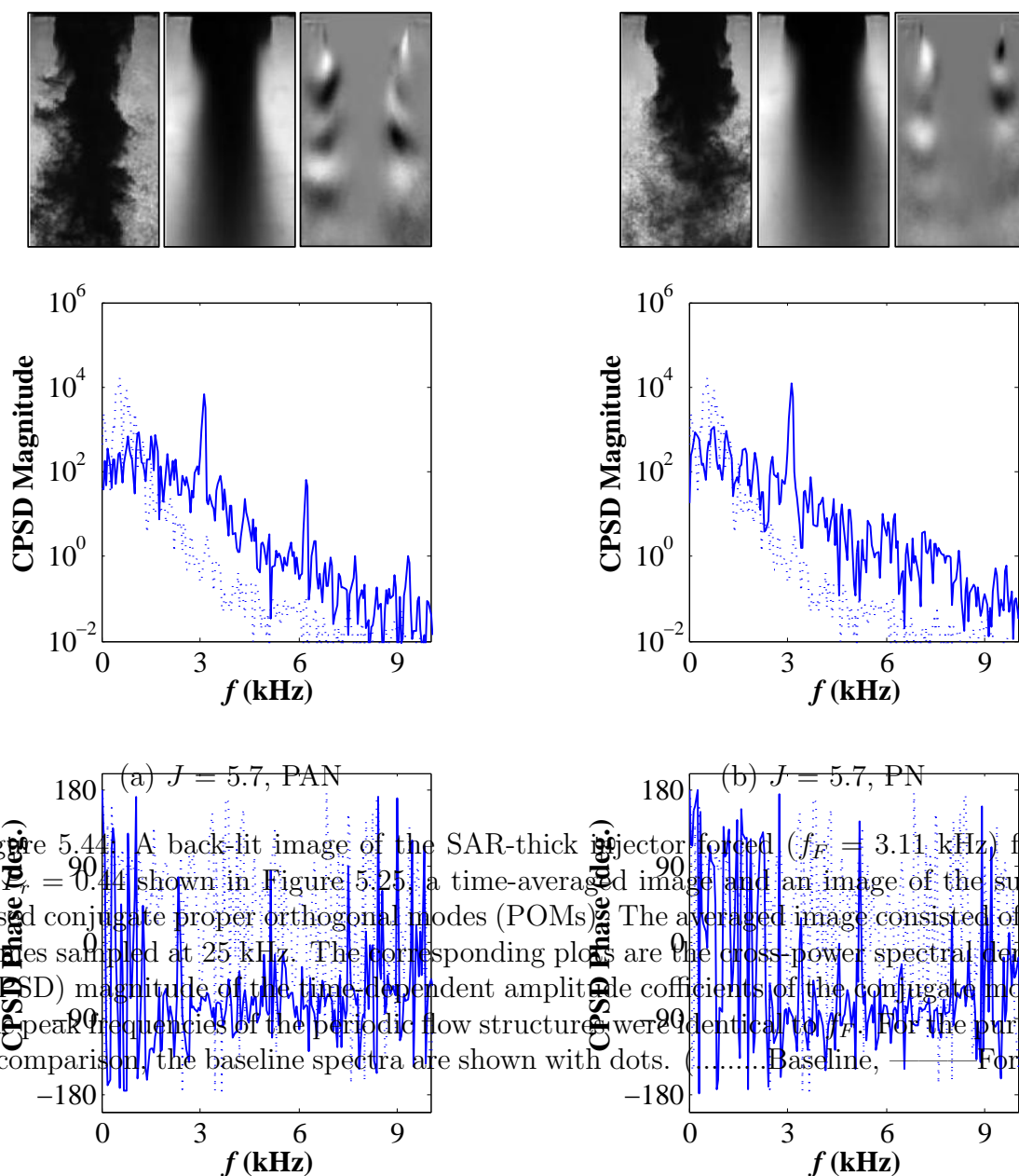


Figure 5.43: A back-lit image of the SAR-thick injector forced, ($f_F = 3.07$ kHz) flows at $J = 0.44$ shown in Figure 5.25, a time-averaged image and an image of the superposed conjugate proper orthogonal modes (POM). The averaged image consisted of 500 frames sampled at 25 kHz. The corresponding plots are the cross-power spectral density (CPSD) magnitude of the time-dependent amplitude coefficients of the conjugate modes. The low frequency peaks associated with the periodic flow structures was not identical to f_F . For the purpose of comparison, the baseline spectra are shown with dots. (—Baseline, — Forced)



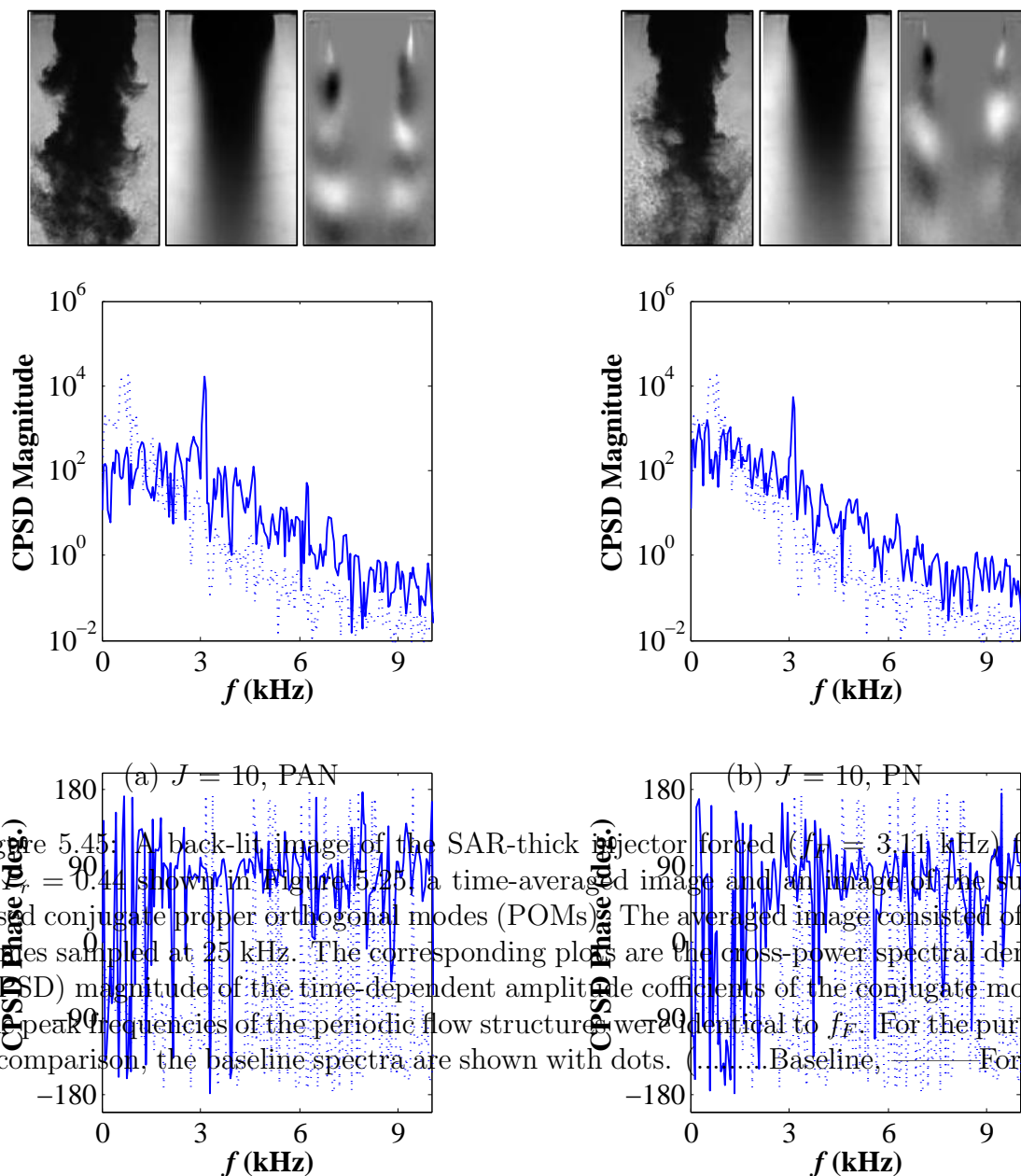


Figure 5.45: A back-lit image of the SAR-thick injector forced ($f_F = 3.11$ kHz) flows at $J = 0.44$ shown in Figure 5.25, a time-averaged image and an image of the superposed conjugate proper orthogonal modes (POMs). The averaged image consisted of 500 frames sampled at 25 kHz. The corresponding plots are the cross-power spectral density (CPSD) magnitude of the time-dependent amplitude coefficients of the conjugate modes. The peak frequencies of the periodic flow structures were identical to f_F . For the purpose of comparison, the baseline spectra are shown with dots. (.....Baseline, — Forced)

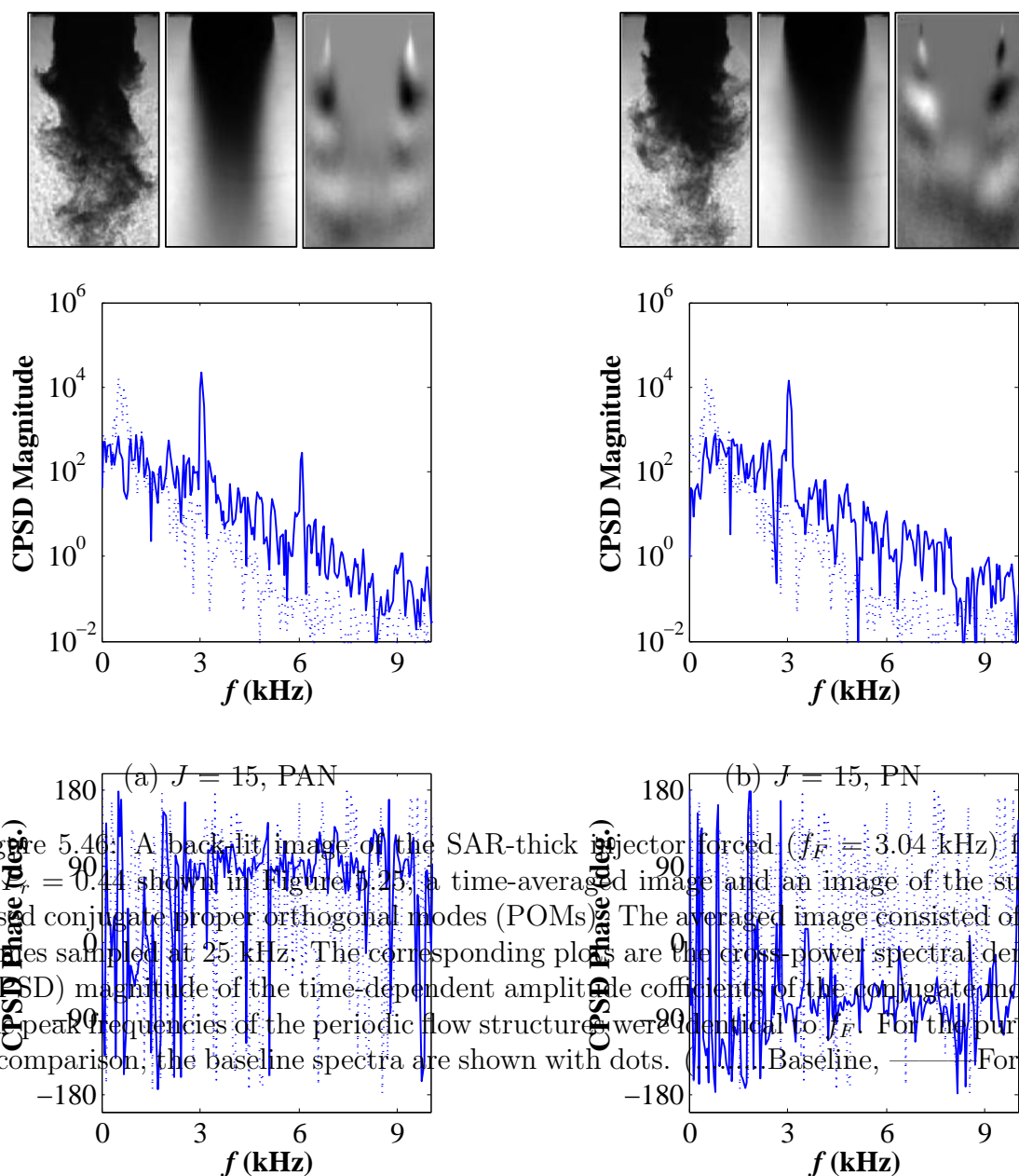


Figure 5.46: A back-lit image of the SAR-thick injector forced ($f_F = 3.04$ kHz) flows at $J = 0.44$ shown in Figure 5.25; a time-averaged image and an image of the superposed conjugate proper orthogonal modes (POMs). The averaged image consisted of 500 frames sampled at 25 kHz. The corresponding plots are the cross-power spectral density (CPSD) magnitude of the time-dependent amplitude coefficients of the conjugate modes. The peak frequencies of the periodic flow structures were identical to f_F . For the purpose of comparison, the baseline spectra are shown with dots. (..... Baseline, — Forced)

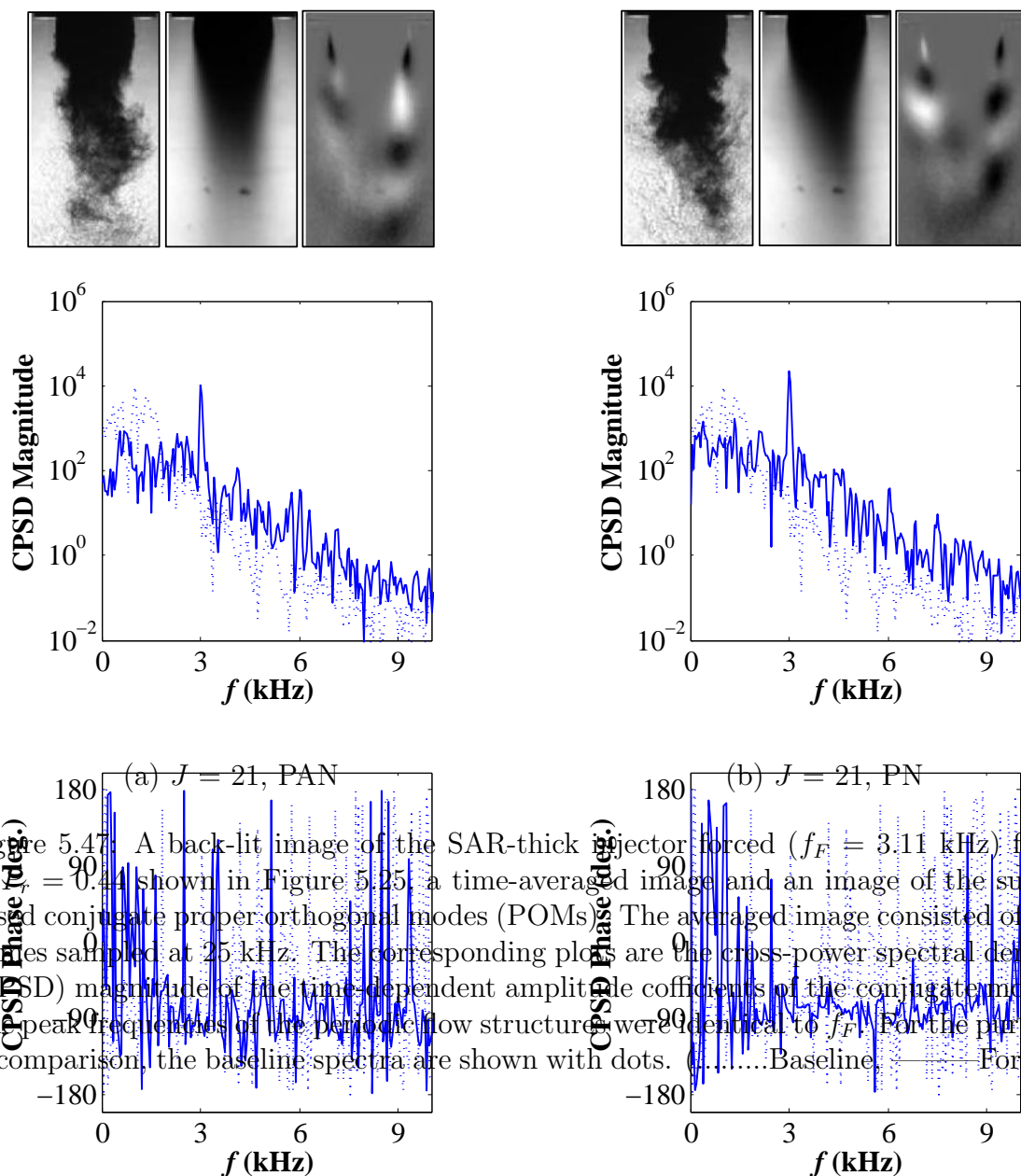


Figure 5.47: A back-lit image of the SAR-thick injector forced ($f_F = 3.11$ kHz) flows at $J = 0.44$ shown in Figure 5.25: a time-averaged image and an image of the superposed conjugate proper orthogonal modes (POMs). The averaged image consisted of 500 frames sampled at 25 kHz. The corresponding plots are the cross-power spectral density (CPSD) magnitude of the time-dependent amplitude coefficients of the conjugate modes. The peak frequencies of the periodic flow structures were identical to f_F . For the purpose of comparison, the baseline spectra are shown with dots. (.....Baseline, — Forced)

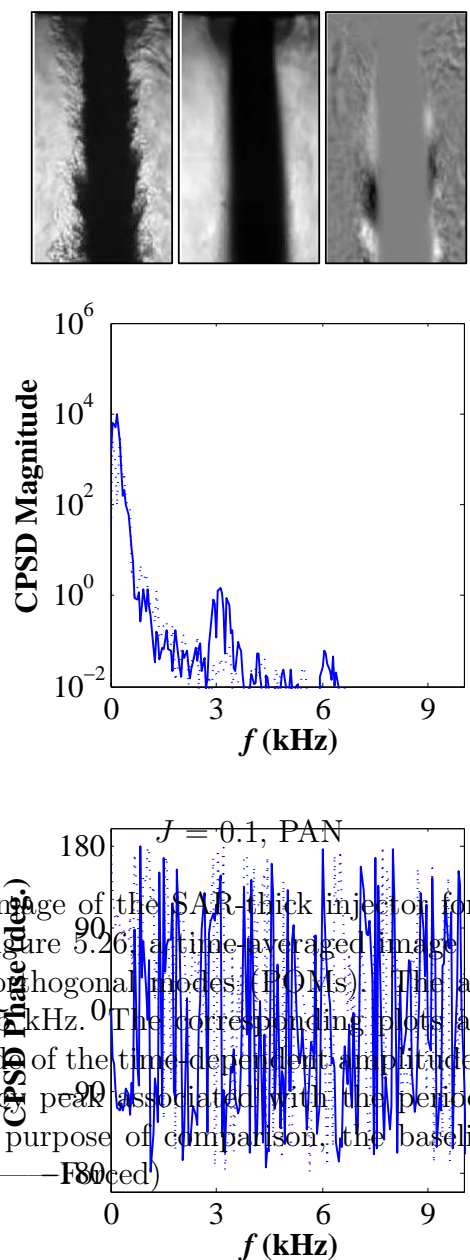


Figure 5.48: A back-lit image of the SAR-thick injector forced ($f_F = 3.12$ kHz) flows at $P_r = 1.05$ shown in Figure 5.26; a time-averaged image and an image of the superposed conjugate proper orthogonal modes (POMs). The averaged image consisted of 500 frames sampled at 25 kHz. The corresponding plots are the cross-power spectral density (CPSD) magnitude of the time-dependent amplitude coefficients of the conjugate modes. The low frequency peak associated with the periodic flow structures was not identical to f_F . For the purpose of comparison, the baseline spectra are shown with dots. (.....Baseline, ——— Forced)

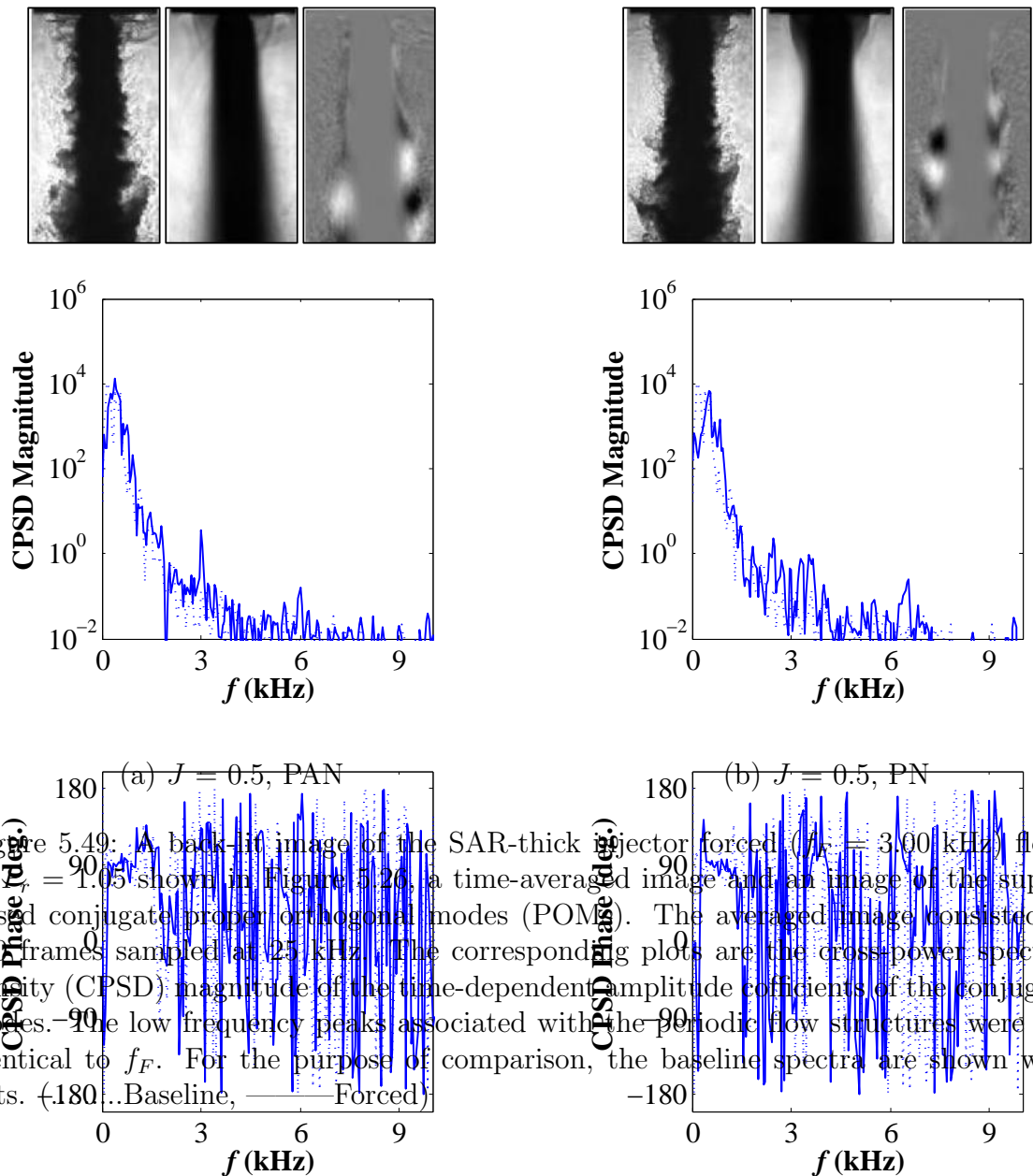
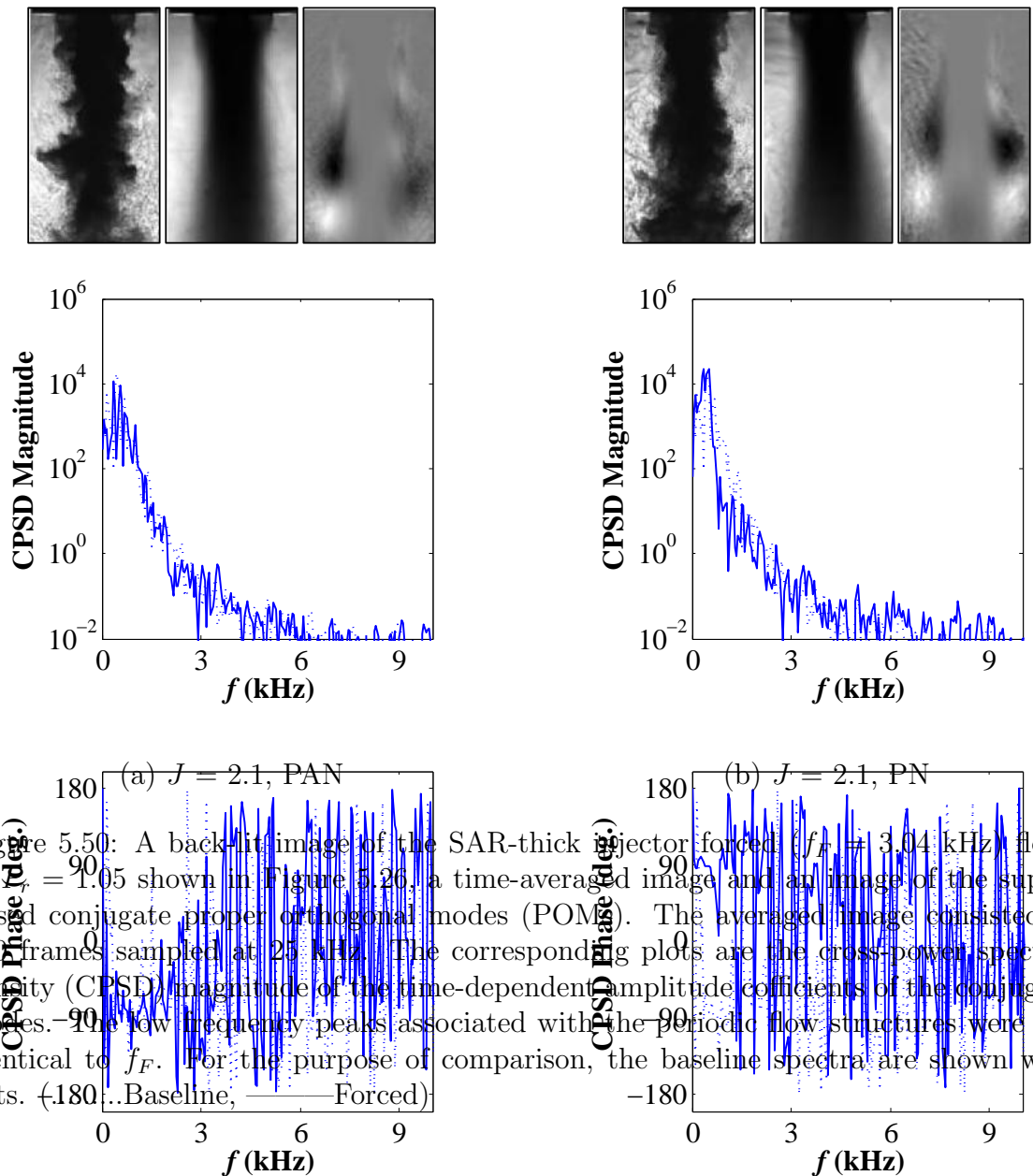


Figure 5.49: (A) back-lit image of the SAR-thick injector forced ($f_F = 3.00$ kHz) flows at $J = 1.05$ shown in Figure 5.26, a time-averaged image and an image of the superposed conjugate proper orthogonal modes (POM). The averaged image consisted of 500 frames sampled at 25 kHz. The corresponding plots are the cross-power spectral density (CPSD) magnitude of the time-dependent amplitude coefficients of the conjugate modes. The low frequency peaks associated with the periodic flow structures were not identical to f_F . For the purpose of comparison, the baseline spectra are shown with dots. (— Baseline, — Forced)



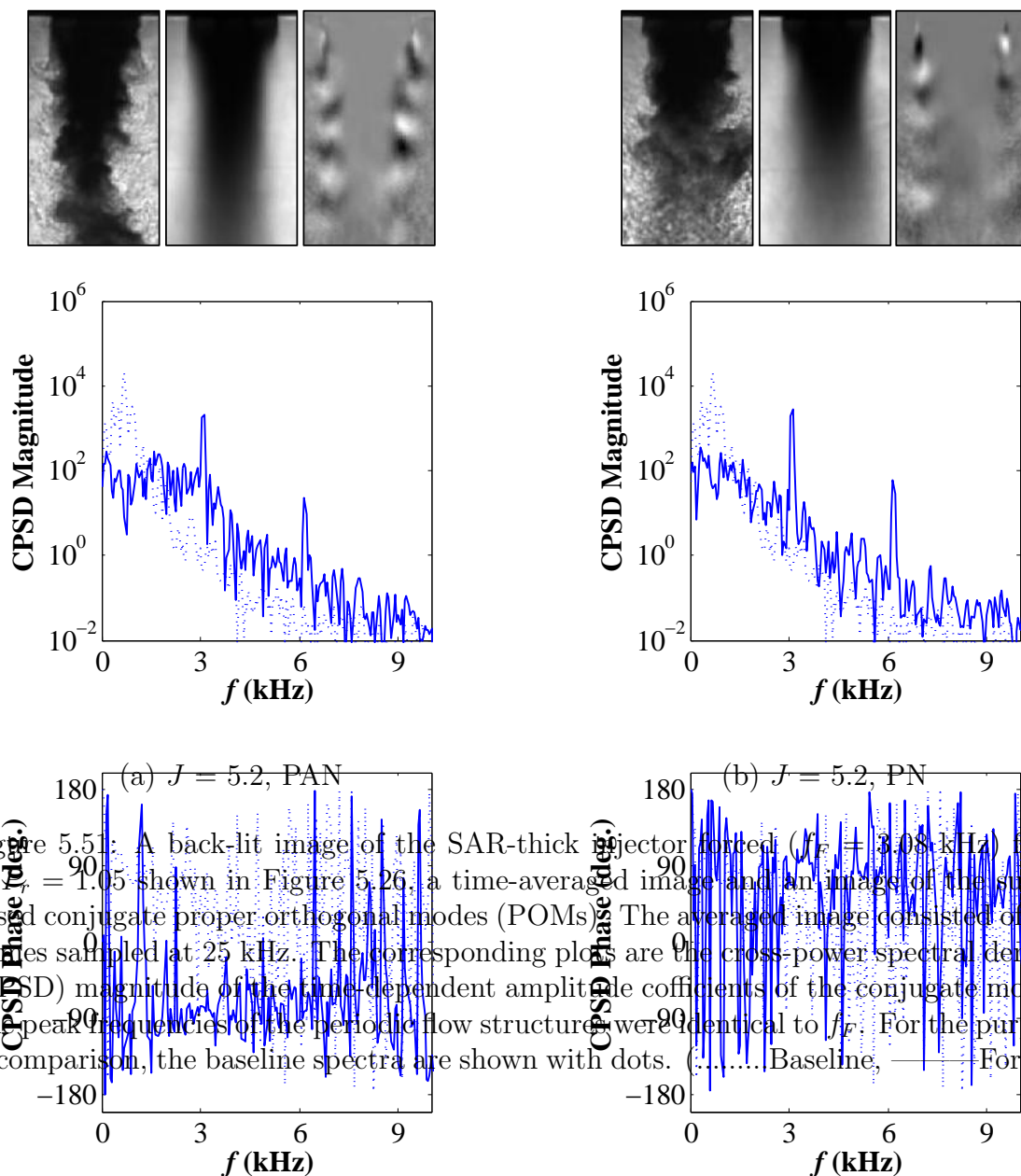


Figure 5.51: A back-lit image of the SAR-thick injector forced ($f_F = 3.08$ kHz) flows at $J = 1.05$ shown in Figure 5.26, a time-averaged image and an image of the superposed conjugate proper orthogonal modes (POMs). The averaged image consisted of 500 frames sampled at 25 kHz. The corresponding plots are the cross-power spectral density (CPSD) magnitude of the time-dependent amplitude coefficients of the conjugate modes. The peak frequencies of the periodic flow structures were identical to f_F . For the purpose of comparison, the baseline spectra are shown with dots. (..... Baseline, — Forced)

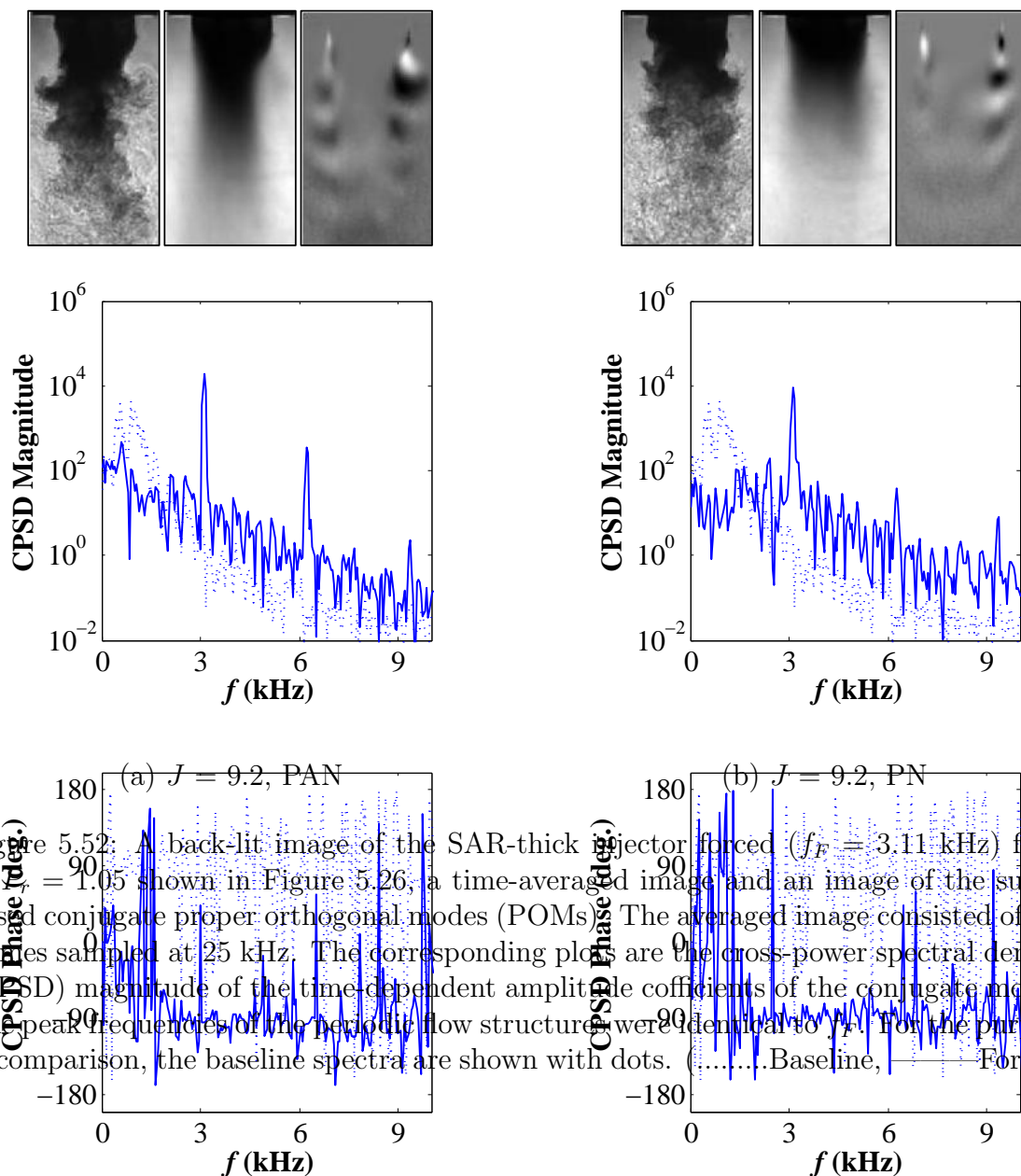


Figure 5.52: A back-lit image of the SAR-thick injector forced ($f_F = 3.11$ kHz) flows at $J = 1.05$ shown in Figure 5.26, a time-averaged image and an image of the superposed conjugate proper orthogonal modes (POMs). The averaged image consisted of 500 frames sampled at 25 kHz. The corresponding plots are the cross-power spectral density (CPSD) magnitude of the time-dependent amplitude coefficients of the conjugate modes. The peak frequencies of the periodic flow structures were identical to f_F . For the purpose of comparison, the baseline spectra are shown with dots. (.....Baseline, — Forced)

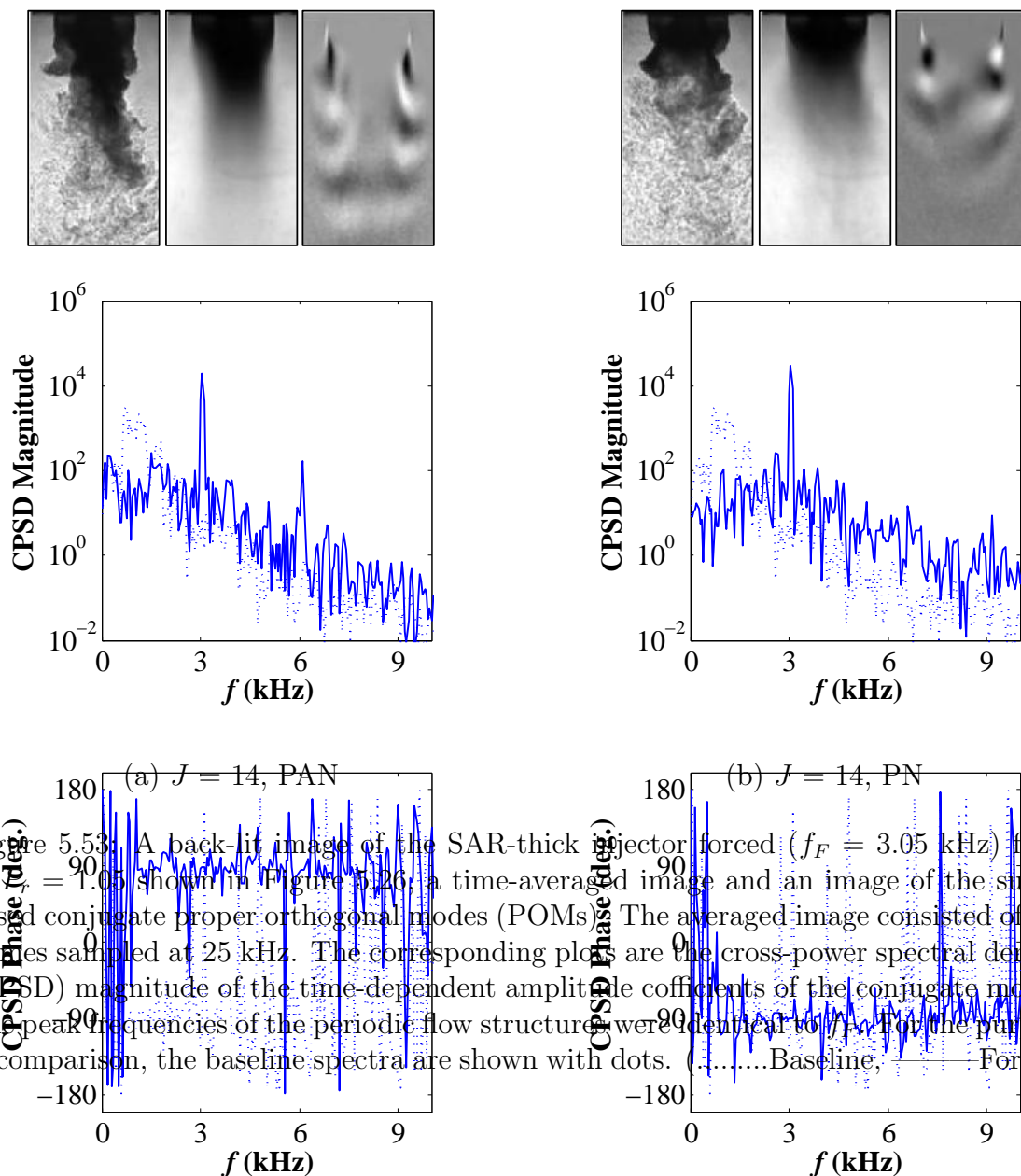


Figure 5.53: A back-lit image of the SAR-thick injector forced ($f_F = 3.05$ kHz) flows at $J = 1.05$ shown in Figure 5.26: a time-averaged image and an image of the superposed conjugate proper orthogonal modes (POMs). The averaged image consisted of 500 frames sampled at 25 kHz. The corresponding plots are the cross-power spectral density (CPSD) magnitude of the time-dependent amplitude coefficients of the conjugate modes. The peak frequencies of the periodic flow structures were identical to f_F . For the purpose of comparison, the baseline spectra are shown with dots. (.....Baseline, — Forced)

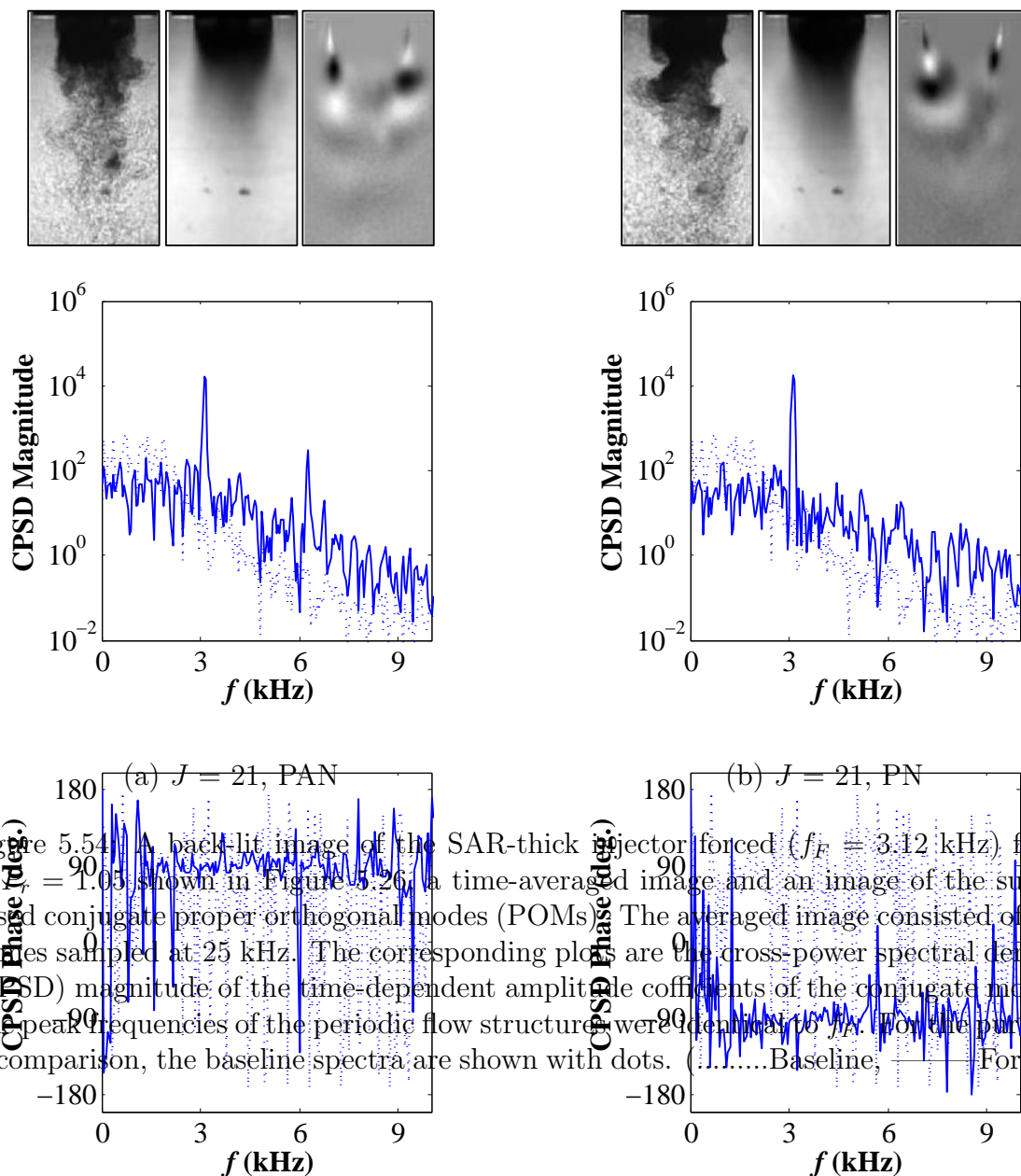


Figure 5.54: A back-lit image of the SAR-thick injector forced ($f_F = 3.12$ kHz) flows at $J = 1.05$ shown in Figure 5.26, a time-averaged image and an image of the superposed conjugate proper orthogonal modes (POMs). The averaged image consisted of 500 frames sampled at 25 kHz. The corresponding plots are the cross-power spectral density (CPSD) magnitude of the time-dependent amplitude coefficients of the conjugate modes. The peak frequencies of the periodic flow structures were identical to f_F . For the purpose of comparison, the baseline spectra are shown with dots. (.....Baseline; — Forced)

CHAPTER 6

Summary, Conclusions and Recommendations for Future Work

6.1 Droplet Combustion

The single fuel droplet experiments allowed for the exploration of alternative fuel combustion characteristics in the presence of acoustic perturbations. These included changes that can occur in the mean burning rates associated with a single burning fuel droplet, and flame extinction limits for a range of acoustic excitation conditions. The flame deflections observed at moderate acoustic intensities were qualitatively in accordance with the predictions of the acoustic radiation force theory. The directions of the theoretical and measured acoustic accelerations were consistent with each other. However, the magnitudes of the measured acoustic accelerations were larger and steeper in the vicinity of the pressure node than predicted by theory. This was contrary to the expected profile, where a maximum acceleration was expected to occur at approximately $\lambda/8$ away from the pressure node. The variation in magnitude of the burning rate constants, despite not being significantly larger than the measurement uncertainties, showed a closer correspondence to the variation in magnitude of the measured acoustic accelerations than the theoretical acoustic accelerations.

Conducting the experiments in normal gravity resulted in natural convection being a significant factor in the magnitude of the burning rate constants at moderate levels of

acoustic forcing, thereby diminishing the impact of the acoustic radiation force. At very high amplitudes of forcing, however, the nearly horizontal deflected flames indicated that g_a exceeded gravitational acceleration by a significant degree.

Based on preliminary extinction strain rate results obtained thus far, there was no significant difference between the alcohols and the hydrocarbon fuels. The current method of evaluating strain rates involved estimating an equivalent bulk flow velocity due to the strong acoustic acceleration and gravitation acceleration. Since the acoustic acceleration was measured based on the degree of flame deflection, and the flame orientation was nearly horizontal at the instant before extinction, the estimated bulk flow velocity was thus very sensitive to measured angles of flame deflection. As little as two to three degrees of uncertainty in the measured flame deflection angle brought about changes in the estimated strain rates of more than 40 s^{-1} . A more refined method of estimating the extinction strain rates for the flames of the different fuels must be sought.

6.2 Non-Reactive Shear-Coaxial Jets

The high pressure, cryogenic shear-coaxial jets experiment provided a means to break down the complex phenomena associated with combustion instabilities, and focus on the non-reactive flow processes that contribute to their growth and sustenance. Chamber pressures below (reduced pressure, $P_r = 0.44$) and just above the critical pressure ($P_r = 1.05$) of nitrogen, and cryogenic jet temperatures allowed for the exploration of different injection phases of the nitrogen test fluid: a liquid inner jet with a cold, gaseous outer jet, and a transcritical inner jet with a supercritical outer jet. A range of momentum flux ratios, $J = 0.1 - 21$, were achieved by holding the inner jet flowrate constant and varying the outer jet flowrate. Two injector configurations that had different outer to inner jet exit area ratio, A_o/A_i , and inner injector post thickness to inner injector inside diameter ratio, t/D_1 , were used. Accordingly, one injector had a large A_o/A_i (LAR)

with a small t/D_1 (thin) while the other had a small A_o/A_i (SAR) with a large t/D_1 (thick). Dark-core lengths based on the silhouette of the dense inner jet fluid were measured for different J flows at $P_r = 0.44$ and $P_r = 1.05$, with and without transverse acoustic forcing, which created either a pressure antinode (PAN) or a pressure node (PN) condition at the coaxial jet location. A proper orthogonal decomposition of the high-speed image data pixel intensities was used to identify the spatial and temporal characteristics of dominant flow structures.

Under baseline or no acoustic forcing condition, the ratio of the dark-core length to inner jet diameter, L_B/D_1 , of the LAR-thin and SAR-thick injector flows at both P_r showed a decreasing trend with increasing J . This decreasing trend also had a steeper gradient for lower J than for higher J values. A power-law curve-fit to the L_B/D_1 variation with J revealed a slightly stronger dependence on J at $P_r = 1.05$, where the LAR-thin injector flow L_B/D_1 varied as $J^{-0.50}$ and that of the SAR-thick injector flow as $J^{-0.54}$, while at $P_r = 0.44$, L_B/D_1 varied as $J^{-0.39}$ and as $J^{-0.35}$ for the LAR-thin and SAR thick injector flows, respectively. For comparable J values, flows at $P_r = 0.44$ had larger L_B/D_1 than those at $P_r = 1.05$. Furthermore, for comparable J values and the same P_r , the SAR-thick injector flows had smaller L_B/D_1 than the LAR-thin injector flows.

The baseline dark-core length measurements for the LAR-thin and SAR-thick injectors were also compared with two other alternate injector exit configurations from previous works in the present experimental facility using a SAR-thin and a LAR-thick injector. Unlike the current work, most of the results obtained using the SAR-thin and LAR-thick injectors had the inner jet injector recessed by $0.5D_1$. However, a similar set of experiments done with and without recess using the SAR-thin injector showed no statistically significant differences in their dark-core lengths. A comparison of L_B/D_1 for the four different injectors showed a large spread for low J flows, where it was the

largest for the LAR-thin injector flows, and the smallest for the SAR-thick and SAR-thin injector flows. For low J flows, the LAR-thick L_B/D_1 were less than the LAR-thin, and greater than both SAR injectors. At high J values, all but the LAR-thin had L_B/D_1 that asymptotically approached the same value. For J values beyond the highest reported in these studies, the trend in the LAR-thin L_B/D_1 also appeared to approach the same asymptotic value as the others. In general, it was found that L_B/D_1 increased with increasing A_o/A_i while it decreased with increasing J and t/D_1 . Thus, the extent of mixing may be controlled by altering these flow and geometric parameters.

In the presence of transverse acoustic excitation, the PAN and PN forcing conditions produced a trend in the LAR-thin injector flow dark-core lengths, L_F , that were different from those of the SAR-thick injector flows. The ratio of the forced to baseline dark-core lengths, L_F/L_B , for the PAN forced LAR-thin injector flows, in general, monotonically increased towards unity with increasing J at both P_r . This implied that the overall mixing characteristics resembled progressively more of the baseline with increasing J . However, lower flowrates resulted in decreased L_F/L_B despite increased J . Thus, the magnitude of the flowrates also influenced the response to external disturbances. Similar behavior in L_F/L_B was observed during the PN forcing condition as well. In contrast, the L_F/L_B for the PAN forced SAR-thick injector deviated from one for higher J ($J \geq 10$) flows only. This attested to the impact of the delayed interaction between the inner and outer jets due to the presence of the recirculating outer jet fluid for lower J flows. However, it was more susceptible to the PN forcing, and became less so with increasing J .

The spatial and temporal characteristics of the dominant flow disturbance structures were identified using proper orthogonal decomposition (POD) of the high-speed image pixel intensities. The LAR-thin injector baseline flows at both P_r and all J were characterized by antisymmetric periodic flow structures that indicated the presence of helical

disturbances in the inner shear layer. The associated peak frequencies of these structures became broader and shifted to higher frequencies with increasing J and increasing outer jet flowrate. On the other hand, the SAR-thick injector showed well-defined antisymmetric flow structures for $J \geq 2$. However, the peak frequencies in the magnitude spectra remained at low frequencies despite increasing J or increasing outer jet flowrate. Unlike the LAR-thin injector, the region immediately downstream of the thick inner jet post formed a flow recirculation zone, which delayed the formation of the inner shear layer. This delayed interaction between the inner and outer jets in addition to the SAR-thick injector's thin annulus outer jet may have been the cause for this limited influence on the spectral characteristics of the inner shear layer disturbances.

The PAN forcing condition had a greater impact on the low J ($J < 5$) LAR-thin injector flows at both P_r . As a result of this forcing condition, periodic and symmetric flow disturbance structures that resembled varicose disturbances, formed in the inner shear layer region. The corresponding magnitude of the cross-power spectra of conjugate modes of the POD showed dominant peaks at the forcing frequency. These strong responses at the forcing frequencies subsided for higher J flows, resulting in the formation of antisymmetric flow structures similar to the ones identified in the baseline flows. The magnitude spectra for these higher J flows also retained the baseline spectral characteristics further indicating a transition to reduced susceptibility to external pressure disturbances. Such variation with J in the degree of sensitivity was not observed for the PN forcing condition, which imposed sinuous disturbances in the form of transverse velocity fluctuations. The magnitude spectra, nevertheless, did retain aspects of the baseline spectral behavior at higher J .

The low J ($J < 2$) SAR-thick injector flow response to the PAN forcing conditions at both P_r was unlike the LAR-thin injector flows. Although direct observation of the high-speed images confirmed the formation of vortical structures in the recirculation zone, as

a result of interaction with the outer shear-layer vortices, there were no symmetric or antisymmetric periodic flow disturbances in the inner shear layer. The absence of dominant peaks at the forcing frequency in the magnitude spectra confirmed this observation. For $J > 5$, the PAN forcing produced symmetric structures below the recirculation zone with associated peaks in the spectra at the forcing frequencies. The low J flows also showed no appreciable response to the PN forcing until about $J > 5$, beyond which antisymmetric structures were formed due to sinuous disturbances.

For a given geometry, the nature of the flow response to an external disturbance depending on the flow condition, namely J , may be used to characterize the state of stability of the flow. Literature [73, 74, 75] on flow stability characterize convectively unstable flows as noise amplifiers; that is, they are prone to external flow disturbances such as acoustic disturbances as used in this study. Their spectral characteristics are such that when exposed to external forcing, their natural instabilities are completely removed and replaced by instabilities whose frequency matches that of the forcing frequency [76]. Absolutely unstable flows, on the other hand, are characterized as naturally self-excited flows that do not respond well to external disturbances. Their spectra preserve the natural instabilities with or without a coexisting frequency content associated with the forcing frequency. These and the flow responses observed may be used to argue that the LAR-thin injector flows can be characterized as convectively unstable for low J flows, and transition into absolutely unstable flows with increasing J values, while the SAR-thick injector flows depicted the behavior of convectively unstable flows at the higher J values. However, this characterization deserves further exploration in future studies.

6.3 Future Work

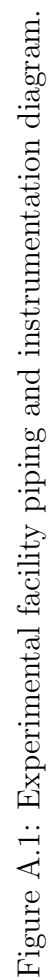
The use of different density coaxial jets in the present study served well to simulate a LOX/GH2 cold flow dynamics albeit both the inner and outer jets were the same species,

N_2 , which has a well-defined critical point. This precludes the added complexity of multi-species flow whose mixture does not have a well-defined critical point but rather critical lines. Thus, this key feature in a GH_2/LOX cold flow may better be simulated using a He outer jet and N_2 inner jet. The large density difference between He and N_2 for a given temperature and pressure will also give better flexibility to do a parametric study on the variation of momentum flux ratio due to the variation in density ratio instead of the variation of velocity ratio as done in the present study.

Then, the next phase of the shear-coaxial jets study will involve reacting species, namely a low temperature GH_2 outer jet and LOX inner jet as the fuel and oxidizer species, respectively. These reactive coaxial jets may then be investigated for a range of momentum flux ratios similar to those examined with non-reactive flow, at and off-stoichiometric conditions, and varying chamber pressures. Additional optical diagnostics may be used including OH^* chemiluminescence, in which the heart of the flame region may be imaged in time, likely in a phase-locked manner. The effect of transverse acoustic excitation on the combustion phenomena may then be studied by examining how pressure oscillations couple with the heat release oscillations depicted by fluctuations in the intensity of the flame front.

APPENDIX A

Shear-Coaxial Jets Experimental Facility: Piping and Instrumentation Diagram



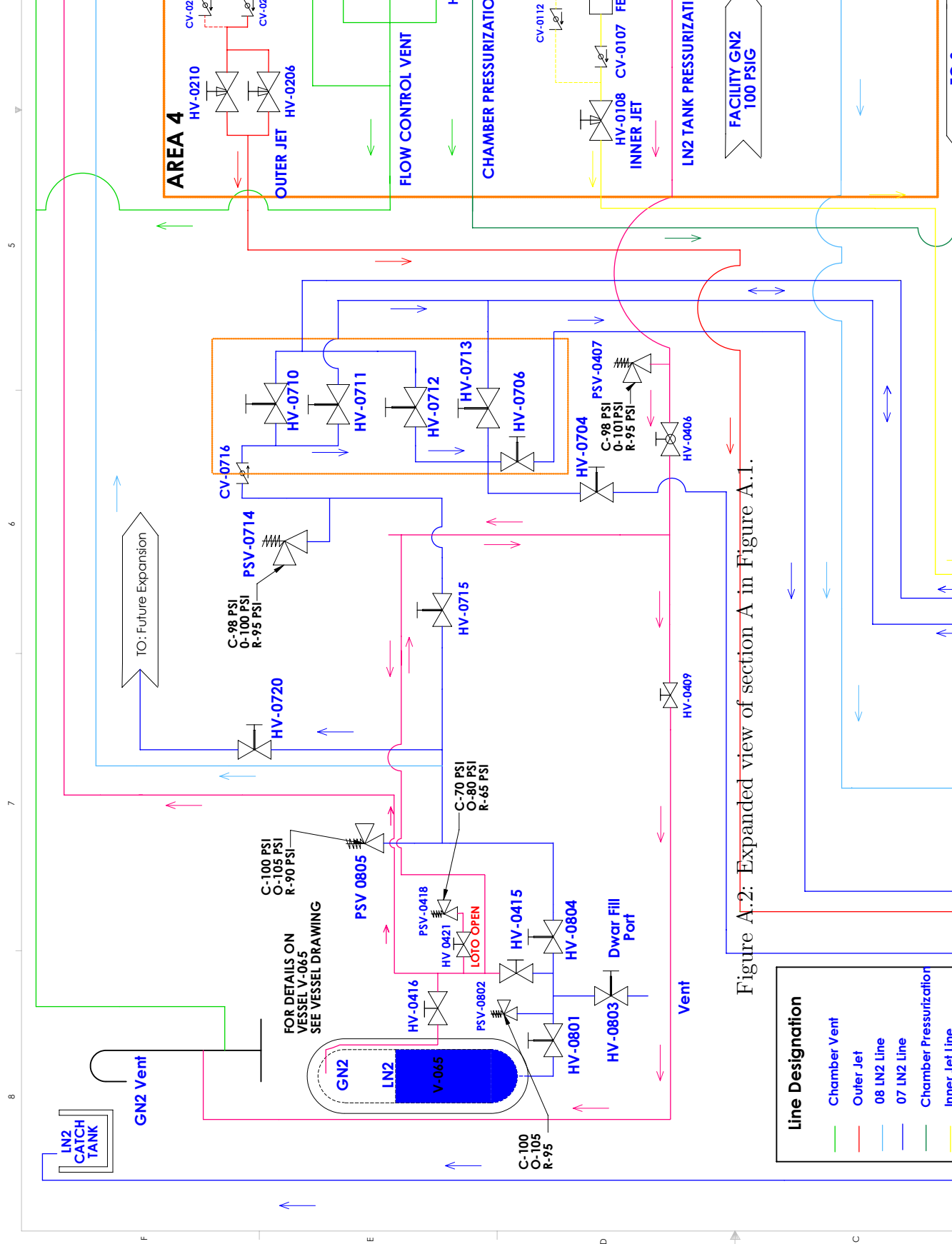
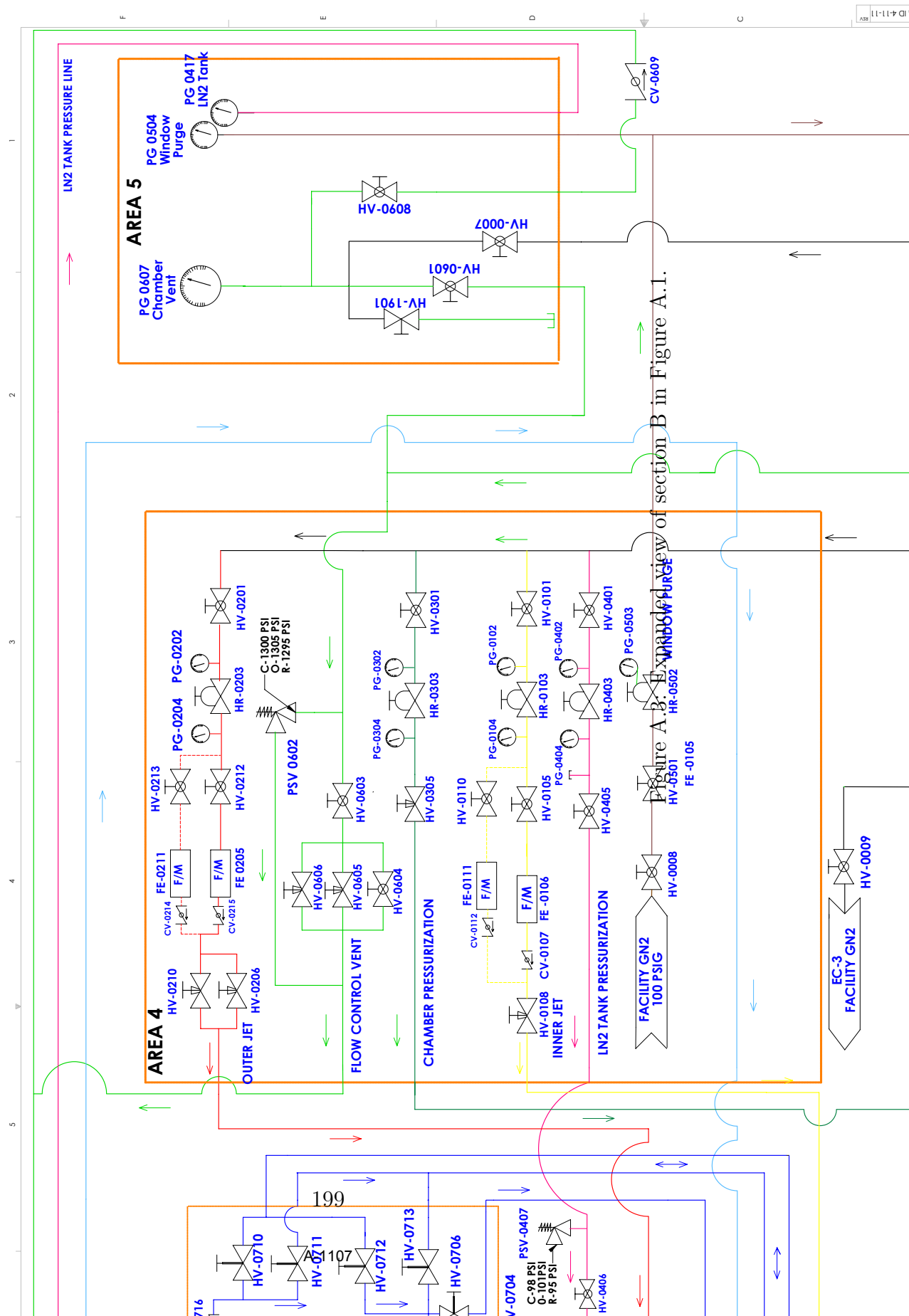


Figure A.2: Expanded view of section A in Figure A.1.

Line Designation	
Chamber Vent	Green
Outer Jet	Red
08 LN2 Line	Blue
07 LN2 Line	Purple
Chamber Pressurization	Yellow
Inner Jet Line	Orange



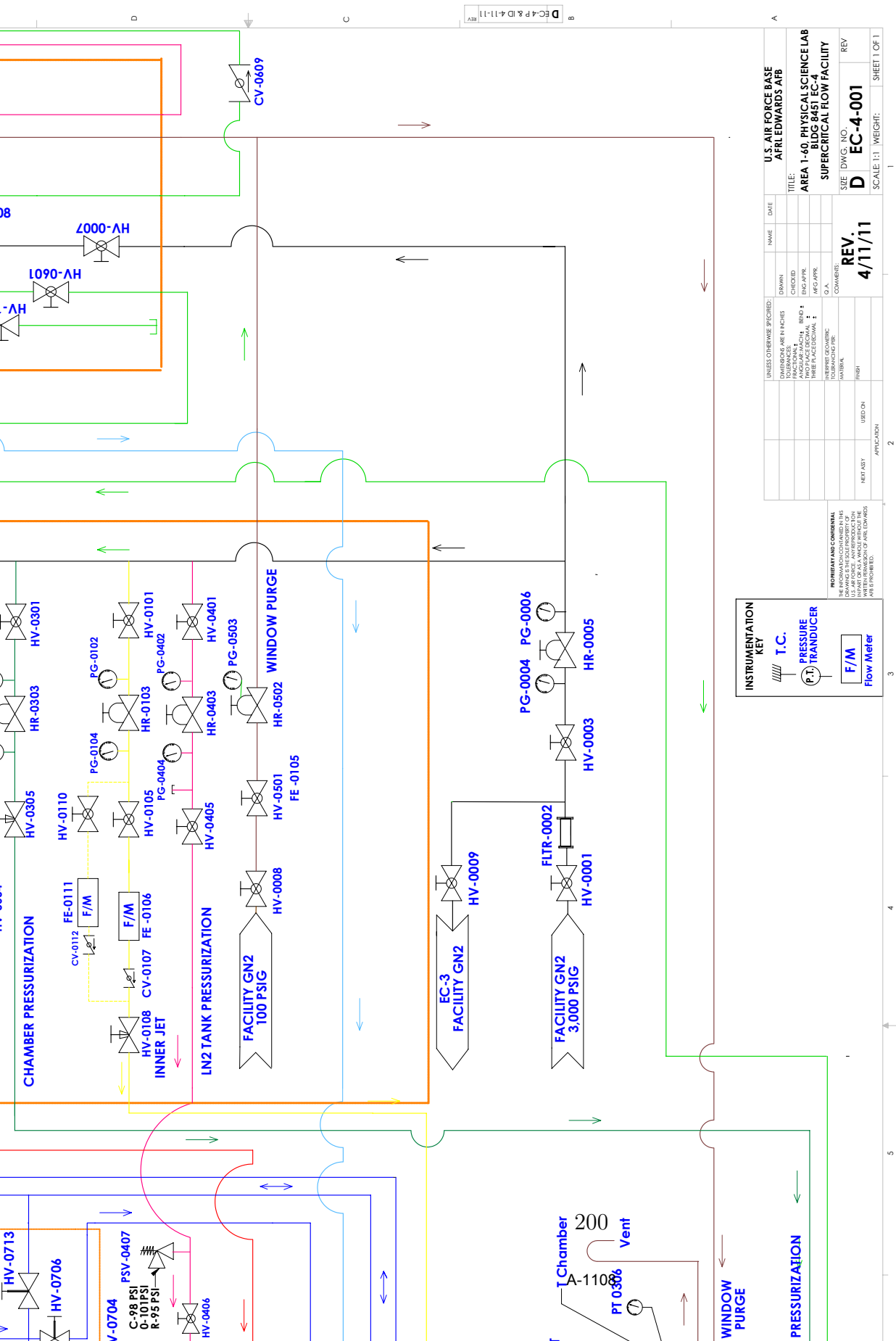


Figure A.4: Expanded view of section C in Figure A.1.

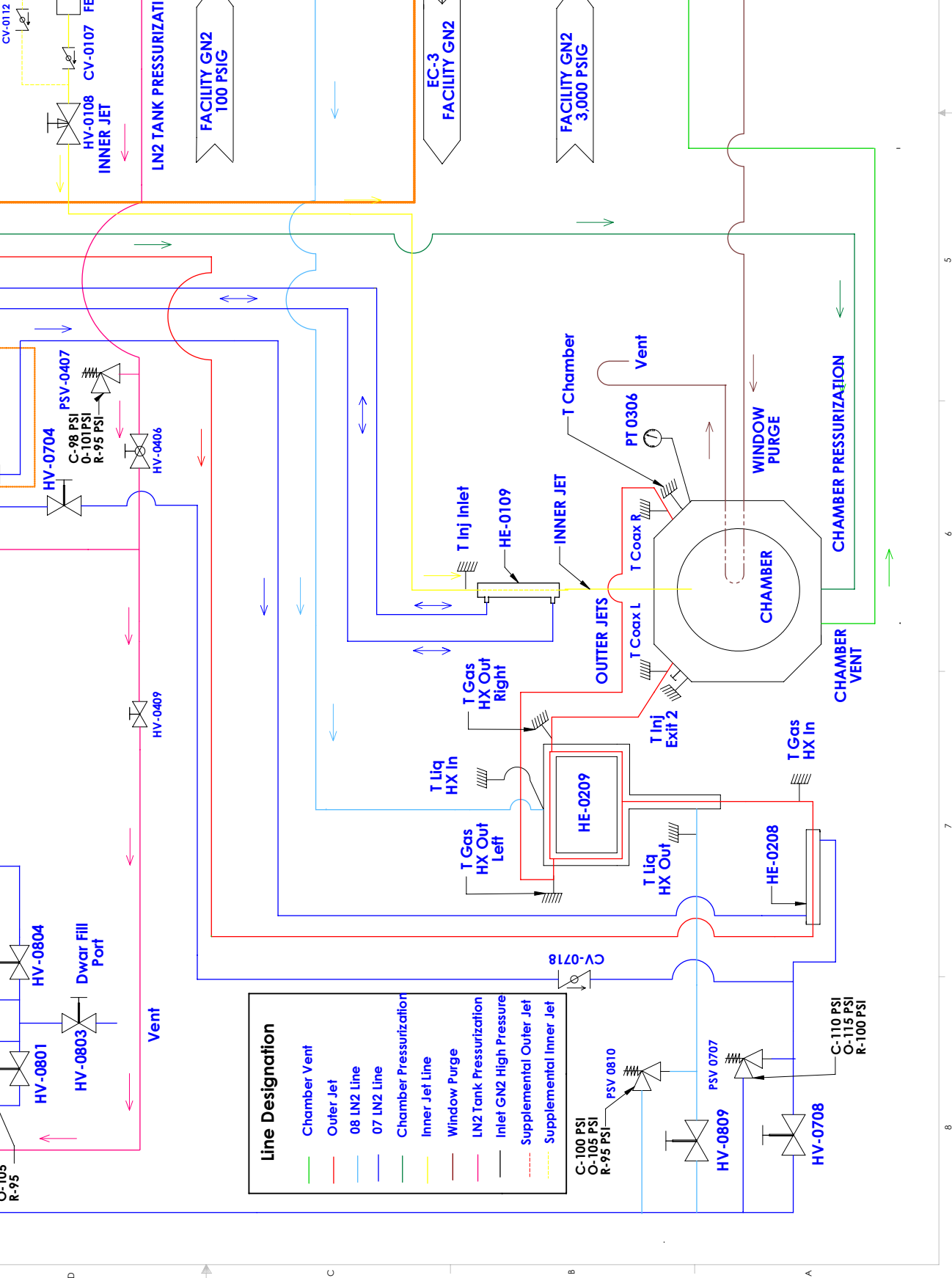


Figure A.5: Expanded view of section D in Figure A.1.

APPENDIX B

Shear-Coaxial Jets Experiment: Standard Operating Procedures

FLUID SUBSYSTEM NUMBER DESIGNATION

The first digit of the number indicates the fluid in the line, where 0 designates nitrogen fluid.

The second digit, ranging from 0 – 8 listed in the Table below, indicates the fluid subsystem based upon its function. The last two digits indicate the component number.

Fluid Subsystem Number Designation.

Subsystem Number	Function
0	High Pressure Facility GN2
1	N ₂ to Feed Inner Injector
2	N ₂ to Feed Outer Injector
3	N ₂ to Pressurize the Chamber
4	N ₂ for Pressurization of LN2 Systems
5	Low Pressure GN2 for Window Purge
6	GN2 Vent
7	LN2 from Dewar
8	LN2 from External Tank

ALL TEST TEAM MEMBERS are responsible for the safe performance of the test, and must have read and understood all portions of the test procedure. Any Test Team Member can declare an emergency or unsafe condition.

____1. ABBREVIATIONS AND ACRYONMS

EC	-	Experimental Cell
ER	-	Engineering Request
FE	-	Flow Element
GN2	-	Gaseous Nitrogen
HE	-	Heat Exchanger
HR	-	Hand Regulator
HV	-	Hand Valve
LN2	-	Liquid Nitrogen
PC	-	Pressure Chamber
PG	-	Pressure Gauge
PPE	-	Personal Protective Equipment
SCF	-	Supercritical Facility
SOCC	-	Site Operations Control Center

____ 2. **PRETEST PREPARATIONS**

- ____ 2.1. DON Test PPE: Lab coat or coveralls, safety goggles, safety shoes, and ear muffs (noise protection as required)
- ____ 2.2. Turn ON and Verify portable oxygen sensors are operational and calibrated
- ____ 2.3. Turn ON or Verify ON EC-4 Air Handler ventilation system.
- ____ 2.4. Turn OFF Air Handler.
- ____ 2.5. UNLOCK EC-4 outside door
- ____ 2.6. NOTE any potential hazards in and outside EC-4
- ____ 2.7. Verify GREEN, AMBER, and RED lights are functional and return to GREEN
- ____ 2.8. Turn on the Attocube power supply
- ____ 2.9. If Acoustic Testing Verify Gain or Turn Gain on Amplifier to the ZERO position
- ____ 2.10. If Acoustic Testing, Turn ON Amplifier to allow warm up as per
ER _____
- ____ 2.11. If Acoustic Testing, POST “HEARING PROTECTION REQUIRED” signs on the
outside of the doors to EC-4, Room 19, foam door and adjacent hallway
- ____ 2.12. Turn on Data Acquisition System and System Electronics
- ____ 2.13. Position “Restricted Area” signs at the exit doors to horseshoe in rooms 39, 41,
and adjacent to room 19 near the LN2 catch tank
- ____ 2.14. Position “DO NOT ENTER” signs outside of the room 19 and EC-4 doors
- ____ 2.15. Place chain in front of entrance to horseshoe

____ **3. INITIAL SETUP**

- ____ **3.1. OPEN / Verify OPEN HV-0001 (EC-3, EC-4 Primary Facility Isolation Valve) - Area 3**
- ____ **3.2. CLOSE / Verify CLOSED HV-0003 (EC-4 Secondary Facility Isolation Valve) - Area 3**
- ____ **3.3. CLOSE / Verify CLOSED HV-0008 (EC-4 Low Pressure Facility Isolation Valve) - Area 3**
- ____ **3.4. CLOSE / Verify CLOSED HV-0009 (EC-3 Secondary Facility Isolation Valve) - Area 3**
- ____ **3.5. CLOSE / Verify CLOSED HV-0406 (Tank GN2 Pressurization Isolation Valve) - Area 2**
- ____ **3.6. CLOSE / Verify CLOSED HV-0409 (LN2 Tank Pressurization Vent Isolation Valve) - Area 2**
- ____ **3.7. OPEN / Verify OPEN HV-0715 (Direct LN2 Supply Valve) - Area 2**
- ____ **3.8. Close/ Verify Closed HV-0720 (Future LN2 Expansion) – Area 2**
- ____ **3.9. OPEN / Verify OPEN HV-0704 (Heat Exchanger LN2 Bypass Valve) – Area 3**
- ____ **3.10. CLOSE / Verify CLOSED HV-0706 (Heat Exchanger Flow Valve) – Area 3**
- ____ **3.11. CLOSE / Verify CLOSED HV-0801 (LN2 Tank Isolation Valve) – Area1**
- ____ **3.12. OPEN / Verify OPEN HV-0803 (LN2 Vent Isolation Valve) – Area1**
- ____ **3.13. CLOSE / Verify CLOSED HV-0804 (LN2 Tank Secondary Isolation Valve) – Area 1**
- ____ **3.14. CLOSE / Verify CLOSED HV-0415 (Vacuum Jacketed Line Purge Valve) – Area 1**

**NOTE: In case the LN2 line needs to be broken, moisture could get in.
This valve permits purging of the line after it is reconnected**

- ____ 3.15. CLOSE / Verify CLOSED HV-0416 (Tank GN2 Pressurization Valve) – Area 1
- ____ 3.16. CLOSE / Verify CLOSED HV-1901 (He System Isolation Valve) - Area 5
- ____ 3.17. CLOSE / Verify CLOSED HV-0601 (PC Vent PG Isolation Valve) - Area 5
- ____ 3.18. OPEN / Verify OPEN HV-0608 (Gauge Vent Valve) - Area 5
- ____ 3.19. CLOSE / Verify CLOSED HV-0007 (Upstream Regulator Pressure Valve) - Area 5
- ____ 3.20. OPEN / Verify OPEN HV-0603 (Chamber Pressure Build Valve) - Area 4
- ____ 3.21. OPEN / Verify OPEN HV-0604 (Primary Chamber Pressure Vent Valve) - Area 4
- ____ 3.22. CLOSE / Verify CLOSED HV-0605 (Secondary Chamber Pressure Vent Valve) - Area 4
- ____ 3.23. CLOSE / Verify CLOSED HV-0606 (Tertiary Chamber Pressure Vent Valve) - Area 4
- ____ 3.24. CLOSE / Verify CLOSED HV-0708 (Heat Exchanger LN2 Throttle Vent Valve) – ceiling between Area 4 & Area 5
- ____ 3.25. CLOSE / Verify CLOSED HV-0809 (Outer Heat Exchanger LN2 Throttle Vent Valve) – ceiling between Area 4 & Area 5
- ____ 3.26. CLOSE / Verify CLOSED HV-0710 (Primary Co-Flow Valve) – Area 4
- ____ 3.27. OPEN / Verify OPEN HV-0711 (Primary Counter Flow Valve) – Area 4
- ____ 3.28. OPEN / Verify OPEN HV-0712 (Secondary Counter Flow Valve) – Area 4
- ____ 3.29. CLOSE / Verify CLOSED HV-0713 (Secondary Co-Flow Valve) – Area 4

- ____ 3.30. Verify PG-0607 (Chamber Pressure Gauge) reads 0 psig– Area 5
- ____ 3.31. Verify PG-0004 (EC-4 System Inlet Pressure Gauge) reads 0 psig – Area 5
- ____ 3.32. DECREASE FULLY / Verify FULLY DECREASED HR-0005 (EC-4 Facility Pressure Regulator) – Area 5
- ____ 3.33. Verify PG-0006 (EC-4 System Outlet Pressure Gauge) reads 0 psig – Area 5
- ____ 3.34. CLOSE / Verify CLOSED HV-0101 (Inner Jet GN2 Isolation Valve) – Area 4
- ____ 3.35. Verify PG-0102 (Inner Jet GN2 System Inlet Pressure Gauge) reads 0 psig – Area 4
- ____ 3.36. DECREASE FULLY / Verify FULLY DECREASED HR-0103 (Inner Jet GN2 Pressure Regulator) – Area 4
- ____ 3.37. Verify PG-0104 (Inner Jet GN2 Regulated Pressure Gauge) reads 0 psig – Area 4
- ____ 3.38. CLOSE / Verify CLOSED HV-0105 (Inner Jet Low Flow Isolation Valve) – Area 4
- ____ 3.39. CLOSE / Verify CLOSED HV-0110 (Inner Jet High Flow Isolation Valve) – Area 4
- ____ 3.40. CLOSE / Verify CLOSED HV-0108 (Inner Jet GN2 Throttle Valve) – Area 4
- ____ 3.41. CLOSE / Verify CLOSED HV-0201 (Outer Jet GN2 Isolation Valve) – Area 4
- ____ 3.42. Verify PG-0202 (Outer Jet GN2 System Inlet Pressure Gauge) reads 0 psig – Area 4
- ____ 3.43. DECREASE FULLY / Verify FULLY DECREASED HR-0203 (Outer Jet GN2 Pressure Regulator) – Area 4
- ____ 3.44. Verify PG-0204 (Outer Jet GN2 Regulated Pressure Gauge) reads 0 psig – Area 4

- ____ 3.45. CLOSE / Verify CLOSED HV-0212 (Outer Jet High Flow Isolation Valve) – Area 4
- ____ 3.46. CLOSE / Verify CLOSED HV-0213 (Outer Jet Low Flow Isolation Valve) – Area 4
- ____ 3.47. CLOSE / Verify CLOSED HV-0206 (fine Outer Jet GN2 Throttle Valve) – Area 4
- ____ 3.48. CLOSE/ Verify CLOSED HV-0210 (coarse Outer Jet GN2 Throttle valve) – Area 4
- ____ 3.49. CLOSE / Verify CLOSED HV-0301 (Chamber Pressurization Isolation Valve) – Area 4
- ____ 3.50. Verify PG-0302 (Chamber Pressurization System Inlet Pressure Gauge) reads 0 psig – Area 4
- ____ 3.51. DECREASE FULLY / Verify FULLY DECREASED HR-0303 (Chamber Pressurization Regulator) – Area 4
- ____ 3.52. Verify PG-0304 (Chamber Pressure Regulated Pressure Gauge) reads 0 psig – Area 4
- ____ 3.53. CLOSE / Verify CLOSED HV-0305 (Chamber Pressurization Throttle Valve) – Area 4
- ____ 3.54. CLOSE / Verify CLOSED HV-0401 (LN2 Tank Pressurization Isolation Valve) – Area 4
- ____ 3.55. Verify PG-0402 (LN2 Tank GN2 System Inlet Pressure Gauge) reads 0 psig – Area 4
- ____ 3.56. DECREASE FULLY / Verify FULLY DECREASED HR-0403 (LN2 Tank GN2 Pressure Regulator) – Area 4
- ____ 3.57. Verify PG-0404 (LN2 Tank Pressurization Pressure Gauge) reads 0 psig – Area 4

- ____3.58. CLOSE / Verify CLOSED HV-0405 (LN2 Supply Tank Isolation Valve) – Area 4
- ____3.59. CLOSE / Verify CLOSED HV-0501 (Window Purge Isolation Valve) – Area 4
- ____3.60. Verify PG-0504 (Window Purge Pressure Gauge) reads 0 psig – Area 5

- ____3.61. DECREASE FULLY / Verify FULLY DECREASED HR-0502 (Window Purge Pressure Regulator) – Area 4
- ____3.62. Verify PG-0417 (LN2 Tank Pressure Gauge) reads 0 psig – Area 5
If not:
A – OPEN HV-0409 – Area 2
B – CLOSE HV-0409 – Area 2

____ 4. **WINDOW PURGE**

____ 4.1. Notify SOCC via hotline (or 5-5632) in EC-1, EC-2 or EC-3 control room that EC-4 is going into a RED condition for SCF testing

____ 4.2. Verify all personnel are wearing Test PPE

____ 4.3. Change EC-4 light to RED

____ 4.4. Record Time _____

____ 4.5. Verify window purge apparatus is in satisfactory condition

____ 4.6. OPEN HV-0008 (EC-4 Low Pressure Facility Isolation Valve) – Area 3

____ 4.7. OPEN HV-0501 (Window Purge Isolation Valve) – Area 4

CAUTION: Do NOT Increase HR-0502 so that PG-0504 reads greater than 5 psig as it will damage PG-0504

____ 4.8. INCREASE HR-0502 (Window Purge Pressure Regulator) until PG-0504 (Window Purge Pressure Gauge) reads 1.5 psig +/- 0.5 psig – Area 4

____ 4.9. Permit window purge to continue according to ER _____

____ 5. **FACILITY GN2 SETUP**

- ____ 5.1. *Slowly* OPEN HV-0003 (EC-4 Facility Isolation Valve) – Area 3
- ____ 5.2. Verify PG-0004 (EC-4 System Inlet Pressure Gauge) reads a pressure greater than 2000 psig – Area 4 _____
- ____ 5.3. OPEN HV-0007 (Upstream Regulator Pressure Valve) – Area 5
- ____ 5.4. CLOSE HV-0608 (Gauge Vent Valve) – Area 5
- ____ 5.5. INCREASE HR-0005 (EC-4 Facility Pressure Regulator) until PG-0607 (Chamber Pressure Gauge) reads 2000 psig +/- 50 psig – Area 5
- ____ **NOTE: Open and quickly close HV-0608 to check if PG-0607 actually reads 2000 psig**
- ____ 5.6. CLOSE HV-0007 (Upstream Regulator Pressure Valve) – Area 5
- ____ 5.7. *Slowly* OPEN HV-0608 (Gauge Vent Valve) – Area 5
- ____ 5.8. Verify PG-0607 (Chamber Pressure Gauge) reads 0 psig – Area 5
- ____ 5.9. OPEN HV-0601 (PC Vent PG Isolation Valve) – Area 5
- ____ 5.10. CLOSE HV-0608 (Gauge Vent Valve) – Area 5
- ____ 5.11. Verify PG-0607 (Chamber Pressure Gauge) reads 0 psig – Area 5
- ____ 5.12. Turn ON Air Handler, *per ER or as necessary*

____ **6. CHAMBER PURGE**

____ 6.1. Record Time _____

____ 6.2. Record zero values for Pressure Transducer (Agilent Ch. 103), Inner Jet Mass Flow Meter (Agilent Ch. 104) and Outer Jet Mass Flow Meter (Agilent Ch. 102).

____ 6.3. *Slowly* OPEN HV-0301 (Chamber Pressurization Isolation Valve) – Area 4

____ 6.4. Verify PG-0302 (Chamber Pressurization System Inlet Pressure Gauge) reads 2000 psig +/- 150 psig – Area 4 _____

____ 6.5. INCREASE HR-0303 (Chamber Pressure GN2 Pressure Regulator) until PG-0304 (Chamber Pressure Regulated Pressure Gauge) reads _____ psig +0/-100 psig as per ER – Area 4

____ 6.6. OPEN HV-0305 (Chamber Pressurization Throttle Valve) as per ER _____
– Area 4

NOTE: Perform next 3 steps in quick succession

____ 6.7. CLOSE HV-0603 (Chamber Pressure Build Valve) – Area 4

____ 6.8. Verify PG-0607 (Chamber Pressure Gauge) indicates that chamber pressure is increasing to indicate purge is flowing. – Area 5

____ 6.9. OPEN HV-0603 (Chamber Pressure Build Valve) – Area 4

____ 6.10 Go to Chamber Pressurization Section if taking ambient T measurements with no flows

____ **7. INNER JET PURGE**

____ 7.1. *Slowly* OPEN HV-0101 (Inner Jet GN2 Isolation Valve) – Area 4

____ 7.2. Verify PG-0102 (Inner Jet GN2 System Inlet Pressure Gauge) reads 2000 psig +/- 150 psig – Area 4 _____

____ 7.3. OPEN HV-0105 (Inner Jet Low Flow Isolation Valve) for use with FE-0106 (flow rates up to 50 SLPM)
or HV-0110 (Inner Jet High Flow Isolation Valve) for use with FE-0111 (flow rates up to 200 SLPM) as per ER _____

____ 7.4. INCREASE HR-0103 (Inner Jet GN2 Pressure Regulator) until PG-0104 (Inner Jet GN2 Regulated Pressure Gauge) reads _____ psig +0/-100 psig as per ER – Area 4

____ 7.5. OPEN HV-0108 (Inner Jet GN2 Throttle Valve) as per ER _____ – Area 4
NOTE: Check chamber pressure periodically Ch. 103 in Agilent (at least every 500 mg/s)

____ 7.6. Verify FE-0106 (Inner Jet GN2 Flow Meter) indicates purge is flowing
NOTE: Ch. 104 in Agilent

____ 8. OUTER JET PURGE

____ 8.1. *Slowly* OPEN HV-0201 (Outer Jet GN2 Isolation Valve) – Area 4

____ 8.2. Verify PG-0202 (Outer Jet GN2 System Inlet Pressure Gauge) reads 2000 psig +/- 150 psig – Area 4 _____

____ 8.3. Open HV-0212 (Outer Jet High Flow Isolation Valve) for use with FE-0205 (flow rates up to 500 SLPM)
or HV-0213 (Outer Jet High Flow Isolation Valve) for use with FE-0211 (lower flow rates) as per ER _____

____ 8.4. INCREASE HR-0203 (Outer Jet GN2 Pressure Regulator) until PG-0204 (Outer Jet GN2 Regulated Pressure Gauge) reads _____ psig +0/-100 psig as per ER – Area 4
NOTE: 1100 psig is the high limit for PG-0204. The calibration curve available does not go beyond this pressure.

____ 8.5. OPEN HV-0206 (Outer Jet GN2 Throttle Valve) as per ER _____ – Area 4
NOTE: Check chamber pressure periodically Ch. 103 in Agilent (at least every 500 mg/s)

____ 8.6. Verify FE-0205 (Outer Jet GN2 Flow Meter) indicates purge is flowing

NOTE: Ch. 102 in Agilent

____ 9. **CHAMBER PRESSURIZATION**

____ 9.1. OPEN HV-0605 (Secondary Chamber Pressure Vent Valve) 2 turns – Area 4

____ 9.2. OPEN HV-0606 (Tertiary Chamber Pressure Vent Valve) 8 turns – Area 4

____ 9.3. CLOSE HV-0604 (Primary Chamber Pressure Vent Valve) – Area 4

____ 9.4. ADJUST HV-0605 (Secondary Chamber Pressure Vent Valve) and HV-0606 (Tertiary Chamber Pressure Vent Valve) until PG-0607 (Chamber Pressure Gauge) reads INITIAL CHAMBER PRESSURE as per ER_____ – Area 4

____ 9.5. Wait for required time to elapse from step 13.1 as per ER_____

____ 9.6. IF taking measurements at room temperature

A - Take measurements

B - Reduce chamber pressure after measurements

C - Return to “Inner Jet Purge” section

____10. **SYSTEM CHILL DOWN**

- ____10.1. Verify Red Crew has donned Cryogenic PPE as outlined in Step 5.2
- ____10.2. CLOSE HV-0803 (LN2 Vent Isolation Valve) – Area 1
- ____10.3. OPEN HV-0801 (LN2 Tank Isolation Valve) – Area 1
- ____10.4. OPEN HV-0804 (LN2 Tank Secondary Isolation Valve) – Area 1
- ____10.5. OPEN HV-0416 (pressurize tank with GN2) – Area 1
- ____10.6. Remove Cryogenic PPE and don Test PPE as listed in Step 5.2
- ____10.7. *Slowly* OPEN HV-0401 (LN2 Tank Pressurization Isolation Valve) – Area 4
- ____10.8. Verify PG-0402 (LN2 Tank GN2 System Inlet Pressure Gauge) reads 2000 psig +/-150 psig – Area 4 _____
- ____10.9. Increase HR-0403 (LN2 Tank GN2 Pressure Regulator) until PG-0404 (Dewar and Tank Pressurization Pressure Gauge) reads as per ER – Area 4 _____
- ____10.10. OPEN HV-0405 (LN2 Supply Tank Isolation Valve) – Area 4
- ____10.11. OPEN HV-0406 (LN2 Tank GN2 Pressurization Isolation Valve) – Area 2
- ____10.12. Record Time _____
- ____10.13. OPEN HV-0809 (Outer Heat Exchanger LN2 Throttle Vent Valve) as per ER_____ ceiling between Area 4 & 5
NOTE: Rotate valve ¼ of a turn and wait 10 minutes
- ____10.14. OPEN HV-0708 (Heat Exchanger LN2 Throttle Vent Valve) as per ER_____ ceiling between Area 4 & 5
NOTE: Rotate valve ¼ of a turn and wait 10 minutes
- ____10.15. Wait Required time for chill down as per ER_____

____11. **TESTING**

____11.1. If acoustic testing, follow the procedure for setting up the acoustic drivers

____11.2. Verify all personnel are wearing ear muffs if acoustic testing

____11.3. Adjust HR-0103 (Inner Jet GN2 Pressure Regulator) to maintain desired flow rates

NOTE: Ch. 104 in Agilent

____11.4. Adjust HR-0203 (Outer Jet GN2 Pressure Regulator) to maintain desired flow rates

NOTE: Ch. 102 in Agilent

____11.5. Adjust HV-0606 (Tertiary Chamber Pressure Vent Valve) and HV-0605 (Secondary Chamber Pressure Vent Valve) to maintain desired chamber pressure

NOTE: Ch. 103 in Agilent

____11.6. Direct red crew leader to operate system as per test needs

____11.7. OPERATE System as directed by test conductor

____12. **SHUT DOWN**

- ____12.1. CLOSE HV-0003 (EC-4 Secondary Facility Isolation Valve) – Area 2
- ____12.2. CLOSE HV-0008 (EC-4 Low Pressure Facility Isolation Valve) – Area 2
- ____12.3. Turn OFF/ Verify OFF air handler
- ____12.4. DON Cryogenic PPE
- ____12.5. CLOSE HV-0801 (LN2 Tank Isolation Valve) – Area 1
- ____12.6. CLOSE HV-0416 (Tank GN2 Pressurization Isolation Valve) – Area 1
- ____12.7. REMOVE Cryogenic PPE
- ____12.8. OPEN HV-0409 (LN2 Tank Pressurization Vent Isolation Valve) – Area 2
- ____12.9. Wait for PG-0004 (EC-4 System Inlet Pressure Gauge) to read 0 psig – Area 5
- ____12.10. Fully DECREASE HR-0005 (EC-4 Facility Pressure Regulator) – Area 5
- ____12.11. Verify PG-0006 (EC-4 System Regulated Pressure Gauge) reads 0 psig – Area 5
- ____12.12. Verify PG-0102 (Inner Jet GN2 System Inlet Pressure Gauge) reads 0 psig – Area 4
- ____12.13. CLOSE HV-0101 (Inner Jet GN2 Isolation Valve) – Area 4
- ____12.14. Fully DECREASE HR-0103 (Inner Jet GN2 Pressure Regulator) – Area 4
- ____12.15. Verify PG-0104 (Inner Jet GN2 Regulated Pressure Gauge) reads 0 psig – Area 4
- ____12.16. CLOSE HV-0105 (Inner Jet Low Flow Isolation Valve) – Area 4
- ____12.17. CLOSE HV-0110 (Inner Jet High Flow Isolation Valve) – Area 4
- ____12.18. CLOSE HV-0108 (Inner Jet GN2 Throttle Valve) – Area 4

- ____12.19. Verify PG-0202 (Outer Jet GN2 System Inlet Pressure Gauge) reads 0 psig — Area 4
- ____12.20. CLOSE HV-0201 (Outer Jet GN2 Isolation Valve) – Area 4
- ____12.21. Fully DECREASE HR-0203 (Outer Jet GN2 Pressure Regulator) – Area 4
- ____12.22. Verify PG-0204 (Outer Jet GN2 Regulated Pressure Gauge) reads 0 psig – Area 4
- ____12.23. CLOSE HV-0212 (Outer Jet High Flow Isolation Valve) – Area 4
- ____12.24. CLOSE HV-0213 (Outer Jet Low Flow Isolation Valve) – Area 4
- ____12.25. CLOSE HV-0206 (fine Outer Jet GN2 Throttle Valve) – Area 4
- ____12.26. CLOSE HV-0210 (coarse Outer Jet GN2 Throttle Valve) – Area 4
- ____12.27. Verify PG-0302 (Chamber Pressurization System Inlet Pressure Gauge) reads 0 psig – Area 4
- ____12.28. CLOSE HV-0301 (Chamber Pressurization Isolation Valve) – Area 4
- ____12.29. Fully DECREASE HR-0303 (Chamber Pressurization Regulator) – Area 4
- ____12.30. Verify PG-0304 (Chamber Pressure Regulated Pressure Gauge) reads 0 psig – Area 4
- ____12.31. CLOSE HV-0305 (Chamber Pressurization Throttle Valve) – Area 4
- ____12.32. Verify PG-0402 (LN2 Tank GN2 System Inlet Pressure Gauge) read 0 psig – Area 4

NOTE: Current readout sticks

- ____12.33. CLOSE HV-0401 (LN2 Tank Pressurization Isolation Valve) – Area 4
- ____12.34. Fully DECREASE HR-0403 (LN2 Tank GN2 Pressure Regulator) – Area 4

- ____12.35. Verify PG-0404 (LN2 Tank Pressurization Pressure Gauge) reads 0 psig – Area 4
- ____12.36. OPEN HV-0405 (LN2 Supply Tank Isolation Valve) – Area 4
- ____12.37. OPEN/Verify OPEN HV-0406 (Tank GN2 Pressurization Isolation Valve) – Area 2
- ____12.38. Verify PG-0504 (Window Purge Pressure Gauge) reads 0 psig – Area 5
- ____12.39. CLOSE HV-0501 (Window Purge Isolation Valve) – Area 4
- ____12.40. Fully DECREASE HR-0502 (Window Purge Pressure Regulator) – Area 4
- ____12.41. OPEN HV-0608 (Gauge Vent Valve) – Area 5
- ____12.42. Verify PG-0607 (Chamber Pressure Gauge) reads 0 psig – Area 5
- ____12.43. CLOSE HV-0601 (PC Vent PG Isolation Valve) – Area 5
- ____12.44. OPEN / Verify OPEN HV-0603 (Chamber Pressure Build Valve) – Area 4
- ____12.45. OPEN HV-0604 (Primary Chamber Pressure Vent Valve) – Area 4
- ____12.46. CLOSE HV-0605 (Secondary Chamber Pressure Vent Valve) – Area 4
- ____12.47. CLOSE HV-0606 (Tertiary Chamber Pressure Vent Valve) – Area 4
- ____12.48. OPEN HV-0708 (Heat Exchanger LN2 Throttle Vent Valve) – ceiling between Area 4&5
- ____12.49. OPEN HV-0809 (Outer Heat Exchanger LN2 Throttle Vent Valve) – ceiling between Area 4&5
- ____12.50. OPEN / Verify OPEN HV-0715 (Direct LN2 Supply Valve) - Area 2
- ____12.51. Don Cryogenic PPE

- ____12.52. CLOSE HV-0804 (LN2 Tank Secondary Isolation Valve) – Area 1
- ____12.53. OPEN HV-0803 (LN2 Vent Isolation Valve - vent trapped LN2 between 0801 and 0804) - Area 1
- ____12.54. Remove Cryogenic PPE
- ____12.55. Verify PG-0417 (LN2 Tank Pressure Gauge) reads 0 psig – Area 5
- ____12.56. Notify SOCC EC-4 is going back to green condition
- ____12.57. Turn off portable O₂ sensors
- ____12.58. Turn EC-4 lights back to green
- ____12.59. Remove “DO NOT ENTER”, “Restricted Area” and “HEARING PROTECTION REQUIRED” signs
- ____12.60. Remove chain from entrance to horseshoe
- ____12.61. Turn off the acoustic drivers

____13. **EMERGENCY PROCEDURE (GN₂ or LN₂ line leak or burst)**

IF OXYGEN MONITORING ALARMS GO OFF:

- ____13.1. Exit the facility to a safe zone given in safety brief.
- ____13.2. Contact SOCC 5-5632 and report the emergency. Have SOCC contact the Fire Dept. 5-5181
- ____13.3. Contact the Facility Manager and isolate the cell or area.

IF POSSIBLE AND WHEN SAFE, DO THE FOLLOWING:

____13.4. CLOSE HV-0001 (EC-3, EC-4 Primary Facility Isolation Valve)

____13.5. CLOSE HV-0801 (Tank LN2 Isolation Valve)

**NOTE: WHEN SAFE TO DO SO COMPLETE THE STEPS OF THE
"SHUT DOWN" SECTION 12**

ACOUSTIC DRIVERS OPERATION

Settings to be verified every time something new is installed or there is an upgrade of the testing equipment that is directly involved with the operation of the acoustic drivers:

- ____1.1. Verify the wire from Channel 1 of the Tektronix oscilloscope (Model No. 2235A) comes from the strain gauge and during testing the signal should NEVER go over 43V peak-to-peak.
- ____1.2. Verify the setting of the Tektronix oscilloscope is such that Channel 1 has a range of 5V per division (for a total of 40V that can be seen on the screen, since there are 8 divisions)
- ____1.3. Verify the wire on Channel 1 of the Tenma oscilloscope (Model No. 72-6800) comes from the output voltage monitor on the Trek-1 amplifier and the wires on Channel 2 of the Tektronix and Tenma oscilloscopes come from the output voltage monitor on the Trek-2 amplifier
- ____1.4. Verify the setting of both oscilloscopes is such that Channel 2 has a range of 1V per division (for a total of 8V that can be seen on the screen, since the oscilloscope has 8 divisions)
- ____1.5. Verify the wire from Channel 1 of the Fluke Signal Generator goes to the Trek-1 amplifier and then the signal is amplified (200 times) and goes to the old (left as seen from the point where the high-speed camera is placed) acoustic driver (piezo-siren)
- ____1.6. Verify the wire from Channel 2 of the Fluke Signal Generator goes to the Trek-2 amplifier and then the signal is amplified (200 times) and goes to the new (right as seen from the point where the high-speed camera is placed) acoustic driver (piezo-siren)

____2. **ACOUSTIC DRIVERS START UP**

- ____2.1. Verify that the Fluke Signal Generator is on
- ____2.2. Verify that the Tektronix and Tenma oscilloscopes are on

- ____ 2.3. Lock Channel 1 to Channel 2 using the “Inter Channel” button on Fluke Signal Generator. Channel 1 setting is “Master/Frequency” and Channel 2 setting is “Slave”
NOTE: Make sure “Status” is ON after the appropriate mode settings on Channels 1 and 2
- ____ 2.4. Verify the phase difference between the two channels is 0 degrees
- ____ 2.5. Use the Fluke Signal Generator to assign Channel 1 an amplitude of 2 V peak-to-peak and a frequency of 3.00 kHz
- ____ 2.6. Verify that the signal (waveform) from Channel 1 is a sine function. [Use the “status” button on the Fluke Signal Generator]
- ____ 2.7. Use the Fluke Signal Generator to assign Channel 2 an amplitude of 2 V peak-to-peak (if there is an attempt to modify the frequency, a warning saying “Tracking Master Channel” should appear on the screen)
- ____ 2.8. Verify that the signal (waveform) from Channel 2 is a sine function. [Use the “status” button on the Fluke Signal Generator]
- ____ 2.9. Verify the LED lights of the Channel 1 and Channel 2 buttons of the Fluke Signal Generator are off. These buttons are used to send the signal to both amplifiers
- ____ 2.10. Verify the **output signal** and **high voltage connectors** of the acoustic drivers (piezo-siren) are **plugged in**
- ____ 2.11. Verify the Trek amplifiers are off and wall outlet power cords are disconnected
- ____ 2.12. Verify the wires of the input signal are disconnected and the wires of the output monitoring signal are connected
- ____ 2.13. Plug in high voltage connection of both Trek amplifiers (clear/red cable)
- ____ 2.14. Connect the wire from Channel 1 of the Fluke Signal Generator to the “Input Signal” slot on the Trek-1 amplifier and the wire from Channel 2 of the Fluke Signal Generator to the “Input Signal” slot on the Trek-2 amplifier

- ____ 2.15. Plug in wall outlet power cords of the Trek amplifiers
- ____ 2.16. Turn the (white) Trek amplifiers (switches) on
- ____ 2.17. Put on acoustic protection (ear plugs and ear muffs)
- ____ 2.18. Verify the **silver** acoustic-protection **foam door** is **in place**
- ____ 2.19. Pull gray high voltage enabling button of Trek amplifiers
NOTE: If the red light switch does not come on, push the start switch on the Trek amplifier

NOTES:

- Make sure waveforms are as expected on the Oscilloscope. The output signal from the strain gauge attached to the right acoustic driver (piezo-siren) should never go over 43V at any point during a test.
- Adjust driving frequency (selecting Channel 1 and using the “Frequency” button) and amplitude as needed for the particular test and case to be run.
- If there is an emergency and the room has to be evacuated: just leave. If there is time, press the grey button on the Trek amplifiers, and turn the main switches off.

____ 3. **ACOUSTIC DRIVERS SHUT DOWN**

- ____ 3.1. Once **acoustic testing** is **over**, verify that the lights of Channels 1 and 2 of the Fluke Signal Generator are off
- ____ 3.2. Press the grey button on the Trek amplifier
- ____ 3.3. Turn off the (white) main switch of the Trek amplifiers
- ____ 3.4. Disconnect the wall outlet power cord of the Trek amplifiers
- ____ 3.5. Disconnect the high voltage (clear/red) cable of the Trek amplifiers
- ____ 3.6. Disconnect the (input) cables from the Trek amplifiers
- ____ 3.7. Turn off Fluke Signal Generator
- ____ 3.8. **Uncouple connectors** from the right acoustic source (piezo-siren) and plug in 1 megaohm resistance connectors

APPENDIX C

Shear-Coaxial Jets Experiment: Summary Tables of Flow Conditions

Table C.1: Summary table of flow conditions for the LAR-thin injector.

J	R	S	T_c (K)	ρ_c (kg/m ³)	P_c (MPa)	T_o (K)	\dot{m}_o (mg/s)	ρ_o (kg/m ³)	U_o (m/s)	Re_o ($\times 10^{-4}$)	T_i (K)	\dot{m}_i (mg/s)	ρ_i (kg/m ³)	U_i (m/s)	Re_i ($\times 10^{-4}$)
$P_r = 0.44$															
0.1	1.6	0.040	243	21	1.50	198	500	26	4.7	1.4	107	722	646	2.9	2.1
0.5	3.5	0.042	217	24	1.50	204	1106	26	11	3.1	110	727	622	3.0	2.4
2.1	7.4	0.039	220	23	1.50	205	2212	25	22	6.3	107	725	646	2.9	2.1
5.2	11	0.041	221	23	1.50	203	3531	26	34	10	108	733	639	3.0	2.2
11	17	0.040	216	24	1.51	204	4991	26	48	14	107	722	646	2.9	2.1
14	19	0.041	221	23	1.50	201	3889	26	37	11	109	483	630	2.0	1.5
20	22	0.042	220	23	1.50	204	4633	26	45	13	110	482	622	2.0	1.6
$P_r = 1.05$															
0.1	0.9	0.11	252	49	3.57	195	773	67	2.8	2.2	114	725	613	3.1	2.5
0.5	2.1	0.11	223	56	3.56	199	1742	65	6.6	4.8	115	724	605	3.1	2.5
1.9	4.1	0.11	221	57	3.56	200	3479	65	13	9.6	118	724	577	3.3	2.8
5.0	6.5	0.12	223	57	3.58	203	4189	64	16	11	122	511	531	2.5	2.4
8.5	8.5	0.12	225	56	3.56	208	5135	61	21	14	123	483	515	2.4	2.4
12	9.9	0.12	223	56	3.57	208	6217	62	25	17	124	482	497	2.5	2.5

Table C.2: Summary table of flow conditions for the SAR-thick injector.

J	R	S	T_c (K)	ρ_c (kg/m ³)	P_c (MPa)	T_o (K)	\dot{m}_o (mg/s)	ρ_o (kg/m ³)	U_o (m/s)	Re_o (x10 ⁻⁴)	T_i (K)	\dot{m}_i (mg/s)	ρ_i (kg/m ³)	U_i (m/s)	Re_i (x10 ⁻⁴)
$P_r = 0.44$															
0.1	1.6	0.043	242	21	1.50	192	404	27	3.0	3.1	110	1991	622	1.9	0.5
0.5	3.4	0.043	218	24	1.50	196	928	27	6.9	1.0	110	2143	622	2.0	3.3
2.1	7.3	0.039	205	25	1.50	212	1789	24	15	1.9	110	2130	622	2.0	3.3
5.7	12	0.040	193	27	1.50	208	3008	25	24	3.2	110	2135	622	2.0	3.3
10	16	0.040	194	27	1.50	208	4075	25	33	4.4	110	2153	622	2.0	3.3
15	19	0.040	203	26	1.50	204	3604	26	28	3.9	107	1598	646	1.5	2.2
21	23	0.039	196	27	1.50	206	4385	25	35	4.7	107	1658	646	1.5	2.3
$P_r = 1.05$															
0.1	0.9	0.113	236	53	3.57	186	649	72	1.8	0.7	111	2126	636	2.0	3.1
0.5	2.1	0.109	229	55	3.57	198	1400	66	4.3	1.5	115	2056	605	2.0	3.4
2.1	4.4	0.106	208	61	3.56	202	2805	64	8.8	2.9	115	2041	605	2.0	3.4
5.2	6.8	0.109	208	61	3.56	203	4219	63	13	4.4	118	1908	577	1.9	3.5
9.2	9.0	0.113	205	63	3.56	203	5990	63	19	6.2	120	1985	556	2.1	4.0
14	11	0.122	206	62	3.56	204	7154	63	23	7.5	123	1885	515	2.2	4.4
21	14	0.104	205	63	3.57	206	7526	62	24	7.8	116	1724	596	1.7	3.0

Table C.3: Summary table of acoustic forcing conditions and dark-core length measurements for the LAR-thin injector.

	J	Baseline		f_F (kHz)	PAN		PN	
		p'_{pk-pk}/P_c	L_B/D_I		p'_{pk-pk}/P_c	L_{PAN}/D_I	p'_{pk-pk}/P_c	L_{PN}/D_I
$P_r = 0.44$	0.1	0.01%	-	3.13	0.82%	-	0.09%	-
	0.5	0.01%	-	3.14	0.96%	-	0.25%	-
	2.1	0.01%	18 ± 3	3.12	1.39%	15 ± 2	0.13%	11 ± 1
	5.2	0.01%	14 ± 2	3.12	1.42%	11 ± 1	0.23%	9.7 ± 0.9
	11	0.01%	11 ± 2	3.10	1.00%	10 ± 1	0.19%	10 ± 1
	14	0.01%	9 ± 2	3.11	1.04%	7.4 ± 0.9	0.30%	6.8 ± 0.6
	20	0.01%	8 ± 1	3.11	1.03%	6.7 ± 0.8	0.19%	6.8 ± 0.6
$P_r = 1.05$	0.1	0.01%	-	3.16	0.77%	-	-	-
	0.5	0.00%	-	3.10	0.98%	-	0.11%	-
	1.9	0.01%	11.9 ± 0.9	3.10	1.22%	8 ± 1	-	-
	5.0	0.01%	7.6 ± 0.7	3.41	0.54%	5.9 ± 0.5	0.05%	6.2 ± 0.4
	9	0.01%	5.9 ± 0.6	3.10	0.75%	5.0 ± 0.4	-	-
	12	0.01%	4.5 ± 0.4	3.10	1.02%	4.4 ± 0.4	-	-

Table C.4: Summary table of acoustic forcing conditions and dark-core length measurements for the SAR-thick injector.

	J	Baseline		f_F (kHz)	PAN		PN	
		p'_{pk-pk}/P_c	L_B/D_I		p'_{pk-pk}/P_c	L_{PAN}/D_I	p'_{pk-pk}/P_c	L_{PN}/D_I
$P_r = 0.44$	0.1	0.02%	-	3.10	1.32%	-	0.21%	-
	0.5	0.02%	-	3.04	1.27%	-	0.19%	-
	2.1	0.02%	10 ± 2	3.07	1.42%	10 ± 3	0.28%	8 ± 1
	5.7	0.02%	7 ± 1	3.11	1.06%	7 ± 1	0.14%	5.5 ± 0.8
	10	0.02%	5.2 ± 0.5	3.11	1.11%	5.4 ± 0.7	0.23%	4.7 ± 0.5
	15	0.02%	5.0 ± 0.5	3.04	1.48%	4.7 ± 0.5	0.25%	4.5 ± 0.5
	21	0.02%	4.6 ± 0.5	3.01	1.51%	4.1 ± 0.4	0.45%	4.3 ± 0.4
$P_r = 1.05$	0.1	0.01%	-	3.12	0.69%	-	0.13%	-
	0.5	0.01%	-	3.00	0.67%	-	0.40%	-
	2.1	0.01%	7 ± 1	3.04	1.17%	7.5 ± 1	0.23%	7.1 ± 0.8
	5.2	0.01%	5.1 ± 0.5	3.08	0.93%	5.3 ± 0.6	0.14%	3.8 ± 0.4
	9.2	0.01%	2.9 ± 0.2	3.11	0.99%	3.4 ± 0.4	0.19%	2.2 ± 0.2
	14	0.01%	2.4 ± 0.2	3.05	1.22%	2.8 ± 0.3	0.25%	2.1 ± 0.3
	21	0.01%	2.4 ± 0.2	3.12	1.11%	2.2 ± 0.3	0.13%	2.4 ± 0.3

REFERENCES

- [1] A. R. Karagozian, W. J. A. Dahm, E. Glasgow, R. Howe, I. Kroo, R. Murray, and H. Shyu. Technology options for improved air vehicle fuel efficiency. Technical Report SAB-TR-06-04, Air Force Scientific Advisory Board Report, 2006.
- [2] G. A. Mills and E. E. Ecklund. Alcohols as components of transportation fuels. *Annual review of energy*, 12(1):47–80, 1987.
- [3] F. Fischer. *The Conversion of Coal*. Ernst Benn, Ltd., 1925.
- [4] U.S. Air Force. B-52 flight uses synthetic fuel in all eight engines, 2006. <http://www.af.mil/news/story.asp?id=123035568>.
- [5] J. Hernandez. Secaf certifies synthetic fuel blends for b-52h, 2007. <http://www.af.mil/news/story.asp?id=123063866>.
- [6] A. Williams. Combustion of droplets of liquid fuels - a review. *Combustion and Flame*, 21, 1973.
- [7] G. A. E. Godsave. Burning of fuel droplets. In *Combustion and Flame*, pages 818–830, Baltimore, 1953. Williams and Wilkins.
- [8] C. K. Law and G. M. Faeth. Opportunities and challenges of combustion in microgravity. *Progress in Energy and Combustion Science*, 20, 1994.
- [9] C. K. Law. Recent advances in droplet vaporization and combustion. *Progress in Energy and Combustion Science*, 8(3):171–201, 1982.
- [10] S. R. Turns. *An Introduction to Combustion*. McGraw Hill, 2000.
- [11] J. Blaszczyk. Acoustically disturbed fuel droplet combustion. *Fuel*, 70(9):1023 – 1025, 1991.
- [12] S. Kumagai and H. Isoda. Combustion of fuel droplets in a vibrating air field. In *Fifth Symposium (International) on Combustion*, 1955.
- [13] P. M. Struk, M. Ackerman, V. Nayagam, and D. L. Dietrich. On calculating burning rates during fibre supported droplet combustion. *Microgravity Science and Technology*, 11, 1998.
- [14] M. Saito, M. Sato, and I. Suzuki. Evaporation and combustion of a single fuel droplet in acoustic fields. *Fuel*, 73, 1994.
- [15] M. Saito, M. Hoshikawa, and M. Sato. Enhancement of evaporation/combustion rate coefficient of a single fuel droplet by acoustic oscillation. *Fuel*, 75, 1996.

- [16] K. Okai, O. Moriue, M. Araki, M. Tsue, M. Kono, J. Sato, D. L. Dietrich, and F. A. Williams. Combustion of single droplets and droplet pairs in a vibrating field under microgravity. *Proceedings of the Combustion Institute*, 28, 200.
- [17] M. Tanabe, T. Morita, K. Aoki, K. Satoh, T. Fujimori, and J. Sato. Influence of standing sound waves on droplet combustion. *Proceedings of the Combustion Institute*, 28, 2000.
- [18] M. Tanabe, T. Kuwahara, K. Satoh, T. Fujimori, J. Sato, and M. Kono. Droplet combustion in standing sound waves. *Proceedings of the Combustion Institute*, 30, 2005.
- [19] Lord Rayleigh. On the circulation of air observed in kundt's tubes, and some allied acoustical problems. *Philosophical Transactions of the Royal Society of London*, 175, 1884.
- [20] S. Dattarajan, A. Lutomirski, R. Lobbia, O. I. Smith, and A. R. Karagozian. Acoustic excitation of droplet combustion in microgravity and normal gravity. *Combustion and Flame*, 144, 2006.
- [21] S. Dattarajan. *Acoustically Excited Droplet Combustion in Normal Gravity and Microgravity*. Ph.d. dissertation, UCLA, 2004.
- [22] J. I. Rodriguez. *Acoustic Excitation of Liquid Fuel Droplets and Coaxial Jets*. Ph.d. dissertation, UCLA, 2009.
- [23] D. B. Spalding. The combustion of liquid fuels. *Fourth Symposium (International) on Combustion*, 1953.
- [24] G. A. Agoston, H. Wise, and W. A. Rosser. Dynamic factors affecting the combustion of liquid spheres. *Symposium (International) on Combustion*, 1957.
- [25] D.T. Harrje and F.H. Reardon. Liquid propellant rocket combustion instability. nasa sp-194. *NASA Special Publication*, 194, 1972.
- [26] K.C. Schadow, E. Gutmark, T.P. Parr, D.M. Parr, K.J. Wilson, and J.E. Crump. Large-scale coherent structures as drivers of combustion instability. *Combustion Science and Technology*, 64(4-6):167–186, 1989.
- [27] N.A. Chigier and J.M. Beer. The flow region near the nozzle in double concentric jets. *Journal of Basic Engineering*, 86:797, 1964.
- [28] W. Forstall and A.H. Shapiro. Momentum and mass transfer in coaxial gas jets. *Journal of Applied Mechanics*, pages 399–407, 1950.

- [29] N.W.M. Ko and A.S.H. Kwan. The initial region of subsonic coaxial jets. *Journal of Fluid Mechanics*, 73(2):305–332, 1976.
- [30] R.B. Wicker and J.K. Eaton. Near field of a coaxial jet with and without axial excitation. *AIAA Journal*, 32(3):542–546, 1994.
- [31] E. Villiermaux, H. Rehab, and E.J. Hopfinger. Breakup regimes and self-sustained pulsations in coaxial jets. *Meccanica*, 29(4):393–401, 1994.
- [32] F.H. Champagne and I.J. Wygnanski. An experimental investigation of coaxial turbulent jets. *International Journal of Heat and Mass Transfer*, 14(9):1445–1464, 1971.
- [33] H. Rehab, E. Villiermaux, and E.J. Hopfinger. Flow regimes of large-velocity-ratio coaxial jets. *Journal of Fluid Mechanics*, 345:357–381, 1997.
- [34] H. Au and N.W.M. Ko. Coaxial jets of different mean velocity ratios, part 2. *Journal of Sound and Vibration*, 116(3):427–443, 1987.
- [35] A. Sevilla, J.M. Gordillo, and C. Martinez-Bazan. The effect of the diameter ratio on the absolute and convective instability of free coflowing jets. *Physics of Fluids*, 14:3028, 2002.
- [36] N.W.M. Ko and H. Au. Coaxial jets of different mean velocity ratios. *Journal of Sound and Vibration*, 100(2):211–232, 1985.
- [37] W.J.A. Dahm, C.E. Frieler, and G. Tryggvason. Vortex structure and dynamics in the near field of a coaxial jet. *Journal of Fluid Mechanics*, 241(1):371–402, 1992.
- [38] H. Rehab, E. Villiermaux, and E.J. Hopfinger. Geometrical effects on the near-field flow structure of coaxial jets. *AIAA Journal*, 36(5):867–869, 1998.
- [39] P.G. Gladnick, A.C. Enotiadis, J.C. LaRue, and G.S. Samuelsen. Near-field characteristics of a turbulent coflowing jet. *AIAA Journal*, 28(8):1405–1414, 1990.
- [40] M. Favre-Marinet, E.B. Camano, and J. Sarboch. Near-field of coaxial jets with large density differences. *Experiments in Fluids*, 26(1):97–106, 1999.
- [41] M. Favre-Marinet and E.B. Camano Schettini. The density field of coaxial jets with large velocity ratio and large density differences. *International Journal of Heat and Mass Transfer*, 44(10):1913–1924, 2001.
- [42] P.E. Dimotakis. Two-dimensional shear-layer entrainment. *AIAA Journal*, 1986.
- [43] H. Eroglu, N. Chigier, and Z. Farago. Coaxial atomizer liquid intact lengths. *Physics of Fluids A: Fluid Dynamics*, 3:303, 1991.

- [44] J.C. Lasheras, E. Villiermaux, and E.J. Hopfinger. Break-up and atomization of a round water jet by a high-speed annular air jet. *Journal of Fluid Mechanics*, 357(1):351–379, 1998.
- [45] D.W. Davis and B. Chehroudi. Measurements in an acoustically driven coaxial jet under sub-, near-, and supercritical conditions. *Journal of Propulsion and Power*, 23(2):364–374, 2007.
- [46] I.A. Leyva, B. Chehroudi, and D. Talley. Dark core analysis of coaxial injectors at sub-, near-, and supercritical pressures in a transverse acoustic field. In *43rd AIAA/ASME/SAE/ASEE Joint Propulsion Conference & Exhibit*, AIAA 2007-5456.
- [47] J. Cohen and I. Wygnanski. The evolution of instabilities in the axisymmetric jet. part 1. the linear growth of disturbances near the nozzle. *J. Fluid Mech*, 176:191–219, 1987.
- [48] A. Michalke and G. Hermann. On the inviscid instability of a circular jet with external flow. *Journal of Fluid Mechanics*, 114(1):343–359, 1982.
- [49] D. Perrault-Joncas and S.A. Maslowe. Linear stability of a compressible coaxial jet with continuous velocity and temperature profiles. *Physics of Fluids*, 20(7):074102, 2008.
- [50] A. Talamelli and I. Gavarini. Linear instability characteristics of incompressible coaxial jets. *Flow, Turbulence and Combustion*, 76(3):221–240, 2006.
- [51] C.C. Miesse. The effect of ambient pressure oscillations on the disintegration and dispersion of a liquid jet. *Jet Propulsion*, 25:525–530, 1955.
- [52] J.A. Newman. A preliminary study of the effects of vaporization and transverse oscillations on liquid jet breakup. Technical Report CR-72258, NASA, 1967.
- [53] M.F. Heidmann and J.F. Groeneweg. *Analysis of the dynamic response of liquid jet atomization to acoustic oscillations*. National Aeronautics and Space Administration, 1969.
- [54] G. Balarac, O. Métais, and M. Lesieur. Mixing enhancement in coaxial jets through inflow forcing: A numerical study. *Physics of Fluids*, 19:075102, 2007.
- [55] F. Richecoeur, P. Scoufflaire, S. Ducruix, and S. Candel. Interactions between propellant jets and acoustic modes in liquid rocket engines: experiments and simulations. In *42nd AIAA/ASME/SAE/ASEE Joint Propulsion Conference & Exhibit*, AIAA 2006-4397.

- [56] A. Ghosh, Q. Diao, G. Young, and K. Yu. Effect of density ratio on shear-coaxial injector flame-acoustic interaction. In *42nd AIAA/ASME/SAE/ASEE Joint Propulsion Conference & Exhibit*, AIAA 2006-4528.
- [57] A. Ghosh. *The Role of Density Gradient in Liquid Rocket Engine Combustion Instability*. PhD thesis, University of Maryland, College Park.
- [58] D.W. Davis. *On the Behavior of a Shear-Coaxial Jet, Spanning Sub- to Supercritical Pressures, with and without an Externally Imposed Transverse Acoustic Field*. Ph.d. dissertation, Pennsylvania State University, 2006.
- [59] W. L. Nyborg. Radiation pressure on a small rigid sphere. *The Journal of the Acoustical Society of America*, 42(5), 1967.
- [60] R. L. Panton. *Incompressible Flow*. John Wiley & Sons, Inc., Hoboken, NJ, third edition, 2005.
- [61] A. F. Mills and B. H. Chang. Error analysis of experiments. UCLA, Los Angeles, CA, 2004.
- [62] B.R. Munson, D.F. Young, and T.H. Okiishi. *Fundamentals of Fluid Mechanics*. John Wiley, New York, 2002.
- [63] National Institute of Standards and Technology. Thermophysical properties of fluid systems, 2011. <http://webbook.nist.gov/chemistry/fluid/>.
- [64] N. Otsu. A threshold selection method from gray-level histograms. *IEEE Trans. Sys., Man., Cyber*, 1979.
- [65] G. Berkooz, P. Holmes, and J.L. Lumley. The proper orthogonal decomposition in the analysis of turbulent flows. *Annual Review of Fluid Mechanics*, 25(1):539–575, 1993.
- [66] A. Chatterjee. An introduction to the proper orthogonal decomposition. *Current Science*, 78(7):808–817, 2000.
- [67] M. Arienti and M.C. Soteriou. Time-resolved proper orthogonal decomposition of liquid jet dynamics. *Physics of Fluids*, 21:112104, 2009.
- [68] J.R. Taylor. *An Introduction to Error Analysis: The Study of Uncertainties in Physical Measurements*. University Science Books.
- [69] J.C. Lasheras and E.J. Hopfinger. Liquid jet instability and atomization in a coaxial gas stream. *Annual Review of Fluid Mechanics*, 32(1):275–308, 2000.

- [70] J.J. Graham, I.A. Leyva, J.I. Rodriguez, and D. Talley. On the effect of a transverse acoustic field on a flush shear coaxial injector. In *45th AIAA/ASME/SAE/ASEE Joint Propulsion Conference & Exhibit*, AIAA 2009-5142.
- [71] G.P. Sutton and O. Biblarz. *Rocket Propulsion Elements*. John Wiley & Sons, 2001.
- [72] M.H. Yu and P.A. Monkewitz. The effect of nonuniform density on the absolute instability of two-dimensional inertial jets and wakes. *Physics of Fluids A: Fluid Dynamics*, 2:1175, 1990.
- [73] P. Huerre and P.A. Monkewitz. Local and global instabilities in spatially developing flows. *Annual Review of Fluid Mechanics*, 22(1):473–537, 1990.
- [74] P. Huerre. Open shear flow instabilities. *Perspectives in Fluid Dynamics*, pages 159–229, 2000.
- [75] S. Jendoubi and P.J. Strykowski. Absolute and convective instability of axisymmetric jets with external flow. *Physics of Fluids*, 6:3000, 1994.
- [76] S. Megerian, J. Davitian, L.S. de B. Alves, and A.R. Karagozian. Transverse-jet shear-layer instabilities. part 1. experimental studies. *Journal of Fluid Mechanics*, 593(1):93–129, 2007.

Experiments and numerical simulation of mixing under supercritical conditions

T. Schmitt,¹ J. Rodriguez,^{1,2} I. A. Leyva,² and S. Candel¹

¹EM2C, CNRS, Ecole Centrale Paris, 92295 Châtenay-Malabry, France

²AFRL/RZSA, Edwards AFB, California 93524, USA

(Received 10 October 2011; accepted 24 October 2011; published online 16 May 2012)

Supercritical pressure conditions designate a situation where the working fluid pressure is above the critical point. Among these conditions, it is interesting to identify a transcritical range which corresponds to cases where the pressure is above the critical point, but the injection temperature is below the critical value. This situation is of special interest because it raises fundamental issues which have technological relevance in the analysis of flows in liquid rocket engines. This situation is here envisaged by analyzing the behavior of a nitrogen shear coaxial jet comprising an inner stream injected at temperatures close to the critical temperature and a coaxial flow at a higher temperature. Experiments are carried out both in the absence of external modulation and by imposing a large amplitude transverse acoustic field. Real gas large eddy simulations are performed for selected experiments. The combination of experiments and calculations is used to evaluate effects of injector geometry and operating parameters. Calculations retrieve what is observed experimentally when the momentum flux ratio of the outer to the inner stream $J = (\rho_e u_e^2)/(\rho_i u_i^2)$ is varied. Results exhibit the change in flow structure and the development of a recirculation region when this parameter exceeds a critical value. The instantaneous flow patterns for different momentum flux ratios are used in a second stage to characterize the dynamical behavior of the flow in terms of power spectral density of velocity and density fluctuations. Results obtained under acoustic modulation provide insight into mixing enhancement of coaxial streams with a view of its possible consequences in high frequency combustion instabilities. It is shown in particular that the presence of strong acoustic modulations notably reduces the high density jet core length, indicating an increased mixing efficiency. This behavior is more pronounced when the jet is placed at the location of maximum transverse velocity fluctuations. © 2012 American Institute of Physics. [<http://dx.doi.org/10.1063/1.3701374>]

I. INTRODUCTION

This study focuses on turbulent cryogenic flows issuing from coaxial injectors operating at supercritical pressure (i.e., pressure above the critical value). Attention is given to the role of injection conditions (temperature, velocity) on mixing efficiency, and on the influence of a transverse acoustic modulation on jets dynamics. In addition to the fundamental interest they raise, flows formed by coaxial injectors are of practical relevance for high performance cryogenic liquid rocket engines (LREs) and more generally for combustion processes operating at high pressure. It is important to understand the basic processes taking place in these flows to improve the design methodology for future cryogenic LREs. Another potential application of research reported in this article lies in the area of combustion instability. It is known that mechanisms driving combustion oscillations result from the coupling between the injector flow, the combustion process and the chamber acoustic modes. The manner in which the inner and outer streams originating from a coaxial element interact with each other and with their surroundings may affect the temporal and spatial release of chemical energy within the chamber leading to undesired oscillations associated with a resonant acoustic motion. In most LREs, performance has been enhanced by augmenting the chamber pressure. Current LOx/H₂

engines, such as the SSME, Vulcain2, and RS-68, operate at values exceeding the critical pressure of their individual propellants. The inner jet, oxygen, is generally injected in a transcritical or liquidlike state (i.e., at a pressure higher than the critical value but at a temperature lower than the critical temperature) and it is surrounded by a higher velocity hydrogen stream at supercritical temperature.¹ The inner fluid stream injected in a transcritical form evolves to a supercritical state as its temperature rises because of mixing and possibly combustion. Under such thermodynamic conditions, the system exhibits particular features that differ from those of a two-phase flow or of a pure gaseous injection. The objective of the present work is to compare experiments and simulations in which shear coaxial jet configurations are established at pressures above the critical point of the injected fluid, but at transcritical temperatures without and with acoustic excitation. For this study, nitrogen (N_2) is the only fluid used in the inner, outer, and chamber flows.

At this point it is worth reviewing previous work dealing with supercritical injection. Starting with single round-jets, experiments have been carried out at AFRL (Air Force Research Laboratory)² and DLR (Deutsches Zentrum für Luft- und Raumfahrt)^{3,4} (see also Oschwald *et al.*⁵ for a review up to 2006). Some recent investigations are reported by Segal and Polikhov⁶ and Roy and Segal.⁷ These studies indicate that the liquid break-up and atomization mechanism which prevail at subcritical pressure are no longer observable because surface tension and latent heat of vaporization vanish at supercritical pressures.⁸ The jet of fluid then dissolves in the ambient gas, with no evidence of droplets. The flow features “comblike” structures at the edge of the dense stream, a type of pattern which is not observed at subcritical pressures.² The geometry of the flow is reminiscent of that of a variable density turbulent gas stream.² This behavior has been confirmed by experimental measurements of visual spreading rates in the initial region which are found to be consistent with theoretical growth rate expressions for incompressible variable-density turbulent mixing layers. Quantitative measurements of density,^{3,4,9} spreading rate and axial decay coefficients obtained by DLR (Refs. 5 and 10) using spontaneous Raman scattering also convey the same type of information.

Coaxial injection is investigated by several researchers at AFRL (Refs. 11–16) who examine the single-species case, and by Mayer and Smith¹⁷ who consider a stream of nitrogen injected at low temperature (high density) surrounded by a high velocity stream of moderate temperature helium. Quantitative measurement of species density are reported by Oschwald *et al.*¹⁸ for a coaxial nitrogen/hydrogen injection, using spontaneous Raman scattering. When compared with the round jet configuration, a strong reduction of the jet density potential core length is observed.⁵ For shear coaxial jets, it has been found that the momentum flux ratio between the outer stream and the inner jet ($J = (\rho_e u_e^2)/(\rho_i u_i^2)$) is of major importance for the mixing efficiency.^{19,20} It has also been found that combustion is more stable and more efficient at high values of this quantity.²¹ Different flow regimes may be obtained by varying this ratio²² and it is found that the inner jet core length decreases as the momentum flux ratio increases.^{12,13}

The dynamics of coaxial transcritical jets is of interest for the study of combustion instability. This can be examined by considering the interaction of acoustic waves with transcritical flows and its influence on mixing efficiency. The effect of an acoustic modulation on a single round jet at sub- and supercritical pressure is investigated by Chehroudi and Talley²³ who find that effects on the jet structure are more profound in the subcritical case. The impact of the modulation is reduced as the initial jet velocity is augmented. The impact of acoustics on a non-reacting shear coaxial jet has been investigated experimentally by Leyva and Rodriguez.^{13–16} They have assessed the effects of acoustics on the jet by measuring the spreading angle of the inner and outer jets and the length of the inner jet before its first break-up. It has been found that the injector geometry has an effect on the susceptibility of coaxial flows to acoustic modulation. For the injector geometry studied here, acoustics have a measurable effect on the reduction of the inner jet dark core length for an intermediate value of J at pressures varying from 1.5 to 5.0 MPa. Reactive cases were also experimentally investigated (see Refs. 21, 24–27 for example, and Refs. 28 and 29 for acoustically modulated cases) but will not be detailed here since they are out of the scope of the present article.

The numerical modeling of such complex flows has been considered more recently by various groups. It is first noted that in the transcritical range, thermodynamic properties notably differ from

those of a perfect gas and cannot be accurately represented with the standard perfect gas equation of state (EOS). Thermodynamics and “real-gas” EOS are required.^{8,30,31} Cubic equations of state are generally used to this purpose,³² but more precise (and numerically expensive) equations may also be employed.³¹ This issue and the modeling of transport properties are extensively reviewed in Refs. 32–35.

The models described in the previous studies are used in various calculations. Mixing at supercritical pressure is examined with direct numerical simulation in a mixing layer configuration, to show the role of density gradients on the global layer stability and turbulence characteristics and the strong effect on the molecular mixing of the reduced species diffusion near critical conditions.³⁵ This highlights the need for appropriate subgrid-scale models for large eddy simulation (LES) under supercritical pressure conditions.^{36,37}

A few LES have been performed under transcritical conditions. An extensive review of non-reacting LES in the period ending in 2006 can be found in Zong and Yang.³⁸ A single nitrogen round jet was studied by Zong^{39,40} and recently by Schmitt *et al.*⁴¹ Again, the stabilizing effect of the density gradient, and its role on turbulent energy redistribution along the mixing layer was identified.³⁹ Shear coaxial injection of oxygen and methane has also been simulated by Zong and Yang.⁴² This has been continued by considering a non-reactive coaxial injector submitted to acoustic modulations⁴³ where a significant reduction of the jet intact core length is observed when acoustic perturbations are present.

One also notes that LES have been used for reactive cases at supercritical pressures. Shear coaxial jet flames were investigated by Oefelein,^{32,44} Oefelein and Yang,⁴⁵ Zong and Yang,⁴⁶ Matsuyama *et al.*,⁴⁷ Masquelet *et al.*,⁴⁸ and Schmitt *et al.*⁴⁹ The problem is also considered in the Reynolds averaged Navier-Stokes framework (see, for example, Refs. 50–52).

The present investigation focuses on the mixing behavior in the flow originating from a shear coaxial injector in the absence or in the presence of external acoustic modulation. Three operating points are considered corresponding to different momentum flux ratios. The coaxial jet geometry corresponds to a thick inner jet post (the wall which separates the inner and outer streams in the coaxial configuration has a thickness of the order of the jet diameter). In this article each case is defined by the chamber pressure, the momentum flux ratio, and the coaxial jet geometry which is fixed in the present study. The main components of the experimental facility are reviewed in Sec. II. Balance equations and models used in the simulations are briefly described in Sec. III. The definition of the computational domain and other numerical aspects are considered in Sec. IV. The influence of the momentum flux ratio is examined in Sec. V. Results obtained are used to examine the dynamics of the flow and identify the spectral content in the various regions. Effects of a transverse acoustic modulation are investigated in Sec. VI.

II. EXPERIMENTAL CONFIGURATION

The experimental work was carried out at the Supercritical Cryogenic Test Facility (EC-4) of the Air Force Research Laboratory at Edwards Air Force Base, California, using a test chamber that achieves pressures over 5 MPa and cryogenic injection at temperatures below 120 K, with the capability to perform acoustic forcing. Figure 1(a) shows the main test chamber and key components of the facility. A schematic view can be seen in Fig. 1(b). It featured a shear coaxial jet flow with an inner jet denser than the outer jet under typical combustion chamber pressures, resembling conditions found in practice where the inner jet is injected at a lower temperature than the outer stream. In these experiments, the coaxial jet flow parameters were varied and the coaxial jet behavior was observed with and without acoustic excitation.

During a test, high-pressure gaseous nitrogen was fed into the inner and outer flow lines of the coaxial jet and flow rates adjusted to correspond to desired test conditions. Mass flow rates through the inner and outer jets were measured with Porter mass flow meters (models 122 and 123-DKASVDAA). High-pressure nitrogen was also employed in the test chamber to increase its pressure, which is measured with a Stellar 1500 transducer to achieve the required level. Jet temperatures were controlled by adjusting the flow rates of liquid nitrogen through the heat exchangers placed on the feed lines. Densities of the two jets were deduced from the measured temperatures

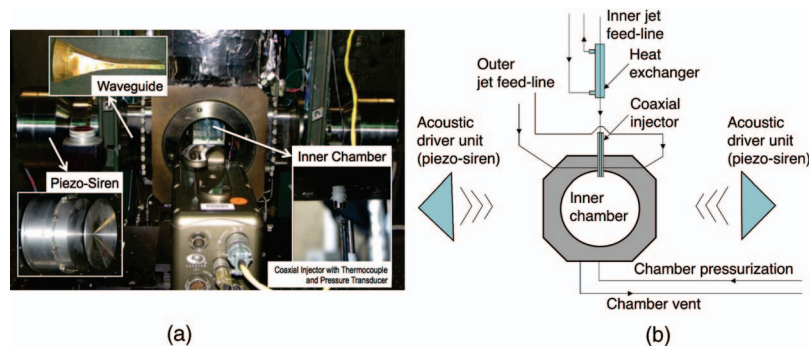


FIG. 1. (a) Photograph of the main test chamber and key instrumentation of EC4, the supercritical cryogenic facility at AFRL, Edwards AFB. (b) Flow diagram of the test chamber and its vicinity.

and pressure using the National Institute of Standards and Technology's thermophysical properties of fluids database.⁵³ These values in conjunction the mass flow rates were used to obtain injection velocities, Reynolds numbers, velocity, and momentum flux ratios. Readings from thermocouples across the heat exchanger and in other locations were used to keep track of the conditions of the flow and maintain the required flow properties. Two images of the shear coaxial injector can be seen in Fig. 2. The first, Fig. 2(a), gives a full view before assembly and the second, Fig. 2(b) shows a plane view of the end section. The inner jet diameter was $d_i = 0.51$ mm, while the outer jet had an inner diameter of 1.59 mm and an outer diameter of 2.42 mm. The outer diameter of the injector was 3.18 mm. The length to inner diameter ratio was 100 for the inner jet and 34 for the outer jet based on the hydraulic diameter. Inner and outer jets were nominally concentric. The inner jet exit plane was recessed by half of d_i (0.255 mm) from the outer jet exit plane in order to mimic coaxial jet configurations used in practice.

An inner chamber within the test chamber was created to augment the level of acoustic modulation acting on the coaxial flow. The inner chamber had a height of 59.4 mm, a width of 76.0 mm, and a depth of 12.7 mm. The coaxial injector was protruding by 5 mm into the inner chamber from the top through an orifice of 17 mm in diameter. The flow was then visualized and was exhausted through another orifice at the bottom.

Temperatures were measured with unshielded traveling type E thermocouples with a bead diameter of 0.1 mm. Immediately prior or after exciting the jet with acoustics and taking films, a temperature profile was recorded at a close distance from the exit plane. Changes that might have occurred during test time were checked by comparing the upstream temperature values of the inner and outer jets, prior, during, and after the test. Since each thermocouple was manually calibrated against a resistance temperature detector, the uncertainty on the temperature measurements at the jet exit plane is about 1 K. Miniature pressure transducers (Kulite Semiconductor Products, either model

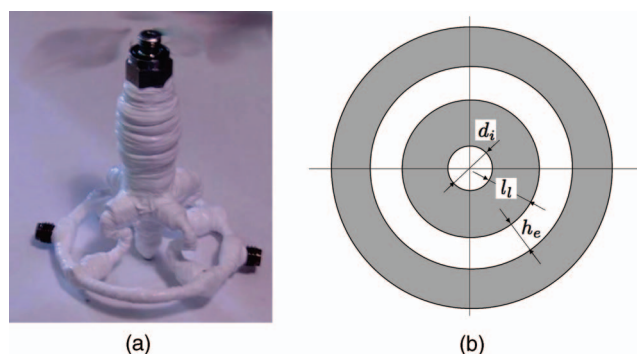


FIG. 2. (a) Photograph of the shear coaxial injector used in this study. (b) Exit plane view of the injector.

CCQ-062-1000A or CCQ-093-750A with 6.9 and 5.2 MPa of absolute pressure range, respectively) record pressure fluctuations at a sampling frequency of 20 kHz. These pressure transducers were used to scan the acoustic field induced by the acoustic driver units prior to experiments. During a test, the acoustic field was also being measured by these high frequency transducers while the films were being recorded.

The coaxial jet was observed with backlighting (shadowgraph) imaging. The flow was illuminated with a Newport variable power arc lamp set at 160 W or 300 W and filmed with a Phantom v7.1 high-speed camera recording up to 160 000 frames per second at a resolution of 32 pixels by 32 pixels.

The camera, equipped with an AF Nikkor 35-105 mm lens and a Nikon No. 1 Close-Up lens, can be seen at the bottom center in Fig. 1(a). The image size in the present experiments varied from 128×224 to 196×400 pixels, depending on chamber pressure and outer-to-inner momentum flux ratio. Images were recorded in grayscale with each pixel taking a value between 0 and 255 for different intensities of gray ranging from white to black. In the images, each pixel represents $0.08 \text{ mm} \times 0.08 \text{ mm}$ approximately. Depending on the resolution chosen, the framing rate was 20, 25, or 41 kHz. The exposure time was generally 1-2 μs and the number of images saved per run was 1000. Then the recorded images were processed using MATLAB. A subroutine based on the Otsu technique⁵⁴ which takes a grayscale image and finds a pixel threshold value was used. All pixel values above this threshold are converted to black and the remaining pixels to white. The subroutine then measures the length of the black region extending from the exit of the coaxial jet. This is referred to as the “dark core length.” A “mean dark core length” l_{dc} is then obtained by averaging the 1000-image sample from each run. The sensitivity of the determined dark core length on threshold values is discussed in Refs. 13 and 55 where it is shown that estimates are only weakly dependent on the selected threshold level.

Two piezo-sirens placed at each end of the chamber, 34 cm away from the jet axis provided acoustic modulation (see Fig. 1(a)). Custom-designed for the Air Force Research Laboratory by Hersh Acoustical Engineering Inc., they received amplified signals from either a Krohn-Hite model 7500 or a Trek model PZD2000A amplifier in the 200–540 V range. A Fluke 100 MS/s arbitrary waveform generator (model 292) produced the two sinusoidal waves sent to the amplifiers with the same frequency but with a prescribed phase between them. A waveguide with a catenary contour (see Fig. 1(a)) transmitted the waves from the circular cross-section of each piezo-siren to a rectangular cross-section. The maximum root-mean-square acoustic pressure fluctuations generated by the two piezo-ceramic acoustic sources in the inner chamber, measured using the three differential Kulite pressure transducers (model XCQ-093-25D) flush mounted on a lateral chamber wall, varied from 8.0 to 22 kPa in the 2.9 to 3.1 kHz range. These operating conditions were obtained by manually varying the frequency on the signal generator and finding the highest possible pressure amplitude, indicating that an eigenfrequency of the chamber is excited (around 3 kHz). This high-frequency value is chosen in order to be comparable with resonant frequencies encountered in transverse high-frequency instabilities of liquid rocket engines.

The prescribed phase difference between the signals sent to the piezo-sirens exposed the coaxial jet to different effective positions in the acoustic field. When the two piezo-sirens generated waves with a 0° phase angle between them, the motion of their radiating membranes was synchronized and vibrated in opposite directions, producing conditions of high pressure perturbations (pressure antinode) and low velocity fluctuations (velocity node) at the center of the chamber where the coaxial jet was located. In contrast, when the two drivers presented a 180° phase difference, then the radiating membranes moved in the same direction, generating high velocity fluctuations with very small variations in pressure at the jet location, producing a pressure node or velocity antinode.

III. BALANCE EQUATIONS AND MODELS

At this stage it is worth briefly reviewing the spatially filtered balance equations and introducing the real gas models and subgrid scale closures used in the large eddy simulations.

A. Governing equations

A single species flow configuration is investigated in the present study. In this situation, the vector of conservative variables for a compressible flow is $\mathbf{w} = (\rho, \rho \mathbf{u}, \rho E)^T$, where ρ is the density, \mathbf{u} is the velocity vector, and E is the total energy (E is the sum of internal energy e_s and kinetic energy $e_k = 1/2 \sum u_i^2$). The present large-eddy simulations are carried out by integrating the mass weighted spatially filtered Navier-Stokes equations. In the following balance equations (for a given variable ϕ , $\bar{\phi}$ designates the spatially filtered variable, while $\tilde{\phi}$ is the mass-weighted (Favre) spatially filtered variable):

$$\frac{\partial \bar{\rho}}{\partial t} + \frac{\partial \bar{\rho} \tilde{u}_j}{\partial x_j} = 0, \quad (1)$$

$$\frac{\partial \bar{\rho} \tilde{u}_i}{\partial t} + \frac{\partial \bar{\rho} \tilde{u}_j \tilde{u}_i}{\partial x_j} = -\frac{\partial \bar{p}}{\partial x_i} + \frac{\partial \bar{\tau}_{ij}}{\partial x_j} - \frac{\partial \tau_{ij}^t}{\partial x_j}, \quad (2)$$

$$\frac{\partial \bar{\rho} \tilde{E}}{\partial t} + \frac{\partial \bar{\rho} \tilde{E} \tilde{u}_j}{\partial x_j} + \frac{\partial \bar{p} \tilde{u}_j}{\partial x_j} = -\frac{\partial \bar{q}_j}{\partial x_j} - \frac{\partial q_j^t}{\partial x_j} + \frac{\partial \tilde{u}_i \bar{\tau}_{ij}}{\partial x_j}. \quad (3)$$

In Eqs. (1)–(3), p is the pressure, \mathbf{x} is the spatial coordinates vector, and t is the time. The laminar viscous stress tensor $\boldsymbol{\tau}$ and heat flux vector \mathbf{q} are expressed as linear functions of the strain rates and temperature gradient, respectively. Laminar viscosity and heat conductivity coefficients are determined with the Chung *et al.* method.⁵⁶ For the single species case investigated in the present article, no additional diffusion terms are needed since the Soret and Dufour effects naturally vanish. The modeling of the subgrid-scale stress tensor τ_{ij}^t and heat flux vector q_j^t requires some discussion. It is known from recent studies that subgrid closure rules for real gases differ from those used for perfect gas flows. In principle, one should take into account additional terms arising from the nonlinearity of the state equation and from the large variations in transport properties as explained in some recent studies by Bellan,³⁵ Selle *et al.*,³⁶ and Taskinoglu and Bellan.³⁷ However, the modeling issues are not completely settled. It is also known from other calculations that the low pressure subgrid scale models yield suitable results for transcritical and supercritical round jets.^{41,57} It was decided for these reasons to keep these low pressure closures for the subgrid scale models as described in more detail in Sec. III C.

B. Real gas thermodynamics and equation of state

Real gas thermodynamics for high pressure flow calculations is envisaged in many recent studies where accurate descriptions of the fluid state are derived from various types of equations.^{31,33} The present simulations rely on the Peng-Robinson equation of state⁵⁸ (Eq. (4)) which is used in the analysis to model the departure from an ideal-gas behavior. This EOS is less accurate than the modified version but it is also simpler and requires a smaller amount of calculations. The fluid state is expressed in the form

$$p = \frac{\rho r T}{1 - \rho b} - \frac{\rho^2 a(T)}{1 + 2\rho b - \rho^2 b^2}, \quad (4)$$

where T is the temperature, $r = R/W$ where R is the perfect-gas constant and W is the molar mass. The Peng-Robinson coefficients $a(T)$ and b for a single-species fluid are⁸

$$a = 0.457236 \frac{(r T_c)^2}{p_c} \left(1 + c(1 - \sqrt{T_R}) \right)^2, \quad (5)$$

$$b = 0.077796 \frac{r T_c}{p_c} \quad (6)$$

with

$$c = 0.37464 + 1.54226\omega - 0.26992\omega^2, \quad (7)$$

where $T_c = 126.2$ K and $p_c = 3.396$ MPa are the critical temperature and pressure of nitrogen, $\omega = 0.0372$ represents its acentric factor and $T_R = T/T_c$ is the reduced temperature. This equation offers a good trade-off between computational cost and precision. The pressure dependence of thermodynamic functions and coefficients is subsequently derived from the EOS.^{31,44,59} Departure energy Δe_s and specific heat Δc_v at constant volume are given by^{8,60}

$$\Delta e_s = - \int_{\rho}^{\rho_0} \left\{ \frac{T}{\rho^2} \left(\frac{\partial p}{\partial T} \right)_{\rho, Y_k} - \frac{p}{\rho^2} \right\}_T d\rho, \quad (8)$$

$$\Delta c_v = -T \int_{\rho}^{\rho_0} \left\{ \left(\frac{1}{\rho^2} \frac{\partial^2 p}{\partial T^2} \right)_{\rho, Y_k} \right\}_T d\rho, \quad (9)$$

where $\Delta e_s = e_s(\rho, T) - e_s^0(T)$ and $\Delta c_v = c_v(\rho, T) - c_v^0(T)$. The enthalpy and specific heat at constant pressure are then deduced from

$$h_s = e_s + \frac{p}{\rho}, \quad c_p = c_v + \frac{T\alpha^2}{\rho\beta}. \quad (10)$$

The thermal expansion coefficient α and the isothermal compressibility coefficient β appearing in the previous expressions are given by

$$\alpha = -\frac{1}{\rho} \left(\frac{\partial \rho}{\partial T} \right)_p, \quad \beta = \frac{1}{\rho} \left(\frac{\partial \rho}{\partial p} \right)_T. \quad (11)$$

The low-pressure references (i.e., e_s^0 and c_v^0) are obtained from the JANAF Thermodynamical Tables⁶¹ and only depend on temperature.

C. Subgrid-scale models and assumptions

As indicated previously, the present simulations rely on a standard (low pressure) subgrid scale closure, the WALE model, in which the stress tensor τ_{ij}^t is conveniently expressed in terms of the spatially resolved strain rates \tilde{S}_{ij} ,⁶²

$$\tau_{ij}^t = 2\nu^t \left(\tilde{S}_{ij} - \frac{1}{3} \delta_{ij} \tilde{S}_{ll} \right), \quad (12)$$

where

$$\nu^t = (C_w \Delta)^2 \frac{(s_{ij}^d s_{ij}^d)^{3/2}}{(\tilde{S}_{ij} \tilde{S}_{ij})^{5/2} + (s_{ij}^d s_{ij}^d)^{5/4}}, \quad (13)$$

$$s_{ij}^d = \frac{1}{2} (\tilde{g}_{ij}^2 + \tilde{g}_{ji}^2) - \frac{1}{3} \tilde{g}_{kk}^2 \delta_{ij}. \quad (14)$$

In the previous expression the WALE model constant $C_w = 0.4929$ and \tilde{g}_{ij} is the irrotational part of the stress tensor

$$\tilde{g}_{ij} = \frac{\partial \tilde{u}_i}{\partial x_j} \quad \text{and} \quad \tilde{g}_{ij}^2 = \tilde{g}_{ik} \tilde{g}_{kj}. \quad (15)$$

The WALE model distinguishes velocity gradients associated with the rotational and pure shear components of the velocity gradients in order to distinguish regions where turbulence is transitional and regions where it is fully developed. It is well suited to the treatment of shear flows of the type considered in this article.

The subgrid scale heat flux is modeled using a standard gradient transport assumption

$$\overline{q_i^t} = -\lambda_t \frac{\partial \tilde{T}}{\partial x_i}. \quad (16)$$

The subgrid scale conductivity is cast in the form $\lambda_t = c_p \mu_t / \text{Pr}_t$ where $\mu_t = \rho \nu_t$ and Pr_t , respectively, designate the subgrid dynamic viscosity and turbulent Prandtl number. As in low pressure simulations a constant value $\text{Pr}_t = 0.7$ is used in the present calculations.

IV. NUMERICAL ASPECTS

The mass weighted spatially filtered compressible Navier-Stokes equations in combination with the subgrid scale models described previously are integrated in the AVBP flow solver.^{63,64} This code has already been used to calculate low and moderate pressure reactive flows of multicomponent mixtures of perfect gases. The spatial discretization on unstructured or hybrid meshes facilitates applications in which the geometry is complex, a feature which is quite useful if one wishes to analyze practical configurations. The LES of turbulent flows requires a low-dissipation algorithm^{65,66} which is often obtained with centered discretization schemes. The present integration method relies on a Taylor-Galerkin weighted residual central distribution scheme, called TTG4A. This scheme is third-order in space and fourth-order in time.⁶⁷

The real gas equation of state, thermodynamics, and transport coefficients have been implemented in AVBP. The convective fluxes Jacobian matrices, used by the scheme, are expressed in terms of real gas thermodynamics to preserve the overall consistency of the code. A fully consistent treatment of associated boundary conditions is based on the characteristic wave decomposition method NSCBC (Refs. 64 and 68) and includes specific expressions provided for real gas thermodynamics in Ref. 69. The highly nonlinear thermodynamics of the transcritical fluid stream induces large density gradients between the dense transcritical fluid and the surrounding gaseous stream which require a specific stabilization procedure. Only the principle of the method is described and the focus is placed on specific issues linked with real gas thermodynamics. The treatment of steep gradients relies on artificial viscosity and is activated when unresolved gradients are detected, using a density-based sensor. More details about the sensor and the operators used to add viscosity can be found in Ref. 41. To deal with the highly nonlinear thermodynamics characterizing supercritical flows, it is necessary to apply artificial dissipation in a consistent way to all variables, to reduce perturbations to the pressure field which may otherwise give rise to strong acoustic waves. Minimization of this parasitic numerical noise was achieved by writing the exact differential of pressure with respect to total energy, density, and momentum

$$dP = \frac{\alpha}{\rho\beta C_v} d(\rho E) + \frac{C_p - \alpha h_s + \alpha e_k}{\rho\beta C_v} d\rho - \frac{\alpha u_i}{\rho\beta C_v} d(\rho u_i). \quad (17)$$

Imposing $dP = 0$ in Eq. (17) provides the variation of ρE , consistent with the modification of ρ and ρu_i introduced by artificial viscosity, that does not generate pressure fluctuations.

One drawback of this strategy is that it is not fully conservative in terms of total energy E . Its impact on the final solution is difficult to estimate, but is probably negligible because this correction is applied locally thanks to the sensor.

The real gas AVBP flow solver has already been used to simulate transcritical cryogenic flames of various types.^{49,70,71}

A. Computational domain and mesh

The geometry of the computational domain essentially matches the experimental configuration. A three-dimensional view of the external boundaries is given in Fig. 3(a). The longitudinal section of the chamber is rectangular (59.4×76.0 mm) and its width is 12.7 mm. The fluid streams are injected by a coaxial element which protrudes by 5 mm into the chamber (Fig. 3(b)). This injector is located in the center of a 17 mm-diameter hole in the inlet wall. No co-flow is directly injected through this orifice during the experiment, but nitrogen gas may traverse this aperture as a result of entrainment by the coaxial streams giving rise to a finite flow velocity in this region. The entrained fluid originates from a large reservoir defined on the upstream side of the central hole. Details

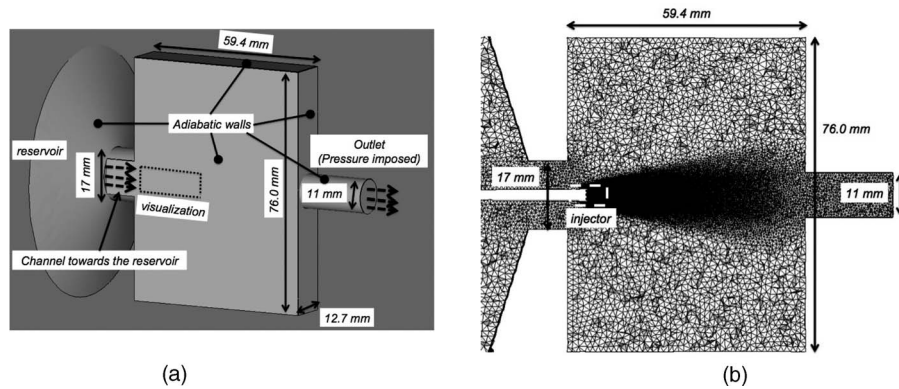


FIG. 3. (a) Three-dimensional visualization of the reservoir. (b) Longitudinal cut of the mesh.

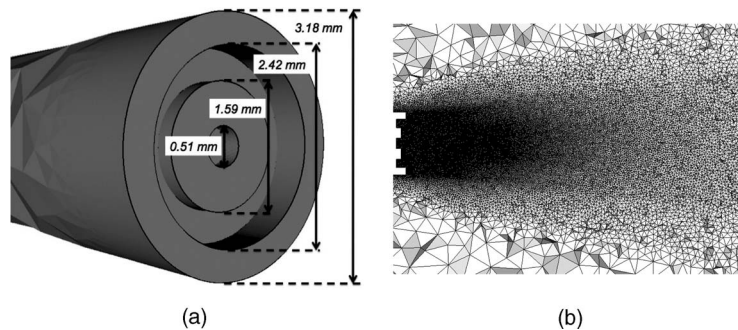


FIG. 4. (a) Closer view of the injector. (b) Longitudinal cut of the mesh (35 inner injector diameters).

about the injector geometry are given in Fig. 4(a). The inner injector diameter, inner duct thickness, annular duct thickness, and outer duct diameter are, respectively, $d_i = 0.51$ mm, $l_i = 0.54$ mm, $h_e = 0.415$ mm, and $d_o = 2.42$ mm. The mesh comprises 2 100 000 nodes corresponding to 10 000 000 tetrahedra. It is highly refined near the injector (Fig. 4(b)), with a constant characteristic size of 0.032 mm on a distance of 10 inner jet diameters. The mesh is then slowly coarsened towards the domain outlet (Fig. 3(b)).

B. Injection characteristics and boundary conditions

Three test conditions are considered in this analysis designated as “N2,” “N6,” and “N8.” Case “N6” serves as a reference simulation (Table I). The two other cases, designated as “N2” and “N8,” are also calculated in order to analyze effects of the momentum flux ratio on the flow behavior (Sec. V). The three cases differ by their injection temperatures and velocities, yielding momentum flux ratios J of 1.05, 3.22, and 9.3 for cases “N2,” “N6,” and “N8,” respectively. The corresponding density ratios S are 5.86, 5.65, and 3.22, respectively. Injection conditions are gathered in Tables

TABLE I. Injection characteristics of the simulated cases. J is the momentum flux ratio between the outer and the inner jets, M is the mass flux ratio, S is the density ratio, and U is the velocity ratio. ρ_i , ρ_e , u_i , and u_e are the inner and outer jet densities and velocities.

Case	$J = \frac{\rho_e u_e^2}{\rho_i u_i^2}$	$M = \frac{\rho_e u_e}{\rho_i u_i}$	$S = \frac{\rho_i}{\rho_e}$	$U = \frac{u_e}{u_i}$
N2	1.05	0.42	5.86	2.48
N6	3.05	0.72	5.65	4.15
N8	9.3	1.70	3.22	5.48

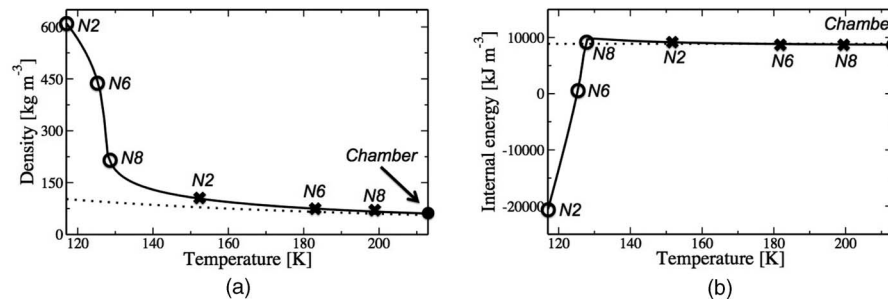


FIG. 5. Thermodynamic state calculated with the PR EOS (—) and the perfect gas EOS (· · ·). (a) Density in terms of temperature. (b) Volumetric internal energy (i.e., ρe_s) in terms of temperature. The pressure is constant and equal to 3.56 MPa. Symbols: \circ inner jet conditions; \times outer stream conditions; \bullet chamber conditions.

XII and XIII which, respectively, correspond to the outer and inner streams. Injection conditions are placed on thermodynamic plots in Fig. 5. The density and volumetric internal energy notably depart from a perfect gas behavior when temperature is close and below the critical value. The influence of acoustic perturbations will only be investigated in a single case corresponding to “N6” (Sec. VI).

In all cases, pressure is maintained at the outlet boundary using non-reflecting characteristic conditions at an adapted level of 3.56 MPa, and the chamber and reservoir are initially filled with nitrogen at the same pressure and a temperature of 213 K (the corresponding density is 59.6 kg m^{-3}). All solid boundaries are treated as adiabatic slip walls. Velocity perturbations (with an amplitude of 3% of the mean flow) are added at injection in order to represent effects of turbulent fluctuations using a procedure described in Refs. 72–74.

C. Simulation procedure

Simulations are carried out on a coarse mesh, with an initial solution corresponding to a uniform fluid at rest. The flow is then qualitatively established after three convective periods. Results are then interpolated on the final mesh. Data averaging can be started after one transient period. The simulated physical time is given in Table II together with the number of simulated convective periods. Finally, the CPU time (equal to the product $n_{\text{core}} \times n_{\text{hours}}$) needed to obtain the average solution (which does not include the CPU time needed for the transient flow and the simulation on the coarse mesh) is also given in this table.

V. EFFECT OF MOMENTUM FLUX RATIO

It is first natural to consider the influence of the momentum flux ratio on the system behavior. Flow patterns calculated numerically and obtained experimentally are first compared in Sec. V A. This is followed by a description of the mean flow in Sec. V B and by an analysis of flow dynamics in Sec. V C.

TABLE II. Averaging time for cases “N2,” “N6,” and “N8.” Δt^a is the physical averaging time. τ_{u_i} represents one convective time over $35 d_i$ for the inner jet and τ_{u_e} represents one convective time over $35 d_i$ for the outer jet. $\tau_{u_i} = (35d_i)/u_i$; $\tau_{u_e} = (35d_i)/u_e$. Calculations have been performed on a SGI Altix ICE 8200 from CINES (Centre Informatique National de l’Enseignement Supérieur).

Case	Δt^a [ms]	$\Delta t^a/\tau_{u_i}$	$\Delta t^a/\tau_{u_e}$	CPU time [h]
N2	14.3	1.9	4.8	35 000
N6	22.7	4.4	18.2	45 000
N8	10.4	4.0	21.2	20 000

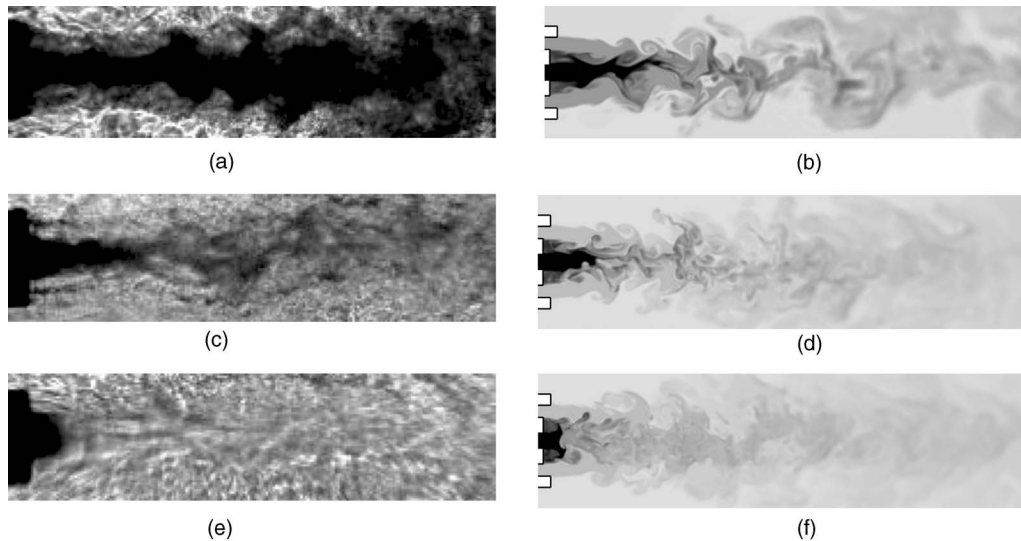


FIG. 6. Comparison between experimental visualizations (backlighting) and typical instantaneous density distributions obtained from simulations (white: 60 kg m^{-3} ; black: inner jet injection density (Table XIII); logarithmic scale). Case “N2” ($J = 1.05$): (a) experimental backlighting image, (b) calculated density. Case “N6” ($J = 3.05$): (c) experimental backlighting image, (d) calculated density. Case “N8” ($J = 9.3$): (e) experimental backlighting image, (f) calculated density.

A. Instantaneous flow patterns

Instantaneous backlighting images obtained experimentally are shown in Figs. 6(a), 6(c), and 6(e). In the dark core light is deviated by changes in the refraction index. This in turn delineates regions where the density takes large values (the deviation can be roughly linked to the second derivative of the density integrated on the line of sight). It is generally admitted that the dark region represents the position of the dense core and qualitatively highlights its external boundaries giving an insight into the main structures present in the flow.⁵ As the momentum flux ratio is increased, the inner jet axial length is reduced. Case “N2” exhibits large scale structures over about 10 inner injector diameters downstream of the injector. These structures are not identifiable in cases “N6” and “N8.” The latter is characterized by a sudden termination of the inner jet at a few inner jet diameters from the exit plane. In contrast with cases “N2” and “N6,” the inner stream appears to be quickly mixed with the surrounding fluid, and the central jet can no longer be clearly identified downstream of this abrupt termination.

Longitudinal slices of instantaneous density distributions extracted from simulations are shown in Figs. 6(b), 6(d), and 6(f) which, respectively, correspond to “N2,” “N6,” and “N8” cases. Comparisons between these figures and the experimental backlighting images are admittedly qualitative. Nevertheless, general experimental features corresponding to these different cases are replicated. One finds that case “N2” features large scale structures which are not present in cases “N6” and “N8.” The abrupt termination noticed in case “N8” is retrieved numerically. This is also made more apparent in the density iso-surfaces corresponding to $\rho = 0.1(\rho_i - \rho_e) + \rho_e$ plotted in Fig. 7. The large scale structures observed experimentally characterize case “N2” and disappear as the momentum flux ratio is increased (cases “N6” and “N8”).

B. Mean flow description

It is first interesting to examine effects of the momentum flux ratio on the mean “dark core” length. Since the density field cannot be directly compared to the experimental light distribution images, it is natural to define a set of density length scales and compare them with the dark core length deduced from the data. The jet core characteristic lengths are defined by considering the axial

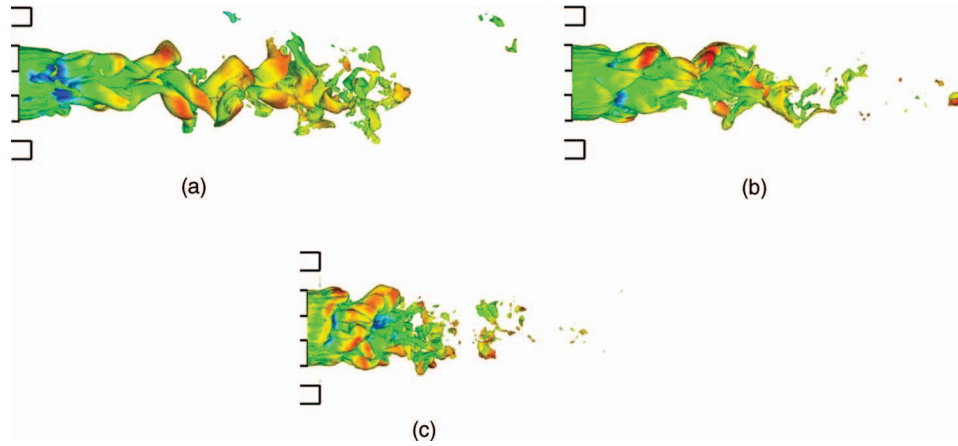


FIG. 7. LES results. Density iso-surface corresponding to $\rho = 0.1(\rho_i - \rho_e) + \rho_e$ colored by the axial velocity. (a) case “N2” ($J = 1.05$) $u_{\min} = -2 \text{ m s}^{-1}$, $u_{\max} = 6.5 \text{ m s}^{-1}$, (b) case “N6” ($J = 3.05$) $u_{\min} = -4 \text{ m s}^{-1}$, $u_{\max} = 16 \text{ m s}^{-1}$, (c) case “N8” ($J = 9.3$) $u_{\min} = -5 \text{ m s}^{-1}$, $u_{\max} = 40 \text{ m s}^{-1}$. The plot corresponds to 20 inner injector diameters.

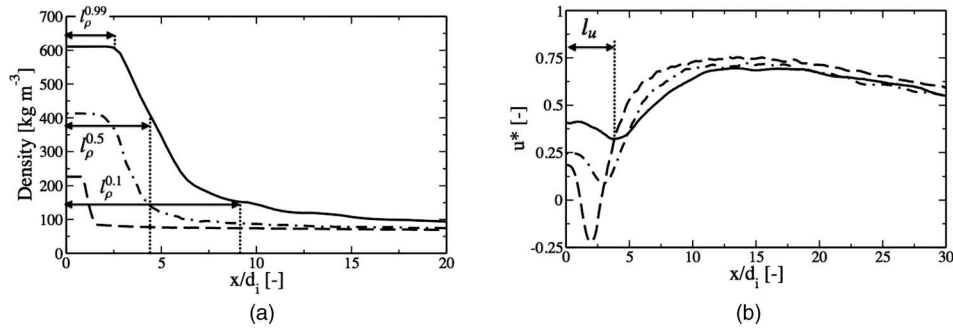


FIG. 8. Centerline profiles deduced by averaging LES results. (a) Density, (b) axial velocity normalized by the outer injection velocity $u^* = u/u_e$. — : Case “N2,” - · - : Case “N6,” and - - : Case “N8.”

TABLE III. Characteristic lengths deduced from simulations based on axial density and velocity profiles and from experimental measurement of the dark core size.

Case	$l_\rho^{0.99}/d_i$	$l_\rho^{0.5}/d_i$	$l_\rho^{0.1}/d_i$	l_u/d_i	l_{dc}/d_i
N2	2.57	4.40	8.66	3.8	15.5
N6	1.81	3.37	5.88	2.95	6.0
N8	0.85	1.17	1.67	1.96	2.5

density distribution

$$l_\rho^{0.99} = x_\rho^{0.99} - x_0 \quad l_\rho^{0.5} = x_\rho^{0.5} - x_0 \quad l_\rho^{0.1} = x_\rho^{0.1} - x_0, \quad (18)$$

where x_0 is the axial position of the inner injector exit, $x_\rho^{0.99}$, $x_\rho^{0.5}$, and $x_\rho^{0.1}$ are positions on the jet axis where density is, respectively, equal to 99% of its initial value, to $0.5(\rho_i - \rho_e) + \rho_e$ or to $0.1(\rho_i - \rho_e) + \rho_e$. These three lengths are shown in Fig. 8(a) together with mean density profiles on the centerline.

It is also useful to define at this point another length scale based on the axial mean velocity profile. The central jets all feature an initial decrease in the axial velocity on the centerline as can be seen in Fig. 8(b). The minimum value is reached at x_u which is used to define a new length scale $l_u = x_u - x_0$.

Characteristic lengths are gathered in Table III for comparison with experimental measurements of the “dark core” length l_{dc} . The latter values are deduced from backlighting images by measuring

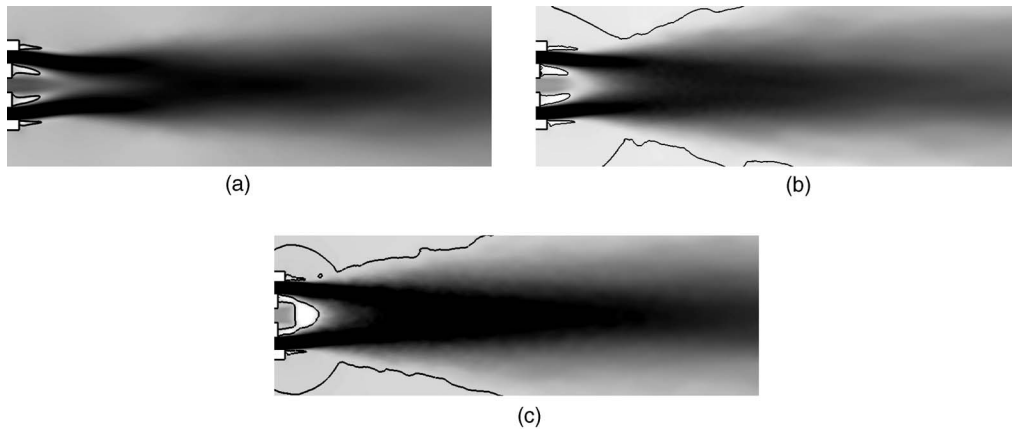


FIG. 9. Distribution of axial velocity (white: minimum; black: maximum). This map corresponds to 35 inner injector diameters. — iso-contour of zero axial velocity. (a) case “N2” ($J = 1.05$), (b) case “N6” ($J = 3.05$), (c) case “N8” ($J = 9.3$).

the “dark region” size from average images. Again, comparison between experiment and simulation is limited. As already noted in Ref. 5, lengths deduced from experimental backlighting data are generally larger than those deduced from density measurements. It is, however, clear that there are similarities between trends in simulations and experiments. In agreement with experiments, numerical results indicate a reduction in the density length scales as the momentum flux ratio is increased. The velocity length scale is reduced and the amplitude of the velocity defect is enhanced as the momentum flux ratio is increased. The flow may also be characterized by the distributions of mean axial velocity plotted in Fig. 9. The outer flow contracts towards the central stream and pinches the central jet to a point where this stream disappears. In the three cases, a small back-flow is generated behind the injector lips. As the momentum flux ratio is increased beyond a certain critical value (case “N8”), the central jet is surrounded by a negative axial velocity region (Fig. 9(c)).

Further downstream, the flows behave in a self-similar fashion in terms of axial velocity normalized by the outer jet injection velocity. Beyond this section, the impact of the inner jet on the flow disappears as this jet is mixed with the outer stream. Since the mass flow rate of the outer jet is much higher than that of the inner jet, the outer jet dominates the flow. Interestingly, the three profiles merge at $x > 15d_i$, indicating a self-similar behavior when profiles are plotted in terms of normalized variables.

Radial profiles of normalized density and axial velocity are plotted in Fig. 10 for case “N6” (case “N2” is not shown here because its behavior is quite similar). The first profiles lie in the potential core region ($x < x_{\rho}^{0.99}$), and feature constant levels of density and velocity in that region. Negative values of axial velocity indicate that back-flow is generated behind the lips. The density profile behind the inner lip shows a rapid variation towards the outer stream. This is attributed to

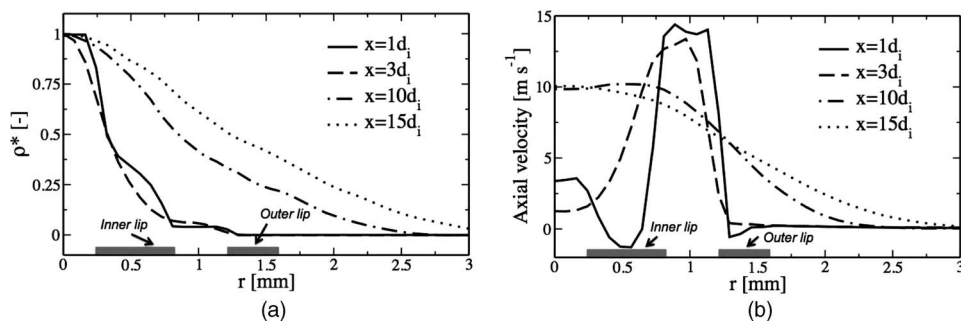


FIG. 10. LES results, case “N6.” (a) Radial profiles of normalized density $\rho^* = (\rho - \rho_{\infty})/(\rho_c - \rho_{\infty})$ and (b) radial profiles of axial velocity.

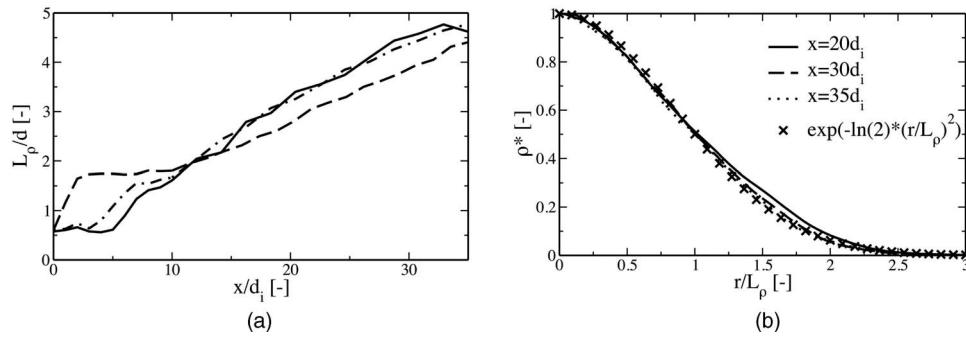


FIG. 11. LES results, (a) half width at half max of density — case “N2,” — case “N6,” and — case “N8.” (b) Radial profiles of normalized density $\rho^* = (\rho - \rho_\infty)/(\rho_c - \rho_\infty)$.

an efficient mixing of inner and outer streams associated with the formation of vortical structures behind the inner lip and the generation of a back flow. In this region, mass is extracted from the central jet by vortical structures and recirculates upstream. Dynamics in this region are discussed in Sec. V C. The profile at $3 d_i$ corresponds to $x = x_u$. The density stratification is still apparent. At $x = 15d_i$, velocity and density are maximum on the centerline, and a jetlike profile is retrieved. Further downstream, the flow behaves like a single round jet and develops in a self-similar fashion. The half width at half maximum (HWHM) of density L_ρ is plotted in Fig. 11(a). For $x > 20d_i$, this quantity evolves quasi-linearly $L_\rho = E_\rho^H(x - x_v)$, where E_ρ^H is the spreading rate of the jet and x_v is a virtual origin. Linear regressions for $20 d_i < x < 35d_i$ give spreading rates of 0.12, 0.11, and 0.11 for cases “N2,” “N6,” and “N8,” respectively. These values are in agreement with those given, for example, by Chen and Rodi⁷⁵ for a single jet and with results obtained from previous high pressure simulations of single species round jets.^{38,41} In this region of the flow, the density profile takes a gaussian shape (Fig. 11(b)). A linear evolution of the density decay is also observed, but not shown here, confirming that the flow is self-similar in the downstream region. Since the flow develops in a confined domain, one may wonder if it is influenced by recirculation in the chamber. Examination of velocity distributions in the domain indicates that the outer recirculation velocities are low and that the reverse flow in the outer region has a limited influence on the coaxial jet structure.

C. Near injector flow dynamics

Large eddy simulations allow detailed analysis of the flow dynamics. This can be accomplished by estimating the spectral content of fluctuations in various regions of the flow to identify the preferred modes of the system. To this end, it is convenient to place a set of sensors in the flow and examine the corresponding velocity and density time series. This is illustrated in Fig. 12. Since the general flow structures of cases “N2” and “N6” differ from that corresponding to “N8,” it is natural to study these two cases separately (Sec. V C 1). Case “N8” is then considered in Sec. V C 2.

1. Cases “N2” and “N6”

To examine the spectral information it is natural to define a set of Strouhal numbers associated with characteristic scales and velocities in the region of interest. The meaningful length scales in this study are the inner injector diameter d_i , the inner lip thickness l_i , and the annular jet thickness h_e . Two velocities characterize the system: the inner and outer jet injection velocities (u_i and u_e , respectively). The resulting Strouhal numbers and the probes used to measure frequencies are shown in Table IV. Probes A and B are used to evaluate the fundamental frequencies of the outer and inner streams. Probe C provides the dominant frequency associated with eddy structures released behind the injector lip and associated with the outer jet. From instantaneous snapshots (see Fig. 12, for example) and animations, these structures are found to originate from the lip corner on the outer-jet side. Positions of the different probes are shown in Fig. 12(a). Note that the axial location of probe B is not the same in cases “N2” and “N6,” because this probe is placed at the end

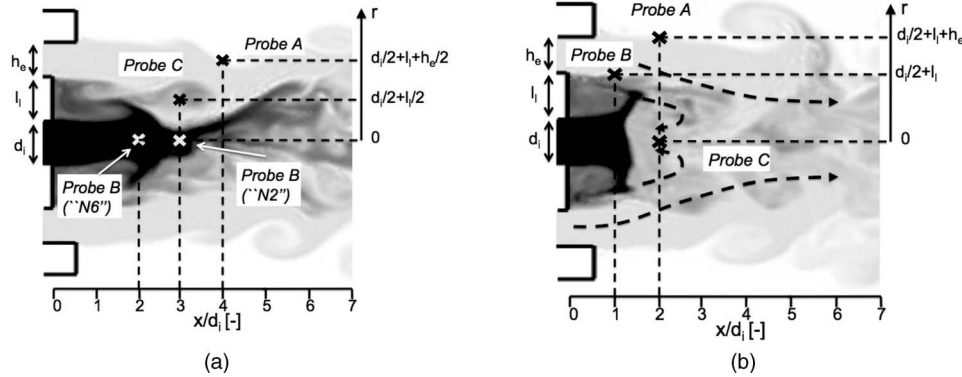


FIG. 12. The three sensor locations. The numerical probes are used to measure characteristic frequencies in the coaxial flow. (a) Case “N6” ($J = 3.05$). Density distribution (white: 60 kg m^{-3} ; black: 410 kg m^{-3} ; logarithmic scale). Sensor B is placed at the end of the inner jet potential core which corresponds to a different location in cases “N2” and “N6.” (b) Case “N8” ($J = 9.3$). Density distribution (white: 60 kg m^{-3} ; black: maximum (Table XIII); logarithmic scale). Sensor C is located in the recirculation region.

of the potential core. Power spectral densities are estimated using Welch’s method of periodograms. Statistical averaging is obtained by segmenting the finite data set in M overlapping blocks (a 50% overlap is employed to augment the number of periodograms used in the averaging procedure). Because the number of samples is limited, the averaging is carried out over $M = 8$ blocks in the outer flow and on $M = 4$ blocks in the inner jet (power is concentrated in the low frequency range and it is important to augment the resolution to distinguish the maximum frequency). The frequency resolution corresponding to the different sensors is given in Table IV.

The outer and central streams are destabilized at a few diameters d_i from the injector exit. The measured frequency for the outer jet (probe A) is 3 600 Hz for case “N2” and 8 550 Hz for case “N6” (Fig. 13), which correspond to $St_{N2}^e = 0.25$ and $St_{N6}^e = 0.25$. The central high-density jet presents a fundamental instability at 1 610 Hz and 1 740 Hz for cases “N2” and “N6” (Fig. 14), respectively (probe B). The associated Strouhal numbers are then $St_{N2}^i = 0.34$ and $St_{N6}^i = 0.26$. For both cases, the fundamental mode of the inner and outer streams falls in the typical range for round jets (0.2–0.4).

The mixing layer between the two jets features eddy structures generated downstream of the central lip. Their dynamics are similar to those observed for vortices shed behind a backward-facing step. The characteristic frequencies are found to be 1620 Hz and 3600 Hz, for cases “N2” and “N6” (Fig. 15), respectively. Such frequencies correspond to Strouhal numbers $St_{N2}^l = 0.15$ and $St_{N6}^l = 0.23$ for cases “N2” and “N6,” which are slightly higher than the commonly determined values for backward-facing step instabilities ($St = O(0.1)$ (Ref. 76)). This could be attributed to a reduction of the “effective” lip thickness as shear is increased. It turns out that the backward-facing step vortical structures induce a back-flow behind the lip (Fig. 9). High-density fluid from the central jet is entrained and recirculates behind the lip. One may then consider that this results

TABLE IV. Definition of characteristic Strouhal numbers. The characteristic length and velocity l and u are given in the second and third columns. The frequency f corresponds to the power spectral density maximum estimated from the simulations. Δf is the frequency resolution.

$St = fl/u$	l	u	Probe (Fig. 12(a))	Δf [Hz]
St^e	h_e (0.41 mm)	u_e	A	N2: 375; N6: 250
St^i	d_i (0.51 mm)	u_i	B	N2: 187; N6: 125
St^l	l_l (0.54 mm)	u_e	C	N2: 375; N6: 250

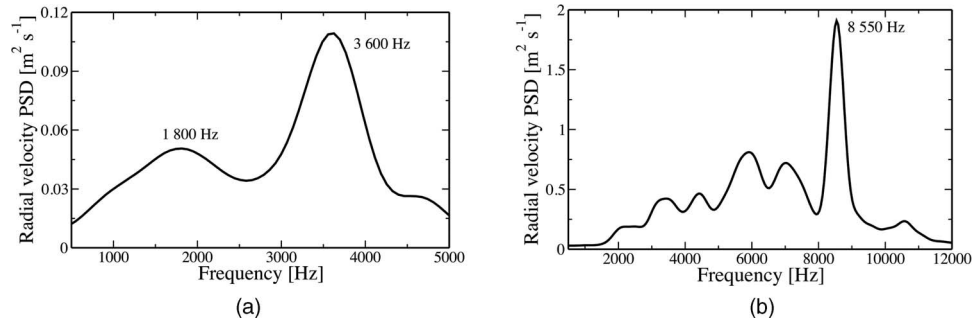


FIG. 13. Power spectral density of the radial velocity in the outer jet (probe A). Averaging is carried out on $M = 8$ blocks with a 50% overlap. (a) Case “N2” ($J = 1.05$) and (b) case “N6” ($J = 3.05$).

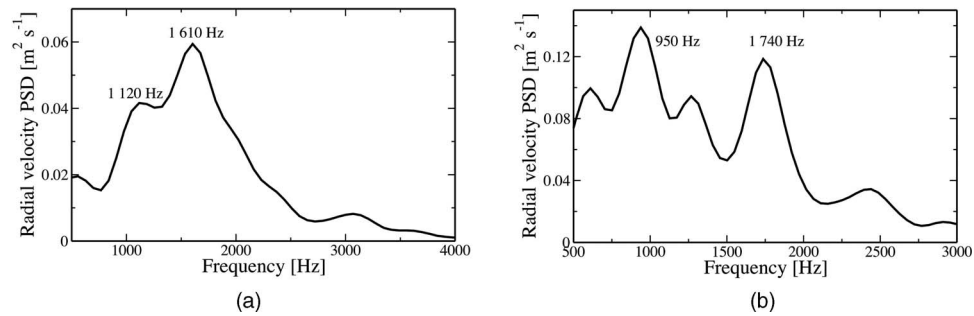


FIG. 14. Power spectral density of radial velocity in the inner jet (probe B). Averaging is carried out on $M = 4$ blocks with a 50% overlap. (a) Case “N2” ($J = 1.05$) and (b) case “N6” ($J = 3.05$).

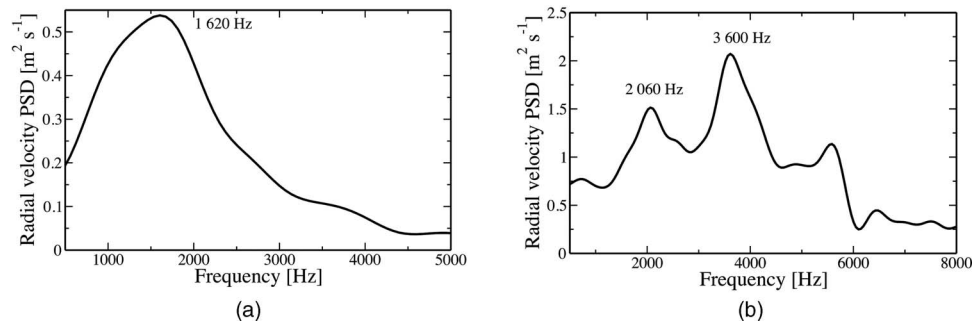


FIG. 15. Power spectral density of radial velocity in the mixing layer behind the inner lip (probe C). Averaging is carried out over $M = 8$ blocks with a 50% overlap. (a) Case “N2” ($J = 1.05$) and (b) case “N6” ($J = 3.05$).

TABLE V. Characteristic Strouhal numbers obtained from the simulations for cases “N2” and “N6.”

Case	St^e (probe A)	St^i (probe B)	St^l (probe C)
N2	0.25	0.34	0.15
N6	0.25	0.26	0.23

in a reduced “effective” lip thickness which intervenes in the formation of the vortical structures, thus limiting their spatial development and increasing the instability frequency. All the Strouhal numbers obtained are gathered in Table V. The frequency obtained for case “N2” is interestingly close to that associated with the inner jet preferred mode. This observation may explain why large scale structures are exclusively observed in this case (Fig. 6).

TABLE VI. Strouhal numbers definitions. l and u are the characteristic length and velocity used to define the Strouhal numbers. f represents the frequency obtained from the simulations.

$St = (fl)/u$	l	u	Probe (Fig. 12(b))
St_{N8}^e	h_e (0.41 mm)	u_e	A
St_{N8}^l	l_l (0.54 mm)	u_e	B
St_{N8}^b	$d_i + l_l$ (0.51 + 0.54 mm)	u_e	C

2. Case “N8”: recirculation regime

The mechanism leading to mixing of the high-density jet with the outer stream is somewhat different for case “N8.” It is already known that the dense jet ends abruptly and that a recirculation bubble is established beyond that point. As done previously for cases “N2” and “N6,” characteristic length scales used to define the relevant Strouhal numbers are given in Table VI, and the probes used to characterize this case are shown in Fig. 12(b). Probe C is inside the recirculation region and is located at $x = x_u$. This case is highly turbulent and features a broadband spectrum so that temporal data are arranged in $M = 16$ blocks to ensure a reasonable statistical convergence. A 50% overlap is used to obtain the maximum possible averaging number. The resulting frequency resolution is in this case 1000 Hz. This value may seem quite high, but should be compared to the spectral range which extends to 25 000 Hz.

The dominant frequency for the outer jet (probe A) is 21 600 Hz (Fig. 16), which corresponds to $St_{N8}^e = 0.25$, as also obtained for the two other cases. The inner jet is notably affected by the recirculation bubble. Its longitudinal development is limited and mass is ejected in the radial direction in the form of thin layers appearing in Fig. 12(b). The resulting structure is similar to a counterflow. This motion leads to the formation of a recirculation ring of high-density fluid behind the inner lip with a characteristic size of the order of the lip thickness. Vortex roll-up is observed behind the inner lip, in the mixing layer established between the inner and outer jets. These structures are similar to those observed in cases “N2” and “N6,” but they strongly interact with higher density layers emerging from the central jet, and their spatial development is limited by the recirculation region. The corresponding Strouhal number is $St_{N8}^l = 0.26$ (Fig. 17(a)). These eddy structures lead to the formation of the recirculation region. The measured frequency corresponds to $St_{N8}^b = 0.18$ (Fig. 17(b)). The dynamics of this bubble are similar to those observed behind a bluff body terminated by a flat face, for which the characteristic Strouhal number is close to 0.2. The Strouhal numbers obtained in this analysis are gathered in Table VII.

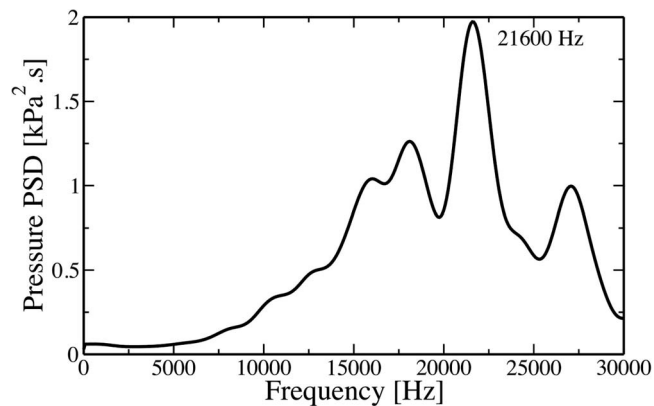


FIG. 16. Case “N8” ($J = 9.3$). Power spectral density of pressure on probe A. Averaging is carried out over $M = 16$ blocks with 50% overlap.

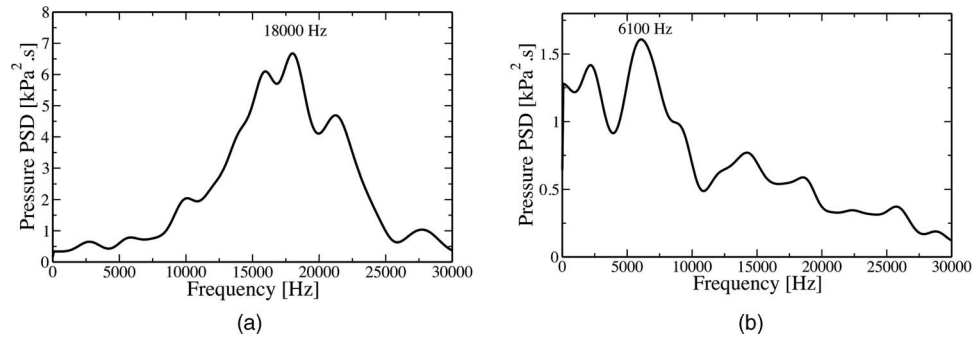


FIG. 17. Case “N8” ($J = 9.3$). (a) Power spectral density of pressure on probe B and (b) power spectral density of pressure in the recirculation bubble. Averaging is carried out over $M = 16$ blocks with 50% overlap.

TABLE VII. Characteristic Strouhal numbers obtained from the simulations for case “N8.”

St_{N8}^e (probe A)	St_{N8}^l (probe B)	St_{N8}^b (probe C)
0.25	0.26	0.18

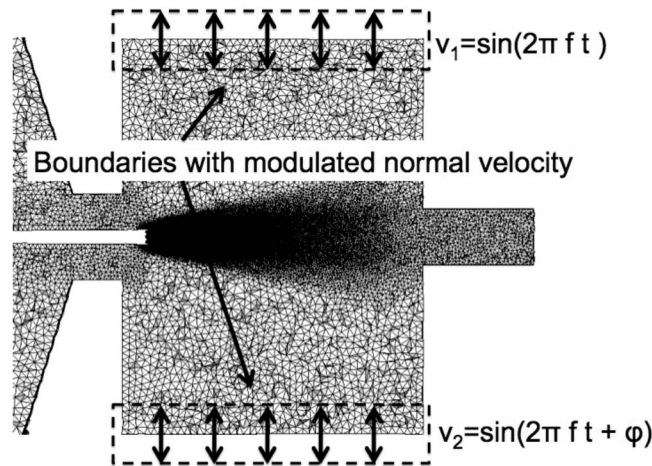


FIG. 18. Longitudinal slice in the computational domain showing the methodology retained to impose acoustic perturbations.

VI. EFFECTS OF A TRANSVERSE ACOUSTIC MODULATION

Effects of an acoustic modulation are now investigated in case “N6.” This operating point is chosen because the core is sufficiently long to allow an examination of external modulation effects. The methodology used to impose an acoustic excitation is described in Sec. VI A. Results are then compared with experimental observations in Sec. VI B and discussed in Sec. VI C.

A. Modulation methodology

An acoustic modulation is obtained by imposing harmonic modulations of the normal velocity at the outer boundaries using a method devised by Rey *et al.*⁷⁷ (Fig. 18). The modulation has the form

$$v_1 = \sin(2\pi ft), \quad v_2 = \sin(2\pi ft + \phi), \quad (19)$$

where v_1 and v_2 are the normal velocities at the lateral boundaries, f is the modulation frequency set equal to 3 kHz, ϕ designates the phase between the imposed modulations. These boundaries are essentially acoustically non-reflecting (with a cut-off frequency of 100 Hz) in order to avoid the

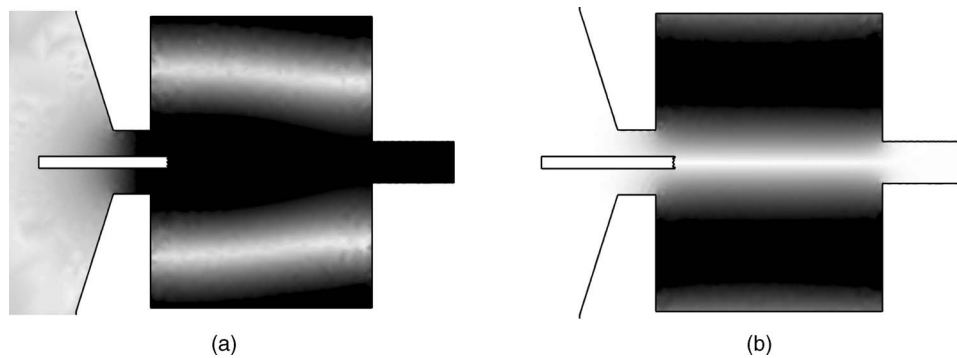


FIG. 19. Results obtained under acoustic modulation in the absence of flow. (a) RMS pressure fluctuations for acoustic perturbations in phase ($\phi = 0$). (b) RMS pressure fluctuations for acoustic perturbations in phase opposition ($\phi = \pi$).

emergence of transverse eigenmodes (the first transverse eigenfrequency, corresponding to totally reflecting boundaries, would be close to 1900 Hz). All other boundaries are treated as in the previous cases (in the absence of modulation). This technique is first validated by simulating an acoustic perturbation in the absence of the central flow. Longitudinal distributions of the rms pressure fluctuations are shown in Fig. 19. When $\phi = 0$ (Fig. 19(a)), the normal velocities at the boundaries are in phase, and this yields a maximum pressure fluctuation on the injector axis. A pressure probe placed at 5 mm from the injector exit confirms this behavior. As expected, pressure fluctuations are observed with a 2% peak-to-peak oscillation with respect to the mean chamber pressure, while the transverse velocity remains unperturbed. When the normal velocities at the boundaries are in phase opposition ($\phi = \pi$), the pressure vanishes on the centerline and the transverse velocity oscillation reaches its maximum (Fig. 19(b)). Spectral analysis also indicates that the perturbed field is dominated by the imposed modulation frequency and that the harmonic content is negligible. The method used to define acoustic boundary conditions reproduces quite reliably the acoustic field generated experimentally by the driver units. In addition, the geometrical complexity of the experimental apparatus is well represented and one can expect that the main features of the system acoustic response will be suitably obtained. The interaction of the transverse acoustic modulation with the coaxial flow should then be fairly quantitative.

The simulated cases are defined in Table VIII. Injection conditions correspond to case “N6.” Modulation amplitudes of 1% and 2% of the mean chamber pressure are imposed. These two cases are studied for $\phi = 0$ and $\phi = \pi$, respectively, corresponding to a pressure antinode and a pressure node on the central axis.

B. Calculated flow dynamics and experimental data

When acoustic modulations are in phase, pressure fluctuations are produced at the injector outlet at the modulation frequency. This leads to oscillations of the axial velocity at the imposed frequency. Such variations in the longitudinal velocity induce a periodic shedding of ringlike patterns (Fig. 20). Structures are created behind the inner lip and in the outer mixing layer. These structures develop in an axisymmetric fashion producing annular vortices that are rapidly affected by turbulence. The vortices produced in the inner jet lip entrain fluid from the inner jet, involving mass from the inner jet in the vortex roll-up. These results are qualitatively consistent with experimental observations

TABLE VIII. Test cases with acoustic modulation.

Case	N6 ^{2%} _{$\phi=0$}	N6 ^{2%} _{$\phi=\pi$}	N6 ^{1%} _{$\phi=0$}	N6 ^{1%} _{$\phi=\pi$}
P_{pp}/P_0	2.0 %	2.0 %	1.0 %	1.0 %
ϕ	0	π	0	π

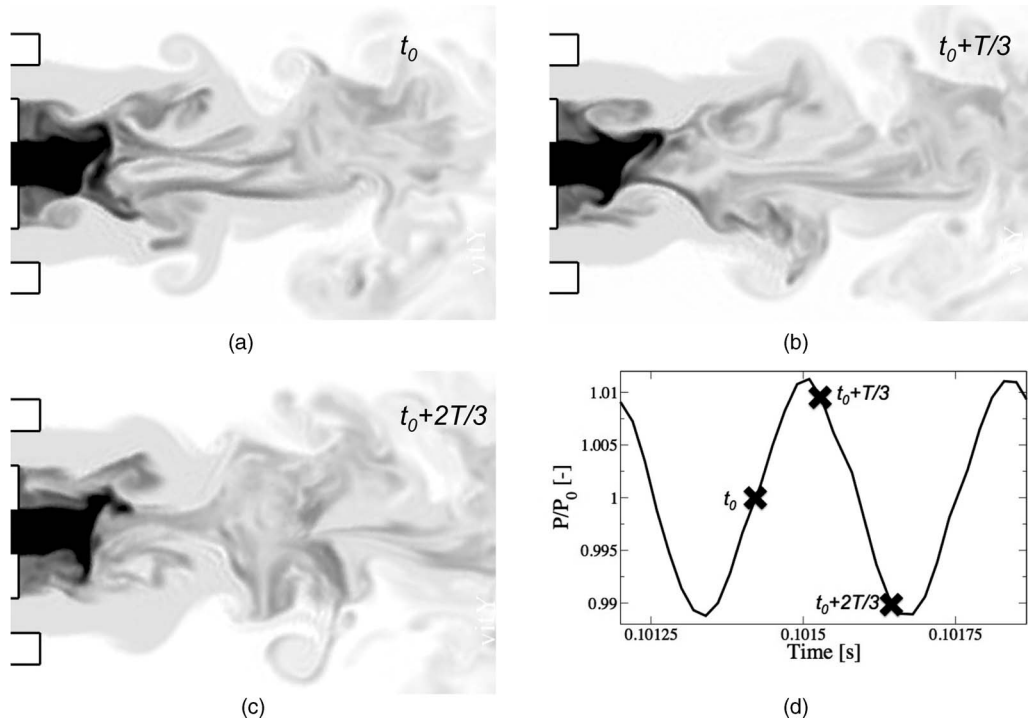


FIG. 20. Case “N6 $_{\phi=0}^{2\%}$ ” ($J = 3.05$). (a), (b), and (c) are longitudinal slices of density (white: 60 kg m^{-3} ; black: 420 kg m^{-3} ; logarithmic scale). (d) Temporal evolution of pressure measured along the jet centerline (5 mm from the injector exit plan).

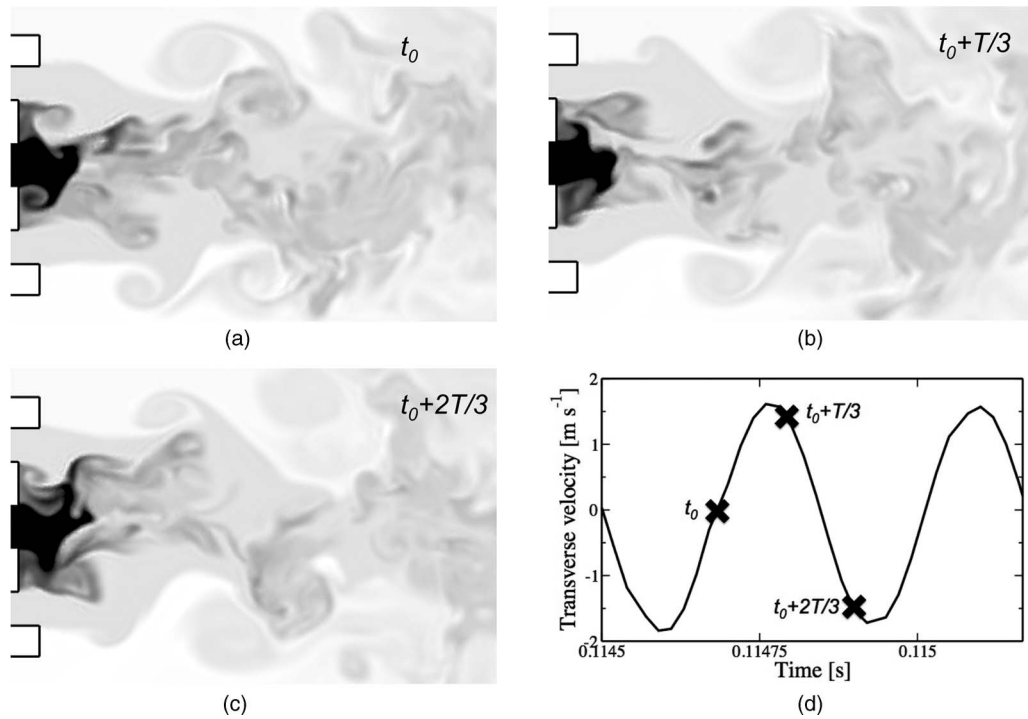


FIG. 21. Case “N6 $_{\phi=\pi}^{2\%}$ ” ($J = 3.05$). (a), (b), and (c) are longitudinal slices of density (white: 60 kg m^{-3} ; black: 420 kg m^{-3} ; logarithmic scale). (d) Temporal evolution of transverse velocity measured along the jet centerline (45 mm from the injector exit plan).

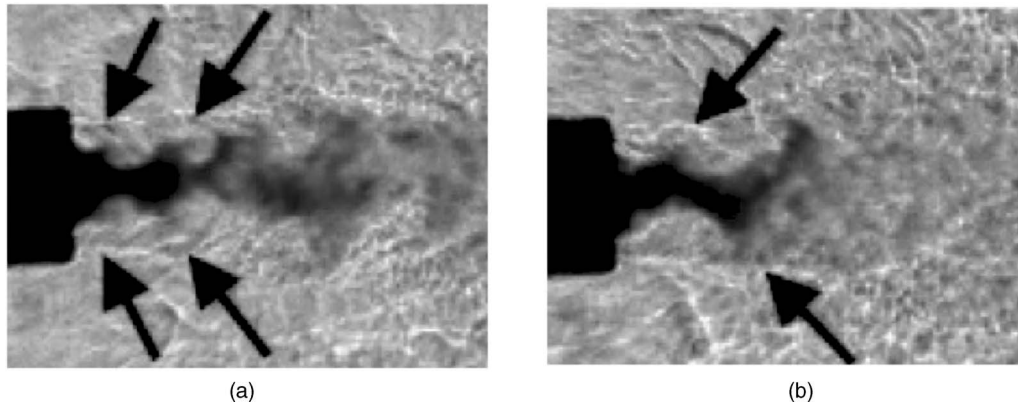


FIG. 22. Experimental shadowgraphs for case “N6.” (a) Acoustic modulation is in phase and (b) acoustic modulation is in phase-opposition.

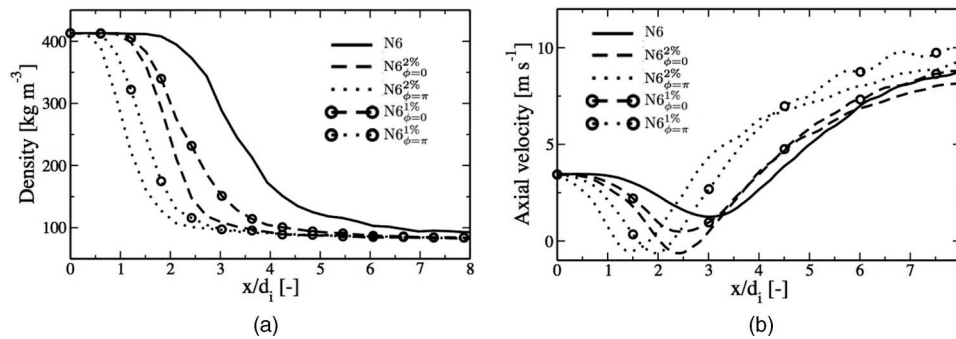


FIG. 23. (a) Density profile on the centerline and (b) axial velocity profile on the centerline.

TABLE IX. Influence of acoustic modulations on the characteristic length in case “N6.” Length scales without modulations are noted $l_{\rho, noac}$.

Case	$N6^{2\%}_{\phi=0}$	$N6^{2\%}_{\phi=\pi}$	$N6^{1\%}_{\phi=0}$	$N6^{1\%}_{\phi=\pi}$
$l_{\rho}^{0.5} / l_{\rho, noac}^{0.5}$	0.60	0.34	0.70	0.45
$l_{\rho}^{0.1} / l_{\rho, noac}^{0.1}$	0.53	0.36	0.66	0.45
Experiments	0.68	0.55

shown in Fig. 22(a), where a varicose motion is clearly identifiable. When acoustic perturbations are in phase-opposition (Fig. 21), the resulting transverse velocity perturbation induces a sinusoidal motion, as observed experimentally in Fig. 22(b), and vortices are shed in an asymmetric fashion.

The centerline density and axial velocity are plotted in Fig. 23. Acoustic perturbations significantly reduce the dense core length and increase the amplitude of the low velocity region just behind the central jet. Characteristic length ratios between acoustically perturbed cases and the reference case “N6” are given in Table IX. These ratios are in agreement with experimental measurements. It is interesting to note that the cases corresponding to phase opposition produce the shortest dense core. It is also found that multiplication of the perturbation amplitude by a factor of two does not lead to a proportional reduction of the dense core.

C. Spectral analysis of acoustic modulation effects

The response of the flow to the external modulation may now be discussed by examining the spectral content of velocity fluctuations. This is done by plotting spectral maps of these fluctuations

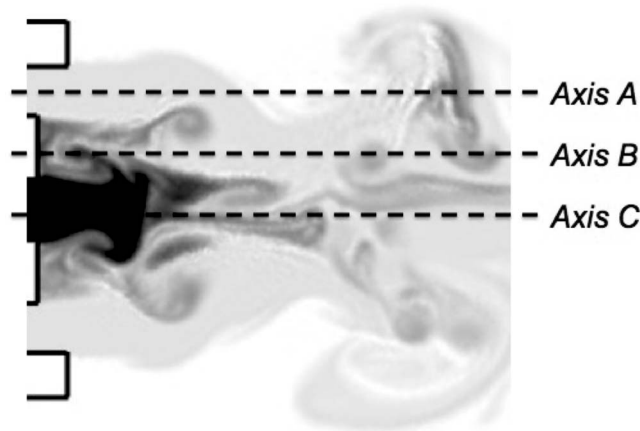


FIG. 24. Case “N6 $_{\phi=0}^{2\%}$ ” ($J = 3.05$). Positions of the three axial lines used in the spatial spectral analysis.

along three axial lines in the flow. The first (line C) corresponds to the centerline, the second (line B) is centered on the lip, the third (line A) is centered on the outer jet annulus (see Fig. 24).

1. Case “N6 $_{\phi=0}^{2\%}$ ”

In-phase excitation induces axial velocity modulations on the centerline. This is clearly seen in Figs. 25(a), 26(a), and 27(a), where the 3000 Hz fluctuations are well retrieved. The amplitude of the axial velocity fluctuation is nevertheless very low in the high-density region (Fig. 28), in the potential core of the inner jet ($x < 1.05 d_i$, defined by the region along the centerline axis where $\rho > 0.99 \rho_i$, see Fig. 23(a)). This region of the flow is less affected by the axial modulation than the surrounding streams. The response of the jets to this modulation is determined by examining the transverse velocity. Both the outer jet and the flow behind the inner lip show a strong response at 3000 Hz (Figs. 25(b) and 26(b)). It means that the axial perturbation promotes a destabilization of these jets and vortex roll-up at the same frequency. This is not the case along the inner jet centerline, where the transverse response at 3000 Hz is not distinguishable (Fig. 27(b)). Since the geometry and the perturbation are both axisymmetric around this axis, such a velocity motion is naturally limited. The dominant frequency after the potential core ($x > 1.05 d_i$) is close to 1000 Hz. The spectral content of the inner jet is shown in Fig. 28 at $x = d_i$, at the end of the potential core. The axial velocity is dominated by the modulation at 3000 Hz, with a low amplitude, but also features a lower frequency component around 1200 Hz. In contrast with the outer jet, the radial velocity responds at half of the imposed frequency (around 1500 Hz). These fluctuations are nevertheless small compared to those measured in the gaseous part of the flow. As a consequence, the high-density part of the inner jet seems to be virtually insensitive to the acoustic modulation. The frequency that dominates at the end of the potential core is close to half of the modulation frequency. This frequency is also observed in the analysis of density fluctuations.

2. Case “N6 $_{\phi=\pi}^{2\%}$ ”

A transverse velocity modulation is again applied at 3000 Hz, but the phase is now equal to π . As in the previous case “N6 $_{\phi=0}^{2\%}$,” this transverse modulation affects all the jets as shown in Figs. 29(b), 30(b), and 31(b). The amplitude of this transverse perturbation is much lower in the high-density part of the inner jet (Figs. 32 and 31(b) for $x < d_i$). Axial velocity perturbations are induced in the outer jet and behind the inner lip (Figs. 29(a) and 30(a)), associated with vortex roll-up at the same frequency. Again, the inner jet is essentially unaffected, since the measured amplitudes are much lower than for the two other cases (Fig. 31(a)). This stream is dominated by an intermediate frequency. A component at 1500 Hz is observed just at the inner injector exit. This is confirmed in

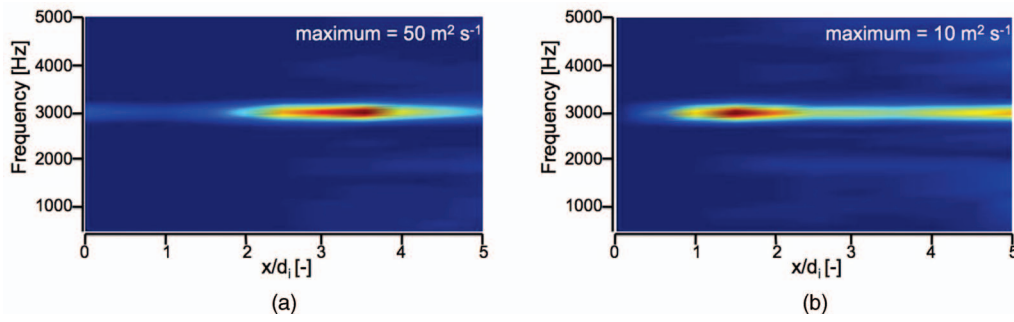


FIG. 25. Case “N6 _{$\phi=0$} ^{2%}” ($J = 3.05$). Spectral map along line A ($r = d_i/2 + l_l + h_c/2$). (a) Axial velocity and (b) radial velocity.

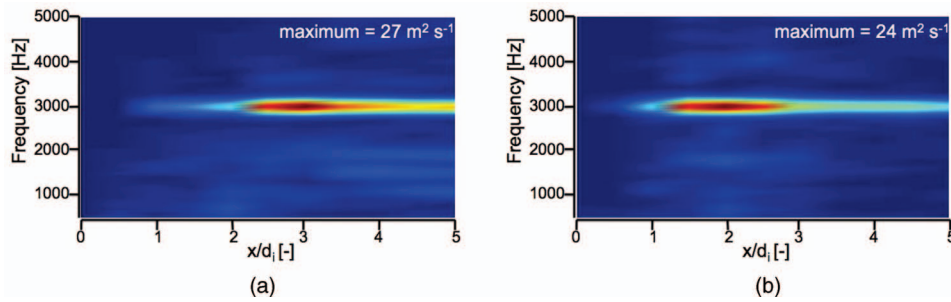


FIG. 26. Case “N6 _{$\phi=0$} ^{2%}” ($J = 3.05$). Spectral map along line B ($r = d_i/2 + l_l/2$). (a) Axial velocity and (b) radial velocity.

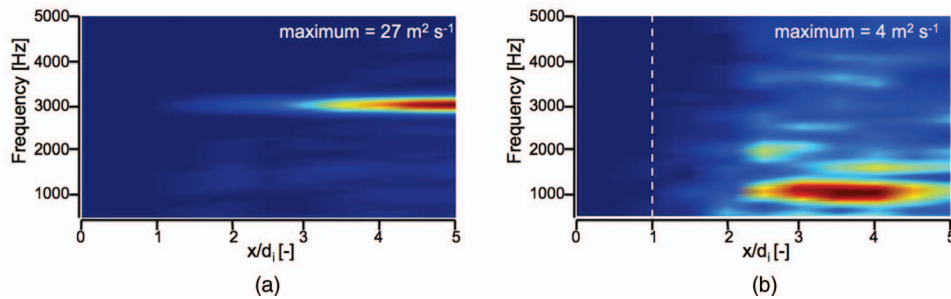


FIG. 27. Case “N6 _{$\phi=0$} ^{2%}” ($J = 3.05$). Spectral map along line C ($r = 0$). (a) Axial velocity and (b) radial velocity. The dashed line represents the axial position at which a power spectral density is shown in Fig. 28.

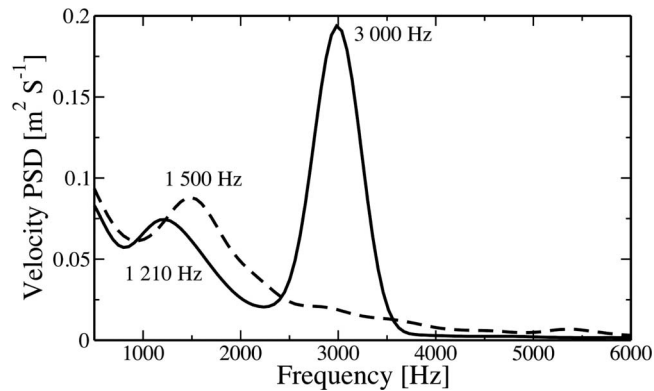


FIG. 28. Case “N6 _{$\phi=0$} ^{2%}” ($J = 3.05$). Power spectral density of axial (—) and radial (---) velocity in the inner jet centerline at $x = d_i$ (end of the potential core).

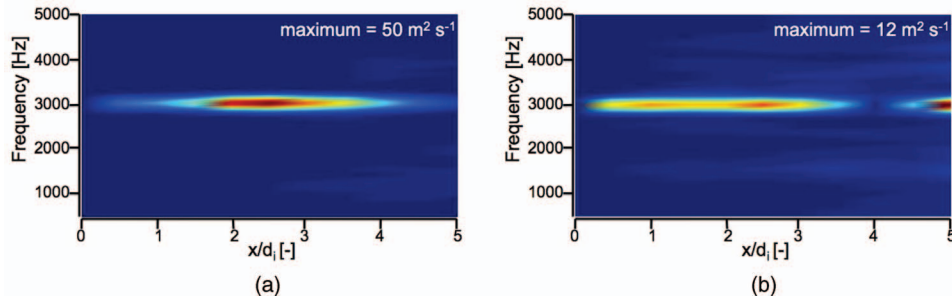


FIG. 29. Case “N6 $_{\phi=\pi}^{2\%}$ ” ($J = 3.05$). Spectral map along line A ($r = d_i/2 + l_i + h_e/2$). (a) Axial velocity and (b) radial velocity.

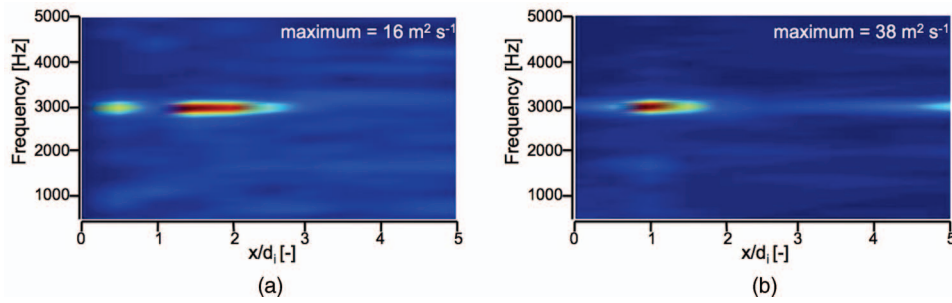


FIG. 30. Case “N6 $_{\phi=\pi}^{2\%}$ ” ($J = 3.05$). Spectral map along line B ($r = d_i/2 + l_i/2$). (a) Axial velocity and (b) radial velocity.

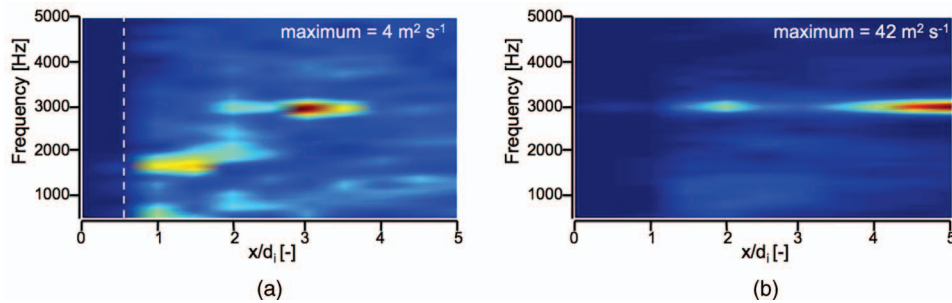


FIG. 31. Case “N6 $_{\phi=\pi}^{2\%}$ ” ($J = 3.05$). Spectral map along line C ($r = 0$). (a) Axial velocity and (b) radial velocity. The dashed line represents the axial position at which a power spectral density is shown in Fig. 32.

Fig. 32, where the transverse modulation at 3000 Hz is visible, but leads to a longitudinal response of the jet close to 1500 Hz. Even though this frequency is clearly identifiable in Figs. 31(a) and 32, its amplitude is lower than that measured behind the lip or in the outer jet. As previously observed for in-phase modulation, the sensitivity of the inner jet to the external modulation is limited. Again, the frequency which dominates at the end of the potential core ($x < 0.55 d_i$, see Fig. 23(a)) is close to half of the modulation frequency and is also observed in density fluctuations.

D. Discussion

It is found that the inner jet, when submitted to an acoustic modulation at 3000 Hz, exhibits fluctuations at the subharmonic frequency of 1500 Hz. This may be explained by considering the stability properties of the central jet and by analyzing the acoustic transmission from the outer medium into the high-density region.

It is first interesting to situate the modulation frequency with respect to the range of unstable frequencies characterizing the jet and, more specifically, with respect to the preferred frequency

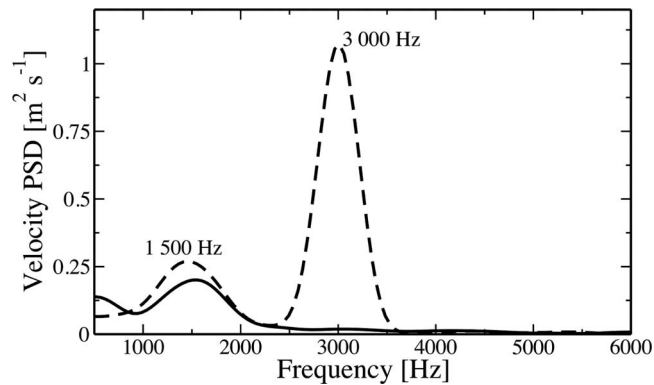


FIG. 32. Case “N6^{2%}” ($J = 3.05$). Power spectral density of axial (—) and radial (---) velocity on the inner jet centerline at $x = 0.5d_i$ (end of the potential core).

TABLE X. Definition of the Strouhal numbers used in this study. f_{ac} represents the modulation frequency (3000 Hz).

$St = (f_{ac}l)/u$	Length scale l	Charac. vel. u	Value
St_{ac}^e	h_e (0.41 mm)	u_e	0.087
St_{ac}^l	l_i (0.54 mm)	u_e	0.115
St_{ac}^i	d_i (0.51 mm)	u_i	0.45

TABLE XI. Specific acoustic impedance in the chamber, inner and outer jets.

Conditions	Impedance ($Z = \rho c$)
Chamber	17 701
Outer jet	19 663
Inner jet	98 700

of the inner jet. It is known (see, for example, Birbaud *et al.*⁷⁸ and references in this article) that when the modulation frequency is well above the preferred mode frequency, the flow is not affected by an external acoustic modulation. This is best expressed in terms of a Strouhal number which can be calculated by considering the acoustic modulation frequency, the characteristic length and velocity associated with each jet. The resulting “acoustic” Strouhal numbers are given in Table X. While St_{ac}^e and St_{ac}^l are lower or close to the natural Strouhal number of the flow for case “N6,” St_{ac}^i is higher than the one measured previously without modulation. As a consequence, the jet does not respond to the modulation frequency, but oscillates at a subharmonic frequency (1500 Hz) which is close to the preferred frequency measured previously in the absence of acoustic modulation (Fig. 14).

Another possible explanation of the absence of modulation at the imposed frequency may be obtained by considering the change in acoustic impedance between the outer stream and the inner jet. It is known that a large impedance mismatch reduces the transmission of waves across the interface. Acoustic impedances gathered in Table XI indicate that a large variation takes place at the inner jet boundary. Under these circumstances acoustic wave transmission into the jet is reduced, explaining the absence of the modulation imposed to the system from the outer region.

The previous arguments provide some clues on the observed response of the coaxial flow to an externally imposed transverse acoustic motion. The strong reduction of the inner jet length is certainly linked to the strong response of the outer jet to the acoustic modulation, which is not observed for the inner stream. The large vortices generated in the annular jet in turn enhance mixing between the outer and inner jets, and thus enhance mixing of the inner fluid with its surroundings, leading to a reduction of the dense core length.

VII. CONCLUSION

The structure of non-reactive transcritical and supercritical jets is investigated by examining the flow formed by a coaxial injector operating at high pressure. This unit injects low temperature dense nitrogen surrounded by an outer stream of higher temperature nitrogen. The analysis relies on large eddy simulations which are compared with experimental results.

The natural development of the coaxial flow is examined for a set of momentum flux ratios. It is shown that the flow patterns observed experimentally are suitably retrieved and that a good correspondence between experimental results and simulations is obtained. It is shown in particular that when the momentum flux ratio exceeds a critical value, the central jet is terminated in an abrupt fashion at a short distance from the injector exhaust. Calculations indicate that this is linked to the formation of a recirculation region located at a short distance from the injection section. This study is complemented with a spectral analysis of the velocity components in the injector nearfield. It is shown that the frequency content is governed by Strouhal numbers which follow standard rules for jets and wakes.

The effect of an external acoustic modulation is then investigated by imposing in-phase and out-of-phase perturbations at the boundaries of the domain. This is used to study the effect of transverse waves on the dark core of the jet. A strong reduction of the jet length is clearly observed, both in experiment and numerics. The spectral content of fluctuations in the coaxial streams is analyzed. In the case considered which corresponds to a Strouhal number (based on the inner jet velocity and diameter) about equal to twice the Strouhal number corresponding to the preferred mode of the jet, it is found that the inner jet responds with a limited amplitude to the external modulation but features a subharmonic motion at half of the modulation frequency. In contrast, the gaseous part of the flow is strongly perturbed by the acoustic modulation. Large scale vortices are released from the outer annulus at the modulation frequency. It is suggested that the relative insensitivity of the inner flow is linked to the fact that the frequency is above the range of unstable frequencies of the central jet. It is also found that the specific acoustic impedance of the central jet is much higher than that corresponding to the surrounding stream and that this may explain why the modulation is not transmitted to the central core.

One objective for the future is to pursue LES development and validation for supercritical/transcritical flow calculations. Validation requires information on the average field, but also on fluctuations. Average and rms profiles of temperature, density, velocity, and main species mass fractions for reactive systems could be useful in this respect, but such measurements are unfortunately not easy to obtain. In general only mean profiles are available for non-reactive cases, most of them having been deduced from thermocouples or spontaneous Raman spectroscopy, which gives information on the mean density field.⁵ Uncertainties are also difficult to estimate and the absence of information on dynamical characteristics limits validations. Comparisons with mean profiles indicate that the flow is well recovered at first order. Direct comparisons with shadowgraphs provides some additional insight. Sensitivity studies, like those carried out in the present article, where injection conditions are changed and different flow regimes are observed (i.e., the recirculation regime of case “N8”), increase the degree of confidence which may be attributed to the simulation and indicate to some extent that the main dynamical features of the flow are retrieved. Further experiments need to be carried out with different injectors to document the effect of geometry, velocity ratio, momentum flux ratio, and thermodynamic state on the mixing of shear coaxial jets with and without acoustic perturbations. This will allow further comparisons with simulations. It is also planned to obtain profiles that could be compared more quantitatively with numerical results. Instantaneous information may also be recovered from shadowgraphs (and from high speed OH* emission visualizations under reactive conditions). In the present investigation, the imaging frequency is higher than the main characteristic frequencies observed in LES. This may give access to the characteristic frequencies of the flow. Recent investigations indicate that some of the flow frequencies may be retrieved in this way. One procedure might also be to reconstruct shadowgraphs from LES results and compare the resulting information with experimental data. It requires further investigations which are underway.

ACKNOWLEDGMENTS

This research was carried out with the partial support from EOARD in the framework of Contract No. FA8655-10-1-3005 and AFOSR under Mitat Birkan, program manager. The AVBP solver used for this study has been developed at Cerfacs. This work was granted access to the HPC resources of CINES under the allocation 2010 - 026176 made by GENCI (Grand Equipement National de Calcul Intensif).

APPENDIX: INJECTION CONDITIONS FOR THE COMPUTED CASES

See Tables XII and XIII for outer and inner jets injection conditions of the computed cases.

TABLE XII. Injection conditions corresponding to the cases “N2,” “N6,” and “N8” for the **outer** jet. \dot{m} denotes the mass flow rate.

Outer jet injection conditions					
Case	T_e [K]	\dot{m}_e [g s ⁻¹]	ρ_e [kg m ⁻³]	u_e [m s ⁻¹]	Re_e
N2	152	1.57	101	5.95	41 600
N6	183	2.69	73.1	14.1	64 800
N8	192	6.46	68.3	36.2	151 000

TABLE XIII. Injection conditions corresponding to the cases “N2,” “N6,” and “N8” for the **inner** jet. \dot{m} denotes the mass flow rate.

Inner jet injection conditions					
Case	T_i [K]	\dot{m}_i [g s ⁻¹]	ρ_i [kg m ⁻³]	u_i [m s ⁻¹]	Re_i
N2	117	0.289	590	2.4	15 000
N6	126	0.292	420	3.4	25 000
N8	128	0.295	220	6.6	52 000

- ¹ V. Yang, M. Habiballah, J. Hulka, and M. Popp, (eds.), “Liquid rocket thrust chambers: Aspects of modeling, analysis, and design,” AIAA Progress in Astronautics and Aeronautics, Vol. 200 (2004), 722 pp.
- ² B. Chehroudi, D. Talley, and E. Coy, “Visual characteristics and initial growth rate of round cryogenic jets at subcritical and supercritical pressures,” *Phys. Fluids* **14**(2), 850–861 (2002).
- ³ W. Mayer, J. Tellar, R. Branam, G. Schneider, and J. Hussong, “Raman measurement of cryogenic injection at supercritical pressure,” *Int. J. Heat Mass Transfer* **39**, 709–719 (2003).
- ⁴ M. Oswald and A. Schik, “Supercritical nitrogen free jet investigated by spontaneous raman scattering,” *Exp. Fluids* **27**, 497–506 (1999).
- ⁵ M. Oswald, J. J. Smith, R. Branam, J. Hussong, A. Shick, B. Chehroudi, and D. Talley, “Injection of fluids into supercritical environments,” *Combust. Sci. Technol.* **178**, 49–100 (2006).
- ⁶ C. Segal and S. A. Polikhov, “Subcritical to supercritical mixing,” *Phys. Fluids* **20**, 052101 (2008).
- ⁷ A. Roy and C. Segal, “Experimental study of fluid jet mixing at supercritical conditions,” *J. Propul. Power* **26**(6), 1205–1211 (2010).
- ⁸ B. E. Poling, J. M. Prausnitz, and J. P. O’Connell, *The Properties of Gases and Liquids*, 5th ed. (McGraw-Hill, 2001).
- ⁹ R. Branam and W. Mayer, “Characterisation of cryogenic injection at supercritical pressure,” *J. Propul. Power* **19**(3), 342–355 (2003).
- ¹⁰ M. Oswald and M. M. Micci, “Spreading angle and centerline variation of density of supercritical nitrogen jets,” *Atomization Sprays* **11**, 91–106 (2002).
- ¹¹ D. W. Davis, B. Chehroudi, and I. Sorensen, “Measurements in an acoustically driven coaxial jet under supercritical conditions,” in *43rd AIAA Aerospace Science Meeting and Exhibit, Reno, NV, Jan. 10–13*, AIAA paper No. 2005-736, 2005.
- ¹² D. W. Davis and B. Chehroudi, “Measurements in an acoustically-driven coaxial jet under sub-, near-, and supercritical conditions,” *J. Propul. Power* **23**(2), 364–374 (2007).
- ¹³ I. A. Leyva, B. Chehroudi, and D. Talley, “Dark core analysis of coaxial injectors at sub-, near-, and supercritical conditions in a transverse acoustic field,” in *43rd AIAA/ASME/SAE/ASEE Joint Propulsion Conference and Exhibit, Cincinnati, OH, July 8–11*, AIAA Paper No. 2007-5456, 2007.

- ¹⁴ I. A. Leyva, J. Rodriguez, B. Chehroudi, and D. Talley, "Preliminary results on coaxial jet spread angles and the effects of variable phase transverse acoustic fields," in *46th AIAA Aerospace Sciences Meeting and Exhibit, Reno, Nevada, Jan. 7-10*, AIAA paper No. 2008-950, 2008.
- ¹⁵ J. Rodriguez, I. Leyva, J. Graham, and D. Talley, "Mixing enhancement of liquid rocket engine injector flow," in *45th AIAA/ASME/SAE/ASEE Joint Propulsion Conference and Exhibit, Denver, Colorado, August 2-5*, AIAA Paper No. 2009-5143, 2009.
- ¹⁶ J. Rodriguez, J. Graham, I. Leyva, and D. Talley, "Effect of variable phase transverse acoustic fields on coaxial jet forced spread angles," in *47th AIAA Aerospace Sciences Meeting including The New Horizons Forum and Aerospace Exposition, Orlando, Florida, 5-8 January*, AIAA Paper No. 2009-231 (American Institute of Aeronautics and Astronautics, 1801 Alexander Bell Dr., Suite 500 Reston, VA 20191-4344, USA).
- ¹⁷ W. O. H. Mayer and R. Branam, "Atomization characteristics on the surface of a round liquid jet," *Exp. Fluid* **36**, 528-539 (2004).
- ¹⁸ M. Oswald, A. Schik, M. Klar, and W. Mayer, "Investigation of coaxial LN₂-GH₂-injection at supercritical pressure by spontaneous Raman scattering," in *35th Joint Propulsion Conference, Los Angeles, CA, 1999*, AIAA Paper No. 99-2887.
- ¹⁹ J. C. Lasheras, E. Villiermaux, and E. J. Hopfinger, "Break-up and atomization of a round water jet by a high-speed annular air jet," *J. Fluid Mech.* **357**, 351-379 (1998).
- ²⁰ E. Villiermaux and H. Rehab, "Mixing in coaxial jets," *J. Fluid Mech.* **425**, 161-185 (2000).
- ²¹ S. Candel, M. Juniper, G. Singla, P. Scoufflaire, and C. Rolon, "Structure and dynamics of cryogenic flames at supercritical pressure," *Combust. Sci. Technol.* **178**, 161-192 (2006).
- ²² H. Rehab, E. Villiermaux, and E. J. Hopfinger, "Flow regimes of large-velocity-ratio coaxial jets," *J. Fluid Mech.* **345**, 357-381 (1997).
- ²³ B. Chehroudi and D. Talley, "Interaction of acoustic waves with a cryogenic nitrogen jet at sub- and supercritical pressures," in *40th AIAA Aerospace Science Meeting and Exhibit, Reno, Nevada, January 14-17*, AIAA Paper No. 2002-342, 2002.
- ²⁴ M. Habiballah, M. Orain, F. Grisch, L. Vingert, and P. Gicquel, "Experimental studies of high-pressure cryogenic flames on the Mascotte facility," *Combust. Sci. Technol.* **178**(1), 101-128 (2006).
- ²⁵ J. J. Smith, G. Schneider, D. Suslov, M. Oswald, and O. Haidn, "Steady-state high pressure lox/h₂ rocket engine combustion," *Aerosp. Sci. Technol.* **11**, 39-47 (2007).
- ²⁶ G. Singla, "Etude des Flamme Cryotechniques Oxygène Liquide/Méthane à Haute Pression," Ph.D. thesis (Ecole Centrale de Paris, 2005).
- ²⁷ G. Singla, P. Scoufflaire, C. Rolon, and S. Candel, "Planar laser-induced fluorescence of OH in high-pressure cryogenic LO_x/GH₂ jet flames," *Combust. Flame* **144**(1-2), 151-169 (2006).
- ²⁸ F. Richecoeur, P. Scoufflaire, S. Ducruix, and S. Candel, "High-frequency transverse acoustic coupling in a multiple-injector cryogenic combustor," *J. Propul. Power* **22**(4), 790-799 (2006).
- ²⁹ Y. Mery, S. Ducruix, P. Scoufflaire, and S. Candel, "Injection coupling with high amplitude transverse modes: Experimentation and simulation," *C. R. Mec.* **337**(6-7), 426-437 (2009).
- ³⁰ R. Dehoff, *Thermodynamics in Materials Science*, 2nd ed. (Taylor & Francis, 2006).
- ³¹ V. Yang, "Modeling of supercritical vaporization, mixing, and combustion processes in liquid-fueled propulsion systems," *Proc. Combust. Inst.* **28**(1), 925-942 (2000).
- ³² J. C. Oefelein, "Thermophysical characteristics of shear-coaxial LOX-H₂ flames at supercritical pressure," *Proc. Combust. Inst.* **30**(2), 2929-2937 (2005).
- ³³ J. Bellan, "Supercritical (and subcritical) fluid behavior and modeling: drops, streams, shear and mixing layers, jets and sprays," *Prog. Energy Combust. Sci.* **26**, 329-366 (2000).
- ³⁴ H. Meng and V. Yang, "A unified treatment of general fluid thermodynamics and its application to a preconditioning scheme," *J. Comput. Phys.* **189**(1), 277-304 (2003).
- ³⁵ J. Bellan, "Theory, modeling and analysis of turbulent supercritical mixing," *Combust. Sci. Technol.* **178**(1), 253-281 (2006).
- ³⁶ L. C. Selle, N. A. Okong'o, J. Bellan, and K. G. Harstad, "Modelling of subgrid-scale phenomena in supercritical transitional mixing layers: an *a priori* study," *J. Fluid Mech.* **593**, 57-91 (2007).
- ³⁷ E. S. Taskinoglu and J. Bellan, "A posteriori study using a DNS database describing fluid disintegration and binary-species mixing under supercritical pressure: heptane and nitrogen," *J. Fluid Mech.* **645**, 211-254 (2010).
- ³⁸ N. Zong and V. Yang, "Cryogenic fluid jets and mixing layers in transcritical and supercritical environments," *Combust. Sci. Technol.* **178**(1), 193-227 (2006).
- ³⁹ N. Zong, H. Meng, S.-Y. Hsieh, and V. Yang, "A numerical study of cryogenic fluid injection and mixing under supercritical conditions," *Phys. Fluids* **16**(12), 4248-4261 (2004).
- ⁴⁰ N. Zong, "Modeling and simulation of cryogenic fluid injection and mixing dynamics under supercritical conditions," Ph.D. dissertation (The Pennsylvania State University, 2005).
- ⁴¹ T. Schmitt, L. Selle, A. Ruiz, and B. Cuenot, "Large-eddy simulation of supercritical-pressure round jets," *AIAA J.* **48**(9), 2133-2144 (2010).
- ⁴² N. Zong and V. Yang, "A numerical study of high-pressure oxygen/methane mixing and combustion of a shear coaxial injector," in *43rd AIAA Aerospace Sciences Meeting and Exhibit*, Vol. AIAA-2005-0152, 2005.
- ⁴³ T. Liu, N. Zong, and V. Yang, "Dynamics of shear-coaxial cryogenic nitrogen jets with acoustic excitation under supercritical conditions," in *44th AIAA Aerospace Sciences Meeting and Exhibit, 9-12 January 2006, Reno, Nevada*, AIAA Paper No. 2006-75, 2006.
- ⁴⁴ J. C. Oefelein, "Mixing and combustion of cryogenic oxygen-hydrogen shear-coaxial jet flames at supercritical pressure," *Combust. Sci. Technol.* **178**(1), 229-252 (2006).
- ⁴⁵ J. C. Oefelein and V. Yang, "Modeling high-pressure mixing and combustion processes in liquid rocket engines," *Journal of Propulsion and Power* **14**(5), 843-857 (1998).

- ⁴⁶ N. Zong and V. Yang, "Near-field flow and flame dynamics of LOX/methane shear-coaxial injector under supercritical conditions," *Proc. Combust. Inst.* **31**(2), 2309–2317 (2007).
- ⁴⁷ S. Matsuyama, J. Shinjo, S. Ogawa, and Y. Mizobuchi, "Large Eddy simulation of LOX/GH2 shear-coaxial jet flame at supercritical pressure," in *48th AIAA Aerospace Sciences Meeting, Orlando, Florida*, Vol. AIAA 2010-208, January 2010.
- ⁴⁸ M. Masquelet, S. Menon, Y. Jin, and R. Friedrich, "Simulation of unsteady combustion in a LOX-GH2 fueled rocket engine," *Aerosp. Sci. Technol.* **13**(8), 466–474 (2009).
- ⁴⁹ T. Schmitt, Y. Méry, M. Boileau, and S. Candel, "Large-eddy simulation of oxygen/methane flames under transcritical conditions," *Proc. Combust. Inst.* **33**(1), 1383–1390 (2011).
- ⁵⁰ F. X. Demoulin, S. Zurbach, and A. Mura, "High-pressure supercritical turbulent cryogenic injection and combustion: A single-phase flow modeling proposal," *J. Propul. Power* **25**(2), 452–464 (2009).
- ⁵¹ G. C. Cheng and R. Farmer, "Real fluid modeling of multiphase flows in liquid rocket engine combustors," *J. Propul. Power* **22**(6), 1373–1381 (2006).
- ⁵² M. M. Poschner and M. Pfitzner, "CFD-simulation of the injection and combustion of LOX and H2 at supercritical pressures," in *Proceedings of the European Combustion Meeting*, 2009.
- ⁵³ E. W. Lemmon, M. O. McLinden, and D. G. Friend, "Thermophysical properties of fluid systems," in *NIST Chemistry WebBook, NIST Standard Reference Database 69*, edited by P. J. Linstrom and W. G. Mallard (National Institute of Standards and Technology, Gaithersburg, MD, 2007).
- ⁵⁴ N. Otsu, "A threshold selection method from gray-level histograms," *Automatica* **11**, 285–296 (1975).
- ⁵⁵ I. A. Leyva, B. Chehroudi, and D. Talley, "Dark core analysis of coaxial injectors at sub-, near-, and supercritical conditions in a transverse acoustic field," in *54th JANNAF Meeting, Denver, CO, May 14-18, 2007*.
- ⁵⁶ T. H. Chung, M. Ajlan, L. L. Lee, and K. E. Starling, "Generalized multiparameter correlation for nonpolar and polar fluid transport properties," *Ind. Eng. Chem. Res.* **27**(4), 671–679 (1988).
- ⁵⁷ L. Selle and T. Schmitt, "Large-eddy simulation of single-species flows under supercritical thermodynamic conditions," *Combust. Sci. Technol.* **182**(4), 392–404 (2010).
- ⁵⁸ D. Peng and D. B. Robinson, "A new two-constant equation of state," *Ind. Eng. Chem. Fundam.* **15**, 59–64 (1976).
- ⁵⁹ R. S. Miller, K. G. Harstad, and J. Bellan, "Direct numerical simulation of supercritical fluid mixing layers applied to heptane-nitrogen," *J. Fluid Mech.* **436**, 1–39 (2001).
- ⁶⁰ J. O. Hirschfelder, C. F. Curtiss, and R. B. Bird, *Molecular Theory of Gases and Liquids* (Wiley, New York, 1954).
- ⁶¹ M. W. Chase, *NIST-JANAF Thermochemical Tables* (American Institute of Physics, 1998).
- ⁶² F. Nicoud and F. Ducros, "Subgrid-scale stress modelling based on the square of the velocity gradient," *Flow, Turbul. Combust.* **62**(3), 183–200 (1999).
- ⁶³ T. Schönfeld and T. Poinso, "Influence of boundary conditions in LES of premixed combustion instabilities," in *Annual Research Briefs* (Center for Turbulence Research, NASA Ames/Stanford University, 1999), pp. 73–84.
- ⁶⁴ V. Moureau, G. Lartigue, Y. Sommerer, C. Angelberger, O. Colin, and T. Poinso, "High-order methods for DNS and LES of compressible multi-component reacting flows on fixed and moving grids," *J. Computat. Phys.* **202**(2), 710–736 (2005).
- ⁶⁵ A. G. Kravchenko and P. Moin, "On the effect of numerical errors in large eddy simulations of turbulent flows," *J. Comput. Phys.* **131**, 310–322 (1996).
- ⁶⁶ J. Gullbrand and F. K. Chow, "The effect of numerical errors of turbulence models in large eddy simulations of channel flow, with and without explicit filtering," *J. Fluid Mech.* **495**, 323–341 (2003).
- ⁶⁷ L. Quartapelle and V. Selmin, "High-order Taylor-Galerkin methods for non-linear multidimensional problems," *Finite Elements in Fluids* **76**, 90 (1993).
- ⁶⁸ T. Poinso and S. Lele, "Boundary conditions for direct simulations of compressible viscous flows," *J. Comput. Phys.* **101**(1), 104–129 (1992).
- ⁶⁹ N. Okong'o and J. Bellan, "Consistent boundary conditions for multicomponent real gas mixtures based on characteristic waves," *J. Comput. Phys.* **176**, 330–344 (2002).
- ⁷⁰ L. Pons, N. Darabiha, S. Candel, T. Schmitt, and B. Cuenot, "The structure of multidimensional strained flames under transcritical conditions," *C. R. Mec.* **337**(6–7), 517–527 (2009).
- ⁷¹ T. Schmitt, L. Selle, B. Cuenot, and T. Poinso, "Large-eddy simulation of transcritical flows," *C. R. Mec.* **337**(6–7), 528–538 (2009).
- ⁷² I. Celik, A. Smirnov, and J. Smith, "Appropriate initial and boundary conditions for LES of a ship wake," in *Proceedings of the 3rd ASME/JSME Joint Fluids Engineering Conference*, Vol. FEDSM99-7851, San Francisco, California, USA, 1999.
- ⁷³ A. Smirnov, S. Shi, and I. Celik, "Random flow generation technique for large eddy simulations and particle-dynamics modeling," *Trans. ASME, J. Appl. Mech.* **123**, 359–371 (2001).
- ⁷⁴ N. Guezennec and T. Poinso, "Acoustically nonreflecting and reflecting boundary conditions for vorticity injection in compressible solvers," *AIAA J.* **47**, 1709–1722 (2009).
- ⁷⁵ C. J. Chen and W. Rodi, *Vertical Turbulent Buoyant Jets: A Review of Experimental Data* (Pergamon, 1980).
- ⁷⁶ D. Wee, T. Yi, A. Annaswamy, and A. F. Ghoniem, "Self-sustained oscillations and vortex shedding in backward-facing step flows: Simulation and linear instability analysis," *Phys. Fluids* **16**, 3361–3373 (2004).
- ⁷⁷ C. Rey, S. Ducruix, and S. Candel, "A method for the transverse modulation of reactive flows with application to combustion instability," *Combust. Theory Modell.* **9**, 5–22 (2005).
- ⁷⁸ A. L. Birbaud, D. Durox, S. Ducruix, and S. Candel, "Dynamics of free jets submitted to upstream acoustic modulations," *Phys. Fluids* **19**, 013602 (2007).

Split Stream Flow Past a Blunt Trailing Edge with Application to Combustion Instabilities

Vicky Tian¹, Beverley McKeon²
California Institute of Technology, Pasadena, CA 91125, USA

Ivett A Leyva³
Air Force Research Lab, Edwards AFB, CA 93524, USA

In shear coaxial injectors, commonly used for cryogenic liquid rocket engines, propellants traveling at different velocities are separated by the inner jet post before they come into contact with each other, mix, and combust. Knowing how the fluids mix and how susceptible they are to hydrodynamic instabilities is paramount for a successful liquid rocket engine. In this study, the wake behind a blunt trailing edge of a long plate, similar to an unwrapped coaxial injector, was studied in a water tunnel. Two fluid streams of different velocities were introduced on opposite sides of the plate. PIV was used to visualize and determine the influence of the velocity ratio of the split stream on the wake behavior. Measurements of the vortex shedding frequency were taken at various velocity ratios and compared with well characterized cases with a uniform free stream.

I. Nomenclature

t	=	plate thickness [m]
U_1	=	mean free stream velocity of faster, unobstructed stream [m s^{-1}]
U_2	=	mean free stream velocity of slower, obstructed stream [m s^{-1}]
ρ	=	density of fluid [N s m^{-2}]
μ	=	dynamic viscosity [kg m^{-2}]
f	=	shedding frequency of vortices from one stream [Hz]
U	=	$\frac{1}{2}(U_1 + U_2)$ mean of two free streams [m s^{-1}]
VR	=	U_1/U_2 velocity ratio
Re	=	Reynolds number using U
St	=	$f t/U$ - Strouhal number using U

II. Introduction

SHEAR coaxial injectors are a common choice for cryogenic liquid rocket engines such as the Shuttle SSME or the Delta IV booster, RS-68. In principle, the injector design is simple. There is an inner tube, carrying liquid oxygen, surrounded by a higher speed stream of hydrogen which flows through a concentric outer tube. As seen in Figure 1, the propellants are separated by the inner jet post before they come into contact with each other, mix, and combust. This type of injector relies on the shear or difference in velocities between the two propellants to achieve good mixing. Therefore, outer to inner jet velocity ratios of the order of 10 or more are typical. When the two fluids are brought together at the end of the inner jet post, the flow is susceptible to hydrodynamic instabilities. The characteristics of a wake behind a cylinder or a blunt body have been widely characterized for the case of a single stream. However, for the case of a split stream with different velocities, there is little knowledge about how the velocity ratio affects the wake structures and shedding frequency.

In this project a shear coaxial injector is simplified into a basic split stream flow over a blunt trailing edge (**Figure 2**). This can be thought of as an “unwrapped” coaxial injector. This simplification was made for ease of visualization and measurements. A good characterization of hydrodynamic instabilities for the case of non-reacting flows is the first step to understand how combustion and heat addition will affect such instabilities. It is expected that avoiding resonances between combustion processes and hydrodynamic instabilities results in more stable injector designs.

¹Undergraduate Student

²Professor of Aeronautics, AIAA Senior Member.

³Sr. Aerospace Engineer, AFRL, RZSA. AIAA Senior Member

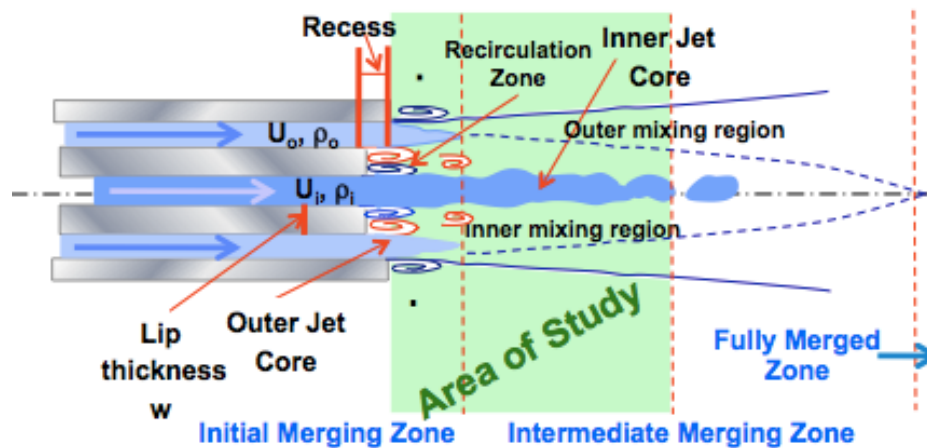


Figure 1. Schematic of shear coaxial injector relevant parameters and features.

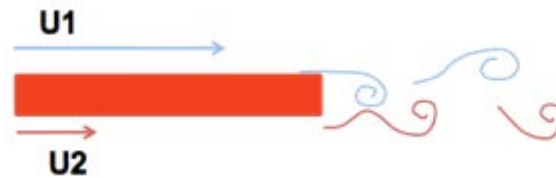


Figure 2. Simplification of shear coaxial jet used in this study.

Few investigators have documented the influence of a split stream flow around a trailing edge using hot wire measurements^{1,2,3,5,6,8}. In the case of flows with a split stream of different velocities, the wake dominates the mixing layer for some distance until the wake structures dissipate and the asymptotic turbulence structures of the mixing layer dominate. The effect of the velocity ratio has been studied mostly as it relates to the mixing layer and not the wake region and its characteristic shedding frequency. Boldman et al., using an air wind tunnel and hot wire measurements, concluded that the average velocity should be used in computing the normalized frequency or Strouhal number⁶. Using four different velocity ratios, his results showed the frequency slightly decreased as the velocity ratio was reduced. The corresponding Strouhal numbers slightly decreased then increased as velocity ratio was reduced. However, studying the Strouhal number was not the focus of his study and he did not make concluding comments about the trend. Tamura et al. having a similar set-up, had similar results using five velocity ratios⁸. They concluded that the Strouhal numbers for velocity ratios greater than 0.78 can be approximated by the Strouhal numbers of the uniform case. Their data also showed that below ratio 0.78, the Strouhal numbers decreased then increased from the uniform case. However, he did not comment on the results for ratios lower than 0.78.

Flows that present a combination of wake and shear layer phenomena are also very interesting from the point of view of linear stability analysis. For example, wakes are a well known example of absolutely unstable flows whereas shear layers are a classical example of convectively unstable flows. Wallace and Redekopp (9), in a computational study, map the stability characteristics (convective vs. absolutely unstable) for plane wake-shear layer as a function of two parameters, a wake deficit parameter (velocity deficit divided by the mean velocity) and a velocity ratio (the velocity difference across the layer of nonzero vorticity divided by the mean velocity). They predict that downstream of the wake region, the vortex pattern should transition into a single row of vortex structures. Bocanegra-Evans and Allen (10) confirmed experimentally those predictions showing that for certain velocity ratios, for the case of a splitter plate with a cylinder at the end, the flow has first a strong Von-Karman street mode which transitions to a single vortex rollup characteristic of shear layers. The single shear layer structures are seen in the high speed side of the flow. Finally, more recently Laizet et al. (11) using DNS studied the effect of the end geometry of the splitter plate (blunt, sharp beveled, truncated bevel) on the flow development. They also showed that for the case of a blunt edge, the wake gives way to a single vortex structure characteristic of shear layers.

The main objective of this study is to characterize the dependence of the hydrodynamic instabilities developed downstream of a blunt edge on the velocity ratio between the two incoming streams. Particle Image Velocimetry (PIV) is used to visualize the flow field and measure the stream velocities and frequencies. Hotwire techniques can only measure velocity at a single point whereas PIV can measure velocity in a plane, thus providing a clearer picture of the structures in the wake.

A. Experimental Set up and ProcedureApparatus

Tests were carried out at the NOAH water tunnel of Graduate Aerospace Laboratories of California Institute of Technology. The experimental set up consisted of an upstream dividing plate 0.057m thick and 3.5m long. It was placed vertically in the water tunnel. Due to its length, the plate was constructed in three sections: two 1.5m long wooden planks treated with water-resistant paint and one 0.5m long acrylic hollow plate with a blunt trailing edge. The wood was placed upstream and the acrylic downstream. The optical clarity of the acrylic allowed light to travel through the plate, which was essential when using PIV.

B. Variation of Velocity Ratio

Using the dividing plate, water was introduced flowing at variable speeds. The velocities in the water tunnel were controlled using honeycomb, wire mesh, and cloth. The plastic honeycomb had cells 1/8-inches in diameter, and blocks of the honeycomb approximately 1-inch and 2-inch thick were used. The wire mesh had a square mesh approximately 1/16-inches in width. The types of cloths used were loosely woven cotton cheesecloth, a slightly denser muslin cheesecloth, and polyester filter felt. To vary the velocity ratio, honeycomb, mesh, and cloth were introduced to one side of the plate while the other velocity remained unchanged. They were placed as far upstream as possible; in this case, at the start of the wooden plate. Because the velocity was not completely uniform across the flow due to boundary layers forming on the plate and walls, free stream velocity of each flow was taken as the time-average velocity measured in the stream.

The following combinations were used to make the resulting velocity ratios:

- 1) 2" honeycomb
VR: 1.00-0.93
- 2) 2" honeycomb, 4 1" honeycomb, 3 screens, 2 muslin cloth
VR: 0.57-0.46
- 3) 2" honeycomb, 4 1" honeycomb, 7 screens, 5 muslin cloth, 1 filter cloth
VR: 0.32-0.30

The Reynolds number was calculated with the properties of water at room temperature and the average velocity of the two streams. The shedding frequency was non-dimensionalized using a Strouhal number ($f t/U$) with the plate thickness (t) as the length scale and the average velocity (U) as the relevant velocity following Boldman⁶.

C. Particle Image Velocimetry (PIV)

A PIV system was used to visualize the flow field, and measure the shedding frequencies and stream velocities. The PIV system used two high-speed cameras mounted below the tunnel and a laser plane emitted from the side of the tunnel across the stream (**Figure 3**). The plane was parallel to the flow aimed at the center height of the trailing edge. The sampling frequency was calculated based on the average velocity U .

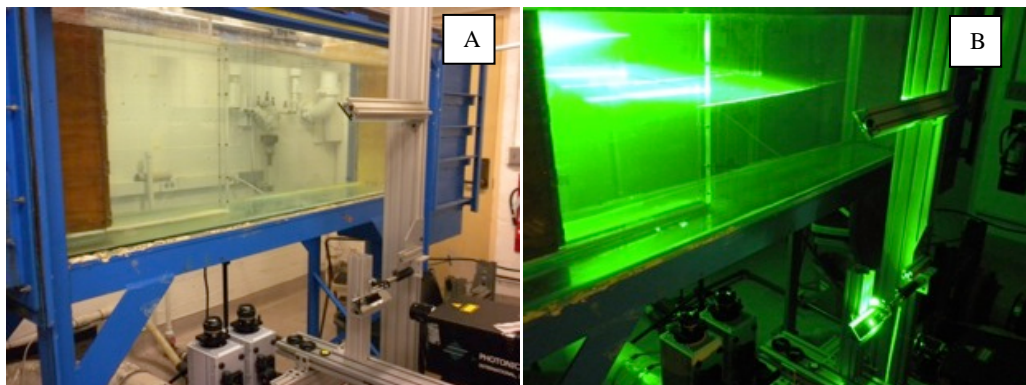


Figure 3. A. PIV Set up. B. PIV running.

III.Results

The experiments presented here closely studied the effect of velocity ratio over three different Reynolds numbers. The specific running conditions are given in Table 1. Each Reynolds number had a base case with a velocity ratio at or close to 1.0. These base cases were used to compare the shedding frequency to the known shedding frequency of non-split stream flows. A goal of this research was to find the trend between the changing velocity ratio and shedding Strouhal number.

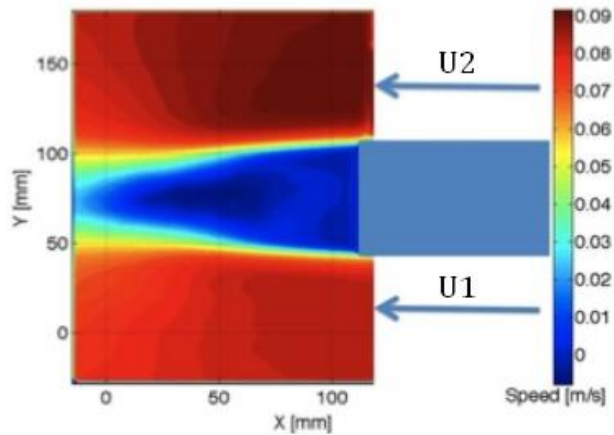
Re	VR	Re	VR	Re	VR
6196	0.93	15,185	0.98	21,430	1.00
6031	0.46	15,676	0.57	22,120	0.55
6043	0.30	14,810	0.32	21,020	0.32

D. Table 1. Running Conditions. Time Averaged Velocity

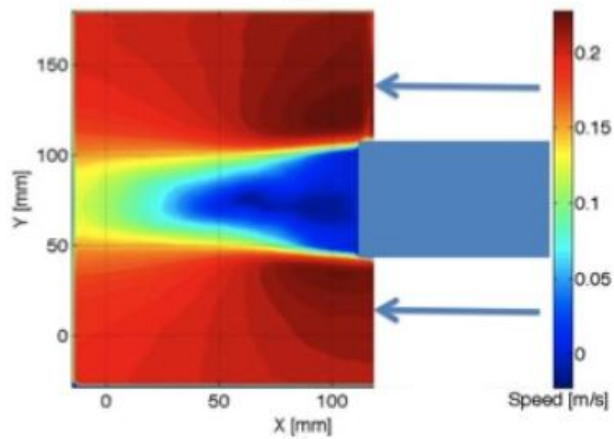
Figures 4-5 present time-averaged U_{mean} and V_{mean} measurements respectively for the baseline cases (velocity ratio ~ 1). We see that in the non-base cases, the slower side of the flow completely dominates the flow immediately behind the plate and the fast stream remained to the side, slightly off center (**Figures 6-9**). Also, as Reynolds number increased, the effects became more pronounced. A more detailed discussion will be presented in the final paper.

The behavior of the flow field in terms of time-averaged U_{rms} and V_{rms} (Figures 10-15) for different Re and velocity ratios will be described next in the full paper.

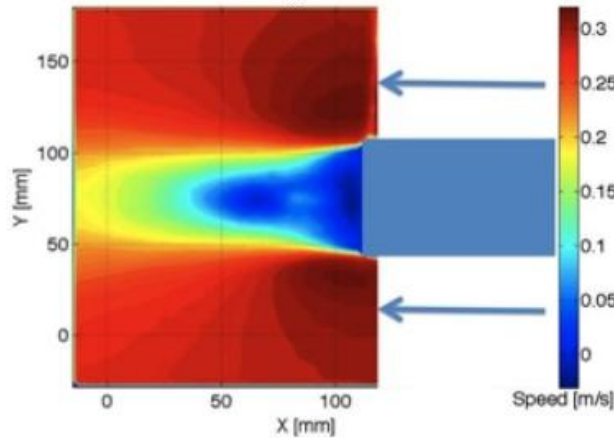
(The naming and size of the figures will be changed for the final paper. The 1-page figures will be compressed)



(a)

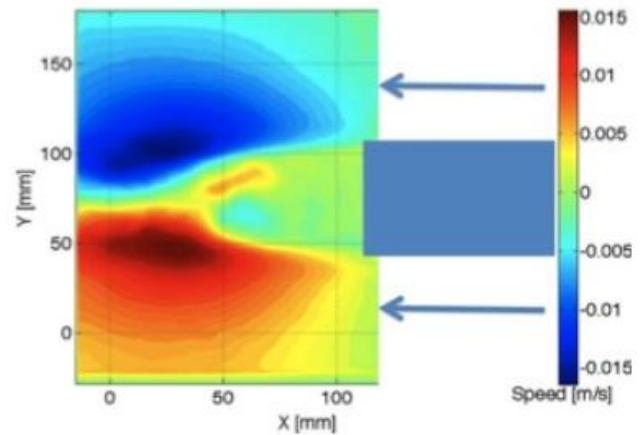


(b)

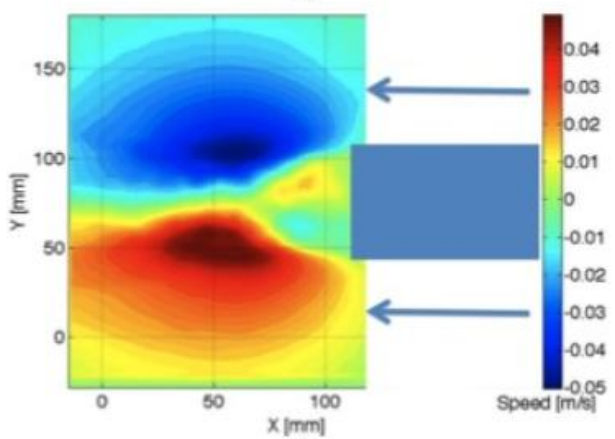


(c)

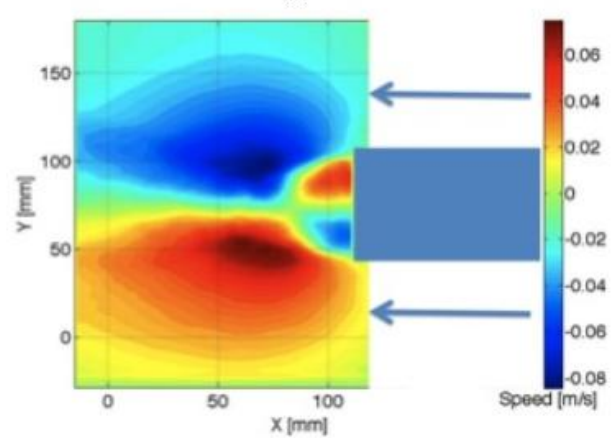
Figure 4 (a-c)
Time-Averaged U_{mean} over 4000 frames
at 70, 200, 290 Hz sampling rate
(a) Re 6169 VR 0.93
(b) Re 15,185 VR 0.98
(c) Re 21,430 VR 1.00



(a)



(b)



(c)

Figure 5 (a-c)
Time-Averaged V_{mean} over 4000 frames
at 70, 200, 190 Hz sampling rate
(a) Re 6169 VR 0.93
(b) Re 15,185 VR 0.98
(c) Re 21,430 VR 1.00

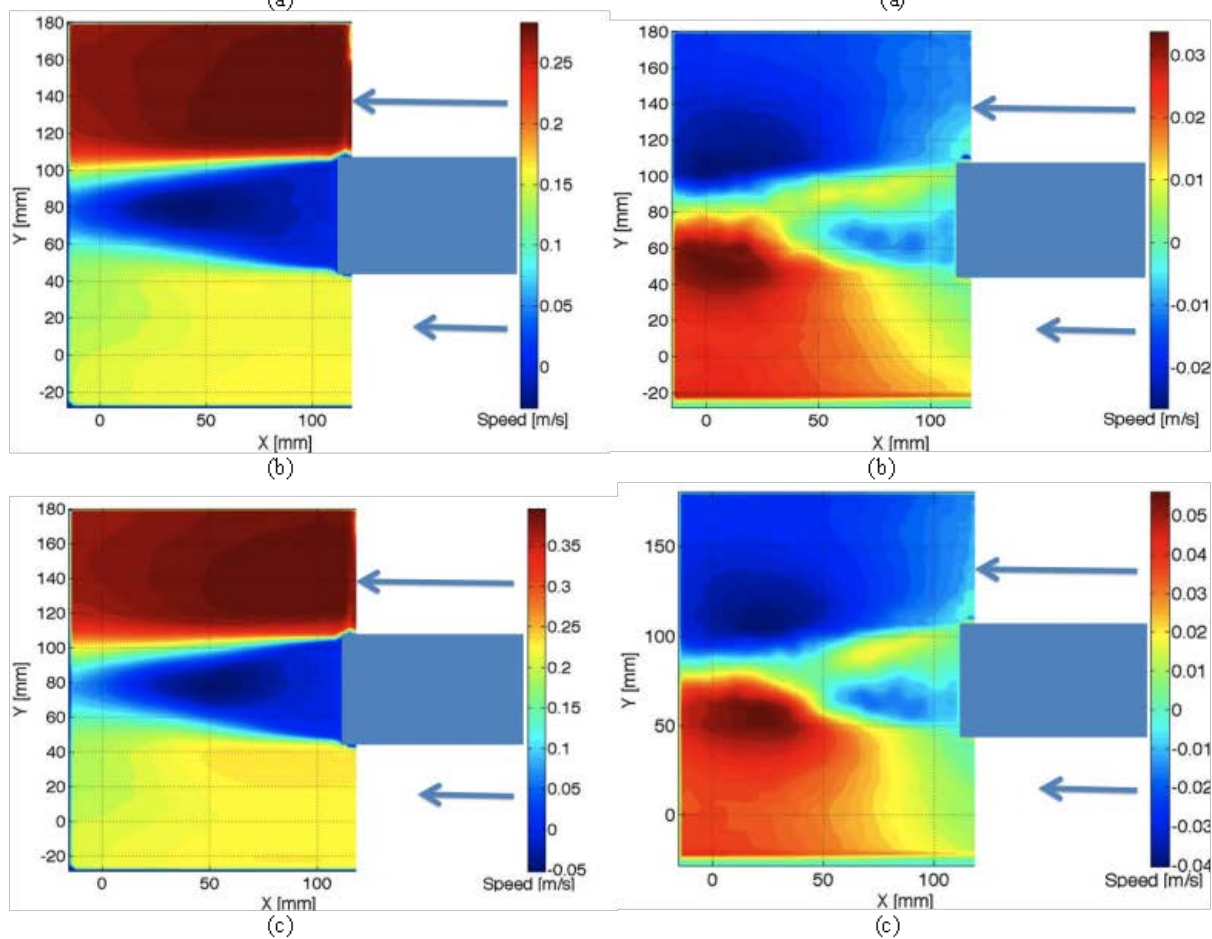
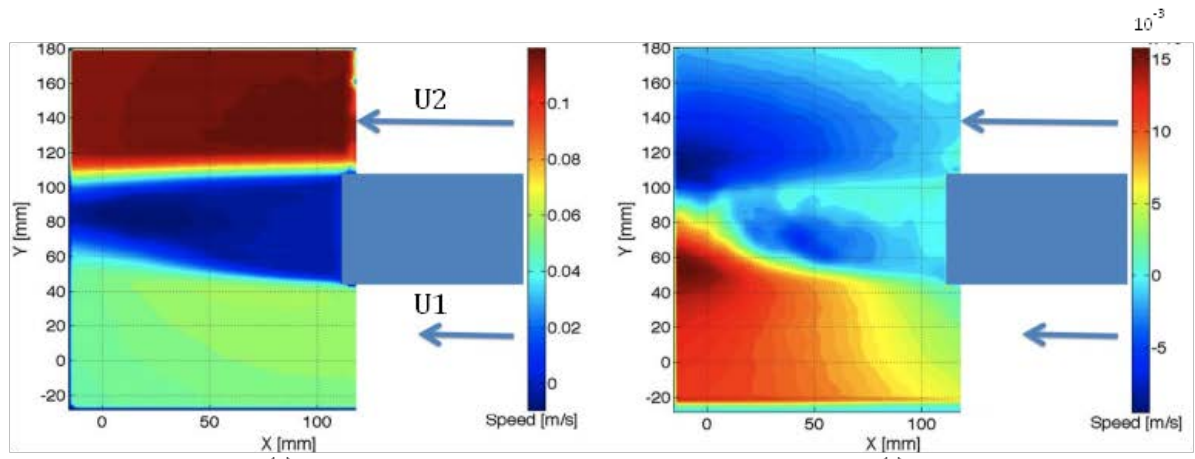


Figure 6(a-c)
Time-Averaged U_{mean} over 20,000
frames at 80, 220, 290Hz sampling rate
(a) Re 6031 VR 0.46
(b) Re 15,676 VR 0.57
(c) Re 22,120 VR 0.55

Figure 7(a-c)
Time-Averaged V_{mean} over 20,000
frames at 80, 220, 290Hz sampling rate
(a) Re 6031 VR 0.46
(b) Re 15,676 VR 0.57
(c) Re 22,120 VR 0.55

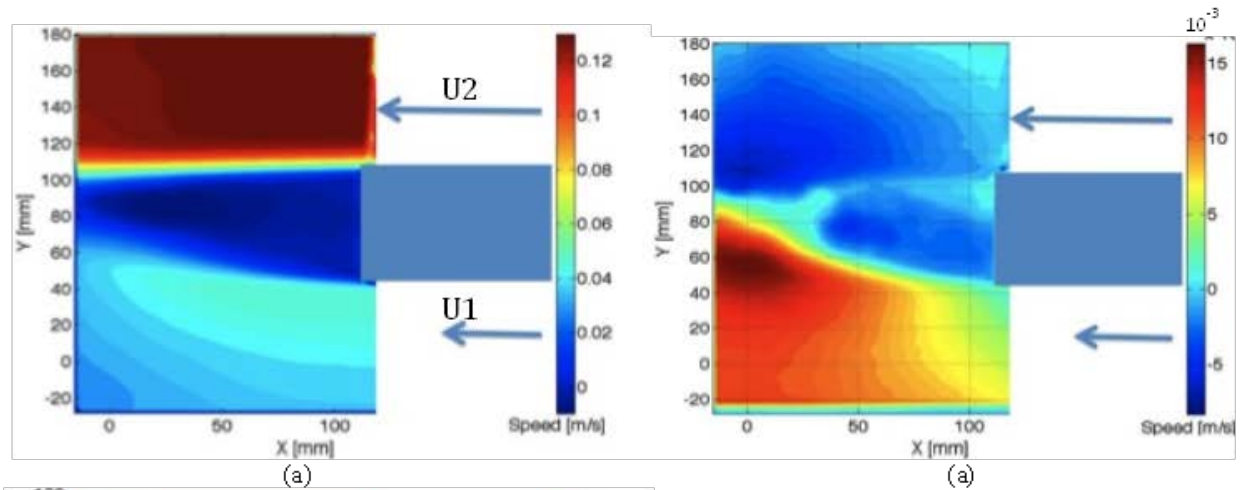
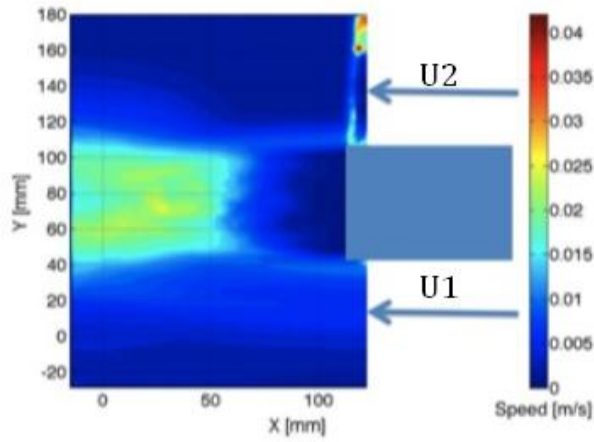
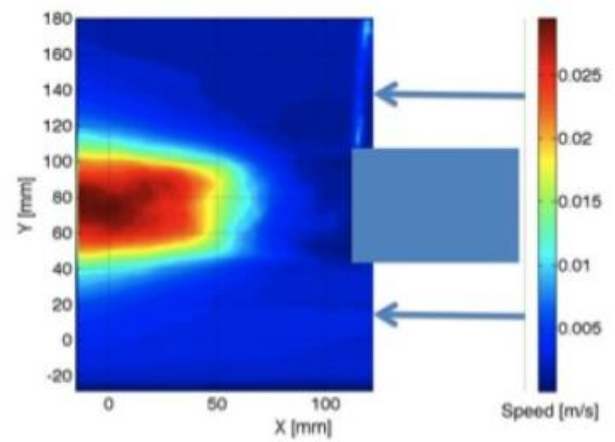


Figure 8(a-c)
Time-Averaged U_{mean} over 20,000
frames at 70, 210, 310Hz sampling rate
(a) Re 6043 VR 0.30
(b) Re 14,818 VR 0.32
(c) Re 21,020 VR 0.32

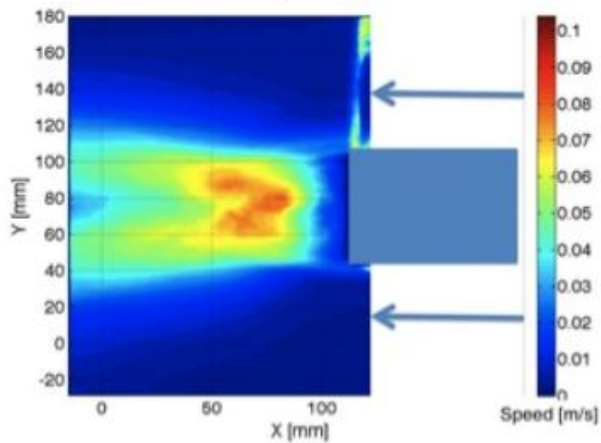
Figure 9(a-c)
Time-Averaged V_{mean} over 20,000
frames at 70, 210, 310Hz sampling rate
(a) Re 6043 VR 0.30
(b) Re 14,818 VR 0.32
(c) Re 21,020 VR 0.32



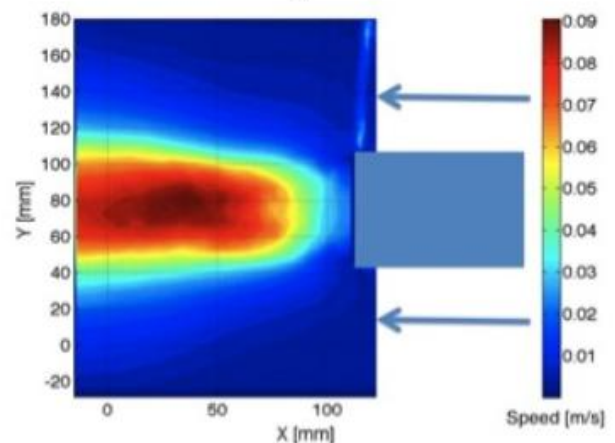
(a)



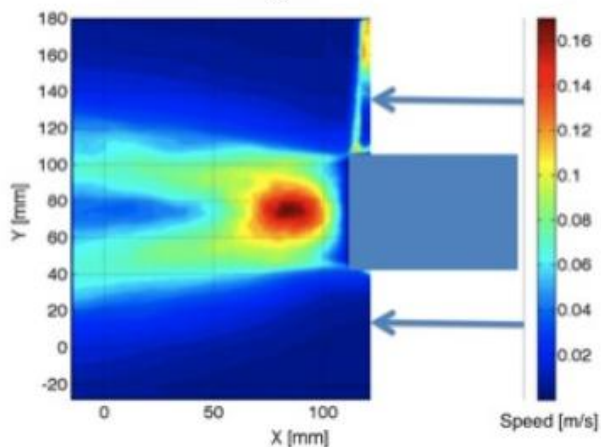
(a)



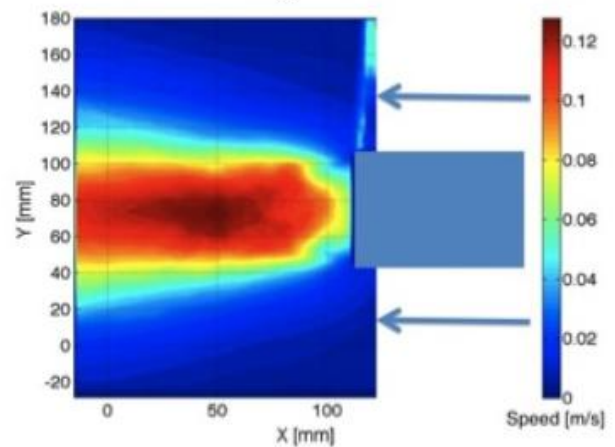
(b)



(b)



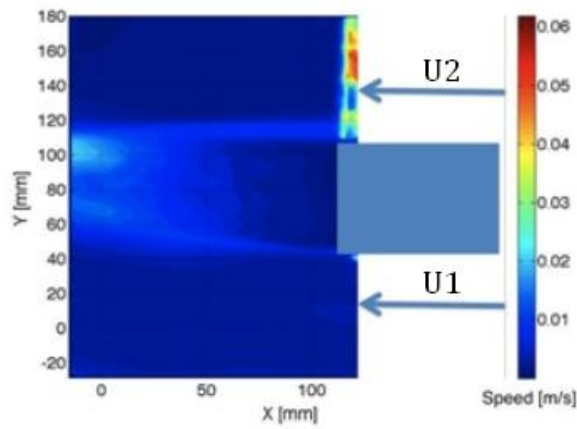
(c)



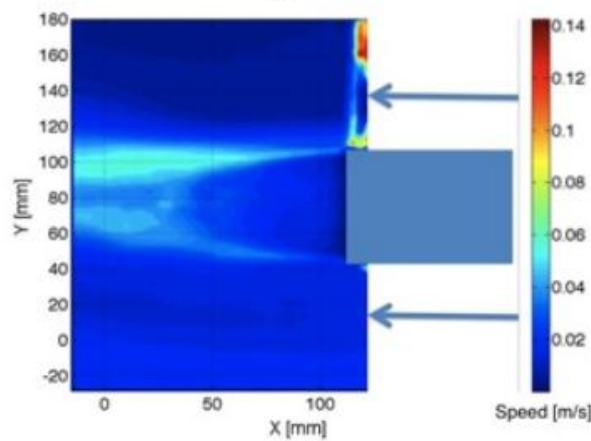
(c)

Figure 10 (a-c)
Time-Averaged U_{RMS} over 4000 frames
at 70, 200, 290 Hz sampling rate
(a) Re 6169 VR 0.93
(b) Re 15,185 VR 0.98
(c) Re 21,430 VR 1.00

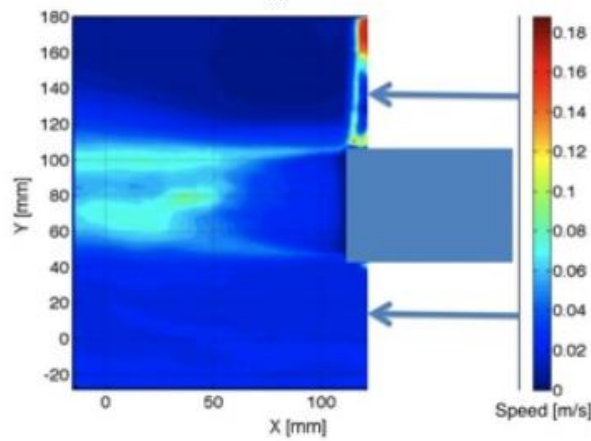
Figure 11 (a-c)
Time-Averaged V_{RMS} over 4000 frames
at 70, 200, 190 Hz sampling rate
(a) Re 6169 VR 0.93
(b) Re 15,185 VR 0.98
(c) Re 21,430 VR 1.00



(a)

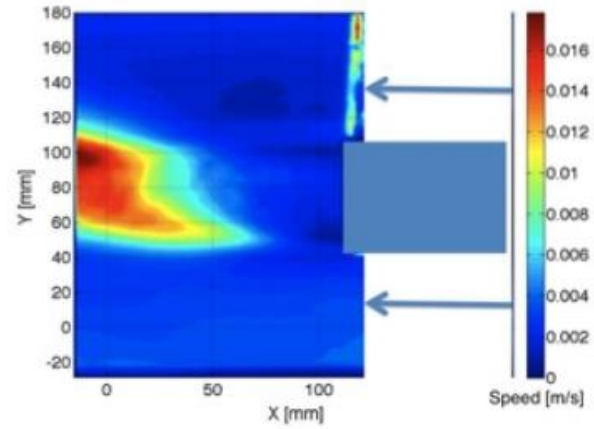


(b)

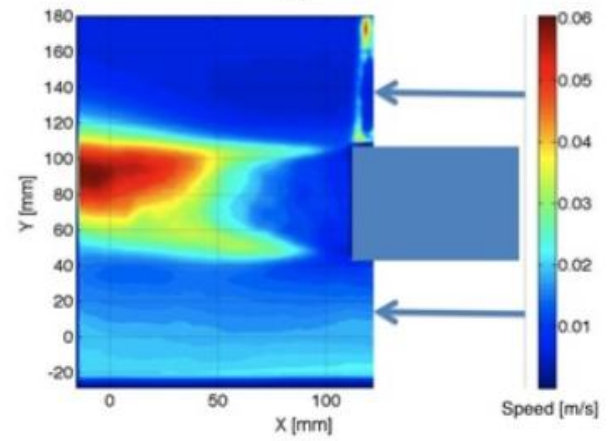


(c)

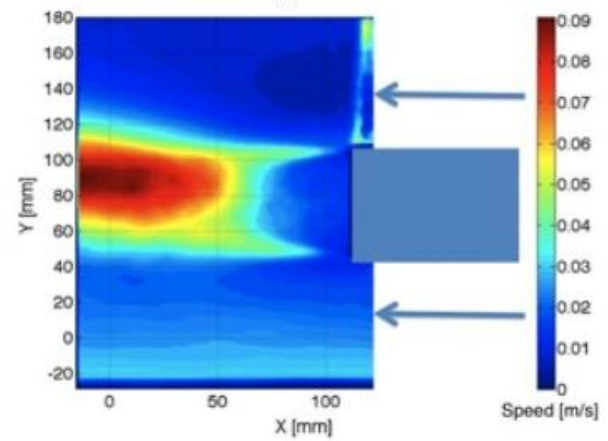
Figure 12 (a-c)
Time-Averaged U_{RMS} over 20,000
frames at 80, 220, 290Hz sampling rate
(a) Re 6031 VR 0.46
(b) Re 15,676 VR 0.57
(c) Re 22,120 VR 0.55



(a)



(b)



(c)

Figure 13 (a-c)
Time-Averaged V_{RMS} over 20,000
frames at 80, 220, 290Hz sampling rate
(a) Re 6031 VR 0.46
(b) Re 15,676 VR 0.57
(c) Re 22,120 VR 0.55

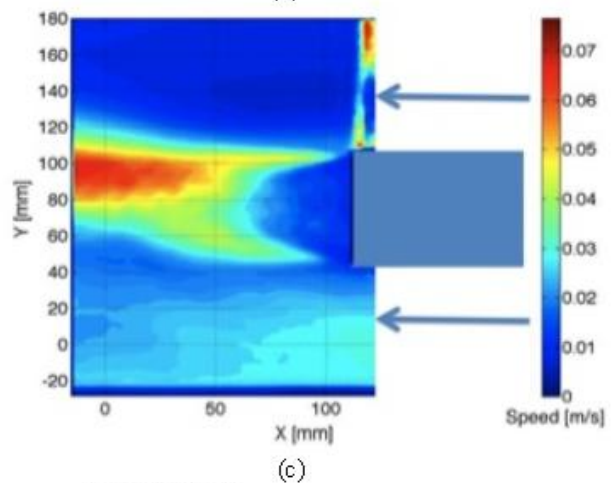
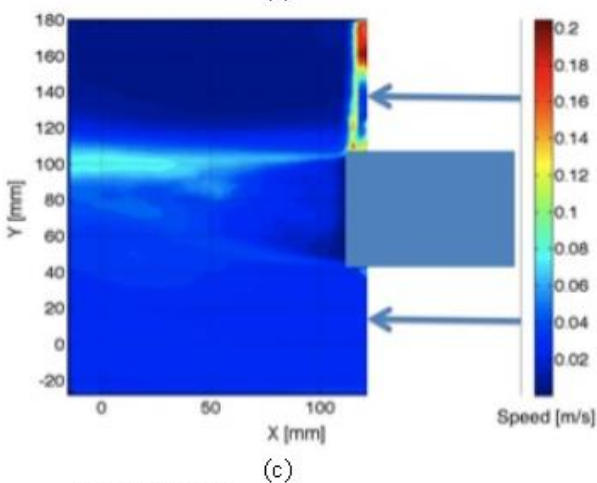
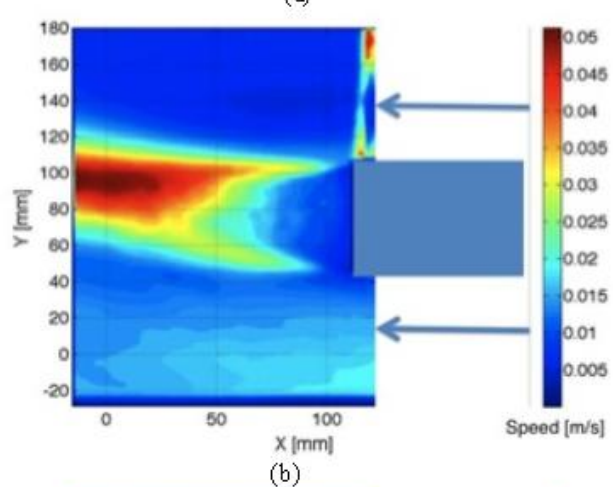
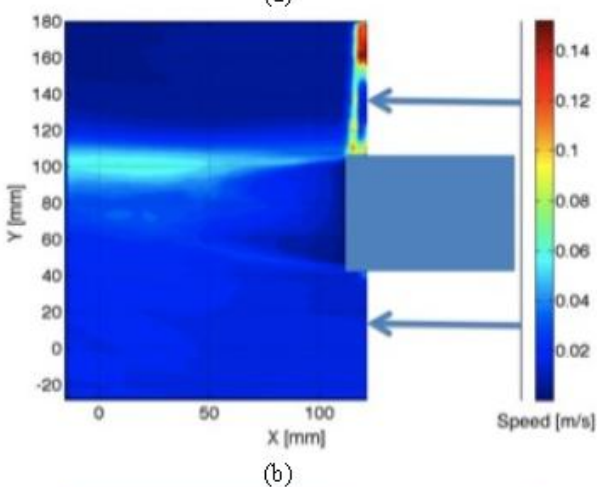
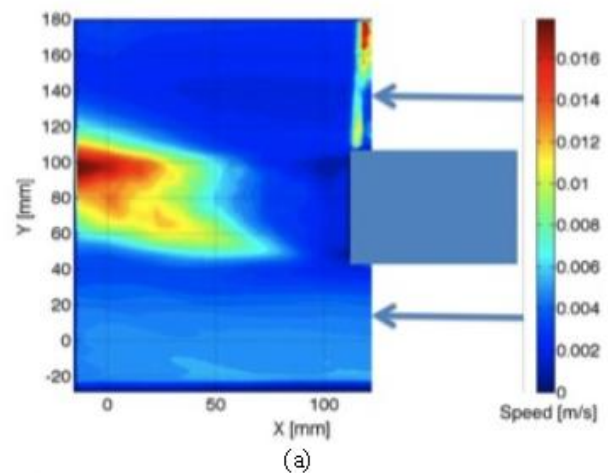
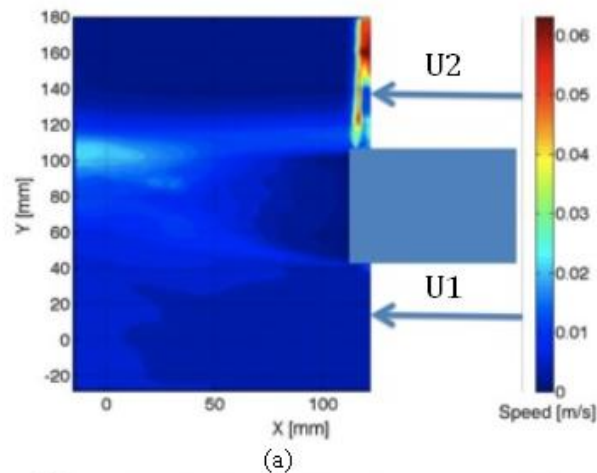


Figure 14 (a-c)
Time-Averaged U_{RMS} over 20,000
frames at 70, 210, 310Hz sampling rate
(a) Re 6043 VR 0.30
(b) Re 14,818 VR 0.32
(c) Re 21,020 VR 0.32

Figure 15 (a-c)
Time-Averaged V_{RMS} over 20,000
frames at 70, 210, 310Hz sampling rate
(a) Re 6043 VR 0.30
(b) Re 14,818 VR 0.32
(c) Re 21,020 VR 0.32

E. Fourier Transform Analysis

Using Fourier Transform analysis, the power spectrum of the flow was estimated using the Welch method of spectral estimation. Picking strategic locations in the stream allowed the shedding frequency to be picked out as the strongest peak in the power spectrum (**Figure 16**).

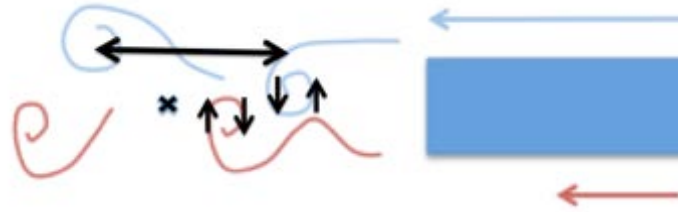


Figure 16. Shedding frequency schematic

Looking at time-instantaneous contour plots the V component of velocity, vortices can be seen with alternating positive and negative V components (**Figure 17**).

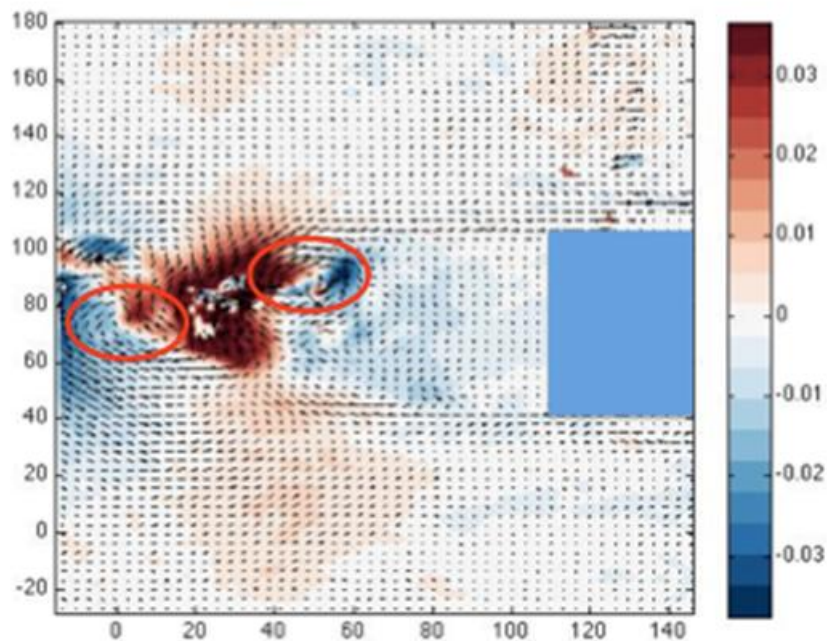
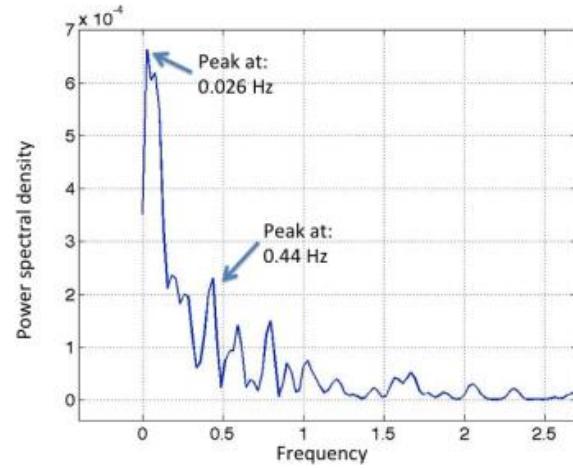
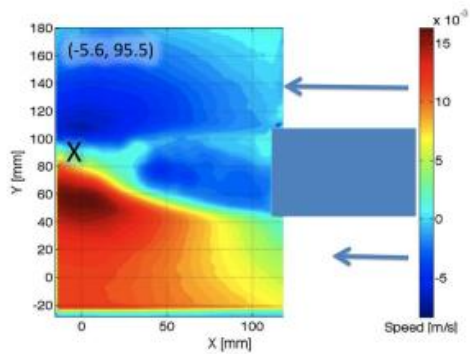
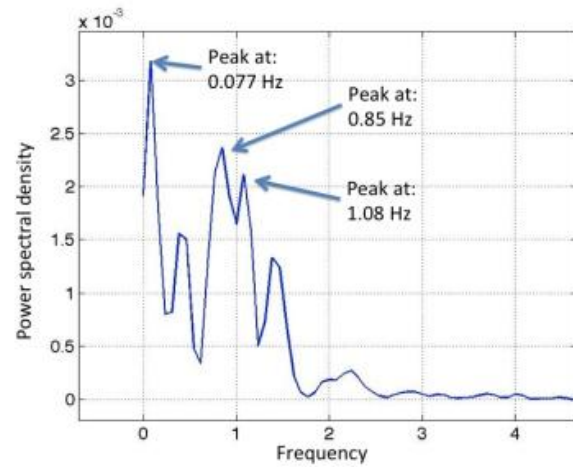
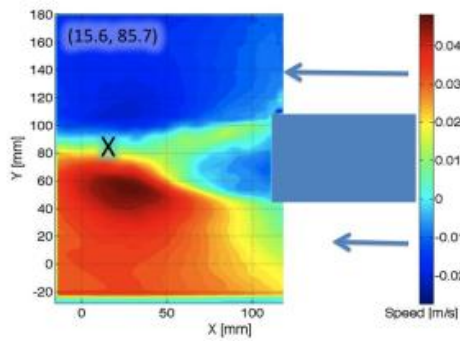


Figure 17. Example of vortices with v-component contours

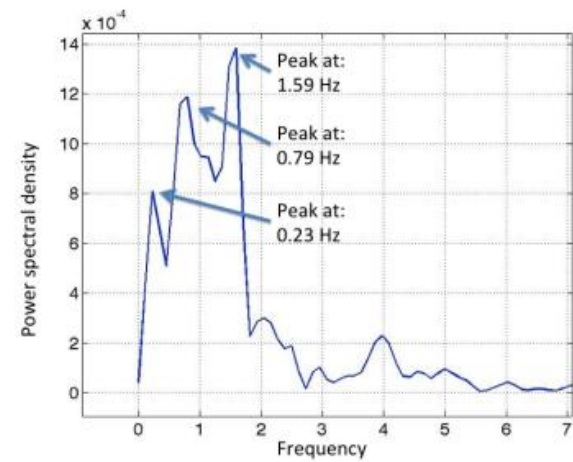
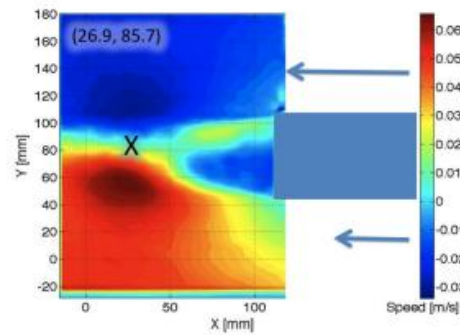
Picking points in the middle of the wake, Fourier analysis was done on the point to find the frequency with the highest power density (**Figures 18-20**). The frequency with the highest power density was most likely to be the shedding frequency of the vortices. The points where the Fourier analysis was done was picked based on the shape of the wake. In the span-wise direction, the point was always chosen at the center of the wake where the contour lines were very close together. In the stream-wise direction, the point was chosen within thickness D of the end of the recirculation region. By watching video of the vortices, the stream-wise distance was chosen by where the vortices were clearly formed. Using this method, the strongest signal for the shedding frequency was analyzed.



(a)



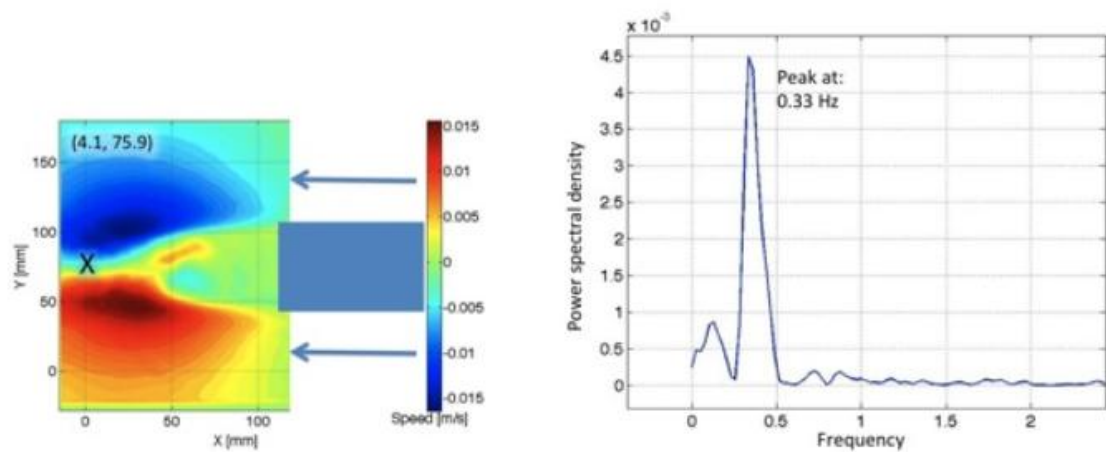
(b)



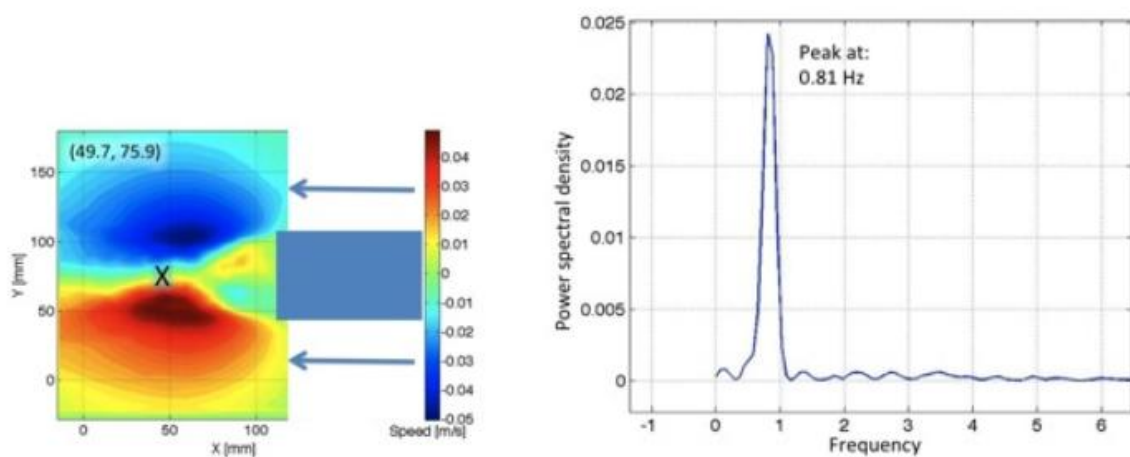
(c)

Figure 20 (a-c)

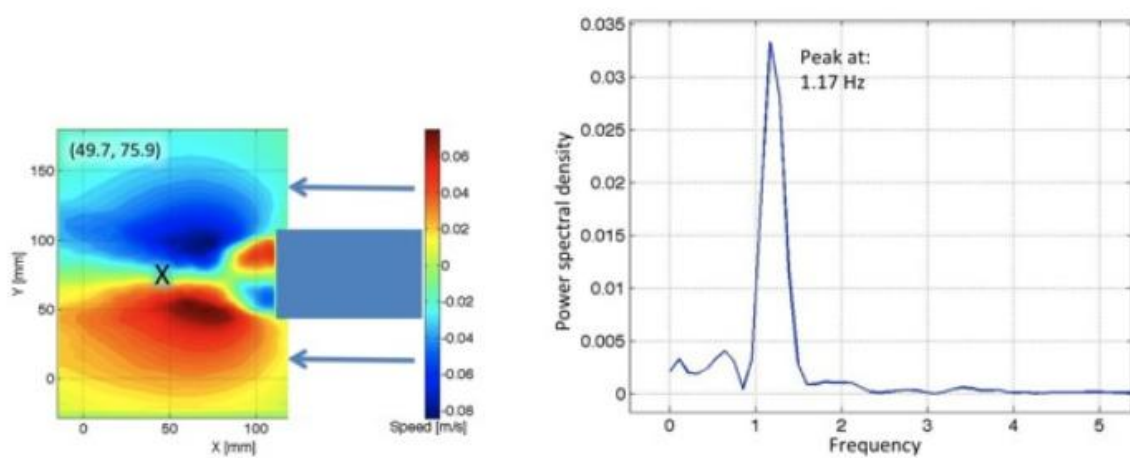
(a) Re 6043	VR 0.30	{Hz 0.026	St 0.017}	or {Hz 0.44	St 0.30}
(b) Re 14,810	VR 0.32	{Hz 0.077	St 0.021}	or {Hz 0.85	St 0.23}
(c) Re 21,020	VR 0.32	{Hz 0.23	St 0.044}	or {Hz 0.79	St 0.15}
				or {Hz 1.08	St 0.30}
				or {Hz 1.59	St 0.31}



(a)



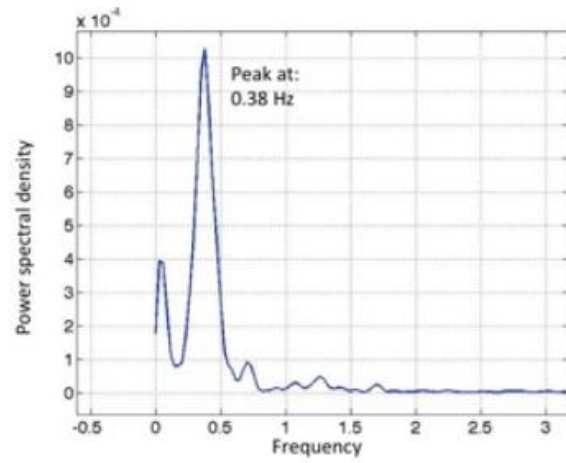
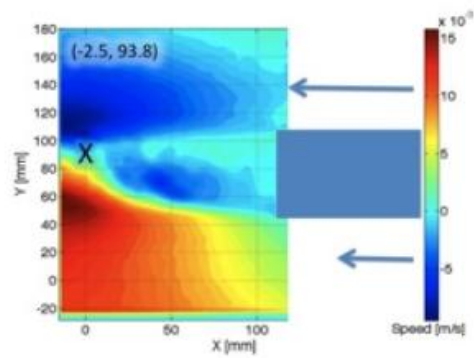
(b)



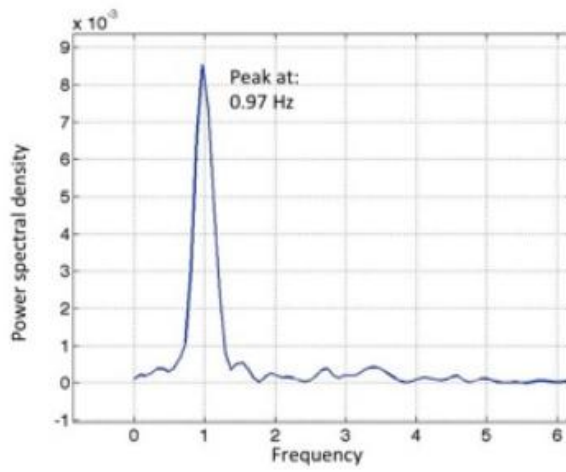
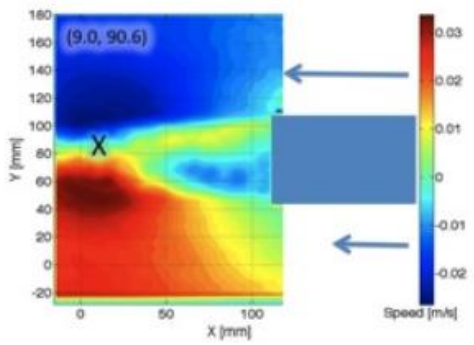
(c)

Figure 18 (a-c)

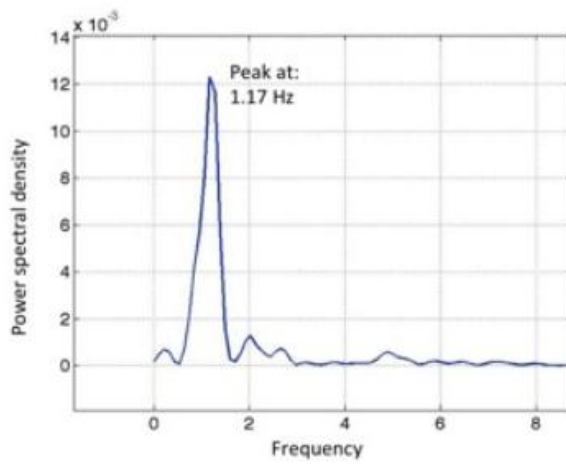
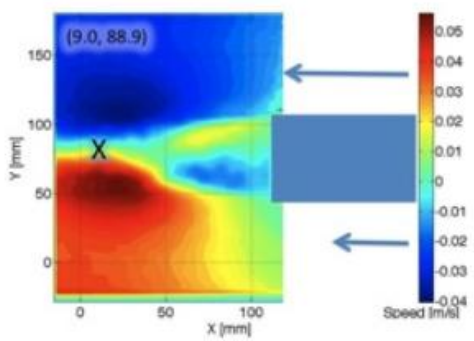
(a) $Re = 6196$	$VR = 0.93$	$Hz = 0.33$	$St = 0.22$
(b) $Re = 15,185$	$VR = 0.98$	$Hz = 0.81$	$St = 0.22$
(c) $Re = 21,430$	$VR = 1.00$	$Hz = 1.17$	$St = 0.22$



(a)



(b)



(c)

Figure 19 (a-c)

(a) Re 6031	VR 0.46	Hz 0.38	St 0.26
(b) Re 15,676	VR 0.57	Hz 0.97	St 0.25
(c) Re 22,020	VR 0.55	Hz 1.17	St 0.22

IV. Discussion

The points where the Fourier analysis was done were picked based on the shape of the wake. In the span-wise direction, the point was always chosen at the center of the wake where the contour lines were very close together. In the stream-wise direction, the point was chosen within thickness D of the end of the recirculation region. By watching video of the vortices, the stream-wise distance was chosen by where the vortices were clearly formed. Using this method, the strongest signal for the shedding frequency was analyzed.

The lower velocity ratios gave power spectra with multiple peaks. This may be due to the flow behind the trailing edge transitioning from a wake to a mixing layer.

Calculating the shedding frequency and Strouhal number was the main objective. In the uniform flow case, the Strouhal number has been shown to be independent of Reynolds numbers in the range of 5,000 to 20,000 [2]. Using this assumption, a generalization of the relationship between velocity ratio and Strouhal number can be seen in (Figure 21).

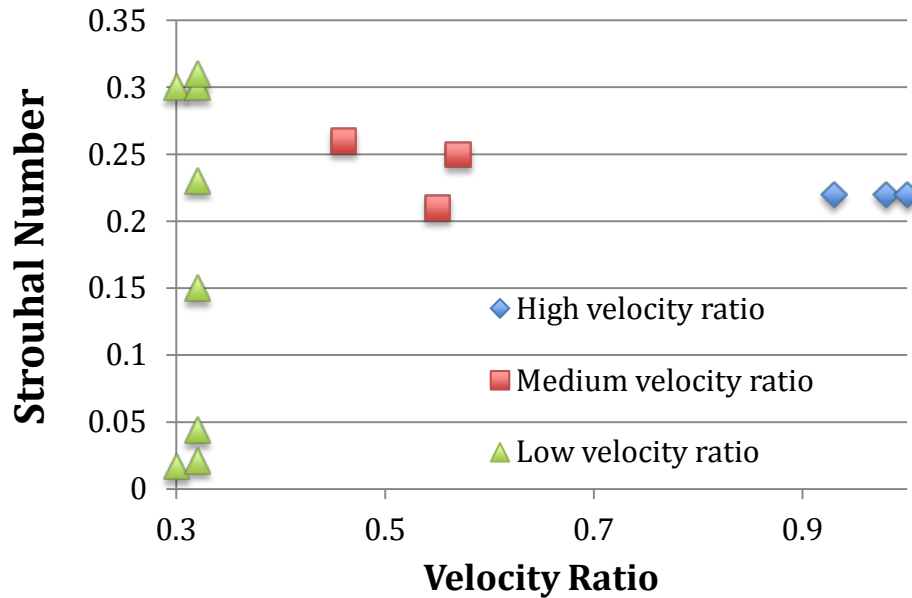


Figure 21. Velocity Ratio vs. Strouhal number

V. Bullet list for Draft Conclusions

- A change of Strouhal number by almost 50% with relation to velocity ratio has been measured.
 - An error analysis is being completed to determine if the increase of Strouhal number with decrease in velocity ratio is a significant change.
 - With this preliminary study, it seems that Strouhal number may change with velocity ratio – this will be compared to other results from literature
- The spectra for the flow field changes from a single dominant frequency to many frequencies as the velocity ratio decreases – newly reported finding.
- A changing frequency due to velocity ratio means a rocket design must account for several shedding frequencies, since matching between a natural frequency and a chamber acoustic frequency could lead to amplification of pressure and heat transfer oscillations.

VI. Acknowledgments

The assistance of the Mechanical Engineering Shop at Caltech and undergraduate and graduate students of Caltech is gratefully acknowledged. The work was supported by the Air Force Research Laboratory, Lester Lees Aeronautics SURF Fellowship, Student Faculty Programs at Caltech, and Graduate Aerospace Laboratories at Caltech.

VII. References

1. Boldman, D.R., Brinidh, P.F., and Goldstein, M.E., "Vortex Shedding from a Blunt Trailing Edge with Equal and Unequal External Mean Velocities," *Journal of Fluid Mechanics*, Vol. 75, No. 4, 1976, pp. 721-735.
2. Buresti, G., Talamelli, A., and Petagna, P., "Experimental Characterization of the Velocity Field of a Coaxial Jet Configuration," *Experimental Thermal and Fluid Science*, Vol. 9, No. 2, 1994, pp. 135-146.
3. Buresti, G., Talamelli, A., and Petagna, P., "Experimental Investigation on the Turbulent Near-Field of Coaxial Jets," *Experimental Thermal and Fluid Science*, Vol. 17, No. 1-2, 1998, pp. 18-26.
4. Mehta, D., "Effect of Velocity Ratio on Plane Mixing Layer Development: Influence of the Splitter Plate Wake," *Experiments in Fluids*, Vol. 10, 1991. pp. 194-204.
5. Olsen, W., and Gutierrez, O., "The Effect of Nozzle Inlet Shape, Lip Thickness, and Exit Shape and Size on Subsonic Jet Noise," *AIAA Paper 73-187*, Jan. 1973.
6. Olsen, W., and Karchmer, A., "Lip Noise Generated by Flow Separation from Nozzle Surfaces," *AIAA Paper 76-3*, Jan. 1976.
7. Rathakrishanan, E., "Effect of Splitter Plate on Bluff Body Drag," *AIAA Journal*, Vol. 37, No. 9, 1999, pp. 135-146.
8. Tamura, H., Kiya, M., and Arie, M., "Vortex Shedding from a Two-Dimensional Blunt Trailing Edge with Unequal External Free-Stream Velocities," *JSME Paper 231-9*, Sept. 1984.
9. Bocanegra-Evans H., Allen, J.J., Wake-shear layer interaction using a soap film tunnel, *Phys. Fluids* 17, 091112 (2005);
10. Wallace, D., Redekopp, L.G., Linear instability characteristics of wake-shear layers, *Physics of Fluids*4, (1), January 1992.
11. Laizet, S., Lardeau, S., Lamballais, E., Direct numerical simulation of a mixing layer downstream a thick splitter plate, *Phys. Fluids* 22, 015104, 2010

Geometry Effects on Steady and Acoustically Forced Shear-Coaxial Jet Sprays

S. Teshome^{*,+}, I.A. Leyva^{+,&}, D. Talley⁺, A. Karagozian^{*}

^{*}UCLA, Los Angeles, CA, USA, ⁺Air Force Research Lab, Edwards, CA, USA

steshome@ucla.edu and ivett.leyva@edwards.af.mil

Abstract

The mixing process on four shear-coaxial injectors with different outer-to-inner jet area ratios and varying inner jet post thickness is examined experimentally. The experiments were conducted at ~1.5MPa with varying outer-to-inner jet momentum flux ratios (0.5 – 20), with and without a pressure antinode perturbation at the jet exit. Nitrogen was used as the test fluid. High speed back-lighting movies, acoustic pressure measurements and temperature exit profiles are the main diagnostics used. Proper orthogonal decomposition was applied to the intensity fluctuation of the high-speed images to extract spatial and temporal characteristics of the dominant flow structures. The extent of the influence of outer-to-inner momentum flux ratio on mixing was dependent on the injector geometry. The inner jet lengths for a large outer-to-inner jet area ratio injector were more influenced by increasing momentum flux ratios. Regardless of injector geometry, lower momentum flux ratio (generally less than 5) flows were found to be more responsive to acoustic forcing. With increasing momentum flux ratio, the flow response to forcing depended on the injector geometry.

Introduction

Coaxial injectors have proven to be one of the most effective and simple means of delivering propellants in combustion devices such as in liquid rocket engines (LREs). Their application in LREs in the United States spans from the development of the J-2 engine to the space shuttle main engine. Since injector flows are directly involved in processes that take place inside combustors, it is crucial to understand how they contribute to, as well as how they are affected by, unsteady physical mechanisms that could lead to rough combustion or even combustion instabilities. A fundamental understanding of the interactions between injector flows and chamber combustion can be aided by first isolating the fluid dynamics aspect from the reactive flow processes, and studying the coupling of non-reactive injector flow instabilities with external pressure perturbations.

Shear-coaxial flows consist of a circular core or inner jet and an annular or outer jet. In the near field region, where the potential cores of both the inner and outer jets exist, two shear-layers develop: an inner one between the inner and outer jet, and an outer one between the outer jet and the ambient fluid¹. The development of instabilities in the individual shear layers and their interactions have a direct impact on the eventual instability characteristics of the entire flow field. Several studies²⁻⁴ investigate the existence and behavior of vortex structures in the near-field region of single-phase coaxial jets with similar and different densities. It is shown that for outer to inner jet velocity ratios exceeding unity ($R = U_o/U_i > 1$), coherent structures in the outer shear layer dominate those in the inner shear layer. The influence of these coherent structures on the overall dynamics of the flow field calls for an understanding of the factors leading to their formation. Detailed studies on the development and growth of natural instabilities in a single circular jet⁶ or a single circular jet with coflow⁷ reveal two of the most significant natural modes of instability: the axisymmetric and the first azimuthal or helical modes. These modes have comparable amplification rates over most of the core region downstream of the exit, with the helical mode eventually dominating the flow field farther downstream. It is shown¹ that the development of the outer shear layer of a coaxial jet behaves as the shear layer of a single jet, while the development of the inner shear layer behaves as that of a single jet issuing into an external coflow.

In LRE applications understanding the mixing between the inner jet, usually the oxidizer, and the outer jet, usually the fuel, is of paramount importance for a successful design. Since the growth and development of the shear layers is integral to the mixing of the two jets, one way of quantifying the degree of mixing is to determine the inner jet potential core length.^{1,8-10} The inner jet potential core ends once the inner shear layer converges on the jet axis. The current study relies on back-lit high speed movies to measure inner jet dark-core lengths, which are related to the potential core.^{13,15}

This study continues the experiments performed in the same facility¹¹⁻¹⁵ examining the behavior of shear-coaxial nitrogen (N_2) jets with and without the presence of a transverse acoustic field. It examines the baseline flow of four injectors with different inner jet post thickness to diameter ratios, different outer to inner jet area ratios, and a range of momentum flux ratios. The flow response to a pressure antinode forcing condition, where the coaxial jet is exposed to the maximum local pressure fluctuations in a transverse acoustic field is also examined. Dark-core length measurements are made to determine the effect of momentum flux ratio and of

[&]Corresponding author: ivett.leyva@edwards.af.mil. Distribution A: Approved for public release; distribution unlimited. PA #12001.

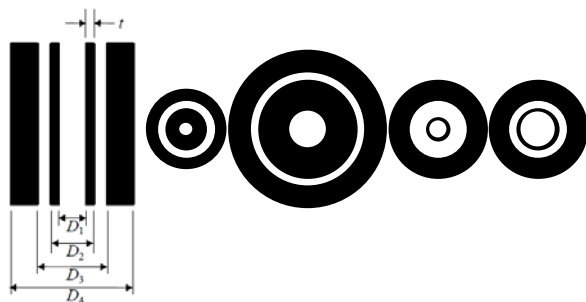
acoustic forcing on mixing. Proper orthogonal decomposition (POD) analysis is also used to extract spatial and temporal dominant flow structures in the inner shear layer of the baseline and acoustically forced flows. The goal is to gain a better understanding of the evolution of flow instabilities and underline the critical differences in the flow stability characteristics of different geometries.

Experimental and Computational Methods

The experiments were carried out at the Air Force Research Laboratory in Edwards, CA. Figure 1 shows a schematic of the experimental facility. The inner and outer jets as well as the chamber pressurization flow were supplied by ambient temperature, high pressure N₂ lines (critical pressure is 3.4 MPa, and critical temperature is 126.2 K). Counter-flow heat exchangers using liquid nitrogen were used to independently cool the inner and outer jets. An unshielded Omega type-E thermocouple with a bead diameter of 0.25mm, mounted on top of a 3D array of linear positioning stages, was used to measure the radial temperature profile of the coaxial jet within one inner jet diameter from the exit plane. Porter mass flow meters (123-DKASVDAA) were used to measure the inner and outer jet flow rates, which were controlled via metering valves. The jets issued into the test section (Fig. 1) of the inner chamber halfway between the two piezo-sirens located at opposite ends of the chamber. Each piezo-siren was fitted with a waveguide that transitioned from a circular to a rectangular cross-section. The inner chamber was used to maximize the amplitude of acoustic oscillations generated by the piezo-sirens. However, both the inner and main chambers were maintained at the same static pressure, which was measured with a Stellar ST1500 pressure transducer.

Figure 1 Schematic of experimental chamber and fluid systems

The outer to inner jet momentum flux ratio ($J = \rho_o U_o^2 / \rho_i U_i^2$), velocity ratio (R), and other flow conditions were determined based on thermophysical properties evaluated at the measured chamber pressure, and jet exit temperatures. Kulite absolute (CCQ-093) and differential (XCQ-093, XCE-093) pressure transducers were used for making high-speed acoustic pressure measurements. These pressure transducers were placed along the inner chamber wall, where one transducer was located directly behind the jet, and two others inside the injector plenums. The acoustic wave signals were generated using a Fluke 292 arbitrary waveform generator. A Trek PZD2000A high-voltage amplifier fed a continuous sine wave from the waveform generator to each piezo-siren. The resulting acoustic waves from each piezo-siren were traveling waves that propagated transversely along the waveguide. Using signals that were in-phase (0° phase difference), a pressure antinode (PAN) condition was



Injector	D1 mm	D2 mm	D3 mm	D4 mm	t/D1	Ao/ Ai	L/D1
LAR_thick	0.51	1.59	2.42	3.18	1.05	12.9	0
SAR_thick	1.47	3.96	4.70	6.35	0.84	2.9	-0.5
LAR_thin	0.70	0.89	2.44	3.94	0.13	10.6	0.2
SAR_thin	1.40	1.65	2.44	3.94	0.09	1.6	0,-0.5

Figure 2. Injector schematics**Table 1.** Summary of injector dimensions

created in the center between the two piezo-sirens where the injector was situated, with maximum pressure perturbation.

Figure 2 shows a schematic of the injector's exit plane view. . Table I provides a summary of the injector exit dimensions. As seen from the table, two injectors have large outer-to-inner jet cross-sectional area ratio (LAR), and two have small area ratios (SAR). Two injectors have small inner jet lip thickness to inner jet diameter ratios (thin) and two have large ratios (thick).

As mentioned above, one of the main parameters used to assess the effect of J and acoustic forcing on coaxial jet mixing is the “dark-core length” of the inner jet measured from high-speed back-lit images. A xenon arc lamp was used to provide a back-lit image of the coaxial jet, which is visualized using a Phantom v7.1 CMOS camera at framing rates exceeding 20 kHz. For a detailed discussion of how the dark-core length is defined and measured see [13]. Briefly, the original images (Fig. 3a) are first converted, or thresholded, to a black and white image using the MATLAB subroutine “im2bw” (Fig. 3b). The threshold level is determined using the MATLAB subroutine “graythresh”. This subroutine uses Otsu's method¹⁶ and it is based on the zeroth and first cumulative moments of the gray-level histogram. Once a black and white image is obtained, the length of the jet is determined by drawing a contour around the black and white image and measuring the axial length of the longest contour attached to the injector (Fig. 3c).

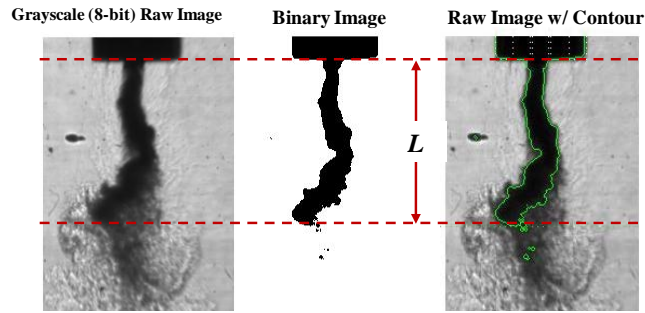


Figure 3. Measurement of dark-core length: (a) original image (b) black and white image after thresholding (c) Contour used to determine axial length (L)

Proper orthogonal decomposition (POD) of the high-speed images has proven to be a powerful means for extracting relevant qualitative and quantitative information from an otherwise complicated and noisy set of images. A pixel intensity data matrix, \mathbf{B} for a set of images may be represented¹⁷⁻¹⁹ as

$$\mathbf{B} = \sum_{k=1}^M a_k(t) \phi_k(x) \quad (1)$$

where a_k are vectors of temporal amplitude coefficients, ϕ_k are vectors of proper orthogonal modes, k is the mode number, and M is the number of modes. The decomposition was achieved by first arranging all the pixel intensity values of all frames into a single data array, whereby the pixel intensities from one frame occupied one row of the data array. Thus, a set of N consecutive frames, each with an $n \times m$ pixel resolution, constituted an N by $n \times m$ data array. The temporal mean of the data array was subtracted in order to eliminate the DC component of the intensity values resulting in a matrix $\tilde{\mathbf{B}}$ of intensity fluctuations. The method of singular value decomposition was implemented in MATLAB using a built-in subroutine to represent the matrix of intensity fluctuations as

$$\tilde{\mathbf{B}} = \mathbf{Q} \mathbf{V}^T \quad (2)$$

where \mathbf{Q} is an N by N matrix composed of column vectors a_k , and \mathbf{V} is an N by $n \times m$ matrix composed of column vectors ϕ_k from Eq. (1). The matrix \mathbf{Q} is the product of an orthogonal matrix of left singular vectors and a diagonal matrix of singular values of $\tilde{\mathbf{B}}$. The different modes were arranged in decreasing order of significance as dictated by the magnitude of the singular values of the decomposition. In order to identify the existence of conjugate mode pairs¹⁸, which have a temporal phase difference of $\pm 90^\circ$ and also have similar ϕ_k , the cross-power spectral density of their amplitude coefficients, a_k and b_k was computed as

$$\text{CPSD} = \sum_{s=0}^{N-1} \text{corr}(a_k, b_k) e^{-i\omega s} \quad (3)$$

where, $\text{corr}(a_k, b_k)$ represents the cross-correlation of a_k and b_k .

Results and Discussion

The experiments described here were performed under subcritical (reduced pressure, $P_r=0.44$) pressure conditions with the inner jet in liquid phase and the outer jet in gas phase at temperatures well above the saturation temperature of N_2 . The flow conditions are summarized in Table 2. The behavior of the inner jet dark-core length for baseline conditions without acoustic excitation is shown in Fig. 4 for the four geometries studied. As previously noted, for coaxial jets of different densities, the outer to inner jet momentum flux ratio, J , is one of the governing parameters of coaxial jet mixing and thus it is chosen as the x-axis. In the present work, for a set of test conditions, the outer-to-inner jet density ratio ($S = \rho_o/\rho_i$) was held approximately constant while R was varied. Thus, the variation in J in these studies resulted mainly due the variation in R . The recess of the inner tube with respect to the outer tube is given in Table 1. The inner jet tube for the LAR-thin injector stuck out by about $0.2D_1$ to allow for visual confirmation that the inner jet injector tube was not oscillating due to the outer jet flow.

Note that there were negligible differences in L_B/D_1 between the flushed and recessed configurations of the SAR-thin injector. Also note that this specific geometry showed the least amount of effect from J . In fact, L_B/D_1 remains almost flat for the range of J studied. Moreover, for low J flows, the SAR-thick and SAR-thin injectors showed comparable L_B/D_1 , which were significantly lower than that of the LAR-thin and LAR-thick injectors. This was in agreement with previous observations^{5,19} that show the potential core is longer for larger area ratios. The large difference in L_B/D_1 between the LAR-thin and LAR-thick injectors may be attributed to the presence of the recirculation zone behind the thick inner tube post of the LAR-thick injector that entrained a significant portion of the inner jet fluid for $J=2$ and higher. For large J , the data for all injectors appeared to asymptote to the same L_B/D_1 . However, due to experimental limitations, large enough J were not attainable to verify this trend.

Next, the behavior of three geometries for a low and high J value will be examined for baseline conditions and when subjected to a pressure antinode (Fig.5). The values of J chosen span about an order of magnitude and are good descriptors of what happens at low J values, when flows are usually more receptive to acoustic disturbances, and at high J values when such receptivity subsides. For all injectors, the forcing frequencies were within 5-10% of the fundamental resonance frequency of the outer jet injector tube. Since the back-lit images reveal best the dense inner jet, the discussion will be limited to the dark-core flow region and the identifiable flow structures on its periphery.

For the SAR thin injector, $J=2.1$, the inner jet breaks into droplets and forms a spray within the field of view. Periodic surface instability flow structures can seen on the periphery of the inner jet. The dominant modes depicted by the light and dark lobes in the proper orthogonal mode (POM) image show what appear to be symmetric flow structures close to the injector exit, but transitioned to antisymmetric structures further downstream. The CPSD magnitude spectrum show that the peak frequencies were unaffected by increasing J . This may be explained by how soon the inner and outer jets attained a single jet behavior, thereby rendering the effect of coflow nonexistent. The baseline case for $J=17$ shows a slightly shorter dark core length, which is surprising since for the other geometries studied, the relative size difference in the dark core length was larger over a similar range of J . Note the large difference on the POM between the two cases. For the large J case, the modes are clearly antisymmetric from the start but their inception is farther downstream from the injector exit plane. The spread angle and the wavelength of the disturbances appears to be also larger.

When subjected to a PAN condition, the lower J value case shows strong symmetric disturbances that annihilate the inner jet flow. For the higher J value, although symmetric disturbances were not as strong, they nevertheless were still prevalent as evident in the POM images and the spectra. As a matter of fact, the spectra showed strong response to external forcing regardless of the J value. This was also evident by the lack of any remnants of the low-frequency peaks present in the baseline spectra. The baseline spectrum is superimposed to the forced spectrum (dashed line) for all three geometries so that a direct comparison can be made.

For the LAR-thin injector, $J=2$, the dark-core region broke up into a fine droplet spray within the field of view. The presence of a larger shear force at the jets' interface than for lower J values also aided in the formation of a fine mist of droplets on the periphery of the inner jet flow. Enhanced entrainment of the inner jet flow into the outer flow was evident in the increased spread of the inner jet compared to lower J values. The dominant flow structures were antisymmetric, their inception being about $1-2D_1$. The CPSD magnitude spectral peak was relatively broad centered around 2kHz. Under a PAN condition, a varicose mode is discernible in the image, with the growth of the resulting symmetric structures relatively subdued.

The higher shear present in the $J=21$ case aided in the break-up and dispersion of the inner jet resulting in rapid mixing with the outer jet at closer distances to the injector exit. Accordingly the dark-core length became shorter. The inception point of the antisymmetric structures seen with POD was closer to the injector exit and the broad peak in the magnitude spectrum shifted to higher frequencies. The flows under PAN forcing were virtually similar to the corresponding baseline flows. Although the sinuous disturbances of the inner jet were considerably

reduced compared to the lower J case, their presence was still evident in the images. Note that while the undulations in the inner jet began close to the injector exit for low J, it was merely limited to the end of the dark-core at the higher J value.

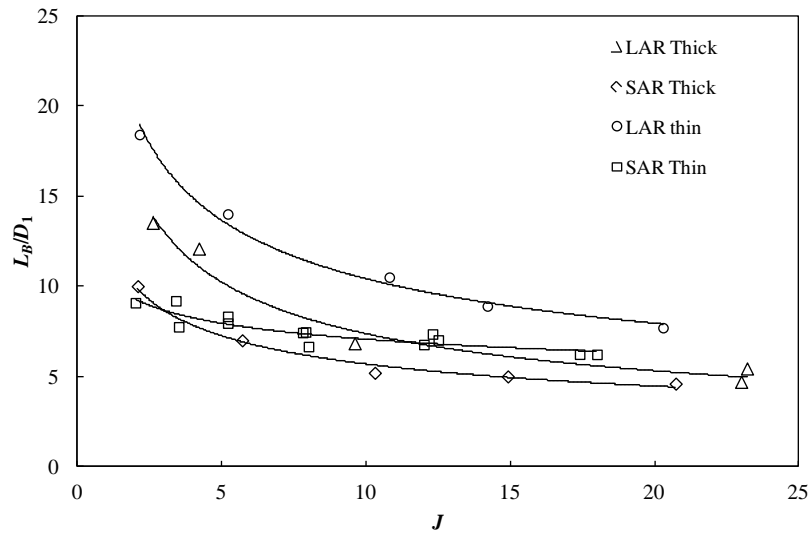


Figure 4. Measurement of dark-core length: (a) original image (b) black and white image after thresholding (c) Contour used to determine axial length (L)

In contrast to the LAR-thin and SAR-thin injector flows, the SAR-thick inner injector post created a larger recirculation zone just below the thick post and surrounding the inner jet flow. For $J = 2.1$, the entrainment by the outer flow caused most of the recirculation zone to be filled with the lower momentum inner jet fluid. The presence of the dense, dark fluid in the recirculation zone created a perception of “necking” in the dark-core flow. Further downstream, the dark-core could no longer maintain its coherence and was fully dispersed into droplets. The POM image shows distinct antisymmetric structures denoting the presence of helical disturbances, and the CPSD magnitude shows a low frequency peak. For PAN conditions the fluid inside the recirculation zone mainly consisted of the lower momentum inner jet fluid, and the sense of rotation was such that a counterflow existed at the inside boundary of the outer jet. Thus, for $J = 2.1$ and higher, the outer shear-layer vortices had the same sense of rotation as the fluid in the recirculation zone, unlike for lower J flows. One would then expect that coupling between these flow regions during varicose disturbances due to the PAN forcing may induce symmetric flow structures on the inner jet surface. However, as Figure 5 shows, besides imparting a merely irregular and dispersive flow pattern, the PAN forcing did not result in a periodic, varicose type of disturbance pattern on the inner jet.

For the case $J=21$, the recirculation zone was completely filled with the inner jet fluid. The remaining inner jet fluid underwent increased dispersion resulting in a shorter dark-core. Together with the recirculation flow, the inner jet started to form a conical dark-core region. The dark-core length has been reduced about 50% compared with the lower J case. The POM also shows antisymmetric structures. However, unlike the LAR-thin flows, the peaks in the magnitude spectra stayed at low frequencies. Under PAN forcing, the higher J value case exhibited the expected symmetric flow disturbances. They appeared to start just beyond the end of the recirculation zone, rolled-up and entrained the inner jet fluid further downstream.

Injector	J	R	T_{ch} K	ρ_{ch} kg/m ³	P_{ch} MPa	T_o K	\dot{m}_o mg/s	ρ_o kg/m ³	U_o m/s	Re_o $\times 10^4$	T_i K	\dot{m}_i mg/s	ρ_i kg/m ³	U_i m/s	Re_i $\times 10^4$
SAR thin	2.0	6.9	246	21	1.49	195	450	27	6.6	1.1	109	925	630	0.96	1.5
SAR thin	17	20	217	24	1.48	194	1300	27	19	3.1	108	925	638	0.95	1.4
LAR thin	2.1	7.4	220	23	1.50	205	2212	25	22	6.3	107	725	646	2.9	2.1
LAR thin	20	22	220	23	1.50	204	4633	26	45	13	110	482	622	2.0	1.6
SAR thick	2.1	7.3	205	25	1.50	212	1789	24	15	1.9	110	2130	622	2.0	3.3
SAR thick	21	23	196	27	1.50	206	4385	25	35	4.7	107	1658	646	1.5	2.3

Table 2. Summary of flow conditions for figure 5.

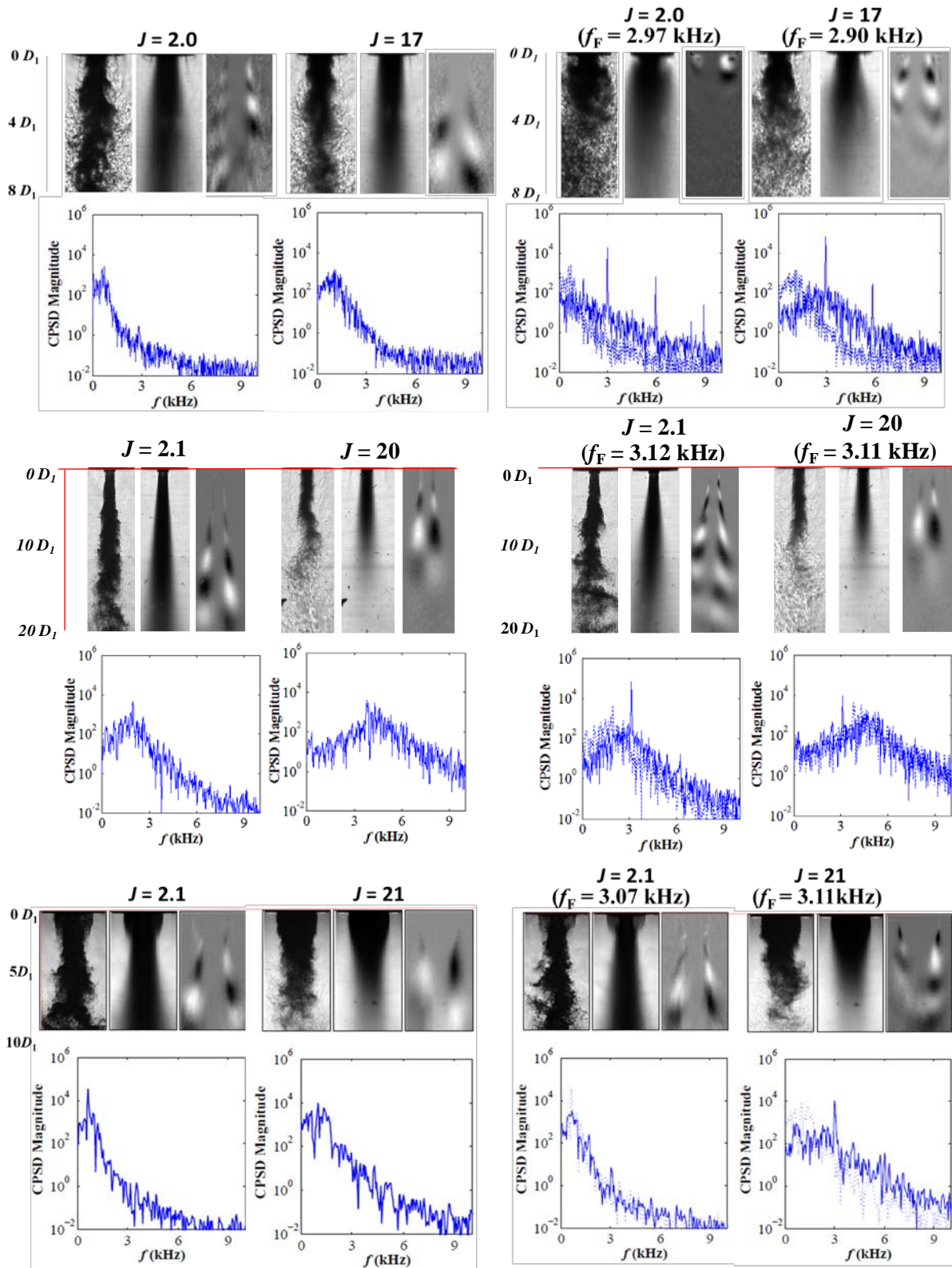


Figure 5. Baseline (left half of page) and PAN conditions (right half of page) for (a) SAR thin (b) LAR thin (c) SAR thick injectors.

Summary and Conclusions

This study examined the effect of different exit geometries on the mixing characteristics as well as the behavior of flow disturbance structures with and without transverse acoustic forcing. The ratios of dark-core lengths to the inner jet diameters, which were used to assess the extent of mixing between the inner and outer jets, were reported for baseline flows using four different injector geometries. These measurements revealed that for low J , the small area ratio (SAR) injector flows, had significantly lower L_B/D_1 than the large area ratio flows. However, L_B/D_1 for all injectors appeared to asymptote to the same value at high enough J . The effect of geometry was also manifested in the response to a pressure antinode (PAN) acoustic forcing of similar J flows of different injector geometries. The low J LAR-thin injector flow showed a strong response at the PAN forcing frequency while the high J appeared less responsive and retained the baseline flow spectral characteristic. In contrast, the SAR-thin injector flow showed strong response at the PAN forcing regardless of J . The low J SAR-thick injector flow showed no response at the forcing frequency, while the high J flow did. Thus, these key traits shed some light on the significance of how simple design alterations in injector geometries may bring about drastic changes in the mixing and response of shear-coaxial jet flows to external pressure disturbances.

Acknowledgements

The authors would like to thank Mr. Randy Harvey for his invaluable contributions in running and maintaining the experimental facility. This work is sponsored by AFOSR under Dr. Mitat Birkan, program manager.

References

- [1] Ko, N. W. M. and Kwan, S. H., *J. Fluid Mech.* 73: 305-332 (1976)
- [2] Dahm, W. J. A., Frieler, C.E., and Tryggvason, G. *J. Fluid Mech.* 241:371-402 (1992)
- [3] Wicker, R.B. and Eaton, J.K., *AIAA Journal* 32:542-546 (1994)
- [4] Balarac, G., Mtais, O. and Lesieur, M. *Phys. Fluids* 19, 075102 (2007).
- [5] Gladnick, P. G., Enotiadis, A. C., LaRue, J. C. and Samuelsen, G. S., *AIAA Journal* 28: 1405-1414 (1990)
- [6] Cohen, J. and Wygnanski, L., *J. Fluid Mech.* 176: 191-219 (1987)
- [7] Michalke, A. and Hermann, G., *J. Fluid Mech.* 114: 343-359 (1982)
- [8] Mayer, W. and Krülle, G., *J. Propulsion and Power* 11: 3 (1995)
- [9] Villiermaux, E., Rehab, H. and Hopfinger, E.J., *Meccanica* 29: 393-401 (1994)
- [10] Rehab, H., Villiermaux, E. and Hopfinger, E.J., *J. Fluid Mech.* 345:357-381 (1997)
- [11] Davis, D.W., *Ph.D. Thesis*, Penn State University (2005)
- [12] Davis, D.W. and Chehroudi, B., *J. Propulsion and Power* 23: 2 (2007)
- [13] Leyva, I.A., Chehroudi, B. and Talley, D., *AIAA 2007-5456*
- [14] Leyva, I.A., Rodriguez, J.I., Chehroudi, B. and Talley, D., *AIAA 2008-950*
- [15] Rodriguez, J. I., *Ph.D. Thesis*, University of California Los Angeles (2009)
- [16] Otsu, N., *IEEE transactions on Systems, Man, and Cybernetics* 9:62-66 (1979)
- [17] Chatterjee, A., *Current Science* 78: 7 (2000)
- [18] Arienti, M. and Soteriou M.C., *Phys. Fluids* 21:112104 (2009)
- [19] Champagne, F.H., and Wygnanski, I.J. *Int. J. Heat Mass Transfer* 14: 1445-1464 (1971)

AFRL-RZ-ED-TR-2012-0031

Primary Distribution of this Report:

AFRL/RQRC (1 CD)
Doug Talley
10 E. Saturn Blvd
Edwards AFB CA 93524-7680

AFRL/RQRC (1 HC)
Record Custodian
10 E. Saturn Blvd
Edwards AFB CA 93524-7680

AFRL/RQ Technical Library (2 CD + 1 HC)
6 Draco Drive
Edwards AFB CA 93524-7130

Chemical Propulsion Information Analysis Center
Attn: Tech Lib (Mary Gannaway) (1 CD)
10630 Little Patuxent Parkway, Suite 202
Columbia MD 21044-3200

Defense Technical Information Center
(1 Electronic Submission via STINT)
Attn: DTIC-ACQS
8725 John J. Kingman Road, Suite 94
Ft. Belvoir VA 22060-6218